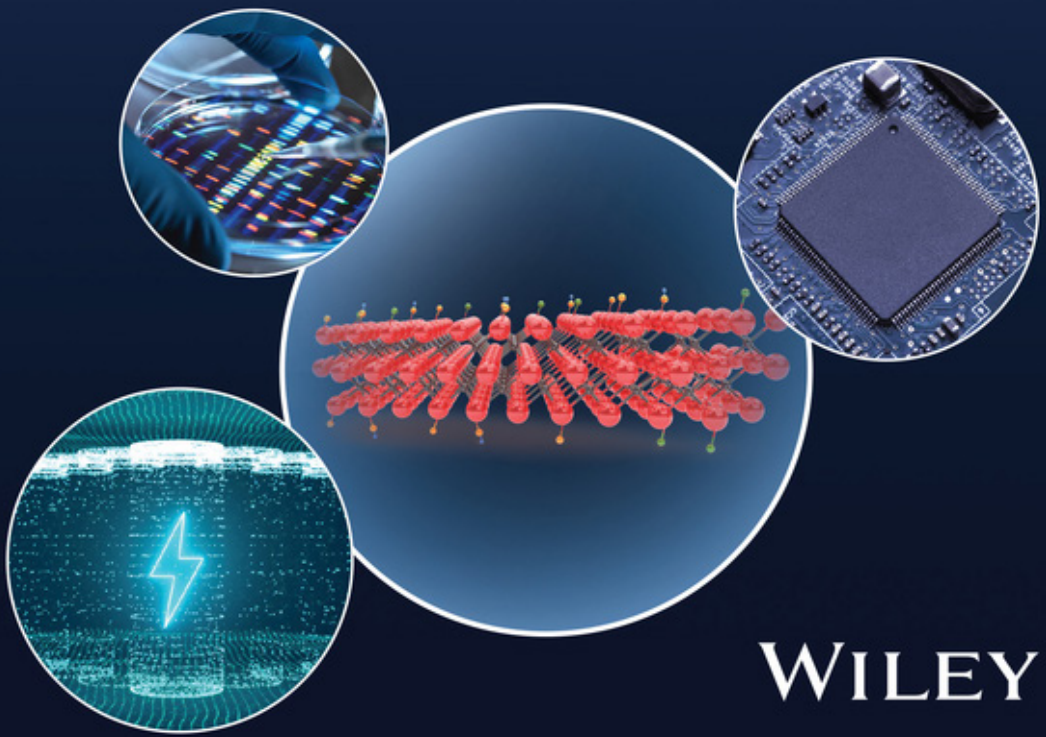
Transition Metal Carbides and Nitrides (MXenes) Handbook

Synthesis, Processing, Properties and Applications

Edited by
Chuanfang Zhang • Michael Naguib



WILEY

Transition Metal Carbides and Nitrides (MXenes) Handbook

Transition Metal Carbides and Nitrides (MXenes) Handbook

Synthesis, Processing, Properties and Applications

Edited by

Chuanfang Zhang
Sichuan University
Chengdu, China

Michael Naguib
Tulane University
New Orleans, LA, US

WILEY

Copyright © 2024 by John Wiley & Sons, Inc. All rights reserved.

Published by John Wiley & Sons, Inc., Hoboken, New Jersey.
Published simultaneously in Canada.

No part of this publication may be reproduced, stored in a retrieval system, or transmitted in any form or by any means, electronic, mechanical, photocopying, recording, scanning, or otherwise, except as permitted under Section 107 or 108 of the 1976 United States Copyright Act, without either the prior written permission of the Publisher, or authorization through payment of the appropriate per-copy fee to the Copyright Clearance Center, Inc., 222 Rosewood Drive, Danvers, MA 01923, (978) 750-8400, fax (978) 750-4470, or on the web at www.copyright.com. Requests to the Publisher for permission should be addressed to the Permissions Department, John Wiley & Sons, Inc., 111 River Street, Hoboken, NJ 07030, (201) 748-6011, fax (201) 748-6008, or online at http://www.wiley.com/go/permission.

Trademarks: Wiley and the Wiley logo are trademarks or registered trademarks of John Wiley & Sons, Inc. and/or its affiliates in the United States and other countries and may not be used without written permission. All other trademarks are the property of their respective owners. John Wiley & Sons, Inc. is not associated with any product or vendor mentioned in this book.

Limit of Liability/Disclaimer of Warranty: While the publisher and author have used their best efforts in preparing this book, they make no representations or warranties with respect to the accuracy or completeness of the contents of this book and specifically disclaim any implied warranties of merchantability or fitness for a particular purpose. No warranty may be created or extended by sales representatives or written sales materials. The advice and strategies contained herein may not be suitable for your situation. You should consult with a professional where appropriate. Further, readers should be aware that websites listed in this work may have changed or disappeared between when this work was written and when it is read. Neither the publisher nor authors shall be liable for any loss of profit or any other commercial damages, including but not limited to special, incidental, consequential, or other damages.

For general information on our other products and services or for technical support, please contact our Customer Care Department within the United States at (800) 762-2974, outside the United States at (317) 572-3993 or fax (317) 572-4002.

Wiley also publishes its books in a variety of electronic formats. Some content that appears in print may not be available in electronic formats. For more information about Wiley products, visit our web site at www.wiley.com.

Library of Congress Cataloging-in-Publication Data
Names: Zhang, Chuanfang, author. | Naguib, Michael, author.
Title: Transition metal carbides and nitrides (MXenes) handbook : synthesis, processing, properties and applications / Chuanfang Zhang, Michael Naguib.
Description: Hoboken, New Jersey : Wiley, [2024] | Includes index.
Identifiers: LCCN 2024007590 (print) | LCCN 2024007591 (ebook) | ISBN 9781119869498 (hardback) | ISBN 9781119869504 (adobe pdf) | ISBN 9781119869511 (epub)
Subjects: LCSH: MXenes.
Classification: LCC QD172.T6 Z46 2024 (print) | LCC QD172.T6 (ebook) | DDC 546/.3–dc23/eng/20240324
LC record available at https://lccn.loc.gov/2024007590
LC ebook record available at https://lccn.loc.gov/2024007591

Cover Design: Wiley
Cover Images: © Westend61/Getty Images, Wentao Zhang from Prof. Chuanfang Zhang group, College of Materials Science and Engineering, Sichuan University, Chengdu, China, © Black_Kira/Shutterstock, © angelo gilardelli/Shutterstock.

Contents

List of Contributors *xvii*
Preface *xxiv*

Part I The Introduction *1*

1 Introduction to the MXene Handbook *3*
Michael Naguib and Chuanfang Zhang
References *7*

Part II Guidelines on MXenes Synthesis, Characterizations and Processing *11*

2 Synthesis of MXene Precursors – Tips and Tricks *13*
Joseph Halim, Jie Zhou, Martin Dahlqvist, and Johanna Rosen
2.1 Structure and Composition of MXene Precursors *13*
2.1.1 MAX Phases (Nitrides/Carbides/Alloys) and *o*-MAX Phases *15*
2.1.2 *i*-MAX Phases *18*
2.1.3 Mo_2Ga_2C and Zr/Hf-based Carbides *18*
2.2 Synthesis of MXene Precursors – Including Good "Tips" and Guidelines *18*
2.2.1 MAX Phases (Nitrides/Carbides/Alloys) and *o*-MAX Phases *18*
2.2.1.1 Preparation for Synthesis *19*
2.2.1.2 Synthesis, Techniques, and Conditions *21*
2.2.1.3 Preparation of Powders for MXene Synthesis *25*
2.2.2 *i*-MAX Phases *27*
2.2.3 Mo_2Ga_2C and Zr/Hf-based Carbides *28*
References *28*

3 Guidelines on Fluorine-based Synthesis of MXenes *34*
Annabelle Bedford, Brian C. Wyatt, Wyatt J. Highland, Srinivasa Kartik Nemani, Krista K. Pulley, Jonah Jordan, and Babak Anasori
3.1 Introduction *34*
3.2 M—A vs. M—X Bonding Roles in Fluorine-based Synthesis *36*
3.3 Interactions of Fluorine with A-group Elements within Precursor Phases *37*
3.4 Effect of Precursor Structure on Fluorine-based MXene Synthesis *43*
3.5 Diversity of Fluorine-based Etchants in MXene Synthesis *46*
3.6 Safety Considerations and Protocols *51*
3.7 Conclusion *52*
Acknowledgments *52*
References *52*

4 Guidelines Low-temperature (LT) F-free Synthesis of MXenes *58*
Changda Wang, Shiqiang Wei, Pengjun Zhang, Kefu Zhu, and Li Song
4.1 Introduction *58*
4.2 Electrochemical Etching Method *59*
4.2.1 Producing Carbide-derived Carbons by Electrochemical Etching *59*
4.2.2 Electrochemical Etching of MAX into 2D MXenes *61*
4.3 Chloride Ion Hydrothermal Etching Method *67*
4.4 Halogen Etching Method *70*
4.5 Alkali Etching Method *73*
4.5.1 Alkali Etching Under Low Concentration *73*
4.5.2 Alkali Etching Under High Concentration *74*
4.5.3 Organic Alkali Etching *77*
4.6 Other F-free Etching Methods *78*
References *81*

5 Guidelines for the Molten Salt Etching of MXenes *85*
Miao Shen and Jian-Qiang Wang
5.1 Introduction *85*
5.2 Reactive Molten Salt Synthesis of MXenes *86*
5.2.1 One-Component Lewis Salt Molten Salt (LAMS) for Etching *86*
5.2.2 Multicomponent Salts Containing Lewis Salts for Etching *87*
5.2.3 Parameters Influencing Molten Salt Etching *92*
5.3 Inert Molten Salt Synthesis of MXenes *95*
5.4 Surface Terminations of MXenes Regulated by Molten Salt *97*
5.5 Electrochemical Etching of MAX in Molten Salt *98*
5.6 Interconversion of MXene and MAX in Molten Salt *100*

5.6.1 From MAX to New MAX *101*
5.6.2 From MAX to New Terminated MXene *101*
5.6.3 From MXene to MAX *101*
5.7 Limitations and Outlook *102*
References *103*

6 Guidelines on the Intercalation of Ions and Molecules in MXenes *109*
Varun Natu and Michel W. Barsoum
6.1 Introduction *109*
6.2 The 002 Peak and the Interlayer Spacing in MXenes *110*
6.3 Ion Exchange Properties and Its Dependence on MXene Synthesis Conditions *112*
6.4 Why Do Cations Intercalate MXene Multilayers? *120*
6.5 Anions and MXene *120*
6.6 Types of Ion/Molecules that Intercalate Between MXene Layers *121*
6.6.1 Inorganic Ions *121*
6.6.2 Organic Molecules *121*
6.7 Complexity of Ion Intercalation in MXenes *124*
6.8 Cation Exchange Capacity *125*
6.9 Hydration and Dehydration of MXene Multilayers *126*
6.10 General Guidelines for Ion Intercalation in MXenes and Possible Pitfalls *128*
6.11 Summary *130*
References *130*

7 MXene Thermal and Chemical Stability and Degradation Mechanism *137*
Shuohan Huang and Vadym N. Mochalin
7.1 Introduction *137*
7.2 Surface Chemistry and Chemical Modification of MXenes *138*
7.3 MXene Chemical Stability and Degradation in Aqueous Solutions *141*
7.3.1 MAX Phase Synthesis *141*
7.3.2 Etchant *144*
7.3.3 Storage Environment *145*
7.3.4 Additives *148*
7.3.5 Annealing *153*
7.4 MXene Thermal Stability *153*
7.4.1 Elimination of MXene Surface Functional Groups *153*
7.4.2 Transformations of MXene Skeleton Structure *155*
7.5 Conclusions and Outlook *157*
References *158*

8 Guidelines on MXene Handling and Storage Strategies *163*
Jizhen Zhang, Dylan Hegh, Peter A. Lynch, and Joselito M. Razal
8.1 Introduction *163*
8.2 The Degradation of MXene *164*
8.2.1 Understanding the Degradation Process of MXenes *166*
8.2.1.1 The Degradation of Wet MXene *166*
8.2.1.2 Oxidation of Dry MXene *170*
8.2.2 Characterizing the Oxidation of MXenes *173*
8.2.2.1 Monitoring the Oxidation Process *173*
8.2.2.2 Characterizing Extent of MXene Oxidation *175*
8.2.3 Parameters Influencing Oxidation Rate *175*
8.2.3.1 MAX Phase Quality and synthetic methods of Synthesis *175*
8.2.3.2 Aqueous Environment *177*
8.2.3.3 Air or Oxygen *177*
8.2.3.4 Temperature *178*
8.2.3.5 UV Light *178*
8.3 Preventing the Oxidation of MXene *179*
8.3.1 Defect Control During MXene Synthesis *179*
8.3.2 Storing MXene in Solvents *180*
8.3.2.1 Isolation of Water *180*
8.3.2.2 Isolation of Oxygen or Air *181*
8.3.2.3 Antioxidants *181*
8.3.2.4 Low Temperature *182*
8.3.2.5 Surface Modification *183*
8.3.3 Coating Protection *184*
8.4 Summary and Outlook *185*
References *186*

9 Beyond Single-M MXenes: Synthesis, Properties, and Applications *189*
Christopher E. Shuck and Yury Gogotsi
9.1 Introduction *189*
9.1.1 Synthesis of MAX *190*
9.2 Random (Disordered) Solid Solutions *193*
9.2.1 Properties and Applications of Random Solid Solutions *194*
9.2.2 High-Entropy MXenes *199*
9.3 Ordered MXenes *199*
9.3.1 Out-of-Plane Ordered *o*-MXenes *199*
9.3.2 In-Plane Ordered *i*-MXenes *202*
9.4 Outlook *203*
Acknowledgments *205*
References *205*

10 Structural Confirmation and Morphological Investigation of MXenes *214*
Kaitlyn Prenger, Anika Tabassum, and Michael Naguib
10.1 Summary and Outlook *226*
References *227*

11 MXene Surface Terminations *229*
Per O.Å. Persson
11.1 Introduction *229*
11.2 Termination Controlled Properties *230*
11.3 Chemical Etching *230*
11.4 Molten Salt Etching *232*
11.5 Termination Site Preference *234*
11.6 MXene Surface Termination Saturation *237*
11.7 Thermal Stability of Terminations *238*
11.8 Post Processing of Terminations *240*
11.9 Summary *242*
References *242*

12 Delamination and Surface Functionalization of MXenes *245*
Mohammad Jafarpour, Sina Abdolhosseinzadeh, Jakob Heier, Frank Nüesch, and Chuanfang Zhang
12.1 Introduction *245*
12.2 Effect of Preparation Routes on the Surface Terminations of MXenes *246*
12.2.1 HF Etching *246*
12.2.2 Fluoride-Containing Solution Etching *249*
12.2.3 Fluoride-Free Etching *251*
12.3 Intercalation and Delamination of Single and Few-Layer MXenes *253*
12.3.1 Metal Cation and Inorganic Intercalants *255*
12.3.2 Organic-Base Molecules *256*
12.3.3 Ultrasonication and Physical Delamination *258*
12.3.4 Dispersibility and Stability of Delaminated MXene Flakes *262*
12.4 Other Methods for Delamination and Surface Engineering *263*
12.4.1 Hydrothermal-Assisted Intercalation (HAI) *263*
12.4.2 Microwave-Assisted Delamination *264*
12.4.3 Freeze-and-Thaw (FAT)-Assisted Method *265*
12.4.4 Low-Temperature Plasma Techniques *266*
12.5 Summary and Outlooks *267*
References *267*

13 Solution Processing of MXenes for Printing, Wet Coating, and 2D Film Formation *272*
Sina Abdolhosseinzadeh, Mohammad Jafarpour, Jakob Heier, Frank Nüesch, and Chuanfang Zhang
13.1 Introduction *272*
13.2 Preparing Stable MXene Dispersions *273*
13.3 Tuning the Rheological Properties of MXene Dispersions *277*
13.4 Ink Formulation and Printing of MXenes *279*
13.5 2D Printing of MXenes *280*
13.6 Wet Coating of MXenes *285*
13.7 Summary and Outlook *289*
References *289*

14 Three-Dimensional (3D) Printing of MXenes *294*
Elnaz Jamshidi, Mackenzie B. Woods, Virginia A. Davis, and Majid Beidaghi
14.1 Introduction *294*
14.2 MXene Inks for DIW *295*
14.2.1 Rheological Properties of DIW Inks *297*
14.2.2 Additive-Free MXene Inks *300*
14.2.3 Multicomponent MXene Inks *301*
14.3 3D Printing of MXene-based Devices *305*
14.4 Conclusion *311*
Acknowledgments *311*
References *312*

15 Assembling of MXenes from Liquid to Solid, Including Liquid Crystals, Fibers *315*
Yu Long, Zhitan Wu, Ying Tao, and Quan-Hong Yang
15.1 Introduction *315*
15.2 1D Macroscopic MXene Fibers *317*
15.2.1 Neat MXene Fibers *318*
15.2.2 MXene Composite Fibers *321*
15.2.2.1 Coated MXene Composite Fibers *321*
15.2.2.2 Spun MXene Composite Fibers *323*
15.2.2.3 Biscrolled MXene Composite Fibers *325*
15.3 2D Macroscopic MXene Films *325*
15.3.1 Neat MXene Films *327*
15.3.1.1 Lamellar Structure *328*
15.3.1.2 In-Plane Nanochannel Structure *331*
15.3.1.3 Porous Structure *331*

15.3.2 MXene-based Composite Films *335*
15.3.2.1 MXene-Inorganics Composite Films *335*
15.3.2.2 MXene-Organics Composite Films *341*
15.4 3D MXene Assemblies, Including Hydrogels and Aerogels *345*
15.4.1 3D MXene Assemblies with Crumpled Structures *345*
15.4.2 Template-assisted 3D MXene Assemblies *348*
15.4.3 MXene-Inorganics Hydrogels and Aerogels *354*
15.4.3.1 Cation-Crosslinked Hydrogels *354*
15.4.3.2 GO-assisted MXene Hydrogels and Aerogels *356*
15.4.3.3 Other MXene-Inorganics Hybrid Assemblies *361*
15.4.4 MXene-Organics Composite Hydrogels and Aerogels *362*
15.4.4.1 Organic Molecule Crosslinked MXene Hydrogels *362*
15.4.4.2 MXene-Polymer Composite Hydrogels *364*
15.5 Summary *369*
Acknowledgments *370*
References *371*

Part III Guidelines on Obtaining MXenes Properties *385*

16 Insights into the Properties of MXenes and MXene Analogs from Atomistic Simulation *387*
Murali Gopal Muraleedharan, Rabi Khanal, Stephan Irle, and Paul R. C. Kent
16.1 Introduction *387*
16.2 Computational Methods *388*
16.3 Structures of MXenes and MXene Analogs *389*
16.4 Predicted Structures and Thermodynamic Stabilities *391*
16.4.1 Structure Prediction *391*
16.4.2 Stability Prediction *394*
16.5 Electronic Properties *397*
16.6 Energy Storage Properties *401*
16.6.1 Rechargeable Metal-Ion Batteries *401*
16.6.2 Supercapacitors *405*
16.6.3 Ion Mobility *409*
16.7 Insights from Molecular Dynamics *412*
16.7.1 *Ab initio* Molecular Dynamics and Approximate Quantum Chemical Simulations *413*
16.7.2 Reactive and Classical Force Field Simulations *417*
16.8 Summary and Future Opportunities *420*
Acknowledgments *421*
References *421*

17 MXenes' Optical and Optoelectronic Properties and Related Applications *429*
Danzhen Zhang, Kanit Hantanasirisakul, and Yury Gogotsi
17.1 Introduction *429*
17.2 Plasmonic Properties *431*
17.3 Plasmonic Applications *433*
17.4 Ultrafast Carrier Dynamics *435*
17.5 Nonlinear Optical Properties *438*
17.6 Nonlinear Optical Applications *440*
17.7 Optoelectronic Properties *442*
17.8 Optoelectronic Applications *444*
17.9 Conclusions and Outlook *447*
Acknowledgments *448*
References *448*

18 Mechanical Properties and Reinforcement Effect of Single MXene Flakes and MXene Composites *453*
Qunfeng Cheng and Alexander Sinitskii
18.1 Introduction *453*
18.2 Mechanical Measurements of Individual $Ti_3C_2T_x$ Flakes *454*
18.3 Mechanical Properties of MXene Composites *462*
18.3.1 1D Fiber MXene Composites *464*
18.3.2 2D Film MXene Composites *466*
18.3.3 3D Bulk MXene Composites *469*
18.4 Effective Strategy to Reduce Voids and Strengthening Interface Interactions *471*
18.4.1 Sequential Bridging of Hydrogen and Ionic Bonding *471*
18.4.2 Sequential Bridging of Hydrogen and Covalent Bonding *475*
18.5 Outlook and Perspectives *477*
Acknowledgments *478*
References *478*

Part IV MXene Applications *485*

19 MXene Capacitive Behaviors and Supercapacitor Devices *487*
Zifeng Lin, Liyuan Liu, and Patrice Simon
19.1 Capacitive Behaviors of MXenes Electrodes in Aqueous Electrolytes *487*
19.2 MXenes as Capacitive Electrodes in Non-Aqueous Electrolytes *492*
19.3 Achieving High Electrochemical Properties by MXene Electrode Construction *497*

19.4 Tuning of MXene Surface Chemistry *500*
19.5 MXene-based Supercapacitor Devices *502*
19.5.1 MXene-based Asymmetric Supercapacitors *502*
19.5.2 MXene-based Micro-Supercapacitors (MSCs) *504*
19.6 Conclusion *508*
References *510*

20 MXene Application in Lithium-Ion Batteries *514*
Majid Farahmandjou, Xin Guo, Zefu Huang, Bijay Janardhanan, A. M. Ruhul, and Guoxiu Wang
20.1 Introduction *514*
20.2 MXenes as Electrode Active Materials *516*
20.2.1 MXenes with Various Formula *517*
20.2.2 Functionalized MXenes *519*
20.2.2.1 Modification of Functional Surface Groups *519*
20.2.2.2 Defect Engineering *520*
20.2.2.3 Intercalation-Interlayer Space Engineering *520*
20.2.2.4 Three-Dimensional (3D) MXene Engineering *521*
20.2.2.5 Doping/Heteroatom Doping *523*
20.3 MXenes-based Composites *524*
20.3.1 MXene Derivatives *524*
20.3.1.1 Completely Oxidized MXenes *525*
20.3.1.2 Partially Oxidized MXenes *526*
20.3.1.3 Other MXene Derivatives *528*
20.3.2 MXene/Metal Chalcogenides *529*
20.3.3 MXene/Alloy-type Materials *530*
20.3.4 Other Composites *533*
20.4 Conclusions *535*
Acknowledgment *536*
References *537*

21 MXenes in Rechargeable Batteries Beyond Li-Ion Battery *541*
Zhuoqi Cen, Qing Huang, and Kun Liang
21.1 Introduction *541*
21.2 Metal-Ion Batteries *542*
21.2.1 Sodium-Ion Batteries *542*
21.2.1.1 Multilayer MXenes *557*
21.2.1.2 Single/Few-Layer MXenes *557*
21.2.1.3 MXenes with an Expanded Interlayer Spacing *559*
21.2.1.4 MXenes with Porous Structure *559*
21.2.1.5 MXene-based Composites *560*
21.2.2 Potassium-Ion Batteries *564*

21.2.3 Magnesium-Ion Batteries *568*
21.2.4 Aluminum-Ion Batteries *571*
21.3 Metal-Sulfur Batteries *572*
21.3.1 Lithium-Sulfur Batteries *575*
21.3.1.1 MXene on the Sulfur Cathode in LSBs *577*
21.3.1.2 MXene as Separator in LSBs *581*
21.3.1.3 MXene on Alkali-Metal (Li, Na, and K) Anodes *582*
21.3.2 Sodium-Sulfur Batteries *584*
21.3.3 Magnesium-Sulfur Batteries *584*
21.4 Conclusions and Perspectives *587*
References *590*

22 Electromagnetic Interference Shielding of MXene/Polymer Composites *602*
Hao-Bin Zhang and Xinfeng Zhou
22.1 Introduction *602*
22.2 MXene as EMI Shielding Materials *607*
22.3 MXene/Polymer Composites as EMI Shielding Materials *609*
22.3.1 The Modulation of MXene-Polymer Interfaces *609*
22.3.1.1 Hydrogen Bonding Interactions *610*
22.3.1.2 Covalent Bonding Interaction *611*
22.3.1.3 Electrostatic Interactions *612*
22.3.2 Preformed of 3D Conductive Architectures *616*
22.4 Outlook *618*
References *618*

23 MXenes in Electronics and Communication Devices *621*
Xiangming Xu and Husam N. Alshareef
23.1 Introduction *621*
23.2 MXene in Oxide Electronics *622*
23.3 MXene in 2D Electronics *625*
23.4 MXene in Flexible and Wearable Electronics *629*
23.5 MXene in Iontronics and Neuromorphic Devices *635*
23.6 MXene in Wireless Communication Devices *640*
23.7 Conclusion and Outlook *643*
References *645*

24 MXene in Sensing Devices *651*
Seon Joon Kim
24.1 Increasing Demand of Sensors *651*
24.2 Use of 2D Nanomaterials for Sensors *652*
24.2.1 Merits of 2D Nanomaterials *652*

24.3 MXenes for Sensors *653*
24.3.1 Sensing Mechanism of MXenes *653*
24.3.2 Factors of MXene Nanomaterials That Can Influence Sensing Properties *654*
24.3.2.1 MXene Flake Morphology *654*
24.3.2.2 Surface Functional Groups and Defects *655*
24.3.2.3 Adsorbents and Intercalants *655*
24.3.2.4 Oxidation *656*
24.4 MXenes for Chemical Sensors *656*
24.4.1 Important Factors in Chemical Sensors *656*
24.4.2 Theoretical Estimations *658*
24.4.2.1 DFT Calculations *658*
24.4.2.2 Gaps Between Theory and Experiment *658*
24.4.3 Guidelines and Considerations for Chemical Sensors *659*
24.4.3.1 Guidelines and Considerations for MXene Synthesis in Chemical Sensors *659*
24.4.3.2 Guidelines and Considerations for MXene Processing in Chemical Sensors *664*
24.4.3.3 Guidelines for Sensor Fabrication and Testing Conditions *666*
24.4.4 Considerations in the Interpretation of Sensing Data *667*
24.4.5 Summary *667*
24.5 MXenes for Mechanical (or Tactile) Sensors *668*
24.5.1 Important Factors in Mechanical Sensors *668*
24.5.2 Comparisons with Other 2D Materials *669*
24.5.3 Guidelines and Considerations for Mechanical Sensors *670*
24.5.3.1 Guidelines and Considerations for MXene Synthesis in Mechanical Sensors *670*
24.5.3.2 Guidelines and Considerations for Sensor Fabrication *670*
24.5.4 Summary *671*
24.6 Conclusions and Outlook *675*
References *675*

25 MXenes for Environmental Treatments *678*
Jie Wang, Zhenjun Wu, Xiuqiang Xie, and Nan Zhang
25.1 Introduction *678*
25.2 MXenes for Adsorption Toward Water Purification *679*
25.3 MXenes Membranes Toward Separation of Pollutants *682*
25.4 MXenes for Water Desalination *683*
25.5 MXenes for Photocatalytic Degradation *686*
25.6 MXenes for Anti-biofouling Applications *691*
25.7 MXenes for Contaminants Detection *692*

25.8 Sustainability of MXenes *694*
25.9 Conclusions and Outlook *697*
References *698*

26 MXenes in Healthcare Technologies *706*
Natalia Noriega, Tochukwu Ozulumba, Grace Cooksley, Emma J. Ward, and Susan Sandeman
26.1 Introduction *706*
26.2 The Biocompatibility of MXenes *706*
26.3 MXenes, Inflammation, Infection, and the Wound Healing Response *711*
26.4 MXenes Sensors and Biosensors in Diagnostics *713*
26.4.1 MXene-based Mechanical Sensors *715*
26.4.2 MXene-based Electrical Sensors *715*
26.4.3 MXene-based Electrochemical Sensors and Biosensors *716*
26.4.4 MXene-based Optical Sensors and Biosensors *717*
26.5 MXenes in Photothermal Therapy *719*
26.6 MXenes in Theranostics *722*
26.7 Perspective on Future Outlook *723*
Acknowledgments *725*
References *725*

Part V Conclusions and Perspectives *735*

27 Summary and Outlook *737*
Chuanfang Zhang and Michael Naguib
References *740*

Index *742*

List of Contributors

Sina Abdolhosseinzadeh
Department of Advanced Materials and Surfaces, Laboratory for Functional Polymers, Swiss Federal Laboratories for Materials Science and Technology (Empa), ETH Domain, Dübendorf, Switzerland

Husam N. Alshareef
Materials Science and Engineering, Physical Science and Engineering Division, King Abdullah University of Science and Technology, Thuwal, Kingdom of Saudi Arabia

Babak Anasori
School of Materials Engineering, Purdue University, West Lafayette, IN, USA; Department of Mechanical and Energy Engineering, and Integrated Nanosystems Development Institute (INDI), Indiana University-Purdue University, Indianapolis, IN, USA; School of Mechanical Engineering, Purdue University, West Lafayette, IN, USA

Michel W. Barsoum
Department of Materials Science and Engineering, Drexel University, Philadelphia, PA, USA

Annabelle Bedford
School of Materials Engineering, Purdue University, West Lafayette, IN, USA; Department of Mechanical and Energy Engineering, and Integrated Nanosystems Development Institute (INDI), Indiana University-Purdue University, Indianapolis, IN, USA

Majid Beidaghi
Department of Mechanical and Materials Engineering, Auburn University, Auburn, AL, USA; Department of Aerospace and Mechanical Engineering University of Arizona, Tucson, AZ, USA

Zhuoqi Cen
Zhejiang Key Laboratory of Data-Driven High-Safety Energy Materials and Applications, Ningbo Key Laboratory of Special Energy Materials and Chemistry, Ningbo Institute of Materials Technology and Engineering, Chinese Academy of Sciences, Ningbo, Zhejiang, China; Qianwan Institute of CNITECH, Ningbo, Zhejiang, China

Qunfeng Cheng
School of Chemistry, Key Laboratory of Bio-inspired Smart Interfacial Science and Technology of Ministry of Education, Beihang University, Beijing, China

Grace Cooksley
Centre for Regenerative Medicine and Devices (CRMD), Centre for Life long Health, School of Applied Sciences, University of Brighton, Brighton, East Sussex, UK

Martin Dahlqvist
Materials Design division, Department of Physics, Chemistry, and Biology (IFM), Linköping University, Linköping, Sweden

Virginia A. Davis
Department of Chemical Engineering, Auburn University, Auburn, AL, USA

Majid Farahmandjou
Centre for Clean Energy Technology, School of Mathematical and Physical Sciences, Faculty of Science, University of Technology Sydney, Sydney, New South Wales, Australia

Yury Gogotsi
Department of Materials Science and Engineering, A. J. Drexel Nanomaterials Institute, Drexel University, Philadelphia, PA, USA

Xin Guo
Centre for Clean Energy Technology, School of Mathematical and Physical Sciences, Faculty of Science, University of Technology Sydney, Sydney, New South Wales, Australia

Joseph Halim
Materials Design division, Department of Physics, Chemistry, and Biology (IFM), Linköping University, Linköping, Sweden

Kanit Hantanasirisakul
Department of Materials Science and Engineering, A. J. Drexel Nanomaterials Institute, Drexel University, Philadelphia, PA, USA

Dylan Hegh
Institute for Frontier Materials, Deakin University, Geelong, Victoria, Australia

Jakob Heier
Department of Advanced Materials and Surfaces, Laboratory for Functional Polymers, Swiss Federal Laboratories for Materials Science and Technology (Empa), ETH Domain, Dübendorf, Switzerland

Wyatt J. Highland
Department of Mechanical and Energy Engineering, and Integrated Nanosystems Development Institute (INDI), Indiana University-Purdue University, Indianapolis, IN, USA

Qing Huang
Zhejiang Key Laboratory of Data-Driven High-Safety Energy Materials and Applications, Ningbo Key Laboratory of Special Energy Materials and Chemistry, Ningbo Institute of Materials Technology and Engineering, Chinese Academy of Sciences, Ningbo, Zhejiang, China; Qianwan Institute of CNITECH, Ningbo, Zhejiang, China

Shuohan Huang
State Key Laboratory for Modification of Chemical Fibers and Polymer Materials, College of Materials Science and Engineering, Donghua University, Shanghai, China

Zefu Huang
Centre for Clean Energy Technology, School of Mathematical and Physical Sciences, Faculty of Science, University of Technology Sydney, Sydney, New South Wales, Australia

Stephan Irle
Computational Sciences and Engineering Division, Oak Ridge National Laboratory, Oak Ridge, TN, USA

Mohammad Jafarpour
Department of Advanced Materials and Surfaces, Laboratory for Functional Polymers, Swiss Federal Laboratories for Materials Science and Technology (Empa), ETH Domain, Dübendorf, Switzerland; Institute of Materials Science and Engineering, Swiss Federal Institute of Technology Lausanne (EPFL), Lausanne, Switzerland

Elnaz Jamshidi
Department of Mechanical and Materials Engineering, Auburn University, Auburn, AL, USA

Bijay Janardhanan
Centre for Clean Energy Technology, School of Mathematical and Physical Sciences, Faculty of Science, University of Technology Sydney, Sydney, New South Wales, Australia

Jonah Jordan
Department of Mechanical and Energy Engineering, and Integrated Nanosystems Development Institute (INDI), Indiana University-Purdue University, Indianapolis, IN, USA

Paul R. C. Kent
Computational Sciences and Engineering Division, Oak Ridge National Laboratory, Oak Ridge, TN, USA

Rabi Khanal
Computational Sciences and Engineering Division, Oak Ridge National Laboratory, Oak Ridge, TN, USA

Seon Joon Kim
Materials Architecturing Research Center, Korea Institute of Science and Technology, Seoul, Republic of Korea

Kun Liang
Zhejiang Key Laboratory of Data-Driven High-Safety Energy Materials and Applications, Ningbo Key Laboratory of Special Energy Materials and Chemistry, Ningbo Institute of Materials Technology and Engineering, Chinese Academy of Sciences, Ningbo, Zhejiang, China; Qianwan Institute of CNITECH, Ningbo, Zhejiang, China

Zifeng Lin
College of Materials Science and Engineering, Sichuan University, Chengdu, China

Liyuan Liu
CIRIMAT UMR CNRS 5085, Université Toulouse III Paul Sabatier, Toulouse, France

Yu Long
Nanoyang Group, State Key Laboratory of Chemical Engineering, School of Chemical Engineering and Technology, Tianjin University, Tianjin, China

Peter A. Lynch
Institute for Frontier Materials, Deakin University, Geelong, Victoria, Australia; Manufacturing BU, Commonwealth Scientific and Industrial Research Organisation (CSIRO), Waurn Ponds, Geelong, Victoria, Australia

Vadym N. Mochalin
Department of Chemistry, Missouri University of Science & Technology, Rolla, MO, USA; Department of Materials Science & Engineering, Missouri University of Science & Technology, Rolla, MO, USA

Murali Gopal Muraleedharan
Computational Sciences and Engineering Division, Oak Ridge National Laboratory, Oak Ridge, TN, USA

Michael Naguib
Department of Physics and Engineering Physics, Tulane University, New Orleans, LA, USA

Varun Natu
Physical and Materials Chemistry Division, National Chemical Laboratory, Pune, Maharashtra, India

Srinivasa Kartik Nemani
Department of Mechanical and Energy Engineering, and Integrated Nanosystems Development Institute (INDI), Indiana University-Purdue University, Indianapolis, IN, USA

Natalia Noriega
Centre for Regenerative Medicine and Devices (CRMD), Centre for Life long Health, School of Applied Sciences, University of Brighton, Brighton, East Sussex, UK

Frank Nüesch
Department of Advanced Materials and Surfaces, Laboratory for Functional Polymers, Swiss Federal Laboratories for Materials Science and Technology (Empa), ETH Domain, Dübendorf, Switzerland; Institute of Materials Science and Engineering, Swiss Federal Institute of Technology Lausanne (EPFL), Lausanne, Switzerland

Tochukwu Ozulumba
Centre for Regenerative Medicine and Devices (CRMD), Centre for Life long Health, School of Applied Sciences, University of Brighton, Brighton, East Sussex, UK; Department of Chemistry, University of Virginia, Charlottesville, VA, USA

Per O.Å. Persson
Thin Film Physics Division, Department of Physics, Chemistry and Biology, Linköping University, Linköping, Sweden

Kaitlyn Prenger
Department of Physics and Engineering Physics, Tulane University, New Orleans, LA, USA

Krista K. Pulley
Department of Mechanical and Energy Engineering, and Integrated Nanosystems Development Institute (INDI), Indiana University-Purdue University, Indianapolis, IN, USA

Joselito M. Razal
Institute for Frontier Materials, Deakin University, Geelong, Victoria, Australia

Johanna Rosen
Materials Design division, Department of Physics, Chemistry, and Biology (IFM), Linköping University Linköping, Sweden

A. M. Ruhul
Centre for Clean Energy Technology, School of Mathematical and Physical Sciences, Faculty of Science, University of Technology Sydney, Sydney, New South Wales, Australia

Susan Sandeman
Centre for Regenerative Medicine and Devices (CRMD), Centre for Life long Health, School of Applied Sciences, University of Brighton, Brighton, East Sussex, UK

Miao Shen
Shanghai Institute of Applied Physics, Chinese Academy of Sciences, Shanghai, China; University of Chinese Academy of Sciences, Beijing, China

Christopher E. Shuck
Department of Chemistry and Chemical Biology, Rutgers University, Piscataway, NJ, USA

Patrice Simon
CIRIMAT UMR CNRS 5085, Université Toulouse III Paul Sabatier, Toulouse, France

Alexander Sinitskii
Department of Chemistry and Nebraska Center for Materials and Nanoscience, University of Nebraska-Lincoln, Lincoln, NE, USA

Li Song
National Synchrotron Radiation Laboratory, CAS Center for Excellence in Nanoscience, Key Laboratory of Precision and Intelligent Chemistry, School of Nuclear Science and Technology, University of Science and Technology of China, Hefei, China

Anika Tabassum
Department of Physics and Engineering Physics, Tulane University, New Orleans, LA, USA

Ying Tao
Nanoyang Group, State Key Laboratory of Chemical Engineering, School of Chemical Engineering and Technology, Tianjin University, Tianjin, China

Changda Wang
National Synchrotron Radiation Laboratory, CAS Center for Excellence in Nanoscience, Key Laboratory of Precision and Intelligent Chemistry, School of Nuclear Science and Technology, University of Science and Technology of China, Hefei, China

Guoxiu Wang
Centre for Clean Energy Technology, School of Mathematical and Physical Sciences, Faculty of Science, University of Technology Sydney, Sydney, New South Wales, Australia

Jian-Qiang Wang
Shanghai Institute of Applied Physics, Chinese Academy of Sciences, Shanghai, China; University of Chinese Academy of Sciences, Beijing, China

Jie Wang
College of Materials Science and Engineering, Hunan University Changsha, PR China

Emma J. Ward
Centre for Regenerative Medicine and Devices (CRMD), Centre for Life long Health, School of Applied Sciences, University of Brighton, Brighton, East Sussex, UK

Shiqiang Wei
National Synchrotron Radiation Laboratory, CAS Center for Excellence in Nanoscience, Key Laboratory of Precision and Intelligent Chemistry, School of Nuclear Science and Technology, University of Science and Technology of China, Hefei, China

Mackenzie B. Woods
Department of Chemical Engineering, Auburn University, Auburn, AL, USA

Zhenjun Wu
College of Chemistry and Chemical Engineering, Hunan University Changsha, PR China

Zhitan Wu
Nanoyang Group, State Key Laboratory of Chemical Engineering, School of Chemical Engineering and Technology, Tianjin University, Tianjin, China

Brian C. Wyatt
Department of Mechanical and Energy Engineering, and Integrated Nanosystems Development Institute (INDI), Indiana University-Purdue University, Indianapolis, IN, USA

Xiuqiang Xie
College of Materials Science and Engineering, Hunan University Changsha, PR China

Xiangming Xu
Materials Science and Engineering, Physical Science and Engineering Division, King Abdullah University of Science and Technology, Thuwal, Kingdom of Saudi Arabia

Quan-Hong Yang
Nanoyang Group, State Key Laboratory of Chemical Engineering, School of Chemical Engineering and Technology, Tianjin University, Tianjin, China

Chuanfang Zhang
College of Materials Science and Engineering, Sichuan University, Chengdu, Sichuan, China

Danzhen Zhang
Department of Materials Science and Engineering, A. J. Drexel Nanomaterials Institute, Drexel University, Philadelphia, PA, USA

Hao-Bin Zhang
State Key Laboratory of Organic-Inorganic Composites, Beijing University of Chemical Technology, Beijing, China

Jizhen Zhang
Institute for Frontier Materials, Deakin University, Geelong, Victoria, Australia; Manufacturing BU, Commonwealth Scientific and Industrial Research Organisation (CSIRO), Waurn Ponds, Geelong, Victoria, Australia

Nan Zhang
College of Materials Science and Engineering, Hunan University Changsha, PR China

Pengjun Zhang
National Synchrotron Radiation Laboratory, CAS Center for Excellence in Nanoscience, Key Laboratory of Precision and Intelligent Chemistry, School of Nuclear Science and Technology, University of Science and Technology of China, Hefei, China

Jie Zhou
Materials Design division, Department of Physics, Chemistry, and Biology (IFM), Linköping University, Linköping, Sweden

Xinfeng Zhou
State Key Laboratory of Organic-Inorganic Composites, Beijing University of Chemical Technology, Beijing, China

Kefu Zhu
National Synchrotron Radiation Laboratory, CAS Center for Excellence in Nanoscience, Key Laboratory of Precision and Intelligent Chemistry, School of Nuclear Science and Technology, University of Science and Technology of China, Hefei, China

Preface

In 2011 came the first report telling a story of the discovery of MXenes, a two-dimensional (2D) transition metal carbide, $Ti_3C_2T_x$, obtained from selective removal of aluminum layers from a 3D-layered Ti_3AlC_2 MAX phase. This discovery was within a year followed by the realization of more MXenes, including Ti_2CT_x, $Ta_4C_3T_x$, and Ti_3CNT_x, and since then, the family of 2D carbides and nitrides has been growing at an unprecedented rate. There are currently more than 50 MXenes reported, including those with out-of-plane and in-plane ordering, solid solutions on both the M and X sites, and high-entropy compositions. Considering the possibility of having both single (Cl, Br, S, etc.) and multiple (O, OH, F, etc.) terminations on these laminates, this family is by far the largest and most diverse family of 2D materials.

Since 2011, more than 20 000 papers have been published by groups from more than 100 countries all over the world (six continents), and the number of publications appearing every year continues to increase. By the most conservative count (Web of Science), more than 70 000 researchers have co-authored MXene papers, following the initial discovery and exploring the enormously rich chemistry and large variety of MXene structures. The fast growth observed in the past five to six years is caused not only by an almost infinite number of new materials that can be synthesized but first and foremost by the unique properties of MXenes. Those include the very high electrical conductivity of $Ti_3C_2T_x$, a wide range of optical properties depending on the composition with absorption peaks from UV to IR wavelength ranges, etc. Biocompatibility and easy processability from aqueous colloids add another advantage. Over the past decade, a major progress has been achieved in increasing the environmental stability of MXenes, with M_3C_2 and M_4C_3 MXenes staying for a year or longer in aqueous solution without degradation, MXene supercapacitor electrodes lasting for 500 000 cycles in acidic electrolytes, and micron-thin films maintaining their conductivity after several years of storage in the ambient environment.

We stand at the crossroads of discovery and applications. While new MXenes are reported regularly and their fundamental properties are being explored, they are also tested for a vast array of potential applications. More than 4200 patent applications were known to be published at the end of 2022, according to Patsnap. Taking into account the 18-month gap between patent filing and publishing by patent offices, this number is much higher today. The initially explored area of application was energy storage, and the largest

number of patents filed address energy, electrochemistry, and separation membranes. However, applications in optics and optoelectronics, as well as biomedical applications, are the fastest areas of growth nowadays. The area closest to commercialization may be electromagnetic interference shielding, where MXenes not only outperform all other materials in performance but also allow controlled reflection or absorption, depending on the choice of MXene and the film architecture, as well as modulation of shielding effectiveness. However, with many other applications being explored, it is difficult to predict where the first large commercial breakthrough will occur. What matters is that, due to their extreme properties, MXenes have already outperformed all known materials in a multitude of applications, from electromagnetic shielding to epidermal electronics and thermal management. By adding their simple processing from colloidal solution in water with no surfactant or additives needed, the chances are high for fast commercialization.

With properties outperforming many of those for currently applied materials, it is crucial to put extra emphasis on how the MXenes, and their precursors, are synthesized. This handbook contains 27 chapters covering synthesis and processing (14 chapters), properties (3 chapters), and applications (8 chapters). A clear emphasis is placed on the synthesis, chemistry, and processing of MXenes. In light of current challenges and demand for cost-efficient, scalable, and not the least sustainable synthesis procedures, the topic of this book *Transition Metal Carbides and Nitrides (MXenes) Handbook: Guidelines for the Synthesis, Processing, Properties, and Applications*, is timely. A comprehensive book that summarizes the current state-of-the-art of MAX and MXene synthesis, also providing details that may sometimes be overlooked in scientific publications, can provide a platform from which we develop MXene synthesis and processing further.

The potential of MXenes will be fully utilized once we have sustainable synthesis methods. While sustainability and materials are often discussed in terms of achieving desired material properties for specific energy and environmental applications, the technology to process the materials is sometimes overlooked. Sustainable MXene synthesis requires minimizing the environmental impact and consumption of resources. It entails principles such as reducing the use of hazardous chemicals (e.g. hydrofluoric acid), optimizing energy efficiency, and recycling raw materials and waste products (salt solutions). Moreover, this approach should also be used to manufacture MAX phases or other MXene precursors. By embracing this way of thinking and with more efforts invested in research on the processing of MXenes, they can play a key role in addressing pressing global challenges, from purification of water, air, and soil to clean energy and beyond.





Johanna Rosen
Linköping University, Sweden

Yury Gogotsi
Drexel University, USA

(*signed using $Ti_3C_2T_x$ MXene ink*)

Part I

The Introduction

1

Introduction to the MXene Handbook

Michael Naguib[1] *and Chuanfang Zhang*[2]

[1] *Department of Physics and Engineering Physics, Tulane University, New Orleans, LA, USA*
[2] *College of Materials Science and Engineering, Sichuan University, Chengdu, Sichuan, China*

Since their discovery in 2011 [1], two-dimensional (2D) transition metal carbides, nitrides, and carbonitrides, collectively known as MXene,[1] have evolved into one of the largest families of 2D materials. MXenes are characterized by the chemical composition $M_{n+1}X_nT_x$, where M represents early transition metals (e.g., Ti, V, Nb, Mo, and Ta), X denotes carbon and/or nitrogen, n varies from 1 to 4, and T_x stands for surface terminations (e.g., O, OH, F, Cl, and Br) [2, 3]. Depending on the value of n, a single-layer MXene may comprise one block, two blocks, three blocks, or four blocks of $M_{n+1}X_n$ octahedrons for $n = 1$, 2, 3, and 4, respectively. Carbon and/or nitrogen fill the centers of these octahedrons, while surface moieties terminate the outermost transition metal atoms. In addition to single metal MXenes, double [4–8], triple [9], and even high-entropy [10–12] transition metal MXenes have been reported. Double transition metal MXenes can exist as solid solutions [4, 6–8] or ordered structures. In the latter case, they can be ordered out-of-plane (for $n > 1$, with one transition metal in the core and the other at the surface) [5] or in-plane (for $n = 1$, with one column of transition metal every two columns of the other transition metal) [6]. To date, more than four dozen MXenes compositions have been synthesized, and this number continues to grow. The electronic structure of MXenes, as well as their properties and performance, depend on their composition and structure [13, 14]. Therefore, this

1 MXene is pronounced as Maxine or mækˈsiːn, and the name was driven from their parent layered carbides/nitrides MAX phases.

Transition Metal Carbides and Nitrides (MXenes) Handbook: Synthesis, Processing, Properties and Applications, First Edition. Edited by Chuanfang Zhang and Michael Naguib.
© 2024 John Wiley & Sons, Inc. Published 2024 by John Wiley & Sons, Inc.

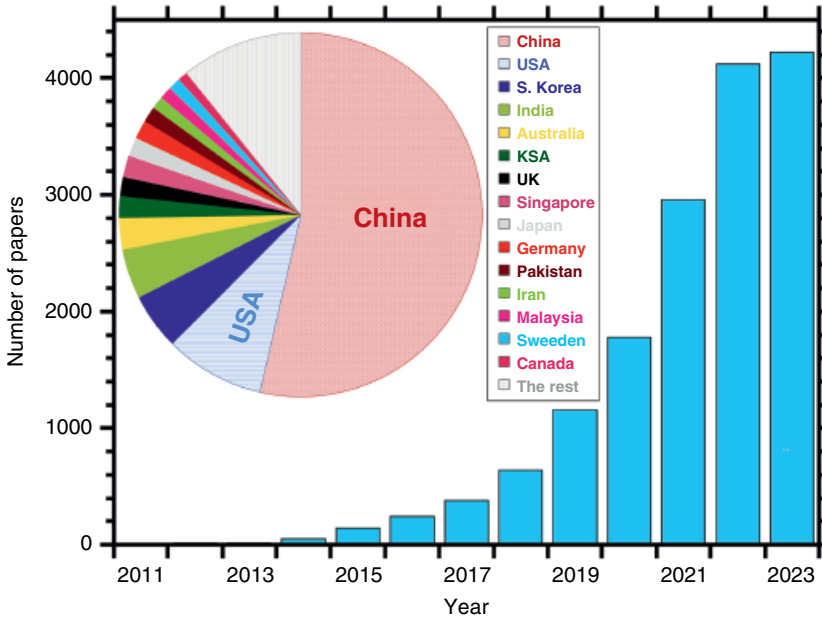


Figure 1.1 Number of papers on MXenes published per year. The inset shows a pie chart for the contribution of the top 15 countries published on MXenes. *Source:* The data plotted here were extracted from the web of science.

vast compositional space makes MXenes highly attractive as a tunable materials platform for various applications.

The interest in MXenes is evident from the significant number of publications, as shown in Figure 1.1. Furthermore, the simplicity of the synthesis process and the affordability of the necessary infrastructure for their processing have made them appealing to research groups worldwide, irrespective of their country's level of development or income (see inset Figure 1.1). With the continuous growth of interest in MXenes research, there is a need for a comprehensive handbook that provides detailed information on various aspects of MXenes, including synthesis, characterization, properties, and applications. Such a handbook should not only cover the current state of the art in MXenes research but, more importantly, provide guidance by the experts on best practices, common pitfalls to avoid, and tips for ensuring high-quality, reproducible outcomes in MXenes research. In this introduction chapter, we walk the handbook readers through the different chapters of the book.

In addition to the Introduction (Part I) and Conclusion (Part V), this handbook consists of three other main parts. Part II (Chapters 2–15) is dedicated to guidelines for the synthesis, characterization, and processing of MXenes. Part III

(Chapters 16–18) delves into MXenes' properties, while Part IV (Chapters 19–26) focuses on important applications of MXenes.

The success of MXene synthesis and the quality of the produced MXenes largely depend on their precursors [15, 16], which include MAX phases and other layered carbides/nitrides. This dependence is often overlooked, especially by researchers who are new to MXene synthesis. Such oversight can lead to frustration when researchers attempt to reproduce MXene synthesis using MAX phases prepared differently, resulting in variations in characteristics, such as particle size distribution. Therefore, it is crucial to exercise precise control over the synthesis of the MAX phases and other layered carbides/nitrides precursors. Furthermore, advancements in the synthesis of MAX phases and the introduction of new compositions of MAX phases and layered carbides/nitrides have paved the way for the creation of new MXenes (Chapter 9) [5, 17]. In Chapter 2, Rosen et al. discuss valuable tips and tricks for synthesizing MXene precursors.

MXene synthesis has undergone significant evolution since the initial reports on MXenes involving the use of hydrofluoric acid (HF)[2] [1, 4]. The capability to utilize fluoride salts dissolved in acids as etchants, rather than employing HF directly [18], has enabled a larger number of researchers to conduct MXene synthesis at their institutions, particularly where the direct use of HF is prohibited. Additionally, the presence of cations from the fluoride salt, along with their intercalation, facilitates the delamination of MXenes [18]. So far, fluorine-based synthesis methods for MXenes (whether through direct use of HF or *in-situ* HF generation using fluoride salts dissolved in acid) are the most widely used due to their simplicity and efficacy. Anasori et al. offer insights into MXene synthesis using fluorine-based etchants in Chapter 3. Alternative fluorine-free synthesis approaches are presented and discussed in Chapter 4 for low-temperature synthesis and in Chapter 5 for the use of molten salts.

Intercalation of ions and molecules in MXenes plays a critical role in the processing of MXenes as it enables large-scale delamination [19] and significantly impacts their properties and performance in various applications [20–23]. Chapter 6

2 The discovery of MXenes resulted from research efforts aimed at utilizing MAX phases as anodes for Li-ion batteries, funded by the US Department of Energy. Initial attempts to insert Li into pristine MAX phases proved unsuccessful. Consequently, Naguib et al. decided to pre-treat the MAX phases using HF that was chosen initially to fulfill two purposes: (i) Deagglomerate the MAX phase particles by etching intermetallic films at the grain boundaries of MAX phases, thereby pulverizing them into small grains. This process is expected to result in faster kinetics for Li storage. (ii) Break through the native metal oxide layer on the surface of MAX phase particles. Subsequently, etch, either partially or fully, the now-exposed A layers, creating more space for Li between the layers of $M_{n+1}X_n$. The first HF treatment at room temperature led to the complete removal of Al from Ti_3AlC_2 resulting in the formation of $Ti_3C_2T_x$, the first-reported MXene.

provides insights into molecules and ions intercalation in MXenes. Zhang and his group discuss the delamination of MXenes in Chapter 12, where MXene flakes serve as the building blocks for various thin films and functional devices. As such, they provide unique strategies for solution processing of these delaminated MXene flakes for coatings, with a particular focus on the ink rheological properties in Chapter 13. Furthermore, Beidaghi et al., in Chapter 14, explore 3D printing of MXene inks following the solution processing, while Tao and Yang' groups provide a comprehensive study for the liquid-based assembly of MXenes into compact films/architectures in Chapter 15. We believe that this order will make it easier for the reader to follow how to intercalate MXene solids and swell their structure until they can be delaminated into homogeneous solutions. Additionally, it provides strategies for processing these dispersions into the desired devices.

Common mistakes and best practices for characterizing the structure and morphology of MXenes are presented in Chapter 10, while Chapter 11 discusses aspects related to the surface terminations of MXenes.

One of the challenges that MXenes encounter relates to their stability specially when delaminated [24]. Chapter 7 delves into this issue, addressing the thermal and chemical stability of MXenes and exploring their degradation mechanisms. In Chapter 8, Razal and colleagues offer excellent guidelines for storing and handling MXenes to maintain their quality.

Many of the properties and applications of MXenes deserve standalone books. In Part III of this handbook, we have chosen to focus on several properties that are commonly explored by researchers and where MXenes demonstrate great potential. Since the first report on MXenes [1], *ab initio* calculations have proven to be a powerful tool for predicting their electronic structure [25], as well as their properties and performance in applications [26–28]. Additionally, *ab initio* calculations have been used to guide the synthesis of new MXenes [5, 29]. Herein, Kent et al. provide, in Chapter 16, expert insights on using atomistic simulation to predict and explain the properties of MXenes. In Chapter 17, Gogotsi et al. discuss the optical and optoelectronic properties of MXenes and their related applications. Chapter 18 offers an insightful overview of the mechanical properties of MXenes and their use as functional reinforcement in composites.

The first explored application for MXenes was their use as electrode materials in electrochemical energy storage devices [22, 30–33]. In fact, this application was the primary motivation for their invention in the first place. To this day, energy storage remains the most extensively studied application for MXenes [34]. Consequently, we have dedicated three chapters to various categories of electrochemical energy storage. In Chapter 19, Lin and Simon delve into the capacitive behavior of MXenes and their applications in supercapacitors. Chapter 20 focuses on the utilization of MXenes in Li-ion batteries (LIBs), while Chapter 21 concentrates on MXenes in rechargeable batteries beyond LIBs, such as Na-ion batteries.

MXenes, with their excellent electrical conductivity and tunable electronic structures, are uniquely positioned for numerous applications. These include their use in electronic and communication devices (Chapter 23) and sensing devices (Chapter 24). Chapter 22 offers insight into the use of MXenes and their composites for electromagnetic interference shielding, which is one of MXenes' most promising applications [35, 36]. MXenes have also made inroads into environmental treatments and healthcare technologies, which are the subjects of Chapters 25 and 26, respectively.

Finally, we conclude the handbook with Part V, which is dedicated to conclusions and perspectives. In this section, we provide a summary of key points and discuss the challenges ahead, presenting them to the readers. We believe that the content of this handbook will be highly beneficial to a diverse audience, including undergraduate and graduate students, postdoctoral fellows, professors, engineers, and scientists in the industry who have an interest in working with MXenes.

References

1 Naguib, M., Kurtoglu, M., Presser, V. et al. (2011). Two-dimensional nanocrystals produced by exfoliation of Ti_3AlC_2. *Advanced Materials* 23 (37): 4248–4253.

2 Naguib, M., Barsoum, M.W., and Gogotsi, Y. (2021). Ten years of progress in the synthesis and development of MXenes. *Advanced Materials* 33 (39): 2103393.

3 Anasori, B. and Naguib, M. (2023). Two-dimensional MXenes. *MRS Bulletin* 48: 238–244.

4 Naguib, M., Mashtalir, O., Carle, J. et al. (2012). Two-dimensional transition metal carbides. *ACS Nano* 6 (2): 1322–1331.

5 Anasori, B., Xie, Y., Beidaghi, M. et al. (2015). Two-dimensional, ordered, double transition metals carbides (MXenes). *ACS Nano* 9 (10): 9507–9516.

6 Persson, I., el Ghazaly, A., Tao, Q. et al. (2018). Tailoring structure, composition, and energy storage properties of MXenes from selective etching of in-plane, chemically ordered MAX phases. *Small* 14 (17): 1703676.

7 Wang, L., Han, M., Shuck, C.E. et al. (2021). Adjustable electrochemical properties of solid-solution MXenes. *Nano Energy* 88: 106308.

8 Yang, J., Naguib, M., Ghidiu, M. et al. (2016). Two-dimensional Nb-based M_4C_3 solid solutions (MXenes). *Journal of the American Ceramic Society* 99 (2): 660–666.

9 Ma, W., Wang, M., Yi, Q. et al. (2022). A new $Ti_2V_{0.9}Cr_{0.1}C_2T_x$ MXene with ultrahigh gravimetric capacitance. *Nano Energy* 96: 107129.

10 Nemani, S.K., Zhang, B., Wyatt, B.C. et al. (2021). High-entropy 2D carbide MXenes: $TiVNbMoC_3$ and $TiVCrMoC_3$. *ACS Nano* 15 (8): 12815–12825.

11 Zhou, J., Tao, Q., Ahmed, B. et al. (2022). High-entropy laminate metal carbide (MAX phase) and its two-dimensional derivative MXene. *Chemistry of Materials* 34 (5): 2098–2106.

12 Chen, L., Li, Y., Liang, K. et al. (2023). Two-dimensional MXenes derived from medium/high-entropy MAX phases M_2GaC (M = Ti/V/Nb/Ta/Mo) and their electrochemical performance. *Small Methods* 7 (8): 2300054.

13 Anasori, B., Shi, C., Moon, E.J. et al. (2016). Control of electronic properties of 2D carbides (MXenes) by manipulating their transition metal layers. *Nanoscale Horizons* 1 (3): 227–234.

14 Bai, Y., Zhou, K., Srikanth, N. et al. (2016). Dependence of elastic and optical properties on surface terminated groups in two-dimensional MXene monolayers: a first-principles study. *RSC Advances* 6 (42): 35731–35739.

15 Mathis, T.S., Maleski, K., Goad, A. et al. (2021). Modified MAX phase synthesis for environmentally stable and highly conductive Ti_3C_2 MXene. *ACS Nano* 15 (4): 6420–6429.

16 Shuck, C.E., Han, M., Maleski, K. et al. (2019). Effect of Ti_3AlC_2 MAX phase on structure and properties of resultant $Ti_3C_2T_x$ MXene. *ACS Applied Nano Materials* 2 (6): 3368–3376.

17 Deysher, G., Shuck, C.E., Hantanasirisakul, K. et al. (2020). Synthesis of Mo_4VAlC_4 MAX phase and two-dimensional Mo_4VC_4 MXene with five atomic layers of transition metals. *ACS Nano* 14 (1): 204–217.

18 Ghidiu, M., Lukatskaya, M.R., Zhao, M.-Q. et al. (2014). Conductive two-dimensional titanium carbide 'clay' with high volumetric capacitance. *Nature* 516: 78.

19 Naguib, M., Unocic, R.R., Armstrong, B.L., and Nanda, J. (2015). Large-scale delamination of multi-layers transition metal carbides and carbonitrides "MXenes". *Dalton Transactions* 44 (20): 9353–9358.

20 Al-Temimy, A., Prenger, K., Golnak, R. et al. (2020). Impact of cation intercalation on the electronic structure of $Ti_3C_2T_x$ MXenes in sulfuric acid. *ACS Applied Materials & Interfaces* 12 (13): 15087–15094.

21 Liang, K., Matsumoto, R.A., Zhao, W. et al. (2021). Engineering the interlayer spacing by pre-intercalation for high performance supercapacitor MXene electrodes in room temperature ionic liquid. *Advanced Functional Materials* 31 (33): 2104007.

22 Lukatskaya, M.R., Mashtalir, O., Ren, C.E. et al. (2013). Cation intercalation and high volumetric capacitance of two-dimensional titanium carbide. *Science* 341 (6153): 1502.

23 Prenger, K., Sun, Y., Ganeshan, K. et al. (2022). Metal cation pre-intercalated $Ti_3C_2T_x$ MXene as ultra high areal capacitance electrodes for aqueous supercapacitors. *ACS Applied Energy Materials* 5 (8): 9373–9382.

24 Cao, F., Zhang, Y., Wang, H. et al. (2022). Recent advances in oxidation stable chemistry of 2D MXenes. *Advanced Materials* 34 (13): 2107554.

25 Khazaei, M., Ranjbar, A., Arai, M. et al. (2017). Electronic properties and applications of MXenes: a theoretical review. *Journal of Materials Chemistry C* 5 (10): 2488–2503.

26 Xie, Y., Dall' Agnese, Y., Naguib, M. et al. (2014). Prediction and characterization of MXene nanosheet anodes for non-lithium-ion batteries. *ACS Nano* 8 (9): 9606–9615.

27 Xie, Y., Naguib, M., Mochalin, V.N. et al. (2014). Role of surface structure on Li-ion energy storage capacity of two-dimensional transition-metal carbides. *Journal of the American Chemical Society* 136 (17): 6385–6394.

28 Zhan, C., Naguib, M., Lukatskaya, M. et al. (2018). Understanding the MXene pseudocapacitance. *The Journal of Physical Chemistry Letters* 9 (6): 1223–1228.

29 Björk, J., Halim, J., Zhou, J., and Rosen, J. (2023). Predicting chemical exfoliation: fundamental insights into the synthesis of MXenes. *npj 2D Materials and Applications* 7 (1): 5.

30 Come, J., Naguib, M., Rozier, P. et al. (2012). A non-aqueous asymmetric cell with a Ti_2C-based two-dimensional negative electrode. *Journal of the Electrochemical Society* 159 (8): A1368.

31 Naguib, M., Come, J., Dyatkin, B. et al. (2012). MXene: a promising transition metal carbide anode for lithium-ion batteries. *Electrochemistry Communications* 16 (1): 61–64.

32 Mashtalir, O., Naguib, M., Mochalin, V.N. et al. (2013). Intercalation and delamination of layered carbides and carbonitrides. *Nature Communications* 4 (1): 1716.

33 Naguib, M., Halim, J., Lu, J. et al. (2013). New two-dimensional niobium and vanadium carbides as promising materials for Li-ion batteries. *Journal of the American Chemical Society* 135 (43): 15966–15969.

34 Anasori, B., Lukatskaya, M.R., and Gogotsi, Y. (2017). 2D metal carbides and nitrides (MXenes) for energy storage. *Nature Reviews Materials* 2 (2): 16098.

35 Shahzad, F., Alhabeb, M., Hatter, C.B. et al. (2016). Electromagnetic interference shielding with 2D transition metal carbides (MXenes). *Science* 353 (6304): 1137–1140.

36 Liu, J., Zhang, H.-B., Sun, R. et al. (2017). Hydrophobic, flexible, and lightweight MXene foams for high-performance electromagnetic-interference shielding. *Advanced Materials* 29 (38): 1702367.

Part II

Guidelines on MXenes Synthesis, Characterizations and Processing

2

Synthesis of MXene Precursors – Tips and Tricks

Joseph Halim, Jie Zhou, Martin Dahlqvist, and Johanna Rosen

Materials Design division, Department of Physics, Chemistry, and Biology (IFM), Linköping University, Linköping, Sweden

2.1 Structure and Composition of MXene Precursors

In the present chapter, we will present the structure and composition of parent materials for experimentally realized MXenes. Naturally, the chapter has a starting point in traditional ternary MAX phases.

MAX phases are a family of hexagonally and atomically laminated materials discovered in the 1960s [1, 2]. Their general composition is given by $M_{n+1}AX_n$ where M is transition metal, A is an A-group element typically from group 13 or 14, X is carbon and/or nitrogen, and $n = 1$, 2, and 3 or even higher. MAX phases are ternary compounds, but it is also possible to mix elements on the M-, A-, and X-sites, which render quaternary or even higher-order MAX phases. The M-site is the most common site for mixing elements which have resulted in solid solution MAX phases (Figure 2.1) and chemically ordered MAX phases depending on the elemental choice (Figures 2.1 and 2.2). Chemically ordered MAX phases have demonstrated to possess either out-of-plane order (*o*-MAX) [3, 4] or in-plane order (*i*-MAX) [5]. Lately, also high-entropy MAX phases have been demonstrated with four or more metals mixed [6–9]. Due to its layered structure and elemental composition, MAX phases consist of strong M–X and relatively weak M–A bonds resulting in a combination of properties bearing ceramic attributes like good oxidation resistance and thermal stability with metallic attributes like being machinable and with good electrical and thermal conductivity [10–12].

In 2011, Naguib et al. managed to produce the first two-dimensional (2D) MXene, $Ti_3C_2T_z$, through selective etching of A-element from its precursor MAX

Transition Metal Carbides and Nitrides (MXenes) Handbook: Synthesis, Processing, Properties and Applications, First Edition. Edited by Chuanfang Zhang and Michael Naguib.
© 2024 John Wiley & Sons, Inc. Published 2024 by John Wiley & Sons, Inc.

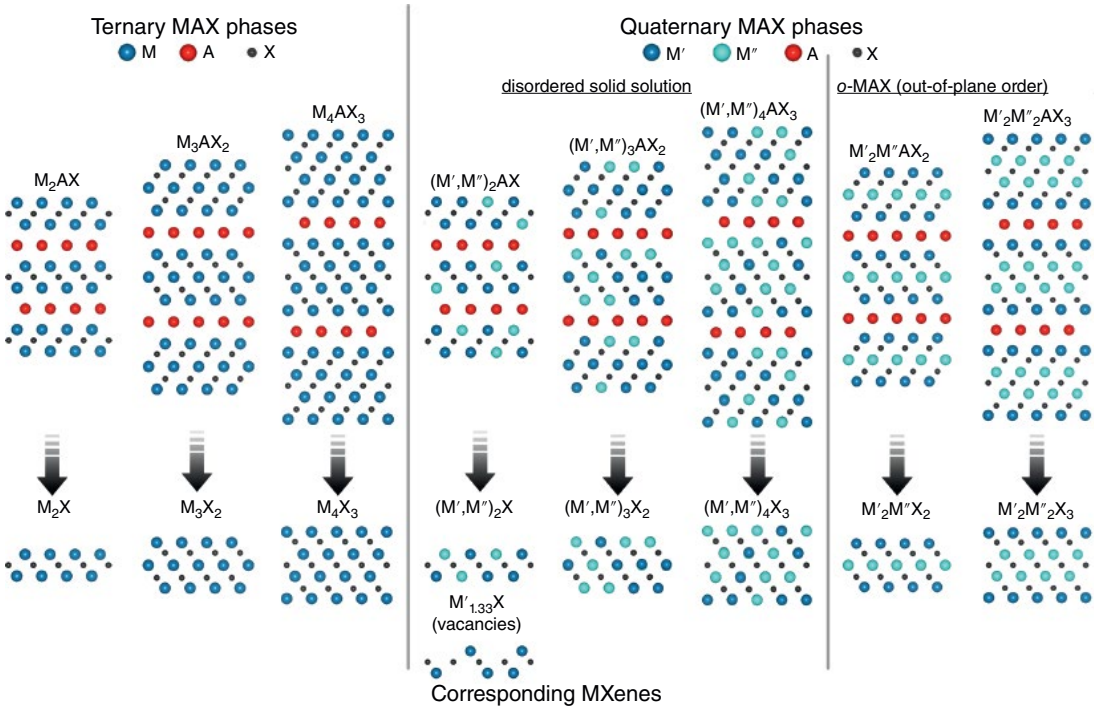


Figure 2.1 Ternary and quaternary MAX phases used as precursors for MXene synthesis. Quaternary MAX phases with metals M″ and M″ distributed as a disordered solid solution, or with out-of-plane chemical ordering in *o*-MAX phases.

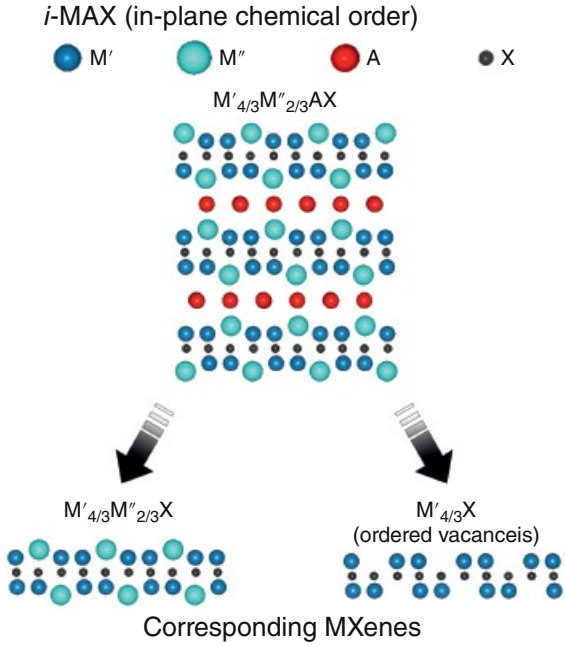


Figure 2.2 *i*-MAX with in-plane chemical order used as precursor for MXenes with elemental order or vacancy order.

phase Ti_3AlC_2 [13]. Since then, many more MXenes have been successfully made as listed in Table 2.1, with corresponding precursor being MAX phase or MAX phase-like, where the latest contributions include chemically ordered MXenes [33, 34] and high-entropy MXenes [7]. Importantly, T_z is the general notation for describing the surface termination of the MXene, where T denotes the termination (which could be O, F, OH, etc.) and z is the amount of corresponding species or molecules, which for ideal surface coverage is equal to 2. For simplicity, we will not use T_z from here on since it can vary depending on the procedure used for etching the MAX phases to realize the MXenes.

2.1.1 MAX Phases (Nitrides/Carbides/Alloys) and *o*-MAX Phases

MAX phases (Figure 2.1) used as precursor for producing $M_{n+1}X_n$ MXenes are listed in Table 2.1.

The first M_2X MXene made was Ti_2C upon etching Al from Ti_2AlC using HF [14]. In this work, Naguib et al. also demonstrated the first M_4X_3 MXene, Ta_4C_3, as well as the first three-component MXenes encompassed by metal solid solution, $(Ti_{0.5}Nb_{0.5})_2C$ and $(V_{0.5}Cr_{0.5})_3C_2$, and X-site solid solution $Ti_3(C_{0.5}N_{0.5})_2$.

Table 2.1 List of synthesized MXenes and their precursor.

General MXene notation	MXene	Precursor
$M_{n+1}X_n$	Ti_2C	Ti_2AlC [14], Ti_2ZnC [15]
	V_2C	V_2AlC [16], V_2ZnC [15]
	Nb_2C	Nb_2AlC [16]
	Mo_2C	Mo_2Ga_2C [17]
	Ti_2N	Ti_2AlN [18]
	Ti_3C_2	Ti_3AlC_2 [13], Ti_3SiC_2 [19], Ti_3ZnC_2 [15]
	Zr_3C_2	$Zr_3Al_3C_5$ [20]
	Hf_3C_2	$Hf_3[Al(Si)]_4C_6$ [21]
	Ta_4C_3	Ta_4AlC_3 [14]
	Nb_4C_3	Nb_4AlC_3 [22]
	V_4C_3	V_4AlC_3 [23]
	Ti_4N_3	Ti_4AlN_3 [24]
$(M',M'')_{n+1}X_n$, disordered solid solution	$(Ti_{1-x}Nb_x)_2C$	$(Ti_{1-x}Nb_x)_2AlC$ [14, 25]
	$(Ti_{1-x}V_x)_2C$	$(Ti_{1-x}V_x)_2AlC$ [25]
	$(V_{1-x}Nb_x)_2C$	$(V_{1-x}Nb_x)_2AlC$ [25]
	$(V_{1-x}Cr_x)_2C$	$(V_{1-x}Cr_x)_2AlC$ [14]
	$(V_{1-x}Cr_x)_3C_2$	$(V_{1-x}Cr_x)_3AlC_2$ [14]
	$(Ti_{1-x}V_x)_3C_2$	$(Ti_{1-x}V_x)_3AlC_2$ [26]
	$(Ta_{1-x}Ti_x)_3C_2$	$(Ta_{1-x}Ti_x)_3AlC_2$ [27]

	$(Nb_{0.8}Ti_{0.2})_4C_3$	$(Nb_{0.8}Ti_{0.2})_4CAl_3$ [28]
	$(Nb_{0.8}Zr_{0.2})_4C_3$	$(Nb_{0.8}Zr_{0.2})_4CAl_3$ [28]
	$(Mo_{1-x}V_x)_4C_3$	$(Mo_{1-x}V_x)_4CAl_3$ [29]
	$(Nb_{0.875}Ta_{0.125})_4C_3$	$(Nb_{0.875}Ta_{0.125})_4AlC_3$ [30]
	$(Nb_{0.975}W_{0.025})_4C_3$	$(Nb_{0.975}W_{0.025})_4AlC_3$ [30]
	$(Mo_{1-x}V_x)_5C_4$	$(Mo_{1-x}V_x)_5AlC_4$ [31]
$(M',M'', M''', M'''')_{n+1}X_n$, disordered solid solution high-entropy MXene	$(Ti_{0.30}V_{0.20}Zr_{0.10}Nb_{0.17}Ta_{0.23})_2C$	$(Ti_{1/5}V_{1/5}Zr_{1/5}Nb_{1/5}Ta_{1/5})_2AlC$ [6]
	$(Ti_{0.28}V_{0.20}Zr_{0.09}Nb_{0.20}Ta_{0.24})_2(C_{1-x}N_x)$	$(Ti_{1/3}V_{1/6}Zr_{1/6}Nb_{1/6}Ta_{1/6})_2Al(C_{1-x}N_x)$ [8]
	$(Ti_{0.225}V_{0.25}Nb_{0.25}Mo_{0.225})_4C_3$	$(Ti_{1/4}V_{1/4}Nb_{1/4}Mo_{1/4})_4AlC_3$ [7]
	$(Ti_{0.275}V_{0.275}Cr_{0.225}Mo_{0.25})_4C_3$	$(Ti_{1/4}V_{1/4}Cr_{1/4}Mo_{1/4})_4AlC_3$ [7]
	$(Ti_{0.275}V_{0.175}Cr_xNb_{0.25}Ta_{0.15})C_3$	$Ti_{1.0}V_{0.7}Cr_{0.05}Nb_{1.0}Ta_{1.0}AlC_3$ [9]
$M_{n+1}(X',X'')_n$, disordered solid solution on X-site	$Ti_3(C,N)_2$	$Ti_3Al(C,N)$ [14]
$M'_2M''_{n-1}X_n$, out-of-plane chemical order	Mo_2ScC_2	Mo_2ScAlC_2 [32]
	Mo_2TiC_2	Mo_2TiAlC_2 [33]
	Cr_2TiC_2	Cr_2TiAlC_2 [33]
	$Mo_2Ti_2C_3$	$Mo_2Ti_2AlC_3$ [33]
$M'_{4/3}M''_{2/3}X$, in-plane chemical order	$(Mo_{2/3}Y_{1/3})_2C$	$Mo_{4/3}Y_{2/3}AlC$ [34]
$M_{1.33}X$,disordered vacancies	$Nb_{1.33}C$	$(Nb_{2/3}Sc_{1/3})_2AlC$ [35]
	$V_{2-x}C$	$(V_{1-x}Sc_x)_2AlC$ ($x \leq 0.05$) [36]
$M_{1.33}X$,ordered vacancies	$Mo_{1.33}C$	$Mo_{4/3}Sc_{2/3}AlC$ [5], $Mo_{4/3}Y_{2/3}AlC$ [34], $Mo_{4/3}RE_{2/3}AlC$ (RE = Gd, Tb, Dy, Ho, Er, and Y) [37]
	$W_{1.33}C$	$W_{4/3}Sc_{2/3}AlC$ [38, 39], $W_{4/3}Y_{2/3}AlC$ [38, 39], $W_{4/3}RE_{2/3}AlC$ (RE = Gd, Tb, Dy, Ho, Er, Tm, and Lu) [40]

This was achieved through selective etching of Al from Ta_4AlC_3, $(Ti_{0.5}Nb_{0.5})_2AlC$, $(V_{0.5}Cr_{0.5})_3AlC_2$, and $Ti_3Al(C_{0.5}N_{0.5})_2$ [14]. Later, Halim et al. showed that it is possible to selectively etch both Al and Sc from solid solution $(Nb_{0.67}Sc_{0.33})_2AlC$ to produce $Nb_{1.33}C$ MXene with disordered metal vacancies [35]. Chemically ordered MXene was first shown upon etching of Al from out-of-plane ordered MAX phases (*o*-MAX) resulting in Mo_2TiC_2, Cr_2TiC_2, and $Mo_2Ti_2C_3$ MXenes [33].

2.1.2 *i*-MAX Phases

Quaternary MAX phase with in-plane chemical ordering of two metals, coined *i*-MAX, was introduced in 2017 by Tao et al. in the form of $Mo_{4/3}Sc_{2/3}AlC$ [5]. The *i*-MAX phase is obtained by mixing two metals in a 2 : 1 ratio, and with the minority metal M″ being much larger than M′. Its structure is schematically illustrated in Figure 2.2. Even though the *i*-MAX structure is closely related to the M_2AX structure, it is strictly speaking not a MAX phase due to the lack of a hexagonal space group symmetry. Its crystal structure is monoclinic or orthorhombic, which stems from the larger M″ being closer to the A-layer, which in turn results in a Kagomé-like structure of the A-layer [41].

Etching the *i*-MAX phase can result in two different kinds of MXene. The first example is $M_{1.33}C$ MXene comprised of ordered metal vacancies, for example, $Mo_{1.33}C$ and $W_{1.33}C$, where the minority metal M″ (Sc, Y, or a rare-earth element RE) is selectively etched along with A [5]. By using different etching protocols to the parent *i*-MAX phase, it is also possible to only etch the A-element, as was demonstrated for $(Mo_{2/3}Y_{1/3})_2C$ [34].

2.1.3 Mo_2Ga_2C and Zr/Hf-based Carbides

There are also other layered materials, illustrated in Figure 2.3, used to make MXenes which are closely related to MAX phases. The first example is Mo_2C MXene obtained by immersing Mo_2Ga_2C thin films in HF [17]. Mo_2Ga_2C deviates from the traditional MAX phases by having a double layer of Ga, which thus makes Ga etchable. Another example is when an Al_4C_3 layer is etched from $Zr_3Al_3C_5$ [20] and $Hf_3[Al(Si)]_4C_6$ [21] to make Zr_3C_2 and Hf_3C_2 MXenes.

2.2 Synthesis of MXene Precursors – Including Good "Tips" and Guidelines

2.2.1 MAX Phases (Nitrides/Carbides/Alloys) and *o*-MAX Phases

This section will be divided into three parts, providing guidelines applicable to before, during, and after synthesis of the 3D MXene precursor.

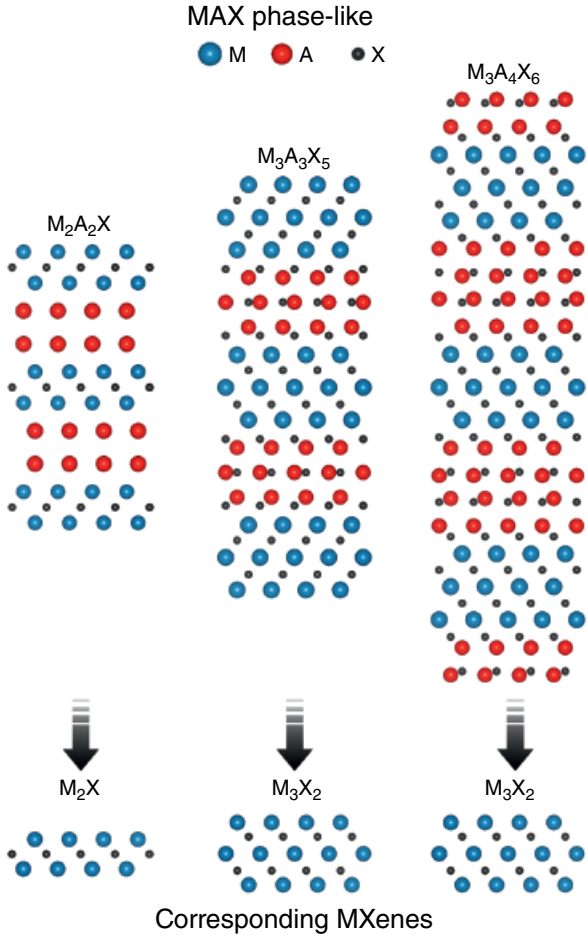


Figure 2.3 MAX phase-like compounds used as precursors for MXenes.

2.2.1.1 Preparation for Synthesis

Molar ratio: The molar ratio of the raw materials used for MAX phase synthesis directly impacts the yield, quality, and properties of the obtained MAX phase and their respective MXenes. As a general rule for the majority of the MAX phases, increasing the amount of the A element to about 10–30 molar percent and/or decreasing the X element, especially in the case of carbide-based MAX phases, increases the purity of the MAX phases by diminishing the growth of binary carbides as secondary phases, and also helps to obtain MAX phases with stoichiometries close to the ideal ones. Using spark plasma sintering (SPS), Zhou et al. obtained a single phase Ti_2AlC, according to XRD, when adding an excess

10–20 mole % of Al to elemental Ti and C of 2 : 1 molar ratio, whereas TiC appeared as a secondary phase when using the stoichiometric ratio as well as both TiC and TiAl appeared when increasing the excess Al to 30 molar percent [42]. Benitez et al. produced a 95.14 wt% Ti_2AlC with less than 0.2 wt% TiC, starting with Ti : Al : TiC molar ratio of 1 : 1.05 : 0.95 using pressureless sintering (PLS) technique [43].

Furthermore, Nb_2AlC as a single phase was reported when mixing Nb : Al : NbC in the molar ratio of 2 : 1.2 : 1 using SPS technique [44]. Mathis et al. showed that starting with TiC, Ti, and Al of 2 : 1.25 : 2.2 molar ratio, improved the crystallinity and carbon stoichiometry of pressureless sintered Ti_3AlC_2 compared to using starting material with a stoichiometric ratio [45]. Moreover, etching the high purity Ti_3AlC_2 led to Ti_3C_2 with increased electronic conductivity up to 20,000 S cm^{-1}, and shelf life up to 10 months, stored in aqueous solution in ambient conditions, compared to conventional Ti_3C_2.

Choice of starting material: The choice of the starting material significantly affects the yield and quality of the produced MAX phase, which ultimately affects the resulting MXene. Elemental powders are the most common form for MAX phase powder and bulk synthesis; however, the use of compounds as starting material has been reported as well. Binary carbides are among the most common starting compounds used for MAX phase synthesis, where the A element intercalates the binary carbide forming a MAX phase. The formation of Ti_3AlC_2 by intercalating Al into TiC is one such example, where extra Ti is added to balance the equation, that is, $2TiC + Al + Ti = Ti_3AlC_2$. The compounds used as starting material can be carbides, such as using TiC and elemental Ti and Al to form Ti_2AlC, and Ti_3AlC_2 [45, 46]. Peng et al. reported on the synthesis of high purity, about 97 wt%, large scale, up to 1 kg, Ti_3AlC_2 by PLS of $2TiC + Ti + Al$ [47]. This reaction is less exothermal than that produced by reacting elemental powders, which leads to a more easily and stable large-scale fabrication of Ti_3AlC_2.

Other synthesis routes include $xTi/Al_4C_3/yC$ to form Ti_3AlC_2 [48] or Ti_2AlC [49], and reduction of transition metal oxide. The latter, considered as a low-cost and environmentally friendly method, has been explored for several Ti-based MAX phases: (i) $xTiO_2/yAl/zC$ to form Ti_2AlC and Ti_3AlC_2 [50–52] and (ii) $xTiO_2/ySiC$ to form Ti_3SiC_2 and Ti_4SiC_3 [53, 54]. Additionally, starting with transition metal hydrides (MH) made it possible to form MAX phases for which their formation is hindered by oxidation; ZrH_2 and HfH_2 were used as sources of Zr and Hf transition metals to produce Zr- and Hf-based MAX phases, respectively, such as Zr_3AlC_2 [55], Zr_2AlC [56], Hf_2AlC, and Hf_3AlC_2 [57].

The source of the starting material has been shown to influence the quality and properties of the produced MAX phase and its MXene. By using three carbon sources (graphite, carbon lampblack, and titanium carbide) to make Ti_3AlC_2, it has been demonstrated that graphite-produced Ti_3C_2 exhibited the highest

conductivity (≈4400 S cm^{-1}) and the longest duration of colloidal stability in water (10.1 days). At the same time, TiC-produced Ti_3C_2 showed a comparable conductivity but lowered colloidal stability (4.8 days), and carbon lampblack-produced Ti_3C_2 had the lowest conductivity (≈1020 S cm^{-1}) and low colloidal stability (5.1 days) [58]. However, when tested as gas sensors for ethanol, acetone, and ammonia, the TiC-produced Ti_3C_2 showed the highest response followed by graphite-produced Ti_3C_2, whereas carbon lampblack-produced Ti_3C_2 had the lowest response.

Pre-treatment of raw material: In some cases, cold pressing the starting powders before sintering can increase the MAX phase yield. This has been demonstrated for Nb_2AlC, V_2AlC, and the in-plane chemically ordered $(Mo_{2/3}Y_{1/3})_2AlC$ and $(W_{2/3}Y_{1/3})_2AlC$, where the increase in yield can reach up to 30 wt% (unpublished results).

2.2.1.2 Synthesis, Techniques, and Conditions

The synthesis of MAX phases can be categorized into three main techniques: (i) solid-state reactions (SSRs), (ii) molten salt synthesis (MS) processes, and (iii) physical vapor deposition (PVD).

In general, the synthesis of MAX phases is not complicated, but very high phase purity (95 wt% or more) is difficult to achieve. One reason is that the MAX phase formation region in the phase diagram is usually very narrow, and several reactions occur during the heating process. Until now, M-A-X phase diagrams are only available for some systems. The synthesized samples typically consist of MAX phases and several competing phases, such as binary carbides, nitrides, and intermetallic compounds [59]. The main limitation is the synthesis of large quantities of MAX phase powders with high-phase purity.

Solid state reaction (SSR): MAX phases are usually synthesized by the SSR approach and the MS method. The phase purity, crystallinity, and grain size of the synthesized MAX phase precursor are key parameters for corresponding MXene synthesis. SSR is the most common method to synthesize MAX phases. This method is based on reactions between the elemental constituting powders or other metal carbides (MX) or MH raw materials at high temperature. Typically, the synthesis temperature ranges between 1000 °C and 1700 °C, and the synthesis is carried out under a protective atmosphere to avoid oxidation.

Pressureless sintering (PLS) is commonly used for MAX phase synthesis. Loose powder or cold-pressed pellets of the mixture of starting raw materials are placed in a crucible and heated under a protected atmosphere to targeted temperatures (1000–1700 °C) for a few hours, where an indirect resistance heating source is used, and the heating rate is 2–10 °C min^{-1}. The heating rate also affects the sample's quality, lower heating rate usually produces more homogenous samples. Especially during large-scale synthesis using sintering method, localized

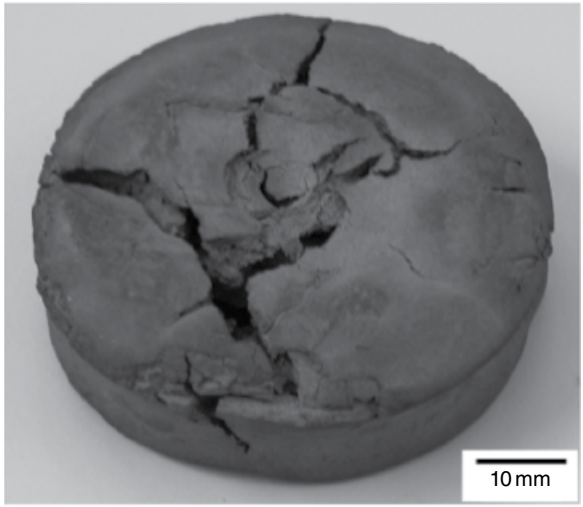


Figure 2.4 Digital image of a thermally exploded Ti_3AlC_2 disc of 20 cm^3 volume after sintering. *Source:* Mingxing et al. [60]/Reproduced from John Wiley & Sons.

self-propagating high-temperature synthesis (SHS) might take place causing thermal explosion, which might impose a threat to the furnace's safety in addition it can cause an increase in the amounts of impurity phases such as transition metal carbides. The thermal explosion can be mitigated using additives such as Sn for the synthesis of Ti_3AlC_2 [60]. Figure 2.4 shows a digital image of a Ti_3AlC_2 disc of 20 cm^3 after thermal explosion during sintering. Generally, the holding temperatures are higher for higher order MAX phases, that is, increased when going from 211 to 312 and 413 type MAX phases. To achieve a relatively high phase purity, a suitable holding temperature should be chosen. This is to get rid of most competing secondary phases and to prohibit the decomposition of MAX phases at higher temperatures. PLS usually leads to porous pellet samples with relatively high phase purity (around 95 wt%), which can be followed by a milling step to obtain fine powders. In addition, holding time should be considered (usually up to several hours) and enough holding temperature contributing to the improved phase purity. A digital image of a Cr_2AlC lightly sintered bulk piece produced by PLS can be seen in Figure 2.5a, b shows an SEM image of typical Ti_3AlC_2 powders.

Microwave synthesis (MW) is a pressureless heating method with high heating rates, a selective heating zone, and direct energy supply and penetration of the raw powder mixture. MW is a fairly recent method used for MAX phase synthesis in comparison to the well-explored processes of SSR methods. To date, a few MAX phases have been reported through the use of MW – V_2AlC, Cr_2AlC, and Ti_2AlN [64–66]. With MW, the starting raw materials are heated under an argon

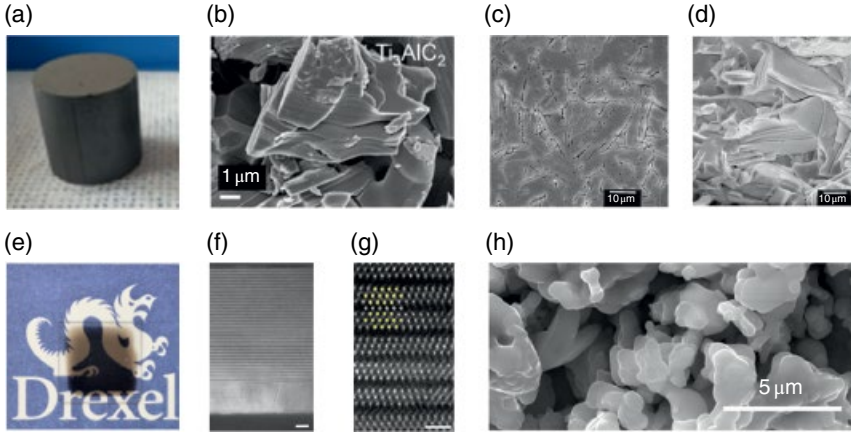


Figure 2.5 Various forms of MAX phase, (a) digital image of a lightly sintered Cr_2AlC sample produced by pressureless sintering. *Source:* Gonzalez-Julian [61]/Reproduced from John Wiley & Sons/CC BY 4.0, (b) SEM of a typical Ti_3AlC_2 powders. *Source:* Alhabeb et al. [62]/Reproduced from American Chemical Society, SEM image of (c) a polished and etched surface and (d) a fracture surface of a Ti_3AlC_2 sample synthetized by HP. *Source:* Tzenov and Barsoum [48]/Reproduced from John Wiley & Sons. (e) A digital image, (f) TEM and (g) HRSTEM images of a Ti_3AlC_2 thin film produced by PVD. *Source:* Halim et al. [63]/Reproduced from American Chemical Society, and (h) SEM image of Ti_2ZnN produced by molten salt method. *Source:* Li et al. [15]/Reproduced with permission from American Chemical Society.

atmosphere with heating rates up to 200 °C min^{-1}, with holding temperatures between 850 °C and 1500 °C, and dwell times up to 30 min. Due to the interaction between starting raw materials and the microwaves, enhanced diffusion of species is expected, and thus results in lower holding temperature. The synthesized pellets exhibit high purity, with values up to 97.5%, and grain size in the range of 1–10 µm. Synthesized pellets are typically porous, and a milling step is also added to obtain powders. MW presents some limitations in synthesizing large-size or large-quantity samples due to temperature gradients.

For synthesis process with pressure, hot-pressing (HP), hot isostatic pressing (HIP), and SPS are usually considered. The simultaneous application of heat and pressure (pressure-assisted synthesis/sintering) during the synthesis process can lead to dense MAX phases samples with higher phase purity (>95 wt%), and can also control the purity more precisely. Dense bulk samples with high purity produced by SPS typically have fine grains (around 1–15 µm), while those produced by HIP and HP have elongated coarse grains (>15 µm). Figure 2.5c, d represents a dense Ti_3AlC_2 sample produced by HP, showing large grains.

Hot-pressing (HP): The starting powder is transferred into a graphite die and is uniaxially pressed between two graphite punches, followed by a thermal

treatment under protected atmosphere. The uniaxial pressure is applied during the whole thermal cycle, and the maximum pressure is up to 50 MPa. The holding temperatures are usually between 1200 °C and 1700 °C, while heating rate is often up to 20 °C min^{-1} with holding times of up to 10 hours at the holding temperature. Highly pure dense samples contain large grains (>10–20 μm) that are oriented perpendicular to the applied pressure are usually obtained. ElMelegy et al. have shown that high purity of the *i*-MAX phases $(Mo_{2/3}Y_{1/3})_2AlC$, $(W_{2/3}Y_{1/3})_2AlC$, and $(Cr_{2/3}Y)_2AlC$ is attainable using the HP method [67].

Hot isostatic pressing (HIP) leads to highly pure and dense MAX phases as HP, but without preferential orientation of the grains due to the applied isostatic pressure. The starting materials are encapsulated into a suitable glass or metallic container, followed by a thermal treatment under argon at high pressures (100–300 MPa) for several hours. As a result, although the synthesis is possible, HIP is not commonly used. However, grain size of Ti_3AlC_2 MAX phase can reach up to more than 50 μm by HIP, which paves the way for the synthesis of MXene sheets with large lateral size [68].

Spark plasma sintering (SPS): Sample preparation is similar to HP but the main difference resides in the heating cycle. In SPS, the mold is directly connected to electrical power. The resistivity of the mold and the powder part generates the heat directly in the mold. This results in very high heating rates. Additionally, this leads to a significant increase in the sintering activity of raw materials, which makes short cycle times of a few minutes possible. Further, this process lowers the threshold sintering temperature and pressure compared to that required in conventional heating processes. Cao et al. have used this method to produce Ti_3AlC_2, the precursor of $Ti_3C_2T_z$ [69].

In summary, faster heating rate (50–200 °C min^{-1}) and shorter dwell times (usually < 20 minutes) are used in SPS, and dense samples with limited grain growth (<10 μm) can be obtained at lower holding temperature (1100 °C–1400 °C).

Molten salt synthesis (MS): A synthesis method performed at high temperature where reactions and diffusion of ions and cations are facilitated in a "liquid media" (molten salt). Diffusion is enhanced in molten salt in comparison to an SSR; thus synthesis temperatures can be lowered. Processing is relatively simple, and it involves mixing the starting raw materials with salt, followed by cold pressing to form pellets. Depending on the required synthesis temperature, single halogen salt, such as NaCl or a eutectic combination, such as NaCl and KCl, are considered. Pellets are then placed in a crucible and heated to temperatures up to 1300 °C under protected atmosphere. Maximum temperature depends on the chosen system, with values in the range of 1000–1300 °C. After cooling, the pellets were washed in water to remove the residual salt and then filtered to obtain loose powders. The purity of powders is high (>95 wt%). Particle size is usually in the range of 100 nm–10 μm, and which depends on the raw starting materials used, raw materials to salt ratio, and the heating program.

Furthermore, the MS process can be used to synthesize novel MAX phases through the replacement of the "A" element in Lewis acidic molten salt. For example, using the replacement reaction between the Zn element from molten $ZnCl_2$ and the Al element in MAX phase precursors (Ti_3AlC_2, Ti_2AlC, Ti_2AlN, and V_2AlC), novel MAX phases Ti_3ZnC_2, Ti_2ZnC, Ti_2ZnN (SEM image shown in Figure 2.5h), and V_2ZnC have been synthesized [15].

Physical vapor deposition (PVD): Magnetron sputtering, cathodic arc deposition, and pulsed laser deposition are the primary methods considered for the synthesis of thin films with high phase purity and density, being performed at substrate temperatures between 450 °C and 1000 °C. Magnetron sputtering is the most used PVD method due to the good process control, attainable high phase purity, and controlled composition and microstructure. For MAX phases carbides, individual elemental targets or MAX phases compound targets are usually used for the deposition, where the latter typically provides a film composition diverging from the target composition. For the nitride counterparts, reactive sputtering using nitrogen gas as N source is typically used. The fabrication of $\sim 1 \times 1\,cm^2$ Ti_3C_2 films with a thickness about 19 nm was reported by selective etching of Al, from sputter-deposited epitaxial Ti_3AlC_2 films, in aqueous HF or NH_4HF_2. The prepared film transmits ~90% of the light in the visible-to-infrared range and exhibit metallic conductivity down to ~100 K [63]. Figure 2.5e, f, g shows a digital image of the Ti_3AlC_2, TEM of the cross-section of the thin film, and HRSTEM of the cross-section of the thin film, respectively.

2.2.1.3 Preparation of Powders for MXene Synthesis

Storage: Generally, the synthesized MAX phases powders are considered to be stable in air. However, several chemical reactions are involved during the etching process. As-prepared MAX phases powders need to be as fresh as possible, and proper storage of the as-prepared MAX phases powders in a glove box (under argon or nitrogen protection) is highly recommended, especially for those MAX phases containing highly active M elements, for example Sc, Y, rare-earth (RE) elements, W, Zr, and Hf. For the as-prepared bulk samples, a surface oxide layer and/or a carbide layer is usually formed during the high-temperature synthesis process, which needs to be removed by grinding paper. An example is shown in Figure 2.6, which depicts a top view of an *i*-MAX $(Mo_{2/3}Sc_{1/3})_2AlC$ lightly dense sample, the inner part of the sample (grey part) comprised of the *i*-MAX phase while the outer part (black part) consists of the secondary phase $ScAl_3C_3$.

Grain size selection: The MAX phase grain size is an important factor in determining the size and quality of the MXene produced. MAX phase size selection is generally done by sieving; however, this method provides a wide range of particle sizes, which can affect the quality and yield of the MXene produced; longer etching time will result in higher yield but the smaller grains will be over-etched

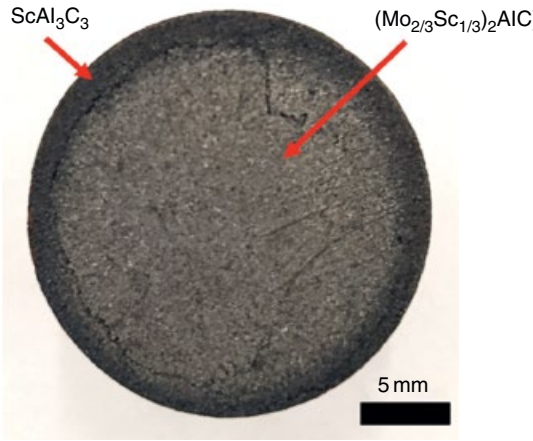


Figure 2.6 Top view digital image of lightly dense sintered *i*-MAX $(Mo_{2/3}Sc_{1/3})_2AlC$ sample (unpublished).

producing flakes with lots of defects, while on the other hand shorter etching durations is not sufficient for etching the large grains hence decreasing the yield of MXene. To narrow down the grain size range, Zhang et al. dispersed Ti_3AlC_2 powder in water of a certain height, and from the fact that grains with different size have different weights and therefore will sediment in different times, they used the equation: $v = \frac{2(\rho_p - \rho_f)gR^2}{9\mu}$ where g is the gravitational acceleration ($m\,s^{-2}$), R is the radius of the spherical particle, ρ_p is the mass density of the MAX phase particles, ρ_f is the mass density of water, and μ is the dynamic velocity of water [70]. Using this method, particles between 40 and 10 μm in grain size were selected resulting in MXene flakes of an average lateral size of 10 ± 2.1 μm. MXene freestanding films produced using these large flakes showed a higher flexibility and about 40% increase in the bending times before cracking, and a small change in the electronic resistivity after bending compared to films made of smaller Ti_3C_2 flakes.

Pre-treatment of precursor before etching: Besides proper storage, pre-treatment of the MAX phases precursor is needed for some specified etching methods or processes. Generally, when etching in relatively mild etchants, pre-treatment of the precursors in dilute HCl or HF for up to 20 minutes could help with the removal of the surface oxides and facilitate the concomitant etching process. In addition, pre-treatment also can be used to improve the phase purity of the as-prepared powder precursors by dissolving some intermetallic secondary phases. For example, for the etching of Ti_3AlC_2 MAX phase in mild TMAOH organic base at room temperature [71], pre-treatment of the Ti_3AlC_2 MAX phase powder in

dilute HF solution for up to 20 minutes is required for surface oxide removal. Moreover, in the synthesis processes where excess amount A elements were used, pre-treatment in acids to remove residual A elements is required, for example, residual Ga needs to be removed in synthesized Mo_2Ga_2C [72]. To properly perform the pre-treatment, complementary XRD and SEM characterization before and after pre-treatment is required.

2.2.2 *i*-MAX Phases

In addition to the points mentioned under Section 2.1, special care should be taken when synthesizing the in-plane chemically ordered *i*-MAX phases, that is, the precursors of the MXenes with ordered vacancies. In order to successfully produce *i*-MXene, it is essential to maintain the M′ to M″ molar ratio as close as possible to the ideal ratio (2 : 1). The amounts of the starting elements or compounds should correspond to the ideal molar ratio of the *i*-MAX; increasing the amount of M″ would lead to the complete dissolution of the *i*-MAX phase [73]. Moreover, the *i*-MAX phase yield can be increased by using compounds as a starting material instead of elemental powders. For example, the yield of $(Mo_{2/3}Y_{1/3})_2AlC$ and $(W_{2/3}Y_{1/3})_2AlC$ was increased by 40 [74] and 31 wt% (unpublished results), respectively, when staring with $AlY_{2.23}$ instead of elemental Al and Y using PLS technique. Similar results were also obtained for $(W_{2/3}Y_{1/3})_2AlC$, $(Mo_{2/3}Y_{1/3})_2AlC$, and $(Cr_{2/3}Y_{1/3})_2AlC$ using Hot Isostatic Press (HIP) [67]. Figure 2.7 shows SEM images of as-prepared $Mo_{4/3}Gd_{2/3}AlC$ *i*-MAX grains synthesized by the PLS method. Notably, the layered morphology is not as obvious compared to that of traditional ternary MAX phases.

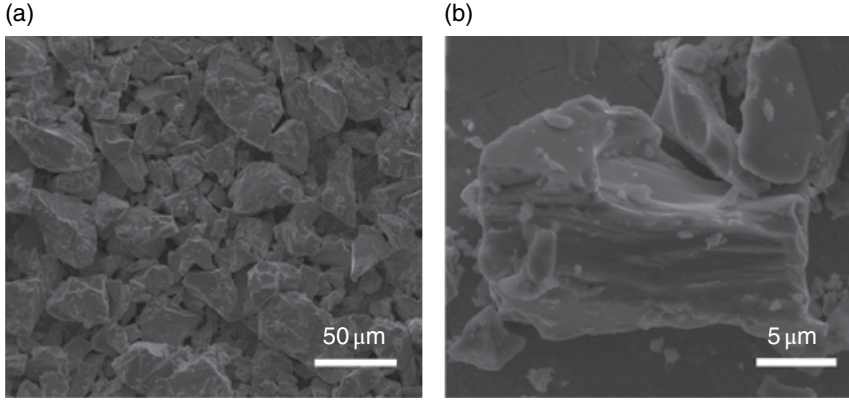


Figure 2.7 (a, b) SEM images of as-prepared $Mo_{4/3}Gd_{2/3}AlC$ *i*-MAX grains prepared by the PLS method (unpublished).

2.2.3 Mo_2Ga_2C and Zr/Hf-based Carbides

Generally, the synthesis methods for Zr/Hf-based laminated carbides are similar to those for traditional MAX phase synthesis mentioned above. Specifically, as the area for the formation of Zr/Hf-based laminated carbides in the phase diagram is even narrower than for the typical MAX phase, and the formation temperature for Zr/Hf-based laminated carbides are higher than those of MAX phases (1600–1900 °C), HP and SPS methods are mainly used for the synthesis. An additional amount of Al (up to 10 at%) is commonly used for the synthesis, probably to compensate for the evaporation loss of the low melting point Al during the synthesis process. Moreover, sub-stoichiometric quantities of carbon (up to 5 at%) are also employed to reduce the formation of secondary phases, and also to count the possible diffusion of carbon from the graphite mold during the synthesis process. Bulk $Zr_3Al_3C_5$ samples were first produced by SPS of Zr/Al/C powder mixture (Zr : Al : C = 3 : 3.2 : 4.8) at 1700 °C for 20 minutes, followed by crushing and milling steps to obtain $Zr_3Al_3C_5$ fine powders, and then served as a precursor for the synthesis of Zr_3C_2 MXene.

The synthesis of Ga-based ternary laminated carbides such as Mo_2Ga_2C requires a lower synthesis temperature than traditional MAX phases (600 °C to 900 °C), and it should be noted that the temperature range for the formation of those two phases is very narrow, about 50 °C–100 °C, and Mo_2GaC is stable at higher temperatures compared to Mo_2Ga_2C [75, 76]. The starting materials for both phases are usually Mo_2C and elemental Ga. It is rather difficult to ensure having a homogenous mixture of the starting materials as liquid Ga does not mix well with the Mo_2C powder. To achieve a higher degree of homogeneity, it is recommended to take the sample out of the furnace after half the sintering duration, crush the sample and put it back in the furnace. The amount of Ga is an influential factor for the synthesis of high-purity phases, and a ratio of 1 Mo_2C to 5 Ga was found to produce the highest purity Mo_2Ga_2C [77]. To reduce the loss of Ga during sintering, it is best to have the sample vacuum sealed in a quartz tube. The sintering reaction for the formation of those phase is slower than for traditional MAX phases; to obtain high purity Mo_2Ga_2C the sintering must proceed for several days up to a week for a more than 95 wt% pure sample. After sintering, excess Ga is removed by soaking the samples in hydrochloric acid.

References

1 Rohde, H. and Kudielka, H. (1960). Strukturuntersuchungen an Carbosulfiden von Titan und Zirkon. *Zeitschrift für Kristallographie* 114 (1-6): 447–456.

2 Jeitschko, W., Nowotny, H., and Benesovsky, F. (1963). Kohlenstoffhaltige ternäre Verbindungen (V-Ge-C, Nb-Ga-C, Ta-Ga-C, Ta-Ge-C, Cr-Ga-C und Cr-Ge-C). *Monatshefte für Chemie / Chemical Monthly* 94 (5): 844–850.

3 Anasori, B., Dahlqvist, M., Halim, J. et al. (2015). Experimental and theoretical characterization of ordered MAX phases Mo_2TiAlC_2 and $Mo_2Ti_2AlC_3$. *Journal of Applied Physics* 118 (9): 094304.

4 Liu, Z., Wu, E., Wang, J. et al. (2014). Crystal structure and formation mechanism of $(Cr_{2/3}Ti_{1/3})_3AlC_2$ MAX phase. *Acta Materialia* 73: 186–193.

5 Tao, Q., Dahlqvist, M., Lu, J. et al. (2017). Two-dimensional $Mo_{1.33}C$ MXene with divacancy ordering prepared from parent 3D laminate with in-plane chemical ordering. *Nature Communications* 8: 14949.

6 Du, Z., Wu, C., Chen, Y. et al. (2021). High-entropy atomic layers of transition-metal carbides (MXenes). *Advanced Materials* 33 (39): 2101473.

7 Nemani, S.K., Zhang, B., Wyatt, B.C. et al. (2021). High-entropy 2D carbide MXenes: $TiVNbMoC_3$ and $TiVCrMoC_3$. *ACS Nano* 15 (8): 12815–12825.

8 Du, Z., Wu, C., Chen, Y. et al. (2021). High-entropy carbonitride MAX phases and their derivative MXenes. *Advanced Energy Materials* 12 (6): 2103228.

9 Zhou, J., Tao, Q., Ahmed, B. et al. (2022). High-entropy laminate metal carbide (MAX phase) and its two-dimensional derivative MXene. *Chemistry of Materials* 34 (5): 2098–2106.

10 Barsoum, M.W. (2013). *MAX Phases, Properties of Machinable Ternary Carbides and Nitrides*. New York: Wiley.

11 Farle, A.-S., Kwakernaak, C., van der Zwaag, S., and Sloof, W.G. (2015). A conceptual study into the potential of $M_{n+1}AX_n$-phase ceramics for self-healing of crack damage. *Journal of the European Ceramic Society* 35 (1): 37–45.

12 Sokol, M., Natu, V., Kota, S., and Barsoum, M.W. (2019). On the chemical diversity of the MAX phases. *Trends in Chemistry* 1 (2): 210–223.

13 Naguib, M., Kurtoglu, M., Presser, V. et al. (2011). Two-dimensional nanocrystals produced by exfoliation of Ti_3AlC_2. *Advanced Materials* 23 (37): 4248–4253.

14 Naguib, M., Mashtalir, O., Carle, J. et al. (2012). Two-dimensional transition metal carbides. *ACS Nano* 6 (2): 1322–1331.

15 Li, M., Lu, J., Luo, K. et al. (2019). Element replacement approach by reaction with lewis acidic molten salts to synthesize nanolaminated MAX phases and MXenes. *Journal of the American Chemical Society* 141 (11): 4730–4737.

16 Naguib, M., Halim, J., Lu, J. et al. (2013). New two-dimensional niobium and vanadium carbides as promising materials for Li-ion batteries. *Journal of the American Chemical Society* 135 (43): 15966–15969.

17 Meshkian, R., Näslund, L.-Å., Halim, J. et al. (2015). Synthesis of two-dimensional molybdenum carbide, Mo_2C, from the gallium based atomic laminate Mo_2Ga_2C. *Scripta Materialia* 108: 147–150.

18 Soundiraraju, B. and George, B.K. (2017). Two-dimensional titanium nitride (Ti_2N) MXene: synthesis, characterization, and potential application as surface-enhanced Raman scattering substrate. *ACS Nano* 11 (9): 8892–8900.

19 Alhabeb, M., Maleski, K., Mathis, T.S. et al. (2018). Selective etching of silicon from Ti_3SiC_2 (MAX) to obtain 2D titanium carbide (MXene). *Angewandte Chemie International Edition* 57 (19): 5444–5448.

20 Zhou, J., Zha, X., Chen, F.Y. et al. (2016). A two-dimensional zirconium carbide by selective etching of Al_3C_3 from nanolaminated $Zr_3Al_3C_5$. *Angewandte Chemie* 128 (16): 5092–5097.

21 Zhou, J., Zha, X., Zhou, X. et al. (2017). Synthesis and electrochemical properties of two-dimensional Hafnium Carbide. *ACS Nano* 11 (4): 3841–3850.

22 Ghidiu, M., Naguib, M., Shi, C. et al. (2014). Synthesis and characterization of two-dimensional Nb_4C_3 (MXene). *Chemical Communications* 50 (67): 9517–9520.

23 Tran, M.H., Schäfer, T., Shahraei, A. et al. (2018). Adding a new member to the MXene family: synthesis, structure, and electrocatalytic activity for the hydrogen evolution reaction of $V_4C_3T_x$. *ACS Applied Energy Materials* 1 (8): 3908–3914.

24 Urbankowski, P., Anasori, B., Makaryan, T. et al. (2016). Synthesis of two-dimensional titanium nitride Ti_4N_3 (MXene). *Nanoscale* 8 (22): 11385–11391.

25 Han, M., Maleski, K., Shuck, C.E. et al. (2020). Tailoring electronic and optical properties of MXenes through forming solid solutions. *Journal of the American Chemical Society* 142 (45): 19110–19118.

26 Shen, Z., Wang, Z., Zhang, M. et al. (2018). A novel solid-solution MXene $(Ti_{0.5}V_{0.5})_3C_2$ with high catalytic activity for hydrogen storage in MgH_2. *Materialia* 1: 114–120.

27 Rigby-Bell, M.T.P., Natu, V., Sokol, M. et al. (2021). Synthesis of new M-layer solid-solution 312 MAX phases $(Ta_{1-x}Ti_x)_3AlC_2$ ($x = 0.4$, 0.62, 0.75, 0.91 or 0.95), and their corresponding MXenes. *RSC Advances* 11 (5): 3110–3114.

28 Yang, J., Naguib, M., Ghidiu, M. et al. (2016). Two-dimensional Nb-based M_4C_3 solid solutions (MXenes). *Journal of the American Ceramic Society* 99 (2): 660–666.

29 Pinto, D., Anasori, B., Avireddy, H. et al. (2020). Synthesis and electrochemical properties of 2D molybdenum vanadium carbides – solid solution MXenes. *Journal of Materials Chemistry A* 8 (18): 8957–8968.

30 Cai, P., He, Q., Wang, L. et al. (2019). Two-dimensional Nb-based $M_4C_3T_x$ MXenes and their sodium storage performances. *Ceramics International* 45 (5): 5761–5767.

31 Deysher, G., Shuck, C.E., Hantanasirisakul, K. et al. (2020). Synthesis of Mo_4VAlC_4 MAX phase and two-dimensional Mo_4VC_4 MXene with five atomic layers of transition metals. *ACS Nano* 14 (1): 204–217.

32 Meshkian, R., Tao, Q., Dahlqvist, M. et al. (2017). Theoretical stability and materials synthesis of a chemically ordered MAX phase, Mo_2ScAlC_2, and its two-dimensional derivate Mo_2ScC_2 MXene. *Acta Materialia* 125: 476–480.

33 Anasori, B., Xie, Y., Beidaghi, M. et al. (2015). Two-dimensional, ordered, double transition metals carbides (MXenes). *ACS Nano* 9 (10): 9507–9516.

34 Persson, I., Ghazaly, A.E., Tao, Q. et al. (2018). Tailoring structure, composition, and energy storage properties of MXenes from selective etching of in-plane, chemically ordered MAX phases. *Small* 14: 1703676.

35 Halim, J., Palisaitis, J., Lu, J. et al. (2018). Synthesis of two-dimensional $Nb_{1.33}C$ (MXene) with randomly distributed vacancies by etching of the quaternary solid solution $(Nb_{2/3}Sc_{1/3})_2AlC$ MAX phase. *ACS Applied Nano Materials* 1 (6): 2455–2460.

36 Thörnberg, J., Halim, J., Lu, J. et al. (2019). Synthesis of $(V_{2/3}Sc_{1/3})_2AlC$ *i*-MAX phase and $V_{2-x}C$ MXene scrolls. *Nanoscale* 11 (31): 14720–14726.

37 Yang, J., Yao, G., Sun, S. et al. (2021). Structural, magnetic properties of in-plane chemically ordered $(Mo_{2/3}R_{1/3})_2AlC$ (R = Gd, Tb, Dy, Ho, Er and Y) MAX phase and enhanced capacitance of $Mo_{1.33}C$ MXene derivatives. *Carbon* 179: 104–110.

38 Meshkian, R., Lind, H., Halim, J. et al. (2019). Theoretical analysis, synthesis, and characterization of 2D $W_{1.33}C$ (MXene) with ordered vacancies. *ACS Applied Nano Materials* 2 (10): 6209–6219.

39 Meshkian, R., Dahlqvist, M., Lu, J. et al. (2018). W-based atomic laminates and their 2D derivative $W_{1.33}C$ MXene with vacancy ordering. *Advanced Materials* 30: 1706409.

40 Yang, J., Liu, R., Jia, N. et al. (2021). Novel W-based in-plane chemically ordered $(W_{2/3}R_{1/3})_2AlC$ (R = Gd, Tb, Dy, Ho, Er, Tm and Lu) MAX phases and their 2D $W_{1.33}C$ MXene derivatives. *Carbon* 183: 76–83.

41 Dahlqvist, M., Petruhins, A., Lu, J. et al. (2018). Origin of chemically ordered atomic laminates (*i*-MAX): expanding the elemental space by a theoretical/experimental approach. *ACS Nano* 12 (8): 7761–7770.

42 Zhou, W.B., Mei, B.C., Zhu, J.Q., and Hong, X.L. (2005). Rapid synthesis of Ti_2AlC by spark plasma sintering technique. *Materials Letters* 59 (1): 131–134.

43 Benitez, R., Kan, W.H., Gao, H. et al. (2016). Room temperature stress-strain hysteresis in Ti_2AlC revisited. *Acta Materialia* 105: 294–305.

44 Zhou, W., Li, K., Zhu, J., and Tian, S. (2018). Rapid synthesis of highly pure Nb_2AlC using the spark plasma sintering technique. *Journal of Physics and Chemistry of Solids* 120: 218–222.

45 Mathis, T.S., Maleski, K., Goad, A. et al. (2021). Modified MAX phase synthesis for environmentally stable and highly conductive Ti_3C_2 MXene. *ACS Nano* 15 (4): 6420–6429.

46 Badie, S., Dash, A., Sohn, Y.J. et al. (2021). Synthesis, sintering, and effect of surface roughness on oxidation of submicron Ti_2AlC ceramics. *Journal of the American Ceramic Society* 104 (4): 1669–1688.

47 Peng, C., Wang, C.-A., Song, Y., and Huang, Y. (2006). A novel simple method to stably synthesize Ti_3AlC_2 powder with high purity. *Materials Science and Engineering: A* 428 (1): 54–58.

48 Tzenov, N.V. and Barsoum, M.W. (2000). Synthesis and characterization of Ti_3AlC_2. *Journal of the American Ceramic Society* 83 (4): 825–832.

49 Gauthier-Brunet, V., Cabioc'h, T., Chartier, P. et al. (2009). Reaction synthesis of layered ternary Ti_2AlC ceramic. *Journal of the European Ceramic Society* 29 (1): 187–194.

50 Hendaoui, A., Vrel, D., Amara, A. et al. (2009). A novel method for synthesis of low-cost Ti-Al-C-based cermets. *International Journal of Self-Propagating High-Temperature Synthesis* 18 (4): 267–272.

51 Jolly, S., Paranthaman, M.P., and Naguib, M. (2021). Synthesis of $Ti_3C_2T_z$ MXene from low-cost and environmentally friendly precursors. *Materials Today Advances* 10: 100139.

52 Li, C., Kota, S., Hu, C., and Barsoum, M.W. (2016). On the synthesis of low-cost, titanium-based MXenes. *Journal of Ceramic Science and Technology* 7 (3): 301–306.

53 Istomin, P., Istomina, E., Nadutkin, A. et al. (2017). Fabrication of Ti_3SiC_2 and Ti_4SiC_3 MAX phase ceramics through reduction of TiO_2 with SiC. *Ceramics International* 43 (18): 16128–16135.

54 Istomin, P., Istomina, E., Nadutkin, A. et al. (2016). Synthesis of a bulk Ti_4SiC_3 MAX phase by reduction of TiO_2 with SiC. *Inorganic Chemistry* 55 (21): 11050–11056.

55 Lapauw, T., Halim, J., Lu, J. et al. (2016). Synthesis of the novel Zr_3AlC_2 MAX phase. *Journal of the European Ceramic Society* 36 (3): 943–947.

56 Lapauw, T., Lambrinou, K., Cabioc'h, T. et al. (2016). Synthesis of the new MAX phase Zr_2AlC. *Journal of the European Ceramic Society* 36 (8): 1847–1853.

57 Lapauw, T., Tunca, B., Cabioc'h, T. et al. (2016). *Synthesis of MAX phases in the Hf–Al–C system. Inorganic Chemistry* 55 (21): 10922–10927.

58 Shuck, C.E., Han, M., Maleski, K. et al. (2019). Effect of Ti_3AlC_2 MAX phase on structure and properties of resultant $Ti_3C_2T_x$ MXene. *ACS Applied Nano Materials* 2 (6): 3368–3376.

59 Barsoum, M.W. (2000). The $M_{N+1}AX_N$ phases: a new class of solids; thermodynamically stable nanolaminates. *Progress in Solid State Chemistry* 28 (1-4): 201–281.

60 Mingxing, A., Hongxiang, Z., Yang, Z. et al. (2006). Synthesis of Ti_3AlC_2 powders using Sn as an additive. *Journal of the American Ceramic Society* 89 (3): 1114–1117.

61 Gonzalez-Julian, J. (2021). Processing of MAX phases: from synthesis to applications. *Journal of the American Ceramic Society* 104 (2): 659–690.

62 Alhabeb, M., Maleski, K., Anasori, B. et al. (2017). Guidelines for synthesis and processing of two-dimensional titanium carbide ($Ti_3C_2T_x$ MXene). *Chemistry of Materials* 29 (18): 7633–7644.

63 Halim, J., Lukatskaya, M.R., Cook, K.M. et al. (2014). Transparent conductive two-dimensional titanium carbide epitaxial thin films. *Chemistry of Materials* 26 (7): 2374–2381.

64 Hossein-Zadeh, M., Ghasali, E., Mirzaee, O. et al. (2019). An investigation into the microstructure and mechanical properties of V_2AlC MAX phase prepared by microwave sintering. *Journal of Alloys and Compounds* 795: 291–303.

65 Guan, C. (2016). Synthesis of fine and high purity Cr_2AlC powders by novel method. *Advances in Applied Ceramics* 115 (8): 505–508.

66 Liu, W., Qiu, C., Zhou, J. et al. (2015). Fabrication of Ti_2AlN ceramics with orientation growth behavior by the microwave sintering method. *Journal of the European Ceramic Society* 35 (5): 1385–1391.

67 ElMelegy, T.A., Sokol, M., and Barsoum, M.W. (2021). Enhanced yield synthesis of bulk dense $(M_{2/3}Y_{1/3})_2AlC$ (M= Cr, W, Mo) in-plane chemically ordered quaternary atomically laminated i-MAX phases and oxidation of $(Cr_{2/3}Y_{1/3})_2AlC$ and $(Mo_{2/3}Y_{1/3})_2AlC$. *Journal of Alloys and Compounds* 867: 158930.

68 Miranda, A., Halim, J., Barsoum, M.W., and Lorke, A. (2016). Electronic properties of freestanding $Ti_3C_2T_x$ MXene monolayers. *Applied Physics Letters* 108 (3): 033102.

69 Cao, H., Escamilla, M., Anas, M. et al. (2021). Synthesis and electronic applications of particle-templated $Ti_3C_2T_z$ MXene–polymer films via pickering emulsion polymerization. *ACS Applied Materials & Interfaces* 13 (43): 51556–51566.

70 Zhang, J., Kong, N., Uzun, S. et al. (2020). Scalable manufacturing of free-standing, strong $Ti_3C_2T_x$ MXene films with outstanding conductivity. *Advanced Materials* 32 (23): 2001093.

71 Xuan, J., Wang, Z., Chen, Y. et al. (2016). Organic-base-driven intercalation and delamination for the production of functionalized titanium carbide nanosheets with superior photothermal therapeutic performance. *Angewandte Chemie International Edition* 55 (47): 14569–14574.

72 Halim, J., Kota, S., Lukatskaya, M.R. et al. (2016). Synthesis and characterization of 2D molybdenum carbide (MXene). *Advanced Functional Materials* 26 (18): 3118–3127.

73 Mockute, A., Tao, Q., Dahlqvist, M. et al. (2019). Materials synthesis, neutron powder diffraction, and first-principles calculations of $(Mo_xSc_{1-x})_2AlC$ *i*-MAX phase used as parent material for MXene derivation. *Physical Review Materials* 3 (11): 113607.

74 Halim, J., Etman, A.S., Elsukova, A. et al. (2020). Tailored synthesis approach of $(Mo_{2/3}Y_{1/3})_2AlC$ *i*-MAX and its two-dimensional derivative $Mo_{1.33}CT_z$ MXene: enhancing the yield, quality, and performance in supercapacitor applications. *Nanoscale* 13 (1): 311–319.

75 Hu, C., Lai, C.C., Tao, Q. et al. (2015). Mo_2Ga_2C: a new ternary nanolaminated carbide. *Chemical Communications* 51 (30): 6560–6563.

76 Hu, C., Li, C., Halim, J. et al. (2015). On the rapid synthesis of the ternary Mo_2GaC. *Journal of the American Ceramic Society* 98 (9): 2713–2715.

77 He, H., Jin, S., Fan, G. et al. (2018). Synthesis mechanisms and thermal stability of ternary carbide Mo_2Ga_2C. *Ceramics International* 44 (18): 22289–22296.

3

Guidelines on Fluorine-based Synthesis of MXenes

Annabelle Bedford[1,2], Brian C. Wyatt[2], Wyatt J. Highland[2], Srinivasa Kartik Nemani[2], Krista K. Pulley[2], Jonah Jordan[2], and Babak Anasori[1,2,3]

[1] *School of Materials Engineering, Purdue University, West Lafayette, IN, USA*
[2] *Department of Mechanical and Energy Engineering, and Integrated Nanosystems Development Institute (INDI), Indiana University-Purdue University, Indianapolis, IN, USA*
[3] *School of Mechanical Engineering, Purdue University, West Lafayette, IN, USA*

3.1 Introduction

The story of MXenes began when Dr. Yury Gogotsi and Dr. Michel Barsoum at Drexel University responded to a call for proposals from the United States Department of Energy seeking alternatives to graphite to be used as anode materials in Li-ion batteries [1]. They proposed that a family of layered transition metal carbides, called MAX phases [2], which displayed favorable electrical conductivity and a relatively high oxidation resistance, may yield promising results. Their hypothesis was based on the knowledge that the A-group elements in MAX phases were capable of alloying with lithium (Li), which may possibly form anodes with a high gravimetric capacity. After initial experimentation with the as-synthesized MAX phases failed to compare to theoretical results, the team looked to both decrease the size of the MAX particles and introduce vacancies within the A layer to better allow for Li insertion.

One of the techniques Barsoum's group used in the synthesis of fully dense MAX phases was hot isostatic pressing (HIPing), where the MAX samples were embedded in glass during the HIP-ing process. After pressing and removing of the sample, the products were usually encased in a layer of glass, and a hydrofluoric acid (HF) solution was used in order to dissolve this glass layer [3]. While it was known that HF does not dissolve the fully dense MAX phase sintered block [3], it was understood that leaving the pressed MAX in the concentrated HF solution for too

Transition Metal Carbides and Nitrides (MXenes) Handbook: Synthesis, Processing, Properties and Applications, First Edition. Edited by Chuanfang Zhang and Michael Naguib.
© 2024 John Wiley & Sons, Inc. Published 2024 by John Wiley & Sons, Inc.

long would cause the dense block to disintegrate into powder. Citing this, M. Naguib suggested the use of HF may serve to further decrease the particle size of the MAX while also achieving full or partial etching of the A layers [1]. Additionally, HF is one of the few etchants capable of dissolving titanium oxide, which often forms on the surface of Ti-containing MAX phases. The team's experimentation with Ti_2AlC and later Ti_3AlC_2 confirmed the successful etching of the A element from the structure, resulting in a graphene-like 2D morphology [4, 5]. As such, the material was named MXene. Because Ti_3AlC_2 and Ti_2AlC are members of a much larger group of transition metal carbides and nitrides, tuning of these etching conditions has allowed for the synthesis of now over 50 different MXene compositions [6], cementing MXenes as members of the 2D material world.

MAX phases are defined as transition metal carbides and nitrides in a hexagonal crystal structure that follow the general chemical formula of $M_{n+1}AX_n$ ($n = 1$–4), where M represents $n + 1$ layers of one or more transition metals from the 3d–5d block of the periodic table of groups 3–6, A represents a layer of one or more A-group elements from groups 11–16 of the periodic table, and X represents n layers of carbon and/or nitrogen interleaving the M layers in their octahedral interstitial sites [7, 8]. MAX phases exhibit bonding between the M and X elements and relatively weaker bonds between the M and the A elements. It is this layering of covalently and ionically bonded M—X and the metallically bonded M—A layers that allow for the etching of MAX phases into MXene when MAX particles are introduced to a corrosive fluorine-containing (F-containing) environment. The first MXene, $Ti_3C_2T_x$, was synthesized via the selective etching of Al from a Ti_3AlC_2 MAX phase using HF, and since then, fluorine-containing solutions, due to their selectivity to break the M—A bonds and etch out the A-layer, have been integral in the production of many MXenes [5]. However, since direct HF (~50 wt%) has environmental and safety risks, the use of a lower concentration of HF mixed with hydrochloric acid (HCl) [9], or the *in-situ* formation of HF via the hydrolysis of fluoride-containing salts [10] or the reaction between fluoride salts with weaker acids, such as HCl [11], have become a commonly used alternative to make the synthesis of MXenes safer and more widely accessible [11, 12]. Figure 3.1 illustrates a schematic representation of the etching of various MAX phases with the variety in elements possible in $M_{n+1}AX_n$ ($n = 1$–4) to MXenes, illustrating an example of a fluorine molecule reaction with Al during etching to form byproduct AlF_3.

However, to date, HF etchants, including *in-situ* HF-forming and direct HF, are the most common etchants used in the top-down liquid exfoliation of MXenes from their MAX precursor [13]. The use of these HF etching techniques has allowed for the successful synthesis of over 50 different MXene compositions [6]. In this chapter, first we focus on the fundamental bonding within the MAX structure that allows A elements to be selectively removed from MAX without impacting the M—X structure. Second, we focus on the fundamentals of why F-containing compounds

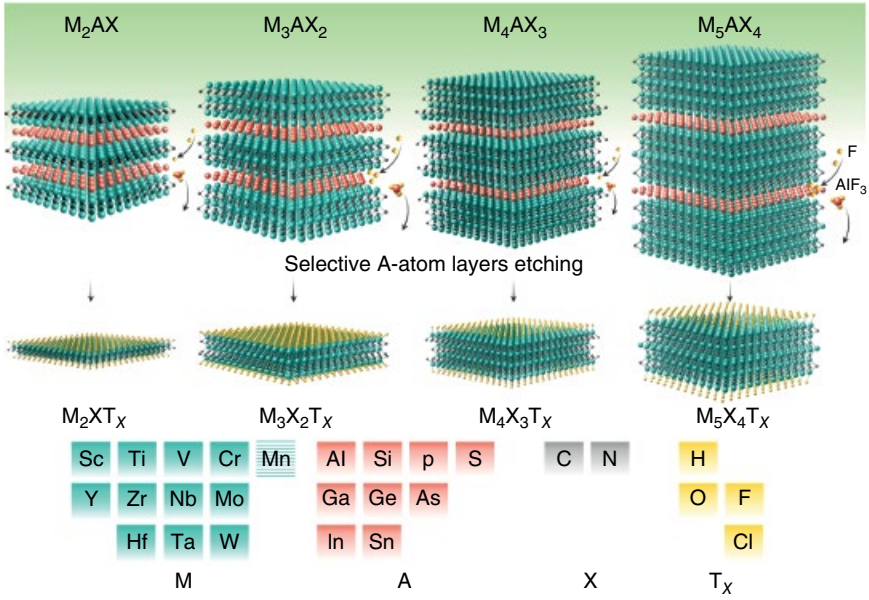


Figure 3.1 Schematic representation of the etching of various MAX phases of $M_{n+1}AX_n$ (n = 1–4) to MXenes. Also shown is an example of fluorine reaction with Al during etching to form byproduct AlF_3. The various compositions of M, A, X, and T_x are shown with matching colors to their possible atom sites. Manganese (Mn) has horizontal bars as its background as it exists in MAX phases but has not been isolated in MXenes through traditional synthesis methods yet.

can selectively remove A groups from the precursor structures. After that, we present the various MAX structures that can be used to form MXenes via HF selective etching. Lastly, we discuss the environmental and safety impacts of using HF and discuss methods to improve their safety for future research in MXenes.

3.2 M—A vs. M—X Bonding Roles in Fluorine-based Synthesis

To understand the fundamentals in fluorine-based (F-based) synthesis, it is important to start with the fundamental bonding behavior in MXenes' precursor, MAX phases. In general, MAX phases exhibit strong bonding between the M and X elements and weaker bonding between the M and the A elements. It is this layering of strongly bonded M—X pairs with comparatively weaker bonding of M—A layers in the out-of-plane direction that allows for the selective etching of MAX phases into MXene flakes when MAX particles are introduced to a corrosive F-containing

environment. Specifically, in the M—X bond, the electrons in the *d* orbital of the M atoms are shared with the electrons in the *p* orbital of the X atoms, which makes this a strong mixed ionic-covalent bond. This is in contrast to M—A bonding, which is metallic due to overlapping *d*-*p* bands in M and A, respectively, which results in weaker bonding as compared to M—X [14]. The comparative bonding between stronger M—X and weaker M—A is what permits selective etching of the A group elements by immersion in an F-containing solvent to yield MXenes from their precursor phases.

Since MAX phases have such a wide array of chemical diversity [7], many different types of MXenes have been synthesized with several more predicted to be capable of synthesis [15]. In general, M—A pairs with relatively long bond lengths, indicating lower bonding energies, paired with M—X bonds that are relatively short bond lengths, indicating higher bonding energies, are necessary to exfoliate MAX phases into MXene flakes, as calculated by exfoliation energy as shown in Figure 3.2 [15]. For example, $Ti_3C_2T_x$ is readily synthesized from both Ti_3AlC_2 and Ti_3SiC_2 MAX phases; however, as Ti—Si is a stronger M—A bond than Ti—Al, Ti_3SiC_2 has a comparatively higher exfoliation energy of $0.186\,eV\,Å^{-2}$ while Ti_3AlC_2 has an exfoliation energy of $0.164\,eV\,Å^{-2}$ [15]. This trend in exfoliation is matched with experimental observations, where Ti_3SiC_2 requires relatively harsher etching conditions (30% $HF + H_2O_2$, 47 hours, 40 °C) to non-complete etching as compared to near-complete etching using Ti_3AlC_2 (5% HF, 24 hours, 27 °C) [16, 17]. Similarly, nitride MAX phases show difficulty in synthesizing MXenes, as their exfoliation energies are typically higher than their carbide counterparts, such as a higher exfoliation energy of theoretical Ti_3AlN_2 of $0.195\,eV\,Å^{-2}$ as compared to the aforementioned Ti_3AlC_2 value of $0.164\,eV\,Å^{-2}$ [15]. This matches experimental observations, where a comparatively harsh molten solution of F-containing salts was necessary to successfully synthesize $Ti_4N_3T_x$ from its Ti_4AlN_3 MAX phase precursor [18]. Therefore, to choose MAX phases which may be exfoliated by immersion in F-containing solvents, careful analyses of the M—X and M—A bonding differences are necessary to choose MAX phases which may be exfoliated using F-based approaches. Next, we look to see how fluorine-containing solutions fundamentally interact with these M—X and M—A bonds to form MXene from their precursor phases.

3.3 Interactions of Fluorine with A-group Elements within Precursor Phases

After establishing the fundamentals of M—X and M—A bonding that permit selective etching and exfoliation of MAX phases into MXenes, we next look to the chemical HF interaction with these bonds to result in MXene. As we discussed, MXene

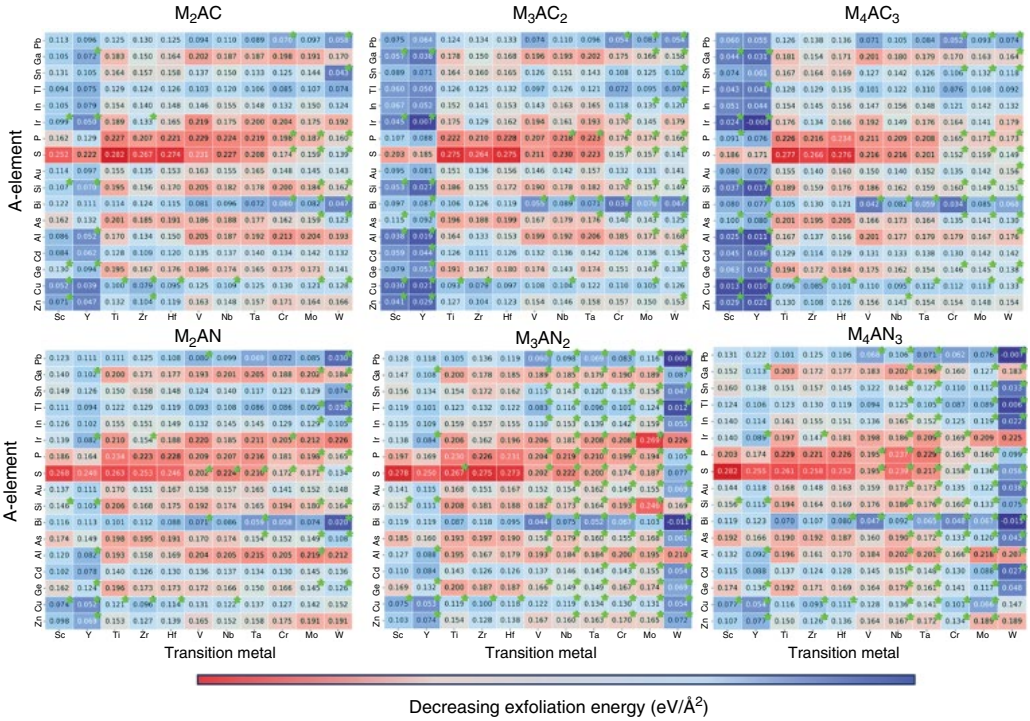


Figure 3.2 Calculated exfoliation energies for M_2AX, M_3AX_2, and M_4AX_3 structures across various compositions of M elements (bottom axis) and A elements (left-axis). The color range indicating a decreasing exfoliation energy, thus increased potential for successful MAX exfoliation to MXene, is shown in the color scale at the bottom. *Source:* Adapted from Khaledialidusti et al. [15].

synthesis has largely been accomplished through the use of fluorine-based compounds [6]. Fluorine-containing etchants are attractive for the synthesis of MXene as they play a key role in selectively etching A group elements from the precursor MAX phase. The mechanisms behind this etching have recently been a growing focus of the MXene community as the importance of the mechanistic perspective of etching is crucial to understanding how the process can be modified to create new MXenes and/or improve the environmental health and safety of the etching process [19].

The effects of F-containing solutions on many variations of MAX phases can be described stepwise. First, we focus on the HF reaction with the most commonly used MAX phase to make MXene, which is the Ti_3AlC_2 MAX phase. As seen in Figure 3.3, in the setting of Ti_3AlC_2 MAX immersed in an HF solution, HF disassociates into hydrogen (H^+) and fluorine (F^-) ions [20]. At first, the under-coordinated Ti atoms at the edge of Ti_3AlC_2 adsorb the H^+ and F^- ions [20]. After adsorption to the under-coordinated Ti atoms, F^- ions replace the H^+ ions and H^+ is lost in the form of H_2 gas [20]. These adsorbed F^- ions weaken the bond between Al and Ti [20], and cause a shift in the oxidation states of Al. As this oxidation state shifts and interlayer distance growth begins, interior Ti and Al atoms will become more accessible to other dissociated F^- ions. When these now under-coordinated Ti layers become exposed, further H^+ and F^- adsorption occurs to the Ti, which results in more significant Ti-interlayer repulsion between flakes. With the interlayer spacing continually enlarging, F^- ions are now able to continually intercalate and continue bonding with Al, which eventually results in its removal as AlF_3 [20]. This process then repeats itself as further Ti and Al atoms are exposed by continual interlayer expansion due to interlayer repulsion by now F-terminated Ti atoms. The capability of this under-coordination and interlayer expansion to

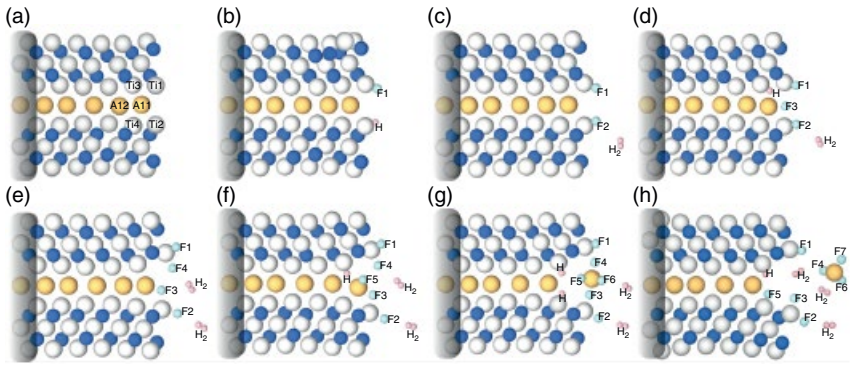


Figure 3.3 Stepwise process of aluminum exfoliation in Ti_3AlC_2 (a) with addition of one, (b) two, (c) three, (d) four, (e) five, (f) six, (g) and seven (h) HF molecules. *Source:* Srivastava et al. [20]/American Chemical Society.

continually etch further into the Al layers out of Ti_3AlC_2 to form $Ti_3C_2T_x$ MXene has been seen in transmission electron microscopy (TEM) studies on HF-etched, epitaxially grown Ti_3AlC_2 MAX (Figure 3.4) [21]. This formation of MXene out of MAX by the selective etching process to etch into the Al layers through continual interlayer expansion due to interlayer repulsion has shown to extend to other MAX phases, such as epitaxially grown V_2AlC to form V_2CT_x [22].

There are several aspects of this mechanistic analysis that exemplify how F-containing compounds allow for the creation of MXene. First, this process illustrates the important role of the H^+ and F^- ions in forming a continuous cycle of under-coordination of Ti and Al followed by interlayer repulsion in the complete etching of MAX phases to MXene flakes. However, it is noted that these processes have been known to work best when the A group element is aluminum, as the

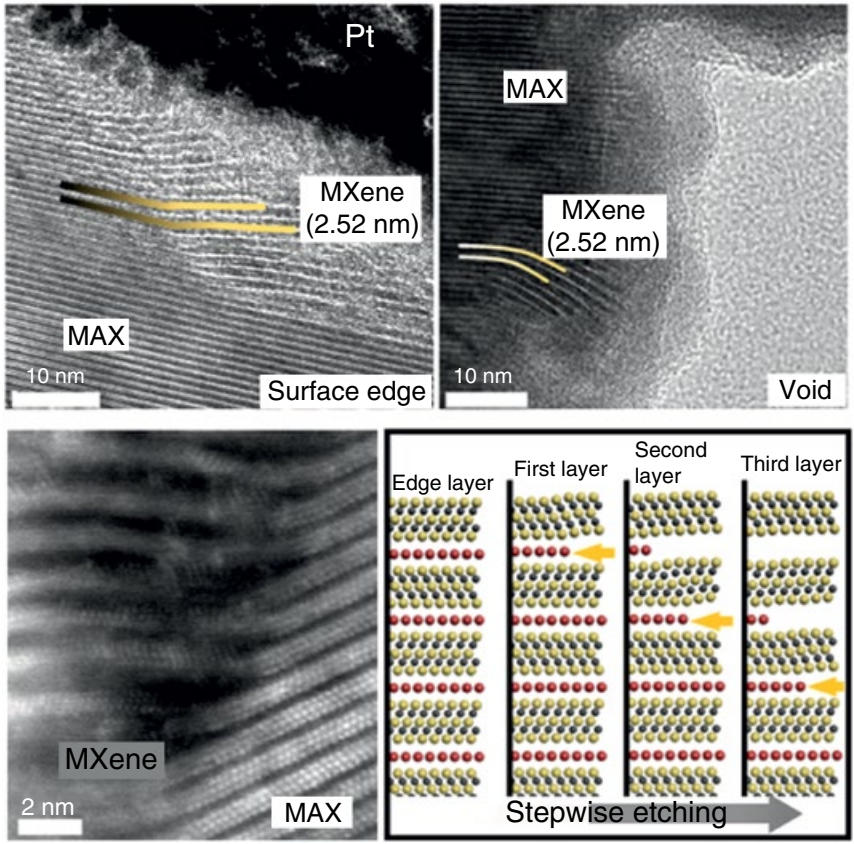


Figure 3.4 Continual etching of HF into the Al layers in Ti_3AlC_2 (MAX) to produce $Ti_3C_2T_x$ (MXene) is shown via transmission electron microscopy imaging. *Source:* Yong-Jae Kim et al. [21]/Reproduced from American Chemical Society.

majority of synthesized MXenes have been derived from aluminum-containing MAX phase precursors [13]. It is hypothesized that the reason most MXenes are synthesized from MAX phases with aluminum as the A group element is due to aluminum having a relatively low reduction potential and electronegativity (1.61) compared to other A group elements [23]. Indeed, Al has the lowest reduction potential compared to the other A-group elements, which might allow for continual under-coordination of the M and Al elements, followed by interlayer repulsion, as described for Ti_3AlC_2 that may be less energetically favorable in non-Al A group MAX phases.

In Al A-group MAX phases, time, temperature, and particle size play a crucial role in the final yield and success of the etching process. For example, in a study observing the effect of time and temperature conditions during etching, it was observed that the dominant Ti_3AlC_2 (002) peak, as measured using X-ray diffraction (XRD), loses intensity, which represents conversion to $Ti_3C_2T_x$ MXene, completely at 50 °C for 2 hours or room temperature (RT) for 15 hours, indicating complete conversion to $Ti_3C_2T_x$ in these conditions. It is important to note that changing the compositions of the MAX phases, such as varying elements and the number of layers, these conditions must be tuned to account for the etching parameters (particle size, composition, structure) of the different MAX phases. This is important because if complete exfoliation is not achieved, the final yield of the MXene and flake size is reduced by the unreacted MAX. For example, particle sizes between 38 and 58 µm can be completely etched in 50% aqueous HF at RT for 2 hours; however, when the particle is larger than 58 µm, the etching is incomplete [24]. This can be attributed to the stepwise nature of etching, which necessitates longer times for larger particles. Therefore, it is recommended that control of particle size will enable better reproducible results when it comes to etching MAX phases to MXenes. One option to achieve this is by using sedimentation processes and tuning centrifugation speeds. For example, it is reported that certain compositions of MAX phases, such as titanium carbonitrides ($Ti_2C_{0.5}N_{0.5}T_x$) are easier synthesized when the MAX particle size is controlled in this manner [25].

After establishing the fundamentals of HF etching of Al-containing MAX phases to form MXene, we next look to studies that do not involve Al as the A group element in MAX. For example, synthesis of MXene derived from silicon-containing Ti_3SiC_2 MAX phase had long been a challenge (Figure 3.5). This is thought to be due to the strong bonds between Ti—Si in Ti_3SiC_2 as compared to the bonding between Ti—Al Ti_3AlC_2 [26]. This results in a difference in etching behavior in HF solutions, as Ti_3SiC_2 results in a poor yield of $Ti_3C_2T_x$ as evidenced by X-ray diffractograms shown in Figure 3.5 [16]. However, previous studies on HF-based cleaning of Si have shown that with a mixture of HF and an oxidant, silicon can be etched in two major steps. The oxidant, such as H_2O_2, can first oxidize the Si and then HF will cause the dissolution of this Si-oxide [27]. This idea was carried over to the synthesis of Ti_3SiC_2-derived MXene

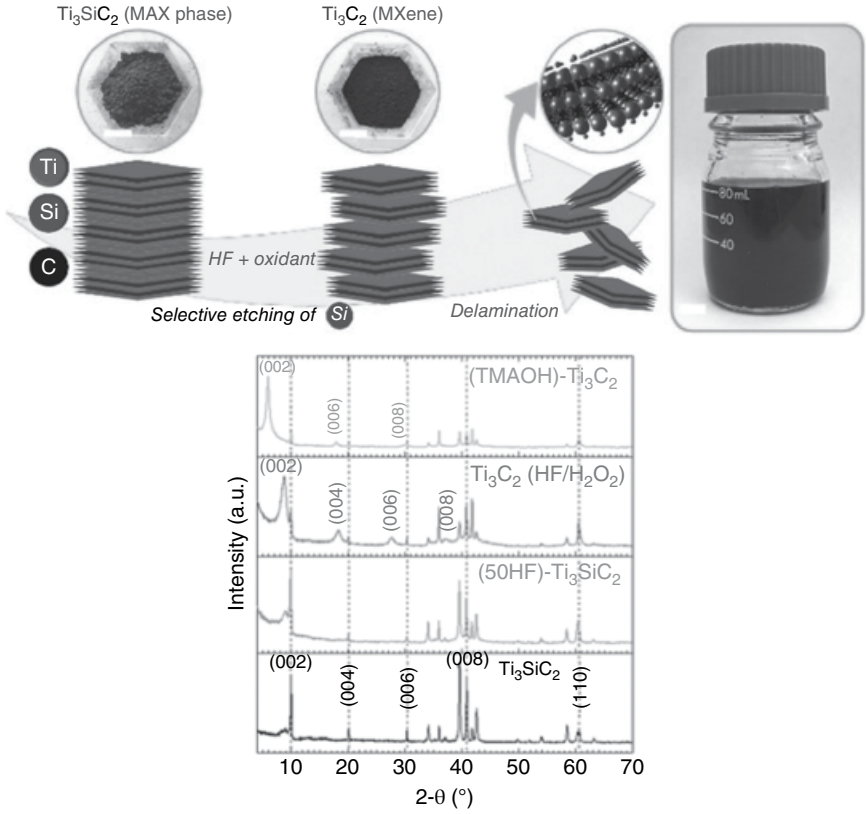


Figure 3.5 H_2O_2-oxidant assisted selective etching of Ti_3SiC_2. *Source:* Adapted from Alhabeb et al. [16]/Reproduced from John Wiley & Sons, Inc.

in 2018, which allowed for the exfoliation of silicon from the Ti_3SiC_2 structure [16]. With a mixture of HF and H_2O_2, Si was selectively etched from Ti_3SiC_2 to create $Ti_3C_2T_x$ MXene. When comparing this to Ti_3AlC_2-derived MXene described in the previous section, it is likely that the stronger bonding between Ti—Si as compared to Ti—Al limits the same cycle of under-coordination and/or interlayer expansion between M—A, which results in a lower yield of $Ti_3C_2T_x$. While the exact mechanism of Ti_3SiC_2 selective etching is not understood yet, the presence of the H_2O_2 oxidant in the etching solution may lead to a change in the bond between Ti—Si in the HF solution, which then may permit the cycle of under-coordination and/or interlayer expansion to then occur to form flakes of $Ti_3C_2T_x$. However, future mechanistic studies are necessary to find other compounds which may be added to HF to synthesize MXenes from non-Al-containing MAX phases.

In addition to non-Al containing MAX phases, HF-based solutions have also been used to synthesize MXene from non-MAX phases, such as Mo_2Ga_2C to form Mo_2CT_x MXene [28], and the only known zirconium- and hafnium-based MXenes from $Zr_3Al_3C_5$ and $Hf_3(Al[Si])_4C_6$, respectively [29, 30]. In the case of the nanolaminated Mo_2Ga_2C precursor, the Mo—Ga bonds are similar to the metallic bonding between M—A in MAX, with the exception that two layers of Ga are present between the Mo_2C layers instead of one [31]. The initial synthesis method of Mo_2C MXene derived from Mo_2Ga_2C was completed through the etching of thin films of mixed Mo_2Ga_2C with Mo_2GaC [28]. Although Mo_2CT_x MXene has been reported through HF treatment of Mo_2GaC MAX [28], the effect of increased layering in Mo_2Ga_2C as compared to the MAX phase Mo_2GaC on the yield of Mo_2CT_x MXene was demonstrated, where the Mo_2Ga_2C phase showed selective removal of Ga in the structure while Ga was still present after immersion of Mo_2GaC in HF at the same thin film form [28]. Similarly, further testing with HF and bulk Mo_2Ga_2C in a powder form allowed for drastically improved selective etching and creation of MXene [32]. In the perspective of F's impact on this synthesis, it is important to compare Mo_2Ga_2C and Mo_2GaC. With the addition of another A layer, Mo_2Ga_2C has Ga—Ga bonds, which do not exist in Mo_2GaC [33]. These bonds drastically change how F^- might behave in the etching process. The greater success in the HF etching of Mo_2Ga_2C may be attributed to the weaker bonds between Ga—Ga as the total Mo—Ga—Ga—Mo bonds might be easier to shift oxidation states, and thus undergo the under-coordination-interlayer expansion cycle in the presence of H^+ and F^-, as compared to Mo and Ga bonding in a Mo—Ga—Mo layer. Overall, the studies on Mo_2GaC and Mo_2Ga_2C illustrate the increased potential that non-MAX phases with the increased number of A-group layering between M—X layers may have toward HF-based synthesis of MXenes.

3.4 Effect of Precursor Structure on Fluorine-based MXene Synthesis

After establishing the fundamentals of how H^+ and F^- interact with M—X and M—A bonds, we next move to discuss the various MAX structures that can be etched to form MXenes. As discussed previously, MAX phases and their resulting MXenes follow a $M_{n+1}AX_n$ and $M_{n+1}X_nT_x$ formula, respectively, with ($n = 1$–4). These structures are typically abbreviated as 211 ($n = 1$), 312 ($n = 2$), and 413 ($n = 3$), and 514 ($n = 4$) in the MAX phase community [8, 34]. Although there are some reports on the effect of layering on etch times of the MXenes with the same M–A composition (48 hours etch for Mo_2TiAlC_2 (312) to $Mo_2TiC_2T_x$ and 90 hours etch for $Mo_2Ti_2AlC_3$ (413) to $Mo_2Ti_2C_3T_x$) [35], other reports use the same etching conditions to etch MAX phases with

different layering with the same M–A composition (48 hours etch for Nb_2AlC to Nb_2CT_x and Nb_4AlC_3 to $Nb_4C_3T_x$) [36]. In theoretical studies, the exfoliation energy for $n = 1$, 2, and 3 structures is close in value, indicating that the exfoliation energy for MAX phases is based on the M–A composition rather than the number of n layers [36]. For example, the exfoliation possibilities for $Ti_{n+1}AlC_n$ to $Ti_{n+1}C_nT_x$ are $0.170\,eV\,Å^{-2}$, $0.164\,eV\,Å^{-2}$, and $0.167\,eV\,Å^{-2}$, for $n = 1$, 2, and 3, respectively [36]. The close values for exfoliation energies indicate that the fundamental F^- and positive ion interactions with undercoordinated sites and subsequent interlayer expansion is likely more affected by M–A chemistry rather than layering; however, further studies are necessary to fully elucidate the effect of layering on etching chemistry and kinetics.

Another major source of research interest is in the formation of double transition metal (DTM) MAX phases and MXenes, in which the atomic structure contains two different M elements, as opposed to just one. These DTM phases (also sometimes referred to as MAX alloys) may follow a random solid-solution or ordered chemical arrangement. The M elements in a solid solution arrangement display no preference for the inner or outer layers of the M layers, dispersing randomly throughout the planes [37]. However, some DTM phases display a preference for an ordered arrangement of transition metals in the various layers and are further subdivided as out-of-plane ordered and in-plane ordered [38]. The out-of-plane ordered MAX phases can be exfoliated into out-of-plane ordered MXene phases (also referred to as *o*-MXenes) using traditional HF methods (Figure 3.6) [35]. Solid solution structures of MAX have also shown to extend to four or more transition metals occupying the transition metal layers, called high-entropy (HE) MAX, which can be synthesized to HE MXenes using traditional HF methods [39, 40].

In 2017, a new family of ordered MAX and MXene phases were introduced, which are referred to as in-plane ordered MAX phases and MXenes (also referred to as *i*-MAX and *i*-MXene, respectively) [41]. In these structures, the two M elements intermingle within a single plane, but maintain a preferred ordering and atomic ratio of $(M^1_{2/3}M^2_{1/3})_2AX$, unlike the more random dispersal of a solid solution [42]. The M element with the smaller atomic radius, which makes up the majority of the structure (e.g. Mo in $(Mo_{2/3}Y_{1/3})_2AC$), tends toward the inner side of the layer while the larger in atomic radius minority M element (e.g. Y in $(Mo_{2/3}Y_{1/3})_2AC$) extends out of the layer, as shown in Figure 3.7 [37].

Etching of the in-plane ordered-MAX phases into in-plane ordered-MXenes is dependent on a few different factors. The structure of the precursor, with closer bonded M^1, which is a transition metal such as Mo, with further bonded M^2, which is an element such as Y, permits choice of HF etching methods to either form in-plane divacancy MXenes, such as $Mo_{1.33}CT_x$ [42] through harsher etching

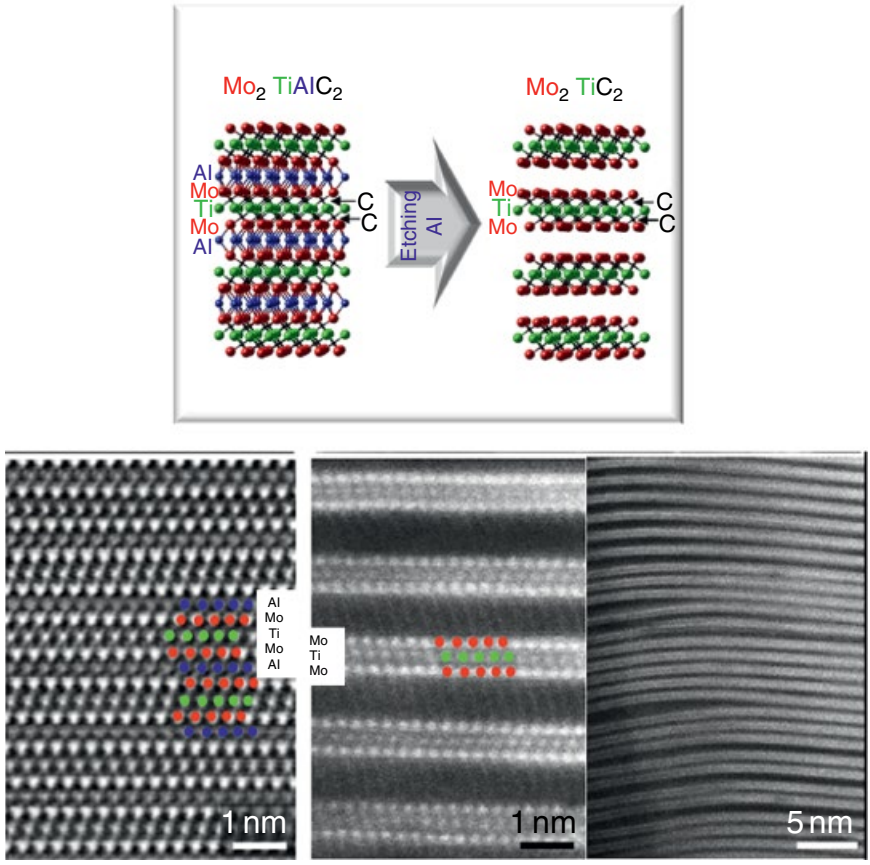


Figure 3.6 Etching of out-of-plane-MAX Mo_2TiAlC_2 to out-of-plane-MXene $Mo_2TiC_2T_x$ via HF methods. Transmission electron microscopy images illustrating the etching of Al layers in Mo_2TiAlC_2 (left) to $Mo_2TiC_2T_x$ (middle) are shown in high magnification with a low magnification image (right) to show the layered structure throughout the sample. *Source:* Adapted from Anasori et al. [35]/Reproduced from American Chemical Society.

methods (48% HF – 12 hours) [43], or retention of in-plane ordered MXene, such as Y in $(Mo_{2/3}Y_{1/3})_2CT_x$, using milder etching methods (10% HF – 72 hours) [43]. The ability to selectively etch just A-layers in the in-plane ordered-MAX $(M^1_{2/3}M^2_{1/3})_2AX$ to yield $(M^1_{2/3}M^2_{1/3})_2XT_x$ or remove both A and M^2 to yield $M^1_{1.33}X$ divacancy MXene likely indicates that both M^2–X and M^1–X are stronger than M^1–A or M^2–A, but M^2–X is weaker than M^1–X, which implies that HF etching conditions must be chosen carefully to yield the desired MXene composition [37]. In Table 3.1, all the currently reported synthesis methods for pure HF synthesis uses of various MXenes are shown.

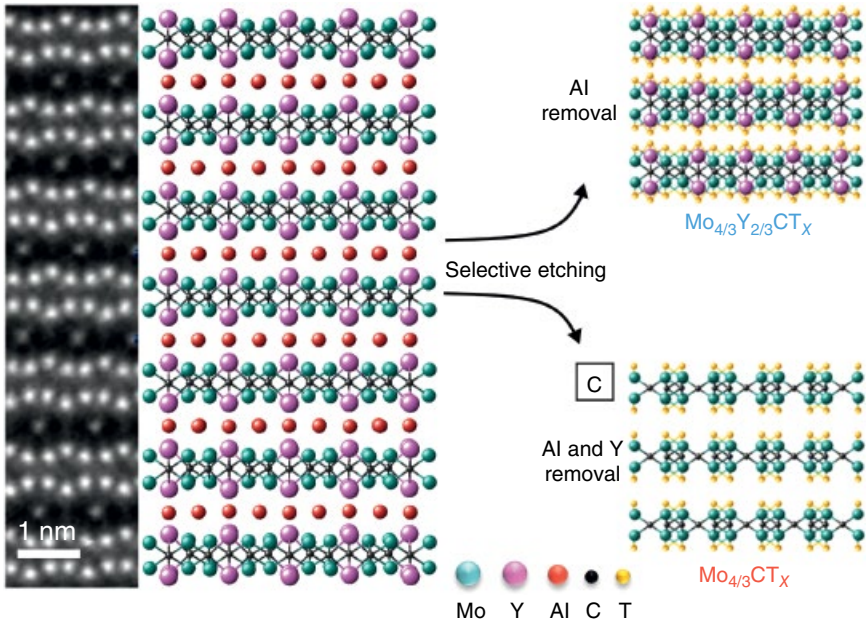


Figure 3.7 Structure of $(Mo_{2/3}Y_{1/3})_2AlC$ *i*-MAX is shown with etching possibilities to $(Mo_{2/3}Y_{1/3})_2CT_x$ or $Mo_{1.33}CT_x$. *Source:* Adapted from Hong et al. [37]/Reproduced from Springer Nature.

3.5 Diversity of Fluorine-based Etchants in MXene Synthesis

HF has been shown as an effective etchant of MXenes; however, alternatives have been found due to the environmental and safety risks associated with working directly with HF. Other methods such as hydrolysis of fluoride-containing salts [10] or the reaction between fluoride salts with other acids, such as HCl [11], are used for the *in-situ* formation of HF [52]. For example, bifluoride salts such as $NaHF_2$, KHF_2, and NH_4HF_2, have been hydrolyzed in the presence of Ti_3AlC_2 at increased temperatures (60 °C) to exfoliate Ti_3AlC_2 to $Ti_3C_2T_x$ [10]. Similarly, hydrothermal methods, such as NH_4F at 150 °C in water, are used to exfoliate Ti_3AlC_2 to $Ti_3C_2T_x$ [53]. Although these methods have been used with some success, these methods have indicated that oxide formation occurs on the $Ti_3C_2T_x$ flakes as evidenced through XRD, X-ray photoelectron spectroscopy, and scanning electron microscopy methods [10, 53].

The mix of lithium fluoride (LiF) and HCl was among the first alternative solutions to form *in-situ* HF for removal of the A group element in the synthesis of

Table 3.1 Synthesis conditions for various MXenes produced using HF methods (RT = room temperature).

Transition metal (M)	MXene	Precursor	Time (h)	Temperature (°C)	HF concentration	Year	References
Ti	Ti_3C_2	Ti_3AlC_2	2	RT	50%	2012	[4]
			20	RT	40%	2013	[44]
			24	RT	5% (60% HCl)	2020	[17]
			5	RT	30%	2017	[12]
			18	RT	10%	2017	[12]
	Ti_3CN	Ti_3AlCN	18	RT	30%	2012	[4]
			24	RT	5% (60% HCl)	2020	[17]
	Ti_2C	Ti_2AlC	10	RT	10%	2012	[4]
		Ti_2AlC_2	24	RT	5% (60% HCl)	2020	[17]
V	V_4C_3	V_4AlC_3	165	RT	40%	2018	[45]
	V_2C	V_2AlC	8	RT	50%	2013	[46]
			90	RT	50%	2013	[46]
Nb	Nb_4C_3	Nb_4AlC_3	90	RT	50%	2013	[46]
			96	RT	50%	2014	[47]
	Nb_2C	Nb_2AlC	90	RT	50%	2013	[46]
	$Nb_{1.33}C$	$(Nb_{0.66}Sc_{0.33})_2AlC$	30	RT	48%	2018	[48]
Ta	Ta_4C_3	Ta_4AlC_3	72	RT	50%	2012	[4]

(*Continued*)

Table 3.1 (Continued)

Transition metal (M)	MXene	Precursor	Time (h)	Temperature (°C)	HF concentration	Year	References
Mo	Mo_2C	Mo_2Ga_2C	3	50	50%	2015	[28]
			160	55	50%	2016	[32]
	$Mo_{1.33}C$	$(Mo_{0.66}Sc_{0.33})_2AlC$	24	RT	50%	2017	[42]
	$(Mo_{0.66}Y_{0.33})_2C$	$(Mo_{0.66}Y_{0.33})_2AlC$	12	RT	48%	2018	[43]
			72	RT	10%	2018	[43]
W	$W_{1.33}C$	$(W_{0.66}Sc_{0.33})_2AlC$	30	RT	48%	2018	[49]
		$(W_{0.66}Y_{0.33})_2AlC$	30	RT	48%	2018	[49]
Hf	Hf_3C_2	$Hf_3(AlSi)_4C_6$	60	RT	35%	2017	[27]
Zr	Zr_3C_2	$Zr_3Al_3C_5$	72	RT	50%	2016	[28]
DTM MXene	$(Ti_{0.5}Nb_{0.5})_2C$	TiNbAlC	28	RT	50%	2012	[4]
	$(Ti_{0.2}Nb_{0.8})_4C_3$	$(Ti_{0.2}Nb_{0.8})_4AlC_3$	96	50	50%	2016	[50]
	$(V_{0.5}Cr_{0.5})_3C_2$	$(V_{0.5}Cr_{0.5})_3AlC_2$	69	RT	50%	2012	[4]
	Mo_2ScC_2	Mo_2ScAlC_2	16	50	48%	2017	[51]
	Mo_2TiC_2	Mo_2TiAlC_2	48	RT	50%	2015	[35]
	$Mo_2Ti_2C_3$	$Mo_2Ti_2AlC_3$	90	55	50%	2015	[35]

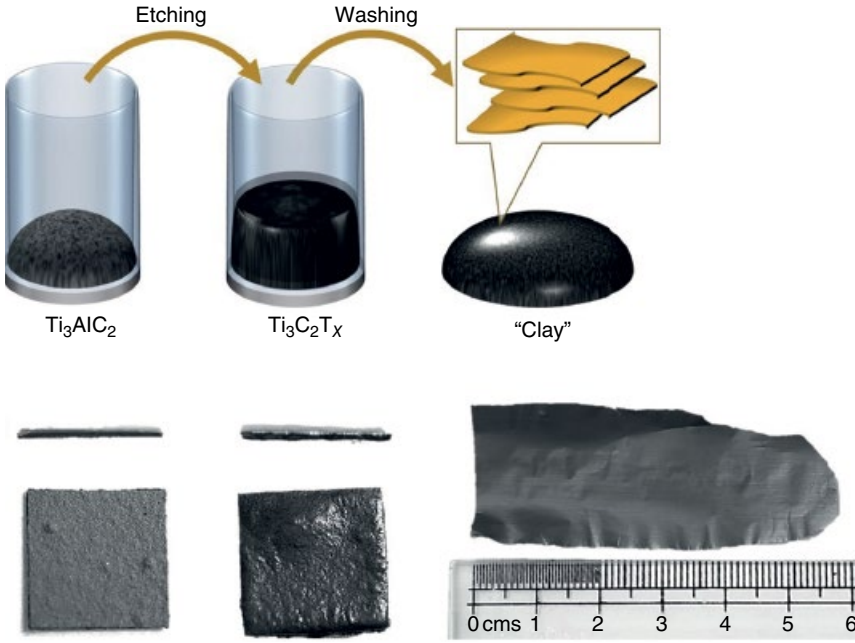


Figure 3.8 $Ti_3C_2T_x$ clay and shaped clay derived from *in-situ* LiF-HCl methods.
Source: Adapted from Ghidiu et al. [11]/Reproduced from Springer Nature.

Ti_3AlC_2 to $Ti_3C_2T_x$ (Figure 3.8) and have been reported for other MXenes such as $(Ti,V)_2AlC$ to $(Ti,V)_2CT_x$ [11, 54], Mo_2CT_x, and V_2CT_x [33, 55]. Studies using X-ray photoelectron spectroscopy as well as nuclear magnetic resonance methods have established that MXenes produced using this method have a reduction in –F surface groups and an increase in –O or –(OH) in comparison to MXene produced using direct high-concentrated HF [54, 56]. Another advantage of the LiF–HCl etching method is the introduction of lithium and chlorine ions during etching, which can result in a process that simultaneously etches the MAX phase to MXene and delaminates the sheets. The intercalation of hydrated Li ions increases the interlayer distance between flakes, which can delaminate the MXene flakes through repeated washing cycles and mechanical agitation [12]. During an experiment that used 3.08M HF concentrated during the LiF–HCl etch, scanning electron microscopy imaging revealed delaminated flakes present after three hours in etchant due to the presence of lithium ions intercalated between layers, delaminating the material unlike the process that only used HF [21]. TEM imaging also showed that unlike HF etching where grain boundary etching occurs, the use of LiF and HCl does not cause such a phenomenon [21]. Clay produced as a result of this process is shown in Figure 3.9. Similar to that of LiF–HCl, processes using

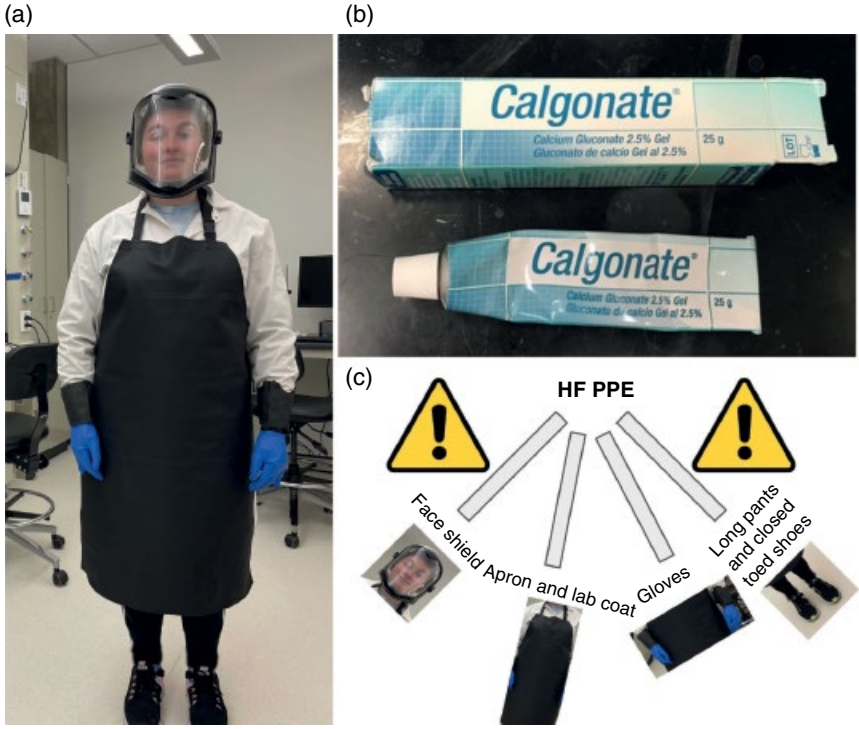


Figure 3.9 Hydrofluoric acid (HF) safety (a) Person wearing HF PPE and (b) calcium gluconate used in the instance of skin exposure to HF (c) personal protective equipment necessary for HF usage.

other fluoride salts, such as NaF, KF, CsF, CaF_2, tetrabutylammonium fluoride (TBAF), and NH_4F have all been combined with HCl to form *in-situ* HF capable of simultaneous A-group etching solutions paired with partial delamination [11, 57], which shows the potential for chemical diversity to form *in-situ* formed HF using this method. This route does present some challenges, such as the difficulty in washing out the excess fluoride salts in the multilayer powder. Therefore, extra washing steps by using a larger volume of water, beyond bringing the solution to a neutral state, are recommended to wash out the salts in this method [58]. Otherwise, impurities can remain in the final MXene powder.

Although research is ongoing toward improvement of the safety of fluorine-based etching MXenes to fluorine-containing salts, important strides have already been completed in offering alternatives to the use of direct HF in the synthesis of MXenes. In combination with further studies on which fluorine compounds can be used to synthesize MXenes from MAX, further research is necessary to relate

the fundamentals of etching of fluorine-containing salts to understand the role of the cations from the fluorine-salts (Na, K, Cs, Ca, NH_4, etc.) in the aforementioned undercoordination-interlayer expansion process mentioned for pure HF. Fundamental understanding of these processes can result in novel synthesis methods of MXenes that can improve both the safety and material behavior of MXenes in applications ranging from energy storage, electronics, and biomedical to extreme environment applications.

3.6 Safety Considerations and Protocols

After establishing the fundamentals of M—X and M—A bonding and the interactions of HF with these bonds to result in MXenes, we next discuss the various methods that can be used to mitigate the safety concerns with using HF. Since the discovery of MXenes in 2011, HF has been the primarily used etchant method to synthesize MXenes from MAX [59]. However, extra safety precautions (Figure 3.9a) are necessary when handling HF as a result of severe health risks due to exposure, which makes it non-optimal as a primary component of synthesis in a laboratory setting or for future large-scale applications [60]. HF can result in chemical burns when it makes contact with human skin, which vary in severity based on HF concentration, surface area contact and duration of exposure [60]. Such burns cause tissue damage by highly concentrating hydrogen ions and releasing fluoride ions, which leads to tissue necrosis [60]. High exposure of HF can lead to organ failure [61]. If exposure occurs, defined by contact of HF acid with the skin, immediate action must be taken [61]. The exposed area must be flushed with water to remove surface HF [61]. Then a topical treatment of calcium gluconate (Figure 3.9b) must be applied to the skin to bind to fluoride ions. After this, the individual should be taken to a hospital for treatment [61]. If inhalation occurs, hospital treatment should be the first course of action [61]. To prevent such incidents, proper personal protective equipment (PPE) should be worn when handling HF. PPE includes a face shield to protect the face, a Neoprene, Viton, or natural rubber apron worn over a lab coat, in addition to long pants and closed-toed shoes. Gloves must be worn at all time in proximity to HF and when handling it, three layers are the best: an initial disposable layer of gloves, a second layer of thick PVC or Neoprene gloves, and a final layer of disposable gloves, as shown in Figure 3.9. Layers are an important aspect of protection when dealing with HF as they increase the distance between the acid and one's skin in the instance of a spill. High-density polyethylene or polypropylene (PP) is a preferable material in which HF can be stored. HF should never be stored in glass containers and it must always be labeled and disposed of as hazardous waste.

3.7 Conclusion

In this chapter, we have summarized the bonding in MAX phases that permits exfoliation into MXenes, the fundamentals of HF etching of MAX phases, relation of MAX structure to HF etching conditions and structural possibilities, and advances in the environmental health and safety of MXene synthesis away from the use of dangerous direct HF. Overall, since MXenes' first report of $Ti_3C_2T_x$ in 2011 using 50% HF, significant strides have been made in MXene literature toward understanding the fundamentals behind HF etching and method–property relations in MXene synthesis using fluorine-containing compounds. In future research, scientists should focus on continually elucidating the fundamentals behind MXene synthesis from the perspective of M—A and M—X bonding, the effect of various cations with fluorine-containing salts, and expanding on processes toward industry-level scalability of MXene synthesis to make MXene synthesis using fluorine-based methods a more safe and environmentally safe process. In general, fluorine-containing synthesis methods using MXenes are ever-expanding and will continue to provide researchers with capabilities to create current and novel MXenes to address a wide array of technological challenges.

Acknowledgments

We thank the support of the US National Science Foundation under grant number DMR-SSMC 2124478. B.C.W. acknowledges financial support from the National Defense Engineering and Science Graduate Fellowship Program.

References

1 Anasori, B. and Gogotsi, Y. (2019). *2D Metal Carbides and Nitrides (MXenes), Structure, Properties and Applications*. Springer.
2 Barsoum, M.W. (2013). *MAX Phases: Properties of Machinable Ternary Carbides and Nitrides*. Wiley.
3 Tzenov, N.V. and Barsoum, M.W. (2000). Synthesis and characterization of Ti_3AlC_2. *Journal of the American Ceramic Society* 83 (4): 825–832.
4 Naguib, M., Mashtalir, O., Carle, J. et al. (2012). Two-dimensional transition metal carbides. *ACS Nano* 6 (2): 1322–1331. https://doi.org/10.1021/nn204153h.
5 Naguib, M., Kurtoglu, M., Presser, V. et al. (2011). Two-dimensional nanocrystals produced by exfoliation of Ti_3AlC_2. *Advanced Materials* 23 (37): 4248–4253. https://doi.org/10.1002/adma.201102306.

6 Naguib, M., Barsoum, M.W., and Gogotsi, Y. (2021). Ten years of progress in the synthesis and development of MXenes. *Advanced Materials* 33 (39): 2103393.

7 Sokol, M., Natu, V., Kota, S., and Barsoum, M.W. (2019). On the chemical diversity of the MAX Phases. *Trends in Chemistry* 1 (2): 210–223. https://doi.org/10.1016/j.trechm.2019.02.016.

8 Eklund, P., Rosen, J., and Persson, P.O.Å. (2017). Layered ternary $M_{n+1}AX_n$ phases and their 2D derivative MXene: an overview from a thin-film perspective. *Journal of Physics D: Applied Physics* 50 (11): 113001. https://doi.org/10.1088/1361-6463/aa57bc.

9 Shahzad, F., Alhabeb, M., Hatter, C.B. et al. (2016). Electromagnetic interference shielding with 2D transition metal carbides (MXenes). *Science* 353 (6304): 1137–1140. https://doi.org/10.1126/science.aag2421.

10 Feng, A., Yu, Y., Wang, Y. et al. (2017). Two-dimensional MXene Ti_3C_2 produced by exfoliation of Ti_3AlC_2. *Materials & Design* 114: 161–166. https://doi.org/10.1016/j.matdes.2016.10.053.

11 Ghidiu, M., Lukatskaya, M.R., Zhao, M.-Q. et al. (2014). Conductive two-dimensional titanium carbide 'clay' with high volumetric capacitance. *Nature* 516 (7529): 78–81. https://doi.org/10.1038/nature13970.

12 Alhabeb, M., Maleski, K., Anasori, B. et al. (2017). Guidelines for synthesis and processing of two-dimensional titanium carbide ($Ti_3C_2T_x$ MXene). *Chemistry of Materials* 29 (18): 7633–7644. https://doi.org/10.1021/acs.chemmater.7b02847.

13 Anasori, B., Lukatskaya, M.R., and Gogotsi, Y. (2017). 2D metal carbides and nitrides (MXenes) for energy storage. *Nature Reviews Materials* 2 (2): 16098. https://doi.org/10.1038/natrevmats.2016.98.

14 Magnuson, M. and Mattesini, M. (2017). Chemical bonding and electronic-structure in MAX phases as viewed by Xray spectroscopy and density functional theory. *Thin Solid Films* 621: 108–130.

15 Khaledialidusti, R., Khazaei, M., Khazaei, S., and Ohno, K. (2021). High-throughput computational discovery of ternary-layered MAX phases and prediction of their exfoliation for formation of 2D MXenes. *Nanoscale* 13 (15): 7294–7307. https://doi.org/10.1039/d0nr08791b.

16 Alhabeb, M., Maleski, K., Mathis, T.S. et al. (2018). Selective etching of silicon from Ti_3SiC_2 (MAX) to obtain 2D titanium carbide (MXene). *Angewandte Chemie (International Ed. in English)* 57 (19): 5444–5448. https://doi.org/10.1002/anie.201802232.

17 Han, M., Shuck, C.E., Rakhmanov, R. et al. (2020). Beyond $Ti_3C_2T_x$: MXenes for electromagnetic interference shielding. *ACS Nano* 14 (4): 5008–5016. https://doi.org/10.1021/acsnano.0c01312.

18 Urbankowski, P., Anasori, B., Makaryan, T. et al. (2016). Synthesis of two-dimensional titanium nitride Ti_4N_3 (MXene). *Nanoscale* 8 (22): 11385–11391. https://doi.org/10.1039/c6nr02253g.

19 Wei, Y., Zhang, P., Soomro, R.A. et al. (2021). Advances in the synthesis of 2D MXenes. *Advanced Materials* 33 (39): 2103148. https://doi.org/10.1002/adma.202103148.

20 Srivastava, P., Mishra, A., Mizuseki, H. et al. (2016). Mechanistic insight into the chemical exfoliation and functionalization of Ti_3C_2 MXene. *ACS Applied Materials & Interfaces* 8 (36): 24256–24264. https://doi.org/10.1021/acsami.6b08413.

21 Kim, Y.-J., Kim, S.J., Seo, D. et al. (2021). Etching mechanism of monoatomic aluminum layers during MXene synthesis. *Chemistry of Materials* 33 (16): 6346–6355. https://doi.org/10.1021/acs.chemmater.1c01263.

22 Kim, Y., Gkountaras, A., Chaix-Pluchery, O. et al. (2020). Elementary processes governing V_2AlC chemical etching in HF. *RSC Advances* 10 (42): 25266–25274. https://doi.org/10.1039/d0ra00842g.

23 Li, W., Cochell, T., and Manthiram, A. (2013). "Activation of aluminum as an effective reducing agent by pitting corrosion for wet-chemical synthesis," (in eng). *Scientific Reports* 3: 1229–1229. https://doi.org/10.1038/srep01229.

24 Mashtalir, O., Naguib, M., Dyatkin, B. et al. (2013). "Kinetics of aluminum extraction from Ti_3AlC_2 in hydrofluoric acid," (in English). *Materials Chemistry and Physics* 139 (1): 147–152. https://doi.org/10.1016/j.matchemphys.2013.01.008.

25 Liang, K., Tabassum, A., Majed, A. et al. (2021). Synthesis of new two-dimensional titanium carbonitride $Ti_2C_{0.5}N_{0.5}T_x$ MXene and its performance as an electrode material for sodium-ion battery. *InfoMat* 3 (12): 1422–1430. https://doi.org/10.1002/inf2.12269.

26 Noor, Q., Zahra, S.A., Serna, M.I. et al. (2020). Silicon carbide-assisted co-existence of magnetic phases in well-optimized Ti_3SiC_2-etched MXene. *Ceramics International* 46 (17): 27419–27425. https://doi.org/10.1016/j.ceramint.2020.07.228.

27 Robbins, H. and Schwartz, B. (1959). Chemical etching of silicon. *Journal of the Electrochemical Society* 106 (6): 505. https://doi.org/10.1149/1.2427397.

28 Meshkian, R., Näslund, L.-Å., Halim, J. et al. (2015). Synthesis of two-dimensional molybdenum carbide, Mo_2C, from the gallium based atomic laminate Mo_2Ga_2C. *Scripta Materialia* 108: 147–150. https://doi.org/10.1016/j.scriptamat.2015.07.003.

29 Zhou, J., Zha, X., Chen, F.Y. et al. (2016). A two-dimensional zirconium carbide by selective etching of Al_3C_3 from nanolaminated $Zr_3Al_3C_5$. *Angewandte Chemie* 128 (16): 5092–5097. https://doi.org/10.1002/anie.201510432.

30 Zhou, J., Zha, X., Zhou, X. et al. (2017). Synthesis and electrochemical properties of two-dimensional hafnium carbide. *ACS Nano* 11: 3841–3850. https://doi.org/10.1021/acsnano.7b00030.

31 Hu, C., Lai, C.-C., Tao, Q. et al. (2015). Mo_2Ga_2C: a new ternary nanolaminated carbide. *Chemical Communications* 51 (30): 6560–6563. https://doi.org/10.1039/C5CC00980D.

32 Halim, J., Kota, S., Lukatskaya, M.R. et al. (2016). Synthesis and characterization of 2D molybdenum carbide (MXene). *Advanced Functional Materials* 26 (18): 3118–3127. https://doi.org/10.1002/adfm.201505328.

33 Hadi, M.A. (2016). New ternary nanolaminated carbide Mo_2Ga_2C: a first-principles comparison with the MAX phase counterpart Mo_2GaC. *Computational Materials Science* 117: 422–427. https://doi.org/10.1016/j.commatsci.2016.02.018.

34 Deysher, G., Shuck, C.E., Hantanasirisakul, K. et al. (2020). Synthesis of Mo_4VAlC_4 MAX phase and two-dimensional Mo_4VC_4 MXene with five atomic layers of transition metals. *ACS Nano* 14 (1): 204–217. https://doi.org/10.1021/acsnano.9b07708.

35 Anasori, B., Xie, Y., Beidaghi, M. et al. (2015). Two-dimensional, ordered, double transition metals carbides (MXenes). *ACS Nano* 9 (10): 9507–9516.

36 Jastrzebska, A., Szuplewska, A., Rozmysłowska-Wojciechowska, A. et al. (2020). Juggling surface charges of 2D niobium carbide MXenes for a reactive oxygen species scavenging and effective targeting of the malignant melanoma cell cycle into programmed cell death. *ACS Sustainable Chemistry & Engineering* 8 (21): 7942–7951. https://doi.org/10.1021/acssuschemeng.0c01609.

37 Hong, W., Wyatt, B.C., Nemani, S.K., and Anasori, B. (2020). Double transition-metal MXenes: atomistic design of two-dimensional carbides and nitrides. *MRS Bulletin* 45 (10): 850–861. https://doi.org/10.1557/mrs.2020.251.

38 Anasori, B., Halim, J., Lu, J. et al. (2015). Mo_2TiAlC_2: a new ordered layered ternary carbide. *Scripta Materialia* 101: 5–7. https://doi.org/10.1016/j.scriptamat.2014.12.024.

39 Nemani, S.K., Zhang, B., Wyatt, B.C. et al. (2021). High-entropy 2D carbide MXenes: $TiVNbMoC_3$ and $TiVCrMoC_3$. *ACS Nano* 15 (8): 12815–12825. https://doi.org/10.1021/acsnano.1c02775.

40 Zhou, J., Tao, Q., Ahmed, B. et al. (2022). High-entropy laminate metal carbide (MAX phase) and its two-dimensional derivative MXene. *Chemistry of Materials* 34 (5): 2098–2106. https://doi.org/10.1021/acs.chemmater.1c3348.

41 Martin Dahlqvist, J.L., Meshkian, R., Tao, Q. et al. (2017). Prediction and synthesis of a family of atomic laminate phases with Kagomé-like and in-plane chemical ordering. *Science Advances* 3: e1700642.

42 Tao, Q., Dahlqvist, M., Lu, J. et al. (2017). Two-dimensional $Mo_{1.33}C$ MXene with divacancy ordering prepared from parent 3D laminate with in-plane chemical ordering. *Nature Communications* 8: 14949. https://doi.org/10.1038/ncomms14949.

43 Persson, I., el Ghazaly, A., Tao, Q. et al. (2018). Tailoring structure, composition, and energy storage properties of MXenes from selective etching of in-plane, chemically ordered MAX phases. *Small* 14 (17): e1703676. https://doi.org/10.1002/smll.201703676.

44 Chang, F., Li, C., Yang, J. et al. (2013). "Synthesis of a new graphene-like transition metal carbide by de-intercalating Ti_3AlC_2," (in English). *Materials Letters* 109: 295–298. https://doi.org/10.1016/j.matlet.2013.07.102.

45 Tran, M.H., Schäfer, T., Shahraei, A. et al. (2018). Adding a new member to the MXene family: synthesis, structure, and electrocatalytic activity for the hydrogen evolution reaction of $V_4C_3T_x$. *ACS Applied Energy Materials* 1 (8): 3908–3914. https://doi.org/10.1021/acsaem.8b00652.

46 Naguib, M., Halim, J., Lu, J. et al. (2013). New two-dimensional niobium and vanadium carbides as promising materials for Li-ion batteries. *Journal of the American Chemical Society* 135 (43): 15966–15969. https://doi.org/10.1021/ja405735d.

47 Ghidiu, M., Naguib, M., Shi, C. et al. (2014). Synthesis and characterization of two-dimensional Nb_4C_3 (MXene). *Chemical Communications* 50 (67): 9517–9520.

48 Halim, J., Palisaitis, J., Lu, J. et al. (2018). Synthesis of two-dimensional $Nb_{1.33}C$ (MXene) with randomly distributed vacancies by etching of the quaternary solid solution $(Nb_{2/3}Sc_{1/3})_2AlC$ MAX phase. *ACS Applied Nano Materials* 1 (6): 2455–2460. https://doi.org/10.1021/acsanm.8b00332.

49 Meshkian, R., Dahlqvist, M., Lu, J. et al. (2018). W-based atomic laminates and their 2D derivative $W_{1.33}C$ MXene with vacancy ordering. *Advanced Materials* 30 (21): 1706409. https://doi.org/10.1002/adma.201706409.

50 Yang, J., Naguib, M., Ghidiu, M. et al. (2016). Two-dimensional Nb-based M_4C_3 solid solutions (MXenes). *Journal of the American Ceramic Society* 99 (2): 660–666. https://doi.org/10.1111/jace.13922.

51 Meshkian, R., Tao, Q., Dahlqvist, M. et al. (2017). Theoretical stability and materials synthesis of a chemically ordered MAX phase, Mo_2ScAlC_2, and its two-dimensional derivate Mo_2ScC_2 MXene. *Acta Materialia* 125: 476–480.

52 Jin, S., Guo, Y., Wang, F., and Zhou, A. (2023). The synthesis of MXenes. *MRS Bulletin* 48 (3).

53 Wang, L., Zhang, H., Wang, B. et al. (2016). Synthesis and electrochemical performance of $Ti_3C_2T_x$ with hydrothermal process. *Electronic Materials Letters* 12 (5): 702–710.

54 Yazdanparast, S., Soltanmohammad, S., Fash-White, A. et al. (2020). Synthesis and surface chemistry of 2D TiVC solid-solution MXenes. *ACS Applied Materials & Interfaces* 12 (17): 20129–20137. https://doi.org/10.1021/acsami.0c3181.

55 Matthews, K., Zhang, T., Shuck, C.E. et al. (2021). Guidelines for synthesis and processing of chemically stable two-dimensional V_2CT_x MXene. *Chemistry of Materials* https://doi.org/10.1021/acs.chemmater.1c3508.

56 Hope, M.A., Forse, A.C., Griffith, K.J. et al. (2016). NMR reveals the surface functionalisation of Ti_3C_2 MXene. *Physical Chemistry Chemical Physics* 18 (7): 5099–5102. https://doi.org/10.1039/c6cp00330c.

57 Guo, Y., Jin, S., Wang, L. et al. (2020). Synthesis of two-dimensional carbide Mo_2CT_x MXene by hydrothermal etching with fluorides and its thermal stability. *Ceramics International* 46 (11): 19550–19556. https://doi.org/10.1016/j.ceramint.2020.05.008.

58 Thakur, A., Chandran, B.S.N., Davidson, K. et al. Step-by-step guide for synthesis and delamination of $Ti_3C_2T_x$ MXene. *Small Methods* 2300030. https://doi.org/10.1002/smtd.202300030.

59 VahidMohammadi, A., Rosen, J., and Gogotsi, Y. (2021). The world of two-dimensional carbides and nitrides (MXenes). *Science* 372: 1–14. https://doi.org/10.1126/science.abf1581.

60 Shuck, C.E., Ventura-Martinez, K., Goad, A. et al. (2021). Safe synthesis of MAX and MXene: guidelines to reduce risk during synthesis. *ACS Chemical Health and Safety* 28 (5): 326–338. https://doi.org/10.1021/acs.chas.1c00051.

61 Ozcan, M., Allahbeickaraghi, A., and Dundar, M. (2012). Possible hazardous effects of hydrofluoric acid and recommendations for treatment approach: a review. *Clinical Oral Investigations* 16 (1): 15–23. https://doi.org/10.1007/s00784-011-0636-6.

4

Guidelines Low-temperature (LT) F-free Synthesis of MXenes

Changda Wang, Shiqiang Wei, Pengjun Zhang, Kefu Zhu, and Li Song

National Synchrotron Radiation Laboratory, CAS Center for Excellence in Nanoscience, Key Laboratory of Precision and Intelligent Chemistry, School of Nuclear Science and Technology, University of Science and Technology of China, Hefei, China

4.1 Introduction

From the initial research of MXenes, hydrofluoric acid [1, 2], and *in-situ* generation of HF (LiF/HCl [3], NH_4HF_2 [4]) from F-containing reagents are the most widely used methods to etch MAX materials. However, F-containing etchants especially HF are dangerous and have to be handled with extreme care. The high toxicity is harmful to human body and environment, hence, inhibit their large-scale and specific applications. On the other hand, the generation of F-containing terminations often shows negative effects on the property of MXenes, for instances, hindering the transportation and reducing the storage capacity of Li^+ [5]. Therefore, substitutable synthesis strategies without involving fluoride atoms are vital and inevitable [6]. In the past several years, the nonaqueous molten salt etching route using Lewis acidic salts as the etchants under high temperature over 500 °C has been used to produce accordion-like MXenes with controllable surface terminations [7, 8]. Presently, several potential methods have been proposed to synthesize MXenes under room temperature or relatively low temperature (LT) without F-involvement, and these methods include electrochemical etching [9], Cl^- hydrothermal etching [10], halogen etching [11], and concentrated alkaline hydrothermal etching [12, 13]. Here, we will summarize the progress of those methods and indicate the guidelines for audiences to successfully synthesize F-free MXenes.

Transition Metal Carbides and Nitrides (MXenes) Handbook: Synthesis, Processing, Properties and Applications, First Edition. Edited by Chuanfang Zhang and Michael Naguib.
© 2024 John Wiley & Sons, Inc. Published 2024 by John Wiley & Sons, Inc.

4.2 Electrochemical Etching Method

In a MAX phase structure, the M—A bond is commonly weaker than the M—X bond [9], and offers the feasibility to selectively etch atoms in the A layer with the help of external forces, such as an electric field. Therefore, the preparation of MXenes by electrochemical etching is used to remove specific atoms under the electrochemical effect. Due to the difference between M—A bond and M—X bond, the electrochemical etching could be characterized by two phases (Figure 4.1a) [14]. During the first stage, the metallic A atoms are electrochemically etched accompanied with M–A breaking. This precisely A sites etching is used for the preparation of MXenes under suitable etching potential and time. During the second stage, over-etching, exerting higher voltage or longer time could further etch the metallic M atoms, which is initially used for producing carbide-derived carbons (CDCs). According to the chronological order of the occurrence of these two etching applications, we will discuss CDCs first followed by etching of MXenes.

4.2.1 Producing Carbide-derived Carbons by Electrochemical Etching

The chlorine gas (Cl_2) is commonly used as an etchant for simultaneous removal of metallic A and M atoms in the MAX phase to produce CDCs [17]. Nevertheless, this procedure features some flaws for applications, such as high temperatures or the residual of metal chlorides [18, 19]. Gogotsi et al. proposed synthesis of CDCs through an electrochemical etching route at room temperature [15]. In detail, three MAX phases of (Ti_3AlC_2, Ti_2AlC, and Ti_3SiC_2) and three dilute aqueous solutions (5.0 wt% NaCl; 10.0 wt% HCl; and 5.0 wt% HF) were chosen as carbide precursors and electrolytes, respectively (Figure 4.1b). When applying anodic potentials, the above-mentioned MAX phases are electrochemically etched into ordered or amorphous CDC (Figure 4.1c, d) with a very narrow pore size distribution of 0.5 nm (Figure 4.1e). This research shows the feasibility of etching MAX phases, indicating the possibility of extracting M and A atoms from MAX layers by electrochemistry methods.

Subsequently, a Ti_2SC MAX phase was utilized for the synthesis of carbon/sulfur nano-laminates through an electrochemically etching route [16]. Evidently, only metallic Ti atoms were chemically active enough to be electrochemically etched for preparing CDCs, reflecting the comparative electrochemical inertness of S atoms in Ti_2SC MAX. The X-ray diffraction (XRD) and energy dispersive spectroscopy (EDS) analysis reveal that the Ti atoms could be optionally removed between 0.3 and 1.0 V during electrochemically etching the Ti_2SC MAX in NH_4F aqueous solution (Figure 4.1f, g). When the applied potential > 1.0 V, the S atoms could also be etched along with the formation of a TiO_2 passive layer. Therefore, by controlling the electrochemical etching potential, the carbon/sulfur

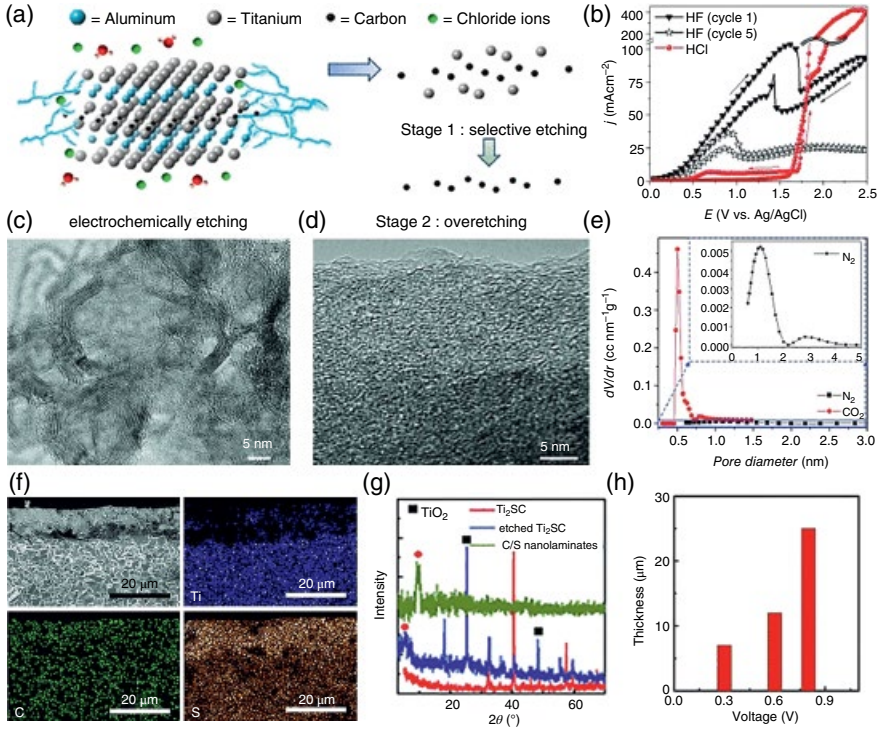


Figure 4.1 Producing carbide-derived carbons (CDCs) by electrochemical etching. (a) The sketch map for proposed electrochemical etching route. *Source:* Reproduced with permission from Pang et al. [14]. Copyright 2019 American Chemical Society. (b) Cyclic voltammograms curves obtained in HF and HCl (circles) for Ti_3AlC_2 MAX phase. (c, d) TEM of CDCs produced by electrochemical etching of Ti_3AlC_2 in 5 wt% HF. (e) Pore size distribution for the Ti_3AlC_2 CDC. *Source:* Reproduced with permission from Lukatskaya et al. [15]. Copyright 2014 WILEY-VCH. (f) Cross-sectional EDS mapping of the Ti_2SC MAX after etched at 0.6 V for one hour. (g) XRD patterns of Ti_2SC, after etched for three hours at 0.8 V before and after dissolving the TiO_2 in HF. (h) The thickness of C/S layers after being etched at different voltages between 0.3 and 1.0 V for one hour. *Source:* Zhao et al. [16]/Reproduced with permission from John Wiley & Sons, Inc.

nano-laminates (C/S) could be successfully prepared between 0.3 and 1.0 V. In addition, the thicknesses of the etched C/S laminates could also be regulated. For example, the thicknesses of the C/S layers after 1 hour etching at 0.3, 0.6, and 0.8 V are c. 7, 12, and 25 mm, respectively (Figure 4.1h). It is worth noting that the formation of TiO_2 is ineluctable in the C/S nano-laminates, but these impurities could dissolve in dilute HF solution in the latter treatment.

Therefore, as guidelines, during the investigation of CDC from MAX materials, the electrochemical etching method has proved to be an available route to extract

M and A layers from MAX phases. It has also proved to be a promising strategy to produce MXenes at LT without F-involvement in the future. Meanwhile, the etching process highly depends on the applied etching voltage, electrolyte, and the etching time, which provides a reference for the follow-up research.

4.2.2 Electrochemical Etching of MAX into 2D MXenes

Based on the research experience from CDCs, the metallic A is vulnerable to be selectively etched from the parent MAX phase by optimizing electrochemical etching conditions. The specific electrochemical etching of Al from porous Ti_2AlC electrodes in dilute hydrochloric acid was explored as a less hazardous method to process and handle MXenes in 2017 [20]. Briefly, Ti_2CT_x MXenes can be etched from Ti_2AlC via electrochemical etching in HCl aqueous electrolyte. In contrast to the chemical etching approach using HF or LiF/HCl, this electrochemical etching approach does not involve any fluoride ions during etching, and results in MXenes with only -Cl, -O, and -OH terminal groups. During the etching process, homemade porous Ti_2AlC electrodes are used as the working electrode and diluted HCl (1 or 2 M) aqueous solution is used as the electrolyte, while a Pt foil is used as the counter electrode. By varying the voltage, etching time, and electrolyte concentration in a three-electrode setup, Ti_2CT_x MXenes can be obtained. The detailed Ti_2AlC MAX etching mechanism in HCl is proposed as shown in formula [1]. On the Ti_2AlC electrode side, the Al atoms are firstly attacked and removed by Cl^- in HCl electrolyte. In the meantime, the -Cl, -O, and -OH terminal groups graft on the surface of Ti_2C MXenes, forming $Ti_2C(OH)_{2x}Cl_yO_z$.

$$\begin{aligned} Ti_2AlC + yCl^- + (2x+z)H_2O \rightarrow Ti_2C(OH)_{2x}Cl_yO_z \\ + Al^{3+} + (x+z)H_2 + (y+3)e^- \end{aligned} \tag{4.1}$$

The Al^{3+} in solution is reduced into Al metal on the counter Pt electrode.

$$Al^{3+} + 3e^- \rightarrow Al \tag{4.2}$$

After being etched, the XRD result indicates a broad peak at 8° assigned to (002) peak, which successfully proves the existence of Ti_2CT_x MXenes at the etching condition of 2 M-0.6 V-5 Days (Figure 4.2a). It is interesting to note that a smaller *d*-spacing is observed in electrochemically etched Ti_2CT_x MXenes, compared with the conventionally etched MXenes in LiF/HCl solutions. The uniqueness of electrochemically etched Ti_2CT_x MXenes is –Cl, –O, and –OH termination groups, rather than –F groups (Figure 4.2b). However, over-etching is unavoidable during electrochemical etching process, which introduces CDC confounding in the MXenes. In addition, the MAX phase during the etching features a core-shell

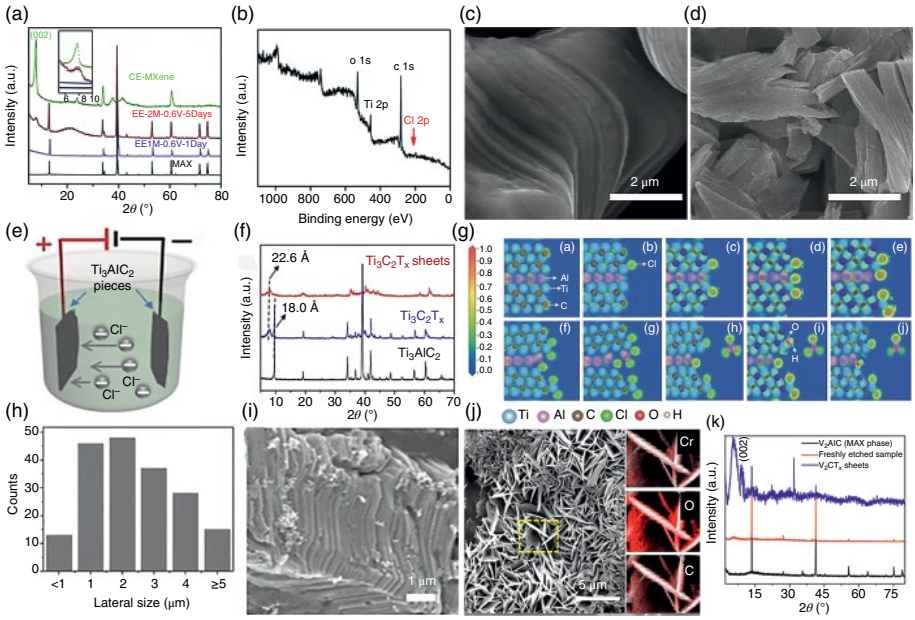


Figure 4.2 Characterizations of the electrochemical etching of Ti_2AlC to Ti_2CT_x and CDC, (a) XRD patterns, and (b) XPS survey spectra of EE-2 M-0.6 V-5 days-sediment. (c) Electrochemically etched Ti_2CT_x MXenes. (d) Chemically etched Ti_2CT_x MXenes. *Source:* Sun et al. [20]/ Reproduced with permission from Royal Society of Chemistry. (e) The configuration for electrochemical etching. (f) XRD patterns of Ti_3AlC_2, $Ti_3C_2T_x$, and $Ti_3C_2T_x$ film. (g) DFT calculations. (h) The statistical size distribution of $Ti_3C_2T_x$ sheets. *Source:* Reproduced with permission from Yang et al. [21]. Copyright 2018 WILEY-VCH. (i) SEM image of etched Ti_2CT_x. (j) SEM image with the elemental mapping analysis of etched Cr_2CT_x. (k) XRD patterns of V_2AlC, freshly E-etched V_2AlC and V_2CT_x sheets. *Source:* Pang et al. [14]/Reproduced with permission from American Chemical Society. Copyright 2019 American Chemical Society.

structure containing CDC on the shell surface, MXenes intermediate transition layer, and MAX phase core. The electrochemically etched Ti_2CT_x MXenes display mixed components of MXenes and CDCs. After separating the final samples through bath-sonicating in water, the sediment is an accordion-like Ti_2CT_x MXenes (Figure 4.2c), which is distinctive from chemically etched Ti_2CT_x MXenes (Figure 4.2d). Although there are still some undesired impurity CDCs in the etched MXenes, this is an important progress for electrochemical etching MAX phase at LT without fluoride.

The above electrochemical etching route achieved a relatively low yield for Ti_2CT_x MXenes. The amorphous carbon protective layer on etched MXenes has been a contributor to blocking the further etching process. In order to solve the low productivity of electrochemical etching, Feng et al. proposed an F-free etching procedure through optimally designed electrolytes using a binary aqueous system in a two-electrode system [21]. The electrolyte is composed of 1 M NH_4Cl and 0.2 M tetramethylammonium hydroxide (TMAOH) with a pH value > 9. In this approach, chloride ions enable rapid anodic Al etching and break the Ti—Al bonds similar to the above. Moreover, the subsequent intercalation of ammonium hydroxide (NH_4OH) can open the edges of the etched anode and facilitate the etching underlying the surfaces. The anode (Ti_3AlC_2) can be completely etched in a short period of time (five hours) under ambient conditions without forming CDC. The configuration for etching is shown in Figure 4.2e, consisting of two pieces of bulk Ti_3AlC_2 MAX phase as both working and counter electrodes, 1 M NH_4Cl with 0.2 M TMAOH as electrolyte. When exerting a working bias of +2.48 V (vs. SCE), the anodic etching of aluminum introduces a multilayer $Ti_3C_2T_x$ MXenes functionalized with –OH groups, which is further delaminated into $Ti_2C_2T_x$ with the simultaneous intercalation of ammonium species. The XRD results indicate that the parameters of the c lattice of etched $Ti_3C_2T_x$ MXenes increased from 18.0 to 22.6 Å (Figure 4.2f). These experimental results have proved the effectiveness of the designed electrochemical etching route. Thus, the etching mechanism is given by the following equations:

$$Ti_3AlC_2 - 3e^- + 3Cl^- = Ti_3C_2 + AlCl_3 \tag{4.3}$$

$$Ti_3C_2 + 2OH^- - 2e^- = Ti_3C_2\left(OH\right)_2 \tag{4.4}$$

$$Ti_3C_2 + H_2O = Ti_3C_2\left(OH\right)_2 + H_2 \tag{4.5}$$

Especially, the etching mechanism is further simulated by Density Functional Theory (DFT) calculations. As shown in Figure 4.2g, Cl^- ions are settled one by one to approach the border of Ti_3AlC_2 MAX. Not surprisingly, the pristine Ti_3AlC_2 MAX fails to be etched without the electric field. After positively charging the

Ti_3AlC_2 MAX, the Cl^- would attack the Al atoms at the periphery. Consequently, the attacked Al atoms would be dissolved forming $AlCl_3$. The deficiency of Al atoms would furnish opportunities for the intercalation and termination of –Cl groups, which further attenuates the binding force of Ti—Al bonds. Meanwhile, based on the atomic force microscope analysis, it is found that the majority (> 90%) of nano-sheets' thickness is in the range of 1.2 nm (Figure 4.2h). Therefore, the preponderance of this binary aqueous etching system is the ability to produce single or bilayer nano-sheets, particularly with a > 90% high yield and large dimension. The combination of Cl^- etching, and expansion of interlayers further indicates a more ideal research direction for electrochemical etching.

The above-mentioned protocol for electrochemical etching is all applied at room temperature, which indirectly causes a comparative long etching time. Hao et al. in 2019 suggested that exerting expedient heating temperature accelerates the etching process so that the required time is reduced [14]. To be further elaborated in detail, they projected a 3D electrode assembled with Ti_2AlC MAX, carbon black additive, and carbon fiber cloth porous substrate for electrochemical etching in a standard three-electrode configuration. In view of the smaller oxidation potential of Al than that of Ti, applying a high voltage close to Ti^{3+} oxidation potential (at 0.74 V vs. RHE) provokes nonselective etching of Ti and Al atoms resulting in over-etching. After exploration, the optimal etching conditions are determined as a 0.3 V (vs. RHE), 1 M HCl aqueous solutions, 50 °C heating temperature, and nine hours' time of duration. It should be noted that carbon black facilitates E-etching on Ti_2AlC due to better delamination. Under these conditions, the etching process complies with the expression [6]. From the SEM image of etched $Ti_2C(OH)_{2x}Cl_yO_z$ MXenes, the laminar structure with a rough surface is displayed, vindicating successful etching of the Ti_2AlC MAX phase (Figure 4.2i).

$$\begin{aligned} &Ti_2AlC + yCl^- + (2x+z)H_2O = \\ &\quad Ti_2C(OH)_{2x}Cl_yO_z + Al^{3+} + (x+z)H_2 + (y+3)e^- \end{aligned} \tag{4.6}$$

The electrochemical etching has barely been tested and verified on the Ti-based MAX phase in the reported works of literature. This report has extended to Cr and V-based MAX phase, namely Cr_2AlC and V_2AlC for illustrating the universality of the developed thermal-assisted electrochemical etching route (Figure 4.2j, k). These two MAX materials have been chosen on account of the difficulties in preparing corresponding MXenes. V_2CT_x MXenes needs a longer time and higher HF concentration for production, and Cr_2CT_x MXenes is scarcely possible to be obtained under strong acid or high temperature [9, 22, 23]. Nevertheless, this strategy plays an important role in mild etching conditions although 50 °C heating (not high temperature like the 700 °C in molten salt etching [8]) has been applied

in the process. As result, the Cr_2C and V_2C MXenes could be readily etched by using this scheme under fixed etching conditions (1.0 and 0.5 V vs. RHE etching voltage for Cr_2C and V_2C, respectively, the remaining conditions are the same as for Ti_2CT_x). Based on these etching voltages, it is not hard to find that the MAX phases with larger atomic number of M atoms (Cr > V > Ti) demand stronger external electric field driving forces to obtain MXenes due to the stronger M—Al bond. Hao et al. prepared fluoride-free Nb_2CT_x nanosheets via this facile strategy of electrochemical etching exfoliation under 1 V for 4 hours at 0.5 M HCl electrolyte, and at 50 °C [24].

According to the above-reported works, warm Cl-containing electrolytes and alkali solutions are able to etch Al owing to the high reactivity of Cl^-/OH^- ions with Al. Therefore, Wong et al. developed a time-saving electrochemical etching method to synthesize F-free and Cl-containing $Ti_3C_2T_x$ [25]. The electrochemical etching is carried out in a two-electrode system, where two Ti_3AlC_2 blocks are used as cathode and anode, respectively. An aqueous solution with 0.8 M LiOH and 1.0 M LiCl is used as the electrolyte and gives an etching efficiency of 92.2% at the constant voltage of 5.5 V for 5 hours. Meanwhile, a key factor should be noticed during the etching process. Li^+ ions in the electrolyte can intercalate into $Ti_3C_2T_x$ layers, which can weaken the interactions between adjacent layers, and expand the interlayer spacing, not only promoting the etching process but also facilitating the delamination of $Ti_3C_2T_x$. Afterward, delaminated $Ti_3C_2T_x$ can be obtained directly after sonication without using other intercalants. And the obtained delaminated $Ti_3C_2T_x$ is more stable and possesses better electrochemical performance compared to the samples synthesized by traditional HF-etching and LiF/HCl-etching methods.

Besides the aqueous condition, anhydrous electrochemical etching in organic ionic liquid such as [EMIm]Cl/$AlCl_3$ is another option. Fluorine-free and anhydrous electrochemical etching of V_2AlC, Ti_3AlC_2, and Nb_2AlC is realized via a constant-voltage electrochemical strategy in an organic ionic liquid aluminum battery at ambient temperature [26]. The constant-voltage etching process is mainly divided into the following three stages: pouch cell assembly, pouch cell constant current charging (100 mA g^{-1}), and pouch cell constant-voltage charging. The process prevents the MXenes from contacting water and air, and the MXenes etched in the aluminum battery are more conducive to the intercalation/deintercalation of Al^{3+}. The applied voltage plays a vital role during the constant-voltage etching. For V_2AlC, Al extraction can be achieved in the range of 2.2–2.3 V (V vs. Al/Al^{3+}) for about 75 hours. However, when the voltage is higher than 2.4 V (V vs. Al/Al^{3+}), the structure of the V atomic layer will be destroyed. Additionally, the Al extraction of Ti_3AlC_2 and Nb_2AlC can be realized under a constant voltage of 2.2 V (V vs. Al/Al^{3+}). Moreover, the extraction of Al will not happen below 2.1 V and will be over-etched above 2.5 V for Ti_3AlC_2.

Therefore, as guidelines, electrochemical etching has been developed as a feasible and efficient strategy for the production of MXenes from the original MAX phases. The etching conditions and attained products are summarized in Table 4.1. For the future synthesis of MXenes, we suggest several vital issues to implement the electrochemical etching process: the etchant is important which tends to be Cl-containing reagents (other halogen ions are also worth investigating) due to the strong interactions between Cl^- ions and Al; for unique MAX materials, proper voltage is essential to get high-quality MXenes, preventing the extraction of both Al and M atoms; not only aqueous solutions, organic ion solutions are also alternative and may diminish the oxidation; the etching process can be accelerated by gentle heating; intercalation agent is the key role to open the edges of etched MAX, which facilitates the further etching from the thin protective carbon layer.

Table 4.1 The summarized etching conditions of electrochemical etching.

MAXs	Electrolytes	Time (h)	Temperature (°C)	Voltages (V)	Products	References
Ti_3AlC_2	HF (5 wt%),	—	RT	0–2.5 V (Ag/AgCl)	CDCs	[15]
Ti_2AlC	HCl (10 wt%),	—	RT			
Ti_3SiC_2	NaCl (5 wt%)	—	RT			
Ti_2SC	0.5 M NH_4F	—	RT	0–2.0 V (Ag/AgCl)	C/S	[16]
Ti_2AlC	2 M HCl	120	RT	0.6 V	Ti_2C@CDC	[20]
Ti_3AlC_2	1 M NH_4Cl + 0.2 M TMAOH	5	RT	2.48 V (vs. SCE)	$Ti_3C_2T_x$	[21]
Ti_2AlC	1 M HCl	9	50	0.3 V (vs. RHE)	Ti_2CT_x	[14]
V_2AlC	1 M HCl	9	50	0.5 V (vs. RHE)	V_2CT_x	
Cr_2AlC	1 M HCl	9	50	1.0 V (vs. RHE)	Cr_2CT_x	
Nb_2AlC	0.5 M HCl	4	50	1.0 V	Nb_2CT_x	[24]
Ti_3AlC_2	0.8 M LiOH+ 1.0 M LiCl	5	RT	5.5 V	$Ti_3C_2T_x$	[25]
V_2AlC	[EMIm]Cl +	58	RT	2.2–2.3 V (vs. Al/Al^{3+})	V_2CT_x	[26]
Ti_3AlC_2	$AlCl_3$ (molar ratio 1 : 1.35)	56		2.2 V (vs. Al/Al^{3+})	$Ti_3C_2T_x$	
Nb_2AlC		56			Nb_2CT_x	

RT = room temperature.

4.3 Chloride Ion Hydrothermal Etching Method

Inspired by the electrochemical etching process, especially the reaction of Cl^- and "A" elements under certain voltages, various MAX materials with Al/Ga layers could in principle be etched by Cl-containing reagents with other appropriate external power by forming soluble $AlCl_3$ and $GaCl_3$. Based on this conception, Prof. Song et al. proposed the Cl^- hydrothermal etching method driven under proper temperature and pressure [10]. The HCl etching feasibility is simulated for various MAX materials with Al and Ga interlayer elements with the DFT calculations, predicting the decisive etching conditions of temperature and pressure as shown in Figure 4.3a, b. As a result, $\mu_{Al}(AlCl_3)$ gradually decreases with the reduction of both temperature and pressure, which is thermodynamically conducive to the etching of MAX phases. However, from kinetics point of view, higher temperature improves the etching efficiency in practical experiments. Therefore, it is essential to provide proper temperature and pressure during the HCl etching. Then, the reaction-limiting temperature (T_{RL}) is studied based on pressure, which is the critical point of reaction (the dotted lines in Figure 4.3a, b). Accordingly, it is predicted that Cr_2GaC, Mo_2GaC, Mo_2Ga_2C, and Mn_2GaC could be successfully etched into corresponding MXenes (Cr_2CT_x, Mo_2CT_x, Mo_2CT_x, and Mn_2CT_x) in HCl solution, and the T_{RL} at 1 atm are 385 K, 435 K, 455 K, and 485 K, respectively.

As a proof-of-concept demonstration, Mo_2Ga_2C is successfully etched via a controllable hydrothermal reaction in HCl. Based on the calculated T_{RL}, the etching efficiency of Mo_2Ga_2C is explored in concentrated HCl solution under 140 °C with different pressure. During the etching process, pressure is adjusted by changing the volume fraction of HCl in Teflon liner from 30% to 60% in customized autoclave (Figure 4.3c). XRD results of obtained Mo_2CT_x-30%/40%/50%/60% MXenes (Figure 4.3d) exhibit the increase of etching efficiency with lower pressure as shown in Figure 4.3e in detail. Meanwhile, the etching in concentrated HCl does not lead to deep oxidation of MXenes. However, it is noted that decreasing the temperature to 120 °C with a pressure about 10 bar, needs longer time to achieve the etching of Mo_2Ga_2C. And this results in more impurities like molybdenum oxide with diluted hydrochloric acid (6 M, ~5 bar) under 140 °C. Therefore, we implement the experiment with 40% volume fraction of concentrated HCl and the temperature is set as 140 °C with pressure about 15 bar. After five days of etching, Mo_2CT_x MXenes with high purity are finally obtained (Figure 4.3f), vindicating another strategy of synthesizing fluoride-free MXenes.

However, high pressure of 15 bar and concentrated HCl restrict further development of this method. Consequently, we use ammonium chloride instead of hydrochloric acid for the etching of Mo_2Ga_2C [27]. In order to avoid the oxidation in aqueous NH_4Cl, DMSO is added as a sulfur source to fabricate endogenous heterojunction (Figure 4.3g). The concentration of NH_4Cl solution is

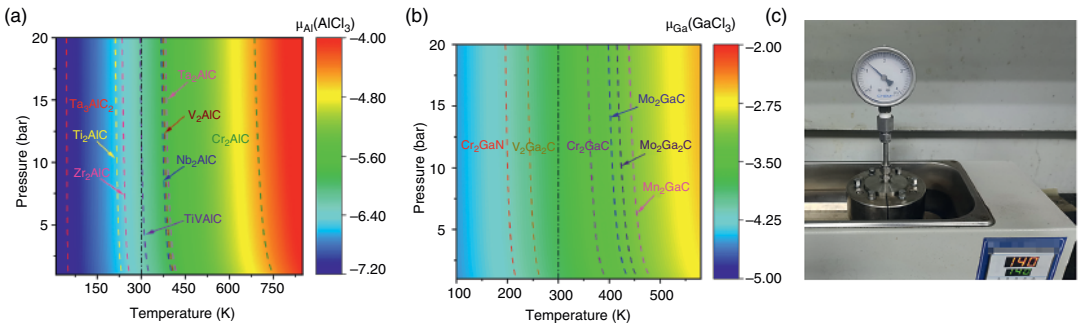


Figure 4.3 (a, b) Feasibility of HCl-assisted hydrothermal etching strategy for various MAX phases. (a) and (b) are the mapping of chemical potential of Al in $AlCl_3$ ($\mu_{Al}(AlCl_3)$), Ga in $GaCl_3$ ($\mu_{Ga}(GaCl_3)$) influenced by temperature and pressure, respectively. The dotted line indicates the $\Delta G = 0$ ($\Delta G = \mu_{Al}(AlCl_3) - \mu_{Al}(MAX)$ and $\Delta G = \mu_{Ga}(GaCl_3) - \mu_{Ga}(MAX)$), left and right areas of dotted line indicate $\Delta G < 0$ and $\Delta G > 0$, respectively. The single point line stands for room temperature. (c) Photo of the high-pressure reactor under 140 °C with HCl volume fraction of 30%. (d) X-ray diffraction patterns of Mo_2CT_x MXenes obtained via hydrothermal with different volume fractions of HCl (Mo_2CT_x-30%/40%/50%/60%) in Teflon liner. (e) Etching efficiency of Mo_2Ga_2C in HCl solution influenced by pressure under 140 °C. (f) XPS survey spectrum of Mo_2Ga_2C and Mo_2CT_x MXenes. *Source:* Wang et al. [10]/Reproduced with permission from John Wiley & Sons, Inc. (g) Diagram of specific synthesis process of hetero-Mo_2C from Cl^--hydrothermal etching of Mo_2Ga_2C. (h) XRD spectra of Mo_2Ga_2C, Mo_2CT_x obtained from HF-etching and hetero-Mo_2C samples. (i) Cross-sectional TEM image of the hetero-Mo_2C prepared by focused ion beam (FIB) technique. *Source:* Zhu et al. [27]/Reproduced with permission from John Wiley & Sons, Inc.

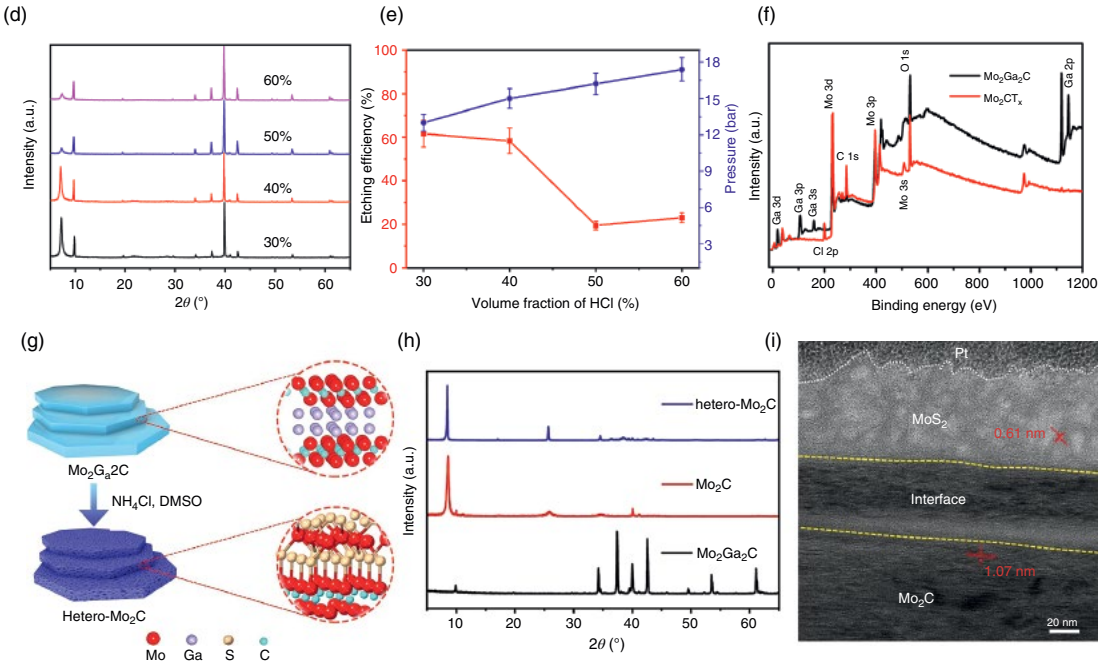


Figure 4.3 (Continued)

7.5 mol l^{-1} with total volume of 20 ml. Afterward, 20 mmol DMSO is added. After the reaction under 180 °C for 5 days, Ga atoms are successfully extracted as shown from the XRD results (Figure 4.3h). At the same time, amorphous MoS_2 layers with a thickness about a dozen nanometers are formed as shown in Figure 4.3i. Therefore, the etching of Mo_2Ga_2C and endogenous heterojunction of amorphous MoS_2 coupled with fluoride-free Mo_2CT_x MXenes (hetero-Mo_2C) are achieved simultaneously. Meanwhile, the antioxidation of Mo_2CT_x is improved due to amorphous MoS_2, and the structural stability during lithium-ion storage is highly improved as well.

Therefore, as guidelines, Cl^- hydrothermal etching method, as another fluoride-free strategy, is expected to achieve massive synthesis of MXenes. It is also a promising strategy with high flexibility for the construction and design of new hetero-MXenes, which is beneficial for the extension and practical application of MXenes. However, this method still needs further investigation to improve. During the operation, proper temperature is vital, and low pressure is preferred. Other halogen ions like Br^- and I^- may also be feasible for the etching of MAX materials. The concentration of halogen ions in the solution and the solvent itself is important for the controlling of oxidation of MXenes during the etching process. Other chemical reagents may also be helpful for the successful etching by forming variable heterojunction structures.

4.4 Halogen Etching Method

As investigated, electrochemical etching in both aqueous and organic ion liquid, and chloride ion hydrothermal etching methods are all based on the reaction of halogen ions like Cl^- with "A" atoms such as Al and Ga driven by electrochemistry and temperature/pressure, respectively. Therefore, the directly etching of MAX materials via halogen molecule is another option. And it has been successfully implemented at room temperature or under heating by utilizing halogens including Br_2, I_2, ICl, and IBr in anhydrous media to etch Ti_3AlC_2 [11, 28].

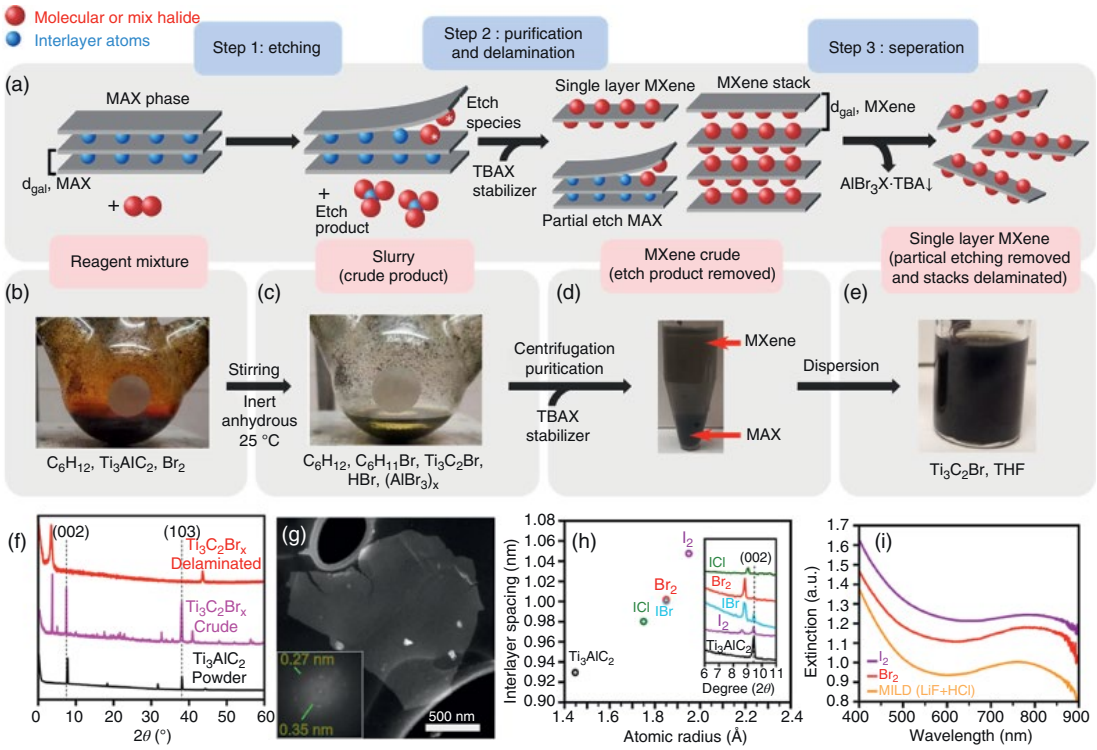
In 2021, Vaia et al. proposed an efficient halogen etching method at room temperature and investigated several decisive factors [11]. They successfully synthesized $Ti_3C_2T_x$ MXenes with homogeneous Cl, Br, or I-terminal groups from Ti_3AlC_2 by Br_2, I_2, ICl, and IBr in anhydrous media. And they also expanded to other MAX phases such as Cr_2AlC, Ti_2AlC, and V_2AlC. During the experiment, all chemical processes involving halogen reaction are carried out in a glove box or using a Schlenk line to inhibit the hydrolysis of $AlBr_3$ byproduct. As shown in Figure 4.4a, the introduction of Br_2 into aluminum-containing materials produces $(AlBr_3)_x$ [29], in which x-monomer is easy to decompose into monomer $AlBr_3$. Therefore, the initial mixed solution (Figure 4.4b–e) changes from deep red to light yellow ($AlBr_3$) under inert atmosphere stirring. It is found that Ti_3AlC_2

surfaces could act as catalysis sites for Br_2 homolysis. The surface Br–Br dissociation is solvent dielectric dependent. The high dielectric solvent increases the reactivity of Br_2 after surface adsorption through solvent coordination, subsequently expands the types of surface sites that may produce free radicals (Br*), and thus reduces the selectivity. Therefore, it is preferred to enhance the selectivity in nonpolar solvents such as anhydrous cyclohexane (CH). Note that $AlBr_3$ is highly soluble in nonpolar solvents. The etching process is also highly dependent on the concentration of halogens. Low-concentrated halogens decrease the etching rate, while high-concentrated halogens reduce the effectiveness of etching due to the specificity reduction via side effects.

As noted, the most effective etching condition occurs in cyclohexane with a medium concentration of Br_2 (~10 vol%) with tetrabutylammonium bromide (TBAX) to stabilize etched byproducts. Figure 4.4f shows the XRD patterns of synthetic $Ti_3C_2Br_x$. After adding TBAX and purification (centrifugation), only $Ti_3C_2Br_x$ is present. Ti–C main chain structure is not damaged during the etching process (Figure 4.4g), indicating the successful etching of Ti_3AlC_2. Furthermore, halogen groups are also considered. Figure 4.4h and 4.4i summarize the results using I_2, ICl, and IBr. For interhalogen compounds, halogen atoms with stronger electronegativity act as active etching substance and terminate the surface (Figure 4.4h). Generally, these halogenated MXenes can easily form stable colloidal suspensions in low-dielectric organic solvents. Moreover, the difference in electronegativity of halogen atoms on $Ti_3C_2T_x$ shows an influence on the surface plasmon resonance (Figure 4.4i) [30]. This is because the polarization of the halogen metal bond is directly proportional to the electronegativity of the halogen atom (F > Cl > Br > I), which causes electron density rearrangement and changes the plasmon structure.

Feng et al. also implemented the halogen etching of Ti_3AlC_2 by I_2 in anhydrous acetonitrile (CH_3CN) under heating [28]. About 0.5 mmol Ti_3AlC_2 powder, 1.5 mmol I_2 nanocrystals, and 5 ml CH_3CN are put in a glass ampoule. The ampoule is then sealed under vacuum after three times freeze-pump-thaw cycles to avoid oxygen and water. The etching is finally achieved under heating up to 100 °C for four days. The process enables the formation of $Ti_3C_2I_x$, and it further transforms into $Ti_3C_2T_x$ (T = O, OH) flakes with moderate sizes about 1.8 μm and high oxygen content of 18.7 wt%. Most of the flakes (71%) are thinner than 5 nm, and they are stable in dispersions for at least two weeks and results in high electrical conductivity (1250 S cm^{-1}) and excellent properties in supercapacitor.

Therefore, as guidelines, when conducting this halogen etching experiment, it is important to be fully aware of safety protocols because of highly reactive, toxic, and corrosive materials. Additionally, water should be avoided as much as possible due to the hydrolysis of AlX_3 species, which reduces the etching efficiency. Due to different atomic radius and endothermic homolysis of halogens, temperature is tunable for better etching. Proper concentration of halogen is also important for


Molecular or mix halide
Interlayer atoms
Step 1: etching
Step 2 : purification and delamination
Step 3 : seperation
(a)
MAX phase
d_{gal}, MAX
+
Etch species
TBAX stabilizer
+
Etch product
Single layer MXene
MXene stack
Partial etch MAX
d_{gal}, MXene
$AlBr_3X$·TBA↓
Reagent mixture
Slurry (crude product)
MXene crude (etch product removed)
Single layer MXene (partical etching removed and stacks delaminated)
(b)
(c)
(d)
(e)
Stirring
Inert anhydrous 25 °C
Centrifugation puritication
TBAX stabilizer
MXene
MAX
Dispersion
C_6H_{12}, Ti_3AlC_2, Br_2
C_6H_{12}, $C_6H_{11}Br$, Ti_3C_2Br, HBr, $(AlBr_3)_x$
Ti_3C_2Br, THF

(f)
(002)
(103)
$Ti_3C_2Br_x$ Delaminated
$Ti_3C_2Br_x$ Crude
Ti_3AlC_2 Powder
2θ (°)
(g)
0.27 nm
0.35 nm
500 nm
(h)
Interlayer spacing (nm)
Atomic radius (Å)
I_2
ICl
Br_2
IBr
Ti_3AlC_2
(002)
Degree (2θ)
(i)
Extinction (a.u.)
Wavelength (nm)
I_2
Br_2
MILD (LiF+HCl)

the successful etching with high quality, since too low or too high concentration are both unfavorable. Low-dielectric solvent is also preferred to avoid violent reaction with MAX. Moreover, other extra solvents should also be considered together to ensure the etching process by stabilizing byproducts.

4.5 Alkali Etching Method

As mentioned above, the successful synthesis of MXenes can be attributed to the fact that the bonds of M—A are more chemically active than that of M—X. Therefore, "A" atoms can be removed from the corresponding MAX phase by the reaction of halogen ions including fluorine, chlorine, bromine and iodine ions by forming AF_3, ACl_3, ABr_3, and AI_3, respectively under corresponding conditions [9, 11]. On the other hand, since aluminum is an amphoteric element, the MAX materials with Al layers are possible to be etched by alkali through the reaction of Al and OH^-. Ultimately, etching methods via both inorganic and organic alkali especially for Al-based MAX materials are investigated.

4.5.1 Alkali Etching Under Low Concentration

Thermodynamically, Al atoms in MAX phases such as Ti_3AlC_2 can react with OH^- to fabricated MXene [13]. Therefore, alkali etching is another alternative method to synthesize MXenes and introduces more −OH functional groups on the surface [31]. Wei et al. etched the MAX phase into $Ti_3C_2T_x$ MXenes by immersing Ti_3AlC_2 in 1 M NaOH solution at 80 °C for 100 hours, as illustrated in

Figure 4.4 (a) Generalized process for the formation of MXenes. (b) The addition of Br_2 and Ti_3AlC_2 produces a deep red solution in anhydrous cyclohexane. (c) When Br_2 reacts with Al, the supernatant turns pale yellow to form $AlBr_3$ species. The addition of stabilizer (TBAX) makes $AlBr_3$ inert. (d) The MXenes crude is purified via repeated redispersion in nonpolar solvent. (e) The purified size-selected MXenes is obtained via centrifugation and dispersed in tetrahydrofuran (THF). (f) XRD patterns of bulk Ti_3AlC_2 (black) and resulting crude (magenta) and purified (red) $Ti_3C_2Br_x$ synthesized with 10% Br_2/CH. The addition of tetrabutylammonium bromide (TBAB) to the crude enables the separation of dispersed $Ti_3C_2Br_x$ flakes from the etched byproducts. (g) STEM image of a purified, exfoliated $Ti_3C_2Br_x$ MXenes flake (inset, FFT of an HRTEM image). (h) The interlayer spacing between Ti_3AlC_2 and various halogen-terminated MXenes. The layer spacing increases with the increase of halogen atom radius. (i) The comparison between the extinction of $Ti_3C_2I_x$ and $Ti_3C_2Br_x$ and that of traditional light etching Ti_3AlC_2 ($Ti_3C_2T_x$: T = F, OH, O) shows that the plasma resonance redshifts with the decrease of surface terminal electronegativity. *Source:* Jawaid et al. [11]/Reproduced with permission from American Chemical Society.

Figure 4.5a [32]. Due to the ultra-high chemical stability of Ti_3AlC_2 and poor etching ability of NaOH, the etching of Al atoms occurs on the surface. After the following procedure to further remove exposed Al atoms by socking the pre-etched material in 100 ml of 1 M H_2SO_4 at 80 °C for 2 hours, the thickness of etched $Ti_3C_2T_x$ on Ti_3AlC_2 surface is about 100 nm (Figure 4.5b). Notably, the BET surface area of the sample is increased from 1.18 $m^2\ g^{-1}$ (Ti_3AlC_2) to 10.35 $m^2\ g^{-1}$ (Figure 4.5c). Meanwhile, there are several experiments executed under higher temperature of 200 °C in low concentrated alkali solution (0.1–5 M). Some Al atoms are removed, but the final products are Na / K-Ti-O compounds rather than MXenes [34, 35]. Therefore, it seems that the etching strategy based on alkali including NaOH and KOH with low concentration is still challenge to effectively produce MXenes from MAX phases.

4.5.2 Alkali Etching Under High Concentration

After the study of low concentrated alkali, high concentrated alkali is investigated on the etching of MAX, which is expected to show distinct results. To produce a high-concentration alkali environment, potassium hydroxide (0.35 g), Ti_3AlC_2 (0.1 g), and a small amount of water (0.05 ml) are mixed and ground into a paste. The paste is then transferred into a polytetrafluoroethylene-lined stainless-steel autoclave under 180 °C for 24 hours [12]. As demonstrated in Figure 4.5d, the Ti_3AlC_2 can be successfully etched by KOH to form $Ti_3C_2(OH)_2$:

$$Ti_3AlC_2 + KOH + H_2O = Ti_3C_2 + KAlO_2 + 3/2H_2 \tag{4.7}$$

$$Ti_3C_2 + 2H_2O = Ti_3C_2\left(OH\right)_2 + H_2 \tag{4.8}$$

The total delaminated $Ti_3C_2(OH)_2$ nanosheets can easily be obtained by a simple washing process to move $KAlO_2$ and residual KOH. By changing the amount of KOH, heating temperature, and reaction time, the synthesis process is well controlled. Accordingly, $Ti_3C_2(OH)_2$ nanoribbons is obtained [36]. The formation of $Ti_3C_2(OH)_2$ MXenes with nanobelt morphology mainly depends on the saturated water vapor pressure, which is about 10^6 Pa under 180 °C together with KOH. During the etching process, a sugarcane-like structure is firstly produced due to surface tension. Simultaneously, high-pressure water vapors promote sugarcane-like products to expand to ribbons with $KAlO_2$ byproducts and further exfoliat to thin nanoribbons.

When handling this small amount of water-assisted alkali hydrothermal etching method, proper content of inorganic alkali is conducive to the process of etching; vapor of water is essential to promote the etching; temperature is also important as it barely begins at lower temperature and over etch at the higher temperature.

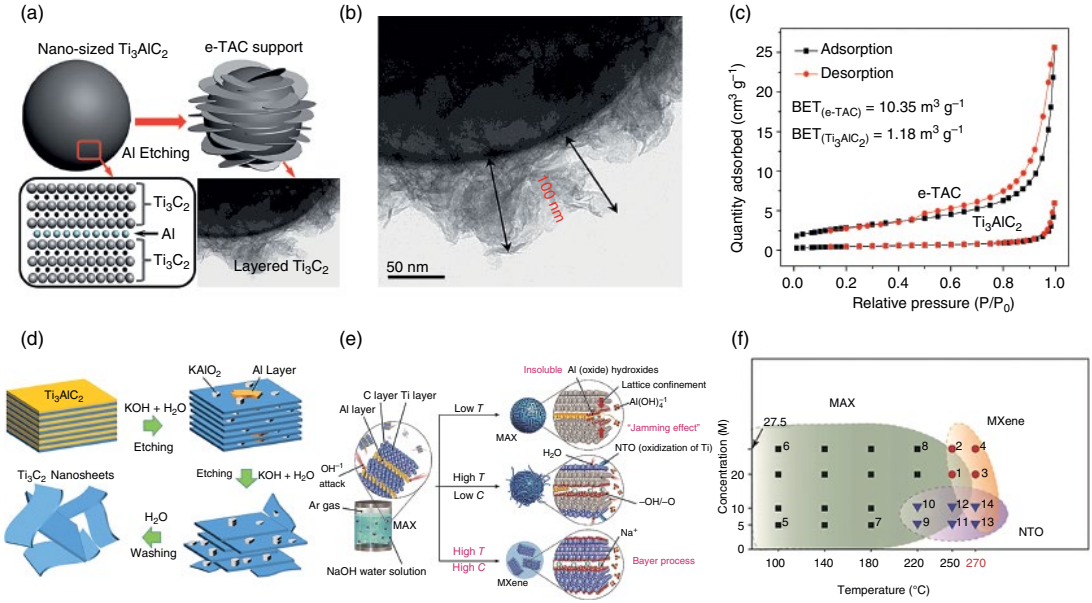


Figure 4.5 (a) Schematic diagram for the formation process, (b) HRTEM image, and (c) Nitrogen adsorption/desorption isotherms of layered $Ti_3C_2T_x$ on the surface of Ti_3AlC_2. *Source:* Xie et al. [32]/Reproduced with permission from Royal Society of Chemistry. (d) Schematic for the etching and exfoliation of Ti_3AlC_2 by KOH in the presence of a small amount of water at 180 °C. *Source:* Reproduced with permission from Li et al. [12]. Copyright 2017, American Chemical Society. (e) The hydrothermal method for etching Ti_3AlC_2 by NaOH water solution under different conditions. (f) 24 batches of samples are prepared under different conditions. Cycle: MXenes; squares: MAX; triangle: NTOs. *Source:* Reproduced with permission from Li et al. [13]. Copyright 2018 Wiley-VCH.

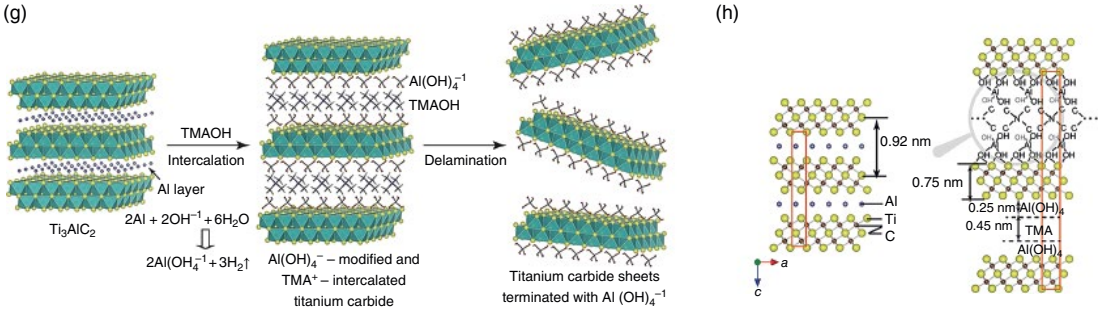


Figure 4.5 (Continued) (g) Schematic illustration of the intercalation and delamination process of Ti_3C_2 terminated with $Al(OH)_4^-$. (h) Structural illustration of the Ti_3AlC_2 and Ti_3C_2 terminated with $Al(OH)_4^-$. *Source:* Reproduced with permission from Xuan et al. [33]. Copyright 2016 Wiley-VCH.

Finally, the shape and morphology of MXenes can be tuned by controlling alkali content, etching temperature, and time.

As reported, the difficulty in achieving MXenes via alkali attack is a kinetic problem that could be attributed to the formation of insoluble Al hydroxides ($Al(OH)_3$) and dehydrated oxide hydroxides (AlO-(OH)) on the Ti_3AlC_2 surface [33]. However, the Al (oxide) hydroxides can further dissolve in high-concentration alkali to form $Al(OH)_4^-$. Therefore, the etching of Ti_3AlC_2 at different concentrations of NaOH water solutions at a series of hydrothermal temperatures under the argon atmosphere is explored (Figure 4.5e, f). The results suggest that $Ti_3C_2T_x$ with high purity of 92 wt% can be obtained at 270 °C in 27.5 M NaOH. While at a lower temperature, the reaction between NaOH and Al (oxide) hydroxides is hindered. This can be reasonably attributed to its endothermic process. In other words, the decreased temperature hinders the dissolution of $Al(OH)_4^-$, resulting in the lower yield of MXenes. When temperature is further decreased (below 220 °C), no MXenes form under any concentration of NaOH water solutions. For a lower concentration of NaOH solutions at 270 °C, the Na–Ti–O compounds are generated due to the oxidation of Ti atoms [34, 35]. Therefore, temperature and concentration of NaOH are two key factors for the preparation of MXenes [37]. These results confirm that MXenes with high yield and purity can be synthesized from Al-based MAX materials via inorganic alkali hydrothermal etching under high concentration and high temperature.

4.5.3 Organic Alkali Etching

The organic base, tetramethylammonium hydroxide (TMAOH), is another etchant to extract the Al layer from Ti_3AlC_2. However, before etching, the Ti_3AlC_2 needs to be pretreated with dilute HF to remove the passivation layer of the surface oxidant. The synthesis process is divided into two steps, as shown in Figure 4.5g. The Al layer is attached and reacted with TMAOH to form $Al(OH)_4^-$. However, the $Al(OH)_4^-$ cannot be removed and serves as titanium-mediation moiety on the surface of the Ti_3C_2 layer, thus resulting in a structure with Ti_3C_2 sheets terminated by $Al(OH)_4^-$ and sandwiching TMA^+. Owing to the intercalation of TMA^+, the continuous reaction between Al layer and TMAOH is protected, resulting in high yield and further delamination of MXenes. According to the inductively coupled plasma analysis, the atomic ratio of Al : Ti is 0.89 : 3, which is similar to Ti_3AlC_2. Thus, the reaction mechanism is different from that Al layer removed by HF (the atomic ratio of Al : Ti is less than 0.1 : 3) [38, 39]. As shown in Figure 4.5h, due to the negative charge of $Al(OH)_4^-$, it is easy to bond with Ti metal on the surface of the Ti_3C_2 unit through O–Ti. In such a configuration, the Al atom is firstly removed and then replaced by $Al(OH)_4^-$, resulting in a similar atomic ratio of Al : Ti in Ti_3AlC_2. Meanwhile, there is no electron transfer from the Ti_3C_2 unit to surface

terminations, which can be reasonably ascribed to the electron and equilibrium injected by Al through the Al—O bond. All these results verify the correctness of this structural model and confirm the successful preparation of Ti_3C_2 terminated with $Al(OH)_4^-$.

Therefore, as guidelines, Al-based MAX materials including Ti_3AlC_2 and Ti_2AlC [40] can be successfully etched by (in)organic alkali. To obtain MXenes with high quality via inorganic alkali, the concentration and temperature are crucial. Etching with low concentration of alkali will produce impurities such as oxides. Etching with LT will suffer from the reaction between OH^- and Al (oxide) hydroxides, further restricting the etching process. Meanwhile, organic alkali is another available etchant to extract the Al layer from MAX. However, pretreatment is necessary to remove the oxidation passivation layer and expose Al layers. Initial break of Ti—Al bonds via OH^- is essential, and bulky-ion intercalation including $Al(OH)_4^-$ and cations can further facilitate the subsequent etching process. The alkali etching strategy is still expected for further etching of more MAX materials with amphoteric elements including Al.

4.6 Other F-free Etching Methods

Besides the methods discussed above, researchers are also working on developing other effective etching strategies under low temperature without fluoride. For instances, Mei et al. in 2020 used a UV-induced selective etching method in phosphoric acid to fabricate fluorine-free mesoporous Mo_2C MXenes from Mo_2Ga_2C [41]. Due to the promising UV absorbing property of Mo_2Ga_2C [42], Sun et al. obtained the fluoride-free Mo_2C with porous structure by starring Mo_2Ga_2C in phosphoric acid (85%) under UV light (100 W) radiation for three to five hours. It is proved that UV-irradiation could be an indispensable factor since there is no involvement of hazardous and highly corrosive acids. For those MAX materials that are sensitive to UV lights, this UV-irradiation-assisted etching method is another choice, but it still needs more investigations to obtain MXenes with high quality.

The above wet etching processes are admitted to serve as the most employed methods for MXenes to produce large quantity samples. However, there is a big challenge to the quality and uniformity of MXenes products. Meanwhile, it seems impossible to fabricate MXenes without terminations by using the wet etching methods. At this point, chemical vapor deposition (CVD) may provide compelling benefits over other alternatives in controllability, uniformity and scalability. Therefore, the progresses on synthesizing 2D MXenes by CVD are also implemented via modulating the temperature, pressure, gas flow rate, and catalysts types [43]. Herein, we will have a brief discussion on CVD method although it is generally operated under high temperature.

Ren et al. in 2015 demonstrated the fabrication of large-area and uniform 2D ultrathin α-Mo_2C crystals over 100 μm by CVD, using CH_4 as carbon source and a Cu foil put on a Mo foil as catalyst over 1085 °C [44]. It exhibits the tunability of α-Mo_2C on size and thickness by changing growth temperature and time. Afterward, the hexagonal Mo_2C crystals in centimeter range are obtained and the growth mechanism is systematically demonstrated by Kian Ping Loh and the co-workers [45]. They use liquid Cu on the supporting Mo foil as the catalyst, CH_4 as the carbon precursor, and H_2 as the reducing and carrier gas at the growth temperature of 1100 °C (Figure 4.6a). As temperature is higher than 1086 °C, the melting Cu can act as a catalyst to form Mo_2C. Moreover, thick Mo_2C crystals with different shapes are randomly distributed on the Cu surface at low CH_4 concentration, whereas at higher CH_4 concentration, the growth of predominantly hexagonal-shaped, thin Mo_2C flakes on graphene is seen. Note that at high CH_4 condition, monolayer graphene can grow rapidly and serve as a blocking layer, cutting off the vertical supply of Mo, resulting in the drastically decreased thickness of Mo_2C (Figure 4.6b). The graphene may also play the role of a template in controlling the shape of the crystals. The growth of Mo_2C is a time-dependent process that can be realized to a centimeter scale (Figure 4.6c, d).

Au could also serve as the metal catalyst working for the growth of 2D Mo_2C crystals in CVD process, with a lower melting point (1064 °C) and moderate higher catalytic capacity compared to those of Cu [47]. It shows a unique sunk growth mode and the ratio of methane to hydrogen (C : H) is crucial. The growth of Mo_2C is energy favored at high H_2 flux and suppressed at lower hydrogen flux due to formation of graphene. Moreover, gallium (Ga) with low melting point is chosen to serve as the liquid solvent to achieve the co-segregation of W and C atoms for the synthesis of WC under ambient pressure [48]. It is found that growth temperature will determine the number of heteroatoms and cooling rates will result in thicker WC flakes.

MXenes such as Mo_2C are also possible to be obtained through the chemical conversion from a pre-deposited MoS_2 film via CVD method (Figure 4.6e), which was implemented by Lee et al. in 2019 [46]. MoS_2 films are grown on the SiO_2/Si substrates firstly. The carburization is then performed at 840 °C for four hours by using a CH_4 source and Cu catalyst to chemically convert the MoS_2 to a Mo_2C. It is successfully achieved under 100 sccm CH_4, 5 sccm H_2, and 100 sccm Ar as shown in HRTEM image (Figure 4.6f).

Therefore, as guidelines, CVD methods including direct synthesis and chemical conversion, are promising strategies to fabricate 2D MXenes with full controllability and without surface terminations which is beyond wet etching methods. It also provides alternative methods to prepare series MXenes heterostructures by precisely controlling the growth conditions. The CVD methods are highly tunable and dependent on growth temperature, gas pressure, gas flow rate, catalysts type, and even cooling procedure.

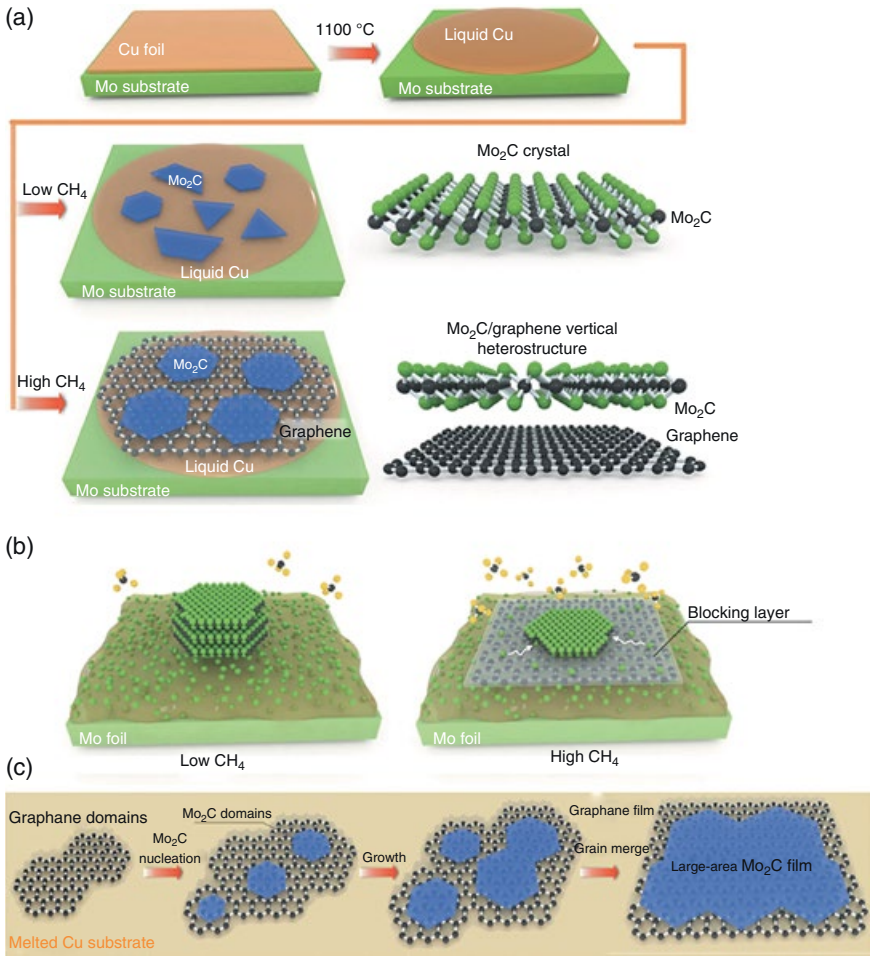


Figure 4.6 (a) Schematic showing the growth of Mo_2C crystals under low and high flow rates of CH_4. (b) Schematic showing the growth mechanism of Mo_2C at low and high CH_4, respectively. (c) Schematic showing the nucleation and coalescence of Mo_2C crystals grown on graphene. (d) Typical optical images of Mo_2C grains on graphene for growth times of 5, 30, 60, and 120 minutes, respectively, with 3 sccm CH_4 at 1100 °C. *Source:* Geng et al. [45]/Reproduced with permission from John Wiley & Sons, Inc. (e) Schematic diagram of the preparation process from MoS_2 to Mo_2C. (f) Cross-sectional HRTEM image of MoS_2/Mo_2C. *Source:* Jeon et al. [46]/Reproduced with permission from John Wiley & Sons, Inc.

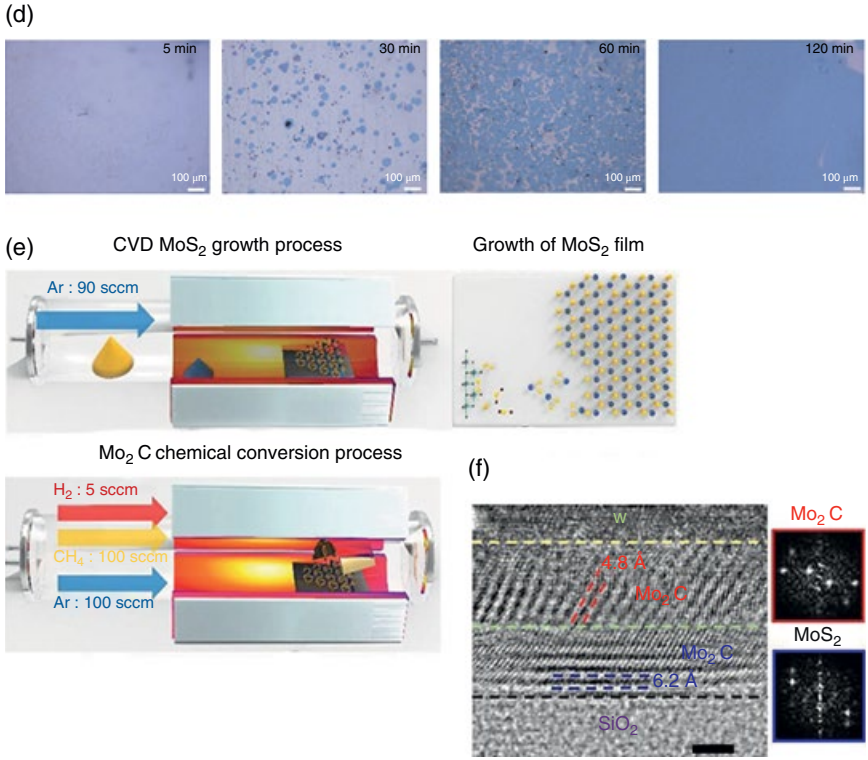


Figure 4.6 (Continued)

Based on the summary of above etching methods without fluoride, we hope to show some guidelines for synthesizing MXenes in future with much more efficiency. Meanwhile, inspired by the diverse current etching methods and mechanisms, more efforts are expected to improve the existing methods and develop new synthesis methods for more MXenes with specific morphology, terminations, layers, and heterostructures.

References

1 Naguib, M., Kurtoglu, M., Presser, V. et al. (2011). Two-dimensional nanocrystals produced by exfoliation of Ti_3AlC_2. *Advanced Materials* 23 (37): 4248–4253.

2 Srivastava, P., Mishra, A., Mizuseki, H. et al. (2016). Mechanistic insight into the chemical exfoliation and functionalization of Ti_3C_2 MXene. *ACS Applied Materials & Interfaces* 8 (36): 24256–24264.

3 Ghidiu, M., Lukatskaya, M.R., Zhao, M.Q. et al. (2014). Conductive two-dimensional titanium carbide 'clay' with high volumetric capacitance. *Nature* 516 (7529): 78–81.

4 Halim, J., Lukatskaya, M.R., Cook, K.M. et al. (2014). Transparent conductive two-dimensional titanium carbide epitaxial thin films. *Chemistry of Materials* 26 (7): 2374–2381.

5 Tang, Q., Zhou, Z., and Shen, P. (2012). Are MXenes promising anode materials for Li ion batteries? Computational studies on electronic properties and Li storage capability of Ti_3C_2 and $Ti_3C_2X_2$ (X = F, OH) monolayer. *Journal of the American Chemical Society* 134 (40): 16909–16916.

6 Wei, Y., Zhang, P., Soomro, R.A. et al. (2021). Advances in the synthesis of 2D MXenes. *Advanced Materials* 33 (39): e2103148.

7 Li, M., Lu, J., Luo, K. et al. (2019). Element replacement approach by reaction with Lewis acidic molten salts to synthesize nanolaminated MAX phases and MXenes. *Journal of the American Chemical Society* 141 (11): 4730–4737.

8 Li, Y., Shao, H., Lin, Z. et al. (2020). A general Lewis acidic etching route for preparing MXenes with enhanced electrochemical performance in non-aqueous electrolyte. *Nature Materials* 19 (8): 894–899.

9 Anasori, B., Lukatskaya, M.R., and Gogotsi, Y. (2017). 2D metal carbides and nitrides (MXenes) for energy storage. *Nature Reviews Materials* 2 (2): 16098.

10 Wang, C., Shou, H., Chen, S. et al. (2021). HCl-based hydrothermal etching strategy toward fluoride-free MXenes. *Advanced Materials* 33 (27): e2101015.

11 Jawaid, A., Hassan, A., Neher, G. et al. (2021). Halogen etch of Ti_3AlC_2 MAX phase for MXene fabrication. *ACS Nano* 15 (2): 2771–2777.

12 Li, G., Tan, L., Zhang, Y. et al. (2017). Highly efficiently delaminated single-layered MXene nanosheets with large lateral size. *Langmuir* 33 (36): 9000–9006.

13 Li, T., Yao, L., Liu, Q. et al. (2018). Fluorine-free synthesis of high-purity $Ti_3C_2T_x$ (T=OH, O) via alkali treatment. *Angewandte Chemie, International Edition* 57 (21): 6115–6119.

14 Pang, S.Y., Wong, Y.T., Yuan, S. et al. (2019). Universal strategy for HF-free facile and rapid synthesis of two-dimensional MXenes as multifunctional energy materials. *Journal of the American Chemical Society* 141 (24): 9610–9616.

15 Lukatskaya, M.R., Halim, J., Dyatkin, B. et al. (2014). Room-temperature carbide-derived carbon synthesis by electrochemical etching of MAX phases. *Angewandte Chemie, International Edition* 53 (19): 4877–4880.

16 Zhao, M.Q., Sedran, M., Ling, Z. et al. (2015). Synthesis of carbon/sulfur nanolaminates by electrochemical extraction of titanium from Ti_2SC. *Angewandte Chemie, International Edition* 54 (16): 4810–4814.

17 Presser, V., Heon, M., and Gogotsi, Y. (2011). Carbide-derived carbons - from porous networks to nanotubes and graphene. *Advanced Functional Materials* 21 (5): 810–833.

18 Cambaz, Z.G., Yushin, G., Osswald, S. et al. (2008). Noncatalytic synthesis of carbon nanotubes, graphene and graphite on SiC. *Carbon* 46 (6): 841–849.

19 Jänes, A., Thomberg, T., and Lust, E. (2007). Synthesis and characterisation of nanoporous carbide-derived carbon by chlorination of vanadium carbide. *Carbon* 45 (14): 2717–2722.

20 Sun, W., Shah, S.A., Chen, Y. et al. (2017). Electrochemical etching of Ti_2AlC to Ti_2CT_x (MXene) in low-concentration hydrochloric acid solution. *Journal of Materials Chemistry A* 5 (41): 21663–21668.

21 Yang, S., Zhang, P., Wang, F. et al. (2018). Fluoride-free synthesis of two-dimensional titanium carbide (MXene) using a binary aqueous system. *Angewandte Chemie, International Edition* 57 (47): 15491–15495.

22 Frey, N.C., Wang, J., Vega Bellido, G.I. et al. (2019). Prediction of synthesis of 2D metal carbides and nitrides (MXenes) and their precursors with positive and unlabeled machine learning. *ACS Nano* 13 (3): 3031–3041.

23 VahidMohammadi, A., Hadjikhani, A., Shahbazmohamadi, S., and Beidaghi, M. (2017). Two-dimensional vanadium carbide (MXene) as a high-capacity cathode material for rechargeable aluminum batteries. *ACS Nano* 11 (11): 11135–11144.

24 Song, M., Pang, S.Y., Guo, F. et al. (2020). Fluoride-free 2D niobium carbide MXenes as stable and biocompatible nanoplatforms for electrochemical biosensors with ultrahigh sensitivity. *Advancement of Science* 7 (24): 2001546.

25 Chen, J., Chen, M., Zhou, W. et al. (2022). Simplified synthesis of fluoride-free $Ti_3C_2T_x$ via electrochemical etching toward high-performance electrochemical capacitors. *ACS Nano* 16 (2): 2461–2470.

26 Huo, X., Zhong, J., Yang, Z. et al. (2021). In situ preparation of MXenes in ambient-temperature organic ionic liquid aluminum batteries with ultrastable cycle performance. *ACS Applied Materials and Interfaces* 13 (46): 55112–55122.

27 Zhu, S., Wang, C., Shou, H. et al. (2022). In situ architecting endogenous heterojunction of MoS_2 coupling with Mo_2CT_x MXenes for optimized Li^+ storage. *Advanced Materials* 34 (5): e2108809.

28 Shi, H., Zhang, P., Liu, Z. et al. (2021). Ambient-stable two-dimensional titanium carbide (MXene) enabled by iodine etching. *Angewandte Chemie, International Edition* 60 (16): 8689–8693.

29 Glasebrook, A.L. and Lovell, W.G. (1939). The isomerization of cyclohexane and methylcyclopentane. *Journal of the American Chemical Society* 61: 1717–1720.

30 El-Demellawi, J.K., Lopatin, S., Yin, J. et al. (2018). Tunable multipolar surface plasmons in 2D $Ti_3C_2T_x$ MXene flakes. *ACS Nano* 12 (8): 8485–8493.

31 Wei, Y., Zhang, P., Soomro, R.A. et al. (2021). Advances in the synthesis of 2D MXenes. *Advanced Materials* 33 (39): 2103148.

32 Xie, X., Xue, Y., Li, L. et al. (2014). Surface Al leached Ti_3AlC_2 as a substitute for carbon for use as a catalyst support in a harsh corrosive electrochemical system. *Nanoscale* 6 (19): 11035–11040.

33 Xuan, J., Wang, Z., Chen, Y. et al. (2016). Organic-base-driven intercalation and delamination for the production of functionalized titanium carbide nanosheets with superior photothermal therapeutic performance. *Angewandte Chemie, International Edition* 55 (47): 14569–14574.

34 Zou, G., Guo, J., Liu, X. et al. (2017). Hydrogenated core–shell MAX@$K_2Ti_8O_{17}$ pseudocapacitance with ultrafast sodium storage and long-term cycling. *Advanced Energy Materials* 7 (18): 1700700.

35 Zou, G., Zhang, Q., Fernandez, C. et al. (2017). Heterogeneous Ti_3SiC_2@C-containing $Na_2Ti_7O_{15}$ architecture for high-performance sodium storage at elevated temperatures. *ACS Nano* 11 (12): 12219–12229.

36 Zhang, B., Zhu, J., Shi, P. et al. (2019). Fluoride-free synthesis and microstructure evolution of novel two-dimensional $Ti_3C_2(OH)_2$ nanoribbons as high-performance anode materials for lithium-ion batteries. *Ceramics International* 45 (7): 8395–8405.

37 Huang, L., Li, T., Liu, Q., and Gu, J. (2019). Fluorine-free $Ti_3C_2T_x$ as anode materials for Li-ion batteries. *Electrochemistry Communications* 104: 106472.

38 Naguib, M., Halim, J., Lu, J. et al. (2013). New two-dimensional niobium and vanadium carbides as promising materials for Li-ion batteries. *Journal of the American Chemical Society* 135 (43): 15966–15969.

39 Naguib, M., Mochalin, V.N., Barsoum, M.W., and Gogotsi, Y. (2014). 25th anniversary article: MXenes: a new family of two-dimensional materials. *Advanced Materials* 26 (7): 992–1005.

40 Xue, N., Li, X., Han, L. et al. (2022). Fluorine-free synthesis of ambient-stable delaminated Ti_2CT_x (MXene). *Journal of Materials Chemistry A* 10 (14): 7960–7967.

41 Mei, J., Ayoko, G.A., Hu, C.F. et al. (2020). Two-dimensional fluorine-free mesoporous Mo_2C MXene via UV-induced selective etching of Mo_2Ga_2C for energy storage. *Sustainable Materials and Technologies* 25: e00156.

42 Ali, M.A., Khatun, M.R., Jahan, N., and Hossain, M.M. (2017). Comparative study of Mo_2Ga_2C with superconducting MAX phase Mo_2GaC: first-principles calculations. *Chinese Physics B* 26 (3): 033102.

43 Fan, Y., Li, L., Zhang, Y. et al. (2022). Recent advances in growth of transition metal carbides and nitrides (MXenes) crystals. *Advanced Functional Materials* 32 (16): 2111357.

44 Xu, C., Wang, L., Liu, Z. et al. (2015). Large-area high-quality 2D ultrathin Mo_2C superconducting crystals. *Nature Materials* 14 (11): 1135–1141.

45 Geng, D., Zhao, X., Chen, Z. et al. (2017). Direct synthesis of large-area 2D Mo_2C on in situ grown graphene. *Advanced Materials* 29 (35): 1700072.

46 Jeon, J., Choi, H., Choi, S. et al. (2019). Transition-metal-carbide (Mo_2C) multiperiod gratings for realization of high-sensitivity and broad-spectrum photodetection. *Advanced Functional Materials* 29 (48): 1905384.

47 Sun, W., Wang, X., Feng, J. et al. (2019). Controlled synthesis of 2D Mo_2C/graphene heterostructure on liquid Au substrates as enhanced electrocatalytic electrodes. *Nanotechnology* 30 (38): 385601.

48 Zeng, M.Q., Chen, Y.X., Li, J.X. et al. (2017). 2D WC single crystal embedded in

5

Guidelines for the Molten Salt Etching of MXenes

Miao Shen[1,2] *and Jian-Qiang Wang*[1,2]

[1] *Shanghai Institute of Applied Physics, Chinese Academy of Sciences, Shanghai, China*
[2] *University of Chinese Academy of Sciences, Beijing, China*

5.1 Introduction

Molten salts, which are ionic liquids that typically have melting points of >200 °C, have enabled the large-scale production of some of the most useful metals. The best example of a metal refined in this manner is aluminum, which is currently the second most widely used metal in the world. The industrial primary production of aluminum is entirely based on the Hall–Héroult smelting process, which involves the electrolysis of alumina dissolved in molten cryolite [1]. Another example is lithium, which is typically refined by the electrolysis of LiCl-based molten salts [2, 3] and has been used in various applications, such as in alloys and lithium-ion batteries. Magnesium [4] and calcium [5] are also examples of metals produced using molten salts.

Over the last 20 years, molten-salt-based processes have facilitated the preparation of various novel, valuable materials that are otherwise difficult or expensive to fabricate. These include the molten salt production of materials based on metals such as Ti [6], Nb [7], Cr [8], W [9], U [10], Ni [11], Fe [12], V [13], and Si [14]; intermetallic compounds such as $TiAl_3$ [15], ZrSi, and $ZrSi_2$ [16]; nanocomposites such as ZrC/ZrSi [17]; complex alloys such as $La(Ni_{0.7}Co_{0.3})_5$ [18]; and ceramics such as Cr_2AlC nanostructures [19], Ti_2AlC [19, 20], Ti_3SiC_2 [21, 22], and Ti_2AlN [22, 23].

In addition, molten-salt-based processes have provided various strategies for the preparation of carbon nanostructures [24, 25], graphene [26, 27], and two-dimensional (2D) MXenes [28–32]. Among these, the synthesis of MXenes by the

Transition Metal Carbides and Nitrides (MXenes) Handbook: Synthesis, Processing, Properties and Applications, First Edition. Edited by Chuanfang Zhang and Michael Naguib.
© 2024 John Wiley & Sons, Inc. Published 2024 by John Wiley & Sons, Inc.

selective etching of A-layer elements in MAX phase precursors has attracted attention in the last five years. Both reactive and relatively inert molten salts can be used to etch the A-layer in MAX materials by providing uniform ionically conductive heating media. In the naked state, the desolvation of solvent ions that occurs in conventional aqueous solutions and the need to overcome a high activation energy barrier are avoided [33]. More importantly, the nonsolvated ions in the molten salt allow for strong template or structure guidance, which causes the ions to be effectively adsorbed on the high-energy surface of the material and stabilize it during crystal nucleus growth. Hence, molten salts are beneficial for the synthesis of dynamically stable products that cannot be synthesized using conventional methods. In this chapter, an overview of molten salt etching techniques is presented.

5.2 Reactive Molten Salt Synthesis of MXenes

In general, the preparation of MXenes begins when HF is inserted into the edges of the MAX phase [34], followed by the surface functionalization of Ti atoms. The continued insertion of HF results in fluorinated MXenes with expanded interlayer spacing, accompanied by the continuous oxidation of Al to Al^{3+} (AlF_3) and the reduction of H^+ (HF) to H_2. Thus, all MAX phase etching techniques involve electron transfer as part of the surface reaction. Similarly, molten salts can serve as acids or bases to accept or donate electrons, respectively. According to Lewis theory [35], acids are electron-pair acceptors, and bases are electron-pair donors. In many metal–halide salt systems, the acids are polyvalent metal components (MX_q), and the bases are halide ions (X^-). The acid–base neutralization process involves the formation of a complex ion of the type MX_{q+r}^{r-} form, as follows:

$$MX_q + rX^- = MX_{q+r}^{r-}, \tag{5.1}$$

where $q =$ is the oxidation state of metal ion M, $q + r$ is the coordination number of metal ion M, and r is the net charge on the complex.

Acidic molten salts contain an excess of acidic components; consequently, there is a deficiency of halide ions in molten salts to coordinate with and stabilize all the polyvalent metal ions. Conversely, basic molten salts contain more halide ions than required to stabilize the polyvalent metal ions. These halide ions are supplied by alkali metal salts with weak coordination bonds between the monovalent metal ions and halide ions and can thus be referred to as "free" halide ions.

5.2.1 One-Component Lewis Salt Molten Salt (LAMS) for Etching

The chloracidity of a molten salt has a significant influence on electron gain and loss [35]. $ZnCl_2$ is a Lewis acid salt that is ionized to Zn^{2+} and tetrahedral $ZnCl_4^{2-}$ in its molten state [36–39]. In this context, Li et al. [28] etched Ti_3AlC_2 and Ti_2AlC

MAX phases in a $ZnCl_2$ molten salt under a nitrogen-protected environment at 550 °C (Figure 5.1a), and the weakly bound Al atoms in Ti_3AlC_2 were easily converted to Al^{3+} by a redox reaction in this acidic environment. The as-produced Al^{3+} further bonded with Cl^- to form $AlCl_3$, which has a boiling point of approximately 180 °C and likely rapidly evaporated at the reaction temperature. Meanwhile, the *in-situ* reduced Zn atoms intercalated into the Ti_3C_2 layers that filled the A-sites of the MAX phase previously occupied by Al atoms, resulting in the formation of Ti_3ZnC_2 (Eq. (5.2)). With the excess $ZnCl_2$ molten salt, the weakly bonded Zn atoms in Ti_3ZnC_2 were easily extracted from the 2D A-site plane and dissolved in the $ZnCl_2$ molten salt due to the redox reaction between Zn and Zn^{2+} [40, 41]. Moreover, the Cl^- anions spontaneously intercalated into the A-site plane and bonded with the specific site between the Ti_3C_2 sublayers to form a more stable phase, $Ti_3C_2Cl_2$ (Eq. (5.3)). Thus, the proportion of $ZnCl_2$ and the Al-containing MAX phase significantly influenced the final products; a molar ratio of Al-MAX/$ZnCl_2$ = 1 : 1.5 resulted in the Zn-MAX phase (Figure 5.1b, c), while a molar ratio of 1 : 6 led to MXenes with an abundance of –Cl terminations (Figure 5.1d, e). However, owing to their low melting and boiling points (283 °C and 732 °C, respectively) and because the evaporation rate is proportional to the mole fraction of $ZnCl_2$ in a salt, etching in single-component $ZnCl_2$ salt at 550 °C may lead to strong volatilization [42].

$$Ti_3AlC_2 + 1.5ZnCl_2 = Ti_3ZnC_2 + 0.5Zn + AlCl_3 \uparrow \tag{5.2}$$

$$Ti_3ZnC_2 + 1.5ZnCl_2 = Ti_3C_2Cl_2 + 2Zn \tag{5.3}$$

5.2.2 Multicomponent Salts Containing Lewis Salts for Etching

To avoid using volatile compounds alone, alkali or alkali earth metal halides were selected as inert media to dissolve the molten etchant. There are a few essential criteria to consider when selecting favorable inert media for etching MAX materials [43]. The molten salt should (i) have a low melting point, (ii) be compatible with reactants, (iii) possess high aqueous solubility for easy removal after synthesis by washing with water, (iv) have high thermal and chemical stability, (v) be nontoxic, inert, cheap, and readily available, and (vi) have low vapor pressure to avoid evaporation loss during operation. The melting points of frequently used chemically inert metal–halide systems are listed in Table 5.1. Notably, "inert" refers to a wide window of electrochemical operation. Therefore, alkali or alkali earth metal–halide systems, especially fluorides and chlorides, which are stable in the presence of strong reducing or oxidizing precursors, are considered inert in this context [43–45].

An NaCl–KCl medium with a higher electrochemical redox potential (V vs. Cl_2/Cl^-) than those of A-site elements (V vs. Cl_2/Cl^-) was proposed by Li et al. [29] to dissolve the Lewis salt. In the case of NaCl–KCl, the chloride activity was equal to

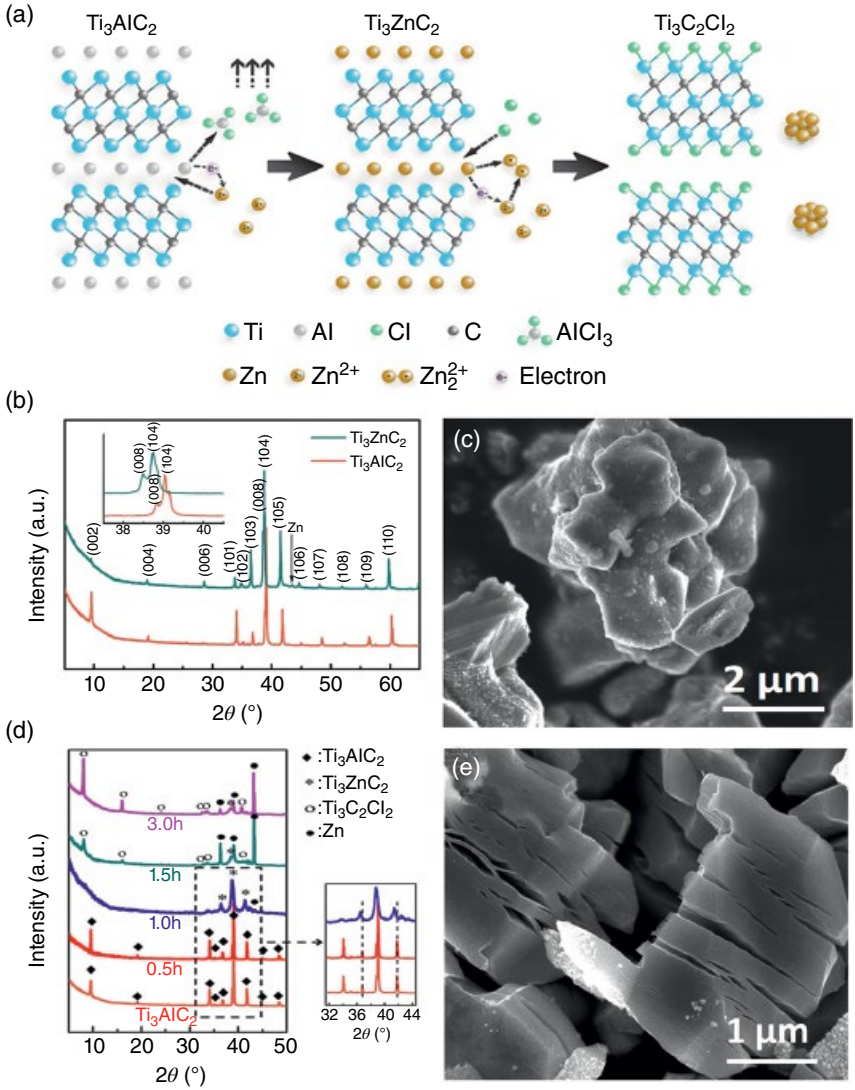


Figure 5.1 (a) Schematic illustration of the preparation procedure for Ti_3ZnC_2 and $Ti_3C_2Cl_2$MXene. (b) X-ray diffraction patterns of Ti_3AlC_2 and Ti_3ZnC_2. (c) SEM image of Ti_3ZnC_2. (d) XRD patterns of the product of the $Ti_3AlC_2/ZnCl_2 = 1 : 6$ system with different reaction times, showing the phase evolution from Ti_3AlC_2 toTi_3ZnC_2 to $Ti_3C_2Cl_2$. (e) SEM image showing $Ti_3C_2Cl_2$ in the as-reacted sample. *Source:* Li et al. [28]/Reproduced from American Chemical Society.

Table 5.1 Melting points and compositions of commonly used metal halides.

Salt system	Composition (mol%)	Melting point (°C)
LiCl : KCl	59 : 41	352
NaCl : KCl	50 : 50	658
$AlCl_3$: NaCl	50 : 50	154
LiF : NaF : KF	46.5 : 11.5 : 42	459
LI : KI	63 : 37	286

Source: Liu et al. [43]/Royal Society of Chemistry/Public Domain CC BY 3.0.

one because this salt was completely dissociated and provided free Cl^- [35]. The category of molten etchants has expanded to include Lewis acid salts, such as molten $CuCl_2$, $NiCl_2$, and $CoCl_2$, which can form complexes with free Cl– and gain electrons. The complexes that these salts form ($CuCl_4^{2-}$ [46, 47], $NiCl_4^{2-}$ [48], and $CoCl_4^{2-}$ [49]) are stabilized and typically exhibit much lower volatility and reactivity than the uncomplexed component, and, thus, the concentration of Lewis salt in NaCl–KCl usually affects the etching degree of the A-element from MAX precursor. The scope for A-site elements was expanded to include Al, Si, Ga, and Zn from various MAX phase precursors. Consider the etching of Ti_3SiC_2 as an example [29]. When the Ti_3SiC_2 MAX precursor is immersed in molten NaCl–KCl–$CuCl_2$ (2 : 2 : 3 mol) at 750 °C(Figure 5.2a), Si atoms are oxidized to Si^{4+} by Lewis acid Cu^{2+} (Figure 5.2b) owing to the higher redox potential of Cu^{2+}/Cu (−0.43 V vs. Cl_2/Cl^-) than that of Si^{4+}/Si (−1.38 V vs. Cl_2/Cl^-). Then, Si^{4+} bonds with Cl^- to form $SiCl_4$, with a boiling point of 57.6 °C, and rapidly evaporates at 750 °C. Simultaneously, Cu^{2+} is reduced to metallic Cu and the Cl^- anions bond with Ti_3C_2 to compensate for the electron gain (Figure 5.2c). The formed Cu particles are removed by ammonium persulfate (Figure 5.2d), affording $Ti_3C_2T_x$ powder with –Cl and –O surface terminations. Generally, the covalent M—X bonds in the MAX phase are very strong, while the M—A bonds are much weaker [50]. Hence, the Ti—C bonds remain unchanged during etching, and the simplified etching mechanism of Ti_3SiC_2 in $CuCl_2$ can be expressed as follows:

$$Si + 2CuCl_2 = SiCl_4\left(gas\right) + 2Cu \tag{5.4}$$

The Gibbs free energies (ΔG) between Si elements from the Ti_3SiC_2 phases and Lewis salts ($CuCl_2$, Eq. (5.4)) were −371.74 kJ at 750 °C, as calculated by HSC chemistry software (HSC 6.0), indicating that the reaction is thermodynamically spontaneous. However, the etching mechanism of Ti_3SiC_2 in $CuCl_2$ is different from those in $ZnCl_2$ and Ti_3AlC_2; no intermediate MAX phase ($Ti_3(Si_xCu_{1-x})C_2$ or

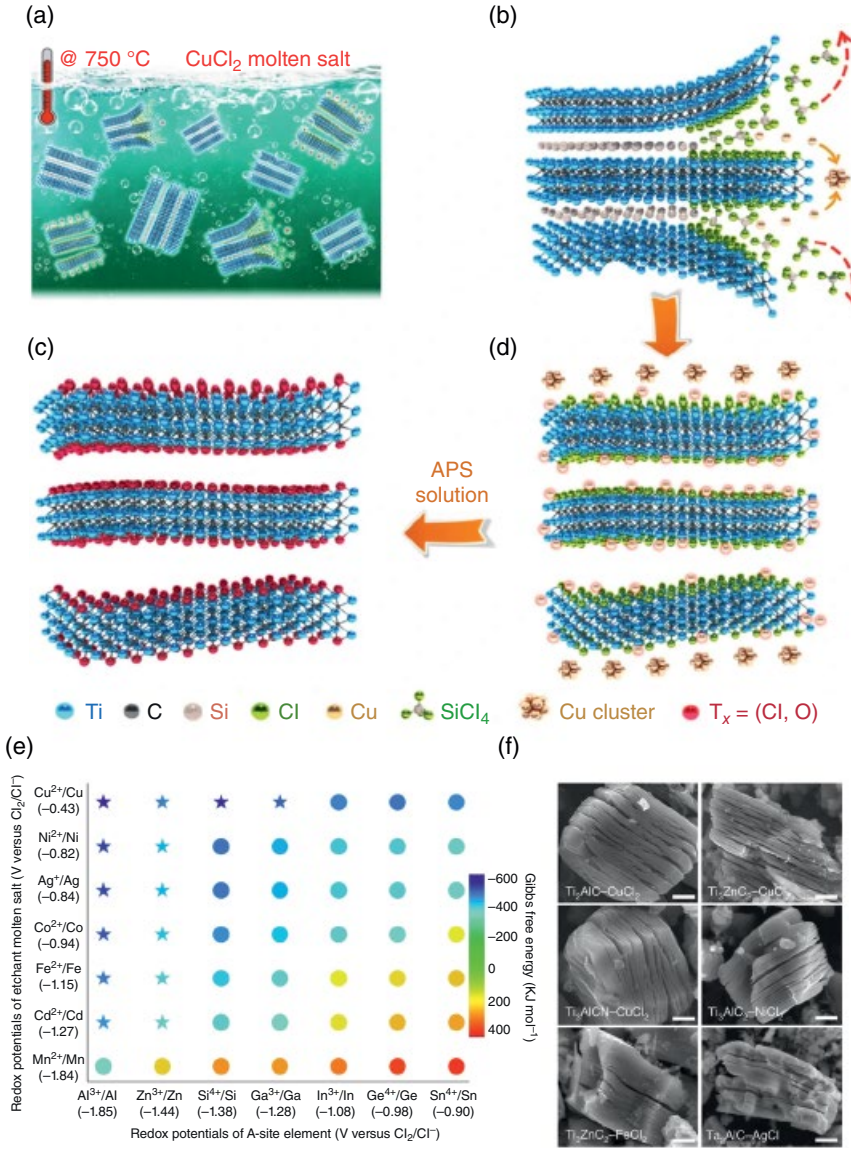


Figure 5.2 Schematic diagram of $Ti_3C_2T_x$ MXene preparation. (a) Ti_3SiC_2 MAX phase is immersed in $CuCl_2$ Lewis molten salt at 750 °C. (b, c) The reaction between Ti_3SiC_2 and $CuCl_2$ results in the formation of $Ti_3C_2T_x$MXene. (d) MS-$Ti_3C_2T_x$ MXene is obtained after further washing in an ammonium persulfate (APS) solution. (e) Gibbs Free Energy mapping (700 °C) guiding the selection of Lewis acid chloride salts according to electrochemical redox potentials of A site elements in MAX phases (*X* axis) and molten salt cations (*Y* axis) in chloride melts. Stars mark corresponding MXenes that are demonstrated in the current study. (f) SEM images reveal the typical accordion morphology of MXenes from different MAX phases etched by varied Lewis acid chlorides, such as Ti_2AlC by$CuCl_2$, Ti_3ZnC_2 by $CuCl_2$, Ti_3AlCN by $CuCl_2$, Ti_3AlC_2 by $NiCl_2$, Ti_3ZnC_2 by $FeCl_2$, and Ta_2AlC by AgCl. Scale bars are 2 μm. *Source:* Li et al. [29]/Reproduced from Springer Nature.

Ti_3CuC_2) was formed. This indicates that the etching mechanism of Ti_3SiC_2 in $CuCl_2$ is influenced by the redox reaction of Si and Cu^{2+}, but not the substitution of Cu for the A-sites.

Subsequently, the direct redox coupling between the A-element and the cation of the Lewis acid molten salt was used as a generic method for MAX phase etching, and the redox potential of the A-elements from the MAX phases or Lewis acid salt can be calculated using the following equations:

$$BCl_n(l) = B(s) + n/2Cl_2(g) \tag{5.5}$$

$$E(\mathrm{V}) = -\Delta G / nF \tag{5.6}$$

where B represents the A-site elements, such as Al, Fe, Zn, In, Ga, Si, and Sn, or Lewis acid salts, such as Mn, Cu, Co, Ni, Cd, and Ag; n denotes the number of electrons involved in the reaction; and ΔG is the Gibbs free energy of Eq. (5.5), which is calculated using HSC 6.0. F is to be 96 485 C mol^{-1}.

Table 5.2 lists the redox potentials of various metallic chlorides at 400–900 °C; the Gibbs free energies between the A-elements from the MAX phases and Lewis salts (BCl_n) can be expressed by Eq. (5.7), as follows:

Table 5.2 Redox potentials of molten salts (V vs. Cl_2/Cl^-) at 400–900 °C.

T(°C)	400	500	600	700	800	900
Al^{3+}/Al	−1.90	−1.88	−1.86	−1.84	−1.82	−1.80
Zn^{2+}/Zn	−1.64	−1.57	−1.50	−1.44	−1.38	−1.32
In^{3+}/In	−1.14	−1.12	−1.10	−1.08	−1.05	−1.03
Ga^{3+}/Ga	−1.35	−1.32	−1.30	−1.27	−1.25	−1.22
Ge^{4+}/Ge	−1.07	−1.04	−1.00	−0.97	−0.94	−0.91
Si^{4+}/Si	−1.48	−1.45	−1.41	−1.38	−1.35	−1.31
Sn^{4+}/Sn	−1.00	−0.97	−0.93	−0.89	−0.86	−0.82
Mn^{2+}/Mn	−1.97	−1.93	−1.88	−1.84	−1.80	−1.76
Fe^{2+}/Fe	−1.32	−1.26	−1.20	−1.15	−1.11	−1.76
Cu^{2+}/Cu	−0.61	−0.54	−0.48	−0.43	−0.37	−0.32
Co^{2+}/Co	−1.13	−1.06	−1.00	−0.94	−0.89	−0.85
Ni^{2+}/Ni	−1.05	−0.97	−0.90	−0.82	−0.75	−0.85
Cd^{2+}/Cd	−1.45	−1.39	−1.32	−1.27	−1.21	−1.16
Ag^{+}/Ag	−0.92	−0.89	−0.87	−0.84	−0.82	−0.79

Source: Adapted from Li et al. [29].

$$xA + y\mathrm{BCl}_n = x\mathrm{ACl}_m + \frac{x \cdot m}{n} B + \left(y - \frac{x \cdot m}{n} \right) \mathrm{BCl}_n \tag{5.7}$$

Figure 5.2e shows the Gibbs free energy mapping prepared from the thermodynamic data to guide the selection of effective Lewis acids for MAX phases with different A-elements. In these calculations, the etching is independent of both the composition of the MX layer and the value of n in $M_{n+1}AX_n$. Based on this map, a series of MAX phases, Ti_2AlC, Ti_3AlC_2, Ti_3AlCN, Nb_2AlC, Ta_2AlC, Ti_2ZnC, and Ti_3ZnC_2, was successfully exfoliated into their corresponding MXenes (Ti_2CT_x, $Ti_3C_2T_x$, Ti_3CNT_x, Nb_2CT_x, Ti_2CT_x, and $Ti_3C_2T_x$) using various chloride molten salts ($CdCl_2$, $FeCl_2$, $CoCl_2$, $CuCl_2$, AgCl, and $NiCl_2$), as indicated by the stars in Figure 5.2e. The scanning electron microscopy (SEM) images in Figure 5.2f show the lamellar microstructures of the various obtained MXenes. Ma et al. [51] recently developed a one-pot molten salt synthesis for MAX phase etching using M, A, and X (carbon) elements as precursors. $Ti_3C_2T_x$ and Ti_2CT_x MXenes were obtained via *in-situ* MAX phase synthesis at 1300 °C, followed by *in-situ* Lewis salt etching at 700 °C. Furthermore, the molten salt synthesis was scaled up from 0.5 to 60 g per batch, and the etching time was reduced from several hours to less than 30 minutes [52]. Although Lewis salts can effectively etch the A-elements in the MAX phase, they still have many limitations. For instance, Nb_2AlC and Ti_2AlC can be etched by a $CuCl_2$ molten salt to synthesize Nb_2C and Ti_2C MXenes with –Cl surface terminations. However, V_2AlC and Ta_2AlC with the same A-element as Al can only be converted into carbides and oxides. Theoretical calculations demonstrated that the success of molten salt etching depends on the exfoliation energy ($E_{\mathrm{Exfoliation}}$), and the exfoliation energy of the molten salts decreases in the following order [53]: $V_2AlC > Ta_2AlC > Nb_2AlC > Ti_2AlC$. Therefore, only when the exfoliation energy is lower than that of Ta_2AlC can this method be used to produce MXenes with an Al layer.

5.2.3 Parameters Influencing Molten Salt Etching

During Lewis salt etching, some etching parameters directly influence the structure and chemistry of the resultant MXenes, ultimately affecting their physicochemical properties. For example, the concentration and anions of etchants and etching temperature have been shown to affect the required etching times and processing of MXenes. Therefore, a deep understanding of how these parameters influence the microscopic and atomic structures of the resulting MXenes is required to optimize their syntheses. Below, an example by our group is presented to demonstrate the relationships between different reaction parameters and the obtained products.

Although the redox potential of Co^{2+}/Co was higher than that of Al^{3+}/Al at 500–900 °C [29], the Ti_3AlC_2 MAX precursor did not change after immersion in

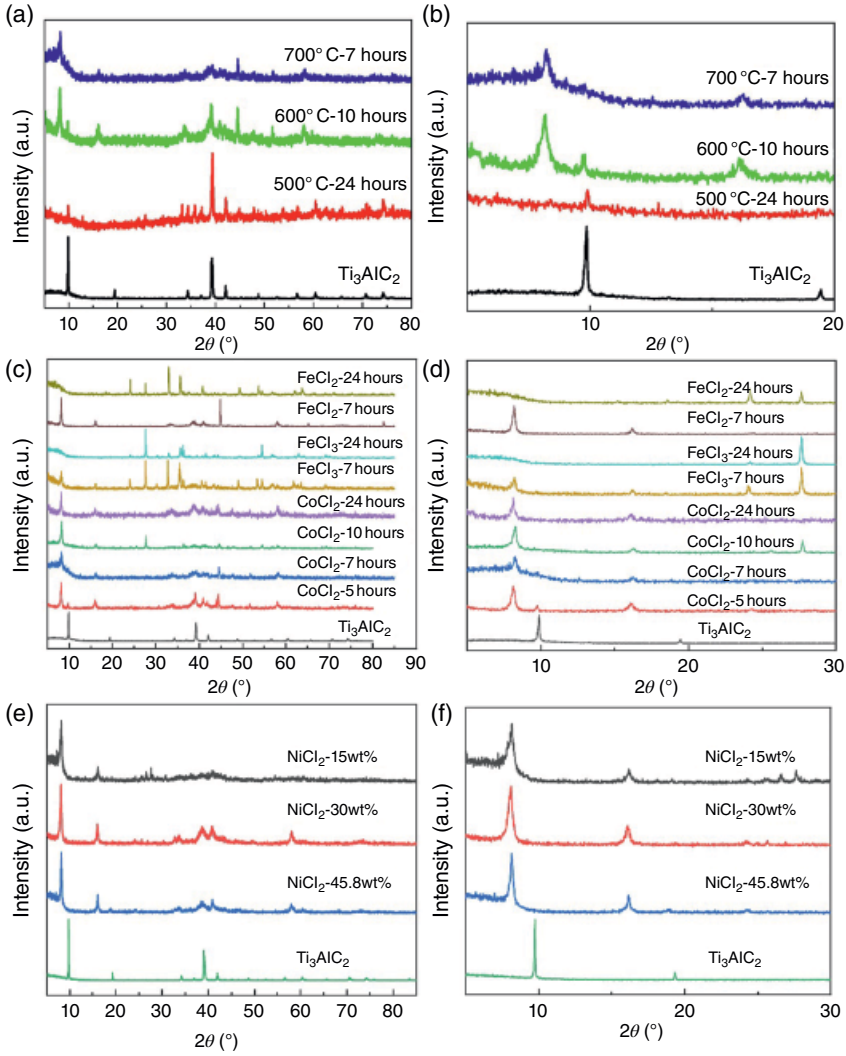


Figure 5.3 X-ray diffraction (XRD) patterns of MXene etching at different conditions; (a, b) Ti_3AlC_2 etched by $CoCl_2$ at different temperature and etching time; (c, d) Ti_3AlC_2 etched by different Lewis salt for different times; (e, f) Ti_3AlC_2 etched by different concentration of $NiCl_2$.

$CoCl_2$ Lewis salt with LiCl–KCl medium at 500 °C for 24 hours (Figure 5.3a, b, and Table 5.3). When the temperature was increased to 600 °C and maintained for 10 hours, most of the Ti_3AlC_2 was converted to $Ti_3C_2Cl_2$, but the characteristic peaks for unetched Ti_3AlC_2 were still detected. When the temperature was further increased to 700 °C and maintained for only 7 hours, the characteristic peaks of

Table 5.3 Etching parameters of molten salt etching.

Lewis acid salt	Etchant concentration (wt%)	LiCl–KCl (1 : 1 mol) (g)	Etching time (h)	Etching temperature (°C)	2θ (°)	d-spacing (Å)
$CoCl_2.6H_2O$	68.1	0.23	5	700	8.15	10.85
	68.1	0.23	7	700	8.23	10.74
	68.1	0.23	24	700	8.17	10.82
$CoCl_2$	45.8	0.23	24	700	8.12	10.89
$NiCl_2$	45.8	0.32	7	700	8.12	10.89
	45.8	0.32	24	700	Over-etched	—
	30	0.63	7	700	8.15	10.84
	15	1.53	7	700	8.06	10.97
$NiCl_2.6H_2O$	60.5	0.32	7	700	Over-etched	—
$FeCl_2$	45.8	0.32	7	700	8.18	10.81
	45.8	0.32	24	700	Over-etched	—
$FeCl_2.4H_2O$	56.2	0.32	7	700	8.14	10.86
$FeCl_3$	51.5	0.32	7	700	8.19	10.79
	51.5	0.32	24	700	Over-etched	—
	51.5	0.32	24	600	8.12	10.88
$FeCl_3.6H_2O$	63.6	0.32	7	700	8.10	10.92
AgCl	64.8	0.32	7	700	8.17	10.82
	64.8	0.32	24	700	8.18	10.81
$ZnCl_2$	100	0	5	550	8.12	10.88
	15.4	1.54	5	550	Ti_3ZnC_2	

unetched Ti_3AlC_2 could not be measured by XRD. Therefore, the kinetics of selective etching of the A-element by Lewis acids is significantly influenced by the temperature.

Suitable etching time is another key parameter that should be considered. For instance, Ti_3AlC_2 could not be completely etched by $CoCl_2$ within 5 hours at 700 °C (Figure 5.3c, d, and Table 5.3). However, when etched for 7 hours, the characteristic peak of the unetched Ti_3AlC_2 was not visible. If the etching time was further extended to 24 hours, the Ti defects in $Ti_3C_2Cl_2$ might have increased because the etchants also attack the carbide layers from complex chemical reactions, leaving defects in the MXene flakes [54]. In addition, the oxidation of the etching agent also affects the structure of the products. For instance, some highly oxidized Lewis acids, such as $FeCl_3$ and $FeCl_2$, over-etch the MAX phase over an extended period,

whereas moderately oxidized Lewis acids, such as $CoCl_2$ and AgCl, only cause defects to the product without damaging the 2D structure (Figure 5.3c, d, and Table 5.3). The crystalline water in Lewis salt also increases its oxidation, for example, in $NiCl_2{\cdot}6H_2O$. After reacting with Ti_3AlC_2 for 7 hours, the products etched by $NiCl_2{\cdot}6H_2O$ were over-etched whereas the products etched by $NiCl_2$ did not destroy the 2D structure (Table 5.3).

The proportion of $ZnCl_2$ and the Al-containing MAX phase significantly influence the final products [28]. A molar ratio of Al-MAX/$ZnCl_2$ = 1 : 1.5 resulted in the Zn-MAX phase, while a molar ratio of 1 : 6 led to MXenes containing a large number of –Cl terminations. However, in the LiCl–KCl salt, only the Zn-MAX phase was formed when the molar ratio of Al-MAX/$ZnCl_2$ was 1 : 10, indicating that the concentration of $ZnCl_2$ greatly influenced the final products (Figure 5.3e, f, and Table 5.3). Furthermore, as the HF concentration affects the etching of the $Ti_3C_2T_x$ MXene and Ti vacancies, a higher HF concentration leads to a higher defect concentration and vacancy clusters [54]. The concentration of Lewis molten salts may also influence these structures (Figure 5.3e, f, and Table 5.3). Atomic defects in 2D materials can directly influence the electronic structure, which, in turn, determines the electronic, optical, and magnetic properties [55–57]. The influence of the method on the creation of atomic defects should be of interest to researchers; in particular, the Ti vacancy in the $Ti_3C_2T_x$ MXene requires further investigation using atomic-resolution aberration-corrected STEM [54].

5.3 Inert Molten Salt Synthesis of MXenes

Recently, researchers have tried to synthesize 2D layered $Ti_{n+1}N_n$ by chemical exfoliation of the $M_{n+1}AN_n$ matrix. However, owing to the poor stability of the $M_{n+1}N_n$ layers during etching (e.g. HF), the aqueous system is not compatible with the MAX phases of the nitrides [58]. Hence, the most effective method to explore 2D layered transition metal nitrides (TMNs) is to use high pressure to prevent the out-diffusion of *N* atoms from the metal lattice at high temperatures [59–61]. The HF-etched Mo_2C can be converted to the Mo_2N MXene through thermal treatment at 600 °C in NH_3 atmosphere (Figure 5.4a) [62]. However, a similar process cannot be applied to V_2CT_x. Figure 5.4b shows the XRD pattern of two carbide MXenes and their corresponding derivatives after NH_3 treatment. The V_2CT_x-derived material exhibits representative peaks of both V_2N and cubic VN owing to structural and compositional degradation during thermal transformation.

The nonsolvated ions in the molten salt cause the ions to be effectively adsorbed on the high-energy surface of the material and stabilize it during the crystal nucleus growth; thus, molten salts are beneficial to the synthesis of dynamically stable products that cannot be synthesized by conventional methods. Hence, alkali molten salts have been used as catalysts to achieve the facile large-scale

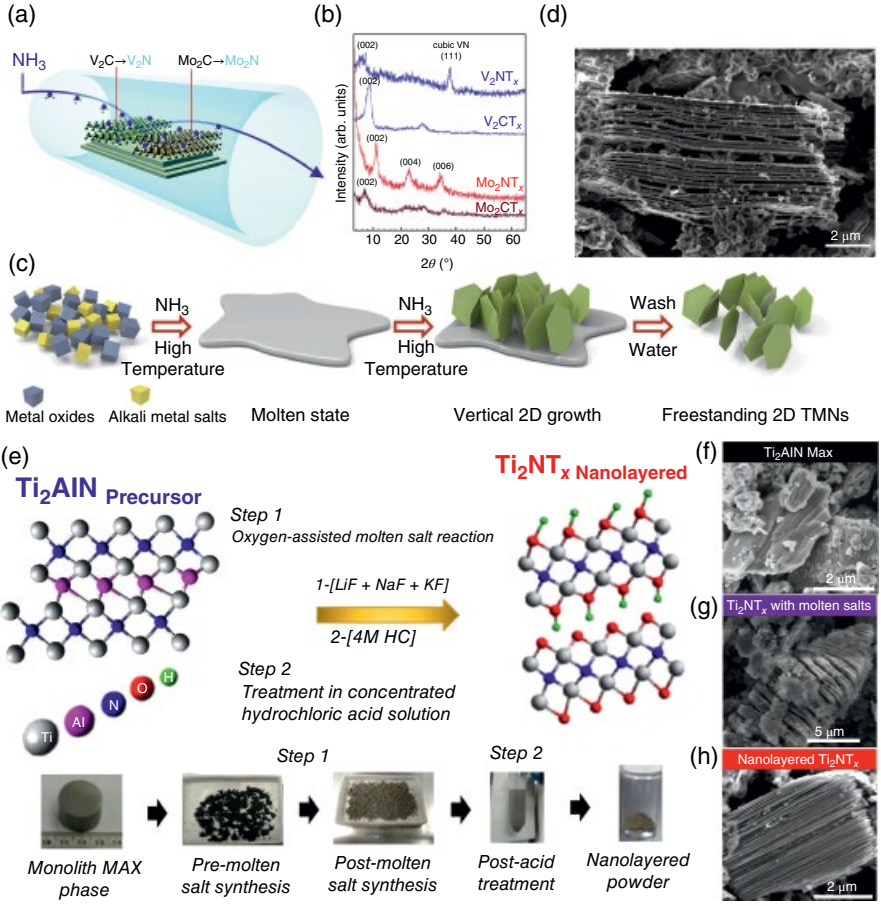


Figure 5.4 (a) Synthesis of materials via the catalytic molten salt method. (b) SEM image of molten-salt-treated Ti_4N_3 at 550 °C for 0.5 hours under Ar flow. (c) Process diagrams of the transformation from carbide MXenes (Mo_2CT_x and V_2CT_x) to nitride MXenes based on ammonization. (d) XRD patterns of Mo_2CT_x and V_2CT_x before and after ammonization at 600 °C for 1 hour. *Source:* Urbankowski et al. [62]/Reproduced from Royal Society of Chemistry. (e) Synthesis procedure for Ti_2NT_x MXene via oxygen-assisted molten salt reaction of Ti_2AlN (MAX phase) at 550 °C for 1 hour under 1% O_2 in N_2 followed by 12 hours under Ar. The excess fluoride salts are removed using concentrated hydrochloric acid to yield nanolayered Ti_2NT_x. We attribute T_x = O and/or OH based on FTIR, Raman, and STEM-EELS data, though T_x = F also may exist. SEM images for (f) Ti_2AlN MAX, (g) Ti_2NT_x with molten salt, and (h) nanolayered Ti_2NT_x. The lateral size of the flakes is 0.5–5 μm.

(over decagram) synthesis of a family of 2D-layered TMNs, $MoN_{1.2}$, $WN_{1.5}$, and $Mo_{0.7}W_{0.3}N_{1.2}$ at atmospheric pressure [63]. *Ex-situ* experiments revealed that molten salt as a medium can lower the formation energy of 2D-layered TMNs by assuring liquid–gas synthesis and forming a TMN–salt–TMN superstructure as an intermediate (Figure 5.4c). In addition, Urbankowski et al. [31] utilized the mixed molten salts LiF, NaF, and KF at 550 °C for 0.5 hours to etch Ti_4AlN_3, which afforded the first $Ti_4N_3T_x$ nitride MXene. The corresponding SEM image in Figure 5.4d further demonstrates the typical accordion-like morphology of the obtained $Ti_4N_3T_x$. In theory, alkali metal fluorides are inert and stable in carbon materials, and the etching mechanism of Ti_4AlN_3 in inert LiF–NaF–KF has not been clarified. Djire et al. [30] proposed the use of an oxygen-assisted molten fluoride salt to produce Ti_2NT_x MXenes. A small volume of 1% O_2 in N_2 was introduced into the reactor, during which the sample expanded in volume and changed color from black to black–brown (Figure 5.4e). The SEM micrographs of the oxygen-assisted molten-salt-treated Ti_2AlN (Figure 5.4f) and nanolayered Ti_2NT_x MXenes (Figure 5.4g) exhibit layered structures, indicating the formation of MXenes. The initial etching mechanism in the presence of small volumes of O_2 involved the formation of aluminum oxides, which then reacted with fluoride salts to form aluminum oxyfluoride compounds. For comparison, when pure argon or nitrogen was used, there was no MXene formation, even with very long reaction times (24 hours). In this study, O_2 was the oxidizing agent and fluoride salts acted as inert media to dissolve the aluminum oxyfluoride. Based on this, the key to the successful etching of Ti_4AlN_3 in LiF–NaF–KF is the dissolution of some oxidizing agents, such as moisture, in molten fluoride. Owing to their hygroscopic nature, these raw LiF–NaF–KF fluorides can absorb water and frequently undergo pyrohydrolysis upon melting [64, 65] and being converted to HF according to Eq. (5.8); then, $Ti_{n+1}AlN_n$ MAX is easily etched in the molten fluoride. As there is no need to use aqueous or organic solvents, the water or hydroxyl content in the molten salts can be limited and controlled, which may be the key to the successful synthesis of nitride MXenes. However, further research is required before this theory can be properly tested.

$$H_2O + 2F^- = O^{2-} + 2HF \tag{5.8}$$

5.4 Surface Terminations of MXenes Regulated by Molten Salt

As the nature of surface termination relies on molten salt anions, the surface chemistry of MXenes can be regulated by varying the type of molten salt etchant used. Li et al. [29] used $CuCl_2/CuBr_2/CuI$ to synthesize $Ti_3C_2T_x$ (T = Cl, Br, and I),

and the proportion of the corresponding halogen groups was controlled by adjusting the proportion of the three salts in the etchants [66]. However, a reduction in the electro-negativity of halogen atoms (the order of electro-negativity is Cl > Br > I) increases the difficulty of etching the MAX phases. In addition to modifying surface termination by molten salt etchants, molten salt can be used as a solvent while other anions are added to replace the functional groups at 300–600 °C [22, 43, 67]. Kamysbayev et al. [68] reported a two-step method for preparing MXenes with adjustable surface terminations. In a typical synthesis, melted chlorine salt or bromine salt was used to etch the MAX phase to produce Cl- or Br-terminated MXenes . By using Li_2O, Li_2S, or Li_2Se molten salts, the –Cl or –Br terminations on the MXenes could be replaced by –O, –S, or –Se terminations at high temperatures, whereas the use of LiH eliminates all the surface terminations. Significantly, the superconducting ability was first observed in MXenes by functionalizing Nb_2CT_x with terminations such as –Cl, –S, –Se, and –NH. This method allowed the substitution or elimination of various terminations on the surface of the MXenes by molten inorganic salts, providing a new pathway for designing surface-selective MXenes for advanced applications. By using this method, Guo et al. and Xu et al. [69, 70] proposed that $Ti_3C_2T_x$ with –F surface terminations can also be treated in molten salt under atmospheric pressure to simultaneously introduce –N and remove –F surface terminations, in which LiCl–KCl salt was used as the solvent and Li_3N was the nitrogen source. Hence, heteroatom doping is easily achieved in high-temperature molten salts.

5.5 Electrochemical Etching of MAX in Molten Salt

Typically, during chemical etching, each active site on the surface participates in both anodic and cathodic reactions. Thus, when using Lewis acidic molten salts (LAMSs) of $ZnCl_2$ or $CuCl_2$ as etchants, the reduction products of metallic Cu or Zn remain in the MXenes [28, 29]. For subsequent surface modification, metallic impurities must be removed by washing with an oxidizing acid, which complicates the surface modifications and produces acidic liquid waste. To develop a simple and environmentally friendly process to prepare MXenes without metallic impurities, Shen et al. [32] proposed the molten-salt-assisted electrochemical etching (MS-E-etching) method to synthesize fluorine-free $Ti_3C_2Cl_2$. Figure 5.5a shows a schematic of the MS etching process in which Ti_3AlC_2 and nickel are used as the anode and cathode, respectively. When a voltage of 2.0 V is applied at 450 °C, the Al atoms are selectively oxidized and removed from the Ti_3AlC_2 phase to form the $Ti_3C_2Cl_2$ product (Figure 5.5b). The oxidized Al subsequently bonds with Cl in the electrolyte to form $AlCl_3$ because of its strong binding capability. Thus, the evaporation of $AlCl_3$ at 450 °C provides the driving force for the outward diffusion of Al atoms. Because the MS-E-etching of Al is thermodynamically preferable [29],

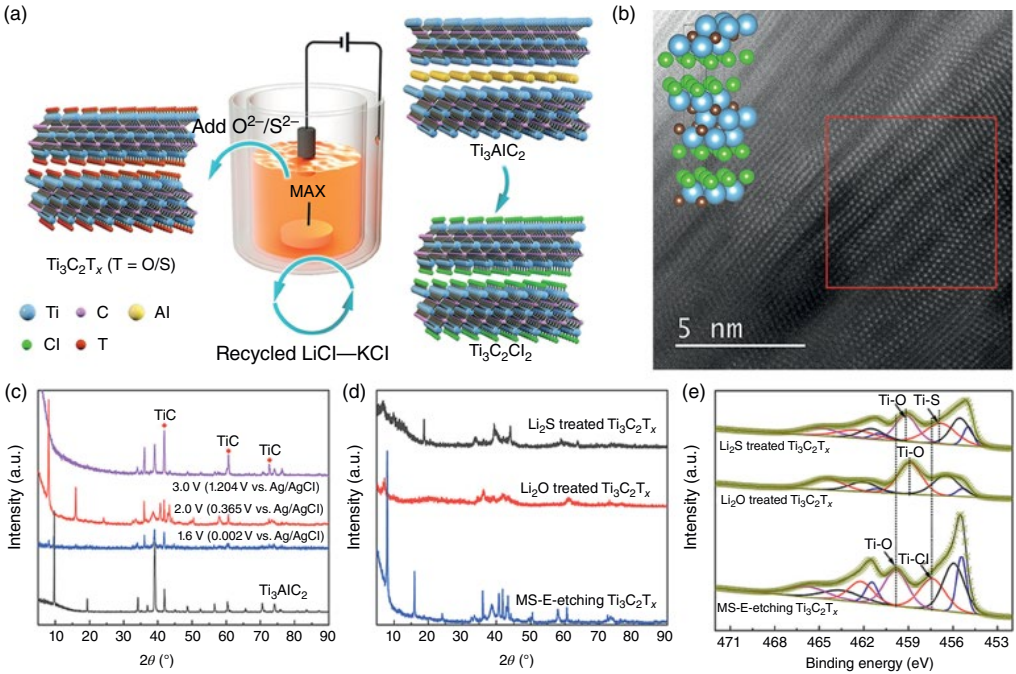


Figure 5.5 (a) Schematic illustration of the synthesis of MXene from the MAX phase by MS-E-etching and the *in-situ* modification of surface terminations. (b) HR-STEM image showing the atomic positions of $Ti_3C_2Cl_2$; (c) XRD patterns of product obtained by MS-E-etching method taken at different voltages in LiCl–KCl system. (d) XRD patterns of obtained $Ti_3C_2T_x$ with various surface terminations. (e) High-resolution Ti 2p spectrum of MSE-etching $Ti_3C_2T_x$ after treated in LiCl–KCl–Li_2O and LiCl–KCl–Li_2S. *Source:* Adapted from Shen et al. [32].

electrochemical potential plays a crucial role. When the applied voltage is reduced to 1.6 V, a large quantity of unetched Ti_3AlC_2 remains in the product. When the applied voltage is increased to 3.0 V, TiC is obtained, indicating that some of the Ti atoms are over-etched (Figure 5.5c) [71, 72]. Because electrons are used as reaction agents, cathode reduction and anode etching can be spatially isolated; thus, metallic impurities are not present in $Ti_3C_2Cl_2$. The synthesis mechanism is as follows:

$$\text{Anode: } Ti_3AlC_2 + 3Cl^- = AlCl_3 \uparrow + Ti_3C_2 + 3e^- \tag{5.9}$$

$$Ti_3C_2 + 2Cl^- = Ti_3C_2Cl_2 + 2e^- \tag{5.10}$$

$$\text{Cathode: } Li^+\left(K^+\right) + e^- = Li\left(K\right) \tag{5.11}$$

$$\text{Overall reaction: } Ti_3AlC_2 + 5\,LiCl\left(KCl\right) = Ti_3C_2Cl_2 + 5\,Li\left(K\right) + AlCl_3 \uparrow \tag{5.12}$$

After MS-E-etching, other inorganic salts, such as Li_2O and Li_2S, are pressed into pellets and directly added to the melting system to modify the –Cl surface terminations *in-situ* with –O or –S (Figure 5.5d, e). Thus, this new MS-E-etching approach is a one-pot molten salt process with short modification steps applicable to a wide variety of surface terminations. Besides, the electrochemical etching of MAX in molten salt is characterized by a large controllable electric field range, wide electrochemical window (>3.5 V), and high ionic conductivity (about 10^2 times that of water); these characteristics may be beneficial for etching a nonypical MAX with high stripping energy, such as Mo_2Ga_2C. Relevant research is ongoing to determine whether the range of A-site elements can be broadened to include Si, Ga, and Zn, and whether the range of MAX can be extended to precursors with high stripping energy barriers.

5.6 Interconversion of MXene and MAX in Molten Salt

Above work is mainly based on the selective oxidation of A-element from MAX phase to MXene in molten salts by chemical or electrochemical methods and the anion-exchange reaction with chlorinated or brominated MXenes to produce terminations of –O, –S, –Se, –Te, and –NH. However, the direct use of oxide or chalcogenide with strong covalent bonds to supply –O and chalcogen terminations would be a difficult task owing to their high melting temperature and low solubility. Recently, Huang et al. [73] reported chemical-scissor-mediated intercalation chemistry for structural editing of non-vdW MAX phases and vdW MXenes. The etching and intercalating steps are regulated separately to achieve the mutual structural transformation between MAX and MXene phases.

5.6.1 From MAX to New MAX

The LAMS is applied to etch out the Al atoms from a series of $M_{n+1}AlX_n$ phases (e.g. Ti_3AlC_2, Ti_3AlCN, Nb_2AlC, and Ta_2AlC), and then, the vdW vacancies in gaps $M_{n+1}X_n$ are reoccupied by the predissolved metal elements with low melting points in molten salts, resulting in the formation of new $M_{n+1}AX_n$ phases (A = Ga, In, Sn, and Ge). The LAMS scissor must preferentially etch the A atoms (e.g. Al) out of MAX phases but avoid the oxidation of intercalating metals (e.g. Bi, Ge, Sn, In, and Ga) [74]. According to this intercalation chemistry, Sb is successfully incorporated, creating unknown MAX phases, such as Ti_3SbC_2, Ti_3SbCN, Nb_2SbC, and $Ti_3(Sb_{0.5}Sn_{0.5})CN$. In addition, during etching, some noble elements can be added into LAMS to form low-eutectic-point alloys. For instance, the LAMS scissor $CdCl_2$ can open the non-vdW gap of Nb_2AlC, and itself be reduced into Cd metal. The Cd–Au alloy with 629 °C eutectic point is formed in molten salt, which is conducive to the insertion of gold atoms into the gap of Nb_2C and the formation of completely substituted Nb_2AuC. The prealloying strategy can also reduce the melting point of noble metals and promote the diffusion and intercalation of these noble atoms in the interlayer gap of Nb_2C. For example, Ag–Sb (m.p. 484 °C) [75], Pd–Sn (m.p. 600 °C) [76], Pt–Cd (m.p. 670 °C) [77], and Rh–Sn (m.p. 660 °C) [78] alloys can be added to Lewis salt to synthesize the noble-metal-containing MAX phases.

5.6.2 From MAX to New Terminated MXene

As reported above, the LAMS acted as an etchant to draw A-site atoms out of MAX phases, while producing metal atoms. If the chalcogenide elements are added in advance, they react with metal products to form metal chalcogenide compounds, which may change the surface termination of MXenes according to the hard/soft acid/base principle [79]. For example, $CuCl_2$ LAMS first etched Al from Nb_2AlC and opened the gap between Nb_2C layers. The added Te reacted with the generated Cu in the chloride salt to form Cu_2Te alloy with a eutectic point around 610 °C. The diluted Te atoms in Cu_2Te become active and withdraw electrons from electropositive Nb atoms to form Te^{2-} anions, which further coordinate with oxidized Nb in Nb_2C to form Nb_2CTe_x MXene. Antimony follows the same intercalation mechanism and two antimony-terminated MXenes, Ta_2CSb_x and $Ta_4C_3Sb_x$, were synthesized.

5.6.3 From MXene to MAX

Some reducing metals can act as scissors to remove the surface terminations of MXene, which provides the opportunity for reverse transformation from MXenes to MAX phases and metal-intercalated 2D carbides. Taking the well-known

$Ti_3C_2Cl_2$ MXene as an example, the reducing Ga, Al, Sn, and Cd metals react with Cl ligands, and the $Ti_3C_2Cl_2$ is converted into a nonterminated Ti_3C_2. The resultant reopened gap in Ti_3C_2 is available to accommodate metal atom to form a new MAX phase of Ti_3GaC_2, Ti_3AlC_2, Ti_3SnC_2, or Ti_3CdC_2. The metal scissors of Al and Zn can also remove the Cl ligand and promote the insertion of some other metal atoms into defunctionalized Ti_3C_2 MXene to form a series of unconventional MAX phases, such as $Ti_3(Cd_{0.5}Zn_{0.5})C_2$ and even double-A $Ti_3Cd_2C_2$. Furthermore, when metal scissor-mediated atom intercalation is controlled, the structure of adjacent $M_{n+1}X_n$ slabs can be intercalated with a layer of metal atoms, but the surface termination groups are retained. These metal-intercalated carbides combine the functional features of MXenes, such as tunable surface termination, with the structural features of MAX phases, such as oxidation-resistant interlayers, and the specific applications of these materials need to be further explored.

5.7 Limitations and Outlook

The synthesis of MXene in molten salt with naked ions can avoid the desolvation process that occurs in traditional aqueous solutions, which effectively weakens the metallic bonding in the precursor material owing to a strong polarization effect, thus promoting rapid synthesis under mild conditions. Molten salt medium has a wider electrochemical operation window (>3.5 V) and higher ionic conductivity (about 10^2 times that of water) than aqueous solutions; hence, the regulation of redox reaction in the molten salt system is more applicable to the etching of a nontypical MAX with high stripping energy, such as nitride MXenes.

The application of MXene can be theoretically predicted based on its surface terminations and electronic properties, but the mainstream HF etching method usually produces MXene with complex surface groups, such as –F, –O, and –OH. Hence, complex terminations result in a wide gap between the predicted properties and the actual behavior. It is theoretically possible to synthesize MXenes with exclusively controllable functional groups in a molten salt environment by varying the anions. Furthermore, the molten salts can dissolve many specific inorganic anions, including VIIA (F^-, Cl^-, Br^-, and I^-), VIA (O^{2-}, S^{2-}, Se^{2-}, and Te^{2-}), and VA (N^{3-}, P^{3-}, and Sb^{3-}), which provide the possibility to achieve the new surface terminations, such as –O, –S, –Se, –Te, –Sb, –P, and –NH. The intercalation and diffusion of metals into MXene occur only at high temperatures; hence, some new noble-metal-containing MAX phases and the interconversion of MXene and MAX can only be achieved in high-temperature molten salt. This may help discover a series of 2D metal-intercalated layered carbides and expand the application scope of MXene. Although the nonaqueous molten salt etching method has expanded the scope for A-site elements to Al, Si, Ga, and Zn from

various MAX phase precursors and the range of surface terminations to chalcogenide and phosphor elements, the research is still in an early stage. For instance, Nb_2AlC and Ti_2AlC can be etched by a $CuCl_2$ molten salt to synthesize Nb_2C and Ti_2C MXenes, respectively, with –Cl surface terminations. However, V_2AlC and Ta_2AlC with the same A-element as Al can only be converted into carbides and oxides. How to etch the nontypical MAX with high stripping energy in molten salt still needs to be studied. Nitride MXenes are difficult to synthesize by means other than molten salt etching, but the mechanism of 2D layered $Ti_{n+1}N_n$ etched in molten salt method is still unclear; thus, the molten salt etching method for the synthesis of nitrides should be explored in the future. Although some noble-metal-containing MAX phases can be synthesized by adding low-eutectic-point noble alloys into LAMS and MXene can also be directly converted to traditional MAX, the conversion mechanism should be further studied. In summary, owing to the complex conditions of molten salt, such as high temperature, weak solvation, and electron transfer effect, some special MXene materials that cannot be synthesized by conventional aqueous solutions probably can be synthesized by molten salt etching.

References

1 Alamdari, H. (2017). Aluminium production process: challenges and opportunities. *Metals* 7 (4): 133.

2 Vikstrom, H., Davidsson, S., and Hook, M. (2013). Lithium availability and future production outlooks. *Applied Energy* 110: 252–266.

3 Sadoway, D.R. (1998). Toward new technologies for the production of lithium. *JOM* 50 (5): 24–26.

4 Demirci, G. and Karakaya, I. (2007). Collection of magnesium in an Mg-Pb alloy cathode placed at the bottom of the cell in $MgCl_2$ electrolysis. *Journal of Alloys and Compounds* 439 (1-2): 237–242.

5 Frary, F.C., Bicknell, H.R., and Tronson, C.A. (1910). Efficiency in the electrolytic production of metallic calcium. *Journal of Industrial & Engineering Chemistry* 2 (12): 522–524.

6 Chen, G.Z., Fray, D.J., and Farthing, T.W. (2000). Direct electrochemical reduction of titanium dioxide to titanium in molten calcium chloride. *Nature* 407 (6802): 361–364.

7 Vishnu, D.S.M., Sanil, N., Mohandas, K.S., and Nagarajan, K. (2017). Factors influencing the direct electrochemical reduction of Nb_2O_5 pellets to Nb metal in molten chloride salts. *Acta Metallurgica Sinica-English Letters* 30 (3): 218–227.

8 Ge, X., Jin, S., Zhang, M. et al. (2015). Synthesis of chromium and ferrochromium alloy in molten salts by the electro-reduction method. *Journal of Mining and Metallurgy Section B-Metallurgy* 51 (2): 185–191.

9 Abdulaziz, R., Brown, L.D., Inman, D. et al. (2014). Novel fluidised cathode approach for the electrochemical reduction of tungsten oxide in molten LiCl-KCl eutectic. *Electrochemistry Communications* 41: 44–46.

10 Brown, L.D., Abdulaziz, R., Jervis, R. et al. (2017). A novel molten-salt electrochemical cell for investigatingthe reduction of uranium dioxide to uranium metal by lithium using in situ synchrotron radiation. *Journal of Synchrotron Radiation* 24: 439–444.

11 Tang, D., Yin, H., Cheng, X. et al. (2016). Green production of nickel powder by electroreduction of NiO in molten Na_2CO_3-K_2CO_3. *International Journal of Hydrogen Energy* 41 (41): 18699–18705.

12 Xie, K. and Kamali, A.R. (2019). Electro-reduction of hematite using water as the redox mediator. *Green Chemistry* 21 (2): 198–204.

13 Xu, Y., Jiao, H., Wang, M., and Jiao, S. (2019). Direct preparation of V-Al alloy by molten salt electrolysis of soluble $NaVO_3$ on a liquid Al cathode. *Journal of Alloys and Compounds* 779: 22–29.

14 Zhao, J., Lu, S., Hu, L., and Li, C. (2013). Nano Si preparation by constant cell voltage electrolysis of FFC-cambridge process in molten $CaCl_2$. *Journal of Energy Chemistry* 22 (6): 819–825.

15 Li, S., Zou, X., Zheng, K. et al. (2017). Direct production of $TiAl_3$ from Ti/Al-containing oxides precursors by solid oxide membrane (SOM) process. *Journal of Alloys and Compounds* 727: 1243–1252.

16 Liu, H., Cai, Y., Xu, Q. et al. (2015). A novel preparation of Zr-Si intermetallics by electrochemical reduction of $ZrSiO_4$ in molten salts. *New Journal of Chemistry* 39 (12): 9969–9975.

17 Liu, H., Cai, Y., Xu, Q. et al. (2017). In situ nano-sized ZrC/ZrSi composite powder fabricated by a one-pot electrochemical process in molten salts. *Rsc Advances* 7 (4): 2301–2307.

18 Anik, M., Hatirnaz, N.B., and Aybar, A.B. (2016). Molten salt synthesis of $La(Ni_{1-x}Co_x)_5$ (x = 0, 0.1, 0.2, 0.3) type hydrogen storage alloys. *International Journal of Hydrogen Energy* 41 (1): 361–368.

19 Galvin, T., Hyatt, N.C., Rainforth, W.M. et al. (2018). Molten salt synthesis of MAX phases in the Ti-Al-C system. *Journal of the European Ceramic Society* 38 (14): 4585–4589.

20 Nadimi, H., Soltanieh, M., and Sarpoolaky, H. (2021). Molten salt shielded synthesis and formation mechanism of Ti_2AlC in NaCl–KCl medium. *Ceramics International 48* (7): 9024–9029.

21 Dash, A., Sohn, Y.J., Vassen, R. et al. (2019). Synthesis of Ti_3SiC_2 MAX phase powder by a molten salt shielded synthesis (MS^3) method in air. *Journal of the European Ceramic Society* 39 (13): 3651–3659.

22 Dash, A., Vaßen, R., Guillon, O., and Gonzalez-Julian, J. (2019). Molten salt shielded synthesis of oxidation prone materials in air. *Nature Materials* 18 (5): 465–470.

23 Roy, C., Banerjee, P., and Bhattacharyya, S. (2020). Molten salt shielded synthesis (MS^3) of Ti_2AlN and V_2AlC MAX phase powders in open air. *Journal of the European Ceramic Society* 40 (3): 923–929.

24 Yu, Z., Wang, X., Hou, Y.-N. et al. (2017). Nitrogen-doped mesoporous carbon nanosheets derived from metal-organic frameworks in a molten salt medium for efficient desulfurization. *Carbon* 117: 376–382.

25 Zheng, X., Cao, X., Li, X. et al. (2017). Biomass lysine-derived nitrogen-doped carbon hollow cubes via a NaCl crystal template: an efficient bifunctional electrocatalyst for oxygen reduction and evolution reactions. *Nanoscale* 9 (3): 1059–1067.

26 Kamali, A.R. (2016). Eco-friendly production of high quality low cost graphene and its application in lithium ion batteries. *Green Chemistry* 18 (7): 1952–1964.

27 Kamali, A.R. and Fray, D. (2016). Electrochemical interaction between graphite and molten salts to produce nanotubes, nanoparticles, graphene and nanodiamonds. *Journal of Materials Science* 51 (1): 569–576.

28 Li, M., Lu, J., Luo, K. et al. (2019). Element replacement approach by reaction with Lewis acidic molten salts to synthesize nanolaminated MAX phases and MXenes. *Journal of the American Chemical Society* 141 (11): 4730–4737.

29 Li, Y., Shao, H., Lin, Z. et al. (2020). A general Lewis acidic etching route for preparing MXenes with enhanced electrochemical performance in non-aqueous electrolyte. *Nature Materials* 19 (8): 894–899.

30 Djire, A., Bos, A., Liu, J. et al. (2019). Pseudocapacitive storage in nanolayered Ti_2NT_x MXene using Mg-ion electrolyte. *Acs Applied Nano Materials* 2 (5): 2785–2795.

31 Urbankowski, P., Anasori, B., Makaryan, T. et al. (2016). Synthesis of two-dimensional titanium nitride Ti_4N_3 (MXene). *Nanoscale* 8 (22): 11385–11391.

32 Shen, M., Jiang, W., Liang, K. et al. (2021). One-pot green process to synthesize MXene with controllable surface terminations using molten salts. *Angewandte Chemie-International Edition* 60 (52): 27013–27018.

33 Huang, L., Hu, Z., Jin, H. et al. (2020). Salt-assisted synthesis of 2D materials. *Advanced Functional Materials* 30 (19).

34 Naguib, M., Mochalin, V.N., Barsoum, M.W., and Gogotsi, Y. (2014). 25th anniversary article: MXenes: a new family of two-dimensional materials. *Advanced Materials* 26 (7): 992–1005.

35 Williams, D.F., Del Cul, G.D., Toth, L.M., and Collins, E.D. (2001). The influence of Lewis acid/base chemistry on the removal of gallium by volatility from weapons-grade plutonium dissolved in molten chlorides. *Nuclear Technology* 136 (3): 367–370.

36 Zhang, H., Dasbiswas, K., Ludwig, N.B. et al. (2017). Stable colloids in molten inorganic salts. *Nature* 542 (7641): 328–331.

37 Biggin, S. and Enderby, J.E. (1981). The structure of molten zinc chloride. *Journal of Physics C (Solid State Physics)* 14 (22): 3129–3136.

38 Li, H., Lu, K., Wu, Z., and Dong, J. (1994). EXAFS studies of molten $ZnCl_2$, RbCl and Rb_2ZnCl_4. *Journal of Physics: Condensed Matter* 6 (20): 3629–3640.

39 Sun, J., Wang, L., Zhang, S. et al. (2006). $ZnCl_2$/phosphonium halide: an efficient Lewis acid/base catalyst for the synthesis of cyclic carbonate. *Journal of Molecular Catalysis a-Chemical* 256 (1–2): 295–300.

40 Kerridge, D.H. and Tariq, S.A. (1967). The solution of zinc in fused zinc chloride. *Journal of the Chemical Society A: Inorganic, Physical, Theoretical* (0): 1122–1125. https://doi.org/10.1039/J19670001122.

41 Buyers, A.G. (1961). A study of the rate of isotopic exchange for zn^{65} in molten zinc-zinc chloride systems at 433–681°. *The Journal of Physical Chemistry* 65 (12): 2253–2257.

42 Li, P., Molina, E., Wang, K. et al. (2016). Thermal and transport properties of NaCl-KCl-$ZnCl_2$ eutectic salts for new generation high-temperature heat-transfer fluids. *Journal of Solar Energy Engineering-Transactions of the Asme* 138 (5): 054501.

43 Liu, X., Fechler, N., and Antonietti, M. (2013). Salt melt synthesis of ceramics, semiconductors and carbon nanostructures. *Chemical Society Reviews* 42 (21): 8237–8265.

44 Bugaris, D.E. and zur Loye, H.-C. (2012). Materials discovery by flux crystal growth: quaternary and higher order oxides. *Angewandte Chemie-International Edition* 51 (16): 3780–3811.

45 Gonzalo-Juan, I. and Riedel, R. (2016). Ceramic synthesis from condensed phases. *ChemTexts* 2 (2): 6.

46 Von Barner, J.H., Brekke, P.B., and Bjerrum, N.J. (1985). Chloro complexes in molten salts. 10. Potentiometric and spectrophotometric study of the system potassium chloride-aluminum chloride-copper(II) chloride at 300. degree.C. *Inorganic Chemistry* 24 (14): 2162–2168.

47 Smith, G.P. and Griffiths, T.R. (1963). Tetrahedral tetrachlorocopper(II) complex in molten salt solutions. *Journal of the American Chemical Society* 85 (24): 4051–4052.

48 Boston, C.R. and Smith, G.P. (1963). Tetrahedral $NiCl_4^{2-}$ in molten salts. The complete spin-allowed spectrum of 3d orbital transitions. *Journal of the American Chemical Society* 85 (7): 1006–1007.

49 Tumidajski, P.J. and Blander, M. (1995). Solubility of $CoCl_2$ in molten NaCl-$AlCl_3$. *The Journal of Physical Chemistry* 99 (24): 9992–9995.

50 Magnuson, M. and Mattesini, M. (2017). Chemical bonding and electronic-structure in MAX phases as viewed by X-ray spectroscopy and density functional theory. *Thin Solid Films* 621: 108–130.

51 Ma, G., Shao, H., Xu, J. et al. (2021). Li-ion storage properties of two-dimensional titanium-carbide synthesized via fast one-pot method in air atmosphere. *Nature Communications* 12 (1): 1–6.

52 Chen, J., Jin, Q., Li, Y. et al. (2021). Molten salt shielded synthesis (MS^3) of MXene in air. *Energy & Environmental Materials 6* (2): e12328.

53 Khazaei, M., Ranjbar, A., Esfarjani, K. et al. (2018). Insights into exfoliation possibility of MAX phases to MXenes. *Physical Chemistry Chemical Physics* 20 (13): 8579–8592.

54 Sang, X., Xie, Y., Lin, M.-W. et al. (2016). Atomic defects in monolayer titanium carbide ($Ti_3C_2T_x$) MXene. *Acs Nano* 10 (10): 9193–9200.

55 Li, X., Puretzky, A.A., Sang, X. et al. (2017). Suppression of defects and deep levels using isoelectronic tungsten substitution in monolayer $MoSe_2$. *Advanced Functional Materials* 27 (19): 1603850.

56 Santosh, K.C., Longo, R.C., Addou, R. et al. (2014). Impact of intrinsic atomic defects on the electronic structure of MoS_2 monolayers. *Nanotechnology* 25 (37): 375703.

57 Yazyev, O.V. and Helm, L. (2007). Defect-induced magnetism in graphene. *Physical Review B* 75 (12): 125408.

58 Zhang, N., Hong, Y., Yazdanparast, S., and Zaeem, M.A. (2018). Superior structural, elastic and electronic properties of 2D titanium nitride MXenes over carbide MXenes: a comprehensive first principles study. *2d Materials* 5 (4): 045004.

59 Salamat, A., Hector, A.L., Kroll, P., and McMillan, P.F. (2013). Nitrogen-rich transition metal nitrides. *Coordination Chemistry Reviews* 257 (13–14): 2063–2072.

60 Wang, S., Ge, H., Sun, S. et al. (2015). A new molybdenum nitride catalyst with rhombohedral MoS_2 structure for hydrogenation applications. *Journal of the American Chemical Society* 137 (14): 4815–4822.

61 Yu, H., Yang, X., Xiao, X. et al. (2018). Atmospheric-pressure synthesis of 2D nitrogen-rich tungsten nitride. *Advanced Materials* 30 (51): e1805655.

62 Urbankowski, P., Anasori, B., Hantanasirisakul, K. et al. (2017). 2D molybdenum and vanadium nitrides synthesized by ammoniation of 2D transition metal carbides (MXenes). *Nanoscale* 9 (45): 17722–17730.

63 Jin, H., Gu, Q., Chen, B. et al. (2020). Molten salt-directed catalytic synthesis of 2D layered transition-metal nitrides for efficient hydrogen evolution. *Chem* 6 (9): 2382–2394.

64 Lantelme, F. and Groult, H. (2013). *Molten Salts Chemistry: From Lab to Applications*. Newnes.

65 Delpech, S., Cabet, C., Slima, C., and Picard, G.S. (2010). Molten fluorides for nuclear applications. *Materials Today* 13 (12): 34–41.

66 Li, M., Li, X., Qin, G. et al. (2021). Halogenated Ti_3C_2 MXenes with electrochemically active terminals for high-performance zinc ion batteries. *Acs Nano* 15 (1): 1077–1085.

67 Srivastava, V., Kamysbayev, V., Hong, L. et al. (2018). Colloidal chemistry in molten salts: synthesis of luminescent $In_{1-x}Ga_xP$ and $In_{1-x}Ga_xAs$ quantum dots. *Journal of the American Chemical Society* 140 (38): 12144–12151.

68 Kamysbayev, V., Filatov, A.S., Hu, H. et al. (2020). Covalent surface modifications and superconductivity of two-dimensional metal carbide MXenes. *Science* 369 (6506): 979–983.

69 Guo, L., Jiang, W.-Y., Shen, M. et al. (2022). High capacitance of MXene ($Ti_3C_2T_x$) through intercalation and surface modification in molten salt. *Electrochimica Acta* 401: 139476.

70 Xu, C., Jiang, W.-Y., Guo, L. et al. (2022). High supercapacitance performance of nitrogen-doped $Ti_3C_2T_x$ prepared by molten salt thermal treatment. *Electrochimica Acta* 403: 139528.

71 Liu, J.-C., Xiao, H., and Li, J. (2020). Constructing high-loading single-atom/cluster catalysts via an electrochemical potential window strategy. *Journal of the American Chemical Society* 142 (7): 3375–3383.

72 Fu, Z.H., Zhang, Q.F., Legut, D. et al. (2016). Stabilization and strengthening effects of functional groups in two-dimensional titanium carbide. *Physical Review B* 94 (10): 104103.

73 Ding, H.; Li, Y.; Li, M.; Chen, K.; Liang, K.; Guoxin, C.; Lu, J.; Palisaitis, J.; Persson, P.; Eklund, P.; et al. Chemical-scissor-mediated structural editing of layered transition metal carbides; 2022 *Science*, *379* (6637): 1130–1135.

74 Zavabeti, A., Ou, J.Z., Carey, B.J. et al. (2017). A liquid metal reaction environment for the room-temperature synthesis of atomically thin metal oxides. *Science 358* (6361): 332–335.

75 Moser, Z., Gasior, W., Pstrus, J. et al. (2004). Surface tension and density measurements of Sn-Ag-Sb liquid alloys and phase diagram calculations of the Sn-Ag-Sb ternary system. *Materials Transactions 45*: 652–660.

76 Ciccioli, A., Balducci, G., Gigli, G. et al. (2000). Vaporization behaviour and some thermodynamic properties of the Pd-In, Pd-Pb, Pd-Sn systems. *Intermetallics 8*: 195–201.

77 Arnberg, L. (1980). The structures of the γ-phases in the Pd–Cd and Pt–Cd systems. *Acta Crystallographica Section B Structural Crystallography and Crystal Chemistry 36*: 527–532.

78 Massalski, T.B. (1990). *Binary Alloy Phase Diagrams*, 2e. Materials Park, OH: ASM International.

79 Ho, T.-L. (1975). Hard soft acids bases (HSAB) principle and organic chemistry. *Chemical Reviews 75* (1): 1–20.

6

Guidelines on the Intercalation of Ions and Molecules in MXenes

Varun Natu[1] *and Michel W. Barsoum*[2]

[1] *Physical and Materials Chemistry Division, National Chemical Laboratory, Pune, Maharashtra, India*
[2] *Department of Materials Science and Engineering, Drexel University, Philadelphia, PA, USA*

6.1 Introduction

Ion exchange reactions can be simply defined as a reversible interchange of ions between an insoluble solid and its surrounding solution. The ion exchanger solid can be mainly classified into two types based on the type of ions it can exchange namely, (i) cations, and (ii) anions. The exchange reactions can be represented as follows: [1–3]

$$\text{Cation Exchange: } M^{-}A^{+} + B^{+} \leftrightharpoons M^{-}B^{+} + A^{+} \tag{6.1}$$

$$\text{Anion Exchange: } M^{+}A^{-} + B^{-} \leftrightharpoons M^{+}B^{-} + A^{-} \tag{6.2}$$

In Eq. (6.1), the M^{-} is representative of a negatively charged solid matrix with exchangeable counter ions A^{+}, while B^{+} denotes the cations from the surrounding solutions that interchange with the A^{+} cations leading to its substitution into the solid structure. Equation (6.2) is similar to 1 but denotes anion exchange instead. While most ion exchangers can either exclusively exchange cations or anions, few can simultaneously do both and are known as amphoteric exchangers [1–3].

Ion exchange in solids has been a topic of interest to the wide scientific community because understanding this fundamental mechanism is key to enhancing the performance of materials in applications like energy storage [4–7], water filtration [8–13], water softeners [14, 15], isotope separation in the nuclear industry [16–19], ionic actuators [20–22], among many others [2, 23–25].

Transition Metal Carbides and Nitrides (MXenes) Handbook: Synthesis, Processing, Properties and Applications, First Edition. Edited by Chuanfang Zhang and Michael Naguib.
© 2024 John Wiley & Sons, Inc. Published 2024 by John Wiley & Sons, Inc.

Based on the chemical composition of the ion exchangers, they are further divided into two types: (i) inorganic – which comprises materials like clays, hydrous oxides, zeolites, layered phosphates, double-layered hydroxides, DLH, etc. and (ii) organics – which are mainly constituted of resins with different functional surface groups [1–3]. MXenes fall under the category of inorganic, cation exchangers and have been shown to spontaneously intercalate many different types of cations into their interlayer space. Their response is quite similar to that of clays. And if there is one leitmotiv to this chapter, it is the similarity between them.

In this chapter, we will mainly focus on the chemical intercalation of ions and other molecules. Electrochemical ion intercalation will be discussed in detail in other chapters. Also, a section of this book is dedicated to various MXene applications therefore discussion pertaining to them will be kept to a minimum here. Furthermore, and unless explicitly stated, this chapter deals with MXene multilayers, MLs.

6.2 The 002 Peak and the Interlayer Spacing in MXenes

In the X-ray diffraction, XRD, pattern of MXenes, the first peak is generally assigned to the 002 basal plane reflections [26, 27]. The angle at which this peak is located can be used to calculate the spacing between layers, *d,* using Bragg's law. Because the first peak is a (002), and not a (001) peak, *d* is half of the *c* lattice parameter, LP, as measured by XRD (Figure 6.1). This *d* is proportional to the size of intercalated species. Many studies have used this facile technique to analyze and understand the effects of ion and/or solvent intercalation [29–32], surface functionalization [33], degree of dispersion in polymers [34], adsorption of dyes [35], etc. For example, in the case of $Ti_3C_2T_z$ synthesized using only hydrofluoric acid, HF, the 002 peak is typically observed at 9° 2θ corresponding to a $d \sim 9.7$ Å. This value is close to that of the parent MAX phase (9.5° 2θ) and results from the presence of protons between the MXene layers [26, 31]. When $Ti_3C_2T_z$ flakes are synthesized using a mixture of lithium fluoride, LiF, and hydrochloric acid, HCl, the (002) peak occurs at $\approx 5.5°$ 2θ ($d \sim 16$ Å). The expansion is due to the presence of hydrated Li^+ ions intercalated between the layers [27, 29, 30, 36].

This method is quite powerful because of the ease of its use to measure *d* between the MXene layers. Though, for exact quantification of species intercalated between the layers and in the case where the exchanged ions are roughly of the same size, XRD alone, cannot provide useful information, and more involved characterization techniques like inductively coupled plasma mass spectrometry, ICP-MS, X-ray photoelectron spectroscopy, XPS, nuclear magnetic resonance spectroscopy, NMR, etc. need to be used [37–41].

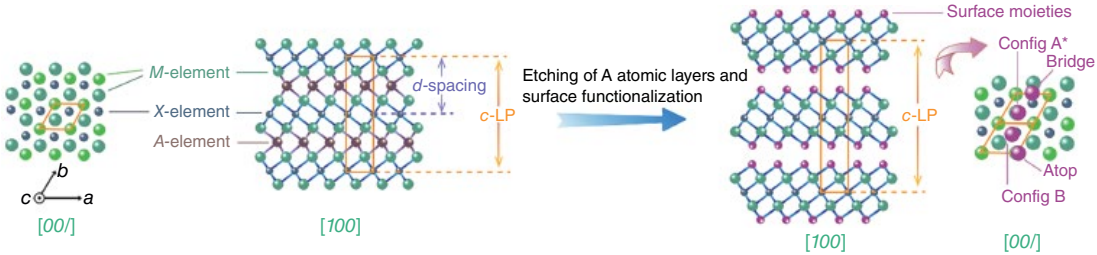


Figure 6.1 Transition of MAX to MXene shown in [00l] and [100] projections. The *c* lattice parameter and *d* spacing are marked in the [001] projections. *Source:* Reproduced from Chen et al. [28]/American Chemical Society.

6.3 Ion Exchange Properties and Its Dependence on MXene Synthesis Conditions

Ion exchange in MXenes is strongly dependent on its method of synthesis [4]. $Ti_3C_2T_z$ synthesized using only HF (henceforth referred to HF-MX in this chapter) is unexchangeable as shown by Ghidiu et al. who immersed HF-MX in a range of chloride salt solutions and found no cation intercalation from the salt solution into the MLs [29]. Lukatskaya et al. discovered that instead of chlorides, nitrates, or other neutral pH ionic solutions, if the MXenes were exposed to basic electrolytes like potassium hydroxide, KOH, potassium acetate, CH_3COOK, ammonium hydroxide, NH_4OH, etc., the respective cations intercalated into the HF-MX MLs [42]. Using neutron and X-ray total scattering, Wang et al. found that in HF-MX hydrogen bonding between the –F and –O terminations of one MXene sheet with the –OH terminations of an adjacent sheet was possible when the sheets were close enough to each other. If these bonds are too strong, they, in turn, explain the lack of ion intercalation in HF-MX layers at neutral pH [43]. In other words, cation exchange was more prevalent in basic solutions than in neutral ones.

The exact reason for this pH-dependent of cation exchange was unclear until the recent work of Natu et al. who showed that after treatment with a base, like sodium hydroxide, NaOH, the OH^- anions replace the –F terminations via a base-induced dehalogenation reaction (Figure 6.2) [4]. Further, the deprotonation of the –OH surface terminations by the basic OH^- anions results in $-O^-$ terminations and a water molecule (Figure 6.2) [4]. The negative charge acquired by the –OH termination after deprotonation gets compensated by Na^+ cations, which lead to their subsequent intercalation into the MXene layers (Figure 6.2) [4]. And since the F—H bond is roughly six times stronger than its O—H counterpart [44–46], reducing the number of *F* terminations *per force* weakens the interlayer bonds [4].

Fully consistent with this picture is the fact that base treatment for cationic intercalation into HF-MX layers is only required initially, that is, to the virgin HF-MX, after which the MLs became fully ion-exchangeable even at neutral pH [4]. Natu et al. showed that the Na^+ ions intercalated after the first NaOH treatment of HF-MX can be exchanged with K^+, Li^+, NH_4^+, $(CH_3)_4N^+$, $(C_{16}H_{33})(CH_3)_3N^+$ cations using just their respective chloride solutions [4]. To sum up this section, once the concentration of the relatively strong F-based H-bonds between MLs is reduced, the latter becomes fully ion-exchangeable.

Many applications of 2D materials require the flakes or layers to be separate and isolated instead of stacked MLs [47–50]. But because of the aforementioned H-bonding in HF-MX layers, it was difficult to exfoliate MXenes into a single to few layers by conventional mechanical routes like sonication, shaking, etc.

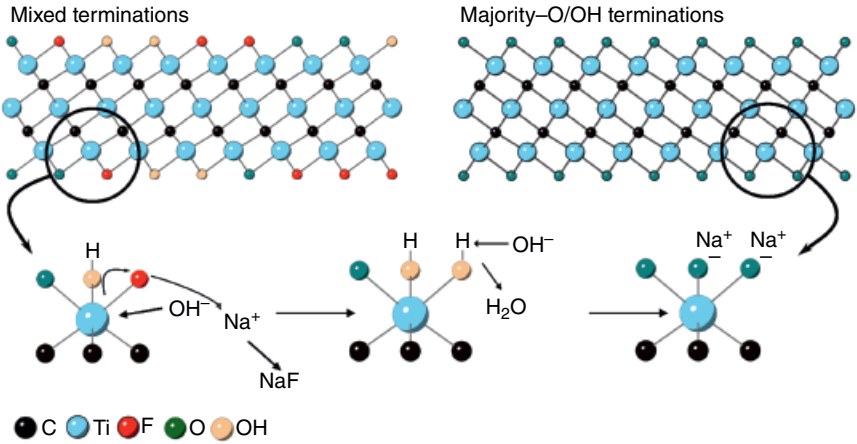


Figure 6.2 Schematic showing possible defluorination and consequent Na^+ ion intercalation reactions during NaOH treatment of HF-MX ML powders. Note Na^+ cations are attracted to the $-O^-$ terminations, most probably forming ionic bonds. Also, H of the –OH terminations are only shown in the magnified octahedra view in the reaction mechanism for simplicity. *Source:* Reproduced from Natu et al. [4]/American Chemical Society.

The most common route in other 2D materials facing the same problem was to treat the MLs with tetrabutylammonium hydroxide, TBAOH, or tetramethylammonium hydroxide, TMAOH, solutions leading to the intercalation of TBA^+/TMA^+ cations, respectively, which in turn results in an expansion of *d* and consequent weakening of the forces between the layers [51–53]. As the most common route of MXene synthesis – other than Ti_3AlC_2 – is by using HF, this creates a delamination problem [54, 55]. Naguib et al. used a similar TBAOH treatment to delaminate several MXene chemistries and found that, similar to other 2D materials, TBA^+ cations intercalate between the layers and sonicating these expanded MLs led to delamination into single to few-layer MXene sheets in the form of stable colloids (Figure 6.3a) [56]. Though at the time of that work and until quite recently, the exact reason why TBA^+ was so effective was not known.

Recently, Natu et al. have shed more light on the subject. They immersed HF-MX MLs into different concentration solutions of TMAOH and tetramethylammonium chloride, TMACl, in two separate experiments and found that the TMA^+ cations only intercalated the MLs when they were soaked in TMAOH (Figure 6.3b, c) as observed by a large shift in the 002 peak in XRD patterns depicted in Figure 6.3b. Crucially, *no* peak shifts were observed for any concentration of TMACl (Figure 6.3c) indicating no ion intercalation between the MLs. The same experiment when carried out with NaOH and NaCl solutions yielded the same result: MLs soaked in

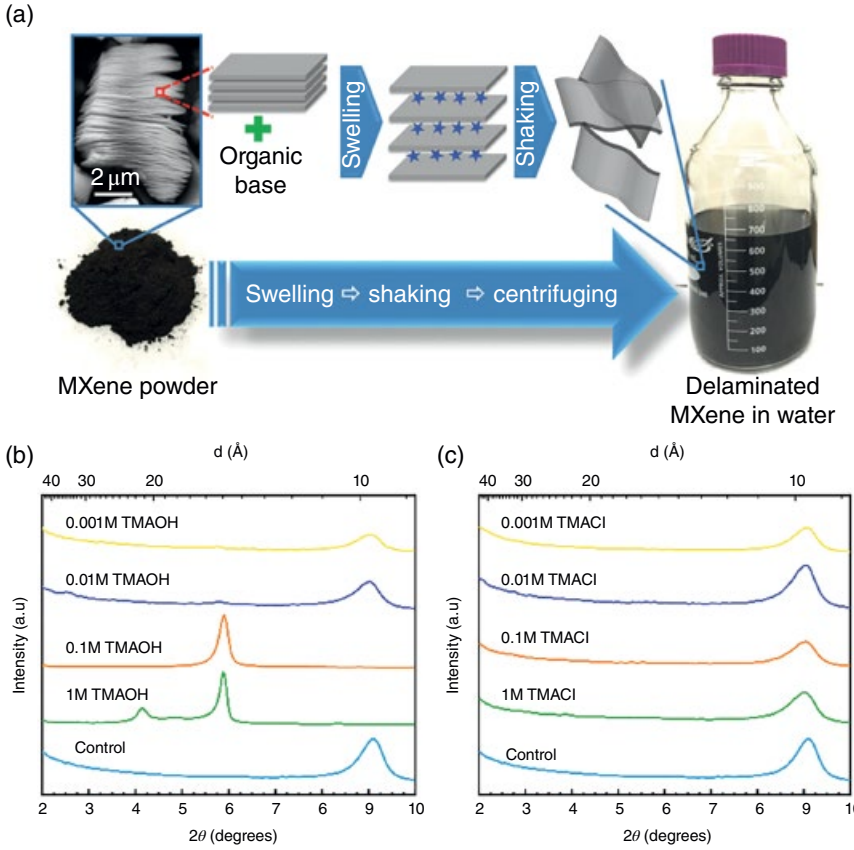


Figure 6.3 (a) Schematic for MXene delamination process by treating MLs with TBAOH. After intercalation of TBA+ cations into the layers, simple hand shaking or mild sonication in water can delaminate the layers forming a stable colloidal solution (right side). Typical SEM image of the as synthesized Ti_3CNT_z MLs is shown at the top left. XRD patterns of HF-MX MLs treated with, (b) TMAOH, and (c) TMACl solutions of concentrations 0.001 M (top), 0.01 M (second), 0.1 M (third), and 1 M (fourth). Control XRD patterns of HF-MX powders before the treatment are shown at the bottom of each panel for reference. *Source:* Natu et al. [4] and Naguib et al. [56].

NaOH delaminated readily, while no intercalation occurred when only NaCl was used. Most importantly, the NaOH-treated MLs were *readily* delaminated to form stable colloids by mere sonication. They also demonstrated that NaOH treatment also works to induce ion intercalation in other MXenes like Nb_2CT_z [4]. To summarize this section, it is the presence of the OH^- anions that is ultimately responsible for the delaminations and not the TBA^+ cations.

In 2014, Ghidiu and co-workers discovered a simpler, safer method for intercalating ions into MLs compared to the ones discussed above [36]. Instead of using HF directly, which is extremely hazardous to handle, they used a mixture of LiF and HCl that forms HF *in-situ* to etch Ti_3AlC_2 and form $Ti_3C_2T_z$ [36]. The resulting MXene already had Li-ion intercalated between the MLs during synthesis [36]. Moreover, this MXene, unlike the HF-MX, was ion exchangeable and interlayer water could also be reversibly inserted and removed as a function of humidity [29, 30, 57]. Ion exchange and hydration in MXene layers are discussed in detail later in the chapter.

After the work of Ghidiu et al., it was assumed that the Li^+ cations intercalate into the MXene layers as the Al from the parent Ti_3AlC_2 is etched away [36, 58]. But later work by Verger et al. showed that the cation intercalation during etching is a more complex process [30]. In their XRD studies, they scanned wet MLs after various washing steps (Figure 6.4) [30]. Right after etching, they measured a wide peak around 6.5° 2θ ($d \sim 14$ Å) (Figure 6.4 which they ascribed to MLs with disordered stacking intercalated with mostly hydrated hydronium ions.

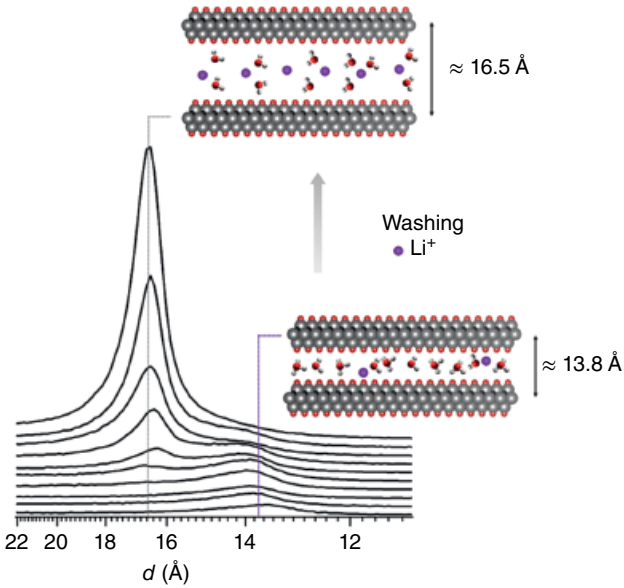


Figure 6.4 XRD patterns acquired on wet as synthesized MXene $Ti_3C_2T_x$ MLs between every wash with DI H_2O. XRD patterns are stacked vertically for clarity. The bottom most scan is of MXene right after synthesis and the scans above are after each subsequent wash. MXene schematics to the right represent what possibly resides between the MXene layers before the first wash, and after the last wash as marked. *Source:* Reproduced from Verger et al. [30]/American Chemical Society.

This peak remained more or less constant after three washes with deionized water, DI. After the fourth wash, the pH was measured to be around three, and two broad peaks were observed around 5.5° 2θ ($d \sim 16.5$ Å) and 6.5° 2θ ($d \sim 14$ Å) (Figure 6.4) indicating partial replacement of hydronium ions with hydrated Li-ions [30]. After the 5th wash, the pH plateaued at 4 and stayed the same for all subsequent washes. Between the 5th and 10th wash, the 6.5° 2θ peak slowly disappeared while the 5.5° 2θ peak grew in intensity and became sharper (Figure 6.4) [30]. From these results, they concluded that during washing, Li^+ ions from the excess LiF used during etching started exchanging with the initially intercalated hydronium ions around wash 5 when the pH is between 2 and 3, and during subsequent washes, the hydronium ions were completely replaced by Li ions and the pH plateaued to around 4 [30]. They concluded that Li^+ ions are not intercalated during etching, but actually intercalate during the washing step [30].

Kajiyama et al. compared the performance Ti_2CT_z synthesized using HF and LiF + HCl methods as electrodes for Li-ion capacitors and found that in the case of MXenes synthesized using LiF + HCl, the energy storage capability was higher compared to the ones synthesized using HF [59]. They attributed this to the increased d spacing caused by the attachment of bulky –Cl terminations to the flakes due to the presence of HCl in the etching mixture [59]. They confirmed the presence of –Cl along with –F, –O, –OH terminations using NMR, XPS, etc. [59].

To delineate the mixed effect of cations present during etching, and the steric repulsion caused due to the presence of bulky surface terminations like –Cl, Voigt et al. designed a series of elegant experiments. They synthesized MXene in a mixture of HF and other mineral acids like HCl/ HBr/ HI or H_3PO_4 [31]. They found that after synthesis, the 002 XRD peak synthesized using only HF was at 9° 2θ (d ~ 9.7 Å) (Figure 6.5a), which they ascribed to dehydrated hydronium ions between the layers [31]. In the case of mixed acids, the (002) peak was observed at 6.5° ($d \sim 14$ Å) (Figure 6.5c) indicating hydrated hydronium ions in the interlayers similar to Verger et al. [30, 31] After washing the samples with a LiCl solution, Voigt et al. found that the 002 peak in case of HF-MX did not shift (Figure 6.5b) but in all cases where different mixed acids were used, the 002 shifted to 5.5° 2θ ($d \sim 16.5$ Å) (Figure 6.5d) indicating the presence of hydrated Li^+ cations between the layers [31].

The studies of Kajiyana et al. [59], Verger et al. [30], Voigt et al. [31], and Natu et al. [4] taken together indicate that MXenes etched in HF alone are not ion exchangeable presumably, as noted above, due to hydrogen bonding between two adjunct layers. To weaken this bonding, either some of the –F terminations need to be replaced with –O/OH terminations using bases like NaOH, TBAOH, etc., or bulkier surface groups like –Cl, –Br, –I, $–PO_4$, etc. which adsorb at the flake edges, prop the layers apart due to steric hindrance after which ions can more freely intercalate between the MLs.

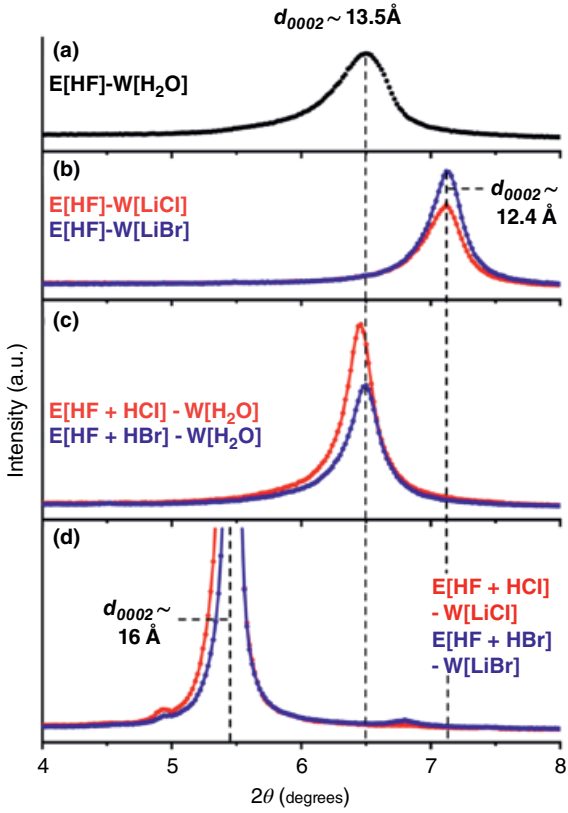


Figure 6.5 Low-angle XRD patterns of wet $Ti_3C_2T_z$ MLs, (a) etched with HF followed by DI water washing; (b) same as (a) but washed in LiCl) or LiBr solution after etching; (c) etched with HF + HCl (red) and with HF + HBr followed by DI water washing; (d) same as (c) but washed in LiCl or LiBr solution after etching. *Source:* Reproduced from Voigt et al. [31]/American Chemical Society.

Even though great progress has been made in linking synthesis conditions and ion exchange in MXenes, a few unknowns remain that need to be explored to complete our understanding. For example, in his thesis, Ghidiu reports Li^+ ion intercalation between MXene layers when a mixture of LiF + HF was used for synthesis [60]. Also work by Halim et al. showed that when using NH_4HF_2 for MXene synthesis, the NH_4^+ cations intercalate between the layers [61]. In the ion exchange studies by Ghidiu et al. [29] (see below) and work by Voigt et al. [31] observed no ion exchange in MXenes synthesized in presence of just F^- anions, that is, HF and Verger et al. [30] showed that the Li^+ cations present in the etching solution intercalate in the layers during washing instead of etching, these results

do not directly agree with the above two examples. Further, Lui et al. recently attempted to completely delaminate –Cl terminated MXenes synthesized in a molten salt and found that it also required a base treatment for initial ion intercalation only after which delamination is possible [62]. This implies that for ion intercalation, big steric terminations may be a necessary, but not sufficient, condition for delamination and more work to understand this phenomenon is needed.

The LiF + HCl combination or HF are the two most commonly used etchants for MXene synthesis, and there are several in-depth studies as discussed above that attempted to understand the effects of synthesis on ion intercalation. Apart from these, some unconventional synthesis methods also report ion exchange or intercalation as discussed below.

Natu et al. showed that it is possible to etch Ti_3AlC_2, using NH_4HF_2 dissolved in a range of polar organic solvents like dioxane (DXN), acetonitrile (ACN), *N*, *N*-dimethylformamide (DMF), dimethyl sulfoxide (DMSO), propylene carbonate (PC) and *N*-Methyl-2-pyrrolidone (NMP) [32]. This method was developed based on the hypothesis that NH_4HF_2 dissociates into NH_4F and HF when dissolved in polar solvents and that the dissolved HF, most probably, plays the same role it does in water mixtures. After etching Ti_3AlC_2 powders in various organic solvents, they observed highly expanded *d* values of nearly 40–50 Å (Figure 6.6a, b) for various solvents except for DMSO for which it was measured to be around 21 Å (Figure 6.6a, b). These highly expanded *d*-spacings implied that NH_4^+ cations, solvated by the organic solvent molecules, intercalated between the MLs. These ammonium cations were also found to be exchangeable as observed from the XRD patterns obtained after washing the as-synthesized $Ti_3C_2T_x$ MLs using HCl-propanol mixtures (Figure 6.6c, d). After washing, the *d* synthesized in different solvents decreased to around 14 Å in all cases except DMSO, where it remained the same even after washing (Figure 6.6c, d) [32]. This again implied that big ammonium complexes were being replaced with protonated propanol [32]. This was the first study that not only demonstrated water-free synthesis of MXene but also showed ion exchange using non-aqueous solvents. Why MXene synthesized using DMSO does not behave like the others is currently not clear. Further, they also showed that compared to MXenes synthesized in water, the ones synthesized in PC showed twice the capacity to store Na ions in Na-ion batteries [32]. This etching method, although slow, is recommended for MXenes to be used in non-aqueous environments, or where water is to be avoided.

Husmann et al. used a mixture of ionic liquids, IL, with F-containing anions and water to synthesize MXenes [63]. They found that anions like BF_4^- or PF_6^- from 1-ethyl-3-ethylimidazolium tetrafluoroborate ($EMIMBF_4$) and 1-butyl-3-methylimidazolium hexafluorophosphate ($BMIMPF_6$) hydrolyze in the presence of water to form HF, which in turn etches the Al from the MAX phase. In the XRD of MXene synthesized using IL + water mixtures, they observed a peak

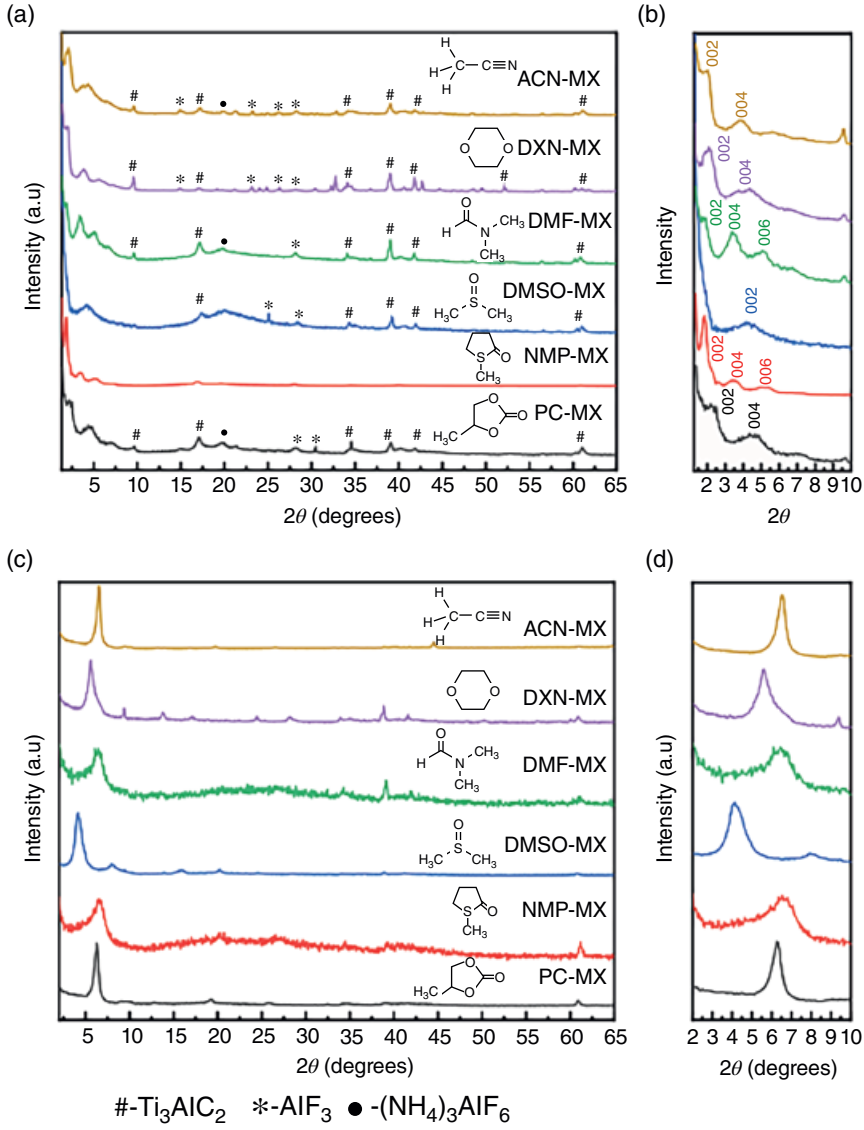


Figure 6.6 XRD patterns of $Ti_3C_2T_z$ synthesized in different organic solvents; (a) before washing, right after etching; (b) same as (a) but focused on low angles for clarity; (c) after washing, drying, and grinding of filtered films; (d) same as (c) but focused on low angles. The molecular structures of the organic solvents used for etching are shown right above the corresponding XRD pattern. Sequence of XRD patterns is the same in all four panels and corresponds to MXenes synthesized in ACN (top), DXN (second), DMF (third), DMSO (fourth), NMP (fifth), and PC (sixth). *Source:* Reproduced from Natu et al. [32]/with permission from Elsevier.

around 4° 2θ ($d \sim 23$ Å), which they assigned to the intercalation of long-chain organic cations between MLs [63]. They found that MXenes synthesized using ILs have higher capacities compared to once synthesized using just HF when tested as anodes in Li-ion batteries [63]. This work, along with that of Natu et al. [4] and Kajiyama et al. [59], proves that the energy storage performance of MXenes is dependent on their synthesis conditions and their interlayer space constituents even for the same MXene composition.

6.4 Why Do Cations Intercalate MXene Multilayers?

As discussed above, cations have a strong affinity to MXenes and readily intercalate between the MXene MLs by mere exposure to various electrolytes. The reason for this phenomenon is attributed to the highly negative surface charges on the MXene sheets as measured by zeta potential studies [56, 64]. And due to electrostatic attraction, this negative charge is balanced by external cations. But the source of the negative charge on MXenes is not completely understood yet, though it likely originates from the –OH terminations on the MXene surface that deprotonate at neutral pH to form $-O^-$ which then electrostatically attract cations [64]. In clay minerals, the surface charge develops due to isomorphic substitutions and defects, which leads to charge imbalance [65–68]. This is another possible mechanism that leads to the negative charges on MXenes as it is known that the acid etchants also create defects in the Ti_3C_2 layers while etching away the Al atoms [69]. And more work needs to be done to understand the origins of the ion exchange capabilities in MXene.

6.5 Anions and MXene

Shpigel et al. recently analyzed electrochemical anion intercalation between MXene MLs using highly concentrated water-in-salt electrolytes. They concluded that even after the application of a positive potential 0.4 V vs. Ag/AgCl, no anions intercalated between the MXene layers, but only cations did, indicating that the local electric field created by the negative surface charge on MXenes is higher than the externally applied voltage [70]. But Natu et al. showed that MXene edges are positively charged possibly due to broken bonds [64]. These positive edges act as sites where anions can be adsorbed due to electrostatic interactions. But since the surface area of the negatively charged MXene sheet faces is significantly larger than the edges, cationic interactions are much more prevalent than their anionic counterparts. Natu et al. demonstrated in a follow-up study that this edge effect can be exploited to cap the highly defective MXene edges with long-chain

polyanions that in turn block their contact with oxygen and water molecules thereby significantly reducing MXene's proclivity to oxidatize [71].

6.6 Types of Ion/Molecules that Intercalate Between MXene Layers

6.6.1 Inorganic Ions

Even though ion intercalation in MXene was observed by Lukatskaya et al. [42] only two years after the discovery of MXene as discussed above, the first systematic study on ion intercalation was carried out by Ghidiu et al. in 2016 [29]. They showed that Li^+ ions intercalated between the MLs during etching with LiF + HCl solutions can be easily exchanged with other alkali and alkali earth ions such as Na^+, K^+, Rb^+, Mg^{2+}, and Ca^{2+} by merely stirring the MXenes in the chloride solution of the desired cation to be exchanged [29]. Verger et al. further found that hydronium ions and alkali cations exchange reversibly multiple times by just alternate washes of MLs with acid and salt solutions, respectively [30]. There is no reason to believe that the exchange between any two ions would be any different.

Using a similar protocol as the alkali ion study, that is, stirring MLs with chloride salt solutions of the desired ions, Ghidiu in this Ph.D. thesis also reports intercalation of transition metal cations. It was shown that it is possible to intercalate Mn^{+2}, Fe^{+2}, Co^{+2}, and Ni^{+2} cations [60]. These ions are of special interest as they could in principle induce magnetic properties in non-magnetic MXene layers after intercalation [72, 73].

6.6.2 Organic Molecules

As discussed above, $Ti_3C_2T_z$ was first obtained by etching Ti_3AlC_2 powders in concentrated HF [26]. The resulting MLs were not easily exfoliated using common processing techniques like sonication, and to delaminate these MLs, the *d* between the MXene sheets first had to be first expanded by the intercalation of organic molecules like DMSO [55], TMAOH [74], TBAOH [56], hydrazine [55, 75], urea [55, 76], isopropyl amines [54], among others. Procedures for intercalating organic molecules generally require simply immersing the MLs into the desired solvent for some time. Similar to inorganic cations, the intercalation is spontaneous at ambient conditions. Again, similar to inorganic cations, intercalation of organic molecules expands the *d-spacing* as readily observed in XRD patterns. Treatments with hydrazine lead to an expansion of *d* to 12.5 Å, from 9 Å, generally observed for HF-MX [55, 75]. While DMSO intercalation leads to an increase in *d* to ≈ 17.5 Å. The intercalated DMSO also tends to draw in water increasing *d* to 22.4 Å [55]. Before

the discovery of the LiF + HCl method for etching and delamination, DMSO and hydrazine were used to expand *d* and delaminate MLs. Later Naguib et al. improved upon this method by using TBAOH to intercalate TBA^+ cations in the range of MXene allowing for a simplified and near-universal method to delaminate any type of MXene [56]. For reasons that are not clear yet, hydrazine and DMSO were unable to delaminate some of the HF etched MXenes, like Ti_2CT_z and V_2CT_z, but worked for $Ti_3C_2T_z$ and $Mo_2TiC_2T_z$ [55, 77]. All molecules discussed above are intercalated directly into HF-MX MLs. Whether uncharged molecules like DMSO, hydrazine, urea, and others can replace the Li^+ cations in MXenes synthesized using LiF + HCl is still an open question. Though there is no reason to believe that TBA^+ and TMA^+ would behave any differently than other cations and should exchange with the Li^+ cations even though it has not been experimentally verified to the best of our knowledge.

Similar to inorganic cations, organic cations can also be intercalated between the MLs via ion exchange. Since, alkyl ammonium, AA, can be engineered to have a larger number of organic groups of varying lengths, their intercalation can be used to tailor *d* [57, 78]. Using AA cations of varying chain lengths, it was shown that in $Ti_3C_2T_z$, MLs, the *d* could be tuned between 14.6 and 38.2 Å (Figure 6.7a) [54]. Interestingly, varying the chain length of AA cations does not lead to a linear

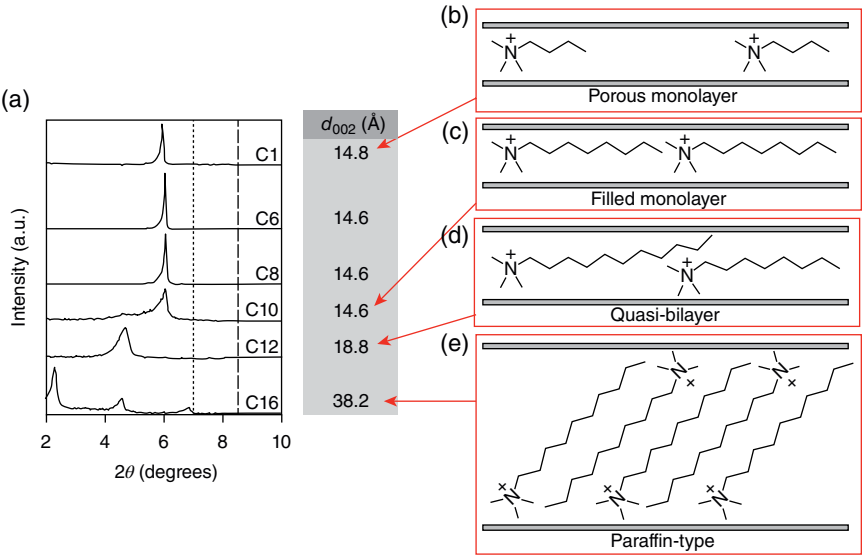


Figure 6.7 (a) Low-angle XRD patterns of $Ti_3C_2T_z$ MLs intercalated with AA cations with different length alkyl chains with extracted basal spacings, represented as d_{002}; (b–e) expected arrangements of cations in the interlayer as a function of C-chain lengths. *Source:* Adapted from Ghidiu et al. [57].

increase in *d*. For chain lengths of 1–8 carbons long, *d* was constant (Figure 6.7b, c) before abruptly increasing when the chain lengths were 10 and 12 (Figure 6.7d, e) [54]. This was attributed to the notion that as long as the AA chains could lie flat on the surface, they would. The longer chained AA, on the other hand, were forced out of the interlayer plane and resulted in increases in *d* [54].

Similar phenomena also occur in other layered materials where increases in *d* proceed through a monolayer (Figure 6.7b) to quasi-bilayer transitions of cation chains (Figure 6.7d) and further expansion is caused by paraffin-type arrangements of long-chain cations (Figure 6.7e). There is no reason to believe anything different is happening here [78–80]. Naguib et al. used these highly expanded MXenes with a carbon chain longer than 10 as electrodes in supercapacitors with IL electrolytes [81]. They show that because of the large cation size of ILs, the expanded *d* makes it easy for their intercalation, compared to MLs with lower *d* values that restrict the intercalation of IL cations [81].

Carey et al. intercalated another AA cation – di(hydrogenated tallow)benzyl methyl ammonium or, DHT – between LiF + HCl MLs by stirring in the chloride salt solution of DHT in ethanol and water. After intercalation, the *d* spacing increased from 16 Å to nearly 36 Å [82]. Further they found that this long-chain alkyl attached to the ammonium cation converted the MLs from hydrophilic to hydrophobic [82]. Using this property, there were able to delaminate and form stable colloids of MXene in several different nonpolar solvents such as chloroform, decalin, hexane, cyclohexane, toluene, and *p*-xylene (Figure 6.8a, b) [82]. And because most polymers are readily soluble in nonpolar solvents, they were able to readily make MXene polymer nanocomposites, NCs, by dissolving the desired polymers in the MXene colloid and then casting the suspension in appropriate molds [82]. This was not possible before this work and opened up a big avenue for MXene research [82].

When electrodes of DHT intercalated MXene were tested in supercapacitors, they resulted in high capacitances at high loadings [82]. Generally, due to the 2D morphology, the tight stacking of flakes results in a tortuous path for ions leading to low capacitances at high electrode loadings. But because of the expanded interlayer space in DHT-MXene, electrodes of roughly ~10 mg cm^{-2} loading and a thickness of 140 μm were tested and the loss in capacitance was low [82]. Pai et al. also used DHT intercalated MXene to form a stable colloid in sulfur-dissolved CS_2 [83]. After the excess CS_2 was evaporated, single to few layers of MXene with a sulfur, S, coating were obtained [83]. This MXene/S composite performed much better as electrodes in Li/S batteries compared to composites made with MXene without DHT and S [83]. In the case where DHT was not used, the S coating was not conformal [83]. Pai et al. later also showed that it was possible to intercalate S_8-molecules into MLs by heating a mixture of S + DHT intercalated MXene in a closed furnace under an inert atmosphere. They found that at 350 °C, the S molecules penetrate the MLs and the DHT molecules are burned off. No S intercalation

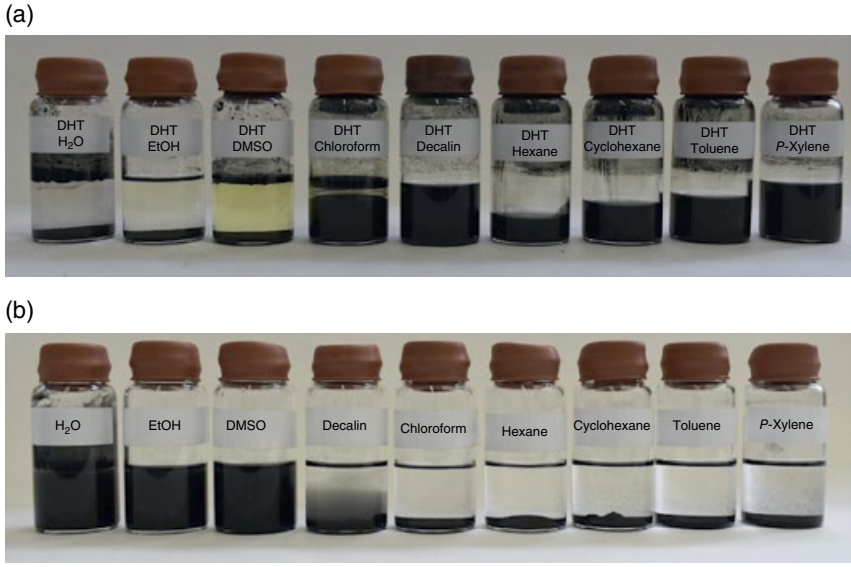


Figure 6.8 Digital photographs of $Ti_3C_2T_z$ suspensions in polar (first three vials) and nonpolar solvents (a) after DHT treatment; (b) without DHT treatment. *Source:* Carey et al. [82]/Reproduced with permission from Elsevier.

was observed when non-DHT-treated MLs were used. The S intercalated MLs showed excellent performance as cathodes in Li, Na, and K ion batteries.

And while to this point, the idea that increasing *d* is beneficial; it is not always the case. For example, Naguib et al. tested $Ti_3C_2T_z$ and Ti_3CNT_z MXenes as catalysts for the hydrogenation of furfural [84]. While they found that both MXenes had comparable activities, the life of the Ti_3CNT_z catalyst was more than that of $Ti_3C_2T_z$ [84]. Upon further inspection, they found that in the case of $Ti_3C_2T_z$, XRD patterns of the MXene after its deactivation as a catalyst showed a large increase in its basal spacing indicating intercalation of the reactants and the reaction products into the MLs, which was conjectured to be the cause of the loss in activity [84]. On the other hand, the 002 peaks in the case of Ti_3CNT_z did not shift before and after the reaction indicating no intercalation of reactants occurred, which is probably why its activity lasted for longer times [84].

6.7 Complexity of Ion Intercalation in MXenes

Based on conventional materials characterization, it was established that in HF-MX the interlayer space is occupied by hydronium ions and water, while in MXene synthesized using LiF + HCl, the interlayer space is occupied by Li^+ cations,

probably some trace hydronium ions, and water [29–31]. But inelastic neutron scattering studies showed that HF-MX samples synthesized using 48% HF have nearly 0.3 wt% H_2 molecules trapped between the MXene layers [85]. The amount of H_2 gas was found to be a function of HF concentration with lower concentration acids leading to a lower concentration of H_2 gas [85]. Intercalating K^+ ions into the layers also displaced trapped H_2 [85]. The source of H_2 is either the gas that is generated during etching due to the following reaction:

$$Ti_3AlC_2 + 3HF \rightarrow Ti_3C_2T_z + AlF_3 + \frac{3}{2}H_2$$

Or, the H_2 source could be due to the decomposition of water on the bare MXene surfaces that results in the formation of the –O/OH terminations during synthesis. A third possibility is electrochemical reduction of hydrogen ions over the MXene surfaces. However, because the amount of H_2 trapped is proportional to the concentration of acid used, the last reason seems to be most probable. But more work is needed to understand this better.

Another example where the catalytic and redox nature of MXene can lead to a complex intercalation mechanism is in the case of urea intercalation. Overbury et al. found that intercalating urea into $Ti_3C_2T_z$ MLs resulted in its decomposition leading to intercalation of NH_4^+ cations between the MLs and the evolution of CO_2 gas [76]. While similar catalytic decomposition may not occur with all the organic molecules intercalated into the MLs, assuming that intercalation of the said species is successful should be avoided only based on XRD and further characterization should be used to confirm its intercalation. Said otherwise, XRD alone will not lead to answering this question.

6.8 Cation Exchange Capacity

The number of intercalated cations that can be exchanged by ion exchange is called as its cation exchange capacity, CEC which is an important parameter for several applications. Various methods exist in the literature for estimating the CEC and direct chemical analysis is possible using ICP-MS, XPS, energy dispersive spectroscopy, EDS, etc. According to the reports in the MXene literature, the CEC ranges from 0.1 to 0.3 for monovalent ions [29, 38, 86]. This variance is most probably due to differences in sample preparation or the method used for analysis. In case of organic AA, Ghidiu et al. reported a CEC of ~0.1, which was confirmed by EDS and XPS [57]. These values might not hold when compared to electrochemically intercalated ions as an external applied voltage changes the local electric fields. Even in the case of $Ti_3C_2T_z$, which is the most studied MXene, hardly any work has been done to determine its CEC. A lot more work is needed to better

understand this aspect and should be carried out on high priority as CEC is one of the most important parameters that dictates the performance of ion exchange materials as it helps to select appropriate ion exchanger for any applications based on the salinity of water used.

6.9 Hydration and Dehydration of MXene Multilayers

Ghidiu et al. studied the effect of relative humidity (RH) on the hydration of the intercalated MXene synthesized using the LiF + HCl method [29]. They found that MXenes intercalated with different cations have different hydration/dehydration behavior. In the case of Na and Li-ions, a peak at 5.5° 2θ ($d \sim 16$ Å) (Figure 6.9a, b) is observed at RH above 60%, which they ascribed to a bilayer of water surrounding the cations. While below 60% RH, the d was ~12 Å (Figure 6.9a, b), which corresponds to a monolayer of water [29]. In the case of K^+ ions, d is not a function of RH and remains at 12 Å (Figure 6.9a, b). In the case of Ca^{2+} ions, the monolayer-to-bilayer transition happens around RH of 40% (Figure 6.9a, b). While in the case of Mg^{2+} ions, the d stays at 16 Å through the whole range of RH except at <20% RH, where it collapses to 12 Å (Figure 6.9a, b) [29]. Ghidiu et al. ascribed these differences to the cationic hydration enthalpies of the various cations [29].

As ion intercalation properties in MXenes were found to be reminiscent of those of clays, most of the XRD peak shifts were analyzed based on prior reports in clay literature. It is commonly accepted in clays that all the interlayer space surrounding the interlayer ions is filled with water and depending on the hydration state, the clay interlayers can have between one and four layers of water [87]. Based on these studies, Ghidiu et al. attributed their peak shifts in their XRD studies as a function of humidity to the presence of one or two layers of water between the layers [29]. This was also supported by the fact the ~2–2.5 Å jump in the d-spacing during hydration and dehydration corresponds well with the size of a water molecule. But Osti et al. studied the intercalated water using inelastic neutron scattering and found that instead of forming a continuous layer between the MXene layers, water molecules tend to form pillars around the intercalated cations; therefore, the amount of water intercalated is a lot less than originally assumed based on the complete filling of interlayer space [88].

Natu et al. found that apart from RH, even pH can be used to control the hydration of the intercalated cations. They found that after exposure of HF-MX MLs to 5 M and 0.1 M NaOH solutions, d increased from ~12 Å to ~16 Å, respectively (Figure 6.9c) [4]. While in the 1 M NaOH case, two peaks appear, the smaller of which is the same as for the 5 M NaOH case the larger peak was centered around $d \sim 15$ Å (Figure 6.9c) [4]. Based on the work of Ghidiu et al. and Osti et al., it is

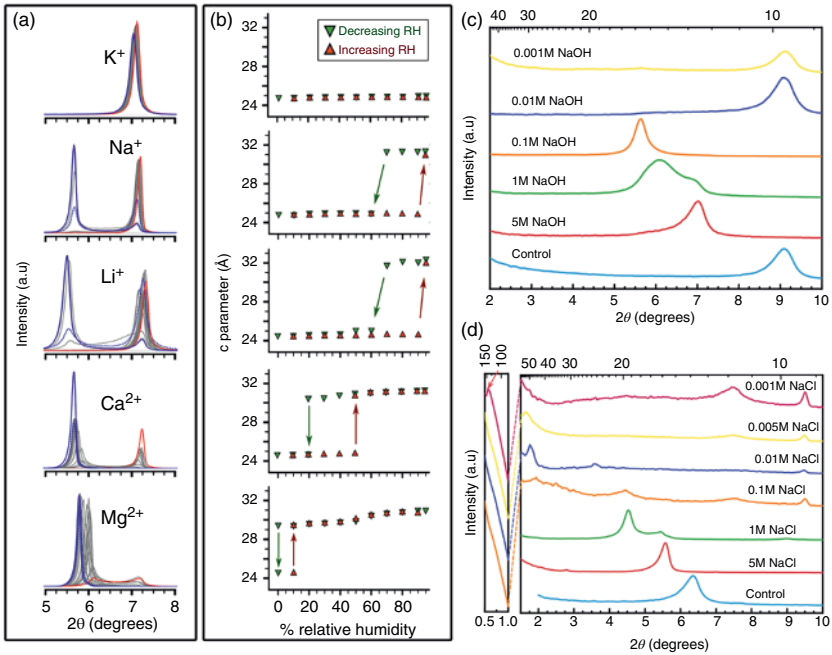


Figure 6.9 (a) XRD plots of the 002 region of $Ti_3C_2T_z$ MLs intercalated with different cations as noted right above the diffractograms as RH was varied from 95% to ~0% and back. (b) *c* parameters extracted from peaks shown in "a" as a function of RH. Triangles plot the changes in *c* from 95% to 0% RH; XRD patterns of (c) HF-MX treated with NaOH, and (d) hydronium ion intercalated MXene synthesized using LiF + HCl method treated with NaCl solutions of various concentrations noted on panel. Control XRD patterns of MXene powders before NaCl or NaOH treatment are shown at the bottom of each panel in blue for reference. *Source:* Adapted from Natu et al. [4] and Ghidiu et al. [29].

reasonable to assume that after treatment with 5 M NaOH, the intercalated Na^+ cations are surrounded by water molecules forming pillars equivalent to 1 monolayer, while after treatment with 0.1 M NaOH the intercalated Na^+ ions are surrounded with 2 "water layers." While in the case of 1 M NaOH, the intercalated cations are likely at an intermediate hydration stage between the two. Exposure to a concentration lower than 0.1 M NaOH did not induce any changes in HF-MX interlayer space.

In the same study, they observed an unusual phenomenon not observed in MXenes before [4]. After exposing $Ti_3C_2T_z$ – synthesized with LiF + HCl and washed with HCl to exchange the intercalated Li^+ ions with hydronium – to various NaCl concentrations, a 002 peak at 5.5° 2θ was detected in the case of the 5 M salt solution (Figure 6.9d) [4]. This peak shifts to 4.2° 2θ when the concentration decreased to 1 M and the position of this peak kept shifting to lower angles as the concentration of the salt decreased. Remarkably, a $d \sim 150$ Å was measured when a 0.001 M NaCl solution was used (Figure 6.9d) [4]. A similar phenomenon has been observed in other 2D materials and is known as osmotic swelling [52, 53, 89, 90]. Osmotic swelling is caused when low-concentration electrolytes are used and the interlayer space attracts cations from the solution due to electrostatic attraction. This leads to a substantially higher number of ions between the layers as compared to the surrounding solution, which in turn causes water to flow between the layers due to concentration-driven osmosis.

Ghidiu et al. also studied the changes in the d of MXenes as a function of applied pressure. What they found was counter-intuitive: d increased with increasing pressure [91]. When pressed uniaxially in the form of a disk to a pressure of 300 MPa, they observed that the d increases roughly by the size of an H_2O molecule (~2.5 Å) [91]. This was attributed to the intercalation of water layer between the MXene layers upon compression. This phenomenon was also observed, but to a lesser degree at a much high pressure of 5 GPa when MXene MLs were compressed using a diamond anvil. From these observations, they concluded that MLs shear under pressure caused higher accessibility to water molecules, which results in the intercalation of water bilayers as measured by XRD [91]. This unusual phenomenon is also observed in some other 2D materials and is termed pseudo-negative compressibility and was observed in MXenes for the first time in this work [91].

6.10 General Guidelines for Ion Intercalation in MXenes and Possible Pitfalls

1) The method of MXene synthesis is very important to achieve ion exchange. To get ion-exchangeable MXenes in the case of $Ti_3C_2T_z$, we suggest using LiF + HCl as the etchant. For other MXenes that need HF for synthesis, a

post-etching treatment with NaOH or TBAOH is suggested to make them ion exchangeable. The former is preferred, since one ends up with Na cations instead of TMA between the layers. We have shown that a simple post-etching treatment with NaOH can result in the delamination of most MXenes. It is worth noting that this post-etching treatment is most probably not restricted to NaOH.

2) When fully exchanging two ions, we recommend to first exchange the ML ions with hydronium ions using several HCl washes. In this case, when the hydronium ions are then replaced by the desired cation by washing with its salt solution, the probability of finding the initial cation is much reduced. If minor impurity ions are acceptable, then directly exchanging the cations using salt solutions is a much faster and easier process.
3) The water used to make the salt solution aliquots for exchange must be ultra-pure. Voigt et al. found that using 15 MΩ DI water instead of the ideal 18 MΩ DI water was enough to cause unwanted ion exchanges and swelling. This can lead to misinterpretation of the results of other experiments.
4) Treatment of HF-MX with intercalants like DMSO, TBAOH, TMAOH, and NaOH should be kept to the minimum possible time. This is because the strong basic nature of these chemicals can also result in the oxidation of MXenes which, in most applications, is undesirable and should be minimized as much as possible. This is especially important for non-$Ti_3C_2T_z$ MXenes, which generally have a higher propensity to oxidation.
5) When measuring d using XRD to compare with other samples, the hydration state of the MXenes should be kept the same, for example, at the same RH. Otherwise, the intercalation/deintercalation of water molecules might be misrepresented as changes in *d* due to other experimental factors.
6) For ion exchange in MLs generally high-concentration salt solutions should be used because they suppress spontaneous delamination of MXene sheets during shaking or stirring; also it will avoid the possibility of osmotic swelling between the layers.
7) Though XRD is a powerful technique to confirm *d*-spacing changes, generally while developing procedures not already reported in the literature, secondary characterization techniques other than XRD, such as XPS, must also be employed to ensure that the desired species is the one causing the changes in *d*, as discussed above. Sometime impurities, or parasitic catalytic reactions can lead to incorrect interpretations of XRD results.
8) In general, MXenes are highly hydrophilic in nature. Therefore, completely dehydrated MXenes must be handled carefully; they can even absorb water from ambient moisture again possibly introducing unknown errors in some measurements.

6.11 Summary

A large variety of small and large ions and molecules can be intercalated in the interlayer space of MXenes. Though spontaneous ion intercalation depends on how the MXenes are synthesized. MXenes synthesized with cations apart from protons present in the etching solution generally tend to allow ion exchange. Ion exchange generally occurs spontaneously at room temperature and just requires exposing the MLs to salt solutions of the desired cations. The intercalated species can cause changes in MXenes such as expansion or contraction of d, change its mechanical strength, affect its catalytic properties, render it hydrophobic or hydrophilic, and affect its energy storage capabilities. The ability of MXenes to spontaneously intercalate and de-intercalate various species, combined with their high conductivities, make them attractive candidates for various sensors as well.

However, there are several open questions that still need to be answered like the interactions of the intercalated species with the surface groups, the arrangement of water molecules into the interlayer space, the sites at which the intercalated ion or molecules reside in the MLs and how the localized positive charges affect the electronic properties of MXenes.

References

1 Harland, C.E. (1994). Discovery and structure of solid inorganic ion exchange materials. In: Ion Exchange: Theory and Practice (2), 1–20. The Royal Society of Chemistry.

2 Zagorodni, A.A. (2007). Chapter 2 - Ion exchangers, their structure and major properties. In: Ion Exchange Materials (ed. A.A. Zagorodni), 9–54. Oxford: Elsevier.

3 Clearfield, A. (1988). Role of ion exchange in solid-state chemistry. *Chemical Reviews* 88 (1): 125–148.

4 Natu, V., Pai, R., Wilson, O. et al. (2022). Effect of base/nucleophile treatment on interlayer ion intercalation, surface terminations, and osmotic swelling of Ti_3C_2Tz MXene multilayers. *Chemistry of Materials* 34 (2): 678–693.

5 Luo, J., Zhang, W., Yuan, H. et al. (2017). Pillared structure design of MXene with ultralarge interlayer spacing for high-performance lithium-ion capacitors. *ACS Nano* 11 (3): 2459–2469.

6 Srimuk, P., Halim, J., Lee, J. et al. (2018). Two-dimensional molybdenum carbide (MXene) with divacancy ordering for brackish and seawater desalination via cation and anion intercalation. *ACS Sustainable Chemistry & Engineering* 6 (3): 3739–3747.

7 Luo, J., Tao, X., Zhang, J. et al. (2016). Sn^{4+} ion decorated highly conductive Ti_3C_2 MXene: promising lithium-ion anodes with enhanced volumetric capacity and cyclic performance. *ACS Nano* 10 (2): 2491–2499.

8 Carrado, K.A., Forman, J.E., Botto, R.E., and Winans, R.E. (1993). Incorporation of phthalocyanines by cationic and anionic clays via ion exchange and direct synthesis. *Chemistry of Materials* 5 (4): 472–478.

9 Beall, G.W. (2003). The use of organo-clays in water treatment. *Applied Clay Science* 24 (1): 11–20.

10 Rožić, M., Cerjan-Stefanović, Š., Kurajica, S. et al. (2000). Ammoniacal nitrogen removal from water by treatment with clays and zeolites. *Water Research* 34 (14): 3675–3681.

11 Ren, C.E., Hatzell, K.B., Alhabeb, M. et al. (2015). Charge- and size-selective ion sieving through Ti_3C_2Tx MXene membranes. *The Journal of Physical Chemistry Letters* 6 (20): 4026–4031.

12 Xing, Y., Akonkwa, G., Liu, Z. et al. (2020). Crumpled two-dimensional Ti_3C_2Tx MXene lamellar membranes for solvent permeation and separation. *ACS Applied Nano Materials* 3 (2): 1526–1534.

13 Xie, X., Chen, C., Zhang, N. et al. (2019). Microstructure and surface control of MXene films for water purification. *Nature Sustainability* 2 (9): 856–862.

14 Loiola, A.R., Andrade, J.C.R.A., Sasaki, J.M., and da Silva, L.R.D. (2012). Structural analysis of zeolite NaA synthesized by a cost-effective hydrothermal method using kaolin and its use as water softener. *Journal of Colloid and Interface Science* 367 (1): 34–39.

15 Cinar, S. and Beler-Baykal, B. (2005). Ion exchange with natural zeolites: an alternative for water softening? *Water Science and Technology* 51 (11): 71–77.

16 Ching, K., Baker, A., Tanaka, R. et al. (2022). Liquid-phase water isotope separation using graphene-oxide membranes. *Carbon* 186: 344–354.

17 Yoneda, Y., Uchijima, T., and Makishima, S. (1959). Separation of boron isotopes by ion exchange. *The Journal of Physical Chemistry* 63 (12): 2057–2058.

18 Kakihana, H. (1974). Ion exchange, isotope exchange and isotope separation. *Journal of Chromatography A* 102: 47–55.

19 Wang, L., Yuan, L., Chen, K. et al. (2016). Loading actinides in multilayered structures for nuclear waste treatment: the first case study of uranium capture with vanadium carbide MXene. *ACS Applied Materials & Interfaces* 8 (25): 16396–16403.

20 Umrao, S., Tabassian, R., Kim, J. et al. (2019). MXene artificial muscles based on ionically cross-linked Ti_3C_2Tx electrode for kinetic soft robotics. *Science Robotics* 4 (33): eaaw7797.

21 Nguyen, V.H., Tabassian, R., Oh, S. et al. (2020). Stimuli-responsive MXene-based actuators. *Advanced Functional Materials* 30 (47): 1909504.

22 Zhao, L., Huang, J., Zhang, Y. et al. (2017). Programmable and bidirectional bending of soft actuators based on Janus structure with sticky tough PAA-clay hydrogel. *ACS Applied Materials & Interfaces* 9 (13): 11866–11873.

23 Roper, D.K. and Lightfoot, E.N. (1995). Separation of biomolecules using adsorptive membranes. *Journal of Chromatography A* 702 (1): 3–26.

24 Felipe, E.C.B., Batista, K.A., and Ladeira, A.C.Q. (2021). Recovery of rare earth elements from acid mine drainage by ion exchange. *Environmental Technology* 42 (17): 2721–2732.

25 Mondal, A., Majumdar, R., Mahata, N., and Bhunia, B. (2019). Separation and purification of uncharged molecules. In: Applications of Ion Exchange Materials in the Environment (ed. M.I. Ahamed and A.M. Asiri), 47–63. Cham: Springer International Publishing.

26 Naguib, M., Kurtoglu, M., Presser, V. et al. (2011). Two-dimensional nanocrystals produced by exfoliation of Ti_3AlC_2. *Advanced Materials* 23 (37): 4248–4253.

27 Ghidiu, M. and Barsoum, M.W. (2017). The {110} reflection in X-ray diffraction of MXene films: misinterpretation and measurement via non-standard orientation. *Journal of the American Ceramic Society* 100 (12): 5395–5399.

28 Chen, H., Ma, H., and Li, C. (2021). Host–guest intercalation chemistry in MXenes and its implications for practical applications. *ACS Nano* 15 (10): 15502–15537.

29 Ghidiu, M., Halim, J., Kota, S. et al. (2016). Ion-exchange and cation solvation reactions in Ti_3C_2 MXene. *Chemistry of Materials* 28 (10): 3507–3514.

30 Verger, L., Natu, V., Ghidiu, M., and Barsoum, M.W. (2019). Effect of cationic exchange on the hydration and swelling behavior of $Ti_3C_2T_z$ MXenes. *The Journal of Physical Chemistry C* 123 (32): 20044–20050.

31 Voigt, C.A., Ghidiu, M., Natu, V., and Barsoum, M.W. (2018). Anion adsorption, $Ti_3C_2T_z$ MXene multilayers, and their effect on claylike swelling. *The Journal of Physical Chemistry C* 122 (40): 23172–23179.

32 Natu, V., Pai, R., Sokol, M. et al. (2020). 2D $Ti_3C_2T_z$ MXene synthesized by water-free etching of Ti_3AlC_2 in polar organic solvents. *Chem* 6 (3): 616–630.

33 McDaniel, R.M., Carey, M.S., Wilson, O.R. et al. (2021). Well-dispersed nanocomposites using covalently modified, multilayer, 2D titanium carbide (MXene) and in-situ "click" polymerization. *Chemistry of Materials* 33 (5): 1648–1656.

34 Carey, M., Hinton, Z., Sokol, M. et al. (2019). Nylon-6/$Ti_3C_2T_z$ MXene nanocomposites synthesized by in situ ring opening polymerization of ε-caprolactam and their water transport properties. *ACS Applied Materials & Interfaces* 11 (22): 20425–20436.

35 Mashtalir, O., Cook, K.M., Mochalin, V.N. et al. (2014). Dye adsorption and decomposition on two-dimensional titanium carbide in aqueous media. *J. Mater. Chem. A* 2 (35): 14334–14338.

36 Ghidiu, M., Lukatskaya, M.R., Zhao, M.-Q. et al. (2014). Conductive two-dimensional titanium carbide 'clay' with high volumetric capacitance. *Nature* 516: 78–81.

37 Halim, J., Cook, K.M., Naguib, M. et al. (2016). X-ray photoelectron spectroscopy of select multi-layered transition metal carbides (MXenes). *Applied Surface Science* 362: 406–417.

38 Sharma, G., Muthuswamy, E., Naguib, M. et al. (2017). Calorimetric study of alkali metal ion (K^+, Na^+, Li^+) exchange in a clay-like MXene. *The Journal of Physical Chemistry C* 121 (28): 15145–15153.

39 Harris, K.J., Bugnet, M., Naguib, M. et al. (2015). Direct measurement of surface termination groups and their connectivity in the 2D MXene V_2CTx using NMR spectroscopy. *The Journal of Physical Chemistry C* 119 (24): 13713–13720.

40 Hope, M.A., Forse, A.C., Griffith, K.J. et al. (2016). NMR reveals the surface functionalisation of Ti_3C_2 MXene. *Physical Chemistry Chemical Physics* 18 (7): 5099–5102.

41 Kobayashi, T., Sun, Y., Prenger, K. et al. (2020). Nature of terminating hydroxyl groups and intercalating water in Ti_3C_2Tx MXenes: a study by ^1H solid-state NMR and DFT calculations. *The Journal of Physical Chemistry C* 124 (25): 13649–13655.

42 Lukatskaya Maria, R., Mashtalir, O., Ren Chang, E. et al. (2013). Cation intercalation and high volumetric capacitance of two-dimensional titanium carbide. *Science* 341 (6153): 1502–1505.

43 Wang, H.-W., Naguib, M., Page, K. et al. (2016). Resolving the structure of Ti_3C_2Tx MXenes through multilevel structural modeling of the atomic pair distribution function. *Chemistry of Materials* 28 (1): 349–359.

44 Markovitch, O. and Agmon, N. (2007). Structure and energetics of the hydronium hydration shells. *The Journal of Physical Chemistry A* 111 (12): 2253–2256.

45 Larson, J.W. and McMahon, T.B. (1984). Gas-phase bihalide and pseudobihalide ions. An ion cyclotron resonance determination of hydrogen bond energies in XHY-species (X, Y = F, Cl, Br, CN). *Inorganic Chemistry* 23 (14): 2029–2033.

46 Emsley, J. (1980). Very strong hydrogen bonding. *Chemical Society Reviews* 9 (1): 91–124.

47 Deng, D., Novoselov, K.S., Fu, Q. et al. (2016). Catalysis with two-dimensional materials and their heterostructures. *Nature Nanotechnology* 11 (3): 218–230.

48 Novoselov, K.S. (2004). Electric field effect in atomically thin carbon films. *Science* 306 (5696): 666–669.

49 Novoselov, K.S., Jiang, D., Schedin, F. et al. (2005). Two-dimensional atomic crystals. *Proceedings of the National Academy of Sciences* 102 (30): 10451–10453.

50 Novoselov, K.S., Mishchenko, A., Carvalho, A., and Castro Neto, A.H. (2016). 2D materials and van der Waals heterostructures. *Science* 353 (6298): aac9439.

51 Hou, J., Zheng, Y., Su, Y. et al. (2015). Macroscopic and strong ribbons of functionality-rich metal oxides from highly ordered assembly of unilamellar sheets. *Journal of the American Chemical Society* 137 (40): 13200–13208.

52 Sasaki, T. and Watanabe, M. (1998). Osmotic swelling to exfoliation. Exceptionally high degrees of hydration of a layered titanate. *Journal of the American Chemical Society* 120 (19): 4682–4689.

53 Song, Y., Iyi, N., Hoshide, T. et al. (2018). Massive hydration-driven swelling of layered perovskite niobate crystals in aqueous solutions of organo-ammonium bases. *Dalton Transactions* 47 (9): 3022–3028.

54 Mashtalir, O., Lukatskaya, M.R., Zhao, M.-Q. et al. (2015). Amine-assisted delamination of Nb_2C MXene for Li-ion energy storage devices. *Advanced Materials* 27 (23): 3501–3506.

55 Mashtalir, O., Naguib, M., Mochalin, V.N. et al. (2013). Intercalation and delamination of layered carbides and carbonitrides. *Nature Communications* 4: 1716–1716.

56 Naguib, M., Unocic, R.R., Armstrong, B.L., and Nanda, J. (2015). Large-scale delamination of multi-layers transition metal carbides and carbonitrides "MXenes". *Dalton Transactions* 44 (20): 9353–9358.

57 Ghidiu, M., Kota, S., Halim, J. et al. (2017). Alkylammonium cation intercalation into Ti_3C_2 (MXene): effects on properties and ion-exchange capacity estimation. *Chemistry of Materials* 29 (3): 1099–1106.

58 Celerier, S., Hurand, S., Garnero, C. et al. (2019). Hydration of $Ti_3C_2T_x$ MXene: an interstratification process with major implications on physical properties. *Chemistry of Materials* 31 (2): 454–461.

59 Kajiyama, S., Szabova, L., Iinuma, H. et al. (2017). Enhanced Li-ion accessibility in MXene titanium carbide by steric chloride termination. *Advanced Energy Materials* 7 (9): 1601873–1601873.

60 Ghidiu, M. J. (2018). Ions in MXene: characterization and control of interlayer cations and their effects on structure and properties of 2D transition metal carbides. Ph.D. thesis. Drexel University.

61 Halim, J., Lukatskaya, M.R., Cook, K.M. et al. (2014). Transparent conductive two-dimensional titanium carbide epitaxial thin films. *Chemistry of Materials* 26 (7): 2374–2381.

62 Liu, L., Orbay, M., Luo, S. et al. (2021). Exfoliation and delamination of Ti_3C_2Tx MXene prepared via molten salt etching route. *ACS Nano* 16 (1): 111–118.

63 Husmann, S., Budak, Ö., Shim, H. et al. (2020). Ionic liquid-based synthesis of MXene. *Chemical Communications* 56 (75): 11082–11085.

64 Natu, V., Sokol, M., Verger, L., and Barsoum, M.W. (2018). Effect of edge charges on stability and aggregation of Ti_3C_2Tz MXene colloidal suspensions. *The Journal of Physical Chemistry C* 122 (48): 27745–27753.

65 Chorom, M. and Rengasamy, P. (1995). Dispersion and zeta potential of pure clays as related to net particle charge under varying pH, electrolyte concentration and cation type. *European Journal of Soil Science* 46 (4): 657–665.

66 Lagaly, G. and Ziesmer, S. (2003). Colloid chemistry of clay minerals: the coagulation of montmorillonite dispersions. *Advances in Colloid and Interface Science* 100-102: 105–128.

67 Missana, T. and Adell, A. (2000). On the applicability of DLVO theory to the prediction of clay colloids stability. *Journal of Colloid and Interface Science* 230 (1): 150–156.

68 Swartzen-Allen, S.L. and Matijevic, E. (1974). Surface and colloid chemistry of clays. *Chemical Reviews* 74 (3): 385–400.

69 Sang, X., Xie, Y., Lin, M.-W. et al. (2016). Atomic defects in monolayer titanium carbide (Ti_3C_2Tx) MXene. *ACS Nano* 10 (10): 9193–9200.

70 Shpigel, N., Chakraborty, A., Malchik, F. et al. (2021). Can anions be inserted into MXene? *Journal of the American Chemical Society* 143 (32): 12552–12559.

71 Natu, V., Hart, J.L., Sokol, M. et al. (2019). Edge capping of 2D-MXene sheets with polyanionic salts to mitigate oxidation in aqueous colloidal suspensions. *Angewandte Chemie International Edition* 131 (36): 12785–12790.

72 Khazaei, M., Arai, M., Sasaki, T. et al. (2013). Novel electronic and magnetic properties of two-dimensional transition metal carbides and nitrides. *Advanced Functional Materials* 23 (17): 2185–2192.

73 Li, K., Chang, T.H., Xie, Q. et al. (2019). Tunable magnetic response in 2D materials via reversible intercalation of paramagnetic ions. *Advanced Electronic Materials* 5 (6): 1900040–1900040.

74 Alhabeb, M., Maleski, K., Anasori, B. et al. (2017). Guidelines for synthesis and processing of two-dimensional titanium carbide (Ti_3C_2Tx MXene). *Chemistry of Materials* 29 (18): 7633–7644.

75 Mashtalir, O., Lukatskaya, M.R., Kolesnikov, A.I. et al. (2016). The effect of hydrazine intercalation on the structure and capacitance of 2D titanium carbide (MXene). *Nanoscale* 8 (17): 9128–9133.

76 Overbury, S.H., Kolesnikov, A.I., Brown, G.M. et al. (2018). Complexity of intercalation in MXenes: destabilization of urea by two-dimensional titanium carbide. *Journal of the American Chemical Society* 140 (32): 10305–10314.

77 Anasori, B., Xie, Y., Beidaghi, M. et al. (2015). Two-dimensional, ordered, double transition metals carbides (MXenes). *ACS Nano* 9 (10): 9507–9516.

78 Lagaly, G. and Malberg, R. (1990). Disaggregation of alkylammonium montmorillonites in organic solvents. *Colloids and Surfaces* 49: 11–27.

79 Lagaly, G. (1986). Interaction of alkylamines with different types of layered compounds. *Solid State Ionics* 22 (1): 43–51.

80 Lagaly, G. and Weiss, A. (1970). Anordnung und orientierung kationischer tenside auf silicatoberflächen. *Kolloid-Zeitschrift und Zeitschrift für Polymere* 238 (1): 485–493.

81 Liang, K., Matsumoto, R.A., Zhao, W. et al. (2021). Engineering the interlayer spacing by pre-intercalation for high performance supercapacitor MXene electrodes in room temperature ionic liquid. *Advanced Functional Materials* 31 (33): 2104007.

82 Carey, M., Hinton, Z., Natu, V. et al. (2020). Dispersion and stabilization of alkylated 2D MXene in nonpolar solvents and their pseudocapacitive behavior. *Cell Reports Physical Science* 1 (4): 100042–100042.

83 Pai, R., Natu, V., Sokol, M. et al. (2021). Tuning functional two-dimensional MXene nanosheets to enable efficient sulfur utilization in lithium-sulfur batteries. *Cell Reports Physical Science* 2 (7): 100480.

84 Naguib, M., Tang, W., Browning, K.L. et al. (2020). Catalytic activity of Ti-based MXenes for the hydrogenation of furfural. *ChemCatChem* 12 (22): 5733–5742.

85 Osti, N.C., Naguib, M., Tyagi, M. et al. (2017). Evidence of molecular hydrogen trapped in two-dimensional layered titanium carbide-based MXene. *Physical Review Materials* 1 (2): 024004.

86 Muckley, E.S., Naguib, M., Wang, H.-W. et al. (2017). Multimodality of structural, electrical, and gravimetric responses of intercalated MXenes to water. *ACS Nano* 11 (11): 11118–11126.

87 Hendricks, S.B., Nelson, R.A., and Alexander, L.T. (1940). Hydration mechanism of the clay mineral montmorillonite saturated with various cations. *Journal of the American Chemical Society* 62 (6): 1457–1464.

88 Osti, N.C., Naguib, M., Ganeshan, K. et al. (2017). Influence of metal ions intercalation on the vibrational dynamics of water confined between MXene layers. *Physical Review Materials* 1 (6): 065406.

89 Daab, M., Eichstaedt, N.J., Habel, C. et al. (2018). Onset of osmotic swelling in highly charged clay minerals. *Langmuir* 34 (28): 8215–8222.

90 Rao, S.M., Thyagaraj, T., and Raghuveer Rao, P. (2013). Crystalline and osmotic swelling of an expansive clay inundated with sodium chloride solutions. *Geotechnical and Geological Engineering* 31 (4): 1399–1404.

91 Ghidiu, M., Kota, S., Drozd, V., and Barsoum, M.W. (2018). Pressure-induced shear and interlayer expansion in Ti_3C_2 MXene in the presence of water. *Science Advances* 4 (1): eaao6850.

7

MXene Thermal and Chemical Stability and Degradation Mechanism

Shuohan Huang[1] *and Vadym N. Mochalin*[2,3]

[1] *State Key Laboratory for Modification of Chemical Fibers and Polymer Materials, College of Materials Science and Engineering, Donghua University, Shanghai, China*
[2] *Department of Chemistry, Missouri University of Science & Technology, Rolla, MO, USA*
[3] *Department of Materials Science & Engineering, Missouri University of Science & Technology, Rolla, MO, USA*

7.1 Introduction

MXenes raised significant interest for various applications; however, they are found to be surprisingly more reactive than their bulk counterparts, transition metal carbides, which are known or their chemical stability in ambient conditions. The large and accessible surface bearing a number of functional groups makes MXenes very sensitive to temperature and environment. Because materials may experience exposure to heat in synthesis processes and application environments, the thermal stability of MXenes is also crucial. Thus, understanding MXene chemical and thermal stability is of critical importance for their synthesis and performance in various applications. In this chapter, we analyze the stability of MXenes with regard to the following aspects: (i) surface chemistry and chemical modification of MXene surface; (ii) key factors that affect the chemical and thermal stability of MXenes and the associated underlying mechanisms; (iii) strategies for chemical stabilization of MXenes by changing the synthesis conditions of the MAX phase, selection of etchants, adjustment of storage conditions, and surface modifications.

Transition Metal Carbides and Nitrides (MXenes) Handbook: Synthesis, Processing, Properties and Applications, First Edition. Edited by Chuanfang Zhang and Michael Naguib.
© 2024 John Wiley & Sons, Inc. Published 2024 by John Wiley & Sons, Inc.

7.2 Surface Chemistry and Chemical Modification of MXenes

Because of the great potential provided by MXenes in many applications, understanding the chemistry and reactivity of MXenes becomes increasingly important. To a large extent, the surface chemistry of MXenes is controlled by the etchants or etching environments [1–3], regardless of the type of M and X elements or the number of atomic layers in the MXene structure [4]. Efforts using various characterization techniques have been made to investigate the surface chemistry of MXenes. Among them, the X-ray photoelectron spectroscopy (XPS) is the most widely used technique [5]. The combination of XPS and EDX (energy dispersive X-ray spectroscopy) provides an efficient way to determine the type (qualitative analysis) and relative proportions of surface functional groups. However, when it comes to quantitative determination of the absolute numbers of –O–, –OH, and other functional groups on MXenes, these techniques are often non-conclusive. Solid-state nuclear magnetic resonance (NMR) has been used as a powerful tool to address this problem [6]. Comparing different etchants, more -F terminations (relative to –O– and –OH) are formed when using HF as the etchant, while more –O– terminations can be found when using LiF/HCl etchant (Figure 7.1). Seredych et al. have demonstrated that TGA-MS could be used to investigate the surface terminations as well as the intercalated species in MXenes synthesized by different etchants. This is an important demonstration as TGA-MS represents a well-established and very sensitive analytical chemistry technique, well suited for quantitative analysis. The results also show that HF concentration affects the ratio of F- to O-containing groups on MXene surface. Also, a higher concentration of HF results in more intercalated water trapped between MXene layers [7].

Surface chemistry of MXenes plays a role in their performance. For example, one of the most efficient ways to improve the electronic conductivity of MXenes, at least in theory, is to remove the surface terminations altogether. In practice, vacuum annealing has been demonstrated to partially remove the functional groups on MXene surface, resulting in an increased conductivity [8]. Besides, Kamysbayev et al. synthesized different MXenes (with M = Ti, Mo, Nb, or V) with none (vacancy), O, S, Cl, Br, Se, Te, or NH surface terminations using Lewis acidic molten salt method (Figure 7.2) [9]. The synthesized MXenes can be beneficial for various applications. Surface functionalization also affects the interlayer distance, allowing to tailor the performance of MXenes for energy storage. For example, Chen et al. functionalized $Ti_3C_2T_x$ MXene with glycine, which increased the d-spacing by 1.19 Å, resulting in a better charge/discharge rate and cycling performance in supercapacitor [10]. A comparative performance of $Ti_3C_2T_x$ MXenes

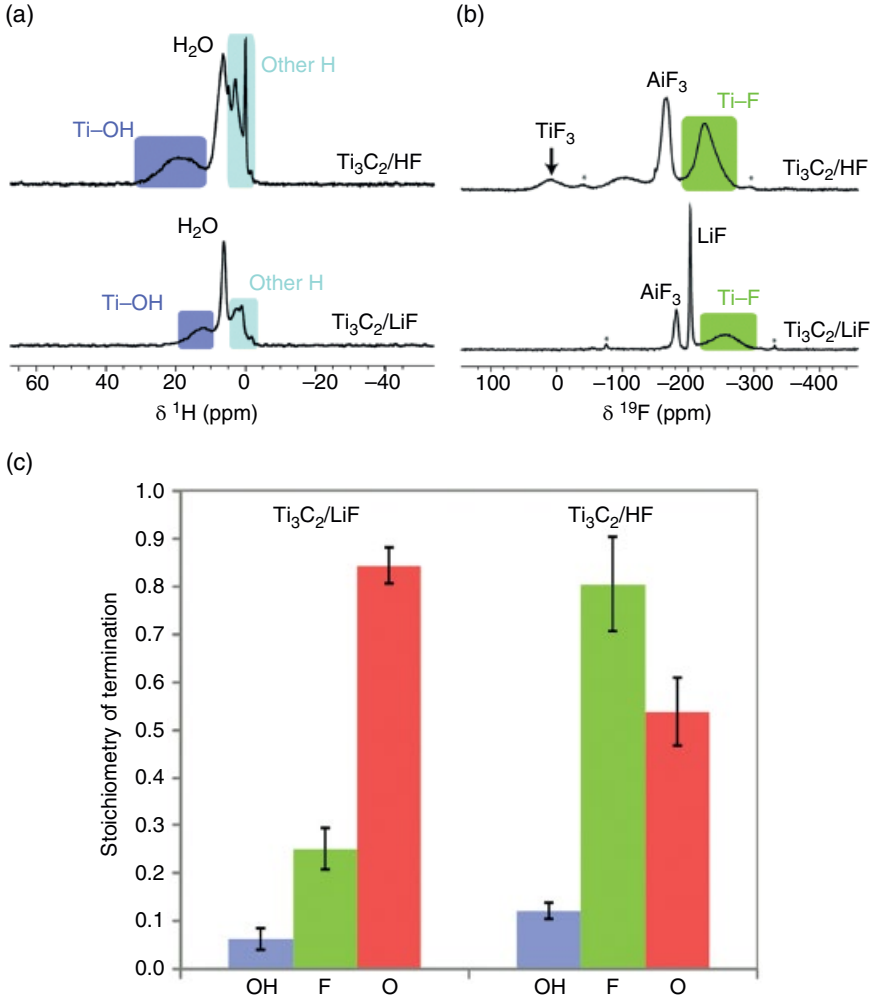


Figure 7.1 Differences in (a) ^{1}H NMR spectra, (b) ^{19}F NMR spectra, and (c) surface functional group composition between Ti_3C_2 MXenes synthesized by using HF and LiF/HCl etchants. *Source:* Hope et al. [6]/Royal Society of Chemistry/CC BY 3.0.

prepared with different etchants (HF, HF/HCl, and HF/H_2SO_4) in Na-ion storage has also been evaluated, and the results show that the MXene synthesized with HF/H_2SO_4 has a better electrochemical performance because of cleaner surface and lower content of structural water [11]. In 2021, Pazniak et al. demonstrated low-energy ion implantation as a new route to modify Ti_3C_2 MXene surface by introducing manganese ions [12]. This modification not only introduced

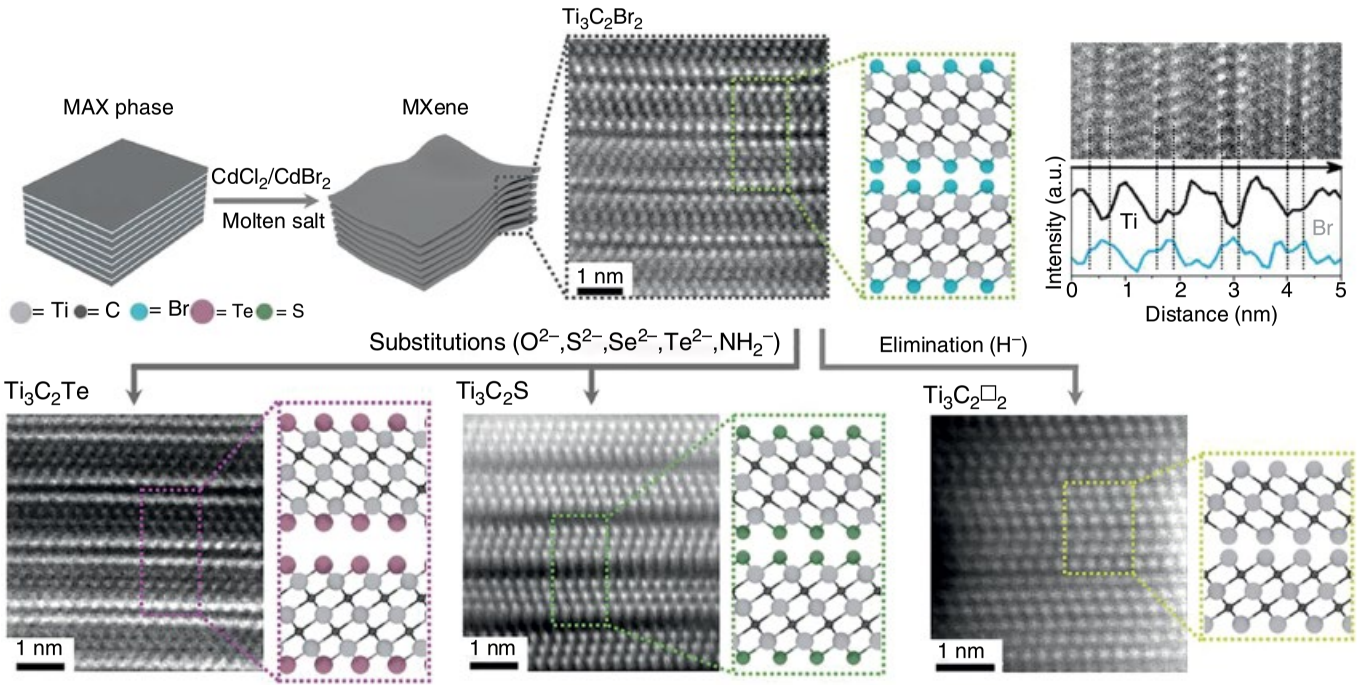


Figure 7.2 Schematics for MXene synthesis using molten salts and atomic resolution high-angle annular dark-field (HAADF) images of $Ti_3C_2Br_2$, Ti_3C_2Te, Ti_3C_2S, and bare $Ti_3C_2\square_2$ MXenes (where □ stands for vacancy). *Source:* Kamysbayev et al. [9]/Reproduced from American Association for the Advancement of Science (AAAS).

manganese ions on the MXene surface, but also created a defective structure that resulted in an increased amount of O on the MXene, and thus could be used to modify its electronic properties.

7.3 MXene Chemical Stability and Degradation in Aqueous Solutions

MXenes offer many advantages in applications compared to other 2D materials. One such advantage is that they can easily form stable aqueous dispersions due to the negatively charged and intrinsically hydrophilic nature of the MXene nanoflakes. However, MXenes also tend to be more reactive than their bulk counterparts, transition metal carbides/nitrides, and, therefore, need more attention with respect to their stability, especially when they are exposed to the environment. In particular, MXenes spontaneously decompose into the corresponding transition metal oxides and gaseous carbon or nitrogen containing products in water- and oxygen-containing environments. MXene flake deterioration often begins at the flake's defects and edges and progresses toward the center. While in optoelectronic applications MXenes will probably be used in a packaged form that excludes their interactions with the environment, for most of their other applications, the instability of MXenes affected by oxidation, hydrolysis or both is a major issue. As a result, different methods have been developed to prevent degradation and extend the shelf life of MXenes, and every stage in the life cycle of MXenes – from the synthesis of the precursor MAX phase to the post-treatment of MXenes as colloidal solutions or solids – has been investigated (Figure 7.3). Below we discuss some of the factors that affect the chemical stability of MXenes.

7.3.1 MAX Phase Synthesis

The flake size and surface imperfections can have a direct impact on the chemical stability of MXenes. The shelf life of the derived MXenes can be increased by adjusting the MAX phase synthesis process or by careful selection of raw materials to produce precursors with larger grains or fewer defects. For example, Ti-containing MAX phases can be synthesized using a variety of Ti and carbon sources, including Ti, TiC, TiH_2, graphite, carbon lampblack, and carbon nanotubes. In comparison to TiC or carbon lampblack sources, the $Ti_3C_2T_x$ MXene produced from the Ti_3AlC_2 MAX phase synthesized using graphite as the carbon source has shown higher conductivity ($4400\,S\,cm^{-1}$) and improved chemical stability (Figure 7.4a–f) [18]. Changing the annealing time for MAX phase synthesis can also affect the grain size of the MAX phase and further influence the lateral size of the corresponding MXene flakes [19].

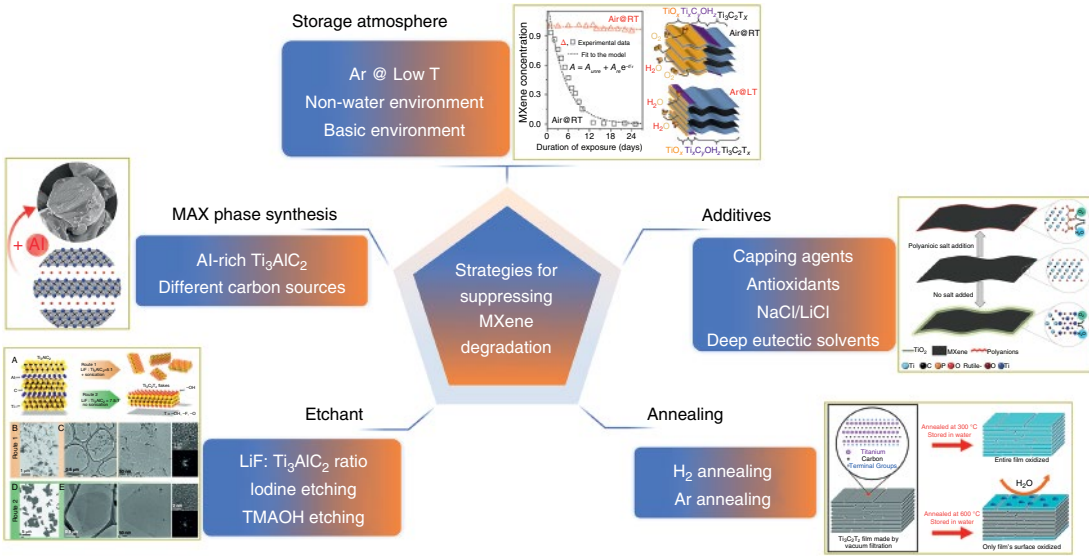


Figure 7.3 Known strategies for suppressing MXene degradation. *Source:* Lipatov et al. [13], Zhang et al. [14], Natu et al. [15], Mathis et al. [16] and Zhao et al. [17].

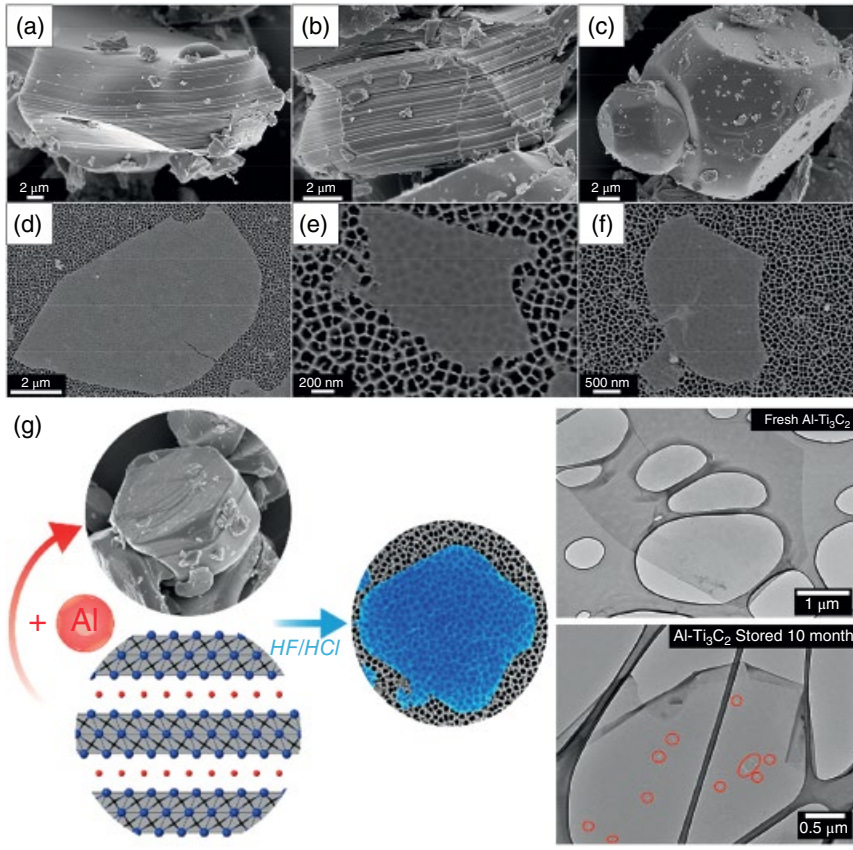


Figure 7.4 SEM images of Ti_3AlC_2 synthesized with (a) graphite, (b) TiC, and (c) carbon lampblack as carbon source. And corresponding SEM images of $Ti_3C_2T_x$ MXene produced by a MILD-like process (40 hours etching in 12 M HCl and 9 M LiF) using (d) graphite, (e) TiC, and (f) carbon lampblack-derived MAX phases and cast from solution on an anodic aluminum oxide membrane for imaging. (g) Schematic illustration of MAX phase synthesis with an excess of Al in the initial mix and of subsequent MXene synthesis, leading to a more stable Ti_3C_2 MXene flakes (shown in TEM images on the right) in colloid (red circles in TEM images show defects in MXene flakes found after 10 months of storage). *Source:* (a) Shuck et al. [18]/Reproduced from American Chemical Society and (b) Mathis et al. [16]/Reproduced from American Chemical Society.

Mathis et al. have demonstrated that the modified synthesis method (changing the composition of TiC : Ti : Al = 2 : 1 : 1 from molar ratio to mass ratio) produces a less defective MAX phase because of the excess of Al in the mix, which upon etching yields less defective MXene sheets (Figure 7.4g). The idea of this method is to provide an excess of Al as sacrificial material to chemically bind any oxygen

either adsorbed on surfaces or present in the atmosphere of the furnace during high-temperature MAX phase synthesis. According to the authors of this method, the produced MXene can be stored for years in an ambient environment [16]. However, gas analysis, which is currently the most sensitive and unambiguous technique to detect early stages of MXene degradation, has not been performed yet to confirm the stability of this MXene [20].

7.3.2 Etchant

Top-down synthesis, whereupon the A layers are selectively etched from the MAX phase or non-MAX phase precursors, has become a general synthesis method for MXenes. *In-situ* formed low concentration HF, as for example in a mixture of LiF + HCl, is a significantly milder etchant than *ex-situ* HF, resulting in flakes of larger lateral dimensions and with much less defects compared to MXenes produced *via ex-situ* HF etching where the concentrations of HF used in the etching solution are usually higher [21]. The minimally intensive layer delamination (MILD) method is recommended for applications requiring excellent electrical conductivity, improved chemical stability, and mechanical performance. To produce more Li^+ ions in the mix for intercalation, the molar ratio of HCl to LiF was doubled, and the molar ratio of LiF to MAX was raised to 7.5 : 1 from 5 : 1 to achieve a more complete removal of aluminum. After the MILD etching, delamination of multi-layered MXene into individual flakes can be achieved simply by manual shaking. The MILD method has become one of the most widely used to synthesize and delaminate MXenes with larger flakes and higher stability [2, 13].

The etching process largely determines the terminating functional groups of MXenes, which also have great effects on chemical stability. Tailoring surface chemistry of MXenes is another approach to prevent oxidation. Etching out Al layers from Ti_3AlC_2 with TMAOH resulted in $Al(OH)_4^-$ passivated Ti_3C_2 MXene [22]. Because of the shielding and passivating effects of $Al(OH)_4^-$, the produced MXenes survived for a longer period of time in water with a strong oxidizer (H_2O_2) added, as compared to the MXenes with usual –OH and –F mix terminated surfaces, synthesized using HF.

It has been demonstrated that surface density of oxygen functional groups and structural defects are strongly relevant for the ambient stability of MXene sheets. The non-aqueous iodine (I_2) aided etching method was discovered for producing $Ti_3C_2T_x$ (T_x = O, OH) with oxygen-rich terminal groups and without fluorine. In comparison to –F terminated MXenes created using conventional etching methods, MXene sheets produced *via* I_2-aided etching have higher structural integrity and are stable in water for at least two weeks [23]. The overall MXene synthesis process *via* I_2-aided etching of a MAX phase can be illustrated by the reactions (7.1–7.3), where the Eq. (7.1) corresponds to the removal of Al layers from the

parent Ti_3AlC_2 in a non-aqueous solvent, while Eqs. (7.2) and (7.3) describe termination of initially I-terminated MXenes with –O and –OH groups at the later stages in the synthesis (washing with water and exposure to ambient air).

$$Ti_3AlC_2 + \frac{x+3}{2}I_2 \rightarrow Ti_3C_2 - I_x + AlI_3 \tag{7.1}$$

$$Ti_3C_2 - I_x + \frac{x}{2}O_2 \rightarrow Ti_3C_2 - O_x + \frac{x}{2}I_2 \tag{7.2}$$

$$Ti_3C_2 - I_x + xH_2O \rightarrow Ti_3C_2 - (OH)_x + xHI \tag{7.3}$$

7.3.3 Storage Environment

In order to devise the appropriate preventive methods, it is crucial to identify the primary factors that affect the degradation of MXenes. Careful attention to storage conditions can reduce MXene degradation. Material degradation in aqueous colloidal solutions upon storage has been noted since the early days of MXene research. Obvious formation of titanium oxide from a titanium carbide MXene pointed researchers toward oxygen-mediated nature of this process and to some extent had diverted their attention from other possible mechanisms capable of yielding the same solid products with respect to transition metal element but proceeding through reactions different from the interaction of MXenes with oxygen gas or dissolved O_2. When a delaminated $Ti_3C_2T_x$ aqueous solution is exposed to air at room temperature, MXene flakes are usually completely oxidized within several days [13, 24]. Zhang et al. proposed refrigeration and de-aerated environment to substantially improve the shelf life of $Ti_3C_2T_x$ and Ti_2CT_x MXenes in aqueous colloidal solutions (Figure 7.5a) [14]. Based on the idea that low temperature slows down many reactions (e.g. exothermic), freezing MXene solutions at low temperatures (below $-20\ ^{\circ}C$) was proposed as an efficient way to suppress the degradation [25, 26]. However, it took the community several years to appreciate other important chemical processes involved in MXene degradation. Although the hints to other reactions besides oxidation were scattered in early MXene papers [27, 28], the commonly accepted opinion in the literature at that time was that the transformation of titanium-containing MXenes into titania observed in aqueous colloidal solutions is mainly due to MXene oxidation, more specifically, reaction of an MXene with dissolved oxygen, while the role of water was reduced to that of merely a solvent. Not surprisingly, numerous recommendations were made to de-aerate water used in colloidal solution preparation and to store the solutions in inert atmosphere. Other attempts to protect MXenes by suppressing their oxidative degradation have also been reported, particularly in aqueous solutions [15, 22, 29].

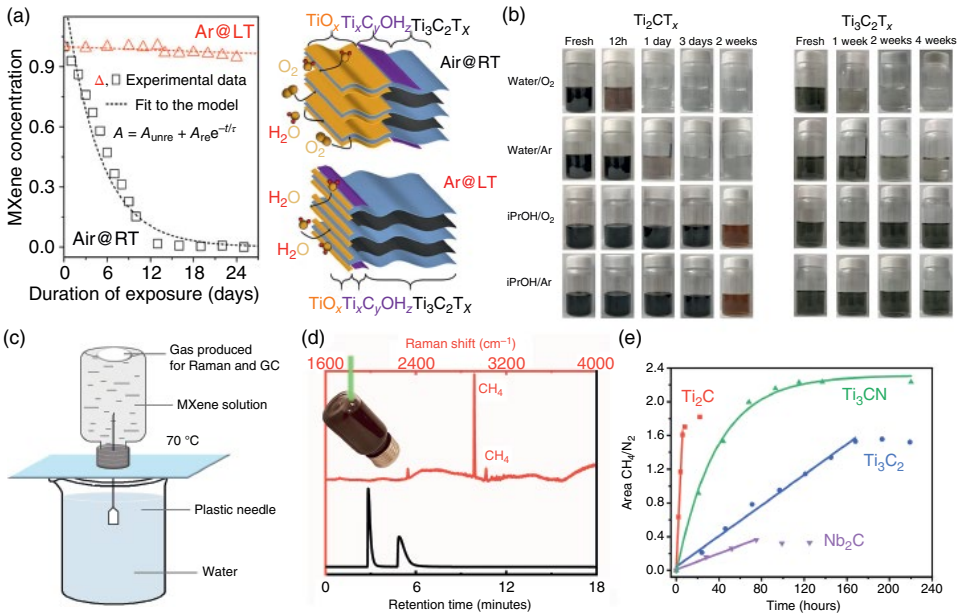


Figure 7.5 (a) Experimental data and schematic illustration of stability of aqueous colloidal $Ti_3C_2T_x$ in argon atmosphere at low temperature (Ar@LT) and in air at room temperature (Air@RT); (b) visual appearance of Ti_2CT_x and $Ti_3C_2T_x$ colloidal solutions in water or isopropanol (iPrOH) saturated with oxygen (O_2) or argon (Ar); (c) schematic illustration of gas collection during MXene degradation experiment for its subsequent analysis *via* spectroscopy and gas chromatography; (d) representative gas chromatogram and Raman spectrum of gaseous products collected during a carbide MXene degradation (GC peak at shorter retention time corresponds to air and at longer retention time to methane); (e) degradation kinetics of several MXenes in aqueous solutions at 70 °C measured with gaseous products analysis. *Source:* (b) Huang et al. [24]/Reproduced from American Chemical Society. (c, d, e) Huang et al. [20]/Reproduced from American Chemical Society. (a) Zhang et al. [14].

The first convincing experimental demonstration of hydrolysis as an alternative, yet overlooked, chemical route of MXene degradation in aqueous colloids, was reported by Huang and Mochalin in 2019 (Figure 7.5b) [24]. This study and a follow-up work have also established analysis of gaseous products of MXene degradation, using sensitive and well-established analytical chemistry techniques of gas chromatography and vibrational spectroscopy (e.g. Raman), as a powerful combination to understand chemistry and reactivity of these materials (Figure 7.5c, d) [20]. Whereas *a priori* carbon oxides (CO, CO_2) were expected to be the main gases formed in oxidation of carbide MXenes such as Ti_2CT_x, $Ti_3C_2T_x$, etc., the results of gas analysis indicate that mainly CH_4 is formed during reactions of carbide MXenes with water, whereas both CH_4 and NH_3 are formed during the degradation of the carbonitride Ti_3CNT_x MXene in water. These gaseous products are products of hydrolysis, not oxidation. Discovery of MXene hydrolysis, that is, direct reaction of MXenes with water not requiring presence of dissolved or gaseous oxygen, clearly showed that merely preventing oxidation of MXenes is not enough to avoid their degradation. To avoid hydrolysis, anhydrous polar organic solvents can be a better choice for MXene processing and storage [27].

Kinetics and reactivity of MXenes have also been studied with gas analysis, showing that the monolayer thickness determines the rate of degradation in water for MXenes with the same chemical composition (e.g. Ti_2CT_x and $Ti_3C_2T_x$). On the other hand, chemical reactivity of carbide MXenes with the same monolayer thickness but with different transition metals in their structure (such as Ti_2CT_x and Nb_2CT_x) is also different, illustrating how the chemical properties of 2D materials vary depending on their chemical composition and type of bonding within the monolayer when the monolayer thickness and structure of material remain essentially the same (Figure 7.5e). The studies of MXene reactivity may have implications far beyond the area of MXenes. Bulk transition metal carbides, such as TiC, VC, NbC, and alike, are well known for their chemical stability and resistance to the action of water as well as acids and bases in ambient conditions [30, 31]. Scattered previous reports of TiC hydrolysis [32] did not receive enough traction in the research community since the results were always questioned due to reactivity of potential minor impurities present in bulk carbides. And even assuming that some amount of the carbide indeed was hydrolyzed, it was anything but important since only a few dozen layers of its surface atoms could react before the reaction ceased, leaving the chemical nature of the bulk carbide solid largely intact. Hydrolysis of 2D transition metal carbides is strikingly different as it leads to complete chemical transformation of the 2D material leaving no room for doubts or alternative interpretations due to impurities, etc. It is also a clear experimental indication of striking differences in reactivity between 2D and bulk forms of solids that are well known to be stable in bulk form under the same conditions. In addition, this discovery challenges our modern

classification of carbides, which is based on their reactivity toward water [33] and may lead to further, more thorough, examination of the differences in chemical properties of materials depending on their dimensionality.

Kinetics of many hydrolysis reactions are pH dependent. Therefore, it is not surprising that pH of MXene aqueous colloidal solutions also has an impact on their chemical stability. The exact nature of this impact is still debated. On the one hand, some researchers believe that the interaction of MXene with hydroxyl anions speeds up MXene oxidation leading to a faster degradation in basic environments (Figure 7.6a) [34], according to the following reaction as the first step:

$$Ti_{n+1}C_nOH + OH^- \rightarrow Ti_{n+1}C_nO^- + H_2O \tag{7.4}$$

On the other hand, however, experiments show that the degradation of MXenes in aqueous solutions is suppressed in basic environments, which was explained by slowing down their hydrolysis, assuming (in analogy to hydrolysis of calcium carbide and other acetylides and methanides) that water acts as acid in the MXene hydrolysis reactions [35, 36]. One hypothetical detailed mechanism could be that hydroxyl groups on the $Ti_3C_2T_x$ surface are protonated by H^+ ions in an acidic environment, making it easier for O atoms in H_2O and O_2 to attack the Ti atoms in acidic media (Figure 7.6b), however, no amorphous carbon was observed to be present in the degradation products of our study. Overall, there is agreement that pH has a significant impact on MXene degradation in colloidal solution, despite different reports on which pH range is beneficial to prolong MXene stability. The different concentration ratios of the acid or base to MXene solution used in different experiments might potentially have a significant impact on the degradation rates. Thus, more studies are needed to understand the effect of pH on MXene stability.

7.3.4 Additives

At present, hydrolysis and oxidation are considered to be parallel processes resulting in MXene degradation in ambient conditions. To protect MXenes, certain passivating additives can be used in order to suppress either hydrolysis, oxidation or both. For example, water-soluble sodium L-ascorbate, a known antioxidant, can be added to protect MXenes from oxidation (Figure 7.7a) [29]. Thermodynamic activity of water in MXene colloids can be influenced by addition of electrolytes. Since the kinetics of hydrolysis depends on water activity (concentration of "free" water), lower activity must reduce the rate of hydrolysis, which was also used to protect MXenes from hydrolytic degradation. As an example, NaCl solution at various concentrations was shown to be an efficient storage agent (Figure 7.7b) [36, 37]. This direction of research seems to be particularly interesting as it offers fundamental mechanisms of

hydrolysis inhibition with a variety of inexpensive water soluble electrolytes and variations in their concentrations available to be explored for this purpose.

It is commonly accepted that the processes leading to MXene degradation (oxidation and hydrolysis) start from the edges and defects of MXene flakes [40]. Natu et al. have discovered that supposedly positively charged edges of MXene flakes could be capped with polyanions: polyphosphates, polysilicates, and polyborates, thus suppressing the degradation of MXenes. The addition of polyanions to aqueous colloids considerably inhibits MXene hydrolysis but has almost no effect on its oxidation (Figure 7.7c) [15, 38, 41]. In this regard, it is

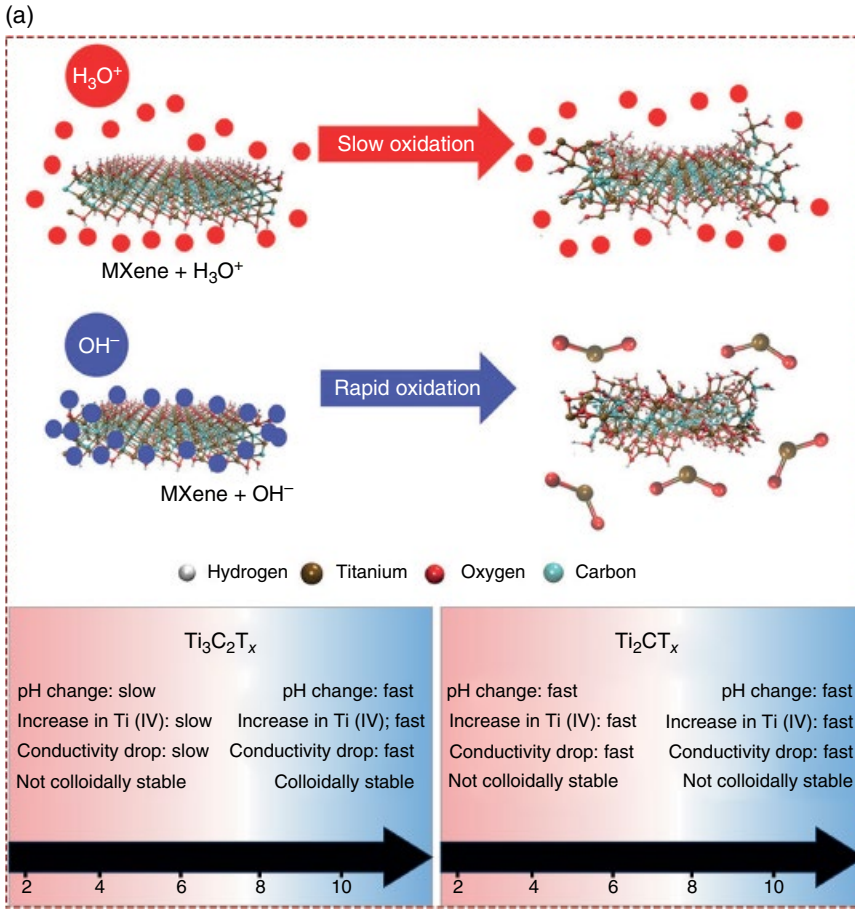


Figure 7.6 (a) Schematic illustration and (b) proposed hypothetical mechanisms for MXene nanosheet degradation in aqueous solutions in acidic or basic environments. *Source:* Zhao et al. [34] and Doo et al. [35].

(b)

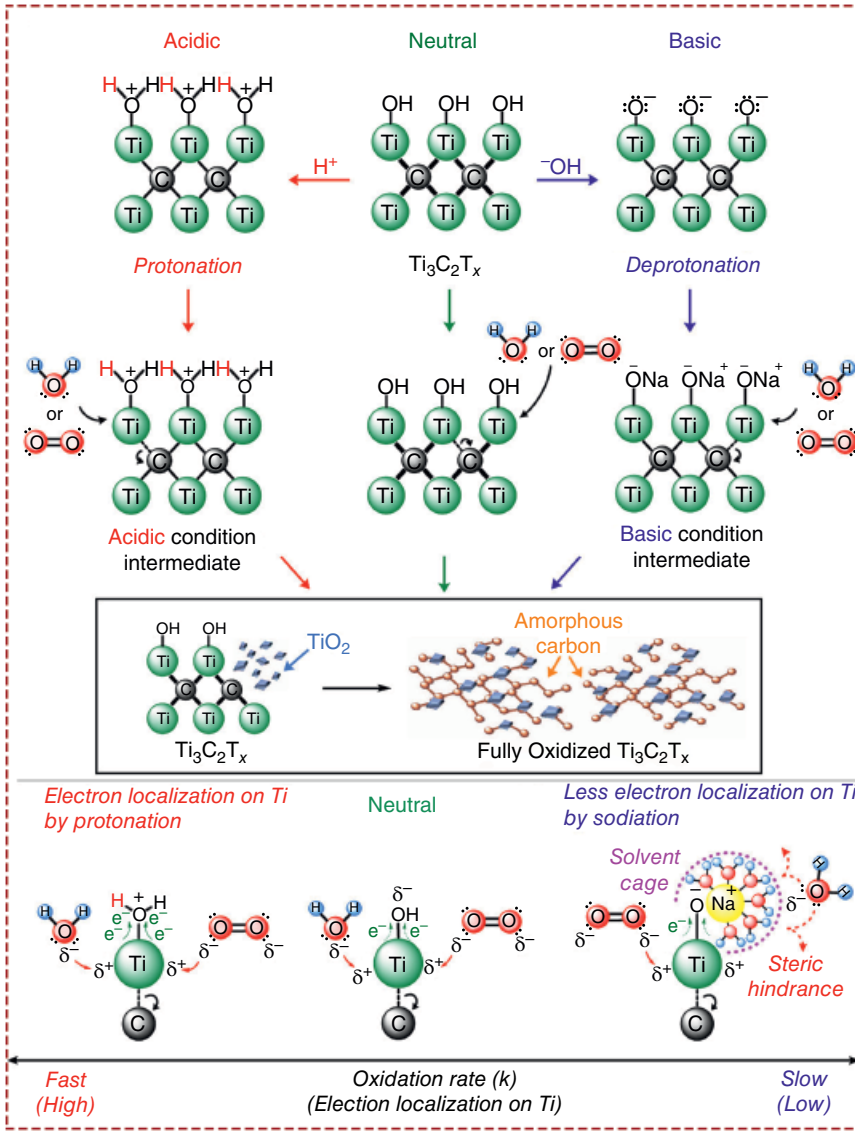


Figure 7.6 (Continued)

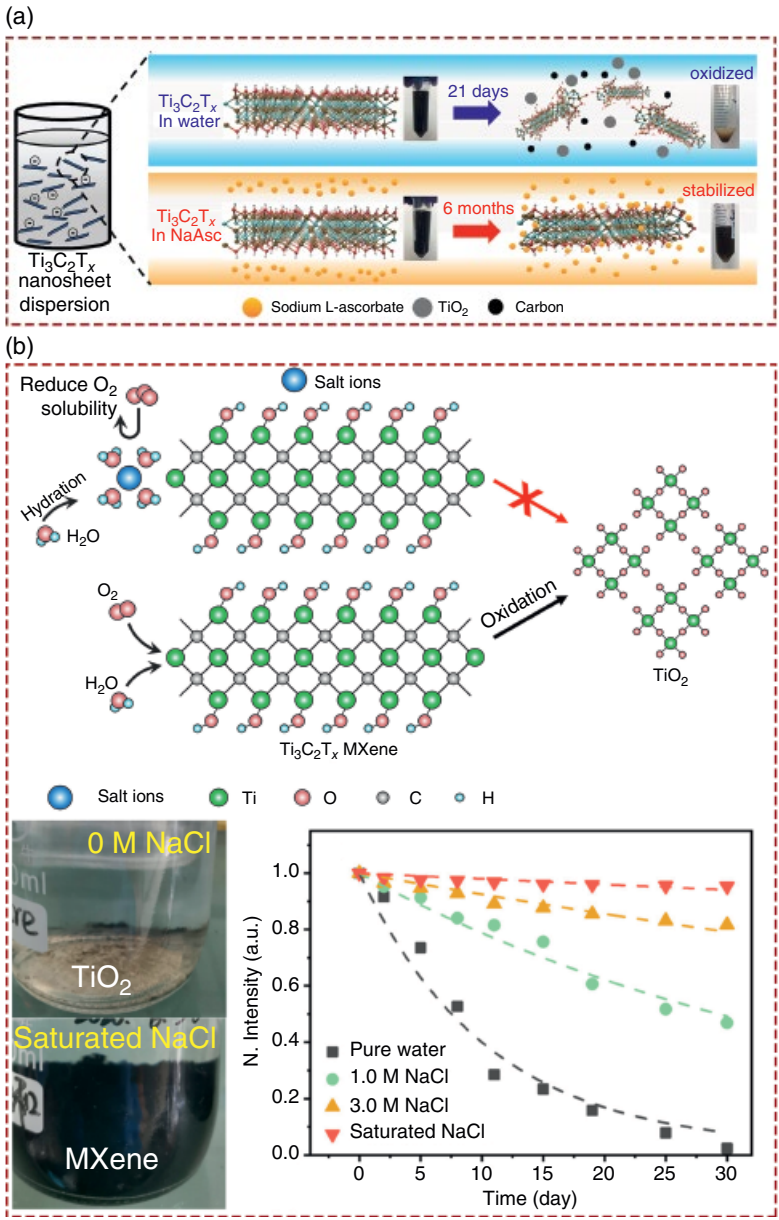


Figure 7.7 (a) Schematics of shelf-stable $Ti_3C_2T_x$ nanosheet dispersion enabled by the antioxidant sodium L-ascorbate; (b) optical photographs and degradation kinetics of $Ti_3C_2T_x$ MXene in NaCl solution measured by UV–vis spectroscopy; (c) schematic and TEM photographs of $Ti_3C_2T_x$ MXene flakes with and without protection by polyanions; (d) schematics of the degradation mechanism of $Ti_3C_2T_x$ MXene in aqueous DES solution [15, 29]. *Source:* (b) Wang et al. [37]/Reproduced from John Wiley & Sons, Inc. (c) Natu et al. [38]/Reproduced from American Chemical Society. (d) Kim et al. [39]/Reproduced from John Wiley & Sons.

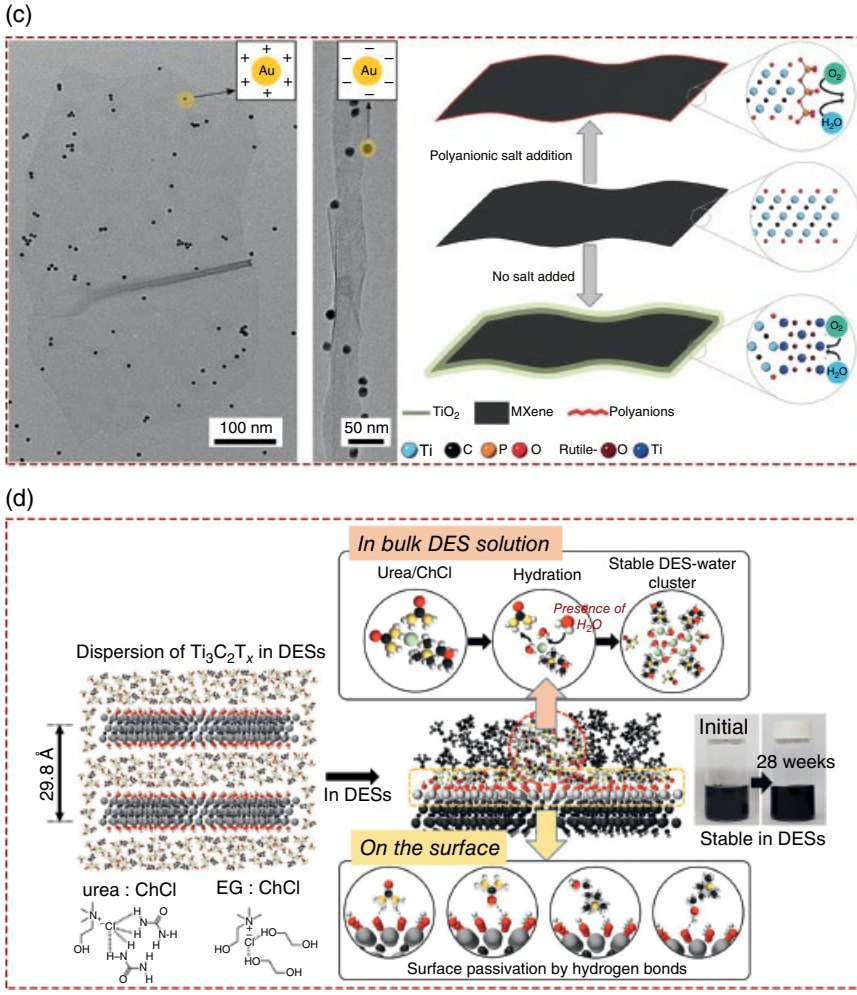


Figure 7.7 (Continued)

important to analyze the role of these polyanions as potent polyelectrolytes capable of reducing the thermodynamic activity of water in MXene colloidal solutions, in addition to the proposed mechanism of their action as capping agents. Kim et al. discovered deep eutectic solvents (DESs) as efficient agents to suppress MXene degradation (Figure 7.7d) [39]. The DES, consisting of choline chloride (ChCl) and urea, can be hydrated in water forming DES-water clusters. The DES used in this study attached to MXene surface *via* hydrogen bonding, thus passivating it and hindering access of oxygen and water to MXene, resulting in suppression of degradation.

The chemical instability of delaminated V_2CT_x MXene in aqueous solutions has been a particular challenge. Researchers explained its high reactivity due to its highly defective nature and large interlayer spacing caused by the intercalation of organic molecules such as TMAOH or TBAOH used for delamination. To address this issue, an ion-exchange protocol was developed to replace the interlayer cations with Li^+. This process not only helps to tune surface chemistry of this MXene, removing the adsorbed ions (TBA^+ or TMA^+) from its surface, but also reduces the interlayer spacing. As a result, the stability of the delaminated V_2CT_x MXene in aqueous solutions has significantly improved from just a few hours to several months [42].

7.3.5 Annealing

Most MXene applications rely on high-performance MXene thin films; nevertheless, MXene flakes are always unstable in the presence of water, and sooner or later they degrade, even if this water is in the form of intercalated water molecules. Thus, the fabrication of MXene films with excellent chemical stability in humid air and at high temperatures is highly desired. The hydrogen/argon-annealing approach considerably increased the oxidation stability of MXene films by (i) forming a dense packing of MXene nanosheets and (ii) increasing the amount of –O-terminations while decreasing the number of –OH and –F terminations [17, 43]. In this case, long-term chemical stability in humid environments and even in aqueous solutions could be achieved for the resulting MXene films.

7.4 MXene Thermal Stability

Understanding MXene thermal stability is crucial for applications in which these materials are used as both solutions and thin films. Depending on the temperature and environment in which MXenes are treated, different levels of modification may occur.

7.4.1 Elimination of MXene Surface Functional Groups

The absorbed water molecules, intercalated species, and terminating functional groups can be desorbed at high temperatures [44–47]. For applications in catalysis, energy storage etc., the surface terminations are often essential for fine-tuning of the MXene properties. The defunctionalization of the MXene surface can also improve its electrical conductivity [13, 48].

Thermal gravimetric analysis with mass spectrometry detection (TGA-MS) is considered as efficient way to investigate surface terminations of MXenes. In a He atmosphere, $Ti_3C_2T_x$ MXene was treated up to 1500 °C. The release of intercalated

H_2O is evidenced by the peak at around 150 °C. The fact that the –OH signal frequently coincides with the H_2O signal suggests that decomposed H_2O mainly contributes to the observed ion current in –OH channel. The loss of –F surface terminations from $Ti_3C_2T_x$, starting at as low as 400 °C, is evidenced by the –F and HF ion currents. Broad peaks in the –F and HF signals centered at 150 °C exactly match the peak in the H_2O channel, proving that these peaks are related to H_2O loss, that is, they originate from residual HF dissolved in intercalated or adsorbed water (Figure 7.8) [7, 8].

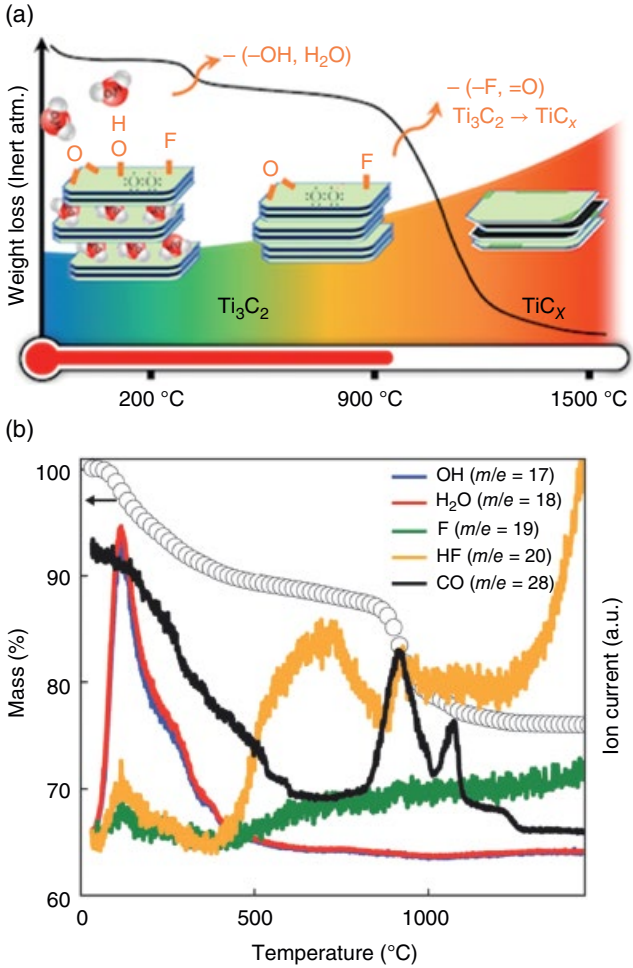


Figure 7.8 (a) Schematic illustration of $Ti_3C_2T_x$ MXene annealed up to 1500 °C in He atmosphere; (b) the corresponding TGA-MS experimental data of $Ti_3C_2T_x$ MXene annealing. *Source:* Seredych et al. [7] and Hart et al. [8].

Li et al. also studied the thermal stability of $Ti_3C_2T_x$ MXene in an Ar atmosphere and investigated the elimination of surface functional groups at various temperatures using TGA and DSC [49]. At the first stage (RT–200 °C), the decrease in mass is mainly caused by the loss of physically adsorbed water on the MXene surface. The second stage (200–800 °C) shows the elimination of –OH from the surface, which can be represented by the equation:

$$Ti_3C_2F_2OH(s) \rightarrow Ti_3C_2F_2O_{0.5}(s) + 0.5H_2O(g) \tag{7.5}$$

The third stage (>800 °C) shows the loss of O and F, which can be represented by the following equation:

$$Ti_3C_2F_2O_{0.5}(s) \rightarrow Ti_3C_2F_2(s) + 0.25O_2(g) \tag{7.6}$$

At these high temperatures, however, MXenes may undergo phase transformations, which are discussed in the following section.

7.4.2 Transformations of MXene Skeleton Structure

The transformation of MXene structure depends on temperature, the atmosphere, and even heating rates. When $Ti_3C_2T_x$ MXene was heated in air, TiO_2-C hybrid structures were produced [50]. The *in-situ* TEM analysis was used to study the transformation of $Ti_3C_2T_x$ at different heating rates [51]. Flash oxidation was performed by gradually increasing the temperature to 950 °C and holding for 1 minute (Figure 7.9a–c). This led to preferential oxidation of Ti surface layers, resulting in quick formation of TiO_2 with much less oxidation of inner layers of carbon atoms (Figure 7.9a1, b1). The complete transformation of MXene flakes finally resulted in the formation of anatase nanoparticles on carbon sheets (Figure 7.9c1), which was confirmed by Raman spectrum (Figure 7.9e). Slow oxidation was performed by heating MXene sheets up to 450 °C at a rate of 0.1 °C s^{-1} and holding for 2 hours (Figure 7.9a, d). In contrast to flash heating, O_2 concentration around MXene was in equilibrium with the solid at all times during the slow oxidation process, producing directly thin sheets of (mainly) rutile on the carbon sheet (Figure 7.9a1, d1, f). Furthermore, the ReaxFF-based molecular dynamics (MD) simulations also provide evidence for the formation of carbon-supported nanotitania structures through an increase in the average bond orders of C—C and Ti—O, and a decrease in the average bond orders of Ti—C. The transformation rate can be controlled by adjusting the oxidation atmosphere, with the strong oxidant H_2O_2 exhibiting the fastest transformation rate, followed by wet air and dry air [53]. When HF etched $Ti_3C_2T_x$ MXene was heated in O_2 atmosphere, anatase nano-crystals were primarily formed on MXene nanostructures at low temperatures (~200 °C), followed by the transformation of anatase to rutile during a

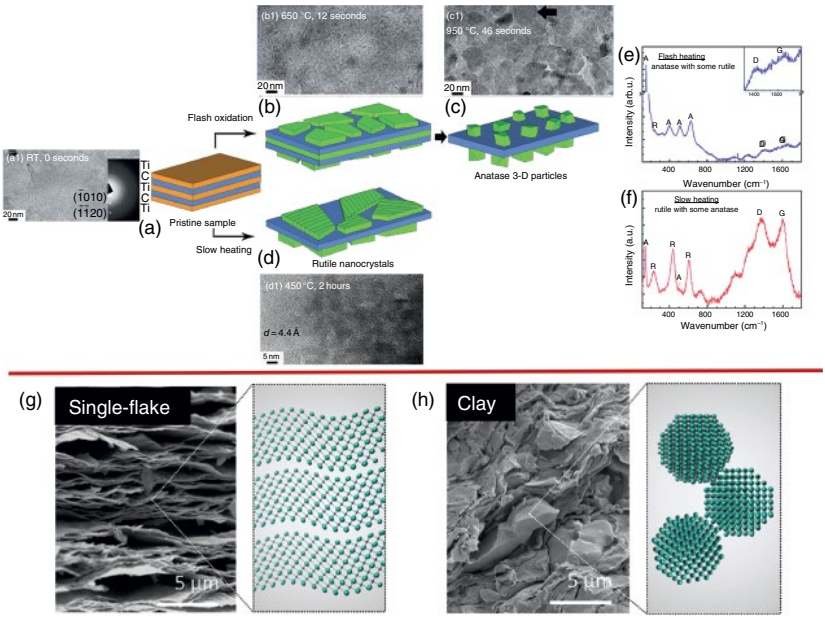


Figure 7.9 Top row: Schematic illustrations and TEM images of $Ti_3C_2T_x$ thermally treated at different heating rates: (a, a1) pristine MXene, (b, b1) and (c, c1) same MXene after the flash oxidation treatment (gradually increasing the temperature to 950 °C and holding for 1 minute), and (d, d1) after the slow oxidation treatment (increasing the temperature to 450 °C at a rate of 0.1 °C s^{-1} and holding for 2 hours). Raman spectra of the final products of (e) flash oxidation and (f) slow oxidation treatments. Bottom row: Cross-section SEM images of (g) single-flake and (h) clay $Ti_3C_2T_x$ MXene films after annealing at 1000 °C for 2 hours under Ar. *Source:* (a) Ghassemi et al. [51]/Reproduced from Royal Society of Chemistry. (b) Wyatt et al. [52]/Reproduced from IOP Publishing Ltd.

high-temperature process (1000 °C) [49]. The transformation of $Ti_3C_2T_x$ MXene was also investigated when heated in an inert (Ar) atmosphere and was found to be much slower than in other environments. The resulting structure was also observed to depend on the initial morphology of the MXene films, whether made from MXene single flakes or MXene clay. The analysis revealed that MXene could maintain its 2D layered structure up to 600 °C under Ar atmosphere, beyond which it transformed to form stable 3D crystalline Ti_2C and TiC_y phases up to annealing temperatures of 1000 °C in both single-flake films and multilayer clay films of $Ti_3C_2T_x$ MXene. Interestingly, annealing delaminated $Ti_3C_2T_x$ single-flake films resulted in TiC_y grains with a preferred orientation and lamellar grains; however, annealing multilayer clay $Ti_3C_2T_x$ films produced 3D crystals with no preferred orientation (Figure 7.9g, h) [52].

Therefore, by adjusting initial morphology, atmosphere, oxidation temperature, and heating rate, it may be possible to obtain the required phase composition and structure of MXenes for the desired applications. Moreover, when NH_4HF_2 was applied as the etchant, the resulting $Ti_3C_2T_x$ showed a better thermal stability and higher transformation temperature in air (above 500 °C), while less than 350 °C was enough to initiate thermal transformation of HF-etched MXene. This could be due to the plentiful NH_4^+ adsorbed onto MXene surface in the NH_4HF_2 etched MXene, which prevents and hinders the interaction between O_2 and the MXene, slowing down its oxidation [54].

Despite the fact that MXenes show many promising applications, their thermal stability is sensitive to the atmosphere, presence of humidity, and structural defects. Classical MD simulations show that the estimated onset temperatures of thermal degradation for bare Ti_2C, Ti_3C_2, and Ti_4C_3 MXenes are 1050, 1500, and 1700 K, respectively [55]. Eliminating the influence of the environment and surface functional groups is also crucial for increasing the thermal stability of MXenes. As an example, Xiao et al. reported a high O2 adsorption material, extracted bentonite (EB), which, when added to MXene, has dramatically improved the thermal stability of $Ti_3C_2T_x$/EB composite in air even at temperatures higher than 400 °C [56].

7.5 Conclusions and Outlook

In this chapter, chemical and thermal stability of MXenes and their underlying mechanisms have been discussed. The chemical stability of MXenes is largely dependent on their structure, chemical composition, and storage environment. Different strategies for suppressing the degradation of MXenes have been classified and analyzed based on the above mentioned factors, including optimizing MAX phase synthesis, investigating the role of different etchants, optimizing the

storage environment, introducing additives for further protection of MXenes, as well as applying thermal annealing treatments. The thermal stability of MXenes is strongly influenced by the environment, heating rate, and their chemical composition. The absorbed water, intercalated species, and terminating functional groups will desorb/detach during heating at high temperatures, resulting in an increased concentration of defects, which may lead to a faster degradation for MXenes.

Understanding the stability of MXenes is of critical importance for their synthesis and robust performance in various applications. Experimental and theoretical studies (similar to [57] but in more realistic storage conditions where no electric potential is applied to MXene and the amount of water accessible for reaction is much larger) of chemical as well as thermal stability of MXenes should be conducted in parallel and in greater detail, involving novel varieties of MXenes with different transition metals or variations of the structure of atomic layers, as well as terminated by different functional groups.

References

1 Naguib, M., Mochalin, V.N., Barsoum, M.W., and Gogotsi, Y. (2014). 25th anniversary article: MXenes: a new family of two-dimensional materials. *Advanced Materials* 26: 992–1005.

2 Alhabeb, M., Maleski, K., Anasori, B. et al. (2017). Guidelines for synthesis and processing of two-dimensional titanium carbide ($Ti_3C_2T_x$ MXene). *Chemistry of Materials* 29: 7633–7644.

3 Natu, V., Pai, R., Sokol, M. et al. (2020). 2D $Ti_3C_2T_z$ MXene synthesized by water-free etching of Ti_3AlC_2 in polar organic solvents. *Chem* 6: 616–630.

4 Rina Ibragimova, P.E., Rinke, P., and Koms, H.-P. (2021). Surface functionalization of 2D MXenes: trends in distribution, composition, and electronic properties. *Journal of Physical Chemistry Letters* 12: 2377–2384.

5 Halim, J., Cook, K.M., Naguib, M. et al. (2016). X-ray photoelectron spectroscopy of select multi-layered transition metal carbides (MXenes). *Applied Surface Science* 362: 406–417.

6 Hope, M.A., Forse, A.C., Griffith, K.J. et al. (2016). NMR reveals the surface functionalization of Ti_3C_2 MXene. *Physical Chemistry Chemical Physics* 18: 5099–5102.

7 Seredych, M., Shuck, C., Pinto, D. et al. (2019). High-temperature behavior and surface chemistry of carbide MXenes studied by thermal analysis. *Chemistry of Materials* 31: 3324–3332.

8 Hart, J.L., Hantanasirisakul, K., Lang, A.C. et al. (2019). Control of MXenes' electronic properties through termination and intercalation. *Nature Communications* 10: 1–10.

9 Kamysbayev, V., Filatov, A.S., Hu, H. et al. (2020). Covalent surface modifications and superconductivity of two-dimensional metal carbide MXenes. *Science* 369: 979–983.

10 Chen, C., Boota, M., Urbankowski, P. et al. (2018). Effect of glycine functionalization of 2D titanium carbide (MXene) on charge storage. *Journal of Materials Chemistry A* 6: 4617–4622.

11 Anayee, M., Kurra, N., Alhabeb, M. et al. (2020). Role of acid mixtures etching on the surface chemistry and sodium ion storage in $Ti_3C_2T_x$ MXene. *Chemical Communications* 56: 6090–6093.

12 Pazniak, H., Benchakar, M., Bilyk, T. et al. (2021). Ion implantation as an approach for structural modifications and functionalization of $Ti_3C_2T_x$ MXenes. *ACS Nano* 15: 4245–4255.

13 Lipatov, A., Alhabeb, M., Lukatskaya, M.R. et al. (2016). Effect of synthesis on quality, electronic properties and environmental stability of individual monolayer Ti_3C_2 MXene flakes. *Advanced Electronic Materials* 2: 1600255.

14 Zhang, C., Pinilla, S., McEvoy, N. et al. (2017). Oxidation stability of colloidal 2D titanium carbides (MXenes). *Chemistry of Materials* 29: 4848–4856.

15 Natu, V., Hart, J.L., Sokol, M. et al. (2019). Edge capping of 2D-MXene sheets with polyanionic salts to mitigate oxidation in aqueous colloidal suspensions. *Angewandte Chemie, International Edition* 58: 12655–12660.

16 Mathis, T.S., Maleski, K., Goad, A. et al. (2021). Modified MAX phase synthesis for environmentally stable and highly conductive Ti_3C_2 MXene. *ACS Nano* 15: 6420–6429.

17 Zhao, X., Holta, D.E., Tan, Z. et al. (2020). Annealed $Ti_3C_2T_z$ MXene films for oxidation-resistant functional coatings. *ACS Applied Nano Materials* 3: 10578–10585.

18 Shuck, C.E., Han, M., Maleski, K. et al. (2019). Effect of Ti_3AlC_2 MAX phase on structure and properties of resultant $Ti_3C_2T_x$ MXene. *ACS Applied Nano Materials* 2: 3368–3376.

19 Shekhirev, M., Busa, J., Shuck, C.E. et al. (2022). Ultralarge flakes of $Ti_3C_2T_x$ MXene via soft delamination. *ACS Nano* 16: 13695–13703.

20 Huang, S. and Mochalin, V.N. (2020). Understanding chemistry of two-dimensional transition metal carbides and carbonitrides (MXenes) with gas analysis. *ACS Nano* 14: 10251–10257.

21 Ghidiu, M., Lukatskaya, M.R., Zhao, M.Q. et al. (2014). Conductive two-dimensional titanium carbide 'clay' with high volumetric capacitance. *Nature* 516: 78–81.

22 Li, G., Jiang, K., Zaman, S. et al. (2019). Ti_3C_2 sheets with an adjustable surface and feature sizes to regulate the chemical stability. *Inorganic Chemistry* 58: 9397–9403.

23 Shi, H., Zhang, P., Liu, Z. et al. (2021). Ambient-stable two-dimensional titanium carbide (MXene) enabled by iodine etching. *Angewandte Chemie, International Edition* 60: 8689–8693.

24 Huang, S. and Mochalin, V.N. (2019). Hydrolysis of 2D transition-metal carbides (MXenes) in colloidal solutions. *Inorganic Chemistry* 58: 1958–1966.

25 Chae, Y., Kim, S.J., Cho, S.-Y. et al. (2019). An investigation into the factors governing the oxidation of two-dimensional Ti_3C_2 MXene. *Nanoscale* 11: 8387–8393.

26 Zhang, J., Kong, N., Hegh, D. et al. (2020). Freezing titanium carbide aqueous dispersions for ultra-long-term storage. *ACS Applied Materials & Interfaces* 12: 34032–34040.

27 Maleski, K., Mochalin, V.N., and Gogotsi, Y. (2017). Dispersions of two-dimensional titanium carbide MXene in organic solvents. *Chemistry of Materials* 29: 1632–1640.

28 Mashtalir, O., Cook, K.M., Mochalin, V.N. et al. (2014). Dye adsorption and decomposition on two-dimensional titanium carbide in aqueous media. *Journal of Materials Chemistry A* 2: 14334–14338.

29 Zhao, X., Vashisth, A., Prehn, E. et al. (2019). Antioxidants unlock shelf-stable $Ti_3C_2T_x$ (MXene) nanosheet dispersions. *Matter* 1: 513–526.

30 Sneed, M.C. (1953). *Comprehensive Inorganic Chemistry*, vol. 7. New York: Van Nostrand.

31 Remy, H. (1956). *Treatise on Inorganic Chemistry*, 11e, vol. 1. Amsterdam: Elsevier.

32 Avgustinik, A.I., Drozdetskaya, G.V., and Ordan'yan, S.S. (1967). Reaction of titanium carbide with water. *Soviet Powder Metallurgy and Metal Ceramics* 6: 470–473.

33 G.N.H. (1896). Metallic carbides. *Nature* 54: 357–357.

34 Zhao, X., Vashisth, A., Blivin, J.W. et al. (2020). pH, nanosheet concentration, and antioxidant affect the oxidation of $Ti_3C_2T_x$ and Ti_2CT_x MXene dispersions. *Advanced Materials Interfaces* 7: 2000845.

35 Doo, S., Chae, A., Kim, D. et al. (2021). Mechanism and kinetics of oxidation reaction of aqueous $Ti_3C_2T_x$ suspensions at different pHs and temperatures. *ACS Applied Materials & Interfaces* 13: 22855–22865.

36 Huang, S. and Mochalin, V.N. (2022). Combination of high pH and an antioxidant improves chemical stability of two-dimensional transition-metal carbides and carbonitrides (MXenes) in aqueous colloidal solutions. *Inorganic Chemistry* 61: 9877–9887.

37 Wang, X., Wang, Z., and Qiu, J. (2021). Stabilizing the MXene by hydration chemistry in aqueous solution. *Angewandte Chemie, International Edition* 60: 26587–26591.

38 Natu, V., Sokol, M., Verger, L., and Barsoum, M.W. (2018). Effect of edge charges on stability and aggregation of $Ti_3C_2T_z$ MXene colloidal suspensions. *Journal of Physical Chemistry C* 122: 27745–27753.

39 Kim, J., Yoon, Y., Kim, S.K. et al. (2021). Chemically stabilized and functionalized 2D-MXene with deep eutectic solvents as versatile dispersion medium. *Advanced Functional Materials* 31: 2008722.

40 Xia, F., Lao, J., Yu, R. et al. (2019). Ambient oxidation of Ti_3C_2 MXene initialized by atomic defects. *Nanoscale* 11: 23330–23337.

41 Huang, S., Natu, V., Tao, J. et al. (2022). Understanding the effect of sodium polyphosphate on improving the chemical stability of $Ti_3C_2T_z$ MXene in water. *Journal of Materials Chemistry A* 10: 22016–22024.

42 Matthews, K., Zhang, T., Shuck, C.E. et al. (2022). Guidelines for synthesis and processing of chemically stable two-dimensional V_2CT_x MXene. *Chemistry of Materials* 34: 499–509.

43 Lee, Y., Kim, S.J., Kim, Y.-J. et al. (2020). Oxidation-resistant titanium carbide MXene films. *Journal of Materials Chemistry A* 8: 573–581.

44 Wang, K., Zhou, Y., Xu, W. et al. (2016). Fabrication and thermal stability of two-dimensional carbide Ti_3C_2 nanosheets. *Ceramics International* 42: 8419–8424.

45 Li, J., Du, Y., Huo, C. et al. (2015). Thermal stability of two-dimensional Ti_2C nanosheets. *Ceramics International* 41: 2631–2635.

46 Hu, S., Li, S., Xu, W. et al. (2019). Rapid preparation, thermal stability and electromagnetic interference shielding properties of two-dimensional Ti_3C_2 MXene. *Ceramics International* 45: 19902–19909.

47 Persson, I., Näslund, L.-Å., Halim, J. et al. (2018). On the organization and thermal behavior of functional groups on Ti_3C_2 MXene surfaces in vacuum. *2D Materials* 5: 015002.

48 Zhang, C., Ma, Y., Zhang, X. et al. (2020). Two-dimensional transition metal carbides and nitrides (MXenes): synthesis, properties, and electrochemical energy storage applications. *Energy and Environmental Materials* 3: 29–55.

49 Li, Z., Wang, L., Sun, D. et al. (2015). Synthesis and thermal stability of two-dimensional carbide MXene Ti_3C_2. *Materials Science and Engineering B* 191: 33–40.

50 Naguib, M., Mashtalir, O., Lukatskaya, M.R. et al. (2014). One-step synthesis of nanocrystalline transition metal oxides on thin sheets of disordered graphitic carbon by oxidation of MXenes. *Chemical Communications* 50: 7420–7423.

51 Ghassemi, H., Harlow, W., Mashtalir, O. et al. (2014). In situ environmental transmission electron microscopy study of oxidation of two-dimensional Ti_3C_2 and formation of carbon-supported TiO_2. *Journal of Materials Chemistry A* 2: 14339–14343.

52 Wyatt, B.C., Nemani, S.K., Desai, K. et al. (2021). High-temperature stability and phase transformations of titanium carbide ($Ti_3C_2T_x$) MXene. *Journal of Physics. Condensed Matter* 33: 224002.

53 Lotfi, R., Naguib, M., Yilmaz, D.E. et al. (2018). A comparative study on the oxidation of two-dimensional Ti_3C_2 MXene structures in different environments. *Journal of Materials Chemistry A* 6: 12733–12743.

54 Feng, A., Yu, Y., Jiang, F. et al. (2017). Fabrication and thermal stability of NH_4HF_2-etched Ti_3C_2 MXene. *Ceramics International* 43: 6322–6328.

55 Borysiuk, V. and Mochalin, V.N. (2019). Thermal stability of two-dimensional titanium carbides $Ti_{n+1}C_n$ (MXenes) from classical molecular dynamics simulations. *MRS Communications* 9: 203–208.

56 Liu, N., Li, Q., Wan, H. et al. (2022). High-temperature stability in air of $Ti_3C_2T_x$ MXene-based composite with extracted bentonite. *Nature Communications* 13: 1–10.

57 Wu, T., Kent, P.R., Gogotsi, Y., and Jiang, D.-E. (2022). How water attacks MXene. *Chemistry of Materials* 34: 4975–4982.

8

Guidelines on MXene Handling and Storage Strategies

Jizhen Zhang[1,2], Dylan Hegh[1], Peter A. Lynch[1,2], and Joselito M. Razal[1]

[1] *Institute for Frontier Materials, Deakin University, Geelong, Victoria, Australia*
[2] *Manufacturing BU, Commonwealth Scientific and Industrial Research Organisation (CSIRO), Waurn Ponds, Geelong, Victoria, Australia*

8.1 Introduction

MXenes, an emerging family of 2D transition metal carbides and nitrides, have shown promise in various applications, such as energy storage, electromagnetic interference shielding, conductive thin films, photonics, and photothermal therapy [1]. In general, MXenes are obtained from atomically laminated parent MAX phases, typically described by the formula $M_{n+1}AX_n$ ($n = 1 - 4$). The MAX structure consists of transition metal layers (M) that interleave carbon and/or nitrogen layers (X). The strongly bonded MX domains are further separated by an atomically thin layer consisting of a group 13 or 14 element (A). MXenes are typically produced from MAX phases by chemical etching of the weakly bonded A layers with fluorinated acids. During etching, the highly reactive transition metal surfaces are instantly terminated by species (T_x) originating from the etchant resulting in the general MXene formula $M_{n+1}X_nT_x$. Varying M and/or X elements, or alloying these species, has been extensively demonstrated [2] and more than 30 MXenes have been realized [1]. The metallic nature, wide range of optical absorption, and tunable surface chemistry of MXenes are the key to their success in those applications. However, maintaining the quality and integrity of MXene structures remains one of the greatest challenges preventing the widespread adoption of MXenes in applications, especially since the development of scalable production and practical application of MXenes [3, 4].

Transition Metal Carbides and Nitrides (MXenes) Handbook: Synthesis, Processing, Properties and Applications, First Edition. Edited by Chuanfang Zhang and Michael Naguib.
© 2024 John Wiley & Sons, Inc. Published 2024 by John Wiley & Sons, Inc.

Specifically, the issue for MXenes is the liberal presence of active terminals and/or structural defects, inducing spontaneous degradation [5], which reduces the electrical conductivity and passivates of the reactive interface. MXene degradation is pervasive, occurring in both aqueous dispersion and solid state, such as powder, film, and aerogels [6–9]. As a consequence, the MXene degrades and turns into metal oxide or a hybrid of metal oxides incorporating various X elements depending on the conditions. *In-situ* transmission electron microscopy (TEM) analysis and Raman spectroscopy revealed that the oxidation of the most common $Ti_3C_2T_x$ MXene results in the formation of TiO_2 [6]. While Naguib and co-workers found that heating $Ti_3C_2T_x$ MXene in air induced its degradation into disordered graphitic carbon whose edge was decorated with TiO_2 nanoparticles [7]. A $Ti_3C_2T_x$ MXene-TiO_2 nanosheet hybrid can also be prepared by a hydrothermal method [10]. Although the formation of metal oxides endows this hybrid material with high catalytic efficiency, the original crystal structures changed resulting in a significant drop in electrochemical properties [11]. Therefore, maintaining the integrity of MXene is a critical requirement for applications that demand aqueous MXene dispersions, such as the production of films [12], fibers [13], hydrogel/aerogels [14, 15], and aqueous-based supercapacitors [16].

In this chapter, discussion of the characterization methods for MXene degradation is presented to demonstrate the methods that recognize and monitor the extent of MXene degradation. Most importantly, a summary of different methods to prevent the degradation of MXenes is expected to provide a guideline for storing MXene-based products. The outlook section also points out a few of the most pressing research questions that have not been fully addressed and the proposed strategies for developing environmentally stable MXenes.

8.2 The Degradation of MXene

MXene oxidation is the general and widely used description for the degradation process of MXenes; however, the oxidation is only part of the degradation process, which not only includes the metallic elements oxidizing and other elements reacting with environmental components, such as water and oxygen, but also includes structural deformation of the layers. For the most widely used titanium-based MXenes, oxidation typically results in flake edge or surface TiO_2 formation, as shown in Figure 8.1a. The oxidation occurring at the MXene edge MXenes can also be regarded as the start of the degradation process of the MXenes. The primary disadvantage of MXene oxidation is the resulting irreversible loss of excellent electrical conductivity and energy storage performance. For instance, the TiO_2–Ti_3C_2 composites exhibited a decreased specific capacitance of $143\,F\,g^{-1}$ at $5\,mV\,s^{-1}$, much lower than that of fresh MXene ($>400\,F\,g^{-1}$) [16]. However, new

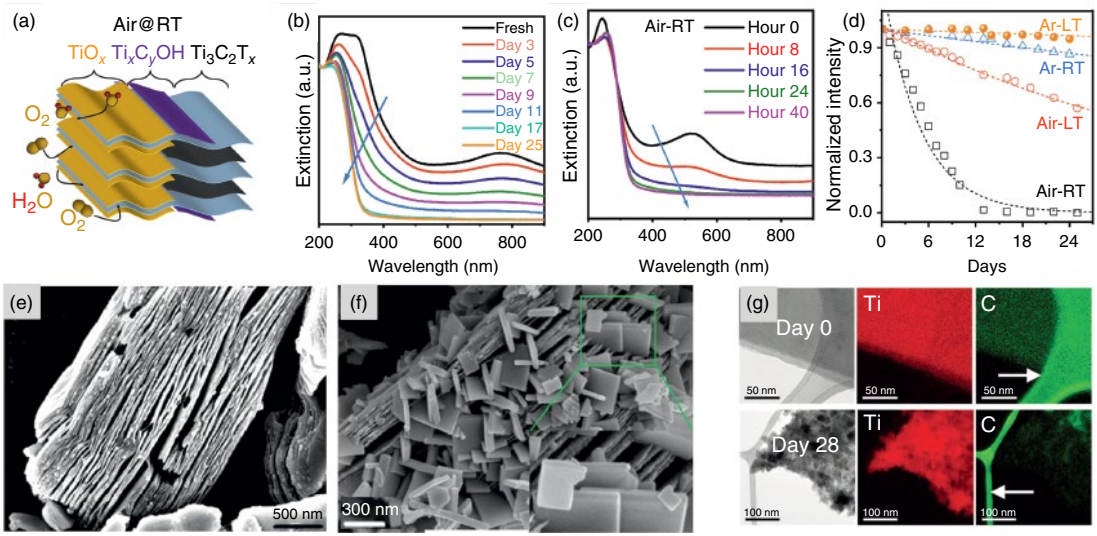


Figure 8.1 (a) The oxidation of aqueous $Ti_3C_2T_x$ MXene exposed to air at room temperature (Air@RT). Normalized UV–Vis extinction spectra of aqueous dispersions of (b) $Ti_3C_2T_x$ and (c) Ti_2CT_x MXene stored in Air@RT. (d) Normalized intact $Ti_3C_2T_x$ MXene sheets in aqueous solution as a function of storage time. *Source:* Adapted from Zhang et al. [8]. (e) SEM of as-synthesized multilayer $Ti_3C_2T_x$ MXene and (f) hybrid (001)TiO_2/$Ti_3C_2T_x$ hydrothermally incubated at 160 °C for 12 hours. The inset shows the enlarged HRSEM image of the TiO_2–Ti_3C_2 heterojunctions in the area highlighted by the green square, and a schematic diagram of an anatase TiO_2 crystal exposing (001) and (101) facets. *Source:* Zhang et al. [13]/Reproduced from American Chemical Society. (g) The TEM and energy-filtered TEM (EFTEM) image of the selected area of fresh few layer MXene (top) and oxidized MXene (day 28) in water (bottom). *Source:* Seyedin et al. [17]/Reproduced from John Wiley & Sons, Inc./CC BY 4.0.

properties may be introduced due to the presence of metal oxides which may be exploited for alternative applications. For example, the formation of TiO_2 nanoparticles on $Ti_3C_2T_x$ flakes facilitated dye adsorption and decomposition [18], while the partially oxidized flakes also demonstrated enhanced photocatalytic CO_2 reduction activity [19]. It should be noted, however, that the oxidation process does not stop at the metal oxide-hybrid stage; instead, the complex will eventually become fully oxidized with the flake structure degrading down to pure metal oxides [20]. Regarding the oxidation process, since 2014 [6] researchers have dedicated particular efforts in elucidating the mechanism of how MXene converts to metallic oxides, the production of side products, and the impact of various factors influencing these processes. The significant progress achieved to date is of great importance in identifying the impact of environmental parameters toward developing standard methods to handle MXenes to support their increasing use in scientific endeavors and eventual commercial applications.

8.2.1 Understanding the Degradation Process of MXenes

8.2.1.1 The Degradation of Wet MXene

Although the first description of MXene oxidation was presented as early as 2014, which investigated flash heating on $Ti_3C_2T_x$ using *in-situ* TEM techniques [6], the first systematic study on MXene oxidation was not carried out until 2017. Professor Gogotsi and his team quantified the degradation process of $Ti_3C_2T_x$ MXenes in aqueous conditions using UV–Vis spectroscopy, as increasing oxidation was tightly correlated with decreases in the extinction coefficient [8]. The extinction spectra and the normalized spectra (to the local minima) are shown in Figure 8.1b, c, with the intensity 785 nm (λ_{max}) chosen as the metric for MXene, and the normalized intensity plotted as a function of time (Figure 8.1d). In this work, aqueous dark green MXene in open vials degraded by 42%, 85%, and 100% after 5, 10, and 15 days, respectively, eventually forming a cloudy-white colloidal solution containing primarily anatase (TiO_2) [8]. Under varying conditions, such as temperature [20], MXene concentration [21], and MXene type [22], the time to reach 100% oxidation varied significantly, which will be discussed in later sections.

In general, spontaneous oxidation of MXene primarily results in anatase TiO_2 with poor catalytic activity. By modifying the oxidation conditions, controlled TiO_2 structures can be achieved. For example, Peng et al. [10] employed a hydrothermal technique at 160 °C to synthesize a TiO_2-MXene nanosheet hybrid, selectively exposing (001) facets and 2D Ti_3C_2 MXene ($(001)TiO_2/Ti_3C_2$), as shown in Figure 8.1e, f. The hydrothermal method involved fast treatment of the MXene dispersion at high temperature, leading to quick formation of TiO_2 on MXene surface while maintaining the underlying structure, particularly the embedded

carbon layer. Recently, a hydrothermal method has been widely used to modify MXenes to synthesize nanobipyramid Ti_3C_2 [23], nanocomposite decorated MXenes [24, 25], and increase the yield of MXene by assisting the interaction of ions [26]. Nevertheless, the fast hydrothermal process could result in the oxidation of metal layers, but the carbon layers could survive. Additionally, the study of high-resolution electron energy loss spectroscopy (HREELS) has found that bulk Ti_3C_2 is capable of dissociating water molecules into H_2 [27]. Therefore, without considering the influence of air, the proposed reaction in water can be regarded as follows [28, 29]:

$$Ti_3C_2T_x + H_2O \rightarrow TiO_2 + C + H_2 \tag{8.1}$$

Crucially, energy-filtered TEM (EFTEM) of fully oxidized MXene (day 28 in the atmosphere) showed that the carbon layer was dispersed after oxidation was complete (Figure 8.1g) [17]. This result confirmed that the final solid oxidation products were pure metal oxides. However, a new question arose – what happens to the carbon elements? In a study of carbon and TiO_2 composites, adsorption of the oxidizing precursor on the carbon surface, followed by a photon-stimulated reaction (induced by TiO_2) resulted in the production of volatile C-containing products [30]. Therefore, it was proposed that the C lattice reacted with O_2 and water through the presence of catalytic TiO_2 particles, finally decomposing into CO or CO_2.

To further understand the reaction mechanism and the resultant products of the MXene oxidation process with respect to the slow oxidation at room temperature, researchers studied the changes in properties of the MXene dispersions as a function of storage time. For example, Huang et al. [22] summarized the changes of pH values of aqueous Ti_2C, Ti_3C_2, Ti_3CN, and Nb_2C MXenes, as shown in Figure 8.2a. All MXenes experienced various drops in pH, especially Ti_2C, the most unstable MXene known, while Ti_3CN showed an initial decline followed by an increase in pH after 20 hours. Such changes in pH suggest some acidic products were dissolved in water. In a succeeding study, Zhao et al. [21] adjusted the pH of a Ti_3C_2 MXene dispersion and found that the pH decrease was more significant under basic conditions. Unsurprisingly, these conditions were correlated with more rapid oxidation than acidic ones, which held for other Ti-based MXenes such as Ti_2CT_x. For acidic systems, it was observed that the added protons interact with water molecules to form H_3O^+. The mutual repulsion arising from the positive charges of this species and MXene results in minimal oxidation, while OH^- readily interacts with the cationic nanosheets. However, this study did not elucidate the mechanism causing the pH drop during oxidation. Two hypotheses have been proposed to explain this phenomenon either (i) attributed to dissolved

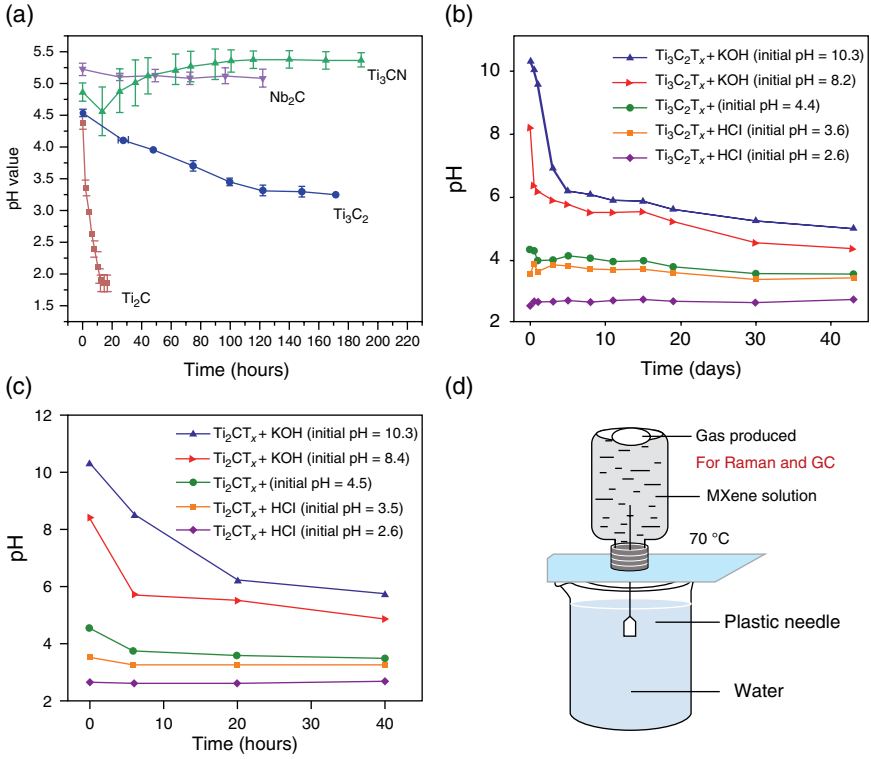


Figure 8.2 (a) Average pH values of colloidal aqueous solutions of Ti_2C, Ti_3C_2, Ti_3CN, and Nb_2C MXenes incubated at 70 °C. Error bars indicate standard deviations in time and pH values. The change in pH of (b) $Ti_3C_2T_x$ and (c) Ti_2CT_x MXene aqueous dispersions with different initial pH. (d) The experimental set-up used to collect the gas products during MXene oxidization. (e) GC analysis of gaseous products of Ti_2C, Ti_3C_2, Ti_3CN, and Nb_2C MXene oxidized in water and standard H_2, CO, CO_2, and CH_4 gases. (f) Raman spectra of gas bubbles collected and analyzed in sealed vials in the course of Ti_2C, Ti_3C_2, Ti_3CN, and Nb_2C MXene oxidized in water. (a and d-f) Copyright © 2020 American Chemical Society. (b and c) Copyright © 2020 Wiley-VCH GmbH & Co. *Source:* (a, d, f, e) Zhao [21]/John Wiley & Sons. (b, c) Huang et al. [22]/John Wiley & Sons.

CO_2, or (ii) release of the intercalated acidic species (HF or HCl) upon structural degradation of MXene. Considering the role of oxygen in the oxidation process [21], the reaction of MXene oxidation in water was revised to follow [31]:

$$Ti_3C_2T_x + H_2O + O_2 \rightarrow TiO_2 + CO + CO_2 + CH_4 + H_2 \quad (8.2)$$

To confirm this mechanism, Huang et al. [22] designed a set-up to collect the gas products during such oxidation (Figure 8.2d). Figure 8.2e shows chromatograms of the corresponding gas phases with different MXenes, as well as pure

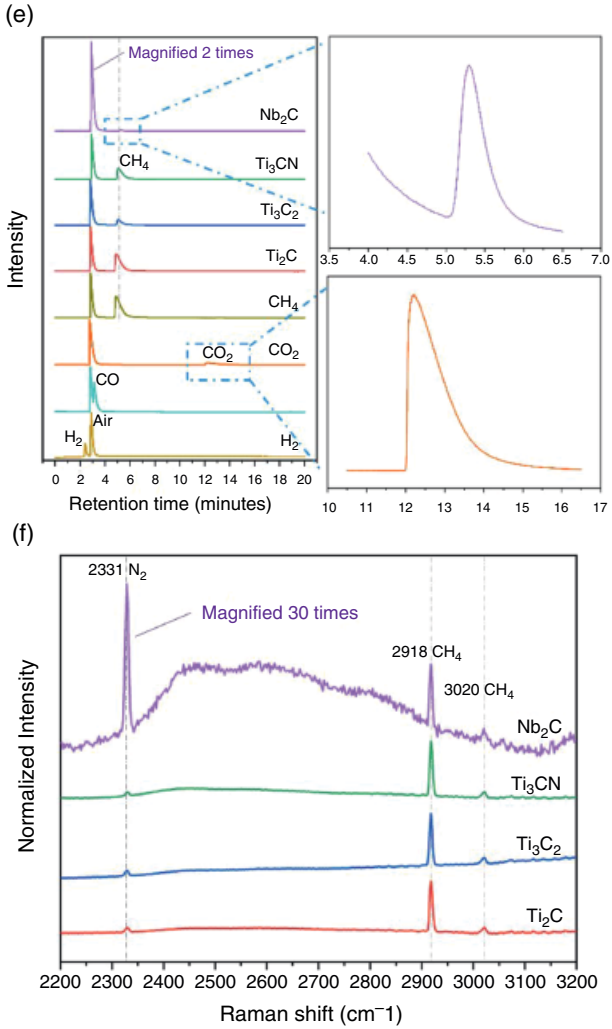


Figure 8.2 (Continued)

H_2, CO, CO_2, and CH_4 gases used as references. Comparison of the retention times allowed for unambiguous identification of CH_4 as the main gaseous product of all four aqueous MXenes studied and strongly suggested it as the main product of all carbide and carbonitride MXene structures in water. To confirm these observations, Raman spectra of the gas phase bubbles produced were recorded. In contrast to the previous hypothesis, no traces of CO and CO_2 were observed despite recognizable peaks of CH_4 (Figure 8.2f). Specifically, it should be mentioned that

the experimental design has some drawbacks (Figure 8.2d) like the significant amounts of water the MXene dispersion was exposed to, causing exchange. Additionally, such a gas collector can effectively collect species with low aqueous solubility but may be inaccurate for gasses such as CO_2, which is >65 times more soluble than CH_4 at room temperature.

In another study, Low et al. [19] demonstrated that a TiO_2/Ti_3C_2 composite exhibited 3.7× performance in CH_4 production ($0.22\,\mu mol\,h^{-1}$) from photocatalytic CO_2 reduction compared to commercial TiO_2 (P25). The detailed photocatalytic CO_2 reduction mechanism using TiO_2/Ti_3C_2 was confirmed through $^{13}CO_2$ isotopic tests and *in-situ* diffuse reflectance infrared Fourier transform spectroscopy. This result implies that the production of CH_4 occurred during the CO_2 reduction, which also resulted in Previously unknown of converting CO_2 to CH_4, as shown in Eq. (8.3)

$$CO_2 + e^- + H^+ \rightarrow CH_4 + H_2O \tag{8.3}$$

8.2.1.2 Oxidation of Dry MXene

Regarding MXene, other than aqueous dispersions, its oxidation also occurs in a dry state. Due to the presence of oxygen and water in air, MXene slowly oxidises under ambient conditions when dried into powder or films with humid, or high-temperature, air significantly accelerating this process. Although the degradation mechanism in such an environment is significantly different from that in aqueous dispersions, they share the same origin – starting from the edge of the MXene sheet, as evidenced by atomic force microscopy (AFM) (Figure 8.3a, b) [32]. Taking single layer $Ti_3C_2T_x$ as an example, the structural layers were maintained, but the thickness increased from 1.5 nm to over 3 nm and that MXene oxidation is initiated from the defect at the flake edge. In general, MXenes tend to maintain this typical layer structure after atmospheric oxidization compared to aqueous dispersions. For example, as-synthesized $Ti_3C_2T_x$ exhibits a layered morphology (Figure 8.3c) [7]. After flash oxidation in air at 1150 °C for 30 seconds, this structure is retained with TiO_2 nanocrystals grown at the edges and between the layers (Figure 8.3d). The TiO_2 size and crystal type can differ at various positions of the flakes, depending on the microenvironment (Figure 8.3d and inset). Although the degree of oxidation at fast oxidation is unknown, the oxidation rate at flash oxidation is much faster than that in water at atmospheric pressure.

The temperature during treatment plays an important role in degree of oxidation. For example, Low et al. [19] prepared TiO_2/Ti_3C_2 (TT) composites by heating MXene powders at different temperatures up to 650 °C. Specifically, a Ti_3C_2 solution dried at 80 °C for 12 hours underwent partial oxidation (Figure 8.3e), while at 650 °C was fully transformed into white TiO_2 (Figure 8.3f), which was confirmed

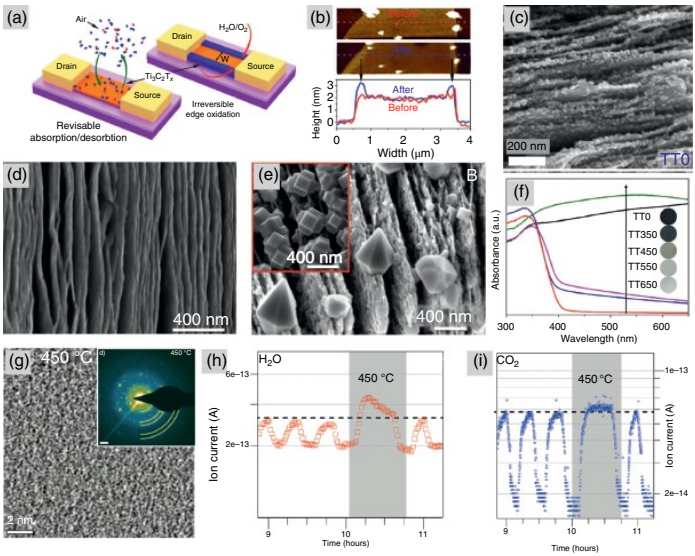


Figure 8.3 $Ti_3C_2T_x$ MXene oxidized under dry conditions. (a) Schematic of the oxidation process of a single $Ti_3C_2T_x$ MXene sheet in air, with corresponding (b) before and after AFM images. *Source:* Lipatov et al. [32]/Reproduced from John Wiley & Sons, Inc. (c) SEM image of an edge of typical as-synthesized multilayer $Ti_3C_2T_x$. (d) SEM image after flash oxidation in air at 1150 °C for 30 seconds. Top left inset is another SEM image at a different location of the same sample. *Source:* Naguib et al. [7]/Reproduced from Royal Society of Chemistry/CC BY 3.0. (e) SEM image of multilayer $Ti_3C_2T_x$ oxidized without heating. (f) Comparison of UV–Vis absorption spectra and corresponding optical photographs (inset) of the prepared samples. *Source:* Low et al. [19]/with permission from Elsevier. (g) Plane-view HRTEM images acquired from $Ti_3C_2T_x$ stacked single flakes after exposure to 2 mbar O_2 gas at 450 °C for 0.5 hours and inset is the corresponding electron diffraction pattern. The residual gas analysis (RGA) of (h) H_2O and (i) CO_2, specifically in temperature window of 450 °C (indicated by the shaded area). The dashed lines identify the max current prior to the 450 °C cycle. Scale bars indicate 2 ($1\,nm^{-1}$). *Source:* Persson et al. [33]/John Wiley & Sons/Public Domain CC BY 3.0.

by thermogravimetric analysis (TGA) under air, giving a white powder at over 600 °C. This suggests the removal of carbon layers of Ti_3C_2 during calcination in air. Recently, Persson et al. [33] studied single $Ti_3C_2T_x$ MXene sheets *in-situ* using an environmental transmission electron microscope (TEM). The inherently F and O terminated nanosheets were defluorinated by heating in vacuum and subsequent exposure to O_2 at temperatures up to 450 °C. It was shown that O supersaturation at the elevated high temperature induced atomic disorder among the surface Ti and ultimately led to complete breakdown of the sheets structural integrity (Figure 8.3g). Finally, with extended oxidation at 450 °C, the MXene sheet was structurally transformed into crystalline TiO_2.

Taking $Ti_3C_2T_x$ as the starting material, atomic oxygen initially occupies the preferred edge site, while upon saturation, the O atoms occupy less favored but energetically comparable alternative sites [33]. Using residual gas analysis (RGA), it was shown that H_2O and CO_2 are desorbed when MXene transforms into TiO_2 (Figure 8.3h, i). CO_2 is a product of the TiO_2 transformation, while H_2O is proposed to originate from chemisorbed water on the MXene surface that is subsequently released due to its lower desorption temperature of TiO_2 compared to MXenes. Put together, for the extended oxidation of $Ti_3C_2T_x$ at increasing temperature, the following irreversible reaction path of MXene decomposition into TiO_2 has been proposed [33].

$$Ti_3C_2T_x + O_2 \rightarrow H2O + Ti_3C_2O_2 \tag{8.4}$$

$$Ti_3C_2O_2 + O_2 \rightarrow TiO_2 + CO_2 \tag{8.5}$$

In contrast, if the aerobic environment was replaced with either an inert gas such as argon or pure vacuum, the heat treatment induces de-intercalation of H_2O [34], rather than MXene oxidation. Moreover, such oxygen-free annealing processes cause selective partial removal of surface termination groups [35], leading to improved environmental stability [36]. For instance, Lee et al. [28] annealed Ti_3C_2 MXene under a hydrogen atmosphere, which significantly enhanced MXene stability in humid, oxidizing conditions (100% RH, 70 °C). Generally using an oxygen-free atmosphere, the thermal treatment results in MXene with oxidation-resistant edge with maintained carbon layers: [6, 7, 28]

$$Ti_3C_2T_x + H_2O(\text{infiltrated}) \rightarrow TiO_2 + C + H_2 \tag{8.6}$$

In summary, the degradation mechanism of MXene is environment dependent and is yet to be fully elucidated. With respect to the metal component, oxidation generally leads to pure metal oxides, or a mixture of metal oxides and MXene layers. However, the variety of other products already observed arising from the

carbon layers suggests further study is required to fully determine the complete mechanism regarding the loss of carbon layers.

8.2.2 Characterizing the Oxidation of MXenes

With the increasing study of MXene oxidation processes under different conditions, various technical characterization methods have been developed to monitor the structural and/or elemental changes within this material. In this section, we summarize the majority of characterization methods that have been utilized in previous studies and discuss their advantages and disadvantages regarding convenience and accuracy, etc. of particular methods.

8.2.2.1 Monitoring the Oxidation Process

The intuitive observation of MXene oxidation is the color change as a function of storage time. Such color change of MXene dispersions is the most obvious evidence of the formation of TiO_2, and straightforward photos of MXene dispersions are a routinely accepted evidence. However, visual color changes can only be a qualitative method to record MXene oxidation [20]. For detailed quantitative study, the changes can be recorded using UV–vis spectrophotometry [31], which exhibits a strong absorption below 400 nm, which is sensitive to the flake size, and a broad peak between 600 and 1000 nm [8], relating to visible light absorption by MXene (Figure 8.1b, c). For practical analysis, Zhang et al. [8] monitored the peak changes at 785 nm for the $Ti_3C_2T_x$ MXene and fitted these points to an empirical function,

$$A = A_{\text{unre}} + A_{\text{re}} e^{-t/\tau} \tag{8.7}$$

where A_{unre} and A_{re} represent the stable/unreactive and reactive/unstable MXene nanosheets, respectively, and τ is the time constant (days). Quite interestingly, the MXene nanosheets followed the exponential decay with a time constant of only 4.8 days (Figure 8.1d). In another study, Huang et al. found the time constant for Ti_2CT_x nanosheets in water/O_2 was small (0.31 days or 7 hours), meaning that only $\sim 1/e \approx 0.37$ of initial MXene is left after 7 hours in this environment [31].

Although continual monitoring of the UV–vis spectra can reveal changes in the dispersion, their absorbance intensity is influenced by solvent type, the concentration of MXene, and aggregation. Therefore, simultaneous monitoring of MXene flake size and the solution properties is required, typically through dynamic light scattering (DLS), zeta-potential, and pH measurements. DLS provides information on the flake size distribution and aggregation [17], while zeta-potential measures its surface charge, which is sensitive to pH fluctuations [21, 37]. As mentioned above, the pH is easily measured to determine changes within dispersions (Figure 8.2a).

Besides observing the MXene dispersion directly, the dispersion can be dried into a solid at various oxidation time intervals to monitor the morphology, crystal structure, and elemental component changes using alternative characterization methods. For example, SEM and TEM can be used to monitor the morphology changes of single MXene flakes or films. Regarding dry oxidation, TEM is a particularly powerful tool to undertake *in-situ* studies by heating MXene flakes [6, 33]. Xia et al. [29] used aberration-corrected scanning transmission electron microscopy (STEM) to monitor MXene flake oxidation under ambient conditions, which identified that the heterogeneous growth of titanium oxide occurred both in the vicinity of atomic defects on the MXene basal plane as well as on the edges of MXene flakes. Using energy dispersive X-ray detection, elemental mapping can be acquired to record the composition changes within the flake structure, which may be correlated with structural changes [10, 17]. When MXene dispersions are filtered or drop cast on a substrate, they form films or coating layers that can be used for characterization techniques requiring a dry sample, such as X-ray diffraction (XRD) analysis, X-ray photoelectron spectroscopy (XPS), and Raman spectroscopy. XRD patterns of MXene films can reveal the changes of inner spacing between MXene flakes, additionally with the crystal formation of TiO_2 [17, 28, 34]. The XPS data can provide the high-resolution Ti 2p and C 1s spectra to indicate the chemical states of Ti and C elements, respectively, while an increasing TiO_2 $2p_{3/2}$ peak is the most significant evidence regarding MXene oxidation [8, 10, 32]. Alternatively, Raman spectroscopy is also capable of detecting the oxidation by peaks at 156, 399, 528, and 630 cm^{-1}, which are attributed to Eg(1), B1g(1), A1g, and B1g(2), and Eg(3) vibrational modes of anatase, respectively [8]. Raman spectroscopy can also provide information on the changes in MXene composition, surface groups, intercalated species, and stacking density [38]. However, both XPS and Raman only provide information of the surface of MXene samples. Meanwhile, electron energy loss spectroscopy (EELS) is a powerful alternative tool to trace the changes in chemical bonds, which is using electrons passing through the sample. It can provide information of the type and quantity of atoms present, chemical state of atoms, and the collective interactions of atoms with their neighbors, which has been used to study the influence of oxygen content and treatment temperature [33]. EELS has also been used to study the oxidation of other MXenes, such as Nb_2C MXene [39].

In several studies, the electrical resistance of MXene films was also used to evaluate the extent of oxidation [21, 28, 40, 41]. Although the electrical resistance of vacuum-filtered films made from MXene dispersions demonstrated a negative correlation with increasing aging, resistance is also influenced by many factors, such as stacking density, size, and alignment of flakes [20, 42]. Such extensive confounding factors make the resistance of films a poor proxy for MXene oxidation. Furthermore, flake aggregation may lead to uneven films, unsuitable for measuring conductivity.

The methods discussed above are good options for understanding MXene oxidation mechanisms and the parameters that influence these mechanisms and rates. However, it should be noted that without a baseline, or unoxidized MXene, these methods cannot precisely identify the oxidation state.

8.2.2.2 Characterizing Extent of MXene Oxidation

As discussed above, some characterization methods can help understand the oxidation kinetics and influencing factors, but such techniques have difficulty in determining the quality of MXene. In other words, if we want to determine the quality of an MXene sample during storage and correlate the degree of oxidation, quantitative characterization methods are required.

In Zhang et al.'s work [20], AFM was found to be a fast approach to characterize the states of MXene by profiling the height within single flakes. In particular, AFM is sufficiently sensitive to recognize the presence of flake-edge nanoscale TiO_2 particles and indication of early-stage oxidation (within two days). Additionally, AFM allows consistent observation of the same MXene flakes over time. For instance, Lipatov et al. [32] found the oxidation of single flakes starts from the edge in the region with the most active structural defects.

In general, EDX and XPS analysis provide the elemental distribution and percentage ratio and can elucidate the changes in MXene before and after different treatments, such as annealing [28] or modification [25]. However, these techniques can often be inaccurate due to the presence of residual water and fluoride salts in the interlayer spacing of MXenes, which may be mistakenly assigned to terminal groups on MXene surfaces. In order to determine the precise type and relative quantities of the termination groups, nuclear magnetic resonance (NMR) spectroscopy has been utilized to study MXene surface functionalization [43]. In particular, ^{1}H and ^{19}F NMR experiments were used to quantify –OH and –F surface functional groups, which were found to be synthesis dependent with the LiF–HCl and HF methods producing $Ti_3C_2(OH)_{0.06}F_{0.25}O_{0.84}$ and $Ti_3C_2(OH)_{0.12}F_{0.8}O_{0.54}$, respectively. The degree of –F termination on HF synthesized MXene was almost four times higher than that of LiF–HCl synthesized MXene, while the latter led to more oxygenic groups which is viewed as beneficial for improving the capacitance when used as energy storage electrodes [44]. Unfortunately, NMR cannot provide information on the chemical state of Ti and it has not been used to study the oxidation of MXene.

8.2.3 Parameters Influencing Oxidation Rate

8.2.3.1 MAX Phase Quality and Synthetic Methods of Synthesis

With the increasing popularity and focus on MXenes, over 30 types have been synthesized, which is one of the primary influences regarding oxidation rate. As revealed in a previous study, the oxidation rate exhibits a general trend, with

higher "n" MXenes more oxidatively stable. For example, $Ti_3C_2T_x$ exhibits better stability than Ti_2CT_x [21] and $Nb_4C_3T_x$ more stable than Nb_2CT_x [45]. Additionally, the quality of MAX phases is also important for the quality of MXene. Taking $Ti_3C_2T_x$ produced from Ti_3AlC_2 MAX phase as an example, Shuck et al. [35] used graphite, active carbon, and graphene as carbon sources for the MAX phase synthesis and found that MAX phase produced using graphite as the carbon source exhibited the best quality. MXene subsequently produced from graphite derived MAX phase showed the highest electrical conductivity ($\sim$4400 S cm^{-1}) and longest stable shelf time (10.1 days), while TiC produced MXene exhibited significantly reduced conductivity ($\sim$3480 S cm^{-1}). In another study, Mathis and co-workers found that including excess aluminum during the synthesis of the Ti_3AlC_2 MAX phase precursor leads to Ti_3AlC_2 grains with improved crystallinity and carbon stoichiometry (termed Al–Ti_3AlC_2). MXene nanosheets (Al–Ti_3C_2) produced from this precursor are of higher quality, as evidenced by their increased resistance to oxidation and an increase in their electronic conductivity up to 20 000 S cm^{-1} [46]. Aqueous suspensions of stoichiometric single- to few-layer Al–Ti_3C_2 flakes produced from the modified Al–Ti_3AlC_2 have a shelf life of over ten months, compared to one to two weeks for Ti_3C_2, even when stored in ambient conditions.

The strong M—X bonds in MAX phases allow the selective etching of M—A bonds, which requires strong acid. High-concentration hydrofluoric (HF) was the first, and remains the most common, etchant to overcome the metallic bonds between M and A elements [2]. DFT calculations combined with aberration-corrected STEM imaging showed that high concentrations of HF resulted in more crystal defects on the MXene flakes and those atomic defects in nanometer-thick MXene layers are highly active sites for oxidation, which are promoted by an intrinsic electric field [5], and it is the number of these defects that determines the oxidation rate. As previously mentioned, degradation rate is dependent on the nanosheet size, as large MXene flakes are the most stable, followed by medium and small ones, indicating the relative magnitude of edge-driven reactions [8]. Due to this effect, the sonication procedure used during the exfoliation of MXene significantly reduces flake size and thus determines the oxidation rate due to the resulting increased flake edges and defects [47].

In 2014, the *in-situ* HF method was developed [48], in which acid contributes H^+ while fluoride salt provides F^-, offering a wide range and combination of acid and fluoride salts. But the component of etchant may affect the quality of synthesized MXenes. For example, Liu et al. [49] synthesized $Ti_3C_2T_x$ and Ti_2CT_x using the mixture of different fluoride salts (lithium fluoride, sodium fluoride, potassium fluoride, and ammonium fluoride) and HCl solutions, and found that MXenes made from LiF and NH_4F can absorb methane under high pressure and can keep methane under normal pressure. These MXenes may have important

application in capturing methane or other hazardous gas molecules. Otherwise, MXenes made from NaF and KF can absorb methane under high pressure and release methane under low pressure. They can have important application in the adsorption and storage of natural gas. The reactivity of metal ions may also influence the quality of synthesized MXenes. Wang et al. [50] used a mixture of iron fluoride (FeF_3) and HCl, which produced partially oxidized MXene decorated with TiO_2 (rutile or anatase) particles directly. In general, mild etching conditions and absence of sonication tend to produce larger defect-free MXene flakes, which demonstrate good environmental stability [32].

8.2.3.2 Aqueous Environment

As mentioned above, water is directly involved in, and required for MXene oxidation, the rate of which can be strongly influenced by various dissolved species [8, 51]. Water acts not only as a solvent of dissolved oxygen, but also as a proton source, promoting MXene degradation to methane and metal oxides [22]. When MXene is stored as a dry solid, water present in air still induces oxidation, albeit at a significantly reduced rate [32]. It has also been demonstrated that MXene concentration strongly influences oxidation kinetics, in which oxidation is accelerated at lower concentrations [21]. However, this is dependent on the concentration of oxygen in water. The pH of the dispersion also affects the MXene oxidation rate. Specifically, MXene oxidation is accelerated in basic media by reaction with hydroxyl anions [21]. Recent studies also showed that the additives in the dispersion may also influence the oxidation rate [21]. For example, the oxidation is initially fast in the alkaline buffer (pH = 10.0), where the OH– ions react with the –OH terminations of the MXene surface and result in less stable O– groups, making the MXene surfaces more reactive. Regarding additives, adding oxidizing agents (such as H_2O_2) into the solution effectively promotes the oxidation of V_2CT_x [52] and $Ti_3C_2T_x$ [53, 54]. In contrast, oxidation can be slowed significantly by adding antioxidants, such as such as sodium L-ascorbate [41], tannic acid, and ascorbic acid [55] in sufficient concentrations, and are often used for MXene longevity.

8.2.3.3 Air or Oxygen

Regarding gaseous species, oxygen is regarded as the reactive portion of air for the oxidation of MXene, which was indirectly proven by control experiments between water purged with air or argon [8, 17, 40]. For instance, Ar@RT removes the oxygen from water effectively minimizing the accessibility of MXene to oxygen, thus slowing down the degradation rate of MXene [8]. Demonstrating the important role oxygen plays in the process. Although an Ar-purged aqueous environment is capable of minimizing the oxidation process, aggregation of $Ti_3C_2T_x$ cannot be avoided. To have an insight into the oxidation reaction between MXene and

oxygen, Persson et al. [33] studied single sheets of $Ti_3C_2T_x$ MXene by heating in vacuum and subsequentially exposed to O_2 gas at temperatures up to 450 °C with controlled O_2 concentration. The *in-situ* TEM results include exclusive termination by O on the MXene surfaces and eventual supersaturation ($x > 2$) with a retained MXene sheet structure. Upon extended O exposure, the MXene structure transforms into TiO_2 and desorbs surface-bound H_2O and CO_2 reaction products. These results are direct evidence of the role of oxygen in the degradation of MXenes. In aqueous dispersion, Zhao et al. [21] found that the oxidation kinetics of $Ti_3C_2T_x$ changes for varying concentrations of MXene dispersions in a fixed volume of air and showed that a higher oxygen and MXene ratio results in a faster oxidation rate.

8.2.3.4 Temperature

In general, an increase in temperature will raise the average kinetic energy of the reactant molecules and a greater proportion of molecules will have the minimum energy necessary for an effective collision and subsequent reaction. The above also applies to the oxidation of MXenes. Under aqueous conditions, MXene oxidation is completed in 2–3 weeks at room temperature, while at 90 °C only takes 24 hours [20]. Such a trend is also observed for dry MXene. The temperature-programmed desorption mass spectroscopy data for $Ti_3C_2T_x$ demonstrates the thermal desorption of surface functional groups occurs in region of 100–200 °C, while the MXene layers themselves formed cubic Ti_3C_2, TiO_2, and evolved CO/CO_2 gasses in the range of 400–1000 °C [56]. In subsequent studies, Persson et al. [33] found that the oxidation of MXene powder occurred at 450 °C in the presence of oxygen. However, the temperature could be increased to over 1000 °C under vacuum before complete oxidation was observed [6, 7, 28, 34, 35].

8.2.3.5 UV Light

In previous studies, $Ti_3C_2T_x$ dispersions have demonstrated a strong absorbance in the wavelength range of 250–300 nm [8]. Therefore, it is reasonable to hypothesize that the exposure of $Ti_3C_2T_x$ to UV light in this wavelength range would accelerate oxidation. Green et al. [11] found that there is a strong decrease in conductivity with a longer UV exposure, suggesting an increase in oxidation. The first stage in this process is the transformation of UV light to heat, leading to increased oxidation kinetics [57]. The second is the generation of radicals under UV light that may attack the $Ti_3C_2T_x$ surface, causing further oxidation. We surmise that the UV light interacts with the TiO_2 causing O· and OH· radical formation from the functional groups, and oxygen and moisture present in the environment [58]. With longer UV exposure times, more radicals were generated, leading to more oxidation. Even so, additional experiments need to be done to properly assess the UV effects on $Ti_3C_2T_x$ oxidation.

8.3 Preventing the Oxidation of MXene

Investigations into the preservation of MXene flakes have demonstrated that the degradation rate is influenced by the MXene quality, surrounding media [11, 51], and can be slowed down by using organic solvents [17, 51], air-free water [8], antioxidant [41], or polymer media [11]. To have a better understanding of how to handle and store MXenes, we have summarized different strategies based on their mechanisms related to the parameters influencing the degradation rate. As shown in Figure 8.4, the physical methods aim to isolate the parameters or decrease the degradation rate, while the chemical methods focus on improving the stability of pristine MXene by alternating the synthetic method or inducing chemical modifications to occupy the active sites with less-reactive functional groups.

8.3.1 Defect Control During MXene Synthesis

Due to the degradation beginning at the defect sites, minimizing the defects during MXene synthesis is the first step to improving its environmental stability. As mentioned previously, the structure and properties of MXenes are highly affected by the quantity of the precursor of MAX phase. Therefore, using high-quality MAX phase is the first criteria for preparing highly stable MXenes. For instance, to illustrate the effect of MAX phase, Ti_3AlC_2 was synthesized using three carbon sources (graphite, carbon lampblack, and titanium carbide [TiC]) at 1650 °C for 2 hours [59]. Thermal analysis was utilized to examine the reaction mechanism, indicating that the three carbon sources undergo different reaction pathways to MXene. The products revealed

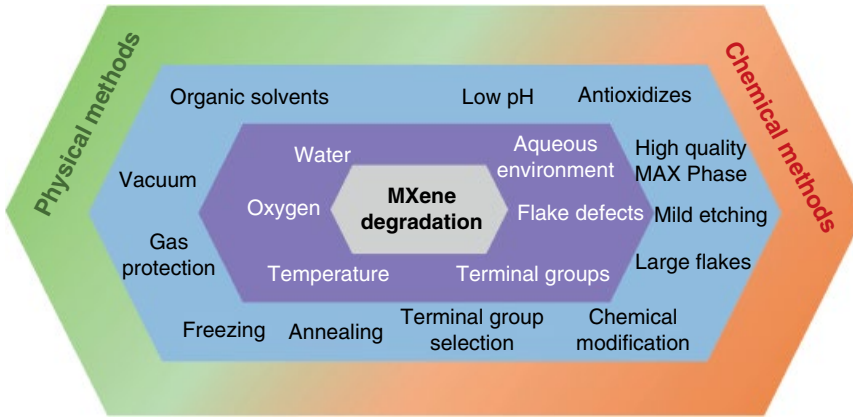


Figure 8.4 Graphic illustration of the impact parameters for the degradation of MXenes and different storing strategies developed based on corresponding parameters.

differences with respect to lateral flake size, chemical composition, chemical stability in deionized water, and electrical conductivity. Graphite-produced $Ti_3C_2T_x$ showed the highest conductivity (~4400 S cm^{-1}) and is the most stable (time constant of 10.1 days), while TiC-produced MXene has a comparable conductivity (~3480 S cm^{-1}), but the lowest colloidal stability (4.8 days), while carbon lampblack has the lowest conductivity (~1020 S cm^{-1}) and low chemical stability (5.1 days) [59]. Recently, Mathis and co-workers found that including excess aluminum during synthesis of the Ti_3AlC_2 MAX phase precursor leads to Ti_3AlC_2 grains with improved crystallinity and carbon stoichiometry (termed Al–Ti_3AlC_2). MXene nanosheets (Al–Ti_3C_2) produced from this precursor are of higher quality, as evidenced by their increased resistance to oxidation and high electronic conductivities (~20 000 S cm^{-1}) [46]. Aqueous suspensions of stoichiometric single- to few-layer Al–Ti_3C_2 flakes produced from the modified Al–Ti_3AlC_2 have a shelf life of over 10 months, compared to 1–2 weeks for previously published Ti_3C_2, even when stored in ambient conditions.

Besides the quality of MAX phase, the mild and controllable synthetic method is also required to minimize the defects and quality of MXene. Following the MILD HCl–LiF method, a wide range of chemicals have been used to synthesize MXene, such as ammonium bifluoride (NH_4HF_2) [60], $NaHF_2$, and KHF_2 [61]. To achieve exfoliated single-layer MXenes without sonication exfoliation, Cao et al. [62] developed a convenient liquid phase exfoliation method to fabricate fewer-layer MXene nanosheets on a large scale. The Hansen solubility parameters (HSPs) and surface tension component ratio were estimated and further applied to detect a green low-boiling-point water/acetone cosolvent for the better exfoliation of MXene. It was found that the exfoliation efficiency is improved efficiently by matching HSPs and surface tension component ratio of MXene to that of solvents. For example, a highly concentrated MXene dispersion of up to 1.73 mg ml^{-1} could be produced in the optimum composition of the water/acetone mixture, which is approximately 78 and 5 times higher than that in pure acetone and water, respectively.

8.3.2 Storing MXene in Solvents

8.3.2.1 Isolation of Water

Since water is an important factor in the degradation of MXene, isolation from water is required to prevent the degradation of MXenes, such as replacing water with organic solvents. For example, Yury and co-workers [51] reported the oxidation stability of $Ti_3C_2T_x$ MXene in various organic solvents, such as DMSO, DMF, NMP, PC, and ethanol, can be significantly enhanced enabling storage for over months. The following study showed that isopropyl alcohol (IPA) [31] and acetone [62] are also good solvents for MXenes. In general, solvent exchange by replacing the water with non-aqueous polar solvents (e.g. IPA, NMP, DMSO, and

ethanol) is a reasonably straightforward and effective method to prevent MXene degradation [17, 31, 51].

To obtain highly dispersed MXene materials in organic solvents without the time-consuming solvent exchange procedures. Zhang et al. [63] developed a method called the tuned microenvironment method (TMM). TMM involves preparing a highly concentrated $Ti_3C_2T_x$ organic solvent dispersion by tuning the microenvironment of $Ti_3C_2T_x$ through direct dispersal in *N*,*N*-dimethylformamide and other solvents using stirring and shaking for a short time, mitigating the need for sonication. Using this delaminated single-layer MXene, yields can reach 90% or greater, and a large-scale synthesis has also been demonstrated with TMM by delaminating 30 g of multilayer $Ti_3C_2T_x$ raw powder in a one-pot synthesis. The $Ti_3C_2T_x$ dispersed in an organic solvent exhibits excellent oxidation resistance even under aerobic conditions at room temperature. Through the experimental investigation, the successful preparation of a highly concentrated $Ti_3C_2T_x$ organic solvent dispersion *via* TMM can be attributed to the following factors: (i) the intercalation of the cation can lead to a change in the hydrophobicity and surface functionalization of the material, and (ii) proper solvent properties are required to disperse MXene nanosheets well. Moreover, various types of MXenes, such as Nb_2CT_x, $Nb_4C_3T_x$, and $Mo_2Ti_2C_3T_x$, can also be prepared as highly concentrated MXene organic solvent dispersions *via* TMM, which proves the universality of this method. However, the poor dispersibility of MXenes in most organics and the tedious removal of these toxic solvents further raise the processing complexity and the cost of MXene storage.

8.3.2.2 Isolation of Oxygen or Air

Isolation of oxygen or air can prevent the degradation of MXene, and the most simple and widely utilized approach is purging such dispersions with argon [8, 31]. However, it is noteworthy that the active sites on MXene flakes can still react with water to form nanosize TiO_2 on flake edges [8]. Storing MXenes in vacuum as powder or films is a simple alternative, but restacking of MXene flakes cannot be avoided. In Huang's study [31], they compared MXene in IPA with oxygen and MXene in water with argon and the results indicate that MXene flakes maintained good quality without oxidation even in the presence of dissolved oxygen in the organic solvent. This observation suggests that isolation of oxygen is only required in the presence of water, which has been verified with other solvents, such as DMSO and NMP [17].

8.3.2.3 Antioxidants

Antioxidants are widely used chemicals to improve the environmental stability of materials. Green's group [41] first reported that the degradation of colloidal $Ti_3C_2T_x$ MXene nanosheets can be slowed significantly by using sodium

L-ascorbate as an antioxidant. The electrical conductivity of $Ti_3C_2T_x$ nanosheets treated with sodium ascorbate was orders of magnitude higher after 21 days as compared with untreated ones. While subsequent studies with aqueous MXene inks prepared with sodium ascorbate have demonstrated low oxidation resistance even after 80 days of storage at ambient temperature and exposed to air [64]. Molecular dynamics simulation showed L-ascorbate anions interact with the edges of $Ti_3C_2T_x$ nanosheets, which prevents detrimental oxidation reactions [41].

Another study showed that decreasing the pH could also slow down the oxidation rate of a dispersion. For instance, Green's team [21] discovered that a weak organic tricarboxylic acid–citric acid (CA), which is one of the components of the acidic buffer solution (pH = 3), is an effective antioxidant for protecting MXenes from oxidation and degradation. Both $Ti_3C_2T_x$ and Ti_2CT_x MXene in this acidic buffer did not show much oxidation, as indicated by the relatively stable electrical conductivities and small changes in the Ti(IV) percentage. Additionally, Jiang et al. found that adding CA could improve the stability of MXene during the thermal treatment at 90 °C for the reduction of graphene/MXene composites [37]. However, the removal of additives was not discussed in those studies, which may increase the cost of storing MXenes with antioxidants.

8.3.2.4 Low Temperature

Decreasing the temperature is a common approach to reduce the reaction rate, which is also applicable to preventing MXene oxidation. As studied by Chae [40], the oxidation stability of the $Ti_3C_2T_x$ flakes is dramatically improved in a system where water molecules and temperature were well-controlled. It was found that aqueous solutions of $Ti_3C_2T_x$ MXene can be chemically stable for more than 39 weeks when the storage temperature (−80 °C) was sufficiently low to halt oxidation processes. It was also found that if the $Ti_3C_2T_x$ flakes are dispersed in ethanol, the degradation process can be significantly delayed even at 5 °C. Moreover, the oxidation stability of the $Ti_3C_2T_x$ flakes is dramatically improved in both cases, even in the presence of an oxygen-containing atmosphere. Recently, Zhang et al. [20] undertook a detailed study on the temperature effects and found that when an aqeous dispersion was frozen the MXene could be stored for up to two years and remained as good as fresh MXene. It is believed that the solid ice matrix surrounding the MXene isolates the flakes from direct exposure to air. Additionally, the solid ice significantly decreases the diffusion rate of oxygen from air to MXene flakes. The third reason is that the amount of dissolved oxygen decreased when the aqueous dispersion was frozen, reducing the contact of MXene flakes with oxygenated water molecules. The combination of these three factors inhibits oxidation, enabling long-term preservation of $Ti_3C_2T_x$ MXene dispersions. Although low-temperature storage increases the cost of large-scale production of MXenes, it provides the easiest approach to storing MXene in aqueous environments by

simply placing it in the freezer directly after synthesis, which can be defrosted when used without the need to remove additives or undertake solvent exchange.

8.3.2.5 Surface Modification

Surface modification takes advantage of the terminal groups on MXene flakes to graft small molecules or polymer chains, which not only occupy the active sites on flakes, but also form a coating layer to prevent MXene from degradation. Ji et al. [65] found that (3-aminopropyl) triethoxysilane functionalized MXene (APTES-MXene) exhibited superior stability against structural degradation and improved surface properties with adjustable hydrophilicity. By measuring UV–Vis absorbance changes of samples stability can be monitored, with MXene in air exhibiting degradation of 95.6% after 11 days while APTES-MXene only reduced 20.8% over the same period. In another work, Jiang et al. [66] modified $Ti_3C_2T_x$ MXene *via* diazonium covalent chemistry. The 4-nitrophenyl group was grafted onto the surface of MXene through a solid–liquid reaction, which was confirmed by various characterization methods, including XPS, Fourier transform infrared spectroscopy, EELS, AFM, and TEM. The degree of modification of MXene is expediently tunable by adjusting the concentration of the diazonium salt solution. Chen et al. [67] produced MXene-based conjugated microporous polymers (M-CMPs) by covalently sandwiching MXene between CMPs using *p*-iodophenyl functionalized MXene as templates. The as-prepared M-CMPs inherit the 2D architecture and high conductivity of MXene in terms of hierarchical porous structure and large specific surface area of CMPs. Moreover, the restacking and oxidation of MXene are simultaneously suppressed.

It should be noted that the surface modification also changes the dispersibility of MXene flakes. For instance, Kim et al. [68] demonstrated that upon the grafting of alkyl phosphonic acid ligands on hydroxyl terminal groups of $Ti_3C_2T_x$ flakes, at the liquid–liquid interface between water and water-immiscible organic medium, a covalent Ti—O—P bond was formed via interfacial nucleophilic addition and sequential condensation reactions. As a result, $Ti_3C_2T_x$ MXene could be stably dispersed in nonpolar organic solvents at room temperature. Unlike conventional surface chemical modification methods that require many complex and tedious steps, this is a simple and easy process for fabricating a $Ti_3C_2T_x$ organic dispersion invarious organic solvents, ranging from highly polar to nonpolar. The nonpolar chloroform $Ti_3C_2T_x$ dispersion also exhibits strong degradation resistance and long-term storage stability. This approach provides an opportunity for preparing MXene nanocomposites with nonpolar polymeric matrices that are soluble in organic media for future applications such as stretchable electrodes.

Besides chemical modification of the terminal groups on MXene flakes, removing the terminals is also a possible strategy to improve the stability. As demonstrated by Lee et al. [28], hydrogen annealing is also an effective strategy to

improve MXene stability. When MXene films were annealed at a temperature ranging from 300 °C to 900 °C for 30 minutes in a vacuum chamber with hydrogen gas, it dramatically improved the oxidation stability of MXene films under harsh conditions (100% relative humidity, 70 °C). Additionally, hydrogen annealing also changed the surface functional groups of the MXene. The relative number of –OH terminations on the surface decreased, whereas the number of –O terminations increased, accompanied by a decrease in the amount of Ti–H_2O species. This change decreased the inner layer spacing in MXene films and increased the electrical conductivity of films. Interestingly, they found that the partly oxidized MXene film exhibited a recovery of conductivity after hydrogen post-annealing, suggesting such treatment eliminated poorly conductive TiO_2 nanoparticles on the surface. However, the removal of hydrophilic groups from MXene flakes caused a loss of dispersibility and surface reactivity, which limits this approach to treating MXene-based structures and is not applicable to MXene dispersions.

Etching of the aluminum layer of a parent MAX phase Ti_3AlC_2 layered material with HF acid leads to the MXene Ti_3C_2 with various surface terminations (T_x). In contrast, molten salts can achieve uniform chloride terminations, but these are difficult to further modify. Recently, Kamysbayev et al. [69] showed that etching of MAX phases in molten cadmium bromide leads to bromide-terminated MXenes that can then be substituted with oxygen, sulfur, selenium, tellurium, amine groups, as well as with vacancy sites. This approach not only potentially provides more reactive groups on MXene flakes for modification but is also capable of introducing more stable groups for enhancing the environmental stability of MXenes.

8.3.3 Coating Protection

MXenes ($Ti_3C_2T_x$) are two-dimensional transition-metal carbides and carbonitrides with high conductivity and optical transparency. However, transparent MXene electrodes with high environmental stability, suitable for various flexible organic electronic devices, have rarely been demonstrated. By laminating a thin polymer film onto a solution-processed MXene layer to protect the MXene film from harsh environmental conditions, transparent and flexible MXene electronic devices can be produced [70]. A thin polymer layer spin-coated onto a transparent MXene electrode provides environmental stability even under air exposure longer than 7 days at up to 70 °C and 50% humidity without degrading the electrodes transparency. The resulting polymer-laminated MXene electrode facilitates the development of a variety of field-driven photoelectronic devices by exploiting the electric field exerted between the MXene layer and the counter electrode through

the insulating polymer. Field-induced electroluminescent displays, based on both organic and inorganic phosphors, with PL-MXene electrodes are demonstrated with high transparency and mechanical flexibility. Furthermore, PL-MXene electrode exhibits high versatility through successful implementation in capacitive-type pressure sensors and triboelectric nanogenerators, resulting in field-driven sensing and energy-harvesting electronic devices with excellent operational reliability.

8.4 Summary and Outlook

Degradation remains one of the biggest challenges for improving the durability of MXene-based materials. This metastable nature of MXenes can be attributed to structural defects and active terminal groups, as mentioned above. Minimizing such structural defects and enhancing the stability of terminal groups is the fundamental approach to prevent degradation, which requires continued efforts in developing efficient synthetic methods. For example, improving the crystallinity and carbon stoichiometry of the Ti_3AlC_2 MAX phase precursor by adding excess aluminum during synthesis [46], or etching of MAX phases in Lewis acidic melts to achieve uniform and stable terminal groups [69, 71]. Another important strategy of storing MXene is control of the environment and parameters, which retards the degradation rate of MXenes and has been used to great success to extend the shelf life of MXene from weeks to years. Unfortunately, the degradation continues during use.

Regarding the degradation mechanism, a few questions have yet to be fully addressed. This includes: how is the carbon layer consumed during the oxidation and what causes the decrease in solution pH? There is also disagreement over whether or not CO_2 is one of the oxidation products [22]. For a long time, it has been believed that CO_2 was formed during the oxidation, which contributed to the drop in pH value. However, a detailed study on compositional changes of MXene dispersion is required. Importantly, the focus of research has been on $Ti_3C_2T_x$ MXene due to its excellent performance in a range of applications; however, there are limited studies on the oxidation of more exotic Nb-, V-, and Mo-based MXenes, which may undergo different mechanisms or be influenced by other environmental parameters. Additionally, developing characterization methods to rigorously define the oxidation stages of MXenes is also required. Currently, the performance of MXene in electrical conductivity and environmental stability varies throughout the literature and the quality of MXenes differs across research groups. Clearly, a systematic standard or characterization method is required to define the fresh MXene, slightly oxidized MXene, TiO_2/MXene hybrids and oxidized MXenes.

Completely preventing the degradation of $Ti_3C_2T_x$ and other MXenes remains challenging, especially when technologies are translated from laboratories to industries for the development of commercial products. To mitigate this challenge, the scientific community continues to investigate MXene oxidation kinetics and mechanisms and develop new strategies to improve their oxidation stability.

References

1 Gogotsi, Y. and Anasori, B. (2019). *ACS Nano* 13: 8491.
2 Naguib, M., Mashtalir, O., Carle, J. et al. (2012). *ACS Nano* 6: 1322.
3 Shuck, C.E., Sarycheva, A., Anayee, M. et al. (2020). *Advanced Engineering Materials* 22: 1901241.
4 Lakhe, P., Prehn, E.M., Habib, T. et al. (2019). *Industrial & Engineering Chemistry Research* 58: 1570.
5 Sang, X., Xie, Y., Lin, M.-W. et al. (2016). *ACS Nano* 10: 9193.
6 Ghassemi, H., Harlow, W., Mashtalir, O. et al. (2014). *Journal of Materials Chemistry A* 2: 14339.
7 Naguib, M., Mashtalir, O., Lukatskaya, M.R. et al. (2014). *Chemical Communications* 50: 7420.
8 Zhang, C.J., Pinilla, S., McEvoy, N. et al. (2017). *Chemistry of Materials* 29: 4848.
9 Iqbal, A., Hong, J., Ko, T.Y., and Koo, C.M. (2021). *Nano Convergence* 8: 9.
10 Peng, C., Yang, X., Li, Y. et al. (2016). *ACS Applied Materials & Interfaces* 8: 6051.
11 Habib, T., Zhao, X., Shah, S.A. et al. (2019). *npj 2D Materials and Applications* 3: 8.
12 Wang, C.-H., Kurra, N., Alhabeb, M. et al. (2018). *ACS Omega* 3: 12489.
13 Zhang, J., Uzun, S., Seyedin, S. et al. (2020). *ACS Central Science* 6: 254.
14 Zhang, Y.-Z., Lee, K.H., Anjum, D.H. et al. (2018). *Science Advances* 4: eaat0098.
15 Han, M., Yin, X., Hantanasirisakul, K. et al. (2019). *Advanced Optical Materials* 7: 1900267.
16 Xia, Y., Mathis, T.S., Zhao, M.-Q. et al. (2018). *Nature* 557: 409.
17 Seyedin, S., Zhang, J., Usman, K.A.S. et al. (2019). *Global Challenges* 3: 1900037.
18 Mashtalir, O., Cook, K.M., Mochalin, V.N. et al. (2014). *Journal of Materials Chemistry A* 2: 14334.
19 Low, J., Zhang, L., Tong, T. et al. (2018). *Journal of Catalysis* 361: 255.
20 Zhang, J., Kong, N., Hegh, D. et al. (2020). *ACS Applied Materials & Interfaces* 12: 34032.
21 Zhao, X., Vashisth, A., Blivin, J.W. et al. (2020). *Advanced Materials Interfaces* 7: 2000845.
22 Huang, S. and Mochalin, V.N. (2020). *ACS Nano* 14: 10251.
23 Singh, B., Bahadur, R., Neekhra, S. et al. (2021). *ACS Applied Materials & Interfaces* 13: 3011.

24 Cai, C., Wang, R., Liu, S. et al. (2020). *Colloids and Surfaces A: Physicochemical and Engineering Aspects* 589: 124468.
25 Liu, H., Yang, C., Jin, X. et al. (2020). *Colloids and Surfaces A: Physicochemical and Engineering Aspects* 603: 125239.
26 Han, F., Luo, S., Xie, L. et al. (2019). *ACS Applied Materials & Interfaces* 11: 8443.
27 Didziulis, S.V., Frantz, P., Perry, S.S. et al. (1999). *The Journal of Physical Chemistry B* 103: 11129.
28 Lee, Y., Kim, S.J., Kim, Y.-J. et al. (2020). *Journal of Materials Chemistry A* 8: 573.
29 Xia, F., Lao, J., Yu, R. et al. (2019). *Nanoscale* 11: 23330.
30 Faradzhev, N.S. and Hill, S.B. (2016). *Surface Science* 652: 200.
31 Huang, S. and Mochalin, V.N. (1958). *Inorganic Chemistry* 2019: 58.
32 Lipatov, A., Alhabeb, M., Lukatskaya, M.R. et al. (2016). *Advanced Electronic Materials* 2: 1600255.
33 Persson, I., Halim, J., Hansen, T.W. et al. (2020). *Advanced Functional Materials* 30: 1909005.
34 Hart, J.L., Hantanasirisakul, K., Lang, A.C. et al. (2019). *Nature Communications* 10: 522.
35 Seredych, M., Shuck, C.E., Pinto, D. et al. (2019). *Chemistry of Materials* 31: 3324.
36 Chen, H., Wen, Y., Qi, Y. et al. (2019). *Advanced Functional Materials* 30: 1906996.
37 Jiang, D., Zhang, J., Qin, S. et al. (2021). *ACS Nano* 15: 5000.
38 Sarycheva, A. and Gogotsi, Y. (2020). *Chemistry of Materials* 32: 3480.
39 Palisaitis, J., Persson, I., Halim, J. et al. (2018). *Nanoscale* 10: 10850.
40 Chae, Y., Kim, S.J., Cho, S.Y. et al. (2019). *Nanoscale* 11: 8387.
41 Zhao, X., Vashisth, A., Prehn, E. et al. (2019). *Matter* 1: 513.
42 Zhang, J., Kong, N., Uzun, S. et al. (2020). *Advanced Materials* 32: 2001093.
43 Hope, M.A., Forse, A.C., Griffith, K.J. et al. (2016). *Physical Chemistry Chemical Physics* 18: 5099.
44 Dall'Agnese, Y., Taberna, P.-L., Gogotsi, Y., and Simon, P. (2015). *Journal of Physical Chemistry C* 6: 2305.
45 Echols, I.J., Holta, D.E., Kotasthane, V.S. et al. (2021). *The Journal of Physical Chemistry C* 125: 13990.
46 Mathis, T.S., Maleski, K., Goad, A. et al. (2021). *ACS Nano* 15: 6420.
47 Tao, N., Zhang, D., Li, X. et al. (2019). *Chemical Science* 10: 10765.
48 Ghidiu, M., Lukatskaya, M.R., Zhao, M.-Q. et al. (2014). *Nature* 516: 78.
49 Liu, F., Zhou, A., Chen, J. et al. (2017). *Applied Surface Science* 416: 781.
50 Wang, X., Garnero, C., Rochard, G. et al. (2017). *Journal of Materials Chemistry A* 5: 22012.
51 Maleski, K., Mochalin, V.N., and Gogotsi, Y. (2017). *Chemistry of Materials* 29: 1632.
52 Luo, W., Liu, Y., Li, F. et al. (2020). *Applied Surface Science* 523: 146387.
53 Ahmed, B., Anjum, D.H., Hedhili, M.N. et al. (2016). *Nanoscale* 8: 7580.
54 Li, S., Gu, W., Sun, Y. et al. (2021). *Ceramics International* 47: 29930.

55 Limbu, T.B., Chitara, B., Orlando, J.D. et al. (2020). *Journal of Materials Chemistry C* 8: 4722.
56 Mashtalir, O., Lukatskaya, M.R., Kolesnikov, A.I. et al. (2016). *Nanoscale* 8: 9128.
57 Li, R., Zhang, L., Shi, L., and Wang, P. (2017). *ACS Nano* 11: 3752.
58 Hirakawa, T. and Nosaka, Y. (2002). *Langmuir* 18: 3247.
59 Shuck, C.E., Han, M., Maleski, K. et al. (2019). *ACS Applied Nano Materials* 2: 3368.
60 Halim, J., Lukatskaya, M.R., Cook, K.M. et al. (2014). *Chemistry of Materials* 26: 2374.
61 Feng, A., Yu, Y., Wang, Y. et al. (2017). *Materials & Design* 114: 161.
62 Zhou, Z., Li, L., Liu, X. et al. (2021). *Journal of Molecular Liquids* 324: 115116.
63 Zhang, Q., Lai, H., Fan, R. et al. (2021). *ACS Nano* 15: 5249.
64 Wu, C.-W., Unnikrishnan, B., Chen, I.W.P. et al. (2020). *Energy Storage Materials* 25: 563.
65 Ji, J., Zhao, L., Shen, Y. et al. (2019). *FlatChem* 17: 100128.
66 Jing, H., Yeo, H., Lyu, B. et al. (2021). *ACS Nano* 15: 1388.
67 Yang, W., Huang, B., Li, L. et al. (2020). *Small Methods* 4: 2000434.
68 Kim, D., Ko, T.Y., Kim, H. et al. (2019). *ACS Nano* 13: 13818.
69 Kamysbayev, V., Filatov, A.S., Hu, H. et al. (2020). *Science* 369: 979.
70 Lee, S., Kim, E.H., Yu, S. et al. (2021). *ACS Nano* 15: 8940.
71 Li, M., Lu, J., Luo, K. et al. (2019). *Journal of the American Chemical Society* 141: 4730.

9

Beyond Single-M MXenes: Synthesis, Properties, and Applications

Christopher E. Shuck[1] *and Yury Gogotsi*[2]

[1] *Department of Chemistry and Chemical Biology, Rutgers University, Piscataway, NJ, USA*
[2] *A. J. Drexel Nanomaterials Institute, and Department of Materials Science and Engineering, Drexel University, Philadelphia, PA, USA*

9.1 Introduction

Within materials science, alloying elements together to improve properties has led to nearly every major modern advance, from the advent of steel to the production of semiconductors. Once a base type of useful material is discovered, over time, the scientific community uses alloying to tailor the properties to enhance specific quantities of interest or to better align with target applications. This includes metals, complex compounds, ceramics, 2D materials, superconductors, and likely every class of materials synthesized. MXenes are no exception.

Since the initial report of the first MXene in 2011, the research community has primarily focused on one MXene, $Ti_3C_2T_x$ [1]. However, just one year after the report of $Ti_3C_2T_x$, the first solid solution MXene, $(Ti_{0.5}Nb_{0.5})_2CT_x$ was reported [2]. This early report illustrates the foresight and desire of the MXene community to understand the relationship between the MXene chemistry and their observed properties. This direction naturally follows the initial discovery of a material – finding ways to modify properties is necessary to best fit specific applications. Within single-M MXenes, the optical, electronic, and chemical properties are essentially fixed; modifications can be accomplished by altering the surface chemistry or through intercalation, but these changes are relatively minor compared to direct modification of the base chemistry. However, due to the MXene

Transition Metal Carbides and Nitrides (MXenes) Handbook: Synthesis, Processing, Properties and Applications, First Edition. Edited by Chuanfang Zhang and Michael Naguib.
© 2024 John Wiley & Sons, Inc. Published 2024 by John Wiley & Sons, Inc.

structure/synthesis approach, the relationship between chemistry and properties is often difficult to determine directly; to understand this, it is vital to first consider MAX phases.

MAX phases have the typical formula: $M_{n+1}AX_n$, where M are early transition metals (Ti, V, Nb, Ta, etc.), A is typically a group 13/14 element (Al, Si, Ga, Sn, etc.), X is C and/or N, and n is 1–4 [3, 4]. While the definition of this family is quite broad in scope, not all permutations of chemistry and structure are thermodynamically possible. Hence, Ti_2AlC and Ti_3AlC_2 exist, but not Ti_4AlC_3. Likewise, Ti_3AlC_2, Ta_3AlC_2, and Zr_3AlC_2 have been reported, but not Mo_3AlC_2, Nb_3AlC_2, V_3AlC_2, etc. [4, 5]. This further extends to every structure (n) of MAX phases and every M, A, and X element. Using multiple-M chemistries expands the total compositional space tremendously; a variety of viable MXene chemistries and structures are only possible due to the use of multiple metallic elements [3, 6, 7]. Because MXenes are directly derived from MAX phases (or similarly layered ceramics), MXenes inherit their M–X chemistry from these precursors; therefore, it is imperative to understand the MAX phase chemistry prior to producing MXenes.

When considering multi-M MXenes, they maintain many of the fundamental properties that make MXenes as a class attractive, such as ease of processibility in water, redox-capable surfaces, scalability of manufacturing, and so forth [8–10], but the individual MXene-based properties vary. Within MXene literature, there are two primary types of multi-M MXenes presented (Figure 9.1), disordered and ordered MXenes [6, 11, 12]. For the disordered types of MXenes, often called solid-solution MXenes, the multiple-M elements are randomly distributed throughout the layers, with no long- or short-range order. For the ordered MXenes, there are two types reported: out-of-plane ordered MXenes and in-plane ordered MXenes, both have specific available chemistries and result from thermodynamic ordering in the precursor MAX phase structure. Both disordered and ordered MXenes lead to different, often unique properties, but in different ways, making both classes of MXenes inherently valuable for different applications. Herein, the scope of this chapter will first focus on the synthesis of MAX phases with multiple-M chemistries and how to know if this MAX can be used for MXene synthesis. Then, the synthesis, properties, and applications of random solid-solution MXenes, followed by ordered MXenes, will be discussed. Finally, the outlook and future directions will be considered.

9.1.1 Synthesis of MAX

Within the MAX phase community are a variety of approaches to produce these ceramic precursors, including high-temperature reactions of the powders in a furnace [1, 13], hot isostatic pressing [14, 15], self-propagating high-temperature synthesis [16–18], microwave synthesis [19, 20], spark plasma synthesis [21, 22],

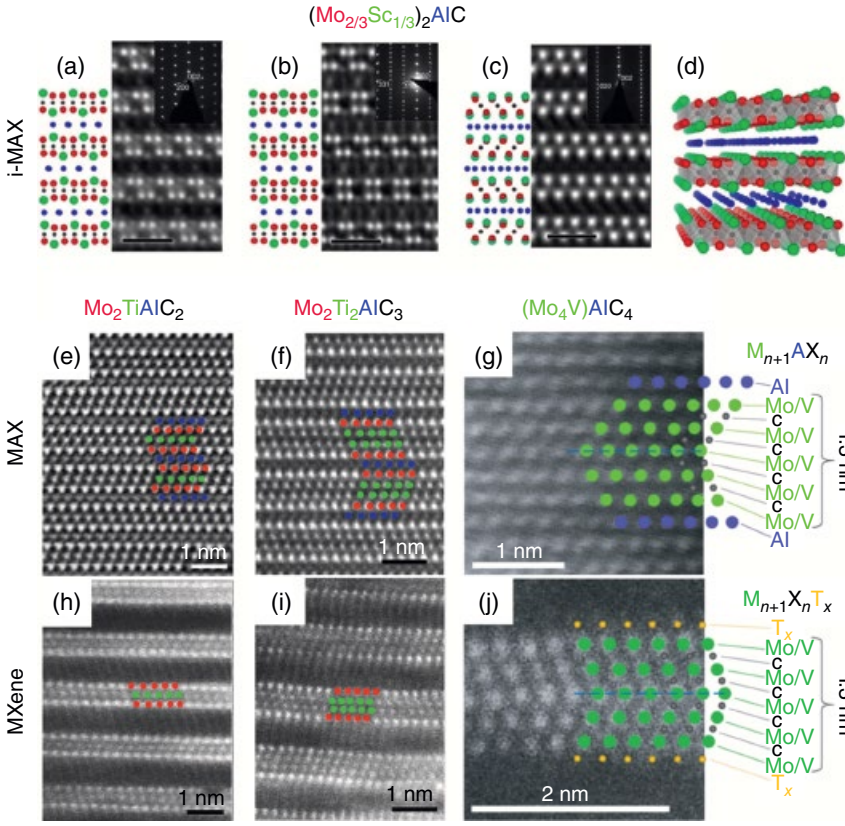


Figure 9.1 High-resolution scanning transmission electron microscopy (HRSTEM) and corresponding selected area electron diffraction (SAED) patterns of $(Mo_{2/3}Sc_{1/3})_2AlC$ along the (a) [010], (b) [110], and (c) [100] crystal orientation, together with schematics based on a monoclinic C_2/c symmetry. The shaded spheres in the schematics are Mo, Sc, Al, and C, respectively. (d) Three-dimensional schematic of the *i*-MAX phase. (e) HRSTEM of Mo_2TiAlC_2, (f) $Mo_2Ti_2AlC_3$, and (g) Mo_4VAlC_4 MAX phases. STEM images of (h) $Mo_2TiC_2T_x$, (i) $Mo_2Ti_2C_3T_x$, and (j) $Mo_4VC_4T_x$ MXenes. For the panels (e, f, h, i), the shaded spheres represent Al, Mo, and Ti, respectively. For the panels (g, j), the shaded spheres represent Mo/V, Al, and surface terminations T_x. Images in (g) and (j) demonstrate a herringbone-type structure with an atomic schematic and mirror plane shown by solid circles on the right and a dashed line, respectively. *Source:* Shekhirev et al. [11]/Reproduced with permission from Elsevier.

molten salt synthesis [23, 24], molten metal synthesis [25–27], and others [28–30]. Each approach leads to different MAX phase morphologies and properties. The most common approach for MXene literature is via high-temperature synthesis of powder mixtures [11], but it is important to note that there are a few reports of MAX phases that can only be produced through specific routes [19, 31].

Considering these different approaches, in addition to the variety of MAX phases available, it is necessary to consider if the MAX is appropriate to use for MXene synthesis. Due to the nature of MAX phases, it is common for there to be multiple MAX phases present after synthesis (M_2AX, M_3AX_2, M_4AX_3, M_5AX_4; Figure 9.2), and this is especially the case when multiple chemistries are present. For any MAX to be suitable for MXene synthesis, there must only be one MAX phase present; if there are multiple MAX phases present, it is impossible to separate the two resultant MXenes; moreover, understanding the chemistry of the MAX phases present becomes increasingly difficult. Considering this, it is important to note that the presence of metals, intermetallics, and bulk carbides/nitrides are not concerning because the MXene can be delaminated and separated from these bulk components. If the MXene is going to be used as multilayer powder, then it is also important to minimize the bulk carbides/nitrides, as the metals/intermetallics can be removed by acid washing [13].

The best way to confirm phase purity of MAX phases is with X-ray diffraction (XRD) because the *c*-lattice parameter is directly related to the number of MX layers, making is easy to distinguish between the different structures (M_2AX vs. M_3AX_2, for example) by comparing the (002) peak (Figure 9.2). For multiple

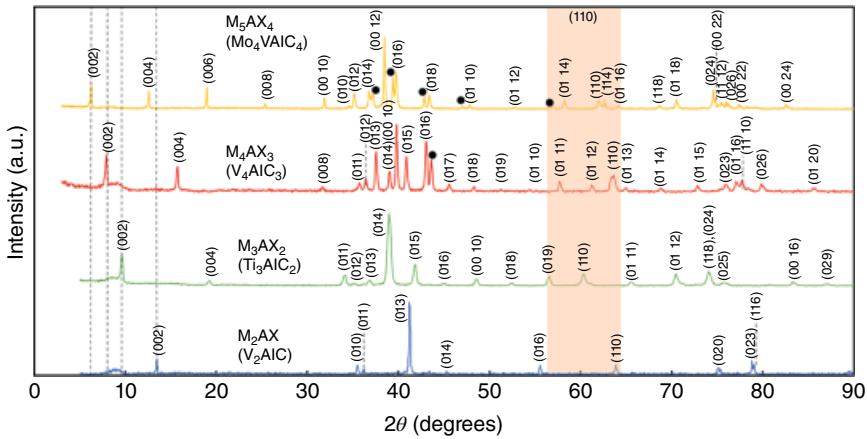


Figure 9.2 Representative X-ray diffraction (XRD) patterns of an M_2AX, M_3AX_2, M_4AX_3, and M_5AX_4 structure with texturing (pressure) applied. The (002) peak is the primary identification peak to determine *n* of the MAX phase in the precursor mixture. The (002) peak is characteristic of the *c*-lattice parameter in MAX phases, and it is imperative that experiments are conducted with only one MAX phase prior to topochemical synthesis to MXene. The box highlights the location of the (110) peak, which is characteristic of the *a*-lattice parameter. The XRD patterns of MAX phases (V_2AlC, Ti_3AlC_2, V_4AlC_3, and Mo_4VAlC_4; synthesized according to the references) show impurity phases (carbide and intermetallic impurities are marked with a circle), but contain only a single MAX phase. *Source:* Reproduced from Shekhirev et al. [11]/with permission from Elsevier.

M-chemistries, it is vital to also ensure that there are not multiple MAX phases of the same structure (two M_2AX phases, for example), by examining if two (002) peaks occur in the same proximity. Once it is confirmed that there is only a single MAX phase, it is then appropriate to use those conditions for MXene synthesis.

In addition to use for synthesis, it is invaluable to properly characterize the MAX phase as produced. As previously mentioned, the chemical ordering of MAX phases carries over to MXenes, so characterization at this step is often easier than for MXenes. For example, transmission electron microscopy (TEM) analysis of MAX phases is significantly easier than MXenes because MAX phases are very resistant to beam damage, and conventional TEM sample preparation techniques apply. Indeed, a significant portion of structural characterization and TEM imaging is done primarily on the MAX phases, rather than MXene [3, 7, 32–34]. This is the case for a wide variety of spectroscopic and imaging techniques, from XRD to Raman spectroscopy [11, 35, 36]. MAX phases are air-stable, oxidation, and high-temperature resistant [5], making structural characterization less of a challenge. Moreover, for techniques such as XRD, it is easier to correlate the c and a-lattice parameters with the chemistry for MAX phases [11, 37], rather than MXenes, due to the added complication of intercalation for MXenes.

9.2 Random (Disordered) Solid Solutions

Solid-solution MXenes are the most common type of multi-M (or multi-X) [109] MXene. In these cases, the M layer is a random mixture of all metals, with no specific ordering; the elements are truly homogeneously mixed and randomly oriented [37, 38]. Structurally, these follow Vegard's law and have a continuous shift in the lattice parameters from one extreme to the other. There have been a variety of solid-solution MXenes discovered, including $Ti_{2-y}Nb_yT_x$ [37], $Nb_{2-y}V_yT_x$ [37], $Ti_{2-y}V_yT_x$ [37], $Ti_{3-y}Ta_yT_x$ [39], $Mo_{4-y}V_yT_x$ [40], $Nb_{4-y}Zr_yT_x$ [41], $Nb_{4-y}Ti_yT_x$ [41], and $Mo_4VC_4T_x$ [3] being the only family of MXenes that spans $n = 1$–4 to date. There have been a large number of solid-solution MAX phases that have been synthesized, but the majority have not been converted to MXenes yet [4].

For many single-M MXenes, their fundamental properties are relatively constant due to their base chemistry. This is one feature of solid-solution MXenes that makes them attractive; the continuous modification of chemistry will carry over to their properties. This allows solid-solution MXenes to be synthesized with targeted properties in mind – if the extremes of each chemistry are known, one can interpolate the solid-solution properties to target specifics. It is important to note that some properties of solid-solution MXenes linearly follow these relationships, while others are nonlinear. For the linear properties, it is the case that the property-values can be directly targeted, such as electrical conductivity, but for some

others, the nonlinear relationship between chemistry and properties provides additional complication, but opens the field to new, exciting applications that could not be targeted otherwise.

Generally, for solid-solution MXenes, synthesis of the MXene from MAX is not the same for all compositions. Using $Ti_{2-y}V_yT_x$ as an example, it is well known that the synthesis of Ti_2CT_x from Ti_2AlC is a relatively short, mild approach, with low-HF concentrations and low temperatures [42–44]. On the other extreme, V_2CT_x is synthesized using high-HF concentrations, often coupled with elevated temperatures [45–47]. For solid-solution MXenes, this leads to intermediate conditions to synthesize each middle composition; $Ti_{0.4}V_{1.6}T_x$ (50 wt% HF), $Ti_{0.8}V_{1.2}CT_x$ and $Ti_{1.2}V_{0.8}CT_x$ (30 wt% HF), and $Ti_{1.6}V_{0.4}CT_x$ (10 wt% HF) all were produced for 24 hours at 35 °C, with the only difference being the HF concentration [37]. This adds a bit of difficulty to directly comparing the effect of chemistry on MXene properties. Since differences in etching lead to differences in the kind and concentration of defects, surface chemistry, and flake size [11, 48–51], this adds some uncertainty to direct comparison between the different MXene compositions. These effects will also carry over to specific properties, such as gas sensing and electrochemistry [52–55]. Further studies focusing on kinetics and the relationship between the surface chemistry and etching approach for solid-solution MXenes are necessary to fully understand and quantify these differences.

9.2.1 Properties and Applications of Random Solid Solutions

For solid-solution MXenes, some properties appear to be linearly related to the chemistry, while others are nonlinearly related. The electrical conductivity of solid-solution MXenes, appear to be directly related to the chemistry in a linear way (Figure 9.3). Nb_2CT_x is well known to have a low electrical conductivity, typically measured ~25 S cm^{-1} in multilayer films [56]. Whereas Ti_2CT_x and V_2CT_x have conductivities >1000 S cm^{-1} [42, 45, 56]. Using $Ti_{2-y}Nb_yCT_x$ and $V_{2-y}Nb_yCT_x$ as examples, as the Nb content increases, the conductivity decreases. This monotonic trend continues over the entire compositional range, with the measured film conductivities being predictable based on the composition alone. All of the measured films also show similar resistivity vs. temperature trends, demonstrating semiconductor-like dependences, likely due to the dominant role of interflake hopping or localization of charge carriers in the disordered metal sites.

Controlling the MXene electrical conductivity to such a degree gives unparalleled control over some applications, such as electromagnetic interference shielding (EMI). Within EMI shielding, there is a direct relationship between the conductivity and EMI shielding effectiveness (SE), for example [56–58]. This means that the EMI-SE can be rationally chosen based purely on the initial MXene chemistry. Other applications that rely on conductivity similarly benefit, such as

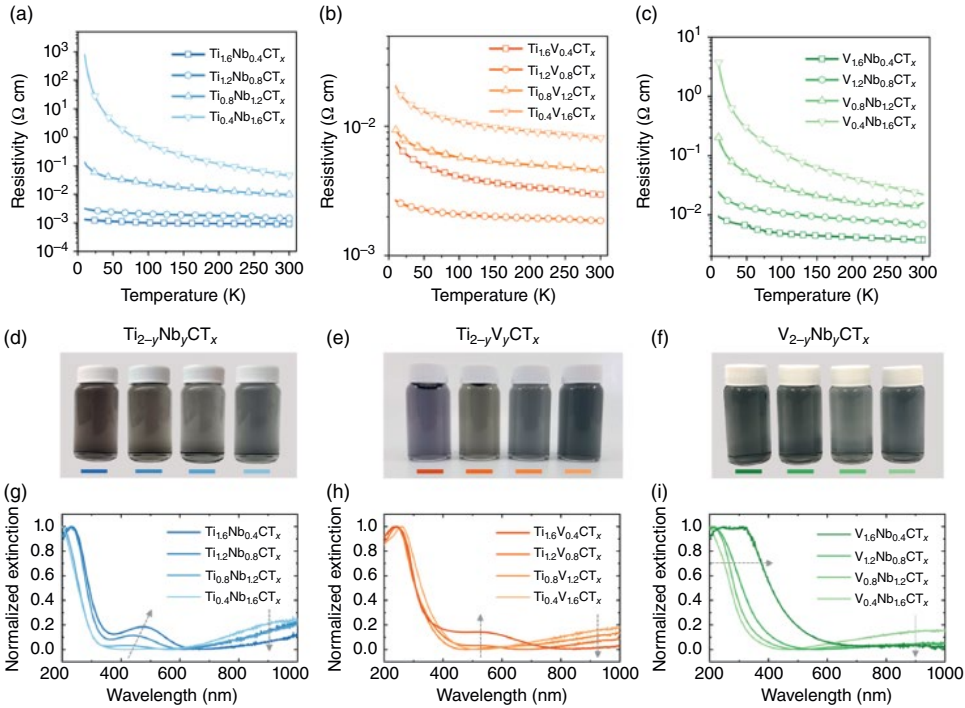


Figure 9.3 The temperature-dependent electrical properties of (a) $Ti_{2-y}Nb_yCT_x$, (b) $Ti_{2-y}V_yCT_x$, and (c) $V_{2-y}Nb_yCT_x$. The optical properties of solid-solution (d) $Ti_{2-y}Nb_yCT_x$, (e) $Ti_{2-y}V_yCT_x$, and (f) $V_{2-y}Nb_yCT_x$ colloidal solutions in deionized water. In all three systems, the gradual change in color resulting from the different stoichiometries can be observed. The quantitative UV–vis spectra normalized to a maximum extinction of 1 of the (g) $Ti_{2-y}Nb_yCT_x$, (h) $Ti_{2-y}V_yCT_x$, and (i) $V_{2y}Nb_yCT_x$ systems. For all systems, multiple features are visible with a nonlinear shift in the absorbance with changes in the composition. *Source:* Reproduced from Han et al. [37]/American Chemical Society.

gas sensing. Typically, gas sensing for MXenes utilized the change in conductivity as gases adsorb onto the surface [59–61]. Broadly, to date, most MXene gas sensors rely purely on $Ti_3C_2T_x$, but this is a limited approach because mixtures of gases will lead to changes in conductivity that cannot be correlated with the change in conductivity. The solution to this problem relies on the use of multiple MXenes, and solid-solution MXenes provide the ideal solution to this problem. Arrays of solid-solution MXenes can be developed that can sense gases, and due to the rationally tailored electrical conductivity, even mixtures of gases can be detected and correlated to the changes in conductivity of arrays.

Other properties of solid-solution MXenes are not linearly related to the chemistry. One key example of this is the optical properties of MXenes (Figure 9.3). For single-M MXenes, there will be a single plasmon resonance peak that depends on the etching/delamination conditions [42, 62]. For solid-solution MXenes, there is instead a double plasmon resonance peak. Both peaks are related to the chemistry of the MXenes themselves, but shift in relation to each other. This is due to the modification of the electronic states of each M element due to the other, as was shown with electron energy loss spectroscopy [63] in addition to computational predictions [37]. It is important to note that not all M elements experience a change in their electronic states. Using $Ti_{2-y}Nb_yCT_x$ and $V_{2-y}Nb_yCT_x$ as examples again, Ti in this case does not experience a modification of its electronic state, but V does. The fact implies that the electronic properties of solid-solution MXenes will require significant future study to truly understand the observed trends and predict the properties of other solid-solution MXenes. In these cases, it was noted that carbon itself does not experience a change in its oxidation state, but only the metals.

These nonlinear properties tend themselves to interesting applications that take advantage of this complication. Consider, for example, the nonlinear plasmon resonance change. MXenes are known to be electrochromic [64, 65]. When a charge is injected into the MXene, the plasmon resonance peak shifts accordingly, thereby visually changing the MXene color, but also affecting the oxidation state (Fermi level) of the metals. With solid-solution MXenes, this dual plasmon resonance leads to a further nonlinear trend where both plasmon resonance peaks shift when a charge is injected [44]. This leads to optoelectronic device performance that cannot be attained with conventional single-M MXenes, and therefore to applications that require absorption at two wavelengths in a controllable manner, such as photocatalysis, light-to-heat conversion, surface-enhanced Raman spectroscopy, or for other optoelectronic applications [66–69]. Understanding this nonlinearity by studying the chemistry and structure relationships will lead to novel applications that no other class of MXene can fulfill.

The electrochemistry of solid-solution MXenes benefits from the multiple chemistries. While the electrochemistry of single-M MXenes, such as $Ti_3C_2T_x$, has

been extensively studied [70], there are very few studies focused on the electrochemical properties and applications of solid-solution MXenes [40, 71]. For $Ti_{2-y}Nb_yCT_x$ and $V_{2-y}Nb_yCT_x$, it was shown that the cyclic voltammograms (CVs) change with their chemistry (Figure 9.4) [71]. Depending on the specific chemistry, the volumetric (gravimetric) capacitance ranged from 680 to 1070 F cm^{-3} (245–490 F g^{-1}) in 3 M H_2SO_4. Notably, there is no visible redox peak for Nb_2CT_x, but there is for V_2CT_x and Ti_2CT_x. The electrochemical CV appears to be a convolution of both types of MXene, with the redox peak for each element present in similar locations to their pure counterparts. The solid-solution MXenes benefit from the other element – both Ti_2CT_x and V_2CT_x are relatively unstable, whereas Nb_2CT_x is quite stable electrochemically. Conversely, Nb_2CT_x has a low capacitance relative to Ti_2CT_x or V_2CT_x. The solid-solutions, however, contain the benefits of both chemistries – enhanced stability and increased capacitance. The addition of Nb stabilizes the solid-solution MXenes, giving them a higher capacitance retention, while Ti or V increases the overall capacitance. In some cases, such as $V_{1.2}Nb_{0.8}CT_x$, the gravimetric capacitance exceeds either extreme, even though Nb is roughly double the atomic weight of V [71]. This same outperformance was observed for other solid-solution MXenes as well, such as $Mo_{4-y}V_yC_3T_x$ [40]. This illustrates the potential for solid-solution MXenes. They experience different properties than single-M MXenes, and can lead to enhanced properties that outperform either extreme. Understanding the why behind this enhancement will pave the way to improve the performance of all MXenes.

One enigmatic member of the disordered solid-solution family are $M_5X_4T_x$ MXenes [3]. To date, only solid-solution MXenes have been demonstrated to form $M_5X_4T_x$ MXenes, including $Mo_4VC_4T_x$, $Ti_{2.5}Ta_{2.5}C_4T_x$, and $Ti_{2.675}Nb_{2.325}C_4T_x$, even though many more MXenes have been predicted to exist in this system. Using $Mo_4VC_4T_x$ as an example, the Mo/V layers are randomly distributed throughout all five layers; however, this MXene, and the other $M_5X_4T_x$ MXenes, is only stable at one composition. It was reported that modification of the chemical composition by ~5% in either direction leads to formation of other phases. This MXene possesses unique properties, beginning with its structure – $Mo_4VC_4T_x$ has a twinned structure (Figure 9.1) centered on one of the metallic layers; this is unlike any other MXene discovered to date. Using TEM, it was reported that there was evidence of even higher-ordered MAX phases present at the impurity level. Moreover, $Mo_4VC_4T_x$ possessed the highest thermal stability of any MXene, low optical absorption in the visible range, and was highly resistant to the effects of organic intercalants on its electrical properties [3, 11, 72]. Further study is necessary for this class of solid-solution MXenes. Understanding why this MXene has its peculiar structure and properties may enable targeted discovery of novel MXenes with different structures and chemistries that may be nonobvious or compositionally strict.

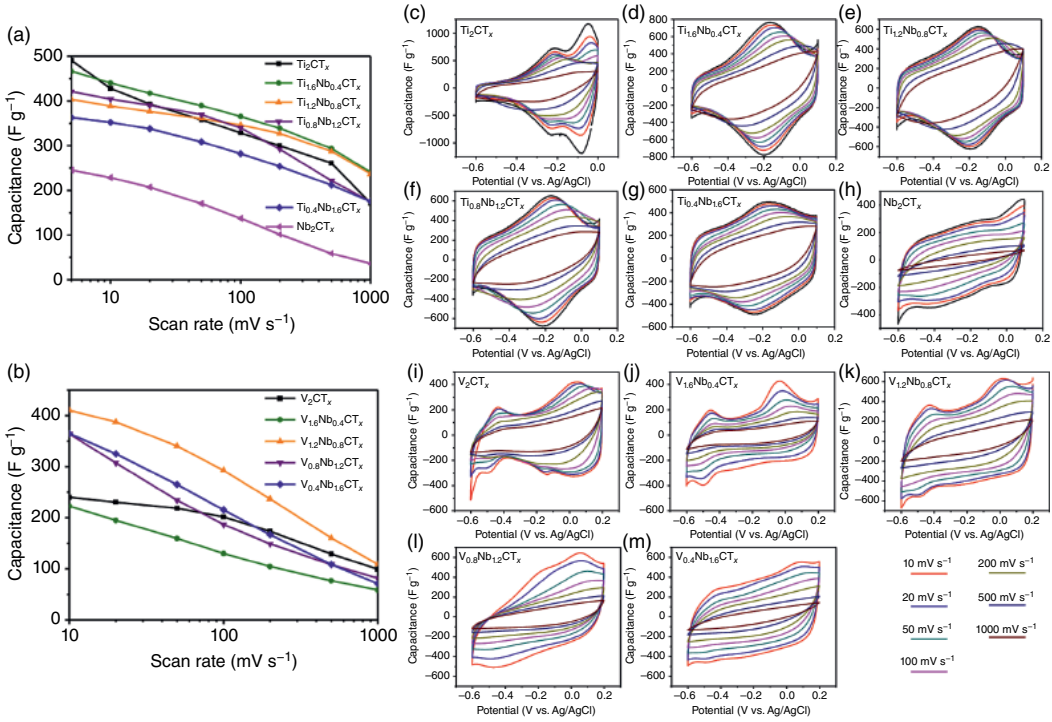


Figure 9.4 Specific capacitance of (a) $Ti_{2-y}Nb_yCT_x$ and (b) $Nb_{2-y}V_yCT_x$ as a function of scan rate. Cyclic voltammetry (CV) curves of $Ti_{2-y}Nb_yCT_x$ (from (c) to (h)): y = 0, 0.4, 0.8, 1.2, 1.6, and 2, and $Nb_{2-y}V_yCT_x$ ((i) to (m)): y = 0.4, 0.8, 1.2, 1.6, and 2, respectively, obtained in 3 M H_2SO_4 electrolyte at scan rates from 5 mV s^{-1} to 1000 mV s^{-1}. *Source:* Reproduced from Gauthier et al. [71]/with permission from Elsevier.

9.2.2 High-Entropy MXenes

One extreme example of solid-solution MXenes is the recently synthesized high-entropy MXenes that contain several M elements, rather than just two [73, 74]. These high-entropy systems have been synthesized as both M_2XT_x and $M_4X_3T_x$, with multiple observed chemistries for each. These classes of MXene provide a new direction that can incorporate the benefits of many chemistries into MXene structures. They have been proposed for use as catalysts, electrochemical materials, or for applications in extreme environments. However, significant experimental and theoretical work needs to be done to understand the relationship between chemistry and properties in these systems. Moreover, the synthesis of these phases poses quite the challenge to ensure that there is only a single MAX phase, without separation of the elements into multiple MAX phases, even of the same structure [75]. Due to the complex structure of these materials, it is unlikely that they will retain the high electrical conductivity present in some MXenes, yet may provide attractive electronic properties and chemical properties.

9.3 Ordered MXenes

Within some MXene chemistries, instead of randomness within the structure, it is more thermodynamically favorable to form ordered structures. Depending on the structure of the precursor MAX phase (e.g. M_2AX against M_3AX_2/M_4AX_3/etc.), this can take the form of in-plane ordered structures (*i*-MAX) or out-of-plane (*o*-MAX) ordered structures (Figure 9.1). Notable, to date, M_2AX structures only showed in-plane ordering, while M_3AX_2 and M_4AX_3 only have out-of-plane ordering. Due to this thermodynamic ordering of the MAX phase, the respective MXenes with unique chemical, optical, and electronic properties can be produced. However, it is important to note that these MXenes only have one thermodynamically stable composition, so they should be considered stoichiometric MXenes, similar to single-M MXenes. This, in turn, leads to less property customizability than solid-solution MXenes, but grants different properties compared to single-M MXenes.

9.3.1 Out-of-Plane Ordered *o*-MXenes

Out-of-plane ordered MXenes, initially called ordered double transition metal MXenes, such as $Mo_2Ti_2C_3T_x$, $Mo_2TiC_2T_x$, $Mo_2ScC_2T_x$ [76], or $Cr_2TiC_2T_x$ [6], have two metal elements that are separated into two different layers (Figure 9.1). In these, the Mo/Cr layers are on the outer surface, with Ti/Sc being in the middle layer. Even though more than 20 *o*-MXenes were predicted to exist, this class of

MXenes is still relatively small in number, with only a few other MAX precursor of this type currently synthesized: Cr_2VAlC_2 [77], Ti_2ZrAlC_2 [78], and $Cr_2V_2AlC_3$ [77]. While these MAX phases have been synthesized, they have not been successfully topochemically converted to MXenes.

The out-of-plane MXenes offer novel chemistries that cannot be easily accessed (or at all) with single-M MXenes. To date, there has not been a successful, high-quality synthesis of Cr_2CT_x, but because $Cr_2TiC_2T_x$ exists [79, 80], it is possible to study how Cr acts on the outer surface. For other chemistries, such as Mo-based MXenes, it is difficult, expensive, and time-consuming to produce Mo_2Ga_2C as a precursor for Mo_2CT_x [81], but producing $Mo_2Ti_2AlC_3$ or Mo_2TiAlC_2 [6], and the following MXenes, is simple and follows standard powder metallurgical synthesis approaches. These MXenes have pure Mo surfaces, allowing one to probe this chemistry, avoiding the alternative difficult route.

Another benefit of this class of MXenes is in the modification of the electronic, optical, and chemical properties. It was shown that the metal on the inner layer affects the outer transition metal electronic state and vice versa both experimentally [82–84] and computationally [85–87]. Moreover, it was shown that the surface terminations do not significantly affect the electronic structure of the internal metal layer [82]. This implies that there are essentially two levers to control the surface metal electronic state, surface terminations (which occur due to the etching approach) and the subsurface metal. Correspondingly, *o*-MXenes have optical properties that differ from single-M MXenes [42]. $Mo_2TiC_2T_x$ has a transverse surface plasmon resonance peak at 476 nm, whereas $Ti_3C_2T_x$ is at 780 nm. This implies that $Mo_2TiC_2T_x$ should have a higher free electron density, but this has not been confirmed with the electrical conductivity measurements so far (~1500 S cm^{-1} for $Mo_2TiC_2T_x$ against >20,000 S cm^{-1} for $Ti_3C_2T_x$) [25, 88], however, this has been the case with other MXenes as well. Moreover, $Cr_2TiC_2T_x$ is currently the only MXene incorporating Cr on the surface that can be produced in high quality [79, 80]. $Cr_2TiC_2T_x$ is also unique among discovered MXenes; it is the only one to have an experimentally measured magnetic transition resulting from the MXene itself (Figure 9.5). The magnetic transition appears to be a spin-freezing transition where the local interactions are strong, but the mixed surface terminations and random orientation of flakes of the vacuum-filtered film prevent long-range magnetic order [80]. Further studies on single-flake $Cr_2TiC_2T_x$ are needed to determine the exact nature of this transition.

Computationally, *o*-MXenes have been predicted to have many exciting electronic and chemical properties [89, 90], such as topological semiconductor bandgaps ranging from 0.12 to 1.26 eV [86], depending on the specific chemistry and surface termination. Ferromagnetism is a desirable property for 2D materials and has been predicted for a number of *o*-MXenes, including $Ti_2MnC_2T_x$, $Cr_2VC_2T_x$, $Hf_2VC_2O_2$, and others [86, 91]. In some cases, depending on the specific surface

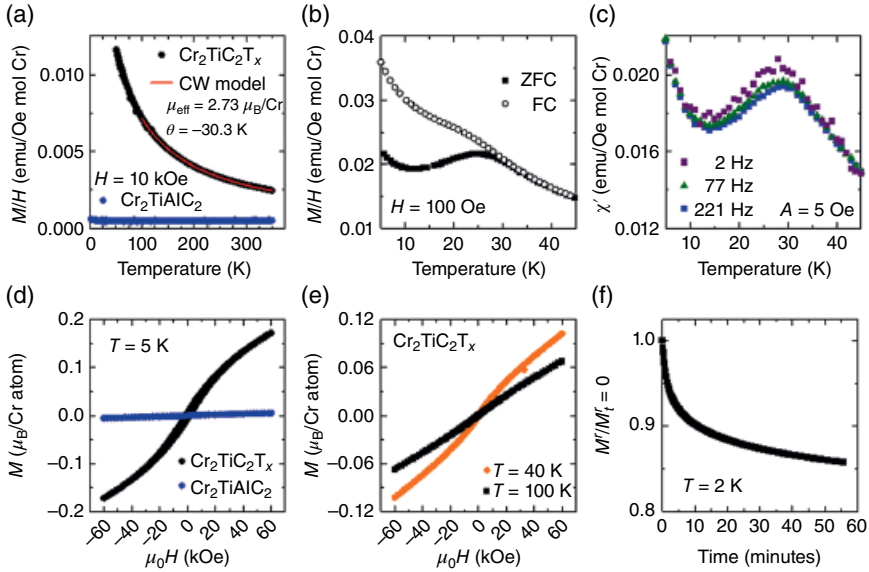


Figure 9.5 Magnetic characterization of $Cr_2TiC_2T_x$ MXene and Cr_2TiAlC_2 MAX phase. (a) Field-cooled (FC) magnetization of $Cr_2TiC_2T_x$ MXene (black) and Cr_2TiAlC_2 MAX phase (blue) measured using 10 kOe external magnetic field. The data from $Cr_2TiC_2T_x$ was fitted with Curie–Weiss (CW) model. (b) Zerofield-cooled (filled squares) and field-cooled (empty circles) magnetization from 5 to 45 K of $Cr_2TiC_2T_x$ MXene. (c) In-phase component of ac susceptibility measured at zero dc field with an amplitude of 5 Oe and frequencies ranging from 2 to 221 Hz. (d) Field-dependent magnetization of $Cr_2TiC_2T_x$ MXene (black) and Cr_2TiAlC_2 MAX phase (medium grey) measured at 5 K. (e) Field-dependent magnetization of $Cr_2TiC_2T_x$ MXene measured at 40 K (light grey) and 100 K (black). (f) Time-dependent magnetization measured after cooling $Cr_2TiC_2T_x$ MXene from 300 to 2 K in 60 kOe external field. *Source:* Reproduced from Hantanasirisakul et al. [80] with permission from the Royal Society of Chemistry.

chemistry or internal strain, the magnetic properties are predicted to change [92, 93]. Unfortunately, due to the difficulty in producing the MAX phase or topochemical conversion of the MAX to MXene, many of these properties have not been experimentally realized.

Out-of-plane MXenes have been explored for a variety of applications to date, ranging from electrochemical energy storage to biomedicine. For example, thermoelectric properties of $Mo_2Ti_2C_3T_x$ and $Mo_2TiC_2T_x$ have been studied, showing Seebeck coefficients of −27.5 and −47.3 $\mu V K^{-1}$, respectively [88]. $Mo_2TiC_2T_x$ was also used for electrochemical energy storage, showing a stable capacity of 176 $mAh g^{-1}$ in 1 M H_2SO_4 [6], and is promising for Na-ion batteries [94]. In addition, it was used as a strengthening additive for Mo-alloys [95] and has been proposed for electrocatalysis [96]. Interestingly, $Mo_2Ti_2C_3T_x$ was found to have

antiviral capabilities against the SARS-CoV-2 virus [97]. While the *o*-MXenes have not been extensively studied, they have already shown promise for multiple applications due to their unique properties.

9.3.2 In-Plane Ordered *i*-MXenes

In-plane ordered MXenes, called *i*-MXenes, are synthesized from $(M'_{2/3}M''_{1/3})_2AlC$ *i*-MAX phases (Figure 9.1) where M′ is typically Mo, W, V, Cr, and M″ is Sc, Zr, or Y, or some lanthanides. These MAX structures generally result from atom size differences (M″ must be >0.2 Å larger than M′) between the M elements being so large that it is more thermodynamically favorable to slightly strain the lattice and reduce the entropy, causing the lower concentration metal element to occupy atomic rows along the MAX phase. The most common in-plane ordered MAX phases are $(Mo_{2/3}Sc_{1/3})_2AlC$ [7] or $(Mo_{2/3}Y_{1/3})_2AlC$ [98], but there are a wide variety of others synthesized to date [12, 34, 99, 100]. These MAX phases have an interesting quirk – depending on the synthesis conditions, it is possible to produce, for example, $(Mo_{2/3}Sc_{1/3})_2CT_x$ or $Mo_{4/3}CT_x$ depending on the harshness of etching [33]. This has obvious benefits related to being able to produce either MXenes with multiple metallic chemistries or to produce MXenes with ordered, controllable defect (M vacancy) sites. It is likely that there will be a mixture of both motifs present, complicating analysis. Moreover, not all MXenes of the formula $M_{4/3}CT_x$ have ordered vacancies [101]. With the majority of the in-plane ordered MAX phase chemistries, synthesis of the MXenes has tended toward formation of the defective structures, rather than the double metal structures.

The defective $M_{4/3}CT_x$ MXenes function as a double-edged sword. On one hand, their highly defective structure gives them the potential to be more chemically active than standard MXenes. This, in some cases, leads to high capacitance or catalytic ability [12]. Moreover, their structure can give insight into the role of defects in MXenes and allow scientists to use them to verify models based on defects. On the other hand, these MXenes tend to be chemically unstable. Oftentimes, the flake sizes are small, with many pinhole defects and significant oxidation [101], leading to rapid degradation of their properties. This especially becomes a problem with applications that require long-term stability, such as catalysis or energy storage. Another issue with these MXenes is the cost associated with them – little research is conducted on Sc/Y containing MXenes due to their high cost, which makes them untenable for applications that have alternative, often orders of magnitude cheaper, materials [102].

The *i*-MXenes have primarily been studied for electrochemical energy storage or catalysis. $Mo_{4/3}CT_x$ was shown to have a volumetric (gravimetric) capacitance of 1153 F cm^{-3} (339 F g^{-1}) [7], which is high among MXenes, but not exceptional; notably, this is ~65% higher than Mo_2CT_x itself [103]. More recent comparisons

between the two indicate that $Mo_{4/3}CT_x$ has a slightly higher volumetric capacitance and energy density, at the exchange of lower stability and a faster self-discharge rate (Figure 9.6) [104]. For the MXenes, such as $(Mo_{2/3}Y_{(1-x)/3})_2CT_x$, the weak bonding in the structure leads to inhomogeneous defects in the Y layer, leading to difficulty in reproducibly synthesizing the same material between experiments; moreover, the mild etching conditions lead to yield issues [33]. Apart from electrochemical energy storage, *i*-MXenes have been explored as an electrocatalyst for use under reducing conditions, such as hydrogen evolution reaction [105].

9.4 Outlook

MXenes have an enormous variety of structures and chemical compositions, offering very attractive and tunable properties. This has led to rapid advances in their synthesis, studies of a wide range of properties, and evaluation for many potential applications. The majority of studies focused on a select few MXenes, namely $Ti_3C_2T_x$, Ti_2CT_x, and V_2CT_x. While these results have been promising so far, there are more than 30 stoichiometric MXenes discovered to date, and about 20 solid solutions and high-entropy compositions that show promising properties and may have applications as well. Taking into account that at least a hundred base stoichiometric compositions of MXenes should be possible, 10 different surface terminations have already been demonstrated and a theoretically infinite number of solid-solution MXenes can be produced, there is a very wide research field open for exploration and discovery science. The wide variety of chemistries and structures available for the MXene family is one of the biggest strengths of this class of materials – the ability to change the structure, metal chemistry, C/N ratio, and surface chemistry gives a degree of tunability that hardly any other class of 2D materials can compete with.

There are broadly three classes of multi-M MXenes, random (disordered) solid-solution MXenes, out-of-plane ordered MXenes, and in-plane ordered MXenes. Each of these classes has its own structural motifs and chemistries available, leading to unique electronic, optical, and chemical properties. In many cases, these MXenes have properties that cannot be accessed by single-M MXenes whatsoever, allowing them to fill applications that no other MXene can, especially since the properties can be finely tuned via the elemental composition within the same structure. These classes of MXenes are newer and have received less attention than single-M MXenes. Due to this, there are many directions to pursue that may bring high-impact discoveries.

Due to the large number of chemistries available, there are many theoretically predicted MAX and MXene compositions, which are expected, based on atomistic simulations, to have desirable properties, but are yet to be synthesized [3, 6, 86, 106, 107].

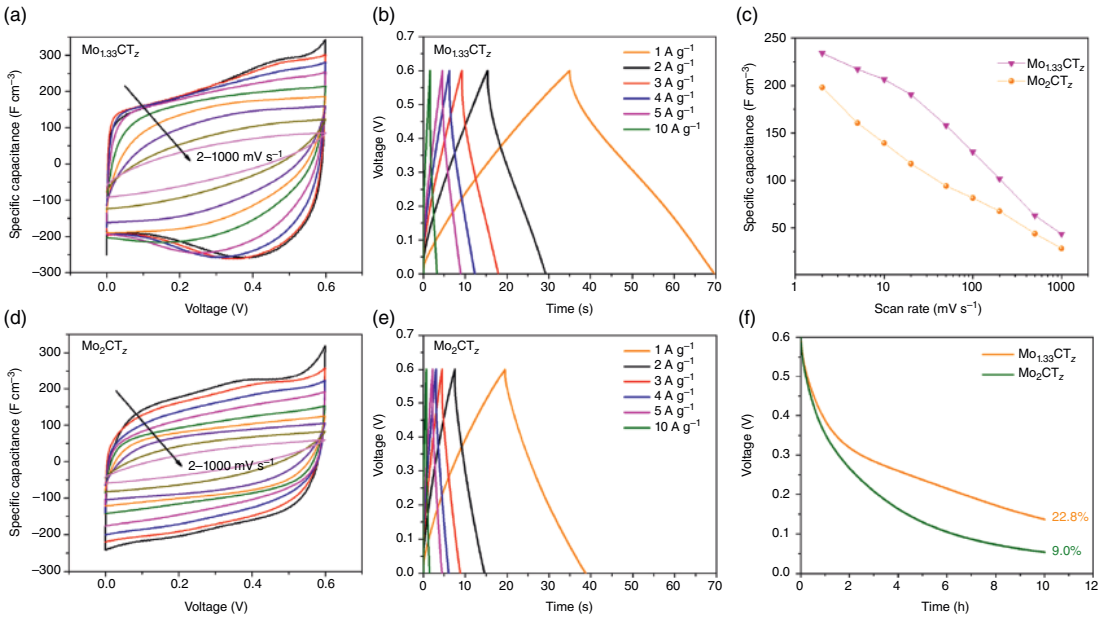


Figure 9.6 Electrochemical performance of $Mo_{4/3}CT_x$ and Mo_2CT_x symmetric supercapacitors in 1 M H_2SO_4 electrolyte. (a) and (d) CV curves of $Mo_{4/3}CT_x$ and Mo_2CT_x symmetric supercapacitors as a function of scan rates from 2 to 1000 mV s^{-1}, respectively, (b) and (e) galvanostatic charge/discharge curves of $Mo_{4/3}CT_x$ and Mo_2CT_x symmetric supercapacitors at different current densities. (c) specific capacitance of $Mo_{4/3}CT_x$ and Mo_2CT_x symmetric supercapacitors as a function of scan rates; (f) self-discharge performance of $Mo_{4/3}CT_x$ and Mo_2CT_x symmetric supercapacitors. *Source:* Reproduced from Zheng et al. [104]/with permission from Elsevier.

There is room for improvement of synthesis procedures for all classes of MXenes, but this is especially the case for mixed-M MXenes because most studies have investigated only one synthesis/delamination condition through the entire process. As more MXenes with different chemistries become available for study, modeling that relates the chemistry and structure to properties will consequently get more accurate, leading to acceleration on both experimental and computational studies of MXenes. This is especially the case for MXenes that are predicted to have interesting magnetic and electronic properties and applications [86, 91, 108]. More systematic studies need to be conducted on different solid-solution MXenes to determine which trends can be generalized, and which are related to interactions of specific elements [37, 40, 56, 71]. Additional work needs dedicated to discovery and understanding of the $M_5X_4T_x$ solid solution MXenes – to date only three have been discovered with only one stable composition each. Does this hold true for all $M_5X_4T_x$ MXenes, or will others be discovered that have more forgiving chemistries? [3] For either disordered/ordered MXenes, is it possible to synthesize both structural motifs with the same chemistry? If so, how will the properties change due to disorder/order?

Multiple-M chemistry represents an important future direction of MXene development. There is significant work dedicated to surface chemistry and synthesis optimization of common MXenes, and the same degree of effort needs to be applied to multiple-M MXenes. Predictive modeling and simulation should guide the experiments and help navigate. Combining the customization of multiple-M MXenes with precise control over the surface chemistry, flake size, and defect density will provide a platform for unparalleled property control, leading to optimized, rationally designed MXenes for each specific application.

Acknowledgments

The authors acknowledge support from the US National Science Foundation under grant DMR-2041050.

References

1 Naguib, M., Kurtoglu, M., Presser, V. et al. (2011). Two-dimensional nanocrystals produced by exfoliation of Ti_3AlC_2. *Advanced Materials* 23 (37): 4248–4253.

2 Naguib, M., Mashtalir, O., Carle, J. et al. (2012). Two-dimensional transition metal carbides. *ACS Nano* 6 (2): 1322–1331.

3 Deysher, G., Shuck, C.E., Hantanasirisakul, K. et al. (2020). Synthesis of Mo_4VAlC_4 MAX phase and two-dimensional Mo_4VC_4 MXene with five atomic layers of transition metals. *ACS Nano* 14 (1): 204–217.

4 Sokol, M., Natu, V., Kota, S., and Barsoum, M.W. (2019). On the chemical diversity of the MAX phases. *Trends in Chemistry* 1 (2): 210–223.

5 Barsoum, M.W. (2000). The $M_{N+1}AX_N$ phases: a new class of solids. *Progress in Solid State Chemistry* 28 (1-4): 201–281.

6 Anasori, B., Xie, Y., Beidaghi, M. et al. (2015). Two-dimensional, ordered, double transition metals carbides (MXenes). *ACS Nano* 9 (10): 9507–9516.

7 Tao, Q., Dahlqvist, M., Lu, J. et al. (2017). Two-dimensional $Mo_{1.33}C$ MXene with divacancy ordering prepared from parent 3D laminate with in-plane chemical ordering. *Nature Communications* 8: 14949.

8 Maleski, K., Mochalin, V.N., and Gogotsi, Y. (2017). Dispersions of two-dimensional titanium carbide MXene in organic solvents. *Chemistry of Materials* 29 (4): 1632–1640.

9 Akuzum, B., Maleski, K., Anasori, B. et al. (2018). Rheological characteristics of 2D titanium carbide (MXene) dispersions: a guide for processing MXenes. *ACS Nano* 12 (3): 2685–2694.

10 Shuck, C.E., Sarycheva, A., Anayee, M. et al. (2020). Scalable synthesis of $Ti_3C_2T_x$ MXene. *Advanced Engineering Materials* 22 (3): 1901241.

11 Shekhirev, M., Shuck, C.E., Sarycheva, A., and Gogotsi, Y. (2021). Characterization of MXenes at every step, from their precursors to single flakes and assembled films. *Progress in Materials Science* 120: 100757.

12 Ahmed, B., Ghazaly, A.E., and Rosen, J. (2020). i-MXenes for energy storage and catalysis. *Advanced Functional Materials* 30 (47): 2000894.

13 Shuck, C.E., Ventura-Martinez, K., Goad, A. et al. (2021). Safe synthesis of MAX and MXene: guidelines to reduce risk during synthesis. *ACS Chemical Health and Safety* 28 (5): 326–338.

14 Yang, J., Chen, B., Song, H. et al. (2014). Synthesis, characterization, and tribological properties of two-dimensional Ti_3C_2. *Crystal Research and Technology* 49 (11): 926–932.

15 Wang, X. and Zhou, Y. (2002). Microstructure and properties of Ti_3AlC_2 prepared by the solid–liquid reaction synthesis and simultaneous in-situ hot pressing process. *Acta Materialia* 50 (12): 3143–3151.

16 Yeh, C., Kuo, C., and Chu, Y. (2010). Formation of Ti_3AlC_2/Al_2O_3 and Ti_2AlC/Al_2O_3 composites by combustion synthesis in Ti–Al–C–TiO_2 systems. *Journal of Alloys and Compounds* 494 (1-2): 132–136.

17 Gauthier, V., Cochepin, B., Dubois, S., and Vrel, D. (2006). Self-propagating high-temperature synthesis of Ti_3SiC_2: study of the reaction mechanisms by time-resolved X-Ray diffraction and infrared thermography. *Journal of the American Ceramic Society* 89 (9): 2899–2907.

18 Mukasyan, A. and Shuck, C. (2017). Kinetics of SHS reactions: a review. *International Journal of Self-Propagating High-Temperature Synthesis* 26 (3): 145–165.

19 Hamm, C.M., Bocarsly, J.D., Seward, G. et al. (2017). Non-conventional synthesis and magnetic properties of MAX Phases $(Cr/Mn)_2AlC$ and $(Cr/Fe)_2AlC$. *Journal of Materials Chemistry C* 5 (23): 5700–5708.

20 Tran, M.H., Schäfer, T., Shahraei, A. et al. (2018). Adding a new member to the MXene family: synthesis, structure, and electrocatalytic activity for the hydrogen evolution reaction of $V_4C_3T_x$. *ACS Applied Energy Materials* 1 (8): 3908–3914.

21 Zhou, A., Wang, C.-A., and Hunag, Y. (2003). Synthesis and mechanical properties of Ti_3AlC_2 by spark plasma sintering. *Journal of Materials Science* 38 (14): 3111–3115.

22 Zhou, W., Mei, B., Zhu, J., and Hong, X. (2005). Synthesis of high-purity Ti_3SiC_2 and Ti_3AlC_2 by spark plasma sintering (SPS) technique. *Journal of Materials Science* 40 (8): 2099–2100.

23 Pang, Z., Zou, X., Li, S. et al. (2020). Molten salt electrochemical synthesis of ternary carbide Ti_3AlC_2 from titanium-rich slag. *Advanced Engineering Materials* 22 (5): 1901300.

24 Bärmann, P., Haneke, L., Wrogemann, J.M. et al. (2021). Scalable synthesis of MAX phase precursors toward titanium-based MXenes for lithium-ion batteries. *ACS Applied Materials and Interfaces* 13 (22): 26074–26083.

25 Mathis, T.S., Maleski, K., Goad, A. et al. (2020). Modified MAX phase synthesis for environmentally stable and highly conductive Ti_3C_2 MXene. *ACS Nano* 15 (4): 6420–6429.

26 Etzkorn, J., Ade, M., and Hillebrecht, H. (2007). V_2AlC, V_4AlC_{3-x} (x approximately 0.31), and $V_{12}Al_3C_8$: synthesis, crystal growth, structure, and superstructure. *Inorganic Chemistry* 46 (18): 7646–7653.

27 Etzkorn, J., Ade, M., and Hillebrecht, H. (2007). Ta_3AlC_2 and Ta_4AlC_3-single-crystal investigations of two new ternary carbides of tantalum synthesized by the molten metal technique. *Inorganic Chemistry* 46 (4): 1410–1418.

28 Siebert, J.P., Bischoff, L., Lepple, M. et al. (2019). Sol–gel based synthesis and enhanced processability of MAX phase Cr_2GaC. *Journal of Materials Chemistry C* 7 (20): 6034–6040.

29 Jordan, J. L.; Thadhani, N. N. In *Effect of Shock-Activation on Post-shock Reaction Synthesis of Ternary Ceramics*, AIP Conference Proceedings, American Institute of Physics: 2002; pp 1097–1100.

30 Davydov, D.M., Amosov, A.P., and Latukhin, E.I. (2015). *Synthesis of MAX-phase of titanium silicon carbide (Ti_3SiC_2) as a promising electric contact material by SHS pressing method. Applied Mechanics and Materials* 792 Trans. Tech. Publ: 596–601.

31 Istomin, P., Istomina, E., Nadutkin, A. et al. (2016). Synthesis of a bulk Ti_4SiC_3 MAX phase by reduction of TiO_2 with SiC. *Inorganic Chemistry* 55 (21): 11050–11056.

32 Lu, J., Thore, A., Meshkian, R. et al. (2017). Theoretical and experimental exploration of a novel in-plane chemically ordered $(Cr_{2/3}M_{1/3})_2AlC$ i-MAX phase with M = Sc and Y. *Crystal Growth & Design* 17 (11): 5704–5711.

33 Persson, I., El Ghazaly, A., Tao, Q. et al. (2018). Tailoring structure, composition, and energy storage properties of MXenes from selective etching of in-plane, chemically ordered MAX phases. *Small* 14 (17): e1703676.

34 Tao, Q., Lu, J., Dahlqvist, M. et al. (2019). Atomically layered and ordered rare-earth i-MAX phases: a new class of magnetic quaternary compounds. *Chemistry of Materials* 31 (7): 2476–2485.

35 Sarycheva, A. and Gogotsi, Y. (2020). Raman spectroscopy analysis of the structure and surface chemistry of $Ti_3C_2T_x$ MXene. *Chemistry of Materials* 32 (8): 3480–3488.

36 Kim, Y.-J., Kim, S.J., Seo, D. et al. (2021). Etching mechanism of monoatomic aluminum layers during MXene synthesis. *Chemistry of Materials* 33 (16): 6346–6355.

37 Han, M., Maleski, K., Shuck, C.E. et al. (2020). Tailoring electronic and optical properties of MXenes through forming solid solution. *Journal of the American Chemical Society* 142 (45): 19110–19118.

38 Sun, W., Wang, H.W., Vlcek, L. et al. (2020). Multiscale and multimodal characterization of 2D titanium carbonitride MXene. *Advanced Materials Interfaces* 7 (11): 1902207.

39 Rigby, M.T., Natu, V., Sokol, M. et al. (2021). Synthesis of new M-layer solid-solution 312 MAX phases $(Ta_{1-x}Ti_x)_3AlC_2$ (x= 0.4, 0.62, 0.75, 0.91 or 0.95), and their corresponding MXenes. *RSC Advances* 11 (5): 3110–3114.

40 Pinto, D., Anasori, B., Avireddy, H. et al. (2020). Synthesis and electrochemical properties of 2D molybdenum vanadium carbides–solid solution MXenes. *Journal of Materials Chemistry A* 8 (18): 8957–8968.

41 Yang, J., Naguib, M., Ghidiu, M. et al. (2016). Two-dimensional Nb-based M_4C_3 solid solutions (MXenes). *Journal of the American Ceramic Society* 99 (2): 660–666.

42 Maleski, K., Shuck, C.E., Fafarman, A.T., and Gogotsi, Y. (2021). The broad chromatic range of two-dimensional transition metal carbides. *Advanced Optical Materials* 9 (4): 2001563.

43 Halim, J., Persson, I., Moon, E.J. et al. (2019). Electronic and optical characterization of 2D Ti_2C and Nb_2C (MXene) thin films. *Journal of Physics: Condensed Matter* 31 (16): 165301.

44 Valurouthu, G., Maleski, K., Kurra, N. et al. (2020). Tunable electrochromic behavior of titanium-based MXenes. *Nanoscale* 12 (26): 14204–14212.

45 Matthews, K., Zhang, T., Shuck, C.E. et al. (2021). Guidelines for synthesis and processing of chemically stable two-dimensional $V2CT_x$ MXene. *Chemistry of Materials* 34: 499–509.

46 Shan, Q., Mu, X., Alhabeb, M. et al. (2018). Two-dimensional vanadium carbide (V_2C) MXene as electrode for supercapacitors with aqueous electrolytes. *Electrochemistry Communications* 96: 103–107.

47 Wu, M., Wang, B., Hu, Q. et al. (2018). The synthesis process and thermal stability of V_2C MXene. *Materials* 11 (11): 2112.

48 Sang, X., Xie, Y., Lin, M.W. et al. (2016). Atomic defects in monolayer titanium carbide ($Ti_3C_2T_x$) MXene. *ACS Nano* 10 (10): 9193–9200.

49 Anayee, M., Kurra, N., Alhabeb, M. et al. (2020). Role of acid mixtures etching on the surface chemistry and sodium ion storage in $Ti_3C_2T_x$ MXene. *Chemical Communications* 56 (45): 6090–6093.

50 Harris, K.J., Bugnet, M., Naguib, M. et al. (2015). Direct measurement of surface termination groups and their connectivity in the 2D MXene V_2CT_x using NMR spectroscopy. *Journal of Physical Chemistry C* 119 (24): 13713–13720.

51 Hope, M.A., Forse, A.C., Griffith, K.J. et al. (2016). NMR reveals the surface functionalisation of Ti_3C_2 MXene. *Physical Chemistry Chemical Physics* 18 (7): 5099–5102.

52 Ho, D.H., Choi, Y.Y., Jo, S.B. et al. (2021). Sensing with MXenes: progress and prospects. *Advanced Materials* 33 (47): 2005846.

53 Tang, J., Mathis, T.S., Kurra, N. et al. (2019). Tuning the electrochemical performance of titanium carbide MXene by controllable in situ anodic oxidation. *Angewandte Chemie, International Edition* 58 (49): 17849–17855.

54 Wang, X., Bak, S.-M., Han, M. et al. (2021). Surface redox pseudocapacitance of partially oxidized titanium carbide MXene in water-in-salt electrolyte. *ACS Energy Letters* 7: 30–35.

55 Bandyopadhyay, A., Ghosh, D., and Pati, S.K. (2018). Effects of point defects on the magnetoelectronic structures of MXenes from first principles. *Physical Chemistry Chemical Physics* 20 (6): 4012–4019.

56 Han, M., Shuck, C.E., Rakhmanov, R. et al. (2020). Beyond $Ti_3C_2T_x$: MXenes for electromagnetic interference shielding. *ACS Nano* 14 (4): 5008–5016.

57 Shahzad, F., Alhabeb, M., Hatter, C.B. et al. (2016). Electromagnetic interference shielding with 2D transition metal carbides (MXenes). *Science* 353 (6304): 1137–1140.

58 Iqbal, A., Sambyal, P., and Koo, C.M. (2020). 2D MXenes for electromagnetic shielding: a review. *Advanced Functional Materials* 30 (47): 2000883.

59 Kim, S.J., Koh, H.J., Ren, C.E. et al. (2018). Metallic $Ti_3C_2T_x$ MXene gas sensors with ultrahigh signal-to-noise ratio. *ACS Nano* 12 (2): 986–993.

60 Shuck, C.E., Han, M., Maleski, K. et al. (2019). Effect of Ti_3AlC_2 MAX phase on structure and properties of resultant $Ti_3C_2T_x$ MXene. *ACS Applied Nano Materials* 2 (6): 3368–3376.

61 Yang, K., Zhu, K., Wang, Y. et al. (2021). $Ti_3C_2T_x$ MXene-loaded 3D substrate toward on-chip multi-gas sensing with surface-enhanced raman spectroscopy (SERS) barcode readout. *ACS Nano* 15 (8): 12996–13006.

62 Hantanasirisakul, K. and Gogotsi, Y. (2018). Electronic and optical properties of 2D transition metal carbides and nitrides (MXenes). *Advanced Materials* 30 (52): e1804779.

63 Foucher, A.C., Han, M., Shuck, C.E. et al. (2022). Shifts in valence states in bimetallic MXenes revealed by electron energy-loss spectroscopy (EELS). *2D Materials* 9: 025004.

64 Salles, P., Pinto, D., Hantanasirisakul, K. et al. (2019). Electrochromic effect in titanium carbide MXene thin films produced by dip-coating. *Advanced Functional Materials* 29 (17): 1809223.

65 Li, J., Wang, X., Sun, W. et al. (2021). Intercalation-induced reversible electrochromic behavior of two-dimensional $Ti_3C_2T_x$ MXene in organic electrolytes. *ChemElectroChem* 8 (1): 151–156.

66 Kuang, P., Low, J., Cheng, B. et al. (2020). MXene-based photocatalysts. *Journal of Materials Science and Technology* 56: 18–44.

67 Sarycheva, A., Makaryan, T., Maleski, K. et al. (2017). Two-dimensional titanium carbide (MXene) as surface-enhanced raman scattering substrate. *Journal of Physical Chemistry C* 121 (36): 19983–19988.

68 Wu, L., Jiang, X., Zhao, J. et al. (2018). MXene-based nonlinear optical information converter for all-optical modulator and switcher. *Laser & Photonics Reviews* 12 (12): 1800215.

69 Dong, Y., Chertopalov, S., Maleski, K. et al. (2018). Saturable absorption in 2D Ti_3C_2 MXene thin films for passive photonic diodes. *Advanced Materials* 30 (10): 1705714.

70 Anasori, B., Lukatskaya, M.R., and Gogotsi, Y. (2017). 2D metal carbides and nitrides (MXenes) for energy storage. *Nature Reviews Materials* 2 (2): 16098.

71 Wang, L., Han, M., Shuck, C.E. et al. (2021). Adjustable electrochemical properties of solid-solution MXenes. *Nano Energy* 88: 106308.

72 Seredych, M., Shuck, C.E., Pinto, D. et al. (2019). High-temperature behavior and surface chemistry of carbide MXenes studied by thermal analysis. *Chemistry of Materials* 31 (9): 3324–3332.

73 Nemani, S.K., Zhang, B., Wyatt, B.C. et al. (2021). High-entropy 2D carbide MXenes: $TiVNbMoC_3$ and $TiVCrMoC_3$. *ACS Nano* 15 (8): 12815–12825.

74 Du, Z., Wu, C., Chen, Y. et al. (2021). High-entropy atomic layers of transition-metal carbides (MXenes). *Advanced Materials* 33 (39): 2101473.

75 Tunca, B., Huang, S., Goossens, N. et al. (2022). Chemically complex double solid solution MAX phase-based ceramics in the (Ti, Zr, Hf, V, Nb)-(Al, Sn)-C system. *Materials Research Letters* 10 (2): 52–61.

76 Meshkian, R., Tao, Q., Dahlqvist, M. et al. (2017). Theoretical stability and materials synthesis of a chemically ordered MAX phase, Mo_2ScAlC_2, and its two-dimensional derivate Mo_2ScC_2 MXene. *Acta Materialia* 125: 476–480.

77 Caspi, E.N., Chartier, P., Porcher, F. et al. (2015). Ordering of (Cr, V) layers in nanolamellar $(Cr_{0.5}V_{0.5})_{n+1}AlC_n$ compounds. *Materials Research Letters* 3 (2): 100–106.

78 Tunca, B., Lapauw, T., Karakulina, O.M. et al. (2017). Synthesis of MAX phases in the Zr-Ti-Al-C system. *Inorganic Chemistry* 56 (6): 3489–3498.

79 Hart, J.L., Hantanasirisakul, K., Lang, A.C. et al. (2021). Multimodal spectroscopic study of surface termination evolution in $Cr_2TiC_2T_x$ MXene. *Advanced Materials Interfaces* 8 (5): 2001789.

80 Hantanasirisakul, K., Anasori, B., Nemsak, S. et al. (2020). Evidence of a magnetic transition in atomically thin $Cr_2TiC_2T_x$ MXene. *Nanoscale Horizons* 5 (12): 1557–1565.

81 Meshkian, R., Näslund, L.-Å., Halim, J. et al. (2015). Synthesis of two-dimensional molybdenum carbide, Mo_2C, from the gallium based atomic laminate Mo_2Ga_2C. *Scripta Materialia* 108: 147–150.

82 Yang, Y., Hantanasirisakul, K., Frey, N. et al. (2020). Distinguishing electronic contributions of surface and sub-surface transition metal atoms in Ti-based MXenes. *2D Materials* 7 (2): 025015.

83 Anasori, B., Shi, C., Moon, E.J. et al. (2016). Control of electronic properties of 2D carbides (MXenes) by manipulating their transition metal layers. *Nanoscale Horizons* 1: 227–234.

84 Hart, J.L., Hantanasirisakul, K., Lang, A.C. et al. (2019). Control of MXenes' electronic properties through termination and intercalation. *Nature Communications* 10 (1): 522.

85 Khazaei, M., Ranjbar, A., Arai, M., and Yunoki, S. (2016). Topological insulators in the ordered double transition metals $M_2'M''C_2$ MXenes (M′=Mo, W;M″=Ti, Zr, Hf). *Physical Review B* 94 (12): 125152.

86 Dong, L., Kumar, H., Anasori, B. et al. (2017). Rational design of two-dimensional metallic and semiconducting spintronic materials based on ordered double-transition-metal MXenes. *Journal of Physical Chemistry Letters* 8 (2): 422–428.

87 Sun, W., Xie, Y., and Kent, P.R. (2018). Double transition metal MXenes with wide band gaps and novel magnetic properties. *Nanoscale* 10 (25): 11962–11968.

88 Kim, H., Anasori, B., Gogotsi, Y., and Alshareef, H.N. (2017). Thermoelectric properties of two-dimensional molybdenum-based MXenes. *Chemistry of Materials* 29 (15): 6472–6479.

89 He, J., Ding, G., Zhong, C. et al. (2018). Cr_2TiC_2-based double MXenes: novel 2D bipolar antiferromagnetic semiconductor with gate-controllable spin orientation toward antiferromagnetic spintronics. *Nanoscale* 11 (1): 356–364.

90 Siriwardane, E.M. and Çakir, D. (2019). Strain engineering of electronic and magnetic properties of double-transition metal ferromagnetic semiconductor MXenes. *Journal of Applied Physics* 125 (8): 082527.

91 Yang, J., Zhou, X., Luo, X. et al. (2016). Tunable electronic and magnetic properties of $Cr_2M'C_2T_2$ (M′ = Ti or V; T = O, OH or F). *Applied Physics Letters* 109 (20): 203109.

92 Frey, N.C., Bandyopadhyay, A., Kumar, H. et al. (2019). Surface-engineered MXenes: electric field control of magnetism and enhanced magnetic anisotropy. *ACS Nano* 13 (3): 2831–2839.

93 Yang, J., Luo, X., Zhou, X. et al. (2017). Tuning magnetic properties of $Cr_2M_2C_3T_2$ (M= Ti and V) using extensile strain. *Computational Materials Science* 139: 313–319.

94 Maughan, P.A., Bouscarrat, L., Seymour, V.R. et al. (2021). Pillared Mo_2TiC_2 MXene for high-power and long-life lithium and sodium-ion batteries. *Nanoscale Advances* 3 (11): 3145–3158.

95 Chen, X., Li, R., Li, B. et al. (2021). Achieving ultra-high ductility and fracture toughness in molybdenum via Mo_2TiC_2 MXene addition. *Materials Science and Engineering A* 818: 141422.

96 Gao, Y., Cao, Y., Zhuo, H. et al. (2020). Mo_2TiC_2 MXene: a promising catalyst for electrocatalytic ammonia synthesis. *Catalysis Today* 339: 120–126.

97 Unal, M.A., Bayrakdar, F., Fusco, L. et al. (2021). 2D MXenes with antiviral and immunomodulatory properties: a pilot study against SARS-CoV-2. *Nano Today* 38: 101136.

98 Dahlqvist, M., Lu, J., Meshkian, R. et al. (2017). Prediction and synthesis of a family of atomic laminate phases with kagome-like and in-plane chemical ordering. *Science Advances* 3 (7): e1700642.

99 Meshkian, R., Dahlqvist, M., Lu, J. et al. (2018). W-based atomic laminates and their 2D derivative $W_{1.33}C$ MXene with vacancy ordering. *Advanced Materials* 30 (21): e1706409.

100 Thörnberg, J., Halim, J., Lu, J. et al. (2019). Synthesis of $(V_{2/3}Sc_{1/3})_2AlC$ i-MAX phase and $V_{2-x}C$ MXene scrolls. *Nanoscale* 11 (31): 14720–14726.

101 Halim, J., Palisaitis, J., Lu, J. et al. (2018). Synthesis of two-dimensional $Nb_{1.33}C$ (MXene) with randomly distributed vacancies by etching of the quaternary solid solution $(Nb_{2/3}Sc_{1/3})_2AlC$ MAX phase. *ACS Applied Nano Materials* 1 (6): 2455–2460.

102 Shuck, C.E. and Gogotsi, Y. (2020). Taking MXenes from the lab to commercial products. *Chemical Engineering Journal* 401: 125786.

103 Halim, J., Kota, S., Lukatskaya, M.R. et al. (2016). Synthesis and characterization of 2D molybdenum carbide (MXene). *Advanced Functional Materials* 26 (18): 3118–3127.

104 Zheng, W., Halim, J., Persson, P.O. et al. (2022). Effect of vacancies on the electrochemical behavior of Mo-based MXenes in aqueous supercapacitors. *Journal of Power Sources* 525: 231064.

105 Kang, Z., Khan, M.A., Gong, Y. et al. (2021). Recent progress of MXenes and MXene-based nanomaterials for the electrocatalytic hydrogen evolution reaction. *Journal of Materials Chemistry A* 9 (10): 6089–6108.

106 Dahlqvist, M. and Rosen, J. (2020). Predictive theoretical screening of phase stability for chemical order and disorder in quaternary 312 and 413 MAX phases. *Nanoscale* 12 (2): 785–794.

107 Tan, T.L., Jin, H.M., Sullivan, M.B. et al. (2017). High-throughput survey of ordering configurations in MXene alloys across compositions and temperatures. *ACS Nano* 11 (5): 4407–4418.

108 Hu, Y., Fan, X.L., Guo, W.J. et al. (2019). Ordered double-M elements MXenes TiMC: large in-plane stiffness and ferromagnetism. *Journal of Magnetism and Magnetic Materials* 486: 165280.

109 Synthesis of Three Families of Titanium Carbonitride MXenes J. Am. Chem. Soc. 2023, 145, 41, 22374–22383.

10

Structural Confirmation and Morphological Investigation of MXenes

Kaitlyn Prenger, Anika Tabassum, and Michael Naguib

Department of Physics and Engineering Physics, Tulane University, New Orleans, LA, USA

Appropriate and thorough characterization of the structure and morphology of MXenes and the parent MAX phases is essential to ensure reproducibility in MXenes research. When reporting MXene results in literature, it should be clearly demonstrated that MXene of suitable purity has been produced, and confirming consistent results should be a standard laboratory process to verify the product before proceeding to any property or application testing. Structural analyses are essential for understanding the phenomena observed when testing MXenes. For structural analysis, X-ray diffraction (XRD), transmission electron microscopy (TEM), and neutron and X-ray pair distribution function (nPDF and xPDF) provide key information. Morphology can be assessed through the use of scanning electron microscopy (SEM), atomic force microscopy (AFM), optical microscopy (OM), and gas sorption analysis.

Laboratory scale powder XRD is a powerful tool for MXene research. It provides quick evidence to verify the MAX phase structure, it can be used to calculate lattice parameters, and, when combined with Rietveld refinement, can give precise structural information. MXene XRD should always be compared to the corresponding parent MAX phase pattern. Since MAX phases are crystalline, acquiring XRD patterns for them is usually not challenging and Rietveld refinement can be utilized to quantify the crystalline impurities/secondary phases in the sample (e.g. binary carbide/nitrides, intermetallic, and oxides). After the selective etching of the A layer from MAX phases, out-of-plane ordering becomes very weak, therefore, when performing XRD on MXene, it is important to achieve preferred orientation by applying pressure to the sample to line up the basal planes (00*l*). XRD scans should start at a low enough 2θ to capture the (002) peak (usually ~3° 2θ, for

Transition Metal Carbides and Nitrides (MXenes) Handbook: Synthesis, Processing, Properties and Applications, First Edition. Edited by Chuanfang Zhang and Michael Naguib.
© 2024 John Wiley & Sons, Inc. Published 2024 by John Wiley & Sons, Inc.

Cu K_α source, is sufficient) and finish high enough to capture all major peaks (typically 65°–80° 2θ, for Cu K_α source). Step sizes of 0.01°–0.04° produce scans of reasonable quality and dwell times should be selected based on the instrument, usually 1°–3° per minute. If XRD patterns are particularly noisy, slower scans should be used. When processing MAX phase XRD, it is often useful to add an internal standard. For most MAX phases, elemental silicon is an appropriate internal standard as its peaks do not tend to overlap with key MAX peaks. However, some phases may require selecting a different standard. Since the peak positions for silicon are well established, these internal standard peaks can be used to align XRD patterns and correct for any instrument shifts. Internal standard amounts should be kept uniform across all samples; 10 mass% silicon is a typical value. The internal standard is not typically necessary for MXene products. Since lab-scale syntheses may not produce enough MXene to dedicate ~0.2–0.3 g for XRD only, it is appropriate to skip the use of internal standard. However, when looking at *d*-spacing and small shifts in *d*-spacing, it may be necessary to use an internal standard to accurately determine the peak positions.

When analyzing XRD data, it is often useful to compare it to other published patterns. The use of a database with peak searching functions makes this process easier, although it should be noted that these databases may not contain all phases. Predicted XRD patterns for known crystal structures can be generated through software such as CrystalMaker or Vesta. Unless comparing to an established pattern, care should be taken to make sure that peaks are assigned correctly to appropriate Miller indices. MAX and MXene phases have hexagonal lattices, and peak assignments are not always trivial.

Even before etching MAX phases into MXenes, use of XRD can guide researchers when selecting an appropriate sample of MAX phase ceramic. It is not uncommon for a MAX phase sample to contain secondary phases, either of binary carbide/nitride, intermetallic, oxide, or even another MAX phase of higher or lower order (i.e. different n in $M_{n+1}AX_n$). Figure 10.1a shows XRD patterns of two different sample batches of Ti_3AlC_2. The pattern shown on top in grey exhibits a small amount of titanium carbide (peaks indicated with diamonds at ~36°, ~42°, and ~60° 2θ), but it does have a small amount of the 211 MAX Ti_2AlC (peak indicated with a square at ~12° 2θ). The black pattern on the bottom lacks the 211 peak but has large amounts of titanium carbide. However, both of these MAX materials can be used, but the selection depends on the synthesis procedure required. If etching in HF, the 211 will be completely dissolved during etching, resulting in a slightly lower yield, but a pure MXene product. If the MXene is to be delaminated, any TiC will sediment to the bottom during the centrifuging steps and not be present in the final delaminated product. This will affect the overall yield but not the MXene produced. While an ideal MAX phase for producing MXene will not have impurity phases, some impurities are difficult to eliminate

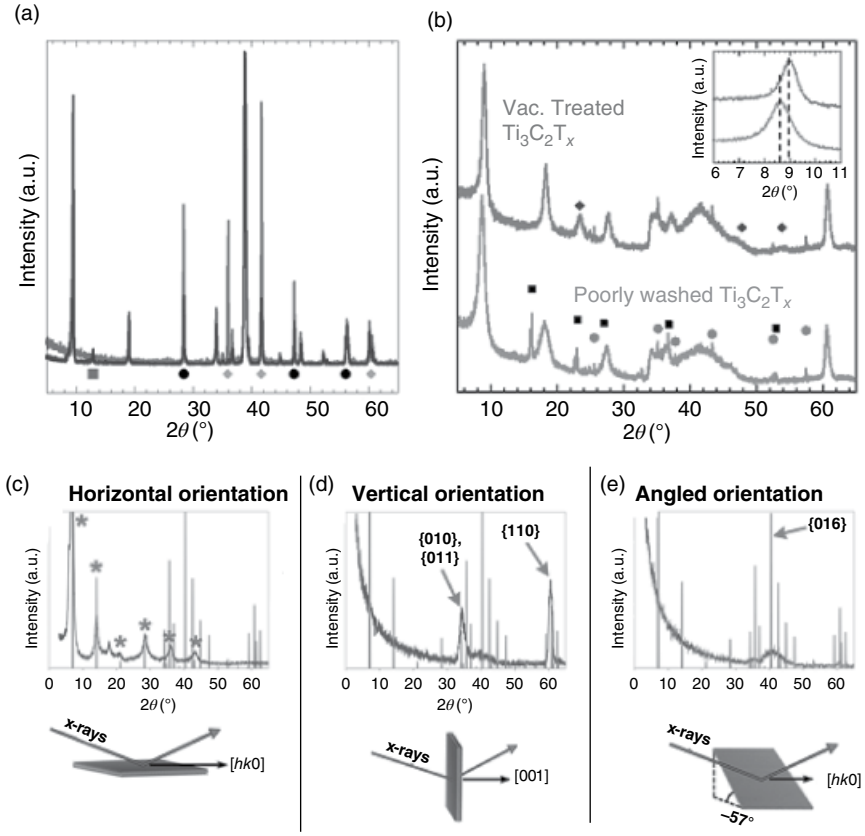


Figure 10.1 (a) XRD patterns of Ti_3AlC_2 samples synthesized differently. Square indicates peak position of Ti_2AlC (002) peak, gray diamonds indicate TiC peaks and black filled circles for Si (added as an internal reference), (b) poorly washed and dried $Ti_3C_2T_x$ (produced by HF treatment of Ti_3AlC_2) before and after vacuum annealing at 200 °C for 20 hours under a vacuum pressure of 1 kPa. The black squares represent the peak position of $AlF_3{\cdot}3H_2O$ [PDF#35-0827], the red circles those of Al_2O_3 [PDF#46-1212], and the blue diamonds those of $TiOF_2$ [PDF#01-0490]. Inset shows the expanded XRD pattern around the (002) peak, clearly illustrating the effect of vacuum annealing [1]. The effect of sample orientation on XRD patterns is shown for horizontally (c), vertically (d), and angled (e) samples [2].

due to the narrow window for synthesis conditions producing these ternary phases. Understanding which impurities have little to no impact is often the solution to producing the purest product.

When considering MXene XRD, the analysis is not as straightforward as in MAX. One important consideration in looking at MXene XRD is looking for the presence of impurities left over from etching. As shown in Figure 10.1b, insufficient washing of MXene can lead to impurity phases in XRD [1]. The reaction of

MXene with acidic fluoride solutions can lead to the presence of $AlF_3{\cdot}3H_2O$ and Al_2O_3, as well as transition metal oxides and oxyfluorides. Thorough washing can eliminate most of these impurities [1]. Further, since most XRD will be collected in the horizontal orientation (Figure 10.1c), which tends to show primarily the (00*l*) reflections because of preferred orientation [2]. In particular, films made of restacked delaminated MXene exhibit extremely high preferred orientation and will rarely show other reflections. As seen in XRD patterns collected vertically (Figure 10.1d) or at a 57° angle (Figure 10.1e), other planes can be captured using XRD [2]. Measuring XRD in other orientations is not a standard practice and is not necessary for most MXene studies, but can be used if measuring the *a* and *b* lattice parameters is needed.

TEM is another important tool for assessing MXene structure. TEM of delaminated MXene can be obtained by suspending MXene on lacy carbon to visualize individual flakes, as in Figure 10.2a and at high resolution in Figure 10.2b [7]. The inset in Figure 10.2d shows a selected area electron diffraction (SAED) pattern, with the characteristic hexagons demonstrating the hexagonal crystal structure [7]. The single hexagonal pattern also indicates that this is a single crystal (i.e. single flake in this case). In the case of multiple restacked flakes, multiple hexagons, slightly offset from one another can be seen, as in Figure 10.2c (inset) [4]. Even when looking at multiple flakes, the hexagons can still be visualized, and often an accurate count of the layers in the flake can be made.

TEM can also be used to look at cross-sections of multilayer particles prepared with the focused ion beam (FIB) technique. HRTEM of $Mo_2Ti_2AlC_3$ (Figure 10.2d) and $Mo_2Ti_2C_3T_x$ (Figure 10.2e) prepared with FIB shows the individual atoms and shows the ordering of the double transition metals [5]. Here, molybdenum (brightest atom layers) forms the outer layers and titanium (medium grey atom layers) on the inner layers, with the brightness difference in the two atoms clearly visible due to atomic mass [5]. In Figure 10.2d, aluminum can also be seen (darkest atomic layers), but neither image clearly shows the carbon atoms [5]. HRTEM images can also be used to measure inter-layer spacing, as shown in Figure 10.2f [6]. However, since the sampling will only take into account a small number of flakes, this method of measurement prone to inaccuracy and should be supported with spacing calculated from XRD patterns. Similarly, TEM-based energy-dispersive X-ray spectroscopy (EDS) measurements can be useful for individual flakes, but will not provide the global averaging possible from SEM-based EDS measurements.

Extremely accurate structural information can also be obtained through atomic PDF analyses of both synchrotron X-ray (xPDF) and neutron (nPDF) data. These analyses combine diffraction data with modeling to produce information on short-range ordering, distribution of surface terminating species, and position of intercalated species. Figure 10.3a shows the xPDF *G(r)* plots (Fourier transformed

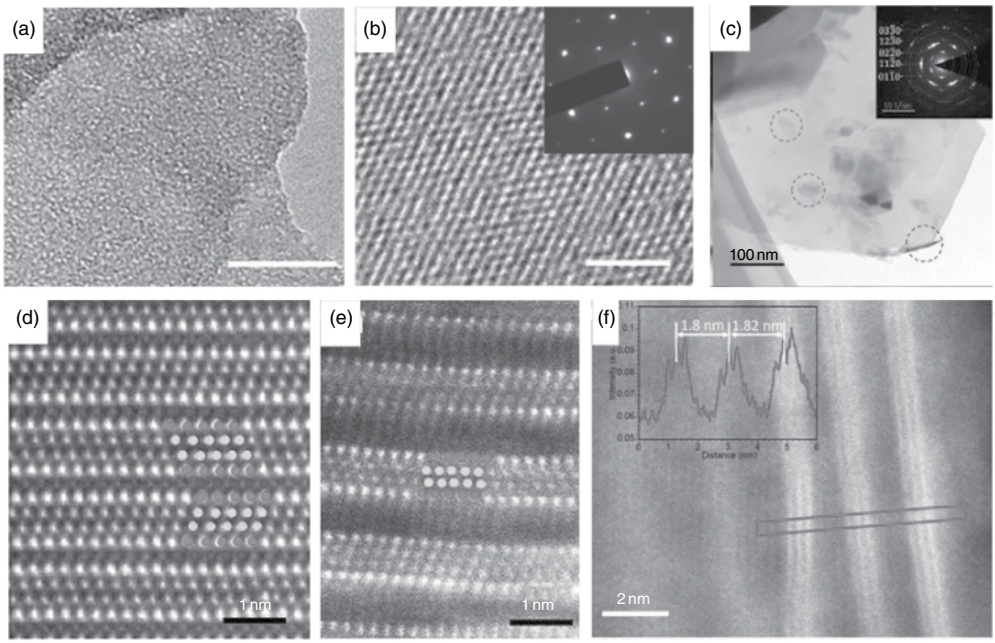


Figure 10.2 (a) and (b) TEM images and corresponding hexagonal pattern SAED (inset of b) of a single sheet of $Ti_3C_2T_x$. *Source:* Mashtalir et al. [3]/Reproduced from Springer Nature. (c) Folded $Ti_3C_2T_x$ sheet with inset SAED showing overlapping and offset hexagonal pattern. *Source:* Han et al. [4]/Reproduced from American Chemical Society. HRSTEM of $Mo_2Ti_2AlC_3$ (d) and $Mo_2Ti_2C_3T_x$ (e) showing atomic positions and ordering. *Source:* Anasori et al. [5]/Reproduced from American Chemical Society. (f) STEM for measuring interlayer spacing in polymer intercalated $Ti_3C_2T_x$. *Source:* Liang et al. [6]/Reproduced from John Wiley & Sons, Inc.

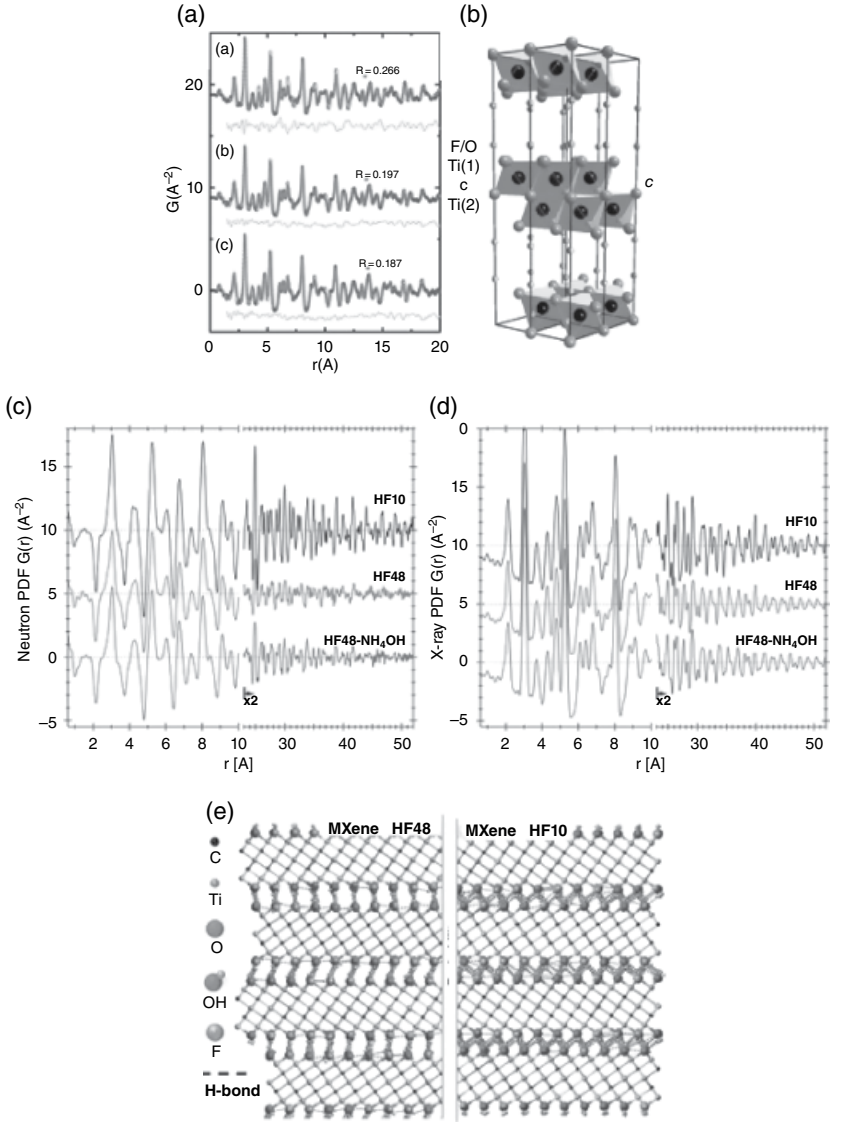


Figure 10.3 (a) PDF fitting for $Ti_3C_2T_x$ (a), Na^+ intercalated (b), and K^+ intercalated MXenes showing the difference between measured data and calculated data with the fit shown below. (b) Shows the polyhedral representation for the optimized structure. *Source:* Shi et al. [8]/American Physical Society. (c) Neutron and (d) synchrotron X-ray PDFs of $Ti_3C_2T_x$ etched with different methods with (e) showing the view across *ab* plane structures generated from pdf data. *Source:* Wang et al. [9]/American Chemical Society. (f) Neutron PDF data for pristine and sodiated MXenes with the classical molecular dynamics simulation results of sodiation sites and distribution based on nPDF data are shown in (g) for pristine and sodiated MXenes with different stoichiometries. *Source:* Brady et al. [10]/American Chemical Society.

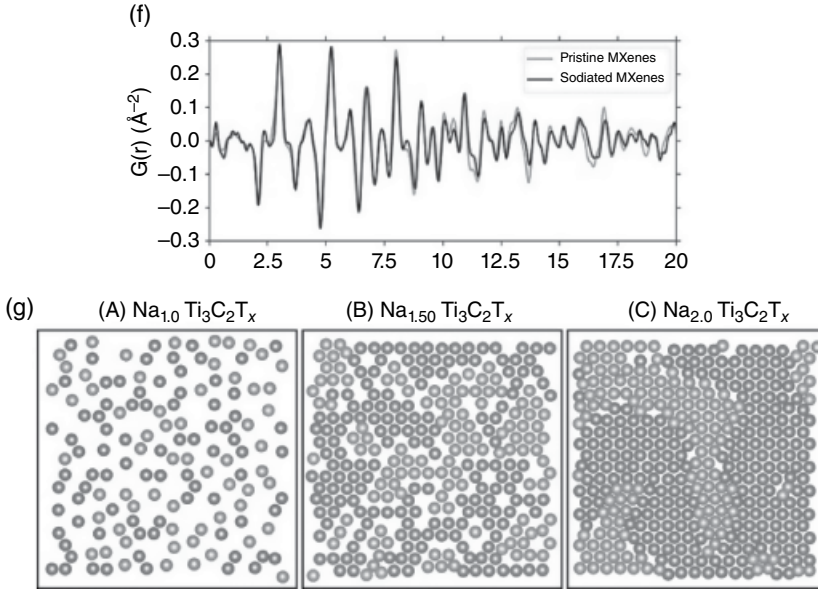


Figure 10.3 (Continued)

raw 2D data) of (a) pristine, (b) Na^+ intercalated, and (c) K^+ intercalated $Ti_3C_2T_x$ [8]. The experimental data and the calculated PDFs are plotted together, with the difference between experiment and calculation shown below. Figure 10.3b shows the optimized structure for $Ti_3C_2T_x$ [8]. X-ray techniques suffer from being insensitive to hydrogen. Since MXenes can be terminated with hydroxyl groups, ignoring the contribution of hydrogen can limit the effectiveness of the xPDF. Indeed, since both neutron and X-ray have different atomic sensitivities, collecting both nPDF and xPDF of the same sample is the optimal way to use PDF data for structural resolution. Figure 10.3c shows nPDF and Figure 10.3d shows xPDF of $Ti_3C_2T_x$ etched with different methods [9]. This data was used to produce the atomistic models in Figure 10.3e, where layer stacking and surface terminations are fully realized for the first time [9]. Resolving the structure gives insights about the nature of bonding between the layers for different synthesis approaches. It was found that HF48 (synthesized using 48% HF) sample has stronger hydrogen bonding than HF10 (synthesized using 10% HF). Figure 10.3f shows the nPDF for pristine and chemically sodiated $Ti_3C_2T_x$, where the subtle differences between the two patterns were used to analyze the preferential loading positions of the intercalated sodium atoms, in combination with atomistic molecular dynamics, as shown in Figure 10.3g [10]. Key for using PDF data is a thorough understanding of the MXene system so that appropriate models can be used in analysis. Unit cell,

or "small box" modeling will not give useful short-range ordering data, and atomistic and coarse-grained approaches must be used to fully utilize data obtained from these techniques [9]. Ensuring that the analysis is performed by someone experienced in handling such data is key.

Morphological study is essential to assess MXene products for sheet size and shape. MXenes are generally produced from the MAX phase ceramics through selective etching, and these multilayer products can be delaminated to produce 2D sheets. Etching and delamination methods can affect the size and shape of these sheets and the multilayer MXenes. Some important techniques for morphological analysis of MXenes can be done using SEM, AFM, OM, and Brunauer–Emmett–Teller (BET) surface area analysis.

SEM is one of the most important techniques in assessing the morphology of MXenes. Both low-magnification and high-magnification images can be useful. Due to their high conductivity, MXenes and MAX phase samples can be mounted on SEM stubs using double-sided tape without the need for conductive coatings. Figure 10.4a shows Ti_3AlC_2 MAX particles before etching, which are clustered together with other particles, whereas in Figure 10.4b accordion-shaped hydrofluoric acid (HF) etched exfoliated $Ti_3C_2T_x$ MXene can be observed [11]. Though this accordion-like morphology is not visible in Figure 10.4c for *in-situ* HF (HCl + KF) etched Ti_2CNT_x MXene, it nevertheless shows exfoliation has taken place due to the visible layers [12]. This demonstrates that changing the etchant can vary the morphology of MXene under SEM. Not all MXenes will show the accordion-like structure, but they will still show definite signs of etching as compared to MAX phase. The lack of accordion-like structure is most prevalent for *in-situ* HF etching methods and/or intercalated MXenes. Figure 10.4d,e shows SEM images of pristine $Ti_3C_2T_x$ MXene and K^+-intercalated MXene with an average thickness of ~40 and ~133 nm, respectively. The latter exhibits a more homogeneous structure with the increased layer stack thicknesses compared to the pristine one for the same size of particle (~6 μm). The insets of Figure 10.4 (d,e) show images taken at lower magnification to demonstrate scale. In this case, SEM images delivered very useful morphological information before and after K^+ intercalation [13]. MXene's purity and/or degradation can be observed using SEM. Figure 10.4g shows SEM image of old (stored for 28 months) $Ti_3C_2T_x$ MXene with small bright agglomerated scattered $TiOF_2$ crystals (confirmed by XRD) on top of the MXene confirming partial degradation [1]. Similarly, Figure 10.4h shows oxide nanocrystals for an intentionally oxidized $Ti_3C_2T_x$ MXene by flash heating in air [14]. In addition to MXene multilayer, the cross-section of highly aligned few layers MXene flakes can also be visualized through SEM. In this case, the freestanding MXene films should be frozen using liquid nitrogen and then fractured to produce straight surfaces for cross sectional SEM imaging. Use of cutting implements or breaking the MXene films at room temperature tends to leave jagged

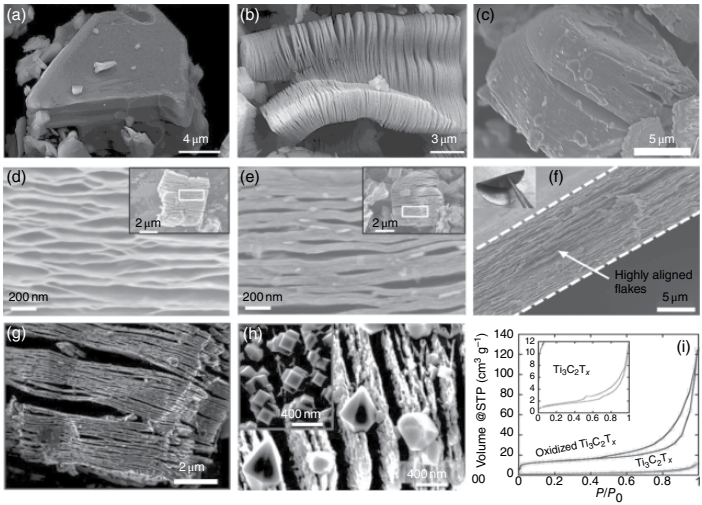


Figure 10.4 SEM images for (a) MAX phase Ti_3AlC_2. (b) Multilayer Ti_3CNT_x produced by HF etching of Ti_3AlCN. *Source:* Naguib et al. [11]/Reproduced from American Chemical Society. (c) Multilayer $Ti_2C_{0.5}N_{0.5}T_x$ produced by HCl/KF etching of $Ti_2AlC_{0.5}N_{0.5}$. *Source:* Liang et al. [12]/Reproduced with permission from John Wiley & Sons, Inc. (d) Multilayer $Ti_3C_2T_x$. (e) K-intercalated $Ti_3C_2T_x$. *Source:* Osti et al. [13]/Reproduced from American Chemical Society. (f) cross-section of $Ti_2C_{0.5}N_{0.5}T_x$ freestanding paper of delaminated and restacked sheets. *Source:* Liang et al. [12]/Reproduced with permission from John Wiley & Sons, Inc. (g) Aged multilayer $Ti_3C_2T_x$ stored for 28 months after synthesis. *Source:* Abdelmalak et al. [1]/Reproduced from Drexel University. (h) Oxidized multilayer $Ti_3C_2T_x$ by flash heating in air. (i) Isotherms of nitrogen adsorption/desorption for $Ti_3C_2T_x$ before and after oxidation. *Source:* Naguib et al. [14]/Reproduced with permission from Royal Society of Chemistry/CC BY 3.0.

breaks, which are difficult to analyze with SEM due to the depth of field capabilities of the technique. A freestanding film of Ti_2CNT_x is shown in Figure 10.4f. Use of SEM for these freestanding films also yields a highly accurate measurement of the thickness of the films, which can be necessary for some electrochemical techniques, measurements of conductivity, and other applications. SEM can be a very powerful tool for comprehensive morphological analysis of MXene sample and hence can guide further steps in analysis.

Energy-dispersive EDS can be performed to analyze the compositions of the MXenes. This technique can generally be done alongside SEM image collection. By calculating the atomic ratio of M : A, the success and extent of MAX to MXene conversion can be evaluated. The atomic ratio M : A in the $M_{n+1}AX_n$ phase should be $(n+1) : 1$ and if A is successfully etched, M : A ratio should be ideally $(n+1) : 0$, small deviation from zero for the A elements can be acceptable as traces of etching products might co-exist in the sample, but efforts should be exerted to minimize it. For presenting EDS results, it is best to normalize the data to the transition metal. For example, $Ti_3C_2T_x$ EDS should be normalized to 3 titanium, whereas $Nb_4C_3T_x$ is best normalized to 4 niobium. Fluorine content as analyzed by EDS is also essential for confirming the quality of the product. High fluorine levels can suggest that salt byproducts were not thoroughly washed away and thus fluorine content should always be monitored using EDS. Since different MXenes and different etching methods will yield different ratios of –O, –OH, and –F terminations, literature should be checked to determine the appropriate range for the MXene and etching method selected. Aluminum stubs sample holders should be avoided in EDS techniques for MXene because most of the parent MAX phases used for MXene synthesis are aluminum-containing ones. In this case, copper SEM stubs are ideal. EDS is an excellent tool to get elemental analysis quickly and reliably, but it does have its limitations. It is often inaccurate in detecting the nitrogen when it co-exists with titanium in nitride and carbonitride MXenes and it cannot detect any hydrogen contributions. Unfortunately, ratios of carbon and oxygen are generally artificially inflated due to the carbon-oxygen-based adhesives on double-sided tapes used for SEM sample mounting. In some cases, an EDS analysis of the tape itself can be useful. Even with those caveats, EDS remains an invaluable technique for monitoring the quality of MXene products and should be performed for each synthesis.

Characterizing the specific surface area (SSA) of MXene is another important quantity for analysis. Typically, this is done using gas sorption analyzers (GSA) with BET theory analysis. SSA of −325 mesh MAX phases is usually less than $10\,m^2\,g^{-1}$ ($1–10\,m^2\,g^{-1}$). For multilayer MXenes, SSA is, larger than MAX phases, usually in the range $10–20\,m^2\,g^{-1}$ and for freestanding paper of delaminated MXenes, it is ~$100\,m^2\,g^{-1}$. Figure 10.4i shows the nitrogen adsorption–desorption of isotherms of $Ti_3C_2T_x$ MXene before and after oxidization. It can be seen in the

figure that due to the oxide nanoparticles and swelling of the layers, the specific surface area is five times greater in the oxidized MXene sample than the pristine MXene. Indeed, a zoomed-in inset of the pristine MXene is needed to see the area encased within the isotherms, as putting it on the same scale as the oxidized MXene does not show this area at all. Pore size analysis using GSA is somewhat challenging for MXene, as most of the models assume round pores, while MXene pores are more slit-shaped, but can have some limited applicability.

To look at the lateral dimensions, layer count, and thickness of delaminated MXene sheets, AFM is a useful technique. MXene colloidal solutions can be drop- or spin-cast on a doped Si wafer (Si/SiO_2) or similar kind of a flat/smooth substrate for AFM imaging. To get good sheet dispersions, colloidal solutions with low concentrations should be used. Since most MXene colloidal solutions have a dark color (usually black) when concentrated, a small volume can be diluted with degassed deionized water until transparent and colorless. Before any type of casting/coating the Si wafers should be thoroughly cleaned by using a solution of methanol, hydrochloric acid (HCl) and sulfuric acid (H_2SO_4), followed by cleaning with ethanol, acetone, and finally deionized water [15]. After cleaning the substrate, plasma cleaning can be employed to etch the surface to allow for a uniform monolayer MXene film deposition. All these processes should ideally be performed in a cleanroom environment to ensure the cleanliness and the purity of the sample. After cleaning via multiple steps, the substrate will be ready to be coated by diluted MXene colloidal solution. Before drop casting, the Si wafer should be heated on a hot plate for a few minutes at 100 °C, after which a micropipette can be used to carefully cast a tiny droplet on the wafer. During the setup of AFM imaging, multiple other parameters are important, such as the selection of tips, mode, scan size, frequency, target amplitude, tuning, etc. Generally, a tip with a force constant of 40–50 $N\,m^{-1}$, resonance frequency of 300–400 kHz and a cantilever length of 100–150 μm is recommended in tapping mode for MXene films.

In case of AFM imaging, a height profile of the film can provide information about the depth of film's layers. Figure 10.5a shows a few layers of $Ti_2C_{0.5}N_{0.5}T_x$ MXene with a thickness of ~2.5 nm, which can be assigned to two to three layers of MXene flakes [12]. AFM imaging can be a valuable resource to determine if samples have begun to oxidize. Figure 10.5b shows AFM images of $Ti_3C_2T_x$ channels before and after oxidation. In this figure, degradation is happening at the edges of the flakes, which is 1 nm thicker than the pristine fresh sample, which has a thickness of 2 nm for both before and after basal planes [16]. Moreover, film uniformity and surface roughness can also be inspected from high-quality AFM images. A large ($100 \times 70\,\mu m^2$) $Ti_3C_2T_x$ film is shown in Figure 10.5c. It has a thickness of ~1.8 nm and a surface roughness of 1.2–1.7 nm indicating the formation of monolayer and uniform $Ti_3C_2T_x$ film. A high-magnified image of the marked area from Figure 10.5c is shown in Figure 10.5d with a depth profile in multiple spots

including edges of the film (2–4 nm thickness) where multiple layers are present [17]. Thus, deeper morphological understanding of the MXene flakes and film can be gained from AFM images.

OM is a lesser-used technique for morphological study of MXenes, but can help in assessing the quality of spin-cast and other MXene thin films. Since assessing film quality is essential for many applications, finding the best way to render flakes visible is a necessary task. Figure 10.5e–l shows how changing the thickness of SiO_2 affects the visual contrast of the $Ti_3C_2T_x$ MXene flakes. When cast on seven different thicknesses of SiO_2, wafers with 223 (Figure 10.5f) and 285 (Figure 10.5e) nm thick SiO_2 layers show the best contrast for single layer MXene flakes [18].

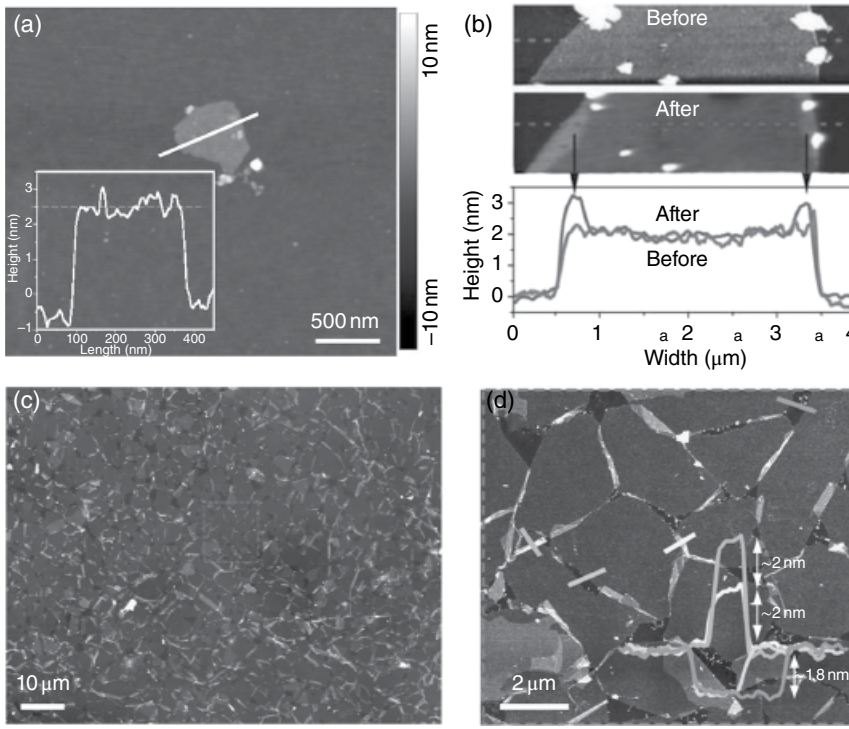


Figure 10.5 AFM images for (a) a $Ti_2C_{0.5}N_{0.5}T_x$ flake and its corresponding height profile. *Source:* Liang et al. [12]/Reproduced with permission from John Wiley & Sons, Inc. (b) $Ti_3C_2T_x$ before and after oxidation and the corresponding height profile showing oxides at the edges. *Source:* Lipatov et al. [16]/Reproduced from John Wiley & Sons, Inc. (c) Thin film of $Ti_3C_2T_x$. (d) Higher magnification AFM image for the film shown in C. *Source:* Mojtabavi et al. [17]/Reproduced from American Chemical Society. (e–k) Optical microscopy images for $Ti_3C_2T_x$ flakes on Si/SiO_2 substrate with different SiO_2 thicknesses. (l) The color difference plot for different SiO_2 thicknesses. *Source:* Miranda et al. [18]/ Reproduced from Taylor and Francis group.

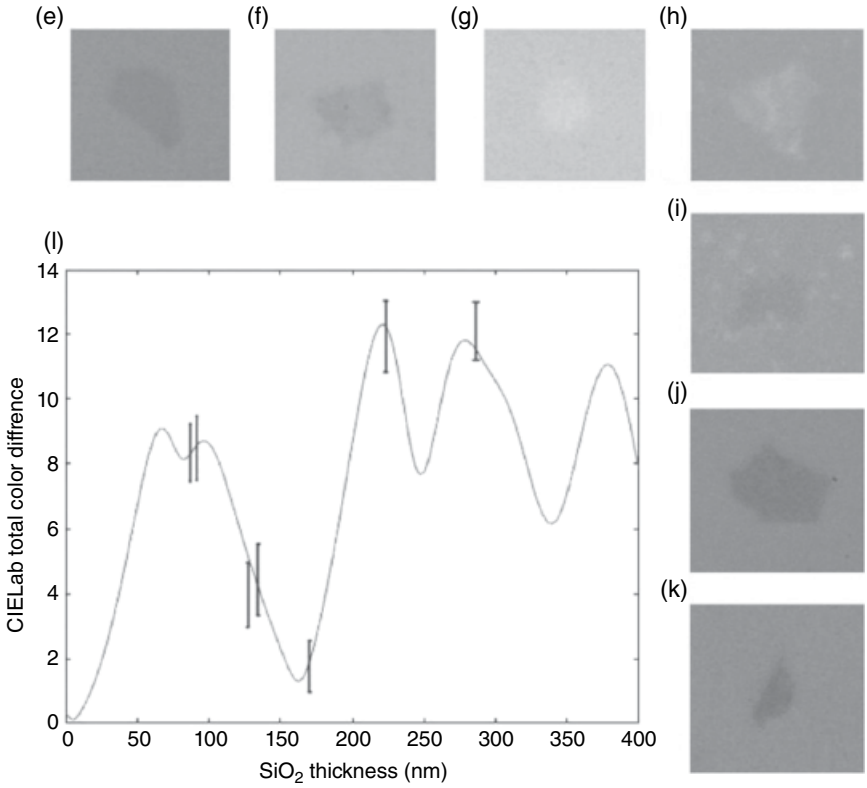


Figure 10.5 (Continued)

Furthermore, the relative intensity of the flakes visualized with OM can be used to determine the number of layers present. While OM remains a lesser-used technique, with proper set up it is a very quick way to assess MXene layers.

10.1 Summary and Outlook

Indeed, appropriate structural and morphological characterization of MXene products throughout the research is essential for consistent and repeatable results. XRD and SEM with EDS should be employed for every MXene sample produced and further exploration of properties and applications should not proceed until the quality of the material is assessed. Techniques such as TEM and neutron and X-ray scattering can provide finer detail for structural analysis but require more specialized equipment and highly trained personnel. AFM is an extremely useful

technique for assessing the dimensions of MXene flakes, including thickness measurements. Finally, techniques such as gas sorption and OM are less often used for MXene analysis but nevertheless have useful applications for structural and morphological characterization.

References

1 Abdelmalak, M.N. (2014). *MXenes: A New Family of Two-Dimensional Materials and its Application as Electrodes for Li-Ion Batteries*. Philadelphia, PA: Drexel University.

2 Ghidiu, M. and Barsoum, M.W. (2017). The {110} reflection in X-ray diffraction of MXene films: misinterpretation and measurement via non-standard orientation. *Journal of the American Ceramic Society* 100 (12): 5395–5399. https://doi.org/10.1111/jace.15124.

3 Mashtalir, O., Naguib, M., Mochalin, V.N. et al. (2013). Intercalation and delamination of layered carbides and carbonitrides. *Nature Communications* 4 (1): 1716. https://doi.org/10.1038/ncomms2664.

4 Han, M., Yin, X., Wu, H. et al. (2016). Ti_3C_2 MXenes with modified surface for high-performance electromagnetic absorption and shielding in the X-band. *ACS Applied Materials & Interfaces* 8 (32): 21011–21019. https://doi.org/10.1021/acsami.6b06455.

5 Anasori, B., Xie, Y., Beidaghi, M. et al. (2015). Two-dimensional, ordered, double transition metals carbides (MXenes). *ACS Nano* 9 (10): 9507–9516. https://doi.org/10.1021/acsnano.5b03591.

6 Liang, K., Matsumoto, R.A., Zhao, W. et al. (2021). Engineering the interlayer spacing by pre-intercalation for high performance supercapacitor MXene electrodes in room temperature ionic liquid. *Advanced Functional Materials* 31 (33): 2104007.

7 Ghidiu, M., Lukatskaya, M.R., Zhao, M.Q. et al. (2014). Conductive two-dimensional titanium carbide 'clay' with high volumetric capacitance. *Nature* 516 (7529): 78–81. https://doi.org/10.1038/nature13970 From NLM.

8 Shi, C., Beidaghi, M., Naguib, M. et al. (2014). Structure of nanocrystalline Ti_3C_2 MXene using atomic pair distribution function. *Physical Review Letters* 112 (12): 125501. https://doi.org/10.1103/PhysRevLett.112.125501.

9 Wang, H.W., Naguib, M., Page, K. et al. (2016). Resolving the structure of $Ti_3C_2T_x$ MXenes through multilevel structural modeling of the atomic pair distribution function. *Chemistry of Materials* 28 (1): 349–359. https://doi.org/10.1021/acs.chemmater.5b04250.

10 Brady, A., Liang, K., Vuong, V.Q. et al. (2021). Pre-sodiated $Ti_3C_2T_x$ MXene structure and behavior as electrode for sodium-ion capacitors. *ACS Nano* 15 (2): 2994–3003. https://doi.org/10.1021/acsnano.0c09301.

11 Naguib, M., Mashtalir, O., Carle, J. et al. (2012). Two-dimensional transition metal carbides. *ACS Nano* 6 (2): 1322–1331. https://doi.org/10.1021/nn204153h.

12 Liang, K., Tabassum, A., Majed, A. et al. (2021). Synthesis of new two-dimensional titanium carbonitride $Ti_2C_{0.5}N_{0.5}T_x$ MXene and its performance as an electrode material for sodium-ion battery. *InfoMat* 3 (12): 1422–1430. https://doi.org/10.1002/inf2.12269.

13 Osti, N.C., Naguib, M., Ostadhossein, A. et al. (2016). Effect of metal ion intercalation on the structure of MXene and water dynamics on its internal surfaces. *ACS Applied Materials & Interfaces* 8 (14): 8859–8863. https://doi.org/10.1021/acsami.6b01490.

14 Naguib, M., Mashtalir, O., Lukatskaya, M.R. et al. (2014). One-step synthesis of nanocrystalline transition metal oxides on thin sheets of disordered graphitic carbon by oxidation of MXenes. *Chemical Communications* 50 (56): 7420–7423.

15 Shi, Y., Osada, M., Ebina, Y., and Sasaki, T. (2020). Single droplet assembly for two-dimensional nanosheet tiling. *ACS Nano* 14 (11): 15216–15226.

16 Lipatov, A., Alhabeb, M., Lukatskaya, M.R. et al. (2016). Effect of synthesis on quality, electronic properties and environmental stability of individual monolayer Ti_3C_2 MXene flakes. *Advanced Electronic Materials* 2 (12): 1600255.

17 Mojtabavi, M., VahidMohammadi, A., Ganeshan, K. et al. (2021). Wafer-scale lateral self-assembly of mosaic $Ti_3C_2T_x$ MXene monolayer films. *ACS Nano* 15 (1): 625–636.

18 Miranda, A., Halim, J., Lorke, A., and Barsoum, M. (2017). Rendering $Ti_3C_2T_x$ (MXene) monolayers visible. *Materials Research Letters* 5 (5): 322–328.

11

MXene Surface Terminations

Per O.Å. Persson

Thin Film Physics Division, Department of Physics, Chemistry and Biology, Linköping University, Linköping, Sweden

11.1 Introduction

First-principles calculations have repeatedly shown the preference for termination of the bare MXene surface. MXenes gain significant negative formation energy upon termination, which indicates the formation of strong bonds between the surface M atoms and the terminating species [1, 2]. Therefore, terminations are viewed as part of the MXene such that the chemical formula for MXene can be described as $M_{n+1}X_nT_z$, where T represents the surface terminating species and the subscript z indicates the coverage of T on the MXene surface. The large variety of synthesis recipes and approaches enables a wide and growing range of terminating species, including single (O, Cl, F, S, etc.) or mixed (O/OH/F) terminations that make MXenes a rich and interesting family among the 2D materials.

The process of initially terminating the MXene surfaces depends on the synthesis protocol. Currently, two main routes are employed to produce MXenes from MAX phases. This include the original method to chemically etch the MAX phases using aqueous-HF and the use of a mixture of hydrochloric acid (HCl) and fluoride salts such as LiF [3–6] or ammonium bifluoride $(NH_4)HF_2$ [7]. There is also the more recently discovered method to utilize Lewis Acid molten salts [8–12]. The methods exhibit some overlap in available terminations but are mostly complementary. Other methods to produce MXenes are also employed, including electrochemical etching [13–16], and hydrothermal etching [17, 18].

Transition Metal Carbides and Nitrides (MXenes) Handbook: Synthesis, Processing, Properties and Applications, First Edition. Edited by Chuanfang Zhang and Michael Naguib.
© 2024 John Wiley & Sons, Inc. Published 2024 by John Wiley & Sons, Inc.

11.2 Termination Controlled Properties

As stated above, surface terminations are essential to the chemistry of MXenes, and deliberate manipulation, as exemplified above, has the potential to provide MXenes with tailored properties.

The well-explored routes for MXene synthesis by traditional etching with HF or HCl/LiF, will leave –O, –OH, and –F surface terminations. Based on theoretical simulation and experiment results, it has been concluded that these archetype terminations degrade the properties of MXenes such as electrical conductivity [19–21] and electron mobility [22]. Accordingly, removal of surface terminations is inferred to improve the electronic properties and experiments to partially remove the terminations have been conducted. As an example, it has been verified how the electrical conductivity of MXenes increased with the removal and reduction of surface terminations [23, 24]. Additionally, the specific capacity of a lithium-ion battery was increased by 69% by decreasing the –F and –OH content on a $Ti_3C_2T_z$ anode [25].

Apart from the termination coverage, the composition is also critical for the emerging properties. While the termination composition has been theoretically shown to affect the catalytic activity [26–28], –F terminated MXenes have also been experimentally shown to contribute to the electrocatalytic hydrogen evolution reaction performance of Ti_2CT_z [29]. It has also been predicted that the thermal conductivity is superior for F-terminated Ti_3C_2 [30]. In contrast, the replacement of –OH and –F by –O will result in the expansion of the band gap and a significant improvement in the Seebeck coefficient [31]. Also, the magnetic properties can be controlled by the surface terminations. For example, Cr_2TiC_2 has been shown to be nonmagnetic when terminated by –O and antiferromagnetic when terminated with OH or F [32]. –OH terminated MXenes were also found to exhibit ultralow work functions, regardless of M-element, in comparison to –O and –F terminated MXenes [33, 34].

Molten salt etching of MAX phases to MXenes has enriched the range of surface terminations considerably. In contrast to MXene with mixed O, OH, and F or pure O terminations, Ti_3C_2 terminated with Cl, S, Se, or NH was shown to be superconducting at different temperatures [11]. Moreover, a series of MXenes with pure halogen terminals, −Cl, −Br, −I, −BrI, and −ClBrI, were synthesized and show functionality for catalysis, ferromagnetism, and electrochemical energy storage [9, 35].

11.3 Chemical Etching

The termination process through chemical etching was nicely demonstrated by theoretical means as shown in Figure 11.1. The simulation shows how the etchant (here HF) interacts with a MAX phase edge (here Ti_3AlC_2), where particularly the

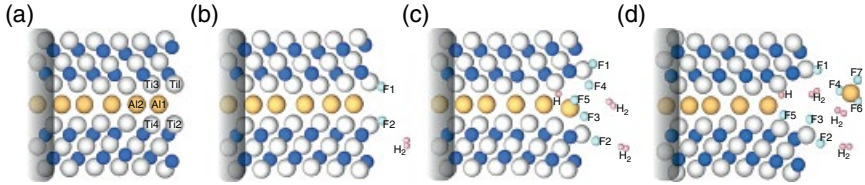


Figure 11.1 Schematic from a simulation of MXene synthesis through chemical etching of MAX phase, showing the lowest energy configurations during the interaction sequence between HF and the Ti_3AlC_2. (a) Shows the edge of the MAX phase, while (b) shows the dissociation of 2 HF molecules, the formation of an H_2 molecule and termination of the Ti_3C_2 edge by F. (c) and (d) Show the continued termination by F and H_2 production along with the gradual formation and final extraction of AlF_3. Silver, blue, orange, cyan, and pink balls represent Ti, C, Al, F, and H atoms, respectively. *Source:* Reproduction with permission Srivastav et al. [36]/American Chemical Society.

A layer is targeted but additionally interacts with the adjacent M elements. In the process, HF dissociates such that F is attracted by the A and M elements. H is moderately attracted by these elements and prefers to form H_2. With increasing HF concentration, the M—A bonds are eventually broken and AlF_3 is formed. Hence, the A element is removed from the MAX phase and the two-dimensional MXene starts to emerge. In the wake of the A element removal, the exposed M element surfaces are terminated by both H and F, though the preferred configuration is F-terminated while H_2 gas emerges as a by-product [36].

The presence of surface terminating species was identified already in the original MXene report wherein Ti_3AlC_2 was etched in 50% aqueous HF [3]. It was proposed that the surface terminations originated from the etching process according to the following simplified reactions:

$$Ti_3AlC_2 + 3HF = AlF_3 + 3/2H_2 + Ti_3C_2 \tag{11.1}$$

$$Ti_3C_2 + 2H_2O = Ti_3C_2\left(OH\right)_2 + H_2 \tag{11.2}$$

$$Ti_3C_2 + 2HF = Ti_3C_2F_2 + H_2 \tag{11.3}$$

Equation (11.1) is required and is followed by Eqs. (11.2) and (11.3), in which the emerging MXene is terminated by species from the etchant. Based on a *c*-parameter obtained from XRD analysis and complementary DFT calculations, the best match was obtained for MXene sheets that were terminated by OH species. Accordingly, Eq. (11.2) was deemed most probable, but additional F terminations according to Eq. (11.3) could not be ruled out. Hence, the surface terminations were proposed to be OH and/or F.

Beyond the presence of –OH and –F, following research using X-ray photoelectron spectroscopy (XPS), experiments have additionally verified the presence of –O [4, 37], which was shown by theoretical means to be stable [1]. The explanation for the observed surface-bound O was proposed [38] to occur as the surface-bound OH recombines into H_2O and O by an equilibrium-driven reaction:

$$Ti_3C_2\left(OH\right)_2 = Ti_3C_2O + H_2O \tag{11.4}$$

The implication of Eq. (11.4) is that one surface site is termination *bare*. In a vacuum environment, this can be sustained momentarily, but at ambient conditions, the bare surface is likely to be immediately terminated according to Eq. (11.2) or (11.3).

11.4 Molten Salt Etching

The use of HF in the synthesis of MXenes is challenging, hazardous, and dangerous. Accordingly, the much less harmful molten salt has been developed as an alternative etchant. Moreover, this reaction is contained during the etching process and requires little exposure to the chemicals. Furthermore, the method has enabled a significant extension in the range of available surface terminations.

The first $Ti_3C_2T_z$ MXene that was synthesized via an element replacement approach, employed a reaction between Ti_3AlC_2 and $ZnCl_2$ [8]. Unlike HF etching, MXene is produced and terminated in a two-step process as described in Figure 11.2. Initially, the Al is replaced by Zn, which is then removed in turn. Following this procedure, the final product is an exclusively Cl-terminated MXene clay, where the final step can be described according to:

$$Ti_3ZnC_2 + ZnCl_2 = Ti_3C_2Cl_2 + 2Zn \tag{11.5}$$

$$Ti_3ZnC_2 + Zn^{2+} = Ti_3C_2 + {Zn_2}^{2+} \tag{11.6}$$

$$Ti_3C_2 + 2Cl^- = Ti_3C_2Cl_2 + 2e^- \tag{11.7}$$

$${Zn_2}^{2+} + 2e^- = 2Zn \tag{11.8}$$

It was later shown that Cl- and, more so, Br-terminated MXenes can efficiently engage in a new type of surface reactions, using a second molten salt etch, wherein the halide ions exchange for other atoms and functional groups as a direct consequence of the relatively weak bond between the transition metal and the -Cl or -Br surface termination. Such MXene surface exchange reactions were achieved using molten alkali metal halides as solvents. For example,

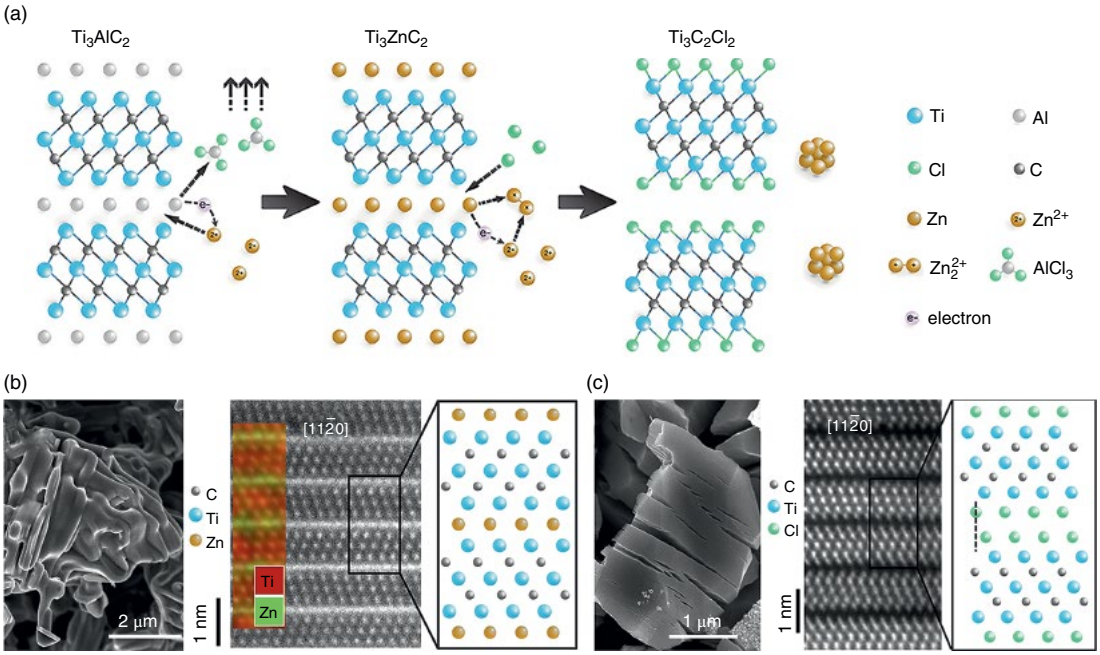


Figure 11.2 Schematic approach to produce MXenes by using $ZnCl_2$ molten salt etching of the Ti_3AlC_2 MAX phase. (a) Shows the initial replacement of the MAX phase A element by Zn, the formation of $AlCl_3$ molecules, and subsequent formation of Cu particles and final Cl termination. The intermediate A-element replacement is verified in (b), where Zn has replaced Al, and the final MXene emerges in (c) exclusively terminated by Cl. *Source:* Li et al. [8]/Reproduced from American Chemical Society.

$Ti_3C_2Br_2$ MXene dispersed in CsBr/KBr/LiBr reacted with Li_2Te and Li_2S to form new Ti_3C_2Te and Ti_3C_2S. This approach resulted in successful surface termination by O, NH, S, Cl, Se, Br, and Te [11].

With a secondary molten salt treatment, the authors were able to exchange the terminal groups. The molten salt method of etching is promising for its versatility in the wide variety of etchable MAX phases and its ability to select the terminal groups of the MXene.

The Lewis-acidic-melt approach was later extended to additionally include Ti_3C_2MXenes with −I, as well as combinations with Cl, Br, and I (−ClBr, −ClI, −BrI, and −ClBrI) halogen surface terminations [35]. While the molten salt method produces MXenes that are difficult to disperse in water, the method is promising for its flexibility, both in terms of etchable MAX phases and for its ability to tailor the MXene surface terminations.

11.5 Termination Site Preference

On the MXene surface, a number of low symmetry site configurations are possible for the terminating species, see Figure 11.3. Although Figure 11.3 employs the M_3X_2 structure to illustrate the most common low symmetry sites, the corresponding configurations can be applied to other MXens as well. The configurations include the threefold coordinated *fcc* and *hcp* sites, as well as the *atop* and the *bridge* positions that position the surface termination above a surface M element or in between two top surface M elements, as shown in Figure 11.3a. These low symmetry sites all represent energetically stable configurations as shown by theoretical means. However, optimization of the structure typically rearranges terminations on both *atop* and bridge configurations into either *fcc* or *hcp* [1, 40]. While MXenes are commonly investigated with the terminations exclusively occupying the *fcc* or *hcp* configurations, MXene allows for mixed configurations. Indeed, configurations with *hcp*-coordinated species on one surface with *fcc*-coordinated species on the other have additionally been investigated [41].

Figure 11.3 (Continued) termination species. TEM images in (b) and (c) show a top-view image of few-layer MXene at ambient temperature and at 400 °C, respectively, revealing the local order among terminations. (d) reveals the UPS valence band spectra of $Ti_3C_2F_{0.8}O_{0.8}$ (solid lines) and $Ti_3C_2F_{0.2}O_{0.8}$ (dashed lines) for different $k_{||}$ values and angle integrated, with corresponding calculated total DOS for $Ti_3C_2F_2$ and $Ti_3C_2O_2$ with terminations at the four low symmetry adsorption sites. The extended arrows indicate the correlations between calculations and experimental data. The measured ARPES spectrum of $Ti_3C_2F_{0.8}O_{0.8}$, including select data from the calculated band structure for the high-symmetry Γ–K and Γ–M directions for $Ti_3C_2O_2$ with O adsorbed only on the bridge site (blue) and for $Ti_3C_2F_2$ with F adsorbed only on the *fcc* site (green). *Source:* (a, d) Schultz et al. [33]/Reproduced from American Chemical Society. (b) Persson et al. [39]/Reproduced from IOP Publishing Ltd.

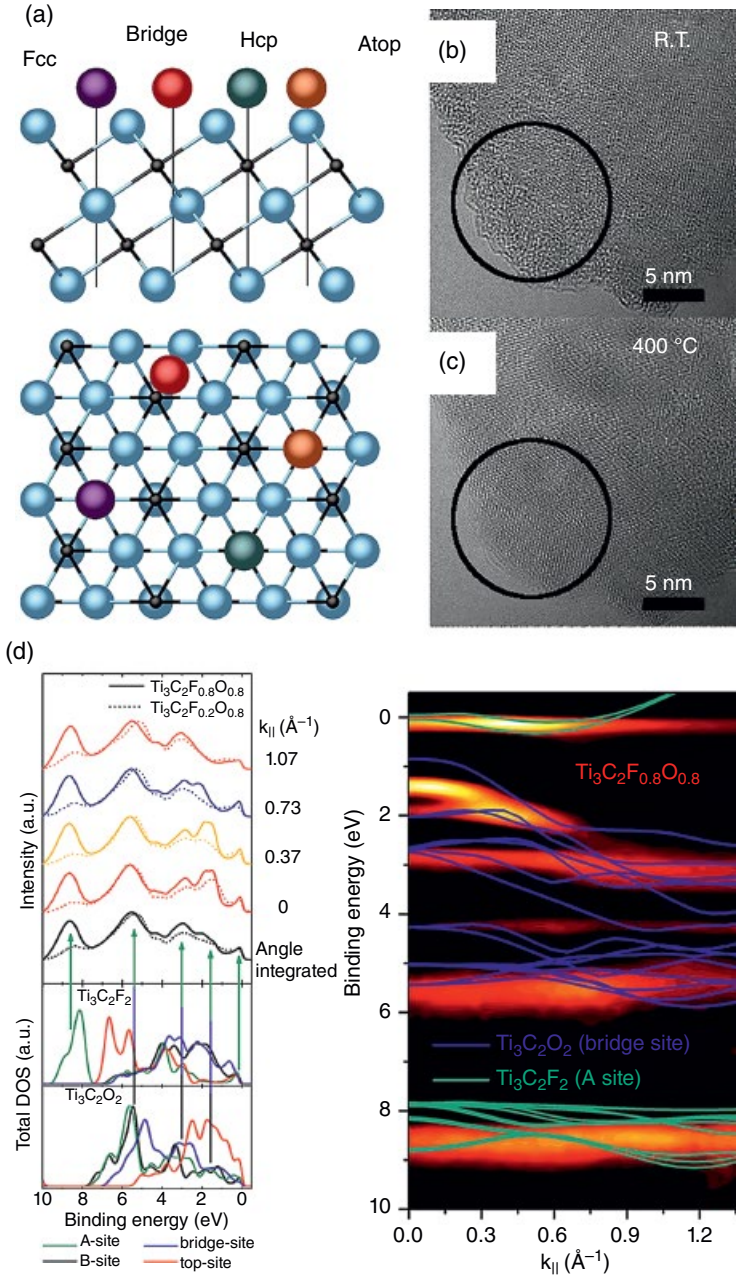


Figure 11.3 (a) Schematic representation of available low symmetry sites on an M_3X_2 type MXene surface, as viewed in cross-section (top) and plan-view (bottom). The four main sites comprise *fcc* (purple), bridge (red), *hcp* (purple), and *atop* (orange), where the vertical position of the terminating species is only representative and changes with

While for both *fcc* and *hcp* sites, the terminating specie is triangulated between three surface M atoms, with the difference that for the *hcp* site, the nearest X element is directly below the terminating specie. For O, OH, and F terminations, the *fcc* is considered to be the most stable site as shown by several investigations [1, 41–46]. The reason that the *hcp* site is the less favored was proposed to originate as a consequence of steric repulsion between the X element and the terminating specie at this site [42]. However, cases have been identified where the terminating specie favors the vicinity of the X atom and hence the *hcp* site in order to gain more electrons [1, 2, 47]. As a general prediction, the relative stability for each model (*fcc*, *hcp*, mixed) depends on the possible ionic state of the surface transition metal atoms. If the transition metals can assume an oxidation state that provides sufficient electrons to both the X element and the adsorbed terminating species, the *fcc* configuration becomes the most stable. Otherwise, *hcp* or mixed emerges as the most stable configuration.

The preference for terminations to occupy the *fcc* site can additionally be understood from the sixfold coordination number of the transition metal (M). Accordingly, the surface M elements form M-X_3T_3 octahedra with the M atom in the center, and together with the adjacent X-element layer atoms and the terminating species layer. It has been observed through PDF analysis that the terminated Ti_3C_2 MXene shows a distortion in the structure, such that the distance between the surface M element and the underlying X layer is different compared to the core M element layer and the adjacent X layers [48]. This was verified through theoretical means, which concluded that the surface Ti 3d orbitals interact more strongly with the terminating specie (O) 2p orbitals compared to the C 2p orbitals, resulting in a distortion of the octahedron [49].

In-situ observations of individual MXene sheets in the (S)TEM and XPS, as prepared by chemical etching, reveal significant disorder among the O surface terminations, while F terminations occupy the preferred *fcc* sites [39]. Only after heating the sheets above 400 °C do surface terminations rearrange to find their minimum energy coordinating sites, see Figure 11.3b, c). These results were corroborated by UPS and ARPES at ambient conditions, together with corresponding total DOS calculations [33], showing a preference for F to occupy the *fcc* site. The same measurements showed best agreement for O at the bridge site, for a mixed terminations sample ($Ti_3C_2O_{0.8}F_{0.8}$). Although alternative sites could not be ruled out, the results are in agreement with *in-situ* (S)TEM observations. While O initially, occupies multiple sites, the preferred site is the *fcc* site. Nearly all *fcc* sites are initially occupied by –F terminations and it is not until F desorbs from the MXene surface at higher temperatures, that the –O species claim the vacated *fcc* sites (see thermal stability below).

In contrast to chemically etched MXenes, material prepared through the molten salt method exhibits surface terminations that exhibit high order, with the

terminations occupying the preferred site [10]. This can presumably be explained by the reaction temperature of the molten salt method, which occurs at significant temperatures in comparison to the temperatures required to organize the surface terminations on chemically etched sheets.

11.6 MXene Surface Termination Saturation

Assuming that all preferred sites are occupied by a termination, then for each surface M element on the MXene sheet, there is one terminating specie. Consequently, the surfaces are saturated for $z = 2$. Yet, other sites remain available and if, for example, both *fcc* and *hcp* sites are terminated, then $z = 4$. Theoretical investigations typically assume $z = 2$, and some experimental investigations commonly normalize the termination ratios with respect to this number. In contrast to the anticipated case, experimental quantifications report termination coverage with z being both larger and smaller than 2 [5, 37, 39]. Storage of MXenes at ambient conditions results in a slow but noticeable oxidation process, increasing the number of –O, and reducing the amount of –F terminations on the MXene sheets, while also transforming the MXene into metal oxyfluorides [37]. Systems in the process of oxidizing to the point of amorphization display $z \sim 3$. However, the increasing occupancy of the MXene surface has been investigated both theoretically and experimentally.

The binding energy vs. surface coverage was calculated for single specie systems on Ti_2C, where it was assumed that the *fcc* sites were first occupied [50]. Additional species were then added to supersaturate the MXene surface by occupation of the *hcp* sites. The binding energy of the *fcc* sites did not change with increasing saturation, regardless of the termination specie. However, with increasing occupancy of the *hcp* site, the binding energy per termination increased significantly, though for all species, the binding energy remained negative, even for saturation of both *fcc* and *hcp* sites. However, the results showed that the surface energy was minimized when all *fcc* sites were occupied and the *hcp* sites were empty.

The oxidation process of single sheet Ti_3C_2 MXene has been investigated, *in-situ*, in an environmental TEM (ETEM), see Figure 11.4a. While following the structural and compositional development during exposure to O_2 gas at increasing temperatures, it was shown that the MXene structure was able to accommodate 1.5 O atoms per surface Ti atom (resulting in a composition of $Ti_3C_2O_3$). Higher temperatures and continued O_2 exposure phases transformed the structure into Titania [51].

The oxidation process at higher temperatures (>1000 °C) was investigated theoretically and suggests that Ti_3C_2 MXene can momentarily hold significant amounts of O prior to phase transforming into carbon-supported Titania [52]. At such

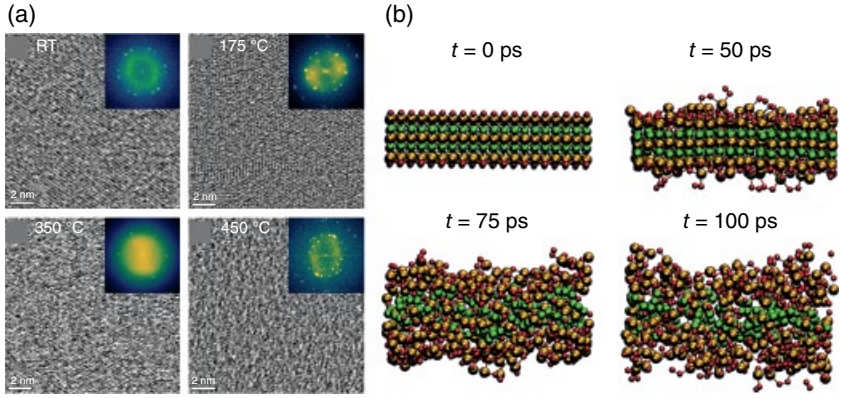


Figure 11.4 (a) Shows the accelerating oxidation and final decomposition of a single Ti_3C_2 MXene sheet, observed under a continuous flow of O_2 gas at increasing temperatures. *Source:* Persson et al. [51]/Reproduced from John Wiley & Sons, Inc./CC BY 4.0. In (b), the simulated rapid oxidation of a Ti_3C_2 sheet in the presence of O_2 molecules at a temperature of 1500 K. *Source:* Reproduction with permission Lotfi et al. [52]/Royal Society of Chemistry.

temperatures, MXene is known to transform into a bulk oxycarbide, but the investigation supports supersaturation of the MXene surface, see Figure 11.4b.

11.7 Thermal Stability of Terminations

The relative stability of the O, OH, and F (as well as H) terminating species has been considered by both theoretical and experimental means. Bader charge and thermodynamic stability analysis has concluded that for *fcc* site saturated MXene surfaces ($z = 2$) the order of stability goes as $Ti_3C_2O_2 > Ti_3C_2F_2 > Ti_3C_2OH_2 > Ti_3C_2H_2$ [2, 49]. Accordingly, it should be feasible to remove these terminations by means of thermal heating, in the reverse order. The stability of the native terminations has been investigated by a range of experimental methods and reveals a complex interplay between F and O terminations, see Figure 11.5.

While –H terminations are not considered to be stable on MXene surfaces, dissociation of –OH has been reported at temperatures above 200 °C for Ti MXenes, but temperatures up to 400 °C has also been observed [23, 53, 54]. Experiments also suggest that –OH terminations may recombine during heat treatment in vacuum or under an inert atmosphere. Two –OH terminations will then be converted to –O and water, where the remaining O termination can resist higher temperatures [23, 25, 38, 39].

The thermal stability of –F terminations varies significantly between reports. Some investigations claim that F dissociation is initiated simultaneously with

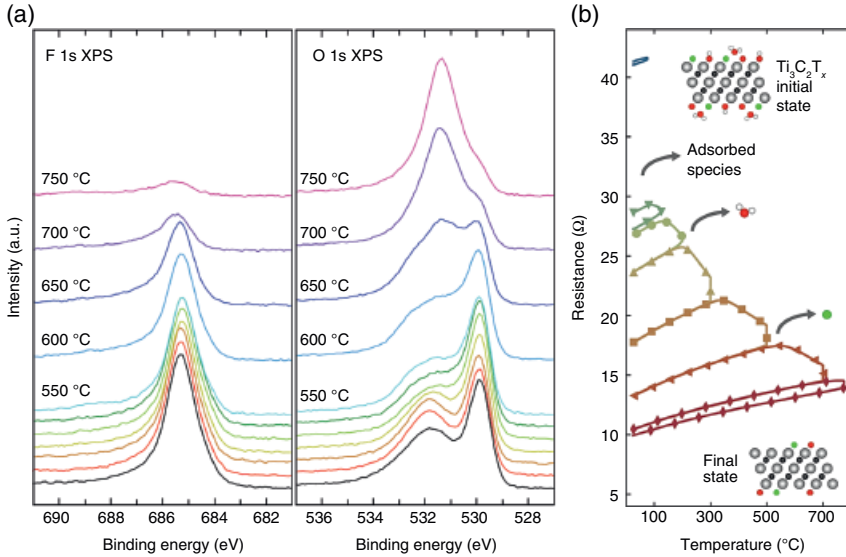


Figure 11.5 Temperature programmed XPS measurements in (a) revealing the temperature-dependent behavior for the gradual desorption of F and the dynamics of O while moving between sites on the surface of $Ti_3C_2T_x$. *Source:* Persson et al. [39]/IOP Publishing/CC BY 3.0. (b) Shows the evolution of the $Ti_3C_2T_x$ electronic properties (resistance) during *in-situ* vacuum annealing in a TEM. The heating and cooling curves are shown for each annealing step. The resistance decreased with each step during annealing. With annealing, the MXene sample resistance is affected by the loss of adsorbed species, intercalants, and terminating species and these processes are shown schematically. *Source:* Adapted from Schultz et al. [33] and Persson et al. [39].

–OH at 200 °C, with the difference between –OH and –F that the dissociation rate of the latter is much slower [22, 25, 29]. In contrast, other reports identify loss of –F terminations at temperatures from 400 °C to 1000 °C, with decreasing dissociation temperature onset with increasing –F content [23, 53, 55].

While much of the reported discrepancies may originate from the quality of the prepared material, one observation has been reported from a single crystal $Ti_3C_2T_x$ thin film, thereby entirely removing contributions from possible residual phases. In the report, the relative changes in Ti, C, O, and F were investigated by temperature-programmed XPS. It was observed F starts to desorb at ~500 °C until –F is entirely removed at ~750 °C as shown in Figure 11.5a [39].

The –O terminations remained on the MXene surface at these temperatures, which is the point of phase transformation of the $Ti_3C_2T_z$ MXene, into a cubic bulk-like Ti(O,C) structure, as reported by several investigations [22, 39, 55, 56]. Accordingly, removal of the –O termination by thermal heating is not a viable route and requires alternative post-processing methods.

Similar to –F, –Cl terminations from molten salt etched MXenes remained stable during heating to temperatures up to ~750 °C, at which point the terminations started to gradually disappear suggesting a more stable termination [10].

11.8 Post Processing of Terminations

An attractive way of tailoring the ratio and composition of surface terminations is by post-etch processing, since this allows for further tuning of MXene properties. Currently, alkalization is the most common post-processing method and consists of two simultaneous processes: surface termination substitution and ion intercalation.

Alkalization predominantly targets the –F terminations on MXene sheets as –F is not stable at high pH values. Accordingly, immersion of MXenes in alkaline solutions at specific concentrations, temperatures, and stirring conditions, enables substitution of –F terminations by –OH, while simultaneously expanding the distance between sheets [57, 58]. Since the intercalation and subsequent increased layer separation, it is proposed that this will enable further interaction between the MXene surface and the alkaline solution to further facilitate the alkalization process.

As an example, through alkalization together with a 1-hour heating process at 550 °C of the processed MXene in vacuum, it as shown that the F/Ti ratio of $Ti_3C_2T_z$ decreased from the initial 0.33–0.016 and changed the O/F ratio to 28 [24]. In contrast to the –F terminations, –O based species remained on the surface where during the alkalization process, they seized the preferred sites, thus becoming more stable than after the initial etching process [39].

Alkalization of MXenes does not only change the chemical and/or electrochemical properties of MXenes but has also been suggested to protect the MXene surfaces from oxidation in air [59]. Apparently, alkalization is a feasible route toward manipulating the surface terminations and their ratios, while thermal heating can remove specific terminations at controlled temperatures. Accordingly, a combination of the two processes may be used to tailor the terminations and accordingly the physical properties of the MXene sheets. Similar to alkalization, salt-like KOAc can produce –OH during hydroxylation and has been employed to produce similar results [60].

In addition to liquid processing, post-processing of MXene sheets by combinations of vacuum heating and gas phase exposures has also been explored theoretically and experimentally to manipulate the native surface terminations, while also enabling surface termination by non-native species [61, 62].

The depletion of MXene surfaces from –F terminations by means of a thermal process, renders –O the remaining termination as described above. Exposures of such –F-depleted sheets to H_2 gas at elevated temperatures were observed *in-situ*

in an environmental TEM. This process rendered the MXene surface nearly termination-free and left a depleted MXene surface, through a reaction between the remaining –O terminations and the H_2 gas, according to:

$$Ti_3C_2\left(O\right)_2 + 2H_2 = Ti_3C_2 + 2H_2O \tag{11.9}$$

The production of H_2O was identified via a residual gas analyzer and the composition was identified by electron energy loss spectroscopy. Consequently, a feasible route for reducing the surface terminations exists, and is schematically described and experimentally shown in Figure 11.6 [62]. This approach enables fundamental investigations of non-terminated MXenes, and additionally allows for re-termination by noninherent species, which was shown for carbon dioxide, see Figure 11.6.

Post-processing of MXenes through a combination of gas exposures at elevated temperatures was also employed to efficiently remove –F terminations. A combination of MXene heating and simultaneous exposure to H_2 gas, was shown to reduce the –F/Ti ratio from 0.2 to 0.05 [25, 63]. Although the applied temperature was on par with observations for thermal removal of –F terminations.

Essentially, surface terminations are most easily chosen through the etchant, but post-processing through alkalization, thermal heating, and gas exposures allows for selective tailoring of inherent surface terminations and addition of noninherent terminations. This enhances the range of available surface chemistries dramatically increases the property space for MXenes.

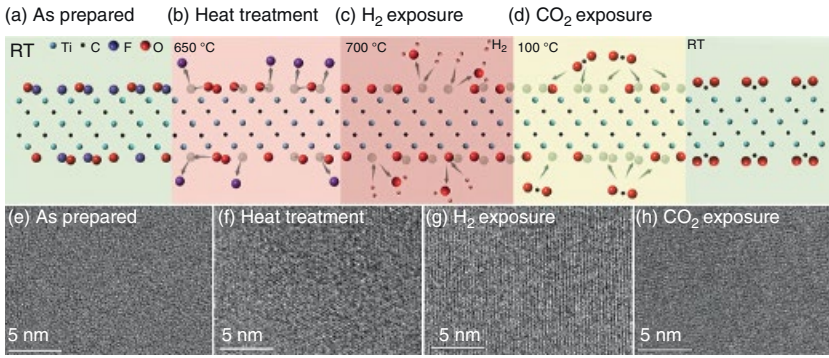


Figure 11.6 Cross-sectional schematics of a $Ti_3C_2T_x$ flake illustrating the applied post-processing that replaces native with non-native terminations. The schematic shows the (a) as prepared, (b) F desorption after heat treatment, (c) H_2O desorption after H_2 exposure of the O terminations, and (d) CO_2 exposure and termination. The plan-view TEM images show the corresponding structure after each step (e–h). *Source:* Persson et al. [62]/Reproduced from John Wiley & Sons, Inc.

11.9 Summary

The MXene properties are critically dependent on the surface terminating species. In the present review article, we have tried to summarize how the different synthesis methods dictate the surface terminations, their coordination, stoichiometry, and composition. It is concluded that traditional MXene synthesis suffers from less control and induces a wider variety of terminations, as well as a higher degree of coordination disorder. Newer MXene synthesis methods, such as molten salt methods, induce much better control of the terminations owing to a more controlled reaction occurring at elevated temperatures. The latter approach furthermore allows for a wider variety of terminations that partly overlap those from traditional methods. It was also shown that post-processing methods, in both gas and liquid, may alter the terminating species, as well as the stoichiometry. Most importantly, a route for termination removal through hydrogen etching was pointed out to prepare termination-depleted surfaces, which in turn enable tailored terminations with unprecedented properties, and applications for MXenes.

Together with progress made in the synthesis of tailored MAX phases and their MXene derivatives, the next generation of 2D materials is here, where the structure and composition are both entirely tailored.

References

1 Khazaei, M., Arai, M., Sasaki, T. et al. (2013). *Advanced Functional Materials* 23: 2185.
2 Ashton, M., Mathew, K., Hennig, R.G., and Sinnott, S.B. (2016). *Journal of Physical Chemistry C* 120: 3550.
3 Naguib, M., Kurtoglu, M., Presser, V. et al. (2011). *Advanced Materials* 23: 4248–4253.
4 Mashtalir, O., Naguib, M., Mochalin, V.N. et al. (2013). *Nature Communications* 4: 1716.
5 Hope, M.A., Forse, A.C., Griffith, K.J. et al. (2016). *Physical Chemistry Chemical Physics* 18: 5099–5102.
6 Ghidiu, M., Lukatskaya, M.R., Zhao, M.-Q. et al. (2014). *Nature* 516: 78–81.
7 Feng, A., Yu, Y., Jiang, F. et al. (2017). *Ceramics International* 43: 6322–6328.
8 Li, M., Lu, J., Luo, K. et al. (2019). *Journal of the American Chemical Society* 141: 4730–4737.
9 Li, Y., Shao, H., Lin, Z. et al. (2020). *Nature Materials* 19: 894–899.
10 Lu, J., Persson, I., Lind, H. et al. (2019). *Nanoscale Advances* 1: 3680–3685.
11 Kamysbayev, V., Filatov, A.S., Hu, H. et al. (2020). *Science* 369: 979–983.
12 Dong, H., Xiao, P., Jin, N. et al. (2021). *Chem Electrochem* 8: 957–962.

13 Sun, W., Shah, S.A., Chen, Y. et al. (2017). *Journal of Materials Chemistry A* 5: 21663–21668.

14 Sun, Z., Yuan, M., Lin, L. et al. (2019). *ACS Materials Letters* 1: 628–632.

15 Yin, T., Li, Y., Wang, R. et al. (2021). *Ceramics International* 47: 28642–28649.

16 Pang, S.Y., Wong, Y.T., Yuan, S. et al. (2019). *Journal of the American Chemical Society* 141: 9610–9616.

17 Wang, C., Shou, H., Chen, S. et al. (2021). *Advanced Materials* 33: e2101015.

18 Li, T., Yao, L., Liu, Q. et al. (2018). *Angewandte Chemie, International Edition in English* 57: 6115–6119.

19 Enyashin, A.N. and Ivanovskii, A.L. (2012). *Computational & Theoretical Chemistry* 989: 27–32.

20 Xie, Y. and Kent, P.R.C. (2013). *Physical Review B: Condensed Matter and Materials Physics* 87 (23): 235441.

21 Li, T., Yan, X., Huang, L. et al. (2019). *Journal of Materials Chemistry A* 7: 14462–14465.

22 Yun, T., Kim, H., Iqbal, A. et al. (2020). *Advanced Materials* 32: e1906769.

23 Hart, J.L., Hantanasirisakul, K., Lang, A.C. et al. (2019). *Nature Communications* 10: 522.

24 Halim, J., Persson, I., Eklund, P. et al. (2018). *RSC Advances* 8: 36785–36790.

25 Lu, M., Li, H., Han, W. et al. (2019). *Journal of Energy Chemistry* 31: 148–153.

26 Morales-García, Á., Calle-Vallejo, F., and Illas, F. (2020). *ACS Catalysis* 10: 13487–13503.

27 Niu, K., Chi, L., Rosen, J., and Björk, J. (2020). *Physical Chemistry Chemical Physics* 22: 18622–18630.

28 Niu, K., Chi, L., Rosen, J., and Björk, J. (2021). *Journal of Physics Condensed Matter* 33: 235201–235207.

29 Li, S., Tuo, P., Xie, J. et al. (2018). *Nano Energy* 47: 512–518.

30 Gholivand, H., Fuladi, S., Hemmat, Z. et al. (2019). *Journal of Applied Physics* 126: 065101–065106.

31 Liu, P., Ding, W., Liu, J. et al. (2020). *Journal of Alloys and Compounds* 829: 154634–154641.

32 Yang, J., Zhou, X., Luo, X. et al. (2016). *Applied Physics Letters* 109: 203109.

33 Schultz, T., Frey, N.C., Hantanasirisakul, K. et al. (2019). *Chemistry of Materials* 31: 6590–6597.

34 Khazaei, M., Arai, M., Sasaki, T. et al. (2015). *Physical Review B: Condensed Matter and Materials Physics* 92: 075411.

35 Li, M., Li, X.-L., Qin, G. et al. (2021). *ACS Nano* 15: 1077.

36 Srivastav, P., Mishra, A., Mizuseki, H. et al. (2016). *ACS Applied Materials & Interfaces* 8 (36): 24256–24264.

37 Halim, J., Cook, K.M., Naguib, M. et al. (2016). *Applied Surface Science* 362: 406–417.

38 Karlsson, L.H., Birch, J., Halim, J. et al. (2015). *Nano Letters* 15: 4955.
39 Persson, I., Näslund, L.-Å., Halim, J. et al. (2017). *2D Materials* 5: 015002.
40 Gan, L.-Y., Huang, D., and Schwingenschlögl, U.J. (2013). *Journal of Materials Chemistry A* 43: 13672–13678.
41 Naguib, M., Mochalin, V.N., Barsoum, M.W., and Gogotsi, Y. (2014). *Advanced Materials* 26: 992–1004.
42 Tang, Q., Zhou, Z., and Shen, P. (2012). *Journal of the American Chemical Society* 134: 16909–16916.
43 Khazaei, M., Arai, M., Sasaki, T. et al. (2014). *Physical Chemistry Chemical Physics* 16: 7841.
44 Zhang, X., Ma, Z., Zhao, X. et al. (2015). *Journal of Materials Chemistry A* 3: 4960.
45 Hu, J., Xu, B., Ouyang, C.Y. et al. (2016). *RSC Advances* 6: 27467–27474.
46 Magne, D., Mauchamp, V., Célérier, S. et al. (2015). *Physical Review B* 91: 201409.
47 Khazaei, M., Ranjbar, A., Arai, M., and Yunoki, S. (2016). *Physical Review B* 94: 125152.
48 Shi, C., Beidaghi, M., Naguib, M. et al. (2014). *Physical Review Letters* 112: 125501.
49 Hu, T., Li, Z., Hu, M. et al. (2017). *Journal of Physical Chemistry C* 121: 19254–19261.
50 Li, L. (2016). *Computational Materials Science* 124: 8–14.
51 Persson, I., Halim, J., Palisaitis, J. et al. (2020). *Advanced Functional Materials* 1909005.
52 Lotfi, R., Naguib, M., Yilmaz, D.E. et al. (2018). *Journal of Materials Chemistry A* 6: 12733.
53 Kong, F., He, X., Liu, Q. et al. (2018). *Electrochimica Acta* 265: 140–150.
54 Zhou, J., Zha, X., Chen, F.Y. et al. (2016). *Angewandte Chemie, International Edition in English* 55: 5008–5013.
55 Seredych, M., Shuck, C.E., Pinto, D. et al. (2019). *Chemistry of Materials* 31: 3324–3332.
56 Wang, H., Wu, Y., Zhang, J. et al. (2015). *Materials Letters* 160: 537–540.
57 Xie, Y., Naguib, M., Mochalin, V.N. et al. (2014). *Journal of the American Chemical Society* 136: 6385–6394.
58 Guo, J., Peng, Q., Fu, H. et al. (2015). *Journal of Physical Chemistry C* 119: 20923–20930.
59 Mu, W., Du, S., Yu, Q. et al. (2018). *Dalton Transactions* 47: 8375–8381.
60 Dall'Agnese, Y., Lukatskaya, M.R., Cook, K.M. et al. (2014). *Electrochemistry Communications* 48: 118–122.
61 Björk, J. and Rosen, J. (2021). *Chemistry of Materials* 33: 9108–9118.
62 Persson, I., Halim, J., Lind, H. et al. (2019). *Advanced Materials* 805472.
63 Lai, S., Jeon, J., Jang, S.K. et al. (2015). *Nanoscale* 7: 19390–19396.

12

Delamination and Surface Functionalization of MXenes

Mohammad Jafarpour[1,2], Sina Abdolhosseinzadeh[1], Jakob Heier[1], Frank Nüesch[1,2], and Chuanfang Zhang[3]

[1] *Department of Advanced Materials and Surfaces, Laboratory for Functional Polymers, Swiss Federal Laboratories for Materials Science and Technology (Empa), ETH Domain, Dübendorf, Switzerland*
[2] *Institute of Materials Science and Engineering, Swiss Federal Institute of Technology Lausanne (EPFL), Lausanne, Switzerland*
[3] *College of Materials Science and Engineering, Sichuan University, Chengdu, Sichuan, China*

12.1 Introduction

Two-dimensional (2D) layered materials started to shine and arouse many interests when a monolayer of graphene was exfoliated from graphite in 2004 [1]. The layers are connected by interplanar forces, which are weaker than their intraplanar binding forces. Separation and isolation of layers and obtaining individual or few layers can lead to remarkable properties in this family of materials. A single layer of 2D materials is formed of a series of a single atomic layer (such as graphene) or a single crystalline layer with several atomic layers (such as MXenes) [2, 3].

MXenes, one of the latest additions to the family of 2D materials, are based on a layered MAX phase with the generic chemical formula of $M_{n+1}X_nT_x$ ($n = 1, 2, 3,$ or 4), whereby the M represents an early transition metal (such as Sc, Y, Ti, Zr, Hf, V, Nb, Ta, Cr, Mo, and W), X corresponds to carbon and/or nitrogen, T represents terminal groups attached to the surface (−OH, −O, and −F), and x is the number of the termination. Currently, there are two main strategies for preparing MXenes: top-down approaches such as etching and exfoliation, and bottom-up methods such as chemical vapor deposition, template method, and plasma-enhanced pulsed laser deposition [4, 5].

Transition Metal Carbides and Nitrides (MXenes) Handbook: Synthesis, Processing, Properties and Applications, First Edition. Edited by Chuanfang Zhang and Michael Naguib.
© 2024 John Wiley & Sons, Inc. Published 2024 by John Wiley & Sons, Inc.

In 2011, Gogotsi et al. [6] discovered that the Al atomic layers in Ti_3AlC_2 (MAX precursors) could be etched, resulting in accordion-like $Ti_3C_2T_x$ powder with van der Waals force and hydrogen bonds formed by surface groups between each layer.

To further develop MXenes and extend their applications, many attempts have been made to modify their properties by applying different approaches. The properties of MXenes are known to be intensely dependent on their surface terminations. So to meet various demands on MXenes' applications, researchers have mainly focused on developing new $M_{n+1}X_n$ chemistries and methods for surface chemistry engineering. Therefore, it is crucial to control the type and content of the surface functional groups by selecting suitable routes for preparation [7–9].

Density functional theory (DFT) calculations can predict the native surface terminations; however, it is still complicated to precisely customize surface chemistries in the experiments [10]. Different outer M atomic layers can modulate surface chemistry. In addition, modifying the terminal surface groups can also be generated by numerous interlayer intercalation agents, delamination, and various surface functionalization strategies.

This chapter will generally explain the relation between MXenes (mostly $Ti_3C_2T_x$) preparation routes and surface terminations. The modulation of surface chemistry with intercalation and delamination steps will be focused on as well.

12.2 Effect of Preparation Routes on the Surface Terminations of MXenes

The surface chemistry of MXenes depends on their crystal structure and synthesis steps. Here, after a short explanation of different preparation routes, we will discuss their consequences and effects on the final surface terminations. The comprehensive information about etching methods can be found in Chapter 3. Currently, the predominant approach for obtaining $Ti_3C_2T_x$ is selective etching. In this method, specific atomic layers (in most cases Al) were removed from the MAX phase precursors by applying different etch solutions and processes, including HF-etching, fluoride-containing solution etching, fluoride-free, and some other modified techniques [11].

12.2.1 HF Etching

Hydrofluoric acid is the most commonly used method to obtain MXenes from their corresponding MAX precursors. The following reactions define the etching process for the synthesis of $Ti_3C_2T_x$ [12]:

$$Ti_3AlC_2 + 3HF = AlF_3 + \frac{3}{2}H_2 + Ti_3C_2 \tag{12.1}$$

$$Ti_3C_2 + 2H_2O = Ti_3C_2\left(OH\right)_2 + H_2 \tag{12.2}$$

$$Ti_3C_2 + 2HF = Ti_3C_2F_2 + H_2 \tag{12.3}$$

As mentioned above, the production of Ti_3C_2 layers from Ti_3AlC_2 is related to Eq. (12.1), and Eqs. (12.2) and/or (12.3) show the formation of surface functional groups in the aqueous etching process and enable the production of Ti_3C_2 with rich terminations, such as −F, −OH, and −O [13].

After the etching process, weak hydrogen or van der Waals bonds replace the strong Ti—Al bonds. Interaction replacements assist the intercalation and delamination of the multilayer stacked MXene into a single or few layers [13, 14]. Indeed, the delamination of MXenes began with the penetration of HF into the edge points of the particles, which caused a gap formation by gradually detaching the interlayers. Step-by-step progression of intercalation by HF shows that HF molecules weaken Al—Ti bonds and generate separated MXene layers with F/H terminal atoms. Therefore, it causes fluorinated MXenes with expanded interlayer spacing, allowing the further intercalation of HF molecules and forming AlF_3 and H_2, as shown in Figure 12.1 [3].

In this case, H_2O facilitates the reaction by terminating the MXene by −OH. It is worth noting that etching is a dynamically controlled process; therefore, surface properties are significantly affected by the etching circumstances, such as the etching period, concentration of HF, and reaction temperature. Thus, different HF concentrations strongly influenced the species of surface terminations during the etching process of $Ti_3C_2T_x$. It was shown that by increasing the concentration of HF, the −F terminations increased, and the proportion of oxygen-containing terminations decreased [3, 12, 15].

The relative number strongly intercalated with water increases with the higher HF concentration. This is based on the water interaction with higher coordination with increased defects; consequently, the ability to insert water between the layers has become greater. Nevertheless, washing the produced powder, a crucial step in the synthesis of MXenes, involves an irreversible reduction in the amount of the introduced water. The adjusting of HF concentration also plays a role in the modification of terminal groups (O/OH ratio) distribution and the stability against surface oxidation. Therefore, the higher the HF etching concentration, the more the −F terminations (Figure 12.2) [15, 16].

Although HF etching is the widely implemented method, the toxicity, highly corrosive nature, operational risks, and environmentally unfriendly effects are the concerns with HF etchant. In addition, the etched products have a large number of −F groups on the surface, which are unfavorable in terms of some applications [17, 18].

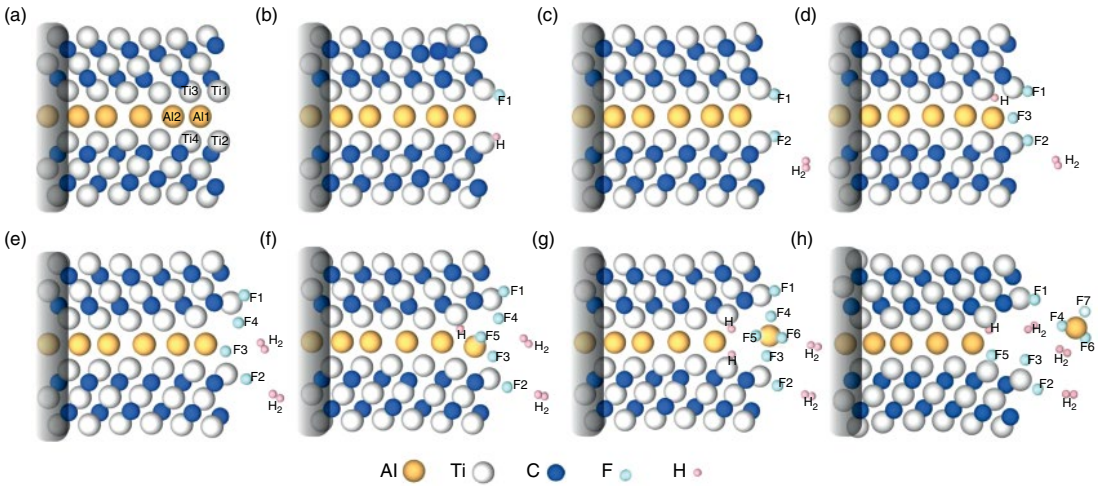


Figure 12.1 Intercalation of HF with MAX phase edge, (a) Ti_3AlC_2 MAX phase with a layer of Al atoms squeezed between the MXenes layers at the lowest energy configurations, (b–h) intercalation steps MAX complexes from the edge with HF and extraction of AlF_3. *Source:* Srivastav et al. [3]/American Chemical Society.

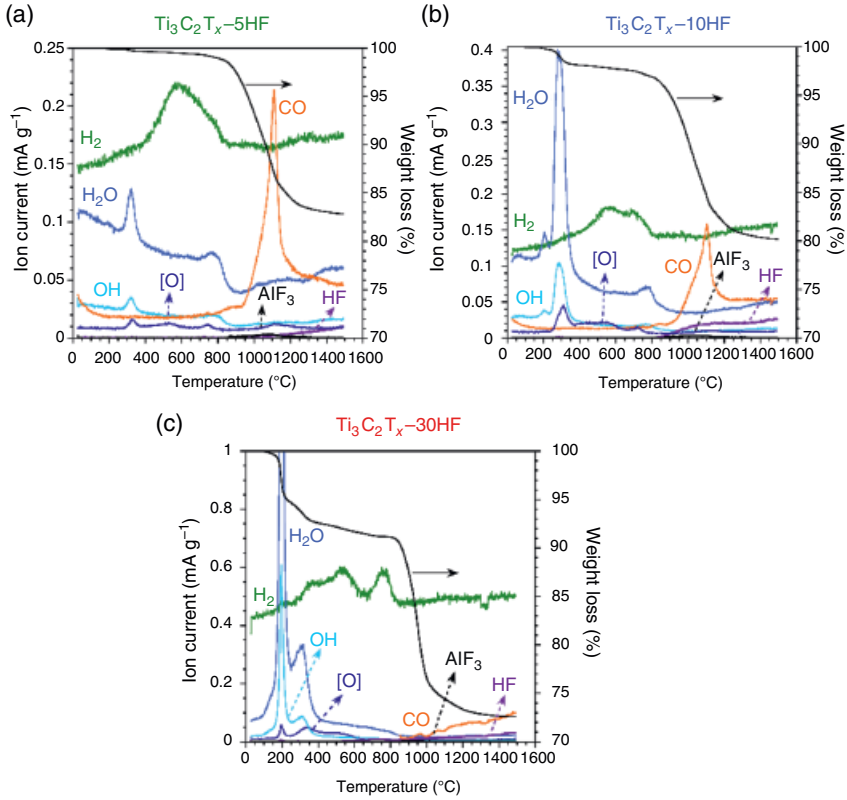


Figure 12.2 Thermal gravimetric TG and mass spectrometry analysis for $Ti_3C_2T_x$. The products were analyzed after etching with different concentrations of HF (wt%) (a) 5, (b) 10, and (c) 30. *Source:* Adapted from Seredych et al. [15].

12.2.2 Fluoride-Containing Solution Etching

To avoid or minimize the use of HFs etchant, alternative etching routes, for instance, fluoride salts with acid or without acid, have been used to produce *in-situ* HF. In the acid-based method, primarily hydrochloric acid (HCl) and lithium fluoride (LiF) are mixed to form HF for the etching of the Al in MAX paternal particles (Eq. [12.4]). The etching process and related reactions are similar to Eqs. (12.1)–(12.3) [19].

$$LiF + HCl = HF + LiCl \tag{12.4}$$

The F^- ions can react with the Al atoms of MAX precursors based on the high reactivity [6]. Li^+ ions could be inserted between the $Ti_3C_2T_x$ layers during the LiF–HCl etching, thus, expanding the interlayer spacing, causing the increasing the distance of $Ti_3C_2T_x$ flakes and the number of terminal hydroxyl groups [20, 21].

Additionally, the hydration of the intercalated lithium during etching results in the incorporation of water molecules into the layered structure of $Ti_3C_2T_x$, which extends the interlayer gap even further [21]. The weakening of interlayer van der Waals forces causes the enlarged interlayer spacing, and these layers can directly be delaminated into monolayer MXene nanosheets by shaking the dispersion even by hand.

Similar to the HF etching process, the *in-situ* HF formation etching route also endows MXenes with surface functionalities, that is, –F, –OH, and –O. According to the Kim et al. [22] studies, they synthesized $Ti_3C_2T_x$ with numerous hydroxyl groups via LiF–HCl etching. The interlayer spacing of MXenes which were produced by the *in-situ* HF forming method, shows a reduction after drying the etching solution due to the disappearance of interlayer water molecules. The type of surface terminations also affects the interlayer spacing. Since the –F termination group has strong hydrophobicity, it shows a distinct opposite relation with the number of water molecules and *d*-spacing. The rising content of the –F groups results from diminishing the interlayer water molecules and the interlayer spacing [23]. Usually, MXene flakes produced by *in-situ* HF formation (and specifically the Minimally Intensive Layer Delamination [MILD]) have larger lateral flakes since the high LiF concentration promotes the intercalation of Li and the removal of Al atomic layers from the MAX phase, resulting in a sizeable lateral size, and fewer defects in comparison with the direct HF etching approach (Figure 12.3) [20].

At present, mixing several fluoride-containing reagents with acid has developed into a sophisticated etching technique to etch the MAX phases. The variation of fluoride salts can change the interlayer spacing of MXenes to meet the desired application requirements. In addition to LiF, other fluoride salts have also been used as a part of the etching route. Liu et al. [24] integrated HCl with various fluoride salts, such as LiF, NaF, KF, and NH_4F, to form a mixed solution for etching the

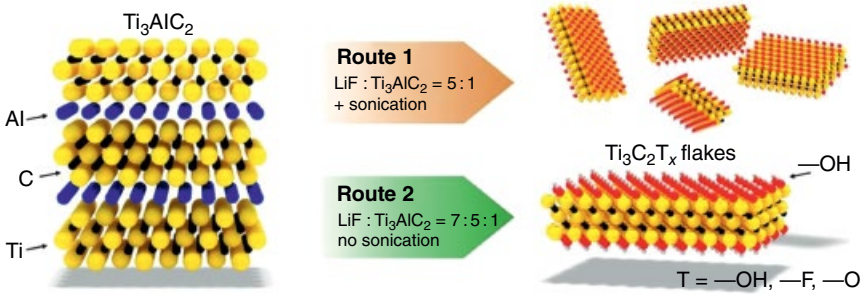


Figure 12.3 Schematic illustration of two different routes for synthesizing $Ti_3C_2T_x$ flakes by implementing different ratios of LiF/Ti_3AlC_2. *Source:* Lipatov et al. [20]/John Wiley & Sons.

Ti_3AlC_2. Mixing the fluoride salts with other acids can also affect the preparation of MXenes. Ghidiu et al. [21] selected some fluoride salts (such as NaF, KF, CsF, CaF_2, and NH_4F) as fluoride sources and utilized H_2SO_4 instead of HCl. The results showed that $Ti_3C_2T_x$ was still be achieved by the *in-situ* HF etching. In addition, a variety of cations, including Na^+, K^+, NH_4^+, Mg^{2+}, and Al^{3+}, as well as water, were intercalated between the $Ti_3C_2T_x$ layers, thus, increasing the interlayer spacing.

Guo et al. [25] considered that substituting H_2SO_4 with HCl could increase the SO_4^- group on the surface of $Ti_3C_2T_x$, which is a large-size electrostatic termination. Conducting the H_2SO_4/LiF etching strategy reveals that the SO_4^- termination expanded the interlayer spacing of as-prepared MXenes. Etching with a complex acidic system, HF/H_2SO_4 or HF/HCl, leads to different surface terminations, resulting in the evolution of other species. Both the HF/H_2SO_4 and HF/HCl systems contain negligible amounts of water.

Additionally, when FeF_3 replaces the LiF, the kinetics of the MAX to MXene transformation is enhanced, even when the initial F/Al ratio is the same, thanks to the oxidation properties of Fe^{3+}, which is interesting to reduce the global cost of the MXene production. On the other hand, this method does not allow spontaneous delamination in water, as in the case of the LiF/HCl etching method [16].

A modified MILD approach, Evaporated-Nitrogen Minimally Intensive Layer Delamination (EN-MILD), minimizes oxidation and increases the acid during the etching stage. Employing EN-MILD results in a high delamination yield and colloidal concentration [26]. As illustrated in Figure 12.4, the etching MAX phase by the EN-MILD process leads to a synthesis (delamination) yield as high as 60%, which is four times higher than that obtained by the MILD approach (≈14%). Considering higher concentrations of Li ions offered by the EN-MILD process is essential. This led to a higher delamination yield of the MXene single layer. Longer etching time also contributed to defect formation (formation of vacancy clusters) in the MXene flakes (30 hours).

On the other hand, longer etching time in EN-MILD increases –O content as a sign of a higher content of oxygen functional groups. Another interesting result is the amount of –F content in the traditional MILD and EN-MILD approaches. At the same etching time, less fluorine was detected for the EN-MILD method, which can benefit electrochemical properties. The results are depicted in Figure 12.4.

12.2.3 Fluoride-Free Etching

A variety of techniques have been widely and effectively employed to synthesize MXenes. The extensive use of hazardous HF or fluoride-based substances like LiF/HCl raises significant concerns about operational safety. Furthermore, the etching procedure generally introduces –F or –O impurity groups to the surface of

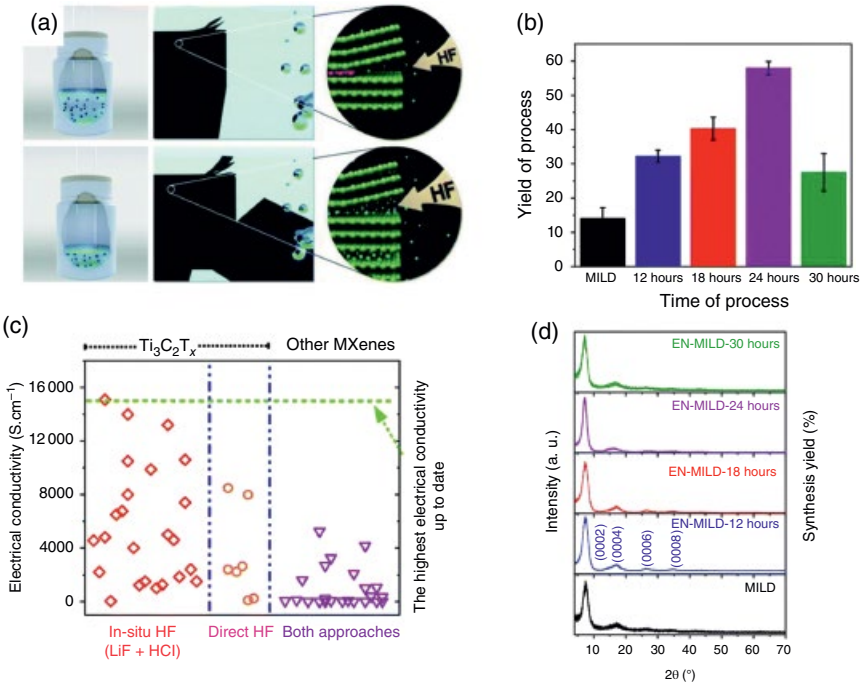


Figure 12.4 Effect of various processes and time in preparation of $Ti_3C_2T_x$ and other MXenes (a) representation of EN-MILD synthesis route depicting etching medium from initial steps and progressing the reactions during the time where evaporating of the liquid media leads a higher acids and Li-ion concentrations, which will improve the removing of Al and yield, (b) the yield of process vs. process time, (c) effect of different routes and consequently the electrical conductivity of different synthesis methods (using direct HF or MILD rout), and (d) the crystal structural studies and differences between MILD and EN-MILD methods. *Source:* Zeraati et al. [26]/Reproduced from Royal Society of Chemistry.

MXenes, affecting their characteristics. The choice of non-fluorinated agents, such as alkali-based compounds, has been shown to significantly impact surface chemistry, delamination ability, and a wide variety of properties [16, 18, 27, 28].

By soaking Ti_3AlC_2 powder in NaOH water solution at 270 °C, Li et al. [29] established an alkali-etching process for synthesizing high-purity multilayer $Ti_3C_2T_x$. The fluorine-free process enabled the production of more –OH and –O terminations on the resulting $Ti_3C_2T_x$. Jawaid et al. [30] recently established a unique room-temperature etching process for preparing $Ti_3C_2T_x$ from Ti_3AlC_2 employing halogens (Br_2, I_2, ICl, and IBr) in anhydrous conditions. The production steps for colloidal stable –Br terminated $Ti_3C_2T_x$ utilizing Br_2 in cyclohexane with tetrabutylammonium bromide (TBAB) as a stabilizer to eliminate the related

by-products are described in Figure 12.5. Parameters such as the concentration of the halogen and the solvent, the molar ratio of the MAX phase to the halogen, and the temperature all play a role in this radical-based etching.

Synthesis of MXenes with a pure –Cl and –Br termination can be achieved by etching the MAX phase in several Lewis acidic molten salts above 500 °C. These pure elemental terminations or bare MXenes result from eliminating unwanted oxidation and hydrolysis during the process. Strong Ti–F and Ti–O terminations from a typical etching method act as a barrier to carrying out any post-synthetic covalent surface modifications of MXenes. However, weaker bonding between Ti and terminal groups, which are generated from the Lewis acidic etching route (–Cl and –Br termination), make it easy to further chemical replacements and alter the MXenes surface terminals to –Te, –S, –Se, –O, –NH in alkali metal halide solvents through the exchange reaction between $Ti_3C_2Br_2$ and molten salts such as Li_2Te, Li_2S, Li_2Se, Li_2O, and $NaNH_2$, respectively [31]. Different terminal groups based on synthesis methods are summarized in Table 12.1.

12.3 Intercalation and Delamination of Single and Few-Layer MXenes

The bonding between MXenes and other 2D materials, such as TMDCs, is fundamentally different due to the nature of the atoms and functional groups involved in their structures. MXenes have a stronger bonding within their layers than TMDCs due to covalent bonds between the transition metal atoms and carbon/nitrogen atoms. Additionally, hydrogen bonding between the surface functional groups (e.g. –OH, –F, and –Cl) and the underlying layers also contributes to the strong bonding in MXenes. On the other hand, the bonding between layers in TMDCs is mainly due to weak van der Waals forces, which are weaker than covalent bonds and hydrogen bonding. This makes TMDCs easier to delaminate into individual layers than MXenes. Furthermore, the presence of different functional groups and surface terminations in MXenes can lead to variation in their bonding and properties, making them more versatile for various applications. In contrast, TMDCs typically have more limited variations in their bonding and properties due to their simpler structures.

To start isolating or decreasing the number of stacked MXene layers, a typical procedure is increasing the interlayer distance by introducing species disrupt bonding between the layers. In other words, the etching process causes the replacement of strong M—A bonds with weaker ones, which enables the insertion of various species (inorganic, organic, and ionic) among the MXene layers. These agents increase the c lattice parameter (c-LP) values, therefore, causing further weakening of the interlayer interactions. As a result, the intercalated multilayer

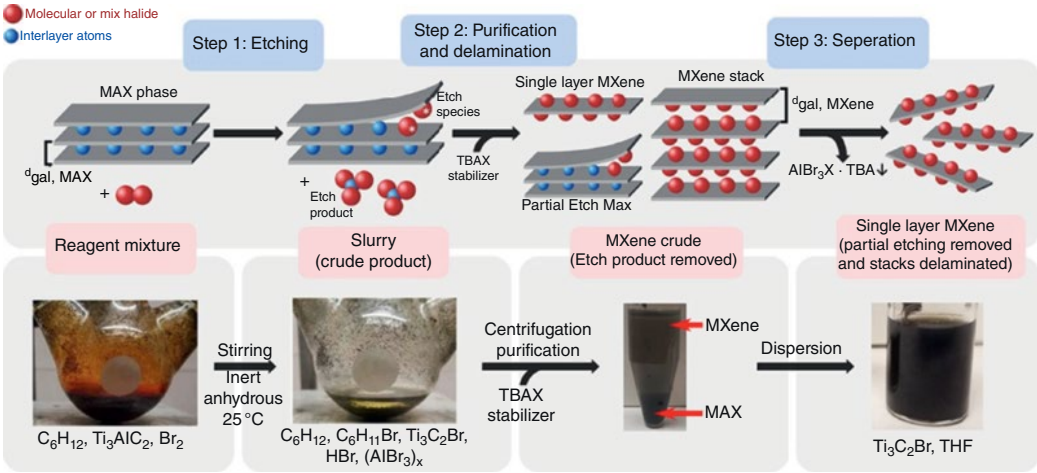


Figure 12.5 Step-by-step formation from the general process of exfoliation by replacement of halide molecules instead of interlayer atoms leads to intercalation and delamination and produces halogen-terminated MXenes. *Source:* Vaia et al. [30]/Reproduced from American Chemical Society.

Table 12.1 Effect of synthesis route on the surface terminations.

Synthesis route	Etchant	Terminal groups	References
Hydrofluoric acid	HF	–F, –O, –OH	[32]
Fluoride-containing solution etching	HCl/LiF	–F, –O, –OH	[20]
	HCl/(Na, K, or NH_4F)	–F, –O, –OH	[21]
	NH_4HF_2	–F, –O, –OH	[33]
Fluoride-free etching	HCl	–Cl, –O, –OH	[28]
	$NaBF_4$/HCl	–F, –O, –OH	[34]
	NaOH	–O, –OH	[29]
	$ZnCl_2$	–Cl	[35]
	$CuCl_2$/NaCl/KCl	–Cl, –O	[36]
	$CdCl_2/CdBr_2$	–Cl, –Br	[30]
	$Li_2Te/Li_2S/Li_2Se/$ $Li_2O/NaNH_2/LiH$	–Te, –S, –Se, –O, –NH, bare	[31]

MXenes can be delaminated into mono or a few layers by sonication or even hand-shaking of dispersion.

The key factor in order to exfoliate the stacked nanosheets of MXenes is to break the interlayer's weak interactions and delamination. To date, organic molecules, inorganic base molecules, and cations are the three types of intercalating agents that facilitate the delamination of multilayer MXenes. Moreover, the surface chemistry of MXenes was found to be affected by the intercalation and delamination strategies.

12.3.1 Metal Cation and Inorganic Intercalants

Several cations, mono- and or multivalent metal cations such as Li^+, Na^+, Mg^{2+}, K^+, Sn^{4+}, and Al^{3+}, have been demonstrated to increase the interlayer spacing (c-LP) of $Ti_3C_2T_x$ MXene. This kind of intercalation was mentioned with the etching process, where metal cations can be used for the spontaneous exfoliation of multilayer $Ti_3C_2T_x$ in aqueous solutions of salts. According to Levi et al. [37], there are more cations, such as Cs^+, Ba^{2+}, Ca^{2+}, that can be employed to intercalate into $Ti_3C_2T_x$ MXene.

Besides the type of intercalating agent, which significantly influences the final expansion of interlayer spacing, the mass and the proportion of components can also be very effective. Shahzad et al. [32] successfully delaminated multilayer $Ti_3C_2T_x$ into single and large flakes without sonication. They optimized the LiF to

Ti_3AlC_2 ratio and changed the concentration of HCl in the etching step. The increasing of protons (H^+) provided by the excessive amount of acid causes improvements in the delamination of $Ti_3C_2T_x$ as a result of Li^+ exchange. Therefore, the strategy uses inorganic materials such as LiCl to enhance the distance between layer spacing by inserting Li cation. This agent is only applicable to the multilayer MXenes etched by the HF/HCl mixture etchant.

An accordion-like $Ti_3C_2T_x$ structure was obtained by Ghidiu et al. [4] with the mixture solution of HF/LiCl. The observations showed that the delamination does not happen appropriately without subsequent ultrasonic treatment. Therefore, it is reasonable to assume that HCl plays a crucial contribution in the delamination. It is worth mentioning that when the Li from the HF/LiCl etchants interacts with the $Ti_3C_2T_x$ interlayer, other ion exchange leads to embedded macromolecular molecules.

Currently, LiF/HCl etching process is the only way for direct delamination of multilayer MXenes into monolayers using the ultrasonic or hand-shaking step. However, the HCl/LiF process without extra intercalation is special compared with other etching processes.

Due to the insertion of Li into the interlayers of multilayer MXenes, enlarges the interlayer spacing of MXenes and weakens the interlayer coupling. The multilayer MXenes generated by this approach may be immediately delaminated without any extra intercalators. Finally, monolayer MXene nanosheets may be generated with a weak ultrasonic treatment or shaking by hands. The delamination could be obtained through a simple hand-shaking treatment with a high concentration ratio (7.5 M LiF/9 M HCl) in comparison with the low concentration (5 M LiF/6 M HCl), which needs more agitation and sonication step to achieve separated individual layers. The other intercalates, such as NH^{4+}, can also be intercalated in bifluoride salts etching solution, but the multilayer MXenes cannot delaminate into monolayers directly [38].

12.3.2 Organic-Base Molecules

Due to some characteristic similarities (such as hydrophilicity and rheological behaviors) between clay and MXenes, researchers thought about using the same intercalating agents used for the clay. Therefore, the organic agents, which are common intercalators for clay, were tested. In 2013, Mashtalir et al. reported that organic molecules such as dimethyl sulfoxide (DMSO) could facilitate the delamination of multilayer $Ti_3C_2T_x$ by expanding the interlayer spacing. Figure 12.6 shows the steps for the delamination of stacked MXene monolayers [39].

The process was started by stirring the dispersion of DMSO and $Ti_3C_2T_x$ for 18 hours at room temperature and followed by a weak sonication treatment in deionized water for 6 hours. The main reason for intercalation with the use of DMSO is

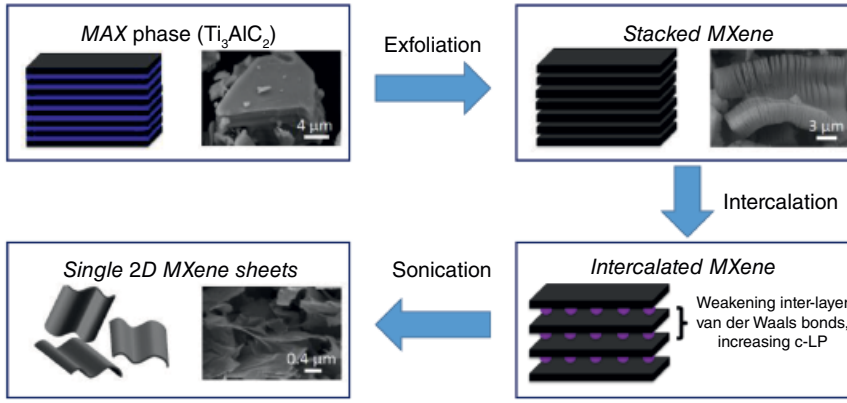


Figure 12.6 Schematic illustration synthesis of $Ti_3C_2T_x$ based on intercalation with DMSO. *Source:* Mashtalir et al. [39]/Reproduced from Springer Nature.

generally related to the repulsion between the methyl group of DMSO and the hydroxyl group on the surface of $Ti_3C_2T_x$. The surface of produced MXenes after intercalating with DMSO is rich in oxygen-containing terminations. As a result, this promotes the delamination of $Ti_3C_2T_x$ nanosheets based on excellent hydrophilicity and a negative-charged surface in deionized water.

Besides DMSO, some other organic materials, like hydrazine monohydrate, *N*-methyl-2-pyrrolidone, *N*, *N*-dimethylformamide, isopropylamine (IPA), and urea, have also been tested as the intercalation agents for the production of multilayer $Ti_3C_2T_x$. However, tetrabutylammonium hydroxide (TBAOH), hydroxyl choline, and n-butylamine, in comparison with DMSO, are all relatively large organic-based molecules, have been determined to have a universal intercalating nature [40].

Among those molecules, ammonium salts such as TBAOH are one of the most studied cations to intercalation. This intercalation leads to a significant increase in the distance between the layers, resulting in swollen MXenes because of penetration and accumulation of cations and weakening the interplanar interaction between the layers. Thus, by gentle hand-shaking, effective delamination is possible to obtain, where other organic intercalators are incapable of etching and delaminating simultaneously. During the TBAOH intercalation, the F content was reduced, and the terminal group of –F was replaced by –O and –OH. Similar swelling behavior was reported in the delamination of V_2CT_x, in which organic bases such as choline hydroxide and *n*-butylamine were used for intercalation [40].

Mashtalir et al. [41] investigated the delamination of the Nb_2CT_x MXene with an organic base solvent. The process begins with the formation of ammonium cation ($R\text{-}NH_3^+$) and a tail (three-carbon-atom alkyl) once IPA is mixed with

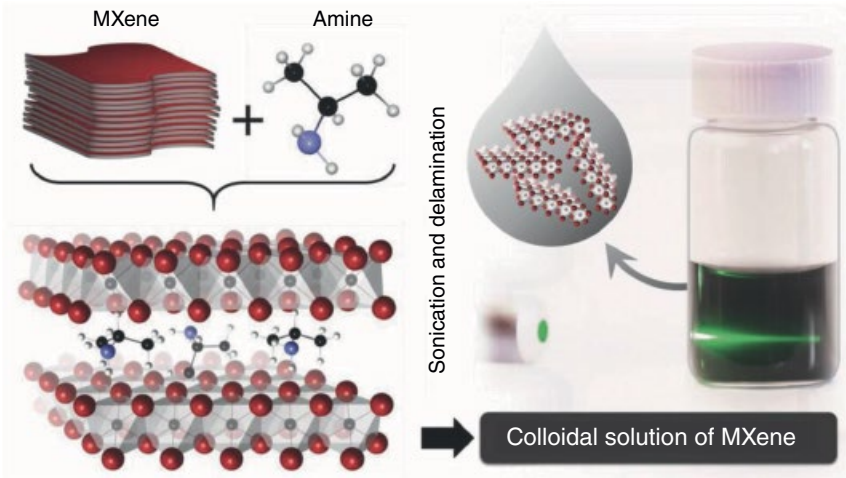


Figure 12.7 The schematic of intercalation and delamination with isopropylamine, an organic-based material. *Source:* Mashtalir et al. [41]/Reproduced from John Wiley & Sons, Inc.

water. They reported that the IPA oriented in the interlayer spacing such that NH_2 or protonated NH_3^+ end pointing toward the Nb_2CT_x layers and the alkyl tail away from the surface. The cationic head is small enough to overcome the steric hindrance, and on the other hand, molecules can enter between the layers causing further expansion of the MXene layers and delamination (Figure 12.7).

A series of trimethyl alkyl ammonium cations with different lengths are other examples of organic intercalators, which generally apply to the $Ti_3C_2T_x$ MXene. The process was explained by ion-exchanging with Li^+ ions, which enlarged the *d* spacing between MXene layers by the *in-situ* growing of alkyl chain length inside the interlayer spacing. As a result, the interlayer space increases.

Some of the intercalation components are listed in Table 12.2 with respect to their application methods.

12.3.3 Ultrasonication and Physical Delamination

In general, the removal of the A-layer from the MAX phase results in a significant weakening of interlayer interactions. MXene multilayers, which are held together by hydrogen bonds and van der Waals interactions, can be separated through mechanical agitation, such as ultrasonication or hand-shaking of the dispersion. The size of the 2D flakes is a crucial factor that affects various properties, as mentioned. Among all solution-based processing methods, ultrasonication stands out as a unique technique for obtaining single-layer MXene sheets. In the absence of

Table 12.2 Some intercalating agents for effective delamination.

Method	Intercalating agent	References
Electrochemical	Li^+, Na^+, K^+, Mg^+, NH_4^+, Al^{3+}	[4, 39, 42]
	Cs^+, Ba^+, Ga^+, $[(CH_3)_4N]^+$	[43]
Mixing and stirring	DMSO	[39, 44]
	TBAOH	[45]
	Isopropylamine	[41]
	Choline hydroxide	[40]
	Urae	[46]
	TMAOH	[47]
Agitation	$[(CH_3)_3NCH_3]^+$	[48]
Hydrothermal	TMAOH	[49]
Freeze-and-thaw	H_2O	[14]
Sonication	Water, ethanol	[50, 51]

sonication, it is particularly challenging, and sometimes impossible, to disperse and exfoliate single flakes.

Ultrasonication not only facilitates the delamination process by mechanically separating the materials into single or few-layer sheets but is also an essential step for using organic solvents, especially with large molecules, such as DMSO, urea, and isopropyl amine. These molecules act as lubricants, weakening interlayer interactions between the atomic layers and assisting exfoliation by ultrasonication. Additionally, ultrasonication appears to be necessary when using Li^+ ions as an intercalant, as delamination will not be successful without it [52].

Moreover, ultrasonication in aqueous media induces the penetration of water molecules between the atomic layers of MXenes, resulting in a noteworthy increase in the lattice *c* parameter and a weakening of the atomic interactions among the flakes. The generation of cavitation microjets can facilitate the removal of reaction by-products from the narrow interlayer chambers and promote the etching process by creating new active sites. Furthermore, the microjets can impede other chemical bonds between the layers. Studies have indicated that ultrasonic irradiation is capable of breaking flakes into smaller particles, with probe sonication systems having significant irradiation intensities, resulting in smaller flake sizes during MXene delamination.

Proper precautions are necessary during the MXene synthesis process to avoid the introduction of impurities and nano defects. Bubble implosions during sonication can lead to the formation of impurities, which may result from oxidation.

To prevent this, an argon protective covering should be used, and dissolved oxygen must be degassed from the mixture. Moreover, the reaction time should be carefully controlled since increasing it may lead to the generation of impurities such as AlF3, which reduces the sharpness of the (002) plane peak. It is important to note that over-processing through extended sonication (60 hours or more) may cause complete MXene disappearance.

Ultrasonic cavitation phenomena are influenced by various factors, including amplitude, power, frequency, temperature, time, and properties of the medium being sonicated, such as viscosity, surface tension, compressibility, vapor pressure, and dispersed particles.

The impact of ultrasonic operating parameters on the removal efficiency of Al in the presence and absence of ultrasound was investigated in a study. The findings revealed that increasing the amplitude (which represents ultrasonic power) and frequency of the applied ultrasound significantly enhances the removal efficiency of Al. Higher ultrasonic power provides more energy, which improves the removal of Al (Figure 12.8). However, excessive energy may result in smaller flakes and undesirable defects in the MXenes. The removal efficiency of Al is proportional to the applied frequency, as a higher frequency provides more opportunities for the etchant to attack the Ti_3AlC_2 precursor, accelerating the removal of Al. Moreover, as shown in Figure 12.8, the removal efficiency of Al with etching time has a close-to-linear increasing trend, indicating different reaction pathways for the cases with and without ultrasound.

In the absence of ultrasound, the etching process produces AlF3 by-products that adhere to the surface of MXenes, hampering further etching. In contrast, ultrasound removes the generated AlF3, accelerating the removal of Al from Ti_3AlC_2 structures [53].

Conventional delamination methods, such as sonication and shaking, can lead to the fragmentation and breakage of MXene flakes. Investigations have shown that, in contrast, lateral flake sizes can be almost as large as their parent MAX phase size using soft delamination approaches. This method benefits MXene assemblies by improving inter-flake contacts and alignment and allows facile patterning and investigation of their intrinsic physical properties.

The process of delamination, commonly used for the MILD method, is often associated with shaking, which can damage the size of the flakes. As shown in Figure 12.9, the shape of the parent multilayer particle is transferred to the single-layer flakes during delamination. The single-layer MXene flakes are likely separated from the multilayer particles during processing, either by capillary forces or created shear forces.

The size of delaminated $Ti_3C_2T_x$ MXene flakes depends on several factors, including the precursor particles, synthesis approach, and delamination protocol. Sonication and shaking decrease the average size of MXene flakes, causing them to break into smaller particles. On the other hand, eliminating shaking and

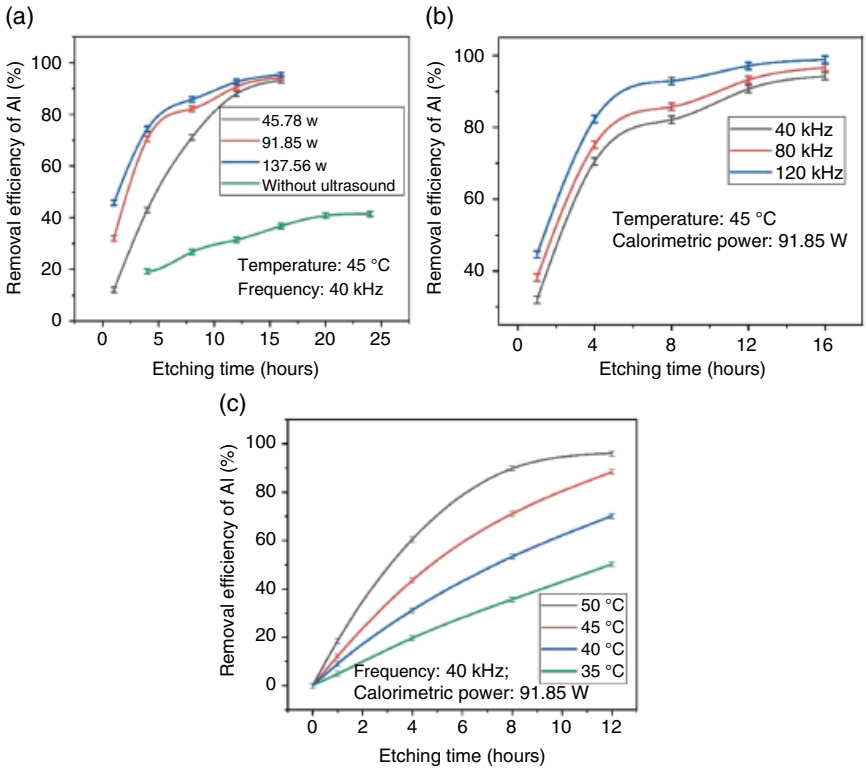


Figure 12.8 The impact of operational variables on the effectiveness of Al removal; (a) the impact of ultrasound's calorimetric power, (b) the influence of ultrasound's applied frequency, and (c) the impact of temperature when ultrasound is present. *Source:* Zhang et al. [53]/With permission of Elsevier.

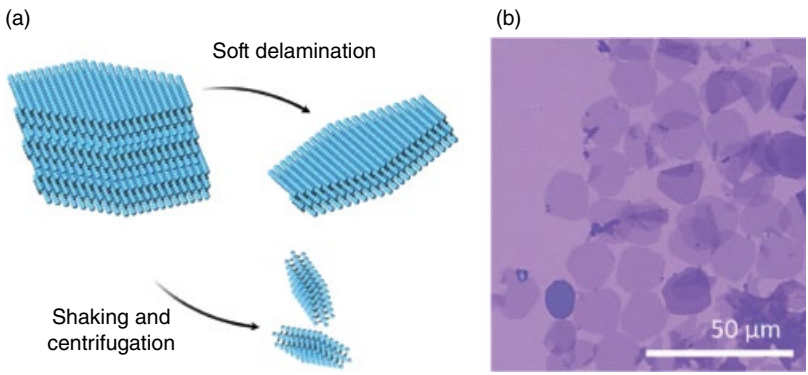


Figure 12.9 Delamination and its effect on flake size. (a) Two different methods of delamination are schematically presented. The first method involves standard delamination, while the second method employs a gentler approach known as soft delamination. (b) Optical micrographs of the flakes on a Si/SiO_2 wafer prepared using soft delamination. *Source:* Shekhirev et al. [54]/Reproduced from American Chemical Society.

employing the soft delamination approach can preserve the lateral flake sizes, allowing the translation of the size of the parent MAX particles into individual MXene flakes. In the soft delamination approach, LiCl intercalation is followed by a 30-minute undisturbed period to precipitate the multilayer MXene particles, and the clear supernatant is then removed via pipetting. The soft delamination approach can facilitate investigations into the intrinsic physical properties of MXenes, such as electrical, mechanical, and barrier properties of MXene films and composites. It can have significant implications for the development of advanced materials and devices [54].

12.3.4 Dispersibility and Stability of Delaminated MXene Flakes

Studies on the aggregation behavior and stability of MXenes have demonstrated that pH, ionic strength, and the type of fluid can significantly impact their colloidal properties, such as zeta potential and hydrodynamic size of flakes. As a result, there has been an improved understanding of the colloidal dispersibility of MXenes. In addition, environmental factors and synthesis procedures can lead to chemical transformations in MXene flakes. Although surface functionalization is an effective way to fully exploit the potential of MXenes, identifying the most stable functionalization strategy can be challenging due to the varying terminal groups that depend on the synthesis procedures and the specific compounds used [55–58].

There has been limited research on the topic, but instability can arise in the system due to the factors mentioned above. A study focused on the impact of the ionic strength of water on the colloidal properties and stabilities of Ti_3C_2 and Ti_2C Mxenes. The pH level was found to be critical to the stability of these materials, with significant effects observed between pH 4 and 10. Moreover, the type of water environment could affect the stability of these MXenes due to electrical double-layer compression. This may be due to the varying amounts of hydroxyl and carbonyl functional groups on the surface of Ti_3C_2 and Ti_2C that can bind with different ions, such as Ca^{2+} [57].

In a separate investigation, scientists examined different types of $Ti_3C_2T_x$ flakes that had undergone different surface modifications because of intercalation agents to assess their dispersion. The researchers analyzed the aggregation behaviors and kinetics of the flakes, studying their mechanisms with the classical DLVO theory. They also investigated certain properties of the flakes using spin-polarized DFT calculations and MD simulations. The surface modifications of the $Ti_3C_2T_x$ flakes using hydrazine and KOH increased their surface electronegativity, which led to a significant improvement in their colloidal stability. Surface-adsorbed K^+ from the KOH intercalation treatment acted as a protective layer that hindered the coupling between Ti^{3+} and reactive oxygen species, thereby shielding the $Ti_3C_2T_x$ flakes from photooxidation. However, this protection gradually decreased as K^+ dissolved [58].

12.4 Other Methods for Delamination and Surface Engineering

12.4.1 Hydrothermal-Assisted Intercalation (HAI)

Some modifications were considered in some MXene preparation routes to boost the yield of MXene (achieving a high value of 74%). For instance, to better intercalation, a hydrothermal process was applied where the intercalating agent could diffuse and intercalate easily into the multilayer MXenes and facilitate the subsequent delamination. Xuan et al. use TMAOH to simultaneously etch and intercalate for the preparation of monolayer $Ti_3C_2T_x$. After the simultaneous etching–delamination process, the reaction between TMAOH and Al atoms produces delaminated MXenes with the $Al(OH)_4$ surface group [49, 59]. Figure 12.10 shows

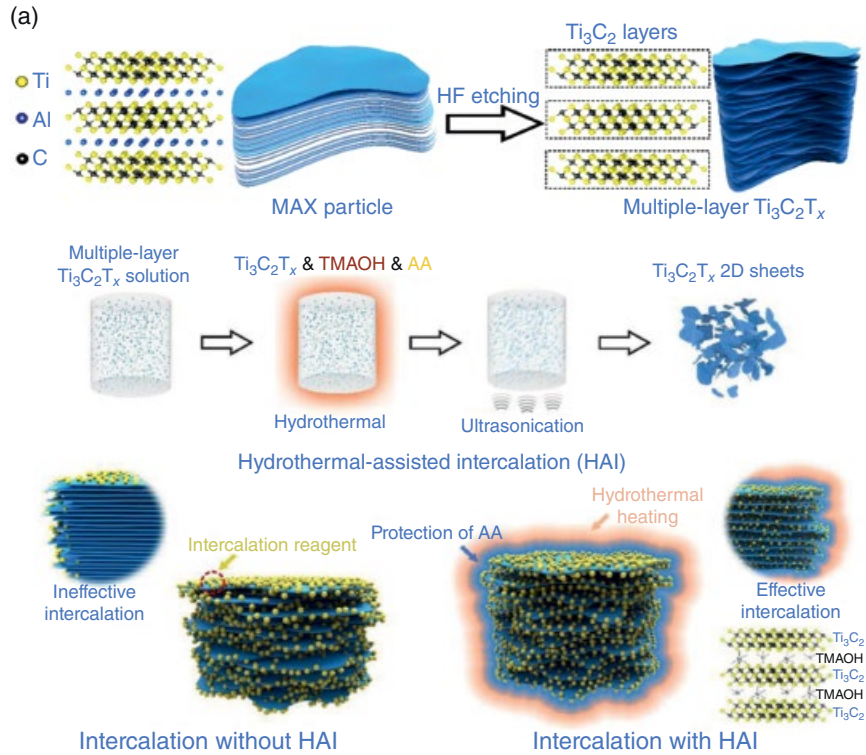


Figure 12.10 Different strategies by the intercalating agent to increase the *d*-spacing. (a) The hydrothermal-assisted intercalation (HAI) strategy to synthesize $Ti_3C_2T_x$, (b) Schematic explanation of how TMAOH plays a role in intercalating and delamination of multilayer MXene, and (c) surface $Al(OH)_4$ groups generation after delamination process. *Source:* Adapted from Han et al. [49] and Xuan et al. [59].

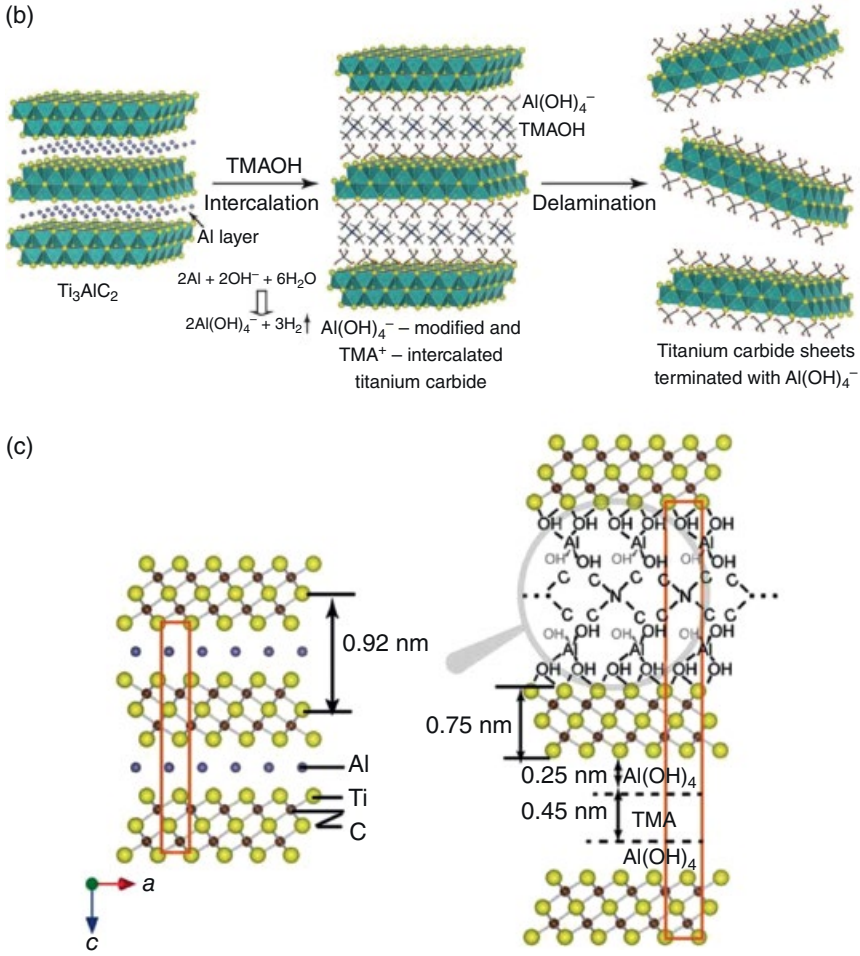


Figure 12.10 (Continued)

the efficiency of TMAOH in instantaneously etching the MAX phase and delaminating the following multilayer MXenes.

12.4.2 Microwave-Assisted Delamination

Another method that can facilitate the delamination step is using a microwave heating system (Figure 12.11), where Ti_3AlC_2 within a mixed solution of HCl/LiF can be prepared in a short period (15 minutes). It is worth mentioning that rapid inductive heating enhances the condition to release H_2 intensively and water

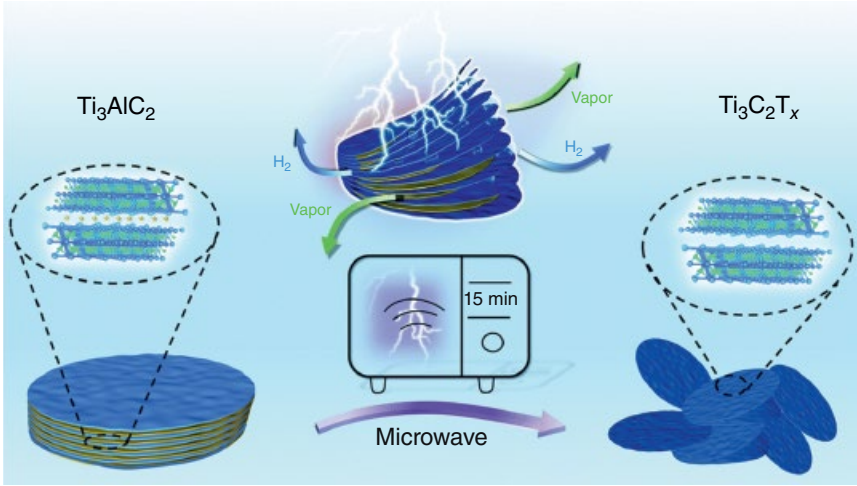


Figure 12.11 Schematic representation of microwave process steps for the preparation of MXenes. *Source:* Zhu et al. [60]/Royal Society of Chemistry.

vapor bubbles, which promotes delaminating the etched $Ti_3C_2T_x$ without using any intercalation agents. After weak ultrasonication, the single-layer and few-layer nanosheets of $Ti_3C_2T_x$ can be prepared with clean surfaces. However, the yield of the process is dissatisfactory (<10%) up to now. With the help of microwave treatment, the TMAOH can be used as an intercalation and delamination agent of $Ti_3C_2T_x$. The yield of single-layer MXene nanosheets was relatively low, limiting its applicability for preliminary applications [60, 61].

12.4.3 Freeze-and-Thaw (FAT)-Assisted Method

Recently, Huang et al. [14] reported a cyclic freezing-thawing-assisted approach for the delamination of MXenes. In this method, multilayer MXenes are dispersed in water, cooling down to −20 °C. Then the frozen dispersion was naturally thawed at room temperature. The process of freezing-thawing was repeated in several cycles. The expansion force of freezing water molecules enlarges the interlayer spacing of multilayer MXenes and therefore weaken the strong van der Waals forces, which allows the easy delamination of MXenes without any intercalation agents (Figure 12.12). Eventually, the thawy dispersion was centrifuged at 3500 rpm for 1 hour. The supernatant dispersion contains large and single MXene. This effort can solve the low-yield problem of delamination. After several cycles of FAT, the yield of the process can reach 39.0% without sonication. While followed by 1-hour sonication, the yield of MXene can increase to a record value of 81.4% even if a decrease in the lateral size has occurred.

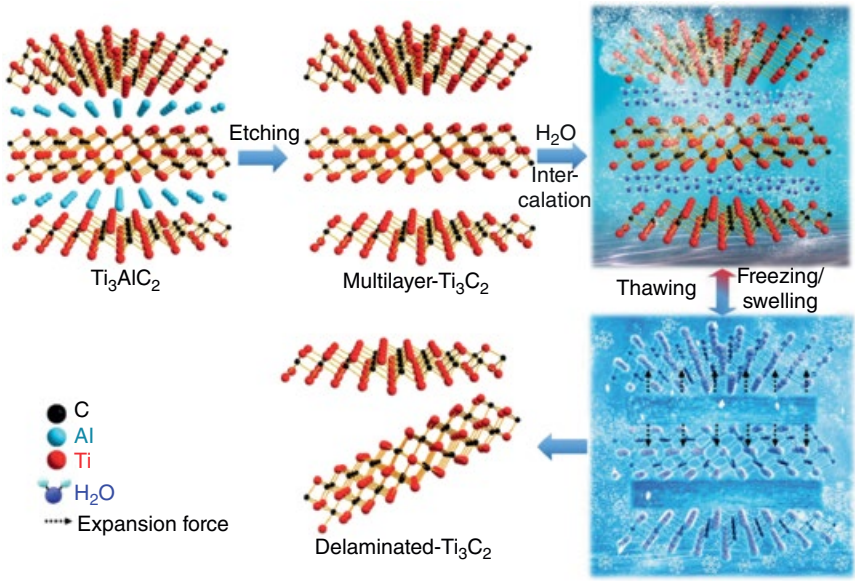


Figure 12.12 Schematic representation of the freeze-and-thaw (FAT) method for the delamination of $Ti_3C_2T_x$. *Source:* Huang et al. [14]/Reproduced from John Wiley & Sons, Inc.

The repetitive freezing and thawing may cause wrinkles on the surface of the nanosheets. Slowly cooling down and freezing the aqueous dispersion (−20 °C) induced the squeezing of the flakes and generated an uneven surface. Studies based on freezing the distribution in liquid nitrogen revealed noticeable folds in the layered MXenes. This indicates that the squeezing approach had a significant impact on the delamination quality of MXenes.

12.4.4 Low-Temperature Plasma Techniques

Despite outstanding achievements in the synthesis and delamination of MXenes, the addition of external molecules and heteroatom incorporation can be problematic in some cases. For instance, organic macromolecules as an intercalating agent could be blocking the active spots on the surface, or higher process temperature during the doping of heteroatom could damage the surface chemistry of MXenes. Indeed, using methods like the Low-temperature plasma technique for rapid delamination is not only an efficient one-step process for synthesizing heteroatom-doped MXenes but also the way that the surface can be modified without disturbing the bulk properties.

Based on Chen et al. [62] studies, nitrogen-doped $Ti_3C_2T_x$ MXene was produced at low temperatures. They applied dielectric barrier discharge (DBD) plasma treatment to obtain delaminated and nitrogen-doped MXene. The NH_4HCO_3 as a precursor of the system decomposes into NH_3, CO_2, and H_2O gases during the plasma treatment, which attacks the intralayer van der Waals interactions. Besides delamination nitrogen, doping on the MXene surface is successfully carried out, and the nitrogen content is adjustable by controlling the volume ratio of gases in the chamber.

12.5 Summary and Outlooks

Scalable synthesis of a single layer or a few layers of MXene plays a critical role in fulfilling their remarkable application potential. The frontier of these attempts is synthesizing $Ti_3C_2T_x$ MXenes primarily based on aqueous-based etching and subsequent delamination. Recently, researchers focused on fluorine-free and different strategies for delamination as well as adjusting the surface functional groups. Throughout this chapter, we discussed different synthesizing routes and their roles on surface terminals. It is mentioned that several parameters, such as process time, temperature, the concentration of components and their ratio, and the type of MAX phase precursor, can affect the final properties of products. Moreover, recent developments in intercalation with different species, such as metal cations, Inorganic and organic molecules, and delamination techniques, are introduced. Unless there is not any well-established and specific delamination mechanism, in some studies, a high yield of around 82% was reported.

We believe that optimizing the newborn techniques and conducting systematic and reproducible processes that are still missing may lead to the development of synthesizing this new generation of 2D materials. Therefore, we recommend that future work in this area should focus on the systematic studies of the effect of the different independent and dependent parameters for intercalation and delamination to synthesize single-/few-layer MXene flakes of various compositions.

References

1 Novoselov, K.S., Gem, A.K., Morozov, S.V. et al. (2004). Electric field in atomically thin carbon films. *Science* 306 (5696): 666–669.

2 Nicolosi, V., Chhowalla, M., Kanatzidis, M.G. et al. (2013). Liquid exfoliation of layered materials. *Science* 340 (6139).

3 Srivastava, P., Mishra, A., Mizuseki, H. et al. (2016). Mechanistic insight into the chemical exfoliation and functionalization of Ti_3C_2 MXene. *ACS Applied Materials & Interfaces* 8 (36): 24256–24264.

4 Ghidiu, M., Halim, J., Kota, S. et al. (2016). Ion-exchange and cation solvation reactions in Ti_3C_2 MXene. *Chemistry of Materials* 28 (10): 3507–3514.

5 Abdolhosseinzadeh, S., Jiang, X., Zhang, H. et al. (2021). Perspectives on solution processing of two-dimensional MXenes. *Materials Today* 48: 214–240.

6 Naguib, M., Kurtoglu, M., Presser, V. et al. (2011). Two-dimensional nanocrystals produced by exfoliation of Ti_3AlC_2. *Advanced Materials* 23 (37): 4248–4253.

7 Hart, J.L., Hantanasirisakul, K., Lang, A.C. et al. (2019). Control of MXenes' electronic properties through termination and intercalation. *Nature Communications* 10 (1): 1–10.

8 Mozafari, M. and Soroush, M. (2021). Surface functionalization of MXenes. *Materials Advances* 2 (22): 7277–7307.

9 Sharma, V. and Datta, D. (2021). Variation in the interface strength of silicon with surface engineered Ti_3C_2 MXenes. *Physical Chemistry Chemical Physics* 23 (9): 5540–5550.

10 Heckler, J.E., Neher, G.R., Mehmood, F. et al. (2021). Surface functionalization of $Ti_3C_2T_x$ MXene nanosheets with catechols: implication for colloidal processing. *Langmuir* 37 (18): 5447–5456.

11 Zhao, Q.N., Zhang, Y.J., Duan, Z.H. et al. (2021). A review on $Ti_3C_2T_x$-based nanomaterials: synthesis and applications in gas and humidity sensors. *Rare Metals* 40 (6): 1459–1476.

12 Persson, P.O.Å. and Rosen, J. (2019). Current state of the art on tailoring the MXene composition, structure, and surface chemistry. *Current Opinion in Solid State & Materials Science* 23 (6): 100774.

13 Xiong, D., Li, X., Bai, Z. et al. (2018). Recent advances in layered $Ti_3C_2T_x$ MXene for electrochemical energy storage. *Small* 14 (17): 1703419.

14 Huang, X., Wu, P., Huang, X., and Wu, P. (2020). A facile, high-yield, and freeze-and-thaw-assisted approach to fabricate MXene with plentiful wrinkles and its application in on-chip micro-supercapacitors. *Advanced Functional Materials* 30 (12): 1910048.

15 Seredych, M., Shuck, C.E., Pinto, D. et al. (2019). High-temperature behavior and surface chemistry of carbide MXenes studied by thermal analysis. *Chemistry of Materials* 31 (9): 3324–3332.

16 Benchakar, M., Loupias, L., Garnero, C. et al. (2020). One MAX phase, different MXenes: a guideline to understand the crucial role of etching conditions on $Ti_3C_2T_x$ surface chemistry. *Applied Surface Science* 530: 147209.

17 Tang, Q., Zhou, Z., and Shen, P. (2012). Are MXenes promising anode materials for Li ion batteries? Computational studies on electronic properties and Li storage capability of Ti_3C_2 and $Ti_3C_2X_2$ (X = F, OH) monolayer. *Journal of the American Chemical Society* 134 (40): 16909–16916.

18 Pang, S.Y., Wong, Y.T., Yuan, S. et al. (2019). Universal strategy for HF-free facile and rapid synthesis of two-dimensional MXenes as multifunctional energy materials. *Journal of the American Chemical Society* 141 (24): 9610–9616.

19 Folorunso, O., Kumar, N., Hamam, Y. et al. (2021). Recent progress on 2D metal carbide/nitride (MXene) nanocomposites for lithium-based batteries. *FlatChem* 29: 100281.

20 Lipatov, A., Alhabeb, M., Lukatskaya, M.R. et al. (2016). Effect of synthesis on quality, electronic properties and environmental stability of individual monolayer Ti_3C_2 MXene flakes. *Advanced Electronic Materials* 2 (12): 1600255.

21 Ghidiu, M., Lukatskaya, M.R., Zhao, M.Q. et al. (2014). Conductive two-dimensional titanium carbide 'clay' with high volumetric capacitance. *Nature* 516 (7529): 78–81.

22 Kim, S.J., Koh, H.J., Ren, C.E. et al. (2018). Metallic $Ti_3C_2T_x$ MXene gas sensors with ultrahigh signal-to-noise ratio. *ACS Nano* 12 (2): 986–993.

23 Wang, X., Garnero, C., Rochard, G. et al. (2017). A new etching environment (FeF_3/HCl) for the synthesis of two-dimensional titanium carbide MXenes: a route towards selective reactivity vs. water. *Journal of Materials Chemistry A* 5 (41): 22012–22023.

24 Liu, F., Zhou, A., Chen, J. et al. (2017). Preparation of Ti_3C_2 and Ti_2C MXenes by fluoride salts etching and methane adsorptive properties. *Applied Surface Science* 416: 781–789.

25 Guo, M., Geng, W.-C., Liu, C. et al. (2020). Ultrahigh areal capacitance of flexible MXene electrodes: electrostatic and steric effects of terminations. *Chemistry of Materials* 32: 8265.

26 Shayesteh Zeraati, A., Mirkhani, S.A., Sun, P. et al. (2021). Improved synthesis of $Ti_3C_2T_x$ MXenes resulting in exceptional electrical conductivity, high synthesis yield, and enhanced capacitance. *Nanoscale* 13 (6): 3572–3580.

27 Yang, S., Zhang, P., Wang, F. et al. (2018). Fluoride-free synthesis of two-dimensional titanium carbide (MXene) using a binary aqueous system. *Angewandte Chemie, International Edition* 57 (47): 15491–15495.

28 Sun, W., Shah, S.A., Chen, Y. et al. (2017). Electrochemical etching of Ti_2AlC to Ti_2CT_x (MXene) in low-concentration hydrochloric acid solution. *Journal of Materials Chemistry A* 5 (41): 21663–21668.

29 Li, T., Yao, L., Liu, Q. et al. (2018). Fluorine-free synthesis of high-purity $Ti_3C_2T_x$ (T=OH, O) via alkali treatment. *Angewandte Chemie* 130 (21): 6223–6227.

30 Vaia, R.A., Jawaid, A., Hassan, A. et al. (2021). Halogen etch of Ti_3AlC_2 MAX phase for mxene fabrication. *ACS Nano* 15 (2): 2771–2777.

31 Kamysbayev, V., Filatov, A.S., Hu, H. et al. (2020). Covalent surface modifications and superconductivity of two-dimensional metal carbide MXenes. *Science* 369 (6506): 979–983.

32 Shahzad, F., Alhabeb, M., Hatter, C.B. et al. (2016). Electromagnetic interference shielding with 2D transition metal carbides (MXenes). *Science* 353 (6304): 1137–1140.

33 Li, J., Liu, Y., Xu, F. et al. (2020). K^+ intercalation of NH_4HF_2-exfoliated Ti_3C_2 MXene as binder-free electrodes with high electrochemical capacitance. *Physica Status Solidi* 217 (8): 1900806.

34 Peng, C., Wei, P., Chen, X. et al. (2018). A hydrothermal etching route to synthesis of 2D MXene (Ti_3C_2, Nb_2C): enhanced exfoliation and improved adsorption performance. *Ceramics International* 44 (15): 18886–18893.

35 Lu, J., Persson, I., Lind, H. et al. (2019). Ti_{n+1} C_n MXenes with fully saturated and thermally stable Cl terminations. *Nanoscale Advances* 1 (9): 3680–3685.

36 Li, Y., Shao, H., Lin, Z. et al. (2020). A general Lewis acidic etching route for preparing MXenes with enhanced electrochemical performance in non-aqueous electrolyte. *Nature Materials* 19 (8): 894–899.

37 Lei, J.C., Zhang, X., and Zhou, Z. (2015). Recent advances in MXene: preparation, properties, and applications. *Frontiers of Physics* 10 (3): 276–286.

38 Alhabeb, M., Maleski, K., Anasori, B. et al. (2017). Guidelines for synthesis and processing of two-dimensional titanium carbide ($Ti_3C_2T_x$ MXene). *Chemistry of Materials* 29 (18): 7633–7644.

39 Mashtalir, O., Naguib, M., Mochalin, V.N. et al. (2013). Intercalation and delamination of layered carbides and carbonitrides. *Nature Communications* 4 (1): 1–7.

40 Naguib, M., Unocic, R.R., Armstrong, B.L., and Nanda, J. (2015). Large-scale delamination of multi-layers transition metal carbides and carbonitrides "MXenes". *Dalton Transactions* 44 (20): 9353–9358.

41 Mashtalir, O., Lukatskaya, M.R., Zhao, M.-Q. et al. (2015). Amine-assisted delamination of Nb_2C MXene for Li-ion energy storage devices. *Advanced Materials* 27 (23): 3501–3506.

42 Lukatskaya, M.R., Mashtalir, O., Ren, C.E. et al. (2013). Cation intercalation and high volumetric capacitance of two-dimensional titanium carbide. *Science* 341 (6153): 1502–1505.

43 Levi, M.D., Lukatskaya, M.R., Sigalov, S. et al. (2015). Solving the capacitive paradox of 2D MXene using electrochemical quartz-crystal admittance and in situ electronic conductance measurements. *Advanced Energy Materials* 5 (1): 1400815.

44 Lv, G., Wang, J., Shi, Z., and Fan, L. (2018). Intercalation and delamination of two-dimensional MXene ($Ti_3C_2T_x$) and application in sodium-ion batteries. *Materials Letters* 219: 45–50.

45 Vahidmohammadi, A., Hadjikhani, A., Shahbazmohamadi, S., and Beidaghi, M. (2017). Two-dimensional vanadium carbide (MXene) as a high-capacity cathode material for rechargeable aluminum batteries. *ACS Nano* 11 (11): 11135–11144.

46 Al-Temimy, A., Anasori, B., Mazzio, K.A. et al. (2020). Enhancement of Ti_3C_2 MXene pseudocapacitance after urea intercalation studied by soft X-ray absorption spectroscopy. *Journal of Physical Chemistry C* 124 (9): 5079–5086.

47 Tang, J., Wan, H., Chang, L. et al. (2022). Tunable infrared sensing properties of MXenes enabled by intercalants. *Advanced Optical Materials* 10 (17): 2200623.

48 Ghidiu, M., Kota, S., Halim, J. et al. (2017). Alkylammonium cation intercalation into Ti_3C_2 (MXene): effects on properties and ion-exchange capacity estimation. *Chemistry of Materials* 29 (3): 1099–1106.

49 Han, F., Luo, S., Xie, L. et al. (2019). Boosting the yield of MXene 2D sheets via a facile hydrothermal-assisted intercalation. *ACS Applied Materials & Interfaces* 11 (8): 8443–8452.

50 Fredrickson, K.D., Anasori, B., Seh, Z.W. et al. (2016). Effects of applied potential and water intercalation on the surface chemistry of Ti_2C and Mo_2C MXenes. *Journal of Physical Chemistry C* 120 (50): 28432–28440.

51 Lim, G.P., Soon, C.F., Morsin, M. et al. (2020). Synthesis, characterization and antifungal property of $Ti_3C_2T_x$ MXene nanosheets. *Ceramics International* 46 (12): 20306–20312.

52 Malaki, M., Maleki, A., and Varma, R.S. (2019). MXenes and ultrasonication. *Journal of Materials Chemistry A* 7 (18): 10843–10857.

53 Zhang, W. and Zhang, X. (2022). The effect of ultrasound on synthesis and energy storage mechanism of $Ti_3C_2T_x$ MXene. *Ultrasonics Sonochemistry* 89: 106122.

54 Shekhirev, M., Busa, J., Shuck, C.E. et al. (2022). Ultralarge flakes of $Ti_3C_2T_x$ MXene via soft delamination. *ACS Nano* 16 (9): 13695–13703.

55 Natu, V., Sokol, M., Verger, L., and Barsoum, M.W. (2018). Effect of edge charges on stability and aggregation of $Ti_3 C_2 T_z$ MXene colloidal suspensions. *The Journal of Physical Chemistry C* 122: 27745–27753.

56 Zheng, C., Yao, Y., Rui, X. et al. (2022). Functional MXene-based materials for next-generation rechargeable batteries. *Advanced Materials* 34 (51): 2204988.

57 Rozmysłowska, A., Wojciechowski, T., Ziemkowska, W. et al. (2018). Colloidal properties and stability of 2D $Ti_3 C_2$ and Ti_2 C MXenes in water. *International Journal of Electrochemical Science* 13: 10837–10847.

58 Shen, S., Ke, T., Rajavel, K. et al. (2020). Dispersibility and photochemical stability of delaminated MXene flakes in water. *Small* 16 (36): 2002433.

59 Xuan, J., Wang, Z., Chen, Y. et al. (2016). Organic-base-driven intercalation and delamination for the production of functionalized titanium carbide nanosheets with superior photothermal therapeutic performance. *Angewandte Chemie, International Edition* 55 (47): 14569–14574.

60 Zhu, J., Zhang, J., Lin, R. et al. (2021). Rapid one-step scalable microwave synthesis of $Ti_3C_2T_x$ MXene. *Chemical Communications* 57 (94): 12611–12614.

61 Wu, W., Xu, J., Tang, X. et al. (2018). Two-dimensional nanosheets by rapid and efficient microwave exfoliation of layered materials. *Chemistry of Materials* 30 (17): 5932–5940.

62 Chen, X., Zhai, X., Hou, J. et al. (2021). Tunable nitrogen-doped delaminated 2D MXene obtained by NH_3/Ar plasma treatment as highly efficient hydrogen and oxygen evolution reaction electrocatalyst. *Chemical Engineering Journal* 420: 129832.

13

Solution Processing of MXenes for Printing, Wet Coating, and 2D Film Formation

Sina Abdolhosseinzadeh[1], Mohammad Jafarpour[1,2], Jakob Heier[1], Frank Nüesch[1,2], and Chuanfang Zhang[3]

[1] *Department of Advanced Materials and Surfaces, Laboratory for Functional Polymers, Swiss Federal Laboratories for Materials Science and Technology (Empa), ETH Domain, Dübendorf, Switzerland*
[2] *Institute of Materials Science and Engineering, Swiss Federal Institute of Technology Lausanne (EPFL), Lausanne, Switzerland*
[3] *College of Materials Science and Engineering, Sichuan University, Chengdu, Sichuan, China*

13.1 Introduction

Printing is an additive manufacturing technique that enables the deposition of a precise amount of a functional material in the form of an ink in a predefined pattern/location. Usually, in most of the literature, all dispersions of a functional material are considered as inks, and these terms (ink and dispersion) are often used interchangeably. However, to qualify as a printable ink for practical applications, a dispersion should possess certain characteristics that can be classified into two groups: pre-deposition and post-deposition properties.

The pre-deposition characteristics are primarily determined by the printing method and are mainly related to the rheological properties of the ink. Additionally, as a general requirement, an ink should have a reasonable shelf life, meaning that it should be chemically and colloidally stable for at least several months. The colloidal stability can be shorter as inks can be homogenized before deposition, but it should be long enough to enable stable printing [1]. The post-deposition properties are related to the surface on which the ink is deposited (wetting, and chemical compatibility), and the film formation behavior of the ink. While the wetting and the chemical compatibility are

Transition Metal Carbides and Nitrides (MXenes) Handbook: Synthesis, Processing, Properties and Applications, First Edition. Edited by Chuanfang Zhang and Michael Naguib.
© 2024 John Wiley & Sons, Inc. Published 2024 by John Wiley & Sons, Inc.

mainly determined by the carrier solvent (usually the dispersion medium), the film formation behavior depends on numerous parameters such as wetting (adhesion), interparticle interactions (cohesion), ink composition (e.g. particle concentration and binder content), and post-treatments (e.g. drying and sintering) [2].

In the first part of this chapter, the aforementioned properties of dispersions of MXenes will be discussed and then the printing of MXene inks using major 2D printing methods will be reviewed. While it is possible to prepare MXene inks using dried powder, due to the difficulties of redispersing the nanosheets [3], it is often more convenient to use suspensions of MXene, which are usually used to delaminate the etched MAX phase. Since MXenes and their synthesis methods have been comprehensively reviewed in other chapters, the starting point for this chapter's solution processing and ink formulation discussions will begin with the delamination of multilayer MXenes.

13.2 Preparing Stable MXene Dispersions

Water is the most efficient and preferred medium of choice for the delamination and dispersion of multilayer-MXene (*m*-MXene). Depending on the etching method, sometimes (e.g. etching with HF acid) additional intercalation agents may also be required to delaminate the *m*-MXene and separate the MXene nanosheets, which are strongly attached to each other even after the removal of the "A" layers [4]. So far numerous organic molecules such as tetrabutylammonium hydroxide (TBAOH), choline hydroxide, *n*-butylamine, and dimethyl sulfoxide (DMSO) have been successfully used as intercalation agents [5]. Since metal cations (e.g. Li^+) can also efficiently intercalate into the interlayer galleries of the *m*-MXene, when the MAX phase is etched by a mixture of an acid and a fluoride-containing salt (e.g. HCl + LiF), highly stable dispersions of delaminated MXene (*d*-MXene) can be obtained even by gentle agitation of *m*-MXene in water (zeta potential between −30 and −80 mV) [4].

Although water is a green and low-cost solvent, for some applications, it is necessary to formulate non-aqueous inks (e.g. printing on polymeric substrates with low surface energy) [6]. Matching the surface tension of an ink with the surface energy of the printing substrate is very important for proper wetting of the ink and strong adhesion of the film [2]. In this regard, the possibility of dispersing MXenes in solvents with different surface tensions is an important tool for adjusting the surface tension of the inks according to the surface energy of the substrates.

Depending on the permissible amount of water, non-aqueous pristine MXene inks can be formulated in one of the three following methods. The easiest and the

most frequently used method is based on the solvent exchange technique, where the MXene nanosheets (after being delaminated in water) are transferred to a new solvent by repeatedly centrifuging, discarding the supernatant, and redispersing the sedimented nanosheets in the fresh target solvent (Figure 13.1a) [7]. Considering the hydrophilicity of the MXene nanosheets [10] and the strong affinity of the water molecules to bond to the terminal groups of MXene (e.g. by hydrogen bond formation [11]), when using the solvent exchange method, small traces of water will still be present in the final ink composition. Drying the delaminated nanosheets and redispersing the dry powder in the solvent of choice (only possible specific solvents, which will be discussed in the next paragraph) is another approach [3]. Although the water content of the ink is less than in the former method, the yield of the dispersion is lower and the dispersed nanosheets

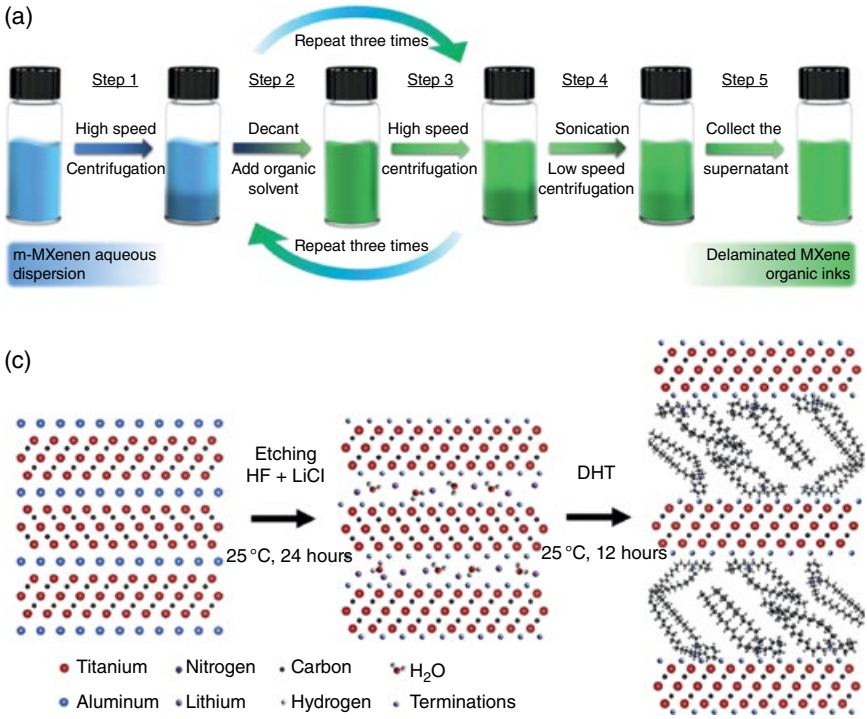


Figure 13.1 (a) Schematic representation of solvent exchange method. *Source:* Adapted from Zhang et al. [7]. (b) Stability of MXene dispersions in different polar and nonpolar solvents. *Source:* Maleski et al. [3]/Reproduced from American Chemical Society. (c) Schematic representation of synthesis steps of DHT-modified MXene. *Source:* Reproduced with permission Carey et al. [8]/Elsevier. (d) Schematic representation of grafting long alkyl chains via chemical condensation method. *Source:* Reproduced with permission Kim et al. [9]/American Chemical Society.

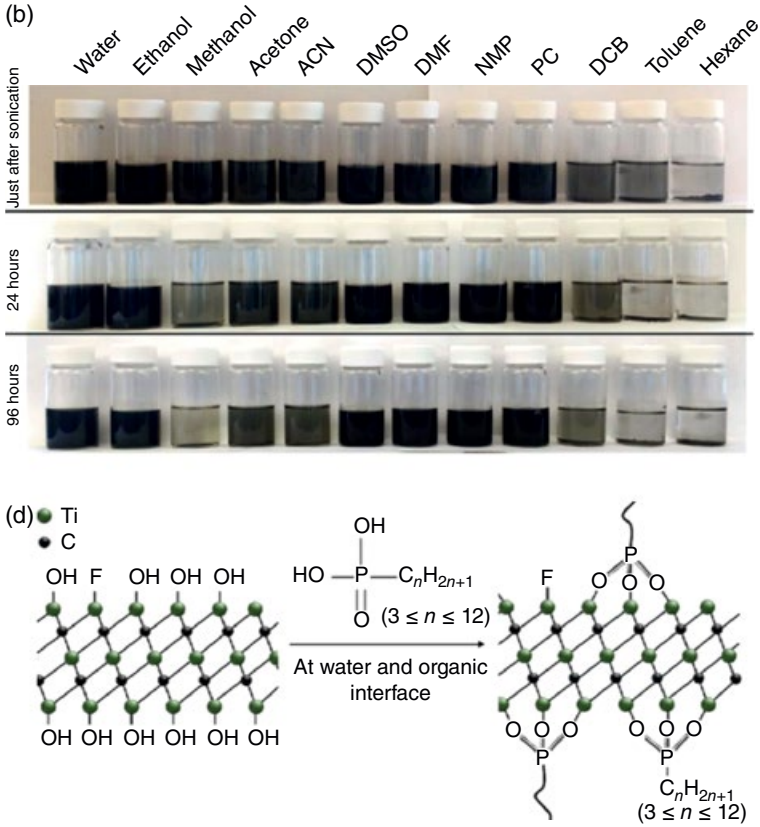


Figure 13.1 (Continued)

tend to have a smaller lateral size (due to the required long sonication process). It is also worth noting that when the MAX phase is etched in acid and fluoride-containing salts, dispersion of dried MXene powder is significantly more difficult, which is mainly attributed to the role of residual metal cations in holding the negatively charged MXene nanosheets together [3]. A relatively more recent approach is based on etching the MAX phase in a non-aqueous system such as NH_4HF_2 dissolved in propylene carbonate (PC) and delaminating the m-MXene in PC [6].

While as-synthesized MXenes (with no chemical/physical modifications) can be easily dispersed in water and in a limited number of polar aprotic solvents such as NMP, PC, DMSO, and DMF (dimethyl formamide), they have very limited dispersibility in other types of polar solvents and no dispersibility in nonpolar solvents (Figure 13.1b) [3]. To overcome this problem and formulate MXene inks

in nonpolar solvents, it is necessary to process the *m*-MXene further. It has been shown that when the residual Li^+ cations between *m*-MXene layers are exchanged with di(hydrogenated tallow)benzyl methyl ammonium chloride (DHT), they become organophilic and form highly stable colloidal suspensions in nonpolar solvents (Figure 13.1c) [8]. For this purpose, after etching the MAX phase and purifying the obtained *m*-MXene, a solution of DHT (in an ethanol-water mixture) is added to the *m*-MXene dispersion, and the mixture is stirred for 12 hours. Finally, the DHT-modified *m*-MXene powder is obtained after multiple washing steps (with water) and drying at ambient pressure (at 100 °C). This dry powder is readily dispersible in a wide range of nonpolar solvents such as chloroform, decalin, *p*-xylene, etc. Grafting long alkyl chains via chemical condensation between the hydroxyl groups of MXenes and alkoxy or chloro groups of such molecules [9, 12, 13] is another approach that can efficiently make MXene nanosheets dispersible in nonpolar solvents (Figure 13.1d). In this case, the dispersibility of the nanosheets is not from the electrostatic repulsive interactions, but mainly from the steric stabilization of long alkyl chains as well as the solvation effect of long alkyl chain-grafted flakes with organic solvents due to the strong nonpolar interactions [9].

In addition to colloidal stability, a suitable dispersion for ink formulation (especially for industrial applications) should also be chemically stable. Unfortunately, pristine MXenes are very prone to oxidation in aqueous media and in presence of oxygen [14], which can drastically limit the shelf life of aqueous MXene inks to a few weeks. So far, numerous solutions such as controlling the quality of the parent MAX phase and chemical etching conditions as well as the passivation of defects and tailoring the composition of the dispersion media [15] have been proposed to slow down the kinetics of MXene oxidation. Some of these approaches are out of the scope of this chapter; hence, here only the techniques that are related to ink formulation will be discussed.

Deoxygenation of the inks and storing them in hermetic vessels at low temperatures can significantly decelerate the oxidation rate and prolong the shelf life from a few days to several months (Figure 13.2a) [16]. Fortunately, the oxidation of MXenes in non-aqueous dispersions is much slower than their aqueous counterparts [17]. Even adding organic solvents such as ethylene glycol to aqueous dispersions can improve the oxidation resistance of MXenes [18]. Capping the edges of the nanosheets (Figure 13.2c) and passivating the defects are other effective solutions as they are more prone to oxidation. Capping agents such as sodium ascorbate [19] can block water molecules and dissolved oxygen, thereby improving the oxidation stability [15]. This is an important strategy for the formulation of inkjet printing (IJP) inks (and similar methods) that require small flakes (will be discussed later), which are more prone to oxidation (Figure 13.2b).

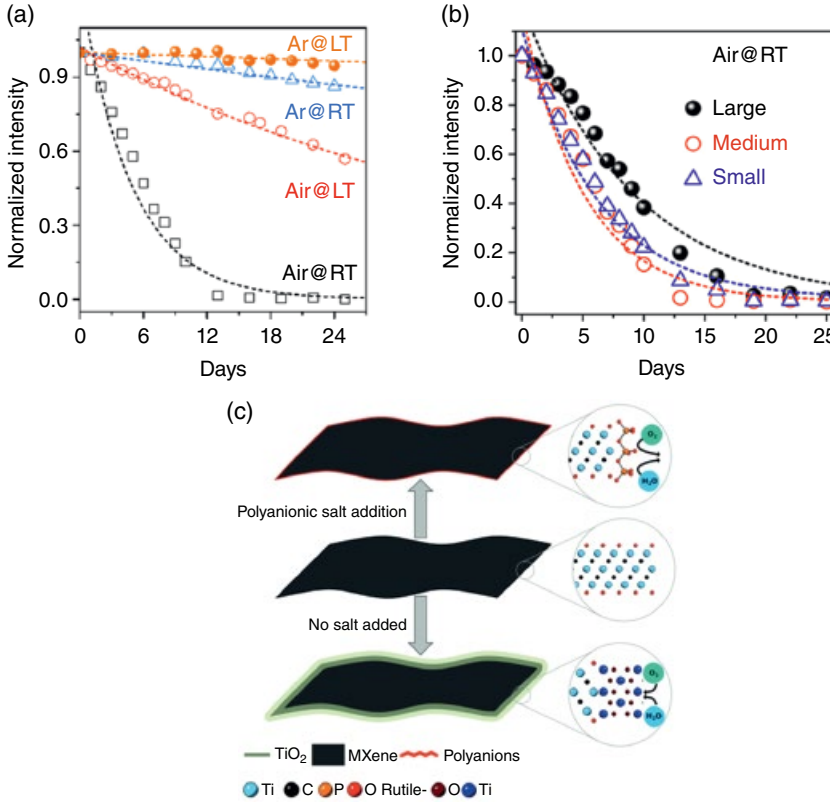


Figure 13.2 (a) Oxidation stability of MXene at different storage conditions. (b) Oxidation stability of MXene nanosheets with different sizes stored in air and at room temperature. *Source:* Reproduced with permission Zhang et al. [16]/American Chemical Society. (c) Edge capping of a MXene nanosheet and blocking of oxygen and water. *Source:* Reproduced with permission Natu et al. [17]/John Wiley & Sons.

13.3 Tuning the Rheological Properties of MXene Dispersions

Even at very low concentrations, due to their unique two-dimensional morphology, substantial particle-particle interactions are observed in MXene dispersions. As a result, the concentration, and the morphological characteristics of MXene nanosheets strongly govern the rheological properties of their dispersions [20]. As discussed in the previous section, stable dispersions of MXenes can be prepared in a wide range of concentrations (when the dispersion solvent is properly selected). Therefore, by adjusting these parameters, the flow behavior of the MXene inks can be easily tuned for various printing and coating methods (will be discussed later).

Single-layer MXene (*d*-MXene) dispersions exhibit substantially different rheological properties than those prepared with multilayer flakes. The viscosity of *d*-MXene dispersions increases rapidly even at very low volume fractions $\varnothing \approx 10^{-4}$. A similar power law increase in the viscosity of *m*-MXene is only observed at 3–4 orders of magnitude higher volume fractions (Figure 13.3a) [21]. Therefore, *d*-MXene is more suitable for printing/coating thin and transparent layers [21] and *m*-MXene for thick film deposition [22]. In dispersions of *d*-MXene, gelation occurs at very low concentrations (Figure 13.3b), which is not suitable

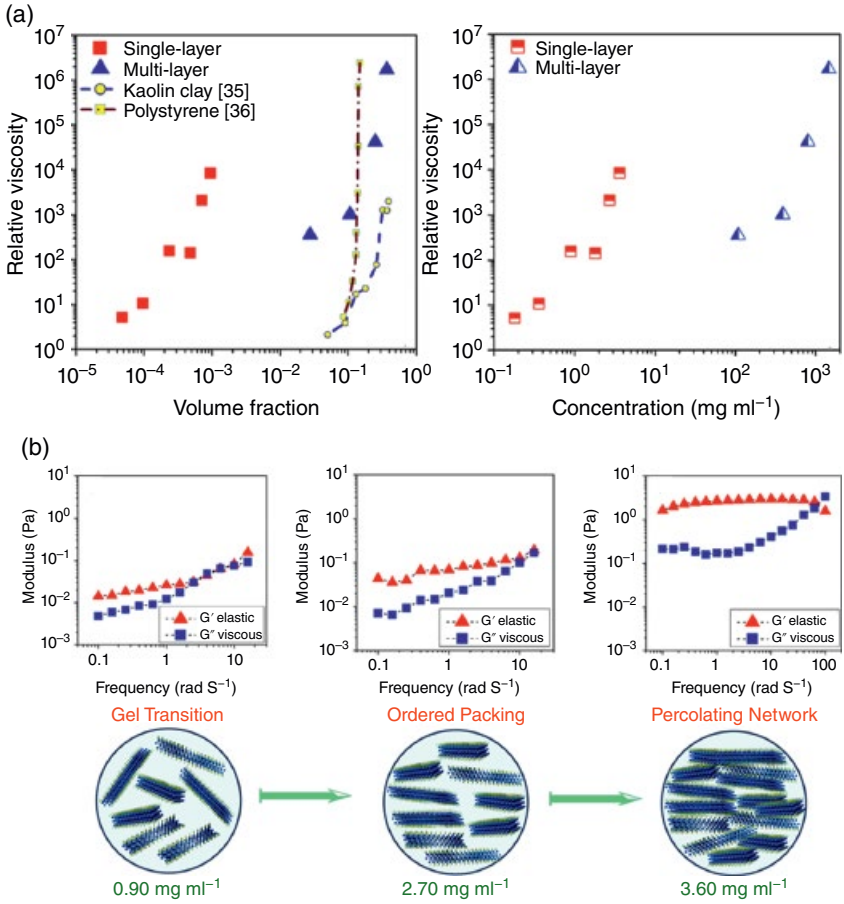


Figure 13.3 (a) Relation between viscosity and volume fraction/concentration of *d*-MXene and *m*-MXene. (b) Frequency sweep test results for *d*-MXene at different concentrations with the schematic representation of the state of dispersion at the given concentrations. *Source:* Reproduced with permission Akuzum et al. [21]/American Chemical Society.

for printing techniques that require inks with liquid-like behavior (e.g. gravure printing, GP).

It is worth noting that the mechanical properties of binder-free 2D-material-based films strongly depend on the exfoliation/delamination degree of the flakes. Single- or few-layer flakes can often form more robust films as they can establish a larger number of interflake interactions and more efficient interlocks (with each other) [23]. Thus, the choice of *d*-MXene or *m*-MXene (or a mixture of both) for ink formulation should be made while also considering the expected mechanical properties of the films for every specific application.

At an identical delamination/exfoliation level, the rheological properties are mainly determined by the size of the flakes. Similar to other liquid-phase exfoliated 2D materials, the product of MXene delamination often has polydisperse size distribution, and when a specific size is needed, a size screening process would be necessary [24]. Since the flake size has major effects on (opto)electronic properties of the printed films, size selection should be done by considering the requirements of every specific application. For instance, defect-free large single-layer nanosheets are the best choices for maximizing the transparency of a thin MXene film. In some cases, restrictions on the flake size may be dictated by the printing method (e.g. to avoid clogging the nozzle in IJP). Generally, the interparticle interactions are more extensive in dispersions with larger flakes, and particle jamming occurs at significantly lower concentrations. In dispersions with an equal concentration of MXene, larger flakes exhibit higher zero-shear viscosity than their smaller counterparts. For instance, the zero-shear viscosity (measured at $0.01\,s^{-1}$) of a MXene dispersion with an average flake size of ~3.1 μm is ~5050 Pa s at ~26.5 mg ml^{-1}, while similar values for a dispersion of 310 nm flakes (average size) are only observed at concentrations as high as ~150 mg ml^{-1} [25]. There are also several other parameters related to the MXene particles and their dispersions such as elemental composition, surface terminations, sample age, ionic strength, pH, and zeta potential that can affect the rheology of MXene inks and require further research and more systematic investigations [26].

13.4 Ink Formulation and Printing of MXenes

As discussed in the previous sections, the surface tension, and the rheological properties of the MXenes dispersions can be adjusted in a wide range, which enables the formulation of inks for various printing and coating methods. It is worth noting that although controlling these parameters is an important step for ink formulation, further case-specific compositional adjustments may also be needed to meet the requirements of every individual printing method (will be discussed when reviewing each printing method). In other words, the composition of an ink

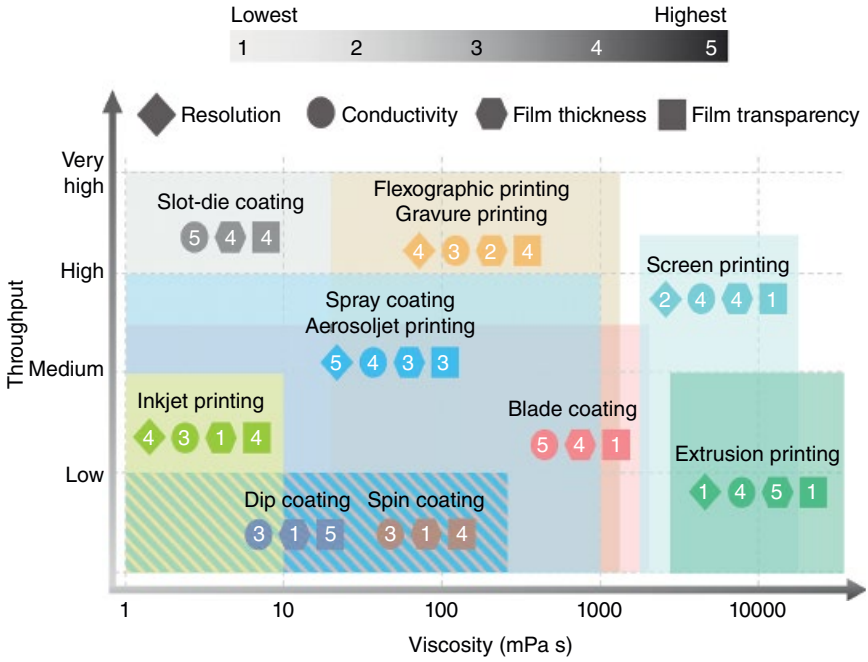


Figure 13.4 Relation between the ink viscosity, throughput, resolution (only applies for printing methods), and various properties of the deposited films for major printing/coating methods. *Source:* Jafarpour et al. [27]/John Wiley & Sons/CC BY 4.0.

is heavily dependent on the selection of the printing method. When choosing the most suitable technique for the deposition of a functional material and fabrication of an electronic device, various issues/limitations should be considered. The expected (opto)electronic properties, the thickness of the film, the size (resolutions) of the printed elements, and the yield/cost of the production are some of the most important considerations (Figure 13.4) [27].

13.5 2D Printing of MXenes

Amongst major 2D printing methods, so far, only inkjet-, electrohydrodynamic-, aerosoljet-, gravure-, and scree-printing methods have been used for the deposition of MXene inks. IJP is arguably one of the most widely used techniques for printing functional materials including MXenes. IJP is a versatile digital printing technique that typically requires small amounts of ink, making it an ideal choice for research and prototyping. Being a noncontact printing method, IJP is also a very suitable

technique for the fabrication of multilayer devices. Since the viscosities of IJP inks are limited to less than ~10 cP, only low-concentration MXene inks can be printed, which is not suitable for thick film deposition [2].

In order to be jettable and form satellite-free droplets, the inks should meet other surface tension and rheological properties as well. For stable droplet formation, the inverse Ohnesorge number of the ink ($Z = \frac{1}{\text{oh}} = \frac{\sqrt{\gamma \rho a}}{\eta}$ where γ, ρ, a, and η are surface tension, density, a nozzle diameter-related constant, and viscosity, respectively) should have a value of $1 < Z < 14$ (in some literature $1 < Z < 10$) [28]. Due to the high surface tension of water, aqueous inks usually suffer from high Z values. By adding a cosolvent (with lower surface tension such as ethanol) and/or increasing the viscosity of the ink (by increasing the MXene concentration), this value can be decreased, and droplet formation can be improved (stable jetting has been reported even at $Z \approx 19$ [29]). It should be noted that the use of larger flakes and higher concentrations of MXene for increasing the viscosity (and decreasing Z), can also lead to clogging of the nozzle [29, 30]. The maximum printable particle size depends on the diameter and the shape of the nozzle, but in the case of MXene inks, a flake size of 300–500 nm has been recommended in most of the literature [30, 31].

Additives such as surfactants can efficiently decrease the surface tension and hence the Z value. However, in this case, a tradeoff between the conductivity of the film and the printability of the ink is inevitable. Amongst various types of surfactants, (i.e. cationic, anionic, and nonionic), nonionic surfactants such as Triton X-100, Tween 20, saponin, Pluronic F-127, and F-68 are proven to be more suitable for MXene ink formulation. Saponin is found to be the best option (between tested surfactants) as it decreases the conductivity less than others. The addition of anionic and cationic surfactants can lead to the formation of branched-like structures, and the precipitation of particles, respectively [30] (Figure 13.5a). Block copolymer-like polypeptides are another class of promising additives for MXene IJP inks as they can increase the viscosity and decrease the surface tension simultaneously [32] (Figure 13.5b). In Table 13.1, the composition and the rheological properties of some previously reported MXene IJP inks are reviewed.

Electrohydrodynamic printing (EHDP) is another noncontact deposition technique that holds great promise for the fabrication of electronics as it can produce sub-micrometer droplets (smaller than the nozzle diameter) and offer highly stable undisrupted droplet jetting under a uniform electric field, enabling high-resolution printing [38] (Figure 13.5c). Since droplet detachment (droplet formation) happens when the applied electrical forces overcome the surface tension of the ink, high surface tension inks such as aqueous MXene inks are not suitable for EHDP (require higher voltage, which can lead to a breakdown between the nozzle and the substrate). In this regard, it is necessary to formulate the ink in

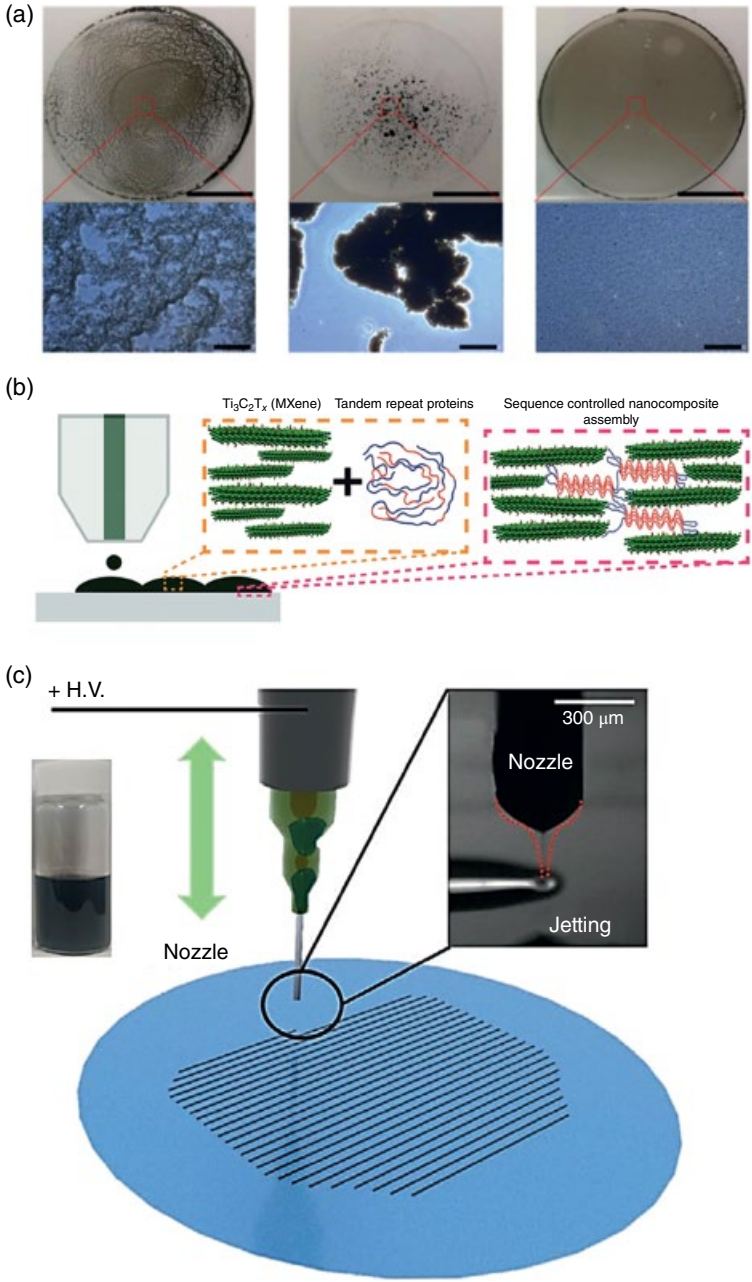


Figure 13.5 (a) Optical photographs of MXene solutions comprising (left) an anionic, (middle) a cationic surfactant, both creating heterogeneous suspensions, and (right) MXene solution with a nonionic surfactant creating a homogeneous suspension. Bottom images are microscope images of the same suspensions. *Source:* Saleh et al. [30]/ Reproduced from IOP Publishing Ltd. (b) Schematic representation of protein-mediated assembly of MXene sheets during inkjet printing. *Source:* Reproduced with permission Vural et al. [32]/John Wiley & Sons. (c) Schematic representation of electrohydrodynamic printing method. *Source:*

Table 13.1 Composition and properties of MXene inkjet printing inks.

Solvent	Concentration (mg ml^{-1})	Viscosity (cP)	Application	Substrate	References
Ethanol NMP DMSO	Ethanol 0.8 NMP 12.5 DMSO 2.1	Ethanol 7.3 NMP 13.8 DMSO12.8	Micro-supercapacitors and resistors	Aluminum oxide-coated PET and glass substrate	[7]
Isopropanol	5	2.4	Photonic devices	Silica glass, SiO_2/Si wafer, PET	[34]
Water	6.8–22.4	5.1	Wearable textile-based electronics	Textiles	[29]
Water + NMP	1.3–13.3	2.3–4.6	Flexible energy storage devices	Printable PET adhesive paper	[35]
Isopropanol	2.1	3.02	Micro-supercapacitors	Photo paper and PET	[36]
Water	30	19.71	Micro-supercapacitors	Photopaper and resin-coated PET	[37]

low-surface tension solvents such as ethanol, which is very challenging as MXene has low dispersibility in such solvents. To address this challenge, Tang et al. have treated the *m*-MXene with trifluoroacetic acid (TFA), which has led to significantly improved dispersibility in ethanol [33]. For this purpose, *m*-MXene obtained from a modified MILD method (Minimally Intensive Layer Delamination) has been treated with an aqueous solution of TFA for 24 hours, and then the product has been purified by water and sedimented by high-speed centrifugation. The ink has been obtained by dispersion/delamination of the sediments in ethanol.

Aerosoljet printing (AJP) is a versatile noncontact digital printing method that can be used for both 2D and 3D printing. AJP is one of the most promising printing technologies as it can deposit inks with a relatively wide viscosity (1–1000 cP). It is a unique printing method since high-resolution patterns (down to 10 μm) can be realized with high throughput [39]. Inks are first atomized into a mist and the aerosol mist is then delivered to the deposition head, where it is focused by a sheath gas, which surrounds the aerosol as an annular ring. Two types of atomization mechanisms are available (i.e. ultrasonic and pneumatic), which can atomize inks with different particle sizes and viscosities. The ultrasonic atomizer is usually used for small particles (<100 nm) and low-viscosity inks (<100 cP), while the pneumatic atomizer can be used for wider ranges (viscosity <1000 cP, and particle size <1 μm).

Since considerable flows of gasses are involved in different stages of printing, controlling the evaporation of the solvent (carrier solvent of the ink) is an important consideration for AJP and affects the quality of the printed structures. For this purpose, AJP inks are usually formulated with cosolvent systems (comprising of a high and a low boiling point solvent) [40], and the carrier and the sheath gases are often saturated in a bubbler with the low-boiling point solvent of the ink. Nevertheless, so far, in all available reports on AJP of MXenes, pure water has been used as the carrier solvent [39, 41–44]. For instance, Borghetti et al. have formulated and printed an aqueous $Ti_3C_2T_x$ MXene with a concentration of ~27 mg ml^{-1} and viscosity of 650 cP (using a pneumatic atomizer). To control the evaporation rate, the carrier gas has been saturated with water in the bubbler [44].

So far, of all the contact and analog 2D printing methods, only GP and screen printing (SP) have been used (reported) for the deposition of MXenes. GP is a very high-throughput printing technique that can deposit films/patterns with low/medium thicknesses. Viscous fingering (i.e. Saffman–Taylor instability) is a common issue (defect) in all contact printing methods (including GP) that requires inks with very specific surface energies and rheological properties [45]. Since aqueous MXene inks cannot meet such strict requirements, it is necessary to formulate organic MXene inks for GP. Organic MXene inks are typically formulated using a group of solvents that are known to be a "good solvent" for dispersing MXenes. However, due to the strong interactions of the MXene nanosheets in such "good solvents," even very low concentrations of MXenes tend to form a gel, which is not suitable for GP. Since low-concentration inks are not suitable for efficient printing and practical applications, formulation of a high-concentration low-viscosity ink is necessary for successful GP of MXene. This can be done using a cosolvent system comprising mostly of a "bad solvent," which is not capable of dispersing MXene, and a small amount of a "good solvent," which acts as a surfactant, helping MXene nanosheets to be dispersed in the main carrier solvent (the "bad solvent"). For instance, it has been shown that stable high-concentration dispersions of Ti_3C_2 MXene can be prepared in a mixture of propylene glycol (80 vol%) and water (20 vol%) that simultaneously exhibit low surface energy and viscosity. Using this approach [45], highly conductive transparent MXene films with minimal traces of viscus fingering have been deposited on a large-scale using GP.

SP is an excellent method for the deposition of thick films and offers one of the highest production throughputs among various printing methods, making it an ideal choice for commercial applications. Nevertheless, due to the simplicity of the method and accessibility of the required instruments, SP is extensively used in research and development as well. It is worth mentioning that a stamping method developed by Zhang et al. [46], which has some similarities with flexographic printing (FGP), can also be considered as another patterned contact deposition technique whose results can be used for developing FGP MXene inks.

Compared to the other printing techniques reviewed before, SP requires inks with higher viscosities (in the range of 2–50 Pa s, at the shear rate 100 s^{-1} [47]), and shear-thinning behavior. This allows the inks to be easily spread over the screen but to stay on the mesh in uncovered areas during the flooding step. A moderate level of thixotropic behavior is also necessary for obtaining smooth films and reduction of the mesh marks on the prints. The viscosity of the MXene dispersions can be increased to the required levels for SP, by either increasing the MXene concentration or by using additives.

Due to the strong interactions between *d*-MXene nanosheets, increasing the concentration of MXene dispersions is very challenging. Alternatively, *m*-MXene can be used for most applications (e.g. for printing conductive elements of a circuit), but the mechanical properties of the inks may not be sufficient. Adding a small amount of *d*-MXene can solve this problem and enable the formulation of high-concentration additive-free inks (Figure 13.6a) [22]. Considering the low yield of MXene delamination, using *m*-Mxene for ink formulation has significant environmental and financial benefits as well. Using rheology modifiers such as xanthan gum [48] is another approach that can increase the viscosity and improve the adhesion of the films. Currently, all Mxene SP inks are formulated in water [22, 48–50], which is not an ideal solvent for SP due to its high evaporation rate, especially for industrial production. Evaporation of the carrier solvent (in this case, water) can lead to significant changes in the rheological properties of the ink (Figure 13.6b, c) and severe reproducibility/reliability issues. Considering the importance of SP for the high-throughput manufacturing of electronics, the development of high-viscosity organic MXene inks is of significant importance [2].

13.6 Wet Coating of MXenes

In addition to printing, solution processing of MXene enables numerous wet coating techniques that can be used for the fabrication of electronics. While patterned structures can also be obtained by wet coating techniques (e.g. using a mask or post-deposition patterning such as laser scribing), unlike printing, wet coating techniques are often used for the deposition of continuous films over an area. For the fabrication of electronic devices with layered (tandem) or sandwiched structures such as solar cells, photodetectors, or batteries/supercapacitors, wet coating methods such as spray-, slot-die-, or blade-coating can offer higher throughput and better quality.

Spray-coating is one of the most used techniques in both academic research and industry as it enables the scalable deposition of both thin (even highly transparent [51]) and thick films [52] with very high throughputs. One of the greatest advantages of the spray-coating technique is the possibility of the deposition of MXenes on 3D and complex surfaces, even conformally (Figure 13.7a) [53]. This

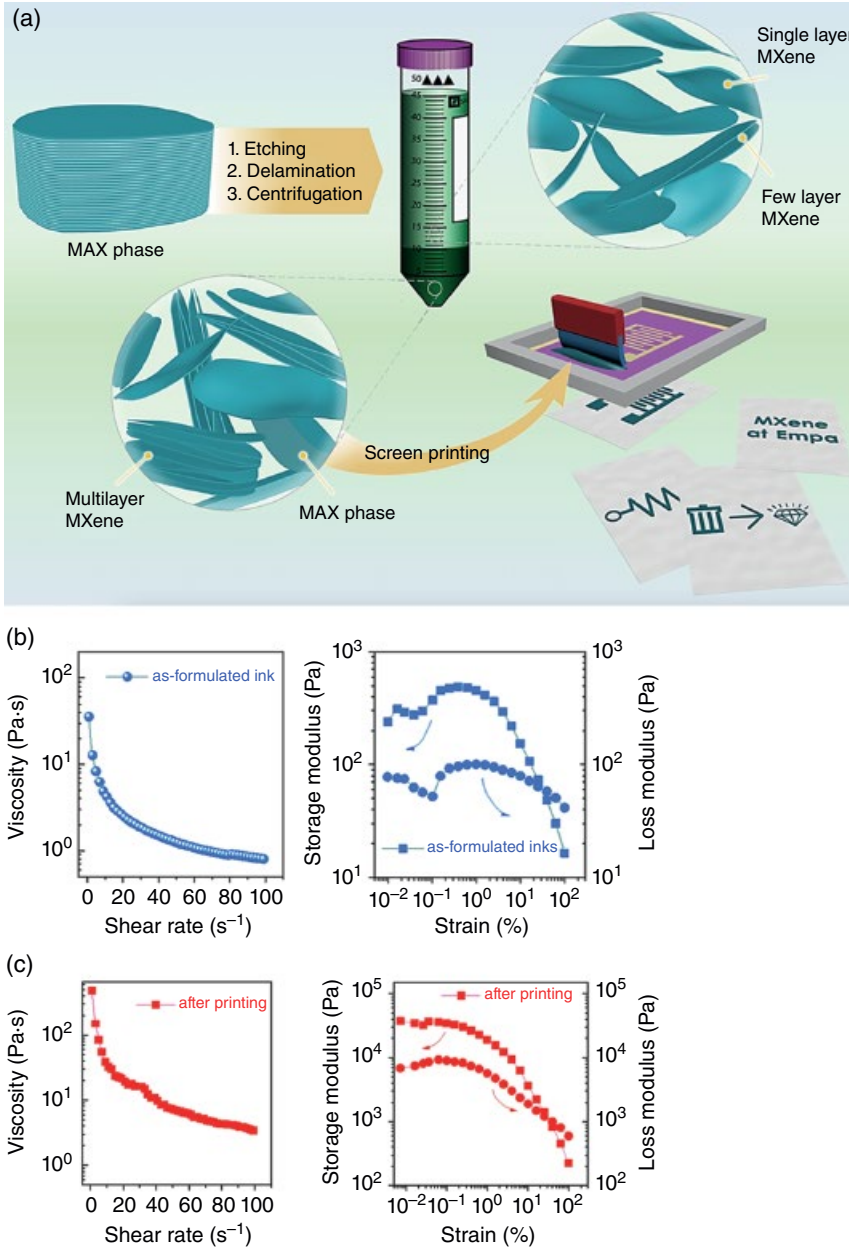


Figure 13.6 (a) Schematic representation of different steps of screen printable *m*-MXene ink formulation. (b) The rheological properties of an aqueous SP ink before printing and (c) after printing. *Source:* Reproduced with permission Abdolhosseinzadeh et al. [22]/John Wiley & Sons.

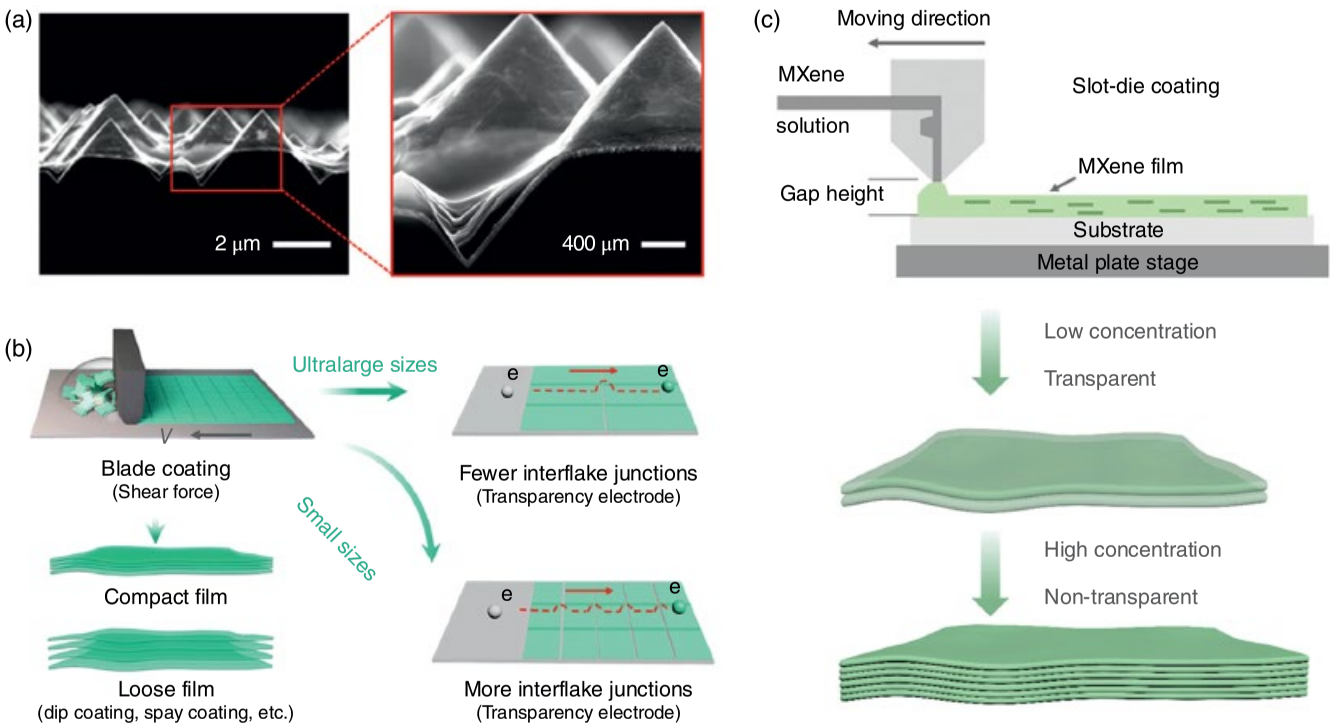


Figure 13.7 (a) SEM images of spray-coated MXene as a rear electrode for a silicon heterojunction solar cell. *Source:* Aydin et al. [53]/Reproduced from American Chemical Society. (b) Schematic representation of blade coating of a compact MXene film. *Source:* Reproduced with permission Guo et al. [54]/American Chemical Society/CC BY 4.0. (c) Schematic representation of slot-die coating method for deposition of MXene films with different thicknesses and transparencies. *Source:* Reproduced with permission Guo et al. [55]/American Chemical Society/CC BY 4.0.

enables various applications such as EMI-shielding [56], integrated thermal management systems [57], rear electrodes for silicon heterojunction solar cells [53], etc. Due to the high conductivity of MXenes and their exceptional film-formation behavior, devices made with spray-coated MXenes can even replace sputtered metallic films (e.g. sputtered silver films for silicon heterojunction solar cells) [53]. Except for a few instances where mixtures of water and a low-boiling point solvent (e.g. ethanol [51]) are used, in almost all cases, MXenes are spray coated from pure aqueous inks. This can be attributed in part to the challenges encountered in formulating non-aqueous spray-coatable inks, mainly due to the high boiling points of the solvents used for dispersing MXenes. Additionally, the considerable benefits of water as a carrier solvent in terms of health, safety, and cost-effectiveness further contribute to the attractiveness of water for spray coating. However, the relatively high vapor pressure, and very high surface tension of water can pose difficulties when attempting to form films on certain substrates during spray coating processes. On porous and rough surfaces, dewetting of aqueous inks is less of an issue but for substrates with low surface energy, the pretreatment of the surface for increasing its surface energy (e.g. using UV/ozone, or oxygen/argon plasma treatments) is crucial for the proper adhesion of the coated films. Heating the substrate during the coating process can assist in mitigating the issue of water's high vapor pressure [53].

Slot-die- and blade-coating are two other prominent large-area wet coating methods that exhibit numerous similarities regarding scalability, film quality, and production throughput. Benefiting from shear-assisted alignment of the flakes during deposition, both methods produce films with highly oriented nanosheets, which can lead to superior electrical (conductivity) and mechanical properties [54, 55, 58]. The deposition of ordered MXene nanosheets (horizontally aligned) leads to higher packing density of the films, maximized interactions of the flakes (better cohesion), and availability of more electron transport paths (Figure 13.7b). While usually used for coating high concentration (high-viscosity) inks and deposition of relatively thick films, both techniques can handle inks with a wide range of viscosities (Figure 13.4) and there is virtually no solvent or particle size limitation for the formulation of the inks (except for the dispersibility of the MXenes). The thickness of the films can be easily controlled from very thin (a few nanometers [55]) to very thick (up to 450 μm [59]) by changing the concentration of the inks and coating parameters (Figure 13.7c).

It is also worth mentioning that in addition to the major coating techniques, numerous other liquid-based deposition techniques such as dip-coating [60], spin-coating [61], interface-assisted self-assembly [62], etc. have also been developed and reported, which are used for less common (less industrial) but very specific applications. As an example, the process of coating a continuous single-layer-thick film of MXene nanosheets can be achieved easily by interfacial self-assembly techniques [63], whereas it poses significant challenges when employing conventional coating and printing methods discussed earlier.

13.7 Summary and Outlook

MXenes are a rapidly expanding category of 2D materials that possess a variety of unique characteristics and offer numerous promising applications. To effectively utilize MXenes in cutting-edge technologies and high-performance devices, it is crucial to efficiently process MXene colloidal dispersions into films/structures. This emphasizes the importance of understanding the solution processing and formulation of functional MXene inks. Equally important is comprehending the colloidal and rheological properties, as well as methods to adjust the flow behavior of the inks, their wetting (and adhesion), drying kinetics, and more. In the past few years, the solution processing (and liquid-based deposition techniques) has emerged as a highly promising technique with immense potential for the cost-effective and high-volume fabrication of diverse devices, ranging from sensors to solar cells and energy storage systems. This shows the significance of development and optimization of the liquid-based MXene-based deposition techniques and their critical role for the successful incorporation of these new group of materials into various applications.

Currently, there is a significant knowledge gap when it comes to understanding the rheological properties and film formation behavior of non-aqueous inks, particularly those involving ink formulations with specific terminal groups. Existing literature mainly focuses on $Ti_3C_2T_x$ MXene with random functional groups and fails to fully comprehend the impact of these specific terminal groups on rheological properties, film formation, and device performance. Additionally, MXene inks have a relatively short shelf-life compared to graphene or metallic inks, which is another area requiring more attention. Although printed or coated MXene films and structures exhibit improved oxidation resistance after the solvent has completely evaporated, further enhancements are necessary for devices exposed to environmental conditions like oxygen and humidity. The application of pre- and post-treatments holds potential for enhancing the chemical stability of MXenes. Although some promising reports have recently been published, significant additional investigations are still needed in this field.

References

1 Abdolhosseinzadeh, S., Heier, J., and Zhang, C.J. (2020). Printing and coating MXenes for electrochemical energy storage devices. *Journal of Physics: Energy* 2: 31004.

2 Abdolhosseinzadeh, S., Jiang, X., Zhang, H. et al. (2021). Perspectives on solution processing of two-dimensional MXenes. *Materials Today* 48: 214–240. https://doi.org/10.1016/j.mattod.2021.02.010.

3 Maleski, K., Mochalin, V.N., and Gogotsi, Y. (2017). Dispersions of two-dimensional titanium carbide MXene in organic solvents. *Chemistry of Materials* 29: 1632–1640.

4 Anasori, B., Lukatskaya, M.R., and Gogotsi, Y. (2017). 2D metal carbides and nitrides (MXenes) for energy storage. *Nature Reviews Materials* 2: 16098.

5 Zhang, C.J., Ma, Y., Zhang, X. et al. (2020). Two-dimensional transition metal carbides and nitrides (MXenes): , properties, and electrochemical energy storage applications synthesis. *Energy & Environmental Materials* 3: 29–55.

6 Natu, V., Pai, R., Sokol, M. et al. (2020). 2D $Ti_3C_2T_z$ MXene synthesized by water-free etching of Ti_3AlC_2 in polar organic solvents. *Chem* 6: 616–630.

7 Zhang, C.J., McKeon, L., Kremer, M.P. et al. (2019). Additive-free MXene inks and direct printing of micro-supercapacitors. *Nature Communications* 10: 1795.

8 Carey, M., Hinton, Z., Natu, V. et al. (2020). Dispersion and stabilization of alkylated 2D MXene in nonpolar solvents and their pseudocapacitive behavior. *Cell Reports Physical Science* 1: 100042.

9 Kim, D., Ko, T.Y., Kim, H. et al. (2019). Nonpolar organic dispersion of 2D Ti_3C_2Tx MXene flakes via simultaneous interfacial chemical grafting and phase transfer method. *ACS Nano* 13: 13818–13828.

10 Zhang, B., Wong, P.W., Guo, J. et al. (2022). Transforming $Ti_3C_2T_x$ MXene's intrinsic hydrophilicity into superhydrophobicity for efficient photothermal membrane desalination. *Nature Communications* 13: 1–10.

11 Wu, T., Kent, P.R.C., Gogotsi, Y., and Jiang, D.E. (2022). How water attacks MXene. *Chemistry of Materials* 34: 4975–4982.

12 Cao, W.T., Feng, W., Jiang, Y.Y. et al. (2019). Two-dimensional MXene-reinforced robust surface superhydrophobicity with self-cleaning and photothermal-actuating binary effects. *Materials Horizons* 6: 1057–1065.

13 Kumar, S., Lei, Y., Alshareef, N.H. et al. (2018). Biofunctionalized two-dimensional Ti_3C_2 MXenes for ultrasensitive detection of cancer biomarker. *Biosensors & Bioelectronics* 121: 243–249.

14 Zhang, C.J., Cui, L., Abdolhosseinzadeh, S., and Heier, J. (2020). Two-dimensional MXenes for lithium-sulfur batteries. *InfoMat* 2: 613–638.

15 Iqbal, A., Hong, J., Ko, T.Y., and Koo, C.M. (2021). Improving oxidation stability of 2D MXenes: synthesis, storage media, and conditions. *Nano Convergence* 8: 1–22.

16 Zhang, C.J., Pinilla, S., McEvoy, N. et al. (2017). Oxidation stability of colloidal two-dimensional titanium carbides (MXenes). *Chemistry of Materials* 29: 4848–4856.

17 Natu, V., Hart, J.L., Sokol, M. et al. (2019). Edge capping of 2D-MXene sheets with polyanionic salts to mitigate oxidation in aqueous colloidal suspensions. *Angewandte Chemie International Edition* 58: 12655–12660.

18 Kong, N., Zhang, J., Hegh, D. et al. (2022). Environmentally stable MXene ink for direct writing flexible electronics. *Nanoscale* 14: 6299–6304.

19 Wu, C.W., Unnikrishnan, B., Chen, I.W.P. et al. (2020). Excellent oxidation resistive MXene aqueous ink for micro-supercapacitor application. *Energy Storage Materials* 25: 563–571.

20 Yang, W., Yang, J., Byun, J.J. et al. (2019). 3D printing of freestanding MXene architectures for current-collector-free supercapacitors. *Advanced Materials* 31: 1902725.

21 Akuzum, B., Maleski, K., Anasori, B. et al. (2018). Rheological characteristics of 2D titanium carbide (MXene) dispersions: a guide for processing MXenes. *ACS Nano* 12: 2685–2694.

22 Abdolhosseinzadeh, S., Schneider, R., Verma, A. et al. (2020). Turning trash into treasure: additive free MXene sediment inks for screen-printed micro-supercapacitors. *Advanced Materials* 32: 2000716.

23 Abdolhosseinzadeh, S., Zhang, C., Schneider, R. et al. (2022). A universal approach for room-temperature printing and coating of 2D materials. *Advanced Materials* 34: 2103660.

24 Maleski, K., Ren, C.E., Zhao, M.Q. et al. (2018). Size-dependent physical and electrochemical properties of two-dimensional MXene flakes. *ACS Applied Materials & Interfaces* 10: 24491–24498.

25 Zhang, J., Uzun, S., Seyedin, S. et al. (2020). Additive-free MXene liquid crystals and fibers. *ACS Central Science* 6: 254–265.

26 Greaves, M., Mende, M., Wang, J. et al. (2021). Investigating the rheology of 2D titanium carbide (MXene) dispersions for colloidal processing: progress and challenges. *Journal of Materials Research* 36: 4578–4600.

27 Jafarpour, M., Nüesch, F., Heier, J., and Abdolhosseinzadeh, S. (2022). Functional ink formulation for printing and coating of graphene and other 2D materials: challenges and solutions. *Small Science* 2: 2200040.

28 Derby, B. (2010). Inkjet printing of functional and structural materials: fluid property requirements, feature stability, and resolution. *Annual Review of Materials Research* 40: 395–414.

29 Uzun, S., Schelling, M., Hantanasirisakul, K. et al. (2021). Additive-free aqueous MXene inks for thermal inkjet printing on textiles. *Small* 17: 2006376.

30 Saleh, A., Wustoni, S., Bihar, E. et al. (2020). Inkjet-printed $Ti_3C_2T_x$ MXene electrodes for multimodal cutaneous biosensing. *Journal of Physics: Materials* 3: 044004.

31 Jiang, X., Li, W., Hai, T. et al. (2019). Inkjet-printed MXene micro-scale devices for integrated broadband ultrafast photonics. *npj 2D Materials and Applications* 3: 1–9.

32 Vural, M., Pena-Francesch, A., Bars-Pomes, J. et al. (2018). Inkjet printing of self-assembled 2D titanium carbide and protein electrodes for stimuli-responsive electromagnetic shielding. *Advanced Functional Materials* 28: 1801972.

33 Tang, X., Murali, G., Lee, H. et al. (2021). Engineering aggregation-resistant MXene nanosheets as highly conductive and stable inks for all-printed electronics. *Advanced Functional Materials* 31: 2010897.

34 Jiang, X., Liu, S., Liang, W. et al. (2018). Broadband nonlinear photonics in few-layer MXene $Ti_3C_2T_x$ (T = F, O, or OH). *Laser & Photonics Reviews* 12: 1700229.

35 Wen, D., Wang, X., Liu, L. et al. (2021). Inkjet printing transparent and conductive MXene ($Ti_3C_2T_x$) films: a strategy for flexible energy storage devices. *ACS Applied Materials & Interfaces* 13: 17766–17780.

36 Sun, P., Liu, J., Liu, Q. et al. (2022). Nitrogen and sulfur co-doped MXene ink without additive for high-performance inkjet-printing micro-supercapacitors. *Chemical Engineering Journal* 450: 138372.

37 Ma, J., Zheng, S., Cao, Y. et al. (2021). Aqueous MXene/PH1000 hybrid inks for inkjet-printing micro-supercapacitors with unprecedented volumetric capacitance and modular self-powered microelectronics. *Advanced Energy Materials* 11: 2100746.

38 Jeong, Y.J., Lee, X., Bae, J. et al. (2016). Direct patterning of conductive carbon nanotube/polystyrene sulfonate composites via electrohydrodynamic jet printing for use in organic field-effect transistors. *Journal of Materials Chemistry C* 4: 4912–4919.

39 Wu, Y., Zhao, D., Zhang, J. et al. (2021). Microscale curling and alignment of $Ti_3C_2T_x$ MXene by confining aerosol droplets for planar micro-supercapacitors. *ACS Omega* 6: 33067–33074.

40 Jabari, E. and Toyserkani, E. (2015). Micro-scale aerosol-jet printing of graphene interconnects. *Carbon* 91: 321–329.

41 Saeidi-Javash, M., Du, Y., Zeng, M. et al. (2021). All-printed MXene-graphene nanosheet-based bimodal sensors for simultaneous strain and temperature sensing. *ACS Applied Electronic Materials* 3: 2341–2348.

42 Wu, Y., Lin, A., Zhang, J. et al. (2022). Crumpled and eccentric nanospheres of $Ti_3C_2T_x$ MXene by aerosol jet printing on heat substrate. *Advanced Engineering Materials* 24: 2101556.

43 Wu, Y., Lin, A., Zhang, J. et al. (2022). Aerosol jet printing of hybrid $Ti_3C_2T_x$/C nanospheres for planar micro-supercapacitors. *Frontiers in Chemistry* 10: 823.

44 Borghetti, M., Serpelloni, M., Sardini, E. et al. (2021). Temperature influence on $Ti_3C_2T_x$ lines printed by aerosol jet printing. *Sensors and Actuators, A: Physical* 332: 113185.

45 Abdolhosseinzadeh, S. (2021). *2D Material Based Inks for Room Temperature Printed Electronics*. Lausanne: École Polytechnique Fédérale de Lausanne.

46 Zhang, C.J., Kremer, M.P., Seral-Ascaso, A. et al. (2018). Stamping of flexible, coplanar micro-supercapacitors using MXene inks. *Advanced Functional Materials* 28: 1705506.

47 Somalu, M.R., Muchtar, A., Daud, W.R.W., and Brandon, N.P. (2017). Screen-printing inks for the fabrication of solid oxide fuel cell films: a review. *Renewable and Sustainable Energy Reviews* 75: 426–439.

48 Wu, H., Xie, Y., Ma, Y. et al. (2022). Aqueous MXene/Xanthan gum hybrid inks for screen-printing electromagnetic shielding, joule heater, and piezoresistive sensor. *Small* 18: 2107087.

49 Yu, L., Fan, Z., Shao, Y. et al. (2019). Versatile N-doped MXene ink for printed electrochemical energy storage application. *Advanced Energy Materials* 9: 1901839.

50 Xu, S., Dall'Agnese, Y., Wei, G. et al. (2018). Screen-printable microscale hybrid device based on MXene and layered double hydroxide electrodes for powering force sensors. *Nano Energy* 50: 479–488.

51 Hantanasirisakul, K., Zhao, M.-Q., Urbankowski, P. et al. (2016). Fabrication of $Ti_3C_2T_x$ MXene transparent thin films with tunable optoelectronic properties. *Advanced Electronic Materials* 2: 1600050.

52 Zhang, C., Schneider, R., Jafarpour, M. et al. (2023). Micro-cup architecture for printing and coating asymmetric 2d-material-based solid-state supercapacitors. *Small* 19 (32): 2300357.

53 Aydin, E., El-Demellawi, J.K., Yarali, E. et al. (2022). Scaled deposition of $Ti_3C_2T_x$ MXene on complex surfaces: application assessment as rear electrodes for silicon heterojunction solar cells. *ACS Nano* 16: 2419–2428.

54 Guo, T., Zhou, D., Deng, S. et al. (2023). Rational design of $Ti_3C_2T_x$ MXene inks for conductive. *Transparent Films ACS Nano* 17: 3737–3749.

55 Guo, T., Zhou, D., Gao, M. et al. (2023). Large-area smooth conductive films enabled by scalable slot-die coating of $Ti_3C_2T_x$ MXene aqueous inks. *Advanced Functional Materials* 33: 2213183.

56 Iqbal, A., Kwon, J., Kim, M.K., and Koo, C.M. (2021). MXenes for electromagnetic interference shielding: experimental and theoretical perspectives. *Materials Today Advances* 9: 100124.

57 Han, M., Zhang, D., Singh, A. et al. (2023). Versatility of infrared properties of MXenes. *Materials Today* 64: 31–39.

58 Zhang, J., Kong, N., Uzun, S. et al. (2020). Scalable manufacturing of free-standing, strong $Ti_3C_2T_x$ MXene films with outstanding conductivity. *Advanced Materials* 32: 2001093.

59 Abdolhosseinzadeh, S., Jiang, X., Zhang, H. et al. (2021). Perspectives on solution processing of two-dimensional MXenes. *Materials Today* 48: 214–240.

60 Salles, P., Pinto, D., Hantanasirisakul, K. et al. (2019). Electrochromic effect in titanium carbide MXene thin films produced by dip-coating. *Advanced Functional Materials* 29: 1809223.

61 Montazeri, K., Currie, M., Verger, L. et al. (2019). Beyond gold: spin-coated Ti_3C_2-based MXene photodetectors. *Advanced Materials* 31: 1903271.

62 Mojtabavi, M., Vahidmohammadi, A., Ganeshan, K. et al. (2021). Wafer-scale lateral self-assembly of Mosaic $Ti_3C_2T_x$ MXene monolayer films. *ACS Nano* 15: 625–636.

63 Yun, T., Kim, H., Iqbal, A. et al. (2020). Electromagnetic shielding of monolayer MXene assemblies. *Advanced Materials* 32: 1906769.

14

Three-Dimensional (3D) Printing of MXenes

Elnaz Jamshidi[1], *Mackenzie B. Woods*[2], *Virginia A. Davis*[2], *and Majid Beidaghi*[1,3]

[1] *Department of Mechanical and Materials Engineering, Auburn University, Auburn, AL, USA*
[2] *Department of Chemical Engineering, Auburn University, Auburn, AL, USA*
[3] *Department of Aerospace and Mechanical Engineering, University of Arizona, Tucson, AZ, USA*

14.1 Introduction

FAs introduced in the earlier chapters of this handbook, MXenes are a large family of two-dimensional (2D) transition metal carbides, nitrides, and carbonitrides with a general formula of $M_{n+1}X_nT_x$ (M represents transition metal, X is carbon/nitrogen, n can be 1–4, and T_x stands for surface functional groups such as OH, O, and F). Due to their high electrical conductivity, high specific area, hydrophilicity, and versatile chemistry, MXenes have been considered for various applications [1, 2], including energy storage devices (such as batteries and supercapacitors) [3], electromagnetic interference (EMI) shielding [4], flexible electronics [5], sensors [6], water desalination and separation membranes [7], and biomedical applications [8], to name a few. A fully developed and reliable three-dimensional (3D) printing process can accelerate the use of MXenes in these applications and provide a route for their scalable manufacturing.

Over the past decade, additive manufacturing, or 3D printing, has shown increasing promise as a rapid and sustainable manufacturing method of functional devices with complex 3D structures. Methods have been developed for printing various materials, including thermoplastic polymers, thermoset resins, metals, waxes, ceramics, and nanomaterials [9]. Fluid phase processing is a preferred route for the bottom-up assembly of nanomaterials into solid structures with controlled microstructures [10]. Additive manufacturing of

Transition Metal Carbides and Nitrides (MXenes) Handbook: Synthesis, Processing, Properties and Applications, First Edition. Edited by Chuanfang Zhang and Michael Naguib.
© 2024 John Wiley & Sons, Inc. Published 2024 by John Wiley & Sons, Inc.

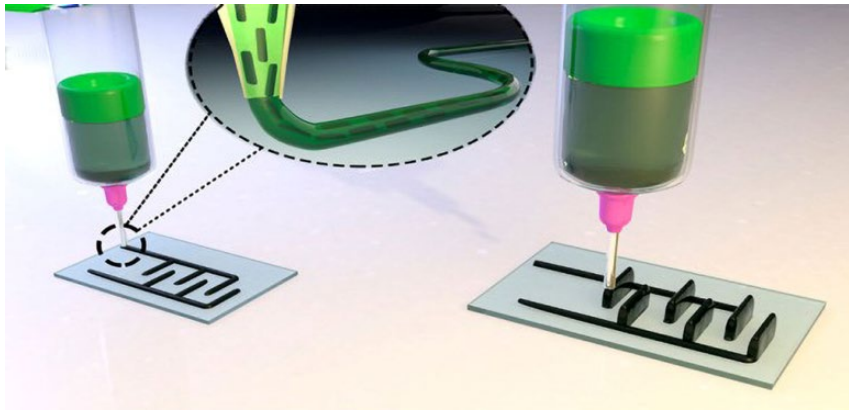


Figure 14.1 Schematic drawing demonstrating the 3D printing of MSCs with interdigital architectures. *Source:* Reproduced with permission Orangi et al. [12]. Copyright (2020), ACS Nano.

nanomaterial dispersions through techniques such as direct ink writing (DIW) permits even greater precision by enabling the production of 3D nanomaterial structures with complex architectures [11]. In DIW, a dispersion is extruded out of a nozzle and deposited on a substrate in a layer-by-layer pattern (Figure 14.1) [10]. The structure is then solidified through solvent evaporation, coagulation, or other methods. As for other fluid-based processing methods, the properties of the printed object are mainly dependent on the dispersions' microstructure and rheological properties. In the past few years, several studies have reported the preparation of 3D printable MXene-based inks and have investigated DIW printing of MXene-based devices [12, 13]. These studies have laid a foundation for understanding the properties of MXene inks and exploring the processing-structure-properties relationships in DIW of MXenes. This chapter will introduce some of the recent work on the preparation of MXene inks and discusses the required properties of MXene inks used in DIW. It will also discuss the properties and performance of some of the 3D MXene-based devices fabricated using DIW.

14.2 MXene Inks for DIW

The properties of DIW inks affect both the processing conditions required for printing and the properties of the printed structures [14]. Although DIW inks can theoretically be prepared using all MXene compositions, $Ti_3C_2T_x$ has been the main MXene used in most studies. This is partly because of reliable methods for

the synthesis $Ti_3C_2T_x$ in sufficient quantities to prepare highly concentrated inks. Also, $Ti_3C_2T_x$ has some unique physical and chemical properties that have made it the most studied MXene composition. In addition, the dispersibility of $Ti_3C_2T_x$ allows for the processing of aqueous inks at room temperature.

Water is one of the more commonly used DIW solvents because it evaporates on a time scale that allows for the deposition of wet dispersions without necessitating overly long drying times at ambient conditions. Solvents with higher vapor pressures can be utilized provided that they do not evaporate too rapidly, which would result in the drying of a layer before the subsequent one is deposited. Lower vapor pressure solvents may be used but typically require removal via immersion in another liquid in a method analogous to coagulation baths in solution spinning of fibers.

The most significant considerations when formulating printing inks are the dispersion microstructure and associated rheological properties. Whether the MXenes are dispersed as completely exfoliated individual sheets, multilayer sheets, loosely associated flocs, or aggregates will affect processability and device performance. The opacity of MXene inks can make assessing the dispersion state using optical microscopy or light scattering challenging. However, rheological methods (see Section 2.1) can be used for quality control. In addition, cast films can be assessed for aggregates through profilometry, atomic force microscopy, or scanning electron microscopy. Many of these methods may provide the most useful information if the inks are diluted to enable the visualization of individual entities [15].

The characteristics above will guide the selection of the most desirable range of MXene concentrations. When considering dispersion microstructure, it is helpful to convert between mass and volume-based concentration. This conversion can be achieved by using the relative densities to calculate the volume fraction of the nanomaterial (ϕ_n)

$$\phi_n = \frac{m_n/\rho_n}{m_n/\rho_n + m_s/\rho_s}$$

where ρ_n is the nanomaterial density and ρ_s is the solvent density, and m_n and m_s are the masses of the nanomaterial and solvent, respectively. For inorganic high-density nanomaterials, such as MXenes, in low-density fluids, the differences between weight- and volume-based concentrations can be significant. For example, the density of $Ti_3C_2T_x$ has been cited as both 3.6 [4] and 5.2 g cc^{-1} because of the possible changes in the surface functional groups [16]. Using the 3.6 g cc^{-1} value that is currently more common in the literature and 1 g ml^{-1} as the density of water, the concentration of a 30 wt% (~30 mg ml^{-1}) dispersion in terms of volume is only 10 vol%. As the volume is increased, the sheets will not be able to exist in isolation from one another and will form a continuous network. The volume fraction at which this occurs is known as the percolation threshold, ϕ_{perc}.

This value scales with the ratio of the sheet's lateral dimension and thickness. As a result, a higher concentration will be needed to achieve percolation for smaller sheets or multilayer sheets. In general, a percolated network is beneficial for printing because it results in desirable rheological properties and facilitates achieving a space-filling structure in the final print. At concentrations above ϕ_{perc}, the sheets are forced into closer proximity to one another, increasing the likelihood of aggregation [15]. However, higher concentrations can also facilitate orientation of the sheets through a process known as liquid crystalline self-assembly. This alignment may be advantageous for applications where a high degree of sheet orientation in the final print is desired.

A key issue with all printing inks is one of stability. Therefore, it is important to evaluate temporal changes in ink microstructure that determine the ink shelf life. All colloidal (and nanomaterial) dispersions, including MXene inks, are subject to changes over time, including flocculation, restacking, aggregation, and sedimentation. In addition, MXenes undergo chemical changes due to oxidation or hydrolysis over time; these changes can affect both dispersion microstructure and device performance. As a result, polymers, surfactants, and other additives are often used in ink formulation to increase stability, modify rheological properties, or enable multifunctional properties that cannot be achieved by MXenes alone.

14.2.1 Rheological Properties of DIW Inks

As for other fluid phase processing methods, ink formulation and processability have become an area of high interest within the realm of DIW. Rheological characterization is a powerful tool for gaining insights structure–process–property relationships between the dispersion microstructure, changes induced during processing and the properties of the final solidified devices. Rheological properties are one of the key determinants of ink processability, print resolution, and device performance. Emerging understanding of MXene dispersions' rheological properties has already facilitated the formulation of inks with higher printability and increased the performance of printed devices; additional knowledge gains will contribute to the development of single and multi-component inks with more tunable properties, better print resolution, and even higher performing devices.

Understanding the structure–process–property relationships of colloidal and nanomaterial dispersions enables the rational selection of dispersion concentrations and processing conditions needed to achieve desired properties in manufactured objects. Rheology refers to the study of how fluids flow and dispersions' rheological properties arise from a combination of solute (nanomaterial) size and shape, solute concentration, solute–solvent interaction. Characterization of rheological properties enables understanding of the dispersion's quiescent microstructure, flow–induced microstructural changes, ink printability, and the required

nozzle sizes and pressures for a given ink. In DIW, an ink is loaded into a syringe or other vessel and then extruded from a nozzle onto a substrate or previously deposited layer. Eom et al. [17] described that rheological characterization determines ink's suitability for each step in the DIW process. To be "printable," DIW inks must exhibit three main rheological properties: shear-thinning behavior, yield stress, and viscoelasticity with more elastic than viscous character. In other words, the ink should flow through the nozzle on-demand without dripping and have enough solid-like character to support subsequent layers while still having enough viscous character to enable intermingling and annealing between layers.

Steady shear rheology, where ink is placed between two rheometer fixtures and subjected to increasing stress or strain, provides information on a fluid's yield stress and flow behavior as a function of shear rate. Viscosity η is a measure of the resistance to flow. Inks of well-dispersed nanomaterials at the concentrations required to produce continuous solid structures can have low shear viscosities, many orders of magnitude higher than that of the solvent. However, shear-thinning behavior causes this viscosity to decrease during extrusion, and thereby enables the ink to flow through the small diameter pressures used in printing at moderate extrusion pressures without nozzle clogging. In colloidal, or nanomaterial, inks of anisotropic materials such as MXenes, shear-thinning is often the result of the alignment of the nanomaterial in the flow direction.

Yield stress is the stress required to initiate flow. In printing, this correlates to the threshold pressure needed for ink to begin flowing through the nozzle for a given nozzle diameter. The yield stress should be low enough that the ink will easily begin to flow through the nozzle upon pressure application. However, the yield stress must also be sufficiently high enough so that the ink will retain the resolution of the print [18].

Printing inks often follow a Herschel–Bulkley model:

$$\tau = \tau_y + K\dot{\gamma}^n$$

where τ is the shear stress, τ_y is the yield stress, K is the consistency factor, γ is the shear rate, and n is the flow index. The flow index parameter n is used to model the rate-dependent viscosity of the ink: if $n < 1$, the ink is shear-thinning, and if $n > 1$, the ink is shear-thickening [19]. The Herschel–Bulkley model assumes steady-state conditions and therefore cannot account for transient behaviors [20].

Inks' viscoelastic behavior is characterized using oscillatory rheology, where a sinusoidal wave is used to determine the ink's storage or elastic modulus G' and loss or viscous modulus G'' as a function of frequency ω. When a fluid has a higher amount of stored energy than dissipated energy ($G' > G''$), it has a greater solid-like (or elastic) character than liquid-like (or viscous) character.

This is a requirement for DIW inks to ensure that the printed layers can support themselves and retain their desired shape post-print processing. However, the ratio of elastic and viscous properties is also important because if the ink is too solid-like, the layers will not intermingle before drying and the structure will not have interconnectivity in the z-direction, resulting in reduced properties and delamination between layers. In the rheology literature, this balance is defined as $\tan \delta = G''/ G'$. However, the inverse of this parameter (G'/G'') is often used to assess an ink's processability by a given fluid phase manufacturing method. For example, Akuzum et al. [21] determined the rheological properties of inks prepared using both single-layer (Figure 14.2a) and multilayer MXenes (Figure 14.2b) and found a 1.8–3.6 mg ml^{-1} (0.18–0.36 wt%) ink of single-layer MXenes was suitable for extrusion printing. However, for inks of multilayer MXenes, orders of magnitude greater concentration, 50–70 wt%, were required, and even these concentrations resulted in lower values of G′/G″. This finding highlights the significant effects the dispersion state has on both rheological properties and processability. Tezel et al. [22] highlighted the potential for tuning an ink's viscoelastic properties with temperature. They demonstrated that the properties of dilute inks could be modeled with a Maxwell-type viscoelastic model that includes temperature dependence. Moreover, they showed that inks that did not possess a percolated network at room temperature transitioned to a predominantly elastic percolated network by decreasing the temperature to 5 °C. This finding provides further motivation for considering both the ink and substrate temperature during printing.

Thixotropy testing is another rheological method that can be useful for assessing an ink's printability at specific processing conditions (e.g. nozzle size and extrusion pressure). This type of testing can be used to determine the time needed for an ink's rheological properties to recover from the shear history. On the one hand, recovery enables the viscosity to increase from the value resulting from shear thinning; this is important for shape retention [19]. On the other hand, it may be desirable to retain some of the alignment 2D materials, such as MXenes, achieve during flow. Regardless, the dispersion must recover to a load-bearing network of particles before the next material layer is deposited. Three-interval thixotropy tests consisting of a low shear interval, a high shear interval, and another low shear interval have been used to mimic the DIW process [17]. The first low shear interval allows for stabilization of the ink. The high shear interval mimics the printing shear resulting in shear-thinning and microstructural deformation. The last interval mimics post-printing structural recovery. The high shear interval can be adjusted to different shear stresses to compare ink behavior. Different shear rates can be studied and used to select the most desirable combinations of nozzle diameter, print speed, and extrusion pressure.

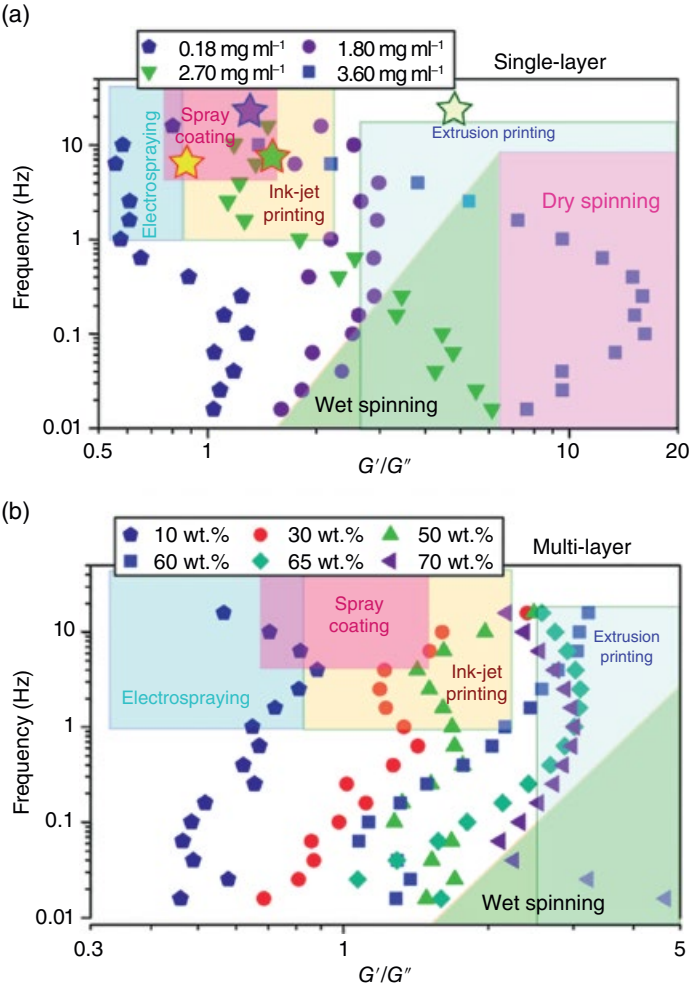


Figure 14.2 Dispersion processability regions for different methods and frequency dependence of G'/G'' for (a) single-layer and (b) multilayer $Ti_3C_2T_x$ MXene flakes. *Source:* Reproduced with permission Akuzum et al. [21]. Copyright (2018), ACS Nano.

14.2.2 Additive-Free MXene Inks

Understanding the rheology and microstructure of the MXene inks is a developing field where most research has been performed within the last few years. In addition to being directly applicable to DIW, researchers have used rheology in conjunction with morphological methods to explore ink stability and microstructure. For example, Seok et al. [23] used rheology to determine which ink

concentrations were unstable against aggregation and used this knowledge to optimize formulation and processing conditions for MXene coatings. Zhang et al. [24] investigated the rheological properties of additive-free MXene inks at various concentrations. These inks were separated into large MXene flakes (L-$Ti_3C_2T_x$) and small flakes resulting from sonication (S-$Ti_3C_2T_x$). This work highlighted the effects that sheet size can have on rheological properties and dispersion microstructure. It also demonstrated that aqueous MXene dispersions could form liquid crystalline phases where the sheets were oriented but could still flow. The authors used this finding to produce aligned MXene fibers, but liquid crystal self-assembly is also promising for increasing the alignment in DIW printed devices.

In terms of DIW, Orangi et al. [12] used an additive-free MXene ink to fabricate 3D, solid-state micro-supercapacitors with excellent electrochemical performance. The inks consisted of 28.9 wt% (290 mg ml^{-1}, 10.5 vol%) aqueous $Ti_3C_2T_x$ dispersions (Figure 14.3a) that were prepared by concentrating a more dilute dispersion using superabsorbent polymer (SAP) beads. Starting from a relatively dilute dispersion is an effective practice for preparing many nanomaterial dispersions and SAP beads are an effective tool when it is desirable to avoid high temperatures or vacuum. As shown in Figure 14.3, the resulting inks met the criteria for DIW. They were shear thinning (Figure 14.3b) had a yield stress (Figure 14.3c), and their viscoelastic properties were indicative of a percolated network (flat G' curve, Figure 14.3d) and G'/G'' ratio (Figure 14.3e) in the range suitable for DIW.

Zhang et al. [13] successfully printed high-performance micro-supercapacitors using inkjet printing and DIW of additive-free MXene inks. They studied MXene dispersions in *n*-methyl-2-pyrrolidone, dimethyl sulfoxide (DMSO), dimethylformamide, and ethanol (EtOH), as well as water (Figure 14.3f). These inks showed high stability without any noticeable sedimentation for a long time after preparation. When kept refrigerated in sealed containers under argon, MXene sheets dispersed in DMSO precipitated after six months, but the other dispersions remained stable for one year. The dispersions prepared using organic solvents displayed lower apparent viscosities than the aqueous dispersion, making them more suitable for the inkjet printing process rather than an extrusion-based process. However, the aqueous ink could be successfully used for DIW.

14.2.3 Multicomponent MXene Inks

In addition to research on printing pure MXene dispersions, several authors have developed printable inks that include other materials to prevent restacking, modify rheological properties, or enable additional functionality. However, the use of additives needs to be considered with caution as they can potentially decrease device performance [12]. Zhou et al. [25] combined one-dimensional cellulose

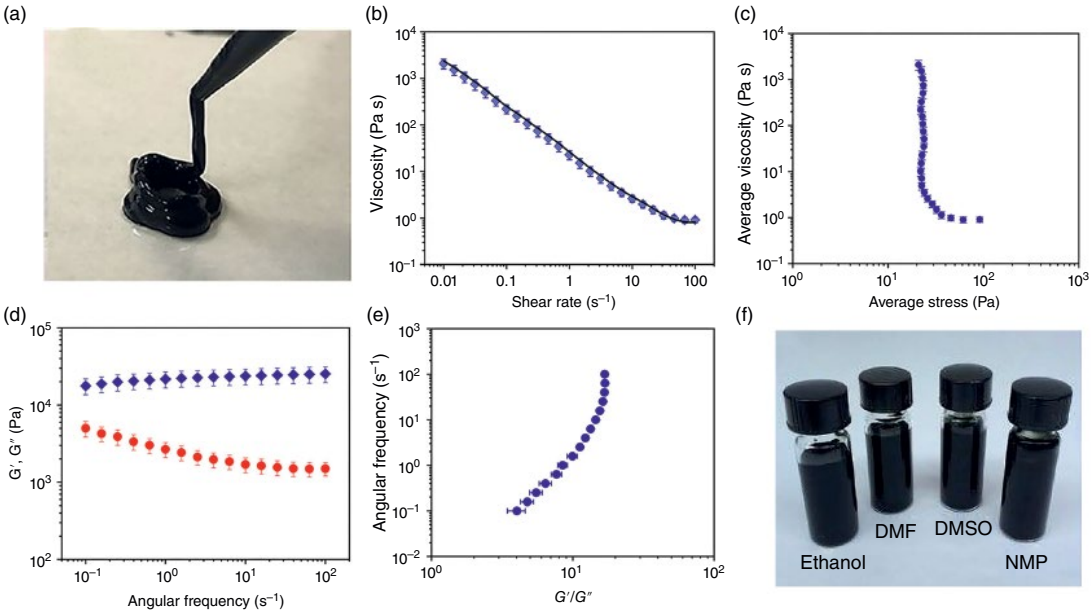


Figure 14.3 (a) A highly concentrated MXene ink prepared for DIW. The prepared ink shows suitable viscoelastic properties. Steady shear rheological behavior (b) Viscosity (blue diamonds) and Herschel–Bulkley (line) model fit for the aqueous MXene ink showed in (a) and (c) Plot of average viscosity vs. average stress showing the dramatic viscosity drop at the yield stress. Small amplitude oscillatory shear (SAOS) data show (e) G' (blue diamonds) > G'' (red diamonds) and G' nearly constant over the measured frequency range. (f) Ratio of G' to G'' over the measured frequency range. Note error bars represent standard error ($n = 5$ for SAOS data and $n = 10$ for steady shear data). *Source:* Orangi et al. [12]/Reproduced from American Chemical Society. (f) Photos of various MXene dispersions in organic solvents. *Source:* Zhang et al. [13]/Reproduced from Springer Nature/CC BY 4.0.

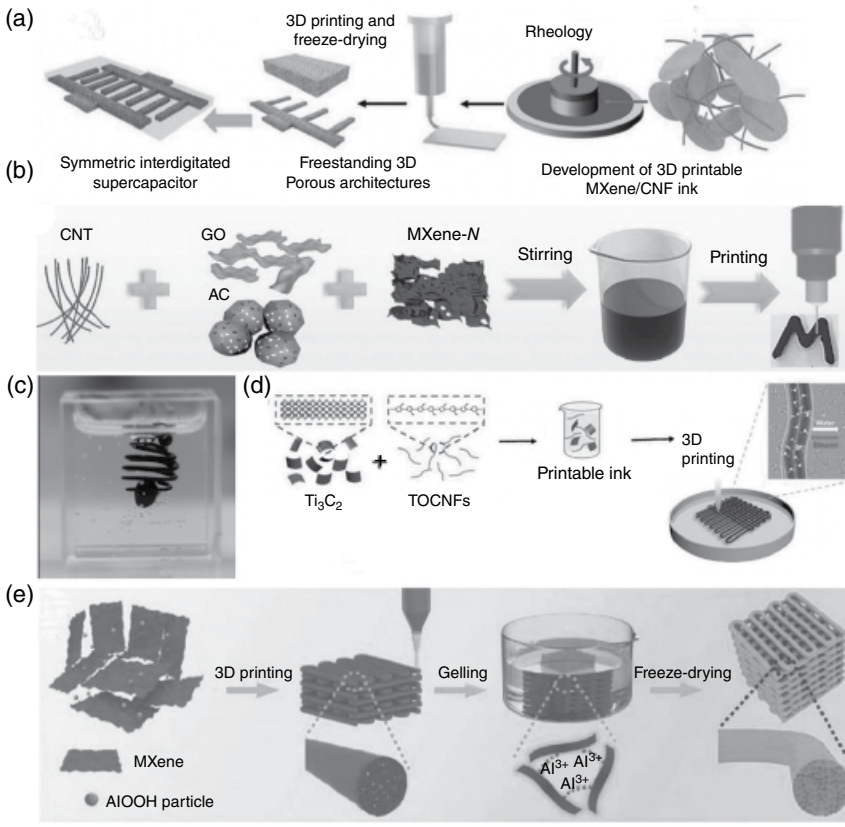


Figure 14.4 (a) Schematic drawing depicting the preparation of MXene/CNF ink and its 3D printing process. *Source:* Reproduced with permission Zhou et al. [25]. Copyright (2022), Advanced Functional Materials. (b) Schematic showing the preparation of binder-free AC/CNT/MXene-*N*/GO ink and its DIW printing. *Source:* Reproduced with permission Yu et al. [26]. Copyright (2019), Advanced Energy Materials. (c) Optical images of threads printed with MXene ink. *Source:* Cain et al. [27]/Reproduced from American Chemical Society. (d) Schematic illustration of preparation of TOCNF/$Ti_3C_2T_x$ inks used in fiber and textiles fabrication. *Source:* Reproduced with permission Cao et al. [28]. Copyright (2019), Advanced Functional Materials. (e) Schematic of constructing a freestanding gelled MXene frame. *Source:* Wu et al. [29]/Springer Nature/CC BY 4.0.

nanofibers (CNF) with MXenes to limit the amount of MXenes required to achieve printable rheological properties (Figure 14.4a). CNF was chosen as the secondary material due to its various morphologies (rod, fiber, etc.), surface chemistry, and facile dispersibility. Due to their size and shape, usually only a low concentration of CNF is enough to achieve rheological properties required for DIW [30], an important consideration when preparation inks based on a material such as

MXene that is still in relatively limited supply and requires high concentrations to obtain properties necessary for printing.

Yu et al. [26] used nitrogen-doped crumpled $Ti_3C_2T_x$ MXenes (MXene-*N*) to prepare inks for screen-printing and DIW and reported that nitrogen doping enhances conductivity and improves the electrochemical properties of the MXene [26]. To synthesize the crumpled MXene-*N*, delaminated $Ti_3C_2T_x$ sheets were first deposited on the surface of melamine-formaldehyde (MF) spheres, which also worked as the source of nitrogen, by electrostatic interaction of the sheets and the positively charged spheres. Subsequently, the templated MXene was annealed in an argon atmosphere to remove the MF templates while the surface of MXene sheets was doped with nitrogen. This MF templating and removal method prevents the restacking of MXene nanosheets by forming a crumpled sheet structure and results in a uniform *N*-doping of MXene during the annealing process. To use the synthesized materials in DIW, hybrid inks were prepared by mixing crumpled *N*-doped MXenes with graphene oxide (GO), activated carbon (AC), and carbon nanotubes (CNTs) to tune the viscosity (Figure 14.4b). The rheological properties of prepared AC/CNT/MXene-*N*/GO ink showed its shear thinning behavior. At a shear rate of $0.06\,s^{-1}$, the ink showed a high viscosity (>104 Pa s) and yield strength of 300 Pa. Therefore, the ink was successfully used for fabricating 3D structures and devices [26].

Cain et al. [27] reported liquid-in-liquid 3D printing of MXene inks enabled by the interfacial assembly of $Ti_3C_2T_x$ MXene nanosheets at oil-water interfaces. The assembly of MXene surfactant at the surface resulted from electrostatic interactions of negatively charged MXene sheets with a positively charged amine-terminated ligand (short-chain organic molecule *n*-butylamine) dissolved in a silicon oil bath. As the MXene ink was extruded into a viscous silicon oil-ligand matrix at a regulated flow rate, a jammed assembly of MXene surfactants was formed at the oil–water interface, preserving the printed thread into a path traced by the printhead and forming a 3D filament-like structure (Figure 14.4c).

Cao et al. [28] reported the preparation of printable hybrid inks made of TEMPO (2,2,6,6-tetramethylpiperidine-1-oxylradi-cal)-mediated oxidized cellulose nanofibrils (TOCNFs) and $Ti_3C_2T_x$. Dispersions of TOCNFs and $Ti_3C_2T_x$ were mixed at room temperature for 12 hours under magnetic stirring to obtain homogenous TOCNFs/$Ti_3C_2T_x$ inks. Steric hinderance of the surface carboxyl groups generates repulsion between TOCNFs, which improves dispersity of $Ti_3C_2T_x$ nanosheets and the stability of the mixed dispersion. In addition, the Coulombic repulsion induced by the negatively charged surfaces $Ti_3C_2T_x$ nanosheets and TOCNFs further improve the stability of the dispersions. Finally, the prepared ink was extruded into an EtOH coagulation bath, forming a continuous and stable gel fiber due to the rapid solvent exchange between EtOH and water inside the ink (Figure 14.4d).

Inorganic nanomaterials have also been used as secondary materials to prepare MXene inks. For example, Wu et al. [29] demonstrated that adding aluminum

oxide hydroxide (AlOOH) nanoparticles to MXene ink improves the rheological properties and flowability, and the resulting hybrid ink can be used in DIW. AlOOH nanoparticles were mixed with an MXene dispersion and grounded in a mortar to achieve a homogenous pasty mixture that was used in 3D printing of MXene-based frames for EMI shielding applications. After printing, the printed frames were freeze-dried, and the electrically insulating AlOOH nanoparticles were removed by inserting the frames in an $AlCl_3$/HCl solution. During this process, MXene sheets are cross-linked by aluminum ions produced from $AlCl_3$ and AlOOH, and gelled MXene frames are formed (Figure 14.4e).

14.3 3D Printing of MXene-based Devices

As mentioned above and explained in other chapters of this handbook, MXenes have shown potential as functional materials for various applications, including electronic, photonic, and electrochemical devices. Many of these potential applications can benefit from printing processes that are specifically developed for the fabrication of MXene-based 3D devices. So far, with only a few exceptions [29, 31], most of the studies in this area have been focused on 3D printing of energy storage devices such as supercapacitors and batteries.

3D energy storage devices can offer higher specific energy and power per footprint area. This is a significant factor for on-chip applications, where the total area available for the energy storage device is limited [32]. Therefore, we have seen a lot of interest in the 3D printing of on-chip micro-supercapacitors (MSCs) and micro-batteries in the past few years. Because of their structural and chemical diversity and tunable surface chemistry, high electrical conductivity, and redox activity, MXenes are considered to be excellent electrode materials for pseudocapacitors and several battery chemistries [3, 33, 34]. Fabrication of 3D interdigitated MXene electrodes with high internal porosity on various substrates, including flexible and wearable substrates, has been demonstrated using DIW printing.

Yu et al. [26] prepared *N*-doped crumpled MXenes (MXene-*N*) ink for direct printing of MSCs on various functional substrates, including polyethylene terephthalate, polyimide, rubber, A4 paper, aluminum (Al) foil, copper (Cu) foil, glass, and stainless steel plate. The MXene-*N* inks were first used in the fabrication of interdigital MSCs using screen printing and the device assembly was completed by using a gel electrolyte of polyvinyl alcohol (PVA)/sulfuric acid (H_2SO_4). The electrochemical tests of quasi-solid-state *N*-MXene MSCs showed near rectangular cyclic voltammetry (CV) profiles (Figure 14.5a) and triangular-like galvanostatic charge/discharge (GCD), indicating the capacitive performance of printed MXene-*N* MSCs. Furthermore, due to properties like the 3D interconnected

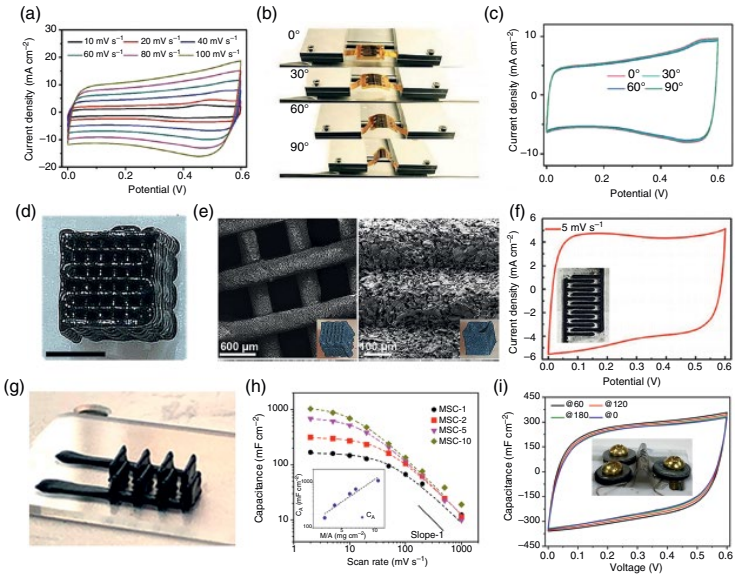


Figure 14.5 (a) CV profiles of an MXene-*N* printed MSC at different scan rates of 10–100 mV s^{-1}. (b) Photographs and (c) CV profiles of MXene-*N* printed MSCs under various bending angles of 0°, 30°, 60°, and 90°. *Source:* Yu et al. [26]/Reproduced from John Wiley & Sons, Inc. (d) Photograph of a 3D printed rectangular hollow prism structure. Scale bar is 3 mm. (e) SEM and optical photographs (inset) of a freestanding MXene microlattice (left) and a hollow rectangular prism (right). (f) Cyclic voltammetry (CV) at 5 mV s^{-1} showing a near-ideal capacitive behavior of MXene MSC with interdigitated electrode configuration shown in the inset (5 mm smallest lateral size). *Source:* Yang et al. [35]/Reproduced with permission from John Wiley & Sons, Inc. (g) Optical image of an MSC (with 10 printed layers) printed on a glass substrate before drying. (h) CV curves at 5 mV s^{-1} of 3D printed MXene MSCs with different numbers of printed layers. (i) Electrochemical performance of an MSC (with one printed layer printed on flexible polymer substrates) at 10 mV s^{-1} scan rate under various bending angles (starting with 60° followed by 120°, 180°, and 0°). *Source:* Orang et al. [12]/Reproduced from American Chemical Society.

conductive network formed in the printed electrodes, the active nitrogen sites, and accessible electrolyte transport passes in the electrode structure, the printed MSCs based on MXene-*N* showed an areal capacitance of 70.1 mF cm^{-2} at 10 mV s^{-1}, much more than that of pure MXene MSCs fabricated in the same study. The CV tests performed under various bending angles (Figure 14.5b) confirmed the mechanical robustness of the printed electrodes and the CV curves remained unchanged as the bending angle increased (Figure 14.5c). Furthermore, to print 3D devices using DIW, the rheological properties of ink were tuned by addition of AC, CNT, and GO to prepare AC/CNT/MXene-*N*/GO ink, as described in the previous section above. This hybrid ink was used to fabricate various structures such as rigid scaffolds and woodpile-like structures. As expected, increasing the nozzle diameter increased the average width of filaments and the printed lines. The electrochemical properties of printed electrodes were studied using symmetric two-electrode configurations based on different printed layer thicknesses. The three-layered electrode showed an areal capacitance of 8.2 F cm^{-2} at a scan rate 10 mV s^{-1}, which is comparatively a high areal capacitance for a 3D-printed MSC. However, due to the large quantity of components with lower capacitance than MXene (AC, CNT, and GO) in the ink composition, the calculated gravimetric capacitance was only 45.1 F g^{-1} and the volumetric energy density was 0.83 mWh cm^{-3}. Therefore, although adding these components enables the rheological properties for DIW, they have little contribution to the overall performance of the device [26].

Yang et al. [35] developed 3D printable MXene inks using $Ti_3C_2T_x$ sheets with large lateral sizes (~8 μm average lateral size) to fabricate symmetric MSCs using DIW printing. First, they demonstrated the properties of additive-free aqueous MXene inks by printing 3D freestanding $Ti_3C_2T_x$ wet structures such as woodpile-like structures, hollow rectangular prisms (Figure 14.5d) and interdigitated electrodes. They then showed that freeze-drying could preserve the well-defined 3D shapes of wet structures as it protects the internal integrity and external shape of the structures while minimizing shrinkage (Figure 14.5e). Furthermore, the freeze-drying approach leads to a high specific surface area of 3D printed architectures (177 m^2 g^{-1}) as the restacking of 2D flakes during drying is prevented and they are assembled into a porous structure. The SEM images of the printed structures showed an interconnected 3D network with no sign of bending in printed filaments as well as well-defined boundaries between individual printed filaments. The electrochemical tests showed that 3D MSCs with a mass loading of ~8.5 mg cm^{-2} had a quasi-rectangular CV shape (Figure 14.5f) and triangular-like GCD curves, indicating a typical capacitive performance. The devices were assembled using a polymer gel electrolyte, a mixture of PVA and H_2SO_4. An areal capacitance of 2.1 F cm^{-2} at a current density of 1.7 mA cm^{-2} was calculated for the printed devices. Also, the tests showed a 90% capacitance retention after 10 000

cycles at $1\,A\,g^{-1}$. An energy density of $0.0244\,mWh\,cm^{-2}$ and power density of $0.64\,mW\,cm^{-2}$ were calculated for the 3D printed MSCs at a current density of $4.3\,mA\,cm^{-2}$.

Orangi et al. [12] reported the fabrication of 3D MSCs based on highly concentrated and additive-free $Ti_3C_2T_x$ MXene ink on various substrates, including glass slides, polymer films, papers, and Si/SiO_2 wafers. As explained in the previous sections, the ink was prepared by concentrating MXene dispersions in water to very high concentrations (~$290\,mg\,ml^{-1}$), using SAP beads to remove the excess water. Then, the prepared ink was used for DIW printing of 3D MSCs with interdigital electrodes. Although the ink showed the required mechanical properties for layer-by-layer deposition without collapsing, it had a very high water content (~71 wt%). Therefore, after drying at room temperature, the electrodes' height significantly decreased due to shrinkage. However, the overall shape of the electrode was preserved due to the good adhesion of the ink to the substrate and the small shrinkage along the width and length of the electrodes. For printing MSCs with higher electrode heights, after printing the current collectors, additional layers were printed on top of each other to reach the required height. SEM showed the horizontal alignment of MXene sheets in the printed electrodes caused by their alignment in the nozzle and in the direction of nozzle movement during the printing process. The MSCs printed on a flexible polymer substrate showed high flexibility and strong attachment to the substrate. A printed device with 10 MXene layers (Figure 14.5g) showed an areal capacitance of $1035\,mF\,cm^{-2}$ at $2\,mV\,s^{-1}$ (Figure 14.5h), an areal energy density of $51.7\,\mu W\,h\,cm^{-2}$, and a power density of $5.7\,mW\,cm^{-2}$ [12]. The mechanical robustness of prints and the flexibility of the devices printed on a flexible polymer substrate were examined by testing these devices at different bending angles. The electrochemical test showed similar performance with negligible change in specific capacitance for devices tested at different bending angles (Figure 14.5i) [12].

Li et al. [36] reported using mixtures of $Ti_3C_2T_x$ MXene nanosheets, manganese dioxide nanowires (MnONWs), silver nanowires (AgNWs), and fullerene (C60) to prepare viscous nanocomposite inks for the fabrication of stretchable MSCs. They reported that 2D MXene nanosheets can form a cross-linked 3D network with 1D AgNWs and MnONWs. MnONWs improve the pseudocapacitive properties in these composite electrodes, whereas AgNWs enhance charge transfer by forming a continuous conductive network throughout the electrode structure. In addition, C60 nanoparticles act as spacers between MXene nanosheets, allowing more effective ion transport and decreasing the friction between adjacent layers, enabling the stretchability of the fabricated MSCs. The stretchable MSCs were printed on oxygen plasma-treated polydimethylsiloxane. Then, using freeze-drying, the MXene-AgNW-MnONW-C60 electrodes were solidified into honeycomb-like porous structures with a layered cell wall architecture (Figure 14.6a, b). Fabrication

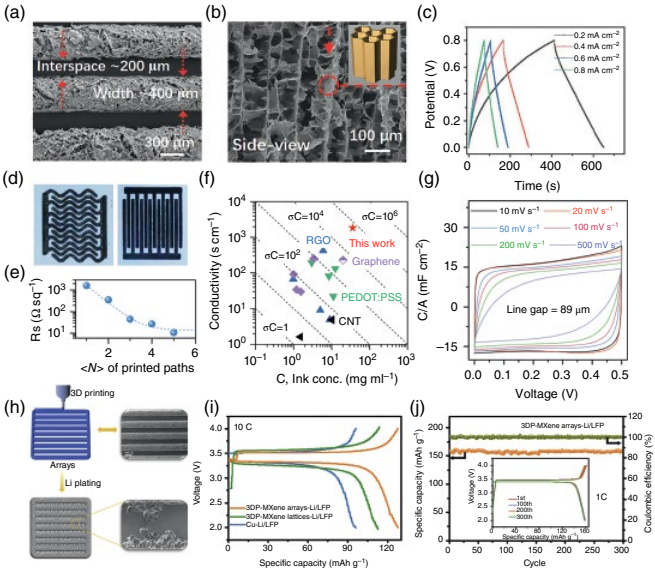


Figure 14.6 SEM images of printed MXene-AgNW-MnONW-C60 electrodes showing (a) the width and interspace distance between the adjacent electrodes (top view) and (b) the thickness of an electrode (lateral view). (c) Electrochemical performance of printed MXene-AgNW-MnONW-C60 MSCs. GCD curves at different current densities. *Source:* Li et al. [36]/Reproduced from John Wiley & Sons, Inc. (d) Optical images of all-MXene printed MSCs with various configurations on paper. (e) The sheet resistance, Rs, plotted as a function of a number of printed layers <*N*> showing an exponential decay of Rs with increasing <*N*>. (f) Comparison of the conductivity of the as-printed lines plotted as a function of concentration for various inks including the reported MXene ink. (g) Normalized CV profiles a typical extrusion-printed MXene MSC (line gap ~89 μm, number of layers <*N*> = 3). *Source:* Zhang et al. [13]/Springer Nature/CC BY 4.0. (h) Schematic drawing and SEM images showing 3D printing MXene arrays to guide the nucleation and growth of lithium. (i) Selected voltage profiles of 3DP-MXene arrays-Li/LFP batteries at a current density of 10 C. (j) Cycling stability of 3DP-MXene arrays-Li/LFP battery. The inset shows typical voltage profiles at various cycles. *Source:* Shen et al. [37]/Reproduced with permission from Elsevier.

of the stretchable MSCs was completed by depositing a PVA-KOH gel electrolyte onto the printed microelectrodes. The assembled MSCs were tested for their electrochemical performance. The GCD curves (Figure 14.6c) showed some asymmetry attributed to the relatively high ion diffusion resistance of PVA-based gel electrolyte, the relatively low electronic and ionic conductivity of the MnONW, and the decomposition of the redox active materials at the end of the charging half cycle. Nonetheless, from the CV tests, an areal capacitance of 216.2 mF cm^{-2}, an energy density of 19.2 Wh cm^{-2}, and a power density of 58.3 mW cm^{-2} were calculated at a scan rate of 10 mV s^{-1}. At this scan rate, the specific areal capacitances of MXene-AgNW and MXene-AgNW-MnONW MSCs with identical electrode thicknesses were 107.1 and 247.8 mF cm^{-2}, respectively. This suggests that incorporating MnONWs can significantly increase the pseudocapacitance of printed MXene MSCs but lower their rate capability [36].

Zhang et al. [13] reported the DIW printing of MSCs using additive-free MXene ink (concentration of ~36 mg ml^{-1}) on various substrates such as porous paper and solid Al foil (Figure 14.6d). The effect of line thickness of MSCs on sheet resistance shows that as the number of printed layers (<*N*>) increases, the sheet resistance significantly decreases (Figure 14.6e). The MSC performance is improved by decreasing the line gap, adding extra pseudocapacitive sites on the MXene nanosheets, and increasing the number of printed layers. A figure of merit, FoM = σC (S cm^{-1}.mg ml^{-1}), was used to describe the electronic properties of the inks based on the ink's concentration (C) and electronic conductivity (σ). A higher FoM means that printed ink can achieve a higher conductivity with a lower number of printed paths (or layers). As shown in Figure 14.6f, the prepared MXene ink showed a significantly higher FoM (66 996 S cm^{-1}.mg ml^{-1}) compared to other reported printable conductive inks such as graphene ink (FoM = 6000 S cm^{-1}.mg ml^{-1}). This higher FoM enables both high-resolution printing and excellent charge-storage performance for the printed MXene MSCs. CV curves of a typical printed MSC with a line gap of 89 μm show near-ideal capacitive performance at various scan rates up to 500 mV s^{-1} (Figure 14.6g). The energy density of printed all-MXene MSCs (<*N*> = 5) assembled using a PVA-H_2SO_4 gel electrolyte was about 0.32 W h cm^{-2}, and its power density was about 0.11 W h cm^{-2} [13].

Shen et al. [37] created a highly concentrated MXene ink (300 mg ml^{-1}) for DIW printing of 3D Li-ion batteries. First, 3D arrays and lattices were fabricated after freeze-drying of the strictures 3D printed a substrate and referred to as 3DP-MXene arrays and 3DP-MXene lattices, respectively. Then, to create the hybrid lithium anodes, 3DP-MXene arrays and lattices were used as substrates for lithium plating. These arrays and lattices homogenized the flow of Li ions and electric field, inhibiting dendrite formation during Li plating. The 3D-printed filament also provided the space to accommodate large Cobblestone-like

lithium features grown during anode cycling (Figure 14.6h). After lithium plating, the 3DP-MXene arrays were evaluated by galvanostatic cycling measurements and showed a low overpotential of 10 mV, long cycle stability of up to 1200 hours, and high rate capabilities of up to 20 mA cm^{-2}.A full cell with a $LiFePO_4$ (LFP) electrode as the cathode and a lithium-plated MXene array as the anode was assembled and showed a capacity of 127.6 mAh g^{-1} at 10C (Figure 14.6i) and a high cycling stability with 99.4% capacity retention after 300 cycles at 1C (Figure 14.6j).

14.4 Conclusion

In this chapter, we briefly presented some of the recent developments in preparation of MXene inks for 3D printing using DIW. Specifically, we highlighted the important role of rheological properties of the ink and how ink formulation can affect properties that are most important for DIW. Several studies have utilized viscoelastic properties of MXene dispersions or hybrid dispersions of MXene and other nanomaterials to 3D print various structures and devices. Most reports are specifically focused on 3D energy storage devices such as MSCs due to the significant advantages of 3D device architectures compared to conventional 2D planar architectures. Here, we reviewed some of the recent efforts on fabrication of MXene-based MSCs by DIW. While preparation of MXene-based inks for 3D printing has seen a lot of advances in the last few years, several issues remain unresolved; for example, only one type of MXene $Ti_3C_2T_x$ has been used in printing out of many existing MXene compositions. Another difficulty that could prevent MXene inks from becoming industrially practical is their stability. The inks have a limited shelf life and must be stored under specific conditions. In addition, improving delamination and etching yields during the synthesis process is critical for lowering total production costs. Furthermore, current research focuses mostly on printing MXene as electrodes for supercapacitors, leaving a wide range of other applications available for subsequent investigations. Because of these difficulties, more research is required to develop functional MXene inks and advance novel preparation processes to expand the applications of 3D MXene-based devices.

Acknowledgments

The authors acknowledge National Science Foundation Award #2005413 for support.

References

1 Anasori, B., Lukatskaya, M.R., and Gogotsi, Y. (2017). 2D metal carbides and nitrides (MXenes) for energy storage. *Nature Reviews Materials* 2 (2): 1–17.

2 VahidMohammadi, A., Rosen, J., and Gogotsi, Y. (2021). The world of two-dimensional carbides and nitrides (MXenes). *Science* 372 (6547): eabf1581.

3 Ghidiu, M., Lukatskaya, M.R., Zhao, M.-Q. et al. (2014). Conductive two-dimensional titanium carbide "clay" with high volumetric capacitance. *Nature* 516 (7529): 78–78.

4 Shahzad, F., Alhabeb, M., Hatter, C.B. et al. (2016). Electromagnetic interference shielding with 2D transition metal carbides (MXenes). *Science* 353 (6304): 1137–1140.

5 Ahn, S., Han, T.-H., Maleski, K. et al. (2020). A 2D titanium carbide MXene flexible electrode for high-efficiency light-emitting diodes. *Advanced Materials* 32 (23): 2000919.

6 Kim, S.J., Koh, H.-J., Ren, C.E. et al. (2018). Metallic $Ti_3C_2T_x$ MXene gas sensors with ultrahigh signal-to-noise ratio. *ACS Nano* 12 (2): 986–993.

7 Ding, L., Wei, Y., Wang, Y. et al. (2017). A two-dimensional lamellar membrane: MXene nanosheet stacks. *Angewandte Chemie (International Ed. in English)* 56 (7): 1825–1829.

8 Li, Z., Zhang, H., Han, J. et al. (2018). Surface nanopore engineering of 2D MXenes for targeted and synergistic multitherapies of hepatocellular carcinoma. *Advanced Materials* 30 (25): 1706981.

9 Bikas, H., Stavropoulos, P., and Chryssolouris, G. (2016). Additive manufacturing methods and modelling approaches: a critical review. *International Journal of Advanced Manufacturing Technology* 83 (1): 389–405.

10 Davis, V.A. (2011). Liquid crystalline assembly of nanocylinders. *Journal of Materials Research* 26 (2): 140–153.

11 Lewis, J.A., Smay, J.E., Stuecker, J., and Cesarano, J. (2006). Direct ink writing of three-dimensional ceramic structures. *Journal of the American Ceramic Society* 89 (12): 3599–3609.

12 Orangi, J., Hamade, F., Davis, V.A., and Beidaghi, M. (2020). 3D printing of additive-free 2D Ti_3C_2Tx (MXene) ink for fabrication of micro-supercapacitors with ultra-high energy densities. *ACS Nano* 14 (1): 640–650.

13 Zhang, C.(J.), McKeon, L., Kremer, M.P. et al. (2019). Additive-free MXene inks and direct printing of micro-supercapacitors. *Nature Communications* 10: 1795.

14 Ng, L.W.T., Hu, G., Howe, R.C.T. et al. (2019). 2D ink design. In: *Printing of Graphene and Related 2D Materials: Technology, Formulation and Applications* (ed. L.W.T. Ng, G. Hu, R.C.T. Howe, et al.), 103–134. Cham: Springer International Publishing.

15 Davis, V.A. and Green, M.J. (2017). Controlling and characterizing anisotropic nanomaterial dispersion. In: *Nanotechnology Commercialization*, 65–99. Wiley.

16 Naguib, M., Mashtalir, O., Carle, J. et al. (2012). Two-dimensional transition metal carbides. *ACS Nano* 6 (2): 1322–1331.

17 Eom, Y., Kim, F., Yang, S.E. et al. (2019). Rheological design of 3D printable all-inorganic inks using BiSbTe-based thermoelectric materials. *Journal of Rheology* 63 (2): 291–304.

18 Corker, A., Ng, H.C.-H., Poole, R.J., and García-Tuñón, E. (2019). 3D printing with 2D colloids: designing rheology protocols to predict 'printability' of soft-materials. *Soft Matter* 15 (6): 1444–1456.

19 Tagliaferri, S., Panagiotopoulos, A., and Mattevi, C. (2021). Direct ink writing of energy materials. *Materials Advances* 2 (2): 540–563.

20 Coussot, P. (2014). Yield stress fluid flows: a review of experimental data. *Journal of Non-Newtonian Fluid Mechanics* 211: 31–49.

21 Akuzum, B., Maleski, K., Anasori, B. et al. (2018). Rheological characteristics of 2D titanium carbide (MXene) dispersions: a guide for processing MXenes. *ACS Nano* 12 (3): 2685–2694.

22 Tezel, G.B., Arole, K., Holta, D.E. et al. (2022). Interparticle interactions and rheological signatures of Ti_3C_2Tz MXene dispersions. *Journal of Colloid and Interface Science* 605: 120–128.

23 Seok, S.-H., Choo, S., Kwak, J. et al. (2021). Synthesis of high-quality 2D carbide MXene flakes using a highly purified MAX precursor for ink applications. *Nanoscale Advances* 3 (2): 517–527.

24 Zhang, J., Uzun, S., Seyedin, S. et al. (2020). Additive-free MXene liquid crystals and fibers. *ACS Central Science* 6 (2): 254–265.

25 Zhou, G., Li, M.-C., Liu, C. et al. 3D printed $Ti_3C_2T_x$ MXene/cellulose nanofiber architectures for solid-state supercapacitors: ink rheology, 3D printability, and electrochemical performance. *Advanced Functional Materials* 32 (14): 2109593.

26 Yu, L., Fan, Z., Shao, Y. et al. (2019). Versatile N-doped MXene ink for printed electrochemical energy storage application. *Advanced Energy Materials* 9 (34): 1901839.

27 Cain, J.D., Azizi, A., Maleski, K. et al. (2019). Sculpting liquids with two-dimensional materials: the assembly of Ti_3C_2Tx MXene sheets at liquid–liquid interfaces. *ACS Nano* 13 (11): 12385–12392.

28 Cao, W.-T., Ma, C., Mao, D.-S. et al. (2019). MXene-reinforced cellulose nanofibril inks for 3D-printed smart fibres and textiles. *Advanced Functional Materials* 29 (51): 1905898.

29 Wu, X., Tu, T., Dai, Y. et al. (2021). Direct ink writing of highly conductive MXene frames for tunable electromagnetic interference shielding and electromagnetic wave-induced thermochromism. *Nano Micro Letters* 13 (1): 148.

30 Chen, Y., Yu, Z., Ye, Y. et al. (2021). Superelastic, hygroscopic, and ionic conducting cellulose nanofibril monoliths by 3D printing. *ACS Nano* 15 (1): 1869–1879.

31 Hong, S.Y., Sun, Y., Lee, J. et al. (2021). 3D printing of free-standing $Ti_3C_2T_x$/PEO architecture for electromagnetic interference shielding. *Polymer* 236: 124312.

32 Beidaghi, M. and Gogotsi, Y. (2014). Capacitive energy storage in micro-scale devices: recent advances in design and fabrication of micro-supercapacitors. *Energy & Environmental Science* 7 (3): 867–884.

33 VahidMohammadi, A., Hadjikhani, A., Shahbazmohamadi, S., and Beidaghi, M. (2017). Two-dimensional vanadium carbide (MXene) as a high-capacity cathode material for rechargeable aluminum batteries. *ACS Nano* 11 (11): 11135–11144.

34 Wang, C.-H., Kurra, N., Alhabeb, M. et al. (2018). Titanium carbide (MXene) as a current collector for lithium-ion batteries. *ACS Omega* 3 (10): 12489–12494.

35 Yang, W., Yang, J., Byun, J.J. et al. (2019). 3D printing of freestanding MXene architectures for current-collector-free supercapacitors. *Advanced Materials* 31 (37): 1902725.

36 Li, X., Li, H., Fan, X. et al. (2020). 3D-printed stretchable micro-supercapacitor with remarkable areal performance. *Advanced Energy Materials* 10 (14): 1903794.

37 Shen, K., Li, B., and Yang, S. (2019). 3D printing dendrite-free lithium anodes based on the nucleated MXene arrays. *Energy Storage Materials* 24.

15

Assembling of MXenes from Liquid to Solid, Including Liquid Crystals, Fibers

Yu Long, Zhitan Wu, Ying Tao, and Quan-Hong Yang

Nanoyang Group, State Key Laboratory of Chemical Engineering, School of Chemical Engineering and Technology, Tianjin University, Tianjin, China

15.1 Introduction

Since the groundbreaking discovery of graphene in 2004, large quantities of two-dimensional (2D) materials with various fascinating properties have been successively prepared by different synthetic methods. These 2D materials possess sheet-like structures, with large lateral sizes (ranging from a few nanometers to micrometers) and atomic layer thickness (less than 5 nm). Owing to their quantum size effect, 2D materials exhibit extraordinary physical, and chemical properties [1–3]. For example, the confinement of charge carriers in two dimensions confers 2D materials with intriguing electronic properties. These unique properties have inspired intense research enthusiasm on the fundamental studies, controlled synthesis, and advanced assembly techniques for the applications of 2D materials, including electronic and optical devices, energy storage, and conversion systems [4–7].

A thriving family of transition metal carbides, nitrides, or carbonitrides (denoted as MXenes) have risen to prominence among the existing 2D materials and attracted ever-increasing attention for their integrated advantages. To date, more than a hundred possible stoichiometric MXenes with distinct properties have been predicted, of which over 30 have been synthesized in the laboratory. Generally, they have a core of transition metal carbides or nitrides, which endows them with excellent electrical conductivity, and abundant active sites. The surfaces of MXenes are terminated with mixed functional groups (–O/OH/F) when they are synthesized in the typical etchant solutions (i.e. LiF/HCl or HF) [8, 9]. By post-treatments (e.g. thermal treatments) or other synthesis routes (e.g. molten salt

Transition Metal Carbides and Nitrides (MXenes) Handbook: Synthesis, Processing, Properties and Applications, First Edition. Edited by Chuanfang Zhang and Michael Naguib.
© 2024 John Wiley & Sons, Inc. Published 2024 by John Wiley & Sons, Inc.

etching routes), the types and ratios of the surface groups can be tuned, which offers opportunities for modifying the surface and building interactions with other species [10–12].

From the viewpoint of practical applications and property integrations, it is vital to assemble MXene sheets or particles from the liquid phase into solid macroscopic architectures. By one-dimensional (1D) macroscopic assembly, the fabricated MXene fibers are integrated with excellent electrical, mechanical, and electrochemical properties, and are promising for powering wearable devices (e.g. fabric supercapacitors), and some heated textiles. By two-dimensional (2D) macroscopic assembly, the fabricated MXene films or papers deliver outstanding performance when used in energy storage devices, electromagnetic interference (EMI) shielding, and sensing. By three-dimensional (3D) macroscopic assembly, the inter-sheet restacking issues can be suppressed, enhancing ion accessibility, and further improving the utilization of MXenes.

Different from graphene, of which the assembly generally starts with graphene oxide (GO), MXenes can be directly applied in diverse solution-based assembly techniques (e.g. spinning, coating, vacuum-assisted filtration, and spray drying) due to their intrinsic hydrophilicity. With these assembly techniques, they can be fabricated into different macroscopic forms effectively. For instance, the MXene flakes can be assembled onto 1D cellulose-based yarns with a dip-coating technique, or into self-supported film with vacuum-assisted filtration [13]. Furthermore, it has been discovered that MXene dispersions exhibit as a nematic liquid crystal (LC) phase when they are of large lateral sizes or high concentrations [14, 15], and the MXene flakes will be packed in arrangement. Accordingly, the LC $Ti_3C_2T_x$ dispersion exhibits enhanced rheological properties, and can be spun into 1D neat MXene fibers [16–18], or be blade-coated into a continuous MXene film [19]. The produced fibers or films possess both high mechanical strength and electrical conductivity [16]. Furthermore, by extrusion printing, customized MXene-based architectures can be fabricated, which opens new opportunities to realize high-performance multiscale and multidimensional devices [20].

In addition to the above, MXene flakes can self-concentrate to construct solid macroscopic architectures, when the electrostatic balance in the original dispersion system is broken. The self-assembly phenomena have been frequently observed at the interfaces formed between MXene dispersions and another phase [21–24]. For instance, when a positively charged solid guest is introduced, the original force balance of the MXene dispersion will be broken by the induced electrostatic attractions, driving MXene flakes to assemble onto the solid surface. These solid surfaces can act as templates to produce designed MXene structures [25–28]. Another typical example is water/oil interfacial assembly. After the MXene flakes are grafted with hydrophobic ligands, the enhanced MXene-solvent interactions will make flakes self-concentrate at the interfaces. Once stable

oil/water Pickering emulsions form, a 3D MXene aerogel can be further obtained after freeze-drying. Furthermore, when crosslinkers (e.g. multivalent metal ions and protonated thionine molecules) are introduced into the dispersion system, bulk gelation will occur easily, resulting in a MXene hydrogel. In this case, the crosslinker can bridge adjacent MXene flakes by forming ionic bonds, chemical bonds, or hydrogen bonds [29–32]. Certainly, MXene flakes can also be integrated into a 3D networked structure by incorporating with other materials (e.g. GO sheets and polymer chains) [33–36]. The restacking issues of MXenes can be effectively prevented in these assemblies, which is of great significance in the application of energy storage, catalysis, sensors, etc.

Overall, assembling 2D materials into macroscopic architectures provides access to optimized properties, structural customizations, and functional diversities, which is of fundamental and practical significance. Various solution-processing techniques by utilization of forces between MXene sheets, solvents, and introduced species as crosslinkers (e.g. van der Waals forces, electrostatic interactions, charge-transfer interactions, hydrogen bonding, and chemical bonding) allow MXenes to be assembled into a broad range of macroscopic architectures, including 1D fibers, 2D films, and 3D hydrogel or aerogels. These macroforms can be applied in numerous fields, such as conductive transparent coatings, electrochemical energy storage, drug delivery, sensing, and EMI shielding. In this chapter, we will provide an overview of the recent advances in rational design and control fabrication, and the potential applications of MXene-based macroscopic assemblies. Moreover, we will present our perspectives on the future of macroscopic MXene-based functional materials.

15.2 1D Macroscopic MXene Fibers

The ever-increasing interest in wearable devices has raised innovative designs of integrating new conductive materials into textiles or fibers. To satisfy the needs of emerging intelligent textile applications, the multifunctional fibers, as key components, must meet the high requirements on conductivity, mechanical properties, safety, as well as electrochemical performance. The most studied MXene, $Ti_3C_2T_x$, has a good solution dispersion ability, due to abundant surface terminations (=O, −F, −OH, −Cl, etc.), which can therefore be functional inks readily and be used to prepare advanced fibers by various solution-processing methods, such as dip coating, spray coating, and extrusion printing. With a deeper understanding of their surface chemistry, colloidal and rheological behaviors, intense attention has been drawn to processing MXenes into advanced functional fibers (or yarns) with excellent electrical, mechanical, and electrochemical properties [37]. Contributed to the development of various fabrication techniques

(e.g. coating [14, 38, 39], wet spinning [40–42], electrospinning [43–45], and biscrolling [46, 47]), MXene-based functional fibers have been developed, which demonstrated outstanding performance in the applications of wearable energy storage devices [48, 49], heated textiles [50, 51], and sensors [52–54]. Based on the component of functional MXene fibers, we divide them into neat MXene fibers and MXene composite fibers.

15.2.1 Neat MXene Fibers

MXenes possess excellent electrical conductivity and good mechanical properties. In order to meet the needs of electronic devices for high electrical conductivity and ion accessibility, it is highly desired to spin MXenes into neat fibers (the MXene content of 100 wt%) without employing additional additives (e.g. polymers, carbon nanotubes (CNTs), and GO sheets) and binders. Contributed to their thermal instability under high temperature, the wet spinning technique is an ideal choice for fabricating neat MXene fibers with ordered microstructures, rather than melt-spinning method. Theoretically, active materials (i.e. MXenes) are dispersed in solvents to prepare homogeneous spinning solutions and then extruded into a coagulation bath for the precipitation in a fiber form [55, 56]. However, a major challenge in wet-spinning for neat MXene fibers is the weak interlayer interactions between sheets with small lateral sizes, which are not sufficiently strong to support a free-standing fiber structure (i.e. spinnability). In addition, the low solid component in dilute MXene dispersion obtained directly from the synthesis cannot satisfy continuous spinning [48, 57].

Studies have shown that addition of other substances, such as GO and polyurethane (PU), can assist $Ti_3C_2T_x$ to achieve LC behavior, thereby preparing LC-assisted fiber spinning. LCs have been demonstrated in diverse materials, including rigid polymers, 1D CNTs, and 2D GO sheets, which are thermodynamically stable, and exhibit both liquid-like fluidity and crystal-like order [29, 58–60]. In the nematic LC phase, the nanomaterials self-align into long-range directional ordering, with surprisingly great fluidity, like original (isotropic) liquids. According to Onsager's theory, the dispersion consisting of 2D randomly oriented flakes will transit into a nematic LC phase, when the concentration and sheet aspect ratio of the materials are increased. This isotropic–nematic (I–N) transition is driven by the competition between rotational entropy (favoring nematic phases) and translational entropy (availability of free volume, favoring isotropic states). Above the critical LC concentration, or for ultra-high sheet aspect ratio, a decrease in free volume results in a higher packing of the MXene flakes, and thus nematic ordering [61]. The formation of nematic LC phases offers great opportunities for 2D materials to achieve highly ordered microstructures, and spinnability with favorable rheological properties (e.g. high viscoelasticity) [57, 62]. Additionally,

the sheet alignment inherited from LCs supports strong interactions between contacted sheets, which contributes to the intense mechanical strength of obtained fibers. Furthermore, the locally crumbled structures of individual sheets endow the fibers with flexibility.

As mentioned above, MXene LCs can be spun into fibers with additives. However, these additives undoubtedly will lower the electrical conductivity and MXene mass loading, thus limiting practical applications. Therefore, the development of additive-free MXene inks is a critical step to realize the wide application of MXene fibers. In 2020, Gogotsi's group first demonstrated that $Ti_3C_2T_x$ MXene sheets could self-assemble into nematic LC phases, and fabricated additive-free fibers, by direct one-step wet spinning [48, 63]. When small $Ti_3C_2T_x$ flakes (S-$Ti_3C_2T_x$, lateral size: ~310 nm) were used, the I–N transition would occur at a high concentration of ~150 mg ml^{-1}, whereas the transition would occur at a relatively low concentration (6.3 mg mL^{-1}) in the case of large flakes (L-$Ti_3C_2T_x$, lateral size: ~3.1 μm). Compared with the isotropic dispersions, the LC $Ti_3C_2T_x$ dispersions (26.5 mg mL^{-1} for L-$Ti_3C_2T_x$; 150 mg mL^{-1} for S-$Ti_3C_2T_x$) demonstrated soft solid-like properties, with both the ratios of elastic modulus and the viscous modulus (G′/G″) exceeding 1. This rheological property indicated the spinnability of LC $Ti_3C_2T_x$ dispersions. As shown in Figure 15.1a, the LC dispersion was injected (needle size: ~170 μm) at a certain spinning rate into a rotating coagulation bath. The applied shear during the spinning induced the alignment of the ordered LC MXene domains, which was well maintained during the coagulation and solidification processes.

The final fiber microstructures can be largely affected by spinning parameters, such as the bath components. For instance, when the pure acetic acid was used as the coagulation bath, it would produce a fast solvent exchange rate between the water and MXene flakes, leading to facilitated coagulation and consequently an open microstructure (Figure 15.1b). In contrast, a chitosan bath slowed down the diffusion of water, resulting in a close-packed microstructure. Therefore, the L-$Ti_3C_2T_x$ fibers spun in a chitosan bath exhibited excellent electrical conductivity (~7750 S cm^{-1}), high tensile strength (~40.5 MPa), and showed a high volumetric capacitance of ~1265 F cm^{-3}, when applied for a fiber-shaped supercapacitor. In addition, this method was successfully extended to other types of MXene (e.g. Ti_2C and $Mo_2Ti_2C_3$), suggesting that it was certainly universal for constructing 1D pure MXene fibers.

Certain ions (e.g. NH_4^+ ions and Mg^{2+}) have been introduced in the coagulation solution for densified MXene fibers with enhanced mechanical properties [18, 64]. As shown in Figure 15.1c, bonding between NH_4^+ ions and MXene sheets increased electrostatic interactions, resulting in a sol–gel transition. This gel induced with NH_4^+ ions manifested outstanding deformability, and structural stability under an external force at a high pH value of 9, which indicated that a

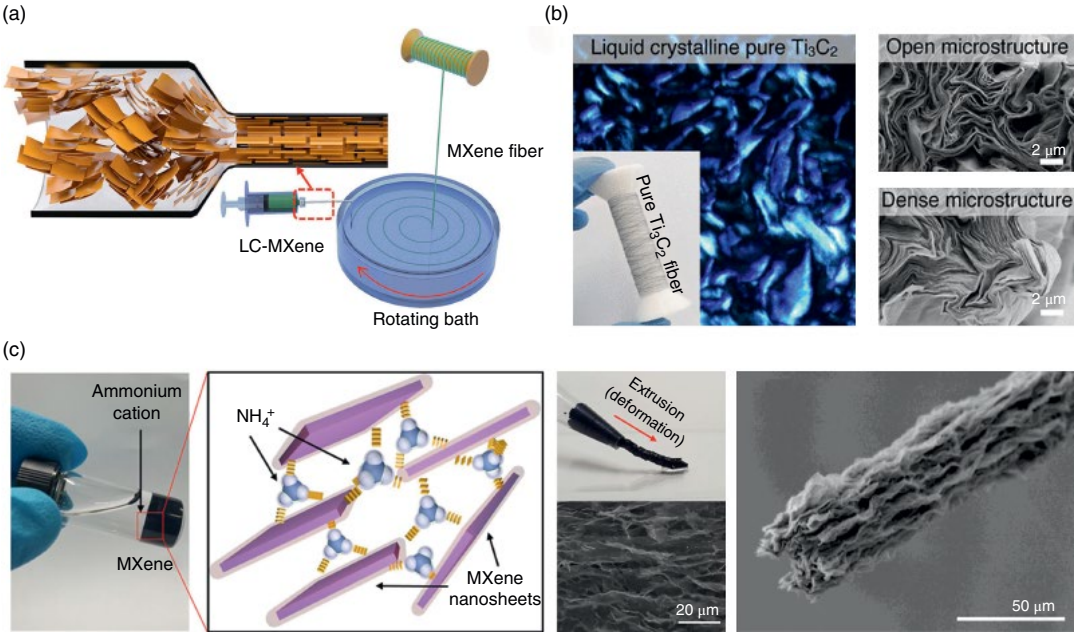


Figure 15.1 Neat MXene fibers. (a) Schematic illustrating the fabrication of LC-MXene fibers via wet-spinning; (b) the optical image of fabricated pure Ti_3C_2 fibers, and cross-sectional SEM images of Ti_3C_2 fibers with open and dense-packed microstructures. *Source:* Reproduced with permission Zhang et al. [16] © 2020, American Chemical Society. (c) NH_4^+ ions could induce the crosslinking of $Ti_3C_2T_x$ sheets, and the induced gel showed outstanding deformability. With NH_4^+ ions introduced in the coagulation bath, highly aligned and densely packed fibers could be achieved. *Source:* Reproduced with permission Shin et al. [64] © 2021, American Chemical Society.

mechanical drawing of MXene gel fibers was allowed during wet spinning to further induce a highly aligned and dense multiscale structure. In this respect, an LC $Ti_3C_2T_x$ dispersion (25 mg mL^{-1}; size: ~5.11 μm) was extruded through a nozzle (needle size: ~210 μm) into a coagulation bath (containing NH_4Cl and NH_4OH; pH: 9). With a drawing ratio of 3, the prepared meter-long MXene fibers showed an ultra-high electrical conductivity of 12 504 S cm^{-1}, high tensile strength of 344 MPa, and Young's modulus of 122 GPa. In a similar mechanism, Li et al. added Mg^{2+} ions into the coagulation bath to force the colloidal filament to precipitate and eventually form intact and densely packed $Ti_3C_2T_x$ fibers [17]. As a consequence of the nanofluidic ion transport channels induced by compact stacking flakes, the fibrillar electrode showed a volumetric capacitance of 1360 F cm^{-3} in a 1.0 M $MgSO_4$ aqueous electrolyte with reversible Mg^{2+} pseudocapacitive intercalation behaviors. Additionally, by integrating subsequent supercritical CO_2 drying with Ca^{2+} crosslinking in coagulation, Li et al. designed MXene aerogel fibers with tunable porosity (96.5–99.3%), and high specific surface area up to 142 m^2 g^{-1} [62].

15.2.2 MXene Composite Fibers

15.2.2.1 Coated MXene Composite Fibers

Various types of coating techniques (e.g. dip coating [14, 65], drop-casting [38], and spray coating [66]) are the easiest and most cost-effective methods to incorporate MXenes into 1D fibers. Typically, homogeneous MXene aqueous dispersions are prepared as coating formulations. With diverse coating techniques and sequential drying, MXene sheets can be coated onto natural fibers (e.g. cotton [39, 53], linen [13], bamboo [67, 68]) and synthetic ones (e.g. nylon [69], polyester [39], silver-coated nylon [70], and carbon-based fabrics [38]). The coating and drying processes may be repeated to achieve the desired MXene loading or functionality. For instance, Jiang et al. chose carbon fabric (CF) as the substrate without additional surface pretreatment, and loaded $Ti_3C_2T_x$ by drop-casting and drying in an oven at 50 °C [38]. When the $Ti_3C_2T_x$-coated CF was coupled with RuO_2-loaded CF, the assembled in-plane asymmetric supercapacitor displayed an energy density of 37 μW h cm^{-2} at power densities of 40 mW cm^{-2}, in a voltage window of 1.5 V.

Due to the rough surfaces, cotton fibers also serve as ideal substrates to provide outstanding adhesion for $Ti_3C_2T_x$ coating. With dip coating, both small- and large-scale Ti_3C_2 MXene flakes (S-Ti_3C_2, 340 nm; L-Ti_3C_2, 1 μm) can be easily deposited onto cotton fibers. Whilst S-Ti_3C_2-coated fibers can retain the original flexibility, the L-Ti_3C_2-coated fibers achieve higher electrical conductivity than the former, but less flexibility. Moreover, L-Ti_3C_2 can be coated exclusively on fiber surfaces. In this regard, Uzun et al. proposed a two-step dip-coating strategy to balance flexibility and conductivity [14]. The fibers were first saturated with S-Ti_3C_2 flakes before being coated with L-Ti_3C_2 ones (Figure 15.2a), resulting in a structure

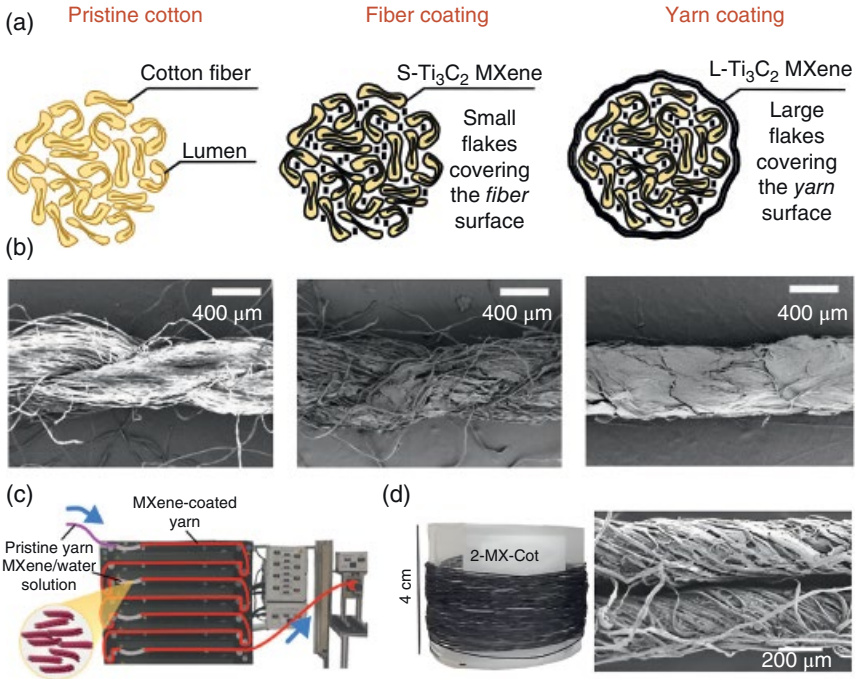


Figure 15.2 MXene coated fibers. (a) Diagrams of cotton yarns before and after coating: pristine, coated with S-Ti_3C_2 MXene flakes, coated with S-Ti_3C_2 and L-Ti_3C_2 MXene flakes; (b) SEM images of the pristine cotton yarns, S-Ti_3C_2 coated cotton yarns, and Ti_3C_2-coated cotton yarns via two-step dip coating. *Source:* Reproduced with permission Uzun et al. [14] © 2019, John Wiley & Sons. (c) Schematic of the large-scale production of MXene-coated yarns; (d) the optical image of 10-meter-long 2-ply MXene-coated cotton yarns (2-MX-Cot) and the SEM image of the coated yarns. *Source:* Reproduced with permission Levitt et al. [13] © 2020, Elsevier.

with S-Ti_3C_2 filled the center and L-Ti_3C_2 covered the surface (Figure 15.2b). As a result, the MXene loading reached 77 wt%, and the electrical conductivity reached $440.3 \pm 0.9\,S\,cm^{-1}$. Moreover, these fibers could be knitted into various stitch patterns, and the resulting MXene-coated yarns were used to prepare a flexible and wearable capacitive pressure sensor, with high sensitivity, a wide sensing range of 20% compression, and excellent cycling stability for 2000 cycles (at ~14.1% strain). With an automated yarn coating facility, Levitt et al. produced ten meters of MXene-coated cotton yarns and multifilament nylon fibers rapidly (Figure 15.2c, d) [13]. The commercial yarns passed through successive baths containing MXene dispersions at a fixed rate for coating, which were then collected onto a yarn winder, and repeatedly fed through the coating line to achieve desired MXene loading. With a flat-bed industrial-scale weft knitting machine,

approximately 66 types of knitted supercapacitors with tuned device geometry and knit structures could be fabricated. The electrochemical performance was optimized, with delivered energy and power densities of 25.4 μWh cm^{-2} and 0.47 mW cm^{-2}, as well as 10 000 stable cycles.

For certain 1D substrates particularly with smooth surfaces that cannot easily bond with MXene, surface pretreatments or binders are needed prior to MXene coating. For example, the adhesion of silver-plated nylon fibers to $Ti_3C_2T_x$ sheets can be enhanced by exposing the pristine fibers to oxygen plasma [70]. Cellulose nanocrystals (CNCs) were introduced to an MXene dispersion to assist MXene dip-coating onto thermoplastic polyurethane (TPU) nonwoven fabric [71]. CNC acted as a binder to enhance the interfacial contact between MXene sheets and TPU substrate via hydrogen bonding, which facilitated the formation of a stable conductive layer, and enhanced the stable sensing performance of the coated fiber. Based on the modulus variances between the rigid MXene-CNC conductive layer and elastic TPU substrate, strain sensors with a special micro-crack structure were prepared after a pre-stretching treatment. The CNC loading also affected the crack density, and consequently sensing performance. Polyethyleneimine (PEI) is a positively charged reagent, which covalently interacts with various materials. With electrostatic assembly, negatively charged $Ti_3C_2T_x$ flakes could spontaneously attach to PEI-modified polyester fabrics and form successive conductive layers [72].

Binders can not only enhance interfacial assembly of MXene onto fiber substrates, but also composite fibers with multiple functions and desired properties [39, 66, 72, 73]. For instance, Wang et al. modified MXene surface with *in-situ* polymerized polypyrrole (PPy) before dip-coating on poly(ethylene terephthalate) (PET) textiles (M-textile) [39]. Contributed to their polar groups, the PPy not only facilitated robust conformal coating, but also further increased the efficiency of EMI shielding. With silicone coated on the surfaces, the M-textile showed water-resistance and an excellent Joule heating performance. Similarly, Zheng et al. used poly(3,4-ethylenedioxythiophene) (PEDOT) modified fabrics to load $Ti_3C_2T_x$ flakes [66]. The fabricated PEDOT/MXene coated fabrics not only exhibited remarkable electrochemical capacitance (1000.2 mF cm^{-2}), but also an excellent EMI shielding effectiveness (36.62 dB), high electrothermal temperature (193.1 °C), as well as impressive strain sensing performance.

15.2.2.2 Spun MXene Composite Fibers

Owing to the good solution processability of MXenes, a wide range of organic or inorganic materials, such as CNTs, GO sheets, poly(3,4-ethylenedioxythiophene): polystyrene sulfonate (PEDOT:PSS), polycaprolactone, polyacrylonitrile (PAN), and polyvinylidene fluoride, have been incorporated with MXenes in spinning formulations, to produce spun MXene-based composite fibers by wet-spinning

and electrospinning [42–44, 74, 75]. The addition of these materials could improve the spinnability of precursor solutions and regulate rheological properties. The loading of MXene in those fibers covered a wide range from 10 to 98 wt%. Functional fibers can be prepared by incorporating materials with high electrical conductivity, and mechanical strength into fibers, which allows them to be used in a wide range of applications, such as strain and pressure sensors, antennas, and heaters. MXenes have the advantages of high electrical conductivity, excellent energy storage properties, and highly hydrophilic surfaces, the combination of which and their processability make MXenes an optimal material for preparing functional fibers.

When certain LC materials (e.g. GO or tungstate sheets) are incorporated, mixed LC MXene-based spinning solutions with long-range ordering can be formed, and thus aligned composite fibers can be directly prepared via wet-spinning [40, 41, 76]. The fabrication process is like that of neat MXene fibers (Section 2.1). The MXene-GO composite fibers fabricated with the MXene as the predominant component exhibit a high volumetric capacitance when used in the supercapacitor. When some conductive polymers are incorporated, the composite fibers show increased conductivity, flexibility, and high stretchability, which are suitable for smart fabric sensory systems. For instance, the $Ti_3C_2T_x$-PU composite fibers prepared by wet spinning have large strains (up to ~152%) with a high gauge factor (GF) of ~12 900 [77]. With an industrial-scale knitting machine, the composite fibers could also be knitted into an elbow sleeve, which could monitor the movement of users. Owing to their sensitivity in both pressure and temperature, the $Ti_3C_2T_x$-Kevlar composite fibers were commonly knitted and sewed into senor masks to monitor human breathing, or temperature-responsive gloves to sense hazards in advance [78].

Different from wet spinning, electrospinning is a technique that produces ultrafine fibers from polymer-based solutions under a high-voltage electric field. Specifically, with a high voltage applied to the needle tip, a polymer-based solution is extruded from the needle to form fibers, which are eventually collected on a metal plate [48]. In this case, the coagulation bath is not needed. The spinning mechanism allows liquid droplets to be charged under high voltage, and induce strong electrostatic repulsion, which counteracts the surface tension, resulting in stretches at a critical point of liquid stream eruption and formation of nanofibers [79].

Numerous polymers have been electrospun with delaminated MXene flakes, including poly(acrylic acid), poly(ethylene oxide) (PEO), poly(vinyl alcohol) (PVA), alginate/PEO, and PAN. Notably, the MXene loading in electrospun composite fibers is usually lower than that in wet-spun fibers [43, 44, 80, 81]. For instance, Mayerberger et al., only 1 wt% MXene was loaded in the fibers, which acted as fillers to change the polymer structures, and tune the mechanical and electrical properties [43]. Levitt et al. fabricated PAN-$Ti_3C_2T_x$ fibers with up to

35 wt% MXene, and the resulting $Ti_3C_2T_x$ flakes were shown to be well aligned with the fiber axis (Figure 15.3a) [45]. With subsequent carbonization, MXene/carbon nanofibers were obtained with stable structure, which displayed an areal capacitance of ~244 mF cm^{-2} at 50 mV s^{-1}. Shao et al. used flexible polyester (PET) yarns to collect the electrospun PEO-$Ti_3C_2T_x$ nanofibers, which could be assembled into asymmetric supercapacitors [80].

15.2.2.3 Biscrolled MXene Composite Fibers

MXene composite fibers prepared by coating and spinning methods will suffer from low mass loading, low durability of powder in fibers, and poor functionality; therefore, the biscrolling technique has been proposed. Unlike the above-mentioned coating method or the spinning method, where MXene is typically coated on the surface of the fiber or dispersed in the spinning solution and then spun into yarns; the biscrolling method is that MXene is first drop-casted, *in-situ* deposited, or dip-coated on the surface of the substrate, and then twist the resulting mixed substrate into yarns [48, 82, 83]. Its unique preparation method traps MXene in a reel structure, not only guaranteeing a high mass-loading with stiff attachment, but also reducing the mass loss during subsequent processing.

To select the appropriate substrate, conductive materials are typically used for spinning, such as conductive polymers, carbon fibers, CNTs, and graphene. CNTs are suitable substrates in biscrolling due to their high conductivity and high strength. As shown in Figure 15.3b, MXene-CNT fibers were produced by drop-casting and twisting, and the MXene sheets were homogeneously dispersed within the CNT network, creating pores and voids of varied sizes [46]. The loading of MXene could reach 98 wt%, and the material possesses nearly identical properties with pure MXene fibers. Expectantly, the MXene-CNT fibers displayed ultra-high specific volumetric, areal, gravimetric, and linear capacitance of 1083 F cm^{-3}, 3188 mF cm^{-2}, 428 F g^{-1}, and 118 mF cm^{-1}, respectively. When a well-aligned CNT scaffold is used, MXene-CNT fibers with helical structures could be successfully fabricated [47]. However, this method bears some disadvantages, such as limited fiber length, and the high cost of CNTs. Furthermore, health concerns may be caused regarding to the biosafety of CNTs in wearable textiles.

15.3 2D Macroscopic MXene Films

Compared with other macroscopic assemblies, such as 1D fibers, 3D monoliths, or powders, the majority of free-standing 2D films can be directly used in various applications (e.g. energy conversion and storage, EMI shielding, and sensing) without further processing [84, 85]. Nevertheless, it is still challenging to fabricate

high-performance MXene films for application in different fields. For instance, the common flake-restacking issue severely limits ion transport, and lowers the rate capabilities displayed by 2D MXene film electrodes, when used for supercapacitors. Recent studies have shown that this issue is expected to be solved by introducing interlayer spacers or crosslinkers [25]. Therefore, it is of great significance to develop novel assembly strategies for fabricating multi-functional MXene-based 2D films with microscopic interlayers and structures.

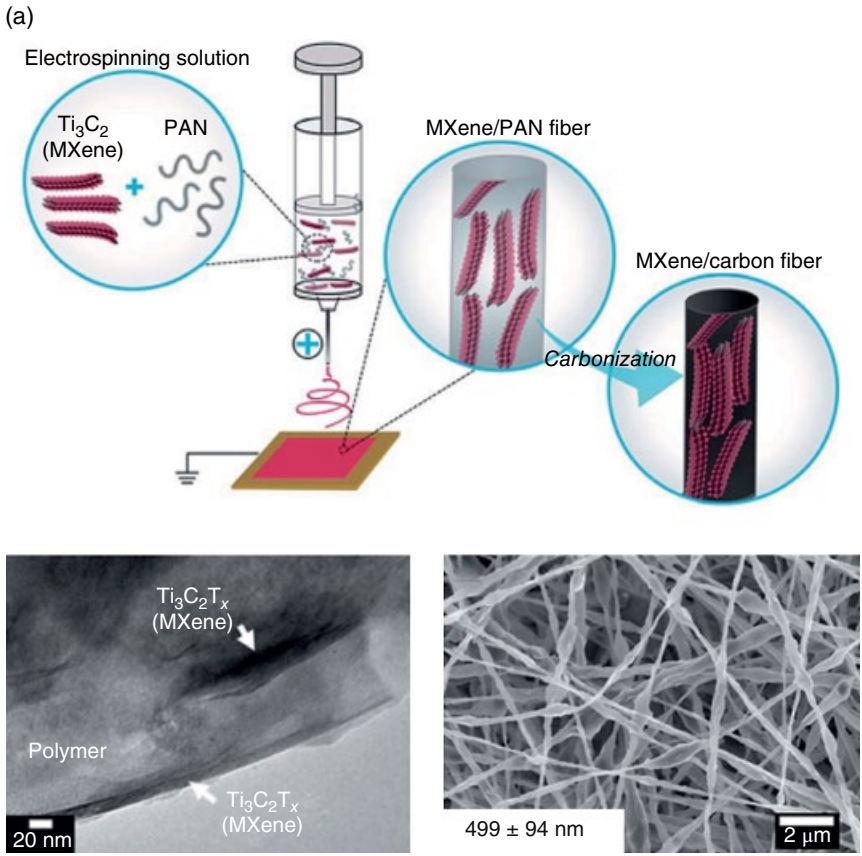


Figure 15.3 Spun MXene composite fibers and Biscrolled MXene composite fibers. (a) Schematic of the production of PAN-$Ti_3C_2T_x$ nanofibers via electrospinning; the inset SEM and TEM images show the structure and morphology of electrospun PAN-$Ti_3C_2T_x$ nanofibers. *Source:* Reproduced with permission [45] © 2019, Royal Society of Chemistry. (b) Biscrolling method: Schematic of the fabrication for MXene-CNT yarns via the biscrolling method; the inset SEM images show the cross-section morphology of the composite yarn. *Source:* Reproduced with permission Wang et al. [46] © 2018, John Wiley & Sons.

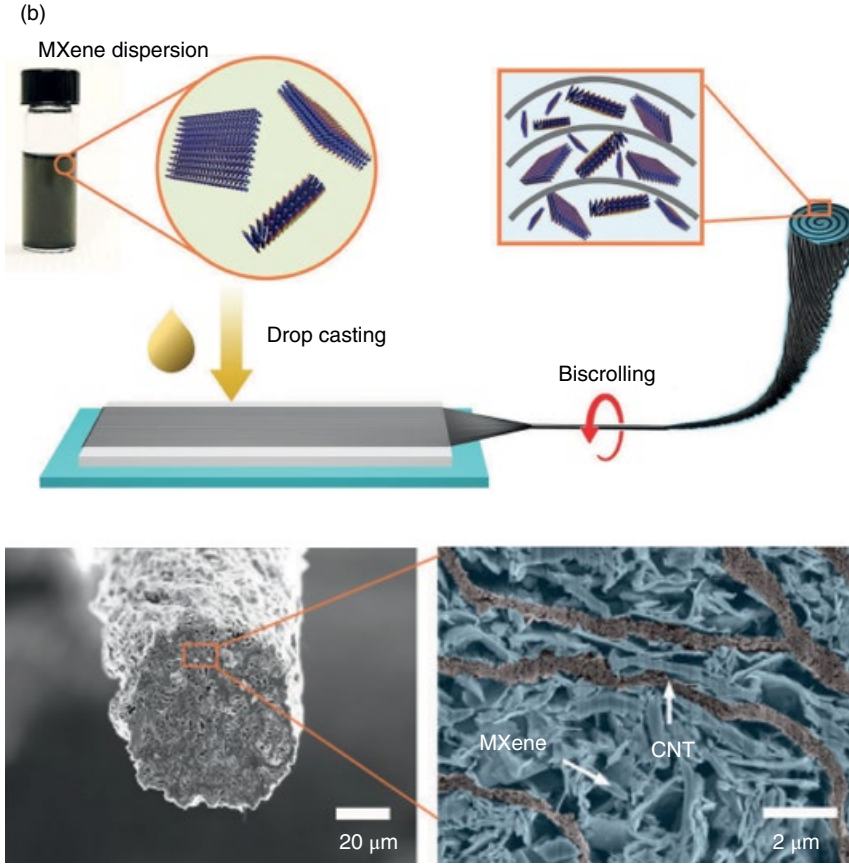


Figure 15.3 (Continued)

In this section, we simply classify the 2D MXene films into neat MXene films and composite films, and then elaborate them detailly according to the subdivision of structural characteristics and compositions. The relationships between the performance and structure will also be discussed to deepen the understanding of the design principles of 2D MXene assemblies.

15.3.1 Neat MXene Films

MXene nanosheets exhibit outstanding electrical conductivity and high mechanical strength. The development of neat MXene films theoretically allows these outstanding properties to be inherited by their corresponding macroscopic assemblies. However, challenges still exist to take full advantage of the property

(or performance) benefits in real applications. One the one hand, these properties are difficult to be preserved during the solution processing for film assembly. For instance, an individual $Ti_3C_2T_x$ nanosheet has a superior Young's modulus (~330 GPa) and a high tensile strength (~17.3 GPa) [86], while the directly filtrated MXene film only exhibits a tensile strength of 20 MPa [19]. In this regard, novel assembly techniques are needed to enhance the inter-flake interactions, and narrow the property gap between MXenes and the fabricated films, which will be discussed in Section 3.1.1 in detail. One the other hand, the flake-restacking issue, as mentioned earlier, still exists, affecting the utilization efficiency of MXenes. In this regard, some in-plane nanochannels, or microscopic pores, are needed to be fast ion-diffusion pathways, as discussed in the following Sections 3.1.2 and 3.1.3.

15.3.1.1 Lamellar Structure

It has been found that the size, orientation, and packing density of MXene flakes during solution processing have great effects on the inter-flake interactions, thus the electrical conductivity and mechanical strength of the fabricated MXene films. Zhang et al. prepared a free-standing neat MXene film, with both high tensile strength and exceptional electrical conductivity by blade-coating large-size $Ti_3C_2T_x$ flakes [19]. As discussed in Section 2.1, a high aspect ratio of flakes favors MXene dispersions (concentration of ~30 mg mL^{-1}) to form LC, where the MXene flakes self-assemble into oriented domains. Meanwhile, the LC formation will enhance the rheological properties, and the applicability of the dispersion for blade-coating, which is advantageous in producing large-scale films with tunable thickness. As shown in Figure 15.4a, b, LC domains of ordered large MXene flakes could be highly aligned under sheer force of blade-coating. Moreover, with blade-coating, a 1 m long film was impressively produced (Figure 15.4c), and its density reached a high value of 4.3 g cm^{-3}, when the thickness was increased to 940 nm. The tensile strength was up to 568 ± 24 MPa, which was approximately 15 times higher than that of vacuum-filtrated films, and a high electrical conductivity of ~15 100 S cm^{-1} was realized, after annealing treatment (Figure 15.4d). These were originated from the highly aligned flakes that reduced the voids among the flakes and induced strong inter-flake interactions. As expected, this blade-coated film exhibited a high EMI shielding effectiveness of 53.5 dB at 8.2 GHz, which was far superior to other similar materials.

The excluding of intercalants between the MXene flakes can also lead to enhanced inter-flake interactions, thus improving the film performance. Chen et al. proposed a proton-acid colloidal processing strategy to remove the extrinsic intercalants of $Ti_3C_2T_x$ films, which were introduced during the selective etching of MAX phases (Figure 15.4e) [87]. By introducing 0.1 M HCl into the dispersion, the adsorbed (or intercalated) Li^+ was stripped via ion-exchange, and then MXene

flakes were stacked into films by vacuum filtration. Additionally, water molecules were destabilized in the absence of Li^+, and thus could be fully removed by vacuum drying. Compared with original $Ti_3C_2T_x$ films, the films after the removal of intercalants not only showed higher packing density, but also exhibited improved mechanical strength and electrical conductivity.

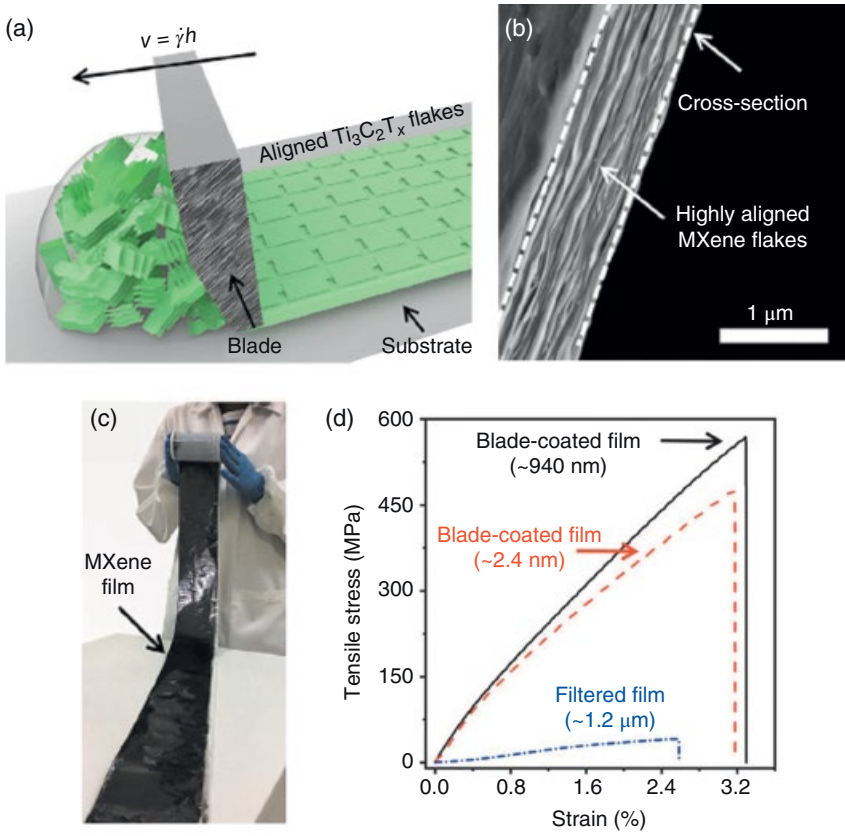


Figure 15.4 Neat MXene films with lamellar structures. (a) Schematic for the fabrication of strong and highly conducting pure MXene films by blade coating; (b) cross-sectional SEM image of a blade-coated film containing highly aligned large MXene flakes; (c) digital photograph of a 1 m long and 10 cm wide film produced from large MXene flakes, which were blade-coated onto a Celgard membrane (thickness of the $Ti_3C_2T_x$ film is 940 nm); (d) typical stress–strain curves of blade-coated and vacuum-filtered films prepared from large MXene flakes. *Source:* Reproduced with permission Zhang et al. [19] © 2020, John Wiley & Sons. (e) Fabrication and structural characteristics of pristine $Ti_3C_2T_x$ films and the comparison with original films, wherein H_2O molecules are not presented; (f, g) digital photos and cross-sectional SEM images of original and 0.1 M H^+ induced $Ti_3C_2T_x$ films. *Source:* Reproduced with permission Chen et al. [87] © 2019/John Wiley & Sons.

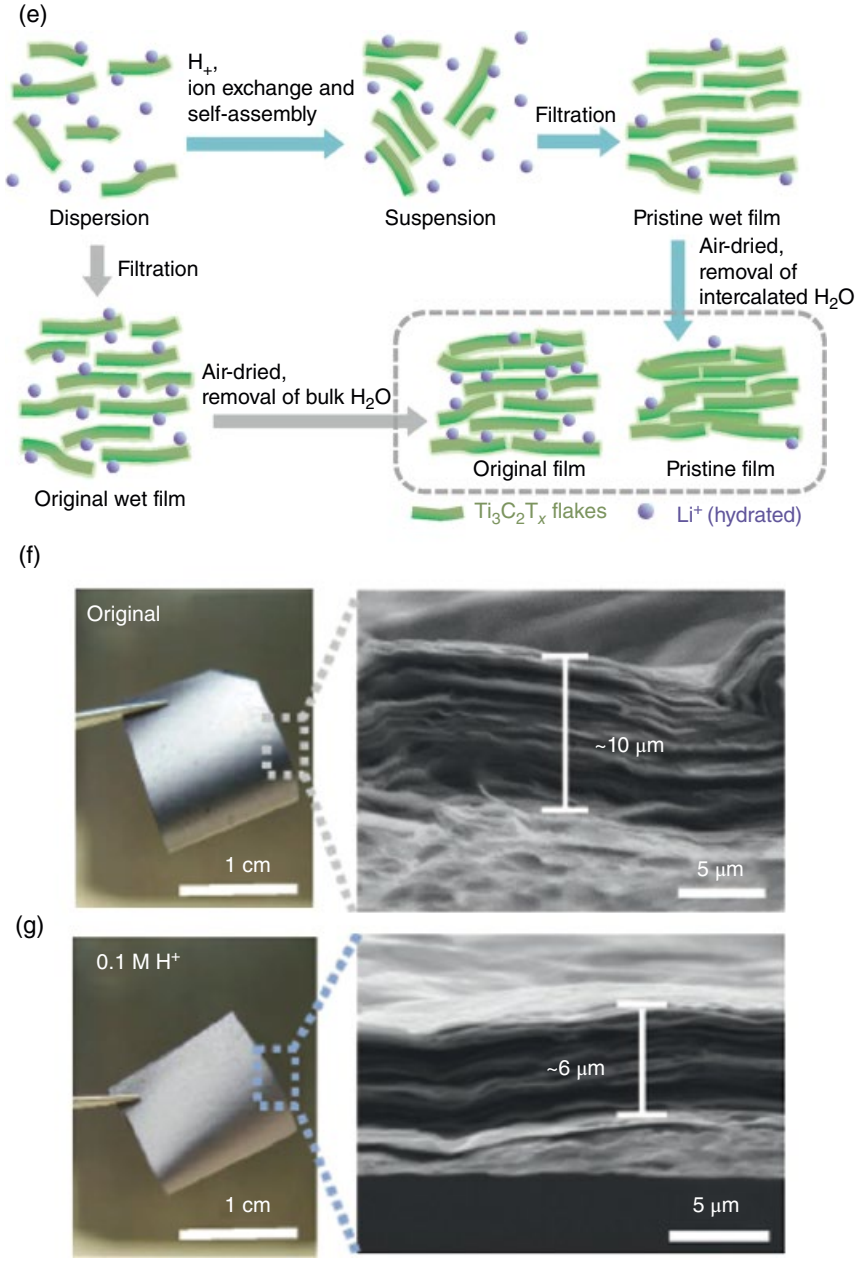


Figure 15.4 (Continued)

15.3.1.2 In-Plane Nanochannel Structure

High electrical conductivity, packing density, and pseudo-capacitance qualify 2D MXene films for high-energy-density supercapacitors. Nevertheless, these highly packed MXene films severely suffer from sluggish ion transport, resulting in poor rate capability. Although there have been some achievements in improving the rate capability of MXene films [88, 89], their volumetric performance will be largely sacrificed accordingly because of the introduction of intercalants and excess space. To simultaneously achieve high volumetric capacitance and excellent rate capability of MXene electrodes, it is necessary to engineer ion-transport channels and improve the space utilization. The in-plane nanochannel structure can shorten the ion-transport paths through the electrodes without changing the stacking structure of 2D nanosheets. Tang et al. proposed a controlled H_2SO_4 oxidation method to construct ion transport highways by introducing relative amounts of holes on MXene nanosheets (Figure 15.5a, b) [90]. In this case, the interlayer spacing was simply increased by an atomic level, thus a high packing-density of the as-fabricated electrodes was maintained. Consequently, a superior rate capability was obtained with high volumetric performance, as a 1.1-μm-thick $Ti_3C_2T_x$ film exhibited a high capacitance retention of 64% ($208\,F\,g^{-1}/756\,F\,cm^{-3}$) at a scan rate of $10\,000\,mV\,s^{-1}$, compared with that at $5\,mV\,s^{-1}$. Moreover, the thick electrodes ($12\,mg\,cm^{-2}$, 48 μm thickness) still outperformed the unmodified $Ti_3C_2T_x$ films (with a low mass loading of $1\,mg\,cm^{-2}$) in terms of rate capability, and thus a high areal capacitance ($3.2\,F\,cm^{-2}$) was also achieved.

In addition to supercapacitors, MXenes are also widely used in rechargeable batteries as conductive additives or electrochemical active materials. Similarly, the film electrodes also face the problems of sluggish ion transport, and low utilization of active sites. To excavate the energy storage capability of MXene electrodes, Cui et al. proposed a cold pressing method to assist the formation of the planar macropores and in-plane holes of $Ti_3C_2T_x$ nanosheets, which was followed by annealing process to regulate the functional groups of $Ti_3C_2T_x$ nanosheets, significantly enhancing their interlayer spacing (Figure 15.5c) [91]. As shown in Figure 15.5d, the basal plane of $Ti_3C_2T_x$ nanosheets could be well-maintained after thermal annealing, and the interlayer spacing was around 1.25 nm. Moreover, as shown in the high-resolution TEM, the (101) plane had some discontinuous fringe lattices, and some in-plane defects (diameter: 2 ~ 4 nm) formed (Figure 15.5e**)**. These in-plane defects could provide fast ion transport channels and expose more active sites to store energy.

15.3.1.3 Porous Structure

Compared with in-plane nanochannel engineering, fabricating the porous structure is the most commonly-used method to mitigate the ion-diffusion issues caused by nanosheet stacking. The introduction of pores or voids in MXene films

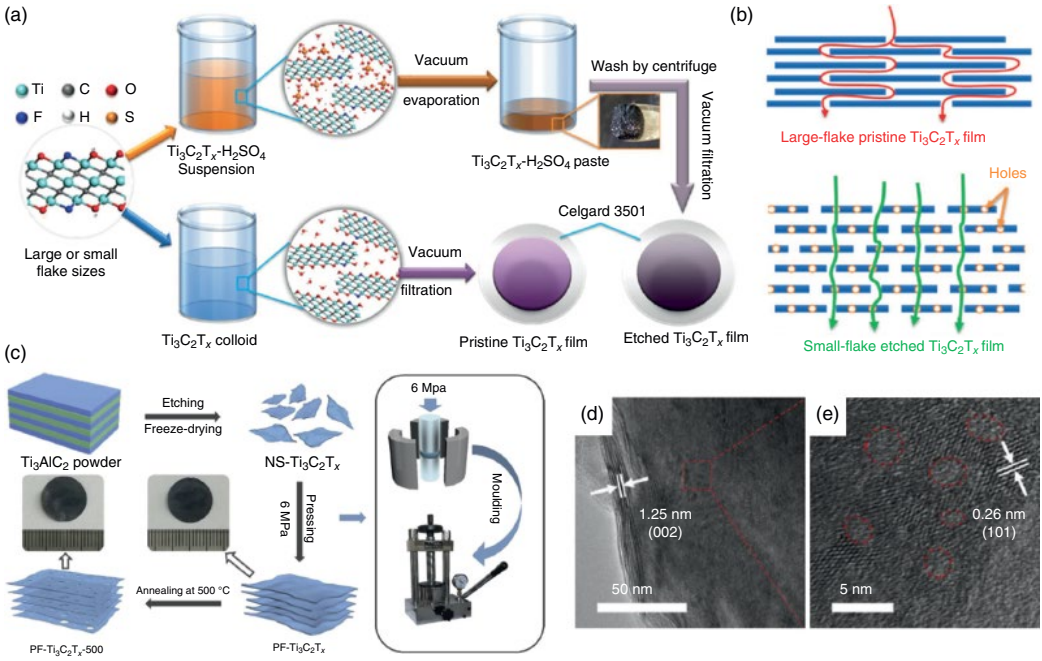


Figure 15.5 Neat MXene films with in-plane nanochannel structures. (a) Schematic illustrations of the etching process of $Ti_3C_2T_x$ nanosheets and the obtained hierarchical nano-porous structure; (b) a schematic illustration of the ion pathway optimization in small-flake etched $Ti_3C_2T_x$ film compared with the large-flake pristine $Ti_3C_2T_x$ film. *Source:* Tang et al. [90]/John Wiley & Sons. (c) A schematic diagram of the procedure to fabricate the free-standing PF-$Ti_3C_2T_x$-500 (inset: the photographs of PF-$Ti_3C_2T_x$ and PF-$Ti_3C_2T_x$-500); TEM (d) and HRTEM (e) images of the PF-$Ti_3C_2T_x$-500 film. *Source:* Reproduced with permission Cui et al. [91] © 2019/Elsevier.

can be effectively achieved by the assistance of 3D templates, and filtration [89, 92–95]. For example, Lukatskaya et al. mixed poly(methyl methacrylate) (PMMA) spheres with the $Ti_3C_2T_x$ dispersion, and filtered the mixture to yield a composite film [89]. Then, this composite film was annealed to remove PMMA spheres, leaving a microporous $Ti_3C_2T_x$ film. As a supercapacitor electrode, it enabled outstanding capacitance retention ($210\,F\,g^{-1}$ at $10\,V\,s^{-1}$; $100\,F\,g^{-1}$ at $40\,V\,s^{-1}$), surpassing the best carbon materials. Freeze-casting is an assembly technique with ice crystals as templates to construction of fast ion-transport channels in the as-fabricated assemblies, which will be detailed discussed in Section 4.2. Based on the conventional freeze-casting, Kong et al. proposed a reduced-repulsion assembly strategy to produce macroscopic 2D MXene films with ordered 3D porous structures [96]. During this process, the –F groups with high electronegativity are substituted by less electronegative –OH groups with the assistance of KOH, thus decreasing electrostatic repulsion between MXene flakes (Figure 15.6a). Moreover, the addition of potassium ions will lead to the formation of electric double layers on the surface of $Ti_3C_2T_x$ nanosheets, thus screening the surface charges and further reducing the interactions between flakes. The decreased electrostatic repulsion makes flake be packed orderly during the freeze-casting process. As shown in Figure 15.6b, c, the KOH-treated $Ti_3C_2T_x$ film shows ordered 3D porous structures after freeze-drying, while the $Ti_3C_2T_x$ nanosheets are randomly aligned and loosely connected without the treatment of KOH. As a result, the assembled films exhibit excellent rate capability (a high capacitance retention of 58.6% from 10 to $10\,000\,mV\,s^{-1}$), which can be well maintained even at a high mass loading of up to $16.18\,mg\,cm^{-2}$.

The strategy of interfacial self-assembly also realizes the fabrication of MXene films, which have both excellent mechanical properties and satisfactory porous structure [98]. It is found that the MXene sheets can be reduced by Zn foil to produce Zn^{2+} ions, and simultaneously some negatively charged functional groups are removed. Under the weakened electrostatic repulsion interaction between MXene sheets, and the crosslinking effects of Zn^{2+} ions, MXene sheets will self-assemble onto the Zn substrate, with some porous structure formed. Based on this mechanism, Zhao et al. have prepared large-area MXene films by controlling the area of Zn substrates [99]. Owing to their high electrical conductivity and excellent porous structures, the flexible MXene films were directly employed as the electrodes of flexible sandwich and micro-sized supercapacitors.

It is also demonstrated that a porous structure conduces EMI performance, besides electrochemical energy storage capacity. Liu et al. used hydrazine as a foaming agent to react with the terminal groups on the $Ti_3C_2T_x$ surface, generating large amounts of gaseous species (Figure 15.6d). The induced high pressure between MXene nanosheets successfully overcome the van der Waals forces. Subsequently, numerous pores were formed in the $Ti_3C_2T_x$ films that significantly

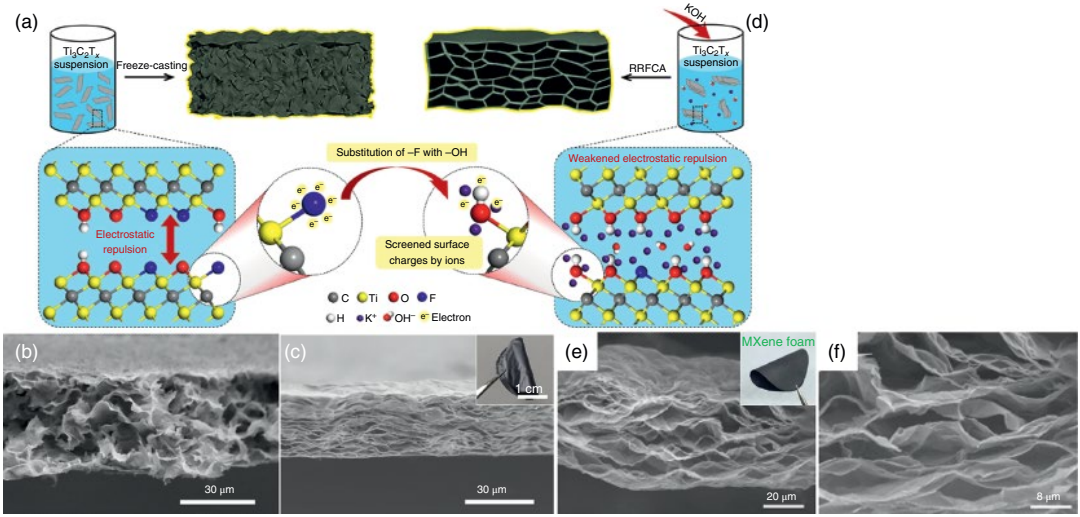


Figure 15.6 Neat MXene films with porous structures. (a) Comparison between conventional freeze-casting and reduced-repulsion freeze-casting assembly (RRFCA) processes; cross-sectional SEM images of randomly aligned $Ti_3C_2T_x$ film (b) and ordered porous $Ti_3C_2T_x$ film (c) with a mass loading of 1.03 mg cm^{-2}. *Source:* Kong et al. [96]/American Chemical Society. (d) A schematic illustration of the fabrication of a hydrophobic and flexible MXene foam; (e, f) cross-sectional SEM images of the MXene foam. *Source:* Reproduced with permission Liu et al. [97] © 2020, John Wiley & Sons.

decreased their density, and enhanced wave attenuation (Figure 15.6e, f). As a result, the as-fabricated MXene foam films showed a highly enhanced EMI shielding effectiveness of ~70 dB compared to that of untreated films (53 dB). Moreover, this reaction led to the variation in the surface chemistry of MXene films, where the wetting behavior was changed from hydrophobic to hydrophilic. The excellent water resistance broadened the practical scenarios of the electronic devices.

15.3.2 MXene-based Composite Films

Due to their layered structure and abundant functional groups, MXenes are promising to be composed with other nanomaterials. On the one hand, these nanomaterials can be spacers to significantly mitigate the sheet-stacking issues, or be additional active sites to enhance electrochemical performance, or be bridges to improve the mechanical properties and flexibility. On the other hand, the MXenes can be the conductive framework for the materials (e.g. oxides and sulfides) with poor conductivities. Compared with neat MXene films, MXene-based composite films are expected to be applied in a broader scope. Here, we have divided the MXene-based composite films into two categories, MXene-inorganics, and MXene-organics composite films.

15.3.2.1 MXene-Inorganics Composite Films

In MXene-inorganics composite films, MXene provides conductive networks, while the inorganic molecules can be intercalated into MXene layers as spacers to increase the interlayer spacing, preventing MXene nanosheets from restacking that causes the reduction of accessible surface area and ion transport efficiency. Graphene, a typical 2D material, is widely used to fabricate 2D/2D composite films with MXenes. For example, Yan et al. first proposed a premodification strategy to prepare flexible and conductive MXene/rGO electrodes [100]. The $Ti_3C_2T_x$ MXene nanosheets are negatively charged and self-assembled with PDDA-modified reduced graphene oxide (rGO) by electrostatic interactions (Figure 15.7a). As shown in Figure 15.7b, the interlayer spacing of MXene nanosheets was enlarged to 1.67 nm as the content of rGO was increased to 10 wt%. As indicated from SEM and TEM images (Figure 15.7c, d), MXene/rGO composite films featured layered structures like the pure MXene films. The MXene and rGO nanosheets were stacked alternately, which effectively prevented the stacking of MXene nanosheets and facilitated the ion transport of as-fabricated films. Fan et al. proposed a method for preparing MXene/holey graphene films, where the holes can function as in-plane nanochannels for ion diffusion [101]. Moreover, with the assistance of NaOH, the electrostatic balance of the MXene and holey graphene dispersion was destroyed by NaOH, leading to the formation of flocculation in a short time. Meanwhile, the –F groups were replaced by OH^- on the MXene surface because

the Ti–O bonds were more stable than Ti–F bonds. The following annealing treatment helped to remove –OH groups, and allowed more Ti atoms to be exposed for improved pseudo-capacitance. The as-fabricated MXene/holey rGO films delivered an ultrahigh volumetric capacitance (1445 F cm^{-3} at 2 mV s^{-1}) and the

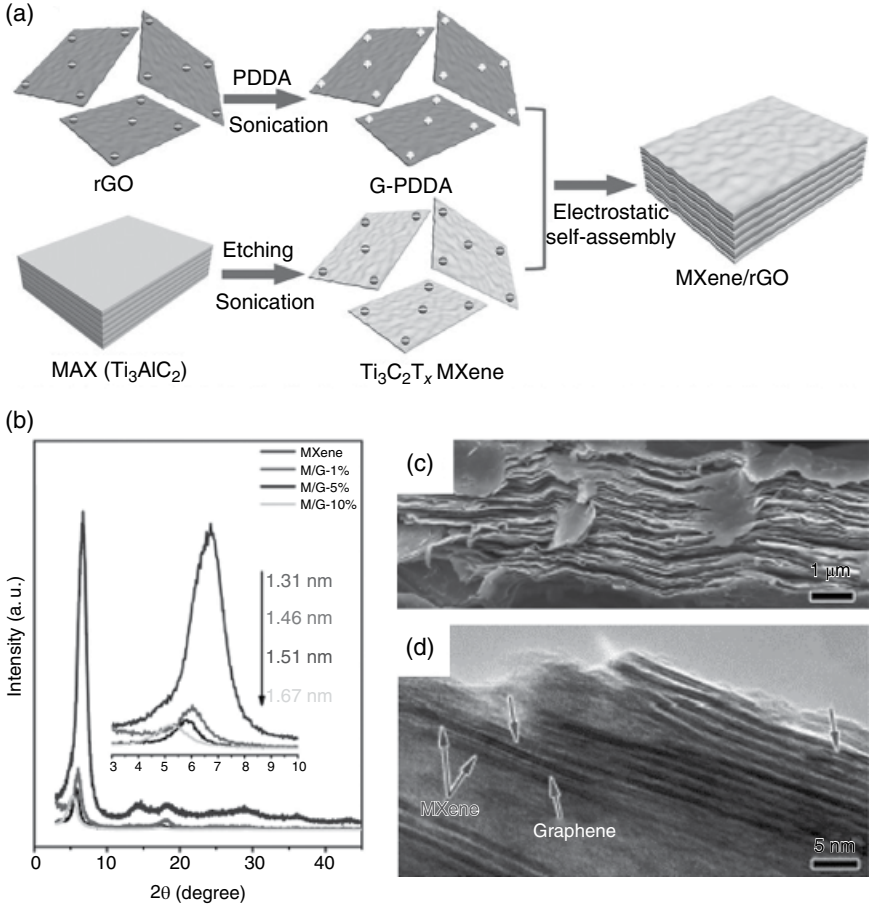


Figure 15.7 MXene-inorganics composite films with 2D nanomaterials. (a) A schematic illustration of the synthesis of the MXene/rGO hybrids; (b) XRD patterns of the MXene and MXene/rGO hybrids; Cross-sectional SEM image. (c) and TEM image (d) of the M/G-5% hybrid. *Source:* Reproduced with permission Yan et al. [100] © 2017, John Wiley & Sons, Inc. (e) Schematics for preparing $Ti_3C_2T_x$ MXene and NbN nanocrystals, pure MXene film and $Ti_3C_2T_x$-NbN hybrid film, and illustration of ion transport. (f) Cross-sectional SEM image of $Ti_3C_2T_x$-NbN hybrid film with 50 wt% $Ti_3C_2T_x$ in the film; (g) top-view SEM image along with elemental maps (Ti and Nb) of a $Ti_3C_2T_x$-NbN hybrid film showing a uniform distribution of the elements. *Source:* Reproduced with permission Wang et al. [102] © 2020, John Wiley & Sons, Inc.

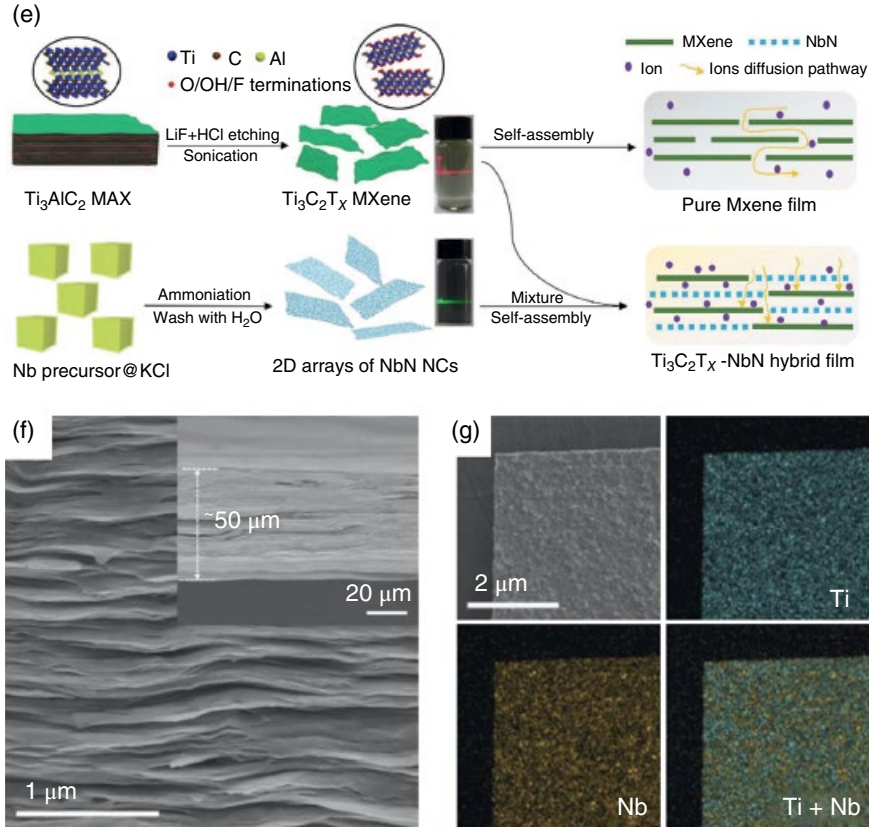


Figure 15.7 (Continued)

corresponding symmetric supercapacitor exhibited an impressive energy density ($38.6\,Wh\,L^{-1}$).

Similarly, other highly conductive 2D nanomaterials have also been cooperated with MXenes to fabricating high-performance composite films. Tang et al. proposed a $Ti_3C_2T_x$-NbN hybrid electrode, where porous NbN arrays with high conductivity served as spacers to prevent $Ti_3C_2T_x$ nanosheets from restacking and bridging adjacent nanosheets [102]. Meanwhile, NbN arrays also participated in redox reactions as active material and provided pseudo-capacitance in acidic electrolytes. As shown in Figure 15.7f, the thick $Ti_3C_2T_x$-NbN hybrid film showed a well-aligned layered structure, and the energy dispersive X-ray spectrum indicated that the $Ti_3C_2T_x$ flakes and NbN nanocrystals were homogeneously distributed (Figure 15.7g). The 2D arrays of NbN nanocrystals between $Ti_3C_2T_x$ nanosheets

accounted for the improved ionic accessibility and ion-transport efficiency in thick and high mass loading electrodes, as illustrated in Figure 15.7e.

Furthermore, MXene can be composed with poorly conductive materials by forming electrostatic interactions or covalent bonding [103–106], where MXenes serve as a highly conductive support or binder. For example, MXene/Fe_3O_4 composite films can be fabricated by electrostatic interactions between PEI-modified Fe_3O_4 nanocrystals with positive charges and negatively charged MXene nanosheets [103]. The Fe_3O_4 particles are anchored between the MXene layers resulting from the physical confinement and the formation of Ti-O-Fe covalent boding, which facilitates the charge polarization and accelerates the lithium-ion transport. Similarly, the free-standing MXene/Si composite films have been obtained by anchoring Si nanospheres on $Ti_3C_2T_x$ nanosheets with covalent bonds [104]. In the as-fabricated films, the aggregation of Si nanospheres and the restacking of MXene nanosheets are both effectively mitigated, attributing to the Si as spacers and MXene nanosheets as 2D walls, which separate Si nanospheres and accommodate volume expansion during the charge/discharge process. Impressively, activated carbon [105] and hard carbon [106] can also be encapsulated between the MXene layers, acting as binder, flexible backbone, and conductive active material to produce flexible composite films. Compared with traditional insulative polymer binders, MXene features high electrical conductivity and a special 2D structure, which is beneficial for constructing 3D networks. Due to the synergistic effect between activated carbon or hard carbon and MXene, the composite films can exhibit excellent electrochemical performance in supercapacitors and Na/K-ion batteries [105, 106]. Additionally, a robust $Ti_3C_2T_x$/S paper has been prepared through sequential filtration and evaporation, which is assembled into Li–S batteries as cathodes [107]. The sulfur particles are deposited on the surface of $Ti_3C_2T_x$ nanosheets with no chemical bonds formed, and the shuttle effect of LiPSs is significantly suppressed by the chemisorption attributed to the interaction between –OH groups and Li_2S_x. The as-fabricated Li-S batteries exhibit a high capacity, excellent rate capability (1383 mAh g^{-1} at 0.1 C and 1075 mAh g^{-1} at 2 C), and outstanding cycling stability (capacity decayed 0.014% after 1500 cycles).

To maximize the ion accessibility and superior rate capability for film electrodes, MXene composites with 3D porous structures have been designed with nanomaterials (e.g. 1D CNTs and 3D assemblies), or crosslinking agents. As shown in Figure 15.8a, an MXene-knitted CNT composite film was fabricated, maximizing the ion accessibility toward superior rate capability in organic electrolytes [108]. As shown in Figure 15.8b–e, some $Ti_3C_2T_x$ flakes were oriented vertically in the porous structures, providing open space, and serving as strong supports for other MXene nanosheets. The corresponding electrodes achieved a high capacitance (276 F cm^{-3}) and excellent rate capability (capacitance retention of ~56% from 10 mV s^{-1} to 10 V s^{-1}) when working in organic electrolytes. Wu et al. fabricated a

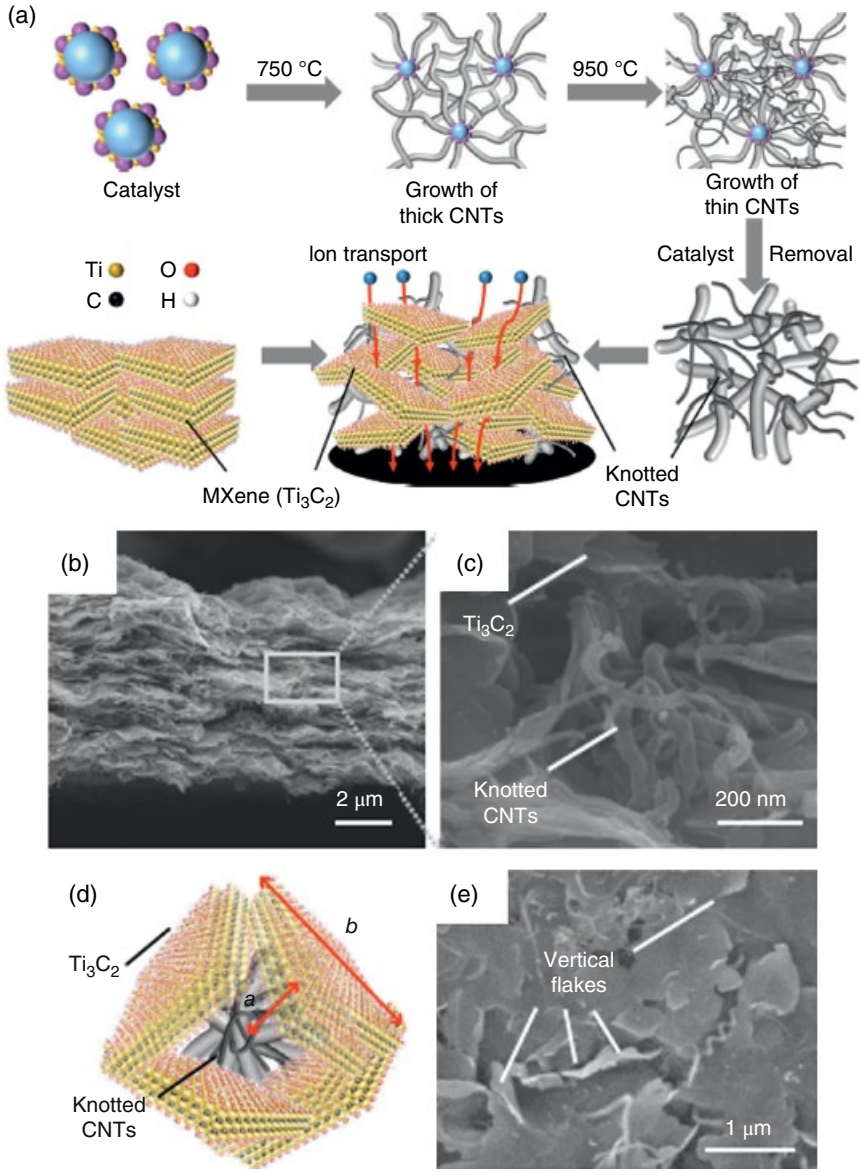


Figure 15.8 MXene-inorganics composite films with 3D porous structures. (a) Schematic of the synthesis of the MXene-knotted CNTs composite electrode with reduced horizontal orientation and lower ion transport tortuosity through the bulk of the electrode; (b) cross-sectional SEM image of an MXene-knotted CNTs composite electrode with 17% CNTs; (c) SEM image and (d) corresponding schematic of how the alignment of the $Ti_3C_2T_x$ flakes was broken by the knotted CNTs to form 3D networked structure; (e) top-view SEM image of an MXene-knotted CNT composite electrode. *Source:* Reproduced with permission Gao et al. [108] © 2020, Springer Nature/CC BY 4.0. (f) Schematic of the preparation of the $Ti_3C_2T_x$ film, RAMX film, and Microgel film; (g) the bulk densities and SSA of the films vs. $Ti_3C_2T_x$ microgel content. *Source:* Reproduced with permission Wu et al. [109]. Copyright 2021, Wiley-VCH.

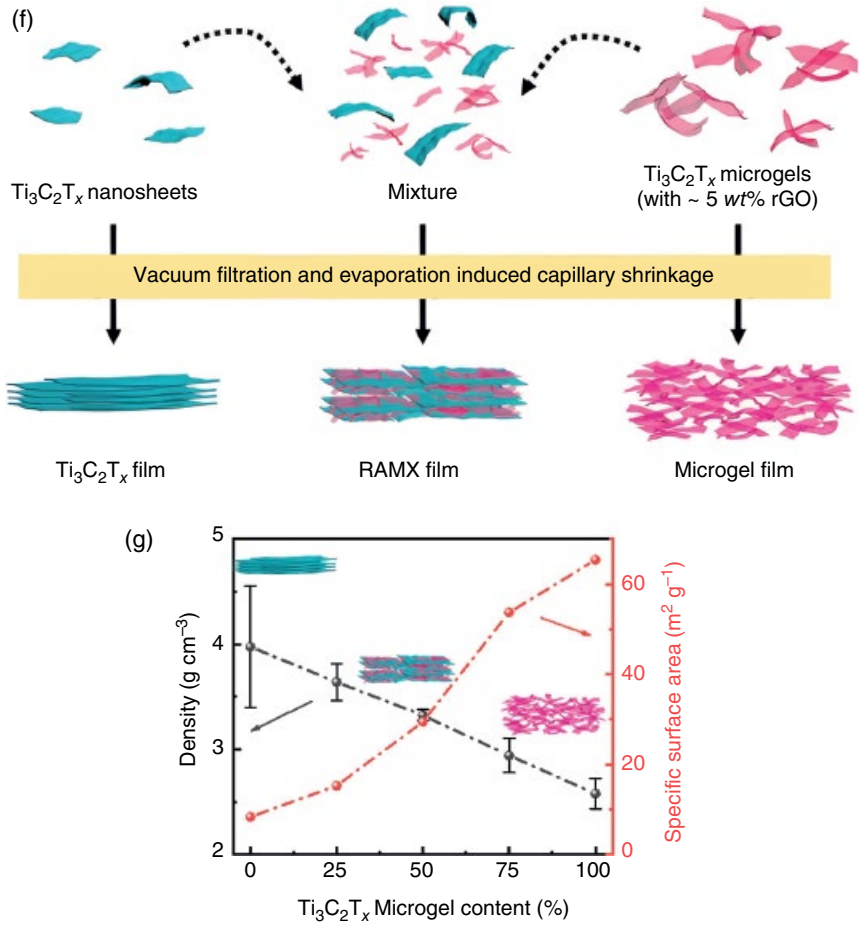


Figure 15.8 (Continued)

flexible and dense composite film (named RAMX film), by vacuum-assisted filtrating the dispersion of $Ti_3C_2T_x$ and $Ti_3C_2T_x$ microgels followed by evaporation-induced capillary shrinkage (Figure 15.8f). The $Ti_3C_2T_x$ microgels with 3D structures were prepared by disassembling $Ti_3C_2T_x$ hydrogels, which were fabricated with the assistance of GO and EDA [33]. Varying the mass ratio of $Ti_3C_2T_x$ nanosheets and microgels, the density and specific surface area of the RAMX film could reach a balance for maximizing the volumetric capacitance ($736\,F\,cm^{-3}$) at an ultrahigh rate of $2000\,mV\,s^{-1}$ (Figure 15.8g). The RAMX electrodes also exhibited superior performance in symmetric configurations, showing great promise in flexible electronics [109]. By electrolyte-induced assembly and vacuum-assisted

filtration, Ma et al. constructed an MXene/rGO film with a 3D porous structure. The electrostatic balance of MXene/GO dispersion was broken by the electrolyte (NH_4HCO_3) and the NH_4^+ linked MXene and GO sheets via hydrogen bonding, resulting in a 3D crosslinked MXene-GO framework. The ultimate hybrid film of MXene/rGO was obtained by vacuum filtration followed by hydrazine vaporing treatment [110].

15.3.2.2 MXene-Organics Composite Films

The abundant surface functional groups of MXene can interact with organics via hydrogen, covalent or ionic bonding, forming organic composite films with outstanding mechanical properties. By introducing CMC and boron to the MXene system, Wan et al. fabricated a highly compact MXene film named SBM film, which exhibited a tensile strength of 583 MPa, a Young's modulus of 27.8 GPa, and a toughness of 15.9 MJ m^{-3}. The CMC formed hydrogen bonding with MXene, and small borate ions covalently crosslinked with the hydroxyl groups on the CMC molecular chains and the surface of MXene platelets. The sequential bridging of hydrogen and covalent bonding effectively removed the voids, as demonstrated in SEM and nano-CT images of cross-sections of SBM film, leading to excellent mechanical properties together with good electrical conductivity and EMI shielding performance [111]. It is confirmed that negatively charged MXene can assemble with positively charged polymer by electrostatic interactions. Hyosung An et al. obtained the conductive and conformal MXene multilayer coatings by the dip or spray coating-assisted methods. MXene sheets and poly(diallyldimethylammonium chloride) (PDAC) were alternately coated onto glass, until the desired number of layers was obtained. Strong electrostatic interactions formed between these two components, giving the PDAC/MXene multilayer strong mechanical integrity. Other organics, such as poly(ethylene terephthalate) (PET) and poly(dimethylsiloxane) (PDMS), were also successfully coated with the MXene. After repeatedly bending or stretching, the MXene-PET or -PDMS multilayer exhibited slightly disrupted in structures. During the process, the cracks and gaps closed and recovered. The conductivity of the composite films maintained as high as 2000 S cm^{-1}, even when they undergone large-scale mechanical deformation [69].

To further broaden the application of MXene-organics composite films, fabricating the freestanding hybrid films of MXene and conductive polymers (e.g. PEDOT:PSS and PANI), is demonstrated as an effective method. VahidMohammadi et al. found that the aniline could be polymerized *in-situ* on the surface of $Ti_3C_2T_x$ MXene sheets to form MXene-PANI composites (Figure 15.9a). By controlling the dispersion concentration during vacuum-assisted filtration, free-standing MXene-PANI composite films of varying thicknesses were obtained. The polymerization mechanism is shown in Figure 15.9b. It is believed that surface functional groups,

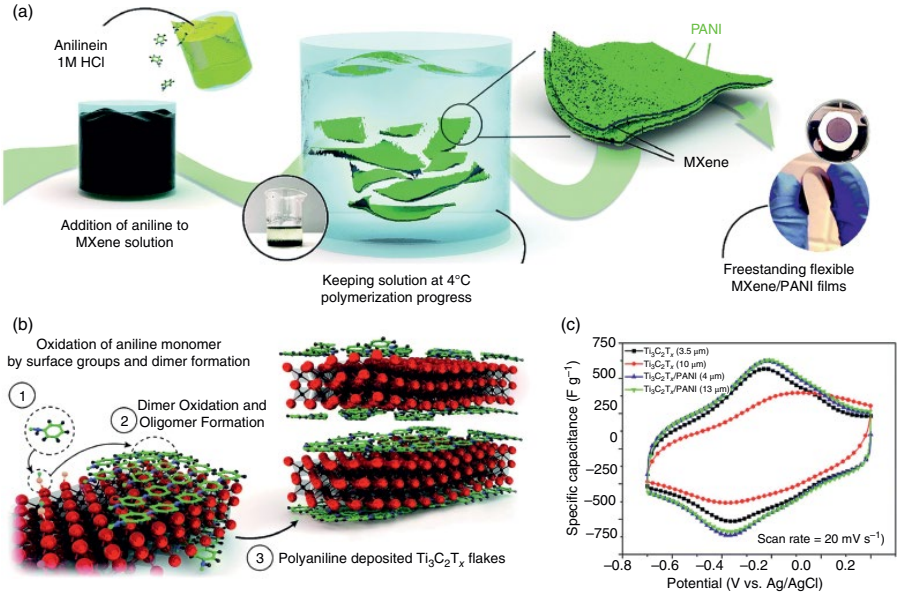


Figure 15.9 MXene-organics composite films with lamellar structures. (a) Schematic of the process used for the synthesis of $Ti_3C_2T_x$/PANI hybrid electrodes; (b) suggested mechanism for the polymerization of aniline on the surface of $Ti_3C_2T_x$ MXene; (c) comparison of the CV profiles of two $Ti_3C_2T_x$/PANI electrodes (4 and 13 μm thicknesses) and two pristine $Ti_3C_2T_x$ electrodes (3.5 and 10 μm thickness). *Source:* Reproduced with permission Vahid Mohammadi et al. [112] © 2018, Royal Society of Chemistry.

specifically —OH and =O, on the MXene, serve as initiation sites for the oxidation of aniline. This oxidation process yields dimers, which can subsequently undergo further oxidation, leading to the formation of oligomers and ultimately resulting in the synthesis of PANI. After PANI deposition, there were notable enhancements in both the ionic and electronic conductivities of the MXene film electrodes. Even with an increase in thickness from 4 to 13 μm, the MXene-PANI electrode maintained a robust pseudocapacitive response (Figure 15.9c), delivering an almost identical gravimetric capacitance of approximately 383 $F g^{-1}$ at a scan rate of 20 $mV s^{-1}$, consistent with the performance of the 4 μm thick electrode (approximately 385 $F g^{-1}$) [112]. Additionally, PANI can be used as an oxidation-resistive layer to prevent MXene from being oxidized [95]. Gund et al. fabricated a porous MXene/conducting polymer hybrid, which was expected to bridge the performance gap between high capacitance and the high-frequency response, ascribing to the synergistic effect of the strong interaction between $Ti_3C_2T_x$ MXene and PEDOT:PSS and the transition of PEDOT:PSS into the more conductive and electrochemically active quinoid phase [113].

Natural biomaterials have attracted much attention ascribing to their abundance, environmental friendliness, and mechanical robustness. Furthermore, they have rich functional groups (e.g. —OH, —COOH, and =O), which are beneficial to form hydrogen bonding with the terminal groups of MXenes. Shahzad et al. intercalated sodium alginate (SA) into MXene layers, which added disorder in stacking and separated MXene flakes. The obtained nacre-like MXene/SA film behaved as a multilevel shield and exhibited good EMI shielding effectiveness. This strategy was universal for other types of MXenes, such as $Mo_2Ti_2C_3T_x$ and $Mo_2TiC_2T_x$ [114].

To solve the sluggish ion transport originating from horizontally stacked nanosheets, porous microstructures are still needed in the design of MXene-organics composite films. Bacterial cellulose (BC), a kind of natural organic material, can help to fabricate fast ion transport channels, owing to its tunable pore structure and hyperfine fiber form [115, 116]. Wang et al. prepared a MXene/BC composite film with a continuous 3D porous framework (Figure 15.10a) with the freeze-casting technique. The composite film had a good mechanical strength of 43.0 MPa, nearly threefold over the pure MXene film. The MXene/BC electrodes exhibited a high gravimetric capacitance of 416 $F g^{-1}$ and a high areal capacitance of 2084 $mF cm^{-2}$ at 3 $mA cm^{-2}$ [117]. By using the property of LC (long-range alignment under machinal shear), Xia et al. constructed an MXene lamellar LC film with vertically aligned pores (Figure 15.10b, c). First, $C_{12}E_{16}$ surfactants were introduced to form hydrogen bonding with —F or —O groups on the surface of the MXene. Subsequently, a uniaxial in-plane mechanical shear force was applied to align the LCs. Compared with the MXene films fabricated by the traditional filtration method, the vertically aligned liquid crystalline MXene

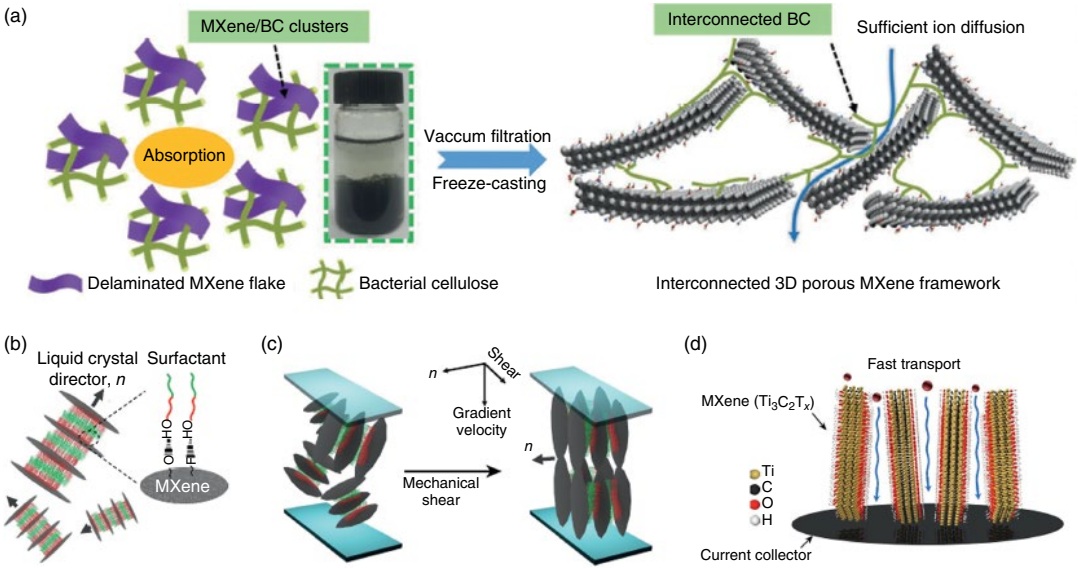


Figure 15.10 MXene-Organics composite films with porous structures. (a) The forming mechanism and photograph of MXene/BC composites with a 3D porous MXene framework. *Source:* Reproduced with permission from Wang et al. [117] © 2019, John Wiley & Sons. (b) Illustration of the surfactant ($C_{12}E_6$)-enhanced lamellar structure of the MXene lamellar LC (MXLLC). The light grey indicates the hydrophilic tail, and the dark black indicates the hydrophobic part of the surfactant; (c) illustration of the alignment process. The plates at the top and bottom represent the shear plates; (d) ion transport pathways in vertically aligned $Ti_3C_2T_x$ MXene films. *Source:* Xia et al. [88]/Springer Nature.

film showed excellent electrochemical performance nearly independent of thickness up to 200 μm, which is attributed to the directional ion transport and high ion-accessible surface area (Figure 15.10d) [88].

15.4 3D MXene Assemblies, Including Hydrogels and Aerogels

Like other 2D materials, MXenes are prone to restacking during processing, due to strong van der Waals attractions and hydrogen bonding between adjacent sheets. Undoubtedly, the inter-sheet restacking blocks the ionic or mass transfer, reduces the accessible surface area of ions, and lowers the efficiency of MXene utilization, resulting in difficulties in fabricating MXene-based functional materials, and limitations in application fields. Conversely, a 3D assembly can well mitigate the above issues. Based on different strategies or methods, MXenes with diverse morphologies, including crumpled, sphere-like, and interconnected structures (i.e. hydrogels and aerogels), as well as with diverse inorganic or organic materials incorporated, have been produced and applied in various fields.

15.4.1 3D MXene Assemblies with Crumpled Structures

Spray drying is a conventional and industrial method to produce dry powders, especially some thermally-sensitive materials (e.g. pharmaceuticals), by aerosolization and drying of colloidal dispersions under a hot gas. Recently, this drying technology has been demonstrated to create scrolled, or crumpled structures for various 2D materials, including graphene, boron nitride, and MXenes [118–120]. As illustrated in Figure 15.11a, after the ultrasonic-assisted aerosolization of MXene colloids, the formed MXene aerosol droplets are heated (e.g. at 600 °C or 220 °C) in the argon gas atmosphere [121]. During the drying process, the trapped solvents in droplets are evaporated rapidly, and the induced capillary force leads to the assembly of MXene nanosheets, and the following crumpling. It has been believed that the crumpling mechanism is heavily influenced by the intrinsic characteristics of MXenes (e.g. high bending stiffness and hydrophilicity), as well as the properties and concentration of MXene colloids [28, 119]. Specifically, evaporation of the solvent from the droplets induces capillary forces onto the nanosheets, which will be further increased by the enhanced wettability, due to the hydrophilic functional groups of MXenes. When the capillary forces are dominant, the nanosheets will overcome electrostatic forces to accumulate and form a continuous shell at the liquid-air interface. Under capillary pressure, the MXene nanosheets of high elastic modulus fold at the edge initially and then bend in the middle. Consequently, numerous wrinkles appear on the surface of dried MXenes shells, as shown in Figure 15.11b, c.

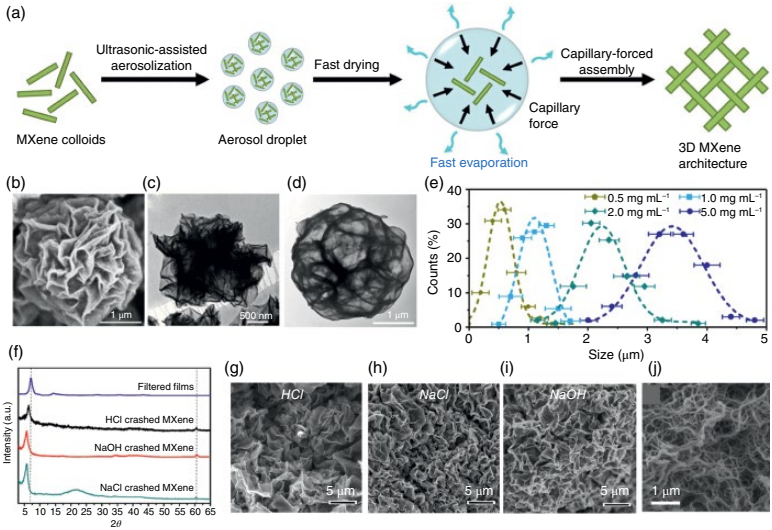


Figure 15.11 3D MXene assemblies with crumpled and open structures. (a) The preparation process of 3D MXene assemblies with the spray drying method; The SEM image (b) and the TEM image (c) of 3D $Ti_3C_2T_x$ MXene with fluffy shape and numerous ridges on the surface; (d) the TEM image of sphere-like 3D MXene assemblies with the utilization of surfactants; (e) size distributions of 3D $Ti_3C_2T_x$ MXene assemblies made by MXene colloids with different concentrations. *Source:* Reproduced with permission Xiu et al. [121] © 2018, American Chemical Society. (f) XRD patterns of 3D crumpled MXene created by the addition of a HCl, or NaCl or NaOH solution; SEM images of 3D crumpled MXene created by HCl (g), NaCl (h), and NaOH (i); scale bar = 5 μm. *Source:* Reproduced with permission Natu et al. [122] © 2018, American Chemical Society. (j) SEM image of MXene nanoribbons prepared by highly concentrated KOH. *Source:* Reproduced with permission Lian et al. [123] © 2017, Elsevier.

The crumpled structure of 3D MXene assemblies could be precisely tailored with formulated MXene colloids. For instance, with the reduced surface tension of precursor colloids by surfactants (e.g. polyvinylpyrrolidone) and capillary forces (Figure 15.11d), sphere-like 3D MXene assemblies with fewer crumples are obtained after droplet evaporation. Moreover, a higher MXene concentration of precursor colloids generally results in a larger size of the as-obtained 3D MXene assembles, with a decreased degree of crumpling. This trend may be ascribed to the thicker nanosheet shells formed during evaporation, and thus a higher effective bending modulus [28]. As shown in Figure 15.11e, the average size of 3D MXene assembles varies from 0.5 to 3.5 μm, with the concentration ranging from 0.5 to 5.0 mg mL^{-1}. Furthermore, the product morphology and structure also are influenced by the processing parameters used, such as inlet temperature and pump speed. Overall, the spray drying technique provides an effective and controllable way to realize MXene 3D assembly, as well as to anchor various functional materials (e.g. Pt clusters, Fe_3O_4, and Si) onto the crumpled MXenes, for enhanced performance in catalysis, and electrochemical energy storage.

The 3D crumpling of MXene flakes can also be created by the addition of an acid, a salt (with high concentrations), or a base to a MXene suspension. Barsoum's group found that the addition of HCl, alkali metal hydroxides (e.g. NaOH and KOH), or NaCl salt could disrupt the stability of $Ti_3C_2T_x$ suspensions, and induce flocculation [122, 124]. Importantly, this flocculation would result in mesoporous crumpled MXene sheets, which could be well maintained after (freeze-) drying. As shown in Figure 15.11f–i, compared to the pristine MXene, the crumpled MXene powders after HCl (or NaCl, or NaOH) have a larger and more disordered interlayer structure. Although the crumpled structures created with HCl, NaOH, and NaCl, share similar morphologies, their crumpling or aggregation mechanisms are found to be distinct [122]. Before further detailed explanations, it is crucial to note that the zeta potential of $Ti_3C_2T_x$ suspension at pH ≈ 7 is −53 mV, contributed by the negatively charged surface groups and the induced electrostatic repulsion between flakes is accounted for the suspension stability. However, the edges of flakes are positively charged and would adsorb anions; thus the external environment of the solution such as the pH value, exerts great effects on the state of MXene suspensions. At low pH, negative charges of faces are weakened by H^+ adsorption, while the edges remain positively charged, as Cl^- ions with larger hydration radii tend not to absorb. In this regard, the electrostatic repulsion decreases, but the interactions between the positively charged edge and negatively charged surface increase, resulting in a final crumpling or aggregation. With the addition of NaCl, the eventual flocculation may be accounted to the decreased Deybe-Huckle length with the increased salt concentration (or ionic strength), which in turn reduces the repulsion between flakes and triggers face-to-face interactions. At high pH, it is thought that the OH– would neutralize the positive edges,

and the Na^+ would adsorb onto negatively charged terminations, resulting in face-to-face interactions.

Surprisingly, some unique 3D MXene structures will be directly generated in specific alkaline environments. For instance, when an ultra-high concentration of the alkali metal hydroxide is used, MXene nanoribbons will be directly induced [125–127]. Typically, $Ti_3C_2T_x$ nanoribbons were prepared by continuous shaking treatment (250 rpm) of pristine MXene in 6 M KOH aqueous solution for 72 hours (Figure 15.11j) [123]. This unique morphology may be explained by the following: all the positive edge sites are passivated by OH^- ions, and the Debye-Huckle lengths at both flake edges and faces are reduced by the high ionic strength of K^+. The induced in-plane edge-face interactions result in a high degree of flake folding and crumping, and the formation of the ribbon-like structure. Another example is that $Ti_3C_2T_x$ hydrogels could be directly obtained after thermal treatments (e.g. at 90 °C for 4 hours) of MXene in ammonia solutions. In this case, a strong reduction agent, thiourea dioxide, is usually introduced to prevent MXene oxidation. During the overall process, the alkali environment and the release of NH_3 gas cause the crumpling of MXene flakes, and the *N*-doping concurrently. The strong chemical bonding between the doped *N* atoms and the terminal O groups of $Ti_3C_2T_x$ flakes facilitates the interconnecting. Eventually, an aerogel can be produced by freeze-drying, which has a large specific surface area of $108\,m^2g^{-1}$ and achieves an improved capacitance of $349\,Fg^{-1}$ in the application of supercapacitors.

15.4.2 Template-assisted 3D MXene Assemblies

Templates have been widely employed to fabricate 3D networks effectively and straightforwardly. They can support the assembly of nanosheets, and promote nanosheet networking, contributing to their porous skeleton, or/and the porous replica structure upon removal. In this regard, the adopted templates for fabricating 3D MXene structures can be briefly divided into four categories: (i) sacrificial templates; (ii) porous templates; (iii) ice templates; (iv) pickering emulsion templates. Precise morphology tailoring, including pore size, pore orientation, as well as uniformity, can be achieved, assisted with the selected types of templates.

The commonly used simple sacrificial templates are PMMA [89, 93, 128], melamine-formaldehyde (MF) [27, 129], and polystyrene (PS) spheres [95, 130]. As introduced in Section 3.1, with vacuum filtration and the following removal of templates, 3D-structured MXene films can be fabricated [89, 128]. For some positively charged templates (e.g. PMMA and MF), they provide strong electrostatic attractions and thus allow the self-assembly of MXene nanosheets to form crumpled structures, without introducing external forces. Here, the MF template is taken as an example to illustrate the typical fabrication process (Figure 15.12a).

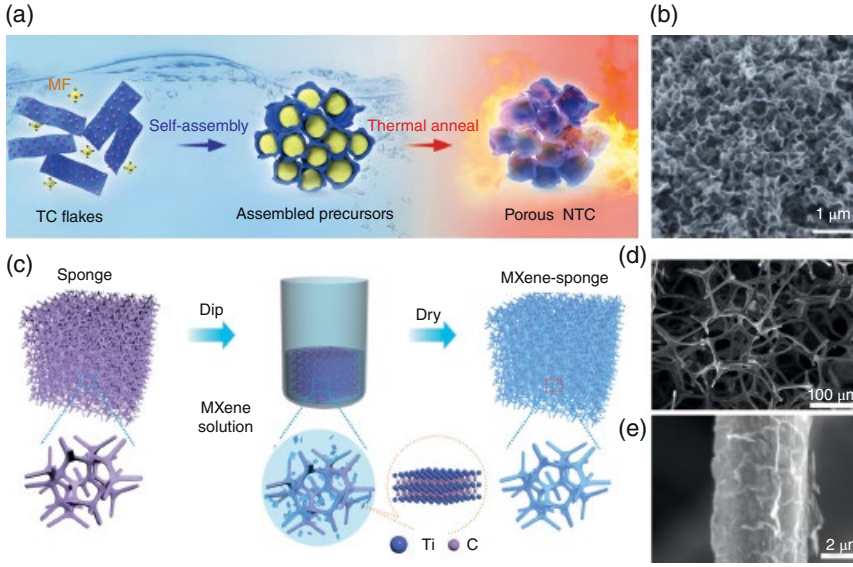


Figure 15.12 3D MXene networks formed with simple sacrificial templates, and porous templates. (a) The illustration of porous N-$Ti_3C_2T_x$ species with MF-templating synthesis; (b) the SEM image of the prepared porous N-$Ti_3C_2T_x$. *Source:* Reproduced with permission Song et al. [27] © 2020, Elsevier. (c) Illustration of fabrication procedure of the MXene-sponge; (d, e) SEM images of the MXene-sponge. *Source:* Reproduced with permission Yue et al. [131] © 2018, Elsevier.

The nitrogen-containing groups (–NH_2, –NH–) of MF spheres interact with the oxygen-containing groups (–O/–OH) of $Ti_3C_2T_x$ flakes, which allows the flakes spontaneously to wrap themselves onto MF spheres [27, 129]. After thermal annealing (e.g. at 500 °C for 2.5 hours), porous N-$Ti_3C_2T_x$ species (P-NTC) are produced (Figure 15.12b). Note that the release of ammonia (NH_3) gas during MF decomposition will facilitate *in-situ N*-doping. With a controlled size of MF spheres and weight ratios (MF:$Ti_3C_2T_x$), the pore structure of the fabricated 3D porous MXene network can be easily tailored. Benefiting from the superb electrical conductivity, large surface area, and strong interactions with lithium polysulfides, P-NTC can facilitate sulfur redox reactions with suppressed shuttling effects. Expectantly, the fabricated S/P-NTC cathode could exhibit excellent cycling stability over 1200 cycles (at 2.0 C). Additionally, sulfur powders [132] and zinc powders [133] can also be used as templates. Yang et al. fabricated a 3D porous MXene/graphene (PMG) structure with the assistance of metallic zinc powders, which acted as *in situ* sacrificial templates and reductants. The *in-situ* released Zn^{2+} ions could induce the self-assembly of the $Ti_3C_2T_x$ MXene and graphene nanosheets and promote 3D networking. The fabricated PMG electrode

showed a specific surface area of $52.5\,m^2\,g^{-1}$ and provided a high-specific capacitance of $393\,F\,g^{-1}$ at $2\,mV\,s^{-1}$. When the PMG was coupled with *N*-doped holey graphene, the assembled asymmetric supercapacitor displayed an ultrahigh energy density of $50.8\,Wh\,kg^{-1}$ with a power density of $215\,W\,kg^{-1}$.

MXenes can also be coated on the skeleton of porous templates to form a 3D network, by simple dip-coating (or impregnation) and drying process. For a typical example, Gao's group chose a melamine sponge as the template, which has a porosity of over 97% with pore sizes ranging from 30 to 130 μm [131]. As illustrated in Figure 15.12c, the sponge was first immersed in the $Ti_3C_2T_x$ MXene dispersion for minutes, and then dried for 24 hours at 80 °C in a vacuum oven. Subsequently, a thin layer of MXene was successfully anchored onto the 3D skeleton, due to the formed hydrogen bonding or electrostatic interactions. As shown in Figure 15.12d, e, the obtained MXene-sponge had a cellular-like network structure, and MXene layers, with a thickness of several hundred nanometers, were attached to the sponge skeleton. When applied for piezoresistive sensors, this MXene-sponge exhibited a low detection limit of 9 Pa, high sensitivity for a broad pressure range, as well as satisfactory durability. The pore structure of obtained MXene sponges is determined by that of the used template. In addition to the melamine sponge, porous carbon skeleton [134, 135], graphene aerogel [136], and PU fiber networks also have been adopted [137]. For instance, Yang et al. prepared a PU mat by electrospinning technique, and MXene sheets penetrated the interlocking network through the fiber intervals when the MXene dispersion was drop-casted on the mat. As a strain sensor, the obtained flexible and stretchable hybrid mat showed excellent performance in detecting physical motion and monitoring physiological signals, which hold great potential in the applications of mechanical dynamic technologies, such as electronic skin and wearable healthcare devices.

Ice templating also called freeze casting, is an inexpensive and environmentally friendly technique to assemble 2D materials into a gel, with a 3D porous structure, including ordered cellular structure, and arrays [92, 138–142]. This approach takes advantage of the "squeezing" effect deriving from the growth of ice crystals. The 2D sheets are squeezed and trapped to the crystal boundaries, which reduce distance and greatly enhance van der Waals forces between adjacent sheets. After the ice gel is directly freeze-dried, aerogel can be yielded, while when the ice gel thaws in an acid (e.g. 5 M HCl), a hydrogel with well-preserved microstructures can be produced instead [143]. As for the latter, if the pre-assembly $Ti_3C_2T_x$ ice gel is thawed by a normal method, it will be redispersed in water with no 3D matrix formed. It can be explained that the ion exchange of as-intercalated Li^+ with water molecules causes interlayer expansion and structure disassembly, which can be prevented by the intercalation of hydrated protons.

The key to obtaining the desired morphology of the final product is the precise control of ice crystals, which is determined by the operational parameters,

including the freezing speed and direction, the temperature gradient, the viscosity of the precursor solution, and even additives [144]. As shown in Figure 15.13, if the $Ti_3C_2T_x$ droplets are dipped into liquid nitrogen, amorphous ice crystals will grow, generating a randomly connected $Ti_3C_2T_x$ matrix (Figure 15.13a_1). If the bulk $Ti_3C_2T_x$ dispersion is frozen, the ice crystal will grow along the direction of the temperature gradient. In this regard, a $Ti_3C_2T_x$ matrix with local or long-range oriented microstructures can be produced upon a multidirectional or uniaxial freezing direction (Figure 15.13b_1, c_1). A honeycomb-like pore structure can be possibly formed under the unidirectional freezing, while isolated solid MXene walls with fewer interconnections are produced under the bidirectional condition [145]. Furthermore, with a controlled freezing speed, the size of the formed ice crystals can also be controlled, and thus the cellular size can be tuned (Figure 15.13c–e). Following the above rules, Yang et al. prepared a $Ti_3C_2T_x$ aerogel of a long-range oriented microstructure with a directional freeze-drying technique and found that the connection, as well as the mechanical strength of the formed network, could be improved by using a high concentration of $Ti_3C_2T_x$ suspensions [146]. This method is also called as freeze-assisted tape casting technique, usually used to fabricate nanosheet arrays [147, 148]. By this, Chen et al. synthesized vertically aligned $Ti_3C_2T_x$ arrays, which could be applied to high-rate

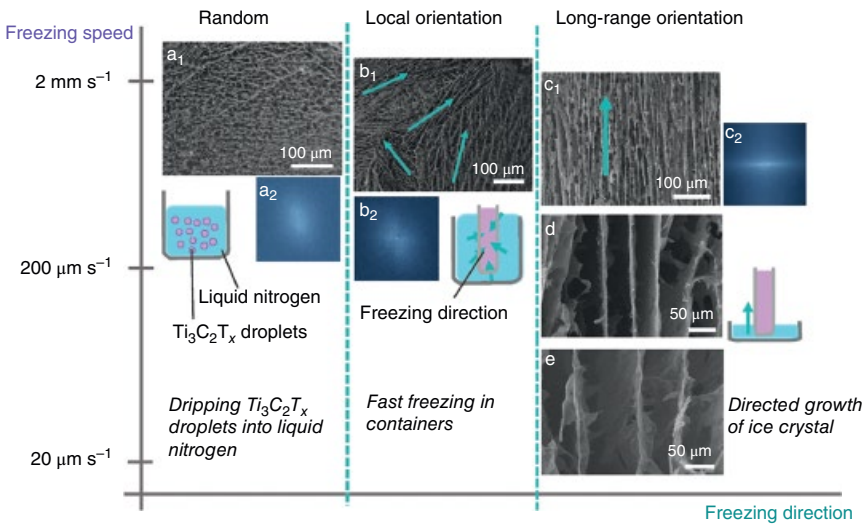


Figure 15.13 Tuning the microstructure of $Ti_3C_2T_x$ matrix with the ice templating method. (a_1, b_1, c_1, d, and e) SEM images of the $Ti_3C_2T_x$ ice gel with random, local oriented, long-range oriented microstructure, respectively; (a_2, b_2, and c_2) Fast Fourier transforms showing the degree of microstructure orientation in (a_1), (b_1), and (c_1), respectively. *Source:* Reproduced with permission Chen et al. [143] © 2020, American Chemical Society.

lithium metal anodes with stable lithium plating/striping behaviors [148]. Overall, ice templating is effective, but there are still some technical hurdles to be addressed before large-scale applications, such as the inhomogeneity of the temperature field, and the volume expansion during freezing [29].

Pickering emulsions, which are emulsions stabilized by solid particles, have been rated as excellent templates for preparing microspheres, and foam materials, because the emulsion droplets will naturally form voids after evaporation or washing [149, 150]. The stabilization of Pickering emulsions is achieved by the self-assembly of these solid particles at the water-oil interface, which is driven by the reduction of interfacial energy. Clays are widely studied stabilizers, after their lipophilicity is enhanced by modification. MXenes, also known as "clay-like materials", possess similar characteristics, particularly hydrophilicity. Moreover, the abundant negatively charged groups of MXenes promote opportunities for surface modifications, and enhance sheet-solvent interactions. In this respect, after being grafted with desired ligands chemically or physically, the MXene flakes will spontaneously migrate to the water-oil interface, and overlap to form layers on the surface of emulsion droplets [11]. An effectively manipulated degree of MXene overlapping will undoubtedly bring a tunability of MXene assemblies, such as in density, or pore wall thickness. When concentrated Pickering emulsions are used, MXene aerogels with excellent mechanical properties can be easily prepared by freeze-drying. For example, Zhao et al. designed Janus MXene nanosheets (JMNs) with amphiphilicity, by selectively grafting PS ligands onto one side of MXene nanosheets [151]. As solid surfactants, these JMNs would aggregate at the water–oil interface, and help form a stable toluene/water emulsion (8 : 1, v/v; 0.1 wt% JMNs), in which these JMNs facilitated the interfacial assembly into microdroplets. Assisted by freeze-drying, a 3D MXene aerogel could be obtained. The well-known surfactant, Cetyl trimethylammonium bromide, can also be used to tune the hydrophilic nature of $Ti_3C_2T_x$ MXene [152]. In a neutral or basic environment, a Pickering emulsion with more than 70 vol% oil droplets could be stabilized, and an MXene foam could be further fabricated.

By using the cooperative assembly of MXene and the oil-soluble amine-functionalized polyhedral oligomeric silsesquioxane (POSS-NH_2) at the oil-water interface, Shi et al. prepared a new type of Janus MXene, termed MXene-surfactants (MXSs) [153]. After freeze-drying, a MXene aerogel with robust and conductive 3D frameworks was fabricated, owing to the dense packing of the MXSs at the interface (Figure 15.14a). Given that the size of emulsion droplets was closely correlated to the MXene concentration used, the pore structure (pore size: c. 60–15 μm) could be effectively tuned. When the MXene concentration was 10 mg ml^{-1}, the obtained aerogel had a pore size of 15 μm, and exhibited excellent mechanical strength, which could support a 20 g weight, as shown in Figure 15.14b. As illustrated in Figure 15.14c, the interfacial assembling mechanism could be

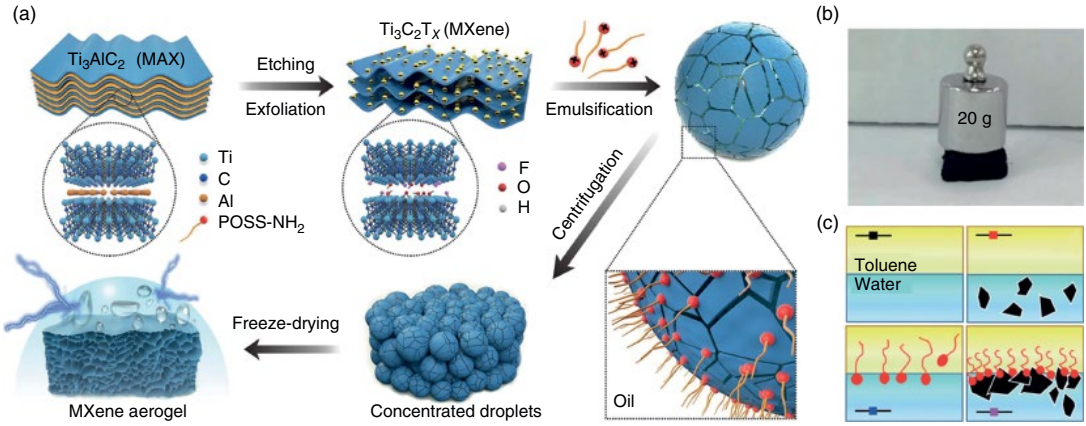


Figure 15.14 3D MXene networks formed with emulsion droplets as templates. (a) The construction process of Pickering emulsions and MXene aerogels; (b) the digital image of a lightweight aerogel (c. 6.4 mg) supporting a 20 g weight; (c) schematics of different oil–water systems: water/toluene, MXene@water/toluene, water/POSS-NH_2@toluene, and MXene@water/POSS-NH_2@toluene. *Source:* Reproduced with permission Shi et al. [153] © 2019, John Wiley & Sons.

explained as the following: The $Ti_3C_2T_x$ was not interfacial active in the MXene@ water/toluene system, as the interfacial tension (35 mN m^{-1}) kept the same as the pure water/toluene system. When POSS-NH_2 molecules were dissolved in toluene, they behaved as surfactants and assembled at the interface, with the interfacial tension decreased to 23 mN m^{-1}. As $Ti_3C_2T_x$ further dispersed in water, a rapid decrease in interfacial tension (21 mN m^{-1}) was detected. Simultaneously, owing to the strong interactions with POSS-NH_2, $Ti_3C_2T_x$ would be continuously adsorbed to the interface to form a random loose packing state.

15.4.3 MXene-Inorganics Hydrogels and Aerogels

15.4.3.1 Cation-Crosslinked Hydrogels

Assisted with selected metal salt solutions, MXene flakes can be directly assembled into hydrogels with crosslinked networks. Typically, a $Ti_3C_2T_x$ MXene dispersion with the concentration of 10 mg mL^{-1} is added into a $FeCl_2{\cdot}4H_2O$ solution. After a few minutes, a liquid-gel transition occurs, and a well-shaped hydrogel is formed (Figure 15.15a) [154]. The interconnected MXene networks are sufficiently stable and can be well maintained after drying (Figure 15.15b). Different from the above crumpling mechanism, the introduced Fe^{2+} cations could break the original electrostatic balance among the initial MXene sheets. Then, the bare ions (with hydration shells removed) function as linkers, and interact with —OH/—O and —F groups on the MXene surface to form Fe—O and Fe—F ionic bonds. Given that the distance for the ionic bond interactions is limited, the MXene hydrogel will not be generated when the concentration of precursor dispersion is low (≤5 mg mL^{-1}). Moreover, not only Fe^{2+} ions but also numerous other multivalent metal ions (e.g. Mg^{2+}, Co^{2+}, Ni^{2+}, Mg^{2+}, Al^{3+}) can act as linkers to induce MXene gelation. Notably, univalent ions (e.g. Li^+, Na^+, K^+) only lead to the flocculation of MXenes, even at a high concentration of $Ti_3C_2T_x$ (15 mg mL^{-1}) and a high concentration of Na^+ (24 M). This is probably explained by the fact that the direct interactions between these cations and functional groups on MXene sheets are shielded by the solvation shells, and thus effective crosslinking could not be achieved. Following the gelation rules, Ding et al. utilized the crosslinking effect of Mg^{2+} ions to prepare a 3D $Ti_3C_2T_x$ aerogel [156]. The pre-prepared $Ti_3C_2T_x$ coating (CT-MXene) with textured structure was immersed in a $MgCl_2$ solution for seconds, and then the wet CT-MXene was then placed on the liquid surface of the $Ti_3C_2T_x$ dispersion (21 mg mL^{-1}). With the loading of Mg^{2+} ions, the MXene sheets were electrostatically assembled into a Mg^{2+}-MXene hydrogel. Subsequently, a Mg^{2+}-MXene aerogel was obtained after the freeze-drying process. The aerogel showed improved structural stability and remained intact after being soaked in water for over a week, even under ultrasonication for 10 minutes. Due to the intersheet crosslinks created by Mg^{2+} ions, the Mg^{2+}-MXene aerogel also showed

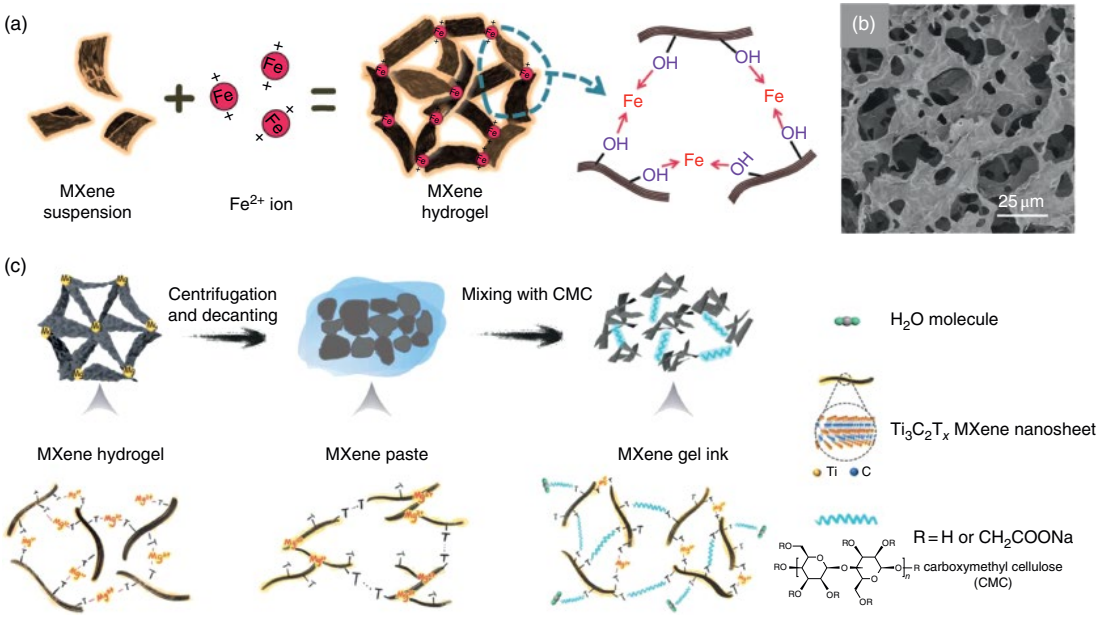


Figure 15.15 Cation-crosslinked hydrogels. (a) Schematic of the metal ion-initiated gelation of MXene nanosheets; (b) the SEM image of obtained MXene aerogel. *Source:* Reproduced with permission Deng et al. [154] © 2019, John Wiley & Sons. (c) The schematic of the preparation of the MXene gel ink. *Source:* Reproduced with permission Chen et al. [155]. Copyright 2022, Wiley-VCH.

increased electrical conductivity ($758.4 \pm 41.6\,S\,m^{-1}$) compared to the MXene aerogel directly obtained by freeze-drying ($471.3 \pm 22.8\,S\,m^{-1}$). When applied in quasi-solid state micro-supercapacitors (QMSCs), the aerogel electrode exhibited a high areal capacitance of $409.3\,mF\,cm^{-2}$, outperforming the state-of-art QMSCs.

Owing to the gelation effects initiated by metal ions, MXene inks with high MXene utilization and tunable rheological properties have been developed. With Zn^{2+}-aided gelation, Li et al. produced 3D-printable Ti_3C_2 MXene inks with satisfactory rheological properties [157]. The MXene ink ($20\,mg\,mL^{-1}$) with the addition of $ZnSO_4$ ($0.03\,mg\,mL^{-1}$) exhibited a high viscosity (up to $10^4\,Pa\,s$ at the shear rate of $10^{-2}\,s$). When the concentration of Zn^{2+} ions (C_Z) was lower than $0.02\,mg\,mL^{-1}$, the ink exhibited a liquid behavior; with the increase of C_Z, the interactions between MXene sheets would be strengthened, which would result in an enlarged storage modulus (G'), and a liquid-solid transition in ink behaviors; once C_Z exceeded $0.05\,mg\,mL^{-1}$, strong van der Waals attractions would occur to cause heavy aggregation, which is not suitable for extrusion printing. With the well-formulated MXene ink, the fabricated 3D-printed MXene cathode exhibited pseudocapacitive storage of H^+ and electrical double-layer capacitive storage of Zn^{2+}, as well as sufficient electrolyte accessibility in a 2 M $ZnSO_4$ solution. Benefiting from the above, an outstanding areal capacitance ($1006.4\,mF\,cm^{-2}$ at $0.38\,mA\,cm^{-2}$) and an excellent rate capability ($184.4\,F\,g^{-1}$ at $10\,A\,g^{-1}$) were delivered, which were superior to most reported Zn-ion hybrid capacitors. Chen et al. designed a versatile $Ti_3C_2T_x$ gel ink in a similar way, but with additional crosslinking induced by sodium carboxymethyl cellulose (CMC) molecules, which could form hydrogen binding with $Ti_3C_2T_x$ sheets and water molecules, as shown in Figure 15.15c. By simply controlling the amount of water within the sol–gel system, this gel ink exhibited a more effective regulation of rheological properties, and could be applicable for various printing and coating techniques, ranging from 3D printing, painting, to stamping, and blade coating. The coating made by the MXene gel ink achieved stable zinc stripping/plating in the aqueous zinc ion batteries, due to the uniform coated surface and the interlinked 3D structure [155].

15.4.3.2 GO-assisted MXene Hydrogels and Aerogels

It is well known that GO nanosheets can easily assemble into a hydrogel in hydrothermal reactions, chemical reductions, or in the presence of chemical or physical cross-linkers. In the former two cases, rGO nanosheets are produced, accompanied by increased hydrophilicity, and enhanced π–π stacking, which enable the cross-linking of rGO through the remaining functional groups (e.g. –OH, –COOH) on the surface. Additionally, it is also widely used to introduce crosslinkers to bridge the GO nanosheets by ionic binding, hydrogen binding, or covalent binding. MXene possesses similar structural characteristics to GO, but the smaller size and limited surface functional groups are not conducive to the assembly like GO.

Inspirationally, controlled and efficient assembly of MXenes into functional hydrogels has been achieved with the assistance of GO colloid chemistry [22].

With the hydrothermal (or solvothermal) assembling, MXene-rGO hybrid hydrogels and aerogels have been fabricated by intermolecular forces (e.g. van der Waals forces, hydrogen bonds, and electrostatic interaction) [34, 158–163]. For instance, Ma et al. fabricated 3D porous MXene hybrid foam by a solvothermal treatment of $Ti_3C_2T_x$-GO mixtures at 180 °C for 12 hours, and the following freeze-drying. Regardless of the contents of MXene, a similar morphology (cellular-like structures) with average pore sizes of ~10 μm would be obtained. Chen et al. proposed a GO-assisted self-convergence strategy to fabricate $Ti_3C_2T_x$-based hydrogel [163]. As shown in Figure 15.16a, a $Ti_3C_2T_x$ dispersion was first mixed with the GO colloidal solution, and the resulting mixture was then heated at 70 °C for 30 hours under an N_2 atmosphere. During the process, GO was partially reduced by $Ti_3C_2T_x$, leading to an increased hydrophobicity and the π-conjugated structures of rGO, and thus a formed 3D rGO framework. Due to the interfacial interactions, $Ti_3C_2T_x$ nanosheets were spontaneously incorporated into the framework, resulting in a $Ti_3C_2T_x$-rGO hydrogel, shown in Figure 15.16b.

The introduction of reductants (e.g. $NaHSO_3$ and ascorbic acid) could also assist the MXene hydrogel formation, without oxidizing MXene. Zhao et al. adopted a method with ascorbic acid introduced as a reductant, and obtained the hydrogel after a 4-hour hydrothermal treatment [34]. Then the obtained MXene-rGO hybrid hydrogel was treated by directional freeze-drying, and a lattice-like cellular structure was formed with vertically grown ice cylinders as templates. This hybrid aerogel showed an outstanding electrical conductivity of 1085 S m^{-1}, considerably higher than the pure graphene aerogel (5.4 S m^{-1}) prepared by the same method. Controlled interactions between MXene and rGO sheets have been achieved by managing the reduction condition and the relative composition of GO. To fabricate super-elastic MXene-rGO aerogels, Jiang et al. adopted a stepwise reduction strategy, followed by temperature-gradient freeze-casting and annealing treatment [158]. As illustrated in Figure 15.16c, with the assistance of ascorbic acid, the GO sheets were partially reduced (zeta potential: −1.1 mV), which were self-assembled with $Ti_3C_2T_x$ sheets (zeta potential: −22.0 mV), as a consequence of a decrease of electrostatic repulsion. Subsequently, during freeze-casting, the vertical growth of ice crystals compressed the partially reduced GO and MXene sheets, leading to the formation of alternating stacked cellular walls (Figure 15.16d, e). The following reduction and the final annealing treatments allowed a complete reduction of GO and elimination of surface functional groups, resulting in enhanced π–π stacking interactions and improved interconnectivity between rGO and MXene layers. Accordingly, the resilient strain properties of the produced MXene-rGO aerogel were enhanced. Remarkably, the aerogel displayed a reversible compressive strain of 95% and a retained

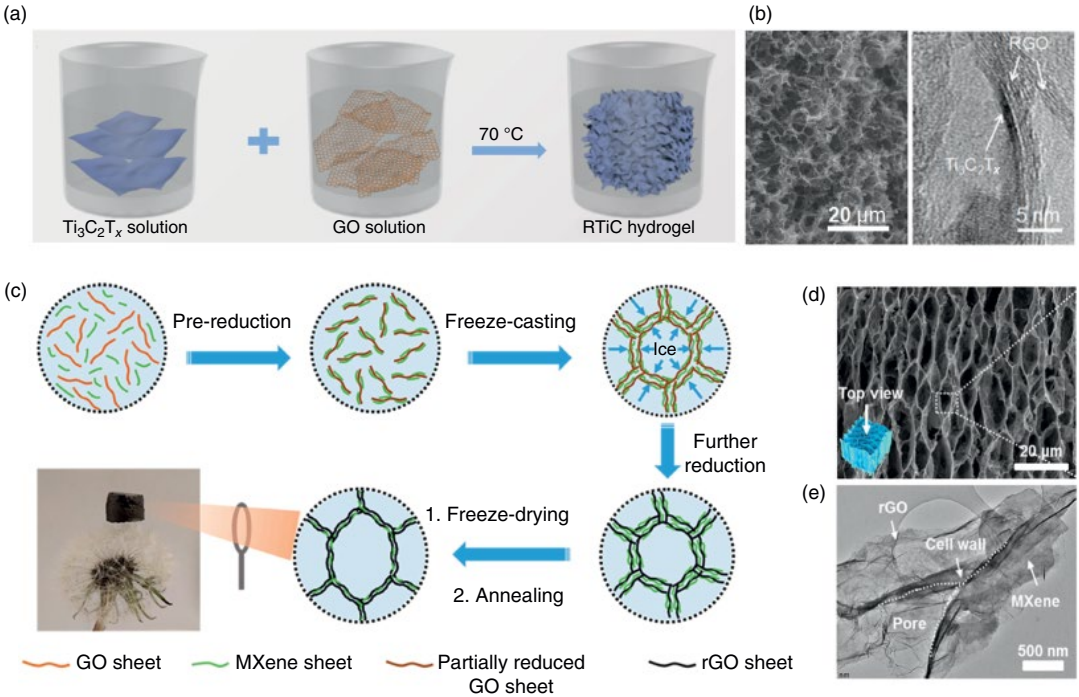


Figure 15.16 MXene-rGO hybrid hydrogels prepared by hydrothermal assembling. (a) The fabrication process of $Ti_3C_2T_x$-based hydrogel, without reductants; (b) SEM and TEM images of the obtained hydrogel. *Source:* Reproduced with permission Chen et al. [163] © 2019, American Chemical Society. (c) Stepwise reduction strategy with freeze-casting for fabricating a $Ti_3C_2T_x$ MXene/RGO hybrid aerogel; (d) the top-view SEM image of the hybrid aerogel; (e) the TEM image showing MXene attached by rGO sheets in the hybrid aerogel. *Source:* Reproduced with permission Jiang et al. [158] © 2021, American Chemical Society.

capacitance of 97.2% when MXene loading was 50 wt%, even after 1000 compression/release cycles in compressible supercapacitors.

Some reductants (e.g. L-cysteine, ethylenediamine (EDA), and $NH_3{\cdot}H_2O$) also act as crosslinkers to promote the assembly of MXene and rGO sheets into 3D macrostructures. Typically, as shown in Figure 15.17a, Shang et al. realized the assembly of $Ti_3C_2T_x$ MXene induced by tiny amounts of GO assisted with crosslinking agent/reductant, EDA. Nucleophilic reactions would occur between EDA and the hydroxyl and epoxy groups on the GO basal planes, and oxygen dangling bonds would form on the rGO, which allow the direct interactions between $Ti_3C_2T_x$ MXene and rGO sheets as well as the crosslinking by the grafted EDA. Eventually, due to the van der Waals forces and π–π stacking interactions, the MXene-rGO hybrid hydrogels (MXH) formed. The MXH slices exhibited outstanding performance ($370\,F\,g^{-1}$ at $5\,A\,g^{-1}$) and could be used as freestanding electrodes in supercapacitors. Impressively, with freeze-drying and capillary-drying, a loose foam (F-MXM) (Figure 15.17b–d) and dense monoliths (D-MXM) with tunable pore structures (Figure 15.17e–g) were obtained, respectively [33]. Similarly, Yang et al. utilized the intense interactions between –OH groups on the MXene or GO surfaces and the $–NH_2$, –SH groups of L-cysteine to construct 3D crosslinked structures. (Figure 15.17h, i) [164]. The L-cysteine acted as the crosslinker/reductant, and the reductant L-ascorbic acid (VC) was used to prevent MXene from being oxidized. The CNTs interconnected with MXene and rGO, leading to improved conductivity. Consequently, the hybrid aerogel was oxidation-resistant, and could maintain high electrical conductivity for 60-day storage in ambient conditions.

Different from the above, divalent metal ions (e.g. Al^{3+}, Ni^{2+}, Fe^{2+}, Zn^{2+}, and Co^{2+}) can achieve desired crosslinking and gelation of MXene and GO sheets under mild conditions, without heating or reduction [160, 165]. Detailed mechanism of the assembly is similar to the self-assembly of pure MXene initiated by cations, as introduced in Section 4.3.1. The MXene-GO assemblies always exhibit enhanced mechanical performance. For example, Lin et al. utilized an efficient and controllable ion diffusion-induced gelation method to fabricate MXene-GO hydrogels, in which a metal foil (e.g. Zn, Al, Co, Fe, and Ni) was placed on the surface of the acidified dispersion consisting of GO and $Ti_3C_2T_x$ sheets. During the gelation process, the metal ions generated from the reactions of the metal foils with acid solutions cross-linked MXene and GO sheets by ionic binding. Simultaneously, GO sheets were partially reduced, which induces their π–π interactions with $Ti_3C_2T_x$. The obtained MXene-GO hybrid foam exhibited excellent structural stability, and significantly excellent terahertz shielding performance of 51 dB at a small thickness of 85 μm [160].

Additionally, there have been other methods proposed to prepare MXene-rGO hydrogels or aerogels [136, 166, 167]. For instance, Wang et al. first prepared rGO

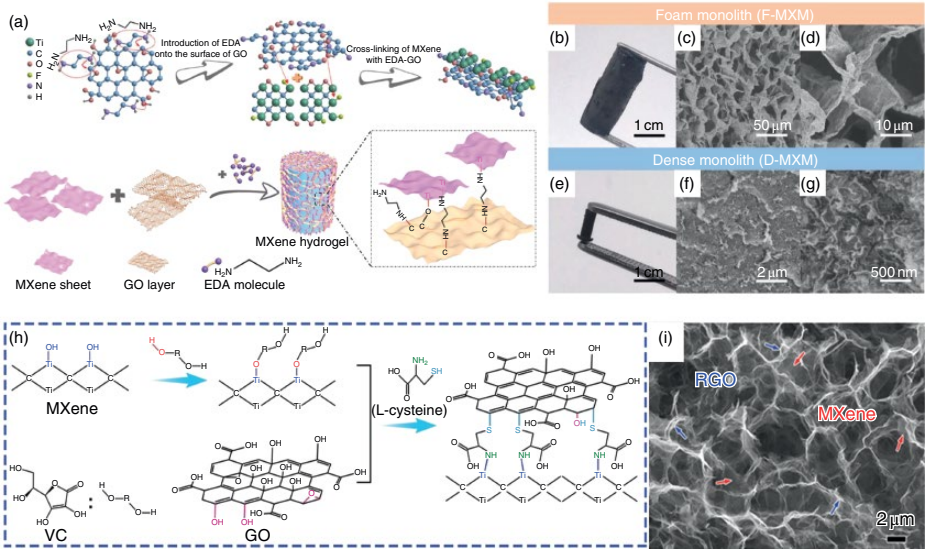


Figure 15.17 MXene based hybrid hydrogels, with assistance of GO and crosslinkers. (a) The mechanism of formation and preparation of 3D MXene hydrogel, with the assistance of GO and EDA. (b–d) The optical photograph and SEM images of MXene foam monolith; (e–g) the optical photograph and SEM images of MXene dense monolith. *Source:* Reproduced with permission Shang et al. [33] © 2019 /John Wiley & Sons. (h) The mechanism of crosslinking of L-cysteine, $Ti_3C_2T_x$ MXene, and rGO; (i) the SEM image of the obtained MXene-rGO hydrogels with L-cysteine crosslinking. *Source:* Reproduced with permission Yang et al. [164] © 2021, John Wiley & Sons.

aerogels by hydrothermal reaction and freeze-drying, and then soaked them in the MXene dispersion to obtain the MXene-rGO aerogels, in which the rGO aerogels acted as porous templates. Li et al. fabricated the $Ti_3C_2T_x$/rGO aerogel by an ice-template freezing technique and low-temperature annealing under Ar/H_2, and neither reductant nor crosslinker was used [166].

15.4.3.3 Other MXene-Inorganics Hybrid Assemblies

In addition to GO or rGO, other inorganic materials, including 0D nanoparticles (e.g. Pd [168], SnO_2 [169], and Fe_2O_3 [170]), 1D materials (e.g. CNTs), and 2D materials (layered double hydroxides, metal-organic frameworks, etc.), could be assembled into MXene-based hydrogel or aerogel frameworks, for multifunctionality, versatility, and enhanced properties. For instance, Tang et al. prepared $Ti_3C_2T_x$-Fe_2O_3 hybrid aerogel by freeze-drying the $Ti_3C_2T_x$ and Fe_2O_3 mixture solutions [170]. Due to the electrostatic interactions, the Fe_2O_3 nanospheres could be adsorbed onto $Ti_3C_2T_x$ interconnected network easily, and act as spacers to avoid MXene restacking. The synergistic effects of MXene and Fe_2O_3 nanospheres endowed the hybrid with excellent electrochemical performance in lithium-ion capacitors, such as a high energy density of $216\,W\,h\,kg^{-1}$ and a power density of $400\,W\,kg^{-1}$. Similarly, Zhang et al. prepared a MXene-CNT aerogel with interconnected and parallel-aligned sandwich structures by the freeze-drying method, which effectively suppressed lithium polysulfide (LiPS) shuttling, and improved the conversion efficiency [171]. Metal-organic frameworks (MOFs) are a special class of materials with abundant porosity, huge surface areas, and coordinatively unsaturated sites. However, the conductivity of traditional MOFs is poor [172]. In this regard, incorporating highly conductive MXene with MOFs can overcome the poor electrical conductivity of MOFs, simultaneously, MOFs as spacers to prevent the stacking of MXene nanosheets and improve the porosity and specific surface areas of the composites [173–175]. Yao et al. designed an MXene-MOFs aerogel, with the *in-situ* growth of MOF particles within an MXene hydrogel framework [176]. As shown in Figure 15.18, Co^{2+} ions acted as crosslinkers to interact with oxygen-containing functional groups of MXene to produce MXene hydrogel, and simultaneously as nucleation sites for the growth of MOFs. With further carbonization and vulcanization, the MOFs could be finally transformed into CoS nanoparticles and a hollow carbon nano box, resulting in the formation of (CoS NP@NHC)@MXene aerogel. Benefiting from the synergistic effect of the components, and the hierarchical porous structure, this hybrid exhibited outstanding electrochemistry performance for alkali metal ion storage, with high capacities of $1145.9\,mAh\,g^{-1}$ at $1\,A\,g^{-1}$ for lithium-ion batteries, $420\,mAh\,g^{-1}$ at $2\,A\,g^{-1}$ for sodium-ion batteries, and $210\,mAh\,g^{-1}$ at $2\,A\,g^{-1}$ for potassium-ion batteries. Zheng et al. fabricated a well-designed 3D MXene-based aerogel by integrating MXene, $NiCo_2$-Layered double hydroxides ($NiCo_2$-LDHs), and rGO with

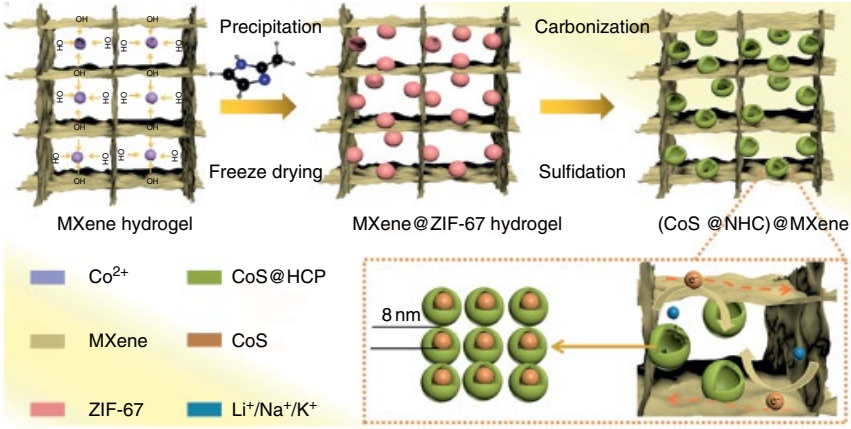


Figure 15.18 A Schematic of the manufacturing of (CoS NP @NHC)@MXene aerogel. *Source:* Yao et al. [176]/American Chemical Society.

hydrothermal and wet chemical techniques [177]. This aerogel delivered a remarkable specific capacity of 332.2 mAh g^{-1} at 1 A g^{-1} and good durability of 87.5% after 5000 cycles at 5 A g^{-1} in a three-electrode system. When it was coupled with a MXene-rGO anode, the fabricated hybrid supercapacitor provided a superior energy density of 65.3 W h kg^{-1}, a power density of 700 W kg^{-1}, and excellent cycling stability over 10 000 cycles at 5 A g^{-1}.

15.4.4 MXene-Organics Composite Hydrogels and Aerogels

Besides inorganics, organics can also be used to construct 3D $Ti_3C_2T_x$ structures [35, 36, 178–196]. To date, several organic-assisted 3D $Ti_3C_2T_x$ structures have been reported and various applications have been developed according to the special properties of the material. Typically, the interactions between MXene nanosheets and other species in the three-dimensional structure include hydrogen and/or covalent bonds.

15.4.4.1 Organic Molecule Crosslinked MXene Hydrogels

Besides the above-mentioned multivalent metal cations, some organic molecules can act as crosslinkers to induce the flake assembly to form MXene hydrogels. For example, Peng et al. prepared a $Ti_3C_2T_x$ MXene hydrogel in seconds, by introducing protonated thionine (Th) molecules into MXene dispersions, as shown in Figure 15.19a [32]. In the gelation process, protonated Th molecules play similar roles with multivalent metal cations. The protonated Th molecules are flanked by amine groups and interact with the negatively charged MXene flakes.

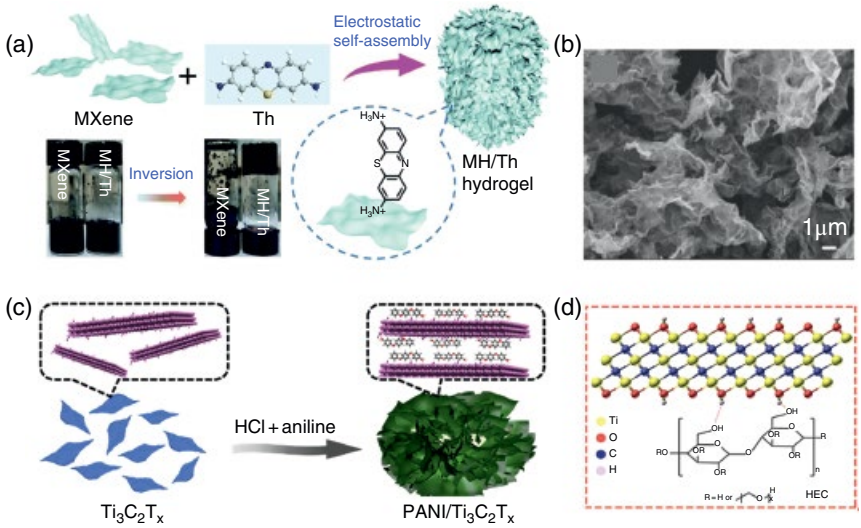


Figure 15.19 3D MXene assembled by organic molecules. (a) Schematic of the preparation of the MH/Th hydrogel; (b) the SEM image of the MH/Th hydrogel. *Source:* Reproduced with permission Peng et al. [32] © 2021, Royal Society of Chemistry. (c) Schematic of preparing 3D PANI/ $Ti_3C_2T_x$ networks. *Source:* Reproduced with permission Wang et al. [180]. Copyright 2020, American Chemical Society. (d) Diagram of hydrogen bonds between $Ti_3C_2T_x$ and hydroxyethyl cellulose. *Source:* Reproduced with permission Huang et al. [186]. Copyright 2021, Wiley-VCH.

Their electrostatic interactions facilitate the self-assembly of $Ti_3C_2T_x$ sheets. Simultaneously, the protonated Th molecules crosslink adjacent $Ti_3C_2T_x$ sheets to form a tough hydrogel with interconnected networks (Figure 15.19b). In addition, Th molecules are redox-reactive and can provide additional pseudocapacitance, when this composite hydrogel is applied as an electrode material for supercapacitors. The weak reducing agent EDA is also found to initiate pristine MXene assembly into hydrogels [178]. Specifically, EDA (100 μL) is added into the as-produced $Ti_3C_2T_x$ dispersion (20 mg mL^{-1}, 5 mL), and then the mixture will transform into hydrogels after heating at 95 °C for 6 hours. Different from when GO is applied, a highly concentrated MXene dispersion is required.

The abundant groups enable polymers to form chemical interactions (e.g. hydrogen bonding and covalent bonding) with MXenes and bridge neighbor nanosheets into interconnected networks or hydrogels. For example, Wang et al. fabricated a 3D PANI/$Ti_3C_2T_x$ network, by mixing a HCl aqueous solution containing positively charged aniline monomers with the $Ti_3C_2T_x$ MXene suspension (Figure 15.19c) [180]. During this process, the aniline monomers firstly adsorbed onto the MXene surface, and then spontaneously polymerized to form PANI,

which generated strong covalent Ti—N bonding with $Ti_3C_2T_x$ nanosheets and eventually the 3D assembly. The self-polymerization could be explained as: the aniline monomers were oxidized by oxygen-containing functional groups (–O and –OH) on $Ti_3C_2T_x$ surfaces to release radicals, and the oxidation products reacted with other anilines to form dimers, oligomers, and polymers. Distinct from the negative potential of the acid-induced assembly, the zeta potential of PANI-induced $Ti_3C_2T_x$ assemblies would become positive. Benefiting from the enlarged interlayer spacing and stable 3D structures, the PANI/$Ti_3C_2T_x$ provided a high specific capacity of 254 mAh g^{-1} at 100 mA g^{-1} for Na^+ ion intercalation. The water-soluble hydroxyethyl cellulose (HEC) with abundant hydroxyl groups can crosslink MXene flakes through hydrogen bonds (Figure 15.19d). With a trace of HEC added and freeze-drying, an MXene aerogel with high mechanical stability and a high conductivity network could be obtained, which exhibited a high EMI shielding performance of 74.5 dB on average [186].

15.4.4.2 MXene-Polymer Composite Hydrogels

Owing to the hydrophilicity and excellent electrical conductivity, MXenes have been proposed as conductive nanofillers in a polymer hydrogel matrix, which endow hydrogels with outstanding multifunctional versatility. The introduced MXene is effective despite its sparsity. Generally, the uniform dispersed MXene nanosheets can interact with the entangled polymer chains, by ionic, hydrogen, and/or covalent bonding. It is believed that the formation of MXene-polymer network structures can significantly improve the elastic modulus and stretchability of the hydrogel, as well as the self-healing ability. The fabricated MXene-polymer composite hydrogels have shown outstanding performance in various applications, such as sensing [36, 182–184], electromagnetic shielding [185, 186], and energy storage [187, 188].

To date, there have been various methods to incorporate MXene nanosheets into a hydrogel matrix, with MXene functioning variously. The simplest and most direct way is mechanical mixing. Husam N. Alshareef's group manually mixed MXene paste with a commercial hydrogel containing PVA, until a homogeneous black MXene-PVA hydrogel was obtained [182, 188]. The MXene nanosheets which were randomly distributed in the hydrogel matrix interacted with PVA chains by hydrogen bonding. The obtained MXene-PVA hydrogel displayed excellent stretchability, adhesiveness, conformability, as well as asymmetrical strain sensitivity, which allow them to be potential materials for wearable electronics, soft robotics, and artificial skin. Incorporating MXene nanosheets before the gelation of hydrogels is beneficial for homogeneous MXene distribution, and thus ensures uniformity in the performance of devices [183, 192, 193]. For example, Zhang et al. firstly mixed the MXene colloidal solution with the aqueous PVA solution, and then added the crosslinking agent, sodium tetraborate, into the

mixture [183]. The MXene-PVA hydrogel was ultimately obtained by gelatinization. In the hydrogel system, di-diol bonds formed between tetrafunctional borate ions and PVA chains, which formed covalent bonds with $Ti_3C_2T_x$ surfaces.

When two or more different polymers are involved, the corresponding crosslinked networks are termed MXene-copolymeric composite hydrogels [35, 184, 187]. For instance, Liao et al. prepared MXene-polyvinylalcohol-polyacrylamide (MXene-PVA-PAAm) hydrogels from the precursor solutions containing $Ti_3C_2T_x$ nanosheets, PVA, and acrylamide (AAm) monomers [35]. The MXene-copolymer hydrogel was subsequently obtained after *in-situ* polymerization of AAm monomers at 60 °C. During gelation and polymerization, *N,N′*-methylene-bis-acrylamide and 2,2′-azobis[2-(2-imidazolin-2-yl)propane] dihydrochloride were used as the chemical crosslinker and initiator, respectively, to polymerize AAm, with sodium tetraborate decahydrate crosslinking PVA chains. As shown in Figure 15.20a, the PVA and PAAm chains were densely entangled together with abundant hydrogen bonds formed among PVA and MXene nanosheets. Zhang et al. fabricated MXene/PPy-PVA composite hydrogels by immersing the MXene-PVA hydrogel in a solution containing dopamine hydrochloride and pyrrole (Py) monomers, followed polymerization with the addition of $FeCl_3$ [187]. The produced PPy nanofibers were within the MXene-PVA hydrogel structure, and formed hydrogen bonding with PVA chains and MXene nanosheets. This obtained composite hydrogel showed a remarkable tensile strength of 10.3 MPa and could be stretched to 380%. When applied to supercapacitors, it provided a high specific capacitance of up to 614 F g^{-1} at 1 A g^{-1} and excellent cycling stability over 10 000 cycles without capacitance decay.

In principle, monomers, an initiator, and a crosslinker are needed to synthesize MXene-polymer composite hydrogels, and in all the aforementioned reports, MXene nanosheets hardly contribute to polymer gelation. Recently, it has been found that MXene nanosheets can initiate gelation or act as a cross-linking agent. Tao et al. demonstrated MXene nanosheets as an initiator for polymerization and gelation of a series of acrylic monomers, including acrylamide, *N*-isopropyl acrylamide (NIPAM), *N,N′*-dimethylacetamide, methyl methacrylate, and hydroxyethyl methacrylate [194]. Polymerization would occur in minutes after monomers were added into a $Ti_3C_2T_x$ suspension in an ice bath. When a high concentration of monomers was used, a hydrogel could be directly obtained, such as 8 wt% for NIPAM. The initiation mechanism is proposed as that two radicals (hydroxyl and peroxyl radicals) will be generated during sonication in the synthesis of $Ti_3C_2T_x$, and initiate the chain propagation reactions. However, for the self-polymerization of aniline monomers on MXene in the previous report, it is presumed that MXene oxidizes the monomer to generate aniline cation radicals and/or neutral radicals, which initiate electrophilic substitution to form aniline dimers. Further investigation is required to fully understand the detailed initiation mechanism. Combining

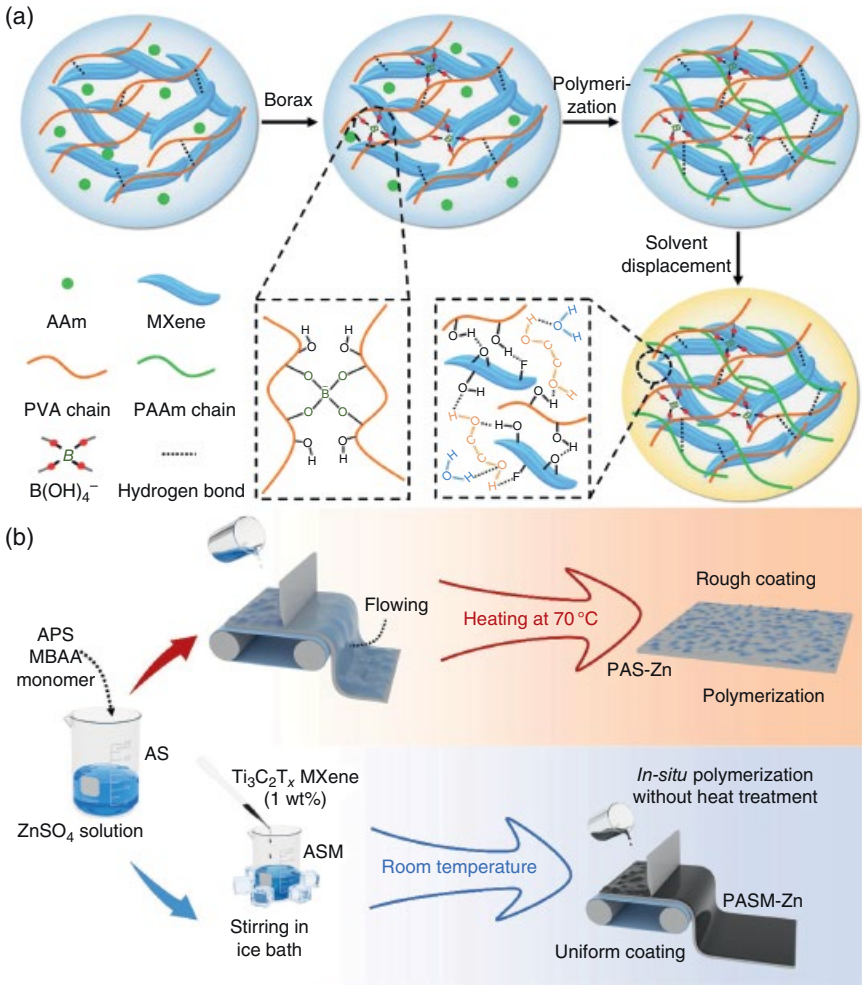


Figure 15.20 A MXene-polymer composite hydrogel. (a) Schematic of the fabrication of a conductive, anti-freezing, and self-healing MXene-PVA-PAAm composite hydrogel. *Source:* Reproduced with permission Liao et al. [35]. Copyright 2019, Wiley-VCH. (b) Schematic of the one-step polymer coating processing from aqueous monomer solution with the assistance of $Ti_3C_2T_x$ MXene. *Source:* Reproduced with permission Wang et al. [197]. Copyright 2022, Elsevier.

the initiation effect and a doctor-blading method, Wang et al. fabricated a uniform, adhesive, and versatile MXene-P(AA-co-AMPS) coating layer on a zinc substrate assisted with a trace of MXene at room temperature (Figure 15.20b) [197]. The –COOH groups of acrylic acid (AA) provide good adhesion on substrates, and the $–SO_3^-$ groups of 2-acrylamido-2-methylpropanesulfonic acid (AMPS) facilitate

the de-solvation and transport of Zn^{2+} ions [198]. When applied for a zinc anode in aqueous zinc batteries, the as-fabricated coating not only suppressed side reactions, but also facilitated uniform zinc deposition, and steady cycling (over 1900 hours, at 0.2 mA cm^{-2}).

MXene nanosheets can also be used as inorganic cross-linking agents in fabricating MXene-polymer hydrogels. For instance, Zhang et al. prepared $Ti_3C_2T_x$-polyacrylamide hydrogel without using any organic crosslinkers [196]. Potassium persulfate was used to initiate polymerization, and the traces $Ti_3C_2T_x$ MXene could crosslink polymer chains by forming hydrogen bonding with the $-CONH_2$ groups of polyacrylamides. Compared with the traditional polyacrylamide hydrogel prepared with *N*, *N*-methylene bisacrylamide crosslinking, this hydrogel exhibited improved mechanical properties and higher degrees of deformations. Furthermore, the mechanical performance could be tuned by controlling the $Ti_3C_2T_x$ content, explicitly, as the content increased from 0.0145% to 0.0436%, the fracture strength expanded from 66.5 to 102.7 kPa, and compressive strength grew from 400.6 to 819.4 kPa. Ge et al. also reported the crosslinking effect of $Ti_3C_2T_x$ MXene as well as the initiation function for polymerization and rapid gelation after monomers were mixed with $Ti_3C_2T_x$ nanosheets [195]. In the presence of ammonium persulfate (APS) and glycerol, the gelation occurred rapidly without heating or ultraviolet (UV) light irradiation. It was explained as the following: (i) The strong chelation between monomers and the $Ti_3C_2T_x$ nanosheets would release heat, which activates the decomposition of APS to generate free radicals for polymerization. (ii) Abundant hydrogen bonding (physical cross-linking) formed among $Ti_3C_2T_x$, glycerol, and PAA chains.

As MXene-organic composite hydrogels are generally prepared by *in-situ* polymerizing or self-assembly in solutions, most of them show disordered, isotropic polymer networks. Assisted by directional freeze-templating (introduced in Section 15.4.2), an anisotropic MXene-polymer hydrogel with ordered orientations can be fabricated, which is expected to exhibit enhanced mechanical properties and anisotropic performance. Yang et al. fabricated a highly anisotropic MXene-gelatin composite aerogel with aligned walls by a simple unidirectional freeze-drying method (Figure 15.21a), which exhibited improved mechanical properties. The anisotropic microstructures also resulted in anisotropic electromagnetic wave absorption properties, with a −59.5 dB minimum reflection loss at 14.04 GHz in the vertical direction and a 6.24 GHz effective absorption bandwidth in the parallel direction (Figure 15.21a) [191]. Jiang et al. used crosslinker epichlorohydrin to build covalent bonds between MXene nanosheets and cellulose through an etherification reaction, and then utilized the freeze-casting technique to fabricate hierarchical structured MXene-cellulose aerogels with lamellar channels, as shown in Figure 15.21b [190]. The cellulose and MXene nanosheets were stacked together to form cell walls of the aerogel, and the average diameter of the channels is

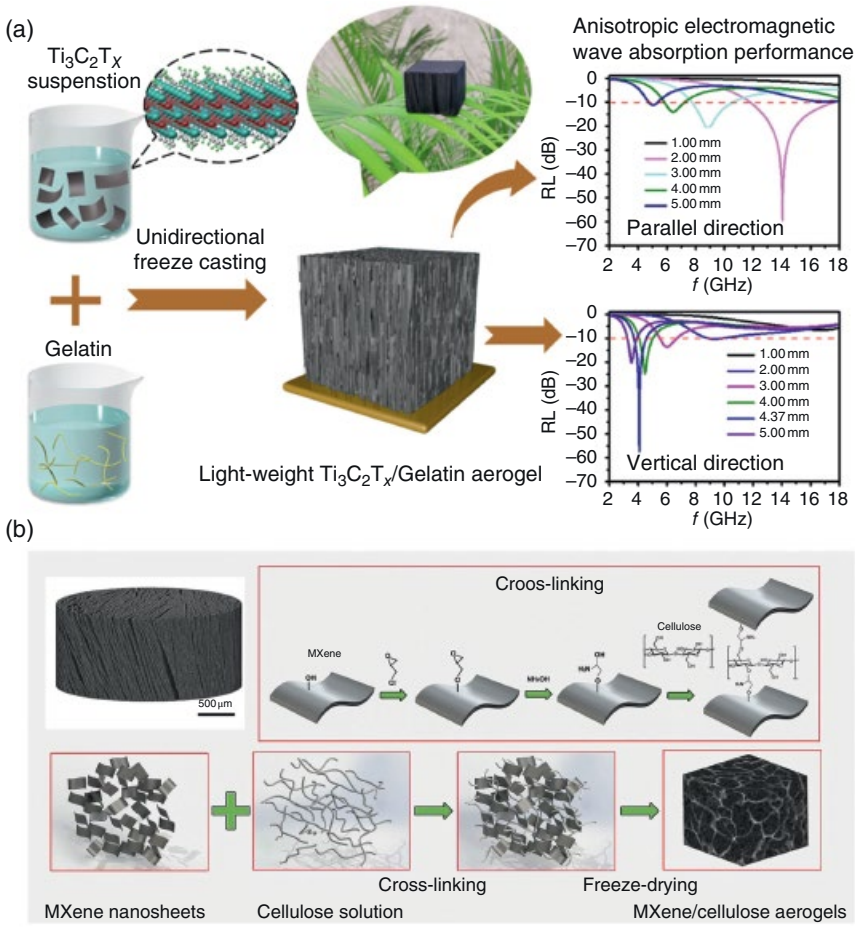


Figure 15.21 3D hydrogels with anisotropic structures. (a) A schematic illustration of the preparation process of the $Ti_3C_2T_x$ MXene@gelatin composite aerogel, which showed anisotropic electromagnetic wave absorption performance. *Source:* Reproduced with permission Yang et al. [191]. Copyright 2020, American Chemical Society. (b) A schematic illustrating the fabrication process of MXene/cellulose aerogel composites. *Source:* Reproduced with permission Jiang et al. [190]. Copyright 2018, Royal Society of Chemistry.

approximately 25 mm. The electrically conductive network provided by $Ti_3C_2T_x$ MXene could enhance the electrical energy storage as well as the loss capability with high real and imaginary permittivity, and the unique structure could provide multiple reflections to further attenuate microwave energy. Therefore, the aerogel exhibited enhanced microwave absorption performance, with an effective absorption bandwidth of 4.5 GHz and excellent minimal reflection loss of −43.4 dB at

11.2 GHz. Feng et al. developed $Ti_3C_2T_x$-PVA hydrogel with an ordered orientation by adding $ZnSO_4$ to the MXene-PVA mixture solutions, and following directional freezing and thawing repeatedly [36]. The introduced Zn^{2+} ions contributed to the production of the cross-linked network, and the directional freezing allowed numerous open channels to form on the surface. This ordered-oriented MXene conductive hydrogel could be applied as wearable flexible sensors for comprehensive human motion biomonitoring.

15.5 Summary

MXenes, a novel and fast-growing class of 2D materials over the past ten years, exhibit outstanding physical and chemical properties and enable numerous promising applications. Cutting-edge technologies and advanced electronic devices require efficient processing of MXene colloidal dispersions into diverse structures (e.g. array, fiber, and film). Here, this chapter highlights the significance of the solution processing to fabricate functional MXene assemblies. Based on the assembly methods and mechanisms, MXene-based macroscopic architectures, including 1D fibers, 2D films, and 3D hydrogel or aerogels, are discussed in detail. Additionally, we present our views on the current progress and future research directions in this interesting field.

For 1D MXene assemblies, various types of assembly techniques like direct dip-coating, wet-spinning, electrospinning, and biscrolling, are used to shape MXene composites into 1D fibers, exhibiting great performance in wearable energy storage devices, heated textiles, and sensors. The discovery of LC behaviors promotes the fabrication of neat MXene fibers, in which the pristine properties of MXene nanosheets can be well preserved, and the mechanical properties are greatly enhanced by the order sheet-alignment. Nevertheless, we still face numerous challenges on the road to large-scale industrialization toward 1D MXene assembled fibers, namely further enhancing the mechanical properties of the MXene-based fibers, choosing the proper substrates with low cost and high conductivity, and designing the specific manufacturing routes for scale-up industrial processing.

The assembly of MXene films is the most straightforward method to realize compact, transparent, and conductive coatings, and has been widely applied in the fields of electrochemical energy storage, EMI, and sensing without further processing. To narrow the property gap between MXenes and the fabricated films, or overcome the sheet restacking issues, strategies to fabricate the neat MXene films with lamellar structures, or in-plane nanochannel and porous structures, have been proposed. To further meet the demands of practical applications, multifunctional MXene composite films are prepared with inorganic and organic materials. The resulting 2D assemblies (or with 3D microstructures) mainly rely on various

inter-molecular interactions between the guest species and the unique surface groups (e.g. –F, –O, and OH) of MXenes. Although the engineering of microscopic structures has proven to be an efficient strategy for the design of 2D macroscopic MXene films, challenges still exist such as large-scale production of MXene films, and fabrication of dense and thick films in the assembly of 2D MXene films.

A phase separation originated from the overbalance of the electrostatic interaction in colloidal dispersions may favor the crumpling or self-concentration of MXene nanosheets. The assembly on the interfaces (e.g. liquid–solid and liquid–liquid) that can act as 3D continuous templates will result in interconnected porous structures. With the help of crosslinking agents or GO sheets, the 3D MXene-based architectures with crosslinking networks are assembled from solutions due to the phase separation and bulk gelation. Assisted with these 3D networks and synergistic effects of other functional materials (e.g. inorganic nanomaterials and polymers), the 3D MXene-based composite assemblies inherit the pristine properties of MXene and show more excellent properties. Thus, assembling 2D MXene nanosheets into 3D macro assemblies plays a significant role in broadening their practical applications. However, compared with GO assembly, the 3D assembly of MXenes still faces challenges in precisely controlling the concentration of MXene input to achieve both stable 3D architectures and avoid the aggregation in the composite precursors, as well as feasible modification of the size and the rigidity of MXene flakes.

Despite the progress on MXene assemblies achieved so far, the solution processing and fabrication of advanced MXene-based macroscopic materials for high-performance devices are still in the primary stage, and there are few examples of industrial uses. Since the lack of understanding of colloidal chemistry of MXenes, the processing techniques of MXene colloidal solutions are still immature. Many bottleneck problems still need to be addressed, such as how to take advantage of the uniqueness of assemblies with different dimensions, how to integrate MXene-based electronics with free-standing and higher conductivity properties into real devices, etc. Therefore, efforts are required to be made in assembling 2D MXene nanosheets into 1D/2D/3D architectures with a tailored structure by well-designed processes so that high-performance, stable, and reliable materials can be targeted in the future.

Acknowledgments

The authors appreciate the financial support from the National Natural Science Foundation of China (No. 51972228) and TJU Nanoyang-Neware Joint Laboratory for Energy Innovation. The authors also appreciate the valuable assistance from Boya Zhang, Derong Chen, Fangbing Li, Jinyang Yu, and Boyang Niu during the preparation of the manuscript.

References

1 Butler, S.Z., Hollen, S.M., Cao, L. et al. (2013). Progress, challenges, and opportunities in two-dimensional materials beyond graphene. *ACS Nano* 7 (4): 2898.

2 Zeng, M., Xiao, Y., Liu, J. et al. (2018). Exploring two-dimensional materials toward the next-generation circuits: from monomer design to assembly control. *Chemical Reviews* 118 (13): 6236.

3 Mannix, A.J., Kiraly, B., Hersam, M.C., and Guisinger, N.P. (2017). Synthesis and chemistry of elemental 2D materials. *Nature Reviews Chemistry* 1 (2): 14.

4 Choi, S.H., Yun, S.J., Won, Y.S. et al. (2022). Large-scale synthesis of graphene and other 2D materials towards industrialization. *Nature Communications* 13 (1): 1484.

5 Peng, J., Liu, Y., Lv, H. et al. (2021). Stoichiometric two-dimensional non-van der Waals $AgCrS_2$ with superionic behaviour at room temperature. *Nature Chemistry* 13 (12): 1235.

6 Wan, J., Lacey, S.D., Dai, J. et al. (2016). Tuning two-dimensional nanomaterials by intercalation: materials, properties and applications. *Chemical Society Reviews* 45 (24): 6742.

7 Ryu, B., Wang, L., Pu, H. et al. (2022). Understanding, discovery, and synthesis of 2D materials enabled by machine learning. *Chemical Society Reviews* 51 (6): 1899.

8 Mohammadi, A.V., Rosen, J., and Gogotsi, Y. (2021). The world of two-dimensional carbides and nitrides (MXenes). *Science* 372 (6547): 1165.

9 Wei, Y., Zhang, P., Soomro, R.A. et al. (2021). Advances in the synthesis of 2D MXenes. *Advanced Materials* 33 (39): e2103148.

10 Li, K., Liang, M., Wang, H. et al. (2020). 3D MXene architectures for eifficient energy storage and conversion. *Advanced Functional Materials* 30 (47): 2000842.

11 Zhang, C. (2021). Interfacial assembly of two-dimensional MXenes. *Journal of Electroanalytical Chemistry* 60: 417.

12 Abdolhosseinzadeh, S., Jiang, X., Zhang, H. et al. (2021). Perspectives on solution processing of two-dimensional MXenes. *Materials Today* 40: 214.

13 Levitt, A., Hegh, D., Phillips, P. et al. (2020). 3D knitted energy storage textiles using MXene-coated yarns. *Materials Today* 34: 17.

14 Uzun, S., Seyedin, S., Stoltzfus, A.L. et al. (2019). Knittable and washable multifunctional MXene-coated cellulose yarns. *Advanced Functional Materials* 29 (45): 1905015.

15 Liu, K., Fan, Y., Ali, A., and Shen, P.K. (2021). A flexible and conductive MXene-coated fabric integrated with in situ sulfur loaded MXene nanosheets for long-life rechargeable Li-S batteries. *Nanoscale* 13 (5): 2963.

16 Zhang, J., Uzun, S., Seyedin, S. et al. (2020). Additive-free MXene liquid crystals and fibers. *ACS Central Science* 6 (2): 254.

17 Li, S., Fan, Z., Wu, G. et al. (2021). Assembly of nanofluidic MXene fibers with enhanced ionic transport and capacitive charge storage by flake orientation. *ACS Nano* 15 (4): 7821.

18 Eom, W., Shin, H., Ambade, R.B. et al. (2020). Large-scale wet-spinning of highly electroconductive MXene fibers. *Nature Communications* 11 (1): 2825.

19 Zhang, J., Kong, N., Uzun, S. et al. (2020). Scalable manufacturing of free-standing, strong $Ti_3C_2T_x$ MXene films with outstanding conductivity. *Advanced Materials* 32 (23): e2001093.

20 Yang, W., Yang, J., Byun, J.J. et al. (2019). 3D printing of freestanding MXene architectures for current-collector-free supercapacitors. *Advanced Materials* 31 (37): e1902725.

21 Long, Y., Tao, Y., Shang, T. et al. (2022). Roles of metal ions in MXene synthesis, processing and applications: a perspective. *Advanced Science* 9 (12): e2200296.

22 Cong, H.P., Chen, J.F., and Yu, S.H. (2014). Graphene-based macroscopic assemblies and architectures: an emerging material system. *Chemical Society Reviews* 43 (21): 7295.

23 Shao, J.J., Lv, W., and Yang, Q.H. (2014). Self-assembly of graphene oxide at interfaces. *Advanced Materials* 26 (32): 5586.

24 Lipton, J., Weng, G.-M., Röhr, J.A. et al. (2020). Layer-by-layer assembly of two-dimensional materials: Meticulous control on the nanoscale. *Matter* 2 (5): 1148.

25 Wu, Z., Shang, T., Deng, Y. et al. (2020). The assembly of MXenes from 2D to 3D. *Advanced Science* 7 (7): 1903077.

26 Bu, J.D., Zhang, W.Q., Su, Y. et al. (2022). Preparation of 3D flower-like $Ti_3C_2T_x$ microspheres by w/o emulsion-assisted assembly and their application for supercapacitors. *Ceramics International* 48 (8): 10834.

27 Song, Y., Sun, Z., Fan, Z. et al. (2020). Rational design of porous nitrogen-doped Ti_3C_2 MXene as a multifunctional electrocatalyst for Li–s chemistry. *Nano Energy* 70: 104555.

28 Shah, S.A., Habib, T., Gao, H. et al. (2016). Template-free 3D titanium carbide ($Ti_3C_2T_x$) MXene particles crumpled by capillary forces. *Chemical Communications* 53 (2): 400.

29 Kim, J.-E., Oh, J.-H., Kotal, M. et al. (2017). Self-assembly and morphological control of three-dimensional macroporous architectures built of two-dimensional materials. *Nano Today* 14: 100.

30 Zhang, Y.Z., El-Demellawi, J.K., Jiang, Q. et al. (2020). MXene hydrogels: fundamentals and applications. *Chemical Society Reviews* 49 (20): 7229.

31 Zhou, J., Xie, M., Wu, F. et al. (2021). Encapsulation of metallic Zn in a hybrid MXene/graphene aerogel as a stable Zn anode for foldable Zn-ion batteries. *Advanced Materials* e2106897.

32 Peng, M., Yang, W., Li, L. et al. (2021). Fast assembly of MXene hydrogels by interfacial electrostatic interaction for supercapacitors. *Chemical Communications* 57 (82): 10731.

33 Shang, T., Lin, Z., Qi, C. et al. (2019). 3D macroscopic architectures from self-assembled MXene hydrogels. *Advanced Functional Materials* 29 (33): 1903960.

34 Zhao, S., Zhang, H.B., Luo, J.Q. et al. (2018). Highly electrically conductive three-dimensional $Ti_3C_2T_x$ MXene/reduced graphene oxide hybrid aerogels with excellent electromagnetic interference shielding performances. *ACS Nano* 12 (11): 11193.

35 Liao, H., Guo, X., Wan, P., and Yu, G. (2019). Conductive MXene nanocomposite organohydrogel for flexible, healable, low-temperature tolerant strain sensors. *Advanced Functional Materials* 29 (39): 1904507.

36 Feng, Y., Liu, H., Zhu, W. et al. (2021). Muscle-inspired MXene conductive hydrogels with anisotropy and low-temperature tolerance for wearable flexible sensors and arrays. *Advanced Functional Materials* 31 (46): 2105264.

37 Anasori, B., Sarycheva, A., Buondonno, S. et al. (2017). 2D metal carbides (MXenes) in fibers. *Materials Today* 20 (8): 481.

38 Jiang, Q., Kurra, N., Alhabeb, M. et al. (2018). All pseudocapacitive MXene-RuO_2 asymmetric supercapacitors. *Advanced Energy Materials* 8 (13): 1703043.

39 Wang, Q.-W., Zhang, H.-B., Liu, J. et al. (2019). Multifunctional and water-resistant MXene-decorated polyester textiles with outstanding electromagnetic interference shielding and joule heating performances. *Advanced Functional Materials* 29 (7): 1806819.

40 Seyedin, S., Yanza, E.R.S., and Razal, J.M. (2017). Knittable energy storing fiber with high volumetric performance made from predominantly MXene nanosheets. *Journal of Materials Chemistry A* 5 (46): 24076.

41 Yang, Q., Xu, Z., Fang, B. et al. (2017). MXene/graphene hybrid fibers for high performance flexible supercapacitors. *Journal of Materials Chemistry A* 5 (42): 22113.

42 Zhang, J., Seyedin, S., Qin, S. et al. (2019). Highly conductive $Ti_3C_2T_x$ MXene hybrid fibers for flexible and elastic fiber-shaped supercapacitors. *Small* 15 (8): e1804732.

43 Mayerberger, E.A., Urbanek, O., McDaniel, R.M. et al. (2017). Preparation and characterization of polymer-$Ti_3C_2T_x$ (MXene) composite nanofibers produced via electrospinning. *Journal of Applied Polymer Science* 134 (37): 45295.

44 Mayerberger, E.A., Street, R.M., McDaniel, R.M. et al. (2018). Antibacterial properties of electrospun $Ti_3C_2T_x$ (MXene)/chitosan nanofibers. *RSC Advances* 8 (62): 35386.

45 Levitt, A.S., Alhabeb, M., Hatter, C.B. et al. (2019). Electrospun MXene/carbon nanofibers as supercapacitor electrodes. *Journal of Materials Chemistry A* 7 (1): 269.

46 Wang, Z., Qin, S., Seyedin, S. et al. (2018). High-performance biscrolled MXene/carbon nanotube yarn supercapacitors. *Small* 14 (37): e1802225.

47 Yu, C., Gong, Y., Chen, R. et al. (2018). A solid-state fibriform supercapacitor boosted by host-guest hybridization between the carbon nanotube scaffold and MXene nanosheets. *Small* 14: e1801203.

48 Levitt, A., Zhang, J., Dion, G. et al. (2020). MXene-based fibers, yarns, and fabrics for wearable energy storage devices. *Advanced Functional Materials* 30 (47): 2000739.

49 Ma, C., Ma, M.G., Si, C. et al. (2021). Flexible MXene-based composites for wearable devices. *Advanced Functional Materials* 31 (22): 2009524.

50 Zhang, X., Wang, X., Lei, Z. et al. (2020). Flexible MXene-decorated fabric with interwoven conductive networks for integrated joule heating, electromagnetic interference shielding, and strain sensing performances. *ACS Applied Materials & Interfaces* 12 (12): 14459.

51 Zhao, X., Wang, L.-Y., Tang, C.-Y. et al. (2020). Smart $Ti_3C_2T_x$ MXene fabric with fast humidity response and joule heating for healthcare and medical therapy applications. *ACS Nano* 14 (7): 8793.

52 Yang, G., Li, X., Guan, Z. et al. (2020). Insights into lithium and sodium storage in porous carbon. *Nano Letters* 20 (5): 3836.

53 Liu, R., Li, J., Li, M. et al. (2020). MXene-coated air-permeable pressure-sensing fabric for smart wear. *ACS Applied Materials & Interfaces* 12 (41): 46446.

54 Riazi, H., Taghizadeh, G., and Soroush, M. (2021). MXene-based nanocomposite sensors. *ACS Omega* 6 (17): 11103.

55 Iwamoto, S., Isogai, A., and Iwata, T. (2011). Structure and mechanical properties of wet-spun fibers made from natural cellulose nanofibers. *Biomacromolecules* 12 (3): 831.

56 Yu, Q., Zhao, B., Ren, X. et al. (2022). Porous pure MXene fibrous network for highly sensitive pressure sensors. *Langmuir* 38 (18): 5494.

57 Qin, S., Usman, K.A.S., Hegh, D. et al. (2021). Development and applications of MXene-based functional fibers. *ACS Applied Materials & Interfaces* 13 (31): 36655.

58 Xu, Z. and Gao, C. (2011). Graphene chiral liquid crystals and macroscopic assembled fibres. *Nature Communications* 2: 571.

59 Davis, V.A., Parra-Vasquez, A.N.G., Green, M.J. et al. (2009). True solutions of single-walled carbon nanotubes for assembly into macroscopic materials. *Nature Nanotechnology* 4 (12): 830.

60 Song, W.H., Kinloch, I.A., and Windle, A.H. (2003). Nematic liquid crystallinity of multiwall carbon nanotubes. *Science* 302 (5649): 1363.

61 Jalili, R., Aboutalebi, S.H., Esrafilzadeh, D. et al. (2014). Formation and processability of liquid crystalline dispersions of graphene oxide. *Materials Horizons* 1 (1): 87.

62 Li, Y. and Zhang, X. (2022). Electrically conductive, optically responsive, and highly orientated $Ti_3C_2T_x$ MXene aerogel fibers. *Advanced Functional Materials* 32 (4): 2107767.

63 Naguib, M. (2020). Multifunctional pure MXene fiber from liquid crystals of only water and MXene. *ACS Central Science* 6 (3): 344.

64 Shin, H., Eom, W., Lee, K.H. et al. (2021). Highly electroconductive and mechanically strong $Ti_3C_2T_x$ MXene fibers using a deformable MXene gel. *ACS Nano* 15 (2): 3320.

65 Li, T., Chen, L., Yang, X. et al. (2019). A flexible pressure sensor based on an MXene-textile network structure. *Journal of Materials Chemistry C* 7 (4): 1022.

66 Zheng, X., Shen, J., Hu, Q. et al. (2021). Vapor phase polymerized conducting polymer/MXene textiles for wearable electronics. *Nanoscale* 13 (3): 1832.

67 Cao, J., Zhou, Z., Song, Q. et al. (2020). Ultrarobust $Ti_3C_2T_x$ MXene-based soft actuators via bamboo-inspired mesoscale assembly of hybrid nanostructures. *ACS Nano* 14 (6): 7055.

68 Zhu, W.-B., Luo, H.-S., Tang, Z.-H. et al. (2022). $Ti_3C_2T_x$ MXene/bamboo fiber/PDMS pressure sensor with simultaneous ultrawide linear sensing range, superb environmental stability, and excellent biocompatibility. *ACS Sustainable Chemistry & Engineering* 10 (11): 3546.

69 An, H., Habib, T., Shah, S. et al. (2018). Surface-agnostic highly stretchable and bendable conductive MXene multilayers. *Science Advances* 4 (3): eaaq0118.

70 Hu, M., Li, Z., Li, G. et al. (2017). All-solid-state flexible fiber-based MXene supercapacitors. *Advanced Materials Technologies* 2 (10): 1700143.

71 Li, Q., Yin, R., Zhang, D. et al. (2020). All-solid-state flexible fiber-based MXene supercapacitors. *Journal of Materials Chemistry A* 8 (40): 21131.

72 Li, X., Hao, J., Liu, R. et al. (2020). Interfacing MXene flakes on fiber fabric as an ultrafast electron transport layer for high performance textile electrodes. *Energy Storage Materials* 33: 62.

73 Duan, S., Lin, Y., Zhang, C. et al. (2022). Machine-learned, waterproof MXene fiber-based glove platform for underwater interactivities. *Nano Energy* 91: 106650.

74 Seyedin, S., Zhang, J., Usman, K.A.S. et al. (2019). Facile solution processing of stable MXene dispersions towards conductive composite fibers. *Global Challenges* 3 (10): 1900037.

75 He, N., Patil, S., Qu, J. et al. (2020). Effects of electrolyte mediation and MXene size in fiber-shaped supercapacitors. *ACS Applied Energy Materials* 3 (3): 2949.

76 Wang, Y., Zheng, Y., Zhao, J., and Li, Y. (2020). Assembling free-standing and aligned tungstate/MXene fiber for flexible lithium and sodium-ion batteries with efficient pseudocapacitive energy storage. *Energy Storage Materials* 33: 82.

77 Seyedin, S., Uzun, S., Levitt, A. et al. (2020). MXene composite and coaxial fibers with high stretchability and conductivity for wearable strain sensing textiles. *Advanced Functional Materials* 30 (12): 1910504.

78 Cheng, B. and Wu, P. (2021). Scalable fabrication of kevlar/$Ti_3C_2T_x$ MXene intelligent wearable fabrics with multiple sensory capabilities. *ACS Nano* 15 (5): 8676.

79 Davoodi, P., Gill, E.L., Wang, W., and Shery Huang, Y.Y. (2021). Chapter two-advances and innovations in electrospinning technology. In: *Biomedical Applications of Electrospinning and Electrospraying* (ed. N. Kasoju and H. Ye), 2. Woodhead Publishing.

80 Shao, W., Tebyetekerwa, M., Marriam, I. et al. (2018). Polyster@MXene nanofibers-based yarn electrodes. *Journal of Power Sources* 396: 683.

81 Hwang, H., Byun, S., Yuk, S. et al. (2021). High-rate electrospun $Ti_3C_2T_x$ MXene/carbon nanofiber electrodes for flexible supercapacitors. *Applied Surface Science* 556: 149710.

82 Choi, C., Kim, K.M., Kim, K.J. et al. (2016). Improvement of system capacitance via weavable superelastic biscrolled yarn supercapacitors. *Nature Communications* 7: 13811.

83 Lima, M.D., Fang, S., Lepro, X. et al. (2011). Biscrolling nanotube sheets and functional guests into yarns. *Science* 331 (6013): 51.

84 Xiong, D., Shi, Y., and Yang, H.Y. (2021). Rational design of MXene-based films for energy storage: progress, prospects. *Materials Today* 46: 183.

85 Li, G., Wyatt, B.C., Song, F. et al. (2021). 2D titanium carbide (MXene) based films: expanding the frontier of functional film materials. *Advanced Functional Materials* 31 (46): 2105043.

86 Lipatov, A., Lu, H., Alhabeb, M. et al. (2018). Elastic properties of 2D $Ti_3C_2T_x$ MXene monolayers and bilayers. *Science Advances* 4 (6): eaat0491.

87 Chen, H., Wen, Y., Qi, Y. et al. (2020). Pristine titanium carbide MXene films with environmentally stable conductivity and superior mechanical strength. *Advanced Functional Materials* 30 (5): 1906996.

88 Xia, Y., Mathis, T., Zhao, M. et al. (2018). Thickness-independent capacitance of vertically aligned liquid-crystalline MXenes. *Nature* 256: 409.

89 Lukatskaya, M.R., Kota, S., Lin, Z. et al. (2017). Ultra-high-rate pseudocapacitive energy storage in two-dimensional transition metal carbides. *Nature Energy* 2 (8): 17105.

90 Tang, J., Mathis, T., Zhong, X. et al. (2021). Optimizing ion pathway in titanium carbide MXene for practical high-rate supercapacitor. *Advanced Energy Materials* 11 (4): 2003025.

91 Cui, Y., Xie, X., Yang, R. et al. (2019). Cold pressing-built microreactors to thermally manipulate microstructure of MXene film as an anode for high-performance lithium-ion batteries. *Electrochimica Acta* 305: 11.

92 Ji, C., Wang, Y., Ye, Z. et al. (2020). Ice-templated MXene/Ag-epoxy nanocomposites as high-performance thermal management materials. *ACS Applied Materials & Interfaces* 12 (21): 24298.

93 Wang, X., Chen, Y., Hu, F. et al. (2022). Electromagnetic interference shielding performance of flexible, hydrophobic honeycomb-structured Ag@$Ti_3C_2T_x$ composites. *Advanced Electronic Materials* 8 (3): 2101028.

94 Min, G.D., Nam, M.G., Kim, D. et al. (2020). Controlled high-capacity storage of lithium-ions using void-incorporated 3D MXene architectures. *Advanced Materials Interfaces* 7 (14): 2000734.

95 Li, K., Wang, X., Li, S. et al. (2020). An ultrafast conducting polymer@MXene positive electrode with high volumetric capacitance for advanced asymmetric supercapacitors. *Small* 16 (4): e1906851.

96 Kong, J., Yang, H., Guo, X. et al. (2020). High-mass-loading porous $Ti_3C_2T_x$ films for ultrahigh-rate pseudocapacitors. *ACS Energy Letters* 5 (7): 2266.

97 Liu, J., Zhang, H.-B., Sun, R. et al. (2017). Hydrophobic, flexible, and lightweight MXene foams for high-performance electromagnetic-interference shielding. *Advanced Materials* 29 (38): 1702367.

98 Yun, T., Lee, G.S., Choi, J. et al. (2021). Multidimensional $Ti_3C_2T_x$ MXene architectures via interfacial electrochemical self-assembly. *ACS Nano* 15 (6): 10058.

99 Zhao, Z., Wang, S., Wan, F. et al. (2021). Scalable 3D self-assembly of MXene films for flexible sandwich and microsized supercapacitors. *Advanced Functional Materials* 31 (23): 2101302.

100 Yan, J., Ren, C.E., Maleski, K. et al. (2017). Flexible MXene/graphene films for ultrafast supercapacitors with outstanding volumetric capacitance. *Advanced Functional Materials* 27 (30): 1701264.

101 Fan, Z., Wang, Y., Xie, Z. et al. (2018). Modified MXene/holey graphene films for advanced supercapacitor electrodes with superior energy storage. *Advanced Science* 5 (10): 1800750.

102 Wang, H., Li, J., Kuai, X. et al. (2020). Enhanced rate capability of ion-accessible $Ti_3C_2T_x$-NbN hybrid electrodes. *Advanced Energy Materials* 10 (35): 2001411.

103 Xu, D., Ma, K., Chen, L. et al. (2020). MXene interlayer anchored Fe_3O_4 nanocrystals for ultrafast Li-ion batteries. *Chemical Engineering Science* 212: 115342.

104 Tian, Y., An, Y., and Feng, J. (2019). Flexible and freestanding silicon/MXene composite papers for high-performance lithium-ion batteries. *ACS Applied Materials & Interfaces* 11 (10): 10004.

105 Yu, L., Hu, L., Anasori, B. et al. (2018). MXene-bonded activated carbon as a flexible electrode for high-performance supercapacitors. *ACS Energy Letters* 3 (7): 1597.

106 Sun, N., Zhu, Q., Anasori, B. et al. (2019). MXene-bonded flexible hard carbon film as anode for stable Na/K-ion storage. *Advanced Functional Materials* 29 (51): 1906282.

107 Tang, H., Li, W., Pan, L. et al. (2019). A robust, freestanding MXene-sulfur conductive paper for long-lifetime Li-S batteries. *Advanced Functional Materials* 29 (30): 1901907.

108 Gao, X., Du, X., Mathis, T.S. et al. (2020). Maximizing ion accessibility in MXene-knotted carbon nanotube composite electrodes for high-rate electrochemical energy storage. *Nature Communications* 11 (1): 6160.

109 Wu, Z., Liu, X., Shang, T. et al. (2021). Reassembly of MXene hydrogels into flexible films towards compact and ultrafast supercapacitors. *Advanced Functional Materials* 31 (41): 2102874.

110 Ma, Z., Zhou, X., Deng, W. et al. (2018). 3D porous MXene (Ti_3C_2)/reduced graphene oxide hybrid films for advanced lithium storage. *ACS Applied Materials & Interfaces* 10 (4): 3634.

111 Wan, S., Li, X., Chen, Y. et al. (2021). High-strength scalable MXene films through bridging-induced densification. *Science* 374: 96.

112 Vahid Mohammadi, A., Moncada, J., Chen, H. et al. (2018). Thick and freestanding MXene/PANI pseudocapacitive electrodes with ultrahigh specific capacitance. *Journal of Materials Chemistry A* 6 (44): 22123.

113 Gund, G.S., Park, J.H., Harpalsinh, R. et al. (2019). MXene/polymer hybrid materials for flexible AC-filtering electrochemical capacitors. *Joule* 3 (1): 164.

114 Shahzad, F., Alhabeb, M., Hatter, C.B. et al. (2016). Electromagnetic interference shielding with 2D transition metal carbides (MXenes). *Science* 353 (6304): 1137.

115 Ma, L., Bi, Z., Xue, Y. et al. (2020). Bacterial cellulose: an encouraging eco-friendly nano-candidate for energy storage and energy conversion. *Journal of Materials Chemistry A* 8 (12): 5812.

116 Wan, Y., Xiong, P., Liu, J. et al. (2021). Ultrathin, strong, and highly flexible $Ti_3C_2T_x$ MXene/bacterial cellulose composite films for high-performance electromagnetic interference shielding. *ACS Nano* 15 (5): 8439.

117 Wang, Y., Wang, X., Li, X. et al. (2019). Engineering 3D ion transport channels for flexible MXene films with superior capacitive performance. *Advanced Functional Materials* 29 (14): 1900326.

118 V. Thirumal, R. Yuvakkumar, P. S. Kumar, G. Ravi, D. Velauthapillai, Si@ MXene/graphene crumbled spherical nanocomposites. *International Journal of Energy Research*, 2022,46 (7), 21548-21557.

119 Parviz, D., Metzler, S.D., Das, S. et al. (2015). Tailored crumpling and unfolding of spray-dried pristine graphene and graphene oxide sheets. *Small* 11 (22): 2661.

120 Li, X., Zhang, M., You, W. et al. (2020). Magnetized MXene microspheres with multiscale magnetic coupling and enhanced polarized interfaces for distinct microwave absorption via a spray-drying method. *ACS Applied Materials & Interfaces* 12 (15): 18138.

121 Xiu, L., Wang, Z., Yu, M. et al. (2018). Aggregation-resistant 3D MXene-based architecture as efficient bifunctional electrocatalyst for overall water splitting. *ACS Nano* 12 (8): 8017.

122 Natu, V., Sokol, M., Verger, L., and Barsoum, M.W. (2018). Effect of edge charges on stability and aggregation of $Ti_3C_2T_z$ MXene colloidal suspensions. *Journal of Physical Chemistry C* 122 (48): 27745.

123 Lian, P., Dong, Y., Wu, Z.-S. et al. (2017). Alkalized Ti_3C_2 MXene nanoribbons with expanded interlayer spacing for high-capacity sodium and potassium ion batteries. *Nano Energy* 40: 1.

124 Zhao, D., Clites, M., Ying, G. et al. (2018). Alkali-induced crumpling of $Ti_3C_2T_x$ (MXene) to form 3D porous networks for sodium ion storage. *Chemical Communications* 54 (36): 4533.

125 Shi, H., Dong, Y., Zheng, S. et al. (2020). Three dimensional Ti_3C_2 MXene nanoribbon frameworks with uniform potassiophilic sites for the dendrite-free potassium metal anodes. *Nanoscale Advances* 2 (9): 4212.

126 He, X., Ni, Y., Li, Y. et al. (2022). MXene-based metal anode with stepped sodiophilic gradient structure enables a large current density for rechargeable Na-O_2 batteries. *Advanced Materials* e2106565.

127 Dong, Y., Zheng, S., Qin, J. et al. (2018). All-MXene-based integrated electrode constructed by Ti_3C_2 nanoribbon framework host and nanosheet interlayer for high-energy-density Li-S batteries. *ACS Nano* 12 (3): 2381.

128 Zhao, M.Q., Xie, X., Ren, C.E. et al. (2017). Hollow MXene spheres and 3D macroporous MXene frameworks for Na-ion storage. *Advanced Materials* 29 (37): 1702410.

129 Fan, Z., Wei, C., Yu, L. et al. (2020). 3D printing of porous nitrogen-doped Ti_3C_2 MXene scaffolds for high-performance sodium-ion hybrid capacitors. *ACS Nano* 14 (1): 867.

130 Kang, J., Byun, S., Kim, S. et al. (2020). Design of three-dimensional hollow-sphere architecture of $Ti_3C_2T_x$ MXene with graphitic carbon nitride nanoshells for efficient photocatalytic hydrogen evolution. *ACS Applied Energy Materials* 3 (9): 9226.

131 Yue, Y., Liu, N., Liu, W. et al. (2018). 3D hybrid porous MXene-sponge network and its application in piezoresistive sensor. *Nano Energy* 50: 79.

132 Zhao, Q., Zhu, Q., Miao, J. et al. (2019). Flexible 3D porous MXene foam for high-performance lithium-ion batteries. *Small* 15 (51): e1904293.

133 Yang, X., Wang, Q., Zhu, K. et al. (2021). 3D porous oxidation-resistant MXene/graphene architectures induced by in situ zinc template toward high-performance supercapacitors. *Advanced Functional Materials* 31 (20): 2101087.

134 Liang, C., Qiu, H., Song, P. et al. (2020). Ultra-light MXene aerogel/wood-derived porous carbon composites with wall-like "mortar/brick" structures for electromagnetic interference shielding. *Science Bulletin* 65 (8): 616.

135 Wang, Y., Yang, J., Chen, Z., and Hu, Y. (2019). A new flexible and ultralight carbon foam/$Ti_3C_2T_x$ MXene hybrid for high-performance electromagnetic wave absorption. *RSC Advances* 9 (70): 41038.

136 Wang, Q., Wang, S., Guo, X. et al. (2019). MXene-reduced graphene oxide aerogel for aqueous zinc-ion hybrid supercapacitor with ultralong cycle life. *Advanced Electronic Materials* 5 (12): 1900537.

137 Yang, K., Yin, F., Xia, D. et al. (2019). A highly flexible and multifunctional strain sensor based on a network-structured MXene/polyurethane mat with ultra-high sensitivity and a broad sensing range. *Nanoscale* 11 (20): 9949.

138 Liu, Z., Xu, K., She, P. et al. (2016). Self-assembly of 2D MnO_2 nanosheets into high-purity aerogels with ultralow density. *Chemical Science* 7 (3): 1926.

139 Qiu, L., Liu, J.Z., Chang, S.L. et al. (2012). Biomimetic superelastic graphene-based cellular monoliths. *Nature Communications* 3: 1241.

140 Zhang, P., Zhu, Q., Soomro, R.A. et al. (2020). In situ ice template approach to fabricate 3D flexible MXene film-based electrode for high performance supercapacitors. *Advanced Functional Materials* 30 (47): 2000922.

141 Cai, C., Wei, Z., Deng, L., and Fu, Y. (2021). Temperature-invariant superelastic multifunctional MXene aerogels for high-performance photoresponsive supercapacitors and wearable strain sensors. *ACS Applied Materials & Interfaces* 13 (45): 54170.

142 Weng, C., Wang, G., Dai, Z. et al. (2019). Buckled AgNw/MXene hybrid hierarchical sponges for high-performance electromagnetic interference shielding. *Nanoscale* 11 (47): 22804.

143 Chen, H., Ma, H., Zhang, P. et al. (2020). Pristine titanium carbide MXene hydrogel matrix. *ACS Nano* 14 (8): 10471.

144 Deville, S. (2013). Ice-templating, freeze casting: Beyond materials processing. *Journal of Materials Research* 28 (17): 2202.

145 Jin, L., Wang, P., Cao, W. et al. (2022). Isolated solid wall-assisted thermal conductive performance of three-dimensional anisotropic MXene/graphene polymeric composites. *ACS Applied Materials & Interfaces* 14 (1): 1747.

146 Yang, J., Wang, J., Li, H. et al. (2022). MoS_2/MXene aerogel with conformal heterogeneous interfaces tailored by atomic layer deposition for tunable microwave absorption. *Advanced Science* 9 (7): e2101988.

147 Yang, W., Byun, J.J., Yang, J. et al. (2020). Freeze-assisted tape casting of vertically aligned MXene films for high rate performance supercapacitors. *Energy & Environmental Materials* 3 (3): 380.

148 Chen, Q., Wei, Y., Zhang, X. et al. (2022). Vertically aligned MXene nanosheet arrays for high-rate lithium metal anodes. *Advanced Energy Materials* 12: 2200072.

149 Jiang, H., Sheng, Y., and Ngai, T. (2020). Pickering emulsions: versatility of colloidal particles and recent applications. *Current Opinion in Colloid & Interface Science* 49: 1.

150 Fujisawa, S. (2020). Material design of nanocellulose/polymer composites via pickering emulsion templating. *Polymer Journal* 53 (1): 103.

151 Zhao, S., Li, L., Zhang, H.-B. et al. (2020). Janus MXene nanosheets for macroscopic assemblies. *Materials Chemistry Frontiers* 4 (3): 910.

152 Bian, R., Lin, R., Wang, G. et al. (2018). 3D assembly of Ti_3C_2 MXene directed by water/oil interfaces. *Nanoscale* 10 (8): 3621.

153 Shi, S.W., Qian, B.Q., Wu, X.Y. et al. (2019). Self-assembly of MXene-surfactants at liquid-liquid interfaces: from structured liquids to 3D aerogels. *Angewandte Chemie-International Edition* 58 (50): 18171.

154 Deng, Y., Shang, T., Wu, Z. et al. (2019). Fast gelation of $Ti_3C_2T_x$ MXene initiated by metal ions. *Advanced Materials* 31 (43): e1902432.

155 Chen, D., Long, Y., Wu, Z. et al. (2022). A gelation-assisted approach for versatile MXene inks. *Advanced Functional Materials* 32 (36): 2204372.

156 Ding, M., Li, S., Guo, L. et al. (2021). Metal ion-induced assembly of MXene aerogels via biomimetic microtextures for electromagnetic interference shielding, capacitive deionization, and microsupercapacitors. *Advanced Energy Materials* 11 (35): 2101494.

157 Fan, Z., Jin, J., Li, C. et al. (2021). 3D-printed Zn-ion hybrid capacitor enabled by universal divalent cation-gelated additive-free Ti_3C_2 MXene ink. *ACS Nano* 15 (2): 3098.

158 Jiang, D., Zhang, J., Qin, S. et al. (2021). Superelastic $Ti_3C_2T_x$ MXene-based hybrid aerogels for compression-resilient devices. *ACS Nano* 15 (3): 5000.

159 Li, Y., Meng, F., Mei, Y. et al. (2020). Electrospun generation of $Ti_3C_2T_x$ MXene@graphene oxide hybrid aerogel microspheres for tunable high-performance microwave absorption. *Chemical Engineering Journal* 391: 123512.

160 Lin, Z., Liu, J., Peng, W. et al. (2020). Highly stable 3D $Ti_3C_2T_x$ MXene-based foam architectures toward high-performance terahertz radiation shielding. *ACS Nano* 14 (2): 2109.

161 Ma, W., Chen, H., Hou, S. et al. (2019). Compressible highly stable 3D porous MXene/GO foam with a tunable high-performance stealth property in the terahertz band. *ACS Applied Materials & Interfaces* 11 (28): 25369.

162 Shao, L., Xu, J., Ma, J. et al. (2020). MXene/rGO composite aerogels with light and high-strength for supercapacitor electrode materials. *Composites Communications* 19: 108.

163 Chen, Y., Xie, X., Xin, X. et al. (2019). $Ti_3C_2T_x$-based three-dimensional hydrogel by a graphene oxide-assisted self-convergence process for enhanced photoredox catalysis. *ACS Nano* 13 (1): 295.

164 Yang, X., Yao, Y., Wang, Q. et al. (2021). 3D macroporous oxidation-resistant $Ti_3C_2T_x$ MXene hybrid hydrogels for enhanced supercapacitive performances with ultralong cycle life. *Advanced Functional Materials* 32 (10): 2109479.

165 Song, F., Hu, J., Li, G. et al. (2021). Room-temperature assembled MXene-based aerogels for high mass-loading sodium-ion storage. *Nanomicro Letters* 14 (1): 37.

166 Ma, Y., Yue, Y., Zhang, H. et al. (2018). 3D synergistical MXene/reduced graphene oxide aerogel for a piezoresistive sensor. *ACS Nano* 12 (4): 3209.

167 Li, W., Li, X., Chang, W. et al. (2020). Vertically aligned reduced graphene oxide/$Ti_3C_2T_x$ MXene hybrid hydrogel for highly efficient solar steam generation. *Nano Research* 13 (11): 3048.

168 Yang, C., He, H., Jiang, Q. et al. (2021). Pd nanocrystals grown on MXene and reduced graphene oxide co-constructed three-dimensional nanoarchitectures for efficient formic acid oxidation reaction. *International Journal of Hydrogen Energy* 46 (1): 589.

169 Zhang, H., Zhang, P., Zheng, W. et al. (2018). 3D d-Ti_3C_2 xerogel framework decorated with core-shell SnO_2@C for high-performance lithium-ion batteries. *Electrochimica Acta* 285: 94.

170 Tang, X., Liu, H., Guo, X. et al. (2018). A novel lithium-ion hybrid capacitor based on an aerogel-like MXene wrapped Fe_2O_3 nanosphere anode and a 3D nitrogen sulphur dual-doped porous carbon cathode. *Materials Chemistry Frontiers* 2 (10): 1811.

171 Zhang, B., Luo, C., Zhou, G. et al. (2021). Lamellar MXene composite aerogels with sandwiched carbon nanotubes enable stable lithium–sulfur batteries with a high sulfur loading. *Advanced Functional Materials* 31 (26): 2100793.

172 Furukawa, H., Cordova, K.E., O'Keeffe, M., and Yaghi, O.M. (2013). The chemistry and applications of metal-organic frameworks. *Science* 341 (6149): 1230444.

173 Hou, T., Jia, Z., Wang, B. et al. (2021). Metal-organic framework-derived $NiSe_2$-$CoSe_2$@C/$Ti_3C_2T_x$ composites as electromagnetic wave absorbers. *Chemical Engineering Journal* 422: 130079.

174 Zhao, W., Peng, J., Wang, W. et al. (2019). Interlayer hydrogen-bonded metal porphyrin frameworks/MXene hybrid film with high capacitance for flexible all-solid-state supercapacitors. *Small* 15 (18): 1901351.

175 Zhao, X., Xu, H., Hui, Z. et al. (2019). Electrostatically assembling 2D nanosheets of MXene and mof-derivatives into 3D hollow frameworks for enhanced lithium storage. *Small* 15 (47): e1904255.

176 Yao, L., Gu, Q., and Yu, X. (2021). Three-dimensional MOFs@MXene aerogel composite derived MXene threaded hollow carbon confined cos nanoparticles toward advanced alkali-ion batteries. *ACS Nano* 15 (2): 3228.

177 Zheng, J., Pan, X., Huang, X. et al. (2020). Integrated $NiCo_2$-LDHs@MXene/rGO aerogel: componential and structural engineering towards enhanced performance stability of hybrid supercapacitor. *Chemical Engineering Journal* 396: 125197.

178 Li, L., Zhang, M., Zhang, X., and Zhang, Z. (2017). New Ti_3C_2 aerogel as promising negative electrode materials for asymmetric supercapacitors. *Journal of Power Sources* 364: 234.

179 Wang, X., Fu, Q., Wen, J. et al. (2018). 3D $Ti_3C_2T_x$ aerogels with enhanced surface area for high performance supercapacitors. *Nanoscale* 10 (44): 20828.

180 Wang, X., Wang, J., Qin, J. et al. (2020). Surface charge engineering for covalently assembling three-dimensional MXene network for all-climate sodium ion batteries. *ACS Applied Materials & Interfaces* 12 (35): 39181.

181 Le, T.A., Tran, N.Q., Hong, Y., and Lee, H. (2019). Intertwined titanium carbide MXene within a 3D tangled polypyrrole nanowires matrix for enhanced supercapacitor performances. *Chemistry* 25 (4): 1037.

182 Zhang, Y.-Z., Lee, K.H., Anjum, D.H. et al. (2018). MXenes stretch hydrogel sensor performance to new limits. *Science Advances* 4: eaat0098.

183 Zhang, J., Wan, L., Gao, Y. et al. (2019). Highly stretchable and self-healable MXene/polyvinyl alcohol hydrogel electrode for wearable capacitive electronic skin. *Advanced Electronic Materials* 5 (7): 1900285.

184 Zhi, H., Zhang, X., Wang, F. et al. (2021). Flexible $Ti_3C_2T_x$ MXene/pani/bacterial cellulose aerogel for e-skins and gas sensing. *ACS Applied Materials & Interfaces* 13 (38): 45987.

185 Wang, L., Song, P., Lin, C.-T. et al. (2020). 3D shapeable, superior electrically conductive cellulose nanofibers/$Ti_3C_2T_x$ MXene aerogels/epoxy nanocomposites for promising emi shielding. *Research* 2020: 1.

186 Huang, J.J., Wang, T., Su, Y.M. et al. (2021). Hydrophobic MXene/hydroxyethyl cellulose/silicone resin composites with electromagnetic interference shielding. *Advanced Materials Interfaces* 8 (11): 2100186.

187 Zhang, W., Ma, J., Zhang, W. et al. (2020). A multidimensional nanostructural design towards electrochemically stable and mechanically strong hydrogel electrodes. *Nanoscale* 12 (12): 6637.

188 Lee, K.H., Zhang, Y.Z., Jiang, Q. et al. (2020). Ultrasound-driven two-dimensional $Ti_3C_2T_x$ MXene hydrogel generator. *ACS Nano* 14 (3): 3199.

189 Peng, C., Kuai, Z., Li, X. et al. (2021). Facile synthesis of Ag nanoparticles/$Ti_3C_2T_x$/polyacrylamide composite hydrogel as efficient catalyst for methylene blue and 4-nitrophenol reduction. *Materials & Design* 210: 110061.

190 Jiang, Y., Xie, X., Chen, Y. et al. (2018). Hierarchically structured cellulose aerogels with interconnected MXene networks and their enhanced microwave absorption properties. *Journal of Materials Chemistry C* 6 (32): 8679.

191 Yang, M., Yuan, Y., Li, Y. et al. (2020). Anisotropic electromagnetic absorption of aligned $Ti_3C_2T_x$ MXene/gelatin nanocomposite aerogels. *ACS Applied Materials & Interfaces* 12 (29): 33128.

192 Rafieerad, A., Sequiera, G.L., Yan, W. et al. (2020). Sweet-MXene hydrogel with mixed-dimensional components for biomedical applications. *Journal of the Mechanical Behavior of Biomedical Materials* 101: 103440.

193 Yang, M., Xu, Y., Zhang, X. et al. (2022). Bioinspired phototropic MXene-reinforced soft tubular actuators for omnidirectional light-tracking and adaptive photovoltaics. *Advanced Functional Materials* 32 (26): 2201884.

194 Tao, N., Zhang, D., Li, X. et al. (2019). Near-infrared light-responsive hydrogels via peroxide-decorated MXene-initiated polymerization. *Chemical Science* 10 (46): 10765.

195 Ge, G., Zhang, Y.Z., Zhang, W. et al. (2021). $Ti_3C_2T_x$ MXene-activated fast gelation of stretchable and self-healing hydrogels: a molecular approach. *ACS Nano* 15 (2): 2698.

196 Zhang, P., Yang, X.J., Li, P. et al. (2020). Fabrication of novel MXene (Ti_3C_2)/polyacrylamide nanocomposite hydrogels with enhanced mechanical and drug release properties. *Soft Matter* 16 (1): 162.

197 Wang, N., Wu, Z., Long, Y. et al. (2022). MXene-assisted polymer coating from aqueous monomer solution towards dendrite-free zinc anodes. *Journal of Energy Chemistry* 73: 277.

198 Yang, J.-L., Li, J., Zhao, J.-W. et al. (2022). Stable zinc anodes enabled by a zincophilic polyanionic hydrogel layer. *Advanced Materials* 34 (27): 2202382.

Part III

Guidelines on Obtaining MXenes Properties

16

Insights into the Properties of MXenes and MXene Analogs from Atomistic Simulation

Murali Gopal Muraleedharan, Rabi Khanal, Stephan Irle, and Paul R. C. Kent

Computational Sciences and Engineering Division, Oak Ridge National Laboratory, Oak Ridge, TN, USA

16.1 Introduction

[1]MXenes (M_nX_{n-1}) were first described by Naguib et al., in 2011 as two-dimensional (2D) freestanding crystals that can be synthesized via room temperature exfoliation or chemical etching of a parent "MAX" phase in hydrofluoric acid, such as in the production of the prototypical MXene Ti_3C_2 from Ti_3AlC_2 [1]. (M is typically an early transition metal, A is aluminum, and X typically a carbon.) Since the first synthesis, the number of publications on MXenes and their analogs has seen nearly exponential growth that currently appears to overtake the rate of publications on graphene [2]. It is interesting to note that the birth of this rapidly rising new class of materials was intimately linked to predictions from atomistic simulations beginning with the very first publication, which included predicted electronic band structures for MXenes with different terminations [1]. The measured and predicted good electronic conductivity of the treated materials was quickly recognized as promising for applications in rechargeable Li-ion batteries,

1 This manuscript has been authored by UT-Battelle, LLC under Contract No. DE-AC05-00OR22725 with the US Department of Energy. The United States Government retains and the publisher, by accepting the article for publication, acknowledges that the United States Government retains a nonexclusive, paid-up, irrevocable, worldwide license to publish or reproduce the published form of this manuscript, or allow others to do so, for United States Government purposes. The Department of Energy will provide public access to these results of federally sponsored research in accordance with the DOE Public Access Plan (https://energy.gov/downloads/doe-public-access-plan).

Transition Metal Carbides and Nitrides (MXenes) Handbook: Synthesis, Processing, Properties and Applications, First Edition. Edited by Chuanfang Zhang and Michael Naguib.
© 2024 John Wiley & Sons, Inc. Published 2024 by John Wiley & Sons, Inc.

supercapacitors, and other electronic applications [3]. Indeed, a majority of applications for MXene and their analogs are in energy storage, most prominently for batteries and supercapacitors, where a substantial number of prior reviews and book chapters have already appeared, encompassing a multitude of computational works [3–11]. Other rapidly growing playing fields are the use of MXenes in electrocatalysis, for example, oxygen evolution reaction, hydrogen evolution reaction (HER), and nitrogen fixation [12, 13] as well as in gas sensors and as polymer matrix composites [14].

In this chapter, we present a comprehensive review of MXene types, structures, stability, electronic properties, ionic storage, and transport from the perspective of energy storage. We cover insights gained from atomistic simulations that share the capability of either explicitly or implicitly, considering electronic structure and thereby allowing the simulation of electron transfer and/or bond-breaking/formation processes. As MXenes are layered 2D materials with nanometer-sized interlayer stacking distances, computational methods need to be able to adequately model materials properties that are highly complex, including a rich structural composition including chemical composition as typical point defects, structural diversity in terms of surface functional groups originating from mixtures of typical surface terminations such as –OH, –O, –F or –Cl, solvation by electrolytes, and surface redox reactions, etc. These complex properties call for a hierarchy of methodologies, loosely coupled in a multiscale simulation framework, as will be detailed in the following sections. It is the purpose of this chapter to compile in a comprehensive manner the relevant surface and electrochemical aspects that need to be considered when designing MXene applications for energy storage applications.

16.2 Computational Methods

In the context of computational materials design for energy storage applications, it is vital that ion storage and transport are faithfully modeled, both in bulk electrolytes and under confinement. In the case of MXenes as electrode materials, an accurate description of the electronic band structure and surface redox chemistry is equally important. Crucially, any physics-based modeling must be able to bridge the necessary length and time scales required to accurately describe electronic, atomic, and cooperative effects occurring on nanometer scales through complimentary, method-specific capabilities.

While it would be ideal to employ electronic density functional theory (DFT) [15, 16] and *ab initio* molecular dynamics (AIMD) [17, 18] on all scales due to its superior transferability and accuracy, DFT is still limited to systems containing merely hundreds of atoms and simulation time lengths on the order of tens of

picoseconds, due to computational resource requirements such as CPU time and memory size. To access greater system sizes (>500 atoms) and timescales (>100 ps), other methods must be employed even on modern-day supercomputers. On the other hand, approximate quantum chemical methods such as the density-functional tight-binding (DFTB) approach [19, 20] can treat systems several orders of magnitude larger, overcoming the limited number of solvation shells and surface functionalization compositions that can be studied with conventional DFT. The approximate quantum chemical DFTB method has been successfully applied to studies of cations solvation shells, proton transport, and diffusion [21–24], indicating that the technique is applicable, and sufficiently accurate DFTB parameterizations can be obtained. For larger scales, for example, >10 000 atoms and >5 ns, it is nevertheless still necessary to utilize reactive classical molecular dynamics (CMD, e.g., ReaxFF [25]) formalisms. It is important to mention that ReaxFF includes dynamic charge updating schemes such as the popular charge equilibration method [26]. Each level of theory (DFT, DFTB, and ReaxFF) can serve to generate reference data for evaluating the performance of the others, that is, either by means of upscaling through parameterization of the approximate methods or in a downscaling approach where localized, rare events occurring in CMD or DFTB simulations are analyzed in greater detail with smaller model systems. Examples of such events are surface protonation, metal aggregation on surfaces, surface redox reactions, and Grotthuss transport mechanisms, etc.

In the following sections, we will first describe the structural complexity of MXenes along with their potential for inverse materials design, before describing static structural and electronic properties that lay the groundwork for dynamic energy storage applications in conjunction with ion storage and transport. We conclude this chapter with a summary and future outlook on the challenges and opportunities that lie ahead for the rapidly growing MXene materials class.

16.3 Structures of MXenes and MXene Analogs

Since their initial discovery, a myriad of compositional and structural variations of MXenes have been subjected to investigation. Figure 16.1 shows a glimpse of the span of transition metal atom (M), nonmetal X atom, and surface functional termination groups T, clearly showing the diversity of various MXene compounds, as well as other variations and analogs that have been either synthesized or simulated. These will be described in more detail in the later sections.

Figure 16.1a, b show the top and side views of traditional carbide MXenes Ti_3C_2 and $Ti_3C_2(OH)_2$, respectively. Carbide MXenes have been by far the most extensively studied MXenes followed at a long distance by nitrides [27, 30–32].

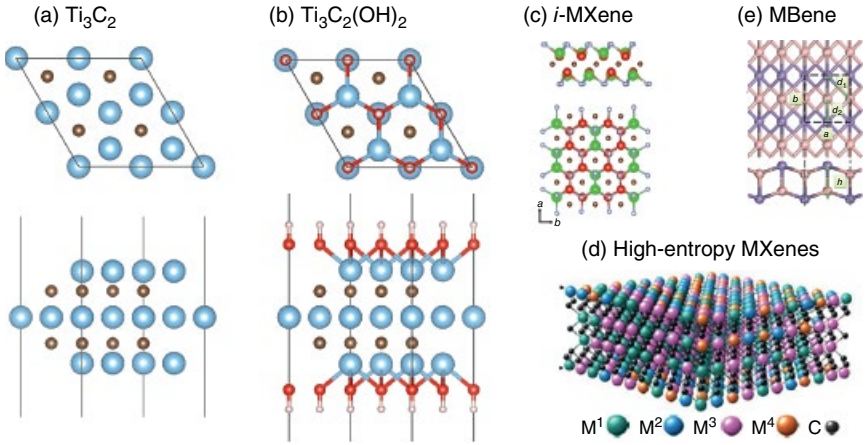


Figure 16.1 Structures of traditional MXenes and their compositional variants. (a) Top and side views of Ti_3C_2 from the Computational 2D-Materials Database (C2DB). (b) Top and side views of $Ti_3C_2(OH)_2$. *Source:* Adapted from Haastrup et al. [27]. (c) Top and side views of functionalized *i*-MXenes with chemical groups (F, O, or OH). The attached chemical groups are indicated by small gray spheres. *Source:* Khazaei et al. [7]/American Physical Society. (d) Isometric view of a high-entropy MXene $TiVNbMoC_3T_x$, and (e) Top and side views of a 2D MnB (MBene) sheet called *i*-MAX phases. Khazaei et al. [28] have investigated the structural, electronic, and piezoelectric properties of experimentally synthesized *i*MAX phases: $(Mo_{2/3}Sc_{1/3})_2AlC$, $(Mo_{2/3}Y_{1/3})_2AlC$, $(W_{2/3}Sc_{1/3})_2AlC$, $(W_{2/3}Y_{1/3})_2AlC$, and $(V_{2/3}Zr_{1/3})_2AlC$) and their possible 2D *i*-MXene derivatives: $(Mo_{2/3}Sc_{1/3})_2C$, $(Mo_{2/3}Y_{1/3})_2C$, $(W_{2/3}Sc_{1/3})_2C$, $(W_{2/3}Y_{1/3})_2C$, and $(V_{2/3}Zr_{1/3})_2C$. (e) The side and top views of functionalized *i*-MXenes with chemical groups (−F, −O, or −OH). The attached chemical groups are indicated by small gray spheres. *Source:* Neman et al. [29]/American Chemical Society.

Besides the conventional MXenes, with chemical formula M_nX_{n-1}, many variations now exist. These include *i*-MXenes [28] (Figure 16.1c), high-entropy MXenes [29], multimetal atom MXenes [33], and doped MXenes [34].

i-MXenes are 2D derivatives of in-plane ordered $(M'_{2/3}M''_{1/3})_2AX$ MAX phases.

High-entropy MXenes, similar to high-entropy alloys, consist of equiatomic concentrations of multiple transition metal atoms randomly dispersed at the metal lattice sites. In the combined DFT-experimental work reported in Reference [29], the authors have considered monolayers of $TiVNbMoC_3T_x$ (Figure 16.1d) and $TiVCrMoC_3T_x$, delaminated from their corresponding MAX phases.

Boride MXenes or MBenes [35] have also been subject to computational studies. For instance, Figure 16.1e shows the top and side views of a 2D MnB MBene sheet reported in Reference [35]. In this work, the authors have considered a range of 2D transitional metal borides with a general formula M_xB_y, and have identified 12

unprecedented 2D MBenes worth exploring further, including MnB, HfB, ZrB, Au_2B, Mo_2B, Nb_5B_2, Nb_3B_4, Ta_3B_4, V_3B_4, OsB_2, FeB_2, and RuB_2. Likewise, analogs of traditional MXenes, that is, partially substituted compounds such as boron-nitrides [36, 37], carbon-nitrides [38], and carbon-borides [39] have also been designed *in silica*, and their structure, stability, and other exotic properties have been investigated solely relying on *ab initia* calculations.

The now very broad range of MXenes and MXene analogs creates enormous opportunities for researchers in the area of materials design and discovery. To aid in the prioritization of which compositions and structures are studied for different applications, high quality guidance from simulation is clearly desirable.

16.4 Predicted Structures and Thermodynamic Stabilities

Prior to conducting rather computationally expensive electronic structure alculations, it is a common practice to determine the static structural properties and stability levels of a newly designed material. In this section, we review existing literature and outline a standard procedure to perform structure and stability calculations of MXenes.

16.4.1 Structure Prediction

Accurate prediction of structural properties (mainly lattice constant [a], layer thickness [L], and bond lengths [d]) is an essential step in any routine computational investigation of material properties. Structural relaxation of MXenes gives the ground state structural properties, which is computationally feasible even for rather large unit cells from a DFT perspective. Moreover, structural properties can be experimentally verified. Xie and Kent [30] have demonstrated how structural properties of MXenes can be systematically predicted using an all-electron projector augment wave method [40]. They used both the Perdew–Burke–Ernzerhof (PBE) version of generalized gradient approximation (GGA), and the Heyd–Scuseria–Ernzerhof (HSE06) hybrid functional to describe the exchange correlation energy. The initial structural models of MXenes were constructed by removing the A atom from bulk "MAX" phases. Table 16.1 compares the PBE versus HSE06 predicted structural properties of Ti-carbon and nitrogen MXenes [28, 30].

Firstly, note the excellent agreement with experimental data for both the functionals indicating that the effect of the choice of functionals on the accuracy of structural properties is minimal. Also note that the HSE06 lattice parameters and bond lengths are about 0.02–0.03 Å smaller than for PBE, except for Ti_2NH_2, where the HSE06 lattice parameter is 0.15 Å longer. Likewise, the O-terminated MXenes have the shortest d_{Ti-T} and the longest d_{Ti-X} bond lengths, implying a

Table 16.1 Equilibrium lattice parameter (a), thickness of the monolayer (L), and bond lengths between surface Ti atom and termination (d_{Ti-T}), and nearest C/N atom (d_{Ti-X}) of selected functionalized MXenes.

$Ti_{n+1}C_nT_2$		a (Å)	L (Å)	d_{Ti-C} (Å)	d_{Ti-T} (Å)	$Ti_{n+1}N_nT_2$		a (Å)	L (Å)	d_{Ti-N} (Å)	d_{Ti-T} (Å)
Ti_2CF_2	Theo.†	3.0587	4.84	2.10	2.16	Ti_2NF_2	Theo.†	3.0704	4.69	2.07	2.16
	PBE	3.0583	4.80	2.10	2.16		PBE	3.0642	4.63	2.07	2.16
	HSE	3.0312	4.72	2.08	2.14		HSE	3.0460	4.55	2.05	2.14
Ti_2CO_2	Theo.†	3.0349	4.47	2.19	1.98	Ti_2NO_2	Theo.†	3.0191	4.28	2.17	1.93
	PBE	3.0329	4.45	2.19	1.98		PBE	3.0030	4.35	2.15	1.98
	HSE	3.0093	4.40	2.17	1.96		HSE	2.9743	4.29	2.13	1.86
$Ti_2C(OH)_2$	Theo.†	3.0715	6.75	2.11	2.18	$Ti_2N(OH)_2$	Theo.†	3.0635	6.68	2.08	2.17
	PBE	3.0712	6.79	2.12	2.18		PBE	3.0635	6.66	2.08	2.17
	HSE	3.0464	6.71	2.09	2.17		HSE	3.0447	6.56	2.06	2.16
Ti_2CH_2	PBE	3.0357	4.28	2.10	2.01	Ti_2NH_2	PBE	2.9882	4.20	2.07	2.00
	HSE	3.0094	4.24	2.08	1.99		HSE	3.0127	4.11	2.04	2.00
$Ti_3C_2F_2$	Theo.†	3.0792	7.23	2.08	2.17	$Ti_3N_2F_2$					
	PBE	3.0775	7.21	2.08	2.17		PBE	3.0226	7.15	2.07	2.15
	HSE	3.0508	7.14	2.06	2.15		HSE	2.9945	7.07	2.04	2.14
$Ti_4C_3F_2$	Theo.†	3.0856	9.70	2.08	2.17	$Ti_4N_3F_2$	Theo.†	3.0287	9.45	2.06	2.15
	PBE	3.0844	9.67	2.07	2.17		PBE	3.0268	9.62	2.06	2.15
	HSE	3.0582	9.58	2.05	2.16		HSE	3.0041	9.49	2.04	2.14
$Ti_5C_4F_2$	Theo.†	3.0828	12.15	2.08	2.17	$Ti_5N_4F_2$					

	PBE	3.0794	12.19	2.08	2.17		PBE	3.0226	12.09	2.07	2.15
	HSE	3.0528	12.09	2.06	2.15		HSE	2.9947	11.96	2.04	2.13
$Ti_6C_5F_2$	PBE	3.0744	14.72	2.08	2.17	$Ti_6N_5F_2$	PBE	3.0235	14.52	2.05	2.16
	HSE	3.0456	14.63	2.06	2.15		HSE	2.9932	14.37	2.04	2.13
$Ti_7C_6F_2$	PBE	3.0719	17.24	2.08	2.17	$Ti_7N_6F_2$	PBE	3.0222	16.97	2.05	2.15
	HSE	3.0441	17.13	2.06	2.15		HSE	2.9945	16.78	2.03	2.14
$Ti_8C_7F_2$	PBE	3.0730	19.73	2.08	2.17	$Ti_8N_7F_2$	PBE	3.0194	19.45	2.05	2.15
	HSE	3.0442	19.61	2.08	2.15		HSE	2.9913	19.23	2.03	2.13
$Ti_9C_8F_2$	PBE	3.0728	22.22	2.08	2.17	$Ti_9N_8F_2$	PBE	3.0200	21.87	2.05	2.15
	HSE	3.0453	22.08	2.06	2.15		HSE	2.9932	21.62	2.03	2.13
$Ti_{10}C_9F_2$	PBE	3.0723	24.72	2.08	2.17	$Ti_{10}N_9F_2$	PBE	3.0179	24.34	2.05	2.15
	HSE	3.0448	24.56	2.06	2.15		HSE	2.9874	24.13	2.03	2.13

Source: Data and table reproduced from Xie and Kent [30], † from Khazaei et al. [28].

strong interaction between surface Ti atoms and O. Carbides, in general have larger lattice constants and longer bond lengths than nitrides, correlating with the atomic radii difference between C and N. The PBE-GGA approach is inexpensive compared with the hybrid functionals, and therefore, may be preferred for structure prediction of single MXenes.

In addition to traditional MXenes, the PBE-GGA approach has been used to predict structural properties of *i*-MXenes [7], MBenes [35], and analogs such as boron-nitrides [36, 37] and carbon-nitrides [38]. For *i*-MXenes [7], the computed lattice parameters of 5 *i*-MAX phases ($(Mo_{2/3}Sc_{1/3})_2AlC$, $(Mo_{2/3}Y_{1/3})_2AlC$, $(W_{2/3}Sc_{1/3})_2AlC$, $(W_{2/3}Y_{1/3})_2AlC$, and $(V_{2/3}Zr_{2/3})_2AlC$) showed excellent agreement with experimental data despite their chemical complexity. On the other hand, for MBenes [35], the predicted structure emerged to be a rectangular lattice with space group *Pmma* unlike the hexagonal lattice of traditional MXenes. The M—B bond lengths were computed to be larger than M—C and M—N bonds owing to the weaker M—B bonds. Likewise, the one-dimensional zigzag chains that one would expect in bulk MnB, CrB, and MoB were also found in the 2D monolayer. Similarly, the PBE-GGA method was employed for structure prediction of novel MXenes analogues such as BN's [36, 37] and CN's [38]; the predicted structural properties showed similarity with traditional carbide MXenes. For instance, a hexagonal unit cell was found to have the lowest energy with Ti-B (2.249 Å) bond lengths larger than Ti-N (2.054 Å) and Ti-C (2.064 Å) bonds. The predicted lattice constant *a* of Ti_3CN was 3.07 Å and that of Ti_3BN was 3.095 Å, both of which are comparable with that of Ti_3C_2 (3.099 Å) [27], again indicating that PBE-GGA yields a relatively accurate yet also computationally inexpensive structure prediction.

16.4.2 Stability Prediction

In the current practice of *in silico* materials discovery, as the first step, a sequence of relatively inexpensive DFT-based stability tests are conducted to filter out stable materials before other computationally expensive properties are calculated and synthesis efforts are suggested. These include thermodynamic/phase stability, phonon (dynamic) stability, mechanical stability, finite temperature stability, and electrochemical stability.

Thermodynamic stability can be quantified by means of energy above convex hull (E-hull) [41]. E-hull distinguishes phases with energies below those for all possible mixtures of competing phases with the same compositions. If the considered compound is stable, its E-hull will be ≤ 0. A positive E-hull indicates that the material would decompose to constituent phases with lower formation energies. However, for MXenes, which are 2D materials etched or exfoliated from bulk MAX phases, we also need to account for the exfoliation energy. This can be accounted for in the form of a slightly positive E-hull. In other words, a stable 2D

material could still have E-hull ≥ 0. DFT-calculation of E-hull of isolated MXene layers has limitations when compared with experiments, which include uncertainties in the energies from the approximate exchange-correlation functional, exclusion of substrate interactions that can stabilize the monolayer, and kinetic barriers that separate the monolayer from other lower energy phases leaving the monolayer in a metastable state [27]. Hence, materials with E-hull < 0.4 eV per atom have been deemed as sufficiently stable, following the rationale in References [27, 42, 43].

Passing the phase stability criterion is one of the first and essential steps in the screening procedure. Several researchers have calculated E-hull from DFT formation energies to adjudicate the thermodynamic stability of MXenes and MAX phases [35, 37, 38, 44–46]. Miao et al. performed a high-throughput discovery of MAB phases (boride variants of MAX) and MBene derivatives. In this work, firstly, E-hull of these MAB phases were calculated and classified them into three categories: stable (<70 meV), metastable (70–400 meV), and unstable (>400 meV) phases. MAB phases such as Hf_2InB_2, Hf_2SnB_2, Zr_2TlB_2, Zr_2PbB_2, Zr_2InB_2, Hf_3PB_4, Zr_3CdB_4, Hf_2BiB, and Hf_2PbB were found to be thermodynamically stable with respect to their competing phases. They found 64 new stable borides whose layered phases can be prepared by applying thermodynamic work such as temperature, pressure, chemical, and surface energy. The role of surface structures in stabilizing the MXene layers has also been explored. Tao et al. [46] varied the content of F, O, and OH terminations on $M_3C_2T_xT'_{2-x}$ MXenes, where M = Ti and Nb, and T = F, O, and OH, respectively. They found that the E-hull showed a linear relationship with the proportion of terminations for all of the kinds of MXenes considered. It was also noted that the slope of the linear relationship is different for different terminations indicating that the functional group's ability to stabilize the monolayer can be assessed from the change in E-hull with x.

Under equilibrium, a crystal is dynamically stable if its energy increases as a function of any combinations of atomic displacements [47]. This constitutes all phonons with real and positive frequencies. In the case of a negative or imaginary phonon frequency, the system will be dynamically unstable, which means that some atomic displacements reduce the energy in the vicinity of the assumed atomic positions. Researchers have utilized density functional perturbation theory (DFPT) [48] and finite displacement methods [47] to obtain the phonon band structures. In the pursuit of discovering phonon-stable boron-nitrides, Wu et al. [37] computed the phonon band structures of Ti, Zr, V, and Nb BN's using DFPT along the high-symmetry Γ–X–M–Γ direction. They found that while Ti_2BN and Zr_2BN possessed all positive phonon modes, V_2BN and Nb_2BN had significant imaginary frequencies at r and X points indicating that these monolayers are dynamically unstable. Meanwhile, several MXene phases with and without phonon stability have been reported in the high-throughput DFT studies of Haastrup

et al. [27, 43] and tabulated in the Computational 2D-Materials Database (C2DB). The readers are advised to visit the C2DB workflow to understand how the phonon stability analysis can be utilized in novel MXene discovery.

Additionally, phonon calculations have also provided insights into synthesizability of MXenes *viz.* exfoliability and chemical etchability. Extensive phonon calculations have been performed to correlate bond stiffness (force constants) to bond-lengths [49]. In essence, they analyzed 82 experimentally observed MAX phases and obtained the interatomic force constants from the second derivative of total energy with respect to finite displacement of atoms. They found that the M—X bonds are stronger than M—A bonds from their higher force constant values, indicating that stable MXenes are exfoliable from corresponding MAX phases by breaking the M—A bonds relatively easily. They also analyzed the effects of charges on bond strength by analyzing force constants as a function of charge injected. An increase in force constant was obtained with the removal of electrons. Especially for Ti—Al bonds, a large enough supply of positive charge weakens the bonds to an extent that the bond breaks and frees up the MXene layers. This analysis gives insights on how the chemical etching-based synthesis of MXenes can be carried out for the specific MAX phase in question.

Mechanical stability and finite temperature structural stability are other aspects that have also been studied in the past. To assess if a MXene monolayer will be mechanically stable, under applied external stress, it will be necessary and sufficient to check the mechanical stability criteria following Mouhat and Coudert [50]. This states that the necessary and sufficient conditions for a 2D hexagonal crystal lattice to be mechanically stable, are, $C_{11}.C_{22}-C_{i2}^{2} > 0$ and $C_{66} > 0$, where $C_{66} = (C_{11}-C_{12})/2$, which is a generalized version of Born stability conditions [50]. Haastrup et al. have employed a straightforward approach, wherein the material is strained by $\pm 1\%$ along one of the axes x or y, and the stress tensor is calculated. Thereafter, the mechanical stability criteria was tested and stable materials were identified. In the discovery of novel MBene structures, Miao et al. have calculated the mechanical stability of thermodynamically stable borides [45]. They have reported a remarkably high mechanical stability (and therefore Young's modulus) for M_2XO_2, $M_2X_2O_2$, and $M_3B_4O_2$, and low stability levels of $M_2X_2Cl_2$. In general, the presence of functional groups yielded higher stiffness than bare MBenes. Finite temperature stability has been assessed by means of AIMD simulations. Since they are computationally expensive, they have been mostly conducted only after a preliminary screening process based on thermodynamic and phonon stability analysis [42]. Contrariwise to this norm, in a recent work that attempted to screen MXenes for Li-ion battery anodes [45], the authors have performed a constant volume and temperature (NVT) AIMD run for 10 ps to filter out the stable materials in the first stage. They have found that the structures of Cr_2C, Cr_2N,

CrN_2, VN_2, and VC_2 underwent severe structural distortions within the 10 ps simulation time. While the other materials were considered to be stable in this time frame, it is unsure whether the materials would distort with time. Therefore, a longer timescale simulation with constant monitoring of energy as a function of time is recommended for practical applications of this strategy.

Eventually, a selected MXene compound for energy storage or catalysis applications will have to be subjected to external potentials and an electrolyte with varying pH levels. Hence, the electrochemical stability also needs to be assessed in the design process. Pourbaix diagram gives insights to aqueous stability at applied potential and pH. It represents electrochemical stability for different redox states of an element as a function of pH. They are phase diagrams that map the conditions of potential and pH (typically in aqueous solutions) where different redox species are stable. Pourbaix diagrams of MXenes have mostly been generated from catalysis perspectives, which is not a focus of this chapter. However, for more insights, readers are advised to follow References [51, 52].

In the next section, we discuss how *ab initio* calculations have been employed to determine the electronic structure of MXenes, which serves as the base for the prediction of their electronic properties.

16.5 Electronic Properties

In this section, we review the fundamental electronic properties of MXenes and MXene analogs from DFT methods. For properties such as the electronic band structure of bulk MXenes, these are computationally cheap enough that they are a standard part of MXene investigations and can also be applied to entire material series to study trends. Indeed, the first paper on MXenes [1] already included a DFT prediction of the band structures of Ti_3C_2, and these as well as other early results, for example, References [28, 30], are still well-supported by current calculations.

The qualitative and quantitative accuracy of approximate density functionals is a concern for many classes of materials, particularly those with strong spin-lattice-charge interactions. Fortunately, in the case of the majority of MXenes studied, standard and computationally cheap density functionals give both useful accurate trends and quantitative results for the structure and band structure. This was originally studied in [30], where hybrid functionals were shown to yield only small refinements over the much cheaper PBE [53] functional. Recently Bae et al. [54] performed a systematic study of M_2CT_2 with M = Ti, Sc, Y, La, Ti, Zr, Hf, V, Nb, Ta, Mo, W, and T = O, F, using the PBE, PBE+U, SCAN [55], and HSE06 [56] functionals. They concluded that, while PBE appears sufficient for most of the MXenes, for five of the studied MXenes, qualitatively different electronic

structures were predicted by the different functionals, leading to different ground-state structures and magnetic configurations. Therefore, general trends can be examined and materials databases constructed, e.g. Reference [27], but some caution is still required, particularly for quantities that are not yet benchmarked. For example, the influence of the van der Waals interaction on MXene stacking has been difficult to validate versus experiments due to the uncertainties in experimental structures, such as their varied terminations.

In Figure 16.2a, b, we show the total and partial densities of states (DOS, PDOS) for the parent MAX bulk phases Ti_2AlC and Ti_2AlN, and for the monolayer MXenes Ti_2CT_2 and Ti_2NT_2, where T are the terminations O, F, H, and OH, computed with the HSE06 density functional. The DOS and PDOS are typical of most of the MXenes that have been studied to-date. As expected, the parent MAX phases are metallic with a large DOS at the Fermi level (aligned with zero energy in Figure 16.2). When examining the bare (or unterminated) MXene we find a metallic DOS, with a large contribution from the Ti 3d states at the Fermi energy. The relatively high DOS at this energy suggests that high electrical conductivity can be expected. For the terminated cases, both carbide and nitride, we see that the terminations do result in significant changes to the PDOS, due to the varying strength of hybridization between the surface titanium atoms and the terminations. However, only in the case of the oxygen termination is a band gap predicted to open, while in all other cases, the MXenes remain metallic. MXenes with mixed terminations will therefore likely retain the metallicity.

The ability to vary the surface terminations of MXenes is a distinguishing feature from many other 2D nanomaterials such as graphene, BN, and MoS_2, and is one key way to tailor their properties. In [58], Schultz et al. showed how the electronic properties of $Ti_3C_2T_x$ including the work function were modified by different surface terminations, on the basis of DFT calculations and in experiments by manipulating the annealing temperatures, and combinations of photoelectron and inverse photoelectron spectroscopies. Work function engineering using MXenes was later employed by Agresti et al. [59] to modify the electron transport in halide perovskite solar cells resulting in enhanced efficiency and reduced hysteresis.

The range of electronic properties displayed by MXenes is significantly expanded in MXene compositions incorporating multiple metal atoms. Depending on the species involved, these can form solid solutions with near-random distribution of different metal atoms on the "M" sites or form ordered structures. In Reference [60], it was shown theoretically that for many of the potential pairs of early transition metals, ordered structures would be energetically preferred, with one on the outside of the MXene and the other in the inner layer. Ordered Mo_2TiC_2, $MoTi_2C_3$, and Cr_2TiC_2 were synthesized and shown to display distinct electrochemical properties from Ti_3C_2. In Reference [61], Sun

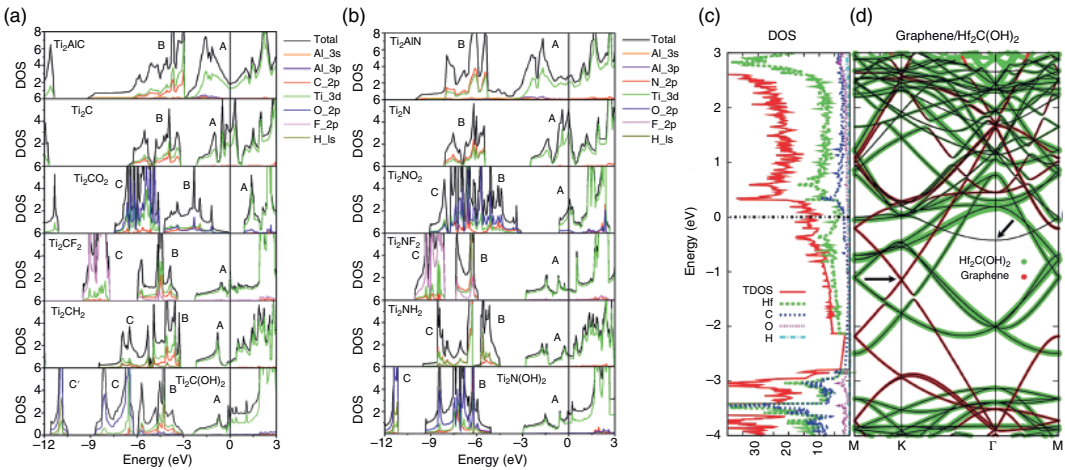


Figure 16.2 Electronic properties of MXenes. Partial density of states of (a) Ti_2CT_2 and (b) Ti_2NT_2, and related MXenes and MAX phase computed using the HSE06 functional. *Source:* Xie and Kent [30]/American Physical Society. (c) and (d) Density of states (DOS in states/eV/cell) and projected band structure of graphene/$Hf_2C(OH)_2$ heterostructure. Arrows in (d) indicate the position of the Dirac cone at K and the nearly free electron band at *r*. The Fermi level is located at zero. *Source:* Khazaei et al. [57]/American Physical Society.

et al. performed calculations for TiM_2X_2T (M = V, Cr, Mn; X = C, N; T = H, F, O, OH). In particular for the ordered chromium and manganese-nitride MXenes, termination-dependent metal-insulator transitions were predicted, including an over 1 eV band gap for $TiMn_2N_2F_2$ using the HSE06 functional. The possibility of achieving large band gaps in MXenes has however yet to be demonstrated experimentally.

In contrast to the ordered multiple-metal atom MXenes, which require fixed ratios of the different species, solid solutions open up the possibility of continuously varying the ratios and composition. As an example, Han et al. [62] systematically investigated binary solid-solutions of Ti, Nb, and/or V at the M-site in M_2XT, with X = C or N. They predicted unlimited solubility of the metal atoms and highly tunable functionality, including optical absorption from ultraviolet to near-infrared wavelength, and electrical conductivity varying by several orders of magnitude, depending on the temperature.

Very recently, high-entropy MAX phases and MXenes have been proposed and synthesized [29, 63, 64], yet again expanding the compositional space of MXenes. These incorporated up to five transition metal elements in equiatomic concentrations. While predicted to be thermodynamically stable, the extent to which these MXenes extend the accessible range of electronic properties remains to be determined.

Beyond the wide interest in MXenes for energy storage (discussed in Section 16.6) and catalysis, they also display a rich range of interesting properties directly related to their electronic structures. In the following, we consider a few: First, already in 2013, Khazaei et al. [28] suggested that narrow gap MXenes would display large Seebeck coefficients and attributed this to the large DOS at the bottom of the conduction band and low DOS at the top of the valence band. Second, certain MXenes, for example, $Ti_3N_2F_2$, display a potentially topologically insulating band structure or can be converted to one through the application of strain [57, 65]. Figure 16.2c, d shows the predicted DOS and band structure, respectively, for a graphene/$Hf_2C(OH)_2$ heterostructure with the Dirac cone at K indicated. (The extent to which topological behavior is retained in imperfect MXenes with varying termination or defects has yet to be studied.) Third, Zhang et al. [66] predicted three types of ferroelectric MXene via high-throughput search and DFT in the phases Nb_2CS_2, Ta_2CS_2, Sc_2CO_2, Y_2CO_2, Sc_2CS_2, and Y_2CS_2. Most intriguingly, Sc_2CS_2 and Y_2CS_2 both show an out-of-plane auxeticity that is triggered by in-plane tensile strains. Fourth, and finally, superconductivity has been both predicted and measured in MXenes. Kamysbayev et al. experimentally found a superconducting transition at 6 K in Nb_2CCl_2 MXene [67], while the parent MAX phase Nb_2AlC has a reported $T_c \sim 0.44$ K. MXene with O, OH, or F termination showed no superconductivity. Bekaert et al. [68] performed DFT calculations. Within Eliashberg theory and the range of MXenes considered, the highest

predicted T_c is 16 K for Mo_2N. While the role of terminations was not studied, this result indicates that MXenes can have favorable electron-phonon couplings, promoting superconductivity.

Overall, despite the decade of study of MXene electronic properties, the recently greatly expanded range of structures, compositions, and terminations – including MXene analogs such as the *i*-MXenes and MBenes – indicates that an expanded survey of the electronic properties is needed and that as-yet unrealized properties may still be achievable in MXenes.

16.6 Energy Storage Properties

Having discussed how relatively inexpensive DFT calculations can be used to compute electronic structure with useful accuracy, in this section and the next, we discuss how *ab initia* methods and molecular simulations can be used to investigate energy storage properties of MXenes *viz.* ion storage and transport in bulk and confinements. In this section, we focus on ion adsorption properties, surface redox reactions, and capacitive double-layer storage, and finally ion mobility, relevant to rechargeable metal-ion batteries and supercapacitor applications.

16.6.1 Rechargeable Metal-Ion Batteries

Ab initio calculations have been useful in shedding light on the ion adsorption behavior and redox reactions on MXene surfaces [31, 32, 69]. In this section, we review the successful applications of different *ab initio* calculations in determining ion storage mechanisms, open circuit voltage prediction, and finally how these descriptors have been used to screen/discover MXenes as rechargeable battery anode materials.

Trends in ion adsorption energy (E_{ads}) and charge transfer reveal ample information on whether a MXene will make a promising anode material. Xie et al. [32] in their combined DFT-experimental study, predicted MXene structures that can be used to develop non-Li-ion battery anodes by assessing trends in E_{ads} and charge transfer. For instance, in the case of $Ti_3C_2O_2$ MXenes, the cations: Na^+, K^+, Mg^{2+}, and Ca^{2+} ions gave negative E_{ads} indicating a favorable chemisorption, whereas Al^{3+} gave a positive E_{ads} suggesting an unfavorable chemisorption (Figure 16.3a). However, upon varying the surface coverage of ions, they found that up to 2/3 Al coverage, a negative E_{ads} was obtained, which turned positive upon the further addition of Al. To further investigate this behavior, charge transfer analysis was performed by means of relatively inexpensive Bader charge analysis. They found that Al transfers 1.09 e per atom charge to the MXene surface

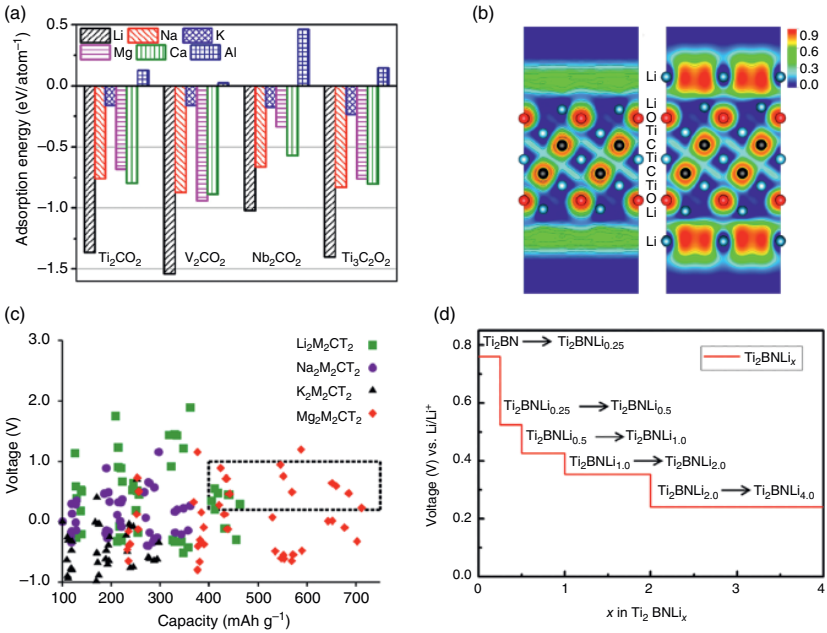


Figure 16.3 (a) ion adsorption energies for O-terminated Ti-MXene nanosheets. *Source:* Xie et al. [32]/American Chemical Society. (b) Valence electron localization function (ELF) of (110) sections of: (i) lithiated $Ti_3C_2O_2Li_2$ monolayer, and (ii) with an extra Li layer. *Source:* Xie et al. [31]/American Chemical Society. (c) Cell voltage and theoretical capacity for intercalation of two ions of Li^+, Na^+, K^+, or Mg^{2+} per formula unit into M_2CT_2 MXenes (where M refers to the transition metal and T to the surface functional group O, OH, H, or F). The dashed box indicates an approximate window of desired voltages (0.2–1.0 V) and capacities (>400 mAh g^{-1}). *Source:* Eames and Saiful Islam [70]/American Chemical Society/CC BY 4.0. (d) Open circuit voltage (OCV) profile as a function of Li concentration in the Ti_2BN monolayer. *Source:* Yi-Yuan et al. [37]/with permission of Elsevier.

indicating that fewer Al are required to satisfy surface O groups. Hence, counterintuitive to a full ion surface coverage, a partial Al coverage was found to be favorable.

E_{ads} trends were also used to conclude that hydroxyl functionalized MXenes such as $Ti_3C_2(OH)_2$ is an inferior anode material from the consistently positive E_{ads} values. In fact, hydroxyl groups react with ions to release an H_2 molecule and subsequently form O-terminated MXenes, thereby, questioning the stability of surface OH structures. The role of surface structure was further explored using a combination of DFT and experiments including X-ray diffraction (XRD), inelastic neutron scattering, and X-ray absorption spectroscopy [31]. Here, a multilayer structure of functionalized MXenes (Sc_2C, Ti_2C, Ti_3C_2, V_2C, Cr_2C, and Nb_2C) was considered, wherein the interlayer interaction was modeled by using van der Waals density functionals. They predicted a positive Li E_{ads} on OH-terminated MXenes with values: 0.124, 0.077, 0.170, and 0.171 eV per Li atom for Ti_2C and V_2C, Nb_2C, and Ti_3C_2, respectively, whereas *O*-MXenes gave favorable (negative) E_{ads}.

In addition to single-layer adsorption, multilayer adsorption was also explored following a similar approach [32, 71]. Herein [32], the ions were found to behave differently: K had the highest positive E_{ads} (>0.6 eV) followed by Li, Na, Ca with moderate (0–0.4 eV per atom), and Mg with negative E_{ads}. They ascribed this peculiar behavior of Mg to its complex adsorption process that is a combination of ion insertion of the first layer and a plating mechanism of other layers. This uniquely stable multilayer ensures a high Mg capacity on MXene surface.

Further insights such as charge transfer at the surface can be obtained from examining the ion-electron interaction. For instance, electron localization function or charge density plots (Figure 16.3c) show a hybridization between adatoms and surface Ti orbitals [32]. By means of electronic structures, the multilayer adsorption mechanism was also explained [32]. In essence, for Li, Na, and Mg, the electrons are dispersed across metal layers forming a negative electron cloud, which screens the Timetal repulsion and thereby stabilizes the adsorbed structure. Moreover, hybridization between Ti orbitals and adatoms near the Fermi level were also found to be absent, which strengthens the bonds. For bare MXenes, the hybridization between Nb and Ca near Fermi level was found to be smaller than the other metals considered. In the grand scheme of things, all known mechanisms of ion storage - reversible conversion, insertion, and plating may be found in MXenes making them promising as rechargeable battery anodes.

DFT energies have been further utilized to approximate an open-circuit voltage (OCV) [31, 37, 70] following the equation:

$$V = \frac{-\left[E\left(\mathrm{Ti_3}X_2T_2\mathrm{Li_2}\right) - E\left(\mathrm{Ti_3}X_2T_2\right) - 2\mu\left(\mathrm{Li}\right)\right]}{2} \tag{16.1}$$

where $E(Ti_3XT_2)$ is the total energy of the MXene compound, $E(Ti_3XT_2Li_2)$ is the total energy of the MXene after intercalation of two Li atoms per formula unit, and μ (Li) is the chemical potential of the Li. The accuracy in OCV predictions has been verified by Xie et al. [31], who estimated the OCVs to be 1.539 V for V_2CO_2, 1.019 V for Nb_2CO_2, 1.364 V for Ti_2CO_2, and 1.404 V for $Ti_3C_2O_2$ with respect to pure Li and found that this trend was found to be in good agreement with experimental results [72].

By relying solely on DFT-based energy calculations of OCV and theoretical capacity, Eames and Islam [70] performed a comprehensive global screening of candidate anodes from 300 M_2C compounds (M = Sc, Ti, V, Cr, Zr, Nb, Mo, Hf, Ta) with functionalizations F, H, O, and OH for the intercalation of ions (Li^+, Na^+, K^+, and Mg^{2+}). The results of their global search are summarized in Figure 16.3b. From Figure 16.3b, we see a strong dependence on intercalating ion on capacity with Mg^{+2}-based compounds giving the highest capacity although the mass of Mg^{2+} is 3.5× that of Li^+. This indicates that the two-electron chemistry offered by Mg^{2+} overshadows the mass disparity. Highest voltage, on the other hand, is offered by Li^+, followed by Mg^{2+}, Na^+, and K^+. They have attributed the low voltage in K^+ and Na^+ ions to a lateral electrostatic repulsion that increases the energy of intercalated compound in Eq. (16.1) and thereby reduces voltage. They also mapped the relation between voltage and metallic species; the higher the electropositivity of metal, the higher the voltage. The surface functional groups were also found to have non-negligible effect on voltage. For the light transition metals (Sc, Ti, V, and Cr), the voltage is ~0.0–1.0 V for bare MXenes, >0.5 V for *O*-MXenes, negative for H or OH MXenes, and a range of values for F termination. The change in voltage with a functional group can be tied to charge density difference following a similar argument of E_{ads}.

Similar to Li-ion battery anode materials, Na-ion battery anode materials based on Zr-MXenes were also created *in silico* and systematically investigated by Meng et al. [73] using DFT calculations. Specifically, they considered Zr_2C, Zr_3C_2, Zr_2CO_2, and $Zr_3C_2O_2$. OCVs of Zr_2CO_2 and $Zr_3C_2O_2$ MXenes were found to decrease monotonously as x was increased, and the OCV for $Zr_3C_2O_2$ was higher than that for Zr_2CO_2 MXene. Combined with the high maximum capacities of 474 and 326 mAh g^{-1} of Na adsorption on Zr_2CO_2 and $Zr_3C_2O_2$ with their good electrical conductivity, these materials were deemed to be promising for Na-ion battery ßanodes.

Recently, analogous to conventional carbide MXenes, boron-nitride MXenes were also investigated for their utility for lithium-ion battery anode applications [37]. Here, an isoelectronic substitution of C with B and N was used to create a Ti_2BN MXene [37]. They were found to be stable, electronically conductive, and had favorable Li E_{ads}. In addition to total OCV calculation, they have also determined the various intermediates (Figure 16.3d): $Ti_2BN \rightarrow Ti_2BNLi_{0.25}$, $Ti_2BNLi_{0.25}$

→ $Ti_2BNLi_{0.5}$ $Ti_2BNLi_{0.5}$ → $Ti_2BNLi_{1.0}$, $Ti_2BNLi_{1.0}$ → $Ti_2BNLi_{2.0}$ and $Ti_2BNLi_{2.0}$ → $Ti_2BNLi_{4.0}$. The OCV for these five plateaus were calculated as 0.76, 0.53, 0.43, 0.35, and 0.24 V, respectively, all of them falling in the range of standard accepted voltage values: 0.1–1.0 V. The theoretical capacity of Ti_2BN was calculated as 889 mAh g^{-1}, which is superior to graphite (372 mAh g^{-1}) and Ti_3C_2 (448 mAh g^{-1}); hence Ti_2BN was discovered as a promising anode material. In summary, *ab initio* calculations have been crucial in fundamentally understanding ion storage properties of MXenes and in rationally designing new MXene structures for battery anodes.

16.6.2 Supercapacitors

MXenes have been extensively tested as electrode materials for capacitive energy storage. Depending on the electrolyte, MXenes exhibit either double-layer capacitance, ion intercalation capacitance, or in the case of acidic electrolytes such as H_2SO_4, surface redox chemistry can result in pseudocapacitance. Fundamentally understanding the capacitive energy storage behavior of MXenes has been a challenging problem for *ab initia* modeling efforts.

Zhan et al. [74] have conducted a rigorous joint DFT (JDFT) study to understand the pseudocapacitance in MXenes. JDFT provides a formally exact variational theory for the free energy of an electronic DFT system combined with classical DFT or a polarizable continuum model. The advantage is that this could reliably predict the solvation behavior and potential at the point of zero charge (PZC) of electrode. In addition, an implicit electrolyte model described by the charge-asymmetric nonlocally determined local-electric (CANDLE) model was used to capture solvation effect and electrolyte response to surface charge. Using $Ti_3C_2O_2$ as a model system, they explain how the applied potential governs the surface redox reactions and double-layer charging simultaneously, their contributions to capacitive performance, and how the electronic structure changes with applied electrode potential.

Firstly, in an attempt to understand the redox pseudocapacitive behavior [74], the proton transfer to MXene surface was analyzed. Here, the surface redox chemistry was found to be dictated by proton adsorption and subsequent electron transfer to electrode. To determine the extent of redox reactions, Gibbs free energy, $G(x, \phi)$ was calculated as a function of H coverage, x and electrode potential, ϕ. For each H coverage, x, at various fixed electrode potentials, ϕ varied from −1.0 to 1.0 V vs. SHE in 1.0 M H_2SO_4. As can be seen from Figure 16.4a, when the applied potential is −1 V, a parabolic shape of $G(x, \phi)$ averaged around $x = 0.68$ was observed. As potential increases, G shifts up and x shifts to smaller values. Furthermore, with an increase in electrode potential, a smooth decrease in H coverage was observed. Figure 16.4b shows the redox charge storage, surface net charge, and the electron transfer number

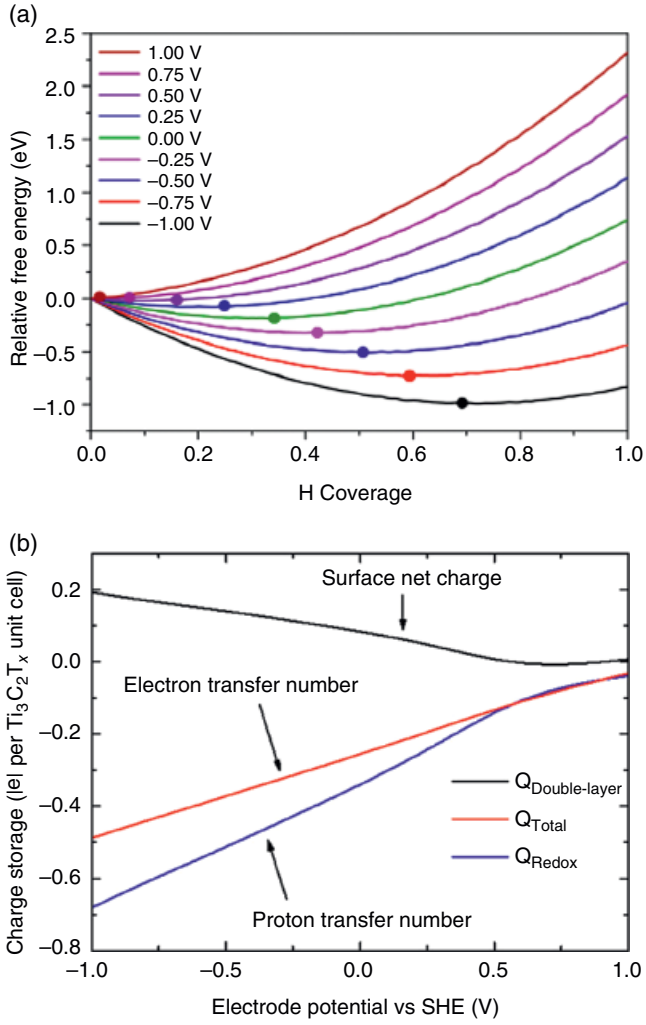


Figure 16.4 (a) Gibbs free energy of $Ti_3C_2T_x$ (T = O, OH) in 1 M H_2SO_4 electrolyte as a function of H coverage x at different electrode potentials, ϕ, relative to standard hydrogen electrode (SHE). The average minimum on each curve is indicated by a dot, (b) Faradaic charge (blue, to balance proton transfer), EDL charge (black, due to surface net charge), and total charge (red, net electron transfer number) stored at different electrode potentials, (c) Predicted integral capacitance of MXene electrodes: (1) specific capacitance of carbide MXenes; (2) specific capacitance of nitride MXenes; (3) areal capacitance of carbide MXenes; and (4) areal capacitance of nitride MXenes. The voltage window is from −0.5 to +0.5 V vs. SHE, and (d) charge storage per formula unit vs. the shift in the potential at the point of zero charge (ΔV_{PZC}) and hydrogen adsorption free energy (ΔG_H). Voltage window is from −1 to +1 V vs. SHE. Values (in |e| per $M_{n+1}X_nT_x$) for the contour lines are given on the right. *Source:* (a) and (b) Zhan et al. [74]/American Chemical Society. (c) and (d) Zhan et al. [5]/American Chemical Society.

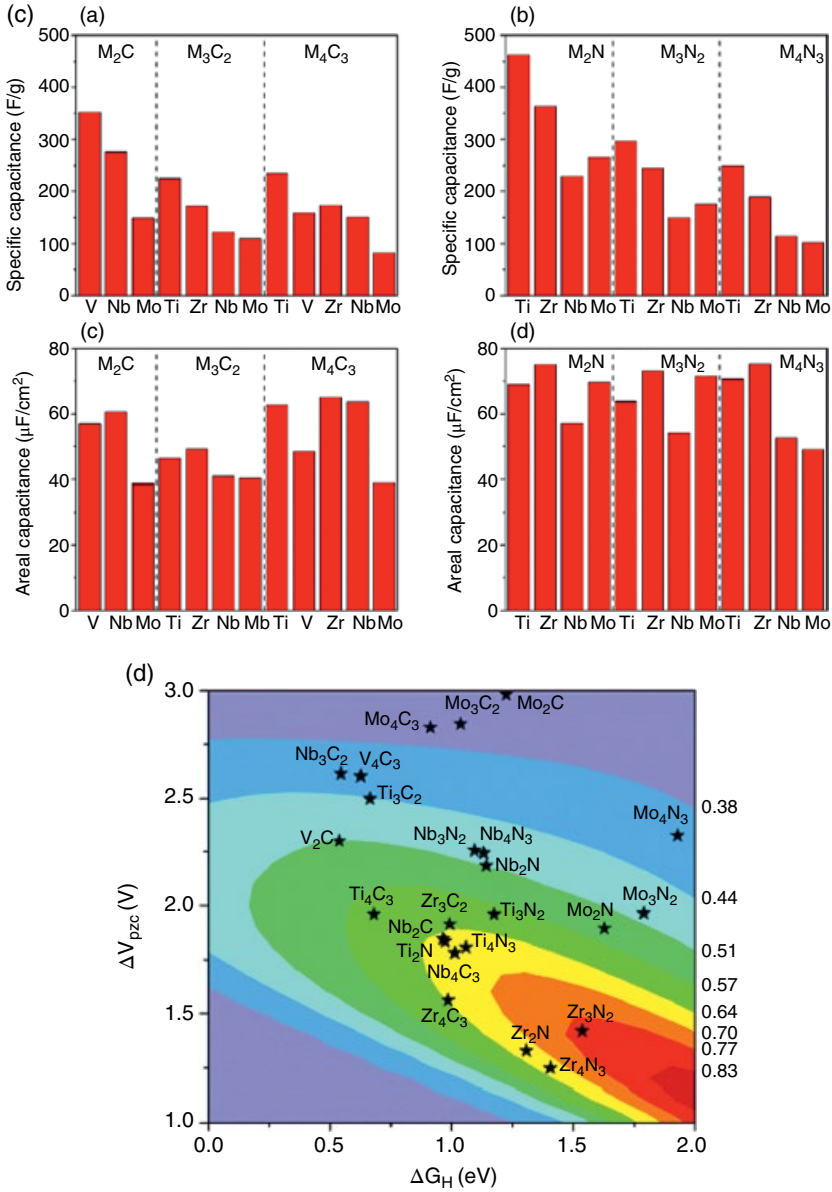


Figure 16.4 (Continued)

as a function of applied potential. Note that the surface charge is responsible for the EDL capacitance. It is apparent that the electrode is positively charged in the voltage window and that the surface charge decreases with voltage. Hence, the EDL acts opposite to the redox storage, which dominates the total capacitive behavior.

One may also find similar observations in ion-solvent confinement systems from the AIMD study by Sun et al. [75]. They investigated the proton transfer mechanism in MXene-confined water layers of different thicknesses using $Ti_3C_2O_2$ MXenes. They found a significant surface redox reaction of protons reversibly with surface O sites and water molecules at the interfaces. The redox rate was found to increase with the reduction in water layer thickness, while the rate reducing with increased thickness.

Importantly, redox charging and EDL capacitive behavior have also been revealed via DFT calculations [74]. To elucidate the redox charging mechanism, a constant charge DFT has been employed and the DOS and local DOS of $Ti_3C_2T_x$ electrode with H coverages of 0.11 and 0.22 corresponding to V = 0.59 and 0.3 V were obtained [74]. From the total DOS, mainly contributed by Ti atom, it was deemed that electron-transfer process mainly happens on the Ti atom. The excess charge on the electrode, however, was found to be mainly distributed on the surface oxygen layer that directly interacts with the electrolyte to form the EDL.

Similar to the *in silico* discovery of battery anode materials, discovery/screening of MXenes for supercapacitors has also been performed [5]. Building on the fundamental knowledge of pseudocapacitance, a series of MXene electrodes ($M_{n+i}X_nT_n$; M = Sc, Ti, V, Zr, Nb, Mo; X = C, N; T = O, OH; n = 1–3) were screened to simulate their performance in aqueous H_2SO_4 electrolyte. As the first step, Sc-based MXene compounds that are too active for HER were screened out using differential hydrogen adsorption-free energy as a descriptor. Secondly, the free energy of solvated MXene electrode at different applied potentials and H coverages, as well as the potential at PZC before and after H binding were computed. From these computed values, the differential and integral capacitances were determined. Figure 16.4c shows the predicted integral capacitances of MXene electrodes. In *C*-MXenes, V_2C exhibits the highest specific capacity of 350 F g^{-1}. In the *N*-MXenes, the highest is from Ti_2N of 450 F g^{-1}. Ti_2N has the highest capacity due to Ti's low atomic weight and favorable redox chemistry. Furthermore, the charge stored was also calculated from ΔG_H and ΔV_{PZC}. As shown in the 2D map, large ΔG_H and low ΔV_{PZC} lead to higher charge storage per formula unit. It is clear that the Zr-MXenes show the highest charge storage, thereby, warranting efforts of synthesis, characterization, and testing of Zr-MXenes for practical supercapacitor applications.

In summary, first principles-based computation has been used to calculate the capacitive energy storage behavior of MXenes with reasonable accuracy. These works suggest that a surface redox reaction mechanism is the dominant mechanism of charge storage while the EDL mechanism counteracts.

16.6.3 Ion Mobility

In addition to favorable adsorption energy and redox chemistry, ion mobility is another important property that determines if the MXene-electrolyte system is promising for practical energy storage devices. Several minimum energy path methods implemented in conjunction with traditional DFT methods provide insights to the diffusion energy barriers [76].

Sun et al. [71] conducted Nudged Elastic Band (NEB) analysis to understand Li/Na diffusion on the Mo_2C monolayer surface. Three possible pathways were considered as shown in Figure 16.5a. For Li diffusion, the lowest barrier is 0.035 eV along the P1 path of length 2.88 Å, whereas the P3 path exhibits the highest of 0.133 eV. On the other hand, Na adsorption P2 and P1 are interchanged, and have a lower activation energy than Li. Likewise, the diffusion pathways and barriers for adsorbed monovalent and multivalent species on O-terminated Ti-MXene surface have also been explored using NEB analysis [32]. Monovalent adatoms displayed a low energy barrier (<0.3 eV), whereas multivalent atoms had higher (>0.5 eV) values. Both these works also point at a general phenomenon of higher ion coverages exhibiting lower mobilities. Hence, on O-terminated MXene nanosheets, Na and K were found to possess high ion mobilities implying good rate capabilities, whereas Mg, Ca, and Al yield lower rate capabilities.

Similar to metallic ions, proton diffusion in water confined within MXene layers has also been investigated rigorously [75] providing additional insights to the states of protons in confinement. Following the same denotation scheme as the authors, let us denote O atom in the hydronium ion as O_0 and its nearest O atom in the first coordination shell as O_{1x} atom; the O_0–O_{1x} interaction is called a special pair. In Figure 16.5b, the upper panel shows the change of density of O_0 and O_{1x} during a 0.5 ps trajectory indicating proton transfer. It is clear that during the short segments, the O_0 identity is short-lived and switches back and forth with the O_{1x} identity. However, during the long segments, the O_0 identity lasts longer, but the O_{1x} identity changes across three O atoms. The short segment corresponds to Zundel state, where O_0 and O_{1x} share a proton, and the O_0—H and O_{1x}—H bond lengths are close. Likewise, the long segments were found to have the eigen state of hydronium ion coordinated by water molecules in the first coordination shell. The proton transfer thereby follows an Eigen-Zundel-Eigen mechanism in MXene-confined water. They also went a step further to calculate the diffusivity of protons in confined water from the mean squared displacement of O_0 atoms by varying the number of water layers obtained from AIMD trajectories. It was found that for a single layer, a 2D-like proton motion was observed and as the number of layers was increased to three, diffusivity started approaching the bulk diffusivity of water.

Contrariwise to an independent ion diffusion model, a correlated metal ion diffusion model has also been reported recently [77]. As noted in the previous studies, a high

ion coverage leads to a higher diffusion barrier due to Coulomb repulsion between ions. Song et al. [77] elucidated the effect of ionic concentration on the diffusion barrier, capturing the mechanism of ion migration in a 2D heterostructure. They considered a system of Li ion intercalated in VS_2/Ti_2CO_2 heterostructure with Li occupancies varying from 0 to 1. They first conducted independent climbing-image-NEB and AIMD simulations to calculate the formation energy of Li vacancy and the activation energy of Li diffusion, respectively, which showed great disparity. This disparity was explained by introducing a new correlated mechanism of ion migration. Figure 16.5c

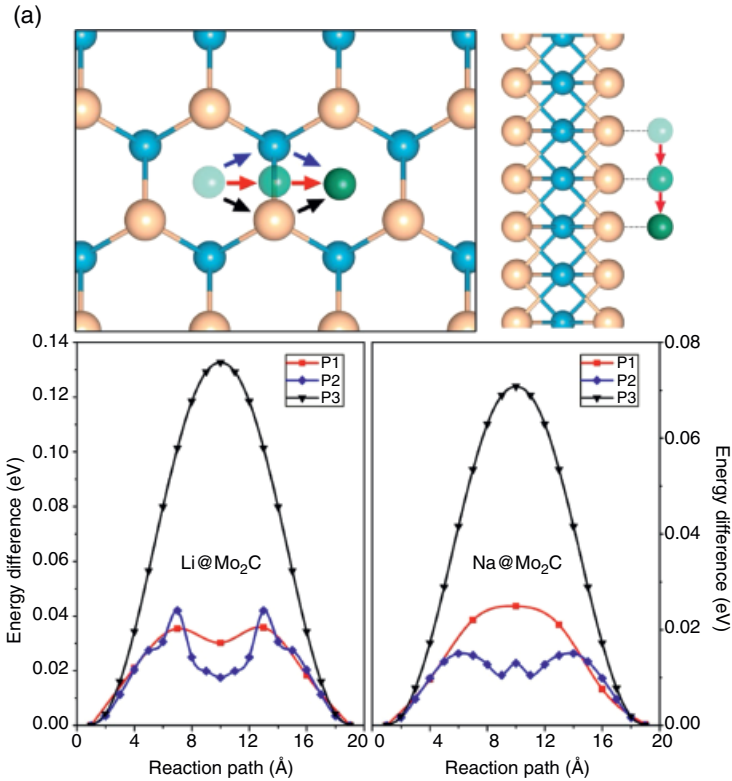


Figure 16.5 (a) Li^+ and Na^+ ion diffusion pathways and energy barriers calculated using NEB. *Source:* Sun et al. [71]/American Chemical Society. (b) Change of O_0 and O_{1x} identity (upper panel) and their O—H bond lengths (lower panel) with time during a typical in-water proton-transfer event. The "long" or "short" labels refer to the relative duration of the O_0 identity. *Source:* Sun et al. [75]/American Chemical Society. (c) Correlated migration snapshots of AIMD and diffusion analysis of the mobile ion by the van Hove correlation function. (1–4) AIMD snapshots, from 10 to 13 ps, of Li ions in a supercell of the VS_2/Ti_2CO_2 heterostructure at 900 K. (d) The self-part and distinct-part of the van Hove correlation function from the AIMD simulation. *Source:* Song et al. [77]/Royal Society of Chemistry.

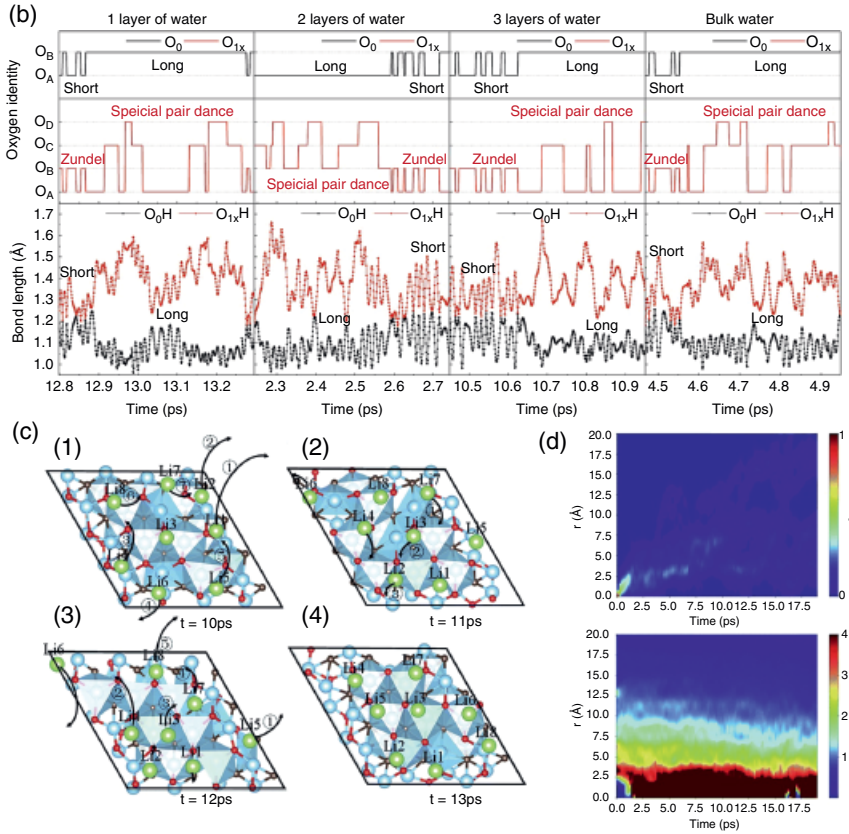


Figure 16.5 (Continued)

(1)–(4) shows the Li intercalated heterostructures between 10 and 13 ps of AIMD simulation. The images show the correlated migration of Li ions. For example, from 10 to 11 ps, the first and second Li jump prompted the fourth, fifth, and sixth Li jumps, which eventually resulted in the migration of an eighth Li that pushes the seventh Li toward the vacancy left by the second Li. To further understand the macroscopic implications of correlated Li migration, the van Hove correlation function (VHF) of Li-ion motion according to the following equation:

$$G_s(r,t) = \frac{1}{4\pi r^2 N_d}\left\langle \sum_{i=1}^{N_d} \delta\left(r - \left|\vec{r}_i(t_0) - \vec{r}_i(t+t_0)\right|\right)\right\rangle_{t_0} \tag{16.2}$$

$$G_d(r,t) = \frac{1}{4\pi r^2 N_d}\left\langle \sum_{i\neq 1}^{N_d} \delta\left(r - \left|\vec{r}_i(t_0) - \vec{r}_j(t+t_0)\right|\right)\right\rangle_{t_0} \tag{16.3}$$

where G_s and G_d are the self and distinct parts of the VHF, δ is the Dirac delta function, $\vec{r}_i(t)$ is the position of the ith particle and time t, N_d is the number of diffusing ions, and r represents the radial distance.

The self (G_s) and distinct (G_d) parts are shown in Figure 16.5d. The high-value range in G_s between 0 and 2.5 Å indicates the distance between adjacent Li sites, which then extends within a few ps. It also implies that Li ions migrate by a displacement of 10 Å in a few ps indicating high diffusivity. Furthermore, a strong time correlation of Li ion diffusion is apparent from the G_d plot; the G_d at $r < 2$ Å indicates that a vacancy left by diffusion of a Li ion is eventually occupied by another Li ion. The diffusion energy barriers of correlated electrons were also found to be significantly lower than that of a single ion diffusion picture. For instance, E_f values of Li site occupation of 0.5 are 0.247, 0.206, and 0.170 eV, which is much lower than the 0.355 eV of noncorrelated mechanism. The reason for reduced barriers in the correlated mechanism was further investigated by comparing the deformation charge densities of the intermediate states of Li diffusion. Essentially, the correlated mechanism creates a favorable chemical environment for Li ions in their transient states and a large Li spacing resulting in lower Coulomb repulsion.

In summary, *ab initio* calculations have been able to qualitatively and quantitatively describe the ion mobility in adsorbed, bulk electrolyte, and confined states with commendable levels of accuracy. While we point out the urgency in need for *ab initio*-quality force fields to address the long timescale and large system size challenges to a satisfactory extent to allow quantitative ion mobility predictions, we note that molecular dynamics simulations have been instrumental in revealing valuable insights on ion transport and reactivity. Recently, AIMD, approximate quantum chemical, or reactive classical MD methodologies have been extensively employed to reveal the interactions of MXene with electrolyte ions and solvents, which will be the focus of discussion in the following section.

16.7 Insights from Molecular Dynamics

Many studies have focused on unraveling the properties of MXene as an electrode and its complex interaction with electrolyte ions and solvents for energy storage applications [11, 78, 79]. In addition, many atomistic studies have used advanced simulation techniques to explore underlying phenomena inside the confinement from dynamic electrolyte properties [11, 80]. The following section reviews mainly the recent studies performed using molecular dynamics (MD) at various levels of accuracy.

16.7.1 *Ab initio* Molecular Dynamics and Approximate Quantum Chemical Simulations

So-called "direct" simulation methods such as AIMD and DFTB/MD involve obtaining the solution of the electronic Schrodinger equation at each MD time step "on-the-fly" to compute the forces on the nuclei. Hence, these methods can provide detailed chemical and electronic interactions of atoms during ion dynamics. However, the computational cost associated with AIMD has limited its applicability to small system sizes to explore the interaction of intercalated ions and their stability in confinement [31, 81].

Performing AIMD simulations on water/$Ti_3C_2O_2$ interface at room temperature, Wu et al. found that the water molecules can attack the basal plane of $Ti_3C_2O_2$ MXenes via the surface Ti atom [80]. The study suggested that one way of increasing the stability of MXenes against water is by negatively charging the surface or converting surface O terminations to OH, which can help to push away water molecules away from the MXenes surface. Intending to enhance energy storage and power delivery performance of MXene, Demiroglu et al. performed AIMD at the MXene/graphene heterointerface to assess the stability of intercalated Na, K, and Ca ions [82]. Three different types of MXenes, namely $Sc_2C(OH)_2$, Ti_2CO_2, and V_2CO_2 were investigated for cation intercalation at the heterostructure. Only Ti_2CO_2/graphene and V_2CO_2/graphene heterostructures were predicted to be stable for cation intercalation. Compared to K and Na, Ca intercalation leads to greater distortion of the graphene atomic structure within these heterostructures. However, none of the three cations considered caused significant structural or phase change of the heterostructures. Based on the reduced energy barrier and calculated voltage, Ti_2CO_2/graphene and V_2CO_2/graphene showed good promise for Na ion battery applications with the possibility of operating at low and high voltage, respectively [82].

Similarly, Gao et al. [83] used AIMD to study the intercalation of aqueous ions (Li^+, Na^+, K^+, Cs^+, and Mg^{2+}) into $Ti_3C_2(OH)_2$ MXenes nanopores. Ions under confinement showed different affinities toward MXene/water interface. For example, Li^+, Na^+, and K^+ were found to be adsorbed on the MXenes surfaces, whereas Cs^+ and Mg^{2+} were located around the pore center, as shown in Figure 16.6a (i). However, the first hydration shell of various cations under confinement remained similar to that of bulk, Figure 16.6a (ii). The extent of water retained inside the nanopore could be linked to the cation-O_w distance, Figure 16.6a (iii). A cation-O_w distance shorter than O_w–O_w leads to extra water entering into the nanopore, whereas larger cation-O_w distances lead to water becoming expelled from it, as observed in electrochemical quartz crystal microbalance experiments [85]. Confinement leads to a significant decrease in the coordination environment of ions compared to the bulk, Figure 16.6a (iv). Comparison

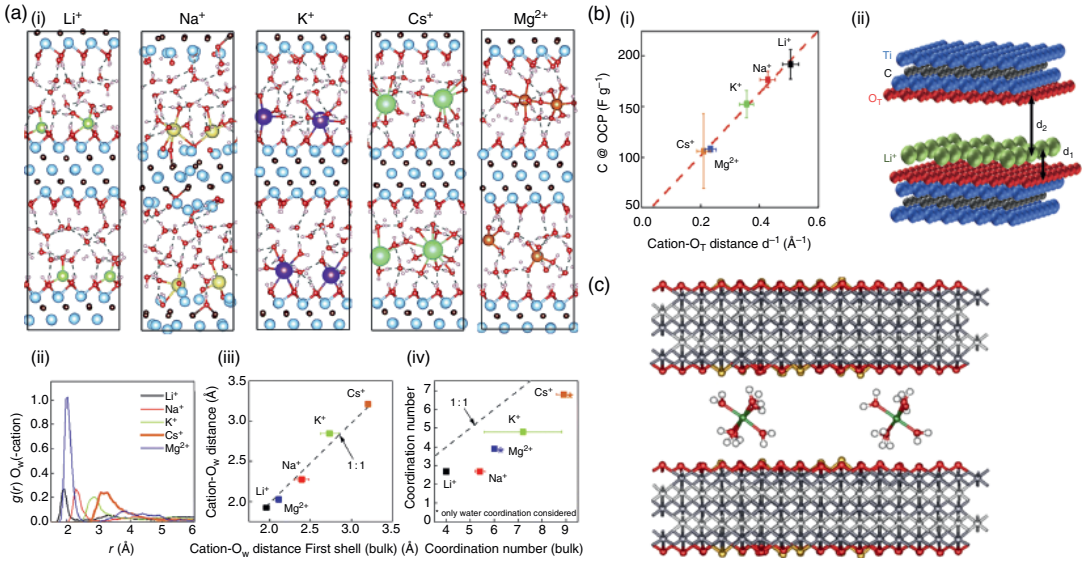


Figure 16.6 Results from AIMD simulations (a) (i) Cation distributions in the interlayer space between MXenes. (ii) Pair distribution functions (PDF) of cation-water(O_w), g(r). (iii) The cation-O_w distances based on the maxima of $g(r)$ correlating with values in bulk solutions. (iv) Coordination numbers extracted from (ii) in comparison with values for bulk solutions. (b) (i) Relationship between cation-MXene distance^{-1} and averaged capacitance at open circuit potential (OCP). (ii) The schematic of modified Helmholtz model in two MXene layers with corresponding distances d_1 and d_2. *Source:* Gao et al. [83]/Royal Society of Chemistry. (c) Mg^{2+} $(H_2O)_6$ clusters in MXene pore, showing pillaring effect. *Source:* Muckley et al. [84]/American Chemical Society.

between experimentally and theoretically estimated heat of reaction led to the conclusion that the heat of proton hydration is rather constant among four cations.

Furthermore, based on simulations of the pair distribution function from MD trajectories, relative distances between cations from the surface were on the order $Li^+ < Na^+ < K^+$. The cation-MXene distances were correlated to the average cation-MXene distance with EDL-type capacitance measured by cyclic voltammograms (CVs) as seen in Figure 16.6b (i). The OCP capacitance had a $1/d$ relationship where d represents the average cation-MXene distance. By measuring distances (d_1 and d_2 as indicated in Figure 16.6b (ii)) of the cations from the two surfaces in confinement, the authors decomposed the total capacitance C, determined from the $\epsilon\epsilon_0(1/d_1 + 1/d_2)$ using the modified Helmholtz model into two C_1 and C_2 partial contributions, one from each cation [83]. The study underscores the importance of details understanding the location and the dynamics of ions in confinement for obtaining a comprehensive picture of energy storage properties and the process of MXenes.

Muckley et al. [84] combined AIMD with the neutron scattering to understand the effect of K^+ and Mg^{2+} ion intercalation and hydration effects in the MXene layers. Ion intercalation resulted in an increase in d-spacing on MXene corresponding to their sizes, that is, K^+ ion leading to a more significant increment than in the case of the smaller Mg^{2+} ion. Furthermore, intercalation of water molecules with the identical H/cation ratio as in the experiment (two for K^+ and five for Mg^{2+}) led to an increase in the c-lattice parameter of MXenes (a crystal structure parameter that is directly proportional to the distance between individual MXene layers). The hydration radius of Mg^{2+} is higher than that of K^+. The increase in the c-lattice parameter with hydrated ions (Mg^{2+}, K^+) was larger for Mg^{2+} and smaller for K^+, corresponding to their hydration radius. The $Mg^{2+}(H_2O)_6$ cluster is considered rigid as it completes the hydration shell on the Mg ion. Two $Mg^{2+}(H_2O)_6$ clusters supported MXene sheets acting as a pillar as shown in Figure 16.6c. Pillaring led to a separation of MXene layers with increased d-spacing separation by 4.7 Å in agreement with an increase by 4.5 Å as observed in the experiment. The stability of the hydrated Mg^{2+} clusters was confirmed using classical MD simulations over more extended periods in an identical setup to the AIMD, that is, two clusters between two MXene layers [84]. This "pillaring" effect of the cations has been reported with other cations as well [86, 87], and MXenes pillared by cations such as Li^+, Na^+, and K^+ exhibit improved energy storage performance [86–88].

Brady et al. [89] explored the correlation of intercalated sodium ion distributions and their surface redox properties by combining DFTB- and CMD-based MD simulations. Three different presodiated sites were identified based on the possibility of sodium bonding with surface O/F atoms as shown in Figure 16.7a,

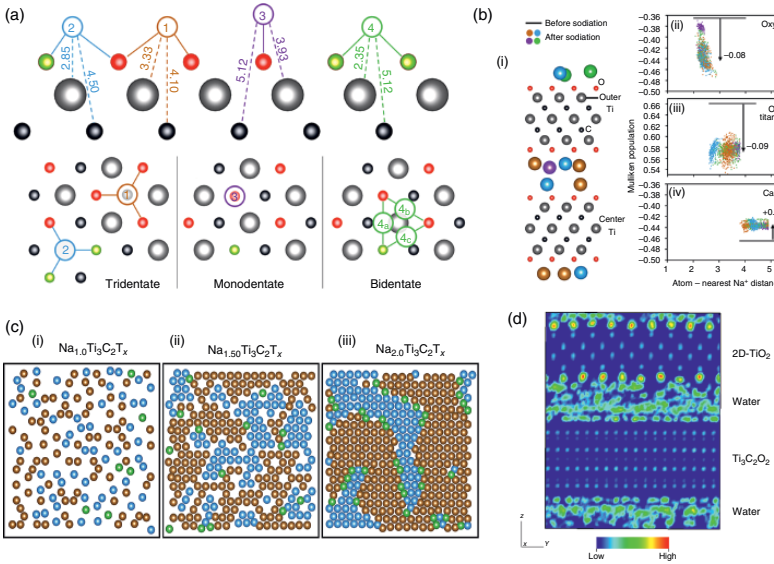


Figure 16.7 (a) Side and top views of four predicted sodiation sites at MXene interfaces/surfaces. (b) (i) Snapshot of sodiated Mxene ($Na_1Ti_3C_2O_2$) structure obtained from DFTB/MD, showing the correlation of four sodiation sites to the $Ti_3C_2O_2$ layers. (ii)–(iv) The corresponding Mulliken atomic charge populations before and after sodium intercalation as a function of distance from the nearest Na^+ ion. (c) Classical MD results of the surface-domain structure with chemical short-range ordering created by the distribution of sodiation sites with concentrations of 1, 1.5, and 2 Na+ per Ti_3C_2 [$O_{0.7}F_{1.3}$] (i)–(iii), respectively. *Source:* Brad et al. [89]/American Chemical Society. (d) Projection of velocity magnitude of all atoms averaged over ReaxFF trajectories for 2D-TiO_2/$Ti_3C_2O_2$ MXene heterostructure. The hotspots around the oxygen ridges on the 2D-TiO_2 surface indicate the region where water molecules have higher mobility. *Source:* Ganeshan et al. [90]/American Chemical Society.

i.e. (i) Na^+ with three nearest neighbor (NN) surface O/F, tridentate. These sites are right above C atoms, two layers below the surface with a Ti-Na distance of 2.85 Å, or right above the Ti atom with a Ti-Na distance of 3.33 Å. (ii) Na with single NN O/F, monodentate. These sites are above O/F, with a Ti-Na distance of 3.93 Å. Finally, (iii) Na^+ with two O/F NN, that is, site saddling along the line between two O/F atoms, with a Ti-Na distance of 2.35 Å. Different sodiation sites have different coordination environments, which led to various deviations in the charge after sodiation from their initial charges. For example, O anions showed a greater range of excess charge distribution. In contrast, surface Ti exhibited only a narrow charge range. Furthermore, Ti atoms below the surface remained practically unchanged, whereas C atoms at the center of the MXene layers were less negative after sodiation, Figure 16.7b (ii)–(iv). Sodium ions oxidized upon intercalation, in agreement with predictions made in other studies [32, 91].

The location of Na^+ with respect to terminal atoms on the MXene surface determines redox chemistry on the surface O/F atom. CMD was performed with three concentrations: 1, 1.5, and 2 Na+ per $Ti_3C_2[O_{0.7}F_{1.3}]$ of nanoconfined sodium ions using DFTB calculated charges. Intercalated sodium formed concentration-dependent domain structures as shown in Figure 16.7c. Low sodium concentration featured sodium-rich and sodium-poor regions, Figure 16.7c (i), and interleaved structure pattern in $Na_{1.5}Ti_3C_2$ $[O_{0.7}F_{1.3}]$, Figure 16.7c (ii) and section of enlarged (positively correlated) supersaturated structures in $Na_2Ti_3C_2$ $[O_{0.7}F_{1.3}]$, Figure 16.7c (iii). The tridentate type (light gray) atom is the most stable, followed by the tridentate type (dark gray), and the next stable is bidentate. The monodentate sites were observed to be the least stable and do not appear in Figure 16.7c. The PDF of the various adsorption sites from CMD simulations agreed with the experimental PDF. Sodium-domain formation in atomistic simulation suggested that sodium sites filled simultaneously and affected the sodium mobility as they became trapped between the layers. The untrapped, remaining ions are electrochemically mobile in agreement with the capacitive measurement. This type of domain structure ultimately provides a way to control the voltage of pseudocapacitive materials.

16.7.2 Reactive and Classical Force Field Simulations

Generally, classical force field-based molecular dynamics is based on molecular mechanics and is not able to describe either bond-breaking or formation. However, the classical force fields can be very useful in modeling large systems (>100 000) for a long time (ns). They can help to capture rare events and describe structural features such as structural functions and PDFs. On the other hand, the Reactive force field (ReaxFF) can simulate bond-breaking and formation as it includes a dynamic charge updating scheme. ReaxFF has allowed determining energy

barrier proton transport under confinement, evaluations of nuclear quantum effects [22] and intercalation of various ions under confinement [92] as well as MXene heterostructures [90]. The costs are significantly closer to conventional classical force fields than *ab initio* calculations.

Osti et al. [92] performed ReaxFF-based MD simulations combined with XRD, small-angle neutron scattering, and quasi-elastic neutron scattering measurement to explore the effect of confinement and intercalation of K^+ on the MXene confined water. The diffusion coefficient of water was reduced by a factor of 2 inside the confinement relative to bulk. The diffusion coefficient of water further decreased due to the intercalation of K^+. Also, intercalation of K^+ led to ordering of MXene layers. In the subsequent study [93], performed by incorporating Li^+, Na^+, and K^+ showed the ordering of water molecules under confinement. The extent of molecular water order inside the MXene surface was correlated to the size of the intercalated ions. For example, Li^+ had the smallest influence, whereas K^+ the greatest, with Na^+ exhibiting an intermediate effect on molecular water ordering within the confinement. Also, the authors observed Na^+ and K^+ having stronger interactions with the water molecules than Li^+. The diffusion coefficient of water further decreased by the intercalation of ions, with Li^+ having the least effect, followed by Na^+ and K^+ as these ions had more interference with the water molecules than Li^+.

CMD studies performed using classical force fields have also predicted the ordering of water molecules under confinement. For instance, MXene annealed at 500 °C ($Ti_3C_2O_{1.185}F_{0.8}(OH)_{0.015}$) led to well-organized compact structure of water molecules, whereas pristine MXene ($Ti_3C_2O_{0.9}F_{0.8}(OH)_{0.3}$) showed disordered orientation of water molecules [94]. Zaman et al. [95] studied the effect of cation intercalation on MXene nanopore combining XRD, ambient-pressure X-ray photoelectron spectroscopy (APXPS), with classical forcefield-based MD. MXenes exhibit volume swilling upon hydration and intercalation of ions; the hydrophilic cations (Li^+) actively help in water adsorption at MXene interfaces. On the other hand, hydrophobic cations (K^+) weakly interact with the water, which accelerates water removal under the nanoconfinement, according to the cation-water distance [83].

The heterostructure of MXene with materials like graphene, metal oxides, metal sulfides, etc. leads to an opportunity to enhance the performance of electrochemical and energy storage applications by combining the advantages of different materials forming the interface [81, 82]. Ganeshan et al. [90] have performed ReaxFF-based MD on the MXenes/2D-TiO_2 with Li^+, Na^+, and K^+ ions intercalation. The $Ti_3C_2O_2$/2D-TiO_2 heterostructure leads to the formation of a planar arrangement of water with hydrogen atoms facing toward the surface of $Ti_3C_2O_2$. $Ti_3C_2(OH)_2$/2D-TiO_2 leads to the long-range ordering of water due to cascading hydrogen bonding perpendicular to the surface. However, long-range ordering

was absent on the $Ti_3C_2(OH)_2/Ti_3C_2(OH)_2$ homostructure due to the surface proton disrupting the water hydrogen bond network. Similar to water confinement on MXenes homostructure, the heterostructure also decreases the diffusion coefficient of water. However, water on $Ti_3C_2O_2$/2D-TiO_2 shows a greater diffusion coefficient than on $Ti_3C_2(OH)_2$/2D-TiO_2 due to the long-range order on the latter. Unlike the MXene surface, where the uniform distribution of the velocity was seen, the 2D-TiO_2 surface shows a hotspot of the velocity, as shown in Figure 16.7d. The higher packing density of water molecules around the oxygen ridge was believed to be the reason for the overall decrease in water diffusion with the 2D-TiO_2 surface. In agreement with the simulation, the neutron experiment also showed an increased jump rate in Ti_3C_2-2D-TiO_2 compared to pristine Ti_3C_2 [90].

Furthermore, different from MXene homostructures, [93] the presence of Li^+ ions leads to increased water intercalation. This somewhat counterintuitive observation can be explained because Li^+ ions lying close to the 2D-TiO_2 surface prevent water from being trapped in the notches there [90]. Among other cations, Na^+ forms a planar layer and decreases diffusivity as it is located in the central region of the MXene interlayer space, hindering water mobility. K^+ has only a minor effect on the diffusivity compared to the ion-free case. Yet, for increased ion concentrations, the presence of K^+ increases the water diffusion coefficient due to an opening created by the repulsion with surface protons. Na^+ favored the proton transfer from –OH terminations into the waters. Those protons reaching the 2D-TiO_2 surface undergo redox reactions instead of diffusion into the water as hydronium ions. For the water confined between MXene layers [75] or MXene/graphene interface [96], reversible redox reactions at the surface and water protonation have been proposed based on AIMD simulations. Increased energy storage is expected due to the accumulation of protons in the 2D-TiO_2/MXene heterostructure.

Room temperature ionic liquids (RTILs) are considered promising alternatives to aqueous electrolytes to achieve a higher energy density due to their wider potential windows and stability. Xu et al. [97] performed CMD studies on the ionic liquid electrolyte 1-ethyl-3-methylimidazolium bis (trifluoromethylsulfonyl) imide ($[EMIM]^+[TFSI]^-$) to understand the charging-discharging mechanism in MXene $Ti_3C_2T_x$. The study used a classical force field to simulate pores between rigid parallel MXenes layers treated as movable plates. They found expansion of the negative electrode and contraction of the positive electrode. The volumetric change in interlayer spacing during charging and discharging was found to be in agreement with the experiment. Two different charging mechanisms at the positive and negative electrodes were predicted by analyzing the nanopore's ionic distribution and structural arrangement. On the negative electrode, the charge storage is primarily achieved by counterion intercalation, whereas ion removal and ion exchange were observed at the positive counterpart. In a similar study

performed by Xu et al. [98], with fixed MXene layers, they observed spontaneous wetting of $Ti_3C_2(OH)_2$. $Ti_3C_2(OH)_2$ This particular MXene structure is expected to have increased power performance compared to $Ti_3C_2O_2$ or $Ti_3C_2F_2$. Similarly, Liang et al. [99] have studied the effect of *c*-lattice spacing $Ti_3C_2T_x$ by introducing different chain lengths of alkylammonium (AA) cation intercalation into MXenes. MD simulations predicted differences in the atomic structures of RTIL, and AA in the interlayer *c*-lattice spacing due to increased spaced corresponding to longer alkyl chains, in agreement with changes in the experimental electrochemical behavior. These studies implied optimization and engineering of the *c*-spacing as one way to increase the energy storage performance of 2D materials like MXenes.

As discussed above, most dynamics-based simulations have been performed to understand the effect of confinement on electrolytes in dilute conditions, namely salt-in-water systems. In contrast, studies are scarce on highly concentrated electrolytes, or water-in-salt (WIS). Most of the commonly used cations such as Li^+, Na^+, K^+, and Mg^{2+} need to be evaluated thoroughly in WIS to understand the diffusion of ions/solvents and the correlated motions of ions in confinement to predict the performance of MXenes with WIS electrolytes.

16.8 Summary and Future Opportunities

Today, MXenes and their analogs represent a very large family of 2D nanomaterials. Simulations are able to afford a good accounting of the structural, electronic, and energy storage-related properties. However, despite a decade's worth of studies, there remain numerous important topics where greater insight from theory is needed and where disconnects remain with current experiments.

First, while many hundreds of MXene compositions have been predicted to be thermodynamically stable, only a small fraction of them have been successfully synthesized. In some cases where conventional etching has been attempted, the etching is unsuccessful, but the reasons for this are unclear. New theory and simulations are needed to provide insight into the etching processes, how they can be tailored for the greatest effectiveness, and to inform alternate synthesis methods.

Second, and methodologically, a major challenge is to simulate realistic MXenes in the presence of electrolytes and multiple charged species, and under applied potentials. If sufficient length and time scales can be achieved, this would give insights into the energy storage mechanisms and detailed information on the complex interactions between the bulk MXene, its surface terminations, and the solvated ions and electrolyte. An effective model would enable the mechanisms and limits of performance to be predicted and understood. Simulations of similar complexity are desired to gain insight into catalytic properties under realistic conditions. Neural network potentials promise this

capability, but they have yet to be demonstrated in non-trivial electrochemical scenarios such as intercalated MXenes.

Finally, the areas of superconductivity and topological behaviors in MXenes both remain little explored. Additional discoveries of novel behaviors would firmly establish MXenes as "quantum materials," expanding MXene's already significant electronic structure repertoire for exciting novel types of quantum applications.

Acknowledgments

This work was supported by the Fluid Interface Reactions, Structures, and Transport (FIRST) Center, an Energy Frontier Research Center funded by the US Department of Energy (DOE), Office of Science, Office of Basic Energy Sciences.

References

1 Naguib, M., Kurtoglu, M., Presser, V. et al. (2011). Two-dimensional nanocrystals produced by exfoliation of Ti_3AlC_2. *Advanced Materials* 23 (37): 4248–4253.

2 Aslam, M.K. and Xu, M. (2020). A mini-review: MXene composites for sodium/potassium-ion batteries. *Nanoscale* 12: 15993–16007.

3 Li, N. and Fan, J. (2021). Computational insights into modulating the performance of MXene based electrode materials for rechargeable batteries. *Nanotechnology* 32 (12): 252001.

4 Zhan, C., Weiwei Sun, Y., Xie, D.e.J., and Kent, P.R.C. (2019). Computational discovery and design of MXenes for energy applications: status, successes, and opportunities. *ACS Applied Materials & Interfaces* 11: 24885–24905.

5 Zhan, C., Sun, W., Kent, P.R.C. et al. (2019). Computational screening of MXene electrodes for pseudocapacitive energy storage. *Journal of Physical Chemistry C* 123 (1): 315–321.

6 Khazaei, M., Ranjbar, A., Arai, M. et al. (2017). Electronic properties and applications of MXenes: a theoretical review. *Journal of Materials Chemistry C* 5 (10): 2488–2503.

7 Khazaei, M., Wang, V., Sevik, C. et al. (2018). Electronic structures of iMAX phases and their two-dimensional derivatives: a family of piezoelectric materials. *Physical Review Materials* 2: 074002.

8 Lee, E. and Kim, D.-J. (2020). Review— recent exploration of two-dimensional MXenes for gas sensing: from a theoretical to an experimental view. *Journal of the Electrochemical Society* 167: 037515.

9 Yorulmaz, U., Demiroglu, I., Cakir, D. et al. (2020). A systematical ab-initio review of promising 2D MXene monolayers towards Li-ion battery applications. *Journal of Physics: Energy* 2 (3): 032006.

10 Zhongheng, F., Wang, N., Legut, D. et al. (2019). Rational design of flexible two-dimensional MXenes with multiple functionalities. *Chemical Reviews* 119 (23): 11980–12031.

11 Lotfi, R., Yilmaz, D.E., Vlcek, L., and van Duin, A. (2019). *Molecular Dynamics Simulations of MXenes: Ab Initio, Reactive, and Non-reactive Empirical Force Fields*, 137–157. Cham: Springer International Publishing.

12 Morales-Garcia, A., Calle-Vallejo, F., and Illas, F. (2020). MXenes: new horizons in catalysis. *ACS Catalysis* 10 (22): 13487–13503.

13 Zhu, J., Ha, E., Zhao, G. et al. (2017). Recent advance in MXenes: a promising 2D material for catalysis, sensor and chemical adsorption. *Coordination Chemistry Reviews* 352: 306–327.

14 Ronchi, R.M., Arantes, J.T., and Santos, S.F. (2019). Synthesis, structure, properties and applications of MXenes: current status and perspectives. *Ceramics International* 45 (15): 18167–18188.

15 Jones, R.O. (2015). Density functional theory: its origins, rise to prominence, and future. *Reviews of Modern Physics* 87: 897–923.

16 Maurer, R.J., Freysoldt, C., Reilly, A.M. et al. (2019). Advances in density-functional calculations for materials modeling. *Annual Review of Materials Research* 49 (1): 1–30.

17 Iftimie, R., Minary, P., and Tuckerman, M.E. (2005). Ab initio molecular dynamics: concepts, recent developments, and future trends. *Proceedings of the National Academy of Sciences* 102 (19): 6654–6659.

18 Marx, D. and Hutter, J. (2009). *Ab Initio Molecular Dynamics: Basic Theory and Advanced Methods*. Cambridge University Press.

19 Cui, Q. and Elstner, M. (2014). Density functional tight binding: values of semi-empirical methods in an ab initio era. *Physical Chemistry Chemical Physics* 16: 14368–14377.

20 Christensen, A.S., Kubar, T., Cui, Q., and Elstner, M. (2016). Semiempirical quantum mechanical methods for noncovalent interactions for chemical and biochemical applications. *Chemical Reviews* 116 (9): 5301–5337.

21 Khanal, R. and Irle, S. (2022). Quantum chemical investigation of the effect of alkali metal ions on the dynamic structure of water in aqueous solutions. *RSC Advances* 12 (39): 25500–25510.

22 Ganeshan, K., Khanal, R., Muraleedharan, M.G. et al. (2022). Importance of nuclear quantum effects on aqueous electrolyte transport under confinement in Ti_3C_2 MXenes. *Journal of Chemical Theory and Computation* 18 (11): 6920–6931.

23 Goyal, P., Qian, H.-J., Irle, S. et al. (2014). Molecular simulation of water and hydration effects in different environments: challenges and developments for DFTB based models. *The Journal of Physical Chemistry B* 118 (38): 11007–11027.

24 Nakai, H., Sakti, A.W., and Nishimura, Y. (2016). Divide-and-conquer-type density-functional tight-binding molecular dynamics simulations of proton diffusion in a bulk water system. *The Journal of Physical Chemistry B* 120 (1): 217–221.

25 Thomas, P.S., Hong, S., Islam, M.M. et al. The ReaxFF reactive force-field: development, applications and future directions. *npj Computational Materials* 2 (1): 1–14.

26 Koski, J.P., Moore, S.G., Clay, R.C. et al. (2022). Water in an external electric field: comparing charge distribution methods using ReaxFF simulations. *Journal of Chemical Theory and Computation* 18 (1): 580–594.

27 Haastrup, S., Strange, M., Pandey, M. et al. (2018). The computational 2D materials database: high-throughput modeling and discovery of atomically thin crystals. *2D Materials* 5 (4): 042002.

28 Khazaei, M., Arai, M., Sasaki, T. et al. (2013). Novel electronic and magnetic properties of two-dimensional transition metal carbides and nitrides. *Advanced Functional Materials* 23 (17): 2185–2192.

29 Nemani, S.K., Zhang, B., Wyatt, B.C. et al. (2021). High-entropy 2D carbide MXenes: $TiVNbMoC_3$ and $TiVCrMoC_3$. *ACS Nano* 15 (8): 12815–12825.

30 Xie, Y. and Kent, P.R.C. (2013). Hybrid density functional study of structural and electronic properties of functionalized $Ti_{n+1}X_n$ (X = C, N) monolayers. *Physical Review B* 87: 235441.

31 Xie, Y., Naguib, M., Mochalin, V.N. et al. (2014). Role of surface structure on Li-ion energy storage capacity of two-dimensional transition-metal carbides. *Journal of the American Chemical Society* 136 (17): 6385–6394.

32 Xie, Y., Dall'Agnese, Y., Naguib, M. et al. (2014). Prediction and characterization of MXene nanosheet anodes for non-lithium-ion batteries. *ACS Nano* 8 (9): 9606–9615.

33 Rajan, A.C., Mishra, A., Satsangi, S. et al. (2018). Machine-learning-assisted accurate band gap predictions of functionalized MXene. *Chemistry of Materials* 30 (12): 4031–4038.

34 Chengjie, L., Yang, L., Yan, B. et al. (2020). Nitrogen-doped Ti_3C_2 MXene: mechanism investigation and electrochemical analysis. *Advanced Functional Materials* 30 (47): 2000852.

35 Jiang, Z., Wang, P., Jiang, X., and Zhao, J. (2018). MBene (MnB): a new type of 2D metallic ferromagnet with high Curie temperature. *Nanoscale Horizons* 3: https://doi.org/10.1039/C7NH00197E.

36 Wang, D., Sun, Z.H., Han, D.X. et al. (2017). Ti_3BN monolayer: the MXene-like material predicted by first-principles calculations. *RSC Advances* 7 (20): 11834–11839.

37 Yi-Yuan, W., Bo, T., Zhu, X. et al. (2020). Two-dimensional tetragonal Ti_2BN: a novel potential anode material for Li-ion batteries. *Applied Surface Science* 513: 145821.

38 Chen, X., Kong, Z., Li, N. et al. (2016). Proposing the prospects of Ti_3CN transition metal carbides (MXenes) as anodes of Li-ion batteries: a DFT study. *Physical Chemistry Chemical Physics* 18 (48): 32937–32943.

39 Luo, X., Yang, J., Liu, H. et al. (2011). Predicting two-dimensional boron–carbon compounds by the global optimization method. *Journal of the American Chemical Society* 133 (40): 16285–16290.

40 Blochl, P.E. (1994). Projector augmented-wave method. *Physical Review B* 50 (24): 17953.

41 Liu, M., Rong, Z., Malik, R. et al. (2015). Spinel compounds as multivalent battery cathodes: a systematic evaluation based on ab initio calculations. *Energy & Environmental Science* 8 (3): 964–974.

42 Malyi, O.I., Sopiha, K.V., and Persson, C. (2019). Energy, phonon, and dynamic stability criteria of two-dimensional materials. *ACS Applied Materials & Interfaces* 11 (28): 24876–24884.

43 Gjerding, M.N., Taghizadeh, A., Rasmussen, A. et al. (2021). Recent progress of the computational 2D materials database (C2DB). *2D Materials* 8 (4): 044002.

44 Zhao, X., Wang, P., Lv, E. et al. (2021). Screening MXenes for novel anode material of lithium-ion batteries with high capacity and stability: a DFT calculation. *Applied Surface Science* 569: 151050.

45 Miao, N., Wang, J., Gong, Y. et al. (2020). Computational prediction of boron-based MAX phases and MXene derivatives. *Chemistry of Materials* 32 (16): 6947–6957.

46 Tao, H., Minmin, H., Gao, B. et al. (2018). Screening surface structure of MXenes by high-throughput computation and vibrational spectroscopic confirmation. *Journal of Physical Chemistry C* 122 (32): 18501–18509.

47 Togo, A. and Tanaka, I. (2015). First principles phonon calculations in materials science. *Scripta Materialia* 108: 1–5.

48 Baroni, S., De Gironcoli, S., Dal Corso, A., and Giannozzi, P. (2001). Phonons and related crystal properties from density-functional perturbation theory. *Reviews of Modern Physics* 73 (2): 515.

49 Khazaei, M., Ranjbar, A., Esfarjani, K. et al. (2018). Insights into exfoliation possibility of MAX phases to MXenes. *Physical Chemistry Chemical Physics* 20 (13): 8579–8592.

50 Mouhat, F. and Coudert, F.-X. (2014). Necessary and sufficient elastic stability conditions in various crystal systems. *Physical Review B* 90 (22): 224104.

51 Fredrickson, K.D., Anasori, B., Seh, Z.W. et al. (2016). Effects of applied potential and water intercalation on the surface chemistry of Ti_2C and Mo_2C MXenes. *Journal of Physical Chemistry C* 120 (50): 28432–28440.

52 Gao, G., O'Mullane, A.P., and Aijun, D. (2017). 2D MXenes: a new family of promising catalysts for the hydrogen evolution reaction. *ACS Catalysis* 7 (1): 494–500.

53 Perdew, J.P., Burke, K., and Ernzerhof, M. (1996). Generalized gradient approximation made simple. *Physical Review Letters* 77 (18): 3865.

54 Bae, S., Kang, Y.-G., Khazaei, M. et al. (2021). Electronic and magnetic properties of carbide MXenes—the role of electron correlations. *Materials Today Advances* 9: 100118.

55 Sun, J., Ruzsinszky, A., and Perdew, J.P. (2015). Strongly constrained and appropriately normed semilocal density functional. *Physical Review Letters* 115 (3): 036402.

56 Heyd, J. and Scuseria, G.E. (2004). Assessment and validation of a screened Coulomb hybrid density functional. *Journal of Chemical Physics* 120 (16): 7274–7280.

57 Khazaei, M., Ranjbar, A., Ghorbani-Asl, M. et al. (2016). Nearly free electron states in MXenes. *Physical Review B* 93 (20): 205125.

58 Schultz, T., Frey, N.C., Hantanasirisakul, K. et al. (2019). Surface termination dependent work function and electronic properties of $Ti_3C_2T_x$ MXene. *Chemistry of Materials* 31 (17): 6590–6597.

59 Agresti, A., Pazniak, A., Pescetelli, S. et al. (2019). Titanium-carbide MXenes for work function and interface engineering in perovskite solar cells. *Nature Materials* 1–7.

60 Babak Anasori, Y., Xie, M.B., Jun, L. et al. (2015). Two-dimensional, ordered, double transition metals carbides (MXenes). *ACS Nano* 9 (10): 9507–9516.

61 Sun, W., Xie, Y., and Kent, P.R.C. (2018). Double transition metal MXenes with wide band gaps and novel magnetic properties. *Nanoscale* 10 (25): 11962–11968.

62 Han, M., Maleski, K., Shuck, C.E. et al. (2020). Tailoring electronic and optical properties of MXenes through forming solid solutions. *Journal of the American Chemical Society* 142 (45): 19110–19118.

63 Zhiguo, D., Cheng, W., Chen, Y. et al. (2021). High-entropy atomic layers of transition-metal carbides (MXenes). *Advanced Materials* 33 (39): 2101473.

64 Zhiguo, D., Cheng, W., Chen, Y. et al. (2021). High-entropy carbonitride MAX phases and their derivative MXenes. *Advanced Energy Materials* 12 (6): 2103228.

65 Liang, Y., Khazaei, M., Ranjbar, A. et al. (2017). Theoretical prediction of two-dimensional functionalized MXene nitrides as topological insulators. *Physical Review B* 96 (19): 195414.

66 Zhang, L., Tang, C., Zhang, C., and Aijun, D. (2020). First-principles screening of novel ferroelectric MXene phases with a large piezoelectric response and unusual auxeticity. *Nanoscale* 12 (41): 21291–21298.

67 Kamysbayev, V., Filatov, A.S., Huicheng, H. et al. (2020). Covalent surface modifications and superconductivity of two-dimensional metal carbide MXenes. *Science* 369 (6506): 979–983.

68 Bekaert, J., Sevik, C., and Milosevic, M.V. (2020). First-principles exploration of superconductivity in MXenes. *Nanoscale* 12 (33): 17354–17361.

69 Tang, Q., Zhou, Z., and Shen, P. (2012). Are MXenes promising anode materials for li ion batteries? Computational studies on electronic properties and li storage

capability of Ti_3C_2 and $Ti_3C_2X_2$ (X= F, OH) monolayer. *Journal of the American Chemical Society* 134 (40): 16909–16916.

70 Eames, C. and Saiful Islam, M. (2014). Ion intercalation into two-dimensional transition-metal carbides: global screening for new high-capacity battery materials. *Journal of the American Chemical Society* 136 (46): 16270–16276.

71 Sun, Q., Dai, Y., Ma, Y. et al. (2016). Ab initio prediction and characterization of Mo_2C monolayer as anodes for lithium-ion and sodium-ion batteries. *Journal of Physical Chemistry Letters* 7 (6): 937–943.

72 Naguib, M., Halim, J., Jun, L. et al. (2013). New two-dimensional niobium and vanadium carbides as promising materials for Li-ion batteries. *Journal of the American Chemical Society* 135 (43): 15966–15969.

73 Meng, Q., Ma, J., Zhang, Y. et al. (2018). Theoretical investigation of zirconium carbide MXenes as prospective high capacity anode materials for Na-ion batteries. *Journal of Materials Chemistry A* 6 (28): 13652–13660.

74 Zhan, C., Naguib, M., Lukatskaya, M. et al. (2018). Understanding the MXene pseudocapacitance. *Journal of Physical Chemistry Letters* 9 (6): 1223–1228.

75 Sun, Y., Zhan, C., Kent, P.R.C. et al. (2019). Proton redox and transport in MXene-confined water. *ACS Applied Materials & Interfaces* 12 (1): 763–770.

76 Sheppard, D., Terrell, R., and Henkelman, G. (2008). Optimization methods for finding minimum energy paths. *The Journal of Chemical Physics* 128 (13): 134106.

77 Song, D.-X., Ma, W.-G., and Zhang, X. (2020). Correlated migration of ions in a 2D heterostructure anode: guaranteeing a low barrier for a high site occupancy. *Journal of Materials Chemistry A* 8 (34): 17463–17470.

78 Al-Hamadani, Y.A.J., Jun, B.-M., Yoon, M. et al. (2020). Applications of MXene-based membranes in water purification: a review. *Chemosphere* 254: 126821.

79 Kui, X., Shao, H., Lin, Z. et al. (2020). Computational insights into charge storage mechanisms of supercapacitors. *Energy & Environmental Materials* 3 (3): 235–246.

80 Tao, W., Kent, P.R.C., Gogotsi, Y., and Jiang, D.-e. (2022). How water attacks MXene. *Chemistry of Materials* 34 (11): 4975–4982.

81 Aierken, Y., Sevik, C., Gülseren, O. et al. (2018). MXenes/graphene heterostructures for Li battery applications: a first principles study. *Journal of Materials Chemistry A* 6 (5): 2337–2345.

82 Demiroglu, I., Peeters, F.M., Gülseren, O. et al. (2019). Alkali metal intercalation in MXene/graphene heterostructures: a new platform for ion battery applications. *Journal of Physical Chemistry Letters* 10 (4): 727–734.

83 Gao, Q., Sun, W., Ilani-Kashkouli, P. et al. (2020). Tracking ion intercalation into layered Ti_3C_2 MXene films across length scales. *Energy & Environmental Science* 13 (8): 2549–2558.

84 Muckley, E.S., Naguib, M., Wang, H.-W. et al. (2017). Multimodality of structural, electrical, and gravimetric responses of intercalated MXenes to water. *ACS Nano* 11 (11): 11118–11126.

85 Shpigel, N., Levi, M.D., Sigalov, S. et al. (2018). Direct assessment of nanoconfined water in 2D Ti_3C_2 electrode interspaces by a surface acoustic technique. *Journal of the American Chemical Society* 140 (28): 8910–8917.

86 Luo, J., Zhang, W., Yuan, H. et al. (2017). Pillared structure design of MXene with ultralarge interlayer spacing for high-performance lithium-ion capacitors. *ACS Nano* 11 (3): 2459–2469.

87 Luo, J., Fang, C., Jin, C. et al. (2018). Tunable pseudocapacitance storage of MXene by cation pillaring for high performance sodium ion capacitors. *Journal of Materials Chemistry A* 6 (17): 7794–7806.

88 Lukatskaya, M.R., Mashtalir, O., Ren, C.E. et al. (2013). Cation intercalation and high volumetric capacitance of two-dimensional titanium carbide. *Science* 341 (6153): 1502–1505.

89 Brady, A., Liang, K., Vuong, V.Q. et al. (2021). Pre-sodiated $Ti_3C_2T_x$ MXene structure and behavior as electrode for sodium-ion capacitors. *ACS Nano* 15 (2): 2994–3003.

90 Ganeshan, K., Shin, Y.K., Osti, N.C. et al. (2020). Structure and dynamics of aqueous electrolytes confined in 2D-TiO_2/$Ti_3C_2T_2$ MXene heterostructures. *ACS Applied Materials & Interfaces* 12 (52): 58378–58389.

91 Yang-Xin, Y. (2016). Prediction of mobility, enhanced storage capacity, and volume change during sodiation on interlayer-expanded functionalized Ti_3C_2 MXene anode materials for sodium-ion batteries. *Journal of Physical Chemistry C* 120 (10): 5288–5296.

92 Osti, N.C., Naguib, M., Alireza Ostadhossein, Y. et al. (2016). Effect of metal ion intercalation on the structure of MXene and water dynamics on its internal surfaces. *ACS Applied Materials & Interfaces* 8 (14): 8859–8863.

93 Osti, N.C., Naguib, M., Ganeshan, K. et al. (2017). Influence of metal ions intercalation on the vibrational dynamics of water confined between MXene layers. *Physical Review Materials* 1 (6): 065406.

94 Shao, H., Kui, X., Yih-Chyng, W. et al. (2020). Unraveling the charge storage mechanism of $Ti_3C_2T_x$ MXene electrode in acidic electrolyte. *ACS Energy Letters* 5 (9): 2873–2880.

95 Zaman, W., Matsumoto, R.A., Thompson, M.W. et al. (2021). In situ investigation of water on MXene interfaces. *Proceedings of the National Academy of Sciences* 118 (49): e2108325118.

96 Lihua, X. and Jiang, D.-e. (2021). Proton dynamics in water confined at the interface of the graphene-MXene heterostructure. *Journal of Chemical Physics* 155 (23): 234707.

97 Kui, X., Lin, Z., Merlet, C.'l. et al. (2018). Tracking ionic rearrangements and interpreting dynamic volumetric changes in two-dimensional metal carbide supercapacitors: a molecular dynamics simulation study. *ChemSusChem* 11 (12): 1892–1899.

98 Kui, X., Ji, X., Zhang, B. et al. (2016). Charging/discharging dynamics in two-dimensional titanium carbide (MXene) slit nanopore: insights from molecular dynamic study. *Electrochimica Acta* 196: 75–83.

99 Liang, K., Matsumoto, R.A., Zhao, W. et al. (2021). Engineering the interlayer spacing by pre-intercalation for high performance supercapacitor MXene electrodes in room temperature ionic liquid. *Advanced Functional Materials* 31 (33): 2104007.

17

MXenes' Optical and Optoelectronic Properties and Related Applications

Danzhen Zhang, Kanit Hantanasirisakul, and Yury Gogotsi

Department of Materials Science and Engineering, A. J. Drexel Nanomaterials Institute, Drexel University, Philadelphia, PA, USA

17.1 Introduction

Recently, nanomaterials have found great potential in optics and optoelectronics as their tunable bandgaps and quantum confinement effects [1, 2]. Most of MXenes are metallic 2D materials that have high carrier concentration comparable to bulk metals, setting MXenes apart from the majority of semiconducting or insulating 2D materials. This determines many of their properties, such as surface plasmon resonance with transverse surface plasmons in the ultraviolet (UV), visible or near-infrared (IR) ranges. Moreover, unlike in conventional metals, the plasmon resonance peak position can be reversibly shifted – one can consider MXenes as 2D metals with tunable Fermi level, like in semiconductors. Beyond that, several kinds of MXenes with pure oxygen or fluorine terminations showed insulating behavior, such as Ti_2CO_2, $Mo_2TiC_2O_2$, and $Ti_3N_2F_2$, which may provide a possibility of using MXenes in transistors with a high on/off ratio or as topological insulators for practical applications at room temperature [3–5]. The variety of MXene compositions, structures, and tunable surface terminations enable numerous optical, photonic, and optoelectronic applications [6, 7].

With over 30 stoichiometric MXenes reported and a growing number of predicted structures and compositions, the diverse family of MXenes provides unprecedented tunability of optical properties, as shown in Figure 17.1. In the visible-near IR range, composition and structure variation resulted in strong extinction peaks with broad spectral diversity. For example, $Ti_3C_2T_x$ exhibited an extinction peak around 800 nm, which is attributed to plasmonic resonance [9].

Transition Metal Carbides and Nitrides (MXenes) Handbook: Synthesis, Processing, Properties and Applications, First Edition. Edited by Chuanfang Zhang and Michael Naguib.
© 2024 John Wiley & Sons, Inc. Published 2024 by John Wiley & Sons, Inc.

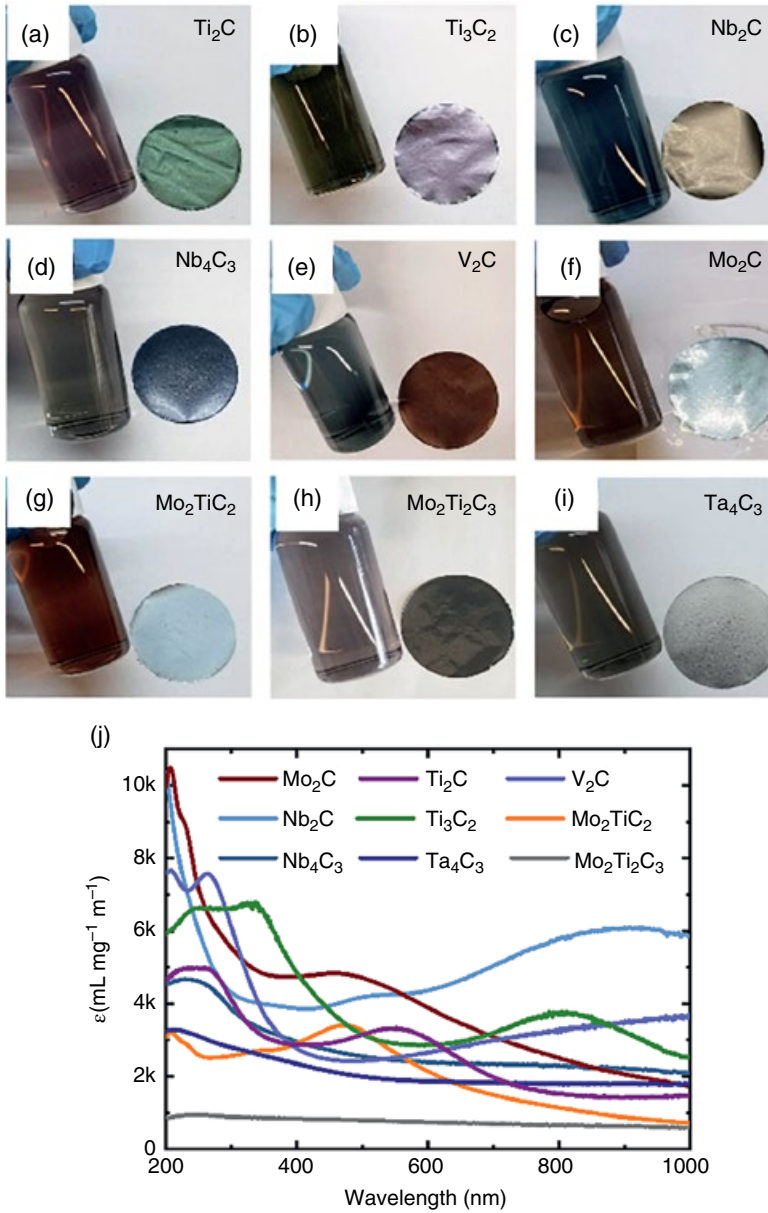


Figure 17.1 Optical properties of representative MXenes in the UV–vis–NIR range. (a–i) Digital photographs of MXene colloidal dispersions and corresponding free-standing films fabricated by vacuum-assisted filtration for (a) Ti_2CT_x, (b) $Ti_3C_2T_x$, (c) Nb_2CT_x, (d) $Nb_4C_3T_x$, (e) V_2CT_x, (f) Mo_2CT_x, (g) $Mo_2TiC_2T_x$, (h) $Mo_2Ti_2C_3T_x$, and (i) $Ta_4C_3T_x$. The MXene film diameters are 4.0 cm. (j) UV–vis–NIR optical extinction properties of the MXene solution shown in (a–i). Wavelength-dependent extinction coefficient for each MXene calculated by determining the extinction coefficient at each wavelength from 200 to 1000 nm ($h\nu$ = 6.2–1.2 eV). *Source:* Maleski

On the other hand, its structural analogue with one less Ti-C layer, Ti_2CT_x, exhibited a qualitatively similar spectrum but with the extinction peak at around 550 nm [8]. In addition, the extinction peak changed drastically when comparing MXenes with different transition metals. This demonstrates that each MXene has its own optical signature and the optical properties can be tuned by varying the chemical composition and the number of layers. Based on this, we will highlight the plasmonic, ultrafast dynamic, nonlinear absorption, and optoelectronic properties as well as related applications in this chapter and target the current challenges and future outlook.

17.2 Plasmonic Properties

Plasmonic properties refer to the interaction of light with a metal that generates the cloud of free electrons and induces charge density fluctuation on the surface of the metal. This is called surface plasmon wave and can be used in a variety of applications, such as surface-enhanced Raman spectroscopy (SERS), photodetectors, and photothermal cancer therapy. The coupling effect between surface plasmons and light greatly enhances the light-matter interaction; therefore, the light can be confined to a small area and the local electromagnetic field intensity can be enhanced largely [10].

While noble metals are considered the primary choice for plasmonic materials, MXenes have gained much attention recently due to the tunability of their plasmonic properties, while maintaining high carrier concentration. The first discovered and most thoroughly studied MXene, $Ti_3C_2T_x$, exhibits intense surface plasmons that can be detected at the nanometer scale with the energy as low as 0.30 eV [11]. Moreover, $Ti_3C_2T_x$ was found to have a tunable electronic structure. Altering its surface termination from =O to –OH and removing -F leads to change of the interband transition and surface plasmon energy. The removal of fluorine atoms from the surface and reduction of MXene increased the free electron density and led to a blue shift of surface plasmon mode. Electron energy loss spectroscopy (EELS) investigation of localized surface plasmon modes of $Ti_3C_2T_x$ identified six distinct peaks at 0.44, 0.66, 0.80, and 0.95 eV, which were assigned to multipolar longitudinal surface plasmon, 1.70 eV, assigned to transverse surface plasmon mode, and 3.50 eV assigned to an interband transition (Figure 17.2a) [9]. Beyond $Ti_3C_2T_x$, other MXene such as Mo_2CT_x also demonstrates surface plasmon mode by EELS measurement (Figure 17.2b) [13]. The distinct peaks located at 0.30 and 0.39 eV were interpreted as dipole and quadrupole modes of surface plasmon, while the peak at 2.45 eV was assigned to transversal surface plasmon mode, which is solely related to free electron concentration. By designing a patterned nanostructure of MXene, the localized surface plasmon resonances can be enhanced further, leading to broadband absorption (85–90%), as shown in

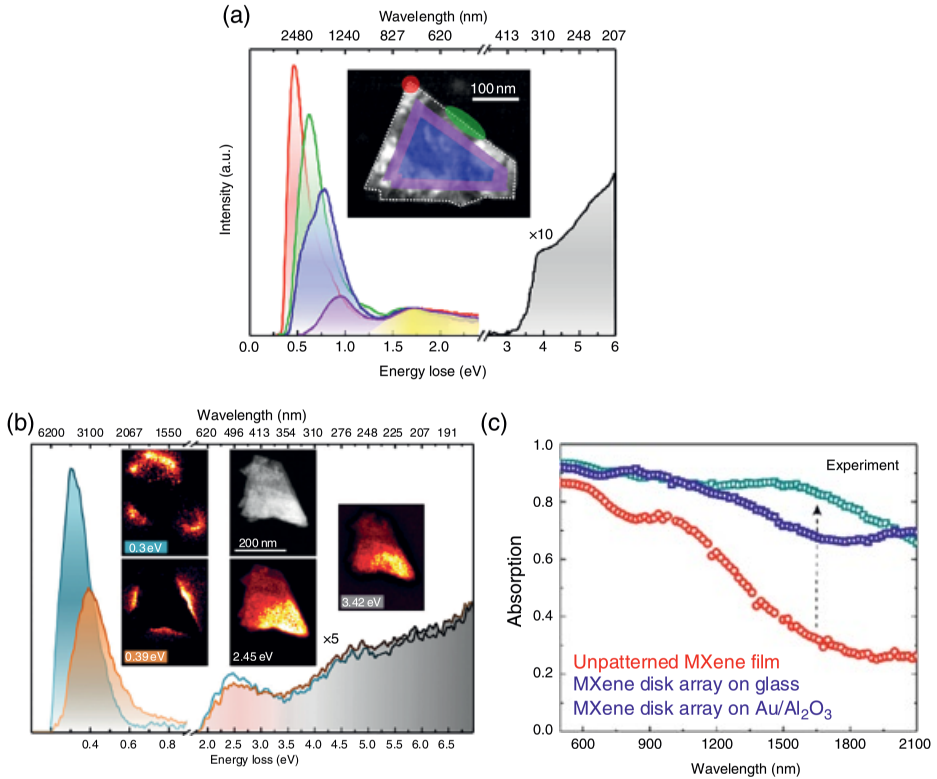


Figure 17.2 (a) Zero loss peak (ZLP)-subtracted electron energy loss spectra (EELS) acquired on a truncated triangular flake of $Ti_3C_2T_x$ (7.50±0.04 nm). Inset: STEM-HAADF micrograph of the $Ti_3C_2T_x$ flake on a Si_3N_4 supporting membrane (black area). Circle at top corner and ellipse on the edge mark the most intense excitation positions for the dipole and quadrupole modes, respectively. Blue and purple regions denote the strongest excitation areas for the central modes. White dotted contour defines the perimeter within which the transversal mode (1.70 eV) and interband transition (3.50 eV) could be excited. *Source:* El-Demellawi et al. [9]/Reproduced from American Chemical Society. (b) ZLP-subtracted EELS acquired on a truncated triangular nanosheet of Mo_2CT_x (≈58±1 nm). Insets in (b): ADF-STEM micrograph of the Mo_2CT_x nanosheet Si_3N_4 supporting membrane (black area), and the EELS fitted intensity maps of the corresponding longitudinal SP modes, namely, dipole (0.30 eV) and quadrupole (0.39 eV), addition to the transversal SP mode (2.45 eV) and the interband transition (starting at 3.42 eV). *Source:* Velusamy et al. [13]/John Wiley & Sons, Inc. (c) Measured absorption spectra comparison for the two types of disk arrays and unpatterned MXene film. *Source:* Chaudhuri et al. [12]/Reproduced from American Chemical Society.

Figure 17.2c. Due to their multiple plasmonic features that are tunable, MXenes are promising candidates for plasmonic applications such as photothermal materials for cancer treatment, water desalination, SERS substrates, and photodetectors.

17.3 Plasmonic Applications

One notable plasmonic application of MXenes is photothermal conversion, as they can efficiently convert light into thermal energy. They exhibit high extinction coefficients and high light-to-heat conversion efficiency. While the precise mechanisms of the interactions between MXenes and electromagnetic waves are not fully understood, the photothermal effect in $Ti_3C_2T_x$ has been attributed to surface plasmon resonances that enhance the absorption in the near-IR range. The internal light-to-heat conversion of $Ti_3C_2T_x$ was measured to be nearly 100%, while the water evaporation efficiency was measured to approach 84%, which is similar to the state-of-the-art conversion efficiency for photothermal evaporation systems [14]. Upon irradiation, the temperature of a droplet of $Ti_3C_2T_x$ solution increased by 15 °C in less than 60 seconds, showing the capability of light-to-heat conversion at different wavelengths, as shown in Figure 17.3a. Under sunlight illumination, MXene-coated PVDF was able to achieve an equilibrium temperature of around 75 °C which is obviously much higher than the unmodified PVDF membrane, demonstrating the efficient interfacial water heating by freestanding MXene-PVDF membrane (Figure 17.3b). Beyond $Ti_3C_2T_x$, Nb_2CT_x, and $Ta_4C_3T_x$ also exhibited extraordinarily high intrinsic photothermal conversion efficiency, which was used for *in vivo* photothermal ablation and cancer theranostics applications [17, 18].

Moreover, due to the strong tunability of surface plasmons, MXenes have also been explored as SERS substrates with high enhancement factors (EF) and detection sensitivity. Generally, SERS enhancement can be attributed to surface plasmon resonance effect excited by incident light on rough surface of metallic materials. Spray-coated $Ti_3C_2T_x$ demonstrated a significant increase in the EF on the order of 10^5 for detecting Rhodamine 6G with a low concentration of 10^{-7} M, as shown in Figure 17.3c [15]. Beyond $Ti_3C_2T_x$, Ta_2CT_x, and Nb_2CT_x also demonstrated detection limits of 10^{-7} and 10^{-8} M for methyl violet and methylene blue molecules, respectively [19]. In 2022, the SERS EF was increased to 10^{12} and the sensitivity was increased to femtomolar concentration using Rhodamine 6G as a model molecule with a solid-solution MXene, TiVC [20]. Shevchuk et al. showed capability of MXenes beyond $Ti_3C_2T_x$ to perform as a SERS substrate [21]. They elucidated that Ti_3CNT_x and Ti_2CT_x have relatively high EF due to higher carrier concentration, whereas Mo_2CT_x, $Mo_2TiC_2T_x$, and Nb_2CT_x had lower carrier concentrations and thus lower EF values. Moreover, V_2CT_x exhibited an order of

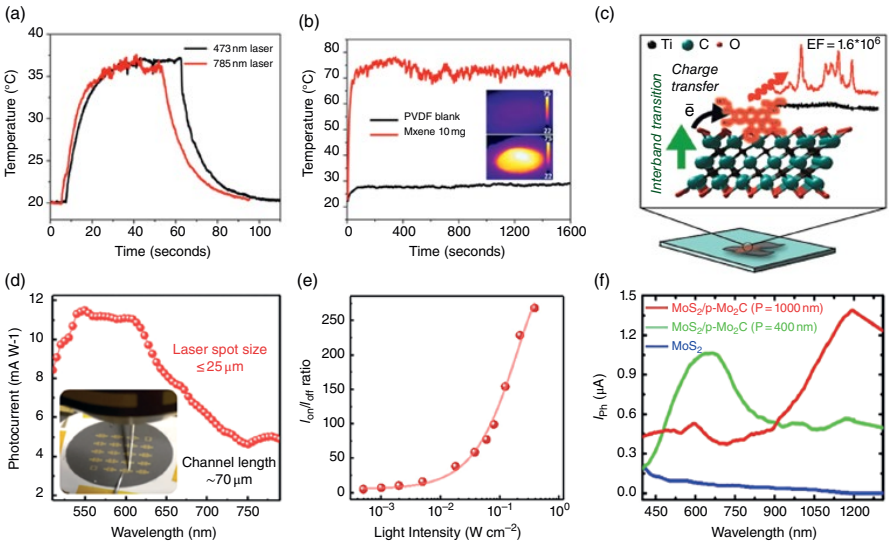


Figure 17.3 (a) Temperature profile of a droplet containing 0.10 mg ml^{-1} MXene in the light-to-heat conversion experiment under two separate laser irradiations. (b) Temperature profile of polydimethylsiloxane (PDMS) modified polyvinylidene fluoride (PVDF) membrane and MXene-PVDF membrane in air under one sun illumination. Top and bottom insets are IR photos of PDMS-modified PVDF membrane and MXene membrane, respectively. *Source:* Li et al. [14]/American Chemical Society/CC BY 4.0. (c) A possible SERS mechanism of MXene as a substrate for organic dye detection. *Source:* Sarycheva et al. [15]/American Chemical Society. (d) Photoresponse of a Mo_2CT_x thin film photodetector as a function of wavelength, under 0.70 V bias voltage. Inset: Photograph of the photocurrent setup showing one of the investigated samples, illumination objective, and the contact electrodes. (e) Ratios of the photocurrent to the dark current of the Mo_2CT_x thin film photodetector as function of different light intensities. *Source:* Velusamy et al. [13]/John Wiley & Sons. (f) Spectral photocurrent curves from the MoS_2 photodetector device with and without hybrid structures. *Source:* Jeon et al. [16]/John Wiley & Sons.

magnitude lower EF since the etching process introduced more defects. These demonstrated plasmonic properties and hence photothermal conversion, as well as SERS performance, can be tuned by altering MXene composition.

The high conductivity and surface plasmon-assisted hot electron generation of MXenes make them great candidates for photodetection. The localized surface plasmons are able to enhance the local electromagnetic fields, thereby resulting in increasing optical absorption [22]. In a comparative study, Mo_2CT_x exhibited the highest photodetection performance among the different MXenes studied, that is, Mo_2CT_x, $Ti_3C_2T_x$, Ti_2CT_x, and V_2CT_x [13]. The Mo_2CT_x-based photodetector showed a broadband and high photocurrent in the visible range (400–800 nm), as shown in Figure 17.3d. The transversal surface plasmon mode at 2.45 eV enhanced the photocurrent generation in the visible range. With the high mechanical and chemical stability of MXenes, high-performance plasmonic photodetection devices can be fabricated. Integrated with other 2D materials such as MoS_2, Mo_2CT_x has demonstrated an enhanced photoresponsivity of $10^3\,A\,W^{-1}$ within a broad spectral response range from 400 to 1300 nm (Figure 17.3f) [16]. This integrated heterostructure makes it possible to fabricate multiperiod gratings and reduce the Schottky barrier at the interface, which paves the way to innovative photodetector applications.

17.4 Ultrafast Carrier Dynamics

Unambiguous determination of the optical ultrafast carrier dynamics in MXenes is necessary for their reliable use in applications such as electromagnetic interference (EMI) shielding and laser systems. Ultrafast spectroscopy has been utilized to elucidate the dynamic processes of electrons and photons in MXenes, which occur at femto- to picoseconds time scale. The dependence of the ultrafast transient spectra on the different excitation wavelengths (325, 500, and 780 nm) was studied using pump–probe spectroscopy, as shown in Figure 17.4a [23]. All the transient spectra exhibited a photo-induced absorption enhancement in the visible range from 450 to 680 nm and near-IR range from 850 to 1100 nm. Notably, there were two electronic absorption peaks at the early stage following the photoexcitation, which comes from the internal electronic excitations. Then the peaks broadened and shifted at the later stage, since the electronic absorption was converted into thermal energy. Similar to ultrafast absorption measurement, simultaneous ultrafast transmission and reflection (SUTR) pump–probe technique allows the determination of true transient absorption. Combined with other techniques such as complementary spectroscopic ellipsometry, the origin of optical absorption of $Ti_3C_2T_x$ was further elucidated. From SUTR pump–probe measurements, the 800 nm resonance exhibited a time domain response indicative of a surface

plasmon with qualitative differences from the time domain response of interband transitions, as shown in Figure 17.4b [24]. For all probe wavelength studied, there was a pump-induced reduction of reflection and a positive change in transmission. The transient absorption at 520 and 700 nm was positive at a time scale greater than a picosecond and this was attributed to electron-phonon coupling. This change in transmission, reflection, and absorption demonstrates that $Ti_3C_2T_x$

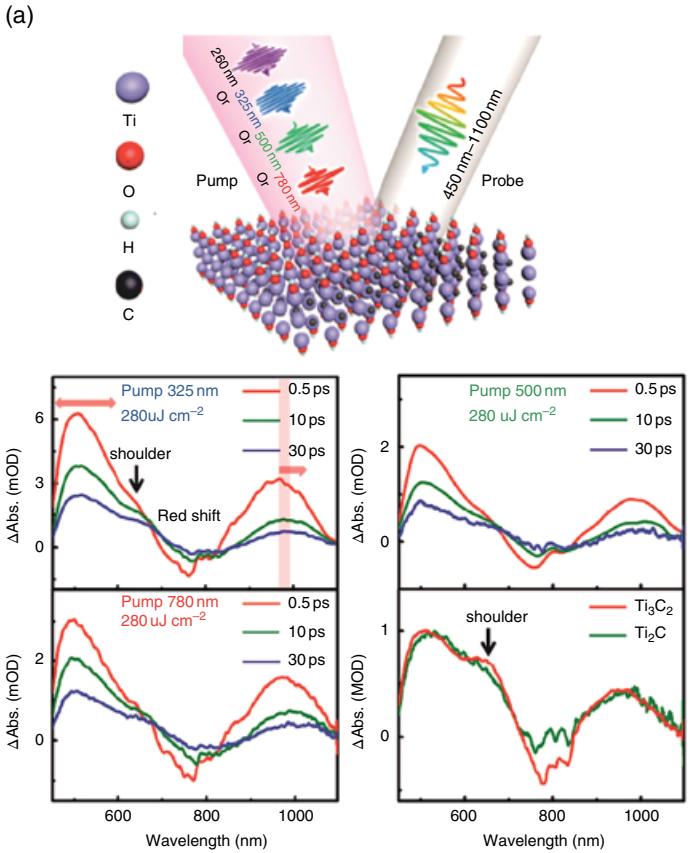


Figure 17.4 (a) A schematic of pump–probe spectroscopy of MXenes and transient spectra under different pump excitation. *Source:* Zhang et al. [23]/American Chemical Society. (b) Transmission, reflection, and obtained absorption transient spectra of $Ti_3C_2T_x$ probed at 520, 700, 1020, and 1320 nm with 785 nm pump pulse. *Source:* Lioi et al. [24]/American Chemical Society. (c) Photo-induced change in EMI SE at different times following excitation with 800 nm, 950 μJ cm^{-2} pulse. *Source:* Li et al. [25]/American Chemical Society. (d) Transient absorption spectrum of the Nb_2CT_x dispersion as a function of probe delay time with different pump intensities at wavelengths of 1064 nm. *Source:* Wang et al. [26]/American Chemical Society.

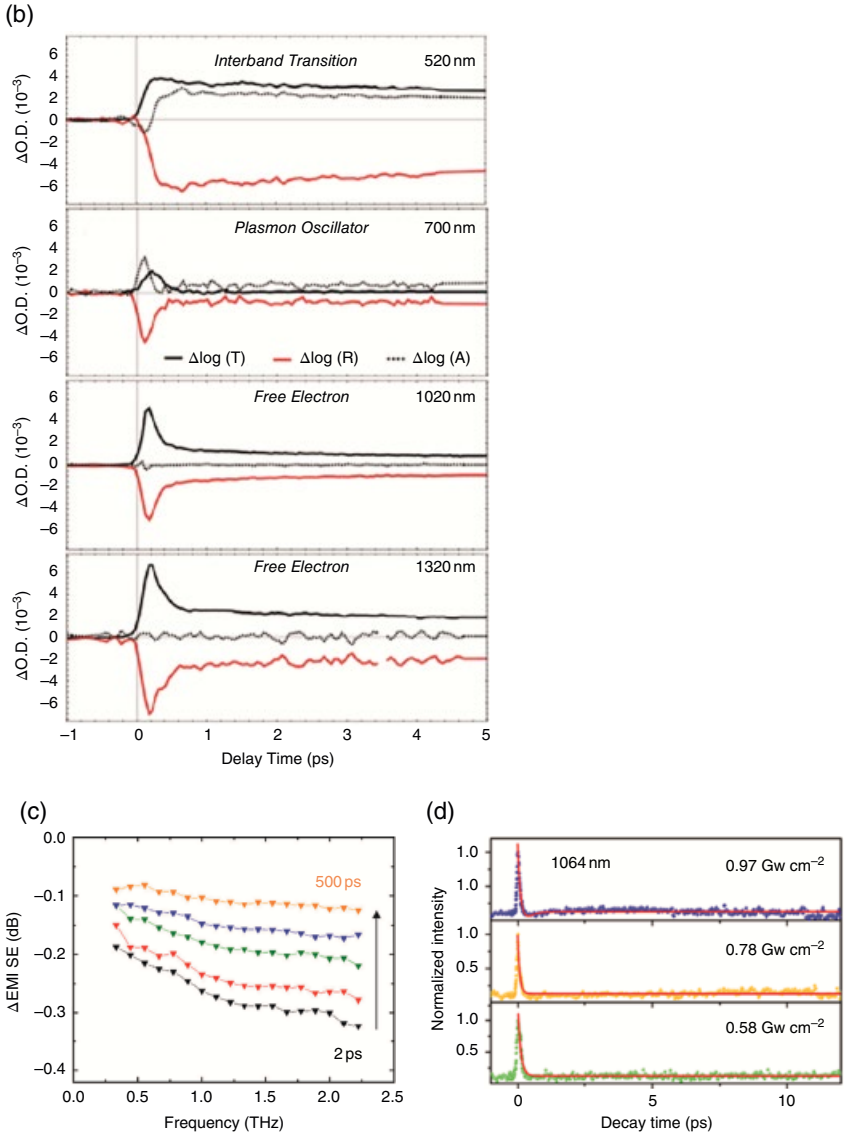


Figure 17.4 (Continued)

is a potential saturable absorber, which can be integrated in laser systems. These studies on the ultrafast carrier dynamics have provided a more complete picture of the underlying ultrafast processes in MXenes. Given the excellent light-to-heat conversion that MXenes provide, investigations on the ultrafast photon–phonon

interactions provide an important step in successfully employing MXenes in future photonic devices.

Beyond the UV–vis–NIR range, MXenes also show high absorption of electromagnetic irradiation in the gigahertz (GHz) and terahertz (THz) frequency range. $Ti_3C_2T_x$ MXene has been recently suggested as a promising material for EMI shielding in the 8–18 GHz frequency range with a shielding efficiency of >50 dB for a 2.5 μm film [27]. In a new study, both 800 and 400 nm optical excitation pulses was demonstrated a transient suppression of THz absorption that lasts over nanoseconds. The EMI shielding efficiency was suppressed over the THz probe (0.25–2.25 THz) with the magnitude exhibiting a slow monotonous increase with time, as shown in Figure 17.4c [25]. This suppression is a direct result of photoinduced transient decrease in conductivity, which comes from the carrier-phonon scattering. The capability of reducing EMI shielding efficiency by ultrashort optical pulses make $Ti_3C_2T_x$ MXene promising for dynamic control of THz EMI shielding, such as in THz communication channel. Moreover, $Ti_3C_2T_x$ is not the only MXene with ultrafast electron-phonon scattering. Nb_2CT_x exhibited ultrafast cooling and recombination processes of hot carriers within a time scale of 3 ps under a 400 nm pulse (Figure 17.4d). The ultrafast dynamics of MXenes combined with their versatility is extremely promising for designing photonic devices such as ultrahigh-speed optical modulators and ultrafast response photodetectors.

17.5 Nonlinear Optical Properties

Nonlinear optical properties involve light-matter interactions, where the electromagnetic field is strong enough to cause a nonlinear response. Highly nonlinear materials are crucial for various optics applications such as laser optics, ultrafast signal processing, and sensing. In the nonlinear regime, many 2D materials exhibit decreased absorption with increasing light intensities due to saturable absorption. Saturable absorption arises from an event when the energy of incident light is higher than the optical bandgap; the electrons at the ground state could be promoted to excited states. According to Pauli exclusion principal, two identical electrons cannot occupy the same state, which results in optical bleaching, as shown in Figure 17.5a. Z-scan measurements (Figure 17.5b) showed the saturable absorption behavior at 1064 nm of a $Ti_3C_2T_x$ thin film arising from plasmon-induced ground state absorption [29]. The modulation depth and saturation fluence varies with film thickness, as shown in Figure 17.5c. The saturation fluence decreased significantly with increasing film thickness, which comes from a strong optical absorption and higher imaginary component of dielectric parameters for thicker $Ti_3C_2T_x$ films. A maximum modulation depth of ≈50% was observed at 70.0 mJ cm^{-2} for a 67-nm-thick $Ti_3C_2T_x$ film, which demonstrated that MXenes

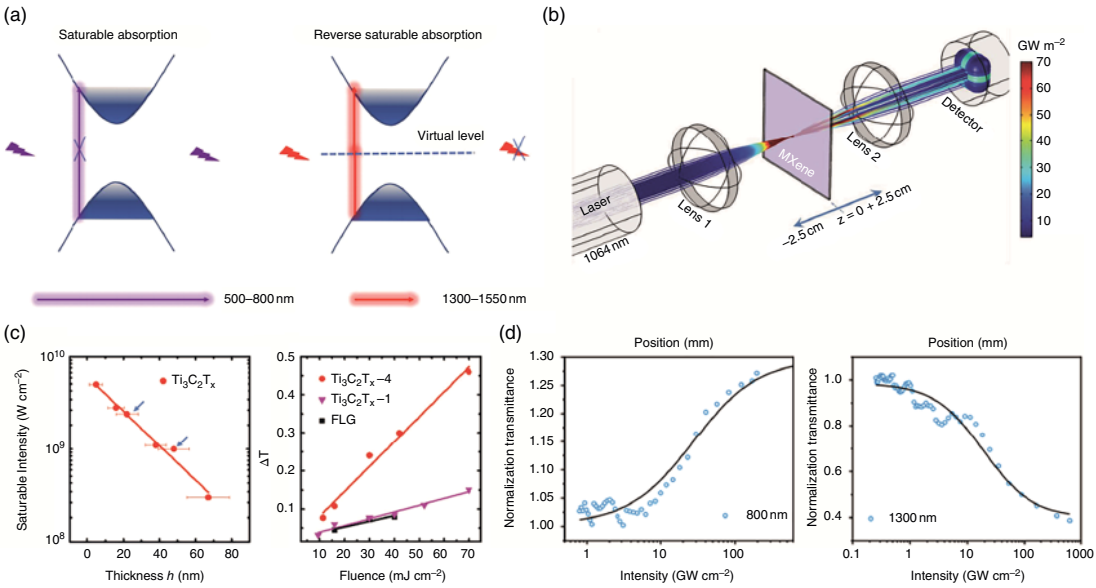


Figure 17.5 (a) A schematic diagram for saturable absorption processes (Pauli Blocking) and reversible saturable absorption processes (two-phonon absorption). *Source:* Adapted from Gao et al. [28]. (b) A schematic Z-scan measurement of MXene thin film. (c) Thickness-dependent saturable fluence intensity and the saturable absorption behavior as a function of laser pulses. *Source:* Dong et al. [29]/John Wiley & Sons. (d) Nonlinear optical properties of Ti_3CNT_x showing normalized transmittance intensity versus incident optical pulse at 800 and 1300 nm. *Source:* Gao et al. [28]/American Chemical Society.

are more favorable compared to other 2D materials due to their higher damage threshold. Nonlinear properties of other MXenes, such as Ti_3CNT_x and Nb_2CT_x, were also reported recently [26, 28]. With the open-aperture Z-scan technique, Ti_3CNT_x performed as a typical saturable absorber under 800 nm ultrafast laser irradiation and a reverse-saturable absorber under 1300 nm laser, as shown in Figure 17.5d, while the reverse-saturable absorption was ascribed to multiphoton absorption [30]. For Nb_2CT_x, the reverse-saturable absorption transition occurs in the range of 1500–1600 nm, which suggests that it has a potential for near-IR photonic applications such as optical switches and saturable absorbers.

17.6 Nonlinear Optical Applications

The currently used saturable absorption materials still have some drawbacks such as long recovery time, large indirect bandgap, and instability [31]. Compared with traditional saturable absorption materials, MXenes have broadband optical responses, tunable optical bandgap, high electrical conductivity, which enable their use in ultrafast lasers, where MXenes serve as a spectral filter to induce mode-locked laser pulses. Various ultrafast pulsed lasers utilizing MXene saturable absorbers have been investigated at wavelengths of 1, 1.5, 2, and 3 μm. A few-layer $Ti_3C_2T_x$-based saturable absorber is implemented in a Yb-doped fiber ring cavity for mode-locking operation [32]. A typical bell-shaped mode-locked optical spectrum centered at 1065.89 nm was observed. The broadband optical switching capabilities were demonstrated via a similar fiber ring with an Er-doped fiber cavity. In this case, the mode-locked wavelength ranges from 1550 to 1620 nm and covers the whole conventional telecommunication band, enabling applications in materials processing and laser probing, as shown in Figure 17.6a [32]. Beyond the near-IR range, mid-IR (MIR) ultrafast lasers have also gained much interest since their diverse applications, such as MIR spectroscopy and gas detection. $Ti_3C_2T_x$ was used to generate ultrafast pulses in the MIR range centered at 2788 nm with a duration of 640 ns, as shown in Figure 17.6b. The pulse duration is shorter than for many other 2D materials such as graphene (2.90 μs), black phosphorus (1.18 μs), and MoS_2 (806 ns), indicating that $Ti_3C_2T_x$ possesses more advanced capability of pulse generation [33]. Ultrafast lasers at other wavelengths were also possible between 1895 and 2050 nm with a short during of 2.4 μs [36]. A square wave pulse mode-locked fiber laser was also fabricated using Nb_2CT_x as saturable absorber with rectangular spectra centered around 1031 nm, as shown in Figure 17.6c [34]. Nonlinearity of Ti_2CT_x and V_2CT_x was also utilized in a mode-locked laser centered at 1565 and 1559 nm [37, 38]. Additionally, a Ti_2CT_x saturable absorber was used as a Q-switcher to realize a pulsed fiber laser operating at 2.8 μm, which showed excellent nonlinear absorption performance in the MIR regime [38].

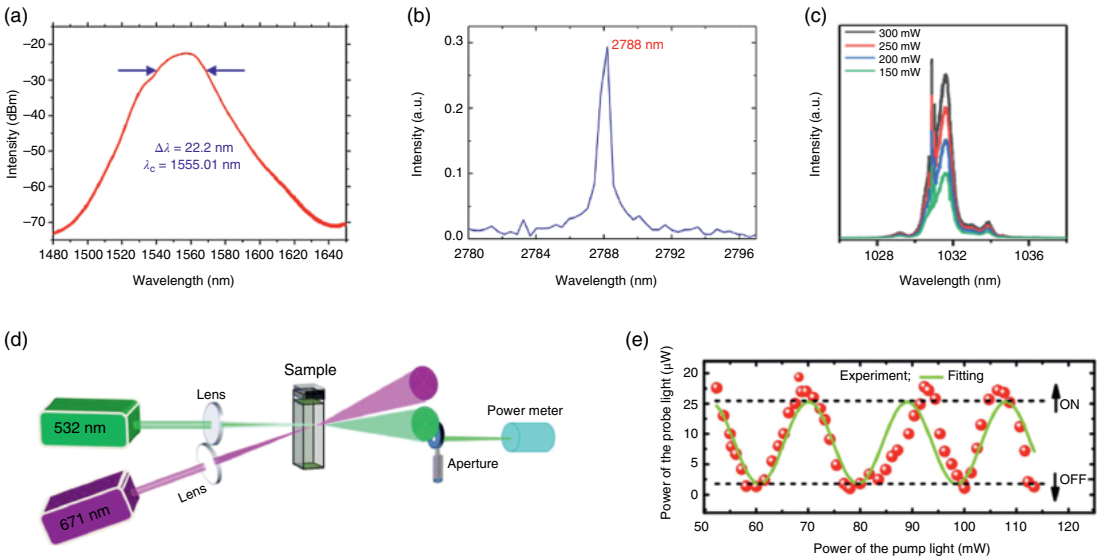


Figure 17.6 (a) Spectrum of erbium-doped fiber laser passively mode locked using a MXene $Ti_3C_2T_x$ saturable absorber centered at 1555.1 nm under the pump power of 238 mW. *Source:* Jiang et al. [32]/John Wiley & Sons. (b) Optical spectrum of mid-IR (MIR) fiber lasers centered at 2788 nm. *Source:* Wang et al. [33]/American Chemical Society. (c) Output spectra with various pump power of Nb_2CT_x-based mode-locked Yb-fiber laser. *Source:* Li et al. [34]/John Wiley & Sons. (d) $Ti_3C_2T_x$ MXene nanosheet–based all-optical switcher. (e) The probe light modulated by the pump light to realize "ON" and "OFF" modes in all-optical switcher. *Source:* Wu et al. [35]/John Wiley & Sons.

By taking the advantage of high optical nonlinearity of $Ti_3C_2T_x$, a novel light-control-light system spatial based on self-phase modulation was designed as an information converter in the all-optical switcher [35]. With pump light introduced to modulate the propagation of probe light, both the ring numbers and diameters can be tuned by the pump light. When the pump light intersecting with the probe light (Figure 17.6d) was directed into MXene dispersions, the phase of probe light was modulated to produce the diffraction rings due to the nonlinear Kerr effect, which means one can obtain a strip interference signal from the probe light by controlling the power of the pump light. With the power of the pump light increasing to 60 mW, the power on the dark stripe was measured to reach the minimum of 1.3 μW. With increasing pump light power, the power increased to the bright strip with the maximum power of 17 μW, as shown in Figure 17.6e. This phenomenon exhibited by MXenes is promising for use in all-optical switchers and modulators. A photonic diode was also fabricated using MXene as a saturable absorber and C_{60} as a reversible saturable absorber. The forward direction ($Ti_3C_2T_x/C_{60}$) and reverse direction ($C_{60}/Ti_3C_2T_x$) showed inverse changes with the input influence increasing [29]. A maximum nonreciprocity factor as high as 4 dB was achieved with this bilayer structure, which provides the basis for MXenes in the photonic diodes and optical isolators. With the studies of nonlinearity in MXenes proliferating, MXene-based nonlinear optical devices may find numerous applications.

17.7 Optoelectronic Properties

MXenes are promising candidates for transparent electrodes because of their high electrical conductivity, 2D morphology, processability, and excellent mechanical properties. Since MXenes are easily dispersed in aqueous solution, many thin film deposition methods, such as spray-coating, spin-coating, dip-coating, and interfacial assembly, can be readily be used to fabricate MXene thin films [29, 39–42]. The first transparent MXene film was produced via a top-down method, using magnetron-sputtered Ti_3AlC_2 MAX phase on a sapphire substrate and etched with NH_4HF_2 [43]. The resulting films exhibited high optoelectronic properties with ~5000 S cm^{-1}electronic conductivity at 85% optical transmittance. The solution-processed, bottom-up technique, such as spray-coating method was used to fabricate transparent thin films with the thickness from 5 to 70 nm [39]. The transmittance spectra of films with different thicknesses are shown in Figure 17.7a. A transmittance of 91.2% was achieved for a 5 nm thick $Ti_3C_2T_x$ thin film with a sheet resistance of 30 kΩ sq^{-1}. The electrical figure of merit (σ_{DC}/σ_{opt}) for the $Ti_3C_2T_x$ thin film was reported up to reach ~15, which surpassed that of reduced graphene oxide, single-wall carbon nanotubes, and conductive polymer thin films (0.02–13), demonstrating the superiority of MXenes as transparent electrodes [41, 47].

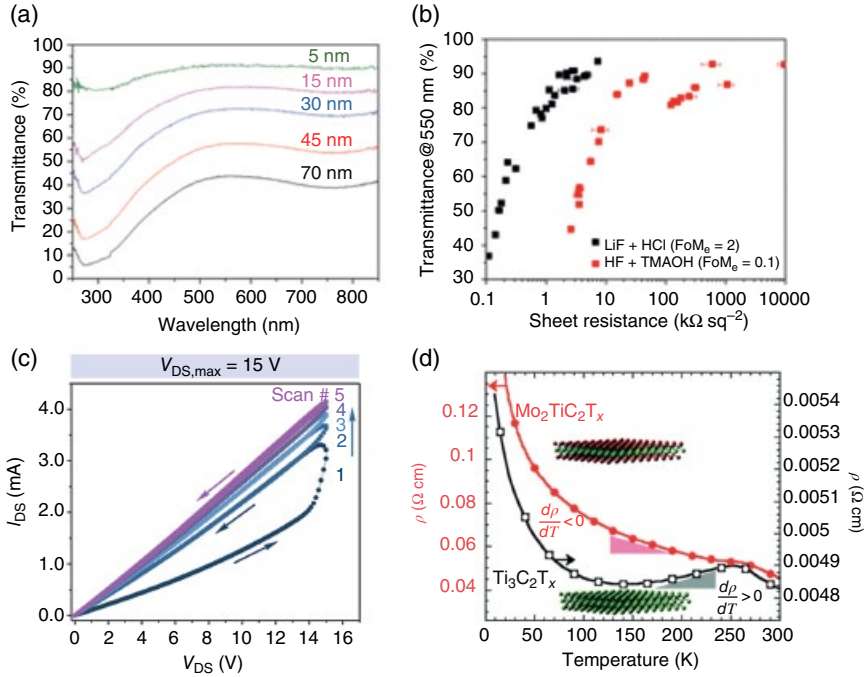


Figure 17.7 (a) UV–vis spectra of $Ti_3C_2T_x$ films with different thicknesses. *Source:* Hantanasirisakul et al. [39]/John Wiley & Sons. (b) Sheet resistance versus transmittance at 550 nm of Ti_3CNT_x synthesized by different methods. *Source:* Hantanasirisakul et al. [44]/American Chemical Society. (c) Stepwise current annealing and electrical breakdown of a monolayer $Nb_4C_3T_x$ flake at $V_{DS,max}$ = 15 V. *Source:* Lipatov et al. [45]/American Chemical Society. (d) Comparison of $Mo_2TiC_2T_x$ (dots left side *y*-axis) and $Ti_3C_2T_x$ (squares, right-side *y*-axis) temperature-dependent resistivity results. *Source:* Anasori et al. [46]/Royal Society of Chemistry.

Other MXenes thin films, such as Ti_2CT_x and Ti_3CNT_x, also have relatively high figures of merit, indicating the potential of the MXene family in optoelectronic applications [44, 48]. Beyond the chemical composition tuning, the optical properties, especially the transmittance of few-layer MXenes, could be tunable via varying the intercalation of cations, which clearly showed promise for thin film sensors and electrochromic applications [39].

Electronic properties of MXenes are essential for the optoelectronic applications. Transparent conductive MXene films have been fabricated and used as the transparent conductor and active material for high-performance capacitive charge storage due to their high electrical conductivity (~10 000 S cm^{-1}) [47]. However, the above-mentioned conductivity was measured on compressed discs, supported

films or free-standing films, and was governed by intra-flake and inter-flake electron transport. Thus, most of the resistance measured could come from the inter-flake hopping and contact resistance. Based on this, the experimental measurement of MXene single-flake is important to understand the intrinsic transport mechanisms of MXenes. The field effect transistors (FETs) were fabricated on monolayer $Ti_3C_2T_x$ to measure the intraflake conductivity [49, 50]. The output and transfer characteristics of the devices showed metallic nature of single-flake $Ti_3C_2T_x$ and the conductivity is measured as high as 11 000 S cm^{-1}, higher than other 2D materials such as CVD graphene and 1T MoS_2 [51, 52]. In addition, the MXene-based FET devices showed very high breakdown current density of 1.2×10^8 A cm^{-2}, which is also comparable to graphene. Other MXenes, such as $Nb_4C_3T_x$ and Ti_3CNT_x, were also demonstrated to have high conductivity and breakdown current density (Figure 17.7c) [45]. The temperature-dependent conductivity was reported for different MXenes [46, 53]. Metallic $Ti_3C_2T_x$ and Ti_3CNT_x showed positive dR/dT above room temperature, while after several cycles of annealing the conductivity increased further, which was interpreted as the contraction of the *c*-lattice parameter due to the water de-intercalation [53]. During the initial annealing process, Ti_3CNT_x showed negative dR/dT, which may come from the inter-flake hopping process. Interestingly, $Mo_2TiC_2T_x$ showed a negative dR/dT (Figure 17.7d) as well in the early stage and transition from negative to positive at 500 °C; this behavior was due to the decomposition and loss of tetrabutylammonium (TBA^+) intercalant, which is usually intercalated for delamination during MXene synthesis. Thus, with annealing, de-intercalation, and de-functionalization, the resistance could be decreased, and it became possible to delineate the effects of intercalation and temperature on MXenes' electronic properties. The electronic conductivity of MXenes can also be increased by modifying the synthesis procedure [44]. The tuning of conductivity of MXenes provides further avenue to improve performance in optoelectronics. The remarkable combination of high electrical conductivity and high current-carrying capacity makes MXenes promising for various applications such as light-emitting diodes (LEDs), solar cells, and electrochromic devices.

17.8 Optoelectronic Applications

The high electrical conductivity of MXene thin films with high optical transparency renders them promising for applications in solar cells, LEDs, and electrochromic devices. The work function of conventional conducting materials is usually less than 4.8 eV, which is the limiting factor in LEDs due to formation of a large energy barrier for hole injection. $Ti_3C_2T_x$ with a high work function of 5.1 eV was used as a transparent conducting electrode after low-temperature vacuum annealing to

modify the surface termination of $Ti_3C_2T_x$ films [40]. The hole-injection capability of $Ti_3C_2T_x$ was evaluated by fabricating the hole-only devices, as shown in Figure 17.8a. The voltage–current density curves at a given bias were even higher than conventional ITO anode, which was attributed to the higher work function of $Ti_3C_2T_x$. Green phosphorescent organic LED was fabricated using $Ti_3C_2T_x$, where the device structure is shown in the right inset of Figure 17.8b. The $Ti_3C_2T_x$-based LED had high current, power, and external quantum efficiency, which is comparable to conventional ITO-based LEDs, but allows flexing and bending without cracking and loss of performance [55]. Mixed with zero-dimensional silver nanoparticles, three-dimensional poly (3, 4-ethylenedioxythiophene): poly(styrenesulfonate) (PEDOT: PSS), the $Ti_3C_2T_x$-based composites endow the electrodes with a much longer operational half-lifetimes and higher retention after 500 bending cycles. The improved mechanical stability minimizes resistance variation of the composites and illustrates a further step toward practical applications of flexible MXene-based LEDs in optoelectronics.

Due to the high optical transmittance, metallic conductivity, and tunable work function, MXenes were explored as additives in light-absorbing layers, electron/hole transport layers (ETL/HTL), and electrodes in perovskite and other types of solar cells. $Ti_3C_2T_x$ was fabricated as an interlayer in perovskite solar cells to accelerate the hole extraction to achieve a high-efficiency carrier transport with low recombination at the interface [54]. The structure of a $CsPbBr_3/Ti_3C_2T_x$-based solar cell is shown in Figure 17.8c. The high work function of $Ti_3C_2T_x$ impeded the transfer of electrons from $CsPbBr_3$ to $Ti_3C_2T_x$ and reduced the carrier recombination. Besides, surface passivation from the bonding surface terminations of $Ti_3C_2T_x$ and Pb atoms provided a direct conducting channel and reduced the Ohmic contact resistance. Consequently, the photovoltaic performance (Figure 17.8d) was improved and the power conversion efficiency increased from 8.21% to 9.01% under the reverse scan. Beyond hole transport layers, MXenes were also used as other parts of solar cells and they showed improved performance compared to other materials [56].

Electrochromism is associated with change in oxidation state and ion intercalation/deintercalation upon reduction and oxidation of materials, which leads to change in the optical absorption spectrum. It is important for many applications, such as color-changing and transparent/translucent windows. In addition to being transparent and conductive, MXenes also capable of reversible surface redox reactions involving the transition metal of the outer M layers. $Ti_3C_2T_x$ has been reported to experience reversible surface redox reactions in acidic electrolytes based on the surface protonation/deprotonation. Switching between =O and —OH results in changing oxidation state of Ti [57]. This mechanism allows for a combination of the capacitive and optoelectronic properties of MXenes to fabricate transparent energy storage and electrochromic devices [41, 47]. As shown in

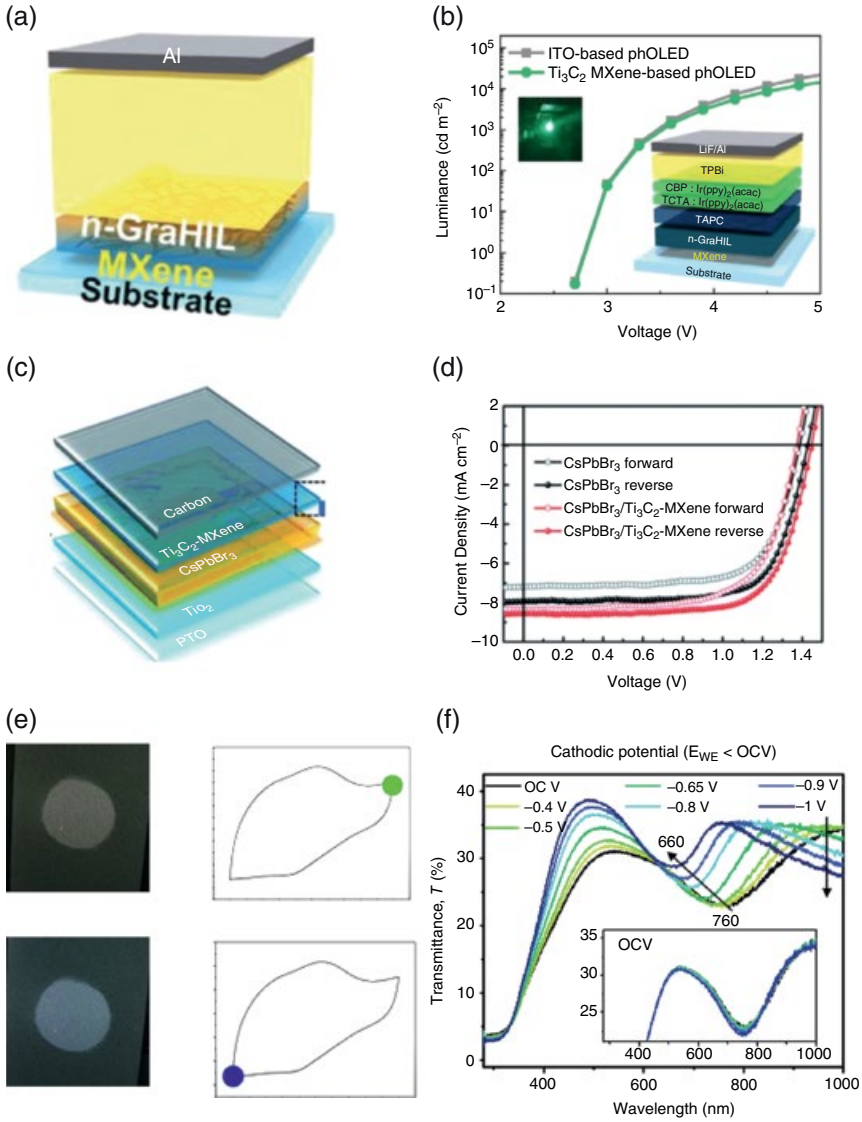


Figure 17.8 (a) Schematic illustration of the hole-only device design to evaluate the hole injection capability. (b) Luminance vs. voltage characteristics of LEDs that have ITO or MXene electrode. Inset: optical image of MXene-based green organic LED (left), and schematic of green phosphorescent organic LED device structure (right). *Source:* Ahn et al. [40]/John Wiley & Sons. (c) Configuration of the perovskite solar cell using MXene as a hole transport layer. (d) J–V curves of the perovskite solar cell using MXene as a hole transport layer. *Source:* Chen et al. [54]/Royal Society of Chemistry. (e) Optical images of $Ti_3C_2T_x$ thin films showing color change from dark (0.0 V vs. Ag) to light gray (−1.0 V vs. Ag). (f) Transmittance spectra from 280 to 1000 nm of the $Ti_3C_2T_x$ electrochromic device during cathodic scans. *Source:* Salles et al. [41]/John Wiley & Sons.

Figure 17.8e, $Ti_3C_2T_x$-based electrochromic devices showed a reversible color change of the $Ti_3C_2T_x$ film from dark (0.0 V vs. Ag) to light gray (−1.0 V vs. Ag). The *in-situ* UV-visible transmittance spectra were collected and a >100 nm shift of the extinction peak to lower wavelength was found upon cathodic scan. The change at 450 nm was recorded and ~20% change in transmittance was observed within 10 seconds. The variation in transmittance and peak shift corresponded to a color change from green to blue which is showing change from dark to light gray in Figure 17.8e. This work corroborated that protonation and redox reaction of a MXene play an important role in electrochromic performance. Based on that, other titanium-based MXenes were explored to have electrochromic effect such as Ti_2CT_x, Ti_3CNT_x [58]. It is important to note that electrochromism of MXenes is caused by a shift of the plasmon resonance peak, not by a typical for oxides shift in the absorption edge due to a change in the band gap. One cannot reversibly change the position of the plasmon resonance peak in conventional metals, such as Au nanoparticles, but it is possible in MXenes. With more electrochemistry of MXenes explored, modulation of the plasmonic electrochromic behavior and other optoelectronic properties will be promoted further.

17.9 Conclusions and Outlook

In this chapter, we have described the selected optical and optoelectronic properties of MXenes, as well as their related applications. This large and rapidly growing family of 2D transition metal carbides, nitrides, and carbonitrides has been demonstrated to exhibit attractive plasmonic, ultrafast dynamics, nonlinear optical properties, which can be controlled by tuning MXene structure and composition. Numerous MXene structures and compositions offer almost infinite possibilities optoelectronic applications of this family of materials. Moreover, plasmonic and optical properties of these metallically conducting 2D materials can be actively tuned by applying a small potential.

There are still remaining challenges in MXenes synthesis and fundamental understanding of MXenes. The current top-down synthesis methods of MXenes require use of acid etching and introduce different surface terminations such as —F, —Cl and =O, which profoundly affect their optoelectronic properties [8]. Exploring chemical vapor deposition to grow ultra-large monolayers of MXenes with uniform and well-controlled surface terminations is important for on-chip devices. Tuning the surface groups of MXenes is also essential for the property's modification. For example, the bandgap of MXenes has been theoretically predicted to vary with surface terminations [59]. However, active switching between metallic and semiconducting MXenes by tuning of the surface terminations is still to be demonstrated experimentally. With a better control of the Fermi level and achievement of tunable bandgaps, the range of optoelectronic applications of MXenes can be further expanded.

MXenes exhibit immense potential in optics and photonics due to their tunable optical, electronic, and optoelectronic properties. Although there are still several issues so far, they will be solved by ongoing and continuous efforts in exploring and controlling fundamental optical and optoelectronic properties of MXenes.

Acknowledgments

Danzhen Zhang and Yury Gogotsi acknowledge funding from NSF Grant DMR-2041050. We thank Marley Downes for editing the manuscript.

References

1 Jariwala, D., Sangwan, V.K., Lauhon, L.J. et al. (2013). Carbon nanomaterials for electronics, optoelectronics, photovoltaics, and sensing. *Chemical Society Reviews* 42: 2824–2860.
2 Chang, H. and Wu, H. (2013). Graphene-based nanomaterials: synthesis, properties, and optical and optoelectronic applications. *Advanced Functional Materials* 23: 1984–1997.
3 Ando, Y. and Watanabe, S. (2016). First-principles study of metal–insulator control by ion adsorption on Ti_2C MXene dioxide monolayers. *Applied Physics Express* 9: 015001.
4 Khazaei, M., Ranjbar, A., Arai, M., and Yunoki, S. (2016). Topological insulators in the ordered double transition metals $M_2'M''C_2$ MXenes (M′=Mo, W; M″=Ti, Zr, Hf). *Physical Review B* 94: 125152.
5 Liang, Y., Khazaei, M., Ranjbar, A. et al. (2017). Theoretical prediction of two-dimensional functionalized MXene nitrides as topological insulators. *Physical Review B* 96: 195414.
6 Hantanasirisakul, K. and Gogotsi, Y. (2018). Electronic and optical properties of 2D transition metal carbides and nitrides (MXenes). *Advanced Materials* 30: e1804779.
7 Zhang, D., Shah, D., Boltasseva, A., and Gogotsi, Y. (2022). MXenes for photonics. *ACS Photonics* 9: 1108–1116.
8 Maleski, K., Shuck, C.E., Fafarman, A.T., and Gogotsi, Y. (2021). The broad chromatic range of two-dimensional transition metal carbides. *Advanced Optical Materials* 9: 2001563.
9 El-Demellawi, J.K., Lopatin, S., Yin, J. et al. (2018). Tunable multipolar surface plasmons in 2D Ti_3C_2Tx MXene flakes. *ACS Nano* 12: 8485–8493.
10 Naik, G.V., Shalaev, V.M., and Boltasseva, A. (2013). Alternative plasmonic materials: beyond gold and silver. *Advanced Materials* 25: 3264–3294.

11 Mauchamp, V., Bugnet, M., Bellido, E.P. et al. (2014). Enhanced and tunable surface plasmons in two-dimensional Ti_3C_2 stacks: electronic structure versus boundary effects. *Physical Review B* 89: 235428.

12 Chaudhuri, K., Alhabeb, M., Wang, Z. et al. (2018). Highly broadband absorber using plasmonic titanium carbide (MXene). *ACS Photonics* 5: 1115–1122.

13 Velusamy, D.B., El-Demellawi, J.K., El-Zohry, A.M. et al. (2019). MXenes for plasmonic photodetection. *Advanced Materials* 31: e1807658.

14 Li, R., Zhang, L., Shi, L., and Wang, P. (2017). MXene Ti_3C_2: an effective 2D light-to-heat conversion material. *ACS Nano* 11: 3752–3759.

15 Sarycheva, A., Makaryan, T., Maleski, K. et al. (2017). Two-dimensional titanium carbide (MXene) as surface-enhanced Raman scattering substrate. *Journal of Physical Chemistry C* 121: 19983–19988.

16 Jeon, J., Choi, H., Choi, S. et al. (2019). Transition-metal-carbide (Mo_2C) multiperiod gratings for realization of high-sensitivity and broad-spectrum photodetection. *Advanced Functional Materials* 29: 1905384.

17 Lin, H., Gao, S., Dai, C. et al. (2017). A two-dimensional biodegradable niobium carbide (MXene) for photothermal tumor eradication in NIR-I and NIR-II biowindows. *Journal of the American Chemical Society* 139: 16235–16247.

18 Dai, C., Chen, Y., Jing, X. et al. (2017). Two-dimensional tantalum carbide (MXenes) composite nanosheets for multiple imaging-guided photothermal tumor ablation. *ACS Nano* 11: 12696–12712.

19 Peng, Y., Lin, C., Long, L. et al. (2021). Charge-transfer resonance and electromagnetic enhancement synergistically enabling MXenes with excellent SERS sensitivity for SARS-CoV-2 S protein detection. *Nano-Micro Letters* 13: 52.

20 He, Z., Rong, T., Li, Y. et al. (2022). Two-dimensional TiVC solid-solution MXene as surface-enhanced Raman scattering substrate. *ACS Nano* 16: 4072–4083.

21 Shevchuk, K., Sarycheva, A., and Gogotsi, Y. (2022). Evaluation of two-dimensional transition-metal carbides and carbonitrides (MXenes) for SERS substrates. *MRS Bulletin* 47: 545–554.

22 Xu, H., Ren, A., Wu, J., and Wang, Z. (2020). Recent advances in 2D MXenes for photodetection. *Advanced Functional Materials* 30: 2000907.

23 Zhang, Q., Yan, L., Yang, M. et al. (2020). Ultrafast transient spectra and dynamics of MXene (Ti_3C_2Tx) in response to light excitations of various wavelengths. *Journal of Physical Chemistry C* 124: 6441–6447.

24 Lioi, D.B., Stevenson, P.R., Seymour, B.T. et al. (2020). Simultaneous ultrafast transmission and reflection of nanometer-thick Ti_3C_2Tx MXene films in the visible and near-infrared: implications for energy storage, electromagnetic shielding, and laser systems. *ACS Applied Nano Materials* 3: 9604–9609.

25 Li, G., Amer, N., Hafez, H.A. et al. (2020). Dynamical control over terahertz electromagnetic interference shielding with 2D Ti_3C_2Ty MXene by ultrafast optical pulses. *Nano Letters* 20: 636–643.

26 Wang, Y., Wang, Y., Chen, K. et al. (2020). Niobium carbide MXenes with broad-band nonlinear optical response and ultrafast carrier dynamics. *ACS Nano* 14: 10492–10502.

27 Shahzad, F., Alhabeb, M., Hatter, C.B. et al. (2016). Electromagnetic interference shielding with 2D transition metal carbides (MXenes). *Science* 353: 1137–1140.

28 Gao, L., Chen, H., Kuklin, A.V. et al. (2022). Optical properties of few-layer Ti_3CN MXene: from experimental observations to theoretical calculations. *ACS Nano* 16: 3059–3069.

29 Dong, Y., Chertopalov, S., Maleski, K. et al. (2018). Saturable absorption in 2D Ti_3C_2 MXene thin films for passive photonic diodes. *Advanced Materials* 30: 1705714.

30 Wang, G., Bennett, D., Zhang, C.J. et al. (2020). Two-photon absorption in monolayer MXenes. *Advanced Optical Materials* 8: 1902021.

31 Fu, B., Sun, J., Wang, C. et al. (2021). MXenes: synthesis, optical properties, and applications in ultrafast photonics. *Small* 17: e2006054.

32 Jiang, X., Liu, S., Liang, W. et al. (2018). Broadband nonlinear photonics in few-layer MXene Ti_3C_2Tx (T = F, O, or OH). *Laser & Photonics Reviews* 12: 1700229.

33 Wang, Z., Li, H., Luo, M. et al. (2020). MXene photonic devices for near-infrared to mid-infrared ultrashort pulse generation. *ACS Applied Nano Materials* 3: 3513–3522.

34 Li, G., Liu, J., Wang, F. et al. (2021). Third-order nonlinear optical response of few-layer MXene Nb_2C and applications for square-wave laser pulse generation. *Advanced Materials Interfaces* 8: 2001805.

35 Wu, L., Jiang, X., Zhao, J. et al. (2018). MXene-based nonlinear optical information converter for all-optical modulator and switcher. *Laser & Photonics Reviews* 12: 1800215.

36 Ahmad, H., Ramli, R., Yusoff, N. et al. (2020). 155 nm-wideband and tunable q-switched fiber laser using an MXene Ti_3C_2Tx coated microfiber based saturable absorber. *Laser Physics Letters* 17: 085103.

37 Huang, W., Ma, C., Li, C. et al. (2020). Highly stable MXene (V_2CTx)-based harmonic pulse generation. *Nanophotonics* 9: 2577–2585.

38 Yi, J., Du, L., Li, J. et al. (2019). Unleashing the potential of Ti_2CTx MXene as a pulse modulator for mid-infrared fiber lasers. *2D Materials* 6: 045038.

39 Hantanasirisakul, K., Zhao, M.-Q., Urbankowski, P. et al. (2016). Fabrication of Ti_3C_2Tx MXene transparent thin films with tunable optoelectronic properties. *Advanced Electronic Materials* 2: 1600050.

40 Ahn, S., Han, T.-H., Maleski, K. et al. (2020). A 2D titanium carbide MXene flexible electrode for high-efficiency light-emitting diodes. *Advanced Materials* 32: e2000919.

41 Salles, P., Pinto, D., Hantanasirisakul, K. et al. (2019). Electrochromic effect in titanium carbide MXene thin films produced by dip-coating. *Advanced Functional Materials* 29: 1809223.

42 Kim, S.J., Choi, J., Maleski, K. et al. (2019). Interfacial assembly of ultrathin, functional MXene films. *ACS Applied Materials & Interfaces* 11: 32320–32327.

43 Halim, J., Lukatskaya, M.R., Cook, K.M. et al. (2014). Transparent conductive two-dimensional titanium carbide epitaxial thin films. *Chemistry of Materials* 26: 2374–2381.

44 Hantanasirisakul, K., Alhabeb, M., Lipatov, A. et al. (2019). Effects of synthesis and processing on optoelectronic properties of titanium carbonitride MXene. *Chemistry of Materials* 31: 2941–2951.

45 Lipatov, A., Loes, M., Vorobeva, N.S. et al. (2021). High breakdown current density in monolayer Nb_4C_3Tx MXene. *ACS Materials Letters* 3: 1088–1094.

46 Anasori, B., Shi, C., Moon, E.J. et al. (2016). Control of electronic properties of 2D carbides (MXenes) by manipulating their transition metal layers. *Nanoscale Horizons* 1: 227–234.

47 Zhang, C.J., Anasori, B., Seral-Ascaso, A. et al. (2017). Transparent, flexible, and conductive 2D titanium carbide (MXene) films with high volumetric capacitance. *Advanced Materials* 29: 1702678.

48 Ying, G., Dillon, A.D., Fafarman, A.T., and Barsoum, M.W. (2017). Transparent, conductive solution processed spincast 2D Ti_2CTx (MXene) films. *Materials Research Letters* 5: 391–398.

49 Lipatov, A., Goad, A., Loes, M. et al. (2021). High electrical conductivity and breakdown current density of individual monolayer Ti_3C_2Tx MXene flakes. *Matter* 4: 1413–1427.

50 Sang, X., Xie, Y., Lin, M.-W. et al. (2016). Atomic defects in monolayer titanium carbide (Ti_3C_2Tx) MXene. *ACS Nano* 10: 9193–9200.

51 Thorsteinsson, S., Wang, F., Petersen, D.H. et al. (2009). Accurate microfour-point probe sheet resistance measurements on small samples. *The Review of Scientific Instruments* 80: 053902.

52 Kappera, R., Voiry, D., Yalcin, S.E. et al. (2014). Phase-engineered low-resistance contacts for ultrathin MoS_2 transistors. *Nature Materials* 13: 1128–1134.

53 Hart, J.L., Hantanasirisakul, K., Lang, A.C. et al. (2019). Control of MXenes' electronic properties through termination and intercalation. *Nature Communications* 10: 522.

54 Chen, T., Tong, G., Xu, E. et al. (2019). Accelerating hole extraction by inserting 2D Ti_3C_2-MXene interlayer to all inorganic perovskite solar cells with long-term stability. *Journal of Materails Chemistry A* 7: 20597–20603.

55 Cao, F., You, M., Kong, L. et al. (2022). Mixed-dimensional MXene-based composite electrodes enable mechanically stable and efficient flexible perovskite light-emitting diodes. *Nano Letters* 22: 4246–4252.

56 Liu, Z. and Alshareef, H.N. (2021). MXenes for optoelectronic devices. *Advanced Electronic Materials* 7: 2100295.

57 Lukatskaya, M.R., Bak, S.-M., Yu, X. et al. (2015). Probing the mechanism of high capacitance in 2D titanium carbide using in situ X-ray absorption spectroscopy. *Advanced Energy Materials* 5: 1500589.

58 Valurouthu, G., Maleski, K., Kurra, N. et al. (2020). Tunable electrochromic behavior of titanium-based MXenes. *Nanoscale* 12: 14204–14212.

59 Bai, Y., Zhou, K., Narasimalu, S. et al. (2016). Dependence of elastic and optical properties on surface terminated groups in two-dimensional MXene monolayers: a first-principles study. *RSC Advances* 6: 35731–35739.

18

Mechanical Properties and Reinforcement Effect of Single MXene Flakes and MXene Composites

Qunfeng Cheng[1] *and Alexander Sinitskii*[2]

[1] *School of Chemistry, Key Laboratory of Bio-inspired Smart Interfacial Science and Technology of Ministry of Education, Beihang University, Beijing, China*
[2] *Department of Chemistry and Nebraska Center for Materials and Nanoscience, University of Nebraska-Lincoln, Lincoln, NE, USA*

18.1 Introduction

MXenes [1–3], new two-dimensional (2D) nanomaterials, show promising mechanical and electrical properties and have a great potential for various applications, such as electronic devices and aerospace. Since 2014 [4], three kinds of MXene composites, including one-dimensional (1D) fiber [5–15], 2D film [4, 16–29], and three-dimensional (3D) bulk composites [30–38], have been fabricated through different kinds of approaches. The MXene composites involving 1D fibers are usually fabricated by wet spinning [5, 6]. Vacuum filtration [4, 23], blade coating [18], layer-by-layer (LbL) [17], evaporation [26], and Langmuir-Blodgett assembly [27] are used to fabricate 2D MXene film composites. For 3D bulk MXene composites [30, 33, 38], several typical approaches are used, such as solution mixing, sol–gel/impregnation, and freeze casting.

In this chapter, we first discuss the outstanding intrinsic mechanical properties of MXenes, which were experimentally determined in nanoindentation measurements performed on individual monolayer MXene flakes. Then, we discuss the experimental challenges in translating the excellent mechanical properties of individual MXene flakes into the properties of bulk MXene composites. One of the challenges with the assembly of MXene composites, especially without applying external force, is that the orientation of MXene flakes is random, so that the

Transition Metal Carbides and Nitrides (MXenes) Handbook: Synthesis, Processing, Properties and Applications, First Edition. Edited by Chuanfang Zhang and Michael Naguib.
© 2024 John Wiley & Sons, Inc. Published 2024 by John Wiley & Sons, Inc.

voids between them could easily form. Furthermore, although many functional groups are on the surface of MXene flakes, the interface interactions still need to be strengthened by other molecules or ions via covalent bonding or ionic bonding. Thus, the flake orientation, voids, and interface interactions are three main issues affecting the low mechanical properties of MXene composites, which are not even nearly as good as the properties demonstrated for individual MXene flakes. It remains a great challenge to realize the intrinsic performance of MXene flakes in macroscale MXene composites.

Although the orientation of MXene flakes has been realized in 1D fiber MXene composites, the voids and interface interactions have not been fully addressed yet. These problems do not exist independently but together. Thus, these problems should be eliminated to obtain high load transfer efficiency and high values of mechanical properties of MXene composites. Recently, several strategies have been developed to fabricate strong MXene composites to enhance the alignment degree of MXene flakes, reduce voids, and strengthen interface interactions in the assembly procedure. In this chapter, we discuss the mechanical properties of 1D fiber, 2D film, and 3D bulk MXene composites, and other functional properties, such as electrical conductivity and electromagnetic interference shielding. Then, the developed effective strategies for enhancing mechanical properties of MXene composites are briefly discussed. Finally, we summarize the progress with our future outlook on the challenges in this promising field.

18.2 Mechanical Measurements of Individual $Ti_3C_2T_x$ Flakes

MXenes have a general formula of $M_{n+1}X_nT_x$, where M is a transition metal, such as Ti, Nb, Ta, V, Cr, etc., X is carbon and/or nitrogen, and T_x represents the surface termination of MXene sheets [39]. MXenes are produced from layered ternary metal carbides/nitrides that are known as MAX phases by chemical extraction of interleaving layers of an "A" element (group IIIA and IVA elements, e.g., Al). This process is schematically illustrated by Figure 18.1a, which demonstrates the synthesis of $Ti_3C_2T_x$, the most popular MXene material so far [44], by etching Al layers from Ti_3AlC_2 MAX phase. Fluoride-containing acidic solutions, such as HF [1, 39], NH_4HF_2 [45] or LiF-HCl [46] are typically used for the aluminum extraction, and the resulting MXene sheets have mixed oxygen- and fluorine-containing surface terminations. In particular, Figure 18.1a demonstrates two synthetic procedures that employ the LiF-HCl treatment of Ti_3AlC_2 MAX phase with different ratios of these chemicals and, more importantly, an optional sonication of the etching products.

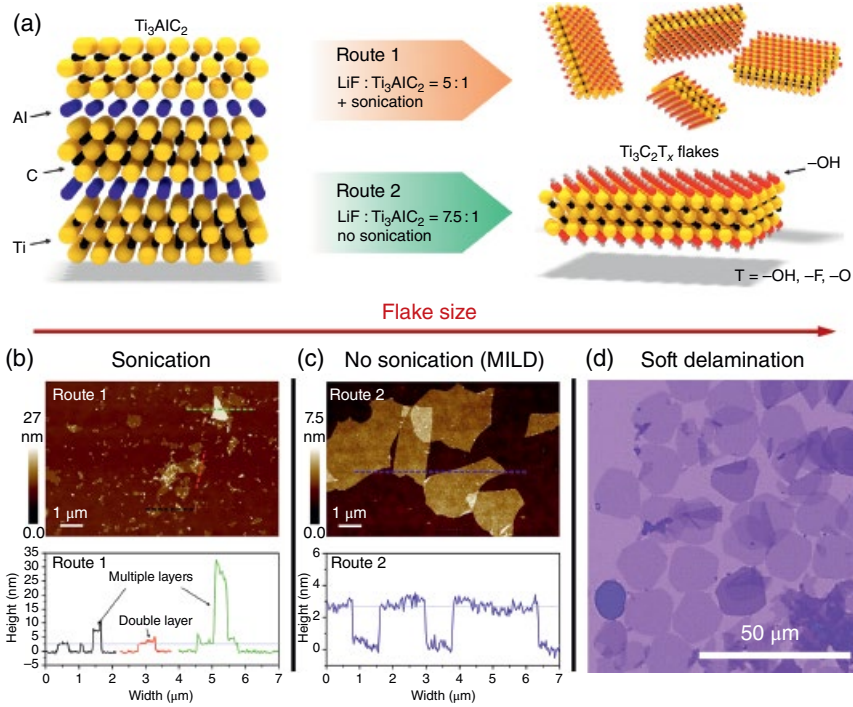


Figure 18.1 Synthesis and microscopy characterization of $Ti_3C_2T_x$ flakes produced by different routes. (a) General approach for $Ti_3C_2T_x$ MXene synthesis by the acid etching of Ti_3AlC_2 MAX phase. Routes 1 and 2 correspond to syntheses with and without sonication of the etching products. The surface T_x functional groups are schematically shown as hydroxyls, although other moieties, such as —O and —F, can also be present on the surface of MXene flakes [40, 41]. (b–d) A comparison of the sizes of $Ti_3C_2T_x$ flakes produced by different methods: (b) with extensive sonication of the etching products (Route 1), (c) without sonication of the etching products (Route 2; the MILD method), and (d) via gentle delamination of the etching products. Panels (b) and (c) show atomic force microscopy (AFM) images of $Ti_3C_2T_x$ MXene flakes and the corresponding height profiles. Panel (d) shows an optical photograph of $Ti_3C_2T_x$ MXene flakes. *Source:* (a–c) Reproduced from Lipatov et al. [42]/Reproduced from John Wiley & Sons, Inc. (d) Shekhirev et al. [43]/Reproduced from American Chemical Society.

For the physical property characterization of MXenes at a single flake level, it is highly preferable to have large MXene flakes. For nanoindentation experiments, the flakes should be sufficiently large to be suspended over prefabricated wells in substrates [3, 47] and have a large contact area with a surface for strong adhesion. In principle, the size of flakes is limited by the size of the precursor MAX phase particles, which are typically employed for MXene synthesis at sizes of several tens of μm. Achieving MXene flakes with sizes comparable to the sizes of the

precursor MAX phase particles requires gentle exfoliation of the products of MAX phase etching, as sonication or vigorous shaking of a MXene solution was previously shown to greatly reduce the average flake size [42]. For example, the original synthesis of $Ti_3C_2T_x$ by Naguib and co-workers employed an extensive sonication of the acid-etched Ti_3AlC_2 MAX phase, and the resulting MXene flakes mostly had sub-micrometer sizes [1]. Later research resulted in the Minimally Intensive Layer Delamination (MILD) method, in which the etching product was not sonicated, and the resulting MXene flakes were considerably larger, in the several μm range, as demonstrated by Lipatov, et al. [42]. A recent study by Shekhirev and co-workers further advanced the synthesis of ultralarge MXene flakes [43], demonstrating that by further minimizing the shaking of the etching product, it is possible to produce $Ti_3C_2T_x$ monolayers of up to 40 μm in lateral size. The improvement in the sizes of $Ti_3C_2T_x$ MXene flakes that was achieved by minimizing the agitation of the etching products is illustrated by Figure 18.1b–d. Each step in this progression resulted in an improvement in the $Ti_3C_2T_x$ flake size by about an order of magnitude. The large flakes prepared by the MILD method and, in particular, the soft delamination method are most suitable for the preparation of suspended MXene membranes [3, 48].

MXene flakes with lateral sizes in the μm range can be used for the fabrication of suspended membranes, as illustrated by Figure 18.2a–c. Such membranes are suitable for mechanical measurements of the elastic modulus and breaking strength of MXene flakes by the AFM indentation. Figure 18.2 primarily focuses on the nanoindentation measurements of monolayer and bilayer $Ti_3C_2T_x$ MXene flakes reported by Lipatov and co-workers [3], although the same methodology was also applied to $Nb_4C_3T_x$ [47] and could be used for characterization of flakes of other MXenes as well. $Ti_3C_2T_x$ MXene flakes (Figure 18.2a) were deposited on a Si/SiO_2 substrate with prefabricated 300-nm-deep wells to produce very clean, well-stretched $Ti_3C_2T_x$ membranes (Figure 18.2b, c). The scheme of the nanoindentation experiment is shown in Figure 18.2d. The AFM tip is positioned over the center of a membrane and slowly moved downward, providing a controlled stretching of a MXene flake. Figure 18.2e shows three consecutive cycles of loading and unloading performed on the same MXene flake with increasing loading. The extension and retraction curves within each loading cycle, as well as the curves for different loads retrace each other, indicating high elasticity of MXene flakes and that no flake detachment occurs during the measurements. The fracture of the 2L $Ti_3C_2T_x$ membrane shown in Figure 18.2e occurred at a load force of about 200 nN and a deflection of 38 nm. The AFM tip punctures the membrane leaving a small hole as seen in the top inset in Figure 18.2e.

Figure 18.2f shows representative force–deflection curves for 1L and 2L $Ti_3C_2T_x$ membranes. Analysis of the force–deflection dependences using Poisson's ratio of $Ti_3C_2T_x$, $\nu = 0.227$ [58], yielded for 1L MXene the E^{2D} elasticity values ranging

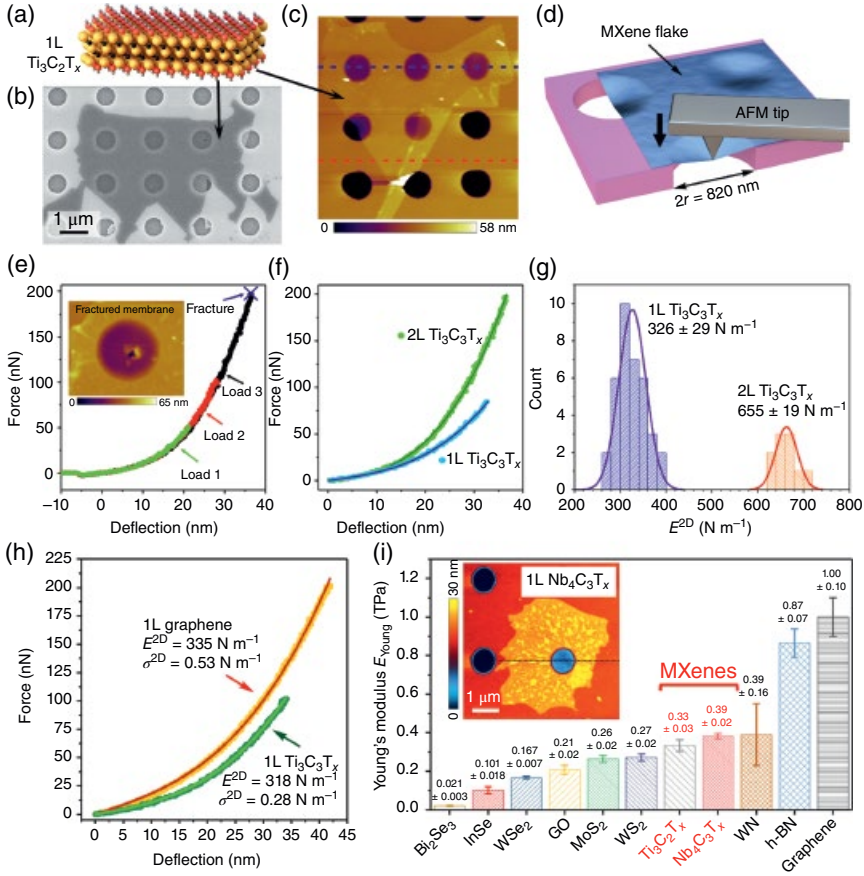


Figure 18.2 Mechanical measurements of individual $Ti_3C_2T_x$ and $Nb_4C_3T_x$ flakes. (a) Scheme of a monolayer (1L) $Ti_3C_2T_x$ MXene flake. (b) Scanning electron microscopy (SEM) image of a $Ti_3C_2T_x$ flake covering an array of circular wells in a Si/SiO_2 substrate with diameters of 820 nm. (c) Noncontact AFM image of a monolayer $Ti_3C_2T_x$ flake placed over an array of wells in a Si/SiO_2 substrate. (d) Scheme of nanoindentation of a suspended MXene membrane with an AFM tip. (e) Force–deflection curves of a bilayer (2L) $Ti_3C_2T_x$ flake at different loads. The inset shows AFM image of the fractured membrane. (f) Comparison of loading curves for monolayer (1L) and bilayer (2L) $Ti_3C_2T_x$ membranes. Hole diameter is 820 nm. (g) Histogram of elastic stiffness for 1L and 2L membranes. Solid lines represent Gaussian fits to the data. (h) Comparison of experimental force–deflection curves for monolayer graphene and $Ti_3C_2T_x$ membranes. *Source:* Lipatov et al. [3]/American Association for the Advancement of Science/CC BY 4.0. (i) Comparison of the effective Young's moduli of monolayer $Ti_3C_2T_x$ and $Nb_4C_3T_x$ MXenes with other 2D materials studied in similar nanoindentation experiments. *Source:* Lipatov et al. [47]/John Wiley & Sons. Other 2D materials in this graph include multilayers of Bi_2Se_3 [49], InSe [50], WSe_2 [51], WN [52], and monolayers of GO [53], MoS_2 [54, 55], WS_2 [55], h-BN [56] and graphene [57]. The inset shows AFM image of an $Nb_4C_3T_x$ flake covering a 820 nm well in a Si/SiO_2 substrate.

from 278 to 393 N m^{-1} with the average of 326 ± 29 N m^{-1}, while for 2L $Ti_3C_2T_x$ flakes the E^{2D} elasticity values ranged from 632 to 683 N m^{-1} with the average of 655 ± 19 N m^{-1} (Figure 18.2g). Both 1L and 2L $Ti_3C_2T_x$ membranes showed a very narrow distribution of the experimental E^{2D} values. The average E^{2D} for 2L $Ti_3C_2T_x$ membranes is exactly twice that determined for monolayer MXene flakes, suggesting a strong interaction between layers that is likely associated with the hydrogen bonding between the $Ti_3C_2T_x$ surface groups. Similar effects were observed for overlapping graphene oxide (GO) membranes [53] and multilayer hexagonal boron nitride (h-BN) flakes [56], where a strong interaction between layers was caused by either hydrogen bonding or interlayer B–N interaction, respectively. In contrast, multilayer graphene exhibits lower E^{2D} than expected from multiplying monolayer E^{2D} by the number of layers due to weaker interlayer interaction and therefore a greater tendency of layers to slide relative to each other upon indentation [56, 57].

Suspended MXene membranes can be deformed elastically up to a certain stress when mechanical failure occurs. The fracture forces for monolayer MXene membranes ranged from 50 to 102 nN with an average value of $F_f = 77 \pm 15$ nN. As shown in the inset in Figure 18.2e, the fracture occurred in the center of a membrane where the stress was applied by the AFM tip.

Considering that graphene is a benchmark 2D material, it is interesting to use it as a reference point for monolayer $Ti_3C_2T_x$ MXene. Figure 18.2h demonstrates that the force–deflection curves for suspended $Ti_3C_2T_x$ and graphene monolayers look very similar and exhibit comparable elasticities (Figure 18.2h). A greater Young's modulus of graphene is attributed to a smaller thickness of its monolayer compared to $Ti_3C_2T_x$ MXene. The effective Young's modulus E_{Young} and breaking strength σ_{max} can be calculated from E^{2D} and σ_{max}^{2D}, respectively, by dividing them by the membrane's thickness. The nominal thickness of a $Ti_3C_2T_x$ monolayer is 0.98 nm, which was obtained from high-resolution transmission electron microscopy analysis and theoretical calculations [45, 59]. The effective Young's modulus for MXene membrane is 333 ± 30 GPa and the breaking strength is 17.3 ± 1.6 GPa. According to the molecular dynamics simulations, an ideal unfunctionalized Ti_3C_2 monolayer has a Young's modulus of 502 GPa [60]. As expected, the experimentally determined value for $Ti_3C_2T_x$ of about 330 GPa is lower because of the structural defects in MXene sheets and their surface functionalization.

Similar nanoindentation experiments were also performed on suspended monolayer flakes of $Nb_4C_3T_x$ MXene [47], see AFM image of a representative membrane in the inset in Figure 18.2i. From these measurements, the effective Young's modulus for $Nb_4C_3T_x$ monolayers was determined to be 386 ± 13 GPa and the breaking strength was determined to be 26 ± 1.6 GPa. Interestingly, the experimental Young's moduli for $Ti_3C_2T_x$ and $Nb_4C_3T_x$ MXenes were close to the moduli of their structurally related cubic carbide counterparts, TiC and NbC,

respectively. An unfunctionalized monolayer of $Ti_3C_2T_x$ can be viewed as a (111) slab of a cubic TiC crystal [47], for which the Young's modulus was measured at 400 GPa [61]. The slightly smaller value of 330 GPa determined for $Ti_3C_2T_x$ MXene monolayers [3] could be explained by the presence of structural defects introduced during the acid etching of the precursor MAX phase, as well as the T_x functionalities. Similarly, the Young's modulus of $Nb_4C_3T_x$ monolayer, which could be similarly viewed as a (111) slab of a cubic NbC crystal, is slightly smaller than that of NbC (452–488 GPa) [62, 63]. Thus, the mechanical properties of bulk carbide materials could serve as reasonable estimates for assessing the mechanical properties of related MXenes. Also, the higher modulus experimentally determined for $Nb_4C_3T_x$ [47] compared $Ti_3C_2T_x$ [3] is in agreement with a comparative assessment of the known mechanical properties of cubic TiC [61] and NbC [62, 63]. In general, bulk transition metal carbides are well known for their exceptional mechanical properties [64]. The available information on other known bulk carbides could be useful for identifying MXene materials with even better mechanical properties than those of the already tested MXenes and inspiring chemists to synthesize such materials in cases when the corresponding MXene compositions have not been experimentally realized yet.

A comparison of the Young's moduli of $Ti_3C_2T_x$ and $Nb_4C_3T_x$ MXenes with other benchmark 2D materials is presented in Figure 18.2i. The effective Young's moduli of $Ti_3C_2T_x$ and $Nb_4C_3T_x$ exceed the reported values for CVD-grown or mechanically exfoliated Bi_2Se_3 [49], InSe [50], WSe_2 [51], MoS_2 [54, 55], WS_2 [55], are comparable to E_{Young} of CVD-grown multilayer WN crystals [52], but are lower than the Young's moduli of perfect monolayers of mechanically exfoliated graphene [57] and h-BN [56]. However, it should be recognized that many of the record properties of graphene and h-BN were measured on small samples prepared by micromechanical exfoliation, a method relevant for fundamental studies, but not large-scale structural applications. Another limitation of pristine graphene and h-BN is their poor solubility in conventional solvents, which complicates their processability and miscibility with other materials, such as polymers, for the preparation of composites. Therefore, it is more appropriate to compare the mechanical properties of $Ti_3C_2T_x$ and $Nb_4C_3T_x$ MXenes to other scalable solution-processable 2D materials, such as GO and reduced GO (rGO). As both GO and rGO can be synthesized in bulk quantities as easily processable dispersions of 2D sheets, they are often discussed with respect to similar applications, such as conductive coatings and polymer composites, for many of which the mechanical characteristics of the sheets are very important. The effective Young's moduli measured for $Ti_3C_2T_x$ and $Nb_4C_3T_x$ MXenes are about 50% higher than the value of about 210 GPa that was previously determined in the experiments on nanoindentation of GO [53], making MXenes superior scalable solution-processable 2D materials in terms of their mechanical properties. Thus, the

nanoindentation experiments on individual MXene flakes demonstrate their promise for structural composites, textiles, protective coatings, membranes, nanoresonators, and other applications that require bulk quantities of solution-processable materials with great mechanical properties.

Some recent studies demonstrated that suspended MXene flakes could be employed not only for nanoindentation measurements, but also in nanoelectromechanical devices. Bagheri and co-workers demonstrated a high-yield transfer of $Ti_3C_2T_x$ flakes on substrates with prefabricated electrodes and trenches, enabling fabrication of numerous electromechanical devices based on suspended MXene monolayers [48]. A scheme of a representative device is shown in Figure 18.3a, which demonstrates a monolayer $Ti_3C_2T_x$ MXene flake suspended over a trench in a Si/Si_3N_4 substrate and connected to a gold contact with a chromium underlayer. An AC voltage is applied between a gold pad and a conductive *p*-doped silicon substrate, resulting in an electrostatic actuation of a MXene membrane. The high electrical conductivity of $Ti_3C_2T_x$ MXene and a good electrical contact that it forms with gold electrodes [42, 72] are both important for this experimental design. The vertical displacement of the MXene membrane is recorded using an AFM tip.

For the experimental realization of these devices, few-μm MXene flakes were synthesized minimizing agitation of the etching products [43, 73] (Figure 18.1) and then transferred on Si/Si_3N_4 substrates with prefabricated electrodes and trenches with gaps ranging from 200 nm to 2 μm by the polydimethylsiloxane (PDMS) stamp-assisted method, as described in Reference [48]. Figure 18.3b shows a representative optical microscopy image of a substrate area with a $Ti_3C_2T_x$ MXene flake (circled) suspended over a trench and making a contact with the gold electrode. The circled MXene flake is also shown in the SEM image in Figure 18.3c, which was recorded at an oblique angle relative to the surface. The image shows that the membrane is well stretched over the trench and that there are no tears in the suspended portion of the flake. A large area contact of the MXene flake with the gold electrode is also evident. The inset in Figure 18.3b shows SEM image of another monolayer $Ti_3C_2T_x$ MXene flake that is suspended over a wider (2 μm) trench.

Figure 18.3d demonstrates a representative cyclic operation of the MXene device shown in Figure 18.3c. The AC voltage waveform applied between the suspended MXene flake and the bottom electrode (*p*-doped Si) is shown in the top panel, while the deflection of the center of the membrane relative to its unbiased position is shown in the bottom panel. As displayed in Figure 18.3a, the deflection is recorded by an AFM tip, which applied a constant force of 2 nN to the membrane. Figure 18.3d shows that the fabricated MXene device responds to the AC voltage and demonstrates periodic vibrations. Regardless of whether the MXene sheet is charged positively and the substrate negatively or vice versa, the

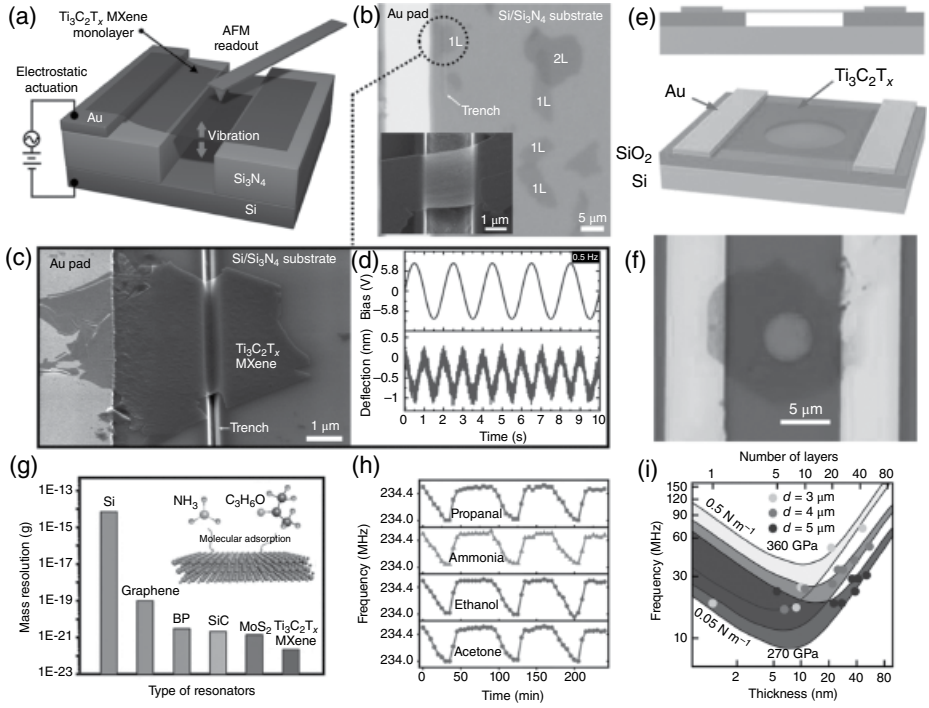


Figure 18.3 Nanoelectromechanical devices based on suspended $Ti_3C_2T_x$ MXene membranes. (a) Scheme of an electrostatically actuated MXene device with a $Ti_3C_2T_x$ flake suspended over a trench. The device was probed by an AFM tip. (b) Optical image of a representative monolayer (1L) MXene flake (in the circle) suspended over a trench in a Si/Si_3N_4 substrate. The inset shows SEM image of a representative suspended monolayer $Ti_3C_2T_x$ flake. (c) SEM image of a device based on a $Ti_3C_2T_x$ MXene flake that is connected to a gold pad and suspended over a trench that is about 400 nm wide. The image was taken at an oblique angle relative to the surface. (d) Cyclic electromechanical operation of the MXene device shown in panel (c). *Source:* Bagheri et al. [48]/Royal Society of Chemistry. (e, f) Scheme and optical image of a MXene resonator suspended over a circular well. *Source:* Xu et al. [65]/Reproduced from American Chemical Society. (g) Mass resolution of a monolayer $Ti_3C_2T_x$ MXene resonator in comparison with resonators based on other materials: Si [66], graphene [67], black phosphorus (BP) [68], SiC [69], MoS_2 [70]. The inset shows a schematic diagram of the adsorption of small molecules on a monolayer $Ti_3C_2T_x$ MXene. (h) Cyclic response of a monolayer $Ti_3C_2T_x$ MXene resonator to adsorbed molecules. The effect of these molecules can be reversed by purging the device with nitrogen gas. *Source:* Tan et al. [71]/John Wiley & Sons. (i) Frequency scaling in $Ti_3C_2T_x$ MXene resonators. Measured (circles) and calculated (lines and areas in between) fundamental resonance frequencies are plotted as functions of device thickness. Different colors represent different device diameters: $d = 3\,\mu m$ (white); $d = 4\,\mu m$ (gray); $d = 5\,\mu m$ (black). In calculated resonance frequency for each device diameter, the top curve represents $E_{Young} = 360\,GPa$ and the device tension (γ) of $0.5\,N\,m^{-1}$; the bottom curve represents $E_{Young} = 270\,GPa$ and $\gamma = 0.05\,N\,m^{-1}$. Results from all combinations of parameters within this range are represented by the colored areas. *Source:* Reproduced from Xu et al. [65]/American Chemical Society.

membrane always experiences an attractive electrostatic force toward the bottom of the trench. Thus, for each period of an AC voltage wave, the membrane has a maximum downward deflection twice, at both positive and negative AC voltage peaks. As a result, the deflection wave doubles the frequency of the AC voltage wave.

Figure 18.3e demonstrates another experimental design of MXene-based nanoelectromechanical devices that were employed in References [65, 71]. In this design, the MXene flake is suspended over a circular well, as in prior nanoindentation studies [3, 47]. An optical photograph of a representative device is shown in Figure 18.3f. Tan and co-workers demonstrated that such nanoelectromechanical resonators based on monolayer $Ti_3C_2T_x$ MXene flakes can function as very sensitive sensors of small molecules with a sub-zeptogram resolution [71]. Figure 18.3g shows that monolayer MXene devices surpass the performance of nanoelectromechanical resonators based on other materials, such as Si [66], graphene [67], black phosphorus (BP) [68], SiC [69], and MoS_2 [70]. The authors attributed the exceptional performance of monolayer $Ti_3C_2T_x$ resonators to the diverse chemical functionalities of MXene flakes [40, 41] that are responsible for strong intermolecular interactions with the surface adsorbates [74, 75]. Figure 18.3h shows the reproducibility of the shift of the resonance frequency of a MXene membrane in response to the surface adsorption of various analyte molecules, such as ethanol, propanol, acetone, and ammonia. Importantly, the sensing response is completely reversible and could be reverted by purging the device with nitrogen gas. Thus, the work by Tan and co-workers demonstrates the great promise of MXene resonators for sensing applications [71].

Xu and co-workers investigated nanoelectromechanical resonators based on $Ti_3C_2T_x$ MXene crystals with thicknesses ranging from a monolayer to more than 50 layers [65]. At various thicknesses, the devices exhibited robust nanomechanical vibrations. By combining experimental results with theoretical calculations, the authors determined the Young's modulus of $Ti_3C_2T_x$ to be 270–360 GPa (Figure 18.3i) [65], which is in excellent agreement with the previous nanoindentation measurements [3] (Figure 18.2). These results further confirm the great mechanical properties of MXenes at a single flake level, and the efforts focused on the translation of these properties from individual flakes to bulk MXene composites are discussed in the following sections.

18.3 Mechanical Properties of MXene Composites

The first report of MXene in 2011 [1] described attractive mechanical properties of MXene flakes [3] and showed their great potential for constructing high-performance composites. For example, Ling et al. [4] first reported MXene

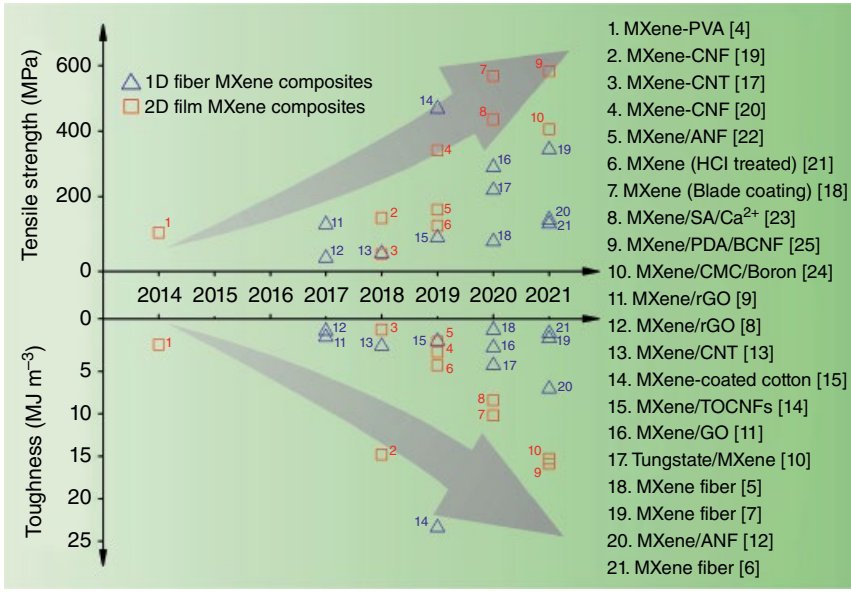


Figure 18.4 Comparison of tensile strength and toughness of 1D fiber and 2D film MXene composites. Since 2014, high values of mechanical properties have been achieved by enhancing the orientation of MXene flakes, reducing voids, and strengthening interface interactions in composites.

composites by assembling the MXene flakes with PVA into 2D film. Later, many 2D film MXene composites were fabricated with different kinds of polymers. Meanwhile, the 1D fiber MXene composites were also fabricated via wet spinning. The tensile strength and toughness of 1D fiber and 2D film MXene composites are shown in Figure 18.4. With the introduction of novel assembly strategies for reducing voids, enhancing orientation, and strengthening interface interactions, the tensile strength and toughness of MXene composites were improved, indicating promising aerospace applications. For example, Eom et al. [5] first fabricated 1D fiber MXene composites with a maximum tensile strength of about 63.9 MPa, toughness of 0.091 MJ m^{-3}, and high electrical conductivity of 7713 S cm^{-1} by the wet-spinning method, in which the ammonium ions were introduced during the coagulation process. After aligning the MXene flakes by controlling spinning speeds and morphology of the spinneret [6], the tensile strength and toughness of 1D fiber MXene composites reach as high as 118 MPa and 1.09 MJ m^{-3}, respectively. Compared with 1D MXene fiber composites, 2D film MXene composites show better properties. Ling et al. [4] first demonstrated MXene/polyvinyl alcohol (PVA) composite film with a tensile strength of 91 MPa and toughness of 1.83 MJ cm^{-3}, respectively. Zhang et al. [18] reported the tensile strength, toughness, and

electrical conductivity of 2D film MXene composites reaching up to 480 MPa, 10.2 MJ cm^{-3}, and 15 100 S cm^{-1} by highly aligning MXene flakes via blade coating. Wan et al. [25] achieved ultrastrong 2D film MXene composites with a tensile strength of 583 MPa and toughness of 15.9 MJ cm^{-3} by reducing voids in composites.

However, compared with 2D film MXene composites, 1D fiber MXene composites show much lower values of mechanical properties due to their random shape structure and high porosity. Compared with 1D fiber and 2D film MXene composites, the investigation of mechanical properties of 3D bulk MXene composites is in early stages. Several approaches, such as solution mixing and sol–gel-assisted impregnation, have been applied to fabricate 3D bulk MXene composites, and the flexural strength and fracture toughness are being investigated extensively [76, 77].

18.3.1 1D Fiber MXene Composites

With their excellent electrical and mechanical properties, MXene flakes are ideal candidate materials for fabricating electrically flexible fibers. The wet-spinning process has been demonstrated as a versatile approach for continuously fabricating MXene fibers. For example, Eom et al. [5] developed continuously controlled, additive/binder-free wet spinning for assembling MXene flakes into fibers, as shown in Figure 18.5a. MXene flakes with an average lateral size of 2.26 μm were incorporated into stable colloidal dispersion with a concentration of 25 mg ml^{-1}. The oriented MXene fibers were obtained through increasing shear stress in the procedure of wet spinning. The cross-section of the MXene fibers showed a lamellar structure with highly compact MXene flakes (Figure 18.5b). Although the maximum tensile strength is about 85 MPa (Figure 18.5c), the electrical conductivity reaches up to 7713 S cm^{-1}. This is because the oriented liquid crystal structure was induced by the external shear force.

To further improve the orientation of MXene flakes in the fiber, Li et al. [6] controlled the cross-sectional structure of the spinneret and the drafting speed in the process of wet spinning, as depicted in Figure 18.5d. The resultant MXene fiber shows a highly oriented lamellar and dense packing structure of MXene flakes (Figure 18.5e). The alignment degree reached up to 0.86 characterized by wide-angle X-ray scattering. Compared with the circular channel, the flat fluid channel effectively restricts the change of the shear force gradient and reduces the defects, such as folds and voids in the MXene fibers, resulting in good mechanical properties (Figure 18.5f), electrical conductivity, and electrochemical properties. Shin et al. [7] demonstrated that the electrostatic interaction between MXene flakes can be further enhanced by controlling the pH value of the dispersion; consequently, high electrical conductivity and strong MXene fibers were successfully fabricated by wet spinning. The MXene fiber had a tensile strength of up to 344 MPa, the Young's modulus was as high as 122 GPa, and it had extremely high electrical conductivity of 12 504 S cm^{-1}.

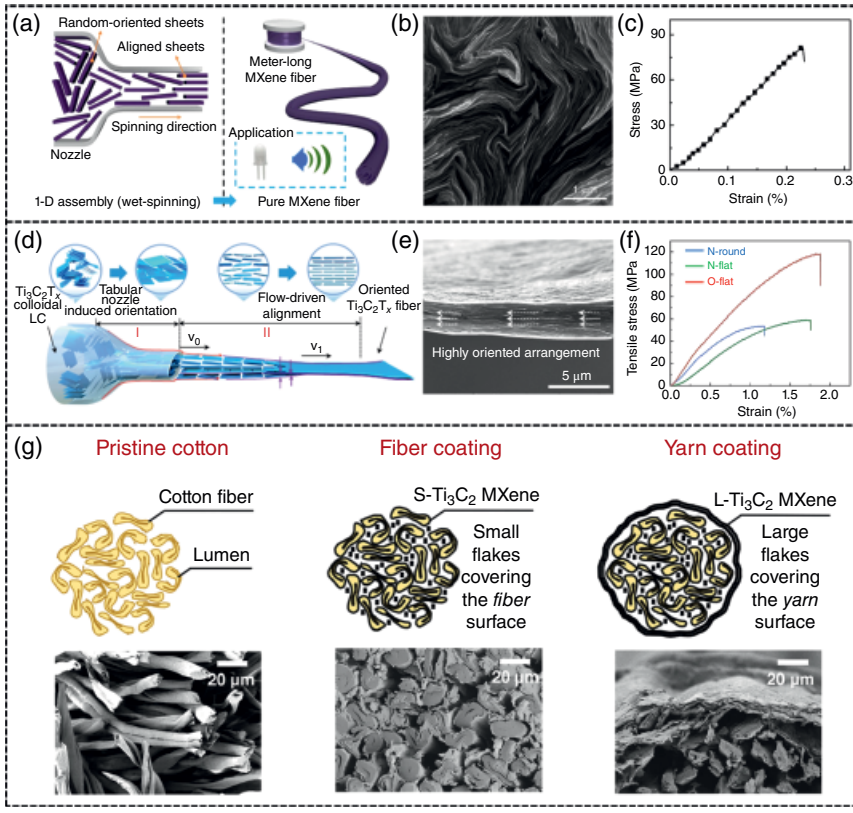


Figure 18.5 1D fiber MXene composites. (a) Schematic illustration of fabrication of fiber MXene by wet spinning, in which the MXene flakes are aligned in the axial direction. (b) The cross-section of MXene fiber. (c) The tensile stress-strain curve of MXene fiber. *Source:* (a, c) Eom et al. [5]/Springer Nature/CC BY 4.0. (d) Schematic illustration of fabrication of highly oriented MXene fiber. (e) Cross-sectional image of highly oriented MXene fiber. (f) The tensile stress-strain curves of MXene fibers. It was noted that "round" in "N-round" and "flat" in "N-flat" and "O-flat" represent the "round" and "flat" spinneret nozzle shapes, respectively. Simultaneously, "N" in "N-round" and "N-flat" means "normal" spinning driving speed, while "O" in "O-flat" stands for oriented MXene flakes. *Source:* Adapted from Li et al. [6]/Reproduced from American Chemical Society. (g) Schematic illustration of the cross-section of pristine cotton, fiber coated with small-size MXene flakes, and yarn coated with large-size MXene flakes. *Source:* Uzun et al. [15]/Reproduced from John Wiley & Sons, Inc.

In the process of wet spinning, the conductive polymers, GO, and carbon nanotubes (CNTs) were also introduced into fiber MXene composites to improve the mechanical properties. For example, the MXene flakes and GO flakes were assembled into orderly MXene-GO fiber composites [8, 9], resulting in a tensile strength of 116.1 MPa after hydroiodic acid reduction treatment. Wang et al. [10]

achieved the aligned fiber tungstate/MXene composites with a tensile strength of 220 MPa. Inspired by the structure of wood, Chen et al. [11] developed a novel approach to the coaxial wet-spinning process to fabricate core-shell MXene@GO fiber composites by using GO as a mechanical layer to wrap MXene flakes, resulting in high tensile strength up to 290 MPa. Wang et al. [12] also reported distinct skin-core structure MXene@aramid composite fibers by the coaxial wet-spinning method. The obtained MXene@aramid fiber composites show a tensile strength of 130 MPa and high toughness of about 7 MJ m^{-3}. Meanwhile, the biscrolling and 3D printing techniques have also been developed to fabricate fiber MXene composites, such as MXene-CNTs yarn [13, 14] and MXene-TEMPO (2,2,6,6-tetramethylpiperidine-1-oxylradi-cal)-mediated oxidized cellulose nanofibrils fiber [14], respectively.

All these fiber MXene composites manufactured by the abovementioned methods exhibited low mechanical properties, far from satisfactory for the smart textile industry. For wearables, fiber MXene composites that can be washed every day, like yarns, have become important for many practical applications. Uzun et al. [15] developed a simple two-step dip-coating process to prepare knittable and washable multifunctional MXene-coated cellulose yarns, through coating cellulose-based yarns (such as cotton, bamboo, and linen) with MXene flakes. In order to maximize MXene flakes' loading on the cellulose-based yarns in the dip-coating process, the colloidal solutions of small- and large-size MXene flakes (as noted S-Ti_3C_2 and L-Ti_3C_2) were used in this two-step coating process (Figure 18.5g). The first coating process used only S-Ti_3C_2 MXene dispersions, and the second coating utilized L-Ti_3C_2 MXene dispersions to achieve MXene coating on the surface of the yarn to provide high electrical conductivity. By the two-step coating procedure, the $Ti_3C_2T_x$ mass loading of up to 78 wt% (2.5 mg cm^{-1}) could be realized with cotton yarns. The obtained fiber MXene composites had a tensile strength of 468.4 MPa, Young's modulus of 5.0 GPa, and electrical conductivity of 198.5 S cm^{-1}.

Fiber MXene composites show many promising applications, however, their mechanical properties and electrical conductivity are not yet high enough to meet commercial production applications. Moreover, these kinds of MXene fibers are difficult to knit into wearable fabrics. Several obstacles, such as voids, wrinkles of MXene flakes, and weak interface interactions also impair the performance of the resultant fiber MXene composites.

18.3.2 2D Film MXene Composites

Ling et al. [4] first reported 2D film MXene composites via simple vacuum-assisted filtration (Figure 18.6). MXene flakes were exfoliated from Ti_3AlC_2 precursor, achieving a large lateral size with over 2 μm. Two kinds of polymers, poly(diallyldimethylammonium chloride) (PDDA) and PVA, were chosen because

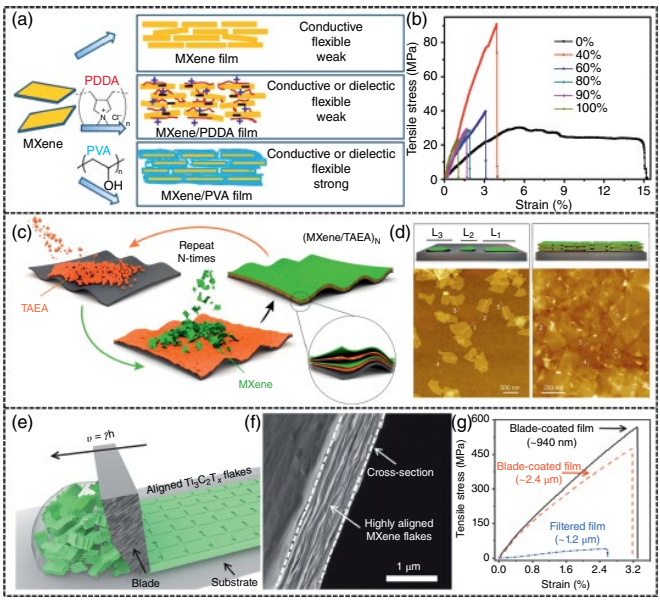


Figure 18.6 2D film MXene composites. (a) Schematic illustration of MXene-PVA composite. (b) Tensile stress-strain curves for MXene-PVA composites with different content of MXene. *Source:* Reproduced from Ling et al. [4] with permission. Copyright 2014, National Academy of Sciences. (c) Schematic illustration of (MXene/TAEA) n composites by LbL assembly. (d) Cross-section model and surface morphology of single MXene flake and (MXene/TAEA) n composites. *Source:* Tian et al. [16]/Reproduced from Springer Nature. (e) Schematic illustration of the blade coating process for preparing MXene film. (f) Cross-section of a blade-coated MXene film showing highly aligned large MXene flakes. (g) Tensile stress-strain curves of blade-coated and vacuum-filtered MXene composites. *Source:* Zhang et al. [18]/Reproduced from John Wiley & Sons, Inc.

PDDA is a cationic polymer, easily interacting with negative MXene flakes, and PVA shows excellent water solubility, having many hydroxyl groups. The MXene-PDDA composites show orderly stacked layers with intercalation of PDDA molecules between the MXene flakes, reducing the electrical conductivity compared with the pure MXene film. Compared with PDDA, the intercalation and confinement of PVA layers were clearly identified, and the spacing between MXene flakes can be controlled by adjusting amounts of PVA. The tensile stress–strain curves of MXene-PVA composites show that the tensile strength increases with decreasing content of MXene. When the MXene loading is 40%, the tensile strength of MXene-PVA composites reached as high as 91 MPa, about four times higher than that for pure MXene film.

Compared with simple vacuum-assisted filtration, LbL assembly is a widely used technique for assembling layered 2D film composites especially for 2D nanomaterials. For example, Tian et al. [16] assembled small molecule tris (2-aminoethyl) amine (TAEA), and MXene flakes into $(MXene/TAEA)_n$ composites by the LbL technique, as shown in Figure 18.6c. The MXene flakes have a thickness of around 2.5 nm and lateral size distribution in the range of several hundreds of nanometers. The in-plane microstructure of the $(MXene/TAEA)_n$ composites characterized by atomic force microscope shows all individual MXene flakes stacked face-to-face, as shown in Figure 18.6d. The interlayer spacing of MXene flakes is expanded only about 1 Å by TAEA, resulting in highly ordered $(MXene/TAEA)_n$ composites with high electronic conductivity of 7.3×10^4 S m^{-1}. The abovementioned MXene composites have been demonstrated as excellent electrodes for flexible all-solid-state supercapacitors. Weng et al. [17] developed a spin spray LbL technique to rapidly fabricate MXene-CNTs composites by an automated apparatus. The PVA and poly (sodium 4-styrene sulfonate) of high molecular weight were selected as main fillers, resulting in low mechanical properties with a tensile strength of 25 MPa but high specific shielding effectiveness up to 58 187 dB cm^2 g^{-1}.

To further improve mechanical properties of MXene composites, the lateral size and alignment of MXene flakes need to be improved, similar to GO-based composites. Zhang et al. [18] demonstrated strong MXene composites by a blade coating approach. The MXene flakes had the lateral size of 10 μm and thickness of ≈1.7 nm, resulting in the aspect ratio of MXene flakes as high as ≈5880. This high aspect ratio resulted in the formation of lyotropic liquid crystals of dispersions of large MXene flakes. The liquid crystal domains of MXene flakes were well-aligned along the shear direction by adjusting the blade speed in the process of blade coating, resulting in an orientation factor of 0.75. The obtained MXene films with a thickness of 2.4 μm showed a tensile strength of 480 MPa, toughness of 7.68 MJ m^{-3}, and electrical conductivity of 15 100 S cm^{-1}, respectively.

18.3.3 3D Bulk MXene Composites

Compared with 1D fiber and 2D film MXene composites, the 3D bulk MXene composites are more investigated because of their flexural strength and fracture toughness. One of the most feasible and effective ways to prepare MXene 3D bulk composites is solution blending, popular in fabricating other nanomaterials like reinforced polymer composites, such as CNTs, nanoclay, and graphene. For example, Liu et al. [30] fabricated the MXene-epoxy composites with a flexural strength of 157 MPa and a fracture toughness of 1.07 MPa $m^{1/2}$ via adding only 0.2 wt% MXene flakes, which is 1.3 and 1.4 times higher than those for pure epoxy. Moreover, the 1D attapulgite (ATP) and 2D MXene flakes were assembled into ATP-MXene hybrid building blocks, used to reinforce the epoxy to obtain high flexural strength of 187.5 MPa and a fracture toughness of 1.84 MPa $m^{1/2}$.

However, improvement in mechanical properties of MXene composites is difficult to realize due to the random structure and weak interface interactions between MXene and polymer matrix. Thus, some new strategies are proposed to fabricate 3D bulk MXene composites, such as sol–gel/impregnation and hot-pressing. Wang et al. [31] prepared the MXene-*C* foam/epoxy composites with a high Young's modulus of 3.96 GPa via a sol–gel and vacuum-assisted impregnation approach. Natural biological materials often provide the inspiration for constructing high-performance composites. Inspired by the wings of a dragonfly, Xu et al. [32] used the 3D-interconnected mechanical framework in a brittle polymer matrix and MXene flakes onto predesigned supramolecular bond crosslinked polymer (SP) microparticles, hot pressed at controllable temperatures. The SP with ureido-4-pyrimidinone group can form hydrogen-bond interactions with polar groups (–OH, –F) of MXene flakes, enhancing stiffness and toughness of SP/MXene (SPM) composites (Figure 18.7a). The flexural strength and fracture toughness of SPM composite were 45.4 MPa and 1.901 MPa $m^{1/2}$ with adding 2 vol% MXene flakes, 25 and 54.3 times higher than those for pure SP (Figure 18.7b). Lossada et al. [33] demonstrated a facile dry hot-pressing approach with poly (ethylene glycolmethacrylamide)-co-hydroxy (ethylene glycol) (EMA) polymer and MXene flakes, showing an internal nacre-mimetic structure (Figure 18.7c). The flexural strength and fracture toughness of MXene/EMA composites was 48 MPa and 1 MPa $m^{1/2}$ (Figure 18.7d). Furthermore, the presence of MXene flakes can improve the interfacial performance of carbon fiber (CF)/epoxy composites. For instance, Liu et al. [34] fabricated CF-MXene-chitosan (CS)/epoxy composites with hierarchical structure. The flexural strength was 992 MPa, higher than that of the CF/epoxy composites at 641 MPa.

Freeze casting, also known as ice-templating, is a very powerful approach for fabricating bulk materials. Peng et al. [78] demonstrated a reduced graphene-oxide

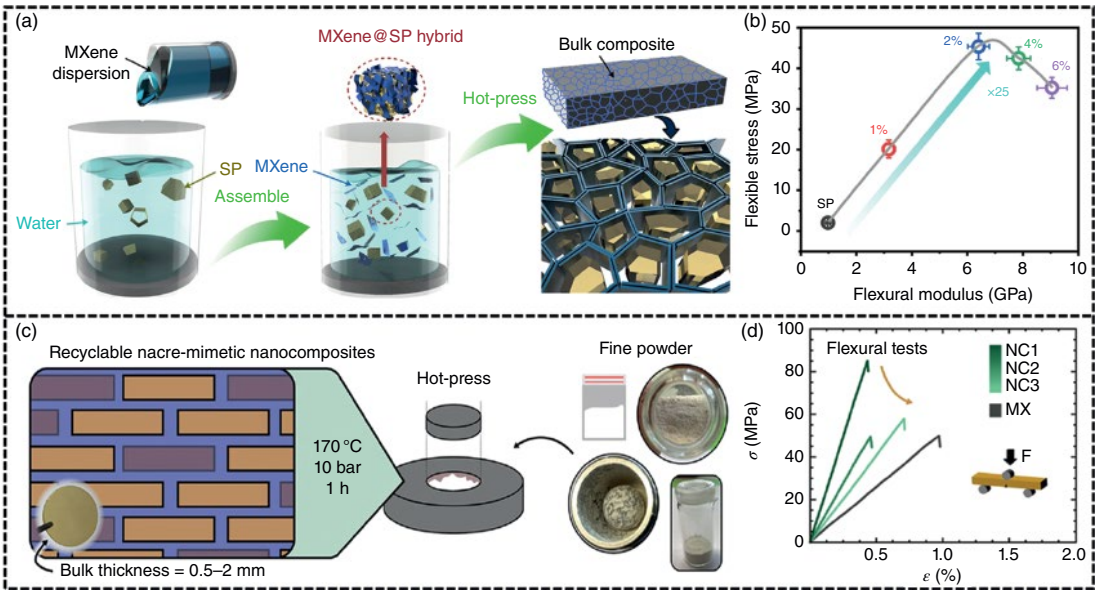


Figure 18.7 3D bulk MXene composites. (a) Schematic fabrication process of supramolecular bond crosslinked polymer-MXene (SPM) bulk composite. (b) Flexural strength and Young's modulus of SPM composites. *Source:* Xu et al. [32]/Reproduced with permission from Elsevier. (c) Schematic illustration process of the dry processing of nacre-mimetic MXene composites. (d) Flexural stress–strain curves of the nacre-mimetic MXene composites. *Source:* Lossada et al. [33]/Reproduced from John Wiley & Sons, Inc./CC BY-NC 4.0.

(rGO)-carboxymethyl cellulose (CMC) sodium scaffold with a lamellar structure via a freeze casting and reducing technique. The epoxy resin was impregnated into the rGO scaffold to fabricate the rGO-CMC/epoxy composites with an "inverse nacre-like" structure, showing the fracture toughness of up to 2.5 MPa $m^{1/2}$. Compared with graphene and its derivatives, the MXene flakes show a layered structure and the tunable surface functional groups (–OH, –F, and –O), which are ideal building blocks for preparing high mechanical performance 3D bulk MXene composites via the ice-templated approach. Recently, Wang et al. [37] demonstrated cellulose nanofibers (CNF)/MXene aerogels (CTA) with high electrical conductivity of 1992 S m^{-1} via the freeze casting technique, and the thermally annealed CTA (TCTA)/epoxy composites were prepared by a vacuum-assisted impregnation approach, resulting in electromagnetic interference shielding effectiveness (EMI SE) of 74 dB via adding 1.38 vol% MXene. Moreover, Wu et al. [38] also prepared the MXene/sodium alginate (SA) (MS) hybrids aerogel scaffold by the freeze casting technique, where the PDMS was impregnated and cured at vacuum environment to achieve the MS composites with an EMI SE of 53.9 dB. However, investigation on mechanical properties of 3D bulk MXene composites fabricated by freeze casting has not yet started.

Moreover, the mechanical properties, electrical conductivity and EMI shielding performance of 1D, 2D, and 3D MXene composites are summarized as shown in Table 18.1.

18.4 Effective Strategy to Reduce Voids and Strengthening Interface Interactions

The sequential bridging strategy has been developed to assemble GO flakes into strong composites and has been found to be very effective for reducing voids [79, 80], aligning GO flakes by stretching [81], and strengthening interface interactions between GO flakes [82–84]. Recently, Cheng's group has also demonstrated the sequential bridging strategy to assemble MXene flakes into high-performance composites.

18.4.1 Sequential Bridging of Hydrogen and Ionic Bonding

Wan et al. [23] demonstrated the formation of high-performance MXene composites through a sequential bridging of hydrogen and ionic bonding. SA was introduced to crosslink MXene flakes through hydrogen bonding, and then Ca^{2+} was further infiltrated into MXene composite, resulting in sequentially bridged MXene (SBM) composites, as shown in Figure 18.8. The SBM composites showed a layered structure. Compared with pure MXene film, the sequential bridging of hydrogen and

Table 18.1 Summary of the mechanical, electrical conductivity, and EMI shielding properties of 1D fiber, 2D film, and 3D bulk MXene composites.

Test type	Composition	MXene content wt%	Tensile strength (MPa)	Young's modulus (GPa)	Toughness ($MJ\,m^{-3}$)	Conductivity ($S\,cm^{-1}$)	Shielding effectiveness (dB)	References
1D fiber	MXene	100	63.9	29.6	0.09	7713	—	[5]
	MXene	100	118	—	~1.09	7200	—	[6]
	MXene	100	343.68	121.97	~0.48	12 503	—	[7]
	MXene/rGO	90	12.9	1.2	~0.22	290	—	[8]
	MXene/rGO	88	116.1	13.3	0.94	72	—	[9]
	MXene/CNT	97.5	26.6	0.09	~2.01	26	—	[13]
	MXene/TOCNFs	50	75.6	4.7	~1.42	2	—	[14]
	MXene-coated cotton yarn	78	468.4	5.0	~23.42	198	—	[15]
	MXene@GO	50	290	30	~2.18	24	70	[11]
	Tungstate/ MXene	10	220	—	~4.29	—	—	[10]
	MXene@ANF	—	130	0.033	~7.02	25	—	[12]
2D film	MXene/PVA	60	91	3.7	1.83	0.0004	—	[4]
	MXene/CNT	—	25	6.25	0.05	130	0.29	[17]
	MXene/CNF	50	135.4	3.8	14.8	0.1	25	[19]
	MXene/CNF	20	341	42.8	2.73	225	—	[20]
	MXene	—	112	4.48	1.48	10 400	60.4	[21]
	MXene/ANF	20	160	4.5	4.3	—	—	[22]
	MXene	—	568	20.6	10.2	11 500	47.9	[18]

	MXene/SA/Ca^{2+}	—	436	14	8.39	2988	46.2	[23]
	PDMM/BCNF	40	406	7.5	15.3	2848	—	[25]
	MXene/CMC/Boron	10	583	27.8	15.9	6115	56.4	[24]
	MXene/MMT/PVA	—	225	10.5	2.25	1.3	20	[29]
	MXene/PDA	5	237	6.8	4.38	4323	58.4	[28]
Test type	**Composition**	**MXene content wt%**	**Bending strength/MPa**	**Bending modulus/GPa**	**Fracture toughness/ MPa $m^{1/2}$**	**Conductivity/ S cm^{-1}**	**shielding efectiveness/dB**	**Reference**
3D bulk	EMA/MXene	50	48	5.5	1	—	—	[33]
	SP/MXene	2 vol%	45.4	6.4	1.9	—	23.5	[32]
	Epoxy/MXene	0.2	157	3.5	1.07	—	—	[30]
	MCF/Epoxy	1.64	—	3.96	—	2	46	[31]
	CF-MXene-CS/Epoxy	—	991.8	89.4	—	—	—	[34]
	MXene/CNTs-BFRP	1	525	25	—	—	—	[36]
	ATP-MXene/Epoxy	0.2	187.5	3.6	1.84	—	—	[35]

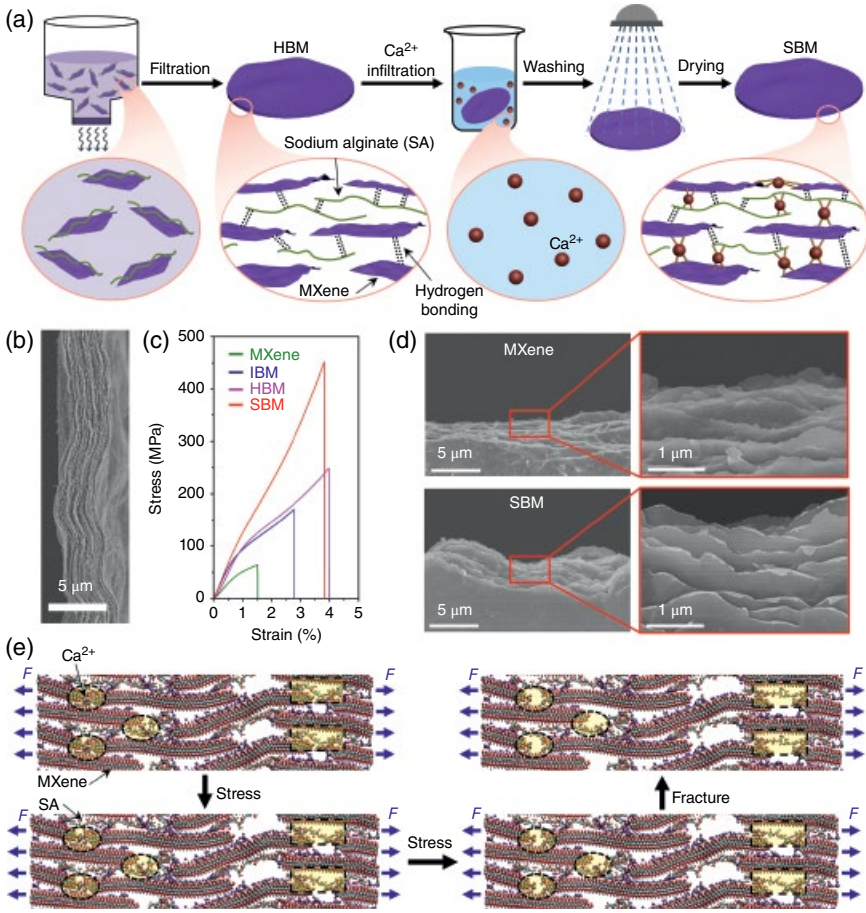


Figure 18.8 Sequential bridging from hydrogen and ionic bonding. (a) The MXene/sodium alginate (SA) layered composites were assembled by introducing the Ca^{2+}, resulting in SBM composite. (b) Scanning electron microscope (SEM) image of the fracture surface of the SBM composite with layered structure. (c) Typical stress–strain curves for the pure MXene film, ionic bonding MXene (IBM), hydrogen bonding MXene (HBM), and SBM composites. (d) Inclined-view SEM images of the fracture surface of the pure MXene film and SBM composites, indicating curling of the MXene flake edges for the SBM composites but not for the pure MXene film. (e) Model snapshots for the SBM composites during simulative tensile stretching showing not only the breakage of hydrogen bonding and stretching of coiled SA molecular chains (dashed rectangular region) but also the breakage of ionic bonding (dashed elliptical region). *Source:* Reproduced from Wan et al. [23] with permission. Copyright 2020, National Academy of Sciences.

ionic bonding in SBM composites plays a key role in enhancing the mechanical properties. As shown in Figure 18.8c, the tensile strength, toughness, and Young's modulus of SBM composites reached as high as 436 ± 15 MPa, 8.39 ± 0.35 MJ m^{-3}, and 14.0 ± 0.2 GPa, respectively, which are 6.9, 13.5, and 2.5 times higher than those for pure MXene film. Figure 18.8d shows the fracture morphology comparison between pure MXene film and MXene composites. It is clear that SBM composites exhibit better curled morphology as compared with pure MXene film, indicating strong interfacial interactions from sequential bridging of hydrogen and ionic bonding.

Molecular-dynamics simulations reveal that the simultaneous improvement in tensile strength and toughness is due to the synergistic effect from hydrogen and ionic bonding. As shown in Figure 18.8e, the adjacent MXene flakes start to slide past each other in the initial loading. The coiled SA molecular chains (dashed rectangular region) are gradually stretched and the hydrogen bonding between SA molecules and MXene flakes is alternately broken and reformed under continuous stretching, dissipating numerous energies. The ionic bonding (dashed elliptical region) also starts to fracture, and the SA molecular chains are sufficiently extended. With further increasing the load, the ionic bonding and hydrogen bonding are simultaneously broken, resulting in high load transfer efficiency.

18.4.2 Sequential Bridging of Hydrogen and Covalent Bonding

Recently, Cheng's group from Beihang University found that the voids that exist in MXene composites are an obstacle to obtaining high-performance MXene composites [25]. The main reasons for the existence of the voids in composites are as follows: (i) the fabrication process, (ii) the intrinsic flexibility of MXene flakes, and (iii) the wrinkling of MXene flakes in the assembly process. Cheng's group developed an effective synergistic strategy for curing the voids using sequential bridging that combines different interfacial interactions. Sodium CMC was first introduced to construct the hydrogen bonding with MXene, and then small borate ions were infiltrated into interlayers of MXene flakes to covalently crosslink with the hydroxyl groups on CMC molecular chains and the surface of MXene flakes, resulting in SBM composites, as shown in Figure 18.9. The void microstructure of pure MXene film and SBM composites was first directly reconstructed using both focused ion beam (FIB) and SEM tomography (FIB/SEMT) and nanoscale X-ray computed tomography (nano-CT). The porosity of MXene film reaches as high as $15.4 \pm 0.6\%$; however, the SBM composites show only $5.35 \pm 0.3\%$ porosity due to the filling of CMC molecules.

The compact SBM composites show great improvement in mechanical properties, including 5.7, 3.6, and 11.2 times the tensile strength, toughness, and Young's modulus as compared with the pure MXene film. Meanwhile, the SBM composites

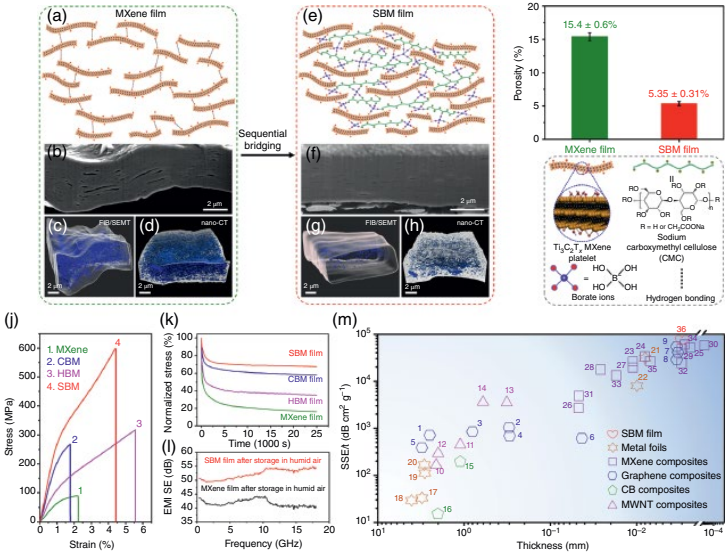


Figure 18.9 Sequentially bridged high-strength MXene composites. (a and e) Structural models of pure MXene film (a) and SBM (e) composites. (b and f) SEM images of cross-sections cut by FIB for pure MXene film (b) and SBM (f) composites. (c and g) 3D-reconstructed void microstructure derived from FIB/SEMT for pure MXene film (c) and SBM composites (g). (d and h) 3D-reconstructed void microstructure derived from nano-CT for pure MXene film (d) and SBM composites (h). (i) Porosities of pure MXene film and SBM composite derived from density measurements. (j) Representative tensile stress–strain curves of pure MXene film, covalent bonding MXene (CBM), HBM, and SBM composites. (k) Stress relaxation curves of pure MXene film, CBM, HBM, and SBM composites at 1.5% strain. (l) EMI SE as a function of frequency for pure MXene film and SBM composite after storage for 10 days in humid air. (m) Comparison of the relationship between SSE/t and thickness for solid materials, MWNT, multiwalled nanotube, and CB, carbon black. *Source:* Wan et al. [25]/Reproduced from American Association for the Advancement of Science - AAAS.

show much higher resistance to sonication damage and stress relaxation than the pure MXene film due to the strong interface interactions between MXene flakes. In particular, the SBM composites show higher shielding capacity retention and a higher electromagnetic interference shielding effectiveness (EMI SE) after storage in humid air for 10 days.

Furthermore, except the sequential bridging strategy, some other strategies, such as filling small-size nanosheets, external force/effect (including magnetic and electric field) induced orientation and hot press strategies also can improve the mechanical properties of 2D materials composites.

18.5 Outlook and Perspectives

In this chapter, we have summarized the recent progress in mechanical characterization of individual MXene flakes, as well as in making MXene composites, including mechanical properties and other functional properties such as electrical conductivity, and electromagnetic interference shielding. Several critical parameters, such as voids, strong interfacial interactions, and large size and high alignment degree of MXene flakes, play a key role in achieving high mechanical properties. For example, less porosity in MXene composites results in higher values of mechanical properties. With the large size of MXene flakes, higher tensile strength is easily obtained. Strong covalent interfacial interactions can also result in higher tensile strength, while much higher toughness is easily obtained through introducing weak hydrogen bonding. The high alignment degree of MXene flakes is very useful for high values of mechanical and electrical properties parallel to the orientation direction. The proposed synergistic effects from sequential bridging are very useful for further enhancing the performance of 1D fiber, 2D film, and 3D bulk MXene composites.

As already indicated, porosity is very harmful for the performance of MXene composites, and needs to be reduced or eliminated in MXene composites. Although the sequential bridging strategy is very useful to reduce voids, other approaches to reduce the voids, such as filling small-size flakes or molecules, should be explored. Compared with other 2D flakes, such as graphene or nanoclay, the orientation is also important to enhance mechanical properties of MXene composites. Therefore, properly aligning the MXene flakes in composites may be the next step for further improvement of the mechanical properties. The external forces, such as the stretching force, centrifugal force, microfluidics force, pressing force, and shearing microlithography force, which have been demonstrated in aligning GO flakes, would also be useful for aligning MXene flakes. However, that approach needs more work due to different intrinsic mechanical properties between GO and MXene flakes. Similar to GO flakes, the MXene flakes show very abundant functional groups, which are very helpful for designing and

constructing the interfacial interactions between MXene flakes by introducing molecules or other nanomaterials, such as black phosphorus.

The defect-free orderly aligned MXene flakes in composites not only enhance the mechanical properties but also improve electrical and thermal conductivities and electromagnetic interference shielding. Although strong and functional MXene composites can be prepared, currently they are produced on only a very small scale. As for practical applications, large-scale fabrication of MXene composites with outstanding performance is still needed. A simple universal strategy is needed and should be explored for rapid preparation of defect-free, orderly aligned MXene composites in the future.

Acknowledgments

This work was supported by the National Key Research and Development Program of China (Grant Number 2021YFA0715700), the National Science Fund for Distinguished Young Scholars (Grant Number 52125302), National Natural Science Foundation of China (Grant Numbers 22075009, 52350012), and 111 Project (Grant Number B14009). The work was also supported by the Nebraska Center for Energy Sciences Research (NCESR) and the National Science Foundation (NSF) through EPSCoR RII Track-1: Emergent Quantum Materials and Technologies (EQUATE), award OIA-2044049.

References

1 Naguib, M., Kurtoglu, M., Presser, V. et al. (2011). Two-dimensional nanocrystals produced by exfoliation of Ti_3AlC_2. *Advanced Materials* 23: 4248–4253.
2 VahidMohammadi, A., Rosen, J., and Gogotsi, Y. (2021). The world of two-dimensional carbides and nitrides (MXenes). *Science* 372: eabf1581.
3 Lipatov, A., Lu, H., Alhabeb, M. et al. (2018). Elastic properties of 2D $Ti_3C_2T_x$ MXene monolayers and bilayers. *Science Advances* 4: eaat0491.
4 Ling, Z., Ren, C.E., Zhao, M.Q. et al. (2014). Flexible and conductive MXene films and nanocomposites with high capacitance. *Proceedings of the National Academy of Sciences of the United States of America* 111: 16676–16681.
5 Eom, W., Shin, H., Ambade, R.B. et al. (2020). Large-scale wet-spinning of highly electroconductive MXene fibers. *Nature Communications* 11: 2825.
6 Li, S., Fan, Z., Wu, G. et al. (2021). Assembly of nanofluidic MXene fibers with enhanced ionic transport and capacitive charge storage by flake orientation. *ACS Nano* 15: 7821–7832.

7 Shin, H., Eom, W., Lee, K.H. et al. (2021). Highly electroconductive and mechanically strong $Ti_3C_2T_x$ MXene fibers using a deformable MXene gel. *ACS Nano* 15: 3320–3329.

8 Yang, Q., Xu, Z., Fang, B. et al. (2017). MXene/graphene hybrid fibers for high performance flexible supercapacitors. *Journal of Materials Chemistry A* 5: 22113–22119.

9 Seyedin, S., Yanza, E.R.S., and Razal, J.M. (2017). Knittable energy storing fiber with high volumetric performance made from predominantly MXene nanosheets. *Journal of Materials Chemistry A* 5: 24076–24082.

10 Wang, Y., Zheng, Y., Zhao, J., and Li, Y. (2020). Assembling free-standing and aligned tungstate/MXene fiber for flexible lithium and sodium-ion batteries with efficient pseudocapacitive energy storage. *Energy Storage Materials* 33: 82–87.

11 Chen, X., Jiang, J., Yang, G. et al. (2020). Bioinspired wood-like coaxial fibers based on MXene@graphene oxide with superior mechanical and electrical properties. *Nanoscale* 12: 21325–21333.

12 Wang, L., Zhang, M., Yang, B., and Tan, J. (2021). Lightweight, robust, conductive composite fibers based on MXene@Aramid nanofibers as sensors for smart fabrics. *ACS Applied Materials & Interfaces* 13: 41933–41945.

13 Wang, Z., Qin, S., Seyedin, S. et al. (2018). High-performance biscrolled MXene/carbon nanotube yarn supercapacitors. *Small* 14: e1802225.

14 Cao, W.T., Ma, C., Mao, D.S. et al. (2019). MXene-reinforced cellulose nanofibril inks for 3D-printed smart fibres and textiles. *Advanced Functional Materials* 29: 1905898.

15 Uzun, S., Seyedin, S., Stoltzfus, A.L. et al. (2019). Knittable and washable multifunctional MXene-coated cellulose yarns. *Advanced Functional Materials* 29: 1905015.

16 Tian, W., VahidMohammadi, A., Wang, Z. et al. (2019). Layer-by-layer self-assembly of pillared two-dimensional multilayers. *Nature Communications* 10: 2558.

17 Weng, G.M., Li, J., Alhabeb, M. et al. (2018). Layer-by-layer assembly of cross-functional semi-transparent MXene-carbon nanotubes composite films for next-generation electromagnetic interference shielding. *Advanced Functional Materials* 28: 1803360.

18 Zhang, J., Kong, N., Uzun, S. et al. (2020). Scalable manufacturing of free-standing, strong $Ti_3C_2T_x$ MXene films with outstanding conductivity. *Advanced Materials* 32: e2001093.

19 Cao, W.T., Chen, F.F., Zhu, Y.J. et al. (2018). Binary strengthening and toughening of MXene/cellulose nanofiber composite paper with nacre-inspired structure and superior electromagnetic interference shielding properties. *ACS Nano* 12: 4583–4593.

20 Tian, W., VahidMohammadi, A., Reid, M.S. et al. (2019). Multifunctional nanocomposites with high strength and capacitance using 2D MXene and 1D nanocellulose. *Advanced Materials* 31: e1902977.

21 Chen, H., Wen, Y., Qi, Y. et al. (2019). Pristine titanium carbide MXene films with environmentally stable conductivity and superior mechanical strength. *Advanced Functional Materials* 30: 1906996.

22 Zhang, Z., Yang, S., Zhang, P. et al. (2019). Mechanically strong MXene/Kevlar nanofiber composite membranes as high-performance nanofluidic osmotic power generators. *Nature Communications* 10: 2920.

23 Sijie, W., Li, X., and Wang, Y. (2020). Strong sequentially bridged MXene sheets. *PNAS* 117: 27154–27161.

24 Yang, L., Cui, J., Zhang, L. et al. (2021). A moisture-driven actuator based on polydopamine-modified MXene/bacterial cellulose nanofiber composite film. *Advanced Functional Materials* 31: 2101378.

25 Wan, S., Li, X., Chen, Y. et al. (2021). High-strength scalable MXene films through bridging-induced densification. *Science* 374: 96–99.

26 Lipton, J., Röhr, J.A., Dang, V. et al. (2020). Scalable, highly conductive, and micropatternable MXene films for enhanced electromagnetic interference shielding. *Matter* 3: 546–557.

27 Yun, T., Kim, H., Iqbal, A. et al. (2020). Electromagnetic shielding of monolayer MXene assemblies. *Advanced Materials* 32: e1906769.

28 Lee, G.S., Yun, T., Kim, H. et al. (2020). Mussel inspired highly aligned $Ti_3C_2T_x$ mxene film with synergistic enhancement of mechanical strength and ambient stability. *ACS Nano* 14: 11722–11732.

29 Lipton, J., Weng, G.M., Alhabeb, M. et al. (2019). Mechanically strong and electrically conductive multilayer MXene nanocomposites. *Nanoscale* 11: 20295–20300.

30 Liu, L., Ying, G., Wen, D. et al. (2021). Aqueous solution-processed MXene ($Ti_3C_2T_x$) for non-hydrophilic epoxy resin-based composites with enhanced mechanical and physical properties. *Materials & Design* 197: 109276.

31 Wang, L., Qiu, H., Song, P. et al. (2019). 3D $Ti_3C_2T_x$ MXene/C hybrid foam/epoxy nanocomposites with superior electromagnetic interference shielding performances and robust mechanical properties. *Composites Part A: Applied Science and Manufacturing* 123: 293–300.

32 Xu, J., Liu, T., Zhang, Y. et al. (2021). Dragonfly wing-inspired architecture makes a stiff yet tough healable material. *Matter* 4: 2474–2489.

33 Lossada, F., Zhu, B., and Walther, A. (2021). Dry processing and recycling of thick nacre–mimetic nanocomposites. *Advanced Functional Materials* 31: 2102677.

34 Liu, L., Yan, F., Liu, H. et al. (2021). Construction of hierarchical "organic-inorganic" structure by self-assembly to enhance the interfacial properties of epoxy composites. *Composites Science and Technology* 210: 108802.

35 Liu, L., Ying, G., Zhao, Y. et al. (2021). Attapulgite-MXene hybrids with $Ti_3C_2T_x$ lamellae surface modified by attapulgite as a mechanical reinforcement for epoxy composites. *Polymers (Basel)* 13: 1820.

36 Qian, Y., Zhong, J., and Ou, J. (2022). Superdurable fiber-reinforced composite enabled by synergistic bridging effects of MXene and carbon nanotubes. *Carbon* 190: 104–114.

37 Wang, L., Song, P., Lin, C.T. et al. (2020). 3D shapeable, superior electrically conductive cellulose nanofibers/ $Ti_3C_2T_x$ MXene aerogels/epoxy nanocomposites for promising EMI shielding. *Research (Washington DC)* 2020: 4093732.

38 Wu, X., Han, B., Zhang, H.-B. et al. (2020). Compressible, durable and conductive polydimethylsiloxane-coated MXene foams for high-performance electromagnetic interference shielding. *Chemical Engineering Journal* 381: 122622.

39 Naguib, M., Mochalin, V.N., Barsoum, M.W., and Gogotsi, Y. (2014). 25th anniversary article: MXenes: a new family of two-dimensional materials. *Advanced Materials* 26: 992–1005.

40 Halim, J., Cook, K.M., Naguib, M. et al. (2016). X-ray photoelectron spectroscopy of select multi-layered transition metal carbides (MXenes). *Applied Surface Science* 362: 406–417.

41 Seredych, M., Shuck, C.E., Pinto, D. et al. (2019). High-temperature behavior and surface chemistry of carbide MXenes studied by thermal analysis. *Chemistry of Materials* 31: 3324–3332.

42 Lipatov, A., Alhabeb, M., Lukatskaya, M.R. et al. (2016). Effect of synthesis on quality, electronic properties and environmental stability of individual monolayer Ti_3C_2 MXene flakes. *Advanced Electronic Materials* 2: 1600255.

43 Shekhirev, M., Busa, J., Shuck, C.E. et al. (2022). Ultralarge flakes of $Ti_3C_2T_x$ MXene via soft delamination. *ACS Nano* 16: 13695–13703.

44 Gogotsi, Y. and Anasori, B. (2019). The rise of MXenes. *ACS Nano* 13: 8491–8494.

45 Halim, J., Lukatskaya, M.R., Cook, K.M. et al. (2014). Transparent conductive two-dimensional titanium carbide epitaxial thin films. *Chemistry of Materials* 26: 2374–2381.

46 Ghidiu, M., Lukatskaya, M.R., Zhao, M.Q. et al. (2014). Conductive two-dimensional titanium carbide 'clay' with high volumetric capacitance. *Nature* 516: 78–81.

47 Lipatov, A., Alhabeb, M., Lu, H. et al. (2020). Electrical and elastic properties of individual single-layer $Nb_4C_3T_x$ MXene flakes. *Advanced Electronic Materials* 6: 1901382.

48 Bagheri, S., Abourahma, J., Lu, H. et al. (2023). High-yield fabrication of electromechanical devices based on suspended $Ti_3C_2T_x$ MXene monolayers. *Nanoscale* 15: 1248–1259.

49 Yan, H., Vajner, C., Kuhlman, M. et al. (2016). Elastic behavior of Bi_2Se_3 2D nanosheets grown by van der Waals epitaxy. *Applied Physics Letters* 109: 032103.

50 Li, Y., Yu, C., Gan, Y. et al. (2019). Elastic properties and intrinsic strength of two-dimensional InSe flakes. *Nanotechnology* 30: 335703.

51 Zhang, R., Koutsos, V., and Cheung, R. (2016). Elastic properties of suspended multilayer WSe_2. *Applied Physics Letters* 108: 042104.
52 Wang, H., Sandoz-Rosado, E.J., Tsang, S.H. et al. (2019). Elastic properties of 2D ultrathin tungsten nitride crystals grown by chemical vapor deposition. *Advanced Functional Materials* 29: 1902663.
53 Suk, J.W., Piner, R.D., An, J., and Ruoff, R.S. (2010). Mechanical properties of monolayer graphene oxide. *ACS Nano* 4: 6557–6564.
54 Bertolazzi, S., Brivio, J., and Kis, A. (2011). Stretching and breaking of ultrathin MoS_2. *ACS Nano* 5: 9703–9709.
55 Liu, K., Yan, Q.M., Chen, M. et al. (2014). Elastic properties of chemical-vapor-deposited monolayer MoS_2, WS_2, and their bilayer heterostructures. *Nano Letters* 14: 5097–5103.
56 Falin, A., Cai, Q., Santos, E.J.G. et al. (2017). Mechanical properties of atomically thin boron nitride and the role of interlayer interactions. *Nature Communications* 8: 15815.
57 Lee, C., Wei, X., Kysar, J.W., and Hone, J. (2008). Measurement of the elastic properties and intrinsic strength of monolayer graphene. *Science* 321: 385–388.
58 Fu, Z.H., Zhang, Q.F., Legut, D. et al. (2016). Stabilization and strengthening effects of functional groups in two-dimensional titanium carbide. *Physical Review B* 94: 104103.
59 Wang, X., Shen, X., Gao, Y. et al. (2015). Atomic-scale recognition of surface structure and intercalation mechanism of Ti_3C_2X. *Journal of the American Chemical Society* 137: 2715–2721.
60 Borysiuk, V.N., Mochalin, V.N., and Gogotsi, Y. (2015). Molecular dynamic study of the mechanical properties of two-dimensional titanium carbides $Ti_{n+1}C_n$ (MXenes). *Nanotechnology* 26: 265705.
61 Chang, R. and Graham, L.J. (1966). Low-temperature elastic properties of ZrC and TiC. *Journal of Applied Physics* 37: 3778–3783.
62 Brenton, R.F., Saunders, C.R., and Kempter, C.P. (1969). Elastic properties and thermal expansion of niobium mono-carbide to high temperatures. *Journal of the Less-Common Metals* 19: 273–278.
63 Brown, H.L., Armstrong, P.E., and Kempter, C.P. (1966). Elastic properties of some polycrystalline transition-metal monocarbides. *The Journal of Chemical Physics* 45: 547–549.
64 Gogotsi, Y. and Andrievski, R.A. (1999). *Materials Science of Carbides, Nitrides and Borides*. Dordrecht, NL: Kluwer.
65 Xu, B., Zhu, J., Xiao, F. et al. (2022). Electrically tunable MXene nanomechanical resonators vibrating at very high frequencies. *ACS Nano* 16: 20229–20237.
66 Pinto, R.M.R., Brito, P., Chu, V., and Conde, J.P. (2019). Thin-film silicon MEMS for dynamic mass sensing in vacuum and air: phase noise, Allan deviation, mass

sensitivity and limits of detection. *Journal of Microelectromechanical Systems* 28: 390–400.

67 Kumar, M. and Bhaskaran, H. (2015). Ultrasensitive room-temperature piezoresistive transduction in graphene-based nanoelectromechanical systems. *Nano Letters* 15: 2562–2567.

68 Wang, Z., Jia, H., Zheng, X. et al. (2015). Black phosphorus nanoelectromechanical resonators vibrating at very high frequencies. *Nanoscale* 7: 877–884.

69 Wang, Z., Lee, J., and Feng, P.X.L. (2014). Spatial mapping of multimode Brownian motions in high-frequency silicon carbide microdisk resonators. *Nature Communications* 5: 5158.

70 Jiang, C., Li, Q., Huang, J. et al. (2020). Single-layer MoS_2 mechanical resonant piezo-sensors with high mass sensitivity. *ACS Applied Materials & Interfaces* 12: 41991–41998.

71 Tan, D., Cao, X., Huang, J. et al. (2022). Monolayer MXene nanoelectromechanical piezo-resonators with 0.2 zeptogram mass resolution. *Advanced Science* 9: 2201443.

72 Lipatov, A., Goad, A., Loes, M.J. et al. (2021). High electrical conductivity and breakdown current density of individual monolayer $Ti_3C_2T_x$ MXene flakes. *Matter* 4: 1413–1427.

73 Vorobeva, N.S., Bagheri, S., Torres, A., and Sinitskii, A. (2022). Negative photoresponse in $Ti_3C_2T_x$ MXene monolayers. *Nanophotonics* 11: 3953–3960.

74 Chertopalov, S. and Mochalin, V.N. (2018). Environment-sensitive photoresponse of spontaneously partially oxidized Ti_3C_2 MXene thin films. *ACS Nano* 12: 6109–6116.

75 Bagheri, S., Chilcott, R., Luo, S., and Sinitskii, A. (2022). Bifunctional amine- and thiol-modified $Ti_3C_2T_x$ MXene for trace detection of heavy metals. *Langmuir* 38: 12924–12934.

76 Lin, Z., Liu, J., Peng, W. et al. (2020). Inverse highly stable 3D $Ti_3C_2T_x$ MXene-based foam architectures toward high-performance terahertz radiation shielding. *ACS Nano* 14: 2109–2117.

77 Li, K., Liang, M., Wang, H. et al. (2020). 3D MXene architectures for efficient energy storage and conversion. *Advanced Functional Materials* 30: 2000842.

78 Peng, J., Huang, C., Cao, C. et al. (2020). Inverse nacre-like epoxy-graphene layered nanocomposites with integration of high toughness and self-monitoring. *Matter* 2: 220–232.

79 Zhou, T., Wu, C., Wang, Y. et al. (2020). Super-tough MXene-functionalized graphene sheets. *Nature Communications* 11: 2077.

80 Zhou, T., Ni, H., Wang, Y. et al. (2020). Ultratough graphene–black phosphorus films. *Proceedings of the National Academy of Sciences* 117: 8727–8735.

81 Wan, S., Chen, Y., Fang, S. et al. (2021). High-strength scalable graphene sheets by freezing stretch-induced alignment. *Nature Materials* 20: 624–631.
82 Wan, S., Li, Y., Mu, J. et al. (2018). Sequentially bridged graphene sheets with high strength, toughness, and electrical conductivity. *Proceedings of the National Academy of Sciences* 115: 5359–5364.
83 Wan, S., Fang, S., Jiang, L. et al. (2018). Strong, conductive, foldable graphene sheets by sequential ionic and π bridging. *Advanced Materials* 30: 1802733.
84 Wan, S., Chen, Y., Wang, Y. et al. (2019). Ultrastrong graphene films via long-chain π-bridging. *Matter* 1: 389–401.

Part IV

MXene Applications

19

MXene Capacitive Behaviors and Supercapacitor Devices

Zifeng Lin[1], Liyuan Liu[2], and Patrice Simon[2]

[1] *College of Materials Science and Engineering, Sichuan University, Chengdu, China*
[2] *CIRIMAT UMR CNRS 5085, Université Toulouse III Paul Sabatier, Toulouse, France*

Electrochemical capacitors, also termed as supercapacitors, are energy storage devices that store charge by electrostatic ion adsorption/desorption or fast redox reaction without diffusion limitation.

19.1 Capacitive Behaviors of MXenes Electrodes in Aqueous Electrolytes

Thanks to their unique 2D layered structure, hydrophilic surface, and metallic conductivity, MXenes show great potential as an electrode material in the electrochemical energy storage field. The first study of MXene as a capacitive electrode dated back to 2013, when Lukatskaya *et al*. reported that $Ti_3C_2T_x$ MXene could achieve high-rate and high capacitance exceeding 300 F cm^{-3} (130 F g^{-1}) in alkaline and neutral aqueous electrolytes containing different cations (including Li^+, Na^+, K^+, NH_4^+, Mg^{2+}, and Al^{3+}). In these experiments, the box-shaped cyclic voltammograms (Figure 19.1a, b) without pronounced redox peaks suggest the capacitive nature of charge storage [1]. *In-situ* XRD studies of the intercalation process showed that the diffraction peaks of $Ti_3C_2T_x$ MXene shift reversibly during cycling, as presented in Figure 19.1c, d, with a slight shrinkage in *c* lattice parameters with increasing voltage and expansion with decreasing voltage was observed in 1 M KOH and 1 M $MgSO_4$ electrolytes.

The key features of the redox capacitive charge storage mechanism of $Ti_3C_2T_x$ MXene in neutral electrolytes containing a variety of cations (Li^+, Na^+, K^+, Cs^+,

Transition Metal Carbides and Nitrides (MXenes) Handbook: Synthesis, Processing, Properties and Applications, First Edition. Edited by Chuanfang Zhang and Michael Naguib.
© 2024 John Wiley & Sons, Inc. Published 2024 by John Wiley & Sons, Inc.

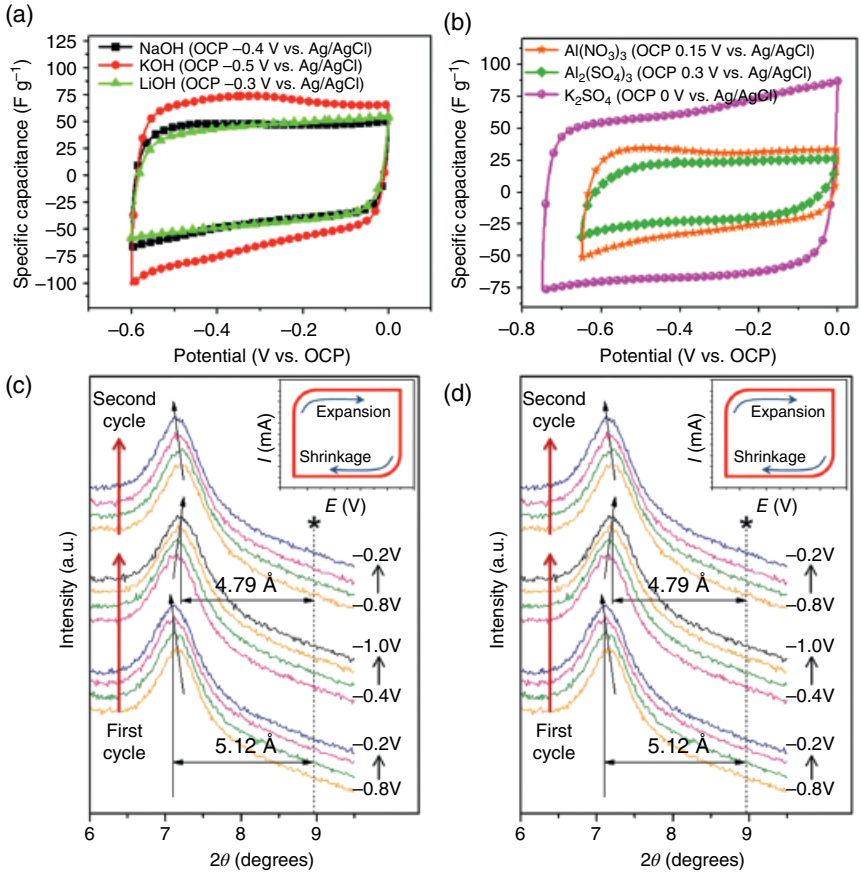


Figure 19.1 (a) CV profiles in NaOH-, KOH-, and LiOH-containing electrolytes at 20 mV s^{-1}. (b) CV profiles in K_2SO_4, $Al_2(SO_4)_3$, and Al $(NO_3)_3$ solutions at 20 mV s^{-1}. (c, d) *In*-situ X-ray diffraction study of exfoliated $Ti_3C_2T_x$ MXene during electrochemical polarization in (c) 1 M KOH and (d) 1 M $MgSO_4$ solutions. Vertical dashed lines indicate the original position of the (0002) peak of the $Ti_3C_2T_x$ electrodes before mounting in a cell. Inclined arrows show the direction of the (0002) peak shift. Insets illustrate cycling direction and concomitant changes in *c* lattice parameters during cycling.
Source: Reproduced with permission from Lukatskaya et al. [1]/American Association for the Advancement of Science.

Mg^{2+}, Ca^{+}, Ba^{+}, and three tetraalkylammonium cations) with both high rate and high capacitance were studied by Levi *et al.* by using electrochemical quartz-crystal admittance and *in-situ* electronic conductance measurements [2]. It was found that the rapid deformation of MXene particles following cationic insertion was similar to 2D ion adsorption at solid liquid interfaces, and the presence of

water molecules between the MXene sheets plays a key role in promoting the cations intercalation. The intercalation of cations (Li^+, Na^+, K^+, Cs^+, and Mg^{2+}) into layered $Ti_3C_2T_x$ MXene was also investigated by Gao *et al.* by using computational simulations, operando calorimetry measurements, and operando liquid Atomic Force Microscope [3]. They showed that cations undergo partial dehydration upon entering the confined spaces between MXene sheets. A modified Helmholtz model is proposed to describe the electrochemical double layer (EDL) capacitance primarily influenced by the distance between cations and the MXene surface. In these studies, the insertion of anionic species is not considered. Based on the observation using *in-situ* gravimetric electrochemical quartz crystal microbalance with dissipation monitoring (EQCM-D) and complementary density functional theory (DFT) calculations, Shpigel *et al.* found that anion insertion was not likely to occur due to the strong negative charge on $Ti_3C_2T_x$ MXene sheets terminated by functional groups [4].

In addition to the numerous studies dealing with MXenes in neutral and alkaline aqueous electrolytes [1, 5–7], more attention has been focused on the investigations on MXene in acidic electrolytes. $Ti_3C_2T_x$ MXene "clay" electrode could achieve high rate and high capacitance of 900 F cm^{-3} (245 F g^{-1}) in 1 M H_2SO_4 electrolyte without significant capacitance degradation over 10000 cycles [8]. However, a narrow potential window of 0.55 V is obtained due to the hydrogen evolution reaction at negative potentials caused by the platinum current collector in use. By replacing the current collector with glassy carbon or titanium foil, the electrochemical potential window could be further extended to 1 V (from −0.2 to −1.2 V vs. Hg/Hg_2SO_4 reference electrode, see Figure 19.2a). Differently from the CVs in neutral electrolytes, a pair of broadening current hump is observed in the CV of $Ti_3C_2T_x$ MXene electrode in 3 M H_2SO_4 electrolyte. Moreover, exceptionally high capacitance of 1500 F cm^{-3} (370 F g^{-1}) was achieved, outperforming the best-reported pseudocapacitive or capacitive electrode materials in aqueous electrolytes [9]. However, such a high capacitance cannot be solely attributed to the electrical double layer capacitance, given the limited specific surface area of a few tens of square meter per gram of $Ti_3C_2T_x$ MXene electrode. Instead, a surface-confined redox reaction of Ti redox centers is involved, leading to a pseudocapacitive contribution. To confirm this hypothesis, *in-situ* X-ray absorption near edge structure spectroscopy (XANES) experiments at the Ti K-edge on pristine-MXene were performed, and change in valency of titanium was observed during charge/discharge of $Ti_3C_2T_x$ MXene electrode, indicating the redox reaction nature and pseudocapacitive charge storage mechanism [10, 13]. As shown in Figure 19.2b, a maximum energy shift of 0.58 eV is observed, corresponding to a change of Ti oxidation state of 0.134 over a 0.9 V potential window, which can be converted into a redox capacitance value of 213 F g^{-1} (65% of total capacitance) [10]. The pseudocapacitive charge storage mechanism can then be described by the following reaction [13, 14]:

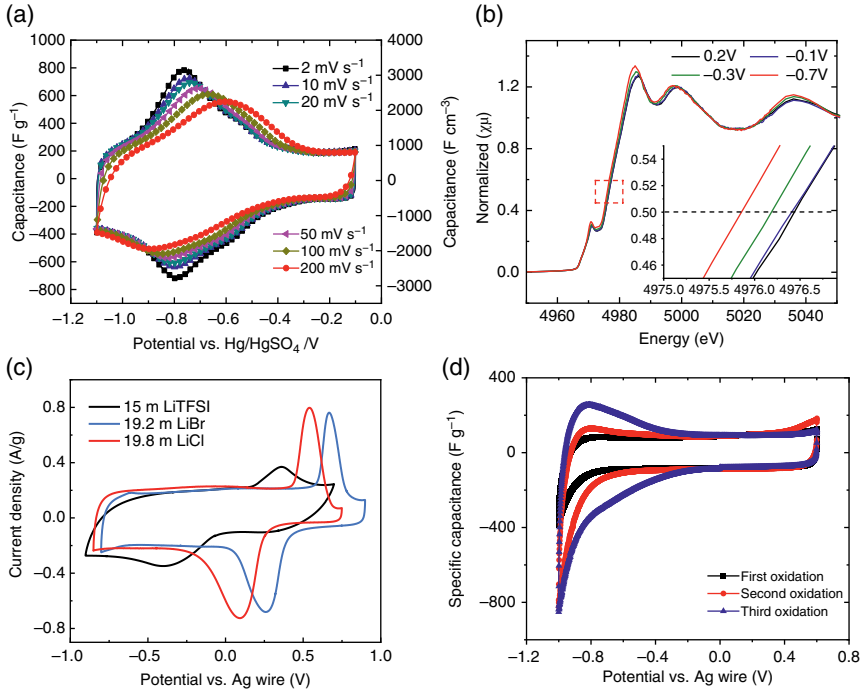


Figure 19.2 (a) Cyclic voltammetry data collected at scan rates from 2 to 200 mV s^{-1} for a $Ti_3C_2T_x$ MXene electrode in a 3 M H_2SO_4 electrolyte. *Source:* Adapted from Lukatskaya et al. [9]. (b) *In-situ* XANES analysis of $Ti_3C_2T_x$ MXene electrode in a 1 M H_2SO_4 electrolyte. Reproduced with permission Shao et al. [10]/American Chemical Society. (c, d) Electrochemical characterization of $Ti_3C_2T_x$ in WIS electrolytes. (c) Cyclic voltammograms for vacuum-filtered $Ti_3C_2T_x$ electrodes collected at 2 mV s^{-1} in 19.8 m LiCl, 19.2 m LiBr, and 15 m LiTFSI. *Source:* Reproduced with permission Wang et al. [11]/American Chemical Society. (d) CVs of $Ti_3C_2T_x$ electrodes *in-situ* oxidized at 1.2 V vs. Ag wire in 19.2 m LiBr. *Source:* Reproduced with permission Wang et al. [12]/American Chemical Society.

$$Ti_3C_2O_x\left(OH\right)_y F_z + \delta H^+ + \delta e^- \leftrightarrow Ti_3C_2O_{x-\delta}\left(OH\right)_{y+\delta} F_z$$

Moreover, the pseudocapacitive nature of the charge storage mechanism was further confirmed by *in situ* XRD investigation during electrochemical polarization. XRD patterns show slight expansion and shrinkage of the *c*-lattice parameter of $Ti_3C_2T_x$ MXene during electrochemical charge/discharge, and DFT calculation reveals the co-insertion of H_2O with proton [14]. The intercalation of the hydrated proton was also further verified by using EQCM measurements, where an average hydration number of 0.72 per proton is measured within the potential range between –0.35 and –0.55 V (vs. Hg/Hg_2SO_4) [10]. Recently, Zheng *et al.* came up

with a novel approach based on *in–situ* EQCM measurements for probing the real-time proton, H_2O population, and hydration evolution dynamic [15]. Populations of proton and H_2O increase with a similar trend during negative polarization and decrease reversibly during positive polarization. Interestingly, the hydration number follows a similar trend, indicating the important role of hydrated H^+ in the potential region of the redox peak, supporting the contribution of hydrated H^+ to the intercalation capacitance. Thus, the charge storage of $Ti_3C_2T_x$ MXene in acidic electrolytes includes redox/intercalation pseudocapacitance and outer surface EDL capacitance. The proton redox and transport in MXene-confined water are studied by Sun *et al.* [16] using first-principles molecular dynamics simulations. Proton transfer follows the same Eigen-Zundel-Eigen mechanism in MXene-confined water as in bulk water, and the proton-based redox process happens reversibly between surface –O sites and water molecules at the interfaces [16]. The numbers of water molecular layers confined in-between MXene sheets have an essential effect on the rate constants of the proton-based surface redox process, and the maximum redox rate constant is achieved with a monolayer of water molecule layer due to higher chances of protons in water to encounter the MXene surfaces when the water molecules layer is thinner. Conversely, the proton mobility is increased with more confined water layers because of less interfacial interaction from the confinement. Although great progress has been made for completing the clear picture of the charge storage mechanism in acidic electrolytes, most of which are based on theoretical predictions, advanced experimental techniques are needed to develop further our basic understanding of the electrochemical behavior of MXene in these electrolytes.

Recently, the study of capacitive behavior of MXenes was extended to highly concentrated aqueous electrolytes or water-in-salt (WIS) electrolytes. Wang *et al.* investigated the electrochemical behavior of $Ti_3C_2T_x$ MXene in WIS electrolytes [11]. Figure 19.2c shows a stable electrochemical potential window of 1.6 V in 19.8 m LiCl WIS electrolyte, which is much larger than the potential windows achieved in conventional aqueous electrolytes. A maximum capacitance of approximately 120 $F g^{-1}$ was achieved – similar to those in neutral and alkaline electrolytes but lower than in acidic electrolytes – with an increased energy density thanks to a larger potential window. Different from the electrochemical signatures in conventional aqueous electrolytes, distinct and separated redox peaks at positive potentials are observed in the CVs of $Ti_3C_2T_x$ MXene in LiTFSI, LiBr, and LiCl WIS electrolytes. More interestingly, this unusual behavior is explained by a surface-controlled partial charge transfer involving fast insertion/desertion of desolvation-free cations. Moreover, Wang *et al.* also demonstrated the surface redox pseudocapacitance of partially oxidized $Ti_3C_2T_x$ MXene in WIS electrolytes [12]. The *in-situ* oxidation of the $Ti_3C_2T_x$ electrode was performed by cycling in 19.2 m LiBr electrolyte within a potential range from −1.1 to +0.5 V vs.

Ag, and after several cycles of oxidation, a pair of significant redox peaks are observed from about –0.4 V to the most negative potential (Figure 19.2d) [12]. Maximum capacitances of 154 F g^{-1} in 19.2 m LiBr and 116 F g^{-1} in 19.8 m LiCl are delivered within a wide potential window of 1.6 V. Outstanding high-rate performance with 40 F g^{-1} at 1000 mV s^{-1} is retained. The evidence of pseudocapacitive behavior is verified by the reversible change of the Ti K-edge energy observed from *in-situ* XANES measurements, which indicates the presence of surface redox reactions during the Li^+ intercalation and deintercalation. These works provide opportunities for developing high-rate and high-energy aqueous energy storage devices and electrochemical actuators using safe and inexpensive aqueous electrolytes.

19.2 MXenes as Capacitive Electrodes in Non-Aqueous Electrolytes

Despite the high specific capacitances obtained in aqueous electrolytes, the narrow potential window (less than 1.6 V even in WIS electrolytes) limits the energy density of MXene materials in the electrolytes. Therefore, investigations of MXenes in non-aqueous electrolytes with larger potential windows have been extensively achieved. Conventional organic electrolytes for supercapacitors consist of acetonitrile (ACN) or propylene carbonate (PC) solvents with conducting salts (e.g. Et_4N-BF_4, Pyr-FSI, EMI-TFSI, and EMI-BF_4) [17]. Generally, the ionic size of organic cations and anions in conventional organic electrolytes are much larger than the metal ions or protons in aqueous electrolytes, which hinders the intercalation of ions into the narrow interlayer space of the restacked MXene sheets. To tackle the issue, Dall'Agnese *et al*. used carbon nanotubes (CNT) as a spacer to limit the restacking of MXene sheets and increase the accessibility of MXene electrodes to large ions [18]. A $Ti_3C_2T_x$/CNT composite electrode was tested in several organic electrolytes (including 1 M EMI-TFSI, 1 M EMI-BF_4, and 1 M TEA-BF_4 in acetonitrile), and a maximum specific capacitance of 85 F g^{-1} (245 F cm^{-3}) within a potential window of 1.8 V is achieved. I*n-situ* XRD study revealed that the energy storage mechanism in EMI^+ cations-containing electrolytes was achieved by reversible cation (de)intercalation.

To further broaden the potential window, Lin *et al*. used neat EMI-TFSI ionic liquid (IL) electrolyte [19]. Instead of using any spacers, IL electrolyte was pre-intercalated in-between the MXene sheets by simply solution exchange during MXene electrode preparation. The prepared $Ti_3C_2T_x$ MXene electrode pre-intercalated with IL was electrochemical stable within a wide voltage window of 3 V in neat EMI-TFSI electrolyte (Figure 19.3a), and a specific capacitance of 70 F g^{-1} was obtained at 20 mV s^{-1}. The rectangular CV shape even at a high scan

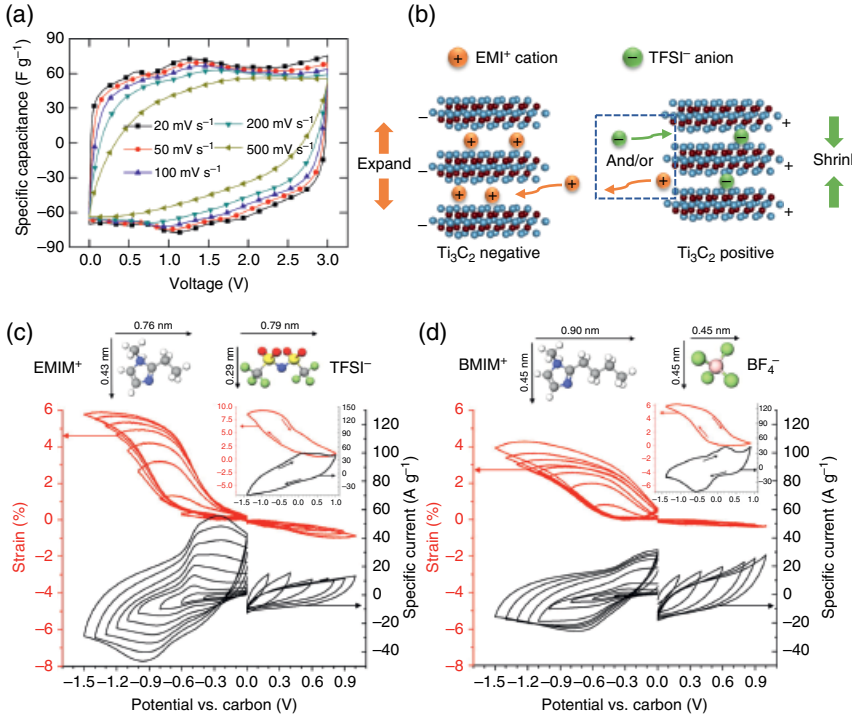


Figure 19.3 MXene EC electrodes in conventional non-aqueous electrolytes. (a, b) $Ti_3C_2T_x$ electrode in neat EMI-TFSI ionic liquid electrolyte, (a) Cyclic voltammetry profile of at 20 mV s^{-1} in the −1.5 to 1.5 V vs. Ag potential range; *Source:* Reproduced with permission Lin et al. [19]/Elsevier. (b) Schematic of the charge storage mechanism – cation insertion at negative polarization and cation deinsertion and/or anion insertion at positive polarization. *Source:* Adapted from Lin et al. [20]. (c, d) Combination of *in-situ* electrical dilatometry and cyclic voltammetry at 1 mV s^{-1} sweep rate. The expansion/contraction is normalized to the equilibrium thickness (after 24 hours) at 0 V vs. carbon. (c) In EMI-TFSI and (d) in BMIM-BF_4. Insets: full-range CV with related displacement with arrows indicating the direction of potential sweeping. *Source:* Adapted from Xu et al. [21].

rate of 500 mV s^{-1} suggests a capacitive charge storage mechanism. Interestingly, the $Ti_3C_2T_x$ MXene electrode exhibits different charge storage behavior when used as positive and negative electrodes. As presented in Figure 19.3b, EMI^+ cation and TFSI− anion exchanges dominate the charge storage process during positive polarization, while reversible (de)intercalation of EMI^+ cations plays a key role during the negative polarization [20]. The molecular dynamic simulation was further used to provide a better understanding of the charge-storage mechanism [21]. EMI^+ population increase/decrease reversibly and TFSI− population remains

constant inside the slit pore in-between MXene sheets during negatively charge–discharge cycles, while EMI^+ population decrease/increase and $TFSI^-$ population increase/decrease reversibly during positive charge and discharge, matching well with the *in-situ* XRD results. Moreover, the volumetric changes of $Ti_3C_2T_x$ MXene electrode in ionic liquids were tracked by complementing electrochemical dilatometry measurements during electrochemical voltage cycling. The strain evolution of $Ti_3C_2T_x$ MXene electrode during cycling in EMI-TFSI and BMI-BF_4 are shown in Figure 19.3c, d. Large strain increases during the negative polarization and slight strain decreases during positive polarization are observed, indicating the large volume expansion during negative sweeping and small volume contraction during positive sweeping, which is in good agreement with *in situ* XRD results. This result is attributed to cation intercalation at negative potentials, but differently from previous results [20, 21], it assumed the sole cations deintercalation at positive potentials.

Although the significant extension of the potential window up to 3 V has been achieved with MXenes in conventional supercapacitor organic electrolytes and ionic liquid electrolytes, low specific capacitances below 100 $F\,g^{-1}$ are far from being satisfactory. In recent years, typical lithium- or sodium-ion batteries organic electrolytes have been investigated for capacitive storage as well. Some metal oxides such as α-MoO_3 and T-Nb_2O_5 were reported with ultrafast lithium-ion (de)intercalation without diffusion limitations in Li-ion batteries electrolytes, resulting in the intercalation pseudocapacitive mechanism [22, 23]. MXenes have been proved to act as excellent ions storage hosts in aqueous, conventional organic, and IL electrolytes, and have been also well investigated as lithium- or sodium-ion batteries electrodes [24, 25]. In 2012, right after the discovery of MXene materials, Come *et al.* reported Ti_2CT_x MXene as a negative electrode for Li^+ storage in 1M $LiPF_6$ in ethylene carbonate (EC) and dimethyl carbonate (DMC) 1:1 electrolyte (LP30) [26]. As presented in Figure 19.4a, the CV profile exhibits a pair of broadening redox peaks similar to the CV shape of $Ti_3C_2T_x$ MXene in acidic aqueous electrolytes, and the kinetic investigation by cavity microelectrode confirmed the high-rate properties of Ti_2CT_x MXene with non-diffusion limited redox processes below scan rates of 5 $mV\,s^{-1}$. A capacity of 160 $mAh\,g^{-1}$ could be obtained within a potential window from 0.5 to 2.7 V vs. Li^+/Li. Combined with activated carbon (YP17) positive electrode, an asymmetric cell exhibited a maximum energy density of 30 $Wh\,kg^{-1}$ at 930 $W\,kg^{-1}$, making Ti_2CT_x suitable as a negative electrode for high-energy density capacitive storage. In addition, Ti_2CT_x MXene was also used as a pseudocapacitive Na ion storage negative electrode in a 1 M $NaPF_6$/ethylene carbonate (EC)–diethyl carbonate (DEC) electrolyte [30]. Combined with an alluaudite $Na_2Fe_2(SO_4)_3$ positive electrode, a Na-ion full cell operates at a relatively high voltage of 2.4 V and delivers 90 and 40 $mAh\,g^{-1}$ at 1.0 and 5.0 $A\,g^{-1}$ (based on the weight of the

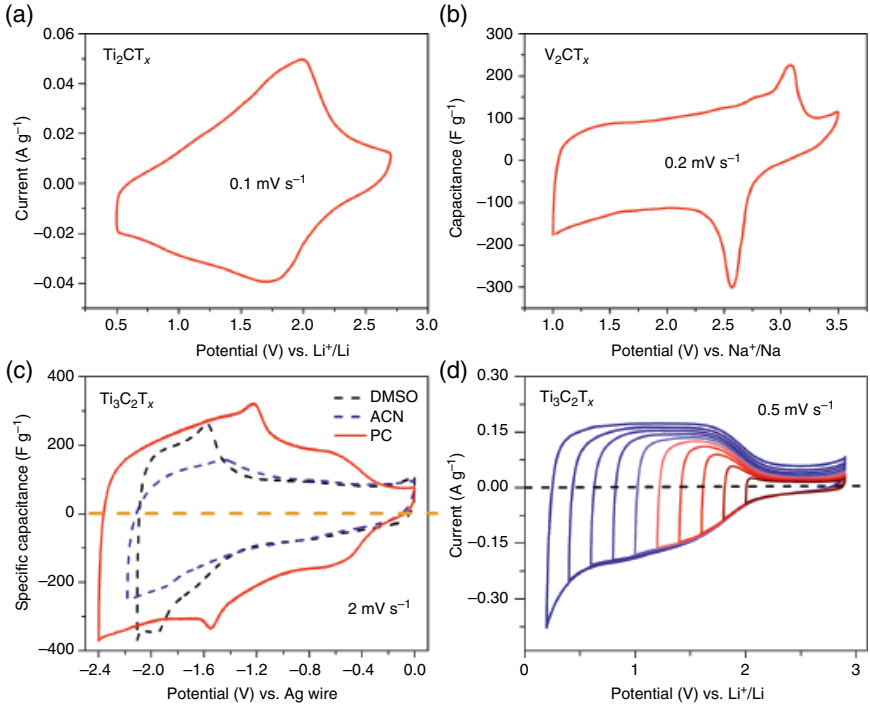


Figure 19.4 MXene electrodes in lithium or sodium-containing organic electrolytes. Cyclic voltammetry profiles of (a) Ti_2CT_x in LP30. *Source:* Adapted from Come et al. [26]. (b) V_2CT_x in 1 M $NaPF_6$ in EC/DMC (1 : 1). *Source:* Adapted from Dall'Agnese et al. [27]. (c) $Ti_3C_2T_x$ in 1M Li-TFSI in DMSO, ACN, PC solvents, the original potential vs. Ag wire is converted into potential vs. Li^+/Li. *Source:* Reproduced with permission Wang et al. [28]/ Springer Nature. (d) $Ti_3C_2T_x$ in LP30. *Source:* Reproduced with permission Li et al. [29]/ Springer Nature.

negative electrode). Moreover, V_2CT_x MXene was investigated as a positive electrode for Na-ion capacitors [27]. As shown in Figure 19.4b, from 1 to 2.2 V vs. Na^+/Na, the rectangular CV shape describes a capacitive storage, and a set of redox peaks at 3 and 2.5 V vs. Na^+/Na were identified. A modest capacitance of 100 F g^{-1} (170 cm^{-3}) was obtained at a slow scanning rate, but 50 F g^{-1} was still delivered at 50 mV s^{-1}, evidencing high-rate performance. The study of Na^+ intercalation mechanism by NMR and DFT calculation show that the interlayer distance of $Ti_3C_2T_x$ MXene was expanded during the first sodiation, but maintained during further cycling due to the pillaring effect of trapped Na^+ and the swelling effect of penetrated solvent molecules [31]. The stable structure and increased interlayer distance act in concert to enable the high-rate intercalation behavior and good cycling stability.

In addition, Wang *et al.* investigated the different electrochemical behavior of a macroporous $Ti_3C_2T_x$ MXene electrode in organic electrolytes with Li-TFSI (1M) as ionic conducting salt and various solvents (Dimethyl sulfoxide (DMSO), Acetonitrile (ACN), Propylene carbonate (PC)). As shown in Figure 19.4c, the best electrochemical properties are obtained in the PC-based electrolyte with a capacity of 130 mAh g^{-1} at 2 mV s^{-1} within 2.4 V potential window, where the CV profiles without distinct redox peaks evidence a pseudocapacitive charge storage behavior. *In-situ* XRD and MD simulation studies suggested that Li^+ in PC solvent was mainly desolvated upon entering the interlayer space in-between MXene sheets, resulting in high Li^+ storage capacity and fast kinetic. On the contrary, the strong interactions between DMSO, ACN solvents, and Li^+ hinder the desolvation process, and the co-intercalation of solvent molecules into the MXene interlayer distance limits the Li^+ storage properties in these electrolytes. This study highlights the important influence of solvents on the Li^+ storage properties of MXene electrodes in organic electrolytes.

More recently, MXenes with –Cl and –O surface terminations were successfully prepared by etching of MAX phase in Lewis acidic salts molten salt electrolytes [29, 32, 33]. Unique electrochemical signature is achieved with these molten salt derived MXenes (MS-MXene) electrodes in an LP30 electrolyte. As presented in Figure 19.4d, mirror-like CV profiles with an almost constant current during reduction and oxidation processes were obtained with an MS-$Ti_3C_2T_x$ electrode, which is characteristic of a high charge/discharge rate pseudocapacitive process. A high capacity of 205 mAh g^{-1} at 0.5 mV s^{-1} is delivered within 0.2–2.8 V vs. Li^+/Li, a potential range, and most of the capacity is achieved below 2 V vs. Li^+/Li [29]. Additionally, the preparation of MS-Ti_2CT_x MXene with an even higher capacity of up to 280 mAh g^{-1} was reported, with similar electrochemical signatures to the MS-$Ti_3C_2T_x$ MXene electrode [32]. However, further delamination of as-prepared multilayer MS-MXenes remains a major challenge. In 2021, *Liu et al.* reported about the successful exfoliation of MS-MXene by using a simple and safe method combining chemical (immersion in tetrabutyl ammonium solution) and mechanical (sonication) treatments, as a result of the successful preparation of a self-supported thin film of MS-MXene [34]. Besides, a high specific capacity of 225 mAh g^{-1} at 1 C and excellent rate capability (95 mAh g^{-1} at 167 C) could be achieved when used as a negative electrode in Li-ion containing electrolyte, indicating improved electrochemical performance versus multilayered (pristine) MS-$Ti_3C_2T_x$. In the same year, by playing with the ratio between NaCl and $ZnCl_2$ molten salt mixture, Zhang *et al.* prepared in-plane porous $Ti_3C_2Cl_2$, which delivers a high capacity of 382 mAh g^{-1} at 0.1 A g^{-1} when used as anode material in Li-ion battery due to an increased surface area and mesoporosity [35]. These remarkable performances positions MS-MXene materials as compelling candidates for high-rate negative electrodes in Li-ion-based high-power devices.

19.3 Achieving High Electrochemical Properties by MXene Electrode Construction

Similar to other two-dimensional materials, the restacking of MXene sheets lowers the surface accessibility to the electrolyte ions which results in limitations in ion diffusion, power performance, and specific capacitance. Therefore, efforts are dedicated to preparing optimized MXene electrode architectures to shorten ion diffusion length and increase the surface accessibility. Many strategies have been applied such as fabricating MXene electrodes with 3D porous macrostructures by methods including induced gelation, freeze-casting, alternative template-assisted techniques, additive manufacturing, and laser writing technique [36].

Top in Figure 19.5a is a conventional $Ti_3C_2T_x$ MXene electrode prepared through vacuum filtration. In this configuration, the well-aligned and restacked 2D MXene sheets contribute to a longer diffusion distance [9]. Differently, the bottom panel shows a macroporous templated $Ti_3C_2T_x$ MXene electrode prepared via a template-assisted method, where the diffusion distance has been shortened greatly. Therefore, excellent high-rate performance is obtained with the macroporous templated $Ti_3C_2T_x$ MXene electrode: 56% capacitance retention is obtained at an ultra-high rate of $10\,V\,s^{-1}$ (Figure 19.5b), exceeding the rate performance of $Ti_3C_2T_x$ MXene hydrogel electrodes (Figure 19.5c). Besides, the vertically aligned $Ti_3C_2T_x$ MXene electrode has been prepared, which allows for faster ion transport into the electrode as compared to conventional horizontally stacked MXene ones (Figure 19.5d) [37]. A vertically aligned $Ti_3C_2T_x$ MXene electrode (Figure 19.5e) with a thickness of up to 200 μm can retain the CV shape without distinct distortion or specific capacitance decrease. However, the electrode weight loading in these architectures has to be kept high enough to reach decent areal capacitance ($F\,cm^2$).

Tang *et al*. used an ultrafast laser writing technique for opening up the stacked layers and creating pores in MXene materials through instantaneous photothermal gasification of interlayer water and partial surface groups [40]. A high capacitance of $322\,F\,g^{-1}$ at $10\,mV\,s^{-1}$ and 48% retention as the scan rate increased by 200-fold are obtained. Initiated by metal ions, a 3D MXene network (Figure 19.5f) has been formed due to the fast gelation between the metal ions and –OH group of MXenes, which avoids MXene nanosheets restacking and greatly improves their surface utilization, thus delivering a high-rate performance of $226\,F\,g^{-1}$ at $1\,V\,s^{-1}$ [38]. Moreover, a hierarchical ion path "highway" in $Ti_3C_2T_x$ film as shown in Figure 19.5g is fabricated with porous structure by a controllable H_2SO_4 oxidation method for tackling the restacking issue, as a result, ultra-high-rate capability (Figure 19.5h) of $208\,F\,g^{-1}$ ($756\,F\,cm^{-3}$) at $10\,V\,s^{-1}$ was achieved [39]. As mentioned above, the key issue of this architecture is the limited electrode weight loading that can be achieved, resulting in low areal electrode capacity.

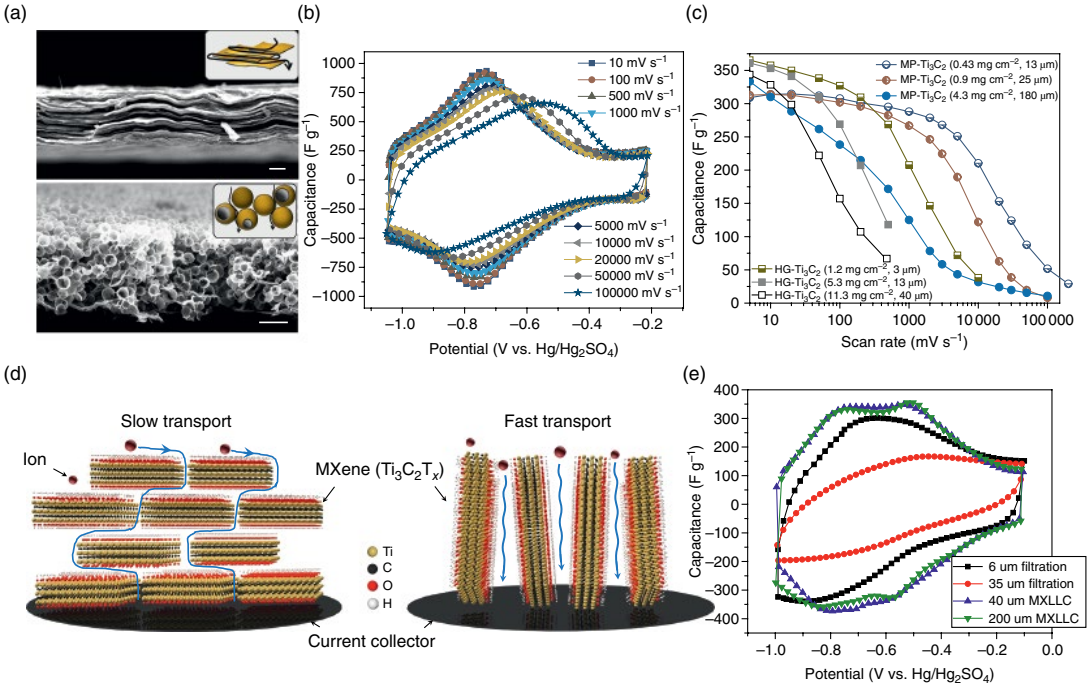


Figure 19.5 (a) SEM image of (top panel) $Ti_3C_2T_x$ MXene hydrogel cross-section and (down panel) macroporous templated $Ti_3C_2T_x$ electrode cross-section. Scale bars: 5 μm. Insets show a schematic representation of the ionic current pathway in electrodes of different architectures. (b) Cyclic voltammetry data collected at scan rates from 10 to 100 000 mV s^{-1} for a 90-nm-thick $Ti_3C_2T_x$ MXene; (c) Comparison of specific capacitances of $Ti_3C_2T_x$ MXene hydrogel and macroporous templated electrodes. (d) Schematic illustration of ion transport in horizontally stacked and vertically aligned $Ti_3C_2T_x$ MXene electrodes; (e) Cyclic voltammograms of the indicated samples at a scan rate of 100 mV s^{-1}.

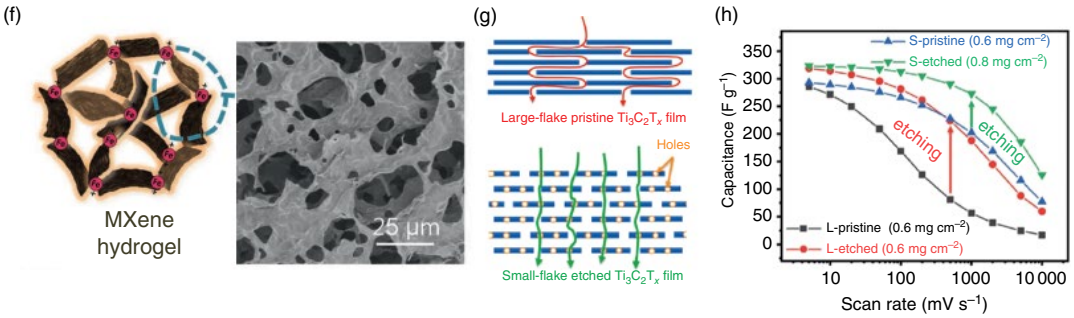


Figure 19.5 (Continued) *Source:* Reproduced with permission Xia et al. [37]/Springer Nature. (f) Schematic of e metal ion-initiated interaction of MXene and SEM image of MXene monolith. *Source:* Reproduced with permission Deng et al. [38]/John Wiley & Sons. (g) The schematic illustration of the ion pathway optimization. (h) Capacitance versus scan rate of $Ti_3C_2T_x$ films before and after etching. *Source:* Reproduced with permission Tang et al. [39]/John Wiley & Sons.

19.4 Tuning of MXene Surface Chemistry

MXenes are typically terminated with various surface groups, which are highly dependent on the synthetic route and post-synthesis treatment. For instance, –O, –OH, –F groups are typically observed with MXenes etched by HF or HF-containing aqueous solution [41]. Experimental and theoretical studies have confirmed the key role of MXene surface terminations on their electrochemical performance [10, 33, 42, 43]. Thus, many strategies have been proposed for tuning the MXene surface chemistry for boosting the capacitive performance of MXenes-based electrodes. Dall'Agnese *et al.* [44] replace –F with –O surface groups by using a chemical treatment in alkaline electrolytes. A fourfold increase in the capacitance could be achieved in the sulfuric acid electrolyte, which is explained by the reversible bond/de-bond with hydroniums ions with –O instead of –F [8]. Yang *et al.* proposed a fluoride-free MXene synthesis method based on the anodic corrosion of titanium aluminum carbide (Ti_3AlC_2) in a binary aqueous electrolyte [45]. Prepared F-free MXenes with –O and –OH surface termination groups exhibit superior capacitive performance to those of LiF/HCl-etched MXenes in aqueous electrolytes. Chen et al. turned the –F and –OH terminal groups to –O groups on the $Ti_3C_2T_x$ MXene by using *n*-butyllithium treatment; MXenes with few –F and more –O surface termination groups showed improved capacitive performance. A record capacitance of $523\,F\,g^{-1}$ at $2\,mV\,s^{-1}$ was obtained for an *n*-butyllithium-treated $Ti_3C_2T_x$ MXene [46]. Those results confirmed that –O contributes to the capacitance of MXene in acidic electrolytes through a pseudocapacitive mechanism.

In addition to the chemical treatments, thermal treatments are also effective routes for tuning the surface chemistry of MXenes. Persson *et al.* reported that O atoms could occupy the sites of F atoms at high temperatures [47]. The effect of the annealing under Ar, N_2, N_2/H_2, and air ambient on the electrochemical properties of the $Ti_3C_2T_x$ MXene was investigated in detail [48]. As shown in Figure 19.6a, b a significant capacitive improvement of $Ti_3C_2T_x$ MXene electrode in 30 wt % KOH aqueous electrolyte is observed upon heat treatment in Ar, N_2, and N_2/H_2 ambientes. This improvement in the electrochemical performance of annealed samples is attributed to the removal of –F content on the surface of the samples by annealing. Besides, Shao *et al.* achieved heat treatment of $Ti_3C_2T_x$ MXene prepared from LiF/HCl-etching, for tuning the surface chemistry [10]. The electrochemical performance was only slightly improved after heat treatment at 500 °C; however, further increase of the treatment temperature to 600 °C results in an obvious decrease in capacitances (Figure 19.6c, d). Heat treatment at 500 °C removed the –F surface groups, but –OH and –O groups were still present. These groups could promote H_2O intercalation in the MXene interlayer, further promoting fast proton transport. Further increase the heating temperature to 600 °C leads

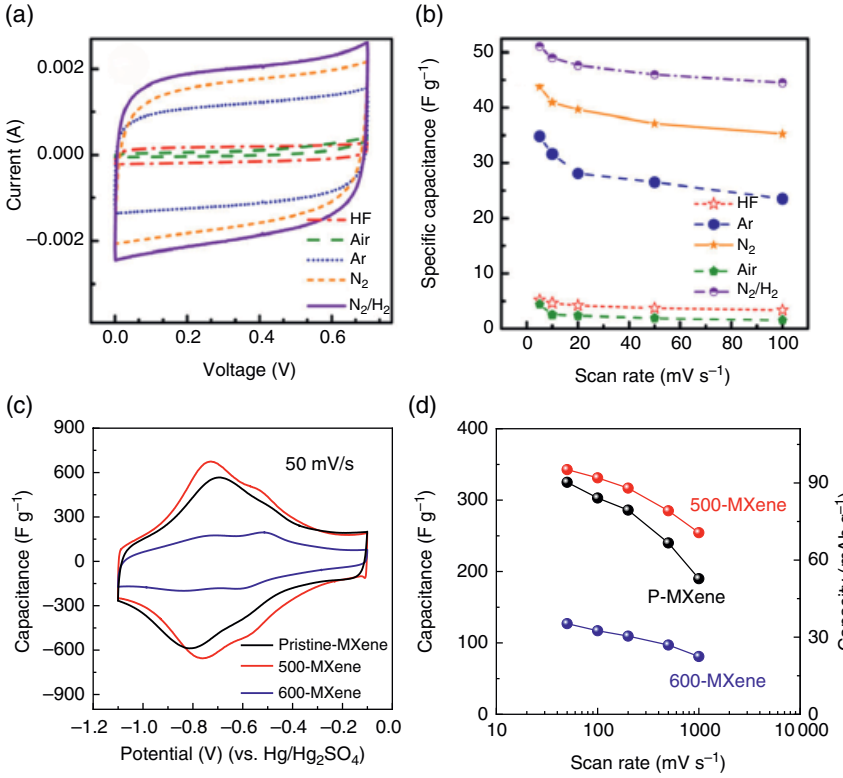


Figure 19.6 (a) Comparison of cyclic voltammograms of MXene samples at a scan rate of 20 mV s^{-1} in sulfuric acid electrolyte. (b) Specific capacitances of MXene samples at different scan rates. *Source:* Reproduced with permission Yoon et al. [49]/American Chemical Society. (c) CV profiles of pristine MXene, samples heat treated at 500 and 600 °C. (d) Specific capacitance and capacity versus scan rates. *Source:* Reproduced with permission [10]/American Chemical Society.

to the removal of most of the –OH and –O groups, resulting in poor electrochemical performance due to the difficulty for H_2O intercalation and proton transportation. Similarly, Li *et al.* removed the surface groups of $Ti_3C_2T_x$ MXene by annealing at 673 °C under Ar atmosphere, with a significant gravimetric capacitance increase (517 F g^{-1} at a discharge rate of 1 A g^{-1}) [42]. Those results show the key importance of the MXene surface termination group on the MXene surface on their electrochemical performance.

Furthermore, heteroatom-doping and defects engineering are also important strategies for surface chemistry modifications. Nitrogen-doped Ti_2CT_x MXene electrodes prepared by MXene with polymeric carbon nitride were able to deliver a higher capacitance of 327 F g^{-1} at 1 A g^{-1} than an origin 230 F g^{-1} of untreated

samples in 6M KOH electrolyte [49]. Nitrogen-doped $Ti_3C_2T_x$ MXene prepared in a similar way exhibited higher capacitances of 192 F g^{-1} in 1 M H_2SO_4 and 82 F g^{-1} in 1 M $MgSO_4$ than the capacitances of undoped $Ti_3C_2T_x$ MXene (34 F g^{-1} in 1 M H_2SO_4 and 52 F g^{-1} in 1 M $MgSO_4$) [50]. Tao *et al.* reported a $Mo_{1.33}C$ MXene with di-vacancy ordering exhibits a volumetric capacitance of 1100 F cm^{-3} that is 65% higher than its counterpart, Mo_2C, with no vacancies. The increase in capacitance was explained by the increase in the electrochemically active sites and/or the fraction of the electrode accessible to the electrolyte [51].

Over the last decade, aqueous solutions containing fluoride ions remained the main etchant to prepare MXenes, which makes it difficult to get F-free MXene. Recently, *Li et al.* reported on the synthesis of Ti_3ZnC_2 MAX phase by reaction of Ti_3AlC_2 in $ZnCl_2$ Lewis acidic molten salt at 550 °C, via a replacement reaction mechanism [52]. Interestingly, Ti_3ZnC_2 could be further transformed into $Ti_3C_2Cl_2$ MXene, as a result of surface F-free, Cl-terminated MXenes. Later on, as mentioned before and shown in Figure 19.7a, b, the synthesis of MS-MXenes was extended to a wide range of elements for the A-site of the MAX precursors (Zn, Al, Si, Ga) and Lewis acid melt composition, leading to the successful preparation of Br and I-terminated MXenes [29]. Following this work, it was proposed to prepare MXene with O, NH, S, Cl, Se, Br, and Te surface terminations [55], as well as bare MXenes (no surface termination) through post-synthesis reactions with the Cl or Br-terminated MXenes, which show distinctive structural and electronic properties. However, the molten salt method requires high temperature, limiting many utilizations. In 2021, Jawaid *et al.* proposed an alternative room-temperature etching method (Figure 19.7c) that utilizes halogens (Br_2, I_2, ICl, IBr) in anhydrous media to synthesize MXenes [53]. In the same year, an iodine (I_2) assisted etching route (Figure 19.7d) was published by *Shi et al.* for the preparation of $Ti_3C_2T_x$ (T = –O, –OH) with oxygen-rich terminal groups [54]. The above progress in the synthesis methods offers great opportunities for controlled surface chemistry to design new MXene materials with improved (electrochemical) properties.

19.5 MXene-based Supercapacitor Devices

19.5.1 MXene-based Asymmetric Supercapacitors

The excellent electrochemical performance of MXenes as capacitive electrodes in terms of capacitance and power clearly places MXene as a key material for assembling supercapacitor devices. However, the limited stability of MXenes with oxidation in aqueous electrolytes limits the operating cell voltage of the device using symmetrical electrodes. As a result, mainly asymmetric devices were assembled by combining a negative MXene electrode together with a different positive

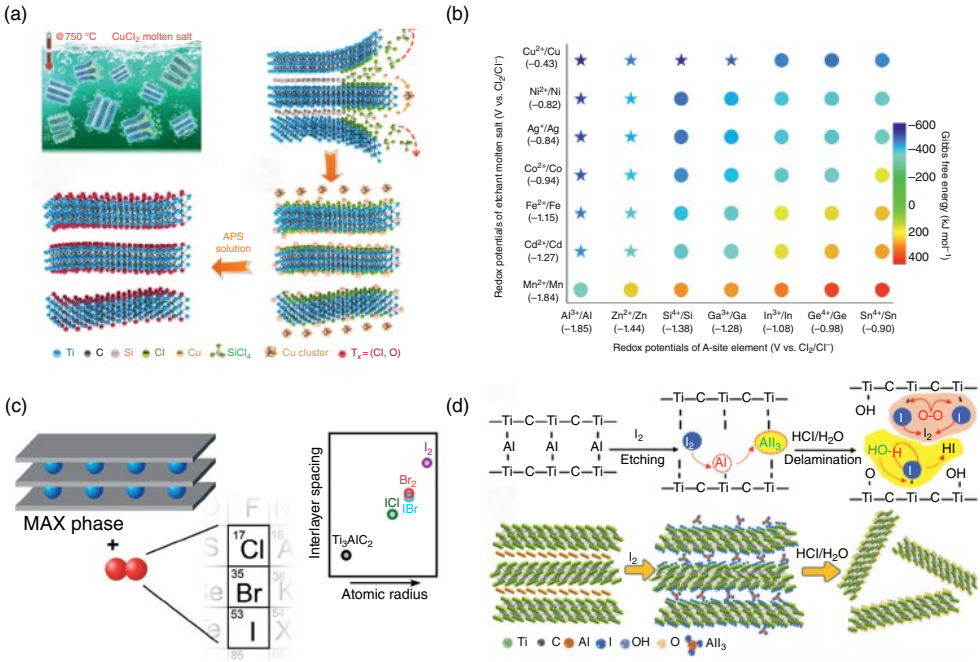


Figure 19.7 Fluorine-free strategies. (a) The schematic diagrams of the molten salt etching method for preparing $Ti_3C_2T_x$ (T = Cl, O). (b) Gibbs free energy mapping (700 °C) guiding the selection of Lewis acid Cl salts according to the electrochemical redox potentials of A-site elements in MAX phases (x-axis) and molten salt cations (y-axis) in Cl melts. *Source:* Li et al. [29]/Reproduced from Springer Nature. (c) The schematic representation of halogen etching of MAX phases. *Source:* Adapted with permission Jawaid et al. [53]. (d) The iodine-assisted etching and delamination of Ti_3AlC_2 toward 2D MXene sheets. *Source:* Reproduced with permission Shi et al. [54]/American Chemical Society.

electrode [9]. For example, a $Ti_3C_2T_x$ MXene electrode with an onset oxidation potential of about −0.1 V vs. Hg/Hg_2SO_4 in H_2SO_4 electrolyte can be combined with a RuO_2 electrode to form an asymmetric supercapacitor (see Figure 19.8a, b) [56]. In this configuration, a wide operation voltage window of 1.5 V together with an energy density of 37 μWh cm^{-2} at a power density of 40 mW cm^{-2} could be achieved. To get rid of expensive RuO_2, Wei *et al.* [58] fabricated a $Ti_3C_2T_x/MnO_2$ asymmetric supercapacitor with 1 M Na_2SO_4 aqueous solution as the electrolyte, which exhibits a wide voltage window of 1.5 V and an energy density of 6.4 Wh kg^{-1} at a power density of 1107.7 W kg^{-1}.

Moreover, Boota and Gogotsi [57] reported an all pseudocapacitive organic-inorganic asymmetric device with the MXene as negative electrode and conducting polymers as positive electrodes (Figure 19.8c). Conducting polymers, including polyaniline (PANI), polypyrrole (PPy), and poly(3,4-ethylenedioxythiophene) (PEDOT), were deposited on reduced graphene oxide (rGO) and further used as positive electrodes. As shown in Figure 19.8d–f, a maximum operating voltage window of 1.45 V was achieved in 3 M H_2SO_4 electrolyte (Figure 19.8g–i). A high energy density of ≈17 Wh kg^{-1} with outstanding capacitance retention of 88% after 20000 cycles was also obtained, which is among the best performance reported for MXene-based asymmetric devices. Besides, Boota *et al.* [59] also reported phenothiazing-MXene asymmetric pseudocapacitors with better cycling stability (over 80% after 30 000 cycles) within the operating voltage window of 1.4V in 3 M H_2SO_4. Even more, an asymmetric pseudocapacitor combining a $Ti_3C_2T_x$ MXene negative electrode with a V-doped MnO_2 positive electrode could reach up to 2.1 V in a neutral 1 M Li_2SO_4 electrolyte [60]. Apart from metal oxides [56, 58, 60–62] and conducting polymers [57, 59], many electrode materials, such as rGO [63], carbon nanofiber film [64], carbon nanotube $MoSe_2$ nanohybrid [65], $NiCo_2S_4$ [66, 67], have been investigated as positive electrodes [68], and extended voltage windows with high electrochemical performance have been achieved. Asymmetric devices assembled with MXene electrodes clearly achieved high power performance thanks to the non-diffusion limited, high redox reaction rate of MXenes in aqueous electrolytes. Future work will be focused on the use of MXene electrodes in non-aqueous electrolyte where higher cell voltage – and then energy density – can be obtained. The recent successful preparation of MXene with tuned surface chemistry by the molten salt route and the associated high capacity in Li-ion containing electrolyte is an example that offers promising perspectives in that aim.

19.5.2 MXene-based Micro-Supercapacitors (MSCs)

The increased miniaturization of microelectronic devices and the rapid development of portable/wearable electronics have boosted the demand for micro energy storage devices, that can offer higher power delivery compared to

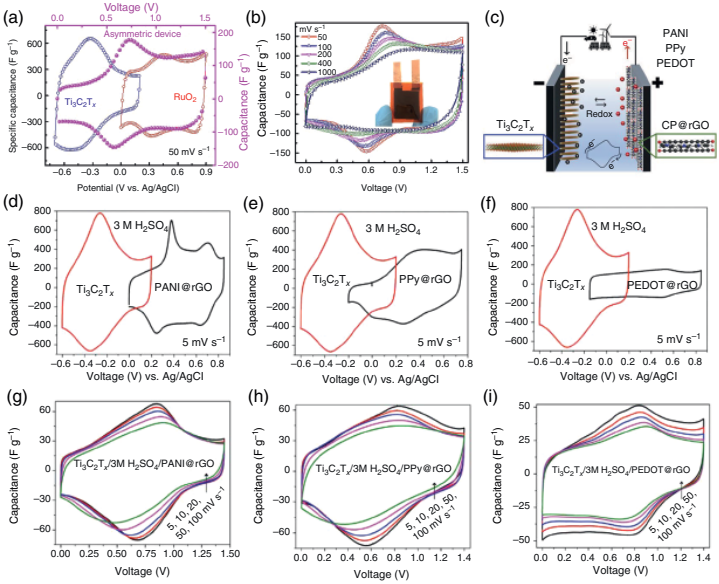


Figure 19.8 Electrochemical performance of RuO_2//$Ti_3C_2T_x$ full-cell device: (a) CVs of RuO_2/carbon fibers, $Ti_3C_2T_x$/carbon fibers, and the asymmetric device at a scan rate of 50 mV s^{-1}; (b) CVs of RuO_2//$Ti_3C_2T_x$ asymmetric sandwich device at different scan rates, inset shows the digital photograph of the asymmetric device. *Source:* Adapted from Jiang et al. [56]. (c) A schematic representation of the organic-inorganic all-pseudocapacitive asymmetric supercapacitor in which CP@rGO and 2D transition metal carbide (MXene) serve as positive and negative electrodes, respectively. CV curves of individual electrodes (d) PANI-, (e) PPy-, (f) PEDOT-containing hybrids and titanium carbide MXene ($Ti_3C_2T_x$). (g–i) CV curves of corresponding devices at scan rates between 5 and 100 mV s^{-1}. All devices were tested in 3 M H_2SO_4 electrolyte. *Source:* Reproduced with permission Boota and Gogotsi [57]/John Wiley & Sons.

batteries [69, 70]. MXene-based MSCs have received increasing attention thanks to flexibility of MXene electrode processing on top of their high capacitance and metallic conductivity properties [68, 71–75]. So far, various patterning techniques have been developed to achieve MSC electrodes on the submillimeter scale, including the direct coating of MXene on the specific substrate with laser scribing, electrochemical polarization, photolithography, or etching (Figure 19.9) [76]. Similarly, different printing techniques such as inkjet printing, extrusion printing or screen printing, were used to transfer the MXene ink onto the patterns [76].

Peng *et al.* [71] proposed a photoresist-free direct laser cutting method to prepare an all-MXene solid-state MSCs. In this process, a layer of large-size $Ti_3C_2T_x$ flakes was firstly spray-coated onto the substrate serving as current collector while another layer of small-size $Ti_3C_2T_x$ flakes was coated on the top as the electroactive layer. The A device could reach a maximal areal capacitance of 27.29 mF cm^{-2} in PVA/H_2SO_4 gel electrolyte and volumetric capacitance of 357 F cm^{-3}. A similar laser machining method (Figure 19.10a) was proposed by *Kurra et al.* to fabricate MXene-on-paper coplanar MSCs with HF-etched $Ti_3C_2T_x$ and clay-like (LiF/HCl etched) $Ti_3C_2T_x$ MXene [74]. As shown in Figure 19.10b, c even with a thick MXene

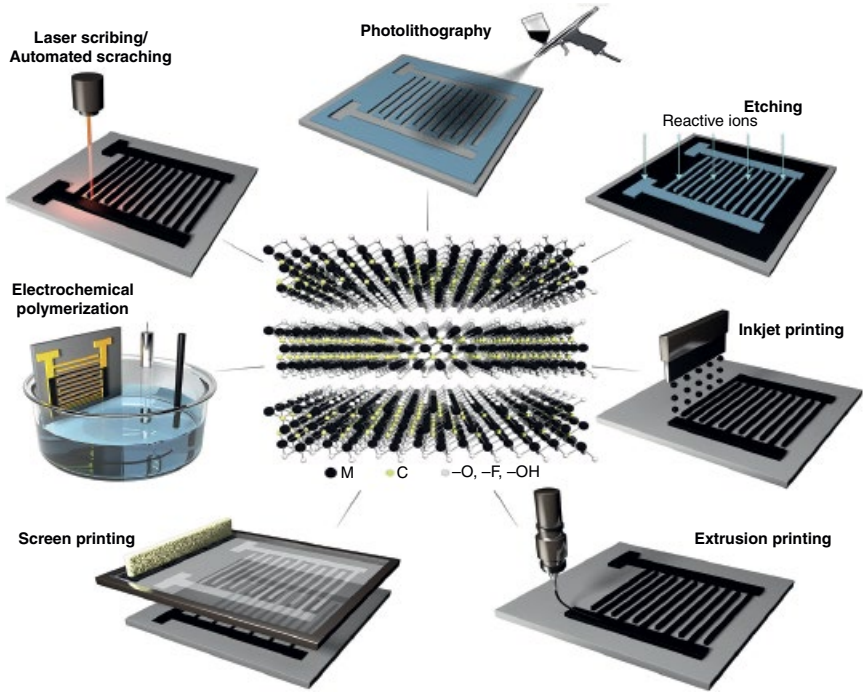


Figure 19.9 Different fabrication methods for interdigital MXene micro-supercapacitors. *Source:* Jiang et al. [76]/Reproduced with permission from Elsevier.

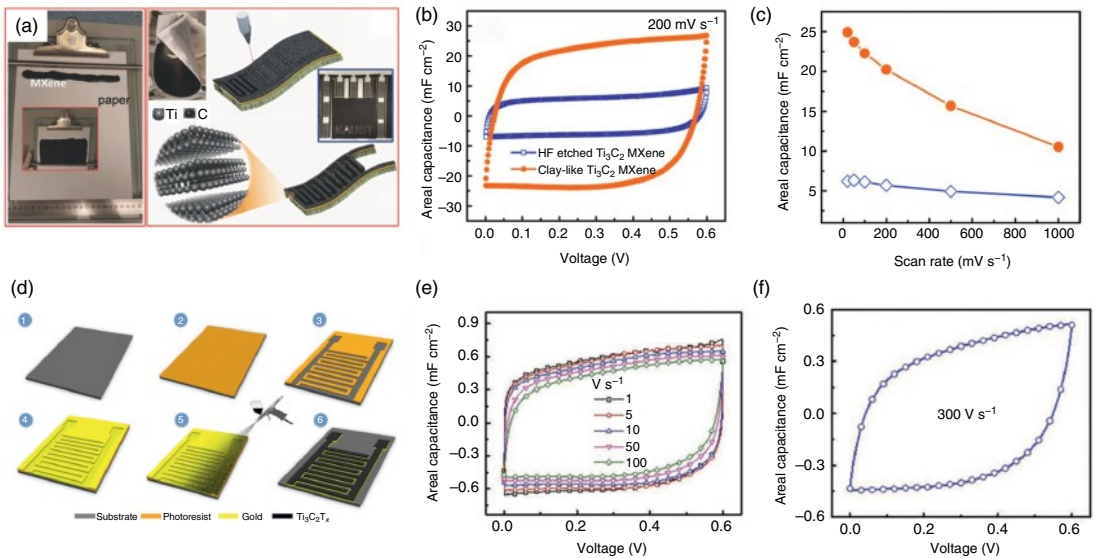


Figure 19.10 (a) The laser machining method for $Ti_3C_2T_x$ MXene micro-supercapacitors fabrication. Electrochemical performance of MXene-on-Paper Coplanar MSCs in 1 M H_2SO_4. (b) Area normalized CV curves at a scan rate of 200 mVs^{-1} and (c) areal capacitance versus scan rate of clay-like MXene. *Source:* Kurra et al. [74]/John Wiley & Sons. (d) Schematic illustration of the fabrication process of MXene MSCs on chip by spray coating. CV of $Ti_3C_2T_x$ —0.3 µm MSCs using PVA/H_3PO_4 gel electrolyte at scan rates (e) from 1 to 100 and (f) 300 Vs^{-1}. *Source:* Jiang et al. [77]/John Wiley & Sons.

film up to 125 μm, the clay-like $Ti_3C_2T_x$ MXene electrodes achieved the areal capacitance of 25 mF cm^{-2} at 20 mV s^{-1}, which is four times higher capacitance than HF-etched $Ti_3C_2T_x$ MXene. In 2019, *Jiang et al.* [77] showed that MXene suspensions could be firmly attached to a gold current collector after an oxygen plasma treatment on the surface of the gold current collector (Figure 19.10d). On-chip MSCs prepared with 100 nm-thick MXene electrodes could achieve high volumetric capacitance of 30 F cm^{-3} at 120 Hz at potential scan rates as high as 300 V s^{-1}, demonstrating an ultra-high rate-capability (Figure 19.10e, f).

Thanks to their negatively charged surface, highly concentrated multilayered MXene suspension (70 wt%) can be prepared without any addition of surfactants or stabilizers, thus forming stable ink for ink-jet printing or extrusion printing. In 2019, *Zhang et al.* [78] developed additive-free aqueous and organic MXene inks for extrusion printing and inkjet printing of the MXene-based MSCs (Figure 19.11a). The prepared all-MXene MSCs show rectangular CV profiles (Figure 19.11b) and ideal-like capacitive galvanostatic charge–discharge signatures (Figure 19.11c) with a H_2SO_4-PVA gel electrolyte even at high scan rates and high charge/discharge specific currents. The energy density of the extrusion-printed MXene MSC reaches 0.32 μW h cm^{-2} at a power density of 11.4 μW cm^{-2}, and 0.11 μW h cm^{-2} can be still maintained at a high-power density of 158 μW cm^{-2}, which is an order of magnitude higher than that of printed graphene MSCs. Besides, a scalable, low-cost stamping strategy has also been proposed for rapid production of flexible MXene-based MSCs [75]. Pre-designed stamp shapes were prepared by three-dimensional (3D)-printing, coated with MXene ink, and then firmly pressed onto different substrates such as paper, polyethylene terephthalate or glass (Figure 19.11d). The interdigitated $Ti_3C_2T_x$ MSCs exhibit high areal capacitance of 61 mF cm^{-2} at 25 μA cm^{-2} and 50 mF cm^{-2} as the current density increases by 32-fold (Figure 19.11e). Moreover, dozens of stamped MSCs can be fabricated in seconds through such a facile, low-cost, but elegant stamping strategy, offering the possibility for large-scale production of these all-MXene MSCs. 3D printing technique has also been applied to the fabrication of all-solid-state MSCs using an additive-free and water-based MXene ink [79]. Thanks to the 3D interdigital electrode architecture, the printed solid-state all MXene MSCs show very high areal capacitance up to 1035 mF cm^{-2}.

Here also, despite excellent electrochemical and mechanical properties, easy electrode formulation, and processing, the main challenge in MXene-based MSCs is to further boost the energy performance.

19.6 Conclusion

MXene materials can achieve excellent electrochemical performance as electrode materials for capacitive energy storage applications. Ultrahigh specific capacitances up to 1500 F cm^{-3} (370 F g^{-1}) in aqueous electrolytes and wide potential

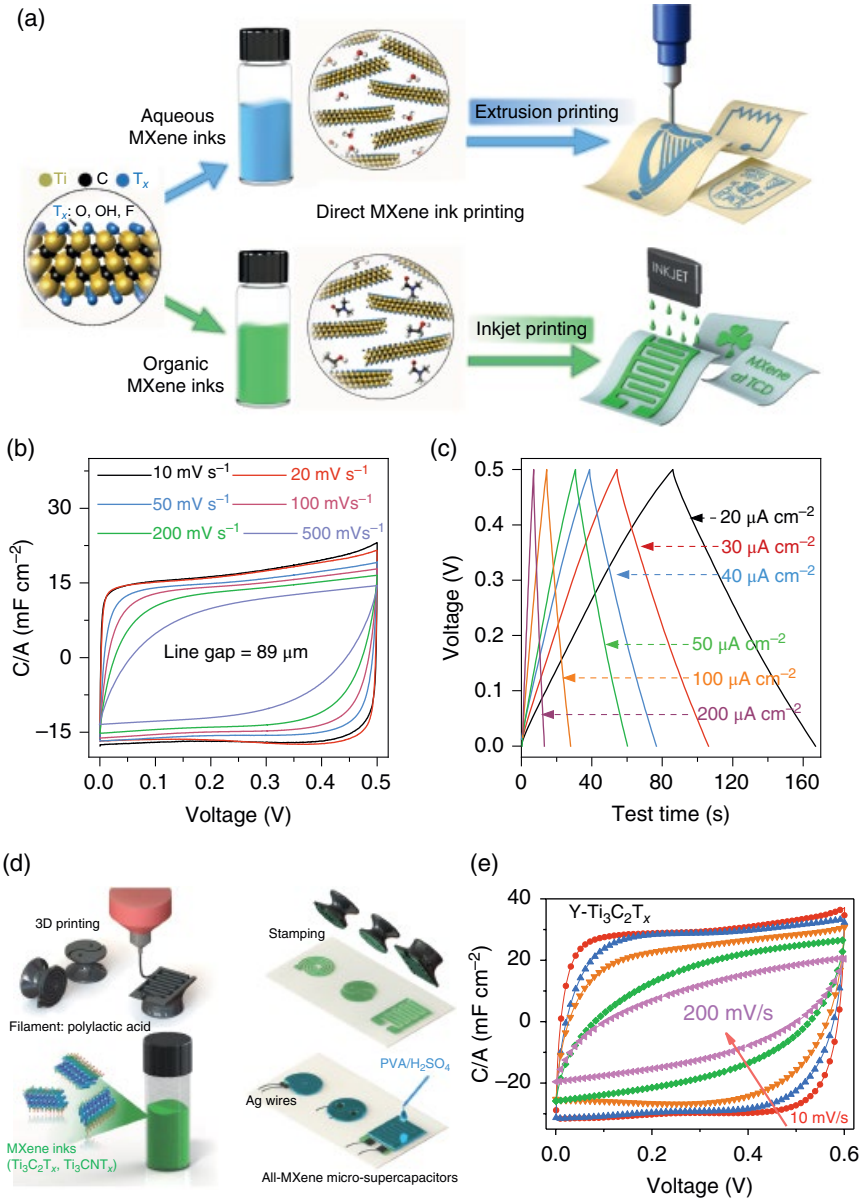


Figure 19.11 (a) Schematic illustration of direct MXene ink printing. The $Ti_3C_2T_x$ organic inks, that is, $Ti_3C_2T_x$-ethanol (molecules shown in the bottom panel) are used for inkjet printing of various patterns, such as MSCs, MXene letters, ohmic resistors, etc. The $Ti_3C_2T_x$ aqueous inks (with water molecules shown in the top panel) are designed for extrusion printing of MSCs and other patterns on flexible substrates. As for the MSCs, a gel electrolyte made of H_2SO_4-PVA, was coated onto the as-printed patterns and dried naturally, forming all-MXene printed, solid-state MSCs. (b, c) Electrochemical response of inkjet- and extrusion-printed MXene MSCs. (b) Normalized cyclic voltammograms (CV) profiles and (c) galvanostatic charge–discharge (GCD) curves of a typical extrusion-printed MSC (line gap ~89 μm, <*N*> = 3). *Source:* Zhang et al. [78]/Springer Nature/CC BY 4.0. (d) Fabrication of all-MXene-based MSCs using the stamping strategy, (e) CV curves of stamp fabricated MSCs. *Source:*

window up to 3 V in non-aqueous electrolytes have been obtained. Recent advances in WIS electrolytes and metal-ion-containing organic electrolytes have suggested the possibility of attaining high specific capacities and wide potential windows at the same time, which reveals great potential for developing high-energy and high-power capacitive devices. Despite great research efforts directed toward clarifying the charge storage mechanisms of MXene electrodes in various electrolytes, the current understanding of pseudocapacitive mechanisms in some systems, such as in WIS electrolytes and organic electrolytes, still needs to be further elaborated. More insights on the charge storage process would definitely provide better guidance toward the preparation of improved MXene-based electrodes for capacitive storage. Other strategies including tuning of the MXene surface groups and electrode architecture design are also effective routes to improve the electrochemical performances and more specifically the energy density. At the same time, attention should also be paid to the fabrication of MXene-based devices by careful selection of the counter electrode. So far, MXenes are promising capacitive electrode materials and efforts are still needed to improve their energy density and bring MXene-based supercapacitors from fundamental research to practical applications.

References

1 Lukatskaya, M.R., Mashtalir, O., Ren, C.E. et al. (2013). *Science* 341: 1502.
2 Levi, M.D., Lukatskaya, M.R., Sigalov, S. et al. (2015). *Advanced Energy Materials* 5: 1400815.
3 Gao, Q., Sun, W., Ilani-Kashkouli, P. et al. (2020). *Energy & Environmental Science* 13: 2549.
4 Shpigel, N., Chakraborty, A., Malchik, F. et al. (2021). *Journal of the American Chemical Society* 143: 12552.
5 Gao, Y., Wang, L., Li, Z. et al. (2015). *Journal of Advanced Ceramics* 4: 130.
6 Shao, H., Lin, Z., Xu, K. et al. (2019). *Energy Storage Materials* 18: 456.
7 Shan, Q., Mu, X., Alhabeb, M. et al. (2018). *Electrochemistry Communications* 96: 103.
8 Ghidiu, M., Lukatskaya, M.R., Zhao, M.-Q. et al. (2014). *Nature* 516: 78.
9 Lukatskaya, M.R., Kota, S., Lin, Z. et al. (2017). *Nature Energy* 2: 17105.
10 Shao, H., Xu, K., Wu, Y.-C. et al. (2020). *ACS Energy Letters* 5: 2873.
11 Wang, X., Mathis, T.S., Sun, Y. et al. (2021). *ACS Nano* 15: 15274.
12 Wang, X., Bak, S.-M., Han, M. et al. (2021). *ACS Energy Letters* 7: 30.
13 Lukatskaya, M.R., Bak, S.-M., Yu, X. et al. (2015). *Advanced Energy Materials* 5: 1500589.
14 Mu, X., Wang, D., Du, F. et al. (2019). *Advanced Functional Materials* 29: 1902953.

15 Zheng, K., Xian, Y., and Lin, Z. (2022). *Advanced Materials Interfaces* 9: 2200112.
16 Sun, Y., Zhan, C., Kent, P.R.C. et al. (2020). *ACS Appl. Mater. Interfaces* 12: 763.
17 Lin, Z., Shao, H., Xu, K. et al. (2020). *Trends in Chemistry* 2: 654.
18 Dall'Agnese, Y., Rozier, P., Taberna, P.-L. et al. (2016). *Journal of Power Sources* 306: 510.
19 Lin, Z., Barbara, D., Taberna, P.-L. et al. (2016). *Journal of Power Sources* 326: 575.
20 Lin, Z., Rozier, P., Duployer, B. et al. (2016). *Electrochemistry Communications* 72: 50.
21 Xu, K., Lin, Z., Merlet, C. et al. (1892). *ChemSusChem* 2018: 11.
22 Brezesinski, T., Wang, J., Tolbert, S.H., and Dunn, B. (2010). *Nature Materials* 9: 146.
23 Augustyn, V., Come, J., Lowe, M.A. et al. (2013). *Nature Materials* 12: 518.
24 Naguib, M., Come, J., Dyatkin, B. et al. (2012). *Electrochemistry Communications* 16: 61.
25 Mashtalir, O., Naguib, M., Mochalin, V.N. et al. (2013). *Nature Communications* 4: 1716.
26 Come, J., Naguib, M., Rozier, P. et al. (2012). *Journal of The Electrochemical Society* 159: A1368.
27 Dall'Agnese, Y., Taberna, P.-L., Gogotsi, Y., and Simon, P. (2015). *The Journal of Physical Chemistry Letters* 6: 2305.
28 Wang, X., Mathis, T.S., Li, K. et al. (2019). *Nature Energy* 4: 241.
29 Li, Y., Shao, H., Lin, Z. et al. (2020). *Nature Materials* 19: 894.
30 Wang, X., Kajiyama, S., Iinuma, H. et al. (2015). *Nature Communications* 6: 6544.
31 Kajiyama, S., Szabova, L., Sodeyama, K. et al. (2016). *ACS Nano* 10: 3334.
32 Ma, G., Shao, H., Xu, J. et al. (2021). *Nature Communications* 12: 5085.
33 Liu, P., Guan, B., Lu, M. et al. (2022). *Electrochemistry Communications* 136: 107236.
34 Liu, L., Orbay, M., Luo, S. et al. (2022). *ACS Nano* 16: 111.
35 Zhang, M., Liang, R., Yang, N. et al. (2022). *Advanced Energy Materials* 12: 2102493.
36 Tontini, G., Greaves, M., Ghosh, S. et al. (2020). *Journal of Physics: Materials* 3: 022001.
37 Xia, Y., Mathis, T.S., Zhao, M.-Q. et al. (2018). *Nature* 557: 409.
38 Deng, Y., Shang, T., Wu, Z. et al. (2019). *Advanced Materials* 31: 1902432.
39 Tang, J., Mathis, T., Zhong, X. et al. (2021). *Advanced Energy Materials* 11: 2003025.
40 Tang, J., Yi, W., Zhong, X. et al. (2020). *Energy Storage Materials* 32: 418.
41 Kobayashi, T., Sun, Y., Prenger, K. et al. (2020). *The Journal of Physical Chemistry C* 124: 13649.
42 Li, J., Yuan, X., Lin, C. et al. (2017). *Advanced Energy Materials.* 7: 1602725.
43 Li, T., Yao, L., Liu, Q. et al. (2018). *Angewandte Chemie International Edition* 57: 6115.

44 Dall'Agnese, Y., Lukatskaya, M.R., Cook, K.M. et al. (2014). *Electrochemistry Communications* 48: 118.
45 Yang, S., Zhang, P., Wang, F. et al. (2018). *Angewandte Chemie* 130: 15717.
46 Chen, X., Zhu, Y., Zhang, M. et al. (2019). *ACS nano* 13: 9449.
47 Persson, I., Näslund, L.-Å., Halim, J. et al. (2017). *2D Materials* 5: 015002.
48 Rakhi, R.B., Ahmed, B., Hedhili, M.N. et al. (2015). *Chemistry of Materials* 27: 5314.
49 Yoon, Y., Lee, M., Kim, S.K. et al. (2018). *Advanced Energy Materials* 8: 1703173.
50 Wen, Y., Rufford, T.E., Chen, X. et al. (2017). *Nano Energy* 38: 368.
51 Tao, Q., Dahlqvist, M., Lu, J. et al. (2017). *Nature Communications* 8: 14949.
52 Li, M., Lu, J., Luo, K. et al. (2019). *Journal of the American Chemical Society* 141: 4730.
53 Jawaid, A., Hassan, A., Neher, G. et al. (2021). *ACS nano* 15: 2771.
54 Shi, H., Zhang, P., Liu, Z. et al. (2021). *Angewandte Chemie* 133: 8771.
55 Kamysbayev, V., Filatov, A.S., Hu, H. et al. (2020). *Science* 369: 979.
56 Jiang, Q., Kurra, N., Alhabeb, M. et al. (2018). *Advanced Energy Materials* 8: 1703043.
57 Boota, M. and Gogotsi, Y. (2019). *Advanced Energy Materials* 9: 1802917.
58 Wei, Y., Zheng, M., Luo, W. et al. (2022). *Journal of Energy Storage* 45: 103715.
59 Boota, M., Bécuwe, M., and Gogotsi, Y. (2020). *ACS Applied Energy Materials* 3: 3144.
60 Wu, J., Li, Q., Shuck, C.E. et al. (2021). *Nano Research* 15: 535.
61 Xia, Q.X., Fu, J., Yun, J.M. et al. (2017). *RSC Advances* 7: 11000.
62 Zhang, Y., Cao, J., Yuan, Z. et al. (2021). *Journal of Colloid and Interface Science* 599: 109.
63 Navarro-Suárez, A.M., Van Aken, K.L., Mathis, T. et al. (2018). *Electrochimica Acta* 259: 752.
64 Li, L., Zhang, M., Zhang, X., and Zhang, Z. (2017). *Journal of Power Sources* 364: 234.
65 Chen, X., Zhu, J., Cai, J. et al. (2021). *Journal of Energy Storage* 40: 102721.
66 Fu, J., Li, L., Yun, J.M. et al. (2019). *Chemical Engineering Journal* 375: 121939.
67 Ruan, C., Zhu, D., Qi, J. et al. (2021). *Surfaces and Interfaces* 25: 101274.
68 Zhao, R., Wang, M., Zhao, D. et al. (2018). *ACS Energy Letters* 3: 132.
69 Wang, J., Li, F., Zhu, F., and Schmidt, O.G. (2019). *Small Methods* 3: 1800367.
70 Lu, X., Yu, M., Wang, G. et al. (2014). *Energy & Environmental Science* 7: 2160.
71 Peng, Y.-Y., Akuzum, B., Kurra, N. et al. (2016). *Energy & Environmental Science* 9: 2847.
72 Li, H., Hou, Y., Wang, F. et al. (2017). *Advanced Energy Materials* 7: 1601847.
73 Qin, L.Q., Tao, Q.Z., El Ghazaly, A. et al. (2018). *Advanced Functional Materials* 28: 1703808.

74 Kurra, N., Ahmed, B., Gogotsi, Y., and Alshareef, H.N. (2016). *Advanced Energy Materials* 6: 1601372.
75 Zhang, C.F., Kremer, M.P., Seral-Ascaso, A. et al. (2018). *Advanced Functional Materials* 28: 1705506.
76 Jiang, Q., Lei, Y., Liang, H. et al. (2020). *Energy Storage Materials* 27: 78.
77 Jiang, Q., Kurra, N., Maleski, K. et al. (2019). *Advanced Energy Materials* 9: 1901061.
78 Zhang, C., McKeon, L., Kremer, M.P. et al. (2019). *Nature Communications* 10: 1795.
79 Orangi, J., Hamade, F., Davis, V.A., and Beidaghi, M. (2020). *ACS Nano* 14: 640.

20

MXene Application in Lithium-Ion Batteries

Majid Farahmandjou, Xin Guo, Zefu Huang, Bijay Janardhanan, A. M. Ruhul, and Guoxiu Wang

Centre for Clean Energy Technology, School of Mathematical and Physical Sciences, Faculty of Science, University of Technology Sydney, Sydney, New South Wales, Australia

20.1 Introduction

Lithium-ion batteries (LIBs) are currently the preferred technology for electrochemical energy storage, and with increasing awareness of the climate crisis, there has been added pressure to expand their applications for electric vehicles (EVs) and renewable energy harvesting. Developing new electrode active materials with properties such as high power and energy density, large reversible capacities, and superior cyclability are essentially required to improve the performance of current LIBs. In LIBs, graphite has been the predominant anode material for many years [1, 2], while the cathode material is often a layered transition metal oxide [3] which allows sufficiently facile lithium-ion (de-)intercalation. These electrodes are connected by an ion-conductive (and electron-insulating) electrolyte. A porous separator prevents the electrodes from physically contacting each other. Figure 20.1 shows the basic working principle of a LIB. During the charge process, lithium-ions are intercalated into a graphite anode, generating graphite intercalation compounds, and the solid electrolyte interphase (SEI) on the first charge. During discharge, the lithium ions migrate toward the cathode.

Graphite delivers a theoretical specific capacity of $372\,\mathrm{mAh\,g^{-1}}$ and is a relatively stable, well studied anode material. However, lithium diffusion is slow, and the material is incapable of handling the fast charge rates required for future EV applications [4]. Therefore, there is an impressive need to improve the rate

Transition Metal Carbides and Nitrides (MXenes) Handbook: Synthesis, Processing, Properties and Applications, First Edition. Edited by Chuanfang Zhang and Michael Naguib.
© 2024 John Wiley & Sons, Inc. Published 2024 by John Wiley & Sons, Inc.

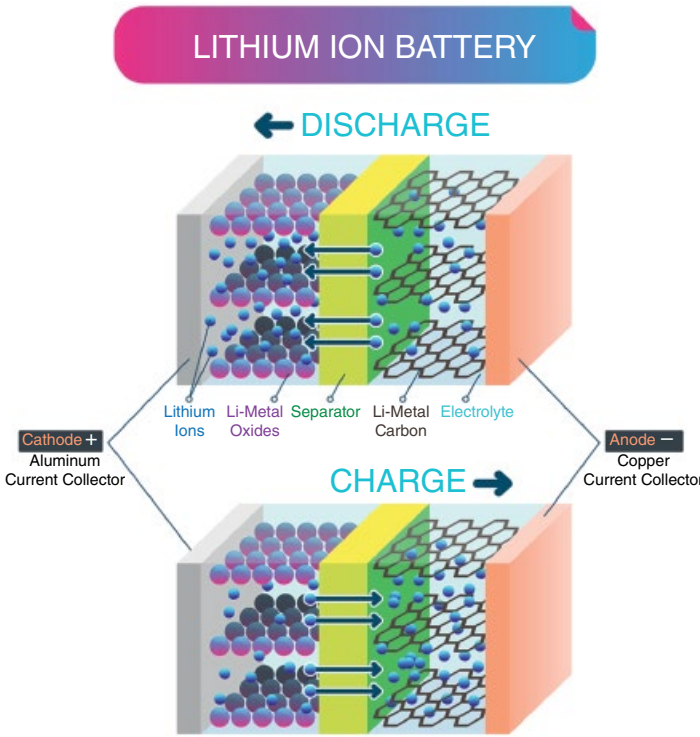


Figure 20.1 The schematic diagram of the working principle of a Li-ion battery.

capability, as well as develop high-capacity electrode materials to increase the energy density of LIBs.

MXenes possess intrinsic properties, including excellent hydrophilicity, metallic conductivity, large specific surface areas for ion intercalation, mechanical stability, and tunable interlayer spacing and morphologies. These qualities lend well to a numerous applications within lithium-based battery architectures. In fact MXenes have been investigated as separator interlayers, conductive additives, and metal anode protective layers [5]. The first investigated use of MXenes was for energy storage [6]. Both theoretical and experimental studies on MXenes as LIB anodes in the past decade have proven they are promising future anode materials. With more than 30 different MXenes already synthesized and further solid solutions with other transition metals (formed on the M and X sites, e.g., $[Ti,Nb]CT_x$), and ordered MXenes with multiple transition metals and ordered vacancies being synthesized (e.g., $Mo_2TiC_2T_x$, $[Mo_{2/3}Y_{1/3}]_2CT_x$, etc.) [6], the potential for further research on this family of materials and their applications are near infinite.

However, when used as electrode active materials for LIBs, MXene nanosheets tend to stack due to strong van der Waals forces between the surfaces, and agglomerate (like other 2D materials), and subsequently suffers from lattice instability and capacity loss upon cycling. Moreover, the presence of undesirable surface functional groups and impurities further limits cation diffusion. These factors, along with the lack of safe, environmentally friendly, and scalable synthesis methods, hinder the application of MXenes as electrode active materials for LIBs. Therefore, researchers continue investigating techniques to overcome these limitations by, investigating different compositions, modifying or eliminating the surface functional groups, engineering the porosity, defects and/or morphology of MXenes, and synthesizing MXene composites with other nano-structured materials.

20.2 MXenes as Electrode Active Materials

The inherent properties of MXenes, such as metallic conductivity which allows rapid electron transport through the electrode, low open circuit voltage vs. Li^+/Li, low diffusion barriers for alkali metal-ions, and plentiful redox active sites, offered by the transition metal oxide like surface, for pseudocapacitive charge storage, make them promising active anode materials [7]. In the past decade or so since their discovery, numerous studies have been conducted to identify, synthesize, and understand the behavior of MXene materials when applied as LIB anodes. Early investigations of MXenes established their suitability for anode application in LIBs [8–10]. For instance, Tang et al. [8] investigated the Li-ion storage capacity of Ti_3C_2 MXenes with F and OH terminations through density functional theory (DFT) calculations. They found that the strong Coulomb interaction between Li^+ ions and negatively charged Ti_3C_2 layers are responsible for Li^+ adsorption on the MXene surface, and that for bare Ti_3C_2, F-terminated Ti_3C_2, and OH-terminated Ti_3C_2, the Li-ion storage capacity would be 320, 130, and 67 mAh g^{-1}, respectively. Later Er et al. [11] indicated that the Li adatom content for Ti_3C_2 monolayers could be as high as 2.8 per formula unit (assuming adsorption on both sides of the monolayer), which corresponds to a specific capacity of 447.8 mAh g^{-1}. Naguib et al. [10] demonstrated that Nb_2CT_x and V_2CT_x showed excellent capability to handle high cycling rates (10 C), due to low diffusion energy barriers. They achieved the reversible capacities of 170 and 260 mAh g^{-1} at 1 C, and 110 and 125 mAh g^{-1} at 10 C for Nb_2C and V_2C based electrodes, respectively.

DFT studies have revealed that the specific capacity of MXene monolayers with higher formula weight (M_3X_2 and M_4X_3) is much lower than the specific capacity of monolayers of lower formula weight such as M_2X. This can be attributed to the inactive M–X layer in the bulk of the larger monolayers. While this may hold true

for monolayers of the same M element, it should be noted that the heavier Nb_2C has been shown to have a higher lithium storage capacity than T_2C [10]. However, the higher surface energies of the M_2X monolayers make them susceptible to stacking and/or oxidation. Thus, M_3X_2 is more commonly seen in the literature concerning the current discussion. These studies in the early half of the last decade laid the groundwork for further experimental and theoretical research. In the following sections, we shall discuss the properties of MXenes and the current progress in engineering for LIB applications.

20.2.1 MXenes with Various Formula

In general, 2D layered materials such as MXenes store energy through ion intercalation. The composition (M and X elements and their ratios) of the MXene monolayer, the surface terminations, and defects from the synthesis process all have profound implications on their mechanical and electrochemical properties and performance as anode active materials. The maximum capacity (C_{Max}) of a monolayer as a function of maximum adatom content (x_{max}) for 2D layered electrodes can be calculated as follows:

$$C_{\mathrm{Max}} = \frac{\left[x_{\mathrm{max}} \times z \times \mathrm{F} \times 10^3\right]}{M} \left(\mathrm{mAh\,g^{-1}}\right) \tag{20.1}$$

where z is the valence number, F is the Faraday Constant, and M is the Molecular Mass of a formula unit of the active species (MXene in this case) [11].

The composition of the MXene monolayer affects the available working voltage, band gap, molecular weight per formula unit, electron conductivity, ion conductivity and many other properties. Several MXene compositions have been investigated for application as electrode active materials for LIBs. Out of the compositions, Ti_2CT_x, $Ti_3C_2T_x$, Ti_3CNT_x, V_2CT_x, Nb_2CT_x, $Nb_3C_2T_x$, $Nb_4C_3T_x$ and their unterminated counterparts might be the most promising for LIB anode application in the short run. Therefore, we shall limit our discussion to these stoichiometries.

Yorulmaz et al. recently screened a series of MXenes using ab-initio high throughput computation for LIB anode application [7]. They used the Arrhenius Law to calculate the Li-ion diffusion energy barriers at room temperature for the above-mentioned stoichiometries (among others – excluding the carbonitride) and determined that for the M_2C systems the diffusion energy barrier was ~0.01 eV. They also calculated theoretical specific capacities of 498, 471, and 271 $\mathrm{mAh\,g^{-1}}$ for T_2C, V_2C, and Nb_2C respectively. For the M_3C_2 systems the diffusion energy barriers were 0.024, 0.025, and 0.054 eV and specific capacities were 320, 303, and 177 $\mathrm{mAh\,g^{-1}}$ for Ti_3C_2, V_3C_2, and Nb_3C_2, respectively. Experimental work conducted earlier has reported capacities of 225 $\mathrm{mAh\,g^{-1}}$ at C/25 for Ti_2CT_x,

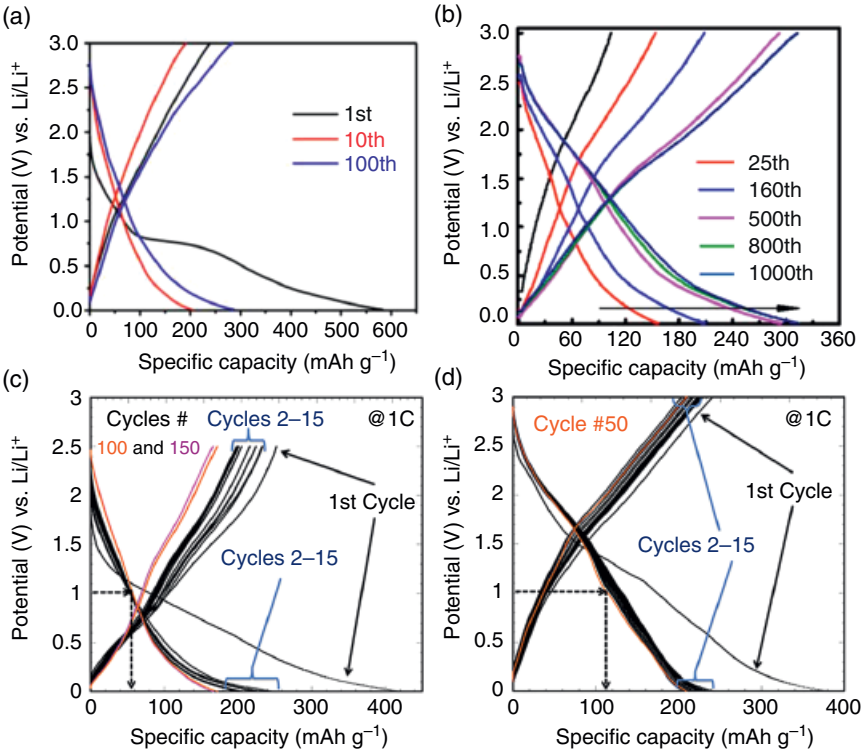


Figure 20.2 (a) Freeze-dried Ti_3CNT_x at 1st, 10th, and 100th under the current density of $0.05\,A\,g^{-1}$ [12]. (b) Charge-discharge curves of $Nb_4C_3T_x$. Electrochemical performance of Nb_2CT_x and V_2CT_x as electrodes in LIB [14]. (c) Voltage profile of Nb_2CT_x between 0 and 2.5 V vs. Li/Li^+. (d) Voltage profile of V_2CT_x. *Source:* Naguib et al. [10]/American Chemical Society.

$410\,mAh\,g^{-1}$ at 1 C for $Ti_3C_2T_x$, $300\,mAh\,g^{-1}$ at $0.5\,A\,g^{-1}$ for Ti_3CNT_x, $260\,mAh\,g^{-1}$ at 1 C for V_2CT_x, and $170\,mAh\,g^{-1}$ at 1 C for Nb_2CT_x, $310\,mAh\,g^{-1}$ at $0.1\,A\,g^{-1}$ and $Nb_4C_3T_x$ (increases to $380\,mAh\,g^{-1}$ after 100 cycles) [9, 10, 12–14] (Figure 20.2). The discrepancy between the theoretically predicted and experimentally observed values for specific capacity, could be explained by the fact that most of these experimental studies were conducted before the true ramifications of surface terminations and defects were understood. Furthermore, MXene stoichiometries display an "electrochemical activation" phenomenon, whereby they require several cycles to achieve a stable SEI and for the *c*-lattice parameter to stabilize into an "open" layered structure. This is indicated by a sudden increase in capacity after several hundred cycles, especially when cycled at high current densities.

20.2.2 Functionalized MXenes

MXene monolayers offer a variety of tunable characteristics for functionalization, or tailoring their properties to fit specific applications. These include, the choosing of M and X elements and their ratios (i.e. the composition), the thickness of the nanosheets, the modification of surface functional groups, engineering the interlayer space, and doping with other elements. Techniques for controlling each of these and their effects on the MXene monolayer are described below.

20.2.2.1 Modification of Functional Surface Groups

Surface terminal groups (or functional groups) are unavoidable by-products of the "top-down" etching techniques used to synthesize MXenes. Conventional etching involves the use of acidic, fluoride containing solutions, and these produce a mixture of –OH, –F, and –O terminations on the surfaces of the nanosheets. Proposed reaction pathways are illustrated by the following equations (using $Ti_3C_2T_x$ as an example):

$$Ti_3AlC_2 + 3HF = AlF_3 + {}^3/_2\, H_2 + Ti_3C_2 \tag{20.2}$$

$$Ti_3C_2 + 2H_2O = Ti_3C_2\left(OH\right)_2 + H_2 \tag{20.3}$$

$$Ti_3C_2 + 2HF = Ti_3C_2F_2 + H_2 \tag{20.4}$$

In a recent computation study, it was determined that the –O terminations are caused by decomposition of the unstable –OH termination into surface bound –O and hydrogen gas [15]. The thermodynamic stability of the functional groups compare as follows: $Ti_3C_2O_2 > Ti_3C_2F_2 > Ti_3C_2(OH)_2$. Functional groups are usually randomly distributed over the surface of the nanosheets. Their location on the monolayer and concentration have great significance on the physical and chemical properties of MXenes, including (but not limited to) conductivity, cation/energy storage capacity, and mechanical strength [4, 7, 16–18]. Pristine (unterminated) MXenes have been computationally and experimentally proven to the better function group, with metallic conductivity and improved capacity, in contrast to most terminated MXenes which tend to show semiconductor like behavior (negative dR/dT at lower temperatures) [7, 8, 18].

Surface functional groups can be tuned by careful selection of the synthesis method, etching agents, and/or post processing techniques [19]. For instance, the ratio of =O, –OH, and –F groups on the MXene surface can be changed by adjusting the types of etchants and concentration. Using the HF as the etchant leads to a higher ratio of –F terminations than that etched by the mixture of HCl and LiF [20, 21]. Wang et al. demonstrated that lower the pH of etchants could increase the F concentration, and they decreased the O/F ratio from 1.4 to 0.8 by increasing

HF concentration from 10% to 48% [22]. Also, the surface terminations can be changed by varying the synthesis solvents. Barsoum et al. prepared fluorine-rich $Ti_3C_2T_x$ in polar organic solvents, and this MXene achieved twice the capacity compared to the conventional water etched MXenes [23]. Besides, a general Lewis acidic etching route was developed to synthesize the Cl- and Br-terminated MXenes, and the surface terminations can be further modified by post-exchange reactions with molten alkali metal halides [24, 25].

Notably, an experimental study conducted by Persson et al. in 2018 has demonstrated that post processing heat treatment of few layered Ti_3C_2 converts initially disordered surface structures into highly ordered structures; and that at temperatures over 550 °C, functional -F can be desorbed leaving the functional O to occupy the vacated co-ordination site [26]. This offers a route for utilizing pristine MXenes. Alternatively, the aforementioned postprocessing techniques, such as ion-exchange in certain solvents [27] and controlled oxidation [28] may offer a possibility for re-termination with more favorable groups to enhance the charge storage capability.

20.2.2.2 Defect Engineering

Vacancies (or point defects) originate from harsh or extended etching processes. The nature of the vacancies have been theoretically predicted to affect both the magnetic and electronic properties of MXenes [29]. Furthermore, through ab-initio computations single point vacancies of carbon in the T_2C monolayer have been shown to improve conductivity and flexibility [30]. Ren et al. created meso-porous monolayers of Ti_3C_2 at room temperature, by catalytic oxidation of MXene flakes using a transition metal salt, followed by an acid treatment to remove the metal oxide. This yielded meso-porous MXene (*p*-MXene) flakes with significantly improved capacities for reversible storage of lithium ions [31]. Figure 20.3 shows the schematic showing the chemical etching of $Ti_3C_2T_x$ flakes to produce porous $Ti_3C_2T_x$ MXene structure. Wang et al. used minimally intensive layer delamination (MILD) method to create free-standing Ti_3C_2 monolayers [32]. They determined that there was a linear relationship between the formation energy of the vacancy and the number of vacancies formed. Also, the formation of defects is proportionally linked to HF concentration. MXenes with ordered divacancies, such as $W_{1.33}CT_x$ and $Mo_{1.33}CT_x$ have been successfully synthesized but are yet to be investigated as electrode active materials for LIBs [33, 34].

20.2.2.3 Intercalation-Interlayer Space Engineering

MXene monolayers have been shown to be theoretically capable of adatom adsorption on either surface of the nanosheet, as mentioned earlier. However, in practice this is often not achievable due to repulsive forces between solvated lithium cations and the limited interlayer space. Therefore, attempts have been made

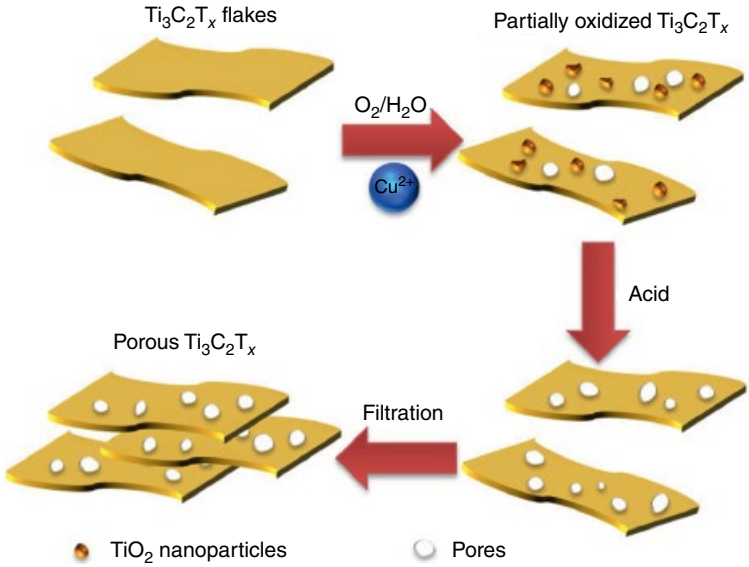


Figure 20.3 Schematic showing the chemical etching of $Ti_3C_2T_x$ flakes to produce porous $Ti_3C_2T_x$ MXene structure. *Source:* Ren et al. [31]/John Wiley & Sons.

to increase the *c*-lattice parameter by pre-intercalation of a variety of cations [4, 35]. For example, Wu et al. synthesized Ti_3C_2 by etching the precursor MAX phase in choline chloride and oxalic acid deep eutectic solvents with the presence of NH_4F [4]. The intercalation of choline cations increased the interlayer space of the MXene by 0.37 nm in comparison to the HF etched Ti_3C_2 and delivered a high reversible capacity of 208 mAh g^{-1} at a current density of 0.5 A g^{-1} for over 400 cycles. Similarly, Lu et al. pre-intercalated Al^{+3} into $Ti_3C_2T_x$, and demonstrated an increase in the interlayer space from 11.6 Å to 12.2 Å [35]. Figure 20.4a shows the schematic illustration of the preparation process for cation (Na^+, Mg^{2+} and Al^{3+}) pre-intercalated $Ti_3C_2T_x$ film electrode. Furthermore, the pre-intercalated MXene enhanced capacity from 128 (for pure $Ti_3C_2T_x$ MXene) to 152 mAh g^{-1} (for pre-intercalated Al^{+3} into $Ti_3C_2T_x$ MXene) at a current density of 320 mA g^{-1} and indicated fast ion diffusion within the enlarged interlayer spaces.

20.2.2.4 Three-Dimensional (3D) MXene Engineering

Another method used to increase the accessible surface area of the MXene monolayer is by constructing a 3D macroporous structure by templating method [38]. A variety of templates have been employed to transform the 2D MXene into 3D architecture, such as sulfur [36], PMMA [37], and ice [39] templates. For example, Xu et al. filtered the MXene/sulfur water dispersion to a film and then removed the

sulfur particles by sublimation at high temperatures to obtain the flexible 3D porous film (Figure 20.4b) [36]. The free-standing film exhibits an enhanced capacity of 455.5 mAh g^{-1} at 50 mA g^{-1}, excellent rate performance and long-term cycle stability. Zhao and co-workers [37] successfully fabricated MXene nanosheets into

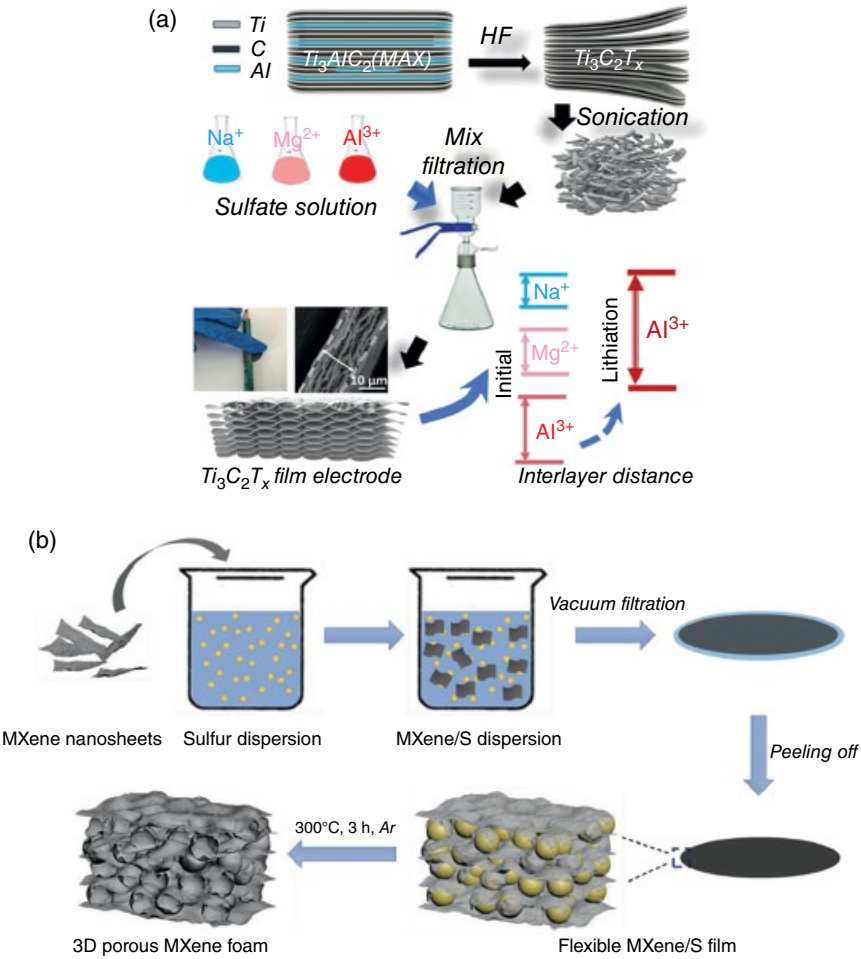


Figure 20.4 (a) Schematic illustration of the preparation process for cation pre-intercalated $Ti_3C_2T_x$ film electrode (inset: photos of flat and rolled shiny $Ti_3C_2T_x$ films on a pencil, cross-sectional SEM image of pristine $Ti_3C_2T_x$ film). *Source:* Lu et al. [35]/With permission of Elsevier. (b) Illustration of the preparation of the flexible 3D porous MXene foam using sulfur particles as template. *Source:* Adapted from Zhao et al. [36]. (c) A schematic of synthesis of 3D macroporous MXene film with PMMA template; (d) Digital photograph showing the flexibility of 3D macroporous MXene film; (e) Cross-sectional SEM image of 3D macroporous MXene film. *Source:* Zhao et al. [37]/Reproduced from John Wiley & Sons, Inc.

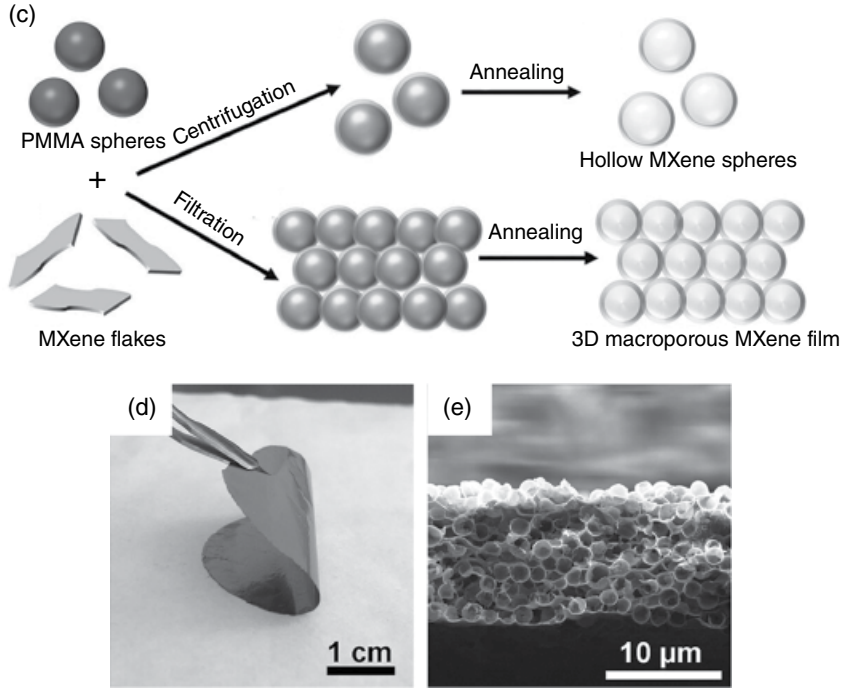


Figure 20.4 (Continued)

3D macroporous MXene films by using PMMA spheres as sacrificial templates. As illustrated in Figure 20.4c, MXene nanosheets can spontaneously wrap the PMMA spheres driven by the interaction between their surface hydroxyl groups. Subsequently, vacuum-assisted filtration can increase the stacking density of PMMA/MXene composite microspheres, producing PMMA spheres/MXene composite films. Finally, the PMMA spheres were removed by calcining at 450 °C to produce 3D macroporous MXene films with excellent flexibility (Figure 20.4d, e). Similarly, Zhang et al. [40] used the as-prepared polystyrene (PS) spheres with an average diameter of 200 nm as sacrificial templates to stop MXene sheets restacking. These macroporous MXenes with massive active sites facilitate the electrolyte impregnation and boost the charge transfer kinetics, leading to significantly improved capacity and fast-charging performance in LIBs.

20.2.2.5 Doping/Heteroatom Doping

Hetero-atom doping is the final strategy for functionalization of MXene monolayers that we shall discuss. This technique involves the doping of MXene surfaces with atoms to improve functionality. Doping has a similar function to the

pre-intercalation of cations described above, but in contrast to it, doping is usually conducted as a post treatment to the etching process. Anions doping/co-doping by sole or a portfolio of nitrogen (N) [41–44], sulfur (S) [45, 46], and phosphorus (P) [47] elements were widely applied to improve the performance of MXene electrodes. Several doping methods used in carbon/graphene structure modification have been leveraged for MXene doping, including thermal treatment, microwave irradiation, and hydrothermal treatment of the mixture of MXene and doped-elements-containing precursors. For instance, Liu et al. has reported the synthesis of nitrogen-doped Nb_2CT_x (N-Nb_2CT_x) MXene via a hydrothermal reaction with urea as an anode for LIBs [44]. The *N*-doping increases *c*-lattice parameter of Nb_2CT_x MXene from 22.32 Å to 34.78 Å, as well as improve its specific surface area and electrical conductivity. The *N*-Nb_2CT_x anodes demonstrated a higher reversible capacity of 360 mAh g^{-1} at 0.2 C in comparison to that of un-doped Nb_2CT_x (190 mAh g^{-1} at 0.2 C). Moreover, heteroatom co-doping with nitrogen and sulfur on V_2CT_x MXene has been demonstrated to achieve a high reversible capacity of 590 mAh g^{-1} after 100 cycles at 0.1 A g^{-1} in LIBs [48]. The *N* and *S* co-doping effectively increases the active sites of V_2CT_x MXene for Li^+ adsorption, promotes the Li^+ insertion capacity by expanded interlayer spacing and enhances the charge transfer kinetics, thereby leading to the improved capacity and rate performance. Beyond the aforementioned anion doping, a few studies also adopted anions and cations co-coping to tune the structure of MXenes and improve the lithium storage performance. For example, Cheng et al. applied the microwave irradiation method to simultaneously incorporate the *N* and *V* into $Ti_3C_2T_x$ to form *N*,*V*-$Ti_3C_2T_x$ which achieved remarkable reversible capacity of 92 mA h g^{-1} at high current rate (3 C) after 1000 cycles [43].

20.3 MXenes-based Composites

Owing to the superior electronic conductivity and unique lamellar structure, MXenes are widely employed as additives or templates to construct MXene-based composites or derivatives for lithium storage, respectively [49, 50]. In the following sections, MXenes based compound and several derivative strategies along with their application in LIBs are discussed.

20.3.1 MXene Derivatives

Derivatives of MXene have come into the spotlight after the first discovery of carbon-supported TiO_2 derived from Ti_3C_2 MXenes with the help of the thermal oxidation process by Naguib et al. [51]. Later on, there are several approaches discovered by the researchers for the synthesis of MXene derivatives and MXene

compounds but the most popular is via oxidation reaction. Chlorination, nitridation, fluorination, and sulfurization are also some alternative routes. The controlled oxidation procedure allowed the synthesis of totally oxidized MXenes, MXene-derived oxides/carbon composites, and MXene-derivative/MXene composites. It is essential to select the optimal oxidation method as the degree of oxidation significantly affects the product as well as structure which leads to distinct performance [52]. The derivative/C and derivative/MXene composites generated from deeply and surface oxidized MXenes use a synergic blend of components to enhance electrochemical performance. The shape and morphology of the derivatives also influence the electrodes ultimate performance depending on synthesis strategies.

20.3.1.1 Completely Oxidized MXenes

MXenes are entirely oxidized to transition metal oxides with the introduction of a suitable oxidation treatment. The most researched MXene $Ti_3C_2T_x$ can be completely transformed to TiO_2 in a highly oxidizing environment, such as air calcination or treatment with powerful oxidants [53]. In this process, the carbon element is oxidized to CO_2 gas where the temperature and the reaction time play a very crucial role in the complete oxidation process. Generally, the amount of oxidation or degree of oxidation is directly proportional to the reaction temperature and duration of reaction [54].

Transition metal oxides-based MXene derivative are considered as potential energy storage electrode materials because of their high safety and outstanding cycling performance, as well as the minimal volume expansion during charge/discharge [55–58]. However, the majority of metal oxides have poor electronic conductivity, limiting their application in energy storage technology [59]. This problem can be addressed by controlling the oxidation process of MXenes to get an MXene-derived oxide/carbon composite since MXenes (carbides) have their own carbon [60]. Naguib et al. [51] reported a one-step synthesis of oxide/C composites by flash oxidizing MXene where multilayer $Ti_3C_2T_x$ MXene powders were deposited in alumina boats and driven into a hot zone furnace at 1150 °C for 30 seconds before being quickly withdrawn. A TiO_2–C composite architecture was produced by inserting TiO_2 nanocrystals in thin layers of irregular amorphous carbon. The Gibbs energy of titanium oxidation is lower than that of carbon oxidation, which explains why a TiO_2–C hybrid structure rather than pure TiO_2 forms.

In comparison to flash oxidation, gradual oxidation of MXenes in the air at a moderate temperature is more regulated, leading to a reduced carbon content [61]. In the hydrothermal process, the generated carbon may dissolve, resulting in a low carbon concentration. Calcination of MXene derivatives in a CO_2 environment may maintain their carbon content. To make C/TiO_2 composites, Yuan

et al. [62] heat-treated Ti_3C_2 MXenes at 700 °C, 800 °C, and 900 °C for 1 hour in CO_2 and discovered that CO_2 oxidation of Ti_3C_2 MXenes started at around 700 °C while carbon oxidation began at 800 °C. Furthermore, the authors noticed that at 900 °C, the carbon was entirely oxidized to CO, putting away TiO_2 as the product. As a result, the MXene-derived oxide/C composite with enhanced carbon content may be simply created by oxidizing CO_2 at a sufficient temperature.

Adding highly conductive components to MXene-derived TiO_2 can further enhance the electronic conductivity of composites and improve the rate performance. For example, Fang et al. [60] have developed a one-step hydrothermal technique to produce MXene-derived TiO_2 nanoparticles/reduced graphene oxide (rGO) composite anodes for LIBs and K-ion batteries. In this process, carbon components are introduced *in-situ* during MXene synthesis. The oxygen-containing functional groups in GO accelerated the transition of Ti_2C MXene sheets into amorphous Ti-based precursors with rough TiO_2 deposition. TiO_2 nanoparticles were created through a 16-hour hydrothermal treatment at 160 °C, while GO was transformed to rGO. In Li-ion batteries, this TiO_2/rGO composite with a well-constructed form outperformed TiO_2 produced from Ti_2C (Figure 20.5a). The XRD pattern of TiO_2/rGO composites showed typical peak centers of anatase TiO_2 crystal faces (Figure 20.5b). The current density, average capacity along with coulombic efficiency is offered TiO_2/rGO is an excellent anode for Li-ion batteries (Figure 20.5c).

Tang et al. [63] investigated two-step oxidation of MXene derivatives of layer-stacked anatase titania (a-TiO_2) from HF-etched $Ti_3C_2T_x$ for LIBs application. In the two-step oxidation process, hydrothermal treatment includes before calcination which improves grain formation and results from two-dimensional morphology formed of TiO_2 nanoparticles (Figure 20.6). This is because carbon is produced during the hydrothermal oxidation of MXene, which may limit mass diffusion over the crystallographic barrier during calcination. The layer-stacked a-TiO_2 particles synthesized through two-step oxidation have enhanced electrochemical characteristics, exhibiting a capacity of 241.9 mAh g^{-1} at 0.3C (1C = 167.5 mA g^{-1}), while directly oxidized thick TiO_2 particles deliver a capacity of 116.4 mAh g^{-1}. The layer-stacked a-TiO_2 also demonstrated impressive rate performance, delivering 131.1 mAh g^{-1} at 12C and outstanding cycle stability, retaining 70% of its capacity after 10 000 cycles at 6C.

20.3.1.2 Partially Oxidized MXenes

Partially oxidized MXenes with a mixed composition of metal oxides and MXenes can be obtained through tailoring the oxidation process. Zhang et al. [64] produced orthorhombic Nb_2O_5@Nb_4C_3 multilayered matrices by oxidizing $Nb_4C_3T_x$ MXenes in CO_2 at 850 °C. This composition performed well, because of the synergistic effects of the hierarchical layered structure. The

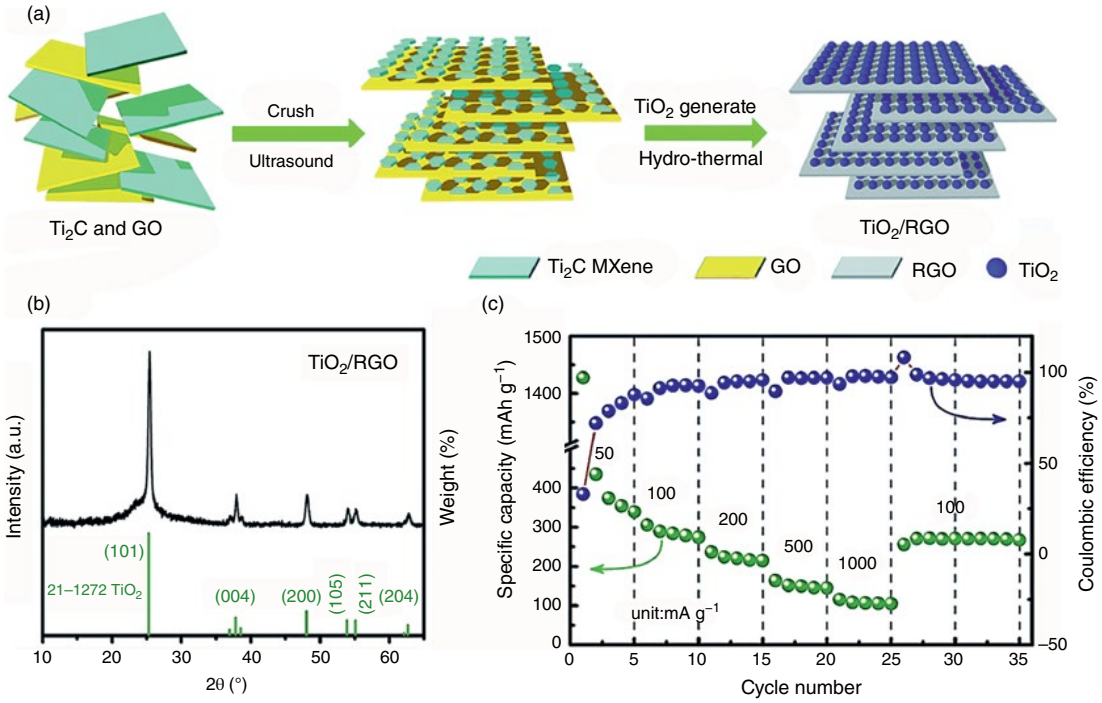


Figure 20.5 (a) One-step formation of TiO_2/rGO composite, (b) XRD of TiO_2/rGO composite, (c) Rate performance of Ti_2C-derived TiO_2/rGO and Ti_2C-derived TiO_2 for LIBs. *Source:* Fang et al. [60]/Royal Society of Chemistry.

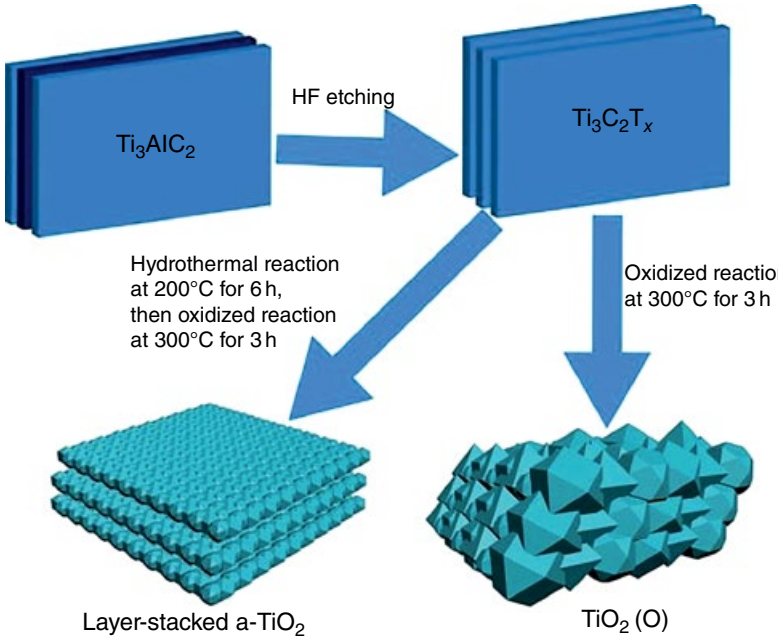


Figure 20.6 Two different oxidation processes of the $Ti_3C_2T_x$ MXene. *Source:* Tang et al. [63]/John Wiley & Sons.

following reactions were used to combine Nb_2O_5 with amorphous carbon in this study to produce amorphous carbon:

$$Nb_4C_3T_x + 5CO_2 \rightarrow 2Nb_2O_5 + 8C \tag{20.5}$$

The Nb_2O_5@Nb_4C_3 electrode demonstrated 208 mAh g^{-1} capacity at 50 mA g^{-1} and strong rate performance with a capacity retention of 60% at 1000 mA g^{-1} as an anode in LIBs. The Nb_2O_5/amorphous carbon/Nb_4C_3 hierarchical architecture was formed after the CO_2 oxidation of MXene layers. The high-capacity Nb_2O_5 nanoparticles were connected to the highly conductive Nb_4C_3 using disordered carbon as an electron "bridge." Also, the equivalent hierarchical structures were generated by oxidizing Mo_2CT_x, Nb_2CT_x, and $Ti_3C_2T_x$ using the same approach [65, 66].

20.3.1.3 Other MXene Derivatives

MXenes can be completely converted to carbon materials for energy storage by using a chlorination process [67, 68]. Ding et al. [69] synthesized carbon nanosheets by heat-treating the Ti_3C_2 MXenes in dry chlorine gas. The Ti

atoms were extracted from Ti_3C_2 MXenes according to the chemical reaction described below:

$$Ti_3C_2(s) + 6Cl_2(g) \rightarrow 3TiCl_4(g) + 2C(s) \tag{20.6}$$

In this process carbon nanosheets possess a considerable interlayer spacing and a lot of in-plane micro/mesopores, resulting in a high specific surface area. MXenes were also converted into a variety of attractive electrode materials with two-dimensional morphology by nitridation or fluorination. For example, Yuan et al. [70]synthesized two-dimensional multilayer carbon surrounded nitrides for energy storage via an one-step nitridation as follow:

$$Ti_3C_2O_2 + 3NH_3 \rightarrow 3TiN + 2C + 2H_2O(g) + 5/2H_2(g) \tag{20.7}$$

Thapaliya et al. [71] converted $Ti_3C_2T_x$ MXenes into $TiOF_2$ layers for LIBs using a direct fluorination process. The fluorination procedure resulted in a phase transition to $TiOF_2$ after 24 hours in the fluorine (F_2) atmosphere. Interestingly, the resultant $TiOF_2$ sheets preserved the MXenes 2D shape, which aided ion transportation. Therefore, the 2D $TiOF_2$ sheets demonstrated more ability than MXene precursors and superior capacity than non-2D-layered $TiOF_2$.

Huang et al. [72] reported sandwich-like extremely thin TiS_2 nanosheets restrained *N*, *S* co-doped porous carbon, which was produced by annealing the polydopamine coated $Ti_3C_2T_x$ MXene in 1 : 9 of H_2S/Ar environment. TiS_2 grew within the polydopamine-derived carbon in this 2D nano space-confined synthesis, resulting in a well-defined shape. The following equation can be used to define the process:

$$Ti_3C_2T_x + H_2S \rightarrow TiS_2 + C + HT_x(g) \tag{20.8}$$

The derived TiS_2@C was employed as a sulfur host in high-performance Li–S batteries because of its good catalytic activity and affinities to polysulfides. Overall, MXene derivatives with unique structure characteristics or compositions show promise to enhance the electrochemical performance of LIBs.

20.3.2 MXene/Metal Chalcogenides

The directly exploitation 2D structure of pure MXenes tends to restack and aggregate, resulting in performance inefficient [73]. Compositing MXenes with complementary materials can overcome the limitations and synergize the advances of individual blocks [74–76]. For this purpose, MXenes have been hybridized with various transition metal chalcogenides (TMCs), such as SnS [77], NiS [78], MoS_2 [79], FeS_2 [80] , $NiSe_2$ [81], and $NiCo_2S_4$ [82] Intercalation/deintercalation

of alkali metal ions in pristine TMC materials causes rapid capacity fading, poor-rate and cycle performance due to their poor electronic conductivity and large volume change, which can be alleviated by the incorporation of MXenes. For example, Tang et al. [83] constructed the Ti_3C_2 MXene@C@SnS hybrids (carbon encapsulated SnS nanoparticles on the surface and interlayer of multilayer Ti_3C_2 MXene) via a hydrothermal and subsequent annealing route for LIBs. They have found huge specific surface area (255.78 $m^2\ g^{-1}$) and porosity which speed up electron/ion exchange. The Ti_3C_2 MXene@C@SnS anode has a better reversible capacity (1473 $mAh\ g^{-1}$ at 0.1 $A\ g^{-1}$), and rate capability (640 $mAh\ g^{-1}$ at 5 $A\ g^{-1}$), and long-cycle stability (1050 $mAh\ g^{-1}$ at 1 $A\ g^{-1}$ over 350 cycles).

20.3.3 MXene/Alloy-type Materials

Due to the remarkable electronic conductivity, elastic properties, and excellent hydrophilicity, MXenes can act as a complementary component to combine with high-capacity alloy-based materials that have low discharge potential and abundant resources, such as Si [84–87], Sn [88, 89], and Sb [90–92]. Among these lithium anode candidates, silicon with the highest theoretical capacity (based on the discharge product $Li_{22}Si_4$: 4200 $mAh\ g^{-1}$) [93], have attracted intense attention from both academic and industry. However, the dramatic volume changes (up to 300%) of the silicon electrode during the cycling severe impact the cycle life and hamper the practical application of lithium-silicon alloy anode [86]. MXene can relieve the volume expansion and increase the conductivity of the Si anode. Kong et al. first synthesized the Si@Ti_3C_2 anode by using ultrasonication to mix Si powder and Ti_3C_2 [85]. Their anode provided a reversible capacity of 188 $mAh\ g^{-1}$ after 150 cycles at a current of 0.2 $A\ g^{-1}$, which is already significantly higher than the pure Si anode (17 $mAh\ g^{-1}$).

Later, Zhang et al. used the MXene inks as the binder to apply in the Si electrode [84]. Their MXene/Si-type cathode is highly scalable because the production just needs the simple and low cost slurry-casting technique (Figure 20.7). In this MXene/Si-type cathode, the highly conductive MXene nanosheet formed a continuous metallic network, which offered fast transport channels for the electrons and Li^+. Furthermore, the viscous MXene ink provided excellent flexibility with sufficient free space to accommodate the volume change of the cathode and provided good mechanical reinforcement for the thick electrode (up to 450 μm) [84].

With advanced electrode synthesis techniques, the distribution of Si on the MXene nanosheet could be more homogenous and thereby offer the Si@MXene electrode a better electrochemical performance. Hui et al. indicated a novel synthesis strategy combining *in-situ* orthosilicate hydrolysis and low-temperature reduction process to synthesize the Si/Ti_3C_2 MXene composites (Figure 20.8) [87]. They used the *in-situ* orthosilicate hydrolysis method to guide the SiO_2 nanoparticles

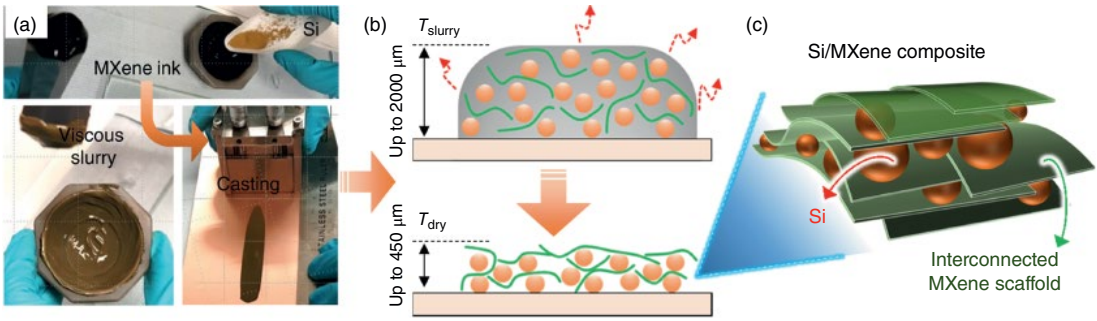


Figure 20.7 (a–c) Schematic of preparing the Si electrode with MXene ink as conductive binder by using the slurry-casting technique. *Source:* Zhang et al. [84]/Reproduced from Springer Nature/CC BY 4.0.

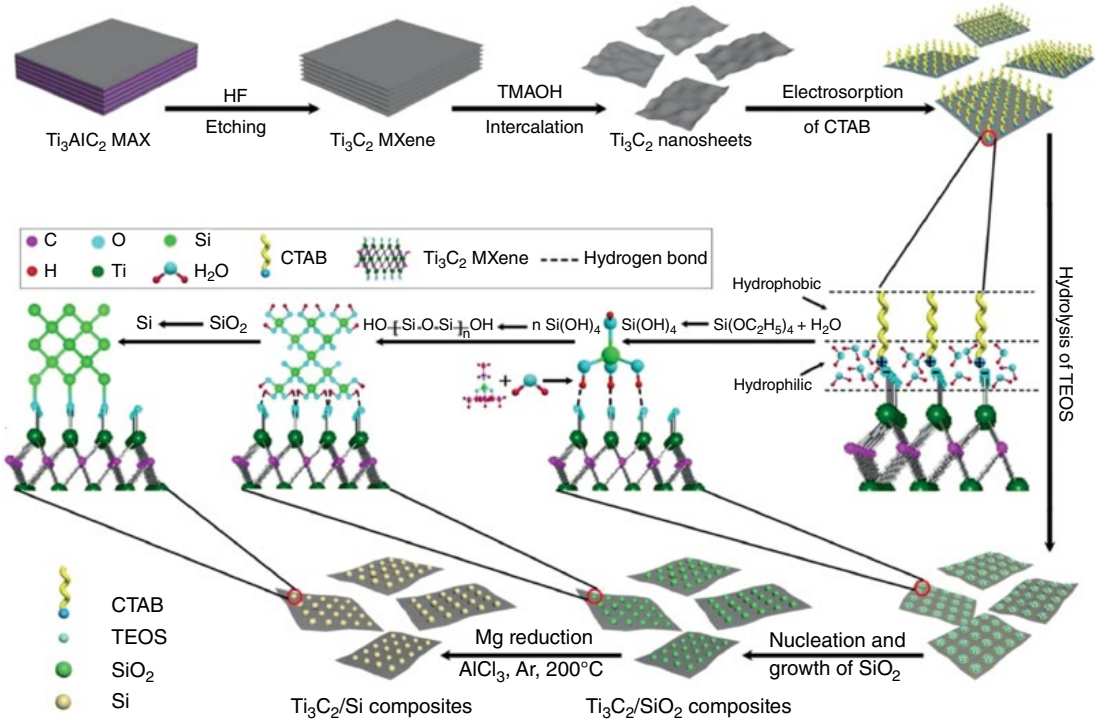


Figure 20.8 Schematic of integrating the *in-situ* orthosilicate hydrolysis and low-temperature reduction process to synthesize the Si/Ti_3C_2 MXene composites. *Source:* Hui et al. [87]/John Wiley & Sons.

nucleated and grew on the surface of MXene nanosheets homogenously, and then the SiO_2 nanoparticles were reduced to Si by the low-temperature (200 °C) reduction process. Through this advanced synthesis technique, their Si/Ti_3C_2 anode provided an excellent cycling performance with a high reversible capacity of 973 mAh g^{-1} after 800 cycles at the high current density of 1 A g^{-1} [87].

Furthermore, Luo et al. decorated the Sn^{4+} ion onto the MXene (Ti_3C_2) nanosheet by using a liquid-phase immersion process assisted with polyvinylpyrrolidone (PVP) [89]. The MXene in the electrode provided the ion-change sites, relieved the volume change during the cycling, and improved the conductivity of the electrode material. On the other hand, Sn^{4+} ions intercalated into the interlayers of MXene and play a "pillar" role, which increase the interlayer spacing for fast lithium-ion transport. Thereby, the anode PVP-Sn(IV)@ Ti_3C_2 they synthesized provided a high reversible capacity of 1374.8 mAh cm^{-3} after 50 cycles at 216.5 mA cm^{-3}, which is much higher than the graphite electrode (550 mAh cm^{-3}) and pure MXene electrode (Ti_3C_2) (197 mAh cm^{-3}) [89].

Similarly, Wang et al. decorated the Sn^{4+} ions onto the V_2C MXene, which can both expand the interlayer spacing and form the V–O–Sn bonding to stabilize the V_2C structure [88]. Their V_2C@Sn electrode delivered a superior cycling performance with the initial discharged capacity of around 1285 mAh g^{-1} and remained 1263 mAh g^{-1} after 90 cycles at 0.1 A g^{-1}.

20.3.4 Other Composites

Beyond the composites mentioned above, MXene can integrate with the traditional carbon-based host for the LIBs with enlarged ion diffusion channels. Lin et al. reported a Ti_3C_2/carbon nanofiber (CNF anode for LIBs by growing the CNF between the MXene layers (Figure 20.9a–c), which can provide the conductive pathway for the electric transport and connect the MXene particles to reduce their contact resistance [94]. Byeon et al. utilized the carbon nanotubes (CNTs) mixed with delaminated MXene (*d*-$Ti_3C_2T_x$) to form the *d*-$Ti_3C_2T_x$/CNT cathode for a hybrid Mg^{2+}/Li^+ battery system (Figure 20.9d) [95]. According to the XRD results, the CNTs effectively increased the space between MXene layers (Figure 20.9e–f). Therefore, the *d*-$Ti_3C_2T_x$/CNT cathode provided a much higher capacity (~105 mAh g^{-1} at 0.1 C) than the pure multilayer MXene (ML-$Ti_3C_2T_x$) (~40 mAh g^{-1} at 0.1 C) [95].

MXene materials integrating with other types of electrode materials such as SnO_2 [96–98], Fe_3O_4/FeS [99], Fe_2O_3 [100], TiO_2 [101], MoS_2 [45, 102, 103], and $C_6H_4O_2/C_6F_4O_2$ [104] can also perform a superior electrochemical performance in the LIB system. Zuo et al. utilized the electrostatic attraction and liquid phase reduction method to realize the homogenous *in-situ* growth of Sn/SnO_x nanoparticles between the interlayers of the MXene nanosheet [96]. The MXene ($Ti_3C_2T_x$) nanosheets effectively suppress the agglomeration and volume expansion of

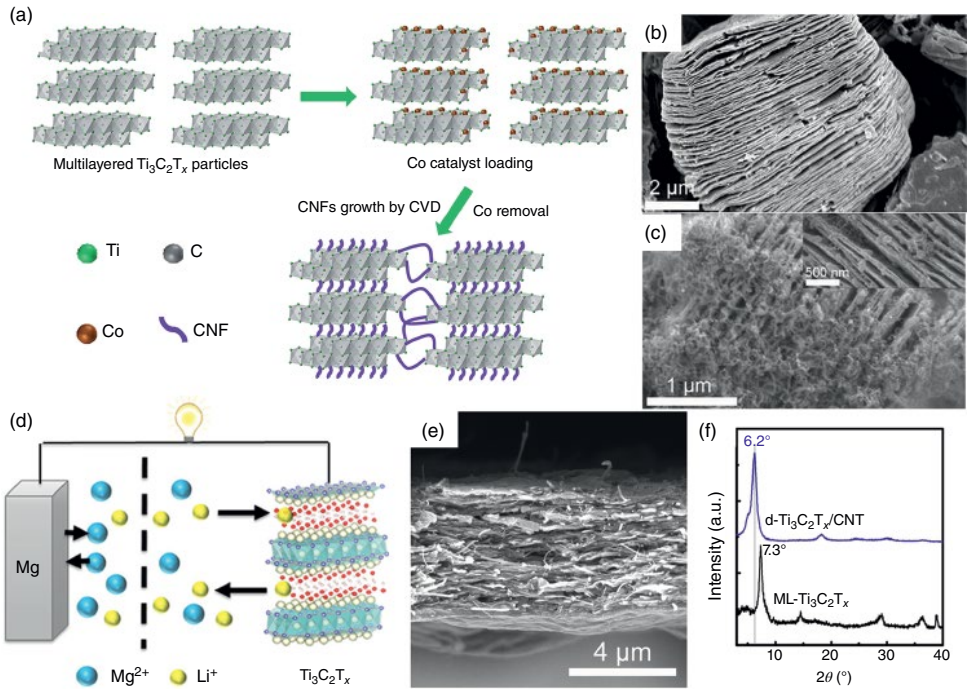


Figure 20.9 (a) Schematic of growing CNF between the MXene layers, and the SEM images of the (b) $Ti_3C_2T_x$ and (c) Ti_3C_2/CNF particles. *Source:* Lin et al. [94]/Reproduced from Royal Society of Chemistry. (d) Schematic of the hybrid Mg^{2+}/Li^+ battery system by using MXene as cathode, (e) SEM images of the cross-section of *d*-$Ti_3C_2T_x$/CNT cathode, and (f) the XRD patterns of both ML-$Ti_3C_2T_x$ and *d*-$Ti_3C_2T_x$/CNT where the shift of (002) peaks from 7.3° to 6.2° indicates the increase in *c*-lattice parameter (*c*-LP) from 24.2 Å to 28.4 Å. *Source:* Byeon et al. [95]/Reproduced from American Chemical Society.

Sn/SnO_x nanoparticles, and the Sn/SnO_x nanoparticles as the pillars that support the spacing between the MXene layers to provide fast Li^+ ion and electron transport channels. Consequently, their $Sn/SnO_x@Ti_3C_2$ anode offered a high reversible capacity of around 594 mAh g^{-1} after 200 cycles at 50 mA g^{-1} [96]. Ruan et al. reported the MXene ($Ti_3C_2T_x$) with 3D crumple and S-functionalization can integrate with Fe_3O_4/FeS heterostructures to form a stable and highly active electrode architecture [99]. They found that the sulfur functional groups on the MXene surface offered extra lithium storage sites and meanwhile the 3D crumpled structure can provide unobstructed paths for the transport of Li^+ ions and electrons inside the electrode and large free spacing to relieve the volume change. Furthermore, the FeS on the outside can modulate the electronic properties of inside Fe_3O_4, which delivered a more stable structure and improved reaction kinetics [99].

Siriwardane et al. used special linker molecules (1,4-benzoquinone ($C_6H_4O_2$) and tetrafluoro-1,4-benzoquinone ($C_6F_4O_2$)) as the pillars to increase and support the spacing between the MXene ($Ti_3C_2O_2$) layers (Figure 20.10) [104]. They indicated the MXene with pillar structure by using the $C_6H_4O_2$ and $C_6F_4O_2$ linkers can provide a very low Li^+ ion diffusion barrier (0.3 eV), as well as intercalate two layers Li between MXene layers without the Li agglomeration or breaking the pillared structure during the intercalation/deintercalation, which significantly reduce the volume change (<1.0%) of the composite during the Li loading/unloading [104].

20.4 Conclusions

Having been discovered in 2011, the MXene material system is relatively new. Most of our understanding of MXenes come from studies conducted on $Ti_3C_2T_x$, other stoichiometries still warrant further studies [105]. Pristine MXenes have shown great promises as electrode materials, additives or even current collectors in Li-ion batteries. Beyond that, the oxidation of MXenes leading to novel architectures of nanohybrid structures of oxides/carbon or oxide/carbon/MXenes synergically enhanced the electrochemical performance. Furthermore, compositing MXenes with many other materials, including carbonaceous materials, layered TMC, alloy- and conversion-type electrode materials and others, can leverage the advantages of each kind of materials and overcome the associated shortcomings, thereby improving the performance of Li-ion batteries. For instance, MXenes can effectively increase the intrinsic weak electrical conductivity of TMCs and alloy-based materials, buffer the volume change, and provide large ion channels for fast lithium ions diffusion, which offer the electrodes with higher power density and longer cycle life.

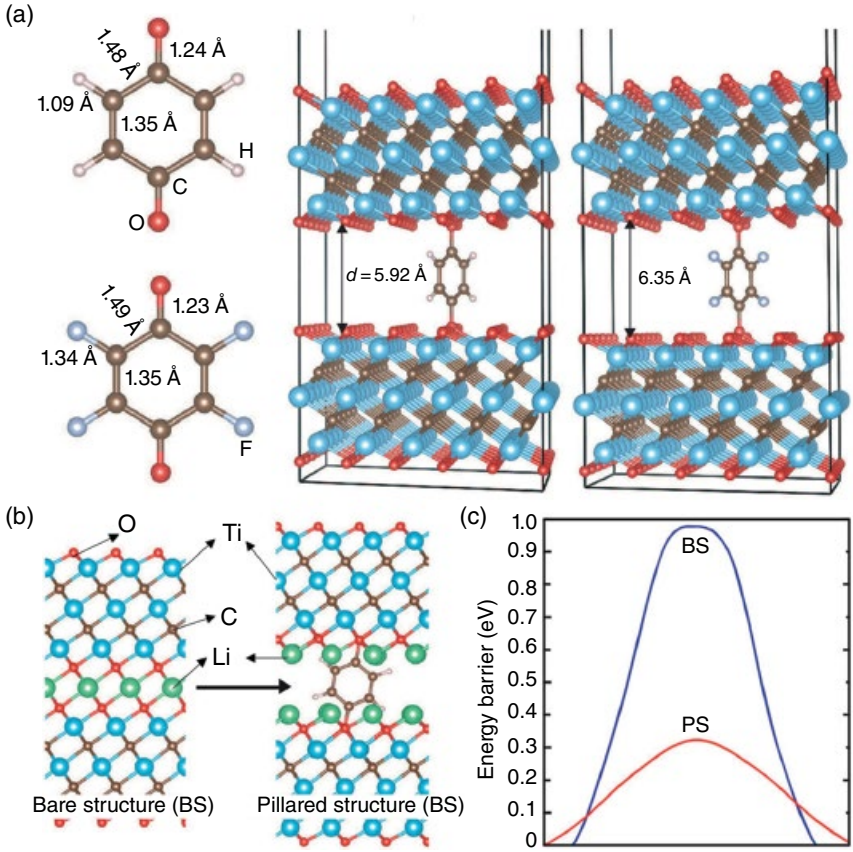


Figure 20.10 (a) Structure of $C_6H_4O_2$ and $C_6F_4O_2$ and they acted as linkers inside the MXene layer. (b) The MXene without $C_6H_4O_2$ pillars (left) and the MXene with $C_6H_4O_2$ pillars (right). (c) The comparison of the diffusion barrier of a single Li ion inside the MXene with and without $C_6H_4O_2$ pillars. *Source:* Siriwardan et al. [104]/American Chemical Society.

As we begin to understand more about this ever-expanding family of 2D materials, with hundreds of compositions theoretically predicted but not yet synthesized, future research could perhaps reveal a MXene, MXene-based composite or MXene derivative with advanced and tailored electrochemical functions for high-performance LIBs.

Acknowledgment

The authors would like to thank the financial support by the Australian Research Council (ARC) through the ARC Discovery Projects (DP200101249, DP210101389) and ARC Research Hub for Integrated Energy Storage Solutions (IH180100020).

References

1 Armand, M. and Tarascon, J.J.N. (2001). *Nature* 414: 359–367.
2 Goodenough, J.B. and Park, K.-S. (2013). *Journal of the American Chemical Society* 135: 1167–1176.
3 Whittingham, M.S. (2004). *Chemical Reviews* 104: 4271–4302.
4 Xie, Y., Naguib, M., Mochalin, V.N. et al. (2014). *Journal of the American Chemical Society* 136: 6385–6394.
5 Ming, F., Liang, H., Huang, G. et al. (2021). *Advanced Materials* 33: 2004039.
6 Yury, G. and Anasori, B. (2019). *Acs Nano* 13: 8491–8494.
7 Yorulmaz, U., Demiroğlu, İ., Çakir, D. et al. (2020). *Journal of Physics: Energy* 2: 032006.
8 Tang, Q., Zhou, Z., and Shen, P. (2012). *Journal of the American Chemical Society* 134: 16909–16916.
9 Naguib, M., Come, J., Dyatkin, B. et al. (2012). *Electrochemistry Communications* 16: 61–64.
10 Naguib, M., Halim, J., Lu, J. et al. (2013). *Journal of the American Chemical Society* 135: 15966–15969.
11 Er, D., Li, J., Naguib, M. et al. (2014). *ECS Meeting Abstracts*, 101. IOP Publishing.
12 Du, F., Tang, H., Pan, L. et al. (2017). *Electrochimica Acta* 235: 690–699.
13 Mashtalir, O., Naguib, M., Mochalin, V.N. et al. (2013). *Nature Communications* 4: 1–7.
14 Zhao, S., Meng, X., Zhu, K. et al. (2017). *Energy Storage Materials* 8: 42–48.
15 Hu, T., Hu, M., Gao, B. et al. (2018). *The Journal of Physical Chemistry C* 122: 18501–18509.
16 Eames, C. and Islam, M.S. (2014). *Journal of the American Chemical Society* 136: 16270–16276.
17 Anasori, B., Lukatskaya, M.R., and Gogotsi, Y. (2017). *Nature Reviews Materials* 2: 1–17.
18 Hart, J.L., Hantanasirisakul, K., Lang, A.C. et al. (2019). *Nature Communications* 10: 1–10.
19 Persson, P.O. and Rosen, J. (2019). *Current Opinion in Solid State and Materials Science* 23: 100774.
20 Sang, X., Xie, Y., Lin, M.-W. et al. (2016). *ACS Nano* 10: 9193–9200.
21 Hope, M.A., Forse, A.C., Griffith, K.J. et al. (2016). *Physical Chemistry Chemical Physics* 18: 5099–5102.
22 Wang, H.-W., Naguib, M., Page, K. et al. (2016). *Chemistry of Materials* 28: 349–359.
23 Natu, V., Pai, R., Sokol, M. et al. (2020). *Chem* 6: 616–630.
24 Li, Y., Shao, H., Lin, Z. et al. (2020). *Nature Materials* 19: 894–899.
25 Kamysbayev, V., Filatov, A.S., Hu, H. et al. (2020). *Science* 369: 979–983.
26 Persson, I., Näslund, L.-Å., Halim, J. et al. (2017). *2D Materials* 5: 015002.

27 Li, S., Tuo, P., Xie, J. et al. (2018). *Nano Energy* 47: 512–518.
28 Ahmed, B., Anjum, D.H., Hedhili, M.N. et al. (2016). *Nanoscale* 8: 7580–7587.
29 Bandyopadhyay, A., Ghosh, D., and Pati, S.K. (2018). *Physical Chemistry Chemical Physics* 20: 4012–4019.
30 Hu, T., Yang, J., and Wang, X. (2017). *Physical Chemistry Chemical Physics* 19: 31773–31780.
31 Ren, C.E., Zhao, M.Q., Makaryan, T. et al. (2016). *ChemElectroChem* 3: 689–693.
32 Wang, S., Li, H., Sawada, H. et al. (2017). *Nanoscale* 9: 6417–6426.
33 Meshkian, R., Dahlqvist, M., Lu, J. et al. (2018). *Advanced Materials* 30: 1706409.
34 Tao, Q., Dahlqvist, M., Lu, J. et al. (2017). *Nature Communications* 8: 1–7.
35 Lu, M., Han, W., Li, H. et al. (2019). *Energy Storage Materials* 16: 163–168.
36 Zhao, Q., Zhu, Q., Miao, J. et al. (2019). *Small* 15: e1904293.
37 Zhao, M.Q., Xie, X., Ren, C.E. et al. (2017). *Advanced Materials* 29: 1702410.
38 Bu, F., Zagho, M.M., Ibrahim, Y. et al. (2020). *Nano Today* 30: 100803.
39 Ji, C., Wang, Y., Ye, Z. et al. (2020). *ACS Applied Materials & Interfaces* 12: 24298–24307.
40 Zhang, Q., Li, Y., Chen, T. et al. (2021). *Journal of Electroanalytical Chemistry* 894: 115338.
41 Zhang, S., Ying, H., Guo, R. et al. (2019). *Journal of Physical Chemistry Letters* 10: 6446–6454.
42 Zhang, Z., Weng, L., Rao, Q. et al. (2019). *Journal of Power Sources* 439: 227107.
43 Cheng, R., Wang, Z., Cui, C. et al. (2020). *Journal of Physical Chemistry C* 124: 6012–6021.
44 Liu, R., Cao, W., Han, D. et al. (2019). *Journal of Alloys and Compounds* 793: 505–511.
45 Chen, C., Xie, X., Anasori, B. et al. (2018). *Angewandte Chemie International Edition* 57: 1846–1850.
46 Zhao, Q., Zhu, Q., Miao, J. et al. (2019). *Small* 15: 1904293.
47 Meng, R., Huang, J., Feng, Y. et al. (2018). *Advanced Energy Materials* 8: 1801514.
48 Zhang, Y., Li, J., Gong, Z. et al. (2021). *Journal of Colloid and Interface Science* 587: 489–498.
49 Yu, Y., Zhou, J., and Sun, Z. (2019). *Nanoscale* 11: 23092–23104.
50 Yang, J., Bao, W., Jaumaux, P. et al. (2019). *Advanced Materials Interfaces* 6: 1802004.
51 Naguib, M., Mashtalir, O., Lukatskaya, M.R. et al. (2014). *Chemical Communications* 50: 7420–7423.
52 He, S., Zhu, Q., Soomro, R.A., and Xu, B. (2020). *Sustainable Energy & Fuels* 4: 4988–5004.
53 Wang, R., Wang, S., Zhang, Y. et al. (2018). *Journal of Materials Chemistry A* 6: 1017–1027.
54 Zou, G., Liu, B., Guo, J. et al. (2017). *ACS Applied Materials & Interfaces* 9: 7611–7618.
55 Deng, D., Kim, M.G., Lee, J.Y., and Cho, J. (2009). *Energy & Environmental Science* 2: 818–837.

56 Saravanan, K., Ananthanarayanan, K., and Balaya, P. (2010). *Energy & Environmental Science* 3: 939–948.
57 Han, H., Song, T., Bae, J.-Y. et al. (2011). *Energy & Environmental Science* 4: 4532–4536.
58 Tian, Y., An, Y., Wei, H. et al. (2020). *Chemistry of Materials* 32: 4054–4064.
59 Maduraiveeran, G., Sasidharan, M., and Jin, W. (2019). *Progress in Materials Science* 106: 100574.
60 Fang, Y., Hu, R., Liu, B. et al. (2019). *Journal of Materials Chemistry A* 7: 5363–5372.
61 Ghassemi, H., Harlow, W., Mashtalir, O. et al. (2014). *Journal of Materials Chemistry A* 2: 14339–14343.
62 Yuan, W., Cheng, L., Zhang, Y. et al. (2017). *Advanced Materials Interfaces* 4: 1700577.
63 Tang, H., Zhuang, S., Bao, Z. et al. (2016). *ChemElectroChem* 3: 871–876.
64 Zhang, C., Kim, S.J., Ghidiu, M. et al. (2016). *Advanced Functional Materials* 26: 4143–4151.
65 Byeon, A., Hatter, C.B., Park, J.H. et al. (2017). *Electrochimica Acta* 258: 979–987.
66 Zhang, H., Wang, L., Shen, C. et al. (2017). *Electrochimica Acta* 248: 178–187.
67 Sun, N., Zhu, Q., Anasori, B. et al. (2019). *Advanced Functional Materials* 29: 1906282.
68 Zhang, P., Soomro, R.A., Guan, Z. et al. (2020). *Energy Storage Materials* 29: 163–171.
69 Ding, B., Wang, J., Wang, Y. et al. (2016). *Nanoscale* 8: 11136–11142.
70 Yuan, W., Cheng, L., Wu, H. et al. (2018). *Chemical Communications* 54: 2755–2758.
71 Thapaliya, B.P., Jafta, C.J., Lyu, H. et al. (2019). *ChemSusChem* 12: 1316–1324.
72 Huang, X., Tang, J., Luo, B. et al. (2019). *Advanced Energy Materials* 9: 1901872.
73 Lai, S., Jeon, J., Jang, S.K. et al. (2015). *Nanoscale* 7: 19390–19396.
74 Jin, J., Xiao, T., Zhang, Y.-f. et al. (2021). *Nanoscale* 13: 19740–19770.
75 Farahmandjou, M. and Jurablu, S. (2014). *International Journal of Bio Inorganic Hybrid Nanomaterials* 3: 84.
76 Farahmandjou, M. and Salehizadeh, S.A.J.G.P. (2013). *Chemistry* 39: 473–479.
77 Choi, W., Choudhary, N., Han, G.H. et al. (2017). *Materials Today* 20: 116–130.
78 Guan, B., Li, Y., Yin, B. et al. (2017). *Chemical Engineering Journal* 308: 1165–1173.
79 Xiao, J., Choi, D., Cosimbescu, L. et al. (2010). *Chemistry of Materials* 22: 4522–4524.
80 Ma, W., Liu, X., Lei, X. et al. (2018). *Chemical Engineering Journal* 334: 725–731.
81 Ye, H., Ma, L., Zhou, Y. et al. (2017). *Proceedings of the National Academy of Sciences U SA* 114: 13091–13096.
82 Li, H., Chen, X., Zalnezhad, E. et al. (2020). *Journal of Industrial and Engineering Chemistry* 82: 309–316.
83 Tang, H., Guo, R., Jiang, M. et al. (2020). *Journal of Power Sources* 462: 228152.
84 Zhang, C.J., Park, S.-H., Seral-Ascaso, A. et al. (2019). *Nature Communications* 10: 849.

85 Kong, F., He, X., Liu, Q. et al. (2018). *Electrochemistry Communications* 97: 16–21.
86 Zhang, Y., Mu, Z., Lai, J. et al. (2019). *ACS Nano* 13: 2167–2175.
87 Hui, X., Zhao, R., Zhang, P. et al. (2019). *Advanced Energy Materials* 9: 1901065.
88 Wang, C., Chen, S., Xie, H. et al. (2019). *Advanced Energy Materials* 9: 1802977.
89 Luo, J., Tao, X., Zhang, J. et al. (2016). *ACS Nano* 10: 2491–2499.
90 Mao, Y., Chen, R., You, H. et al. (2022). *Journal of Alloys and Compounds* 904: 164000.
91 Ren, M., Cao, D., Jiang, W. et al. (2021). *Electrochimica Acta* 373: 137835.
92 Guo, X., Xie, X., Choi, S. et al. (2017). *Journal of Materials Chemistry A* 5: 12445–12452.
93 Liu, X.H. and Huang, J.Y. (2011). *Energy & Environmental Science* 4: 3844–3860.
94 Lin, Z., Sun, D., Huang, Q. et al. (2015). *Journal of Materials Chemistry A* 3: 14096–14100.
95 Byeon, A., Zhao, M.Q., Ren, C.E. et al. (2017). *ACS Applied Materials Interfaces* 9: 4296–4300.
96 Zuo, D.-C., Song, S.-C., An, C.-S. et al. (2019). *Nano Energy* 62: 401–409.
97 Ahmed, B., Anjum, D.H., Gogotsi, Y., and Alshareef, H.N. (2017). *Nano Energy* 34: 249–256.
98 Wang, F., Wang, Z., Zhu, J. et al. (2016). *Journal of Materials Science* 52: 3556–3565.
99 Ruan, T., Wang, B., Yang, Y. et al. (2020). *Advanced Materials* 32: e2000151.
100 Ali, A., Hantanasirisakul, K., Abdala, A. et al. (2018). *Langmuir* 34: 11325–11334.
101 Li, L., Jiang, G., An, C. et al. (2020). *Nanoscale* 12: 10369–10379.
102 Zheng, M., Guo, R., Liu, Z. et al. (2018). *Journal of Alloys and Compounds* 735: 1262–1270.
103 Shen, C., Wang, L., Zhou, A. et al. (2017). *Journal of the Electrochemical Society* 164: A2654–A2659.
104 Siriwardane, E.M.D., Demiroglu, I., Sevik, C., and Çakır, D. (2019). *ACS Applied Energy Materials* 2: 1251–1258.
105 Naguib, M., Barsoum, M.W., and Gogotsi, Y. (2021). *Advanced Materials* 33: 2103393.

21

MXenes in Rechargeable Batteries Beyond Li-Ion Battery

Zhuoqi Cen[1,2], Qing Huang[1,2], and Kun Liang[1,2]

[1] *Zhejiang Key Laboratory of Data-Driven High-Safety Energy Materials and Applications, Ningbo Key Laboratory of Special Energy Materials and Chemistry, Ningbo Institute of Materials Technology and Engineering, Chinese Academy of Sciences, Ningbo, Zhejiang, China*
[2] *Qianwan Institute of CNITECH, Ningbo, Zhejiang, China*

21.1 Introduction

In recent years, with the rapid increase in the use of lithium-ion batteries (LIBs), the shortage of lithium resources has become more and more prominent. However, the unbalanced distribution of global lithium resources and the severe safety concerns of lithium metal anodes limit the penetration of LIBs into these high-capacity markets. Furthermore, material-level advancements are approaching the fundamental limits of LIBs technology after increasing energy densities and cost over the past few decades. Due to the advantages of abundant reserves, lower cost, significant theoretical capability, appropriate potential (negative redox), operational comfort, and environmental friendliness, research on non–Li-ion batteries (NLIBs) has attracted more and more attention. For example, sodium-ion batteries [1], potassium-ion batteries [2], magnesium-ion batteries [3], aluminum-ion batteries [4], and calcium-ion batteries [5]. Similar to LIBs, the electrochemical performance of NLIBs largely depends on their electrode materials structures and properties, where Table 21.1 summarizes the theoretical capacities of different types of batteries.

In the past decade, MXene-based materials have been extensively studied in NLIBs. The representative historical timeline of energy storage applications of MXenes in NLIBs is shown in Figure 21.1: (i) in 2011, the multilayered MXene ($Ti_3C_2T_x$) was discovered [6]; (ii) in 2012, MXene was applied to the LIBs anode [7]; (iii) in 2014, the first-principles density functional theory (DFT)

Transition Metal Carbides and Nitrides (MXenes) Handbook: Synthesis, Processing, Properties and Applications, First Edition. Edited by Chuanfang Zhang and Michael Naguib.
© 2024 John Wiley & Sons, Inc. Published 2024 by John Wiley & Sons, Inc.

Table 21.1 A summary of the theoretical capacities of different types of batteries.

Battery	LIB	SIB	PIB	MIB	AIB	CIB	LSB
Theoretical capacity ($mAh\,g^{-1}$)	3860	1165	687	2205	2980	1340	1675

calculations were used to explore the performance of MXene as electrode material for ion batteries with different metals (Li, Na, K, Mg, Al, and Ca) [5, 8]; (iv) in 2015, MXene was used as a sulfur-host cathode material for lithium sulfur batteries (LSBs) [9]; (v) in 2016, MXene was used as a separator material for LSBs [10]; (vi) in 2017, the experiment proved that MXene can be applied to the cathode material of hybrid Mg^{2+}/Li^{+} batteries (MLIBs) [11], potassium-ion batteries (PIBs) [12] and aluminum-ion batteries (AIBs) [4]; (vii) in 2019, MXene was used as sulfur-host cathode materials for room-temperature sodium-sulfur batteries (RT-SSBs) [13] and magnesium-sulfur batteries (MSBs) [14]. Moreover, the application of MXenes in calcium-ion batteries is only in the stage of theoretical research and has not yet been applied in practice. In this chapter, we summarize the research progress of MXene-based materials in various non-lithium battery energy storage applications, especially in SIBs, PIBs, MIBs, AIBs, LSBs, RT-SSBs, MSBs, etc. To compare the performance of MXenes in various energy storage applications, MXene-based materials for NLIBs are shown in Table 21.2 and Figure 21.2.

21.2 Metal-Ion Batteries

21.2.1 Sodium-Ion Batteries

SIBs are considered promising for large-scale energy storage applications due to their rich sodium resources (the fourth element in the earth), associated low cost, and a storage mechanism similar to LIBs, which depends on the process of sodium-ions embedding/depositioning from the positive and negative poles [96]. However, compared with lithium, Na^{+} has a larger ionic radius (0.102 nm), a higher standard reduction potential (−2.71 V vs. SHE), and a lower electronegativity (0.93), resulting in slower diffusion kinetics of sodium ions in the solid state, a sharp drop in capacity [97]. To solve these problems, an effective solution is to develop nano-electrode materials for SIBs with high capacity and high rate performance [98]. The diffusion time of Na^{+} can be significantly reduced by reducing the sodium-ion embedding/extraction pathway. On the other hand, increasing conductivity can also affect ionic conductivity relative to the neutralization of charge in solid electrode materials [99].

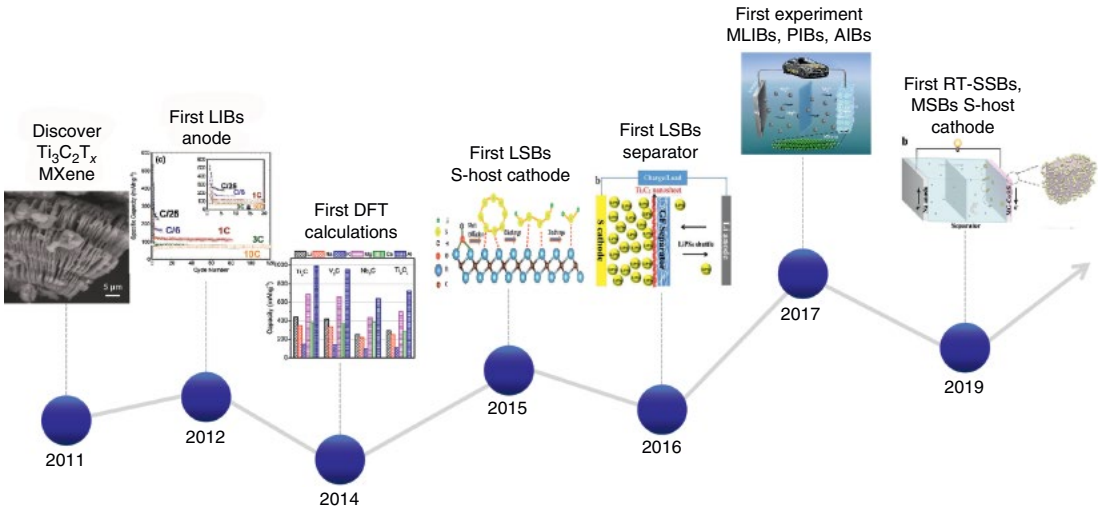


Figure 21.1 The representative historical timeline of energy storage applications of MXenes in NLIBs.

Table 21.2 Summary of electrochemical performance of MXenes for non–lithium-ion batteries.

Material	Electrolyte	Device	Rate performance	Stability (Last cycle capacity [$mAh\,g^{-1}$])/ cycles/current density	References
$Ti_3C_2T_x$	1M $NaClO_4$+ EC/ DEC = 4 : 6(vol%)	SIBs	53.7 $mAh\,g^{-1}$ at 0.8 $A\,g^{-1}$	68.3/1000/0.2 $A\,g^{-1}$	[15]
$Ti_3C_2T_x$	1 M $NaPF_6$+ EC/ DEC = 1 : 1(vol%)	SIBs	70 $mAh\,g^{-1}$ at 0.5 $A\,g^{-1}$, 250 $mAh\,g^{-1}$ at 0.02 $A\,g^{-1}$	90/100/0.02 $A\,g^{-1}$	[16]
$Ti_3C_2T_x$	1M $NaClO_4$+ EC/ PC = 1 : 1(vol%)+ 5 vol% FEC	SIBs	330 $mAh\,g^{-1}$ at 0.25 C, 120 $mAh\,g^{-1}$ at 25 C	295/1000/2.5 C	[17]
V_2CT_x	—	SIBs	340 $mAh\,g^{-1}$ at 0.25 C, 170 $mAh\,g^{-1}$ at 25 C	310/1000/2.5 C	
Mo_2CT_x	—	SIBs	370 $mAh\,g^{-1}$ at 0.25 C, 125 $mAh\,g^{-1}$ at 25 C	290/1000/2.5 C	
V_2CT_x	1M $NNaPF_6$+ EC/ DMC = 3 : 7(vol%)	SIBs	50.4 $mAh\,g^{-1}$ at 1 $A\,g^{-1}$, 90 $mAh\,g^{-1}$ at 0.01 $A\,g^{-1}$, 83 $mAh\,g^{-1}$ at 0.01 $A\,g^{-1}$	78/100/0.02 $A\,g^{-1}$	[18]
$Nb_4C_3T_x$	1M $NaClO_4$+ PC+ 5 wt% FEC	SIBs	71.5 $mAh\,g^{-1}$ at 2 $A\,g^{-1}$, 152 $mAh\,g^{-1}$ at 0.1 $A\,g^{-1}$	69/100/0.1 A g^{-1}	[19]
Ti_3CN	1 M $NaPF_6$+ EC/ DEC = 1 : 1(vol%)	SIBs	98.9 $mAh\,g^{-1}$ at 0.5 $A\,g^{-1}$; 507 $mAh\,g^{-1}$ at 0.02 $A\,g^{-1}$	73.5/500/0.2 A g^{-1}	[20]
a-$Ti_3C_2T_x$	1M $NaCF_3SO_3$ +DME	SIBs	84 $mAh\,g^{-1}$ at 0.2 $A\,g^{-1}$, 168 $mAh\,g^{-1}$ at 0.02 $A\,g^{-1}$	50/500/0.2 A g^{-1}	[21]
	0.8 M KPF_6+ EC/DEC = 1 : 1(vol%)	PIBs	78 $mAh\,g^{-1}$ at 0.2 $A\,g^{-1}$, 136 $mAh\,g^{-1}$ at 0.02 $A\,g^{-1}$	42/500/0.2 A g^{-1}	

c-$Ti_3C_2T_x$	1M $NaClO_4$+ EC/PC = 1 : 1(vol%)+ 5% FEC	SIBs	120 mAh g^{-1} at 0.5 A g^{-1}, 250 mAh g^{-1} at 0.02 A g^{-1}	246/50/0.02 A g^{-1}	[22]
p-$Ti_3C_2T_x$	1M $NaClO_4$+ EC/ PC = 1 : 1(vol%)+ 5 vol% FEC	SIBs	24 mAh g^{-1} at 100 A g^{-1}, 124 mAh g^{-1} at 10 A g^{-1}, 166 mAh g^{-1} at 1 A g^{-1}	189/1000/1 A g^{-1}	[23]
Na- Ti_3C_2	1M $NaClO_4$+ EC/ PC = 1 : 1(vol%)+ 5 wt% FEC	SIBs	175 mAh g^{-1} at 0.1 A g^{-1}, 168 mAh g^{-1} at 0.1 A g^{-1}	85/2000/2 A g^{-1}	[24]
Na-c-$Ti_3C_2T_x$	1M $NaClO_4$+ EC/ DMC = 1 : 1(vol%)+ 5 wt% FEC	SIBs	61 mAh g^{-1} at 1 A g^{-1}	130/500/0.1 A g^{-1}	[25]
Ti_3C_2-M-NTO	1 M $NaCF_3SO_3$+ DME	SIBs	101 mAh g^{-1} at 2 A g^{-1}, 196 mAh g^{-1} at 0.05 A g^{-1}	150/0.2 A g^{-1}	[26]
Ti_3C_2-M-KTO	1 M KPF_6+DME	PIBs	151 mAh g^{-1} at 0.05 A g^{-1}, 88 mAh g^{-1} at 0.3 A g^{-1}	900/0.2 A g^{-1}	
f-$Ti_3C_2T_x$-DMSO	1M $NaClO_4$+ EC/ PC = 1 : 1(vol%)+ 5 wt% FEC	SIBs	110 mAh g^{-1} at 2 A g^{-1}, 267 mAh g^{-1} at 0.1 A g^{-1}	76/1500/1 A g^{-1}	[27]
S-decorated $Ti_3C_2T_x$	1M $NaClO_4$+ EC/ PC = 1 : 1(vol%)	SIBs	136.6 mAh g^{-1} at 5 A g^{-1}	135/1000/2 A g^{-1}	[28]
S-doped $Ti_3C_2T_x$	1M $NaClO_4$+ EC/PC = 1 : 1 (wt%)+ 5 wt% FEC	SIBs	113.9 mAh g^{-1} at 4 A g^{-1}, 121.3 mAh g^{-1} at 2 A g^{-1}	138.2/2000/0.5 A g^{-1}	[29]
CTAB-S@Ti_3C_2-450	1M $NaClO_4$+ EC/ PC = 1 : 1(vol%)+ 5 wt% FEC	SIBs	120 mAh g^{-1} at 15 A g^{-1}	492/100/0.1 A g^{-1}, 77/5000/10 A g^{-1}	[30]
CT-Sn(II)@Ti_3C_2	1M $NaClO_4$+ EC/ DEC = 1 : 1(vol%)	SIBs	100 mAh g^{-1} at 2 C (1 C = 117 mA g^{-1})	95/200/1 C	[31]
$Ti_3C_2T_x$/Sb-0.5	1M $NaClO_4$+ EC/ PC = 1 : 1(vol%)+ 5% FEC	SIBs	127 mAh g^{-1} at 2 A g^{-1}, 212 mAh g^{-1} at 0.1 A g^{-1}	148/8000/1 A g^{-1}	[32]

(*Continued*)

Table 21.2 (Continued)

Material	Electrolyte	Device	Rate performance	Stability (Last cycle capacity [mAh g^{-1}])/ cycles/current density	References
$Ti_3C_2T_x$/BP	1M $NaClO_4$+ EC/ PC = 1 : 1(vol%)	SIBs	67.3 mAh g^{-1} at 1 A g^{-1}, 774.4 mAh g^{-1} at 0.1 A g^{-1},132 mAh g^{-1} at 0.1 A g^{-1}	100/200/0.1 A g^{-1}	[33]
Ti_3C_2/PDDA-BP	1M $NaClO_4$+ EC/DMC/ EMC = 1 : 1 : 1(wt%)+ 5 wt% FEC	SIBs	464 mAh g^{-1} at 2 A g^{-1}, 1767 mAh g^{-1} at 0.1 A g^{-1},1210 mAh g^{-1} at 0.1 A g^{-1}	658/2000/1 A g^{-1}	[34]
$Ti_3C_2T_x$/BPQDs	1M $NaClO_4$+ PC+ 5 wt% FEC	SIBs	120 mAh g^{-1} at 2 A g^{-1}, 723 mAh g^{-1} at 0.05 A g^{-1}	100/1000/1 A g^{-1}	[35]
$Ti_3C_2T_x$/ phosphorene	1M $NaClO_4$+ EC/ PC = 1 : 1(vol%)	SIBs	193 mAh g^{-1} at 5 A g^{-1}, 535 mAh g^{-1} at 0.1 A g^{-1}	298/1000/1 A g^{-1}	[36]
$Ti_3C_2T_x$/CNTs	1M $NaClO_4$+ EC/ PC = 1 : 1(vol%)+ 5vol% FEC	SIBs	89 mAh cm^{-3} at 5 A g^{-1}, 421 mAh cm^{-3} at 0.02 A g^{-1}	345 mAh cm−3/500/0.1 A g^{-1}	[37]
$Ti_3C_2T_x$/SnS	1M $NaClO_4$+ EC/ DEC = 1 : 1(vol%)	SIBs	256 mAh g^{-1} at 1 A g^{-1}, 413 mAh g^{-1} at 0.1 A g^{-1}	320/50/0.5 A g^{-1}	[38]
$Ti_3C_2T_x$/SnS_2(5 : 1)	1M $NaClO_4$+ EC/ PC = 1 : 1(vol%)+ 5 wt% FEC	SIBs	78 mAh g^{-1} at 2 A g^{-1}, 377 mAh g^{-1} at 0.1 A g^{-1}, 230 mAh g^{-1} at 0.1 A g^{-1}	322/200/0.1 A g^{-1}	[39]
$Ti_3C_2T_x$/CoS	1M $NaSO_3CF_3$+DME	SIBs	272 mAh g^{-1} at 5 A g^{-1}	267/1700/2 A g^{-1}	[40]
$Ti_3C_2T_x$/Bi_2S_2	1M $NaSO_3CF_3$+DME	SIBs	168 mAh g^{-1} at 5 A g^{-1},407 mAh g^{-1}at 0.1 A g^{-1}	155/250/0.5 A g^{-1}	[41]
$Ti_3C_2T_x$/MoS_2	1M $NaClO_4$+ EC/ PC = 1 : 1(vol%)+ 5 wt% FEC	SIBs	162.7 mAh g^{-1} at 1 A g^{-1}, 330.6 mAh g^{-1} at 0.1 A g^{-1}	250.9/100/0.1 A g^{-1}	[42]

$Ti_3C_2T_x/MoS_2$	1M $NaClO_4$+ EC/ DEC = 1 : 1(vol%)	SIBs	186.2 mAh g^{-1} at 0.8 A g^{-1}, 411 mAh g^{-1} at 0.05 A g^{-1}	331/70/0.1 A g^{-1}	[43]
MoS_2-in-Ti_3C_2	1M $NaClO_4$+ EC/ DMC = 1 : 1(vol%)+ 5 wt% FEC	SIBs	241 mAh g^{-1} at 3 A g^{-1}	310/1600/1 A g^{-1}	[44]
$Ti_3C_2T_x/FeS_2$	1M $NaClO_4$+PC+ 5% FEC	SIBs	186 mAh g^{-1} at 10 A g^{-1}, 665 mAh g^{-1} at 0.1 A g^{-1},	563/100/0.1 A g^{-1}	[45]
$Ti_3C_2T_x/FePS_3$	1M $NaPF_6$+ EC/ DEC = 1 : 1(vol%)+ 5% FEC	SIBs	449 mAh g^{-1} at 5 A g^{-1}, 767 mAh g^{-1} at 0.1 A g^{-1},792 mAh g^{-1} at 0.1 A g^{-1}	676.1/90/0.1 A g^{-1}	[46]
$Ti_3C_2T_x/MoSe_2$	1M $NaClO_4$+ EC/ PC = 1 : 1(wt%)+ 5 wt% FEC	SIBs	250 mAh g^{-1} at 10 A g^{-1}, 490 mAh g^{-1} at 1 A g^{-1}	434/200/1 A g^{-1}	[47]
$Ti_3C_2T_x/CoSe2$@ NC	1M $NaClO_4$+ EC/ DMC = 1 : 1(vol%)+ 5 wt% FEC	SIBs	343 mAh g^{-1} at 7 A g^{-1}, 507 mAh g^{-1} at 0.2 A g^{-1}	317/200/0.5 A g^{-1}	[48]
	3M KFSI+DGM	PIBs	276mAh g^{-1} at 2 A g^{-1}, 430 mAh g^{-1} at 0.1 A g^{-1},463 mAh g^{-1} at 0.1 A g^{-1}	358/100/0.5 A g^{-1}	
$Cu_{1.75}Se$-MXene-CNRib	1M $NaClO_4$+ EC/ DMC = 1 : 1(vol%)	SIBs	355.3 mAh g^{-1} at 5 A g^{-1}, 611.2 mAh g^{-1} at 0.1 A g^{-1}, 536.3 mAh g^{-1}at 0.1 A g^{-1}	480.7/1000/1 A g^{-1}	[49]
$NiSe_2$-MXene-CNRib	—	SIBs	504.9 mAh g^{-1} at 0.1 A g^{-1}	416.1/1000/1 A g^{-1}	
$CoSe_2$-MXene-CNRib	—	SIBs	415.3 mAh g^{-1} at 0.1 A g^{-1}	302.4/1000/1 A g^{-1}	
$Cu_{1.75}Se$-MXene-CNRib	0.8M KPF_6+ EC/ DMC = 1 : 1(vol%)	PIBs	161.3 mAh g^{-1} at 5 A g^{-1}, 435.3 mAh g^{-1} at 0.1 A g^{-1}, 375.8 mAh g^{-1} at 0.1 A g^{-1}	305.6/400/1 A g^{-1}	

(*Continued*)

Table 21.2 (Continued)

Material	Electrolyte	Device	Rate performance	Stability (Last cycle capacity [mAh g^{-1}])/ cycles/current density	References
$Ti_3C_2T_x/VO_2$	1M $NaClO_4$+ EC/ DEC = 1 : 1(vol%)+ 5 wt% FEC	SIBs	206 mAh g^{-1} at 1.6 A g^{-1}	280.9/200/0.1 A g^{-1}	[50]
$Ti_3C_2T_x/Sb_2O_3$	1M $NaClO_4$+ EC/ PC = 1 : 1(vol%)+ 5% FEC	SIBs	295 mAh g^{-1} at 2 A g^{-1}, 422 mAh g^{-1} at 0.5 A g^{-1},383 mAh g^{-1} at 1 A g^{-1}	472/100/0.1 A g^{-1}	[51]
$Ti_3C_2T_x/TiO_2$	1M $NaClO_4$+ EC/ PC = 1 : 1(vol%)+ 5% FEC	SIBs	68 mAh g^{-1} at 3.84 A g^{-1}, 218 mAh g^{-1} at 0.03 A g^{-1}	110/5000/0.96 A g^{-1}	[52]
$Ti_3C_2T_x/TiO_2$	1M $NaClO_4$+ EC/ DEC = 1 : 1(vol%)	SIBs	52 mAh g^{-1} at 2 A g^{-1}, 156 mAh g^{-1} at 0.05 A g^{-1},148 mAh g^{-1} at 0.05 A g^{-1}	101/500/0.2 A g^{-1}	[53]
$Ti_3C_2T_x/TiO_2$	1M $NaPF_6$+ EC/ DMC = 1 : 1(vol%)+ 5 vol% FEC	SIBs	151.5 mAh g^{-1} at 1 A g^{-1}, 237.8 mAh g^{-1} at 0.1 A g^{-1},209.2 mAh g^{-1} at 0.1 A g^{-1}	153/100/0.6 A g^{-1}	[54]
Nb_2CT_x/Nb_2O_5	1M $NaClO_4$+ EC/ DMC = 1 : 1(vol%)+ 10% FEC	SIBs	99 mAh g^{-1} at 2 A g^{-1}, 262 mAh g^{-1} at 0.1 A g^{-1}, 226 mAh g^{-1} at 0.1 A g^{-1}	102/500/1 A g^{-1}	[55]
$Ti_3C_2/Na_{0.23}TiO_2$	1M $NaClO_4$+ PC+ 5 wt% FEC	SIBs	47 mAh g^{-1} at 3 A g^{-1}, 138 mAh g^{-1} at 0.1 A g^{-1},123 mAh g^{-1} at 0.1 A g^{-1}	56/4000/2 A g^{-1}	[56]
Ti_3C_2/NTO	1M $NaClO_4$+ EC/ PC = 1 : 1(vol%)+ 5wt% FEC	SIBs	78 mAh g^{-1} at 2 A g^{-1}, 157 mAh g^{-1} at 0.05 A g^{-1},152 mAh g^{-1} at 0.05 A g^{-1}	82/1900/2 A g^{-1}	[57]

CoS_2/CNT/TiO_xN_y	1M $NaClO_4$+ EC/ DEC = 1 : 1(vol%)	SIBs	166 mAh g^{-1} at 2 A g^{-1}, 403 mAh g^{-1} at 0.1 A g^{-1}	106/50/1 A g^{-1}	[58]
$Ti_3C_2T_x$/$CoNiO_2$	1M $NaClO_4$+ EC/ DEC = 1 : 1(vol%)	SIBs	188.4 mAh g^{-1} at 0.3 A g^{-1}, 413.4 mAh g^{-1} at 0.02 A g^{-1}	223/140/0.1 A g^{-1}	[59]
$Ti_3C_2T_x$/ $NaTi_2(PO_4)_3$	1M $NaClO_4$+ EC/DEC	SIBs	67 mAh g^{-1} at 2 A g^{-1}, 145 mAh g^{-1} at 0.05 A g^{-1}	121/500/0.2 A g^{-1}	[60]
$Ti_3C_2T_x$/NiCoP	1M $NaClO_4$+ EC/DMC/ EMC = 1 : 1 : 1(wt%)+ 5wt% FEC	SIBs	240.1 mAh g^{-1} at 2 A g^{-1}, 416.9 mAh g^{-1} at 0.1 A g^{-1}	261.7/2000/1 A g^{-1}	[61]
$Ti_3C_2T_x$/HC	1M $NaClO_4$+ EC/ DEC = 1 : 1(vol%)	SIBs	66.7 mAh g^{-1} at 10 A g^{-1}, 98.2 mAh g^{-1} at 2 A g^{-1}, 368.5 mAh g^{-1} at 0.03 A g^{-1}	272.3/1500/0.2 A g^{-1}	[62]
	1M KPF_6+ EC/ DEC = 1 : 1(vol%)	PIBs	102.2 mAh g^{-1} at 0.5 A g^{-1}	210/100/0.05 A g^{-1}	
$Ti_3C_2T_x$@NTP-C	1M $NaClO_4$+ EC/ DEC = 1 : 1(vol%)+ 5 wt% FEC	SIBs	102 mAh g^{-1} at 10 A g^{-1}, 208 mAh g^{-1} at 0.1 A g^{-1},188 mAh g^{-1} at 0.1 A g^{-1}	148/2000/1 A g^{-1}	[63]
Ti_3CNT_x	0.8M KPF_6+ EC/ DEC = 1 : 1(vol%)	PIB	32 mAh g^{-1} at 0.5 A g^{-1}, 90 mAh g^{-1} at 0.01 A g^{-1},80 mAh g^{-1} at 0.01 A g^{-1}	75/100/0.02 A g-1	[12]
$Ti_3C_2T_x$@Sb	5M KFSI+DME	PIB	270 mAh g^{-1} at 0.5 A g^{-1}, 504 mAh g^{-1} at 0.05 A g^{-1},475 mAh g^{-1} at 0.05 A g^{-1}	213.3/500/0.5 A g^{-1}	[64]
PDDA-NPCN/ Ti_3C_2	0.8M KPF_6+ EC/ DEC = 1 : 1(vol%)	PIBs	191.2 mAh g^{-1} at 2 A g^{-1}, 499.8 mAh g^{-1} at 0.1 A g^{-1},363.8 mAh g^{-1} at 0.1 A g^{-1}	252.2/2000/1 A g^{-1}	[65]

(*Continued*)

Table 21.2 (Continued)

Material	Electrolyte	Device	Rate performance	Stability (Last cycle capacity [mAh g^{-1}])/ cycles/current density	References
$MoSe_2$/MXene@C	1M KFSI+ EC/ DEC = 1 : 1(vol%)	PIBs	183 mAh g−1 at 10 A g−1, 350 mAh g−1 at 0.1 A g−1,381 mAh g−1 at 0.1 A g−1	207/300/5 A g^{-1}	[66]
K-V_2C	0.8M KPF_6+ EC/ DEC = 1 : 1(vol%)	PIBs	70 mAh g^{-1} at 3 A g^{-1}, 195 mAh g^{-1} at 0.05 A g^{-1}	152/10/0.1 A g^{-1}	[67]
3D-$Ti_3C_2T_x$	0.8M KPF_6+ EC/ DEC = 1 : 1(vol%)	PIBs	88 mAh g^{-1} at 2 A g^{-1}, 137 mAh g^{-1} at 0.2 A g^{-1},131 mAh g^{-1} at 0.2 A g^{-1}	122/10000/1 A g^{-1}	[68]
BPE@V_2CT_x	0.8M KPF_6+ EC/ DEC = 1 : 1(vol%)	PIBs	229.6 mAh g^{-1} at 2 A g^{-1}, 593.6 mAh g^{-1} at 0.1 A g^{-1},523.8 mAh g^{-1} at 0.1 A g^{-1}	485/3000/0.2 A g^{-1},261/3000/2 A g^{-1},	[69]
Sb/Na-$Ti_3C_2T_x$	4M KTFSI+ EC/ DEC = 1 : 1(vol%)	PIBs	127 mAh g^{-1} at 2 A g^{-1}, 558.9 mAh g^{-1} at 0.1 A g^{-1},398.9 mAh g^{-1} at 0.1 A g^{-1}	392.2/450/0.1 A g g^{-1},258/1200/0.5 A g^{-1}	[70]
3D-a-$Ti_3C_2T_x$	0.8M KFSI+ EC/ DEC = 1 : 1(vol%)	PIBs	82.9 mAh g^{-1} at 0.5 A g^{-1}, 89.9 mAh g^{-1} at 0.3 A g^{-1}	97.5/1000/0.2 A g^{-1}	[71]
$Fe_{x-1}Se_x/Ti_3C_2T_x$/ FCR	1M $NaClO_4$+ EC/ DMC = 1 : 1(vol%)	SIBs	453.1 mAh g^{-1} at 5 A g^{-1}, 677.3 mAh g^{-1} at 0.1 A g^{-1}, 642.9 mAh g^{-1} at 0.1 A g^{-1}	348.1/2000/10 A g^{-1}	[72]
	0.8M KPF_6+ EC/ DMC = 1 : 1(vol%)	PIBs	55.3 mAh g^{-1} at 2 A g^{-1}, 479.6 mAh g^{-1} at 0.1 A g^{-1}, 457.3 mAh g^{-1} at 0.1 A g^{-1}	254.3/900/1 A g^{-1}	
NG/$ReSe_2/Ti_3C_2T_x$	0.8M KPF_6+ EC/ DEC = 1 : 1(vol%)	PIBs	137.5 mAh g^{-1} g^{-1} at 10 A g^{-1}, 395.3 mAh g^{-1} at 0.1 A g^{-1}	90/300/5 A g^{-1}	[73]

GNF/$Ti_3C_2T_x$	1M KFSI+ EC/ PC = 1 : 1(vol%)	PIBs	45.2 mAh g^{-1} at 0.5 A g^{-1}, 263.5 mAh g^{-1} at 0.05 A g^{-1},253.7 mAh g^{-1} at 0.05 A g^{-1}	253.8/100/0.05 A g^{-1}	[74]
o-P-$CoTe_2$/$Ti_3C_2T_x$	0.8M KPF_6+ EC/ DEC = 1 : 1(vol%)	PIBs	168.2 mAh g^{-1} at 20 A g^{-1}, 420.7 mAh g^{-1} at 0.2 A g^{-1},403.6 mAh g^{-1} at 0.2 A g^{-1}	232.3/2000/2 A v	[75]
Ti_3C_2/Sb_2S_3 Nanoflower	3M KFSI + DME	PIBs	102 mAh g^{-1} at 2 A g^{-1}, 357 mAh g^{-1} at 0.1 A g^{-1},294 mAh g^{-1} at 0.1 A g^{-1}	286/500/0.1 A g^{-1}	[76]
MoS_2/$Ti_3C_2T_x$	0.8M KPF_6+ EC/ DEC = 1 : 1(vol%)	PIBs	168.2 mAh g^{-1} at 0.5 A g^{-1}, 290.7 mAh g^{-1} at 0.05 A g^{-1},252.6 mAh g^{-1} at 0.05 A g^{-1}	206/100/0.05 A g^{-1}	[77]
SnS_2 NSs/MXene	1M KFSI + DME	PIBs	162.6 mAh g^{-1} at 1 A g^{-1}, 342.4 mAh g^{-1} at 0.05 A g^{-1}, 303.3 mAh g^{-1} at 0.05 A g^{-1}	206.1/800/0.5 A g^{-1}	[78]
Te-SnS_2/MXene	0.8M KPF_6+ EC/ DEC = 1 : 1(vol%)	PIBs	186.4 mAh g^{-1} at 20 A g^{-1}, 346.6 mAh g^{-1} at 0.2 A g^{-1}	165.8/5000/10 A g^{-1}	[79]
PB@Ti_3C_2	1.5M KFSI+ EC/ DEC = 1 : 1(vol%)	PIBs	170.8 mAh g^{-1} at 10 A g^{-1}, 338.4 mAh g^{-1} at 1 A g^{-1}, 338.3 mAh g^{-1} at 1 A g^{-1}	338.4/100/1 A g^{-1}	[80]
$Ti_3C_2T_x$/CNT	APC + 0.4M LiCl	LMIBs	40 mAh g^{-1} at 10 C, 105 mAh g^{-1} at 0.1 C	80/500/1 C	[11]
V_2CT_x	APC + xM LiCl (x = 0,0.3,0.4,0.5)	LMIBs	82.3 mAh g^{-1} at 0.5 A g^{-1}, 230.3 mAh g^{-1} at 0.02 A g^{-1},169.7 mAh g^{-1} at 0.02 A g^{-1}	116.9/480/0.05 A g-1	[81]
$Ti_3C_2T_x$	APC: 0.4M $(PhMgCl)_2$-$AlCl_3$ + THF	MIBs	55 mAh g^{-1} at 0.5 A g^{-1}, 210 mAh g^{-1} at 0.05 A g^{-1}	50/60/0.1 A g^{-1}	[82]

(*Continued*)

Table 21.2 (Continued)

Material	Electrolyte	Device	Rate performance	Stability (Last cycle capacity [mAh g^{-1}])/ cycles/current density	References
$Ti_3C_2T_x$@C	APC	MIBs	123.3 mAh g^{-1} at 0.2 A g^{-1}, 198.7 mAh g^{-1} at 0.01 A g^{-1}, 201 mAh g^{-1} at 0.01 A g^{-1}	140.6/400/0.05 A g^{-1}	[83]
$Ti_3C_2T_x$/CTAB	APC	MIBs	32 mAh g^{-1}(96 mAh cm^{-3}) at 2 A g^{-1}, 100 mAh g^{-1}(300 mAh cm^{-3}) at 0.05 A g^{-1}	135 mAh cm-3/250 /0.2 A g^{-1}	[3]
$MnO_2/Ti_3C_2T_x$	—	MIBs	21 mAh g^{-1} at 0.5 A g^{-1}, 105 mAh g^{-1} at 0.05 A g^{-1}	58/100/0.05 A g^{-1}	[84]
BC/ Ti_3C_2 film	APC	MIBs	152 mAh g^{-1} at 0.1 A g^{-1}, 203 mAh g^{-1} at 0.02 A g^{-1},212 mAh g^{-1} at 0.02 A g^{-1}	150/100/0.05 A g^{-1}	[85]
MnO_2/V_2C	APC	MIBs	25 mAh g^{-1} at 0.5 A g^{-1}, 65 mAh g^{-1} at 0.1 A g^{-1}, 40 mAh g^{-1} at 0.2 A g^{-1}	59/100/0.1 A g^{-1}	[86]
TiS_2/MXene	APC	MIBs	—	75/50/0.05 A g^{-1}	[87]
$MoS_2/Ti_3C_2T_x$	APC	MIBs	53 mAh g^{-1} at 0.5 A g^{-1}, 165 mAh g^{-1} at 0.05 A g^{-1}, 93 mAh g^{-1} at 0.2 A g^{-1}	108/50/0.05 A g^{-1}	[88]
ML-V_2CT_x	Molar ratio: $AlCl_3$/ [EMIm] Cl = 1.3 : 1	AIBs	335 mAh g^{-1} at 0.01 A g^{-1}, 90 mAh g^{-1} at 0.1 A g^{-1}	112/20/0.01 A g^{-1}	[4]
FL-V_2CT_x	Molar ratio: $AlCl_3$/ [EMIm] Cl = 1.3 : 1	AIBs	50 mAh g^{-1} at 5 A g^{-1}, 162 mAh g^{-1} at 0.1 A g^{-1}	76/100/0.1 A g^{-1}	
TBAOH-FL-V_2CT_x	Molar ratio: $AlCl_3$/ [EMIm] Cl = 1.3 : 1	AIBs	150 mAh g^{-1} at 0.3 A g^{-1}, 300 mAh g^{-1} at 0.1 A g^{-1}	—	

$Ti_3C_2T_x$@S@TiO_2	Molar ratio: $AlCl_3$/ [EMIm] Cl = 1.3 : 1	AIBs	51.8 mAh g^{-1} at 0.5 A g^{-1}, 157.7 mAh g^{-1} at 0.1 A g^{-1}	151.3/120/0.1 A g^{-1}	[89]
Ti_3C_2@CTAB-Se	Molar ratio: $AlCl_3$/ [EMIm] Cl = 1.3 : 1	AIBs	117.7 mAh g^{-1} at 0.5 A g^{-1}, 583.7 mAh g^{-1} at 0.1 A g^{-1}, 440.3 mAh g^{-1} at 0.1 A g^{-1}	132.6/400/0.2 A g^{-1}	[90]
F-$Ti_3C_2T_x$@Te	Molar ratio: $AlCl_3$/ [EMIm] Cl = 1.3 : 1	AIBs	400 mAh g^{-1} at 1.5 A g^{-1}	449/150/0.6 A g^{-1}	[91]
F-$Ti_3C_2T_x$@Ag	Molar ratio: $AlCl_3$/ [EMIm] Cl = 1.3 : 1	AIBs	30 mAh g^{-1} at 2 A g^{-1}, 200 mAh g^{-1} at 0.5 A g^{-1}	150/2000/0.5 A g^{-1}	[92]
MoS_2-$Ti_3C_2T_x$	Molar ratio: $AlCl_3$/ [EMIm] Cl = 1.3 : 1	AIBs	—	166/60/1 A g^{-1}	[93]
Co_9S_8NP@NPC@ MXene	Molar ratio: $AlCl_3$/ [EMIm] Cl = 1.3 : 1	AIBs	241 mAh g^{-1} at 0.1 A g^{-1}	110/1000/1 A g^{-1}	[94]
$CoSe_2$@NPC@ MXene	Molar ratio: $AlCl_3$/ [EMIm] Cl = 1.3 : 1	AIBs	114 mAh g^{-1} at 5 A g^{-1}, 288 mAh g^{-1} at 1 A g^{-1}	155/1000/1 A g-1,220/300/1 A g^{-1}	
$Ni_{0.6}Co_{0.4}S$@ MXene@NC	Molar ratio: $AlCl_3$/ [EMIm] Cl = 1.3 : 1	AIBs	~300 mAh g^{-1} at 1 A g^{-1}, 481.2 mAh g^{-1} at 0.4 A g^{-1}	125.2/300/1 A g^{-1}	[95]

The two-dimensional (2D)-layered material MXene has an open 2D ion transport channel and a significant specific surface area to provide a large number of active sites for sodium-ion storage, as well as excellent electrical conductivity for electron transfer. Therefore, MXenes and their nanocomposites are considered to be excellent anode electrode materials for high-performance SIBs. At present, the application of MXene-based materials in

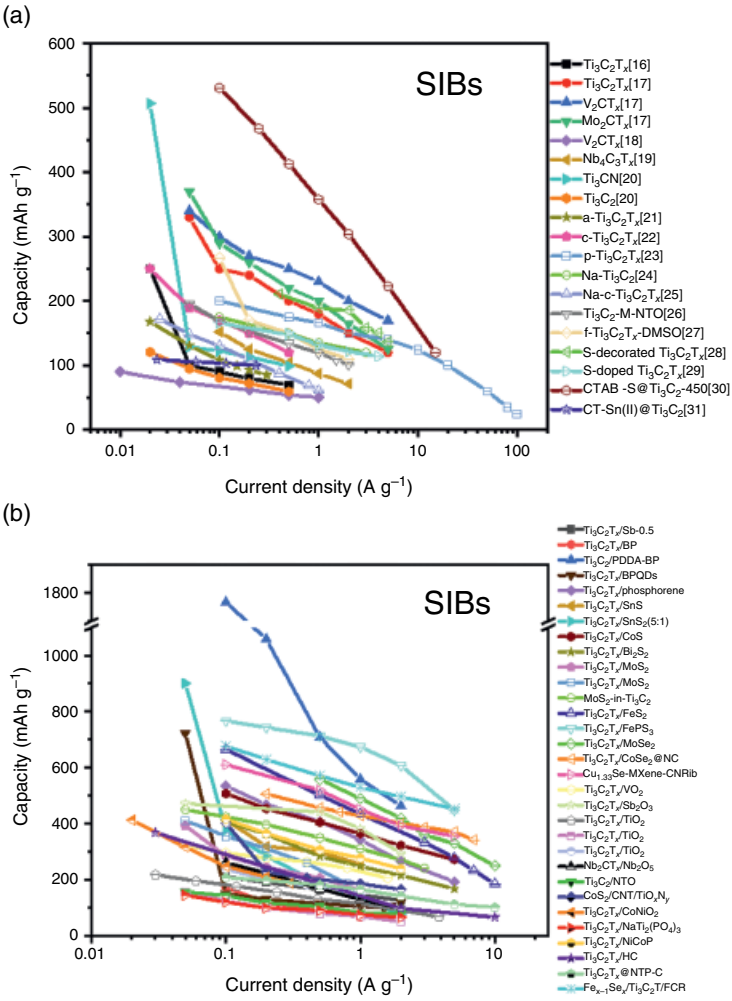


Figure 21.2 Comparison of the rate capability of MXene materials in NLIBs. (a) Pure MXene in SIBs. (b) MXene-based composites in SIBs. (c) MXene in PIBs. (d) MXene in MIBs. (e) MXene in AIBs.

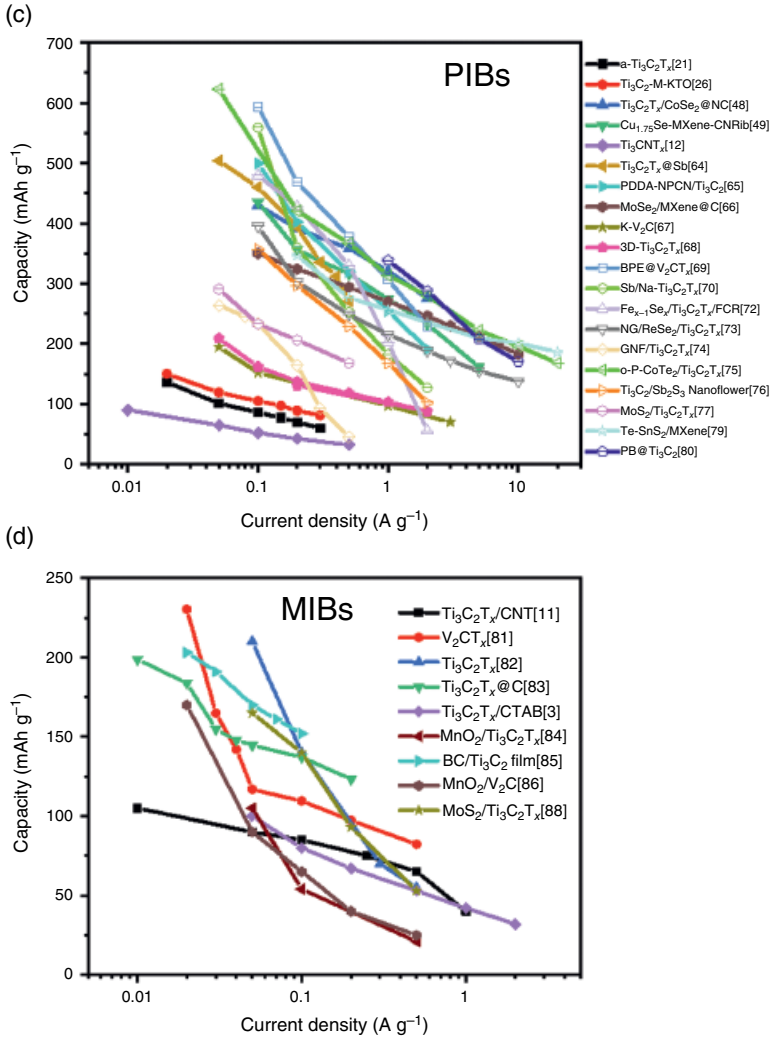


Figure 21.2 (Continued)

sodium-ion storage has been widely studied. According to DFT calculation, the surface terminating group of MXenes has a great influence on the properties of MXenes. For example, Xie et al. [8] found that sodium ions can be well adsorbed on O-functionalized and non-terminal MXene due to good negative adsorption energy, and the initial discharge specific capacity of $Ti_3C_2T_x$ in SIBs is 370 mAh g^{-1}. The presence of functional groups (–F, –OH) of Ti_3N_2 MXene is not conducive to sodium-ion migration and reduces the theoretical capacity

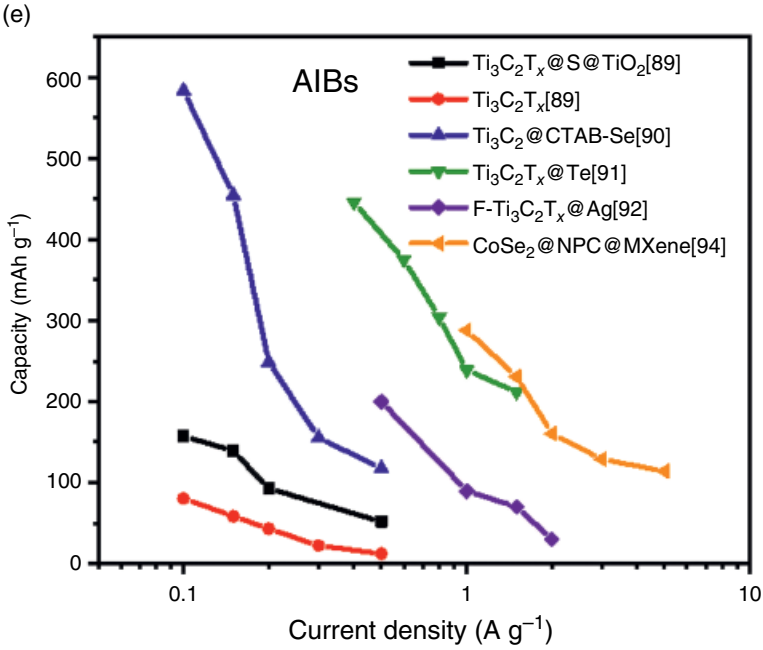


Figure 21.2 (Continued)

except for the –O group [100]. In contrast, $Ti_3C_2S_2$ monolayers have been shown to have multilayer adsorption capacity for sodium, and the theoretical capacity of 463 mAh g^{-1} is greater than that of bare and O-functionalized Ti_3C_2 monolayers [101].

As with most 2D materials, MXenes tend to aggregate or accumulate during the experiment, which limits electrolyte penetration and impedes charge transfer, resulting in limited capacity values. Therefore, compared with other SIBs anode materials, pure MXene electrodes do not exhibit satisfactory reversible capacity, limiting their further application in the field of energy storage.

To optimize the electrochemical performance of MXene, improvements are usually made from two aspects. On the one hand, the performance of pure MXene material itself is improved. Since the electrochemical performance of SIBs is controlled by multiple factors such as the type of MXenes, interlayer spacing, surface groups, and electrode structure, there are three main strategies to accelerate the electrochemical kinetics and improve the capability, including the synthesis of single/few-layer MXenes, the expansion of interlayer spacing of MXenes, and the construction of the three-dimensional (3D) porous structure. Another one is to design composite materials based on MXenes. The unique structure and synergistic effects of the composite materials benefit electrochemical

performance: MXenes can provide interwoven conductive networks that significantly increase electronic conductivity; supporting materials are expected to prevent the aggregation of individual nanosheets. Based on the preparation method and mechanism, MXene matrix composites can be divided into three categories: secondary materials grown on MXenes, self-assembly of MXenes and other materials, and MXene matrix composites formed by *in-situ* transformation reaction [102]. Table 21.1 summarizes and lists the properties of MXenes and its derivatives for sodium-ion storage in recent years, mainly including rate performance and cyclic stability.

21.2.1.1 Multilayer MXenes

Multilayer MXene is usually produced by the selective removal of A layer from the layered structure of the MAX phase, and the layered material with large interlayer spacing is a favorable embedding subject for metal-ions intercalation. Therefore, MXene nanosheets are a promising cathode material for sodium-ion batteries with considerable storage capacity. For example, $Ti_3C_2T_x$ nanosheets show excellent rate performance and long-term cycle stability [15]. Figure 21.3a compares the electrochemical properties of Ti_3AlC_2 and $Ti_3C_2T_x$ for lithium- and sodium-ion storage. The reversible capacities of $Ti_3C_2T_x$ MXenes and Ti_3AlC_2 for SIBs are 100 and 16.8 $mAh\,g^{-1}$, respectively, indicating that Na^+ can be easily diffused electrochemically within $Ti_3C_2T_x$ reversibly (embedded/de-embedded into the MXene lattice and phase transition) by solution reaction. Meanwhile, a reversible capacity of 53.7 or 68.3 $mAh\,g^{-1}$ can be obtained after 1000 cycles at a current density of 0.8 or 0.2 $A\,g^{-1}$. These are attributed to the increased active storage sites and expanded interlayer spacing due to Al removal as well as the double-layer adsorption mechanism.

21.2.1.2 Single/Few-Layer MXenes

For single/few-layer MXenes, they can be conducive to full use of the large surface, allowing for more rapid sodium-ion diffusion. Taking $Ti_3C_2T_x$ MXene as an example. Wu et al. [27] prepared few-layer MXene (f-$Ti_3C_2T_x$-DMSO, Figure 21.3b) with a large specific surface area and layer spacing, good electrolyte path, and short diffusion path of ions and electrons via an organic solvent assisted high-energy mechanical-milling method. Therefore, as a negative electrode of sodium-ion battery, it has excellent performance, including high capacity, high rate performance, and long cycle stability. That is, few-layer MXene nanosheets deliver a high reversible capacity of 267 $mA\,h\,g^{-1}$ at a current density of 0.1 $A\,g^{-1}$. After cycling 1500 cycles at a high rate of 1 $A\,g^{-1}$, a reversible capacity of 76 $mA\,h\,g^{-1}$ could be maintained. The high capacity of 110 $mA\,h\,g^{-1}$ could be achieved at the high current density of 2 $A\,g^{-1}$, which makes the f-$Ti_3C_2T_x$-DMSO electrode a more ideal anode for SIB.

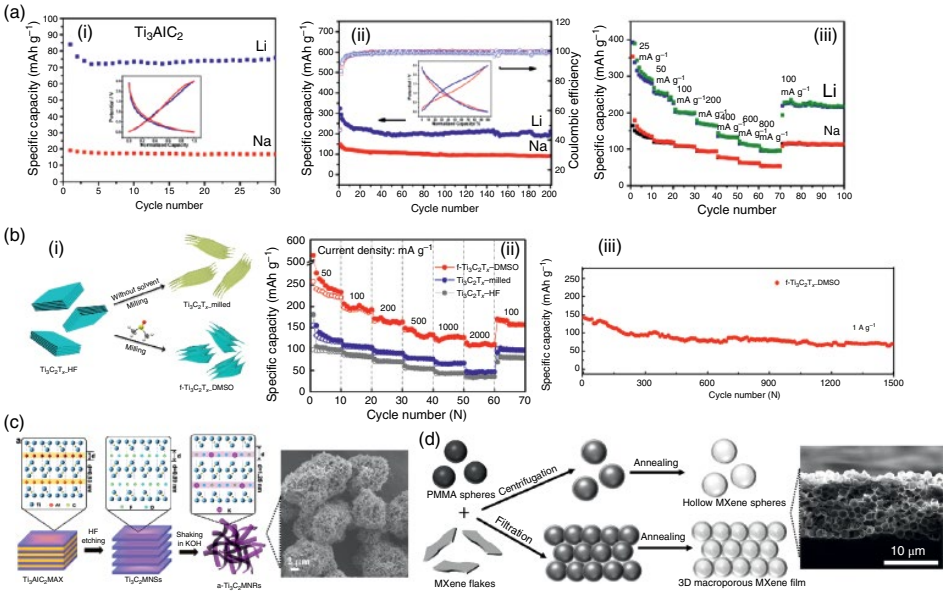


Figure 21.3 (a) Electrochemical performances of Ti_3AlC_2 and $Ti_3C_2T_x$ for LIBs and SIBs. Cycling performance of (i) Ti_3AlC_2 and (ii) $Ti_3C_2T_x$ at 50 mA g^{-1}; (iii) Rate performance of $Ti_3C_2T_x$ for LIBs and SIBs. *Source:* Wang et al. [15]/American Chemical Society. (b) (i) Schematic illustration of scale delamination of few-layer $Ti_3C_2T_x$ nanosheets by HEMM with DMSO solvent; (ii) Rate performance of f-$Ti_3C_2T_x$-DMSO; (iii) Ultralong cycle life of 1500 cycles achieved by f-$Ti_3C_2T_x$-DMSO at 1 A g^{-1}. *Source:* Wu et al. [27]/American Chemical Society. (c) Fabrication and SEM images of a-$Ti_3C_2T_x$ MNRs. *Source:* Lian et al. [21]/Reproduced with permission from Elsevier. (d) The construction of hollow MXene spheres and 3D macroporous MXene frameworks and cross-sectional SEM images of $Ti_3C_2T_x$. *Source:* Zhao et al. [17]/Reproduced from John Wiley & Sons, Inc.

21.2.1.3 MXenes with an Expanded Interlayer Spacing

At present, to improve the electrochemical performance of MXene-based electrodes for SIB, the most effective method is to increase the layer spacing of MXene. Because cations and organic solvents can be easily embedded into MXenes nanosheets, it has been widely used to expand interlamellar space to improve sodium-ion transport dynamics and increase sodium storage sites. In addition, the layer spacing can also be increased by doping heteroatoms in layered MXene because the increase in intrinsic activity caused by heteroatom doping and the redistribution of atomic charge density and/or spin density contribute to improving the electrochemical performance of the heteroatom doped material [103]. Sulfur is one of the most widely doped atoms, and its feasibility and effectiveness have been proven to improve the electrochemical performance of doped materials. For example, Li et al. [29] first used thiourea as an S source and reported an S-doped $Ti_3C_2T_x$ MXene with extended layer spacing as a high-performance anode material for SIB through a simple vulcanization process. S-doped $Ti_3C_2T_x$ MXene has unique multilayer morphology, large surface area, enhanced conductivity, expanded layer spacing, and a capacitance-dominated sodium storage process. Thus, it has a high specific capacity (183.2 mAh g^{-1} at 0.1 A g^{-1}), excellent rate performance (121.3 mAh g^{-1} at 2 A g^{-1} and 113.9 mAh g^{-1} at 4 A g^{-1}), and robust long-term cycling stability with a reversible capacity of 138.2 mAh g^{-1} after 2000 cycles at 0.5 A g^{-1}.

21.2.1.4 MXenes with Porous Structure

Besides controlling the thickness of MXenes, rational design of hierarchical porous structure can also introduce high sodium-ion storage. For example, Lian et al. [21] demonstrated the fabrication of a novel 3D porous framework of alkalized Ti_3C_2 MXene nanoribbons (MNRs) derived from Ti_3C_2 MXene nanosheets (MNSs) in KOH solution, as shown in Figure 21.3c. This unique architecture synergistically combined nanoribbons with expanded interlayer spacing and a 3D open porous network consisting of MNRs, enabling fast electron transport and rapid ion diffusion. As a result, such a-Ti_3C_2 MNRs showed great promise as anodes for SIBs and PIBs with remarkable capacities and excellent rate capability. High reversible capacities of 168 and 136 mAh g^{-1} at 20 mA g^{-1} and 84 and 78 mAh g^{-1} at 200 mA g^{-1} were obtained for SIBs and PIBs, respectively. Notably, a-Ti_3C_2 MNRs possessed outstanding long-term cyclability at a high current density of 200 mA g^{-1}, delivering a capacity of ~50 mAh g^{-1} for SIBs and 42 mAh g^{-1} for PIBs after 500 cycles. Zhao et al. [17] successfully self-assembled 2D MXene flakes ($Ti_3C_2T_x$, V_2CT_x, and Mo_2CT_x) onto polymer (PMMA) surface and hollow spheres and 3D macroporous architectures were made via a sacrificial template approach, as shown in Figure 21.3d. The as-fabricated 3D macroporous $Ti_3C_2T_x$ films were free-standing, flexible, and

highly conductive due to the good contacts between spheres and metallic conductivity of $Ti_3C_2T_x$. And these 3D MXene films were directly used as anodes for sodium-ion storage; no current collectors or binders were needed. Compared with multilayer MXene and MXene/carbon nanotube (CNT) hybrid architectures, these 3D MXene films showed significantly improved performance in terms of capacity, rate capability, and cyclic stability. Therefore, the assembly of 2D materials into 3D porous structures could prove to be a promising solution to the problem of poor charge transport in electrode materials, leading to devices with high performance.

21.2.1.5 MXene-based Composites

MXene-based composites have excellent properties and good interfaces, which have been explored to resist accumulation/agglomeration, optimize charge transfer, and alleviate the volume expansion of batteries, so MXene-based composites also play an important role in enhancing the storage capacity of Na^+. Fabrication of the composite consisting of MXenes and low-dimensional materials with a high specific capacity, such as 0D nanoparticles, is a feasible and effective way to develop advanced MXene-based electrodes for SIBs. $Ti_3C_2T_x$ MXene is a typical example in the application. Currently, MXene/0D heterostructures that have been developed include SnS [38], CoS [40], $CoNiO_2$ [59], $NaTi_2(PO_4)_3$ [60], NiCoP [61], Bi_2S_2 [41], MoS_2 [42, 43], $MoSe_2$ [47], VO_2 [50], Sb_2O_3 [51], Sb [32] etc. Usually, the hydrothermal/annealing method (Figure 21.4a) and solvothermal method or simple solution phase method without heat treatment (such as Sb_2O_3, Sb, Figure 21.4b) are used to make the nanoparticles evenly dispersed in 2D MXene nanosheets/3D porous structure, forming a unique sandwich structure/3D interconnect folded porous structure. MXene composites exhibit excellent electrochemical performance as the anode of sodium-ion batteries, which is mainly attributed to the unique microstructure and synergistic effect between MXene and nanoparticles, as shown in Figure 21.4c.

1) The nanoparticles extend the spacing between MXene layers, prevent the re-stacking of MXene flakes, and provide a large number of active sites for Na^+ adsorption. At the same time, the *in-situ* growth of small nanoparticles can effectively delay the volume expansion, and further shorten the migration path of sodium ions and electrons. In addition, the unique properties of nanoparticles contribute to the improvement of electrochemical performance. For example, NiCoP bimetallic phosphating has more abundant redox reaction sites, higher electrical conductivity, and lower charge transfer resistance. The high electrochemical reactivity of Sb and Na to form Na_3Sb is helpful in obtaining high specific capacity.

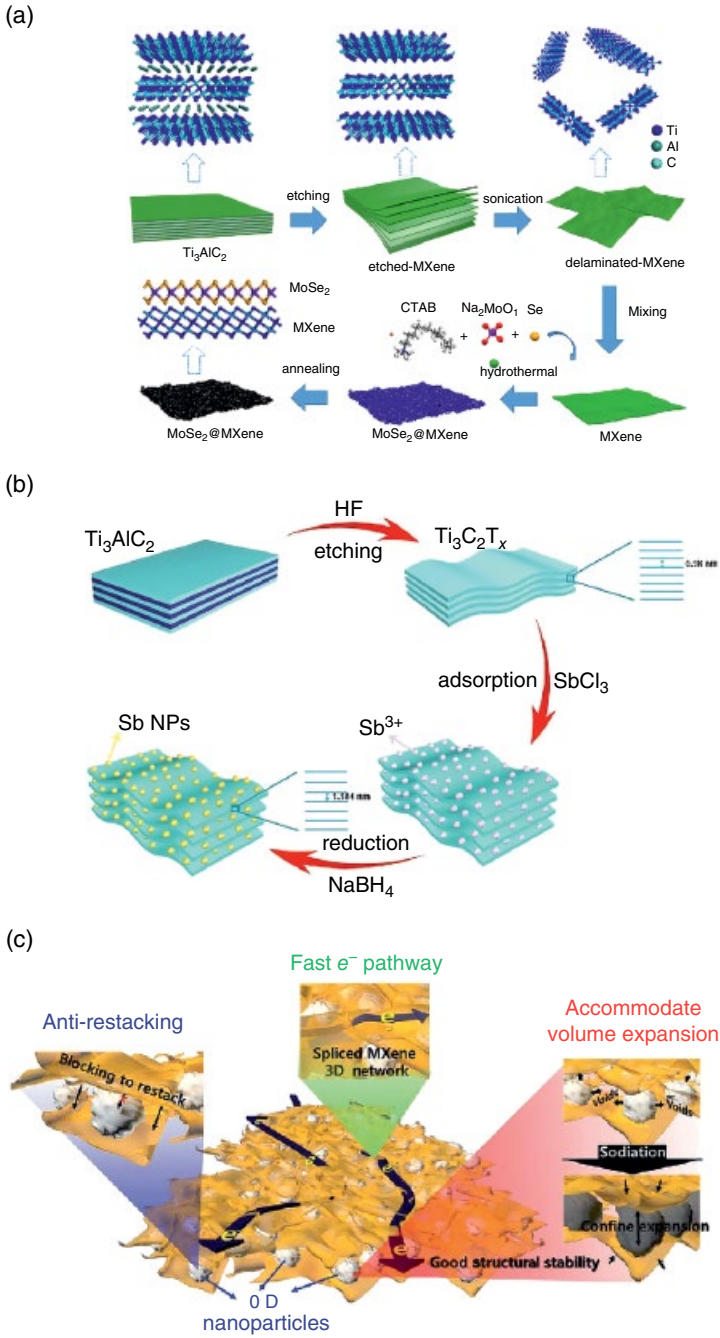


Figure 21.4 (a) Illustration of the synthesis of $MoSe_2/Ti_3C_2T_x$ heterostructures by hydrothermal/annealing method. *Source:* Xu et al. [47]/with permission of Elsevier. (b) Illustration of the synthesis procedure for $Ti_3C_2T_x$ @Sb via a facile solution-phase method. *Source:* Chen et al. [32]/IOP Publishing. (c) Illustration of the enhanced performance mechanism of the nanoparticles/MXene anode in SIBs. *Source:* Guo et al. [51]/Royal Society of Chemistry. (d) Illustration of the synthesis process of the

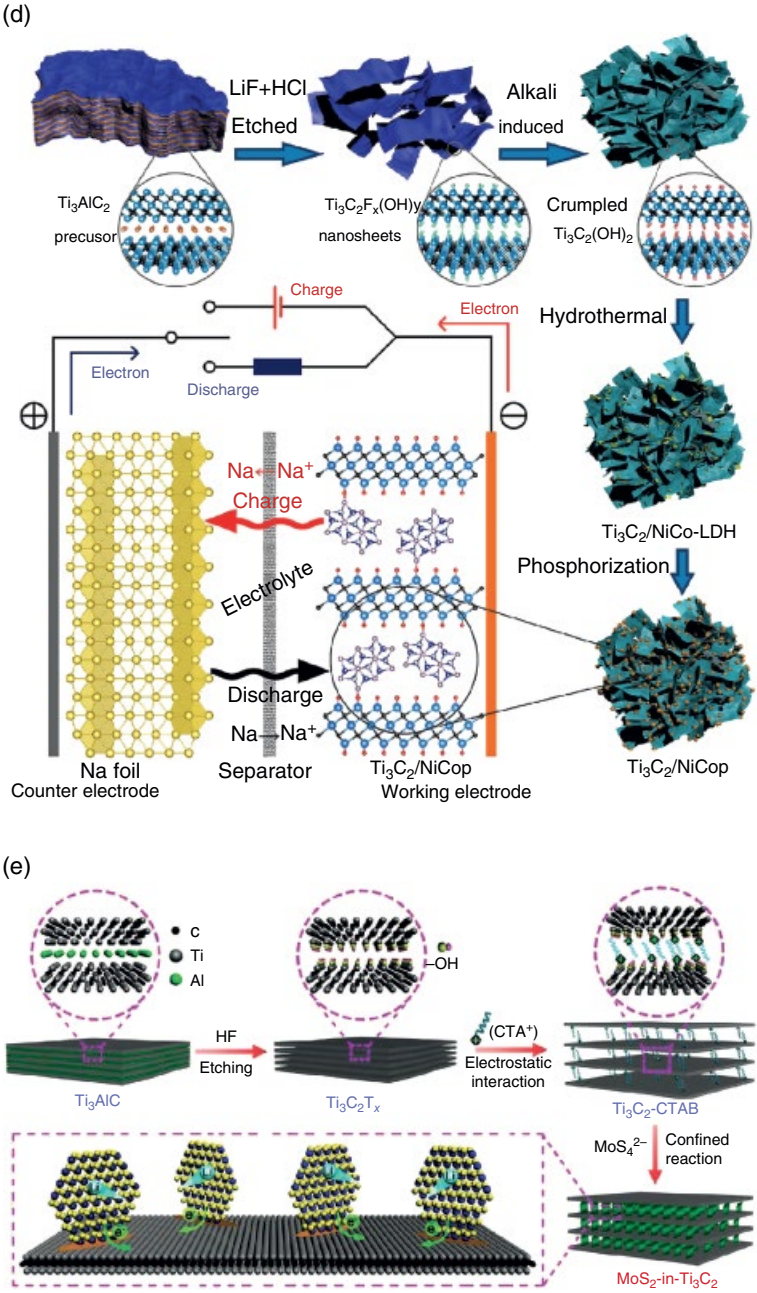


Figure 21.4 (Continued) $Ti_3C_2T_x$/NiCoP with 3D interconnected crinkled porous structure and schematic mechanism of half-cells. *Source:* Zhao et al. [61]/Royal Society of Chemistry. (e) Schematic illustration for the fabrication of the MoS_2-in-$Ti_3C_2T_x$ hybrids by electrostatic self-assembly. *Source:* Ma et al. [44]/John Wiley & Sons. (f) (i) Schematic representation of the formation mechanism for the sandwich-like $Na_{0.23}TiO_2/Ti_3C_2$ composite through an *in-situ* transformation reaction; SEM images (ii), (iii) and TEM images (iv) of the $Na_{0.23}TiO_2/Ti_3C_2$

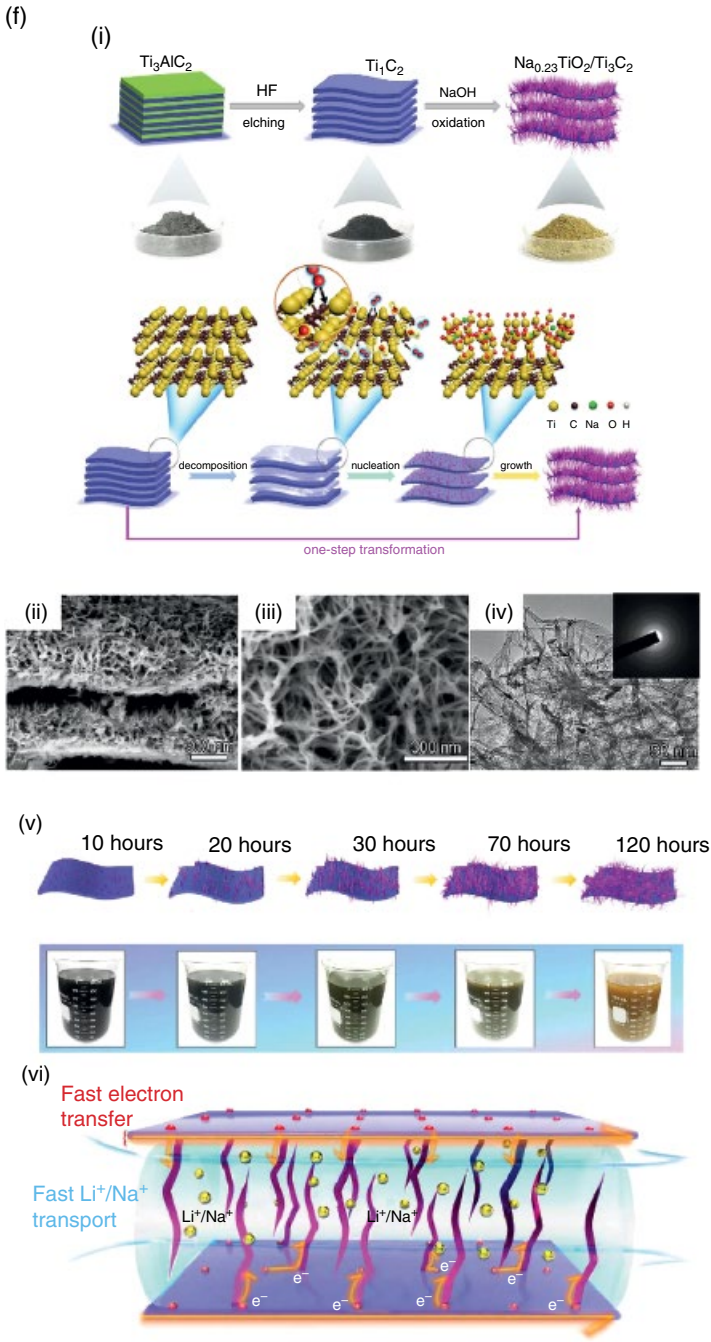


Figure 21.4 (Continued) (iv) is the SAED pattern of $Na_{0.23}TiO_2$ nanobelts; (v) the morphology evolution and solution color change of $Na_{0.23}TiO_2/Ti_3C_2$ composites with transformation reaction proceeding; (vi) energy-storage mechanism in discharge process of $Na_{0.23}TiO_2/Ti_3C_2$ composite. *Source:* Huang et al. [56]/Reproduced from Elsevier.

2) As the matrix of the composite, MXene can provide a stable conductive network skeleton and accelerate the sodium ion and electron transition, thus improving the electronic conductivity of the composite (low diffusion barrier ~0.066 eV between Na^+/MXene). Its open structure can expose more active sites to enhance the charge transfer and redox kinetics. In addition, the agglomeration of nanoparticles can be prevented.
3) Unique structure: sandwich shape stereochemical structure/interconnection 3D skeleton/crossed 3D flower-like hybrid structure (Figure 21.4d) has abundant openings and high specific surface area, which can provide a smooth channel for electrolyte storage and Na^+ transfer, and make the electrode contact with the electrolyte completely close, shortening the diffusion distance of sodium ions. Furthermore, the large number of voids generated between the nanoparticles and MXene not only effectively tolerate volume expansion, but also prevent the aggregation and crushing of nanoparticles during Na^+ insertion/extraction, thus maintaining the stability of the hybrid electrode.

In addition, coupling/hybridization of MXenes with other one-dimensional (1D) and 2D materials has been reported in SIBs. On the one hand, due to the unique desorption behavior of MXenes, the composite materials can usually be prepared by self-assembly, in which the solution is mixed and stirred for a long time and/or ultrasonic treatment. On the other hand, MXenes are negatively charged due to the presence of surface groups, and MXene matrix composites can be self-assembled by electrostatic attraction. For example, coupled with MoS_2, Ma et al. [44] limited the synthesis of 1–3 layers of MoS_2 nanocrystals in a 2D Ti_3C_2 sandwich by electrostatic attraction and directed growth of cetyltrimethylammonium bromide (CTAB), as shown in Figure 21.4e. The obtained MOS_2-in-Ti_3C_2 hybrid can achieve strong coupling between high-energy MoS_2 nanocrystals and high-power Ti_3C_2 due to the unique 2D constraint effect and strong covalent bond. Meanwhile, abundant edges and active centers are generated, which have typical pseudo-capacitive dominant behavior, and achieve ultrafast kinetics for Li^+/Na^+ storage. At present, 2D confined synthesis strategies provide a new approach for precise control of the microstructure of nanomaterials to obtain impressive electrochemical properties. In addition, since MXene can be completely converted to other materials through oxidation or alkalization processes, MXene matrix composites can be obtained *in-situ*, such as TiO_2 [53, 54], $NaTi_2(PO_4)_3$ [63], $Na_{0.23}TiO_2$ nanobelt (Figure 21.4f) [56] or $NaTi_8O_{13}/NaTiO_2$ nanoribbons [57] and so on.

21.2.2 Potassium-Ion Batteries

Due to the similar physical and chemical properties of potassium to sodium, potassium-ion batteries are also a hot research topic in recent years. Specifically, PIBs have the advantages of abundant raw materials, low price, low redox standard

potential (−2.93 V vs. SHE, close to 3.04 V vs. SHE for Li^+/Li), and high mobility and conductivity in electrolytes (Because of the low charge density of K^+, it has weak Lewis acidity, resulting in a small solvation radius). Therefore, theoretically, PIBs can provide higher operating voltage and energy density, and is also an ideal substitute for LIBs. However, the large size and uncontrollable dendrite growth of K^+ bring severe challenges to the practical application of K^+ storage electrode materials. Since K^+ exhibits a larger radius (1.38 Å) than Li^+ and Na^+, the repeated insertion/extraction of potassium ions from the electrode causes a huge volume change that leads to irreparable damage to the structure. Therefore, the development of electrode materials with high cycling stability and large volume strain tolerance is the key to the successful application of PIBs.

It is worth noting that the main advantages of MXene as the anode material for PIBs are good electronic conductivity and low diffusion potential barrier of K^+, resulting in fast charge-discharge capacity and excellent rate performance. These favorable characteristics make MXenes a promising PIB electrode material. However, there are few reports about the application of MXenes in PIBs, many of which are still in the theoretical research stage. To have a clearer understanding of the latest situation of MXene materials applied to PIBs, we prepared a table (Table 21.1) about MXene-related materials and their performance in PIBs. Compared with Li^+, the kinetics of K^+ in active materials is slower, resulting in lower initial coulomb efficiency and poor rate performance in practical applications. Taking $Ti_3C_2T_x$ as an example, the theoretical specific capacity is only 191.8 mAh g^{-1}, and at present $Ti_3C_2T_x$ is prone to irreversible agglomeration and accumulation, resulting in the actual specific capacity being far lower than the theoretical value. In addition, theoretical studies by Xie et al. [8] showed that potassium is not easily absorbed by OH–terminated MXenes, while the O group is more conducive to potassium adsorption. Therefore, in the case that surface groups cannot be removed, MXene should have more O-terminals on its surfaces to obtain better electrochemical performance.

In terms of practical research, Naguib et al. [12] first experimentally studied the electrochemical performance of Ti_3CNT_x as an anode of PIBs. The specific capacity of the first discharge process reached 710 mAh g^{-1} at 20 mA g^{-1}, while the specific capacity of the first charge process was only 202 mAh g^{-1}. The first-Coulomb efficiency is unsatisfactory, probably due to the formation of the SEI layer and the irreversible reaction between K and the water molecules trapped between the MXene layer or the by-product of the etching process. And the capacity remained at only 75 mAh g^{-1} after 100 cycles. Both theoretical and experimental studies have shown that the original MXenes have low potassium storage capacity and fast capacity decay, so pure MXenes are generally not suitable for anodic material of PIB alone [104].

Similar to LIBs and SIBs, the K^+ storage characteristics in PIBs are also controlled by the same factors, the most important of which are layer spacing and morphology control. Therefore, the solution to the above problems is to optimize

the interlayer structure, construct 2D layered heterostructures, reduce the self-stacking effect, build additional potassium storage sites, ensure that it can withstand the volume expansion and rapid transmission of large-size K^+ insertion and de-intercalation, thereby improving the electrochemical performance. For example, Wu et al. [69] designed a novel BPE@V_2CT_x hybrid anode (Figure 21.5a) with a 2D stacked interlamellar structure and large specific surface area using van der Waals interaction interlamellar assembly strategy, in which black phosphene (BPE) and V_2CT_x MXene 2D nanosheets were effectively utilized to create more

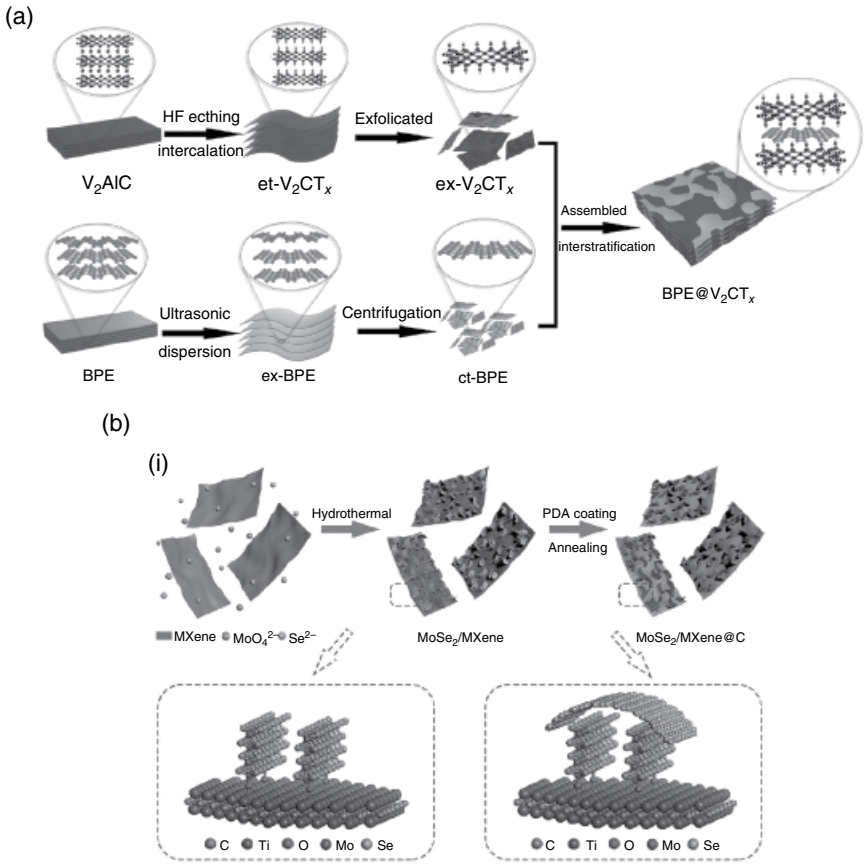


Figure 21.5 (a) Schematic illustration for the fabrication of BPE@V_2CT_x hybrids. *Source:* Wu et al. [69]/Royal Society of Chemistry. (b) (i) Schematic of the preparation of $MoSe_2$/MXene@C; (ii) comparison of rate performance of $MoSe_2$/MXene@C, $MoSe_2$/MXene, $MoSe_2$, and MXene at various current densities; (iii) long-term cycling discharge capacities and Coulombic efficiencies of $MoSe_2$/MXene@C at the current densities of 1.0, 2.0, and 5.0 $A g^{-1}$. *Source:* Huang et al. [66]/American Chemical Society.

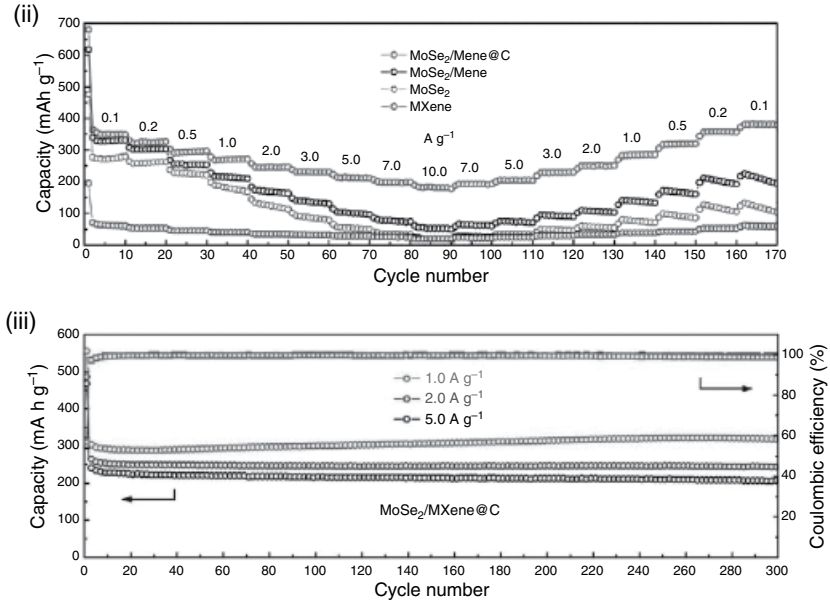


Figure 21.5 (Continued)

active sites. The interlayer hybrid electrode not only provides extended interlayer spacing and an interconnected conductive network to accelerate the K^+ transport rate but also has good resistance to volume changes caused by phase transformation in the process of rapid potassium intercalation/dipotassium. Huang et al. [66] constructed $MoSe_2$/MXene@C composites (Figure 21.5b) by hydrothermal growth of $MoSe_2$ on highly conductive MXene sheets and then covering them with polydopamine-derived carbon coating. The strengthening interaction between $MoSe_2$ nanosheets and MXene flakes and the synergistic effect of carbon coating enables the electrode to obtain excellent structural stability and electrochemical performance, such as high reversible capacity (355 mAh g^{-1} after 100 cycles at 200 mA g^{-1}), and excellent rate performance (a specific capacity of 183 mAh g^{-1} at 10.0 A g^{-1}, which can be well recovered when the current gradually switches back to lower current density).

In general, compared with LIBs and NIBs, the potassium storage capacity of most MXenes is not ideal, and the combination of MXenes and other materials will be the mainstream development direction for a long time. Among them, heterostructure hybrid composites and large-layer interlayer spacing are of great significance to the development of high-performance PIBs. And the careful design of the material structure is the key factor to improve the electrochemical performance of MXene-based materials. Moreover, due to the immature preparation technology and the

lack of varieties of MXenes, the current literature on the application of MXenes in PIBs is dominated by $Ti_3C_2T_x$. Many MXenes materials have not been applied to potassium-ion batteries. With the gradual maturity of preparation technology, MXenes still has great potential in the application of PIBs.

21.2.3 Magnesium-Ion Batteries

For multivalent metal-ion batteries, multivalent cations can transfer two or three electrons, resulting in greater energy density than monovalent ion batteries. Rechargeable magnesium-ion batteries (MIBs) have many advantages, such as rich content in the earth's crust (~10^4 times more than lithium), low cost (the price is only about 1/24 of lithium metal), high theoretical specific capacity (the mass capacity of 2205 mAh g^{-1}, the volumetric capacity of 3833 mAh cm^{-3} is better than that of 2046 mAh cm^{-3} of LIBs, Low redox potential (−2.37 V vs. SHE), good safety (unlike metal lithium and metal sodium, metal magnesium does not form dendrite during repeated magnesium dissolving and deposition processes), and the environmental friendliness of magnesium [84, 85, 105]. As a result, metal magnesium can be used as an anode directly, making rechargeable MIBs widely regarded as one of the most promising next-generation batteries.

Unfortunately, the development of MIBs is still immature, which is mainly hindered by two aspects (cathode material and electrolyte). Therefore, the research on magnesium-ion batteries at home and abroad is also mainly focused on this. In most cases, for the positive poles of the MIBs, magnesium ions are inserted into the main material during discharge and extracted from the main material during charging. However, on the one hand, due to the strong electrostatic interaction between Mg^{2+} and other ions, the diffusion of Mg^{2+} ions is seriously hindered, which limits the practical capacity of the positive electrode. And excellent electrochemical performance can be obtained only at a higher temperature. Therefore, most of the cathode materials in the LIBs system cannot be directly applied to the MIBs system, and there are few cathode materials available [3, 83]. On the other hand, the incompatibility between many cathode materials and electrolytes also limits the practical application of Mg batteries.

To solve the above problems, the most critical method is to find and develop suitable new cathode materials and electrolytes. For example, to develop aqueous MIBs, in organic electrolytes, Mg^{2+} must overcome the difficulty of cracking from the solvated material before insertion. In aqueous electrolytes, by contrast, rapid Mg-ion diffusion kinetics can be obtained with the help of strong bipolar water molecules, thus solving the problem of interfacial diffusion [106]. Another strategy is to design a hybrid battery that could partially replace the power battery. The insertion/exhalation of Mg^{2+} is slowed by more efficient Li^+ or Na^+ diffusion kinetics using a double salt electrolyte. This hybrid design can combine the

advantages of Mg anodes and Li^+ or Na^+ embedded cathodes to endow the device with better safety, rate capability, and cycle stability.

MXene is considered a promising candidate as cathode material for MIBs due to its ability to maintain a layered structure after repeated insertion and extraction reactions, often showing surprising cyclic stability. According to theoretical calculations, MXenes have shown promising theoretical capacities for Mg-ion intercalation (>400 mA h g^{-1}, [105]).

We believe that MXene with pre-expanded layer spacing exhibits excellent kinetic performance in the diffusion process of strong electrostatic Mg^{2+}, and the layer spacing can be increased by pre-insertion. In addition, MXene with a neutral surface can effectively reduce the strong electrostatic interaction between Mg^{2+} and the surface terminal, thus improving the diffusion dynamics of MXene [96]. Meanwhile, the self-standing MXene film, which can be directly used as a MIBs cathode, is attractive because the APC electrolyte will corrode the collector and cause side reactions, and the adhesive will also damage the electrochemical performance of MIBs. Table 21.1 also represents the comparison of different MXene materials used for MIBs.

In 2017, Byeon et al. [11] reported for the first time that $Ti_3C_2T_x$ and Mo_2CT_x MXenes were used as cathodes of mixed Mg^{2+}/Li^+ batteries in combination with metal Mg anodes and traditional APC-THF electrolytes, and showed eminent electrochemical performance, as shown in Figure 21.6a. The free-standing and flexible $Ti_3C_2T_x$/CNT composite "paper" delivered ~100 mAh g^{-1} at 0.1 C and ~50 mAh g^{-1} at 10 C. And 80 mAh g^{-1} was maintained at 1 C after 500 cycles in MLIBs. Then Liu et al. [81] used pre-lithium V_2CT_x MXenes as the cathode of MLIBs (Figure 21.6b), Mg^{2+} and Li^+ co-intercalation layer exhibited an excellent reversible capacity of 230.3 mAh g^{-1} at 0.02 A g^{-1} and great cycling performance (the capacity retention rate was 82% after 480 cycles). This is mainly because Li^+ pre-intercalation can replace lithium sources to effectively alleviate lithium consumption during SEI formation. And the layer spacing of MXenes is enlarged to provide abundant active sites and fast channels for ion transport.

At present, $Ti_3C_2T_x$ MXene is often reported as the cathode of MIBs; however, the reported capacities are far from the theoretical value, which needs to be further investigated. Similar to sodium-ion batteries, enlarging the interlayer spacing is a good strategy to improve the Mg storage capacity of the MXene electrode. It not only provides more magnesium storage sites but also reduces magnesium migration barriers. Meanwhile, the reduction of diffusion length of intercalated ions is crucial for fast charge storage. It has been reported that the electrochemical performance of MXene in MIBs can be improved by pre-embedding of organic molecules (CTAB [3], (phenyl-$MgCl)_2AlCl_3$ [82]), carbon nanospheres [83] or bacterial celluloses (BC) [85]. In addition, MXene-based composites can also be

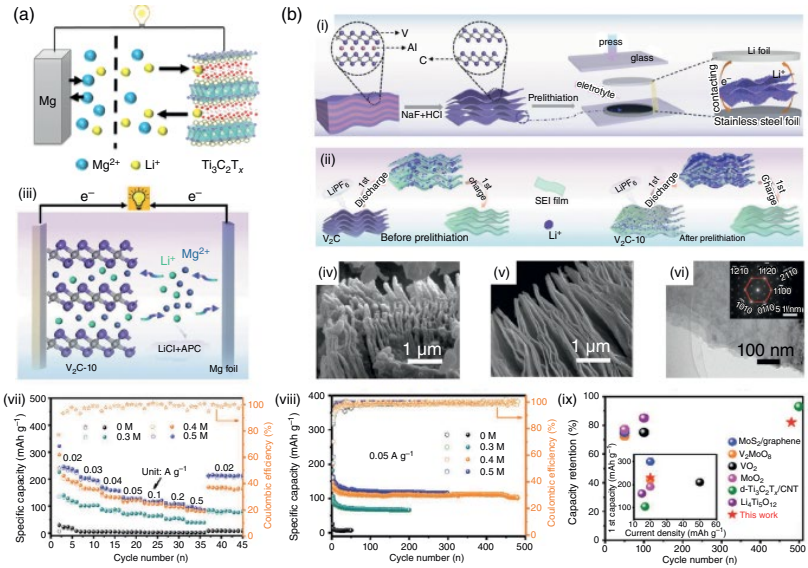


Figure 21.6 (a) Schematic of a hybrid Mg^{2+}/Li^{+} battery using $Ti_3C_2T_x$ MXene as the cathode material. *Source:* Byeon et al. [11]/American Chemical Society. (b) (i) Illustration of the fabrication process for V_2C MXene and prelithiated V_2C; (ii) schematic of a Li-ion battery working. The prelithiation can enlarge the MXene interlayers and compensate for the Li loss in the initial cycle, leading to a high reversible capacity; (iii) schematic illustration of the hybrid battery. This system employs Mg foil as the anode, V_2C-10 as the cathode, and the electrolyte contains both Mg^{2+} and Li^{+}; SEM images of (iv) V_2C and (v) the V_2C after 10 minutes prelithiation, respectively; (vi) TEM image of V_2C, inset is the SAED pattern; (vii) rate capabilities of the V_2C-10 with different electrolytes; (viii) cycling performance of the V_2C-10 electrodes at 0.05 $A g^{-1}$ with different electrolytes; (ix) the reversible capacity and cycling performance comparisons of V_2C-10 and other typical electrode materials used for MLIBs reported. *Source:* Liu et al. [81]/Reproduced from John Wiley & Sons, Inc.

prepared by hydrothermal methods, such as $MoS_2/Ti_3C_2T_x$ [88], $MnO_2/Ti_3C_2T_x$ [84], MnO_2/V_2CT_x [86], $TiS_2/Ti_3C_2T_x$ [87] and so on.

However, to date, there are few experimental reports of MXenes as electrodes for MIBs due to several challenges. All of the above studies have utilized layered $Ti_3C_2T_x$ to obtain highly porous structures with large surface areas by combining molecules with structures. This raises a critical question about the possibility of unsolvated Mg^{2+} intercalation in MXenes, compared to the predominantly surface reactions and/or intercalation of complex ions. The average voltage must be positive, and the ions must have a low enough migration barrier to achieve significant embedding in the particles. To enable competitive energy-dense Mg batteries, intercalation of unsolvated and noncomplexed Mg^{2+} ions is necessary. Another key challenge is the dissociation of Mg^{2+} from the electrolyte, especially in the presence of chloride ions, where the Mg—Cl bond is strong. Therefore, electrolytes with weakly solvated Mg^{2+} must be used, or some mechanism is required to desolvate Mg^{2+} easily enough to intercalate. Furthermore, even if Mg^{2+} desolvation and anion dissociation are successful and the migration barrier inside MXene is low, the intercalation of Mg^{2+} depends on the local environment of the MXene edge. Overall, more research is needed to address the above challenges to realize the theoretical potential of MXenes in the positive poles of energy-intensive MIBs.

21.2.4 Aluminum-Ion Batteries

As one of the rechargeable batteries, aluminum-ion batteries (AIBs) are considered the most promising alternatives to traditional LIBs due to their advantages in cost, energy, and safety. Al^{3+} has the smallest ionic radius (0.54 Å) among the Li^+, Na^+, K^+, Mg^{2+}, Ca^{2+}, and Al^{3+} carrier ions, so the intercalation of Al ions into the MXene layer may result in a relatively small volume expansion of the electrode without significant comminution. Importantly, considering the energy density and charge storage capacity, the aluminum anode has a high theoretical capacity because each Al^{3+} can exchange three electrons in the electrochemical process. The volume capacity (8046 mAh cm^{-3}) is about four times that of lithium metal (2062 mAh cm^{-3}), and the mass capacity (2980 mAh g^{-1}) is close to lithium (3860 mAh g^{-1}). However, the standard reduction potential of aluminum is less negative than that of lithium (−1.7V vs. −3.0V), which leads to a lower energy density of AIBs. Despite this drawback, aluminum is far more abundant in the earth's crust (about 8%) than lithium is on earth (about 0.0065%), reducing battery costs and facilitating the manufacturing process. In addition, AIBs can be treated in the air with high safety in an aqueous solution.

However, like other multivalent metal-ion batteries, the poor cycling performance and slow diffusion dynamics seriously limit the development of AIBs. The

reversible embedding and rapid transmission of Al ions are hindered by the high charge density of Al^{3+} and the strong electrostatic interaction between Al^{3+} and the host material (cathode), resulting in poor capacity and rate performance. Furthermore, the electrode cannot perform optimally due to the complex insertion dynamics of Al ions. And the dissolution of active substances during circulation is also a serious problem in AIBs, resulting in rapid capacity decay. Although the research of aluminum-ion batteries has made great progress in recent years, there are still only a few cathode materials that can satisfy the reversible deintercalation of Al ions. Most of them are difficult to consider from the aspects of capacity and cycle life and lack suitable cathode materials with the ideal capacity and long-term stability. Therefore, the research of cathode materials is the top priority of aluminum-ion batteries, such as carbon materials, oxides, sulfides, selenides, etc. [107, 108].

In recent years, MXenes widely used in electrochemical energy storage have shown the excellent electrochemical performance of MXene. Unlike other electrodes, MXene is unique in that its reactivity toward Al ions can be controlled by modifying surface terminating groups T and/or M elements. However, as far as we know, there are currently few reports on the application of MXenes in AIBs. Theoretically, the electrochemical intercalation of Al ions into $Ti_3C_2T_x$ MXene was reported by Lukatskaya et al. [109]. Experimentally, in 2017, VahidMohammadi et al. [4] demonstrated that V_2CT_x MXene is a high-capacity intercalation cathode material for rechargeable aluminum batteries, as shown in Figure 21.7a. V_2CT_x MXene exhibited an ultrahigh reversible discharge capacity (greater than 300 mAh g^{-1}), but its cycle performance was poor, with the capacity decaying to less than 100 mAh g^{-1} after 100 cycles. Later, the application of MXene in AIBs mainly focuses on the intercalation and surface modification of $Ti_3C_2T_x$ MXene-based composites. For instance, MoS_2@$Ti_3C_2T_x$ [93], F-$Ti_3C_2T_x$@Ag [92], $Ti_3C_2T_x$@Te [91], $Ti_3C_2T_x$@CTAB-Se [90], D-$Ti_3C_2T_x$@S@TiO_2 [89], Co_9S_8NP@NPC@$Ti_3C_2T_x$ (Figure 21.7b) [94], $Ni_{0.6}C$ $o_{0.4}S$@$Ti_3C_2T_x$@NC (Figure 21.7c) [95] and so on. In general, fine structural modulation is of great significance for the further development of MXene as an AIB cathode material with excellent electrochemical performance.

21.3 Metal-Sulfur Batteries

In advanced energy storage systems, metal-sulfur batteries are generally considered as one of the most promising energy storage technologies owing to their high charge storage capacity and energy density, such as lithium-sulfur batteries, sodium-sulfur batteries, magnesium-sulfur batteries, etc. In recent years, the application of MXene materials in metal-sulfur batteries has also attracted extensive attention.

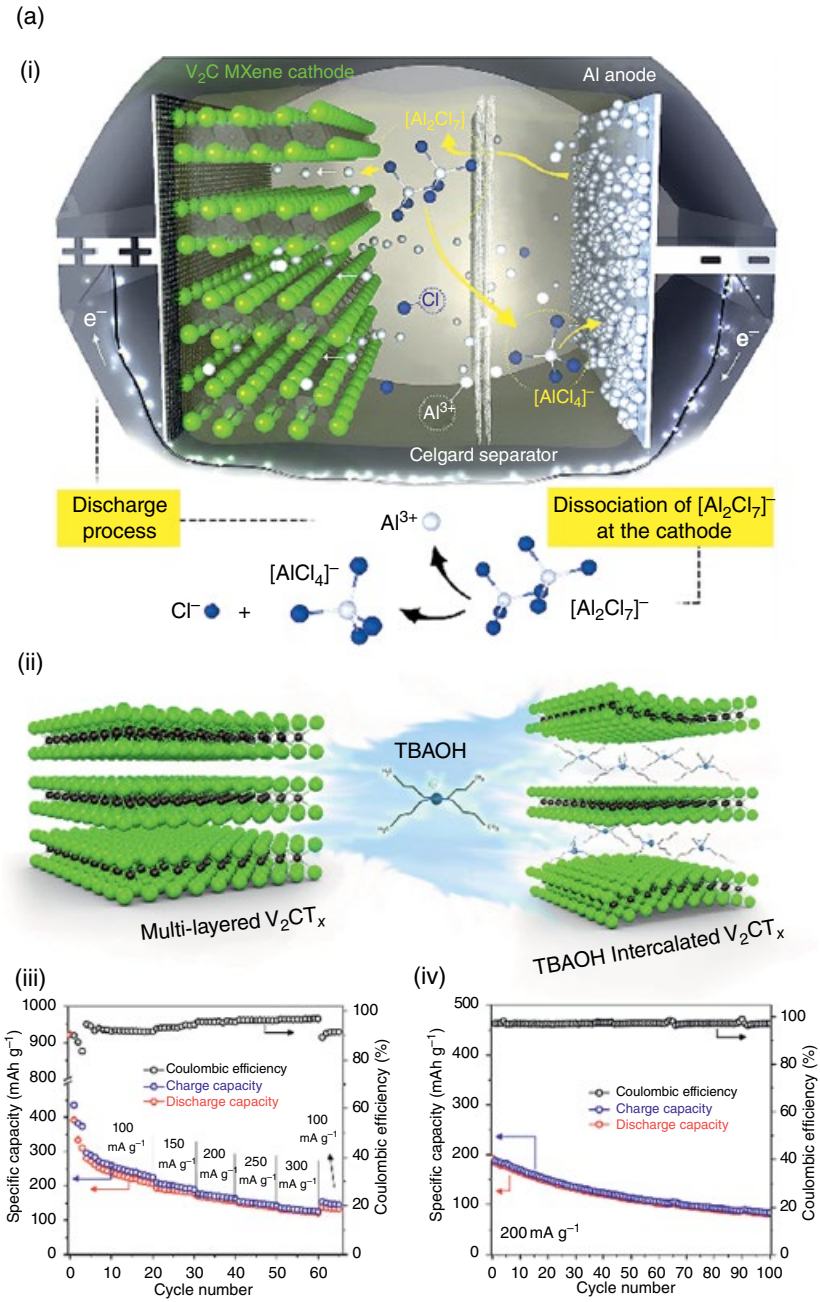


Figure 21.7 (a) (i) Schematic illustration of the proposed mechanism for an Al battery with V_2CT_x MXene as the cathode during discharge in 1.3 : 1 $AlCl_3$/[EMIm]Cl ionic liquid electrolyte; (ii) schematic illustration of interlayer expansion of ML-V_2CT_x MXene through TBAOH intercalation; (iii) rate capability of a TBAOH-FL-V_2CT_x cathode; (iv) cycling performance of TBAOH-FL-V_2CT_x cathode over 100 cycles at 200 mA g^{-1}. *Source:* Vahid Mohammadi et al. [4]/

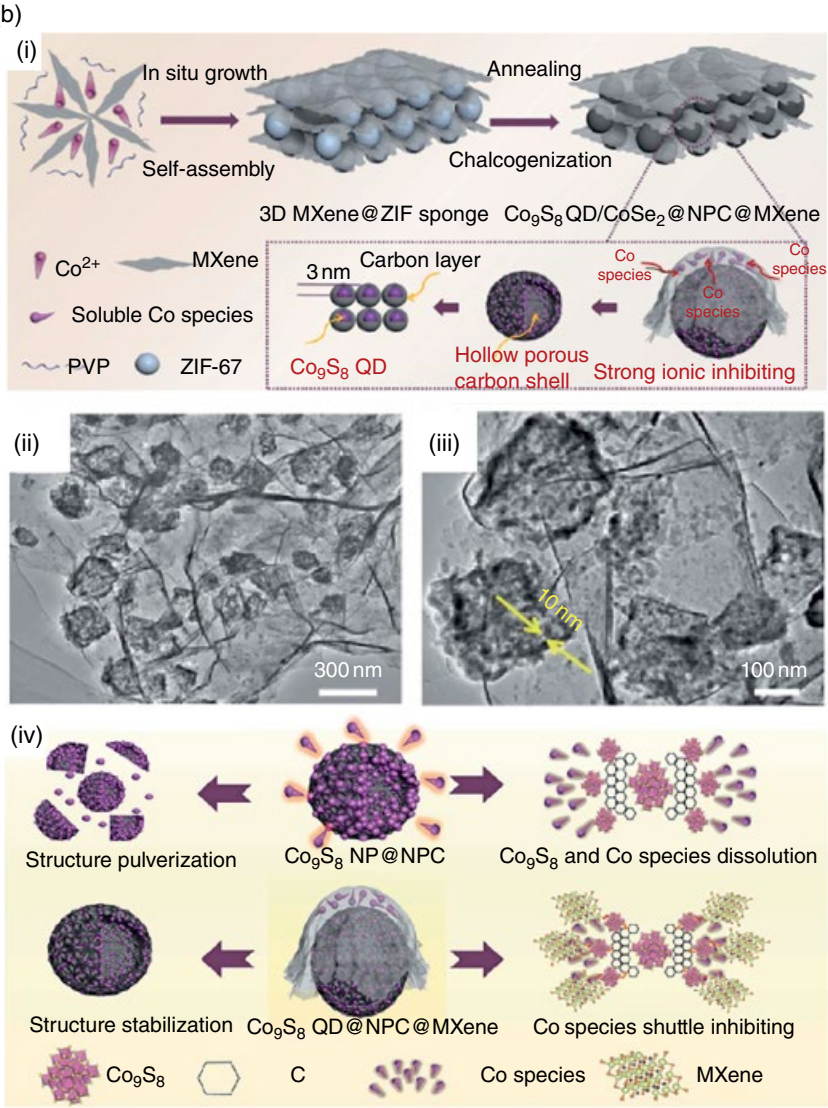


Figure 21.7 (Continued) American Chemical Society. (b) (i) Schematic illustration of the synthetic process of Co_9S_8 NP@NPC@MXene. (ii) and (iii) TEM image of Co_9S_8 NP@NPC@MXene; (iv) the schematic of the performance enhancement of the Co_9S_8 NP@NPC@MXene cathode. *Source:* Yao et al. [94]/Reproduced from Royal Society of Chemistry. (c) (i) Illustration for the synthesis of $Ni_{0.6}Co_{0.4}S$@MXene@NC composite; SEM (ii) and TEM (iii) and (iv) images of $Ni_{0.6}Co_{0.4}S$@MXene@NC; (v) cycling performance of $Ni_{0.6}Co_{0.4}S$@MXene@NC, CoS@MXene@NC, $Ni_{0.6}Co_{0.4}S$@NC, and $Ni_{0.6}Co_{0.4}S$@MXene at 1000 mA g^{-1}. *Source:* Zheng et al. [95]/Reproduced with permission from Elsevier.

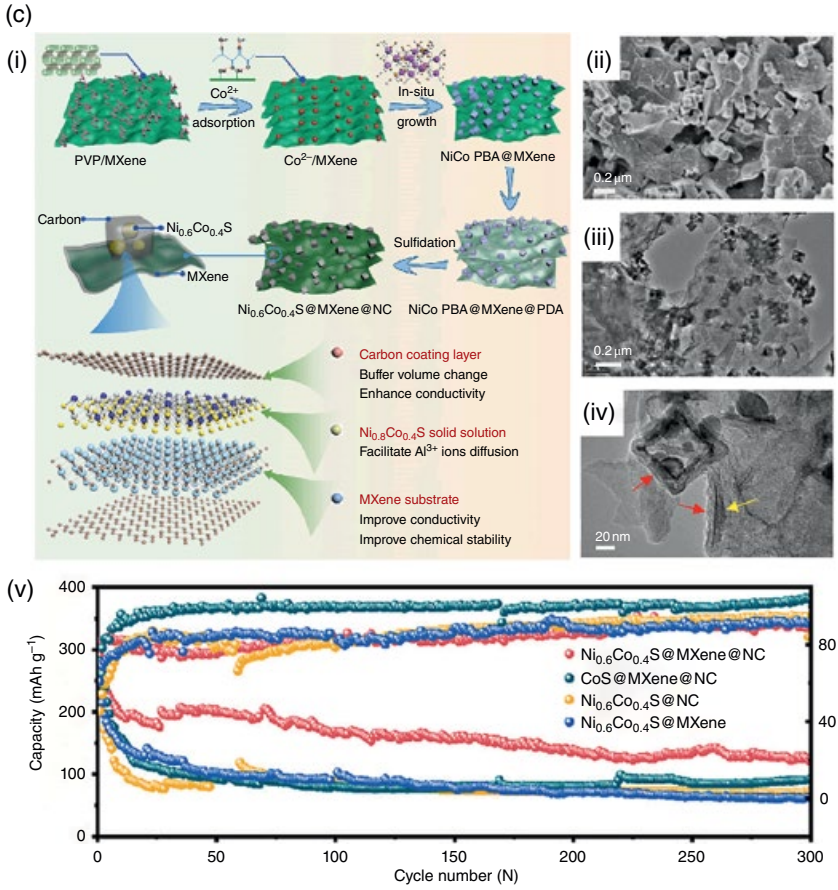


Figure 21.7 (Continued)

21.3.1 Lithium-Sulfur Batteries

Recently, rechargeable LSBs have taken the lead in developing advanced energy storage systems due to high theoretical capacity (1675 mAh g^{-1} for sulfur cathode, 3860 mAh g^{-1} for lithium anode) and high energy density (2567 Wh kg^{-1}, almost 5–10 times that of LIBs). In addition, lithium-sulfur batteries have many advantages such as low cost, high natural sulfur abundance and nontoxic, wide operating temperature range, and long cycle life, which are considered to be promising next-generation energy storage systems. However, large-scale production and commercial application of LSBs have been hindered by the following problems [110, 111]:

1) Shuttle effect: Long chain lithium polysulfide (Li_2S_n, $4 \leq n \leq 8$, LiPS), a soluble intermediate product generated during discharge, dissociates into electrolyte and shuttles between cathode and anode. Owing to the loss of active sulfur caused by the uncontrolled migration of Li_2S_n and the passivation of lithium anode caused by the reaction of Li_2S_n with Li to form an insulating layer (insoluble Li_2S_2/Li_2S), it leads to fast capacity attenuation, short cycle life, low Coulombic efficiency, and serious self-discharge.
2) Low conductivity: Both sulfur (5×10^{-30} S cm^{-1} at 25 °C) and Li_2S (10^{-30} S cm^{-1} at 25 °C) are electrically and ionically insulated, greatly reducing the kinetics of redox reactions, resulting in inadequate sulfur utilization, low productivity, and poor rate performance.
3) Volume expansion: The density difference between S_8 (2.03 g cm^{-3}) and Li_2S (1.66 g cm^{-3}) causes a large volume fluctuation (80%) during lithiation/delithiation, which may lead to structural damage of the electrode.
4) Lithium dendrites: Dendrites are generated on the lithium anode due to repeated dissolution and hetero-deposition of lithium during charge and discharge. The dendrites growing on the surface tend to perforate the separator and contact with the sulfur cathode, potentially shorting the battery.

The above problems make it more arduous to assemble high-energy-density LSBs with high sulfur content and sulfur-loaded area. Therefore, the general approach to overcome the problem is to find a conductive host or modified separator with more abundant polysulfide chemisorption sites in a physical restriction/chemisorption manner to suppress polysulfide migration and promote sulfur redox kinetics, including chemical bonding of polar metal compounds with Li_2S_n, insertion of conductive interlayers between cathode and separator, and the design of an advanced lithium anode to inhibit dendrite growth [112, 113].

2D MXene materials have been widely studied in lithium-sulfur batteries because of their unique properties. They are used as conductive sulfur hosts, separators, and lithium anodes. Specifically, (i) the unique layered structure provides sufficient reaction sites for sulfur conversion and can also be constructed as a 3D porous framework to achieve high sulfur loading and provide good mechanical strength to withstand the stress caused by the bulk expansion of sulfur. (ii) Excellent metal conductivity (Ti—C—Ti bond) promotes electron transfer at the electrode/electrolyte interface and alleviates electrode polarization, thereby improving the utilization of sulfur-active materials and facilitating high-rate response even under high sulfur load. (iii) MXenes exhibit excellent adsorption properties for Li_2S_x species. Soluble Li_2S_4, Li_2S_6, and Li_2S_8 can be captured by bare and hydroxy-terminated MXenes through strong metal-S interaction. On the contrary, Li_2S and Li_2S_2 can be confined by –O groups and bare MXenes, thus inhibiting the shuttle effect, effectively reducing the loss of active materials, and

maintaining high capacity after long-term cycling. (iv) MXenes with abundant terminated groups exhibit low Li_2S decomposition energy barrier and fast Li^+ diffusivity for the transformation between Li_2S_n and Li_2S, resulting in eminent catalytic performance and promoting electrochemical redox reactions. (v) MXenes can also induce uniform nucleation and growth of lithium, and 2D structure provides a wide range of opportunities to construct advanced structures of MXene/Li composites to suppress lithium dendrites. Therefore, MXenes show great potential in realizing high-performance lithium-sulfur batteries, as shown in Figure 21.8a.

21.3.1.1 MXene on the Sulfur Cathode in LSBs

Currently, most of the reported conductive sulfur host MXene/S materials widely used as LSBs are based on $Ti_3C_2T_x$, Ti_2CT_x, V_2CT_x, and Mo_2CT_x. In 2015, the Nazar team [9] proposed to use 2D Ti_2CT_x MXene nanosheets loaded with sulfur as the cathode material of LSBs and to form Ti_2CT_x/S binary composite material with a sulfur content of 70 wt% through the reaction of sulfur and Ti_2CT_x hydrophilic surface. Although the surface area of the prepared MXene (only 67.9 $m^2\ g^{-1}$) was smaller than that of the traditional porous carbonaceous host, Ti_2CT_x could effectively improve the long-term cycling performance of LSBs, with the discharge capacity of 723 $mAh\,g^{-1}$ after 650 cycles at 0.5 C and the decay rate of each cycle was only 0.05%. This is attributed to the high conductivity of Ti_2CT_x MXene and the chemisorption of the S-Ti-C formed between LiPSs and MXene surface, which facilitates the electron transfer and reaction kinetics of LiPSs.

However, the layered MXene sheets are easily restacked due to van der Waals interaction, which limits the diffusion of Li^+ and hinders chemical interactions with polysulfides. To improve the utilization rate of MXene nanosheets and maximize the advantages of MXenes in LSBs, the following three methods are usually adopted for improvement. One strategy is to chemically modify MXenes, that is, to effectively enhance the adsorption capacity and catalytic effect of MXenes on LiPSs by doping heteroatoms (such as N, S, and metal atoms Ni, Co) [121–123]. Secondly, reasonable structural control is carried out on MXene to mitigate restacking and increase the exposed surface area, that is, to expand the layer spacing or to construct a 3D interconnect porous structure [124]. For example, $Ti_3C_2T_x$ nanosheets are introduced into porous carbon skeleton [125] or graphene aerogel [126] as polysulfide reservoirs to construct 3D MXene frameworks, which provide sufficient space to accommodate high sulfur loadings and alleviate sulfur volume expansion. Finally, the construction of MXene-based composites is an effective strategy to promote Li^+ transport.

Some materials with polar sites often form ternary composites with MXene/S, such as nanostructured carbon materials (i.e., CNTs [114, 127–129], carbon

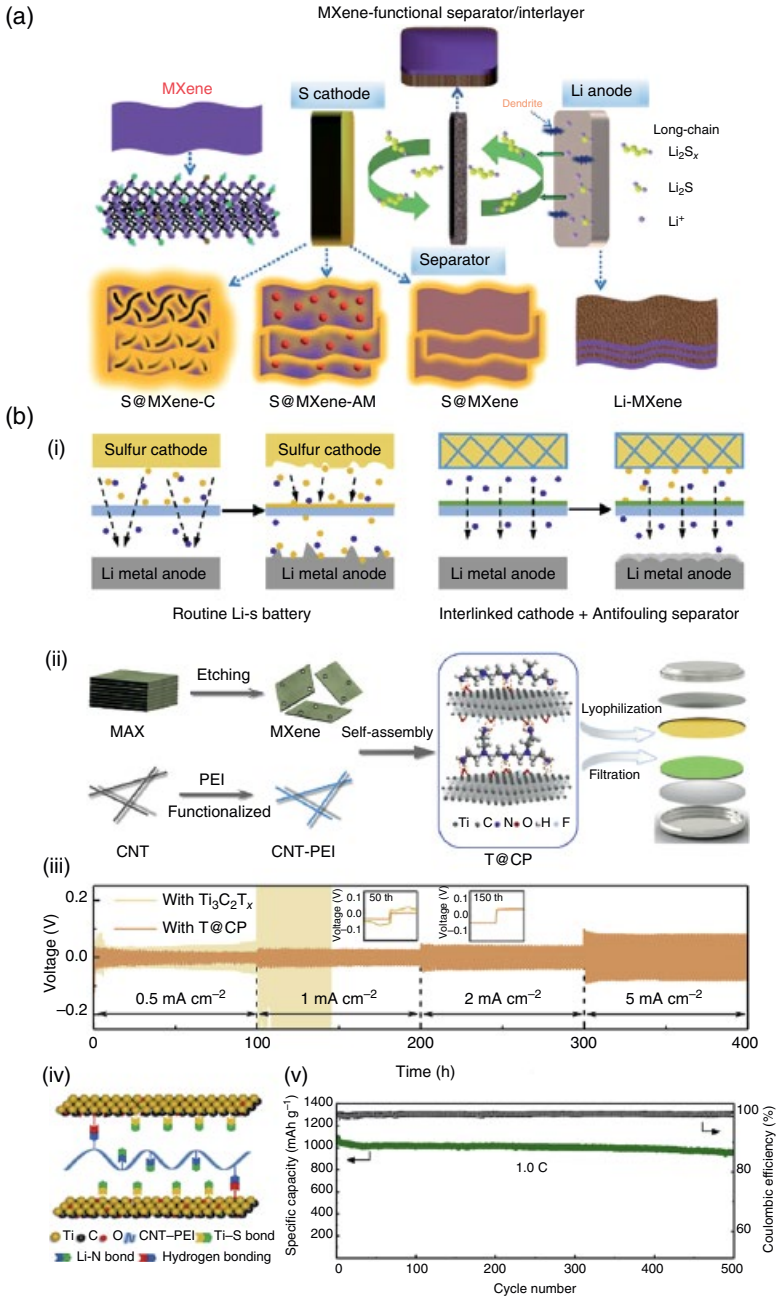


Figure 21.8 (a) Illustration of the MXene-engineered sulfur cathode, Li anode, and separator in LSBs. *Source:* Xiao et al. [110]/Royal Society of Chemistry. (b) (i) Illustration for LSBs with routine configuration and the proposed integrated configuration; (ii) illustration of the fabrication of T@CP nanohybrids for sulfur cathode and modified separator; (iii) voltage-time profiles of Li stripping/plating in Li//Li symmetric cells with 1 mAh cm^{-2} at step-increased current densities; (iv) illustration of the interlamellar nanofluidic channels for LiPS interaction mechanism within the T@CP membrane; (v) performance of T@CP-S|T@CP system at 1 C, sulfur loading is 2.6 mg cm^{-2}. *Source:*

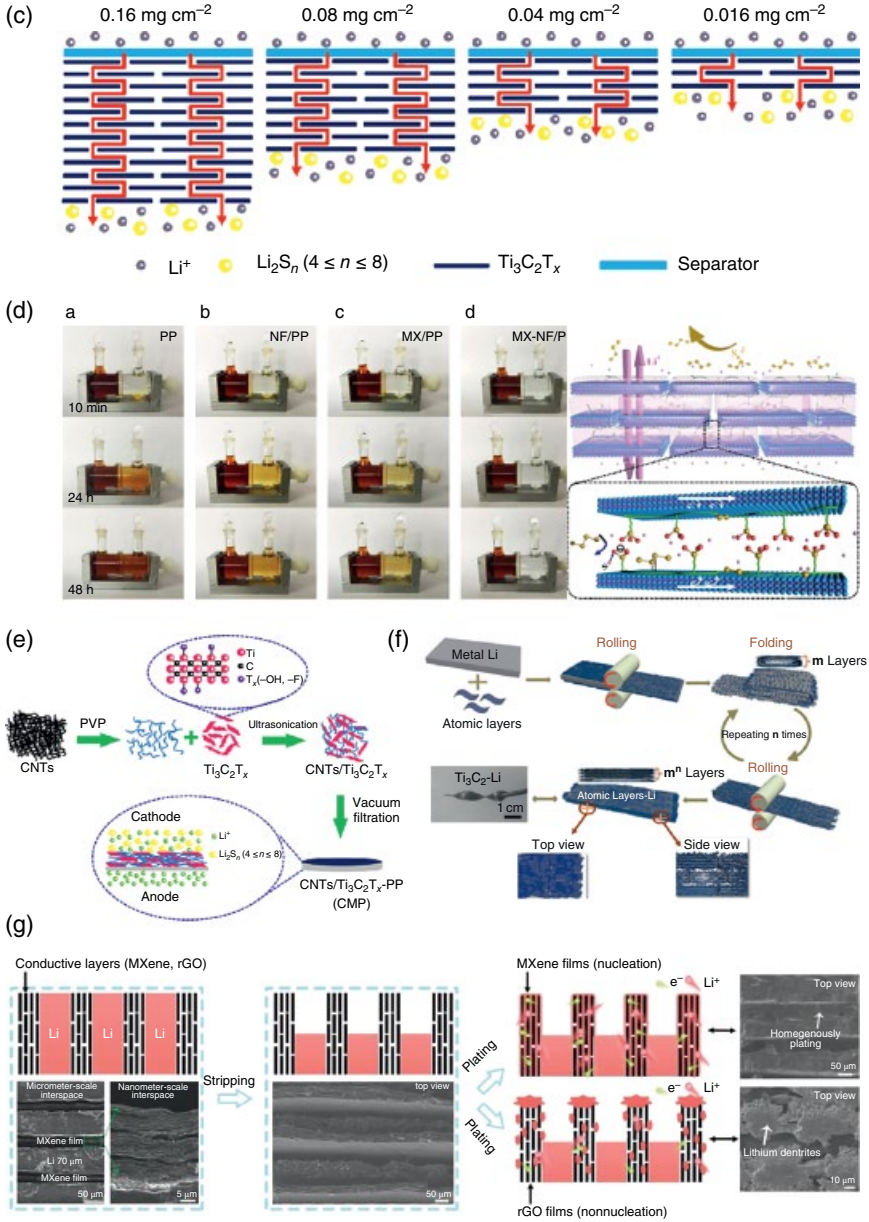


Figure 21.8 (Continued) (c) Schematic illustration of the $Ti_3C_2T_x$-PP separators with different mass loading in LSBs. *Source:* Li et al. [115]/with permission of Elsevier. (d) Polysulfide permeation of PP, NF/PP, MX/PP, and MX-NF/PP separators and the functions of MX-NF/PP separator. *Source:* Wang et al. [116]/with permission of Elsevier. (e) Illustration of the fabrication process for CMP separator. *Source:* Li et al. [117]/with permission of Elsevier. (f) Fabrication of flexible lamellar structured Ti_3C_2 MXene (graphene, BN)-metallic lithium films. *Source:* Li et al. [118]/with permission of Elsevier. (g) Illustration of the stripping and plating states of perpendicular MXene/Li and rGO/Li arrays. The left and middle bottom are the SEM images of

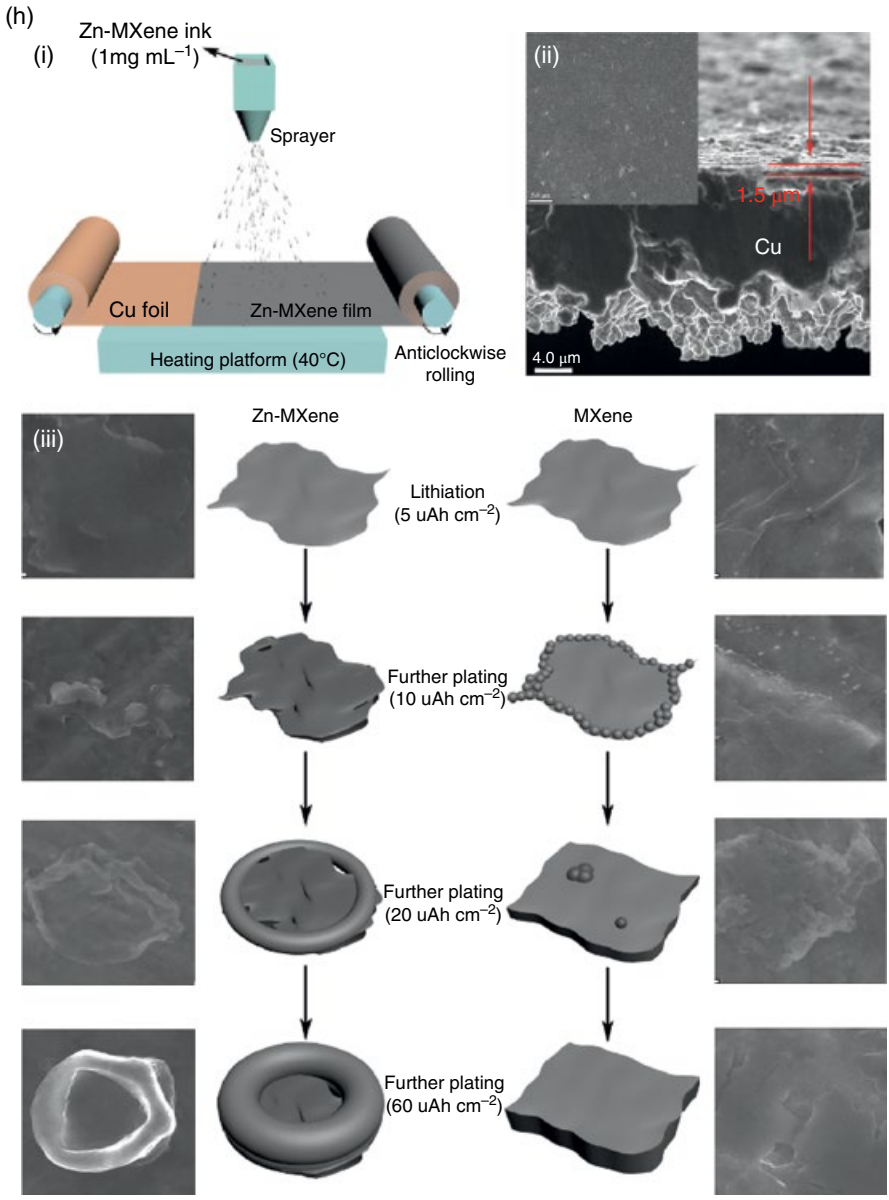


Figure 21.8 (Continued) as-prepared perpendicular MXene/Li arrays and the MXene/Li arrays after lithium stripping, respectively. The right top and right bottom are the top views of SEM images of perpendicular MXene/Li and rGO/Li arrays after initial stripping for 20 mAh cm^{-2} and subsequent plating for 1 mAh cm^{-2}, respectively. *Source:* Cao et al. [119]/John Wiley & Sons. (h) (i) Nucleation and growth SEM diagram of Li on Zn/MXene and MXene nanosheets; (ii) schematic fabrication of Zn/MXene films on large scale by rolling-to-rolling and spray coating technologies; (iii) section and top views (top left corner). *Source:* Gu et al. [120]/ Reproduced from American Chemical Society.

fibers [130], rGO [131], Figure 21.8b), polymers (PDA [132, 133]), metal oxides/sulfides (TiO_2 [134, 135], MnO_2 [136], VO_2 [137], and MoS_2 [138]). In the composites, the obtained MXenes-based heterostructures well preserve the 2D layered geometry, provide a continuous conductive network for fast charge transport, and provide high adsorption and catalysis for LiPSs. In addition to their intrinsic functions, other components can also act as "spacers" to alleviate the re-stacking of MXene and greatly open up more polysulfide entrapping sites and enhance the immobilization ability of LiPSs. Therefore, MXene-based composites generally exhibit prominent electrochemical performance as sulfur hosts. For example, Liang et al. [129] reported a porous and conductive $Ti_3C_2T_x$/CNT structure as a sulfur host.

21.3.1.2 MXene as Separator in LSBs

It is well known that diffusion of LiPSs not only leads to loss of active mass but also leads to unfavorable reactions with the Li anode, resulting in significant polarization. Thence, in addition to designing advanced sulfur hosts, another important aspect of MXenes in LSBs is the use of the separator, which can act both as a barrier to confine LiPS on the cathode side and as an upper current collector to improve LiPSs utilization. Undoubtedly, the MXene-modified separator provides a thin and uniform conductive layer with highly polar "thiophilic" sites to intercept and capture migrating polysulfides, reactivate the trapped active material, and indirectly protect the lithium anode from side reactions and surface passivation, thereby enhancing the electrochemical performance of LSBs. To date, only $Ti_3C_2T_x$ MXene has been used to improve the separator of LSBs, which can stand alone or adhere to the separator by coating/vacuum filtration. Furthermore, the extra weight may be detrimental to the energy density of the battery (Figure 21.8c), and studies have shown that an MXene-based interlayer with a thickness of 100 nm is sufficient to inhibit LiPSs. Therefore, the mass loading of the MXene-modified separator coating is reduced to less than 2% of the weight of the cathode without sacrificing the weight energy density [112, 115, 139].

In 2016, Lin et al. [10] used MXene as a coating for glass fiber separators to suppress the shuttle effect of LSBs for the first time through a simple vacuum filtration method. Compared with original and graphene-coated glass fiber separators, LSBs composed of pure sulfur cathodes (without any heat treatment) and functional $Ti_3C_2T_x$-coated glass fiber separators showed higher capacity (an initial discharge capacity of 820 mAh g^{-1} at 0.5 A g^{-1}) and excellent capacity retention (a discharge capacity of 721 mAh g^{-1} after 100 cycles). Similarly, $Ti_3C_2T_x$ MXene could be applied to biodegradable eggshell membranes [140] and commercial microporous Celgard polypropylene (PP) membranes (Figure 21.8d) [116] to improve the cycling performance of LSBs.

Similar to the case of sulfur hosts, the restacking of layered MXene nanosheets severely hinders the accessibility of ionic and electrolyte components, limiting the full utilization of their surfaces. Meanwhile, the insulating Li S/Li S

continuously accumulates on the separator, which increases interfacial charge transfer resistance and slows ion transport kinetics, resulting in severe polarization and capacity attenuation, especially at high sulfur loadings or high rates. Therefore, the use of MXene-based composites to modify the separator of LSBs can further limit the shuttle effect and promote Li^+ diffusion of the synergistic effect between MXene and other components. Likewise, carbon materials (CNTs, GO) [115, 117, 141], polymers (PEI) [114], and metal oxides (TiO_2, [142]) with strong chemisorption to LiPSs are the most commonly used in combination with MXenes candidate material. For instance, Li et al. [117] coated a 3D interwoven framework structure composed of 1D CNTs and 2D $Ti_3C_2T_x$ MXenes on PP separators (as shown in Figure 21.8e), which significantly improved the electrochemical performance of LSBs. However, it should be noted that the coated MXene-based composites usually have a dense layered structure, which may prevent the efficient penetration of electrolytes. And the MXene-based functionally modified hybrid separator needs to indirectly suppress the growth of lithium dendrites. In general, early capture of polysulfide intermediates by functional coatings can significantly reduce the degradation rate of Li anodes and slow down the growth of Li dendrites, thereby extending the battery life.

21.3.1.3 MXene on Alkali-Metal (Li, Na, and K) Anodes

To alleviate the problems of Li dendrite growth and accommodate the volume expansion, the advanced design of metallic lithium hosts is an effective strategy. MXene materials are considered as a potential lithium host, and the lithiophilicity of terminals can guarantee the efficient combination with lithium and guide nucleation, thereby achieving a stable Li anode. As a result, the application of MXenes to enhance the performance of lithium anodes for high-performance LSBs has received increasing attention.

At present, the application of MXenes in lithium anode is still in the infant stage, mainly focusing on $Ti_3C_2T_x$ MXenes. And a variety of nanostructures on the progress of lithium metal is beneficial to the development of MXene-based lithium-sulfur batteries. For the lamellar structured MXenes, $Ti_3C_2T_x$/Li films were fabricated based on the unique ductility of lithium and the lubricity of atomic layers by a roll-to-roll mechanical approach (Figure 21.8f) [118]. For the vertically structured MXenes, $Ti_3C_2T_x$/Li arrays with bi-periodic interspace were developed by a simple rolling-cutting approach (Figure 21.8g) [119], which significantly facilitated the fast transmission of Li^+ and efficiently mitigated the dendrite formation upon Li stripping/plating. For MXenes with a 3D conductive network structure (such as preparation of 3D porous $Ti_3C_2T_x$/rGO aerogels by hydrothermal approach [110]), the growth of Li dendrites can also be restrained and the volume change upon Li stripping/plating be minimized. In addition, metal atoms doped inside or on the surface of MXenes have also been proven to be

effective nucleating agents, inducing uniform growth of lithium. For example, Gu et al. [120] fixed a single Zn atom on the Ti sites of $Ti_3C_2T_x$ through molten $ZnCl_2$ salt etching, so that Li could homogeneously nucleate on the surface of the formed Zn/MXene films (Figure 21.8h).

Compared with the lithium metal anode, metallic sodium, and potassium have many similarities in electrochemistry, so the application and mechanism of MXene in terms of the stable metal anode are similar. However, sodium metal has higher chemical reactivity than lithium, which makes the application of MXene in sodium metal anode not as much as that in lithium metal anode [143]. To create more internal interlayer space for Na, Luo et al. [31] designed a CT-Sn (II)@Ti_3C_2 fabricated by CTAB pre-pillarization and Sn^{2+} pillarization as the matrix of sodium metal anode by taking advantage of the "pillar effect." The embedded sodiophilic seeds (spot Sn(II) nano complex) not only induce Na to nucleate and grow within MXene interlayers but also endow the volume expansion caused by the alloying reaction with sodium, which further expands the layer spacing and contributes to the uniform deposition of Na. In addition, flexible scaffolds with similar 3D porous structures have been developed to hold Na, such as a fibrous hydroxylated MXene/carbon nanotubes composite (h-Ti_3C_2/CNTs) [144], $Ti_3C_2T_x$-coated carbon cloth host ($Ti_3C_2T_x$-CC) [145], tunable MXene-Derived 1D/2D Hybrid Nanoarchitectures ($Na_3Ti_5O_{12}$-MXene) [146], multifunctional 3D Ti_3C_2 MXene@g-C_3N_4 nanohybrid [147] and V_2CT_x/rGO-CNT MXene microgrid aerogel [148].

Similarly, the chemical reactivity of K is much higher than that of Li and Na, which makes K metal anodes face more severe challenges than Li and Na metal anodes. At present, the introduction of potassiophilic species into 3D conductive frameworks is considered to be one of the most promising methods for producing dendrite-free K metal anodes. Tang et al. [149] prepared a defective and nitrogen-containing MXene/carbon nanotube (DN-MXene/CNTs) independent scaffold as a K metal host for the first time. Among them, potassiophilic DN-MXene nanosheets with high binding energy with K ions as “seeds” can effectively improve the K nucleation and deposition stability. The interconnected CNTs provide 3D conductive networks for fast electronic and ion transport. And 3D host with a large surface area and a porous structure can not only significantly reduce current density to facilitate uniform K plating/stripping but also alleviate volume expansion during cycling to stabilize the electrolyte/electrode interface, resulting in a stable and dendrite-free K metal anode. Shi et al. [71] reasonably designed a 3D alkalized Ti_3C_2 (a-Ti_3C_2) nanoribbon framework with sufficient porous structure and abundant potassiophilic sites as advanced hosts for dendrite-free K deposition via electrodeposition. Owing to the pre-embedded K in the expanded interlayer space, a large number of evenly distributed potassiophilic polar groups, and a 3D conductive porous framework as the host, the nucleation and growth of K metal is well restricted in the 3D skeleton.

21.3.2 Sodium-Sulfur Batteries

Sodium-sulfur batteries (SSBs) are of great research value in the future due to their high theoretical energy density (1274 Wh kg^{-1}) and the natural abundance and low cost of sodium and sulfur resources. However, to maintain good electrical conductivity of electrode materials, traditional SSBs need to operate at 300 °C, and the constant insulation reduces energy conversion efficiency. Therefore, sodium-sulfur batteries at high temperatures are not a long-term solution, focusing on room-temperature sodium-sulfur batteries (RT-SSBs). Similar to LSBs, there are several challenges to be addressed for the large-scale application of RT-SSBs, including the low conductivity of sulfur, uncontrollable shuttle effects of soluble sodium polysulfide (NaPSs), and high-volume expansion during charging and discharging. All of these will lead to the loss of active material sulfur, unsatisfactory reversible capacity, rapid capacity decay, self-discharge, and poor cyclability during the cycle. Therefore, the development of an effective new cathode host material has far-reaching significance for the application of RT-SSBs.

Currently, RT-SSBs are still in their infancy, mainly using carbon materials as the cathode host. So far, MXenes have rarely been used as positive electrodes in RT-SSBs. In 2019, Bao et al. [13] firstly doped heteroatomic sulfur *in-situ* onto the surface of MXene by vacuum freeze-drying method, forming 3D folded MXene nanostructures with high specific surface area, as shown in Figure 21.9a. MXene/S, as the cathode host of RT-SSBS, significantly accelerated the redox reaction and limited the diffusion of sodium polysulfide, which achieved high sulfur loading up to 4.5 mg cm^{-2} and excellent electrochemical performance (reversible capacity of 577 mAh g^{-1} at 2 C after 500 cycles). However, the aggregation and restacking of MXene significantly limit the areal loading of sulfur. The team [33] later prepared porous nitrogen-doped $Ti_3C_2T_x$ MXene microspheres (N-$Ti_3C_2T_x$@MWCNT-MP, Figure 21.9b) with abundant pore structure and heteroatomic functional groups by improved spray drying and annealing approach. It exhibited a high area sulfur load (5.5 mg cm^{-2}), high reversible capacity (980 mAh g^{-1} at 0.5 C), and stable cycling performance (450.1 mAh g^{-1} at 2 C after 1000 cycles).

21.3.3 Magnesium-Sulfur Batteries

Magnesium-sulfur batteries (MSBs) as an emerging technology likewise represent outstanding candidates for cheap, sustainable, energy-intensive, and safe energy storage. Compared with lithium-sulfur batteries, MSBs are attractive because of their rich and nontoxic Mg and S resources, high energy density (1722 Wh kg^{-1}), and inherent dendrite-free properties supported by Mg anode. Similarly, capacity loss, coulomb efficiency attenuation, and anodic corrosion are the biggest development challenges for MSBs, caused by the low conductivity of S and discharge

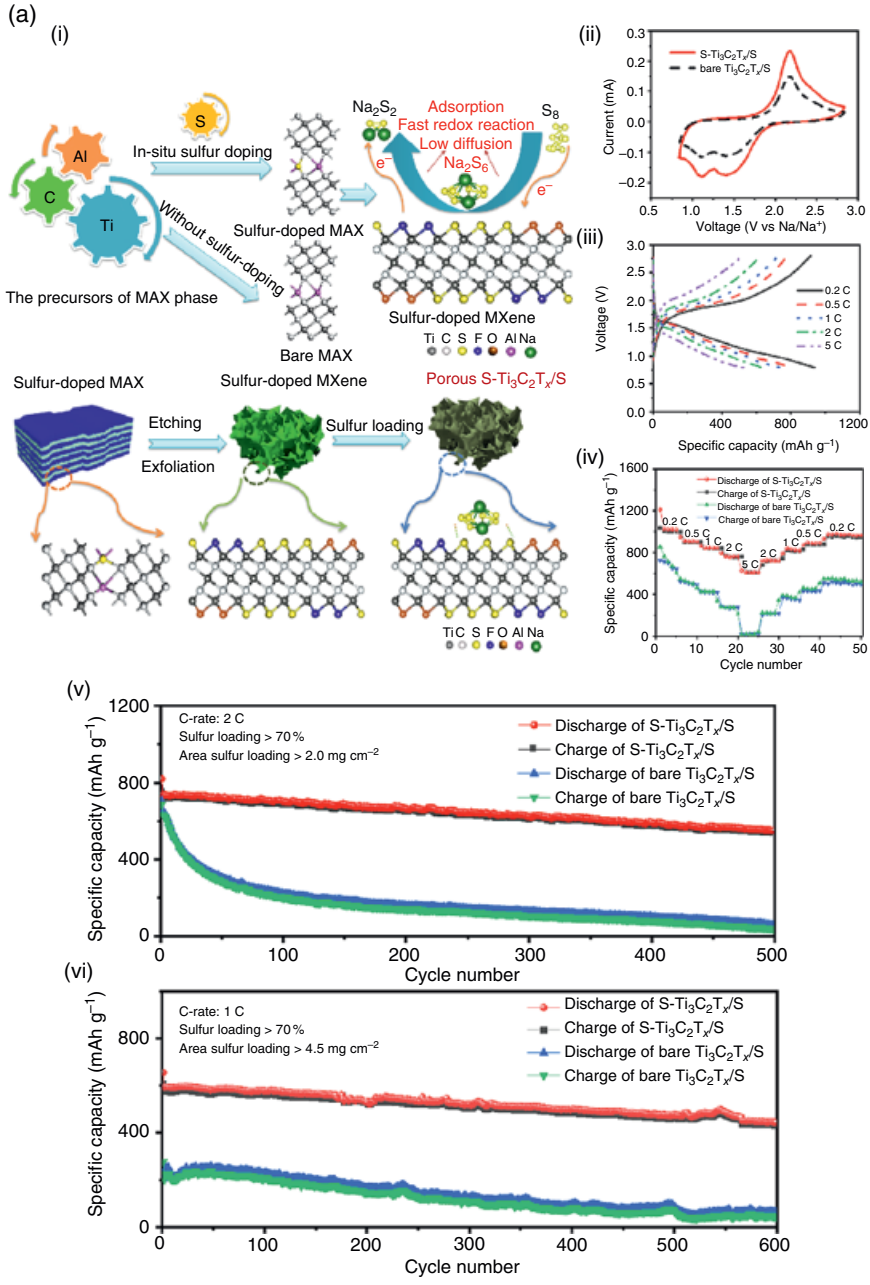


Figure 21.9 (a) (i) Schematic diagram demonstrating the preparation of sulfur-doped MXene, along with the discharge process in sulfur-doped MXene/S cathode; (ii) cyclic voltammograms of SSBs with S-$Ti_3C_2T_x$/S and $Ti_3C_2T_x$/S cathodes at the second cycle at a scan rate of 0.1 mV s^{-1}; (iii) charge/discharge profiles of S-$Ti_3C_2T_x$/S sulfur cathodes at current rates from 0.2 to 5 C; (iv) rate capability of S-$Ti_3C_2T_x$/S and bare $Ti_3C_2T_x$/S cathode at 0.2 to 5 C; (v) cycling performances of S-$Ti_3C_2T_x$/S and bare $Ti_3C_2T_x$/S cathode at 2 C for 500 cycles; (vi) cycling performances of S-$Ti_3C_2T_x$/S and bare $Ti_3C_2T_x$ cells with a high sulfur loading of 4.5 mg cm^{-2} at 1 C for 600 cycles. *Source:*

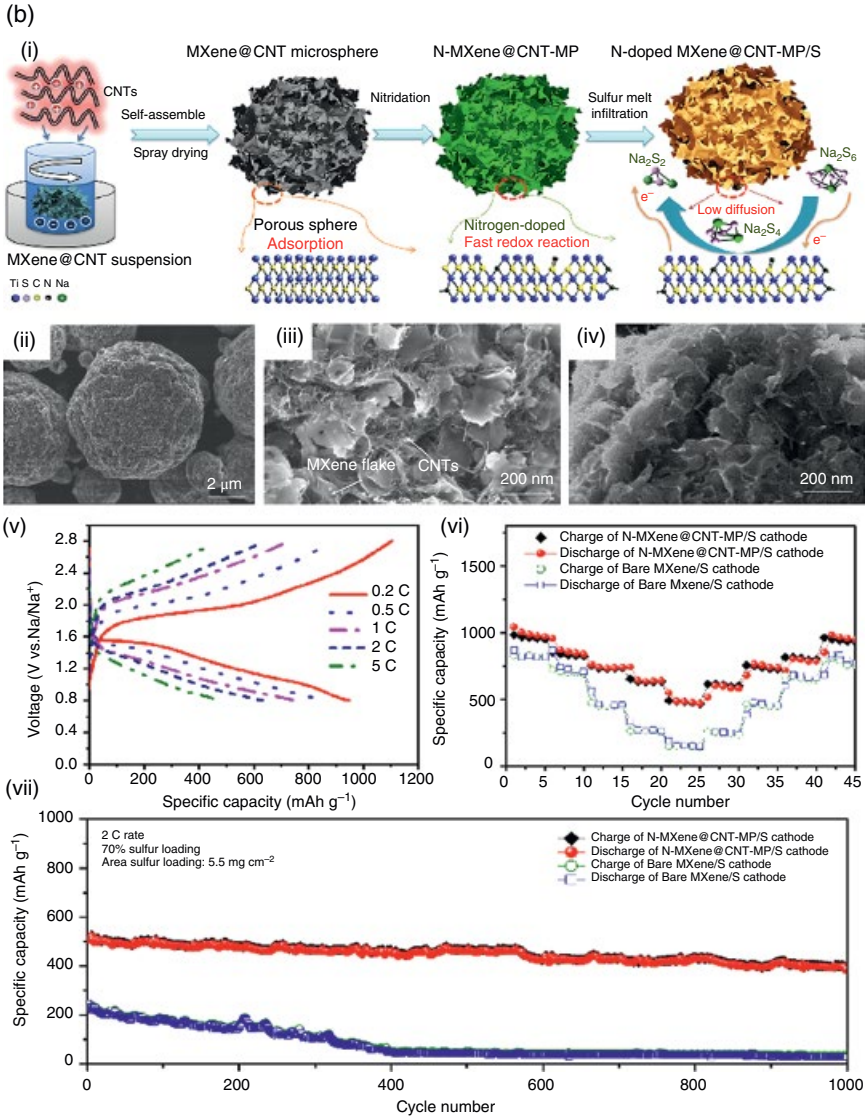


Figure 21.9 (Continued) (b) (i) The schematic preparation procedure of porous N-MXene@MWCNT-MP/S microspheres; (ii), (iii) SEM image of N-MXene@MWCNT-MP sample; (iv) SEM image of N-MXene@MWCNT-MP/S composites; (v) charge/discharge profiles of N-MXene@MWCNT-MP/S sulfur cathodes at 0.2–5 C; (vi) rate capability of N-MXene@ MWCNT-MP/S and bare MXene/S cathodes cathode at 0.2–5 C; (vii) cycling performance of NMXene@MWCNT-MP and bare MXene/S cathodes at 2 C with a high sulfur loading. *Source:* Li et al. [33]/Reproduced from Royal Society of Chemistry.

products and the shuttle effect of soluble magnesium polysulfides (MgPSs), as shown in Figure 21.10a. In particular, during the cycle, electrochemical processes involve the deposition and decomposition of MgPSs intermediates and solid MgS, which is a more complex multi-electron solid–liquid–solid conversion than LSBs. Moreover, the large ion size and slow diffusivity of divalent magnesium ions will further prevent the development of MSBs.

Therefore, the development of appropriate sulfur host materials and electrolytes is crucial for realizing MSBs. Currently, the research on MSBs has mainly focused on non-nucleophilic electrolytes and little attention has been paid to cathode optimization, in stark contrast with LSBs. In most cases, sulfur host materials used in LSBs can serve as relevant models for MSBs, including carbon-based materials (carbon black, graphene, and carbon nanofibers), metal oxides/sulfides, metal-organic frameworks (MOFs) and MXenes et al. There are only three reports on the application of MXene in MSBs so far. Kaland et al. [14] used MXene as the sulfur host material in MSBs for the first time (Figure 21.10b), demonstrating the importance of combining MXene with high surface area co-host materials such as CNTs, which almost doubled the discharge capacity of MSBs (530 vs. 290 mAh g^{-1}), and the capacity retention was 83% after 25 cycles. Zhao et al. [151] constructed a Co_3S_4@MXene heterostructure as an efficient sulfur host for MSBs, as shown in Figure 21.10c. Benefiting from the excellent conductivity of MXene and the catalytic effect of Co_3S_4, the composite effectively improved the electrochemical reaction kinetics of MSBs with a specific capacity of 1220 mAh g^{-1} and the capacity retention of 528 mAh g^{-1} after 100 cycles. Xu et al. [152] successfully prepared a heterogeneous CoO@MXene sulfur host and applied it in MSBs (Figure 21.10d). CoO exhibited stronger adsorption of magnesium polysulfide, while $Ti_3C_2T_x$ promoted the diffusion and transfer of Mg^{2+}, to improve the electrochemical performance of MSBs. The initial discharge capacity was up to 1500 mAh g^{-1} and the capacity of 540 mAh g^{-1} was maintained after 70 cycles at 100 mA g^{-1}. In a nutshell, MXene-base materials are outstanding choices as sulfur host materials for long cycle-life MSBs.

21.4 Conclusions and Perspectives

Different from mature carbon-based materials, the unique 2D structure and tunable surface chemistry of MXene materials will not only facilitate the development of high energy density LIBs but also have enormous potential in other energy storage fields. Herein, we summarize the application progress of MXene-based materials in non–Li-ion storage, showing relatively excellent electrochemical performance. But the development of MXene-based in NLIBs is still in its infancy, and several key hurdles require further optimization for their practical application, including:

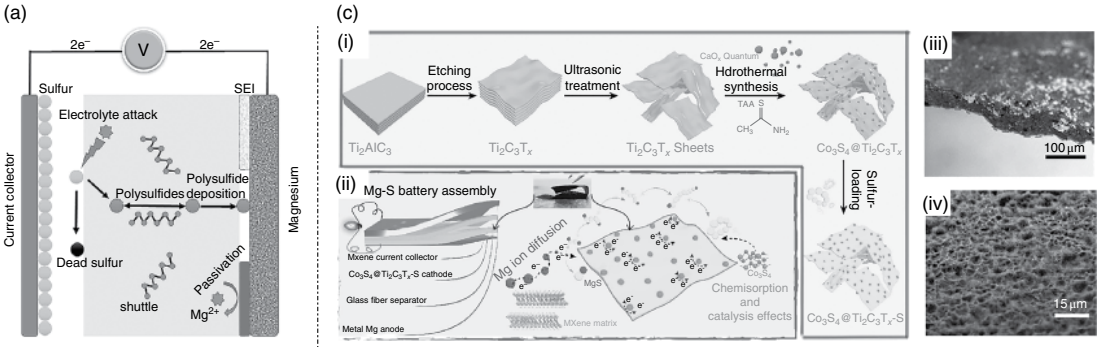


Figure 21.10 (a) Schematic diagram of MSBs showing the working principle and formation of magnesium-polysulfides (Mg-PS), which passivate the anode surface. *Source:* Rashad et al. [150]/with permission of Elsevier. (b) (i) Procedure for preparing PMTT composites from $Ti_3C_2T_x$ MXene, CNT, and PMTT, and (ii) schematic of the resulting films; procedure for preparing (iii) S8-mixed and (iv) S8-sandwich from $Ti_3C_2T_x$ MXene, CNT, and an aqueous S8 nanoparticle dispersion; (v) schematic principle of using MXene as interlayer with the S8-mixed cathode; SEM micrographs of the (vi) S8-mixed and (vii) S8-sandwich film. *Source:* Wu et al. [14]/Reproduced from American Chemical Society. (c) Illustration of (i) the fabricating process of the Co_3S_4@MXene heterostructure and the Co_3S_4@MXene-S cathode material, (ii) scheme of the function of the Co_3S_4@MXene heterostructure in MSBs; SEM images of the flexible Co_3S_4@MXene-S cathode (iii) cross-sectional and (iv) top-view images. *Source:* Zhao et al. [151]/with permission of Elsevier. (d) (i) General methods used to prepare Ti_3C_2 and Ti_3C_2@CoO; (ii) magnesium polysulfide redox mechanism of the S-Ti_3C_2@CoO electrode. *Source:* Xu et al. [152]/with permission of Elsevier.

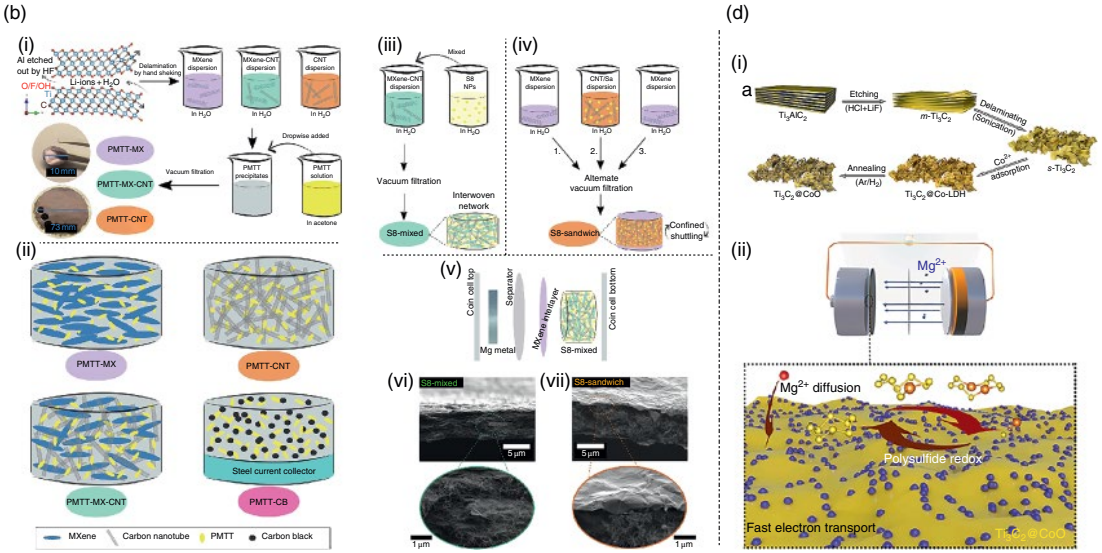


Figure 21.10 (Continued)

1) The ionic dynamics and charge storage mechanism between MXene nanosheets are still unclear. Therefore, the energy storage mechanism of MXene in NLIBs and the composition/structural evolution during charging and discharging need to be further studied in the future, such as *in-situ* tests.
2) Terminals, vacancies, and dopant atoms have a great influence on many properties of MXene, such as electrical conductivity, adsorption capacity, catalytic effect, and affinity with metals. Hence, it is crucial to explore the dynamic change of MXene interlayer spacing, regulation of surface engineering, and chemical modification.
3) The long-term development of MXene materials is strongly hindered by the re-stacking and oxidation, so effective approaches to address these problems are rational structural design and precise morphological control of electrodes.
4) Due to the immature preparation technology and the shortage of MXene types, the current experimental studies mainly focus on $Ti_3C_2T_x$, with a small amount of Ti_2CT_x, V_2CT_x, Mo_2CT_x, and Nb_2CT_x, etc. As a result, the search for novel MXene with different functionalities to develop non–lithium-ion storage is a promising direction.

In conclusion, although there is still giant space for improvement in capacity and stability when MXene is used as an NLIB material, continued extensive research and development will enable MXene to demonstrate unlimited opportunities to build high-performance batteries.

References

1 Chen, M., Liu, Q., Wang, S.-W. et al. (2019). *High-abundance and low-cost metal-based cathode materials for sodium-ion batteries: problems, progress, and key technologies*. *Advanced Energy Materials* 9 (14): 1803609.

2 Wu, Y., Sun, Y., Zheng, J. et al. (2021). *MXenes: advanced materials in potassium ion batteries*. *Chemical Engineering Journal* 404: 126565.

3 Xu, M., Lei, S., Qi, J. et al. (2018). *Opening magnesium storage capability of two-dimensional MXene by intercalation of cationic surfactant*. *ACS Nano* 12 (4): 3733–3740.

4 VahidMohammadi, A., Hadjikhani, A., Shahbazmohamadi, S., and Beidaghi, M. (2017). *Two-dimensional vanadium carbide (MXene) as a high-capacity cathode material for rechargeable aluminum batteries*. *ACS Nano* 11 (11): 11135–11144.

5 Er, D., Li, J., Naguib, M. et al. (2014). *Ti_3C_2 MXene as a high capacity electrode material for metal (Li, Na, K, Ca) ion batteries*. *ACS Applied Materials & Interfaces* 6 (14): 11173–11179.

6 Naguib, M., Kurtoglu, M., Presser, V. et al. (2011). *Two-dimensional nanocrystals produced by exfoliation of Ti_3AlC_2. Advanced Materials* 23 (37): 4248–4253.

7 Naguib, M., Come, J., Dyatkin, B. et al. (2012). *MXene: a promising transition metal carbide anode for lithium-ion batteries. Electrochemistry Communications* 16 (1): 61–64.

8 Xie, Y., Dall'Agnese, Y., Naguib, M. et al. (2014). *Prediction and characterization of MXene nanosheet anodes for non-lithium-ion batteries. ACS Nano* 8 (9): 9606–9615.

9 Liang, X., Garsuch, A., and Nazar, L.F. (2015). *Sulfur cathodes based on conductive MXene nanosheets for high-performance lithium-sulfur batteries. Angewandte Chemie International Edition* 54 (13): 3907–3911.

10 Lin, C., Zhang, W., Wang, L. et al. (2016). *A few-layered Ti_3C_2nanosheet/glass fiber composite separator as a lithium polysulphide reservoir for high-performance lithium-sulfur batteries. Journal of Materials Chemistry A* 4 (16): 5993–5998.

11 Byeon, A., Zhao, M.-Q., Ren, C.E. et al. (2017). *Two-dimensional titanium carbide MXene as a cathode material for hybrid magnesium/lithium-ion batteries. ACS Applied Materials & Interfaces* 9 (5): 4296–4300.

12 Naguib, M., Adams, R.A., Zhao, Y. et al. (2017). *Electrochemical performance of MXenes as K-ion battery anodes. Chemical Communications* 53 (51): 6883–6886.

13 Bao, W., Shuck, C.E., Zhang, W. et al. (2019). *Boosting performance of Na-S batteries using sulfur-doped $Ti_3C_2T_x$ MXene nanosheets with a strong affinity to sodium polysulfides. ACS Nano* 13 (10): 11500–11509.

14 Kaland, H., Fagerli, F.H., Hadler-Jacobsen, J. et al. (2021). *Performance study of MXene/carbon nanotube composites for current collector- and binder-free Mg-S batteries. ChemSusChem* 14 (8): 1864–1873.

15 Wang, X., Shen, X., Gao, Y. et al. (2015). *Atomic-scale recognition of surface structure and intercalation mechanism of $Ti_3C_2T_x$. Journal of the American Chemical Society* 137 (7): 2715–2721.

16 Kajiyama, S., Szabova, L., Sodeyama, K. et al. (2016). *Sodium-ion intercalation mechanism in MXene nanosheets. ACS Nano* 10 (3): 3334–3341.

17 Zhao, M.Q., Xie, X., Ren, C.E. et al. (2017). *Hollow MXene spheres and 3D macroporous MXene frameworks for Na-ion storage. Advanced Materials* 29 (37): 1702410.

18 Bak, S.M., Qiao, R., Yang, W. et al. (2017). *Na-ion intercalation and charge storage mechanism in 2D vanadium carbide. Advanced Energy Materials* 7 (20): 1700959.

19 Cai, P., He, Q., Wang, L. et al. (2019). *Two-dimensional Nb-based $M_4C_3T_x$ MXenes and their sodium storage performances. Ceramics International* 45 (5): 5761–5767.

20 Zhu, J., Wang, M., Lyu, M. et al. (2018). *Two-dimensional titanium carbonitride Mxene for high-performance sodium ion batteries. ACS Applied Nano Materials* 1 (12): 6854–6863.

21 Lian, P., Dong, Y., Wu, Z.-S. et al. (2017). *Alkalized Ti_3C_2 MXene nanoribbons with expanded interlayer spacing for high-capacity sodium and potassium ion batteries. Nano Energy* 40: 1–8.

22 Natu, V., Clites, M., Pomerantseva, E., and Barsoum, M.W. (2018). *Mesoporous MXene powders synthesized by acid induced crumpling and their use as Na-ion battery anodes*. *Materials Research Letters* 6 (4): 230–235.

23 Xie, X., Kretschmer, K., Anasori, B. et al. (2018). *Porous $Ti_3C_2T_x$ MXene for ultrahigh-rate sodium-ion storage with long cycle life*. *ACS Applied Nano Materials* 1 (2): 505–511.

24 Luo, J., Fang, C., Jin, C. et al. (2018). *Tunable pseudocapacitance storage of MXene by cation pillaring for high performance sodium-ion capacitors*. *Journal of Materials Chemistry A* 6 (17): 7794–7806.

25 Zhao, D., Clites, M., Ying, G. et al. (2018). *Alkali-induced crumpling of $Ti_3C_2T_x$ (MXene) to form 3D porous networks for sodium ion storage*. *Chemical Communications* 54 (36): 4533–4536.

26 Dong, Y., Wu, Z.-S., Zheng, S. et al. (2017). *Ti_3C_2 MXene-derived sodium-potassium titanate nanoribbons for high-performance sodium-potassium ion batteries with enhanced capacities*. *ACS Nano* 11 (5): 4792–4800.

27 Wu, Y., Nie, P., Wang, J. et al. (2017). *Few-layer MXenes delaminated via high-energy mechanical milling for enhanced sodium-ion batteries performance*. *ACS Applied Materials & Interfaces* 9 (45): 39610–39617.

28 Sun, S., Xie, Z., Yan, Y., and Wu, S. (2019). *Hybrid energy storage mechanisms for sulfur-decorated Ti_3C_2 MXene anode material for high-rate and long-life sodium-ion batteries*. *Chemical Engineering Journal* 366: 460–467.

29 Li, J., Yan, D., Hou, S. et al. (2018). *Improved sodium-ion storage performance of $Ti_3C_2T_x$ MXenes by sulfur doping*. *Journal of Materials Chemistry A* 6 (3): 1234–1243.

30 Luo, J., Zheng, J., Nai, J. et al. (2019). *Atomic sulfur covalently engineered interlayers of Ti_3C_2 MXene for ultra-fast sodium-ion storage by enhanced pseudocapacitance*. *Advanced Functional Materials* 29 (10): 1808107.

31 Luo, J., Wang, C., Wang, H. et al. (2018). *Pillared MXene with ultralarge interlayer spacing as a stable matrix for high performance sodium metal anodes*. *Advanced Functional Materials* 29 (3): 1805946.

32 Chen, H., Chen, N., Zhang, M. et al. (2019). *$Ti_3C_2T_x$ MXene decorated with Sb nanoparticles as anodes material for sodium-ion batteries*. *Nanotechnology* 30 (13): 134001.

33 Li, H., Liu, A., Ren, X. et al. (2019). *A black phosphorus/Ti_3C_2 MXene nanocomposite for sodium-ion batteries: a combined experimental and theoretical study*. *Nanoscale* 11 (42): 19862–19869.

34 Zhao, R., Qian, Z., Liu, Z. et al. (2019). *Molecular-level heterostructures assembled from layered black phosphorene and Ti_3C_2 MXene as superior anodes for high-performance sodium ion batteries*. *Nano Energy* 65: 104037.

35 Meng, R., Huang, J., Feng, Y. et al. (2018). *Black phosphorus quantum dot/Ti_3C_2 MXene nanosheet composites for efficient electrochemical lithium/sodium-ion storage*. *Advanced Energy Materials* 8 (26): 1801514.

36 Guo, X., Zhang, W., Zhang, J. et al. (2020). *Boosting sodium storage in two-dimensional phosphorene/$Ti_3C_2T_x$ MXene nanoarchitectures with stable fluorinated interphase*. *ACS Nano* 14 (3): 3651–3659.

37 Xie, X., Zhao, M.-Q., Anasori, B. et al. (2016). *Porous heterostructured MXene/carbon nanotube composite paper with high volumetric capacity for sodium-based energy storage devices*. *Nano Energy* 26: 513–523.

38 Zhang, Y., Guo, B., Hu, L. et al. (2018). *Synthesis of SnS nanoparticle-modified MXene ($Ti_3C_2T_x$) composites for enhanced sodium storage*. *Journal of Alloys and Compounds* 732: 448–453.

39 Wu, Y., Nie, P., Wu, L. et al. (2018). *2D MXene/SnS_2 composites as high-performance anodes for sodium ion batteries*. *Chemical Engineering Journal* 334: 932–938.

40 Zhang, Y., Zhan, R., Xu, Q. et al. (2019). *Circuit board-like CoS/MXene composite with superior performance for sodium storage*. *Chemical Engineering Journal* 357: 220–225.

41 Yang, Q., Gao, W., Zhong, W. et al. (2020). *A synergistic Bi_2S_3/MXene composite with enhanced performance as an anode material of sodium-ion batteries*. *New Journal of Chemistry* 44 (7): 3072–3077.

42 Wu, Y., Nie, P., Jiang, J. et al. (2017). *MoS_2-nanosheet-decorated 2D titanium carbide (MXene) as high-performance anodes for sodium-ion batteries*. *ChemElectroChem* 4 (6): 1560–1565.

43 Du, G., Tao, M., Gao, W. et al. (2019). *Preparation of $MoS_2/Ti_3C_2T_x$ composite as anode material with enhanced sodium/lithium storage performance*. *Inorganic Chemistry Frontiers* 6 (1): 117–125.

44 Ma, K., Jiang, H., Hu, Y., and Li, C. (2018). *2D nanospace confined synthesis of pseudocapacitance-dominated MoS_2-in-Ti_3C_2 superstructure for ultrafast and stable Li/Na-ion batteries*. *Advanced Functional Materials* 28 (40): 1804306.

45 Du, C.F., Liang, Q., Zheng, Y. et al. (2018). *Porous MXene frameworks support pyrite nanodots toward high-rate pseudocapacitive Li/Na-ion storage*. *ACS Applied Materials & Interfaces* 10 (40): 33779–33784.

46 Ding, Y., Chen, Y., Xu, N. et al. (2020). *Facile synthesis of $FePS_3$ nanosheets@MXene composite as a high-performance anode material for sodium storage*. *Nano-Micro Letters* 12 (1): 54.

47 Xu, E., Zhang, Y., Wang, H. et al. (2020). *Ultrafast kinetics net electrode assembled via $MoSe_2$/MXene heterojunction for high-performance sodium-ion batteries*. *Chemical Engineering Journal* 385: 123839.

48 Oh, H.G., Yang, S.H., Kang, Y.C., and Park, S.-K. (2021). N-doped carbon-coated $CoSe_2$ nanocrystals anchored on two-dimensional MXene nanosheets for efficient electrochemical sodium- and potassium-ion storage. *International Journal of Energy Research* 45 (12): 17738–17748.

49 Cao, J., Li, J., Li, D. et al. (2021). Strongly coupled 2D transition metal chalcogenide-MXene-carbonaceous nanoribbon heterostructures with ultrafast

ion transport for boosting sodium/potassium ions storage. *Nano-Micro Letters* 13 (1): 113.

50 Wu, F., Jiang, Y., Ye, Z. et al. (2019). A 3D flower-like VO_2/MXene hybrid architecture with superior anode performance for sodium ion batteries. *Journal of Materials Chemistry A* 7 (3): 1315–1322.

51 Guo, X., Xie, X., Choi, S. et al. (2017). Sb_2O_3/MXene($Ti_3C_2T_x$) hybrid anode materials with enhanced performance for sodium-ion batteries. *Journal of Materials Chemistry A* 5 (24): 12445–12452.

52 Guo, X., Zhang, J., Song, J. et al. (2018). MXene encapsulated titanium oxide nanospheres for ultra-stable and fast sodium storage. *Energy Storage Materials* 14: 306–313.

53 Yang, C., Liu, Y., Sun, X. et al. (2018). In-situ construction of hierarchical accordion-like TiO_2/Ti_3C_2 nanohybrid as anode material for lithium and sodium ion batteries. *Electrochimica Acta* 271: 165–172.

54 Wang, P., Lu, X., Boyjoo, Y. et al. (2020). Pillar-free TiO_2/Ti_3C_2 composite with expanded interlayer spacing for high-capacity sodium ion batteries. *Journal of Power Sources* 451: 227756.

55 Du, L., Duan, H., Xia, Q. et al. (2020). Hybrid charge-storage route to Nb_2CT_x MXene as anode for sodium-ion batteries. *ChemistrySelect* 5 (3): 1186–1192.

56 Huang, J., Meng, R., Zu, L. et al. (2018). Sandwich-like $Na_{0.23}TiO_2$ nanobelt/Ti_3C_2 MXene composites from a scalable in situ transformation reaction for long-life high-rate lithium/sodium-ion batteries. *Nano Energy* 46: 20–28.

57 Sun, X., Tan, K., Liu, Y. et al. (2020). In-situ growth of hybrid $NaTi_8O_{13}$/$NaTiO_2$ nanoribbons on layered MXene Ti_3C_2 as a competitive anode for high-performance sodium-ion batteries. *Chinese Chemical Letters* 31 (9): 2254–2258.

58 Tao, M., Du, G., Yang, T. et al. (2020). MXene-derived three-dimensional carbon nanotube network encapsulate CoS_2 nanoparticles as an anode material for solid-state sodium-ion batteries. *Journal of Materials Chemistry A* 8 (6): 3018–3026.

59 Tao, M., Zhang, Y., Zhan, R. et al. (2018). A chemically bonded $CoNiO_2$ nanoparticles/MXene composite as anode for sodium-ion batteries. *Materials Letters* 230: 173–176.

60 Yang, C., Sun, X., Zhang, Y.R. et al. (2019). Facile synthesis of hierarchical $NaTi_2(PO_4)_3$/Ti_3C_2 nanocomposites with superior sodium storage performance. *Materials Letters* 236: 408–411.

61 Zhao, D., Zhao, R., Dong, S. et al. (2019). Alkali-induced 3D crinkled porous Ti_3C_2 MXene architectures coupled with NiCoP bimetallic phosphide nanoparticles as anodes for high-performance sodium-ion batteries. *Energy & Environmental Science* 12 (8): 2422–2432.

62 Sun, N., Zhu, Q., Anasori, B. et al. (2019). MXene-bonded flexible hard carbon film as anode for stable Na/K-ion storage. *Advanced Functional Materials* 29 (51): 1906282.

63 Yang, Q., Jiao, T., Li, M. et al. (2018). In situ formation of $NaTi_2(PO_4)_3$ cubes on Ti_3C_2 MXene for dual-mode sodium storage. *Journal of Materials Chemistry A* 6 (38): 18525–18532.

64 Tian, Y., An, Y., Xiong, S. et al. (2019). A general method for constructing robust, flexible and freestanding MXene@metal anodes for high-performance potassium-ion batteries. *Journal of Materials Chemistry A* 7 (16): 9716–9725.

65 Zhao, R., Di, H., Hui, X. et al. (2020). Self-assembled Ti_3C_2 MXene and N-rich porous carbon hybrids as superior anodes for high-performance potassium-ion batteries. *Energy & Environmental Science* 13 (1): 246–257.

66 Huang, H., Cui, J., Liu, G. et al. (2019). Carbon-coated $MoSe_2$/MXene hybrid nanosheets for superior potassium storage. *ACS Nano* 13 (3): 3448–3456.

67 Ming, F., Liang, H., Zhang, W. et al. (2019). Porous MXenes enable high performance potassium ion capacitors. *Nano Energy* 62: 853–860.

68 Fang, Y.-Z., Hu, R., Zhu, K. et al. (2020). Aggregation-resistant 3D $Ti_3C_2T_x$ MXene with enhanced kinetics for potassium ion hybrid capacitors. *Advanced Functional Materials* 30 (50): 2005663.1–2005663.10.

69 Wu, X., Wang, H., Zhao, Z., and Huang, B. (2020). Interstratification-assembled 2D black phosphorene and V_2CT_x MXene as superior anodes for boosting potassium-ion storage. *Journal of Materials Chemistry A* 8 (25): 12705–12715.

70 Zhao, R., Di, H., Wang, C. et al. (2020). Encapsulating ultrafine Sb nanoparticles in $Na(^+)$ pre-intercalated 3D porous $Ti_3C_2T_x$ MXene nanostructures for enhanced potassium storage performance. *ACS Nano* 14 (10): 13938–13951.

71 Shi, H., Dong, Y., Zheng, S. et al. (2020). Three dimensional Ti_3C_2 MXene nanoribbon frameworks with uniform potassiophilic sites for the dendrite-free potassium metal anodes. *Nanoscale Advances* 2 (9): 4212–4219.

72 Cao, J., Wang, L., Li, D. et al. (2021). $Ti_3C_2T_x$ MXene conductive layers supported bio-derived $Fe_{x\text{-}1}Se_x$/MXene/ carbonaceous nanoribbons for high-performance half/full sodium-ion and potassium-ion batteries. *Advanced Materials* 33 (34): 2101535.

73 Xia, Z., Chen, X., Ci, H. et al. (2021). Designing N-doped graphene/$ReSe_2$/Ti_3C_2 MXene heterostructure frameworks as promising anodes for high-rate potassium-ion batteries. *Journal of Energy Chemistry* 53: 155–162.

74 Cao, B., Liu, H., Zhang, P. et al. (2021). Flexible MXene framework as a fast electron/potassium-ion dual-function conductor boosting stable potassium storage in graphite electrodes. *Advanced Functional Materials* 31 (32): 2102126.

75 Xu, X., Zhang, Y., Sun, H. et al. (2021). Orthorhombic cobalt ditelluride with Te vacancy defects anchoring on elastic MXene enables efficient potassium-ion storage. *Advanced Materials* 33 (31): 2100272.

76 Wang, T., Shen, D., Liu, H. et al. (2020). A Sb_2S_3 nanoflower/MXene composite as an anode for potassium-ion batteries. *ACS Applied Materials & Interfaces* 12 (52): 57907–57915.

77 Li, J., Rui, B., Wei, W. et al. (2020). Nanosheets assembled layered MoS_2/MXene as high performance anode materials for potassium ion batteries. *Journal of Power Sources* 449: 227481.

78 Cao, Y., Chen, H., Shen, Y. et al. (2021). SnS_2 nanosheets anchored on nitrogen and sulfur co-doped MXene sheets for high-performance potassium-ion batteries. *ACS Applied Materials & Interfaces* 13 (15): 17668–17676.

79 Sun, H., Zhang, Y., Xu, X. et al. (2021). Strongly coupled Te-SnS_2/MXene superstructure with self-autoadjustable function for fast and stable potassium ion storage. *Journal of Energy Chemistry* 61: 416–424.

80 Ma, J. and Liu, C. (2021). Ti_3C_2 wrapped Prussian blue skeleton as an anode for potassium-ion battery. *Journal of Power Sources* 484: 229276.

81 Liu, F., Liu, Y., Zhao, X. et al. (2020). Prelithiated V_2C MXene: a high-performance electrode for hybrid magnesium/lithium-ion batteries by ion cointercalation. *Small* 16 (8): 1906076.

82 Zhao, M.-Q., Ren, C.E., Alhabeb, M. et al. (2019). Magnesium-ion storage capability of MXenes. *ACS Applied Energy Materials* 2 (2): 1572–1578.

83 Liu, F., Liu, Y., Zhao, X. et al. (2019). Pursuit of a high-capacity and long-life Mg-storage cathode by tailoring sandwich-structured MXene@carbon nanosphere composites. *Journal of Materials Chemistry A* 7 (28): 16712–16719.

84 Li, Y., Xu, D., Zhang, D. et al. (2019). Study on MnO_2/MXene-Ti_3C_2 composite materials as cathode materials for magnesium batteries. *RSC Advances* 9 (58): 33572–33577.

85 Zhu, J., Shi, R., Liu, Y. et al. (2020). 3D interwoven MXene networks fabricated by the assistance of bacterial celluloses as high-performance cathode material for rechargeable magnesium battery. *Applied Surface Science* 528: 146985.

86 Li, Y., Zhang, R., and Xu, D. (2020). Study on MnO_2/MXene-V_2C composite as cathode for magnesium ion battery. *International Journal of Electrochemical Science* 15: 11227–11237.

87 Li, Y., Xu, D., Zhang, D. et al. (2019). Study on MXene-supported layered TiS_2 as cathode materials for magnesium batteries. *International Journal of Electrochemical Science* 14: 11102–11109.

88 Xu, M., Bai, N., Li, H.-X. et al. (2018). Synthesis of MXene-supported layered MoS_2 with enhanced electrochemical performance for Mg batteries. *Chinese Chemical Letters* 29 (8): 1313–1316.

89 Huo, X., Wang, X., Li, Z. et al. (2020). Two-dimensional composite of D-$Ti_3C_2T_x$@S@TiO_2 (MXene) as the cathode material for aluminum-ion batteries. *Nanoscale* 12 (5): 3387–3399.

90 Li, Z., Wang, X., Zhang, W., and Yang, S. (2020). Two-dimensional Ti_3C_2@CTAB-Se (MXene) composite cathode material for high-performance rechargeable aluminum batteries. *Chemical Engineering Journal* 398: 125679.

91 Huo, X., Wang, X., Li, J. et al. (2022). MXenes@Te as a composite material for high-performance aluminum batteries. *Science China Materials* 65: 85–94.

92 Huo, X., Zhang, B., Li, J. et al. (2021). Two-dimensional F-$Ti_3C_2T_x$@Ag composite for an extraordinary long cycle lifetime with high specific capacity in an aluminum battery. *ACS Applied Materials & Interfaces* 13 (10): 11822–11832.

93 Tan, B., Lu, T., Luo, W. et al. (2021). A novel MoS_2-MXene composite cathode for aluminum-ion batteries. *Energy & Fuels* 35 (15): 12666–12670.

94 Yao, L., Ju, S., and Yu, X. (2021). Rational surface engineering of MXene@N-doped hollow carbon dual-confined cobalt sulfides/selenides for advanced aluminum batteries. *Journal of Materials Chemistry A* 9 (31): 16878–16888.

95 Zheng, J., Ju, S., Yao, L. et al. (2021). Construction of solid solution sulfide embedded in MXene@N-doped carbon dual protection matrix for advanced aluminum ion batteries. *Journal of Power Sources* 511: 230450.

96 Aslam, M.K., Niu, Y., Xu, M. et al. (2020). MXenes for non-lithium-ion (Na, K, Ca, Mg, and Al) batteries and supercapacitors. *Advanced Energy Materials* 11 (2): 2000681.

97 Naguib, M., Halim, J., Lu, J. et al. (2013). New two-dimensional niobium and vanadium carbides as promising materials for Li-ion batteries. *Journal of the American Chemical Society* 135 (43): 15966–15969.

98 Nan, J., Guo, X., Xiao, J. et al. (2021). Nanoengineering of 2D MXene-based materials for energy storage applications. *Small* 17 (9): 1902085.

99 Xu, X., Zhang, Y., Sun, H. et al. (2021). Progress and perspective: MXene and MXene-based nanomaterials for high-performance energy storage devices. *Advanced Electronic Materials* 7 (7): 2000967.

100 Yu, H., Lin, W., Zhang, Y. et al. (2019). Exploring the potentials of Ti_3N_2 and $Ti_3N_2X_2$ (X = O, F, OH) monolayers as anodes for Li or non-Li ion batteries from first-principles calculations. *RSC Advances* 9 (69): 40340–40347.

101 Meng, Q., Ma, J., Zhang, Y. et al. (2018). The S-functionalized Ti_3C_2 Mxene as a high capacity electrode material for Na-ion batteries: a DFT study. *Nanoscale* 10 (7): 3385–3392.

102 Ma, P., Fang, D., Liu, Y. et al. (2021). MXene-based materials for electrochemical sodium-ion storage. *Advanced Science* 8 (11): 2003185.

103 Ni, J., Fu, S., Wu, C. et al. (2016). Superior sodium storage in $Na_2Ti_3O_7$ nanotube arrays through surface engineering. *Advanced Energy Materials* 6 (11): 1502568.

104 Gabaudan, V., Monconduit, L., Stievano, L., and Berthelot, R. (2019). Snapshot on negative electrode materials for potassium-ion batteries. *Frontiers in Energy Research* 7: 46.

105 Kaland, H., Hadler-Jacobsen, J., Fagerli, F.H. et al. (2020). Are MXenes suitable as cathode materials for rechargeable Mg batteries? *Sustainable Energy & Fuels* 4 (6): 2956–2966.

106 Zhang, Y., Liu, G., Zhang, C. et al. (2020). Low-cost $MgFe_xMn_{2-x}O_4$ cathode materials for high-performance aqueous rechargeable magnesium-ion batteries. *Chemical Engineering Journal* 392: 123652.

107 Liu, H., Wang, H., Jing, Z. et al. (2020). Bare Mo-based ordered double-transition metal MXenes as high-performance anode materials for aluminum-ion batteries. *The Journal of Physical Chemistry C* 124 (47): 25769–25774.

108 Lee, S., Wang, H., Jing, Z. et al. (2020). Fe_2CS_2 MXene: a promising electrode for Al-ion batteries. *Nanoscale* 12 (9): 5324–5331.

109 Lukatskaya, M., Mashtalir, O., Ren, C.E. et al. (2013). Cation intercalation and high volumetric capacitance of two-dimensional titanium carbide. *Science* 341 (6153): 1502–1505.

110 Xiao, Z., Li, Z., Menga, X. et al. (2019). MXene-engineered lithium-sulfur batteries. *Journal of Materials Chemistry A* 7 (40): 22730–22743.

111 Zhang, C., Cui, L., Abdolhosseinzadeh, S., and Heier, J. (2020). Two-dimensional MXenes for lithium-sulfur batteries. *InfoMat* 2 (4): 613–638.

112 Giebeler, L. and Balach, J. (2021). MXenes in lithium-sulfur batteries: scratching the surface of a complex 2D material – a minireview. *Materials Today Communications* 27: 102323.

113 Zhao, Q., Zhu, Q., Liu, Y., and Xu, B. (2021). Status and prospects of MXene-based lithium-sulfur batteries. *Advanced Functional Materials* 31 (21): 2100457.

114 Guo, D., Ming, F., Su, H. et al. (2019). MXene based self-assembled cathode and antifouling separator for high-rate and dendrite-inhibited Li-S battery. *Nano Energy* 61: 478–485.

115 Li, N., Xie, Y., Peng, S. et al. (2020). Ultra-lightweight Ti_3C_2T MXene modified separator for Li-S batteries: thickness regulation enabled polysulfide inhibition and lithium ion transportation. *Journal of Energy Chemistry* 42: 116–125.

116 Wang, J., Zhai, P., Zhao, T. et al. (2019). Laminar MXene-Nafion-modified separator with highly inhibited shuttle effect for long-life lithium-sulfur batteries. *Electrochimica Acta* 320: 134558.

117 Li, N., Cao, W., Liu, Y. et al. (2019). Impeding polysulfide shuttling with a three-dimensional conductive carbon nanotubes/MXene framework modified separator for highly efficient lithium-sulfur batteries. *Colloids and Surfaces A: Physicochemical and Engineering Aspects* 573: 128–136.

118 Li, B., Zhang, D., Liu, Y. et al. (2017). Flexible Ti_3C_2 MXene-lithium film with lamellar structure for ultrastable metallic lithium anodes. *Nano Energy* 39: 654–661.

119 Cao, Z., Zhu, Q., Wang, S. et al. (2019). Perpendicular MXene arrays with periodic interspaces toward dendrite-free lithium metal anodes with high-rate capabilities. *Advanced Functional Materials* 30 (5): 1908075.

120 Gu, J., Zhu, Q., Shi, Y. et al. (2020). Single zinc atoms immobilized on MXene ($Ti_3C_2Cl_x$) layers toward dendrite-free lithium metal anodes. *ACS Nano* 14 (1): 891–898.

121 Bao, W., Liu, L., Wang, C. et al. (2018). Facile synthesis of crumpled nitrogen-doped MXene nanosheets as a new sulfur host for lithium-sulfur batteries. *Advanced Energy Materials* 8 (13): 1702485.

122 Zhang, Y., Tang, W., Zhan, R. et al. (2019). An N-doped porous carbon/MXene composite as a sulfur host for lithium-sulfur batteries. *Inorganic Chemistry Frontiers* 6 (10): 2894–2899.

123 Wang, J., Zhao, T., Yang, Z. et al. (2019). MXene-based Co, N-codoped porous carbon nanosheets regulating polysulfides for high-performance lithium-sulfur batteries. *ACS Applied Materials & Interfaces* 11 (42): 38654–38662.

124 Bao, W., Su, D., Zhang, W. et al. (2016). 3D metal carbide@mesoporous carbon hybrid architecture as a new polysulfide reservoir for lithium-sulfur batteries. *Advanced Functional Materials* 26 (47): 8746–8756.

125 Qi, Q., Zhang, H., Zhang, P. et al. (2020). Self-assembled sandwich hollow porous carbon sphere@MXene composites as superior Li-S battery cathode hosts. *2D Materials* 7 (2).

126 Song, J., Guo, X., Zhang, J. et al. (2019). Rational design of free-standing 3D porous MXene/rGO hybrid aerogels as polysulfide reservoirs for high-energy lithium-sulfur batteries. *Journal of Materials Chemistry A* 7 (11): 6507–6513.

127 Lv, L.-P., Guo, C.-F., Sun, W., and Wang, Y. (2019). Strong surface-bound sulfur in carbon nanotube bridged hierarchical Mo_2C-based MXene nanosheets for lithium-sulfur batteries. *Small* 15 (3): 1804338.

128 Chen, Z., Yang, X., Qiao, X. et al. (2020). Lithium-ion-engineered interlayers of V_2C MXene as advanced host for flexible sulfur cathode with enhanced rate performance. *Journal of Physical Chemistry Letters* 11 (3): 885–890.

129 Liang, X., Rangom, Y., Kwok, C.Y. et al. (2017). Interwoven MXene nanosheet/carbon-nanotube composites as Li-S cathode hosts. *Advanced Materials* 29 (3): 1603040.1–1603040.7.

130 Gan, R., Yang, N., Dong, Q. et al. (2020). Enveloping ultrathin Ti_3C_2 nanosheets on carbon fibers: a high-density sulfur loaded lithium-sulfur battery cathode with remarkable cycling stability. *Journal of Materials Chemistry A* 8 (15): 7253–7260.

131 Bao, W., Xie, X., Xu, J. et al. (2017). Confined sulfur in 3D MXene/reduced graphene oxide hybrid nanosheets for lithium-sulfur battery. *Chemistry* 23 (51): 12613–12619.

132 Wang, X., Yang, C., Xiong, X. et al. (2019). A robust sulfur host with dual lithium polysulfide immobilization mechanism for long cycle life and high capacity Li-S batteries. *Energy Storage Materials* 16: 344–353.

133 Yao, Y., Feng, W., Chen, M. et al. (2018). Boosting the electrochemical performance of Li-S batteries with a dual polysulfides confinement strategy. *Small* 14 (42): 1802516.

134 Pan, H., Huang, X., Zhang, R. et al. (2019). Titanium oxide-Ti_3C_2 hybrids as sulfur hosts in lithium-sulfur battery: fast oxidation treatment and enhanced polysulfide adsorption ability. *Chemical Engineering Journal* 358: 1253–1261.

135 Du, C., Wu, J., Yang, P. et al. (2019). Embedding S@TiO_2 nanospheres into MXene layers as high rate cyclability cathodes for lithium-sulfur batteries. *Electrochimica Acta* 295: 1067–1074.

136 Zhang, H., Qi, Q., Zhang, P. et al. (2018). Self-assembled 3D MnO_2 nanosheets@ delaminated-Ti_3C_2 aerogel as sulfur host for lithium-sulfur battery cathodes. *ACS Applied Energy Materials* 2 (1): 705–714.

137 Wang, Z., Yu, K., Feng, Y. et al. (2019). VO_2(p)-V_2C(MXene) grid structure as a lithium polysulfide catalytic host for high-performance Li-S battery. *ACS Applied Materials & Interfaces* 11 (47): 44282–44292.

138 Zhang, Y., Mu, Z., Yang, C. et al. (2018). Rational design of MXene/1T-2H MoS_2C nanohybrids for high-performance lithium-sulfur batteries. *Advanced Functional Materials* 28 (38): 1707578.

139 Balach, J. and Giebeler, L. (2021). MXenes and the progress of Li-S battery development–a perspective. *Journal of Physics: Energy* 3 (2): 021002.

140 Yin, L., Xu, G., Nie, P. et al. (2018). MXene debris modified eggshell membrane as separator for high-performance lithium-sulfur batteries. *Chemical Engineering Journal* 352: 695–703.

141 Liu, P., Qu, L., Tian, X. et al. (2020). $Ti_3C_2T_x$/graphene oxide free-standing membranes as modified separators for lithium–sulfur batteries with enhanced rate performance. *ACS Applied Energy Materials* 3 (3): 2708–2718.

142 Jiao, L., Zhang, C., Geng, C. et al. (2019). Capture and catalytic conversion of polysulfides by in situ built TiO_2-MXene heterostructures for lithium-sulfur batteries. *Advanced Energy Materials* 9 (19): 1900219.

143 Wei, C., Tao, Y., An, Y. et al. (2020). Recent advances of emerging 2D MXene for stable and dendrite-free metal anodes. *Advanced Functional Materials* 30 (45): 2004613.

144 He, X., Jin, S., Miao, L. et al. (2020). A 3D hydroxylated MXene/carbon nanotubes composite as a scaffold for dendrite-free sodium-metal electrodes. *Angewandte Chemie International Edition* 59 (38): 16705–16711.

145 Fang, Y., Lian, R., Li, H. et al. (2020). Induction of planar sodium growth on MXene ($Ti_3C_2T_x$)-modified carbon cloth hosts for flexible sodium metal anodes. *ACS Nano* 14 (7): 8744–8753.

146 Luo, J., Lu, X., Matios, E. et al. (2020). Tunable MXene-derived 1D/2D hybrid nanoarchitectures as a stable matrix for dendrite-free and ultrahigh capacity sodium metal anode. *Nano Letters* 20 (10): 7700–7708.

147 Bao, C., Wang, J., Wang, B. et al. (2022). 3D sodiophilic Ti_3C_2 MXene@g-C_3N_4 hetero-interphase raises the stability of sodium metal anodes. *ACS Nano* 16 (10): 17197–17209.

148 Wang, Z., Huang, Z., Wang, H. et al. (2022). 3D-printed sodiophilic V_2CT_x/ rGO-CNT MXene microgrid aerogel for stable Na metal anode with high areal capacity. *ACS Nano* 16 (6): 9105–9116.

149 Tang, X., Zhou, D., Li, P. et al. (2020). MXene-based dendrite-free potassium metal batteries. *Advanced Materials* 32 (4): 1906739.

150 Rashad, M., Asif, M., and Ali, Z. (2020). Quest for magnesium-sulfur batteries: current challenges in electrolytes and cathode materials developments. *Coordination Chemistry Reviews* 415: 213312.

151 Zhao, Q., Wang, R., Zhang, Y. et al. (2021). The design of Co_3S_4@MXene heterostructure as sulfur host to promote the electrochemical kinetics for reversible magnesium-sulfur batteries. *Journal of Magnesium and Alloys* 9 (1): 78–89.

152 Xu, H., Zhu, D., Zhu, W. et al. (2022). Rational design of high concentration electrolytes and MXene-based sulfur host materials toward high-performance magnesium sulfur batteries. *Chemical Engineering Journal* 428: 131031.

22

Electromagnetic Interference Shielding of MXene/Polymer Composites

Hao-Bin Zhang and Xinfeng Zhou

State Key Laboratory of Organic-Inorganic Composites, Beijing University of Chemical Technology, Beijing, China

22.1 Introduction

Since James Clerk Maxwell proposed the Maxwell's equations in 1865 and predicted the existence of electromagnetic (EM) waves, the research and applications of electromagnetism have made great progress. The EM waves are extensively used to enrich human lives by providing convenient communication and various electronic apparatuses. However, the mismanagement of ubiquitous EM signals may significantly affect the normal function of electronics and public health issues. Hence, it is necessary to fabricate high-performance materials to cope with the increasingly serious electromagnetic interference (EMI) and pollution problems.

When EM wave is projected onto the surface of an EMI shielding material, parts will be reflected to the air because of the large impedance mismatch at the front surface, and the remained part will penetrate into the interior of EMI shielding materials. Then, the incident EM waves will be largely attenuated by conductive loss and polarization loss.

Likewise, the survived EM wave that reached the posterior surface will be again reflected back into the shielding material and further attenuated. The EMI shielding mechanism is depicted in Figure 22.1a. The shielding capability of an EMI shielding material is defined as shielding effectiveness (SE_T) and can be calculated as follows: [1]

Transition Metal Carbides and Nitrides (MXenes) Handbook: Synthesis, Processing, Properties and Applications, First Edition. Edited by Chuanfang Zhang and Michael Naguib.
© 2024 John Wiley & Sons, Inc. Published 2024 by John Wiley & Sons, Inc.

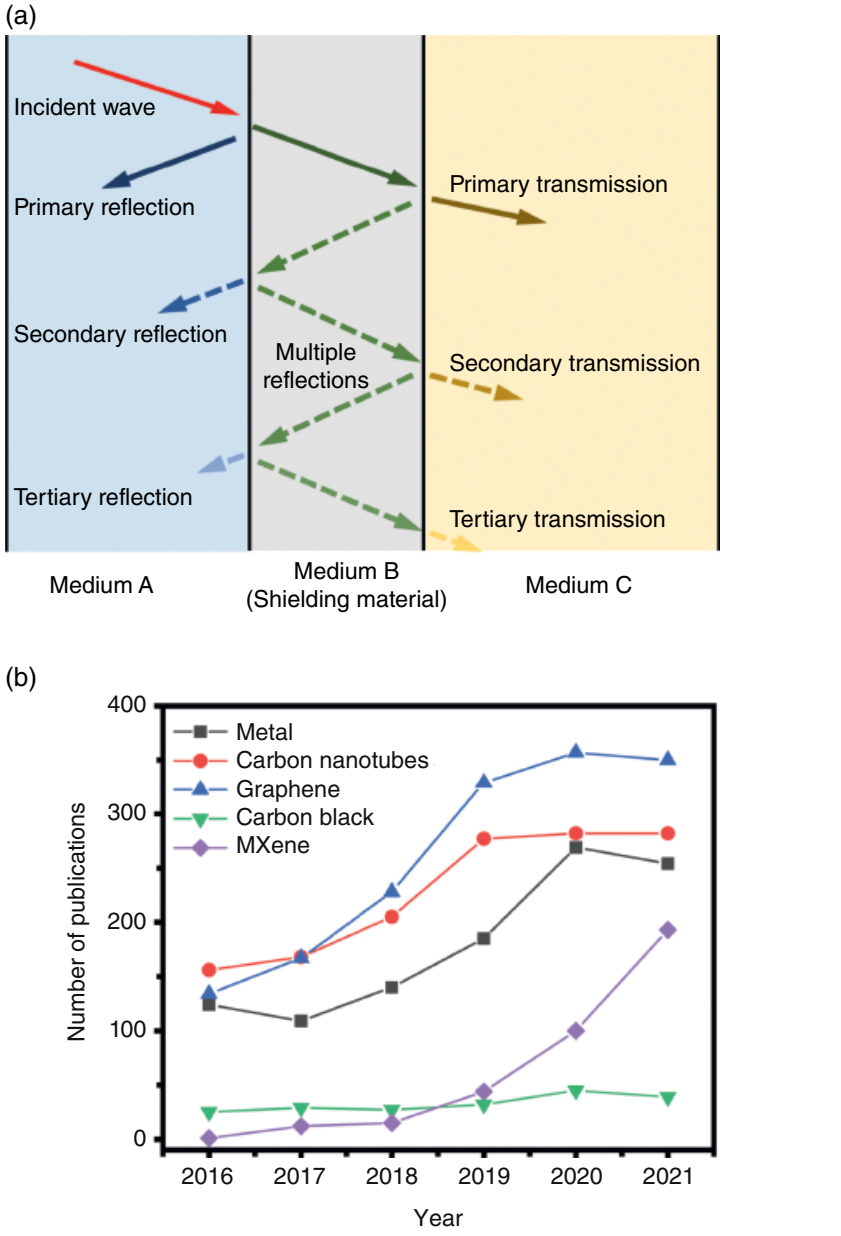


Figure 22.1 (a) Schematic illustration of the propagation of EM waves. (b) The publication trend of the metals, CNTs, graphene, carbon black, MXenes as EMI shielding materials obtained from *Web of Science*.

$$SE_T = 20\log\left(\frac{E_i}{E_t}\right) \tag{22.1}$$

where the E_i and E_t represent the incident and transmitted electric field intensity. The higher the value of SE_T, the better the EMI shielding performance. For example, SE_T values of 20 and 40 dB mean that 99% and 99.99% of incident EM waves are blocked, respectively [2]. In general, the threshold SE_T for commercial EMI shielding materials is higher than 20 dB [3]. In specific, the reflection loss (SE_R), absorption loss (SE_A), and multiple reflection loss (SE_M) contribute to the total shielding effectiveness as described by the Schelkunoffs theory: [4]

$$SE_T(\text{dB}) = SE_R + SE_A + SE_M \tag{22.2}$$

The SE_M will be ignored when the SE_T is larger than 15 dB. According to classical electromagnetic theory, reflection loss is generated by the different impedances of dissimilar mediums. The Fresnel's equation is used to convey the value of amplitude of EM wave reflected by the shielding material: [4]

$$SE_R = 20\log\frac{(Z+Z_0)^2}{4ZZ_0} = 39.5 + 10\log\frac{\sigma}{2\pi f\mu} \tag{22.3}$$

where the Z and Z_0 are the medium and air impedance, σ, μ, and f are the electric conductivity, permeability, and electromagnetic frequency, respectively. From Eq. (22.3), it can be seen that the increment of conductivity or reduction of permeability will enhance SE_R.

The attenuation constant (α) that crucial for EM loss ability is often calculated as follows: [5]

$$\alpha = 2\pi f\sqrt{\frac{\mu\varepsilon}{2}\left[\sqrt{1+\left(\frac{\sigma}{2\pi f\varepsilon}\right)^2}-1\right]} \tag{22.4}$$

where the ε is the permittivity. Clearly, the elevation of electrical conductivity, dielectric and magnetic property benefit the increase of the α value. The EM energy absorption ability can be evaluated by the calculated value of SE_A by the following formula:

$$SE_A = 20\log e^{\alpha d} = 20\left(\frac{d}{\delta}\right)\log_{10} e = 8.68\left(\frac{d}{\delta}\right) = 8.7d\sqrt{\pi f\mu\sigma} \tag{22.5}$$

where δ implies the skin depth, denoting the depth at which the intensity of incident electric field decreases to its *1/e*. d is the thickness of shielding material.

In general, different shielding materials with specific shielding mechanisms can be selected depending on whether secondary contamination of EM needs to be avoided. Massive reports have compared the values of SE_R and SE_A to analyze EMI shielding mechanisms of materials. To a great extent, SE_A represents the parts of incident microwaves that dissipated within the shielding materials. At the same time, the power coefficients of reflectivity and absorptivity are also proposed to evaluate EMI shielding mechanisms [6]. From the EM energy of view, the power of EM waves incident to the shield surface is divided into the reflect (R), absorbed (A), and transmitted (T) power. R represents the reflected EM energy detected in front of the shield, while T represents the EM energy detected behind the shield. Therefore, the A represents the actual absorbed EM energy by shield, and its enhancement can prevent the secondary pollution. Macroscopically, reasonable structural design, such as asymmetric gradient structure [7], porous structure including foam and sponge [8], can make EM waves undergo multiple reflections and scattering as much as possible within the shields to allow their phasic cancelation and consumption rather than just reflection. In addition, constructing dielectric/magnetic loss factors microscopically to convert EM energy into thermal energy is also an effective strategy to prevent secondary pollution [9].

Practical applications in electronics, automotive, and aerospace industries require not only highly efficient EMI shielding performance but also low density and thickness. Therefore, researchers have developed the specific shielding effectiveness (SSE) and the absolute shielding effectiveness (SSE/t) to comprehensively assess the EMI shielding performance of a shielding material.

$$\mathrm{SSE}\left(\mathrm{dB\,cm\,g^{-1}}\right) = \mathrm{EMI\,SE}_T/\rho \tag{22.6}$$

$$\mathrm{SSE}/t\left(\mathrm{dB\,cm^2\,g^{-1}}\right) = \mathrm{EMI\,SE}_T/\rho/t \tag{22.7}$$

Till now, metals, carbon nanotubes (CNTs), graphene, carbon black, and MXenes are widely reported for EMI shielding [10]. Figure 22.1b illustrates a survey about the published literatures of as-mentioned materials on the *Web of Science* from 2016 to 2021, indicating the research hype in this field, especially in the most recent three years. Noteworthy, the sizeable slope of the diamonds curve in Figure 22.1b enunciates that the investigation of MXene-based materials in EMI has continuously been emphasized, which is of great significance for the exploration of high EMI shielding performance. Since the $Ti_3C_2T_x$ MXene was firstly adopted for EMI shielding and demonstrated thin matching thickness as well as outstanding shielding effectiveness by Yury Gogotsi and coworkers in 2016 [11], an extensive series of MXene-based EMI shielding materials have been reported by refining their structure and ingredients. Table 22.1 illustrates the

Table 22.1 Comparison of EMI shielding performance of MXene and their composites with different applied forms.

Materials	Electric conductivity ($S\,cm^{-1}$)	EMI SE (dB)	Thickness (mm)	SE/*t* ($dB\,mm^{-1}$)	SSE ($dB\,cm^3\,g^{-1}$)	SSE/*t* ($dB\,cm^2\,g^{-1}$)	References
$Ti_3C_2T_x$	4665.1	92	0.045	/	/	/	[11]
$Ti_3C_2T_x$-SA	2963	57	0.009	/	/	30 830	[11]
Ti_3CNT_x	1786	116	0.040	/	/	/	[12]
$Ti_3C_2T_x$	5000	20	$\sim 5.5 \times 10^{-5}$	/	/	3.89×10^6	[13]
$Ti_3C_2T_x$	~7000	55.7	0.00326	/	/	48 800	[14]
$Ti_3C_2T_x$-GO	2640	50	0.007	7167.1	/	/	[15]
$Ti_3C_2T_x$/CNF	7.394	~25.8	0.047	/	/	2647	[16]
CNF@$Ti_3C_2T_x$	1.43	40	0.035	/	/	7029	[17]
$Ti_3C_2T_x$/ANF	3.6618	24.5	0.014	/	/	8814.5	[18]
PVA/$Ti_3C_2T_x$	7.16	44.4	0.027	/	/	9343	[19]
$Ti_3C_2T_x$/NR	14	53.6	0.251	213.6	/	/	[20]
PVDF/$Ti_3C_2T_x$	214.6	42.9	0.017	/	/	19 504.8	[21]
$Ti_3C_2T_x$	580	~70	0.060	/	82	136 752	[22]
$Ti_3C_2T_x$	22	75	/	/	9904	/	[23]
$Ti_3C_2T_x$-rGO	10	50.7	3	/	6217	/	[24]
$Ti_3C_2T_x$-rGO	56.718	51	0.085	/	451	/	[14]
$Ti_3C_2T_x$/PC	35.2	71.3	/	/	/	/	[25]
Ti_2CT_x	/	48.5	1	/	/	88 182	[26]
$Ti_3C_2T_x$	1000	53	0.01	/	88.3	88 333	[27]
$Ti_3C_2T_x$-rGO/epoxy	6.959	56.4	2	28.2	/	/	[28]
$Ti_3C_2T_x$/C/epoxy	1.84	46	2	/	/	/	[29]
$Ti_3C_2T_x$/CNTs/paraffin	4.472	90	2	45	/	/	[30]

application of MXene in EMI shielding in recent years. If no special designation is specified, the term MXene in the following represents $Ti_3C_2T_x$.

22.2 MXene as EMI Shielding Materials

As the new addition of 2D materials, two-dimensional transition carbides/nitrides (MXenes) are expected to have more than seventy members depending on the various compositions and structures. Till now, more than 30 types of MXenes have been successfully synthesized by the etching and exfoliation of MAX phase. Among them, $Ti_3C_2T_x$ MXene with superb electrical conductivity (up to 20 000 S cm^{-1}) [31] has been intensively explored for various potential applications, especially for high-level EMI shielding. Zhou et al. [32] simulated the influence of monolayer structure and surface terminations of $Ti_3C_2T_x$ on its electrical conductivity. Pure Ti_3C_2 reveals typical metallic characteristics with a resistivity of $2.31 \pm 0.57\,\mu\Omega\,m$ due to the fundamental electronic states crossing the Fermi level. The surface groups (T_x) could alert the bandgap and electronic states near the Fermi level, and thereby determine the electronic characteristics of $Ti_3C_2T_x$. Reasonably, the electrical conductivity of MXene can be tuned by modifying the functional groups. Ji et al. [33] tried to correlate the surface groups of MXene with its electrical conductivity and EMI shielding characteristic by aligning the heat treatment temperature (800–1550 °C). Below 950 °C, the –O, –OH groups and part of –F groups were removed from MXene surface, significantly enhancing the conductivity and shielding performance. The higher temperature of 1100 °C can even completely eliminate the residual –F groups and further improve the EMI shielding performance to 76.1 dB. However, even higher temperatures will induce obvious phase change of MXene, and seriously deteriorate the conductivity and EMI shielding performance. In accordance, Iqbal and coworkers [12] further confirmed the dependence of electrical conductivity on the variation of *d*-spacing of MXene materials during the heat treatment process. The conductivity of $Ti_3C_2T_x$ and Ti_3CNT_x show a monotonous increment trend below 250 °C. It is understood that the removal of water and small molecules reduces the interlayer spacing, as indicated by the upward shift of (002) peak. The more compact sheet-to-sheet connection facilitates the electron transport and contributes to the enhancement of electric conductivity. Accordingly, the EMI shielding performance of $Ti_3C_2T_x$ and Ti_3CNT_x films increases with the annealing temperature. In addition, the higher SE_T of the Ti_3CNT_x film treated at 350 °C with relatively lower conductivity can be explained by its increased SE_A. Noteworthily, the formed numerous voids in the treated MXene films also significantly contribute to the improved EMI shielding performance.

Moreover, the formed porous structures of MXene films not only can improve the EMI shielding performance by providing abundant interfaces for multiple

scattering and attenuating the EM waves, but also can greatly minimize the apparent density. Typically, the foaming method, template method, and lyophilization method are developed to fabricate low-density MXene foams and aerogels. For example, Liu et al. [22] pioneered the preparation of lightweight porous MXene film with hydrazine hydrate-assisted foaming technique (Figure 22.2a). The reaction of hydrazine hydrate with oxygen-containing groups on MXene generates a large number of gases (CO_2, H_2O), which yield high pressure among the adjacent MXene sheets to conquering the van der Waals forces. Different from the solid MXene film precursor, the foamed MXene film shows continuous cellular structures as clearly identified from the cross-sectional scanning electron microscope (SEM) (Figure 22.2b, c**)**. Interestingly, the MXene foam with a smaller density of $0.2\,g\,cm^{-3}$ exhibits obviously superior shielding performance (70 dB) over the solid MXene film of 53 dB (Figure 22.2d). Its specific SE (SSE) of 136 752 dB $cm^2\,g^{-1}$ is among the record-high values for the shielding materials, including carbon-based solid materials and foams, metal-based solid materials and foams (Figure 22.2e). At the same time, the foaming process also *in–situ* realizes the hydrophilic-to-hydrophobic transition for the MXene films, as evidenced by the

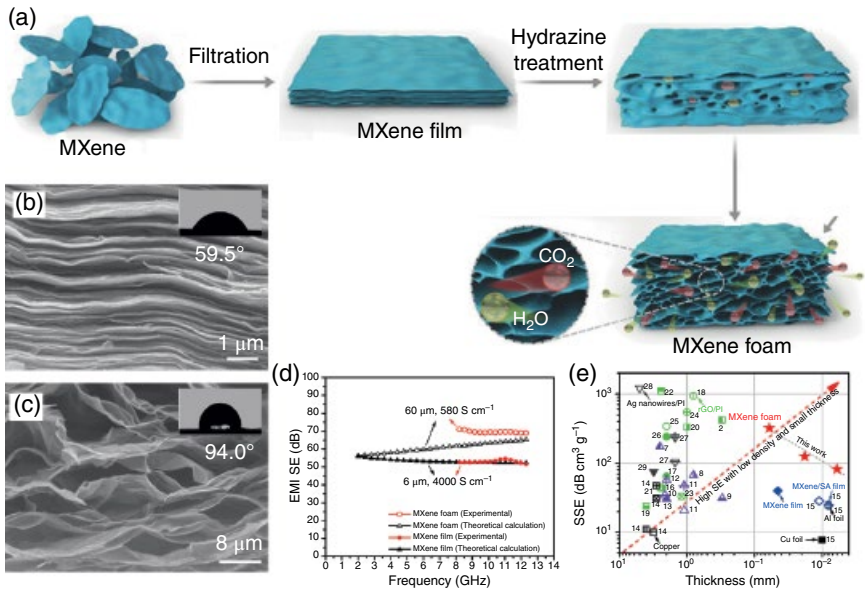


Figure 22.2 (a) Schematic illustration of the fabrication of the MXene foam. Cross-sectional SEM of MXene film (b) and MXene foam (c), respectively, the inset images are their corresponding contact angle. (d) EMI shielding effectiveness of the MXene foams with different thickness. (e) Comparison of the specific SE of reported shielding materials. *Source:* Reproduced from Liu et al. [22] with permission from John Wiley & Sons.

increase in contact angle from 59.5° to 94°, which may provide a promising strategy to alleviate or even avoid the possible oxidation and deterioration of MXene materials.

22.3 MXene/Polymer Composites as EMI Shielding Materials

Except for the bulk EMI shielding materials, the pristine MXene materials can also act as promising conductive nanofillers to endow the electrically insulating polymers with multifunctionalities and mechanical reinforcement. At the same time, the drawbacks of MXene materials including poor mechanical properties and environmental stability can be solved by the presence of polymer matrices. Up to now, the blending method [34], casting method [35], blade coating method [36], and spraying method [10b] are adopted to MXene/polymer composites (MPCs) for EMI shielding, which are anticipated to combine the excellent chemical resistance, good processability, and attractive functionalities. In the MPCs, the MXene dispersion state, the formed conductive network, and interfaces and defects influence the electron transport capability and interactions with EM waves, thereby the electrical and shielding properties. Therefore, the ingenious interfacial modulation and rational geometric configuration of MXene in the polymer matrix are proposed to optimize the EMI shielding effectiveness of MPCs.

22.3.1 The Modulation of MXene-Polymer Interfaces

MXene materials can form various interfacial interactions, such as hydrogen bonding, covalent bonding and electrostatic interactions, with different polymer matrices depending on their surface functional groups. The compatibility of MXene with the polymer matrix and its dispersion can be optimized by manipulating these interactions. The functional groups on MXene surfaces largely determine the bonding types with polymer matrices. For example, Ma et al. [37] systematically explored the interfacial interactions between (001) surfaces of MXene and bacterial celluloses (BCs). Both sides of BCs monomer can adhere to the (001) surface of Ti_3C_2 MXene with identical binding energy. As the acceptor of OH—F bond (HB), the F atom on Ti_3C_2(F) MXene (001) (coverage=1/16ML) surface cannot preserve weak HB with BC monomers. The HB-linked conformation in Ti_3C_2(OH) MXene (001) (coverage = 1/16ML) surface can easily transform to the covalently bonded Ti-O conformation. In other words, when the coverage of –F and –OH is too high to occupy the positions used for Ti–O bonding, hydrogen bonding will dominate the bonding. Therefore, a variety of interactions between

MXene and the polymer matrix can be achieved by modulating the surface terminal groups on MXene. In addition, the robust interactions can prevent the conductive pathways from disruption by external forces, affording excellent fatigue resistance to multiple tensile and compression deformations of MP composites in practical applications.

22.3.1.1 Hydrogen Bonding Interactions

Hydrogen bonds often form between stronger electronegative atoms and H atoms in other functional groups. Similarly, the abundant functional groups (–OH, –O, and –F) on MXene sheets easily construct hydrogen bonds with the groups of polymer molecules, forming robust MXene-polymer interfaces. Liu et al. [38] prepared MXene/polyimide (PI) aerogels by using the strong hydrogen bonding between the MXene surface and the polyamic acid (PAA) and the followed imidization process induced by heat treatment (Figure 22.3a). The increased thickness of MXene nanosheet and the upward shift of –OH peaks in FT-IR also indicate the formation of hydrogen bonds between the functional group and the carbonyl group on the PAA chain, as shown in Figure 22.3b. The numerous hydrogen bonds enhance the interfacial adhesion between MXene and PI and afford excellent compressibility and bending resistance (Figure 22.3c).

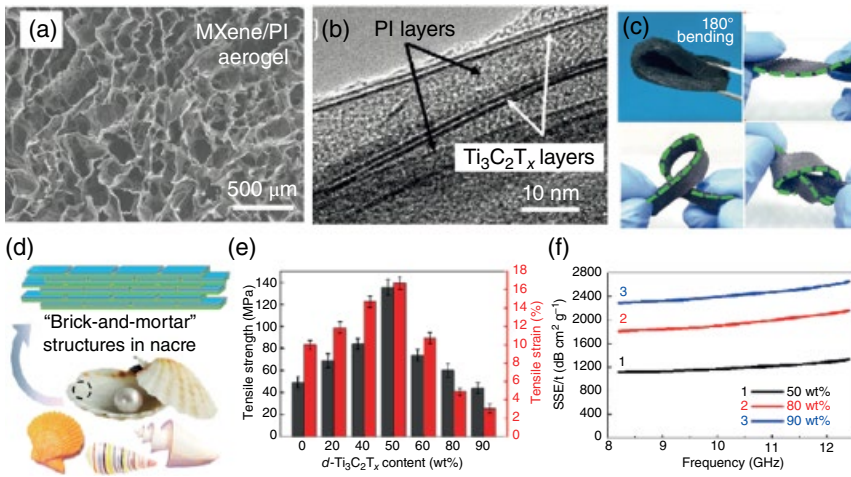


Figure 22.3 (a) SEM and (b) TEM of MXene/PI aerogel. (c) Digital images of MXene/PI aerogel under bending and twisting. *Source:* Liu et al. [38]/Reproduced from John Wiley & Sons, Inc. (d) Schematic illustration of the "brick-and-mortar" structure in nacre and the preparation of the MXene/CNF composite paper. (e) The Tensile strengths and tensile strains. (f) SSE/*t* of the MXene/CNF composite paper. *Source:* Reproduced from Cao et al. [16] with permission from American Chemical Society.

Another example for the formation of hydrogen bond occurs between MXene and cellulose nanofiber (CNF) [39]. The MXene/CNF composite with a nacre-like "brick-and-mortar" multilayer structure was developed by Cao et al. [16] via the vacuum filtration method (Figure 22.3d). The strong hydrogen bonds endow the MXene/CNF composite with a high tensile strength of 135.4 MPa and a fracture strain and 16.7%, as shown in Figure 22.3g. Moreover, the compact lamellar structure also yields an electric conductivity of 739.4 S m^{-1} and the SSE/t of 2647 dB cm^2 g^{-1} even at high contents of non-conductive CNF in Figure 22.3e, f. Besides, other polymers including aramid nanofiber (ANF) [40], BCs [37], PAA [41], and polyurethane [42], are also reported to achieve satisfactory comprehensive performances by establishing strong hydrogen bonding with filled MXene nanosheets.

It is noteworthy that the presence of insulating polymers will inevitably decrease the valuable electrical conductivity of MXene, although they significantly contribute to the comprehensive performances of MXene composites. To ultimately retain intrinsic conductivity of MXene, sodium alginate (SA), a natural polysaccharide polymer, is widely used to modify MXene through constructing hydrogen bonding between –COOH of SA and –OH of MXene. In 2016, Shahzad et al. [11] initially prepared diverse self-supporting MXene ($Ti_3C_2T_x$, $Mo_2TiC_2T_x$, $Mo_2Ti_2C_3T_x$) films and nacre-like $Ti_3C_2T_x$-sodium alginate ($Ti_3C_2T_x$-SA). The $Ti_3C_2T_x$-SA composite film still maintains a similar lamellar stacking architecture with the $Ti_3C_2T_x$ film. The uniformly inserted SA macromolecules among the $Ti_3C_2T_x$ MXene lamellae enhance the interlayer spacing. With the high electron density near the Fermi energy level, $Ti_3C_2T_x$ MXene features a metallic characteristic and shows the highest electrical conductivity as compared to $Mo_2TiC_2T_x$, $Mo_2Ti_2C_3T_x$ MXene. Simultaneously, the conductivity of $Ti_3C_2T_x$-SA composite film is positively correlated with $Ti_3C_2T_x$ content, which is up to 3000 S cm^{-1} with a $Ti_3C_2T_x$ content of 90 wt%. Accordingly, the variance in electrical conductivity induces the corresponding changes in EMI shielding performances. $Ti_3C_2T_x$ MXene film with prominent electrical conductivity of around 5000 S cm^{-1} gives optimal EMI SE_T ranging from 48 to 92 dB depending on its thickness in X-band. The $Ti_3C_2T_x$-SA composite film containing 90 wt% of $Ti_3C_2T_x$ exhibits an SE_T value of 57 dB with a film thickness of 9 μm and the highest SSE/t value is above 30 000 dB cm^2 g^{-1}.

22.3.1.2 Covalent Bonding Interaction

The extensive functional groups on MXene can also act as active sites for the possible covalent modifications to realize versatile functions and structural reinforcement of MPCs. In general, there are three possible chemical approaches for covalent modification of MXene: [43]

i) MXene acts as the initiator to initiate grafting polymerization. The surface functional groups on MXene can graft the polymer chains, forming the periodically arranged MXene-polymer structure. Due to the interaction between

N–H group in pyrrole ring and the oxygen or fluorine on $Ti_3C_2T_x$ surface [44], MXene acts as template for the uniform growth of polypyrrole (PPy). Cross-sectional TEM of MXene-PPy film shows that the PPy intercalated between MXene nanolayers and gives a periodic arrangement structure. As expected, the (002) peak of composite film shows a significant leftward shift from 6.4° to 3.6° compared to that of MXene film. The *in-situ* growth of polymers on MXene offers the anchors for subsequent covalent bridging and brings about attractive mechanical, electrical, and optical properties.

ii) Decoration oxygen-containing groups on MXene surfaces with small molecules such as acid halides, organic amines, epoxy compounds, or alkali metal hydroxides. As shown in Figure 22.4a, Peng et al. [45] used the amino groups to substitute hydroxyl groups on MXene and then resultant MXene-NH_2 was homogenously mixed with carboxymethyl cellulose (CMC) to fabricate CMC/MXene-NH_2 films by infiltration, hot pressing, and amidated treatment. The distinctive N–H characteristic peaks in FTIR spectra and the N1s in XPS spectra prove the amino modification on MXene (Figure 22.4b), consistent with the emerged peak assigned to formed Ti—N bond. Besides, the upward shift of (002) peak implies the reduction of *d*-spacing of MXene owing to the neutralization of the negative repulsion between MXene by positively charged amines (Figure 22.4c). As illustrated in Figure 22.4d, the CMC/MXene film shows EMI SE_T value of exceeding 40 dB. Impressively, the flexible CMC/MXene-NH_2 film presents exceptional mechanical properties with a tensile strength of 240.12 ± 9.4 MPa and a high fracture energy of 661.37 ± 38.2 J mm^{-2} (Figure 22.4e).

iii) Incorporation of single heteroatoms (i.e., N, P, and S) into the MAX phase or MXene phase. For example, triphenylphosphine (TPP) has been used as the P source for the phosphorylation of 2D Vanadium Carbide MXene (V_2CT_x) [46]. The C—P bond and P—V bond in C 1s and P 2p spectra confirm the successful doping of P atoms. The doping enlarges the interlayer spacing, as evidenced by the leftward shift of the (002) peak, facilitating the incorporation of small molecules into MXene nanolayers to grow polymer molecular chains. Furthermore, the surface formation energy calculation shows that the P doping in the form of C—P bonds demonstrates excellent stability even at high temperatures, allowing MXene materials to withstand the severe cross-linking conditions of polymer molecular chains for optimizing the comprehensive performance of composites.

22.3.1.3 Electrostatic Interactions

The electrostatic interactions yield attraction or repelling forces between materials with the opposite or identical charges, which can act as an effective strategy to finely manipulate the distribution of MXene nanosheets in polymer matrix and construct conductive network in MPCs. In general, MXene nanosheets with

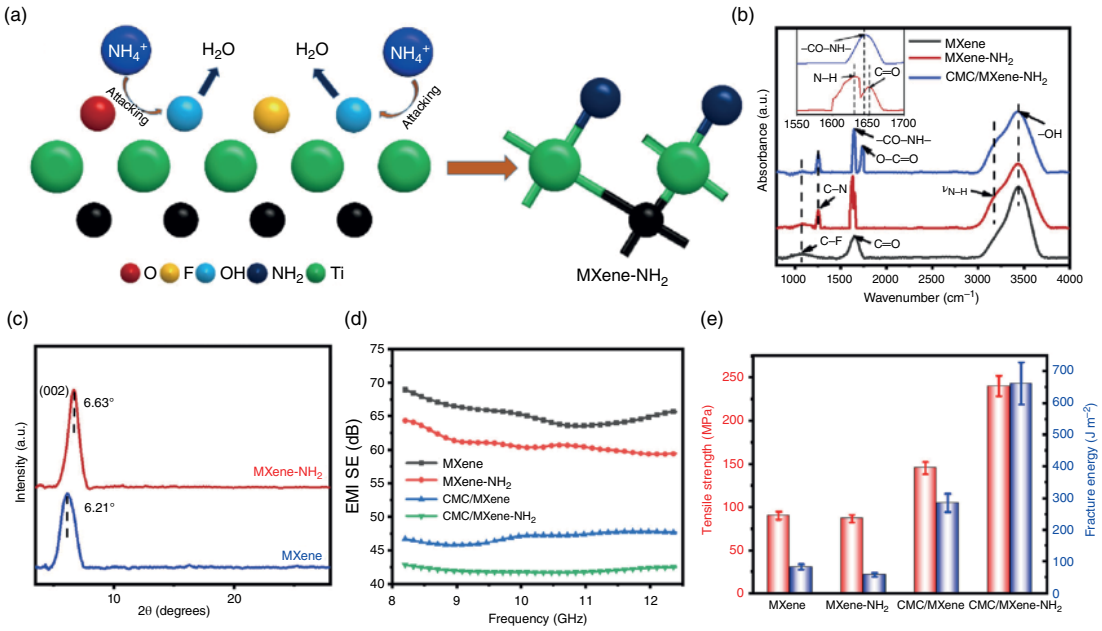


Figure 22.4 (a) Chemical reaction mechanism for the introduction of amino groups on MXene. (b) The FT-IR spectrum of MXene, MXene-NH_2, and CMC/MXene-NH_2 film. (c) XRD patterns of MXene and MXene-NH_2. (d) The EMI SE in X-band and (e) Tensile strength and fracture energy of MXene, MXene-NH_2, CMC/MXene, and CMC/MXene-NH_2 film. *Source:* Reproduced from Peng et al. [45] with permission from Elsevier.

–OH, –F, and –O surface groups are negatively charged. Reasonably, MXene nanosheets tend to assemble on positively charged polymer particles and form efficient 3D conductive networks after post-compression process. The repelling effect of the negatively charged polymer particles can squeeze and realize the compact packing of MXene among the polymer interfaces. For example, Sun et al. [47] first developed core-shell polystyrene (PS)@MXene hybrid by allowing the slow encapsulation of MXene nanosheets on positively charged PS particles under constantly stirring (Figure 22.5a, c). After hot-pression treatment, strong and conductive PS/MXene nanocomposites were prepared and almost all the MXene nanosheets are volume-excluded by the ordered PS domains to form a continuous conductive network (Figure 22.5b). As a result, an outstanding electrical conductivity of 1081 S m^{-1} and a maximum EMI SE of 62 dB is achieved with only 1.90 vol% of MXene (Figure 22.5d, e), which are significantly superior to the reported results for MXene/MPCs. In addition, the similar electrostatic interaction between MXene and poly (3, 4-ethylenedioxythiophene) (PEDOT) was also explored [48]. By removing the insulating poly(styrenesulfonate) (PSS) with acid treatment, the MXene/PEDOT composite film exhibits an EMI SE_T value of 40.5 dB (~6.6 μm) and a tensile strength of 38.5 ± 2.9 MPa.

Oppositely, strong and conductive MXene/natural rubber (NR) nanocomposite film with a similar segregated structure can also be produced by using the electrostatic forces between NR and MXene with the same negative charge (Figure 22.5f) [20]. Because of the efficient transport of electrons along interconnected networks, the MXene/NR composite film delivers a high electric conductivity of 1400 S m^{-1} with 6.71 vol% of MXene. Meanwhile, the film also shows a remarkable EMI shielding performance of 53.6 dB, as well as excellent tensile strength and modulus of 700% and 15 000%, respectively, as shown in Figure 22.5g, h. The potential large-scale production makes the conductive film very promising for flexible and foldable electronic devices.

Actually, there are various types of interactions between MXene and the polymer matrix, and the combination of multiple interactions could yield favorable synergistic effects to afford outstanding comprehensive features for MXene/MPCs. Recently, Wan et al. proposed a sequential bridging strategy to eliminate the voids between lamellae in MXene film [49]. Interestingly, the reduced porosity in the sequential bridging MXene (SBM) film leads to significantly enhanced mechanical performances as compared to MXene film, covalently bridged MXene (CBM) film and hydrogen bridged MXene (HBM) film. The exceptional tensile strength (583 ± 16 MPa), excellent toughness (15.9 ± 1.0 MJ m^3), and high electric conductivity (6115 ± 62 S cm^{-1}) are attributed to the refined alignment, decreased interplanar spacing, and absence of intercalated water. Moreover, the SBM film also exhibits a remarkable shielding performance of 56.4 dB (3.0 μm) over the frequency range from 0.3 to 18 GHz, and its SSE/t is superior than metal foil, MXene, graphene, carbon

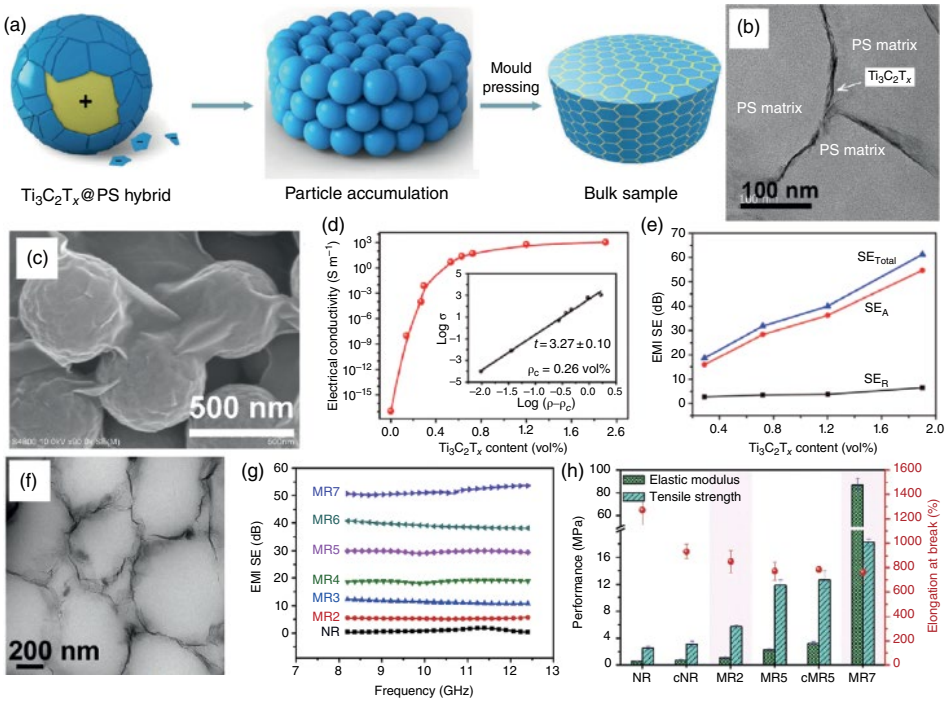


Figure 22.5 (a) The preparation of MXene@PS nanocomposite. (b) TEM of the MXene@PS nanocomposite with 1.20 vol% of MXene. (c) SEM image of the MXene@PS nanocomposite with 1.20 vol% of MXene. (d) The electric conductivity and (e) SE_T, SE_A, and SE_R at 12 GHz of MXene@PS composites with different MXene content. *Source:* Sun et al. [47]/Reproduced from John Wiley & Sons, Inc. (f) TEM image of the MXene/NR film with 3.10 vol% of MXene. (g) The EMI SE_T and (h) Mechanical performance of MXene/NR composite films with different MXene content. *Source:* Luo et al. [20]/Reproduced with permission from Elsevier.

black, and multi-walled nanotube composites. Also, the compact stacked structure endows SBM films with outstanding resistance to humid environments and folding.

22.3.2 Preformed of 3D Conductive Architectures

In MPCs, randomly dispersed nanofillers in the matrix readily aggregate and even high contents often result in greatly compromised electrical and EMI shielding performances, as well as severe deterioration of processing and mechanical properties. Essentially, the electrical conductivity and EM wave attenuation capability of MPCs ultimately derive from the filler distribution and the formed conductive network throughout the polymer matrix. In view of this fact, the strategy of preconstruction of 3D macroscopic porous architectures with various conductive nanomaterials including CNT, graphene, and MXene is proposed to prepare high-performance MPCs with balanced comprehensive properties. Typically, the porous architectures are vacuum-impregnated with polymer precursors or monomers and the followed *in-situ* polymerization to produce the final MPCs.

There are various methods for the production of 3D porous conductive architectures, such as, chemical vapor deposition, ice-template method, and emulsion -template strategy, etc. For example, the ice-template method was adopted to form 3D porous MXene framework by Zhao et al. [28] through the hydrothermal assembly and lyophilization of MXene with the assistance of graphene oxide (Figure 22.6a). During the freezing process, the ice crystals grow along the direction of temperature gradient, and facilitate the arrangement of nanomaterials in the similar direction, producing 3D architectures after freeze-drying. The microstructure analysis reveals that the resultant core-shell architecture consists of GO core and outer MXene nano-shell (Figure 22.6b, c). Based on the preformed 3D framework, the prepared epoxy composites demonstrate a high electrical conductivity of 695.9 S m^{-1} with 0.74 vol% only MXene (Figure 22.6d), and excellent EMI shielding performance above 50 dB within the X-band frequency range with the highest value of 56.4 dB (Figure 22.6e). Therefore, this work offers a promising route for the controllable preparation of MXene/MPCs with optimized EMI shielding performance.

Interestingly, the emulsion droplets with tunable sizes can also act as template to induce the assembly of nanomaterials at the immiscible liquid-liquid interface. Shi et al. [50] reported the co-assembly of water-soluble MXene and oil-soluble end-group functionalized polymer ligands at the water/oil interface (Figure 22.6f). Different from the ice-templated aerogels, the 3D closed cellular structure aerogels were obtained by using size-controlled emulsions as the template (Figure 22.6g, h). Meanwhile, the surface modification of MXene with ligands during the self-assembly process endows the MXene aerogel with favorable hydrophobicity (Figure 22.6i). After the introduction of epoxy, the prepared MXene/epoxy composite presents a relatively high electrical conductivity of 195.3 S m^{-1} and

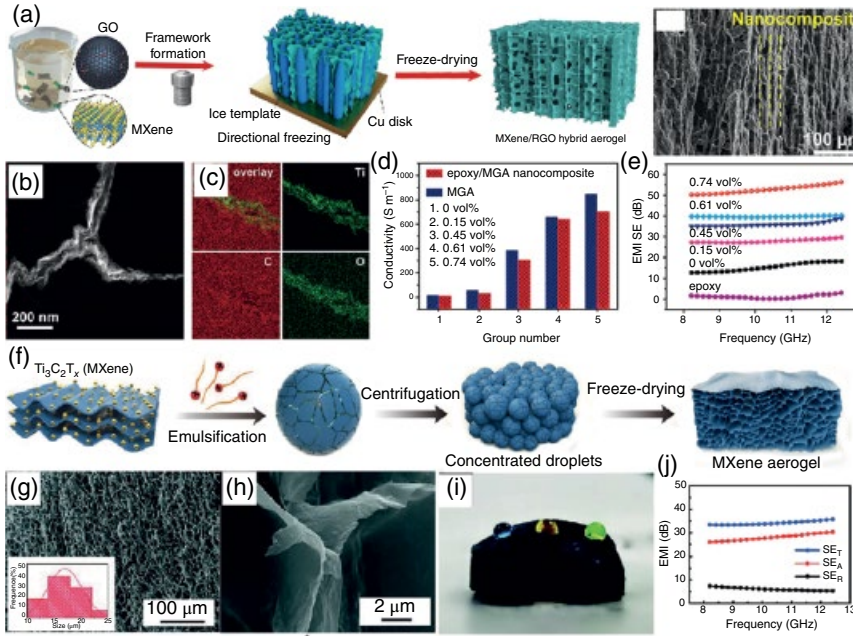


Figure 22.6 (a) Schematic illustration of the preparation and SEM of $Ti_3C_2T_x$ MXene/RGO aerogel. (b) The STEM image of MXene/RGO aerogel. (c) Elemental mapping images of MXene/RGO aerogel. (d) The electric conductivity and (e) EMI SE of aerogel with different MXene content. *Source:* Zhao et al. [28]/Reproduced from American Chemical Society. (f) Schematic illustration of the preparation of MXene aerogel. (g) and (h) SEM images of MXene aerogel. (i) Water droplets on the surface of MXene aerogel. (j) The EMI SE of $Ti_3C_2T_x$@epoxy nanocomposite. *Source:* Shi et al. [50]/Reproduced from John Wiley & Sons, Inc.

excellent EMI shielding capability at X-band was achieved (Figure 22.6j). This liquid–liquid self-assembly proposes a new concept for governing the internal structure of macro MXene composites.

The EMI shielding mechanisms of MXene/MPCs can be mainly attributed to conduction loss and polarization loss. Under EM field, the electron migration along the conductive pathway and rapid traverse through the heterogeneous interfaces produce conduction loss. The polarization loss includes interfacial and dipole polarization losses. The dipoles derive from the structural defects and functional groups of MXene materials, which are redirected along EM field and cause the loss of EM energy. The interfacial polarization loss occurs at heterogeneous interfaces due to the aggregation and rearrangement of electric charges. The 3D network with abundant multiple interfaces will enhance the effective dissipation of EM energy by increasing interface polarization. The lightweight porous

structure design can help satisfy the demands for EMI shielding materials in the electronic industry, self-drive vehicles, and aerospace.

22.4 Outlook

The fast advance of communication technologies calls for various high-performance EMI shielding materials. MXene/MPCs are lightweight, easy-processible, and corrosion-resistant, expressing great potential for electrical industries, automotive, and aerospace applications. Even so, some important yet challenging issues still remain for MXene/MPCs for EMI shielding applications. Firstly, it is still necessary to develop novel methodology and routes for the precise interfacial modulation and structural design of MPCs to provide higher-level EMI shielding efficiency for future high-frequency applications. Secondly, the possible secondary pollution issues caused by the initial surface reflection of highly conductive MPCs should be properly addressed by using the rational structural design and hybridization with other magnetic or dielectric nanomaterials. Besides, the compatibility issues of flexibility, toughness, intelligence, and stability of MPCs should be considered, when they are aimed to be applied in the future flexible and wearable electronic devices. In addition, although some MXenes ($Ti_3C_2T_x$, Ti_2CT_x, Ti_3CNT_x, $Mo_2TiC_2T_x$, and $Mo_2Ti_2C_3T_x$) have been reported for EMI shielding materials, the magnetic MXenes ($M_{n+1}AlN_n$, $M_{n+1}GaN_n$ (M = Cr, Mn; N = C, N)) may offer stirring new opportunities and possibilities for high-performance electromagnetic protective materials.

References

1 Schelkunoff, S.A. (1945). *Electromagnetic Waves*. New York: Van Nostrand.
2 Wang, M., Tang, X.-H., Cai, J.-H. et al. (2021). *Carbon* 177: 377.
3 Li, N., Huang, Y., Du, F. et al. (2006). *Nano Letters* 6: 1141–1145.
4 Liou, B.-T. and Wu, C.-Y. (1996). *Heat and Mass Transfer* 32: 103–107.
5 Ott, H.W. (2011). *Electromagnetic Compatibility Engineering*. Wiley.
6 Peng, M. and Qin, F. (2021). *Journal of Applied Physics* 130: 225108.
7 Xu, L., Wan, S., Heng, Y. et al. (2023). *Composites Science and Technology* 231: 109797.
8 a) Wang, G., Yi, D., Jia, X. et al. (2022). *Materials Today Physics* 22: 100612; b) Duan, H., Zhu, H., Gao, J. et al. (2020). *Journal of Materials Chemistry A* 8: 9146.
9 Zhang, X., Guo, Y., Feng, Y. et al. (2022). *Colloids and Surfaces A: Physicochemical and Engineering Aspects* 651: 129764.
10 a) Jia, H., Kong, Q.-Q., Yang, X. et al. (2021). *Carbon* 171: 329; b) Weng, G.M., Li, J., Alhabeb, M. et al. (2018). *Advanced Functional Materials* 2018: 28; c) Xu, L.,

Lu, H., Zhou, Y. et al. (2021). *Advanced Materials Technologies* 6: 210053; d) Wen, B., Cao, M., Lu, M. et al. (2014). *Advanced Materials* 26: 3484; e) Xu, H., Li, Y., Han, X. et al. (2021). *Materials Letters* 285: 129077.

11 Shahzad, F., Alhabeb, M., Hatter, C.B. et al. (2016). *Science* 353: 1137–1140.

12 Iqbal, A., Shahzad, F., Hantanasirisakul, K. et al. (2020). *Science* 369: 446–450.

13 Yun, T., Kim, H., Iqbal, A. et al. (2020). *Advanced Materials* 32: e1906769.

14 Lin, Z., Liu, J., Peng, W. et al. (2020). *ACS Nano* 14: 2109.

15 Liu, J., Liu, Z., Zhang, H.B. et al. (2019). *Advanced Electronic Materials* 6: 1901094.

16 Cao, W.T., Chen, F.F., Zhu, Y.J. et al. (2018). *ACS Nano* 12: 4583.

17 Zhou, B., Zhang, Z., Li, Y. et al. (2020). *ACS Applied Materials Interfaces* 12: 4895.

18 Lei, C., Zhang, Y., Liu, D. et al. (2020). *ACS Applied Materials Interfaces* 12: 26485.

19 Jin, X., Wang, J., Dai, L. et al. (2020). *Chemical Engineering Journal* 380: 122475.

20 Luo, J.-Q., Zhao, S., Zhang, H.-B. et al. (2019). *Composites Science and Technology* 182: 107754.

21 Li, Y., Zhou, B., Shen, Y. et al. (2021). *Composites Part B: Engineering* 217: 108902.

22 Liu, J., Zhang, H.B., Sun, R. et al. (2017). *Advanced Materials* 29: 1702367.

23 Bian, R., He, G., Zhi, W. et al. (2019). *Journal of Materials Chemistry C* 7: 474.

24 Fan, Z., Wang, D., Yuan, Y. et al. (2020). *Chemical Engineering Journal* 381: 122696.

25 Liang, C., Qiu, H., Song, P. et al. (2020). *Science Bulletin* 65: 616.

26 Han, M., Yin, X., Hantanasirisakul, K. et al. (2019). *Advanced Optical Materials* 7: 1900267.

27 Yin, L., Kang, H., Ma, H. et al. (2021). *Carbon* 182: 124.

28 Zhao, S., Zhang, H.B., Luo, J.Q. et al. (2018). *ACS Nano* 12: 11193.

29 Wang, L., Qiu, H., Song, P. et al. (2019). *Composites Part A: Applied Science and Manufacturing* 123: 293.

30 Deng, Z., Tang, P., Wu, X. et al. (2021). *ACS Applied Materials Interfaces* 13: 20539.

31 Mathis, T.S., Maleski, K., Goad, A. et al. (2021). *ACS Nano* 15: 6420.

32 Tang, Q., Zhou, Z., and Shen, P. (2012). *Journal of American Chemical Society* 134: 16909.

33 Ji, B., Fan, S., Ma, X. et al. (2020). *Carbon* 165: 150.

34 Wan, Y., Xiong, P., Liu, J. et al. (2021). *ACS Nano* 15: 8439.

35 Wei, Q., Pei, S., Qian, X. et al. (2020). *Advanced Materials* 32: e1907411.

36 Zhang, J., Kong, N., Uzun, S. et al. (2020). *Advanced Materials* 32: e2001093.

37 Ma, C., Cao, W.-T., Zhang, W. et al. (2021). *Chemical Engineering Journal* 403: 126438.

38 Liu, J., Zhang, H.B., Xie, X. et al. (2018). *Small* 14: e1802479.

39 Xie, F., Jia, F., Zhuo, L. et al. (2019). *Nanoscale* 11: 23382.

40 Zhan, Z., Song, Q., Zhou, Z., and Lu, C. (2019). *Journal of Materials Chemistry C* 7: 9820.

41 Zhu, Y., Liu, J., Guo, T. et al. (2021). *ACS Nano* 15: 1465.
42 Liu, Z., Wang, W., Tan, J. et al. (2020). *Journal of Materials Chemistry C* 8: 7170.
43 Huang, W., Hu, L., Tang, Y. et al. (2020). *Advanced Functional Materials* 30: 2005223.
44 Boota, M., Anasori, B., Voigt, C. et al. (2016). *Advanced Materials* 28: 1517.
45 Peng, M., Dong, M., Wei, W. et al. (2021). *Carbon* 179: 400.
46 Yoon, Y., Tiwari, A.P., Choi, M. et al. (2019). *Advanced Functional Materials* 29: 1903443.
47 Sun, R., Zhang, H.-B., Liu, J. et al. (2017). *Advanced Functional Materials* 27: 1702807.
48 Wan, Y.-J., Li, X.-M., Zhu, P.-L. et al. (2020). *Composites Part A: Applied Science and Manufacturing* 130: 105764.
49 Wan, S.J., Li, X., Chen, Y. et al. (2021). *Science* 374: 96–99.
50 Shi, S., Qian, B., Wu, X. et al. (2019). *Angewandte Chemie International Edition England* 58: 18171.

23

MXenes in Electronics and Communication Devices

Xiangming Xu and Husam N. Alshareef

Materials Science and Engineering, Physical Science and Engineering Division, King Abdullah University of Science and Technology, Thuwal, Kingdom of Saudi Arabia

23.1 Introduction

MXenes, a large family of two-dimensional (2D) transition metal carbides and nitrides, exhibit many unique properties such as high metallic conductivity, rich surface groups, tunable intercalation, hydrophilicity, and adjustable work function. They have been attracting significant interest since their discovery in 2011 [1] for many applications such as batteries [2], supercapacitors [3], energy conversion [4], water splitting [5], catalysis [6], electromagnetic-interference shielding [7], and water desalination [8]. However, in sharp contrast to other 2D materials which have been extensively researched for nanoelectronics [9], MXenes research for electronic applications [3] is still in the early stage of development. However, it seems that lately the field of MXetronics is starting to take off due to the unique advantages of MXenes, such as excellent conductivity, tunable work function over a wide range [10], rich compositional variety [11], and easy processing without surfactants [12]. This chapter will review the recent progress of MXenes applications in various electronic and wireless communication devices, including oxide electronics, 2D electronics, flexible and wearable electronics, iontronic and neuromorphic devices, and antennas. In the end, important and relevant research directions in this field will be discussed.

Transition Metal Carbides and Nitrides (MXenes) Handbook: Synthesis, Processing, Properties and Applications, First Edition. Edited by Chuanfang Zhang and Michael Naguib.
© 2024 John Wiley & Sons, Inc. Published 2024 by John Wiley & Sons, Inc.

23.2 MXene in Oxide Electronics

Oxide semiconductors play a significant role in transparent electronics and flat panel display technologies. Most oxide semiconductors (*n*-type: SnO_2, ZnO, In_2O_3, $InGaO_3(ZnO)_5$ (or GIZO), etc.; *p*-type: Cu_2O, SnO, NiO, etc.) [13] are wide bandgap, endowing them with excellent visible light transparency. Besides, their amorphous phases can still reserve excellent carrier transport properties. It allows the oxide thin film to be grown at room temperature and is thus very feasible to be applied in the electronic display industry [14]. Oxide semiconductors stand out thanks to their better electronic motilities (1~100 $cm^2\ V^{-1}\ s^{-1}$) compared to amorphous silicon (<1 $cm^2\ V^{-1}\ s^{-1}$) and organic semiconductors (1~10 $cm^2\ V^{-1}\ s^{-1}$) [15]. However, to realize a fully transparent device, conductive electrodes and interconnects should also be highly optical transmittance in visible light wavelength. Electrical conductive oxides such as indium tin oxide (ITO), indium-doped zinc oxide, and $Hf_xZn_{1-x}O_{2-\delta}$ have been developed or widely used [16]. However, most of them are deposited through costly and complicated vacuum deposition systems. The solution process is considered a cost-effective and straightforward method to prepare oxide electronics. It also allows oxide electronic devices to be fabricated on a flexible substrate. However, most of the solution-processed oxides are not stable, and thus high-temperature annealing is necessary [17]. MXenes, as an emerging 2D family, is showing a fantastic combination of high electronic conductivity, ultrathin nature, and good hydrophilicity [18]. Those unique properties make MXenes (especially the $Ti_3C_2T_x$) very promising and attractive conductive electrodes in transparent electronics [19]. MXenes are more advantageous because they can be easily solution-processed and post-annealing is unnecessary. Also, MXene films on the flexible substrate were demonstrated to be much more stable than the ITO even after many-time bending [20]. However, there are few reports on using MXenes in oxide electronics applications.

A pioneer work done by Wang et al. in 2018 confirmed that $Ti_3C_2T_x$ MXene could be suitable metal contacts for both *n*-type ZnO and *p*-type SnO transistor devices [21]. Before starting the device fabrication, they utilized the photoelectron spectroscopy in air (PESA) technique to measure the work function of the metal contact ($Ti_3C_2T_x$), the conduction band of *n*-ZnO, and the valence band of *p*-SnO. The results showed their very close values of 4.60, 4.58, and 4.65 eV, respectively. This indicates MXene $Ti_3C_2T_x$ could be a promising source (S) and drain (D) contact to inject carriers into both semiconductors with a small barrier. They also fabricated *n*-type ZnO and *p*-type SnO thin-film transistors (TFTs) using MXene as all contacts, including S/D and gate (G). The schematic of $Ti_3C_2T_x$-oxide TFTs is illustrated in Figure 23.1a. The $Ti_3C_2T_x$ G layer was first produced by a simple spray coating process, followed by the growth of the HfO_2 dielectric layer through atomic layer deposition (ALD). They confirmed the uniform growth of the HfO_2

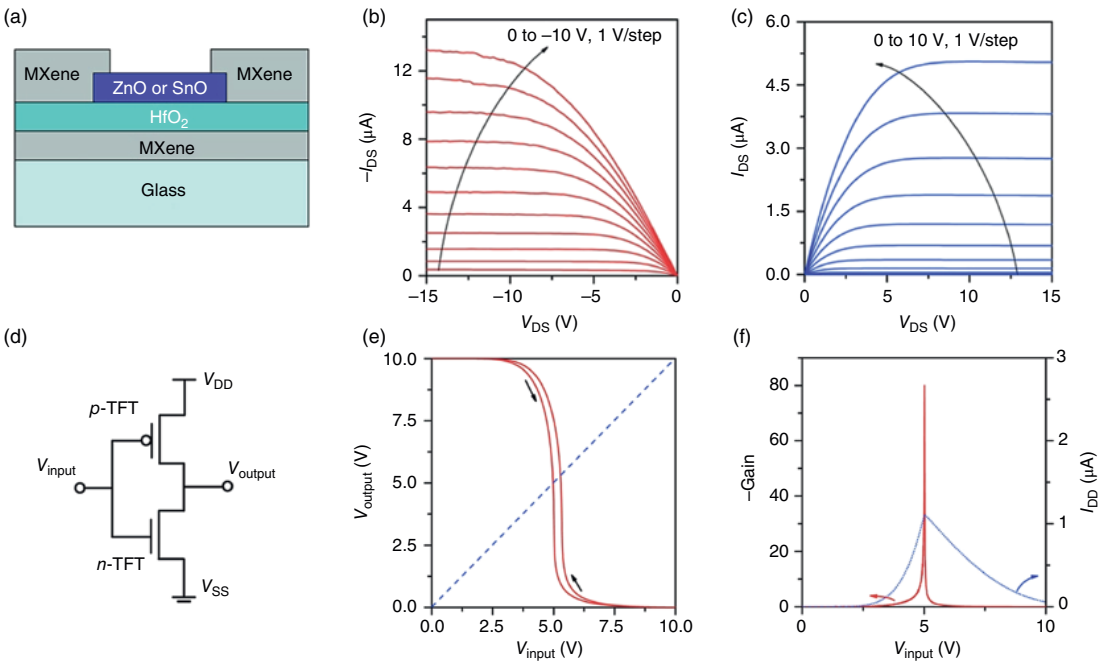


Figure 23.1 Performance of oxide TFTs with all-MXene ($Ti_3C_2T_x$) contacts. (a) Schematic structure of the device. (b, c) Output characteristic for the (b) *p*-type SnO TFT and (c) *n*-type ZnO TFT. (d) CMOS inverter Schematic. (e) VTC and (f) gain and IDD of the CMOS inverter. *Source:* Wang et al. [21]/John Wiley & Sons.

layer. The reason could be the hydrophilic surface of the $Ti_3C_2T_x$ film promoted the homogeneous nucleation of the oxide layer. The uniformity of the dielectric layer guaranteed minimized gate current leakage. Then, semiconductor layers were either grown through ALD for *n*-ZnO or sputtering for *p*-type SnO. The S/D $Ti_3C_2T_x$ layer was processed and patterned by spray coating combined with a lift-off process. The device process indicates the excellent compatibility of MXene in oxide electronics. The output curves are shown in Figure 23.1b,c for *p*-TFT and *n*-TFT, respectively. Both devices have the apparent saturation behavior at the high S/D voltage (V_{SD}) range. It means the S/D current was mainly modulated in the semiconducting channel region instead of the metal/semiconductor (M/S) contact regions. Based on the device operation at different temperatures, they deduced that a minimal barrier exists between $Ti_3C_2T_x$ and ZnO (SnO), which is 0.03 (0.02) eV, constant with the PESA results.

The balanced performance of both *n*-type ZnO and *p*-type SnO TFTs inspired them to fabricate complementary metal-oxide-semiconductor (CMOS) devices further. The performance of the CMOS inverter is illustrated in Figure 23.1d–f. The schematic circuit diagram (Figure 23.1d) indicates that both *n*- and *p*-TFTs connected their G electrodes as the input terminal (V_{IN}); the output terminal (V_{OUT}) is formed at the connected area between Ds of both *n*- and *p*-type TFTs. V_{DD} was settled at S of *p*-TFT and V_{SS} at S of *n*-TFT. They performed a dual-sweep scan to collect the voltage transfer curve (VTC) of this CMOS inverter shown in Figure 23.1e. A slight hysteresis is observed with the maximum V_M variation is 5% of $V_{DD}/2$, indicating that the logic switching is stable regardless of the scan direction. The VTC characteristic exhibits rapid output voltage transition with a peak gain value of about 80 (Figure 23.1f). The CMOS inverter displays a logic swing range of 8.78 V, ~ 87.8% of the ideal case. This excellent CMOS performance indicates MXene conductive electrodes are very promising to be used in oxide electronics. Compared with traditional metals such as gold and aluminum, MXenes are solution processed without using complicated vacuum systems. In addition, MXenes are rich in surface groups that make them intrinsically hydrophilic and work function tunable. This promotes the uniform growth of oxide films on top of MXene films and potentially allows barrier engineering at the MXene/oxide interface. Furthermore, MXenes can be engineered as transparent electrodes, enabling transparent electronic devices.

More efforts are needed to explore the potential of MXenes as transparent contact electrodes in oxide electronics. Zhang et al. already did systematic research on the sheet resistance change with the transparency for the spin-casting MXene films. They found $Ti_3C_2T_x$ films have better carrier conductance (a smaller sheet resistance) than PEDOT/SWCNT, or P3-SWCNT, liquid-exfoliated graphene, and graphene oxide, when they have similar transparency (87%) for 550 nm visible light [19b]. However, the figures of merit (FoM) of $Ti_3C_2T_x$ films, regarding the

ratio of electronic conductivity to optical conductivity, is about 15, which still has a gap in meeting the minimum industrial requirement of about 35 [22]. Therefore, improving the FoM of $Ti_3C_2T_x$ films will be significant for real-world applications. One strategy developed by Chen et al. is to hybridize MXenes with silver nanowires to improve their transparency, indicating its potential in flexible, transparent, and wearable electronics [22]. In reality, transparent electronics using MXene as electrodes require additional evaluation. Realizing the ideal contact between MXenes electrodes and oxide semiconductors is a significant direction for improving the performance of TFTs. Other oxide electronic devices based on the MXenes/oxide semiconductors contacts, such as Schottky junctions, memories, and synaptic devices, are worth designing and investigating. Therefore, there is still a big room for exploring MXenes in oxide electronics.

23.3 MXene in 2D Electronics

2D materials have received the most extensive research since the discovery of graphene in 2004 [24]. Electrons confined in a 2D layer show unique behaviors in contrast to those in a three-dimensional (3D) lattice structure environment. This intrinsic difference creates a powerful platform for researchers to explore many unprecedented and fancy physical properties. The large 2D family, including graphene, h-BN, transition-metal dichalcogenides (TMDCs), BP, Te, and 2D oxides, also MXenes, further enrich physical phenomena in the 2D world. As the firstly discovered member, graphene possesses ultrahigh carrier mobility [25], tunable Fermi level under an electrostatic field [26], and superconducting properties based on magic-angle vdW stacking [27]. *h*-BN is the only 2D material used as the dielectric layer with no dangling bonds [28]. It is super stable in the ambient environment [29], making it a perfect passivation layer to protect 2D devices [30]. Many 2D TMDCs are excellent semiconductors working properly in an atomically thin state, such as MoS_2, $MoSe_2$, WS_2, WSe_2, etc. Since carrier transportation is confined in an atomic-thin layer and thus can be very efficiently modulated by the electrostatic field, they have no concern about the short-channel effect that bothers the silicon transistors. Experts from both academy and industry are planning to employ them to scale down the transistors to extend Moore's Law [31]. BP and Te have also been experimentally confirmed as high-mobility *p*-type 2D semiconductors [32]. MXenes, as emerging 2D family members, are still in the infancy stage for their application in 2D electronics. They are gaining explosive attention recently because of their excellent conductivity, work function tunable in a big range (2 ~ 8 eV), hydrophilic surface, and some MXenes are predicted to be semiconducting [18, 33].

MXenes were investigated as metal contact electrodes with 2D TMDCs semiconducting flakes by Xu et al. in 2016 [34]. They fabricated WSe_2 and MoS_2

FET devices using $Ti_2C(OH)_xF_y$ as one-side S contact. The D side was traditional Cr/Au metal, as shown in Figure 23.2a. The mechanical exfoliation transfer method is performed to prepare WSe_2-$Ti_2C(OH)_xF_y$ and MoS_2-$Ti_2C(OH)_xF_y$ heterostructures. Before the device fabrication, they confirmed that $Ti_2C(OH)_xF_y$ has a high carrier concentration ($\sim 3.5 \times 10^{14}\,cm^{-2}$) and small contact resistance ($\sim 0.243\,\Omega\,mm$) with Cr/Au using a four-probe method. It has a high work function value of about 4.98 eV according to probe force microscopy measurements. Based on the fabricated MXene-TMDCs devices, a series of current-voltage transfer operations can be performed under different temperatures and then be used to extract the Schottky barrier height (ϕ_B) between $Ti_2C(OH)_xF_y$ and WSe_2 (or MoS_2). Figure 23.2b indicates that the effective holes injection ϕ_B from $Ti_2C(OH)_xF_y$ to WSe_2 is about 0.23 eV, and in Figure 23.2c, the electrons injection ϕ_B value from

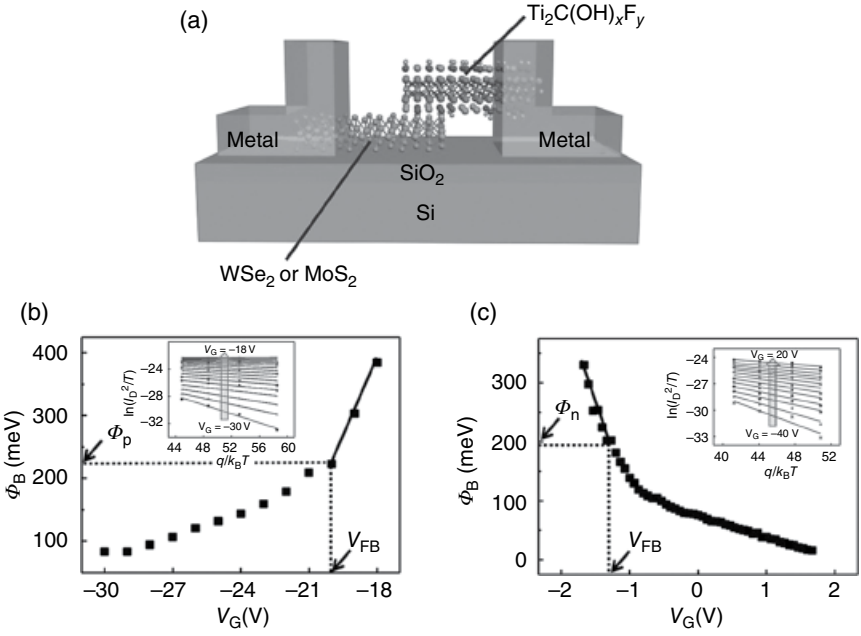


Figure 23.2 2D electronics using MXene contacts. (a) Schematic diagram of a WSe_2 (or MoS_2)/$Ti_2C(OH)_xF_y$ FET device. (b, c) Effective barrier height at the junction of (b) WSe_2-$Ti_2C(OH)_xF_y$ and (c) MoS_2-$Ti_2C(OH)_xF_y$ as a function of the gate voltage, extracted from the Richardson plots in the insets. *Source:* Xu et al. [34]/John Wiley & Sons. (d, e) Band structures (left) and atomic structures (right) for (d) $Hf_2N(OH)_2$-WSe_2 junction and (e) Nb_2CO_2-WSe_2 junction. The Fermi level is set to zero. *Source:* Liu et al. [10]/American Chemical Society. (f) The 3D schematic of $Ti_3C_2T_x$-MoS_2 transistor with sub-10 nm Hf50/Al10 dielectric layer, all layers are labeled. (g) Optical image of the NMOS inverter and (h) its circuit diagram (i) its output voltage transfer curve. *Source:* Xu et al. [35]/John Wiley & Sons.

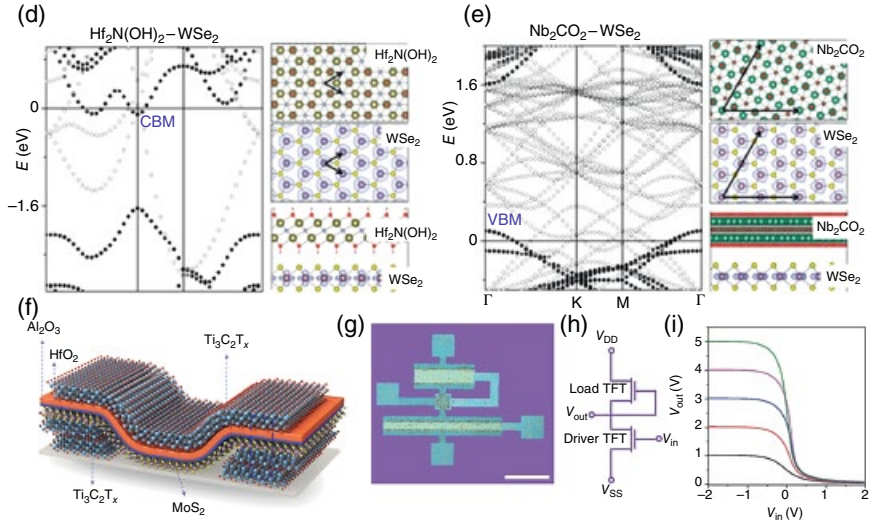


Figure 23.2 (Continued)

$Ti_2C(OH)_xF_y$ to MoS_2 of about 0.19 eV. The above research initially investigated the contact behaviors between $Ti_2C(OH)_xF_y$ (only one type of MXene) and 2D TMDCs experimentally. However, about 50 MXenes have been experimentally demonstrated and about 150 MXenes have been predicted [11]. Such an immense material treasure induces tremendous interest for both theorists and experimenters.

In 2016, Liu et al. [10] applied first-principle calculations to investigate many MXenes with different surface groups. They found that the surface groups strongly affect the Fermi level of MXenes. The =O group tends to increase the work function of most MXenes, while –OH reduces their work function. The –F group can either increase or decrease work function values depending on the type of MXenes. They regarded these phenomena originated from their different dipole behaviors. Notably, they also tried to evaluate and filter out which MXenes with certain surface terminations can be the ideal candidate for the ohmic contact to 2D semiconductors with zero Schottky barriers. M/S junction (MSJ) formed by $Hf_2N(OH)_2$ and WSe_2 (Figure 23.2d) was used as one example to investigate the barrier for the electrons injection from metallic MXenes to 2D semiconductors. They found the Fermi level of the $Hf_2N(OH)_2$ is above the conduction band minimum (CBM) of WSe_2, which means electrons can be freely injected from $Hf_2N(OH)_2$ to WSe_2. They predicted that all the MXenes with –OH groups, because of their shallow work function values of about 2~3 eV, can be promising barrier-free contacts for *n*-type carrier injection in 2D semiconductors. They further investigated the potential MXenes for barrier-free holes injection into 2D

semiconducting WSe_2. Nb_2CO_2 was used as one example to form an MSJ by placing this MXene on top of the WSe_2 layer (Figure 23.2e) because of the minimal strain introduced by lattice mismatch between these two layers. They found the Fermi level of Nb_2CO_2 is below the valence band maximum (VBM) of WSe_2, which means *p*-type carriers (holes) can be freely transported from the MXene layer to the 2D semiconductor layers without an energy barrier. Not only Nb_2CO_2, they expected many other MXenes with –O group could be the barrier-free contact to *p*-type WSe_2, such as Cr_2CO_2, Mo_2CO_2, $Ti_3C_2O_2$, $V_3C_2O_2$, $Ti_4C_3O_2$, $V_4C_3O_2$, Ti_2NO_2, V_2NO_2, and $Ti_4N_3O_2$. The theoretical calculation indicated great chances for some MXenes members to be barrier-free contacts with 2D semiconductors. It needs MXenes with either purified –OH surface groups for *n*-type transportation or –O groups for *p*-type transportation. However, there are still significant challenges in precisely engineering MXenes surface groups based on current fluorine acidic etching methods.

Tunable work function in a wide range is only one of significant reasons for MXenes as promising metal contacts. Several other advantages can significantly contribute to 2D electronics research. Solution processing of MXene electrodes is a low-energy and damage-free method; therefore, defects can be excluded at the MXene-semiconductor interface [18, 36]. Some MXenes, such as $Ti_3C_2T_x$, have high electrical conductivity (~24 000 S cm^{-1}) [37] and high current break-down density [38]. Instead of using single 2D MXene flakes, Xu et al. [39] developed $Ti_3C_2T_x$ MXene films as metal contacts in a large-area 2D MoS_2 transistors array through a simple spray coating process. They designed a top-gate TFT device architecture (Figure 23.2f), which uses $Ti_3C_2T_x$ as S/D/G electrodes, MoS_2 layer as the semiconducting channel, and HfO_2 with or without Al_2O_3 as the dielectric layer. Through vacuum annealing, the work function of the MXene electrodes was reduced from 4.6 to 4.5 eV, resulting in a minor contact barrier (~0.25 eV) for *n*-type carriers injection into the CBM of the MoS_2 layer. This annealing also made MXene films very stable to be patterned through a standard cleanroom process without peeling off phenomena, allowing the large-area transistor array with excellent uniformity in the device performance. Thus, they also achieved a high yield even using an ultrathin dielectric layer of about 8 nm. They further applied the $Ti_3C_2T_x$ MXene as the interconnect to fabricate all MXene-contact circuits, including rectifiers, negative-channel metal-oxide-semiconductor (NMOS) inverters, and voltage-shift NMOS inverters. They confirmed that all these circuit devices were working properly. The optical image of one NMOS inverter is shown in Figure 23.2g, which was designed using a load transistor with channel size width/length 250/50 μm and a driver transistor with 500/25 μm, thus a load ratio of 4. The circuit diagram is shown in Figure 23.2h. The static VTCs with different V_{DD} voltages in Figure 23.2i evidenced the NMOS proper operations.

MXenes have great potential as barrier-free and damage-free contacts to achieve ultralow M/S contact resistance in 2D transistors, which is an essential topic in 2D transistor research and application [40]. It is worth taking more effort in this direction. The practical strategy should first focus on synthesizing MXene with well-controlled surface groups, such as purified –OH or –O groups. MXene synthesis through molten salt etching can be one promising method worthy of further exploration [41]. Another great direction is synthesizing semiconducting MXenes, which will undoubtedly enrich the 2D semiconducting families.

23.4 MXene in Flexible and Wearable Electronics

Flexible electronics have been actively explored recently because flexibility can significantly expand electronic applications from fragile and rigid substrates to soft and conformal interfaces. They also possess several advantages of elasticity, lightweight, roll-to-roll manufacturable, low-cost fabrication, and large area. It is regarded as one essential technique strongly supporting the application scenarios involved with the friendly man–machine interaction. Depending on terminal applications, the scope of flexible electronics may include rollable and foldable displays and sensors, light emitters, electronic textiles, electronic skin, and muscle. The flexibility of electronic devices implies that the electronic device can work properly without obvious performance degradation while bending, twisting, folding, or even stretching the devices [42]. Those require both active materials in devices and the substrate can bear the complex stress environment. Organic polymers stand out because of their flexibility and stretchability and thus receive more attention in this area. Devices based on inorganic semiconductors and metals usually show high performance, but they are still limited in sustaining repeated bending or stretching, though some efforts have been taken [43]. However, MXenes, especially the representative $Ti_3C_2T_x$, have been demonstrated with excellent electrical performance stability after many-time bending [20, 44]. It starts to attract great attention to develop MXene applications in flexible electronics. Initial works using MXenes as electrodes in flexible transistor circuits and OLEDs have been developed recently.

Lyu et al. demonstrated $Ti_3C_2T_x$ MXene as low-cost electrodes in large-area flexible OFETs [45]. They found that the work function of the $Ti_3C_2T_x$ MXene can be engineered through an ammonia doping process and thus used as metal contacts for both *p*-type and *n*-type organic semiconductors. The schematic of using MXene as electrodes in a large-area OFET array is illustrated in Figure 23.3a. They first prepared G MXene patterning on a PEN substrate by spray coating combined with a selected-area O-zone treatment. Then, an organic dielectric layer of the cross-linked poly(4-vinyl phenol) (*c*PVP) was spin-coated and

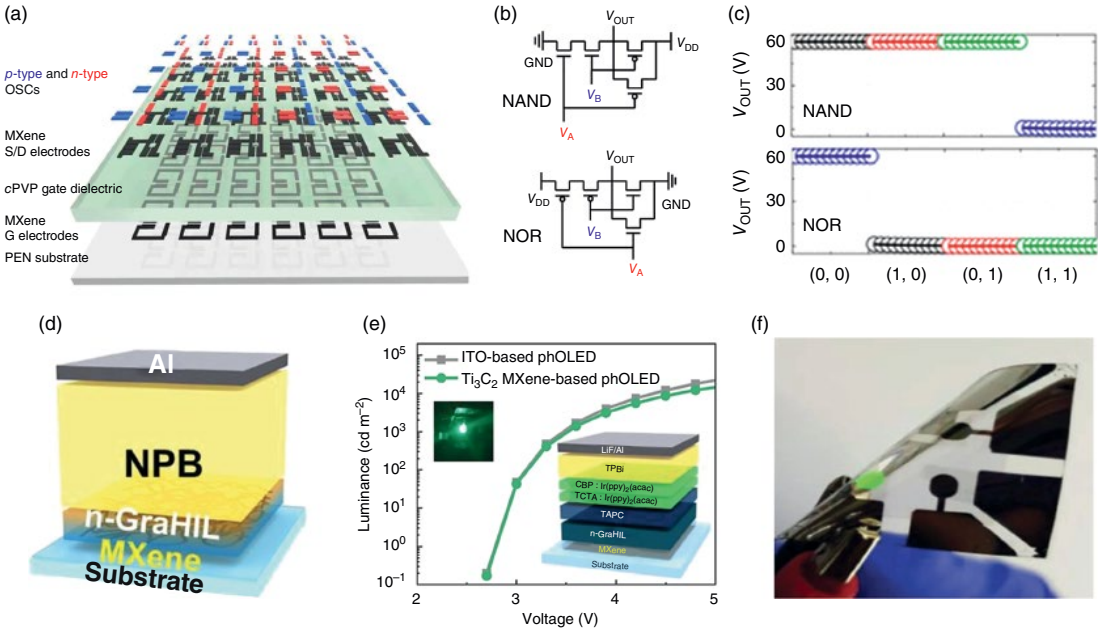


Figure 23.3 Flexible electronics using MXene contacts. (a) Schematic image of organic field-effect transistors (OFETs) device array using $Ti_3C_2T_x$ MXene as electrodes on a flexible polyethylene 2,6-naphthalate (PEN) substrate. (b) Circuit diagrams of single NAND and NOR gates (top and bottom, respectively). (c) Output voltages of NAND (top) and NOR (bottom) gates as functions of input signals. *Source:* Lyu et al. [45]/American Chemical Society. (d) Schematic illustration of the hole-only device (HOD) design. (e) Luminance versus voltage characteristics of organic light-emitting diodes (OLEDs) that have ITO or MXene electrode (inset: the optical image of MXene-based green OLED [left], and the schematic of the light gray glowing OLED structure [right]). (f) The optical image of flexible OLEDs based on MXene electrodes. *Source:* Ahn et al. [20]/Reproduced from John Wiley & Sons, Inc.

thermal-annealed to form a crosslinking network uniformly over the substrate. After which, the S and D MXene electrode patterning was prepared through the same method as the G MXene. However, *n*-type contact MXene needs ammonia solution treatments. Finally, *p*-type pentacene and *n*-type PTCDI-C_8 semiconducting channels were prepared to connect S and D electrodes. This beautiful device can be easily bent since they are fabricated on a flexible plastic substrate. They also demonstrated circuits that require connecting several *p*-type and/or *n*-type transistors. Figure 23.3b illustrates two circuits: NAND and NOR gates, which need four transistors serially or parallelly connected, respectively. They confirmed all these circuits were working properly. Figure 23.3c displays the output signals of the NAND and NOR gates. For the NAND gate, three logic combinations of (0, 0), (1, 0), and (0, 1) all resulted in the NAND output state "1," while another logic combination (1, 1) gave the output state "0." However, the NOR gate circuit operates oppositely. This work demonstrated MXenes as metal electrodes in flexible circuits are very practical in device fabrication and operation. However, more efforts are needed because the performance stability under different stress environments has yet to be investigated.

In the paper of Ahn et al. [20], $Ti_3C_2T_x$ MXene is regarded as a better transparent conducting material than several intensively explored materials such as carbon nanotubes, graphene, and conducting polymers. It is because MXenes have high electrical conductivity, high work function, and are easy to process. These motivated them to use MXene in the flexible OLEDs, a powerful technology in the next-generation display [46]. They first confirmed that $Ti_3C_2T_x$ MXene films prepared through a spin-casting process have acceptable transmittance (~85%) and conductivity (11 668 $S\,cm^{-1}$), which is suitable to be used as the transparent electrode. They further evaluated the electrical stability of $Ti_3C_2T_x$ MXene under different bending times on a flexible substrate. The conductivity of MXene films showed negligible changes after 5000 bendings. However, ITO films degraded sharply after only 1000 bendings. Besides, the vacuum annealing at 200 °C enables $Ti_3C_2T_x$ a high work function value of about 5.1 eV, which is another outstanding feature compared to other transparent conducting materials. It makes $Ti_3C_2T_x$ a very promising electrode candidate for barrier-free hole injection into the light-emitting layer and thus produces a high-efficient light illumination in the OLED. Therefore, they fabricated and evaluated HODs using $Ti_3C_2T_x$ as the hole injection electrode with the schematic shown in Figure 23.3d. It is incredible to find that the HOD with $Ti_3C_2T_x$ anode showed higher hole-current density at a given applied bias than that using an ITO anode (Figure 23.3e). In Figure 23.3e, the authors further fabricated green phosphorescent OLEDs using Ti_3C_2 MXene film as a transparent electrode and achieved the maximum current efficiency of about 102.0 $cd\,A^{-1}$, maximum power efficiency of 103.7 $lm\,W^{-1}$, and maximum external quantum efficiency (EQE) 28.5%, such a good result was very close to the

optical simulation. One flexible device using $Ti_3C_2T_x$ as a hole injection electrode is shown in Figure 23.3f, offering distinguished flexibility against cyclic bending and folding. The achievement above indicates the potential role of MXene as a transparent high-work-function electrode in OLED. However, MXenes can also be promising for electron injection if low-work-function –OH terminated MXenes can be successfully synthesized. Besides, MXenes as transparent electrodes in other OLEDs with different emitting light wavelengths are worth investigating further.

$Ti_3C_2T_x$ MXene films have shown outstanding stability under a flexible bending environment compared to the other transparent conducting films. It implies that MXene can play a significant role in flexible device applications.

Wearable electronics are the typical electronic devices that are lightweight, soft, flexible, and stretchable enough to be patched on human bodies. Unlike flexible electronics, wearable electronics emphasize the excellent biocompatibility of the devices to the human body, ideally similar to or even better than traditional wearable textiles [47]. Conventional textiles provide several well-known functions: keeping warm, preventing direct sunlight irradiation, privacy protection, and adorning. However, advanced wearable electronics would allow many different types of electronic devices to closely interact with specific human organs and precisely collect various physiological information. Such a unique function makes wearable electronics very attractive in personalized health monitoring and care systems, soft robotics, and human–machine interactions [48]. Particularly, wearable sensors can detect human physical and chemical signals in real time [49]. The sensor signals could reflect initial changes in health status and then provide timely reminders of possible diseases. MXenes, one emerging 2D family with unique electrical properties, shows great potential in wearable devices. Recently, MXene hydrogel-based strain sensor [50] and MXene-based biosensor received extensive exploration [51].

Conductive hydrogels, typical cross-linked 3D networks of hydrophilic viscoelastic polymers, are promising materials for wearable strain sensors. However, hydrogel-based sensors have several intrinsic problems such as relatively low sensitivity, unstable noises, and unexpected viscous deformation. Through filling with conductive $Ti_3C_2T_x$ MXenes, Zhang et al. [52] realized the MXene hybrid poly(vinyl alcohol) (PVA) hydrogel (M-hydrogel) with outstanding tensile strain sensitivity with a gauge factor of 25, 10 times higher than the pristine hydrogel. Besides, M-hydrogel also has a remarkable stretchability of more than 3400%, instantaneous self-heal ability, and excellent conformability and adhesiveness of human skin. They consider several reasons for such a fantastic improvement: MXene itself is very sensitive to mechanical strain sensitivity; negatively charged hydrophilic surfaces of MXene nanosheets help to form unique clay-polymer network structure and then significantly improve the hydrogel mechanical

properties, such as elastic modulus and stretchability; –OH groups on MXene surface can help to form more hydrogen bonds in the hydrogel system and realize better self-heal ability. More significantly, M-hydrogel can detect handwriting, facial expressions, and vocal signals accurately and sensitively. As shown in Figure 23.4a, they patched M-hydrogel on Adam's apple and monitored the resistance variation when there were vocal signals. They found that M-hydrogel produces stable and unique patterns. Even similarly sounding single syllables, such as "B" and "D" (Figure 23.4b, c), there are still easily distinguishable patterns for resistance changes.

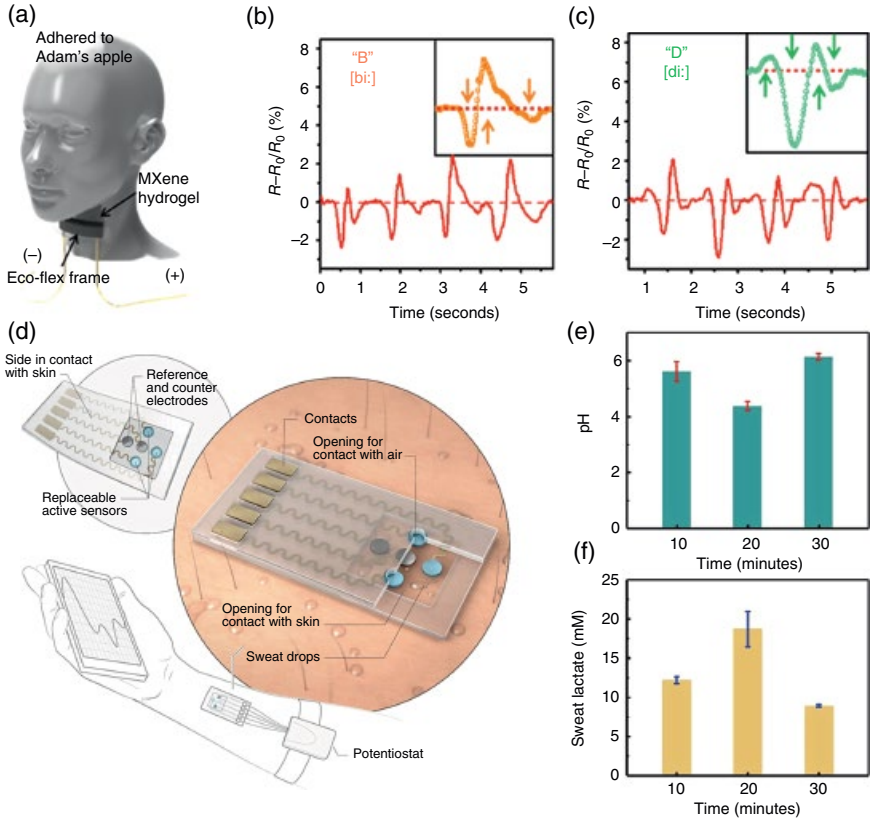


Figure 23.4 MXene involved wearable electronics. (a) Schematic for vocal sensing. (b,c) Resistance change in response to similarly sounding letters (b) "B" and (c) "D." *Source:* Zhang et al. [52]/American Association for the Advancement of Science. (d) Schematic diagram of the MXene-based wearable biosensor system. (e) Comparison of pH levels during the exercise with three different pH sensors. (f) Comparison of lactate levels during the exercise with three different lactate sensors. *Source:* Lei et al. [53]/John Wiley & Sons.

There has been great interest and research upsurge on the MXene hybrid wearable sensors for detecting human physical signals in recent years. Ma et al. [54] fabricated $Ti_3C_2T_x$ MXene-based piezoresistive sensor with high flexibility, excellent sensitivity (Gauge Factor ~ 180.1), fast response (<30 ms), and reversible compressibility. They figured out that the sensor resistance change stems from the great change of interlayer distances under external pressure. Cai et al. designed a multifunctional e-skin system based on a hetero-structured configuration that couples vinyl-hybrid-silica nanoparticle modified polyacrylamide hydrogel with $Ti_3C_2T_x$ MXene bridged by polypyrrole nanowires (PpyNWs) layers. This e-skin device possessed an extraordinary working range (2800%), ultrafast responsiveness (90 ms) and resilience (240 ms), and good linearity (800%) [55]. Chen et al. also fabricated a highly sensitive and flexible MXene-based piezoresistive sensor with bioinspired micro spinous microstructures, which can monitor physiological signals and detect quantitative pressure distributions [56]. A novel microchannel-confined MXene-based flexible piezoresistive sensor designed by Gao et al. can simultaneously achieve multi-types micro-force sensing of pressure, sound, and acceleration [57].

Not only the physical signals but some specific body-produced chemicals (glucose, urea, cholesterol, NO_2^- and adrenaline, etc.) can also be detected by wearable electrochemical biosensors [58]. A MXene-based wearable multifunctional biosensor designed by Lei et al. can detect biomarkers in sweat with good sensitivity values of 35.3 $\mu A\,mm^{-1}\,cm^{-2}$ for glucose and 11.4 $\mu A\,mm^{-1}\,cm^{-2}$. They applied MXene/Prussian blue ($Ti_3C_2T_x$/PB) as active sensing materials and confirmed good repeatability. Figure 23.4a illustrates the schematic of the MXene-based wearable biosensor with the capability of detecting multiple chemical signals, including glucose, lactate, and pH. Soft materials were applied to make the device comfortably wearable. The active sensing, counter, and reference electrodes can be easily replaced so that the whole sensor platform can serve a prolonged working life. Because of the larger linear detection range and the ultrahigh sensitivity, their multifunctional biosensor can simultaneously monitor sweat glucose, lactate, and pH in real time, as evidenced in Figure 23.4e, f. The excellent conductivity and electrochemical activity of exfoliated $Ti_3C_2T_x$, $Ti_3C_2T_x$/PB composites as active sensing materials significantly improved the performance. This achievement indicates MXene can play a significant role in the high-performance wearable biochemical sensor.

Wearable electronics, including strain sensors and biochemical sensors, can reshape personal medical care technologies with a very high chance and enormously benefit human health. MXenes are attracting widespread attention and upspring papers have been published recently. Other kinds of wearable electronics using MXene are also on the rise.

23.5 MXene in Iontronics and Neuromorphic Devices

Iontronics is a novel physical device that involves the modulation of both electronic and ionic transportation, accumulation, and interactions under a specific electrostatic field. It is an emerging interdisciplinary field involving electrochemistry, solid-state physics, electronic engineering, and biological sciences. The electron double-layer transistor (EDLT), using the ionic accumulation layer to modulate the electronic carrier behavior in the channel layer, is one of the representative iontronic device architectures [59]. MXenes, with the combination of excellent electronic conductivity and tunable interlayer ions intercalation and transportation [60], would open up a broad platform for iontronics. MXene-involved EDLTs have been reported recently for biosensing and logic devices.

$Ti_3C_2T_x$ MXene micro-stripes as the transistor channel for an EDLT have been fabricated by Xu et al., as shown in the schematic in Figure 23.5a [61]. The micro-stripe patterning was processed through a simple and easy micro-contact printing technique. Silver electrodes were patterned as the S and D contact, a liquid-like electrolyte as the solution G can provide ions for the EDL formation under a certain gate bias. The gate voltage can be supplied by immersing an Ag/AgCl electrode in the electrolyte. When they applied different gate voltages, the conductance of the $Ti_3C_2T_x$ MXene channel was evidenced with a corresponding modulation, which could result from the EDL formation and disappearance. They also tried to utilize this device to sense biomolecules like dopamine. The actual device displayed in Figure 23.5b illustrated the architecture of the biosensor based on this $Ti_3C_2T_x$ MXene-based EDLT. A biosensing chamber was filled with the liquid electrolyte, and the concentration of biomolecules such as dopamine can be adjusted by the microinjector. The amount of biomolecule in the liquid electrolyte can effectively change the ionic environment around the $Ti_3C_2T_x$ MXene channel so that its electronic conductivity will be adjusted accordingly. Figure 23.5c, while increasing the dopamine concentration through pulsed microinjection in the sensing chamber, the device conductance was modulated accordingly. Amazingly, it has an ultralow detection limit with a dopamine concentration as low as 100×10^{-9} m. Such an excellent sensitivity indicates $Ti_3C_2T_x$ MXene-based iontronics can be a promising biosensor for the quantitative detection of biological molecules. However, more studies should focus on how biomolecules interact with MXene, and whether this interaction is via physical absorption or chemical bonding with the surface groups. The stability of MXenes in bodily fluids requires additional investigation, which might contribute to developing better MXene-based biosensors.

Besides MXenes, MXene-derived materials have also been demonstrated as excellent candidates for electronic and iontronic research since they can inherit

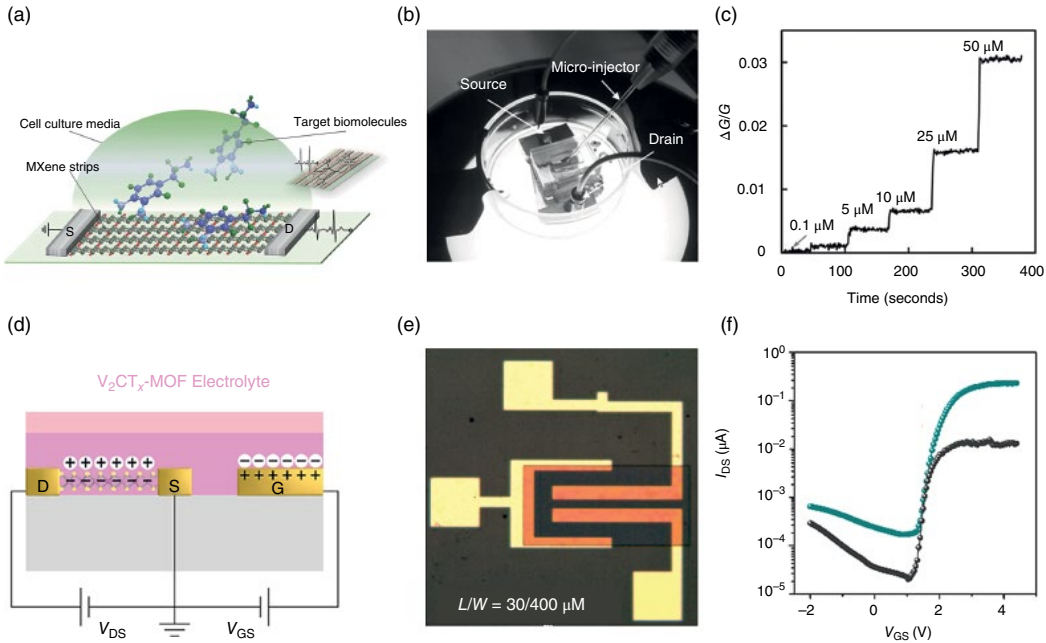


Figure 23.5 MXene in iontronics. (a) Schematic of a biosensor based on MXene ionic gate transistor. (b) Photograph showing the MXene transistor device coupled with a microinjector for precisely controlled pulsed dopamine release in the biosensing chamber. (c) Real-time change of conductivity of an MXene device during variation from 100×10^{-9} m to 50×10^{-6} m of dopamine concentrations. *Source:* Xu et al. [61]/Reproduced from John Wiley & Sons, Inc. (d) Schematic diagram. (e) Photograph of V_2CT_x-MOF/MoS_2 EDL transistor. (f) Logarithmic-scale transfer curves at different S/D voltages (black: V_{DS} = 0.1 V, dark gray: V_{DS} = 1 V). *Source:* Xu et al. [62].

specific unique features from MXenes. For example, Using MXene as the metal precursor, ferroelectric $KNbO_3$ crystals can be synthesized with a high aspect ratio because of the MXene 2D nature, which cannot be realized using traditional precursors [63]. V_2CT_x MXene-derived porous metal-organic frameworks (V_2CT_x-MOFs) have been verified with ultrathin 2D nature and very narrow size distribution, while other metal-derived MOFs were produced with irregular particles [64]. The V_2CT_x-MOFs can be feasibly processed as ultrathin films with a flat surface and large-area uniformity. Xu et al. applied the V_2CT_x-MOFs as the solid electrolyte for hydrogen ions storage, transport, and accumulation and then successfully fabricated EDLTs using MoS_2 as the electron transport channel [62]. The architecture of the V_2CT_x-MOF/MoS_2 EDLT is illustrated in Figure 23.5d, MoS_2 was used as the semiconducting channel, Au/Ti pattern as S/D and side G. V_2CT_x-MOF doped with phosphoric acid was performed as the pattern-able solid electrolyte, the photoresist layer was preserved as a capping layer to keep the acid-doped MX-MOF film as a stable proton-conductive medium. When applying a positive gate voltage, H^+ ions would accumulate as the positively charged layer on the surface of the MoS_2 channel. Then electron layer will gather in the channel, such an accumulation of both positively and negatively charged layers at an electrolyte/channel interface is regarded as the EDL formation. The actual device is shown in Figure 23.5e. The electrical characterization of this EDLT is illustrated in Figure 23.5f, where transfer curves at different S/D voltages were plotted on a logarithmic scale. They found this EDLT had an excellent subthreshold swing (*SS*) value of about $238\,mV\,dec^{-1}$ and an acceptable S/D current on/off ratio of about 10^3. This is the first time using V_2CT_x-MOF for micro-intronic devices; the successful EDLTs demonstration of MXene-derived materials would have a significant impact on iontronics research and development.

The rapid development of advanced information technologies, such as artificial intelligence (AI), machine learning, big data, and the internet of things (IoT), put forward extremely high requirements for computing power. The current underlying hardware architecture is based on conventional von Neumann computing, which has separate data processing and memory systems. Such a construction needs large amounts of data transmission between logic computing processor and data storage, leading to great power consumption and slow data process speed [65]. Inspired by the neuromorphic network in the human brain, which can process and memorize large amounts of data in parallel with ultralow power dissipation [66], many scientists are dreaming of building an artificial neuron network that can mimic recognition, learning, and in-memory computing skills of human brains [67]. Various building units of neuromorphic systems, such as synaptic devices, have been proposed and experimentally investigated. It includes two-terminal devices such as memristors, ferroelectric tunnel junctions,

and phase change memories, also three-terminal devices such as ionic-gate transistors, ferroelectric transistors, and floating-gate transistors. Emerging materials can always bring endless possibilities and great operation space for designing these neuromorphic devices [65]. Some MXenes have also been explored in many kinds of synaptic devices, such as memristors [68], floating-gate transistors [69], and ionic-gate transistors [70].

Lyu et al. implied the surface oxidized $Ti_3C_2T_x$ MXene as the nano-floating gate in a bottom-gated *p*-type organic pentacene transistor and achieved the floating gate transistor memory [69]. They confirmed the distinguished nonvolatile memory characteristics and further investigated its synaptic functions. The schematic of using this MXene floating-gate transistor as the synaptic device is illustrated in Figure 23.6a. In the upper part, they explained the working mechanism of a natural biological synapse with three critical components, including the synaptic cleft, presynaptic, and postsynaptic terminals. Spikes released from the presynaptic terminal would produce a corresponding current change in the postsynaptic, such as the excitatory postsynaptic current (EPSC)/ inhibitory postsynaptic current (IPSC). The below part is the schematic of the MXene floating-gate device that served as an artificial synaptic device. Voltage pulses at the G electrode, performed as the presynaptic sparks, can modulate trapped charges in the MXene core layer and thus change the pentacene channel current in the mode of either the EPSC or the IPSC. The transfer characteristics in Figure 23.6b investigated the role of MXene in the hysteresis behaviors. They found that MXene with a surface oxidized TiO_2 layer causes the floating gate memory with a big memory window up to 35.2 V, high programming/erasing current ratio ($\approx 10^6$), low off-current (<1 pA), long retention (>10^4 s), and cyclic endurance (300 cycles). They investigated the EPSC and IPSC responses in the MXene floating gate transistor memory with relevant curves shown in Figure 23.6c. They first fixed the S/D voltage at +5 V to trace how the channel current (considered the postsynaptic current) responds to the gate voltage pulse (considered the presynaptic spike). When they applied a gate voltage pulse with a magnitude of +10 V and duration (t_d) of 10 ms, the channel current showed a sudden saturation of 0.56 nA, whereas a negative gate voltage pulse of −10 V led to the channel current decreasing to 0.16 nA. The channel current did not return to the level before the voltage spike in 30 s in both situations, verifying the long-term plasticity of the MXene floating gate transistor devices as a three-synaptic device. Other synaptic functions, including the EPSC/IPSC and paired-pulse facilitation, were also successfully emulated. Such a role of oxidized $Ti_3C_2T_x$ in artificial floating-gate synaptic would inspire the application of MXene in the emerging neuromorphic device.

Except that the partially oxidized $Ti_3C_2T_x$ as the floating gate in the synaptic transistor device, the pristine $Ti_3C_2T_x$ has also been demonstrated as the suitable

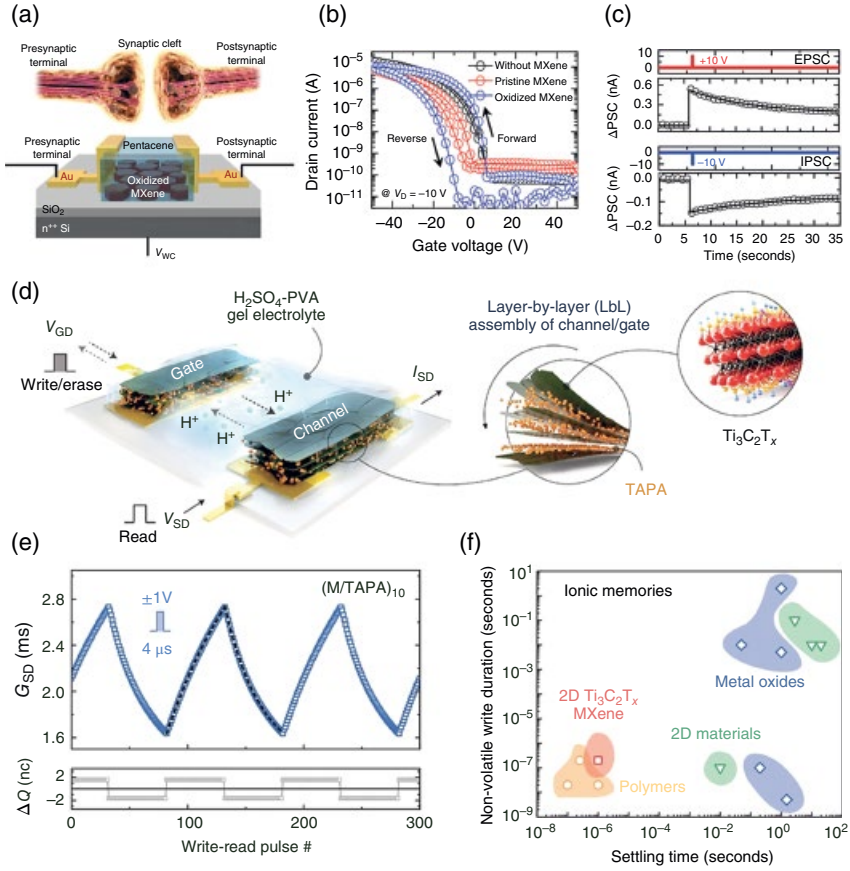


Figure 23.6 MXene in neuromorphic devices. (a) Schematic illustration of the biological synapse (top) and the artificial synapse (bottom). (b) Transfer characteristics of transistors with different hysteresis behaviors. (c) EPSC and IPSC responses of NFGTMs to V_{WC} spike with a magnitude of ±10 V and duration (t_d) of 10 ms. *Source:* Lyu et al. [69]/John Wiley & Sons. (d) The schematic of MXene-ECRAM device architecture. (e) (MXene/TAPA)10 ECRAM cycling using ±1 V 4-µs write pulses (top panel) and ΔQ per write (bottom panel). Cycling is nearly linear, with constant ΔQ per write across the ECRAM dynamic range. (f) Nonvolatile write duration versus settling time in ECRAMs using various classes. *Source:* Melianas et al. [70]/John Wiley & Sons.

channel layer in an ionic electrochemical transistor synaptic device by Melianas et al. [70]. The schematic of the electrochemical synaptic device using the $Ti_3C_2T_x$ film as the channel is illustrated in Figure 23.6d. The $Ti_3C_2T_x$ layer is formed by a layer-by-layer process with spacer molecules such as tris(3-aminopropyl)amine (TAPA), which can help to modify the interlayer chemistry of the MXene channel.

PVA-H_2SO_4 was used as the solid-state electrolyte, laterally connecting the MXene channel to G in the synaptic device. Such a synaptic has the capability of high-speed switching, which can accelerate learning in artificial neural networks. They performed high-speed programming using pulses of −1 V at 4 μs, and confirmed the write-read delay was only about 1 μs and readout parameters of 0.1 V at 10 μs. They also performed continuous writing pulses and found that the ionic MXene channel resistance switching in a nearly linear mode (Figure 23.6e), the switching of this device needs a very small amount of energy with only about 80 fJ μm^{-2}. Such outstanding high-speed programming (Figure 23.6f) and low-power consumption make this MXene-based ionic-gating synaptic device even comparable to the polymer-based device. Besides, MXene Synaptics can stand high-temperature processing and are thus more suitable for on-chip integration than the polymer. This achievement further demonstrated the unique advantage of MXene in artificial synaptic devices.

Research on MXene-based neuromorphic devices is still in the early stage but already showing great promise. MXenes have a combination of excellent electronic conductivity and interlayer ionic transport. At the same time, the operation of most neuromorphic devices is also involved with the control of both electrons and ions. This suggests that MXenes could be the ideal platform for the successful design of high-performance artificial synaptic devices.

23.6 MXene in Wireless Communication Devices

Wireless communication technologies are becoming increasingly impactful because of the explosive development of various portable devices. The IoT requires the information to be collected from targets and then processed and stored in the data processing system, ideally through a wireless propagation method. One of the most popular techniques for wireless communication is based on the emission, propagation, and reception of electromagnetic waves loaded with electrical signals, which operation heavily relies on radio-frequency antenna devices. Metallic conducting materials applied in the antennas are usually silver, copper, or aluminum because of their high electrical conductivity for transmitting and receiving radio waves. However, there are always skin depth phenomena in those kinds of bulky metal plates, where most electrical current flows within a layer close to the surface. The layer thickness is about four times the skin depth. It is reported that skin depths of silver, copper, and aluminum at 2.4 GHz are 1.33, 1.29, and 1.67 μm, respectively. It means the minimum thickness of these metal plates should be at least 5 μm [71]. Such a property limits their applications as the ultrathin and flexible antenna component, which is essential for meeting the fast-growing demands on portable and wearable devices [72]. Relevant researchers

keep seeking alternative materials to replace traditional metals and fabricate ultrathin antenna devices. Many emerging metallic or semi-metallic nanomaterials have been manufactured as wireless communication devices. They include conductive polymers [73] and their hybrids with metal nanoparticles [74], 2D TMDCs [75], BP [76], graphene [77], carbon nanotubes [78], and carbon onions [79]. However, most of them are suffering from relatively low electrical conductance. $Ti_3C_2T_x$, the representative member of the MXene family, has an electrical conductivity value of up to 24 000 S cm^{-1}, which is the best among all solution-processed 2D materials [37]. Besides, it has a well-established synthesis process and received the most profound investigation, making it easy to process and possibly the best candidate material in antenna devices. Recent publications from Gogotsi's group have demonstrated MXenes great potential in wireless communication technologies [71, 80].

Han et al. [80] fabricated microstrip patch antennas for target frequencies of 5.6, 10.9, and 16.4 GHz using solution-processed $Ti_3C_2T_x$ MXene as the conductive films. Figure 23.7a schematically illustrates how the 2D layered $Ti_3C_2T_x$ was synthesized, processed, and then fabricated as flexible antenna devices and how the antennas can be used in wireless communication among various movable and motionless objectives. They got very promising and reliable achievements on the MXene-based antennas through comprehensive testing, including the gain, radiation efficiency, and directivity measurements under different test scenarios. Incredibly, they observed that the antenna fabricated using $Ti_3C_2T_x$ with a thickness of only 5.5 μm had a radiation efficiency of y 99% at 16.4 GHz, comparable with the standard device based on a 35 μm thick copper. Amazingly, MXene applied in the device is only about 15% in thickness and 7% in weight of the copper counterpart. Actually, they compared the performance of the antennas based on MXenes with devices based on many other materials. They found the MXene one is outstanding in radiation efficiency even with a relatively thin feature, as shown in Figure 23.7b. They also demonstrated that MXene-based devices could work in a broad frequency range. It indicates that $Ti_3C_2T_x$ MXene has apparent advantages in making lightweight and flexible 5G communication devices.

Ultrathin MXene-based antenna devices were also investigated by Sarycheva et al. [71]. They fabricated a straight dipole antenna commonly used in broadcasting, cellular phones, and other wireless communications because of their omnidirectional property. The device schematic is illustrated in Figure 23.7c, where $Ti_3C_2T_x$ film was processed as the conductive material. The thinnest MXene antenna devices are only about 100 nm thick, translucent, and can still reach a reflection coefficient of less than −10 dB. The thicker antenna (8 μm) has a reflection coefficient of only −65 dB at about 2.4 GHz as shown in Figure 23.7d. They plotted the attenuations of different antenna materials, directly reflecting the superiority of MXenes. As shown in Figure 23.7e, the 1.4-μm-thick $Ti_3C_2T_x$ MXene

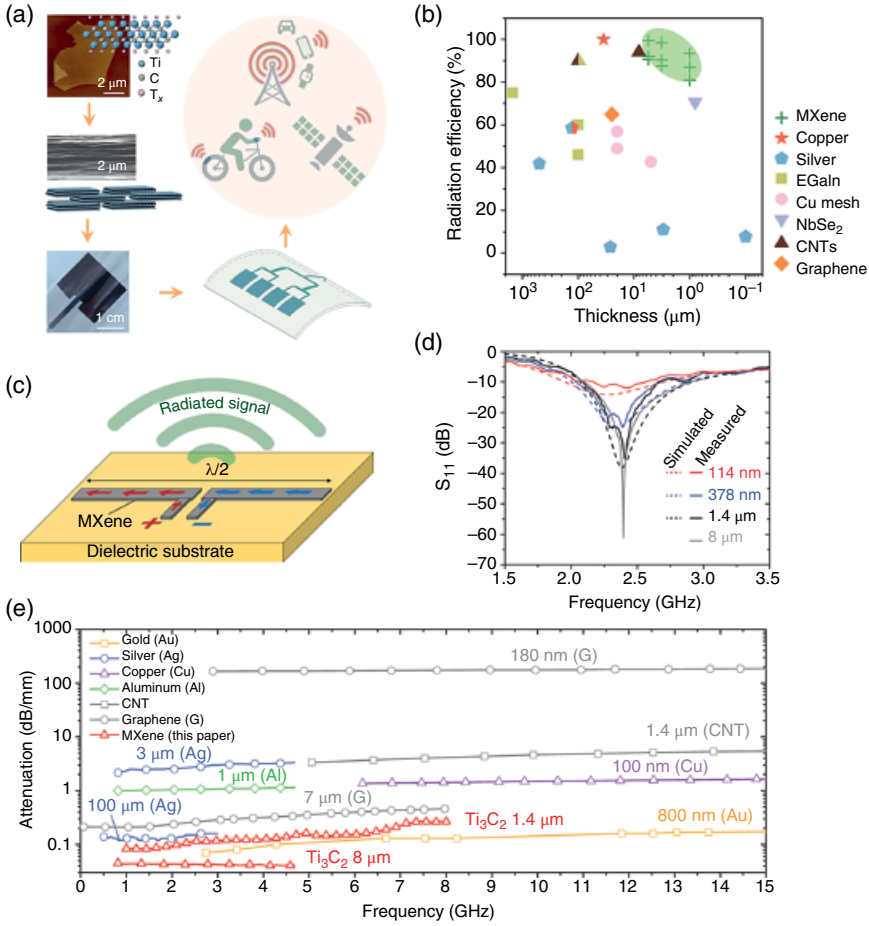


Figure 23.7 MXene in wireless communication devices. (a) The simplified entire process of $Ti_3C_2T_x$ MXene in antenna application from 2D MXene sheet synthesis, MXene film process, device preparation, and the various terminal devices application scenarios. (b) A comparison of radiation efficiency versus thickness for MXene with metals, carbons, and others as patch antennas. *Source:* Han et al. [80]/Reproduced from John Wiley & Sons, Inc. (c) The schematic explaining the working principle of the dipole antenna. The length of the dipole antenna matches half of the wavelength of the radiated signal. (d) S_{11} parameter (reflection coefficient) of dipole antennas of various thicknesses (from 114 nm to 8 μm). Measured values are presented as solid lines and simulated values are presented as dashed lines. (e) Comparison of attenuation in CPW of different materials: graphene, CNT, Ag ink, Ag-polydimethylsiloxane, Au ink, Al, and Cu with 1.4- and 8-μm-thick $Ti_3C_2T_x$ MXene films. *Source:* Sarycheva et al. [71].

film has about 50 times fewer losses at 1 GHz than a 7.7-μm-thick graphene-printed film and 300 times less than a silver ink-printed antenna.

The above results summarize the unique advantages of 2D MXene in wireless communication technologies, especially for designing and fabricating flexible, wearable, or even transparent devices. MXenes also have the advantage of low-cost fabrication because of their ease of processing in aqueous solutions free of toxic organic solvents and surfactants. Many other MXenes, which have already been synthesized or are yet to be synthesized, provide a rich conductive materials library to design more high-performance antenna devices with more advanced functionality.

23.7 Conclusion and Outlook

MXenes are increasingly being considered for electronics and communication device applications. So far, a few studies have been reported for devices involving micro or nanofabrication in the field of oxide electronics, 2D electronics, organic electronics, micro-iontronics, and antennas. However, we expect this area to experience a rapid expansion in the coming years because of the unique properties of MXenes and advances in synthesis strategies. There is substantial exploration potential in the synthesis of new MXenes, the discovery of novel physical properties, the development of advanced MXene processing, and the design of innovative devices. Herein, we will point out the potential directions that can make MXenes play an increasingly significant role in electronics and wireless communication technologies.

There is a great chance for MXenes to be an ideal ohmic contact for semiconducting channels in transistor devices, including *n*-type and *p*-type oxides, 2D TMDCs, and organic semiconductors. This is because the work function of MXenes covers a wide range from 2 to 8 eV according to the theoretical calculation [10]. Another reason for MXenes to be excellent ohmic contact electrodes is the low-energy solution deposition of MXene film. This reduces the chance of introducing interfacial defects and therefore forms a clean MXene/semiconductor interface, excluding the possible Fermi-level pinning effect [36]. Therefore, it makes MXenes more prominent than traditional metal electrodes, which are usually deposited through high-energy vacuum systems that usually introduce interface defects. However, no report has experimentally demonstrated MXene as a barrier-free contact with any semiconductor. To realize this great goal, more efforts should be put into the work function engineering of MXenes by precisely controlling their surface groups. MXenes with only the –OH group have a shallow work function value of about 2 eV and can be promising electrodes for electron injection. The –O group makes MXenes a high work function value of up

to 8 eV and is good for hole injection. Developing new synthesis methods can be a practical method for surface group modification. The current method used is based on a hydrofluoric acid etching process, resulting in mixed groups of —F, =O, and —OH. Therefore, it is almost impossible to achieve a mono-type surface group based on the mixed acid solution etching process. Molten salt etching can be a practical strategy to achieve well-controlled surface termination, $Ti_3C_2T_x$ and Nb_2CT_x with mono-group such as =O, =S, =Se, =Te or $—NH_2$ have been demonstrated, which are worth to be investigated in terms of work function and as the ideal ohmic contact electrodes [41]. Strategies for processing MXene with only the –OH group have not yet been achieved experimentally, requiring more effort. The post-treatment such as chemical doping and thermal annealing under various atmospheres can also effectively modify surface groups and thus work functions.

Preparation of MXene films with a high FoM (high visible transparency without sacrificing conductivity) is necessary for using MXenes as transparent conductive films in transparent oxide displays, OLEDs, and ultra-thin antennas. To our knowledge, the FoM value of $Ti_3C_2T_x$ films is 15, which is far below the requirement for industrial applications (>35) [22]. One direction is to enhance the electrical conductivity of MXenes through developing advanced synthesis methods to improve the MXene crystalline quality so that MXene films with an acceptable sheet resistance can be thinner and thus more transparent. The etching of the Al-rich MAX phase [81] and the evaporated-nitrogen-protected MXene Delamination [37] have been demonstrated as proper methods of improving $Ti_3C_2T_x$ conductivity. Another effective strategy for achieving higher FoM is to engineer the transparency of the MXene film through ions intercalation, which has been initially explored in the Gogotsi group [82]. Therefore, both increasing the conductivity of MXenes and optimizing the formation process of the MXene film should be heavily considered for transparent MXene films with a better FoM value.

MXenes have potential in electronics and telecommunication devices. However, many of these applications are still limited by the development of the MXene synthesis process. Only $Ti_3C_2T_x$ MXene has been reported in these devices because of its relatively well-established synthesis process and more mature experiences. However, many other MXenes, including about 50 members achieved experimentally and another about 150 predicted [51], are certain to expand the field of electronics and communication applications. For example, successfully developing semiconducting MXenes would mean MXene can be used not only as a contact but also as channel material. Most MXenes are prepared through a solution process, limiting the feasibility of further device miniaturization to the nanometer scale and the reliability of nano-device yield. Therefore, developing a strategy for MXene growth by vacuum methods may allow us to overcome those challenges.

Scaling up the MXenes production through an environmentally friendly process flow is necessary for industrial applications. The unique structure of MXenes coupled with the combination of surface groups for dipole formation and the metallic core for fast carrier transport implies that they may present unexpected physical properties that can lead to novel electronic devices. As more MXenes are experimentally synthesized, MXene-based new and improved devices will emerge.

References

1 Naguib, M., Kurtoglu, M., Presser, V. et al. (2011). Two-dimensional nanocrystals produced by exfoliation of Ti_3AlC_2. *Advanced Materials* 23: 4248.
2 Anasori, B., Lukatskaya, M.R., and Gogotsi, Y. (2017). 2D metal carbides and nitrides (MXenes) for energy storage. *Nature Reviews Materials* 2: 1.
3 Jiang, Q., Lei, Y., Liang, H. et al. (2020). Review of MXene electrochemical microsupercapacitors. *Energy Storage Materials* 27: 78.
4 Chaudhari, N.K., Jin, H., Kim, B. et al. (2017). MXene: an emerging two-dimensional material for future energy conversion and storage applications. *Journal of Materials Chemistry A* 5: 24564.
5 Guo, Z., Zhou, J., Zhu, L., and Sun, Z. (2016). MXene: a promising photocatalyst for water splitting. *Journal of Materials Chemistry A* 4: 11446.
6 Zhang, J., Zhao, Y., Guo, X. et al. (2018). Single platinum atoms immobilized on an MXene as an efficient catalyst for the hydrogen evolution reaction. *Nature Catalysis* 1: 985.
7 Liu, J., Zhang, H.B., Sun, R. et al. (2017). Hydrophobic, flexible, and lightweight MXene foams for high-performance electromagnetic-interference shielding. *Advanced Materials* 29: 1702367.
8 Ihsanullah, I. (2020). Potential of MXenes in water desalination: current status and perspectives. *Nano Micro Letters* 12: 1.
9 Xu, X., Guo, T., Kim, H. et al. Growth of two-dimensional materials at the wafer scale. *Advanced Materials* 34: 2108258.
10 Liu, Y., Xiao, H., and Goddard, W.A. (2016). Schottky-barrier-free contacts with two-dimensional semiconductors by surface-engineered MXenes. *Journal of the American Chemical Society* 138: 15853.
11 VahidMohammadi, A., Rosen, J., and Gogotsi, Y. (2021). The world of two-dimensional carbides and nitrides (MXenes). *Science* 372: eabf1581.
12 Zhang, C., McKeon, L., Kremer, M.P. et al. (2019). Additive-free MXene inks and direct printing of micro-supercapacitors. *Nature Communications* 10: 1795.
13 (a) Fortunato, E., Barquinha, P., and Martins, R. (2012). Oxide semiconductor thin-film transistors: a review of recent advances. *Advanced Materials* 24: 2945. (b) Wang, Z., Nayak, P.K., Caraveo-Frescas, J.A., and Alshareef, H.N. (2016). Oxide

thin-film electronics using all-MXene electrical contacts. *Advanced Materials* 28: 3831.

14 Nomura, K., Ohta, H., Takagi, A. et al. (2004). Room-temperature fabrication of transparent flexible thin-film transistors using amorphous oxide semiconductors. *Nature* 432: 488.

15 Park, B., Ho, D., Kwon, G. et al. (2018). Solution-processed rad-hard amorphous metal-oxide thin-film transistors. *Advanced Functional Materials* 28: 1802717.

16 (a) Nayak, P.K., Wang, Z., and Alshareef, H.N. (2016). Solution-processed rad-hard amorphous metal-oxide thin-film transistors. *Advanced Materials* 28: 7736. (b) Alshammari, F.H., Hota, M.K., and Alshareef, H.N. (2018). Transparent electronics using one binary oxide for all transistor layers. *Small* 14: 1803969.

17 Park, J.W., Kang, B.H., and Kim, H.J. (2020). A review of low-temperature solution-processed metal oxide thin-film transistors for flexible electronics. *Advanced Functional Materials* 30: 1904632.

18 Kim, H., Wang, Z., and Alshareef, H.N. (2019). MXetronics: electronic and photonic applications of MXenes. *Nano Energy* 60: 179.

19 (a) Zhang, C. and Nicolosi, V. (2019). *2D Metal Carbides and Nitrides (MXenes): Structure, Properties and Applications*, DOI: 10.1007/978-3-030-19026-2_25 (ed. B. Anasori and Y. Gogotsi), 481. Cham: Springer International Publishing. (b) Zhang, C., Anasori, B., Seral-Ascaso, A. et al. (2017). Transparent, flexible, and conductive 2D titanium carbide (MXene) films with high volumetric capacitance. *Advanced Materials* 29: 1702678.

20 Ahn, S., Han, T.-H., Maleski, K. et al. (2020). A 2D titanium carbide MXene flexible electrode for high-efficiency light-emitting diodes. *Advanced Materials* 32: 2000919.

21 Z. Wang, H. Kim, H. N. Alshareef, Oxide Thin-film electronics using all-MXene electrical contacts *Advanced Materials* 2018, 30, 1706656.

22 De, S., Higgins, T.M., Lyons, P.E. et al. (2009). Silver nanowire networks as flexible, transparent, conducting films: extremely high DC to optical conductivity ratios. *ACS Nano* 3: 1767.

23 (a) Chen, W., Liu, L.-X., Zhang, H.-B., and Yu, Z.-Z. (2020). Flexible, transparent, and conductive $Ti_3C_2T_x$ MXene–silver nanowire films with smart acoustic sensitivity for high-performance electromagnetic interference shielding. *ACS Nano* 14: 16643. (b) Jin, M., Chen, W., Liu, L.-X. et al. (2022). Transparent, conductive and flexible MXene grid/silver nanowire hierarchical films for high-performance electromagnetic interference shielding. *Journal of Materials Chemistry A* 10: 14364.

24 Novoselov, K.S., Geim, A.K., Morozov, S.V. et al. (2004). Electric field effect in atomically thin carbon films. *Science* 306: 666.

25 Bolotin, K.I., Sikes, K.J., Jiang, Z. et al. (2008). Ultrahigh electron mobility in suspended graphene. *Solid State Communications* 146: 351.

26 Yu, Y.-J., Zhao, Y., Ryu, S. et al. (2009). Tuning the graphene work function by electric field effect. *Nano Letters* 9: 3430.

27 Cao, Y., Fatemi, V., Fang, S. et al. (2018). Unconventional superconductivity in magic-angle graphene superlattices. *Nature* 556: 43.

28 Dean, C.R., Young, A.F., Meric, I. et al. (2010). Boron nitride substrates for high-quality graphene electronics. *Nature Nanotechnology* 5: 722.

29 Kostoglou, N., Polychronopoulou, K., and Rebholz, C. (2015). Thermal and chemical stability of hexagonal boron nitride (h-BN) nanoplatelets. *Vacuum* 112: 42.

30 Vu, Q.A., Fan, S., Lee, S.H. et al. (2018). Near-zero hysteresis and near-ideal subthreshold swing in h-BN encapsulated single-layer MoS_2 field-effect transistors. *2D Materials* 5: 031001.

31 (a) Akinwande, D., Huyghebaert, C., Wang, C.-H. et al. (2019). Graphene and two-dimensional materials for silicon technology. *Nature* 573: 507. (b) Samavedam, S. B., Ryckaert, J., Beyne, E. et al. (2020). Future logic scaling: towards atomic channels and deconstructed chips. *Presented at 2020 IEEE International Electron Devices Meeting (IEDM)*, IMEC, Leuven, Belgium, pp. 12–18 (December 2020).

32 (a) Li, L., Yu, Y., Ye, G.J. et al. (2014). Black phosphorus field-effect transistors. *Nature Nanotechnology* 9: 372. (b) Wang, Y., Qiu, G., Wang, R. et al. (2018). Field-effect transistors made from solution-grown two-dimensional tellurene. *Nature Electronics* 1: 228.

33 Kim, H. and Alshareef, H.N. (2020). MXetronics: MXene-enabled electronic and photonic devices. *ACS Materials Letters* 2: 55.

34 Xu, J., Shim, J., Park, J.H., and Lee, S. (2016). MXene electrode for the integration of WSe_2 and MoS_2 field effect transistors. *Advanced Functional Materials* 26: 5328.

35 Xu, X., Guo, T., Hota, M.K. et al. (2022). High-yield $Ti_3C_2T_x$ MXene-MoS_2 integrated circuits. *Advanced Materials* 34: 2107370.

36 Zheng, W., Saiz, F., Shen, Y. et al. (2022). Defect-free metal deposition on 2D materials via inkjet printing technology. *Advanced Materials* 34: 2104138.

37 Zeraati, A.S., Mirkhani, S.A., Sun, P. et al. (2021). Improved synthesis of $Ti_3C_2T_x$ MXenes resulting in exceptional electrical conductivity, high synthesis yield, and enhanced capacitance. *Nanoscale* 13: 3572.

38 (a) Lipatov, A., Goad, A., Loes, M.J. et al. (2021). High electrical conductivity and breakdown current density of individual monolayer $Ti_3C_2T_x$ MXene flakes. *Matter* 4: 1413. (b) Lipatov, A., Loes, M.J., Vorobeva, N.S. et al. (2021). High breakdown current density in monolayer Nb4C3Tx MXene. *ACS Materials Letters* 3: 1088.(c) Wang, H., Yao, Z., Acauan, L. et al. (2021). Toward MXene interconnects. *Matter* 4: 1447.

39 Gong, C., Zhang, H., Wang, W. et al. (2013). Band alignment of two-dimensional transition metal dichalcogenides: application in tunnel field effect transistors. *Applied Physics Letters* 103: 053513.

40 Wang, Y. and Chhowalla, M. (2021). Making clean electrical contacts on 2D transition metal dichalcogenides. *Nature Reviews Physics* 4 (2): 1–12. https://doi.org/10.1038/s42254-021-00389-0.

41 Kamysbayev, V., Filatov, A.S., Hu, H. et al. (2020). Covalent surface modifications and superconductivity of two-dimensional metal carbide MXenes. *Science* 369: 979.

42 (a) Wong, W.S. and Salleo, A. (2009). *Flexible Electronics: Materials and Applications*. Springer Science & Business Media. (b) Kamyshny, A. and Magdassi, S. (2019). Conductive nanomaterials for 2D and 3D printed flexible electronics. *Chemical Society Reviews* 48: 1712.

43 (a) Lu, X. and Xia, Y. (2006). Buckling down for flexible electronics. *Nature Nanotechnology* 1: 163. (b) Gates, B.D. (2009). Flexible electronics. *Science* 323: 1566.

44 Kim, H., Nugraha, M.I., Guan, X. et al. (2021). All-solution-processed quantum dot electrical double-layer transistors enhanced by surface charges of $Ti_3C_2T_x$ MXene contacts. *ACS Nano* 15: 5221.

45 Lyu, B., Kim, M., Jing, H. et al. (2019). Large-area MXene electrode array for flexible electronics. *ACS Nano* 13: 11392.

46 Lee, S.M., Kwon, J.H., Kwon, S., and Choi, K.C. (2017). A review of flexible OLEDs toward highly durable unusual displays. *IEEE Transactions on Electron Devices* 64: 1922.

47 Stoppa, M. and Chiolerio, A. (2014). Wearable electronics and smart textiles: a critical review. *Sensors-Basel* 14: 11957.

48 Wang, C., Xia, K., Wang, H. et al. (2019). Advanced carbon for flexible and wearable electronics. *Advanced Materials* 31: 1801072.

49 (a) Shi, Q., Dong, B., He, T. et al. (2020). Progress in wearable electronics/photonics—moving toward the era of artificial intelligence and internet of things. *InfoMat* 2: 1131. (b) Pang, Y., Yang, Z., Yang, Y., and Ren, T.-L. (2020). Wearable electronics based on 2D materials for human physiological information detection. *Small* 16: 1901124.

50 Zhang, Y., Gong, M., and Wan, P. (2021). MXene hydrogel for wearable electronics. *Matter* 4: 2655.

51 Ma, C., Ma, M.-G., Si, C. et al. (2021). Flexible MXene-based composites for wearable devices. *Advanced Functional Materials* 31: 2009524.

52 Zhang, Y.-Z., Lee, K.H., Anjum, D.H. et al. (2018). MXenes stretch hydrogel sensor performance to new limits. *Science Advances* 4: eaat0098.

53 Lei, Y., Zhao, W., Zhang, Y. et al. (2019). A MXene-based wearable biosensor system for high-performance in vitro perspiration analysis. *Small* 15: 1901190.

54 Ma, Y., Liu, N., Li, L. et al. (2017). A highly flexible and sensitive piezoresistive sensor based on MXene with greatly changed interlayer distances. *Nature Communications* 8: 1207.

55 Cai, Y., Shen, J., Yang, C.-W. et al. (2020). Mixed-dimensional MXene-hydrogel heterostructures for electronic skin sensors with ultrabroad working range. *Science Advances* 6: eabb5367.

56 Cheng, Y., Ma, Y., Li, L. et al. (2020). Bioinspired microspines for a high-performance spray $Ti_3C_2T_x$ MXene-based piezoresistive sensor. *ACS Nano* 14: 2145.

57 Gao, Y., Yan, C., Huang, H. et al. (2020). Microchannel-confined MXene based flexible piezoresistive multifunctional micro-force sensor. *Advanced Functional Materials* 30: 1909603.

58 Khunger, A., Kaur, N., Mishra, Y.K. et al. (2021). Perspective and prospects of 2D MXenes for smart biosensing. *Materials Letters* 304: 130656.

59 Bisri, S.Z., Shimizu, S., Nakano, M., and Iwasa, Y. (2017). Endeavor of iontronics: from fundamentals to applications of ion-controlled electronics. *Advanced Materials* 29: 16070541.

60 Hong, S., Zou, G., Kim, H. et al. (2020). Photothermoelectric response of $Ti_3C_2T_x$ MXene confined ion channels. *ACS Nano* 14: 9042.

61 Xu, B., Zhu, M., Zhang, W. et al. (2016). Ultrathin MXene-micropattern-based field-effect transistor for probing neural activity. *Advanced Materials* 28: 3333.

62 Xu, X., Wu, H., He, X. et al. (2020). Iontronics using V_2CT_x MXene-derived metal–organic framework solid electrolytes. *ACS Nano* 14: 9840.

63 Tu, S., Ming, F., Zhang, J. et al. (2019). MXene-derived ferroelectric crystals. *Advanced Materials* 31: 1806860.

64 Wu, H., Almalki, M., Xu, X. et al. (2019). MXene derived metal-organic frameworks. *Journal of the American Chemical Society* 141: 20037.

65 Kim, M.-K., Park, Y., Kim, I.-J., and Lee, J.-S. (2020). Emerging materials for neuromorphic devices and systems. *Iscience* 23: 101846.

66 Yu, F. and Zhu, L.Q. (2019). Ionotronic neuromorphic devices for bionic neural network applications. *Physica Status Solidi RRL: Rapid Research Letters* 13: 1800674.

67 Ielmini, D. and Ambrogio, S. (2019). Emerging neuromorphic devices. *Nanotechnology* 31: 092001.

68 (a) Yan, X., Wang, K., Zhao, J. et al. (2019). A new memristor with 2D $Ti_3C_2T_x$ MXene flakes as an artificial bio-synapse. *Small* 15: 1900107. (b) Wang, K., Chen, J., and Yan, X. (2021). MXene Ti_3C_2 memristor for neuromorphic behavior and decimal arithmetic operation applications. *Nano Energy* 79: 105453.

69 Lyu, B., Choi, Y., Jing, H. et al. (2020). 2D MXene–TiO_2 core–shell nanosheets as a data-storage medium in memory devices. *Advanced Materials* 32: 1907633.

70 Melianas, A., Kang, M.-A., VahidMohammadi, A. et al. (2022). High-speed ionic synaptic memory based on 2D titanium carbide MXene. *Advanced Functional Materials* 32: 2109970.

71 Sarycheva, A., Polemi, A., Liu, Y. et al. (2018). 2D titanium carbide (MXene) for wireless communication. *Science Advances* 4: eaau0920.

72 He, P., Cao, M.-S., Cao, W.-Q., and Yuan, J. (2021). Developing MXenes from wireless communication to electromagnetic attenuation. *Nano Micro Letters* 13: 115.

73 Chen, S.J., Kaufmann, T., Shepherd, R. et al. (2015). Highly efficient and flexible polymer ultra-wideband antenna. *IEEE Antennas and Wireless Propagation Letters* 14: 1207.

74 O'Carroll, D.M., Hofmann, C.E., and Atwater, H.A. (2010). Conjugated polymer/metal nanowire heterostructure plasmonic antennas. *Advanced Materials* 22: 1223.

75 (a) Aldrigo, M., Masotti, D., and Dragoman, M. (2017). Smart two-dimensional material-based time modulated array for RFID applications. *IET Microwaves, Antennas & Propagation* 11: 2267. (b) Gund, G.S., Jung, M.G., Shin, K.-Y., and Park, H.S. (2019). Two-dimensional metallic niobium diselenide for sub-micrometer-thin antennas in wireless communication systems. *ACS Nano* 13: 14114. (c) Wen, T., Zhang, W., Liu, S. et al. (2020). Steering valley-polarized emission of monolayer MoS_2 sandwiched in plasmonic antennas. *Science Advances* 6: eaao0019.

76 Wang, L., Liu, C., Chen, X. et al. (2017). Toward sensitive room-temperature broadband detection from infrared to terahertz with antenna-integrated black phosphorus photoconductor. *Advanced Functional Materials* 27: 1604414.

77 Perruisseau-Carrier, J. (2012). Graphene for antenna applications: opportunities and challenges from microwaves to THz. *Presented at 2012 Loughborough Antennas & Propagation Conference (LAPC)*, IEEE, Loughborough, UK, pp. 12–13 (November 2012).

78 Bengio, E.A., Senic, D., Taylor, L.W. et al. (2019). Carbon nanotube thin film patch antennas for wireless communications. *Applied Physics Letters* 114: 203102.

79 Vacirca, N.A., McDonough, J.K., Jost, K. et al. (2013). Onion-like carbon and carbon nanotube film antennas. *Applied Physics Letters* 103: 073301.

80 Han, M., Liu, Y., Rakhmanov, R. et al. (2021). Solution-processed $Ti_3C_2T_x$ MXene antennas for radio-frequency communication. *Advanced Materials* 33: 2003225.

81 Mathis, T.S., Maleski, K., Goad, A. et al. (2021). Modified MAX phase synthesis for environmentally stable and highly conductive Ti_3C_2 MXene. *ACS Nano* 15: 6420.

82 Hantanasirisakul, K., Zhao, M.-Q., Urbankowski, P. et al. (2016). Fabrication of $Ti_3C_2T_x$ MXene transparent thin films with tunable optoelectronic properties. *Advanced Electronic Materials* 2: 1600050.

24

MXene in Sensing Devices

Seon Joon Kim

Materials Architecturing Research Center, Korea Institute of Science and Technology, Seoul, Republic of Korea

24.1 Increasing Demand of Sensors

Sensing devices, or sensors, have become an inevitable part of the modern world, where various types of sensors are being used in multiple fields. Major categories of sensors include physical sensors, which measure a physical quantity (such as temperature); optical sensors such as pulse oximeters or proximity detectors; mechanical sensors such as strain gauges or pressure sensors; and chemical sensors such as humidity sensors, gas sensors, or biosensors. Each sensor can act independently or a few sensors can be integrated together to obtain comprehensive information about the surrounding environment. For example, a typical smartphone contains numerous sensors in a single device such as proximity sensors, light sensors, and temperature sensors. Also, a soldier wearing smart equipment may be equipped with chemical sensors, IR sensors, proximity sensors, which can provide the soldier with critical information regarding survival. Recently, autonomous devices are being intensively researched, with the most popularity in the automobile industry. Autonomous devices rely on the machine or vehicle to independently operate without the intervention of other machines or human activity. Therefore, the successful operation of autonomous devices heavily relies on rapidly and accurately obtaining nearby information and using the processed information to make the next action. While the central processors act as the brains of these devices, sensors act as the eyes, ears, and the skin, in which their performance is of paramount importance. Also, the emergence of new pathogens has shown devastating consequences globally, which has been recently demonstrated by the COVID-19 crisis. Due to the advancement in transportation

Transition Metal Carbides and Nitrides (MXenes) Handbook: Synthesis, Processing, Properties and Applications, First Edition. Edited by Chuanfang Zhang and Michael Naguib.
© 2024 John Wiley & Sons, Inc. Published 2024 by John Wiley & Sons, Inc.

and logistics, the current world has the highest degree of global connection. This allows the fast spreading of viruses through multiple channels and makes it increasingly difficult to contain them. While many efforts are being made to delay the spreading of viruses, it is highly important to develop a sensor that can accurately and rapidly detect target viruses at the same time.

Future devices are becoming increasingly sophisticated and enhanced properties of sensors are required to match the demanded performance. Nanomaterials have played a major role in this effort where new nanomaterials and new nanostructures are being researched to fabricate sensors with higher sensitivity, selectivity, and reliability.

24.2 Use of 2D Nanomaterials for Sensors

Nanomaterials of various dimensions and morphologies have been employed in developing sensors. For example, metal nanoparticles and metal nanowires embedded into polymer matrices have been employed in mechanical sensors, and metal oxide semiconductors have been widely used in chemical sensors. Since the discovery of graphene in 2004, two-dimensional (2D) materials have been of great interest in multidisciplinary research fields due to their novel and non-conventional properties that were not achievable using traditional materials. Especially, conducting 2D materials such as graphene and semiconducting 2D materials such as MoS_2 have been extensively studied as various types of sensors.

24.2.1 Merits of 2D Nanomaterials

2D materials have several physicochemical merits compared to conventional materials. First, 2D materials have a very high specific surface area, where graphene has one of the highest surface areas ($2630\,m^2g^{-1}$). This means that a large surface area can be efficiently utilized for sensing activities, which is highly advantageous in achieving high sensitivity and reducing the weight of the overall device. Second, 2D materials have highly tunable properties due to their high surface-to-volume ratio. Due to the atomically thin thickness, the surface comprises most of the bulk material. Therefore, a small change in the surface structure can result in a large shift in the physicochemical properties, which can lead to tunable sensing performances. Third, the sheet-like morphology of 2D materials allows them to be compatible with conventional thin film techniques, whereas 1D nanomaterials such as carbon nanotubes and metal nanowires are difficult to conformally coat into a dense film. Once 2D materials are assembled into films on various substrates, they can be further processed into complex sensor patterns using lithographic techniques.

In addition, 2D materials have advantages in terms of fabricating sensors. In the case of mechanical sensors such as strain gauges, materials with a high surface area have a low percolation threshold. This means that a conductive network can

be formed by adding a very small amount of filler. This allows the better retention of the matrix's (typically polymers) properties such as mechanical strength or flexibility. For the case of gas sensors, sensors based on 2D materials are known to be able to operate at room temperature. Typically, gas sensors fabricated from metal oxide semiconductors are operated at elevated temperatures between 100–300 °C. This requires a substantial amount of power, which can limit the operating lifetime of sensors in portable or wearable devices.

24.3 MXenes for Sensors

MXenes hold a special place in the world of 2D materials due to their unique and outstanding properties. MXenes have a dual-functional structure; The core of the molecular structure is constructed of transition metal carbides. This allows the fast transport of electrons, in which the highest electrical conductivity of MXenes reported so far is over 20 000 $S\,cm^{-1}$ [1]. At the same time, the surface structure is mainly constructed of transition metal oxides, hydroxides, or fluorides with a very high density of surface functional groups. Typically, the electrical conductivity and surface functionality are in a trade-off relation, where a larger density of surface functional groups will decrease the electrical conductivity. This relation can be easily observed in the case of graphene and graphene oxide [2]. However, MXenes simultaneously possess both properties, which make them very unique, allowing to reach areas that were not able to be covered with conventional materials. In general, this property is advantageous for sensors as well. The high density of surface functional groups provides high solubility in solvents. This allows MXenes to be processed using solution-based techniques that can be cost-efficiently applicable to flexible substrates toward wearable sensors. Also, a wide variety of elemental combinations can be utilized in modulating the sensing properties. So far, over 20 types of MXenes have been experimentally synthesized, with each composition having different electrical and physicochemical property.

In this chapter, the main factors and physicochemical mechanisms that influence the MXene sensing properties will be discussed. As many of the important factors overlap for various types of sensors, discussion on the common main factors will be done with an emphasis on chemical sensors, which are among the most heavily influenced by the MXene properties. Aside from the common factors, specific criteria for other types of sensors will be discussed separately.

24.3.1 Sensing Mechanism of MXenes

With the exception of certain specific sensors such as optical sensors, the sensing mechanism of sensors mainly relies on the change of electrical resistance (or electrical conductivity) when the sensing components are exposed to external stimuli

or a change in environment. Therefore, most sensors are entirely composed of or partially contain electrically conducting or semiconducting materials within the active sensing channel. In MXene sensors, MXenes typically act as the conductive component inside a sensing channel where MXenes can be either solely used or embedded into polymer matrices to fabricate sensors.

The sensing mechanism of MXene sensors depends on how the mechanical, physical, and chemical stimuli interact with and change the electrical conductivity of MXene. As MXene is a sheet-like 2D material, the electrical conductivity of MXene structures can be divided into two factors: intra-flake conductivity and inter-flake conductivity. Intra-flake conductivity is simply the electrical conducting behavior within a single MXene flake, typically determined by the in-plane flow of electrons through the basal plane. Inter-flake conductivity is the conductivity between adjacent MXene flakes, determined by the out-of-plane hopping of electrons. MXene-based sensors are typically designed by fabricating films or composite structures that are composed of multiple MXene flakes. Therefore, both intra-flake and inter-flake conductivity will contribute to the sensing properties of MXene sensors. As the sensing mechanism can greatly differ depending on which conduction path dominates the overall structure, it is important to understand how different MXene structures and processing methods influence the conducting behavior.

24.3.2 Factors of MXene Nanomaterials That Can Influence Sensing Properties

24.3.2.1 MXene Flake Morphology

The inter-flake conductivity of MXene flakes is largely influenced by the MXene flake morphology, which takes the form of either delaminated single flakes or multilayer (nondelaminated) flakes (Figure 24.1). When fabricating sensors based on MXene coatings or MXene films, the stacking behavior of delaminated and multilayer flakes must be taken into consideration. Delaminated flakes have a sheet-like 2D morphology, and flakes are able to be stacked into well-ordered structures using methods such as vacuum filtration, spin coating, and spray coating. In this case, the inter-flake conductivity will be relatively high as adjacent flakes will be in good contact. On the other hand, the morphology of multilayer flakes is irregular and does not have a planar morphology. When assembled into a film, the inter-flake conductivity will be poor due to irregular and poor electrical connections between adjacent flakes. Therefore, sensors fabricated from multilayer flakes may show high sensitivity (high resistance change), but the reproducibility and reversibility of sensing properties may be relatively poor.

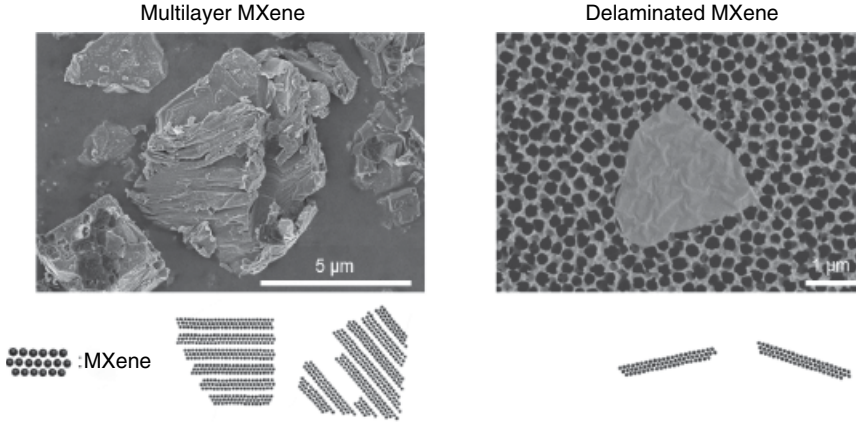


Figure 24.1 Scanning electron microscopy (SEM) images and schematic illustrations of multilayer and delaminated MXene.

24.3.2.2 Surface Functional Groups and Defects

Surface functional groups and defects can influence the intra-flake conductivity of MXenes. The surface of MXenes is comprised of various functional groups, with –OH, –O, –F, and –Cl being the major groups resulting from conventional etching methods. Theoretical results have shown that the type of functional groups influences the electronic band structure of MXene [3, 4], which can alter the electrical conductivity. More importantly, each functional group has a different affinity to various molecules. This is especially important for chemical sensors, where the compositional distribution of functional groups can modulate the selectivity of MXene sensors toward certain analytes. Furthermore, the type of surface functionalities will influence the solubility of MXenes in various solvents including water, polar organic solvents, and nonpolar organic solvents. This aspect is especially important when developing homogenous MXene composites. Atomic defects in the MXene structure also influence the intra-flake conductivity, where defects act as electron scattering points to increase the electrical resistance. At the same time, defects tend to act as strong adsorption sites, which can further influence the properties of chemical sensors.

24.3.2.3 Adsorbents and Intercalants

MXenes have a highly negatively charged surface where the zeta-potential of pristine MXenes at neutral pH is around −40 mV. This allows the spontaneous adsorption of positively charge species, such as metal ions or organic cations, on the surface of MXenes, which can influence the sensing properties. First, adsorbed species can block certain molecules from approaching and chemically interacting

with the MXene surface by preoccupying active sites. Second, when MXene flakes are assembled into films, adsorbed cations can act as intercalated spacers to change the interlayer spacing of MXenes within a film, leading to differences in inter-flake conductivity and interlayer conductivity.

24.3.2.4 Oxidation

MXenes are known to spontaneously oxidize in the presence of oxygen and humidity. For example, Ti-MXenes oxidize into TiO_2 [5] and Nb-MXenes oxidize into Nb_2O_5 [6]. As transition metal oxides are typically semiconductors, the oxidation of MXene results in a decreased intra-flake electrical conductivity. The inter-flake conductivity is also influenced by MXene oxidation. Metal oxide nanocrystals are known to form on the flake edges. Therefore, when individual flakes are assembled into a film, semiconductor-metal contacts (Schottky junctions) are formed instead of metal-metal contacts. Also, as the intrinsic crystal structure of metal oxides is three-dimensional, the formation of oxides will partially deform the intrinsic 2D morphology.

24.4 MXenes for Chemical Sensors

Chemical sensors refer to sensors that detect analytes through chemical interactions. Major devices that fall into this category include electrochemical sensors, gas sensors, ion sensors, and some types of humidity sensors. Among various types of chemical sensors, MXenes and their composites are being intensively researched in gas sensing applications. Especially, MXenes have been of wide interest due to their ability to detect volatile organic compounds (VOCs) and the ability to operate at room temperature, opening the possibility of developing wearable breath sensors [7–9]. Also, MXene chemical sensors are being developed to detect small molecules and bio-chemicals, where in this case, sensors typically operate in liquid environments. MXene chemical sensors share a similar sensing mechanism where gaseous analytes or analytes dissolved in solvents adsorb onto the surface functional groups, which then change the electrical conductivity or electrical current. In the case of electrochemical-type sensors, analytes can be also detected by observing the change in the redox curves. The analytes can also diffuse through the MXene surface and further adsorb on the inner sites of the MXene structure. Typically, a combination of these sensing mechanisms can be used to explain the selective sensing properties toward a specific analyte, as representatively shown in Figure 24.2.

24.4.1 Important Factors in Chemical Sensors

A chemical sensor's performance is largely evaluated by sensitivity and selectivity. The sensitivity is related to the ability of a sensor to detect a small amount of analytes, which is one of the most important aspects to consider in chemical sensors.

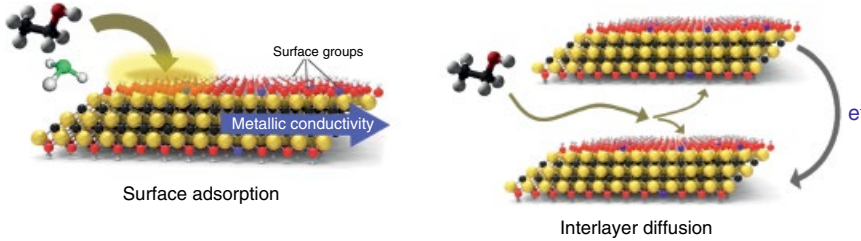


Figure 24.2 Schematic illustration of the chemical sensing mechanism of MXenes based on surface adsorption and intercalation.

For example, certain gases and toxins can be lethal to the human body at very low concentrations. The short-term exposure limit (STEL) during a 15-minute interval of acetone and propane is 1000 ppm. However, the STEL of toxic gases is much lower: 50 ppm for ammonia and carbon monoxide, 5 ppm for nitrogen dioxide, and 0.75 ppm for formaldehyde [10]. For certain biomaterials such as biotoxins, the LD50 (median lethal dose) can even be as low as a few ng kg^{-1}. In order to reliably detect such molecules at low concentrations, the sensing materials and sensors must have high sensitivity. Sensitivity in chemical sensors is typically measured by the change in electrical resistance or electrochemical current upon exposure to target analytes. If a sensor shows a relatively large change in conductivity, it can be said to have high sensitivity. Sensitivity can be also evaluated by the signal-to-noise (SNR) value, where sensors with high sensitivity show a large SNR value upon exposure to analytes. Furthermore, the sensitivity can be comparatively quantified using the limit of detection (LOD) value, which indicates the lowest analyte concentration that a sensor is able to detect. While the LOD can be determined experimentally, it can also be estimated by calculating the analyte concentration at which SNR = 3.

Selectivity is analyzed by comparing the sensitivity of a sensor toward a specific analyte to the sensitivity toward another analyte. Achieving a high selectivity is important as interfering species can make it very difficult to accurately detect the actual targeting species. Interferents can be any molecule besides the target analyte that exists within the same gaseous or liquid environment, where a typical interferent for gas sensors is water molecules (humidity). Where a quantitative criterion for determining the selectivity does not exist, a sensor can be considered to be selective when the response is exceptionally high toward a certain analyte.

MXenes have shown outstanding sensitivity and unique selectivity compared to other similar nanomaterials. When trying to achieve a high SNR value, the optimal case would be a combination of a high signal and low electrical noise. First, a high signal is achievable when target analytes bind strongly to the surface of the sensing material. In terms of surface chemistry, the presence of surface functional groups with high chemical activity typically leads to strong binding energies. The surface of MXenes is nearly completely covered with functional groups, in which

the grafting density is much higher compared to graphenes (reduced graphene oxide and graphene oxide). Such a high density of functionalities provides abundant sites for analytes to bind to the MXene surface. Second, a low noise is achievable when the sensing channel has a high electrical conductivity. As MXenes intrinsically have a high electrical conductivity (~20 000 S cm^{-1}), they show a low electrical noise that is a few orders lower than other 2D materials such as graphene and MoS_2. As MXenes simultaneously possess a high electrical conductivity and a high density of surface functional groups, they are one of the ideal candidates to achieve a high SNR sensor. This property is difficult to achieve with conventional materials.

24.4.2 Theoretical Estimations

24.4.2.1 DFT Calculations

Since the binding of analytes to the sensing surface occurs at a molecular level, density functional theory (DFT) calculations have been widely used to estimate the chemical sensing behavior. Especially, the binding energy of molecules to the MXene surface can be used to estimate the sensitivity and selectivity behavior. In one of the first reports on the DFT calculations of MXene chemical sensors, researchers have estimated that oxygen-terminated Ti_3C_2 MXene has a high selectivity toward ammonia compared to other gases such as hydrogen, CO, CO_2, NO_2, or CH_4 [11]. Also, the binding energy and charge transfer that results from ammonia adsorption on MXene was shown to be higher than those on phosphorene or MoS_2. Another study has shown that the strongly adsorbed ammonia molecules can be better released by injecting electrons into MXenes, which will be advantageous in achieving fast recovery [12].

24.4.2.2 Gaps Between Theory and Experiment

However, as DFT calculations are basically estimations, there are gaps between the estimated behavior and experimental behavior, which researchers should consider when referencing. First, discrepancies exist in the distribution of surface functional groups on MXene. In actual MXene samples, various types of functional groups are randomly distributed on the surface where the exact composition cannot be precisely controlled. On the other hand, MXenes covered with a single type of surface functional group are used to perform DFT calculations, as it is highly difficult to emulate the actual MXene surface. Second, the MXene laminate structure needs to be taken into consideration. Typically, in DFT calculations, the main parameter of interest is the interaction between analyte molecules with the MXene functional groups at their interface, and the remaining space aside from this interest is less considered. In the actual testing environment, the analytes approach the MXene surface from a free space only in the case of sensors

comprised of monolayer MXene films. In all other cases, many molecules would have to diffuse through MXene interlayers to reach the inner layers and bind to the surface functional groups. Therefore, as much as the binding energy of molecules plays a major role in determining the sensitivity and selectivity of MXene sensors, the inter-gallery diffusion of molecules through the MXene layers may also largely influence the sensing properties.

24.4.3 Guidelines and Considerations for Chemical Sensors

24.4.3.1 Guidelines and Considerations for MXene Synthesis in Chemical Sensors

The MXene synthesis method largely determines the flake morphology, surface functional group composition, and native surface adsorbents, thus inevitably influencing the chemical sensing properties.

The flake morphology can range from delaminated single sheets to non-delaminated multilayer flakes. In this manner, one needs to carefully choose the appropriate MXene synthesis method depending on the targeted MXene morphology. Figure 24.3 shows the representative methods that are currently used to synthesize MXenes. The earliest method to synthesize MXenes from MAX uses HF etchants. HF is able to selectively etch the Al atoms from the MAX phases to synthesize multilayer MXene flakes. As etching occurs with a high yield [13], the HF method is the go-to-method if your final target is applying multilayer MXene flakes for sensing applications. However, an additional step is required to delaminate these multilayer MXene flakes due to the lack of cationic intercalants. Here, organic intercalants such as tetramethylammonium hydroxide (TMAOH) or tetrabutylammonium hydroxide (TBAOH) are typically added to delaminate

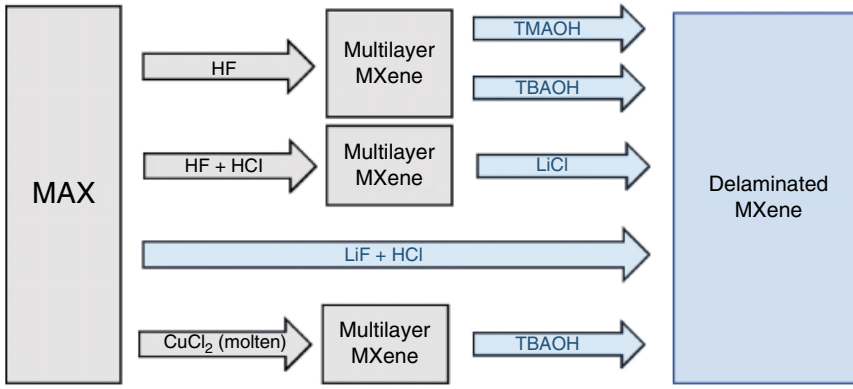


Figure 24.3 Representative etching and delamination methods to synthesize MXenes from MAX.

multilayer MXenes. The recently developed mixed acid etching route, which uses a mixture of HF and other acids such as HCl or H_2SO_4, shows similar behavior where etching the MAX phases with mixed acid etchants leads to multilayer MXenes. In this route, LiCl intercalants are used for further delamination. MXenes synthesized using this etching route is so far known to yield very high electrical conductivity. The LiF/HCl etching route (also known as the MILD method) is widely used to produce delaminated MXene flakes. While the *in-situ*-formed HF etches the Al atoms, the Li^+ ions simultaneously intercalate into the multilayer MXenes and spontaneously delaminate them into single sheets at neutral pH conditions. For the most widely studied Ti_3C_2 MXene, sensors have been fabricated from MXenes that have been synthesized using various routes. On the other hand, various types of etching routes are not yet widely applicable to other MXenes other than Ti_3C_2. Therefore, for other MXenes besides Ti_3C_2, sensors have been majorly fabricated from MXenes etched using the traditional HF etching route. For example, Zhao et al. fabricated acetone sensors using $V_4C_3T_x$ MXenes synthesized by etching V_4AlC_3 MAX phases using HF [14]. For other MXenes, further intercalation was done using TMAOH or TBAOH intercalants, which were used to fabricate sensors based on Mo_2C and V_2C MXenes [15, 16].

The chemical sensing behavior largely differs for sensors fabricated from multilayer and delaminated MXenes. For multilayer MXenes, multiple binding sites exist. As multilayer flakes cannot be assembled into a well-ordered film, the basal plane and edge sites are irregularly exposed to the outer surface. Therefore, target analytes will show various binding behavior depending on the adsorbing site, leading to different changes in intra-flake electrical conductivity. At the same time, target molecules will diffuse through the interlayer galleries to change the inter-flake conductivity of MXenes. Here, the intrinsic chemical structure of the interlayers and the interlayer spacing is largely dependent on the type of etchant. Also, the chemical structure can be modified by post-synthesis treatments using salts. [17] In terms of electrical conductivity, the base electrical resistance is relatively high due to the poor contact between adjacent MXene flakes, which also leads to delicate changes in conductivity upon external stimuli. Thus, chemical sensors fabricated from multilayer flakes tend to visually show a high resistance change. Figure 24.4 shows a study conducted on developing alkalized multilayer $Ti_3C_2T_x$ MXenes for gas sensors [18]. The gas sensor shows the highest response toward ammonia, where the absolute gas response is about 30% toward 100 ppm ammonia.

For delaminated MXenes, binding sites are relatively well defined as the basal planes are dominantly exposed. Here, the interlayer galleries can be largely influenced by the intercalants or post-treatment processes, as individual flakes are restacked into films. The base electrical resistance is low due to the good inter-flake contact throughout the film, which typically leads to a low absolute change

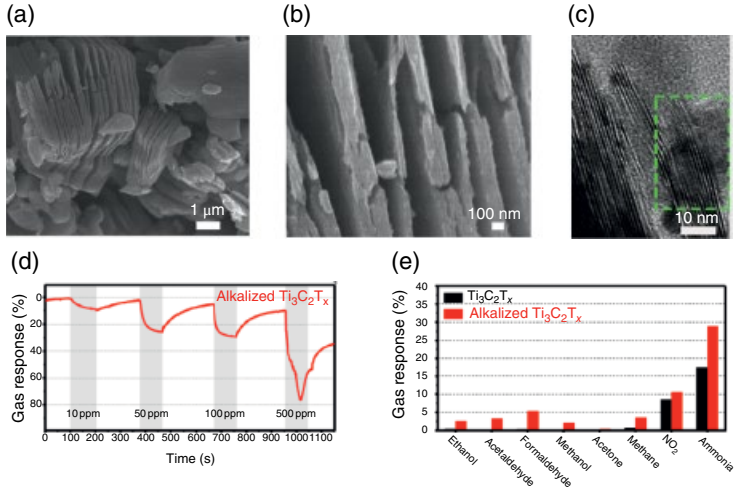


Figure 24.4 (a, b) Typical scanning electron microscopy (SEM) images and (c) TEM images of multilayer $Ti_3C_2T_x$. (d) Dynamic response-recovery curve of the devices based on alkalized multilayer $Ti_3C_2T_x$ to the NH_3 at the concentration of 10, 50, 100, and 500 ppm at 38% RH. (e) Response of the devices based on $Ti_3C_2T_x$ and alkalized $Ti_3C_2T_x$ to various test gases with a concentration of 100 ppm. *Source:* Yang et al. [18]/Reproduced from American Chemical Society.

in resistance. Figure 24.5 shows studies that have used delaminated $Ti_3C_2T_x$ (Figure 24.5a–c) and delaminated Mo_2CT_x (Figure 24.5d–g) for gas sensors [7, 15]. In both studies, sensors show a high selectivity toward VOCs, where the absolute gas response is relatively low, within a range of 1~5%. However, despite the lower absolute change in electrical resistance, the SNR values are high due to the low electrical noise.

Regarding the issues above, an important thing to consider is the phase purity of the MXene material. Some reports that claim to have used delaminated MXene sheets actually turn out to have used a mixture of multilayer and delaminated MXene flakes for their sensors. So, conducting a careful analysis using scanning electron microscopy (SEM) or X-ray diffraction to determine the etching/delamination purity is highly recommended prior to fabricating sensors to obtain reliable and reproducible results.

The MXene synthesis method also influences the surface functional groups. As estimated by DFT calculations, the surface functional group composition and distribution can largely influence behavior. Each synthesis route is known to yield a different composition of surface functional groups. MXenes synthesized by the HF route are known to yield multilayer MXenes with a large amount of fluorine functional groups [19]. But when the multilayer flakes are delaminated

using TMAOH, the resulting sheets tend to majorly have hydroxyl and oxygen groups [20]. On the other hand, the LiF/HCl route is known to yield MXenes with a larger amount of oxygen functional groups. Recently, novel synthesis methods using molten salts such as $CuCl_2$ or $ZnCl_2$ have been developed [21].

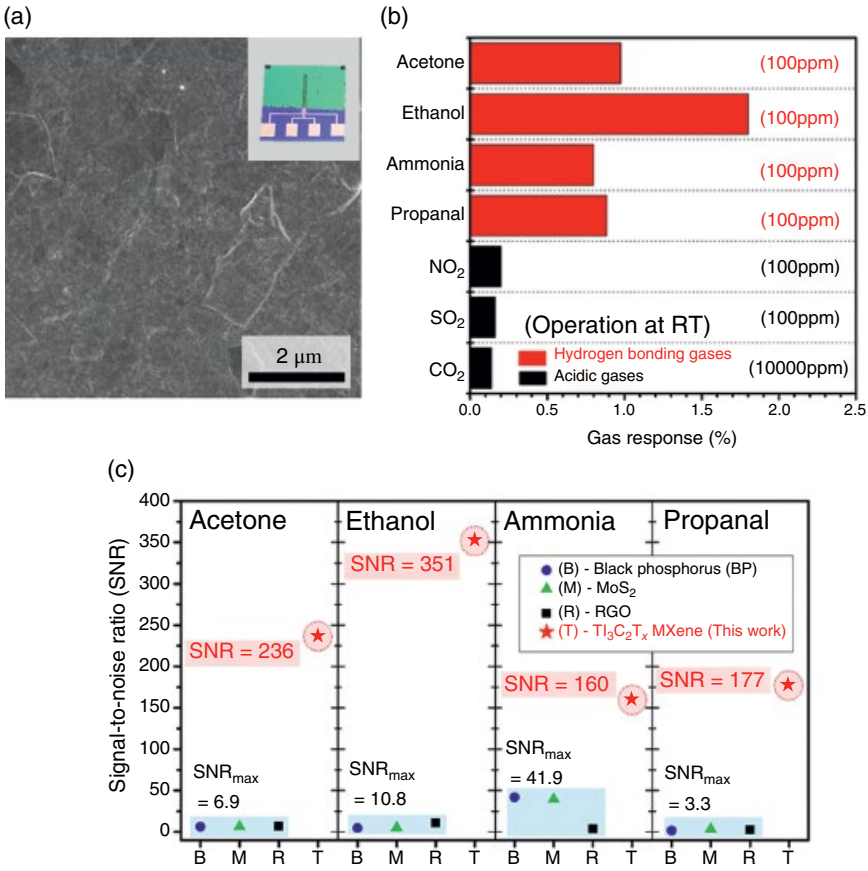


Figure 24.5 (a) Scanning electron microscopy (SEM) image of the $Ti_3C_2T_x$ sensor film surface and a photographic image of a film sensor (inset). (b) Maximal resistance change upon exposure to 100 ppm of acetone, ethanol, ammonia, propanal, NO_2, SO_2, and 10 000 ppm of CO_2 at room temperature. (c) Maximal SNR values of sensors upon exposure to 100 ppm of acetone, ethanol, ammonia, and propanal. *Source:* Kim et al. [7]/ Reproduced from American Chemical Society. (d) SEM images of Mo_2CT_x free-standing film. (e, f) Transient response of Mo_2CT_x to different VOCs for two minutes exposure: (e) toluene and (f) benzene. (g) Response under exposure to toluene, benzene, ethanol, methanol, and acetone at 140 ppm. *Source:* Guo et al. [15]/Reproduced from American Chemical Society.

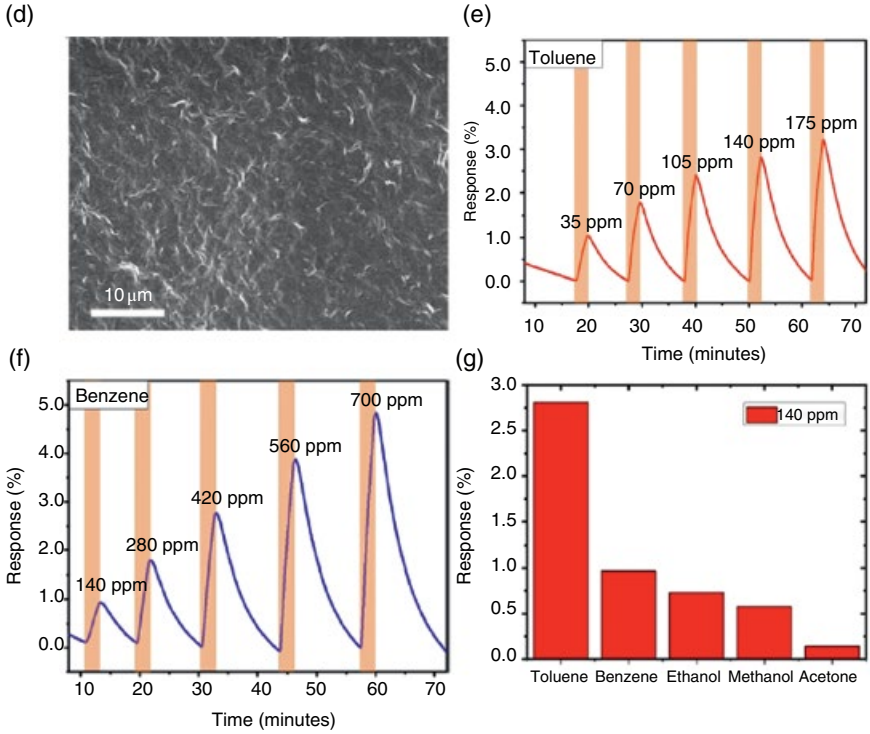


Figure 24.5 (Continued)

Here, the resulting MXenes are known to be chlorine-terminated. Kamysbayev et al. also reported on a method to synthesize Br-terminated MXenes using Lewis acidic $CdBr_2$, which could be further transformed into Te- or S-terminated MXenes [22].

Aside from the synthesis methods themselves, post-treatment methods can further modify the MXene surface functional groups. Studies have shown that treating MXenes using strong bases such as NaOH or KOH can alkalize the MXene surface, partially transforming the surface functional groups to hydroxyl groups. Zhang et al. have shown that such alkalization can largely change the gas-sensing performance of MXenes, where alkalized MXenes showed a higher response toward NO_2 and humidity [23]. A popular method to tune the surface chemistry is the chemical functionalization of MXenes using organic ligand where various ligands have been grafted on the MXene surface. The outermost chemical moieties can alter the binding energy of target analytes toward MXenes and modulate the interlayer structure. For example, Chen et al. reported on gas sensors fabricated from Ti_3C_2 MXene functionalized with chlorine- or fluorine-terminated

silanes [24]. Here, they show that silane-terminated MXenes show a higher gas response toward various gases due to increased interlayer spacing, with a higher stability in humid environments. In another study, fluoroalkyl silane-functionalized Ti_3C_2 MXene was used to develop a skin-attachable and wearable electrochemical pH sensor for real-time sweat detection (Figure 24.6) [25]. Due to the hydrophobicity of fluoroalkyl silanes, the sensors showed high environmental stability in liquid environments. Also, among various cations such as H^+, Na^+, K^+, Mg^{2+}, and Ca^{2+}, functionalized MXenes only showed a response toward changes in pH, demonstrating their good selectivity in the presence of interfering species.

24.4.3.2 Guidelines and Considerations for MXene Processing in Chemical Sensors

In order to fabricate MXene-based sensors, synthesized MXene flakes need to be assembled onto sensing electrodes and substrates using multiple processing methods. In this section, the possible influence of these processing factors on sensing properties will be discussed.

Sonication is often used to create a homogeneous solution of purely MXenes or MXene mixtures in various solutions prior to sensor fabrication. While sonication can be very effective in mixing, elongated sonication durations can break the MXene flakes to decrease the average sheet size. This exposes more edge sites with stronger adsorption toward analytes, which can alter the chemical sensing properties. For example, Kim et al. have shown that MXene flakes with a smaller size show a 10 times higher gas sensing response compared to larger flakes [26]. Therefore, sonication conditions should be carefully controlled to create reproducible sensing results. The pH of a solution can also manipulate the MXene flake dimensions. While basic solutions can alter the surface functional groups, acidic conditions coagulate individual MXene flakes into aggregates as the hydronium ion neutralizes the negative surface charge of MXenes.

When transforming MXene solutions into solid MXene films, heat is typically applied along the way to remove residual solvents. Solvent molecules are intercalated (or trapped) in between MXene interlayers, whereas pristine MXenes are known to largely harbor water molecules due to their hydrophilic surface. Depending on the degree of solvent intercalation, the interlayer spacing and diffusivity will differ, which will then influence the diffusion of analyte molecules into the inner MXene layers. Therefore, the annealing temperature can influence the sensing performance. For example, annealing MXene films at temperatures around 180~200 °C in a vacuum or inert atmosphere will better remove interlayer water, while annealing films at lower temperatures around 60~80 °C will retain more interlayer water. As the change inter-flake conductivity is a major factor determining the chemical sensing properties, understanding the interlayer chemical structure is critical in developing MXene chemical sensors. On the other hand, when the film processing or annealing occurs in ambient or wet

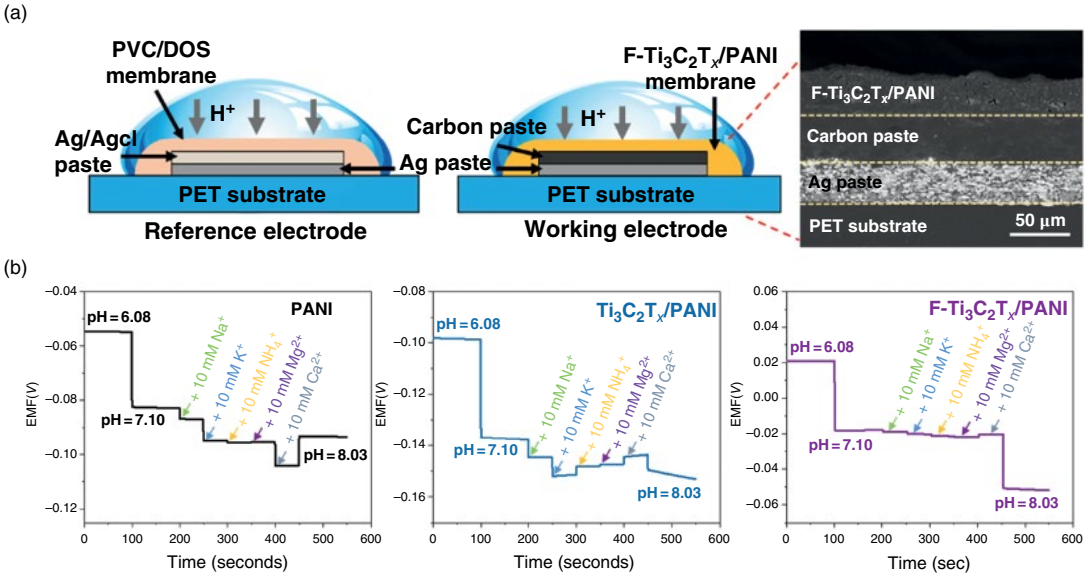


Figure 24.6 (a) Schematic illustration of pH sensor electrodes based on functionalized MXene. (b) Selectivity evaluation of MXene-based sensors by continually adding different interfering ions in the 10 mM concentration. *Source:* Chen et al. [25]/Reproduced from American Chemical Society.

environments, oxidation must be taken into consideration when applying heat. Where the formation of oxides is not always a disadvantage, it will definitely influence the sensing properties. For example, a previous study showed that the sensitivity toward gases greatly increases when Ti_3C_2 MXene is mildly oxidized to create a TiO_2/Ti_3C_2 Schottky junction [27].

24.4.3.3 Guidelines for Sensor Fabrication and Testing Conditions

The majority of chemical sensors exist as solid-state sensors where the sensing material is deposited in between gold or platinum electrodes to act as conducting or semiconducting channels. Thus, the fabrication of MXene sensors requires the coating MXene flakes or films onto sensing electrodes that are printed on rigid or flexible substrates. The most widely used coating method is drop coating due to their simplicity and versatility where diluted MXene solutions are drop-casted onto substrates deposited with Pt or Au electrodes. While this method is rapid and applicable to various sensing substrates, careful control of coating parameters is required to obtain a uniform coating. In other early studies, Kim et al. and Koh et al. prepared thin MXene films by vacuum filtration on anodized aluminum oxide (AAO) membranes, which were transferred onto sensing electrodes by dissolving AAO [7, 8]. Interestingly, this method spontaneously intercalates Na ions into the MXene interlayers, which enhances the gas sensing performance and selectivity toward VOCs at room temperature. In another study, self-assembly methods were employed to fabricate nanometer-scale MXene films, in which films could be easily transferred onto arbitrary substrates. A previous reported that when using acids as the assembling agent, a compactly stacked MXene film is fabricated [26]. The compact stacking led to a smaller interlayer spacing, which can impede the diffusion of target molecules into the inner MXene layers. This will decrease the effective adsorption area, which decreases the gas response. A follow-up study further demonstrated that when using metal ions as the assembling agent instead of acids, MXene thin film with an enlarged interlayer spacing was obtained, which led to an enhanced gas sensing response toward ammonia [9].

Once MXene sensors are prepared on various substrates, they can be either placed inside a gas-flowing chamber for gas sensors or immersed in water for ion sensors, etc. In all cases, the influence of the testing conditions on the reliability and stability of MXene sensors must be considered. For gas sensors, the testing atmosphere is usually nitrogen or air where the testing temperature ranges from room temperature to 300 °C. Whereas gas sensors based on semiconducting metal oxides are optimized at high-temperature testing conditions, room-temperature operation is preferred for MXenes due to the possibility of oxidation. While oxidation could be relatively mild in a nitrogen atmosphere, testing sensors at elevated

temperatures in air atmosphere have a greater chance of oxidizing MXene films, changing the sensing properties over time. For sensors operating in liquids such as ion sensors or some electrochemical sensors, the degradation or deformation of MXene sensors may be an issue in addition to oxidation. MXenes in their pristine form are highly hydrophilic, and an elongated period of immersion in water can swell the MXene interlayers, detaching MXene films from the surface. Therefore, it is important to efficiently bind the MXene flakes to the sensing electrodes using appropriate binders to guarantee stable operation of the sensor.

24.4.4 Considerations in the Interpretation of Sensing Data

The sensing mechanism of MXene-based sensors is largely dependent on the electrical or electrochemical charge transfer between analyte molecules and MXene. Therefore, the electronic structure of MXenes will play a major role in determining the chemical sensing properties, and the interpretation of sensing data should consider this aspect. Especially, the tuning of electronic structure and the band structure of nanomaterials have been important in gas sensors, as semiconducting charge transfer behavior is used to modulate sensing performance. Experimentally synthesized MXenes in their pristine state are known to be metallic. Theoretically, semiconducting MXenes with a small bandgap are known to exist in certain MXenes with a single type of surface functional group, but these MXenes are very difficult to realize. However, extrinsic factors may provide MXene-based sensors with semiconducting-like properties. For example, the adsorption of organic molecules on the surface may manipulate the charge transfer properties [28]. Also, the metal oxides formed on MXenes as a result of oxidation are mostly semiconducting, in which a Schottky function can form at the oxide/MXene interface.

24.4.5 Summary

Many physicochemical properties of MXenes can delicately influence the properties and sensing performance of MXene chemical sensors, and the discussed factors above must be carefully considered for this type of application. Thus, constructing a library of MXene sensing properties depending on the MXene atomic composition, surface functional groups, and intercalated structure would be very helpful in designing appropriate structures for target-oriented MXene chemical sensors. Nevertheless, MXenes comprehensively show unique and interesting chemical sensing properties that are highly difficult to obtain with other nanomaterials, and are expected to be continuously researched with great interest.

24.5 MXenes for Mechanical (or Tactile) Sensors

Mechanical sensors are sensors that detect mechanical stimuli. Major examples that fall into this category include touch sensors, pressure sensors, and strain gauges, in which a majority of them fall into the category of tactile sensors. Compared to chemical sensors, MXenes are relatively less delicate in tactile sensors. This is because while the surface chemistry and related reactions play a major role in chemical sensors, the physical morphology of MXene flakes and their assembling behavior play a dominant role in mechanical sensors. Therefore, MXenes do not necessarily have to be exposed to the outer environment, but can be embedded into other materials such as polymers. This feature makes it easier to practically apply MXenes to sensing applications.

MXene tactile sensors share a similar sensing mechanism where the MXene flake or the inter-flake network is disrupted by the application of mechanical force. First, the mechanical forces can directly stretch or compress the MXene flake in lateral directions or disrupt the lattice structure in the normal direction. As such changes directly manipulate the molecular bonds, the change in electrical resistance can be high. However, the contribution of this sensing mechanism is rather limited in most sensors. Second, mechanical forces can stretch or compress the composite network in which MXene is embedded to alter the inter-flake distance of individual MXene flakes. Here, the electrical resistance of the overall composite will increase as the MXene flakes are increasingly separated, where the resistance can abruptly increase when the percolation network is lost.

24.5.1 Important Factors in Mechanical Sensors

A tactile sensor's performance is largely evaluated by the sensitivity and sensing range. The sensitivity indicates the sensor's ability to detect very small stimuli. Developing sensors with high sensitivity is especially an important factor in touch sensors that are used to copy human motion as it allows delicate interaction with the environment. Sensitivity is typically evaluated by the relative change in electrical resistance compared to the change in mechanical force/stimulus. Thus, a highly sensitive sensor would show a significant change in electrical resistance when a very small force is applied. In strain gauges, this factor is typically quantified through the gauge factor, which is defined as $(\Delta R/R)/\varepsilon$.

The sensing range is another important factor in developing high-performance tactile sensors. When a sensor has a wide sensing range, it means that the sensing material does not show severe deformation or changes in morphology until a large force is applied. Thus, the electrical resistance will continue to gradually

change reversibly across a wide range. On the other hand, the small change in morphology may simultaneously lead to a low sensitivity. Therefore, the sensitivity and sensing range is typically in a trade-off relation; when the sensitivity is high, the sensing range will be narrow and vice-versa. Due to this feature, it is important to design sensors so that they will show high sensitivity in the targeted sensing range for sensors that do not necessarily have to be wide-range sensing. Also, designing heterogeneous or hierarchical structures can be used to achieve sensors with both high sensitivity and wide sensing range.

Aside from the quantitative sensing performance, the damage effect is another important factor to consider as the application of mechanical force will inevitably deform the sensing structure. In a representative sensing structure of MXene flakes dispersed in a polymer matrix, significant deformation can mainly occur at three different regions. First, individual MXene flakes can be torn or punctured upon the application of strong or acute force. In this case, it is nearly impossible to stitch the MXene flake into its original whole shape, leading to a permanently decreased electrical conductivity. Second, mechanical forces can cause plastic deformation of certain types of polymers, which will permanently change the overall morphology. Third, due to the two reasons above or other additional phenomena, the binding between MXene flakes and the matrix can be deteriorated after applying mechanical force. Thus, it is important to carefully design the composite structure and find a safe working range to avoid permanent damage effects and preserve long-term stability and reliability.

24.5.2 Comparisons with Other 2D Materials

As the most widely used 2D material for tactile sensors is graphene, the features of MXene in comparison to graphene will be discussed. First, MXene has a very high solubility in its pristine form with the highest solubility in water. This property has allowed MXenes to be easily mixed with hydrophilic polymers such as poly(vinyl alcohol) (PVA) and poly(acrylic acid). While graphene and its derivatives have also been successfully dissolved in various solvents using surface functionalization, the related processes tend to decrease the original electrical conductivity. Second, the atomic thickness of MXenes is larger than graphene, where the representative $Ti_3C_2T_x$ MXene has 7~9 atomic layers in a single delaminated sheet. Thus, the MXene sheets are relatively stiff compared to graphene, which can influence the sensing properties. Also due to this feature, the percolation threshold (in terms of weight percentage) of MXene composites is higher than that of graphene composites, as the molecular weight of a MXene unit cell is much higher.

24.5.3 Guidelines and Considerations for Mechanical Sensors

24.5.3.1 Guidelines and Considerations for MXene Synthesis in Mechanical Sensors

As most sensors take the form of MXene sheets embedded into polymeric matrices to create a percolated network, delaminated MXenes are highly desired in fabricating mechanical sensors. Therefore, MXenes synthesized using the LiF/HCl route or those delaminated using TMAOH/TBAOH intercalants will be good choices. Although the fabrication of composites can also be partially achieved using few-layer or multilayer MXene flakes, the reversibility would be bad due to poor contact and the percolation threshold would be very high. Another thing to consider would be the surface post-functionalization of MXene using organic ligands as a large number of polymers do not dissolve in water. If the MXene flakes can be further functionalized to dissolve in various polar and nonpolar solvents, MXenes can be efficiently embedded into a wide range of polymers.

The lateral sheet dimensions of the synthesized MXene sheets should also be taken into consideration. In a filler-matrix network, the feature dimensions of the filler and matrix should be similar in order to better form a homogeneous composite. For example, if the MXene sheets are significantly larger than the fibrous structures of the matrix, the movement of the MXene flakes and the backbone will not be synchronized, which will lead to a non-uniform sensing behavior. On the other hand, if the MXene flakes have similar dimensions with the structures within the matrix, flakes can be well-deposited on the backbone. Regarding this issue, the size of MXene sheets can be decreased using ultrasonication, where the sheet dimensions can be roughly controlled by sonication duration.

24.5.3.2 Guidelines and Considerations for Sensor Fabrication

MXenes synthesized using conventional methods are hydrophilic and thus can be uniformly dispersed into aqueous solutions. Therefore, in order to uniformly disperse MXenes in a polymer matrix, it is important to consider using hydrophilic polymers when mixing with as-synthesized MXene solutions. In an early study, Zhang et al. demonstrated an MXene sensor that exhibits a remarkable stretchability of more than 3400% with a gauge factor of 25 [29]. Here, MXene was mixed with "crystal clay," which is a commercial hydrogel that is mainly composed of PVA. MXene hydrogels were fabricated by simply spreading the MXene paste onto the pristine crystal clay, which was then rolled into a ball and flattened by hand, and the process was repeatedly done until a uniform mixture was obtained. Using this sensor, both the direction and speed of motions on the hydrogel surface could be conveniently detected without the need for complex circuitry.

As MXene sensors undergo multiple cycles of morphological changes, retaining the original structure and preventing the detachment of MXenes flakes from the

matrix is critically important. Therefore, it is important to consider methods to enhance the physical or chemical bonding of MXenes within the composite matrix. A widely used strategy is utilizing the hydrogen bonding of the hydroxyl functional groups of MXene. For example, Cai et al. have demonstrated a heterogeneous configuration where MXene was coupled with polyacrylamides through nano-bridging layers of polypyrrole nanowires (Figure 24.7) [30]. Such a structure allows high toughness and low hysteresis, along with a sensor with a wide working range and fast responsiveness.

Aside from using hydrogen bonding, several studies have additionally utilized positively charged species to better bind the negatively charged MXene flakes to the backbone. First, positively charged species can be treated onto sensing substrates to bind the MXenes in film-type sensors. For example, An et al. showed that by coating a positively charged polyelectrolyte (PDAC) onto various substrates, MXenes can be efficiently coated using LbL techniques to show surface agnostic properties (Figure 24.8) [31]. The authors further show that the MXene-PDAC composite film can be used as sensors to detect stretching and bending behavior to be utilized in human motion sensors.

Second, positively charged species can be directly incorporated into the composite in bulk-type composites. For example, Shi et al. fabricated a bioinspired ultrasensitive and stretchable MXene-based strain sensor using a "brick-and-mortar" architecture (Figure 24.9) [32]. Here, the MXene sheets were bound together through hydrogen bonding with the PDA backbone and coordination bonding with Ni ions. The resulting composite showed a larger sensing range and higher sensitivity due to the hierarchical structure.

Finally, to further develop a strategy to enhance the long-term reliable use of MXene sensors, several studies have focused on preventing the plastic deformation of the polymeric matrix by developing self-healable polymers. For example, Liao et al. fabricated an MXene-based organohydrogel sensors where MXene flakes were mixed with polyacrylamide and PVA. Similar to the example above, MXene flakes were firmly attached to the polymer backbone through hydrogen bonding. In this study, tetrahydroxyl borate ions were further added to allow the self-healing of disconnected networks [33]. In another study, MXene-AgNW composite sensing layers were sandwiched between poly(urethane acrylate) self-healing films, in which sensors were able to detect various types of human motion [34].

24.5.4 Summary

The mechanical sensing properties of MXene-based structures have been relatively well-defined among many applications as similar architectures have been previously developed using other conductive nanomaterials such as carbon nanotubes or graphene. At the same time, MXene surfaces are highly functional

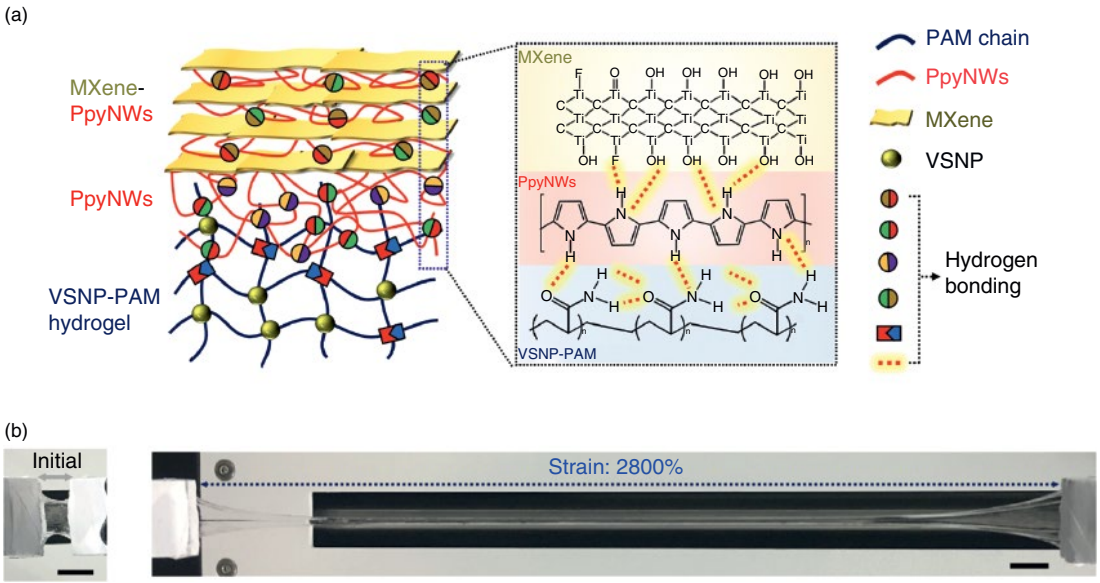


Figure 24.7 (a) Schematic of the MXene-PpyNW-PAM composite in a layer-by-layer fashion. (b) Initial and elongated state of the composite that shows excellent stretchability. *Source:* Cai et al. [30]/Reproduced from American Association for the Advancement of Science - AAAS/CC BY-NC 4.0.

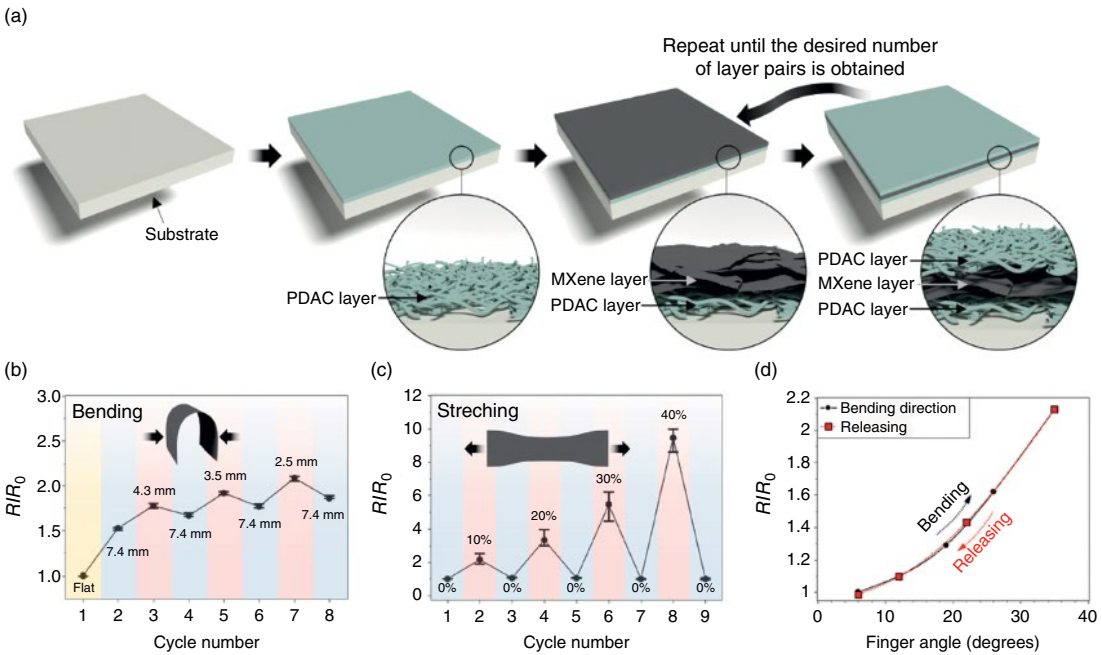


Figure 24.8 (a) Schematic of the PDAC/MXene LbL assembly process. (b) Normalized resistance (R/R_0) vs. bending radius for 20-layer-pair MXene multilayer on PET and (c) vs. strain for 20-layer-pair MXene multilayer on PDMS. (d) Response to finger motion. *Source:* Reprinted with permission from An et al. [31] by CC BY-NC 4.0.

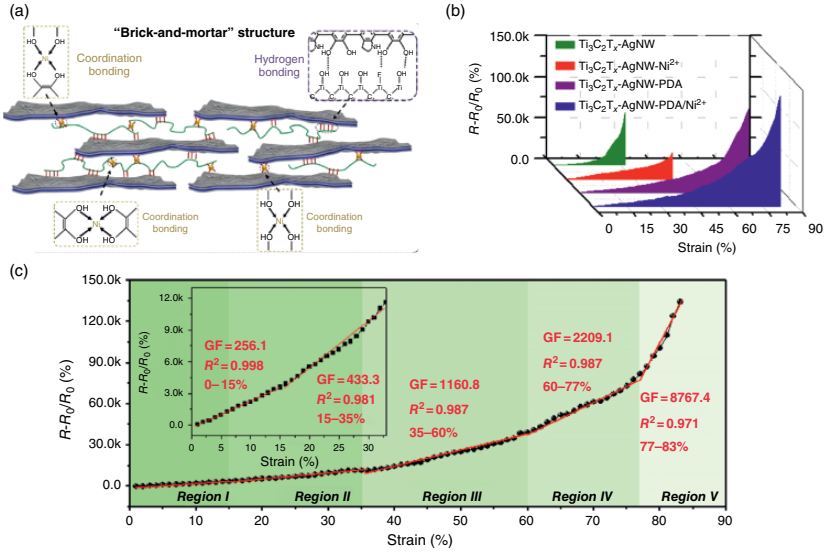


Figure 24.9 (a) Schematic illustration of the $Ti_3C_2T_x$-AgNW-PDA/Ni^{2+} sensor based on the "brick-and-mortar" architecture. (b) Typical relative resistance change as a function of applied strain curves for the $Ti_3C_2T_x$-AgNW, $Ti_3C_2T_x$-AgNW-PDA, $Ti_3C_2T_x$-AgNW-Ni^{2+}, and $Ti_3C_2T_x$-AgNW-PDA/Ni^{2+} sensors. (c) Detailed gauge factor and linear behavior of the $Ti_3C_2T_x$-AgNW-PDA/Ni^{2+} strain sensor. Regions I, II, III, IV, and V represent the fitting lines for strains ranging from 0% to 15% (with a linearity of 0.998), 15% to 35% (with a linearity of 0.981), 35% to 60% (with a linearity of 0.987), 60% to 77% (with a linearity of 0.987), and 77% to 83% (with a linearity of 0.971), respectively (GF = gauge factor). *Source:* Reprinted with permission from Shi et al. [32]. Copyright 2019 American Chemical Society.

compared to conventional materials, which gives a wide range of control regarding the filler-matrix interaction when fabricating sensors. Thus, designing the chemical structure of MXene surfaces and elaborately tailoring the interface and hierarchical structure within the MXene-polymer composite would be of paramount importance in developing high-performance mechanical sensors.

24.6 Conclusions and Outlook

The advancement of MXene synthesis techniques over the past few years has enabled a wide control over the MXene properties. Furthermore, multiple studies on sensors based on MXenes other than Ti_3C_2 have been reported to give more insight toward utilizing MXenes in various sensors. Whereas groundbreaking results are continuously expected in this field, it is also important to consider the practical aspects of applying MXenes to sensing devices. Despite a large amount of publications, there still is a lack of standardized methods to fabricate reliable MXene sensors, in which the sensing performances largely vary between various research groups. To achieve this, an accurate analysis of the MXene physicochemical properties should be preceded. Also, enhancing the large-scale processing, long-term environmental stability of MXenes would greatly improve the feasibility of employing MXenes in sensing devices in an effort to move from fundamental studies toward practical applications.

References

1 Zeraati, A.S., Mirkhani, S.A., Sun, P. et al. (2021). Improved synthesis of $Ti_3C_2T_x$ MXenes resulting in exceptional electrical conductivity, high synthesis yield, and enhanced capacitance. *Nanoscale* 13: 3572–2580.

2 Morimoto, N., Kubo, T., and Nishina, Y. (2016). Tailoring the oxygen content of graphite and reduced graphene oxide for specific applications. *Scientific Reports* 6: 21715.

3 Liu, Y., Xiao, H., and Goddard, W.A. (2016). Schottky-barrier-free contacts with two-dimensional semiconductors by surface-engineered MXenes. *Journal of the American Chemical Society* 138: 15853–15856.

4 Schultz, T., Frey, N.C., Hantanasirisakul, K. et al. (2019). Surface termination dependent work function and electronic properties of $Ti_3C_2T_x$ MXene. *Chemistry of Materials* 31: 6590–6597.

5 Zhang, C.J., Pinilla, S., McEvoy, N. et al. (2017). Oxidation stability of colloidal two-dimensional titanium carbides (MXenes). *Chemistry of Materials* 29: 4848–4856.

6 Zhang, C.J., Kim, S.J., Ghidiu, M. et al. (2016). Layered orthorhombic Nb_2O_5@$Nb_4C_3T_x$ and TiO_2@$Ti_3C_2T_x$ hierarchical composites for high performance Li-ion batteries. *Advanced Functional Materials* 26: 4143–4151.

7 Kim, S.J., Koh, H.-J., Ren, C.E. et al. (2018). Metallic $Ti_3C_2T_x$ MXene gas sensors with ultrahigh signal-to-noise ratio. *ACS Nano* 12: 986–993.

8 Koh, H.J., Kim, S.J., Maleski, K. et al. (2019). Enhanced selectivity of MXene gas sensors through metal ion intercalation: in situ X-ray diffraction study. *ACS Sensors* 4: 1365–1372.

9 Kim, S., Lee, J., Doo, S. et al. (2021). Metal-ion-intercalated MXene nanosheet films for NH_3 gas detection. *ACS Applied Nano Materials* 4: 14249–14257.

10 Jang, J.-S., Winter, L.R., Kim, C. et al. (2021). Selective and sensitive environmental gas sensors enabled by membrane overlayers. *Trends in Chemistry* 3: 547–560.

11 Yu, X.-F., Li, Y.-C., Cheng, J.B. et al. (2015). Monolayer Ti_2CO_2: a promising candidate for NH_3 sensor or capturer with high sensitivity and selectivity. *ACS Applied Materials & Interfaces* 7: 13707–13713.

12 Xiao, B., Li, Y.-C., Yu, X.-F., and Cheng, J.-B. (2016). MXenes: reusable materials for NH_3 sensor or capturer by controlling the charge injection. *Sensors and Actuators B* 235: 103–109.

13 Kim, Y.-J., Kim, S.J., Seo, D. et al. (2021). Etching mechanism of monoatomic aluminum layers during MXene synthesis. *Chemistry of Materials* 33: 6346–6355.

14 Zhao, W.-N., Yun, N., Dai, Z.-H., and Li, Y.-F. (2020). A high-performance trace level acetone sensor using an indispensable $V_4C_3T_x$ MXene. *RSC Advances* 10: 1261–1270.

15 Guo, W., Surya, S.G., Babar, V. et al. (2020). Selective toluene detection with Mo_2CT_x MXene at room temperature. *ACS Applied Materials & Interfaces* 12: 57218–57227.

16 Wu, M., An, Y., Yang, R. et al. (2021). V_2CT_x and $Ti_3C_2T_x$ MXenes nanosheets for gas sensing. *ACS Applied Nano Materials* 4: 6257–6268.

17 Ghidiu, M., Halim, J., Kota, S. et al. (2016). Ion-exchange and cation solvation reactions in Ti_3C_2 MXene. *Chemistry of Materials* 28: 3507–3514.

18 Yang, Z., Liu, A., Wang, C. et al. (2019). Improvement of gas and humidity sensing properties of organ-like MXene by alkaline treatment. *ACS Sensors* 4: 1261–1269.

19 Hope, M.A., Forse, A.C., Griffith, K.J. et al. (2016). NMR reveals the surface functionalization of Ti_3C_2 MXene. *Physical Chemistry Chemical Physics* 18: 5099–5102.

20 Hart, J.L., Hantanasirisakul, K., Lang, A.C. et al. (2019). Control of MXenes' electronic properties through termination and intercalation. *Nature Communications* 10: 522.

21 Li, Y., Shao, H., Lin, Z. et al. (2020). A general Lewis acidic etching route for preparing MXenes with enhanced electrochemical performance in non-aqueous electrolyte. *Nature Materials* 19: 894–899.

22 Kamysbayev, V., Filatov, A.S., Hu, H. et al. (2020). Covalent surface modifications and superconductivity of two-dimensional metal carbide MXenes. *Science* 369: 979–983.

23 Zhang, Y., Jiang, Y., Duan, Z. et al. (2021). Highly sensitive and selective NO_2 sensor of alkalized V_2CT_x MXene driven by interlayer swelling. *Sensors and Actuators B* 344: 130150.

24 Chen, W.Y., Lai, S.-N., Yen, C.-C. et al. (2020). Surface functionalization of $Ti_3C_2T_x$ MXene with highly reliable superhydrophobic protection for volatile organic compounds sensing. *ACS Nano* 14: 11490–11501.

25 Chen, L., Chen, F., Liu, G. et al. (2022). Superhydrophobic functionalized $Ti_3C_2T_x$ MXene-based skin-attachable and wearable electrochemical pH sensor for real-time sweat detection. *Analytical Chemistry* 94: 7319–7328.

26 Kim, S.J., Choi, J., Maleski, K. et al. (2019). Interfacial assembly of ultrathin, functional MXene films. *ACS Applied Materials & Interfaces* 11: 32320–32327.

27 Choi, J., Kim, Y.-J., Cho, S.-Y. et al. (2020). In situ formation of multiple Schottky barriers in a Ti_3C_2 MXene film and its application in highly sensitive gas sensors. *Advanced Functional Materials* 30: 2003998.

28 Choi, J., Chacon, B., Park, H. et al. (2022). N-p-conductor transition of gas sensing behaviors in Mo_2CT_x MXene. *ACS Sensors* https://doi.org/10.1021/acssensors.2c00658.

29 Zhang, Y.-Z., Lee, K.H., Anjum, D.H. et al. (2018). MXenes stretch hydrogel sensor performance to new limits. *Science Advances* 4: eaat 0098.

30 Cai, Y., Shen, J., Yang, C.-W. et al. (2020). Mixed-dimensional MXene-hydrogel heterostructures for electronic skin sensors with ultrabroad working range. *Science Advances* 6: eabb5367.

31 An, H., Habib, T., Shah, S. et al. (2018). Surface-agnostic highly stretchable and bendable conductive MXene multilayers. *Science Advances* 4: eaaq0118.

32 Shi, X., Wang, H., Xie, X. et al. (2019). Bioinspired ultrasensitive and stretchable MXene-based strain sensor via nacre-mimetic microscale "brick-and-mortar" architecture. *ACS Nano* 13: 649–659.

33 Liao, H., Guo, X., Wan, P., and Yu, G. (2019). Conductive MXene nanocomposite organohydrogel for flexible, healable, low-temperature tolerant strain sensors. *Advanced Functional Materials* 29: 1904507.

34 Zhang, L., Zhang, X., Zhang, H. et al. (2022). Semi-embedded robust MXene/AgNW sensor with self-healing, high sensitivity and a wide range for motion detection. *Chemical Engineering Journal* 434: 134751.

25

MXenes for Environmental Treatments

Jie Wang[1], Zhenjun Wu[2], Xiuqiang Xie[1], and Nan Zhang[1]

[1] *College of Materials Science and Engineering, Hunan University, Changsha, PR China*
[2] *College of Chemistry and Chemical Engineering, Hunan University, Changsha, PR China*

25.1 Introduction

The rapid growth of economy and industry has raised severe environmental concerns. One of the critical issues is the production of hazardous wastes, which leads to severe damage to the ecological environment and human health. Pollutants such as heavy metal ions, radioactive ions, dyes, and antibiotic residues are highly harmful and may cause irreversible damages to organisms. Thus, developing appropriate approaches to removing contaminants is a priority. At present, various environmental remediation techniques such as adsorption, membrane separation, photocatalytic degradation, and desalination are considered as practical and economically viable technologies [1–3]. The development of these techniques relies on the search for advanced materials to achieve a better process. In addition to the traditional materials such as ceramics, metal-organic frameworks, and carbon-based nanostructures, MXenes have been intensively investigated as suitable materials for environmental treatments [2].

MXenes have gained significant attention for environmental remediation due to their attracting properties, such as large specific area, hydrophilicity, biological compatibility, tunable interlayer spacing, and abundant functional groups (–OH and –O) [4–6]. And these properties can be easily enhanced by constructing composites. For example, MXene-polymer composites have been fabricated to provide conductive pathway, strengthen the stability, and inhibit agglomeration, thereby cooperatively enhancing the performance of individual components [7].

Transition Metal Carbides and Nitrides (MXenes) Handbook: Synthesis, Processing, Properties and Applications, First Edition. Edited by Chuanfang Zhang and Michael Naguib.
© 2024 John Wiley & Sons, Inc. Published 2024 by John Wiley & Sons, Inc.

Furthermore, benefiting from the "conductive clay-like" characteristic, MXenes-based functional materials can be constructed by a variety of facile methods, such as filtration, painting, spray coating, and electrostatic assembly, which is highly desirable to design functional devices [8]. All these advantages make MXenes potential materials for target applications [9–13].

This chapter will summarize and discuss the extensive applications of MXenes and their composites in environmental remediation, including chemical adsorption, membrane separation, desalination, and photocatalytic degradation for water treatment, and electrocatalytic sensors for pollutant detection. Antibiofouling properties, biocompatibility, and stability will also be discussed.

25.2 MXenes for Adsorption Toward Water Purification

Adsorption as a widely used technique has been popular because of its low cost, high efficiency, easy operation, and extensive availability for water purification. The bourgeoning development of MXenes unveils the potentials as adsorbents for the removal of heavy metal ions, dyes, radioactive ions, as well as antibacterial agents for water purification [5, 14, 15]. For example, owning to the negative charge on the surface, MXenes present a strong ability to easily accommodate Na^+, K^+, NH_4^+, Mg^{2+}, and Al^{3+} cations and organic molecules such as hydrazine, dimethyl sulfoxide, and urea between their layers [16, 17].

Heavy metal ions have the long-lasting toxicity due to their nondegradable and persistent characteristic. MXenes are regarded as favorable adsorbents for heavy metal ions, primarily relying on the surface functional groups and the redox-active M metals sites [18]. Previous reports have demonstrated MXenes have strong adsorption toward different metal ions [19–21]. $Ti_3C_2T_x$ has been used for the effective removal of Pb(II) in synthetic wastewater [22]. It is reported that although $Ti_3C_2T_x$ has a smaller surface area than that of powder activate carbon, it has achieved better adsorption owning to the higher negative surface charge. The Pb(II) adsorption equilibrium by $Ti_3C_2T_x$ is attained quickly as short as 30 minutes, conforming to the Freundlich model. In addition to the physical adsorption on the surface of MXenes, the chemisorption exists between ions and functional group on the surface of MXenes through chemical bonds. $Ti_3C_2T_x$ nanosheets have been applied to adsorb Ba(II), showing more than 90% removal efficiency in the first 10 minutes [23]. The maximum Ba(II) sorption occurs in the pH range from 6 to 9, where $Ti_3C_2T_x$ has highly negative zeta potential. It is proposed that the electrostatic attraction forces between $Ti_3C_2T_x$ and Ba(II) to form $Ba(OH)_2$ and BaF_2 further promote the adsorption capacity.

The adsorption performance can be tailored by surface functionalization. After alkalization intercalation, $Ti_3C_2(OH/ONa)_xF_{2-x}$ has exhibited a preferential and

unique Pb(II) adsorption behavior when competing ions (Ca(II)/Mg(II)) of high concentrations coexisted [18]. The average water treatment capacity is 4500 kg of water per kg of $Ti_3C_2(OH/ONa)_xF_{2-x}$, and the effluent contents of Pb(II) are below $2\,\mu g\,l^{-1}$, meeting the drinking water standard ($10\,\mu g\,l^{-1}$) suggested by the World Health Organization (WHO). The fast sorption behavior is attributed to the –OH groups, which promote the exchange of Pb(II). Furthermore, a high-quality amino-functionalized $Ti_3C_2T_x$ (alk-MXene-NH_2) as Pb(II) adsorbent has been synthesized by an alkalization-grafting process using (3-aminopropyl) triethoxysilane [24]. The interlayer spacing and chemical state can be improved by increasing the amount of grafted organofunctional groups. The alk-MXene-NH_2 has achieved the maximum Pb(II) adsorption capacity of $384.63\,mg\,g^{-1}$ compared with other 2D adsorbents.

Notably, MXenes have been reported to remove some contaminations by *in-situ* reduction, such as Cu^{2+}, Ag^+, and some organic molecules [25, 26]. Benefiting from this merit, $Ti_3C_2T_x$ nanosheets have a more efficient Cr(VI) reductive removal capacity of $250\,mg\,g^{-1}$, which is higher than that of activated carbon ($112.36\,mg\,g^{-1}$) [27], graphene nanocomposites ($1.03\,mg\,g^{-1}$) [28], and TiO_2 particles ($5\,mg\,g^{-1}$) [29]. The concentration of residual Cr(VI) is less than 5 ppb, fulfilling the standard of drinking water by WHO (0.05 ppm) [30]. However, the stability of powder adsorbents is limited by their exposure to the oxidation environment in the way of dispersed nanosheets. For this, the film material not only prolongs their lifetime but also is time- and cost-effective for recycling after water purification. A $Ti_3C_2T_x$-based film intercalated with reduced graphene oxide (rGO) has been prepared for the removal of multiple heavy metal ions (HMIs) from water, as shown in Figure 25.1a. After surface modification by HCl, the fabricated film (HRM) with more hydroxyl groups has exhibited the highest $HCrO_4^-$ adsorption capacity ($84\,mg\,g^{-1}$) compared to the pure $Ti_3C_2T_x$ film (PM) and bare rGO-intercalated $Ti_3C_2T_x$ film (RM) (Figure 25.1b). The progressive effects can be ascribed to the introduction of rGO mitigating the restacking of $Ti_3C_2T_x$ and the increased hydroxyl groups enhancing the adsorption and reduction of HIMs (Figure 25.1c). The HRM film has been also effective for $PdCl_4^{2-}$, $AuCl_4^-$, and Ag^+ with removal capacities of 890, 1241, and $1172\,mg\,g^{-1}$, respectively. In addition, it is found the method of sequential treatment in NaOH and HCl can regenerate the $Ti_3C_2T_x$-based films used for the removal of $HCrO_4^-$ [31]. $Ti_3C_2T_x$ has been further used for the reductive adsorption of Cu^{2+} to Cu_2O and CuO [26]. A maximum removal efficiency of $78.45\,mg\,g^{-1}$ with fast kinetics has been obtained, which is higher than that of activated carbon ($15.07\,mg\,g^{-1}$) [32].

The radioactive pollution has increased with the development of nuclear power, which leads to healthy concerns because of the strong radioactivity, toxicity, and long half-life. MXenes as potential adsorbents have gained enormous attention because of their resistance to radiation-induced damage. Density functional

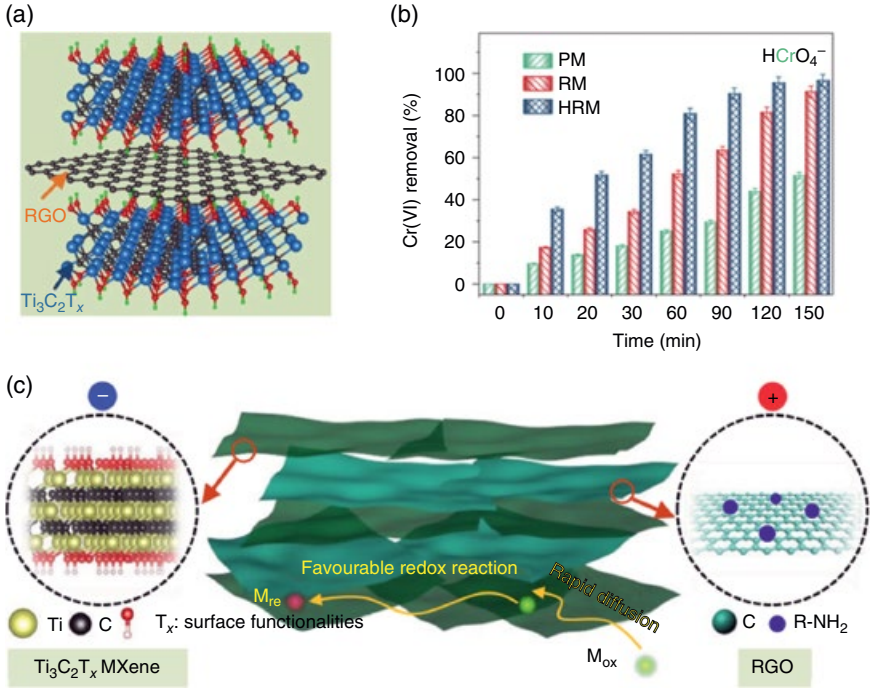


Figure 25.1 (a) Schematic illustration of the mitigated restacking of $Ti_3C_2T_x$ layers by rGO. (b) Performance of $Ti_3C_2T_x$-based films (PM, RM, and HRM) for removing $HCrO_4^-$ under pressure-free conditions. (c) Schematic illustration of the removal of HMIs by the prepared $Ti_3C_2T_x$ films under pressure-free conditions. *Source:* Xie et al. [31]/ Springer Nature.

theory (DFT) calculations have predicted that radionuclide uranyl ions can be efficiently removed by V_2CT_x with an adsorption capacity of 536 mg g^{-1} [33, 34], which is attributed to strong bonding between uranyl ions and the –OH groups of MXenes via bidentate inner-sphere complexes. However, the experimental adsorption capacity of 174 mg g^{-1} is far less than that of theoretical value (536 mg g^{-1}), which highlights the importance of material optimization, such as etching, intercalation, activation, and delamination [34]. A major challenge of MXenes as adsorbents for removing radionuclides is that the interlayer spacing limits the accessibility of adsorbates with large hydrated ion radii [35]. Owning to the presence of hydrophilic groups, a large number of water is attracted into the interlayer spacing of $Ti_3C_2T_x$ ($Ti_3C_2T_x$-hydrated) in aqueous solution, which results in a shift of the (002) peak to 6.78° from 8.81° for dry $Ti_3C_2T_x$ [35]. After treated with NaOH ($Ti_3C_2T_x$-NaOH) and dimethyl sulfoxide (DMSO), the (002) peak of wet $Ti_3C_2T_x$ further shifts to 5.73° and 4.56°, respectively, corresponding

to much larger interlayer spacings. Among the prepared samples, $Ti_3C_2T_x$-DMSO shows the highest U(VI) uptake capacity of 160 mg g^{-1} due to the largest interlayer spacing. Hence, the rational regulation and control to the interlayer spacing can effectively promote the ability of MXenes to adsorb certain species.

MXenes have also shown great potential for the removal of organic dyes in wastewater, which causes severe threats to the ecosystem and environment. The adsorption behavior of MXenes for methylene blue (MB) and acid blue 80 (AB80) is firstly reported by Gogotsi's group [36]. The results show that $Ti_3C_2T_x$ prefers to adsorb cationic MB because of the electrostatic interactions between the positively charged dyes and the negatively charged $Ti_3C_2T_x$. The adsorption capability can be further improved by the interlayer spacing regulation and surface functionalization. After hot alkaline solution treatment, the interlayer spacing of $Ti_3C_2T_x$ increases 29% and the –F groups are replaced by –OH, and a high adsorption capacity of 189 mg g^{-1} are achieved [37]. Moreover, the chemical modification of $Ti_3C_2T_x$ surface by polymers endows it with advanced properties. A novel carboxyl-modified $Ti_3C_2T_x$ combined with polyethylene polyimide and poly acrylic acid (MXene-COOH@$(PEI/PAA)_n$) has been synthesized by a layer-by-layer strategy [38]. Benefiting from the abundant chemical moieties, the composites have significantly increased adsorption capacities for safranine (33.76 mg g^{-1}), neutral red (42.50 mg g^{-1}), and MB (36.69 mg g^{-1}).

25.3 MXenes Membranes Toward Separation of Pollutants

Membrane-based separation technology is a practical method for wastewater treatment, for which membranes with high flux, high selectivity and stability are required. MXenes are regarded as ideal membrane materials due to their high strength, hydrophilicity, and remarkable flexibility. Compared to the small water flux of GO membranes resulting from their limited interlayer spacing, MXenes possess tunable interlayer spacing and surface functional groups, which have more extensive and practical application prospects. The interlayer spacing varies from 2.9 Å for the dry $Ti_3C_2T_x$ films to more than 6.4 Å for the water-containing ones, meeting the sieving needs in extensive applications [39]. The separation mechanism of MXenes is based on their permeation selectivity toward targets, depending on size exclusion and the interaction between the targets and the MXenes layers.

The $Ti_3C_2T_x$ membrane is firstly fabricated on a polyvinylidene difluoride (PVDF) film by the vacuum-assisted filtration and used for selective rejection of ions and molecules [39]. The results reveal that ions (e.g., MB^+) with higher radii than the interlayer spacing are unable to pass through the MXene membrane. In contrast, the permeated ions' rates follow the order of $Na^+ > Li^+ > K^+ > Ca^{2+} > Ni^{2+} > Mg^{2+} > Al^{3+}$, suggesting the synergetic effect of the charge and size of cations.

Compared to GO membrane (6.5 l [Bar h m^2]$^{-1}$) tested in the same way, MXene membranes have a better selectivity for cations and higher water flux of 37.4 l (Bar h m^2)$^{-1}$, which can be explained by the existence of at least one layer of H_2O molecules between $Ti_3C_2T_x$ layers.

Various strategies are reported to enhance the ions separation efficiency of MXene-based membranes, such as covalent binding, surface coating, grafting, and layer-by-layer assembly [40, 41]. Porous $Ti_3C_2T_x$ membrane has been prepared by using $Fe(OH)_3$ as the hard-template (Figure 25.2a) [42]. The tailored membrane has a rough surface morphology with a typical lamellar structure and abundant nanochannels (Figure 25.2b, c), exhibiting an excellent water permeance of 1000 m^{-2} h^{-1} bar^{-1} and favorable rejection rate of 90% for molecules of ~2.5 nm. In order to improve the hydrophilicity and water flux, Han et al. have reported a new 2D $Ti_3C_2T_x$/polyethersulfone (PES) composite membrane for separating dyes from salts [40]. The obtained membrane has achieved high rejections of 92.3% for Congo red dye, 80.3% for Gentian violet, and <23% for inorganic salts with a water flux above 432 l m^{-2} h^{-1} at 0.1 MPa, respectively. Notably, an increased $Ti_3C_2T_x$ content enhances the rejection of dyes and inorganic salts. Kang et al. prepared $Ti_3C_2T_x$-GO composite membrane with a thickness of 90 nm and an interlayer spacing around 5 Å, allowing two layers of water molecules within $Ti_3C_2T_x$ interlayers [41]. The assembled membrane rejects the dyes with radii above 5 Å, including methyl red (68%), MB (99.5%), rose Bengal (93.5%), and brilliant blue (100%), paving a new pathway for engineering separation composite membranes.

The MXenes-based membranes are also expected to realize the effective removal of oil droplets in the wastewater. Recently, one pioneering research about $Ti_3C_2T_x$-based membranes for separating oil from wastewater has been reported. A flexible, hydrophilic, and oleophobic membrane has been constructed by coating $Ti_3C_2T_x$ ink on the substrate of the conventional print paper [43]. The tailored membrane has achieved over 99% separation efficiency for oil/water emulsions and over 450 l m^{-2} h^{-1} bar^{-1} water permeation flux after 8 cycles. In another report, $Ti_3C_2T_x$ membrane has been prepared by a simple vacuum filtration for effective separation of oil-in-water mixture with an oil contact angle of 158° and an oil sliding angle of 7° [44]. The membrane has shown a high separation efficiency of over 99.4% and a permeation flux of 8871 m^{-2} h^{-1} bar^{-1} for crude oil.

25.4 MXenes for Water Desalination

Among strategies for alleviating water crisis, desalination has been universally identified as an attractive alternative to obtain freshwater from seawater or brackish water. By utilizing the spacings between the layers to improve ion transportation, MXenes have been accepted as promising membrane materials for water desalination.

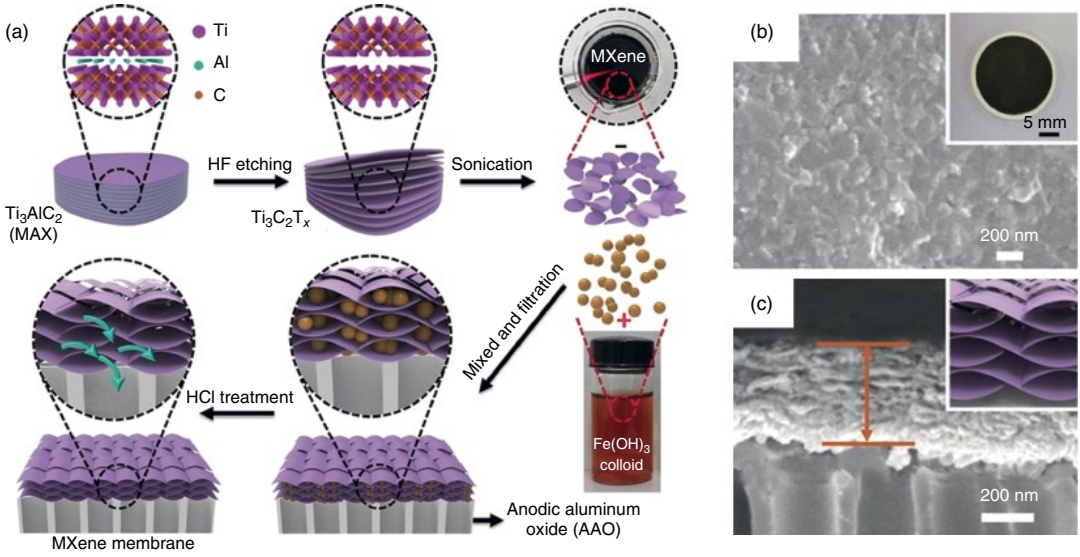


Figure 25.2 (a) Illustration of the fabrication of $Ti_3C_2T_x$ MXene membrane. (b) SEM image of the surface (inset: macroscopic photograph) and (c) the cross-sectional view of $Ti_3C_2T_x$ membrane; the inset represents the layered structure. *Source:* Ding et al. [42]/Reproduced from John Wiley & Sons, Inc.

Capacitive deionization (CDI) is an effective approach for water desalination, which works through electrosorption at ambient temperature and pressure, avoiding the use of expensive high-pressure pumps. Based on the special characteristics of electrodes, such as the surface property, stability, and conductivity, CDI enables the effective separation of cations and anions. Currently, MXenes as promising electrodes for CDI applications have attracted extensive attention. Porous $Ti_3C_2T_x$ electrode with large specific surface area has been used for CDI of saline water, which has demonstrated a high capacity of 118 mg cm^{-3} in the NaCl solution of 10 000 mg l^{-1}, nearly 12 times higher than carbon-based electrode [45]. $NaTi_2(PO_4)_3/Ti_3C_2T_x$ nanohybrid has been synthesized by the transformation of $Ti_3C_2T_x$ under solvothermal conditions for hybrid capacitive deionization (HCDI) [46]. Combining the high theoretical sodium-ion storage of $NaTi_2(PO_4)_3$ and high conductivity of $Ti_3C_2T_x$, the fabricated electrode has exhibited an extraordinary desalination performance, including a high desalination capacity of 128.6 mg g^{-1} and a desalination rate of 29.6 mg g^{-1} min^{-1} with good cycling stability. Asymmetric HCDI cells have been designed for the removal of salt ions using current collector- and binder-free $Ti_3C_2T_x$ electrodes and porous carbon electrodes [47]. The $Ti_3C_2T_x$ electrodes have been fabricated by doctor blade coating method using highly concentrated $Ti_3C_2T_x$ dispersions of 48 mg ml^{-1} consisting of large and small flakes, where large flakes offer mechanical stability with conductive transport, while small flakes provide shorter diffusion pathways. The HCDI system operates at a voltage of +1.2 V and −1.2 V for ions removal and ions release, respectively. The salt removal capacity is 39 mg g^{-1} with cycling stability of 62% over 25 CDI cycles. This research paves a new way for exploring free-standing MXene electrodes in HCDI applications.

Owning to the energy efficiency and easy operation, pervaporation has been used for desalination. In the process of pervaporation, the driving force of the mass transport across the membrane is the chemical potential gradient, which is created by applying a lower vapor pressure on the permeate side than that of the feed side [48]. The permeate vapor is collected by condensing or releasing as expected. During this operation, high performance membranes make a balance between high flux and separation. In terms of MXenes, the hydrophilic nature leads to a high mobility of water molecules and the tunable interlayer spacing achieves controlled ion sieving. $Ti_3C_2T_x$ MXene has been fabricated on the commercial polyacrylonitrile membrane as the ultrathin pervaporation membrane for the first time in 2018 [49]. Owning to unique 2D interlayer channels and high hydrophilicity, the fabricated ultrathin (~60 nm) $Ti_3C_2T_x$ membrane has shown a high water flux of 85.41 m^{-2} h^{-1} and a salt rejection rate of 99.5% for NaCl with a feed concentration of 3.5%. To further improve the performance, maleic acid-crosslinked $Ti_3C_2T_x$ membrane has been designed. Benefiting from the strong covalent bonds, the as-obtained $Ti_3C_2T_x$ membrane has an enlarged interlayer

spacing (0.49 nm), well-packed nanochannels, and enhanced mechanical strength, which has exhibited a water flux of 22.8 kg m^{-2} h^{-1} higher than pure $Ti_3C_2T_x$ membrane (17.3 kg m^{-2} h^{-1}) without sacrificing the selectivity [50].

Solar evaporation is a renewable and environment-friendly strategy for seawater desalination and wastewater treatment. In this process, the thermal energy of solar radiation is transferred to the saline feed by the light-harvesting material, and then water is vaporized along the hydrophilic layer of the salt-rejecting membrane. The ability of the light-harvesting material to absorb solar is crucial for the efficiency of solar evaporation. MXenes are ideal candidates due to their wide range adsorption of solar energy for light-to-heat conversion [4]. A hydrophobic MXene membrane is prepared by filtering delaminated $Ti_3C_2T_x$ modified by trimethoxy (1H,1H,2H,2H-per-uorodecyl) silane (PFDTMS), which plays multiple roles as solar adsorber, vapor evaporator, and salt broker for solar desalination [26]. With high solar utilization efficiency and stability, the self-floatable device has exhibited a high solar evaporation rate of 1.31 kg m^{-2} h^{-1} with a conversation efficiency of 71%, remarkable salt rejection of 99.5%, and stability of over 200 hours in actual seawater. As shown in Figure 25.3a, Zhang et al. have reported a vertically aligned Janus $Ti_3C_2T_x$ aerogels (Janus VA-MXA) with an upper hydrophobic layer and a bottom hydrophilic layer by placing $Ti_3C_2T_x$ aerogels in a ring-shaped sponge mold and then floating on ethanol solution containing fluorinated alkyl silane [51]. The Janus VA-MXA has a black cylinder shape (Figure 25.3b–d), with a microchannel size of 15–20 μm and 20–25 μm for the upper hydrophobic layer and the bottom hydrophilic layer, respectively (Figure 25.3e, f). In this Janus structure, the bottom layer pumps water along the vertical channels based on capillary force and vapor escape, and the upper hydrophobic layer prevents the accumulation of salts on the surface. The Janus VA-MXA shows a high solar-to-heat conversation efficiency of 87% and a water evaporation rate of 1.46 kg m^{-2} h^{-1} with 15 days under 1 sun irradiation (Figure 25.3g).

25.5 MXenes for Photocatalytic Degradation

Photocatalytic degradation of organic pollutants is promising for environmental remediation. In this process, organics are degraded to CO_2 and H_2O as the final product [52]. MXenes can serve as the substrate, electron acceptor, light harvesting material, precursor, and cocatalyst, promoting the performances for photocatalytic degradation of organic pollutants [53].

MXenes are widely considered as the photogenerated electrons acceptor by forming the well-known Schottky barrier to facilitate the separation of photogenerated charge carriers in the photocatalytic degradation process. A novel

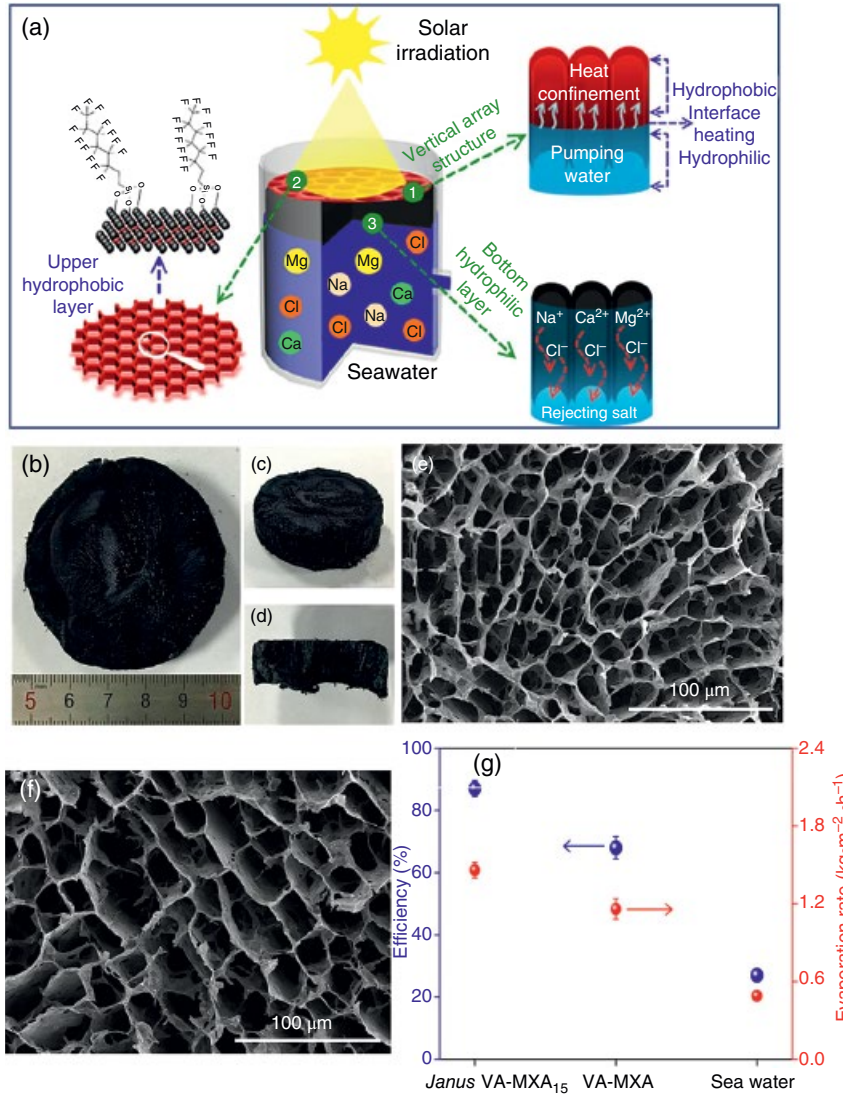


Figure 25.3 (a) Working mechanism of Janus VA-MXA for the fabrication of MXene membrane. (b) Top view, (c) side view, and (d) fracture face of Janus VA-MXA. (e) SEM images of the Janus VA-MXA's upper layer and (f) bottom layer. (g) The water evaporation rates and energy conversation efficiencies. *Source:* Zhang et al. [51]/Reproduced from American Chemical Society.

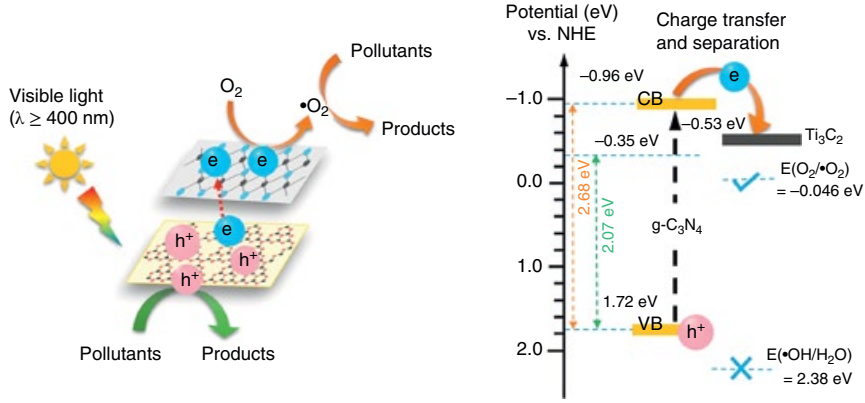
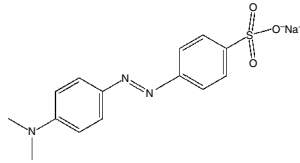
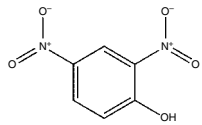
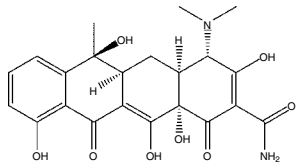
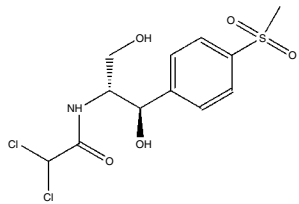
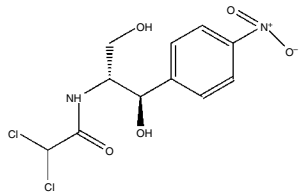


Figure 25.4 Schematic illustration of the production of h^+ and O_2^- and their oxidation reaction toward pollutants. *Source:* Liu et al. [54]/Elsevier.

g-C_3N_4/$Ti_3C_2T_x$ (CNTC) photocatalyst with intimate interfacial contact has been prepared via an evaporation-induced self-assembly method [54]. The Schottky heterojunction in CNTC suppresses the recombination of electron-hole pairs and facilitates the photo-generated separation and migration. Compared to bare g-C_3N_4, CNTC shows a higher photocurrent of 2.2 μA cm^{-1} and a larger kinetic constant for the degradation of ciprofloxacin (CIP). As shown in Figure 25.4, mechanism investigations demonstrate that g-C_3N_4 adsorbs visible light and transfers the photo-induced electrons to $Ti_3C_2T_x$, leaving abundant photogenerated holes (h^+) that degrade CIP. Simultaneously, since the Femi level of $Ti_3C_2T_x$ (−0.53 eV vs. NHE) is lower than that of O_2/O_2^- (−0.46 eV vs. NHE), the dissolved oxygen is reduced to·O_2^-, which also contributes the degradation of CIP. In another report, Ag_3PO_4/$Ti_3C_2T_x$ Schottky catalyst has been prepared by a self-assembly method with a high photocatalytic degradation rate constants superior to the Ag_3PO_4/graphene and pristine Ag_3PO_4 toward the degradation of methyl orange (MO), 2,4-Dinitrophenol (2,4-DPN), tetracycline hydrochloride (TC-H), thiamphenicol (TPL) and chloramphenicol (CPL), as summarized in Table 25.1 [55]. The enhanced photoactivities are ascribed to the intimate contact between Ag_3PO_4 and $Ti_3C_2T_x$, where $Ti_3C_2T_x$ traps unidirectional electron flow over Ag_3PO_4 to limit the charge carrier recombination.

MXenes can also serve as a bridge to form a cascade junction (*Z*-scheme) structure with semiconductor photocatalysts to enhance photocatalytic performances. CdS@Ti_3C_2@TiO_2 has been obtained by a facile calcination and subsequent hydrothermal process [56]. The introduction of $Ti_3C_2T_x$ enhances the activity of CdS@TiO_2 toward the degradation of sulfachloropyridazine, phenol,

Table 25.1 Degradation rate constants of different pollutants over Ag_3PO_4-based catalysts.

Pollutants (20 mg l^{-1})	Structure	Catalysts (0.4 g l^{-1})	Rate constants (min^{-1})
MO		Ag_3PO_4	0.035
		Ag_3PO_4/rGO	0.072
		$Ag_3PO_4/Ti_3C_2T_x$	0.094
2, 4-DNP		Ag_3PO_4	0.0005
		Ag_3PO_4/rGO	0.002
		$Ag_3PO_4/Ti_3C_2T_x$	0.005
TC-H		Ag_3PO_4	0.2
		Ag_3PO_4/rGO	0.22
		$Ag_3PO_4/Ti_3C_2T_x$	0.32
TPL		Ag_3PO_4	0.0025
		Ag_3PO_4/rGO	0.0027
		$Ag_3PO_4/Ti_3C_2T_x$	0.0042
CPL		Ag_3PO_4	0.007
		Ag_3PO_4/rGO	0.012
		$Ag_3PO_4/Ti_3C_2T_x$	0.025

Source: Cai et al. [55]/Elsevier.

and several typical dyes under visible light irradiation ($\lambda \geq 420$ nm). Based on the transient photocurrent response tests and the electron spin resonance technique, the enhanced performance is attributed to the *Z*-scheme type composite promoting the efficient separation and subsequent production of free radicals·O_2^- and OH, which play vital roles in the contaminant photodegradation.

By taking advantage of their light harvesting capability, MXenes have been reported as supporting materials to construct composite photocatalysts. In this context, $Ag_2WO_4/Ti_3C_2T_x$ composites have been prepared for the removal of organic pollutants, exhibiting high degradation efficiencies of 62.9% and 88.6% for tetracycline hydrochloride (TC-H) and sulfadimidine under simulating visible light ($420\,nm \leq \lambda \leq 780\,nm$), respectively [20]. The excellent performance can be attributed to the presence of $Ti_3C_2T_x$ substrate, which facilitates the uniform distribution of Ag_2WO_4, captures and transfers electrons to form electron flow to stabilize $Ag_2WO_4/Ti_3C_2T_x$. In another report, a 2D/2D photocatalyst of Bi_2WO_6/Nb_2CT_x has been fabricated by a facial hydrothermal process for organic pollutants degradation [57]. A batch of experiments suggest that the degradation efficiency reaches the highest when the mass percentage of Nb_2CT_x is 2%. Specially, under visible light irradiation (>420 nm), Bi_2WO_6/Nb_2CT_x exhibits high degradation efficiencies of 99.8, 92.7, and 83.1% for Rhodamine (RhB), MB, and TC-H, respectively. $CeO_2/Ti_3C_2T_x$ nanocomposite has been prepared through a hydrothermal process, where CeO_2 nanorods are well-dispersed on $Ti_3C_2T_x$ [58]. The nanocomposite exhibits an enhanced photocatalytic degradation efficiency of 75% for RhB in 90 minutes under UV-light irradiation, which is higher than that of CeO_2 (24%) and $Ti_3C_2T_x$ (65%). Hematite (α-Fe_2O_3) is also an attractive photocatalyst with low-cost and visible light activity. α-$Fe_2O_3/Ti_3C_2T_x$ composite has been synthesized by an ultrasonic-assisted self-assembly method, where α-Fe_2O_3 is anchored to $Ti_3C_2T_x$ [59]. Benefiting from the heterostructure, the composite achieves a high degradation efficiency of 98% toward MB in 120 minutes under visible light (>420 nm).

It is also worth noting that $Ti_3C_2T_x$ MXenes can also act as the precursors for constructing Ti-based semiconductors. Wang et al. have firstly synthesized $TiO_2/Ti_3C_2T_x$ by partially oxidizing $Ti_3C_2T_x$ via a hydrothermal process [60]. Compared to pure TiO_2, the TiO_2 in the as-prepared $TiO_2/Ti_3C_2T_x$ composite is more regular with less agglomeration, which is attributed to the role of $Ti_3C_2T_x$ as the precursor and growth site for TiO_2. The homogeneous dispersion of TiO_2 provides abundant active sites for photocatalytic reaction. Combining with the high conductivity of $Ti_3C_2T_x$, $TiO_2/Ti_3C_2T_x$ exhibits much better photodegradation activity for MO (98%) than that of pure TiO_2 (77%) and $Ti_3C_2T_x$ (42%) under UV-light irradiation. Furthermore, a hybrid of $Ti_3C_2T_x$ and Ti^{3+}-doped rutile TiO_2 exposing (111) facets ((111) $TiO_{2-x}/Ti_3C_2T_x$) has been prepared [61]. The activity can be optimized by exposing (111) facets of TiO_2, which is regulated by adding different NH_4F contents in the hydrothermal oxidation process. In the meantime, the generation of oxygen vacancies through the reduction by hydrazine hydrate facilitates the charge separation at the interfaces of the (111) $TiO_{2-x}/Ti_3C_2T_x$. Moreover, TiO_2@C has been prepared by high-energy ball milling of Ti_2CT_x [62]. In this process, Ti_2CT_x acts as a structure-directing agent, promoting the uniform distribution of

TiO_2 nanoparticles on the single or few-layered carbon sheets. The results reveal that TiO_2@C exhibits improved degradation efficiency (85.7%) for MB than TiO_2 (68.5%) with good stability.

25.6 MXenes for Anti-biofouling Applications

As mentioned above, the membrane separation method is popular in the field of water treatment because it is efficient and economic. However, the water flux and lifetime of the membrane might be reduced by the formation of biofilms, such as Gram-negative and Gram-positive bacteria, resulting in severe membrane biofouling [63]. Also, bacteria have great impacts on health. Consequently, various antibacterial nanomaterials with antimicrobial potentials have been developed, where MXenes have exhibited strong antibacterial activity by damaging the cell membranes of bacteria.

The antibacterial performance of MXenes originates from the oxidative and physical stress caused by the sharp edges [64]. Gogotsi et al. have firstly demonstrated the antibacterial activity of $Ti_3C_2T_x$, showing that the fresh $Ti_3C_2T_x$-based membrane has shown outstanding bacterial growth inhibition performance against *Bacillus subtilis* (*B. subtilis*) and *Escherichia coli* (*E. coli*) of 73% and 67% as compared to those of PVDF membrane [65]. The aged $Ti_3C_2T_x$ membrane (stored at ambient air and room temperature for >30 days) shows the best antibacterial performance, which results from the synergistic effect between $Ti_3C_2T_x$ and TiO_2/C. When exposed to $Ti_3C_2T_x$ (200 $\mu g\,ml^{-1}$) for 4 hours, more than 98% bacterial (*E. coli* and *B. subtilis*) cell viability loss (Figure 25.5a, b) [66]. The mechanism study reveals the cell membrane is damaged and the cytoplasmic materials are released from the bacterial cells (Figure 25.5c). This antibacterial research features MXenes with more potential in the elimination of water pollution.

It is worth mentioning that the antibacterial activity of MXenes is affected by the structure at the atomic scale. Ti_2CT_x has the same atoms and the same synthetic conditions as $Ti_3C_2T_x$ MXene, while no bacterial growth inhibition has been observed for Ti_2CT_x, which is absolutely different from $Ti_3C_2T_x$ (Figure 25.5d) [67]. This difference might result from the fact that Ti_2CT_x has a higher Ti-C atomic percentage and larger thickness. Additionally, the size of MXenes and the exposure time play key roles in the bactericidal performance [68]. Smaller $Ti_3C_2T_x$ nanosheets have more sharp edges than the larger ones and bring more damage to the bacteria envelope, leading to the release of DNA from the bacteria cytosol in less than three hours. Besides, the anti-fouling properties of MXenes can be further enhanced by hybridizing with other antibacterial materials. For example, silver/$Ti_3C_2T_x$ composite membrane shows an improved anti-biofouling response against *E. coli* compared to

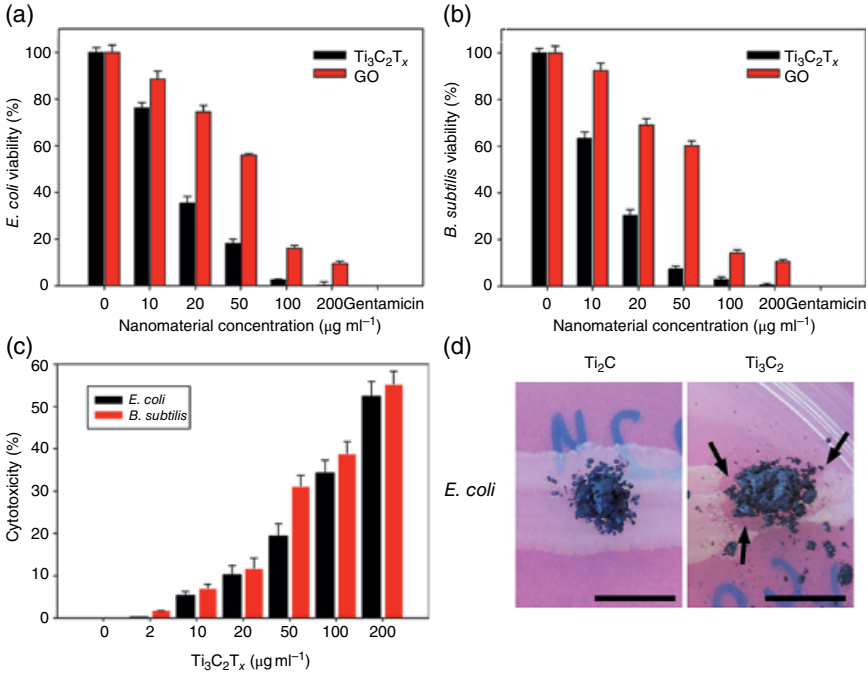


Figure 25.5 Cell viability performance of (a) *E.coli* and (b) *B. subtilis* after treating with $Ti_3C_2T_x$ and graphene oxide (GO). (c) The extent of cell damage measured by lactate dehydrogenase (LDH) release exposed to different concentrations of $Ti_3C_2T_x$. *Source:* Rasool et al. [66]/American Chemical Society/CC BY 4.0. (d) Photographs of the growth of *E. coli* on Petri plates in the presence of $Ti_3C_2T_x$ and Ti_2CT_x. Dark arrows present regions of inhibited bacterial growth. The scale marker was 5 mm. *Source:* Jastrzębska et al. [67]/Reproduced from Springer Nature.

pristine $Ti_3C_2T_x$ [69]. It is suggested that more efforts should be devoted to exploring the factors affecting the antibacterial activity of MXenes, and optimizing the construction and implementation of MXenes-based composite materials for anti-biofouling applications.

25.7 MXenes for Contaminants Detection

Recently, MXenes as suitable 2D materials have been popular in the area of sensors for detecting toxins/pollutants. Compared to the traditional 2D materials with complex synthesis or functionalization process and low-hydrophilicity, MXenes exhibit superiority in many aspects, including high conductivity, tunable surface chemistry, and redox capability. MXenes can be easily decorated/

hybridized with other active materials to further enhance the sensitivity and selectivity, which paves a broad way for the effective detection of contaminants.

As sensors for detecting pollutants, MXenes have been demonstrated to be robust platforms to immobilize active materials for electrochemical sensors. Lu et al. have reported that $Ti_3C_2T_x$ as a platform for the immobilization of tyrosinase, where the –OH termination provides a favorable microenvironment for enzyme immobilization [70]. The prepared $Ti_3C_2T_x$-based tyrosinase biosensors without any media have been employed for detecting phenol with good sensitivity, repeatability, and stability. The detection mechanism is that the phenol is oxidized to *o*-quinone by tyrosinase, followed by the electrochemical reduction to polyhydric phenol to amplify the electrocatalytic phenol signal. It is found that the surface-controlled electrochemical process contributes to the direct electron transfer between tyrosinase biosensors and electrodes, and enables excellent analytical performance. In another case, polyaniline (PANI)-modified $Ti_3C_2T_x$ has been used to detect mercury ions in redox-based sensor systems, which exhibits a detection performance over a wide linear range between 0.1 and 20 $\mu g l^{-1}$ with a detection limit of 0.017 $\mu g l^{-1}$ [71].

Notably, the instability of MXenes during the anodic sweep is still one of the bottlenecks. It is found that $Ti_3C_2T_x$ is partially oxidized along with the reduction of bromate when applied in detecting bromate ions based on redox catalysis [72]. Under the circumstances, the limited stability of MXene-based sensor is a big challenge. A previous study shows that $Ti_3C_2T_x$ is oxidized above 200 mV (vs. Ag/AgCl), which poses a new challenge in direct electrochemical sensing [73]. Therefore, there is still a long way to utilize and configure MXenes for producing reliable, rapid, and sensitive signal output.

Recently, gas detection has played a vital role in air quality control and pollution monitoring. MXenes featuring high conductivity coupled with ample active sites for interfacial interactions are expected to work as sensitive gas sensors with low electrical noise and high signal. Previous studies suggest that $Ti_3C_2T_x$ sensors display typical gas responses when exposed to 100 ppm of acetone, ethanol, ammonia, propanal, nitrogen dioxide, sulfur dioxide, and 10 000 ppm of carbon dioxide, implying the universal gas detection capability (Figure 25.6a) [74]. The responses rely on the change of resistance along with the reduction of conductivity caused by the interaction between the gas molecules and the surface terminations of $Ti_3C_2T_x$, and vary with the thickness of $Ti_3C_2T_x$ films (Figure 25.6b). The DFT calculation confirms that the metallic conductivity together with the strong adsorption energy of the surface functional groups are responsible for the high-sensitivity $Ti_3C_2T_x$ sensors, while another case reveals that the gas detection mechanism might not merely related to adsorption [75]. The gas-induced interlayer swelling of $Ti_3C_2T_x$ is studied by *in-situ* X-ray diffraction, showing better selective swelling toward ethanol than CO_2 gas (Figure 25.6c), where the degree of swelling matches well with the gas response intensity [75]. When treated with

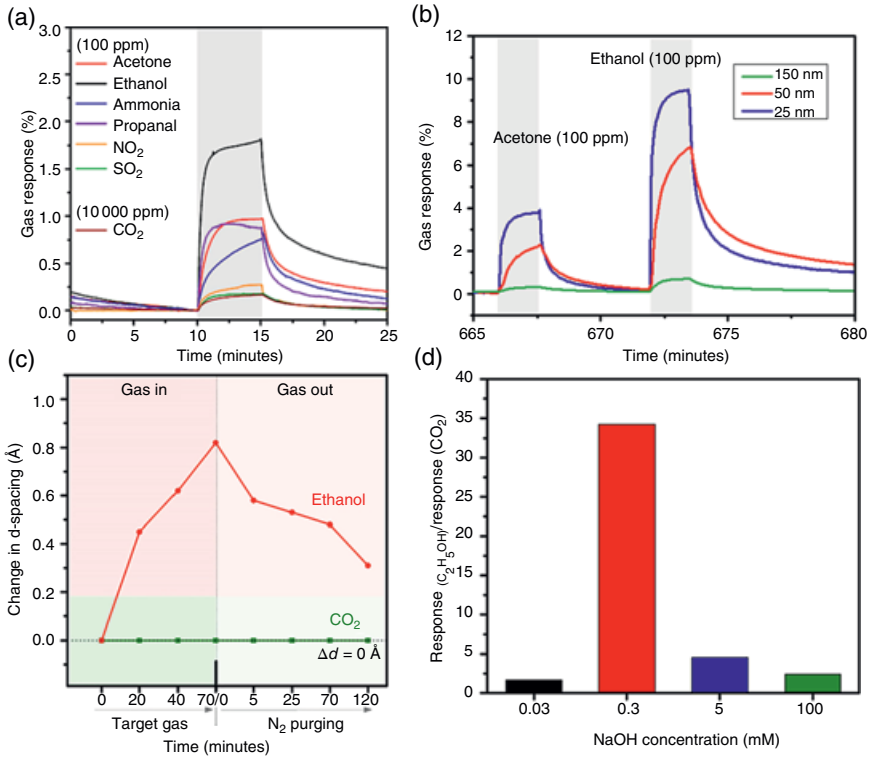


Figure 25.6 (a) Gas response performance of $Ti_3C_2T_x$ sensors toward 100 ppm of acetone, ethanol, ammonia, propanal, NO_2, SO_2, and 10 000 ppm of CO_2. (b) Gas response performance of $Ti_3C_2T_x$ with different thickness exposure to 100 ppm of acetone and ethanol. *Source:* Kim et al. [74]/American Chemical Society. (c) Summarized change of *d*-spacing of $Ti_3C_2T_x$ films after inducing CO_2 and ethanol. (d) Ethanol selectivity of NaOH-treated $Ti_3C_2T_x$ sensors. *Source:* Koh et al. [75]/American Chemical Society.

NaOH, $Ti_3C_2T_x$ accommodates sodium ion in the interlayers, which can tune the swelling behavior and gas sensing performance (Figure 25.6d). This suggests that regulating the interlayer transport of $Ti_3C_2T_x$ is a possible way to enhance the selective sensing of the gas molecules, which extends the understanding of gas sensing mechanism over $Ti_3C_2T_x$.

25.8 Sustainability of MXenes

The sustainability of MXenes plays a key role in their larger-scale practical applications. Considering the effectiveness and economical advantage, recyclability of MXene-based materials is a key factor for environmental treatments. Taking the

application of MXenes for water treatment as an example, exhausted MXene-based adsorbents can be regenerated by acids (HCl or HNO_3) [26, 76], bases (NaOH) [22], inorganic salts ($Ca(NO_3)_2$) [18], and organics (ethanol) [77]. For instance, HCl can realize almost complete desorption (99.69%) of adsorbed Hg^{2+} from $Ti_3C_2T_x$-filled spheres containing sodium alginate, which is the most effective regenerant among reports [76]. Interestingly, HCl, NaOH, and ethanol show a similar level of regeneration capabilities for the desorption of MB from $Ti_3C_2T_x$ [77]. In this context, given the challenges of storage and management, organic solvent may not be suitable while HCl is viewed as the most viable option for the regeneration of MXenes for drinking water treatment.

Swelling is one challenge of MXenes for water desalination, which results in the decreased stability and regeneration capability. When immersed in an aqueous solution, MXenes tend to adsorb water or metal cations, leading to the increased *d*-spacing and thus poor ion rejection efficiency. In recent years, different chemical and physical methods have been used to solve the swelling problem of MXenes, such as thermal self-crossing treatment, ion intercalation, and incorporating other nanomaterials [78–80]. Specifically, self-across-linked $Ti_3C_2T_x$ membranes (SCMM) have been prepared via the self-crosslinking reaction ($-OH + -OH = -O- + H_2O$) between the hydroxyl terminal groups by a facile thermal treatment method (Figure 25.7a) [81]. The formation of Ti—O—Ti bonds between the neighboring $Ti_3C_2T_x$ nanosheets effectively suppresses the swelling behavior of $Ti_3C_2T_x$ membrane for metal ion rejection. SCMM has exhibited reduced permeation rates for K^+, Na^+, and Li^+ of 10^{-3} mol h^{-1} m^{-2} compared to pristine $Ti_3C_2T_x$ membranes (10^{-1} mol h^{-1} m^{-2}) without an obvious decrease in the water flux (Figure 25.7b, c). Even with external voltages, SCMM also has exhibited excellent anti-swelling tolerance with stable interlayer spacing [82]. In another case, cross-linked $Ti_3C_2T_x$/GO composite membrane has been fabricated via the cross-linking reaction ($-OH + -COOH = -COO- + H_2O$) between the carboxyl groups of GO and the hydroxyl group of $Ti_3C_2T_x$, and the ions permeation rates are 7–40 times lower than that of pristine $Ti_3C_2T_x$/GO membrane [80]. The rejection rate of the cross-linked $Ti_3C_2T_x$/GO membrane toward Na^+ is 99.3%, which is higher than that of the pristine $Ti_3C_2T_x$/GO membrane (80.8%). Cation intercalation can also help suppress the swelling and enhance the rejection of ions, where the strong interactions between Al^{3+} and oxygen termination on the MXene surface contribute to the excellent anti-swelling stability for up to 400 hours [78].

Another problem is that MXenes are vulnerable to oxidization in aqueous solution. Due to the partial oxidation, the adsorption capacity of Cu^{2+} on $Ti_3C_2T_x$ decreased from 80% in the first cycle to 47% and 30% in the second and third cycles, respectively [26]. During the reduction of BrO_3^-, $Ti_3C_2T_x$ is oxidized gradually to form TiO_2/C [83]. Consequently, it is difficult to recover the adsorption

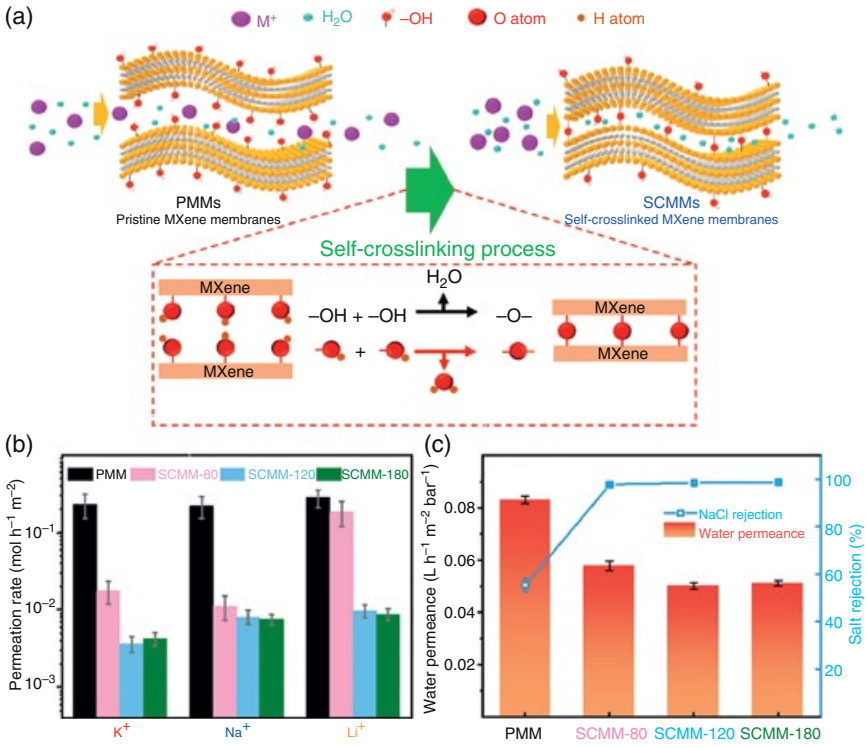


Figure 25.7 (a) Schematic illustration of self-cross-linking process of the MXene membranes. (b) Permeation rates of ions, (c) water permeance and NaCl rejection through the PMM and SCMMs. *Source:* Lu et al. [81]/American Chemical Society.

capacity of $Ti_3C_2T_x$ because of the irreversible reaction in the adsorption process. This case also suggests the regeneration of MXenes after reacting with BrO_3^- might not be possible. More attention should be paid to the stability of MXenes in aqueous media and the development of efficient techniques for the long-term utilization of MXenes without significant degradation.

The ideal materials for environmental treatment are supposed to be biocompatible. Therefore, it is necessary to consider the potential toxicity of MXenes. The toxicity assessment has been studied using a zebrafish embryo model to analyze the possible toxicity of $Ti_3C_2T_x$ *in vivo* and risks on marine biota and ecosystems [84]. The median lethal concentration (LC_{50}) of $Ti_3C_2T_x$ is 257.46 μg ml^{-1}, which is higher than 100 μg ml^{-1} of the "practically nontoxic" group based on the Acute Toxicity Rating Scale by the Fish and Wildlife Service, and no substantial teratogenic effects have been observed on the zebrafish embryos. This work suggests the safe use and discharge of $Ti_3C_2T_x$ should be below 100 μg ml^{-1}. However,

when using avian embryos of 3 and 5 days as an experimental model, ~46% of embryos die after being exposed to $Ti_3C_2T_x$ during 1–5 days [85]. More seriously, seven genes regulating cell proliferation, survival, death, and angiogenesis in $Ti_3C_2T_x$-treated embryos have been deregulated in brain, heart, and liver tissues, which clearly reveals $Ti_3C_2T_x$ at the studied concentration is toxic on the early stage of embryogenesis. Moreover, the degraded metabolites can potentially have harmful consequences. Jastrzebska et al. investigated the toxicity brought on by the oxidation of V_2CT_x nanosheets in cell culture medium [86]. After 48 hours, V_2CT_x nanosheets in cell culture media were observed to undergo fast oxidation, resulting in disintegration and transfer to a mixture of vanadium oxides and carbide-derived-carbon. The vanadium oxides generated were extremely cytotoxic, and the reduction in cell viability was oxidation dependent. Toxicity mechanisms were linked to cell cycle disruption and cell membrane breakdown caused by interaction with oxidized particles. Human umbilical vein endothelial cells were treated with two different concentrations of $Ti_3C_2T_x$ nanosheets (100 and 500 g ml^{-1}), and Zhang et al. found that there was no noticeable acute cytotoxicity [87]. Therefore, it remains uncertain whether the exposure to MXene-based nanomaterials will have adverse health effects on people. Given the vast variety of MXene types and derivatives, as well as the time-consuming and costly nature of toxicity assessments, computer-aided toxicology methodologies, particularly artificial intelligence models, should be used as potent instruments for toxicology prediction and mechanism discovery [88, 89]. Limited by the available data about the toxic effects of MXenes, it is urgently needed to conduct a systematic investigation on the toxicity of MXenes to predict the potential harmful effects on organisms. And the mechanism of the toxicity of MXenes should be explored to ensure the safety of MXenes.

25.9 Conclusions and Outlook

It has been an enduring interest to explore the potential applications of MXenes on environmental treatments. In this chapter, we have summarized recent advances in the applications of MXenes for environmental treatments. Despite these achievements, there are still many challenges and unexplored opportunities. Regarding the adsorption applications, it is difficult to separate the MXenes-based adsorbents from the solution, which limits the in-field practical application for separating pollutants from the solutions of great volume. This problem can be addressed by incorporating MXenes into fibers or fabricating MXenes-derived composites with magnetic nano-architectures. Besides, based on the adsorption mechanism relying on the surface groups, new synthetic routes, and post-treatment methods should be explored to produce MXenes with one type of

uniform terminations to achieve selective sorption. As for membrane separation, the swelling issue leads to the decreased rejection of ions and low selectivity. Consequently, the controllable interlayer spacing should be developed by interlayer engineering to avoid the swelling of MXenes membranes. Several theoretical results reveal superior characteristics of MXenes in desalination [33, 90]. Although MXenes have been extensively employed in water desalination, more investigations are required to bridge the gap between experimentation and theoretical studies [16, 91]. In regards to the photocatalytic applications, the use of MXenes calls for more research being taken in a discreet and reasonable view, rather than rushing to take them as simple replacement of the previous materials to improve the efficacy of semiconductor photocatalysts [92]. Some MXenes have shown antibacterial activity against bacteria, suggesting their potential in water disinfection and anti-biofouling membranes. Yet, more efforts are required to understand the bactericidal mechanisms of MXenes in biofouling applications. At present, the research of MXenes on electrochemical sensors is still in infancy. In most cases, owning to the integration of MXenes, the electrochemical sensors exhibit improved signal sensitivity and detection limit for pollutants. However, the contribution of MXenes is only to increase the conductivity. An in-depth understanding of the effect of MXene surface terminations on the electrochemical behavior is required. It is also worth noting that the stability is a bottleneck issue for MXenes' application in environmental remediation. The understanding of the oxidation kinetics and mechanisms requires in-depth investigations to promote the transformation from laboratories to industries. Currently, $Ti_3C_2T_x$ is the most studied MXene in environmental remediation, while other MXenes such as Nb_2CT_x and V_2CT_x have been less studied. There is still plenty of room to investigate the versatility and potential of MXenes for environmental treatments. We hope that this chapter can give new insights for their use in this field.

References

1 Tunesi, M.M., Soomro, R.A., Han, X. et al. (2021). Application of MXenes in environmental remediation technologies. *Nano Convergence* 8: 5.

2 Jaffari, Z.H., Abuabdou, S.M.A., Ng, D.-Q., and Bashir, M.J.K. (2021). Insight into two-dimensional MXenes for environmental applications: recent progress, challenges, and prospects. *FlatChem* 28: 100256.

3 Chen, J., Huang, Q., Huang, H. et al. (2020). Recent progress and advances in the environmental applications of MXene related materials. *Nanoscale* 12: 3574–3592.

4 Li, R., Zhang, L., Shi, L., and Wang, P. (2017). MXene Ti_3C_2: an effective 2D light-to-heat conversion material. *ACS Nano* 11: 3752–3759.

5 Zhu, J., Ha, E., Zhao, G. et al. (2017). Recent advance in MXenes: a promising 2D material for catalysis, sensor and chemical adsorption. *Coordination Chemistry Reviews* 352: 306–327.

6 Ghidiu, M., Naguib, M., Shi, C. et al. (2014). Synthesis and characterization of two-dimensional Nb_4C_3 (MXene). *Chemical Communications* 50: 9517–9520.

7 Gao, L., Li, C., Huang, W. et al. (2020). MXene/polymer membranes: synthesis, properties, and emerging applications. *Chemistry of Materials* 32: 1703–1747.

8 Wang, H., Wu, Y., Yuan, X. et al. (2018). Clay-inspired MXene-based electrochemical devices and photo-electrocatalyst: state-of-the-art progresses and challenges. *Advanced Materials* 30: e1704561.

9 Anasori, B., Lukatskaya, M.R., and Gogotsi, Y. (2017). 2D metal carbides and nitrides (MXenes) for energy storage. *Nature Reviews Materials* 2: 16098.

10 Liu, J., Jiang, X., Zhang, R. et al. (2018). MXene-enabled electrochemical microfluidic biosensor: applications toward multicomponent continuous monitoring in whole blood. *Advanced Functional Materials* 29: 1807326.

11 Song, P., Liu, B., Qiu, H. et al. (2021). MXenes for polymer matrix electromagnetic interference shielding composites: a review. *Composites Communications* 24: 100653.

12 Morales-García, Á., Calle-Vallejo, F., and Illas, F. (2020). MXenes: new horizons in catalysis. *ACS Catalysis* 10: 13487–13503.

13 Huang, J., Li, Z., Mao, Y., and Li, Z. (2021). Progress and biomedical applications of MXenes. *Nano Select* 2: 1480–1508.

14 Zhang, H., Yang, G., Zuo, X. et al. (2016). Computational studies on the structural, electronic and optical properties of graphene-like MXenes (M_2CT_2, M = Ti, Zr, Hf; T = O, F, OH) and their potential applications as visible-light driven photocatalysts. *Journal of Materials Chemistry A* 4: 12913–12920.

15 Jun, B.-M., Kim, S., Heo, J. et al. (2018). Review of MXenes as new nanomaterials for energy storage/delivery and selected environmental applications. *Nano Research* 12: 471–487.

16 Ihsanullah, I. (2020). MXenes (two-dimensional metal carbides) as emerging nanomaterials for water purification: progress, challenges and prospects. *Chemical Engineering Journal* 388: 124340.

17 Zhang, Q., Du, Q., Hua, M. et al. (2013). Sorption enhancement of lead ions from water by surface charged polystyrene-supported nano-zirconium oxide composites. *Environmental Science & Technology* 47: 6536–6544.

18 Peng, Q., Guo, J., Zhang, Q. et al. (2014). Unique lead adsorption behavior of activated hydroxyl group in two-dimensional titanium carbide. *Journal of the American Chemical Society* 136: 4113–4116.

19 Sun, Y. and Li, Y. (2021). Potential environmental applications of MXenes: a critical review. *Chemosphere* 271: 129578.

20 Fang, Y., Cao, Y., and Chen, Q. (2019). Synthesis of an Ag_2WO_4/Ti_3C_2 Schottky composite by electrostatic traction and its photocatalytic activity. *Ceramics International* 45: 22298–22307.

21 Zhang, Y., Wang, L., Zhang, N., and Zhou, Z. (2018). Adsorptive environmental applications of MXene nanomaterials: a review. *RSC Advances* 8: 19895–19905.

22 Jun, B.-M., Her, N., Park, C.M., and Yoon, Y. (2020). Effective removal of Pb(ii) from synthetic wastewater using $Ti_3C_2T_x$ MXene. *Environmental Science: Water Research & Technology* 6: 173–180.

23 Fard, A.K., McKay, G., Chamoun, R. et al. (2017). Barium removal from synthetic natural and produced water using MXene as two dimensional (2-D) nanosheet adsorbent. *Chemical Engineering Journal* 317: 331–342.

24 Zhang, G., Wang, T., Xu, Z. et al. (2020). Synthesis of amino-functionalized $Ti_3C_2T_x$ MXene by alkalization-grafting modification for efficient lead adsorption. *Chemical Communications* 56: 11283–11286.

25 Zhao, F., Peydayesh, M., Ying, Y. et al. (2020). Transition metal dichalcogenide-silk nanofibril membrane for one-step water purification and precious metal recovery. *ACS Applied Materials & Interfaces* 12: 24521–24530.

26 Shahzad, A., Rasool, K., Miran, W. et al. (2017). Two-dimensional $Ti_3C_2T_x$ MXene nanosheets for efficient copper removal from water. *ACS Sustainable Chemistry & Engineering* 5: 11481–11488.

27 El-Sikaily, A., El Nemr, A., Khaled, A., and Abdelwehab, O. (2007). Removal of toxic chromium from wastewater using green alga Ulva lactuca and its activated carbon. *Journal of Hazardous Materials* 148: 216–228.

28 Zhu, J., Wei, S., Gu, H. et al. (2012). One-pot synthesis of magnetic graphene nanocomposites decorated with core@double-shell nanoparticles for fast chromium removal. *Environmental Science & Technology* 46: 977–985.

29 Liu, E.-t., Zhao, H., Li, H. et al. (2014). Hydrothermal synthesis of porous α-Fe_2O_3 nanostructures for highly efficient Cr(VI) removal. *New Journal of Chemistry* 38: 2911.

30 Ying, Y., Liu, Y., Wang, X. et al. (2015). Two-dimensional titanium carbide for efficiently reductive removal of highly toxic chromium(VI) from water. *ACS Applied Materials & Interfaces* 7: 1795–1803.

31 Xie, X., Chen, C., Zhang, N. et al. (2019). Microstructure and surface control of MXene films for water purification. *Nature Sustainability* 2: 856–862.

32 Demiral, H. and Güngör, C. (2016). Adsorption of copper(II) from aqueous solutions on activated carbon prepared from grape bagasse. *Journal of Cleaner Production* 124: 103–113.

33 Zhang, Y.-J., Zhou, Z.-J., Lan, J.-H. et al. (2017). Theoretical insights into the uranyl adsorption behavior on vanadium carbide MXene. *Applied Surface Science* 426: 572–578.

34 Wang, L., Yuan, L., Chen, K. et al. (2016). Loading actinides in multilayered structures for nuclear waste treatment: the first case study of uranium capture with vanadium carbide MXene. *ACS Applied Materials & Interfaces* 8: 16396–16403.

35 Wang, L., Tao, W., Yuan, L. et al. (2017). Rational control of the interlayer space inside two-dimensional titanium carbides for highly efficient uranium removal and imprisonment. *Chemical Communications* 53: 12084–12087.

36 Mashtalir, O., Cook, K.M., Mochalin, V.N. et al. (2014). Dye adsorption and decomposition on two-dimensional titanium carbide in aqueous media. *Journal of Materials Chemistry A* 2: 14334–14338.

37 Wei, Z., Peigen, Z., Wubian, T. et al. (2018). Alkali treated $Ti_3C_2T_x$ MXenes and their dye adsorption performance. *Materials Chemistry and Physics* 206: 270–276.

38 Li, K., Zou, G., Jiao, T. et al. (2018). Self-assembled MXene-based nanocomposites via layer-by-layer strategy for elevated adsorption capacities. *Colloids and Surfaces A: Physicochemical and Engineering Aspects* 553: 105–113.

39 Ren, C.E., Hatzell, K.B., Alhabeb, M. et al. (2015). Charge- and size-selective ion sieving through $Ti_3C_2T_x$ MXene membranes. *The Journal of Physical Chemistry Letters* 6: 4026–4031.

40 Han, R., Ma, X., Xie, Y. et al. (2017). Preparation of a new 2D MXene/PES composite membrane with excellent hydrophilicity and high flux. *RSC Advances* 7: 56204–56210.

41 Kang, K.M., Kim, D.W., Ren, C.E. et al. (2017). Selective molecular separation on $Ti_3C_2T_x$-graphene oxide membranes during pressure-driven filtration: comparison with graphene oxide and MXenes. *ACS Applied Materials & Interfaces* 9: 44687–44694.

42 Ding, L., Wei, Y., Wang, Y. et al. (2017). A two-dimensional lamellar membrane: MXene nanosheet stacks. *Angewandte Chemie* 56: 1825–1829.

43 Saththasivam, J., Wang, K., Yiming, W. et al. (2019). A flexible $Ti_3C_2T_x$ (MXene)/paper membrane for efficient oil/water separation. *RSC Advances* 9: 16296–16304.

44 Zhang, H., Wang, Z., Shen, Y. et al. (2020). Ultrathin 2D $Ti_3C_2T_x$ MXene membrane for effective separation of oil-in-water emulsions in acidic, alkaline, and salty environment. *Journal of Colloid and Interface Science* 561: 861–869.

45 Bao, W., Tang, X., Guo, X. et al. (2018). Porous cryo-dried MXene for efficient capacitive deionization. *Joule* 2: 778–787.

46 Chen, Z., Xu, X., Ding, Z. et al. (2021). Ti_3C_2 MXenes-derived $NaTi_2(PO_4)_3$/MXene nanohybrid for fast and efficient hybrid capacitive deionization performance. *Chemical Engineering Journal* 407: 127148.

47 Buczek, S., Barsoum, M.L., Uzun, S. et al. (2020). Rational design of titanium carbide MXene electrode architectures for hybrid capacitive deionization. *Energy & Environmental Materials* 3: 398–404.

48 Ahmad, S.A. and Lone, S.R. (2012). Hybrid process (pervaporation-distillation): a review. *International Journal of Scientific & Engineering Research* 3: 1–5.

49 Liu, G., Shen, J., Liu, Q. et al. (2018). Ultrathin two-dimensional MXene membrane for pervaporation desalination. *Journal of Membrane Science* 548: 548–558.

50 Ding, M., Xu, H., Chen, W. et al. (2020). 2D laminar maleic acid-crosslinked MXene membrane with tunable nanochannels for efficient and stable pervaporation desalination. *Journal of Membrane Science* 600: 117871.

51 Zhang, Q., Yi, G., Fu, Z. et al. (2019). Vertically aligned Janus MXene-based aerogels for solar desalination with high efficiency and salt resistance. *ACS Nano* 13: 13196–13207.

52 Jaffari, Z.H., Lam, S.-M., Sin, J.-C. et al. (2020). Magnetically recoverable Pd-loaded $BiFeO_3$ microcomposite with enhanced visible light photocatalytic performance for pollutant, bacterial and fungal elimination. *Separation and Purification Technology* 236: 116195.

53 Huang, K., Li, C., Li, H. et al. (2020). Photocatalytic applications of two-dimensional Ti_3C_2 MXenes: a review. *ACS Applied Nano Materials* 3: 9581–9603.

54 Liu, N., Lu, N., Su, Y. et al. (2019). Fabrication of g-C_3N_4/Ti_3C_2 composite and its visible-light photocatalytic capability for ciprofloxacin degradation. *Separation and Purification Technology* 211: 782–789.

55 Cai, T., Wang, L., Liu, Y. et al. (2018). Ag_3PO_4/Ti_3C_2 MXene interface materials as a Schottky catalyst with enhanced photocatalytic activities and anti-photocorrosion performance. *Applied Catalysis B: Environmental* 239: 545–554.

56 Liu, Q., Tan, X., Wang, S. et al. (2019). MXene as a non-metal charge mediator in 2D layered CdS@Ti_3C_2@TiO_2 composites with superior Z-scheme visible light-driven photocatalytic activity. *Environmental Science: Nano* 6: 3158–3169.

57 Cui, C., Guo, R., Xiao, H. et al. (2020). Bi_2WO_6/Nb_2CT_x MXene hybrid nanosheets with enhanced visible-light-driven photocatalytic activity for organic pollutants degradation. *Applied Surface Science* 505: 144595.

58 Zhou, W., Zhu, J., Wang, F. et al. (2017). One-step synthesis of Ceria/Ti_3C_2 nanocomposites with enhanced photocatalytic activity. *Materials Letters* 206: 237–240.

59 Zhang, H., Li, M., Cao, J. et al. (2018). 2D a-Fe_2O_3 doped Ti_3C_2 MXene composite with enhanced visible light photocatalytic activity for degradation of Rhodamine B. *Ceramics International* 44: 19958–19962.

60 Gao, Y., Wang, L., Zhou, A. et al. (2015). Hydrothermal synthesis of TiO_2/Ti_3C_2 nanocomposites with enhanced photocatalytic activity. *Materials Letters* 150: 62–64.

61 Peng, C., Wang, H., Yu, H., and Peng, F. (2017). (111) TiO_{2-x}/Ti_3C_2: synergy of active facets, interfacial charge transfer and Ti^{3+} doping for enhance photocatalytic activity. *Materials Research Bulletin* 89: 16–25.

62 Li, J., Wang, S., Du, Y., and Liao, W. (2018). Enhanced photocatalytic performance of TiO_2@C nanosheets derived from two-dimensional Ti_2CT_x. *Ceramics International* 44: 7042–7046.

63 Buakaew, T. and Ratanatamskul, C. (2021). Effects of novel anaerobic baffled biofilm membrane bioreactor configurations on membrane fouling mitigation and microbial community in treating liquor condensate. *Bioresource Technology* 335: 125310.

64 Huang, H., Jiang, R., Feng, Y. et al. (2020). Recent development and prospects of surface modification and biomedical applications of MXenes. *Nanoscale* 12: 1325–1338.

65 Rasool, K., Mahmoud, K.A., Johnson, D.J. et al. (2017). Efficient antibacterial membrane based on two-dimensional $Ti_3C_2T_x$ (MXene) nanosheets. *Scientific Reports* 7: 1598.

66 Rasool, K., Helal, M., Ali, A. et al. (2016). Antibacterial activity of $Ti_3C_2T_x$ MXene. *ACS Nano* 10: 3674–3684.

67 Jastrzębska, A.M., Karwowska, E., Wojciechowski, T. et al. (2018). The atomic structure of Ti_2C and Ti_3C_2 MXenes is responsible for their antibacterial activity toward *E. coli* bacteria. *Journal of Materials Engineering and Performance* 28: 1272–1277.

68 Arabi Shamsabadi, A., Sharifian Gh, M., Anasori, B., and Soroush, M. (2018). Antimicrobial mode-of-action of colloidal $Ti_3C_2T_x$ MXene nanosheets. *ACS Sustainable Chemistry & Engineering* 6: 16586–16596.

69 Zhu, X., Zhu, Y., Jia, K. et al. (2020). A near-infrared light-mediated antimicrobial based on Ag/$Ti_3C_2T_x$ for effective synergetic antibacterial applications. *Nanoscale* 12: 19129–19141.

70 Wu, L., Lu, X., Dhanjai, Z.S. et al. (2018). 2D transition metal carbide MXene as a robust biosensing platform for enzyme immobilization and ultrasensitive detection of phenol. *Biosensors & Bioelectronics* 107: 69–75.

71 Cheng, H. (2020). Preparation of Ti_3C_2-PANI composite as sensor for electrochemical determination of Mercury ions in water. *International Journal of Electrochemical Science* 2295–2306.

72 Rasheed, P.A., Pandey, R.P., Rasool, K., and Mahmoud, K.A. (2018). Ultra-sensitive electrocatalytic detection of bromate in drinking water based on Nafion/$Ti_3C_2T_x$ (MXene) modified glassy carbon electrode. *Sensors and Actuators B: Chemical* 265: 652–659.

73 Lorencova, L., Bertok, T., Dosekova, E. et al. (2017). Electrochemical performance of $Ti_3C_2T_x$ MXene in aqueous media: towards ultrasensitive H_2O_2 sensing. *Electrochimica Acta* 235: 471–479.

74 Kim, S.J., Koh, H.-J., Ren, C.E. et al. (2018). Metallic $Ti_3C_2T_x$ MXene gas sensors with ultrahigh signal-to-noise ratio. *ACS Nano* 12: 986–993.

75 Koh, H.J., Kim, S.J., Maleski, K. et al. (2019). Enhanced selectivity of MXene gas sensors through metal ion intercalation: in situ X-ray diffraction study. *ACS Sensors* 4: 1365–1372.

76 Shahzad, A., Nawaz, M., Moztahida, M. et al. (2019). $Ti_3C_2T_x$ MXene core-shell spheres for ultrahigh removal of mercuric ions. *Chemical Engineering Journal* 368: 400–408.

77 Jeon, M., Jun, B.M., Kim, S. et al. (2020). A review on MXene-based nanomaterials as adsorbents in aqueous solution. *Chemosphere* 261: 127781.

78 Ding, L., Li, L., Liu, Y. et al. (2020). Effective ion sieving with $Ti_3C_2T_x$ MXene membranes for production of drinking water from seawater. *Nature Sustainability* 3: 296–302.

79 Feng, X., Yu, Z., Long, R. et al. (2020). Self-assembling 2D/2D (MXene/LDH) materials achieve ultra-high adsorption of heavy metals Ni^{2+} through terminal group modification. *Separation and Purification Technology* 253: 117525.

80 Yin, Z., Lu, Z., Xu, Y. et al. (2021). Supported MXene/GO composite membranes with suppressed swelling for metal ion sieving. *Membranes* 11: 621.

81 Lu, Z., Wei, Y., Deng, J. et al. (2019). Self-crosslinked MXene ($Ti_3C_2T_x$) membranes with good antiswelling property for monovalent metal ion exclusion. *ACS Nano* 13: 10535–10544.

82 Fan, Y., Li, J., Wang, S. et al. (2020). Voltage-enhanced ion sieving and rejection of Pb^{2+} through a thermally cross-linked two-dimensional MXene membrane. *Chemical Engineering Journal* 401: 126073.

83 Pandey, R.P., Rasool, K., Abdul Rasheed, P., and Mahmoud, K.A. (2018). Reductive sequestration of toxic bromate from drinking water using lamellar two-dimensional $Ti_3C_2T_x$ (MXene). *ACS Sustainable Chemistry & Engineering* 6: 7910–7917.

84 Nasrallah, G.K., Al-Asmakh, M., Rasool, K., and Mahmoud, K.A. (2018). Ecotoxicological assessment of $Ti_3C_2T_x$ (MXene) using a zebrafish embryo model. *Environmental Science: Nano* 5: 1002–1011.

85 Alhussain, H., Augustine, R., Hussein, E.A. et al. (2020). MXene nanosheets may induce toxic effect on the early stage of embryogenesis. *Journal of Biomedical Nanotechnology* 16: 364–372.

86 Jastrzębska, A.M., Scheibe, B., Szuplewska, A. et al. (2021). On the rapid in situ oxidation of two-dimensional V_2CT_z MXene in culture cell media and their cytotoxicity. *Materials Science and Engineering: C* 119: 111431.

87 Zhang, D., Zheng, W., Li, X. et al. (2021). Investigating the effect of Ti_3C_2 (MXene) nanosheet on human umbilical vein endothelial cells via a combined untargeted and targeted metabolomics approach. *Carbon* 178: 810–821.

88 Basile, A.O., Yahi, A., and Tatonetti, N.P. (2019). Artificial intelligence for drug toxicity and safety. *Trends in Pharmacological Sciences* 40: 624–635.

89 Wang, J., Su, G., Yan, X. et al. (2022). Predicting cytotoxicity of binary pollutants towards a human cell panel in environmental water by experimentation and deep learning methods. *Chemosphere* 287: 132324.

90 Guo, J., Peng, Q., Fu, H. et al. (2015). Heavy-metal adsorption behavior of two-dimensional alkalization-intercalated MXene by first-principles calculations. *The Journal of Physical Chemistry C* 119: 20923–20930.

91 Sinopoli, A., Othman, Z., Rasool, K., and Mahmoud, K.A. (2019). Electrocatalytic/photocatalytic properties and aqueous media applications of 2D transition metal carbides (MXenes). *Current Opinion in Solid State and Materials Science* 23: 100760.

92 Xie, X. and Zhang, N. (2020). Positioning MXenes in the photocatalysis landscape: competitiveness, challenges, and future perspectives. *Advanced Functional Materials* 30: 2002528.

26

MXenes in Healthcare Technologies

Natalia Noriega[1], Tochukwu Ozulumba[1,2], Grace Cooksley[1], Emma J. Ward[1], and Susan Sandeman[1]

[1] *Centre for Regenerative Medicine and Devices (CRMD), Centre for Life long Health, School of Applied Sciences, University of Brighton, Brighton, East Sussex, UK*
[2] *Department of Chemistry, University of Virginia, Charlottesville, VA, USA*

26.1 Introduction

The MXene family of nanomaterials has unique properties for use in the advancement of healthcare technologies [1, 2]. These two-dimensional (2D), transition metal carbides and nitrides, are characterized by a large surface area and rich surface chemistry, tunable optical [3] and electronic properties [4], mechanical strength, flexibility, and hydrophilicity. Such properties make them suitable for a diverse range of biomedical applications [5, 6] including as antimicrobials, in photothermal therapy (PTT), diagnostics, and theranostics (Figure 26.1). A growing number of synthesized and theorized MXenes has emerged, since the discovery of the first MXene titanium carbide ($Ti_3C_2T_x$) in 2011 [7], for which many of the biologically useful and practically feasible properties have yet to be explored. The following chapter will highlight studies of biocompatibility and summarize the growing breadth of applications in biomedicine and routes to optimize these materials within healthcare technologies to target current clinical challenges.

26.2 The Biocompatibility of MXenes

The application of MXenes to biomedicine inevitably involves contact with cells and other biological tissues requiring initial studies to evaluate biocompatibility. The biocompatibility of a material is specific to the site of use and is defined as the

Transition Metal Carbides and Nitrides (MXenes) Handbook: Synthesis, Processing, Properties and Applications, First Edition. Edited by Chuanfang Zhang and Michael Naguib.
© 2024 John Wiley & Sons, Inc. Published 2024 by John Wiley & Sons, Inc.

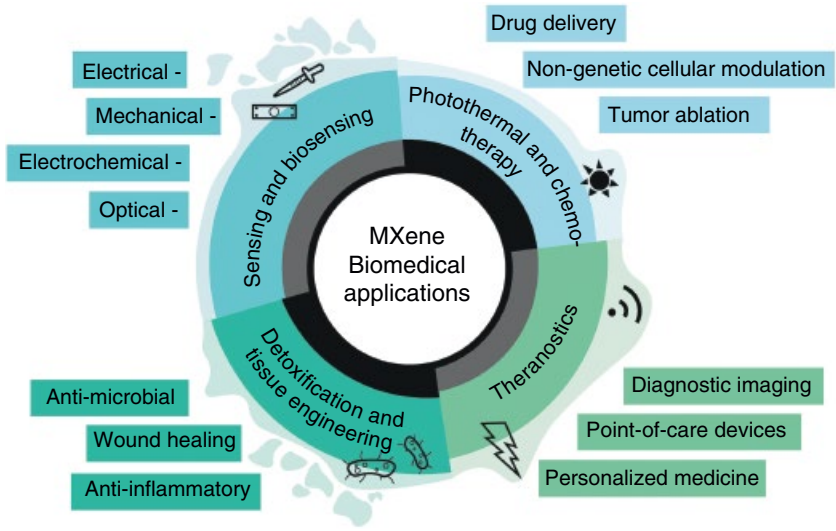


Figure 26.1 Representative examples indicating the range of biomedical applications for MXenes.

ability of a material to function effectively without causing harm to the surrounding tissue or disruption to host physiology. Early biocompatibility studies are carried out using *in vitro*, cell-based investigations to preface those used in later regulatory compliance testing. These *in vitro* cytotoxicity assays may be used in the first instance to assess material impact on cell dynamics by using optical phenomena (absorbance, fluorescence, or luminescence) to measure parameters such as metabolic activity, membrane integrity, apoptosis, production of reactive oxygen species (ROS), DNA damage, and inflammation [8].

As the first discovered MXene [7], $Ti_3C_2T_x$ is the most widely studied for biomedical applications and, therefore, the most commonly used MXene in biocompatibility studies published to date. The majority of studies have found no significant, negative impact on cell physiology using a range of cell types and marker assays. In one of the earliest studies to demonstrate MXene biocompatibility, Meng et al. [9] reported that multilayer (ML) $Ti_3C_2T_x$ had no significant effect on mouse 3T3 fibroblast viability (Figure 26.2a) following 24-hour incubation at a concentration of up to 200 $\mu g\,ml^{-1}$. $Ti_3C_2T_x$ was also hemocompatible, with no induction of clotting cascade activation (Figure 26.2b, c), hemolysis (Figure 26.2d), or platelet activation (Figure 26.2e) after 1-hour incubation with blood. Delamination of ML $Ti_3C_2T_x$ MXene into single and few-layer sheets introduces properties such as a larger surface area and increased electrical conductivity, and thus expands the scope of potential biomedical use, for example, in drug delivery, biosensing, and electrical stimulation. Ward et al. [11] found no significant

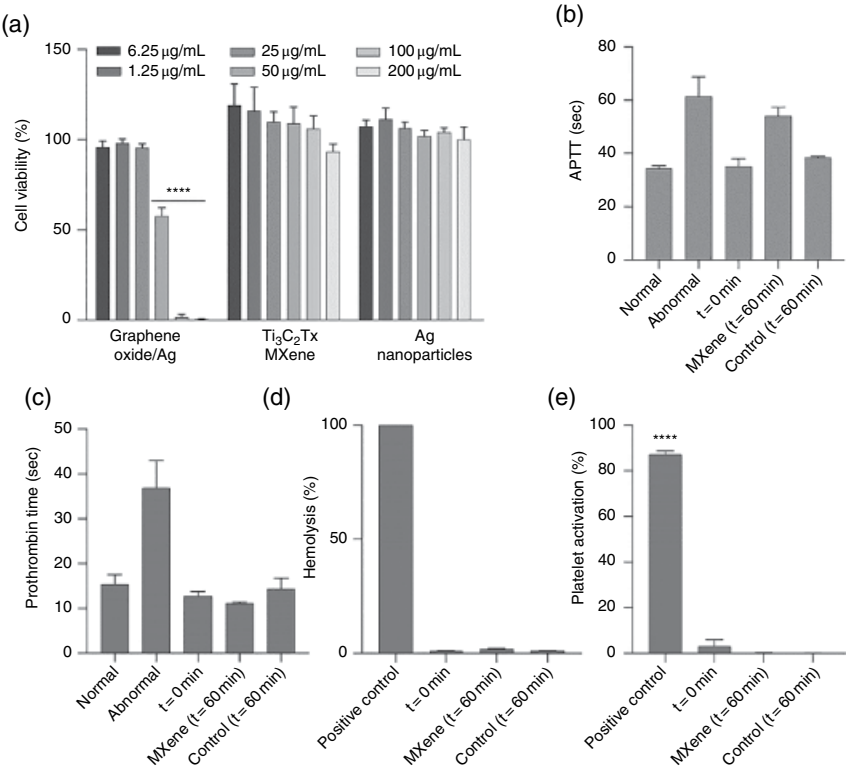


Figure 26.2 Evidence for $Ti_3C_2T_x$ bio- and hemocompatibility on contact with 3T3 fibroblast cells and human blood samples. (a) Direct exposure of murine 3T3 fibroblasts to $Ti_3C_2T_x$ for 24 hours had no significant impact on cell viability, in contrast to graphene oxide-silver (GO-Ag) nanoparticles, which induced a significant reduction in viability at the highest concentration (200 µg ml^{-1}; $p < 0.001$) ($n = 3$, mean ± standard error of the mean). $Ti_3C_2T_x$ did not induce (b) activation of the intrinsic clotting cascade (APTT), (c) activation of the extrinsic clotting cascade (PT), (d) hemolysis, or (e) PAC-1/CD61+ positive platelet activation ($n = 3$, mean ± standard error of the mean). *Source:* Adapted with permission from Meng et al. [9] and Ozulumba et al. [10].

difference in cell viability of human lens epithelial cell line HLE-B3 when incubated with $Ti_3C_2T_x$-coated lenses in comparison to the cell-only control and uncoated IOLs controls. Moreover, the study showed $Ti_3C_2T_x$ coatings did not further incite ROS production nor increase the levels of inflammatory cytokines, interleukin (IL)-6, IL-8, and tumor necrosis factor (TNF)-α.

Multiple reports of delaminated (DL) $Ti_3C_2T_x$ compatibility with mouse 4T1 breast cancer cells have been published [9–12]. Liu et al. [12] confirmed hemocompatibility in a study reporting that DL $Ti_3C_2T_x$ (50–200 µg ml^{-1})

induced minimal hemolysis (<5%) in red blood cells after 8 hours of exposure and was also nontoxic to human colorectal cancer (HCT-116) cells following 24-hour incubation. Using a zebrafish embryo model, Nasrallah et al. [13] showed that DL $Ti_3C_2T_x$ did not cause significant teratogenic effects. In addition to nontoxicity, Zhou et al. [14] demonstrated that DL $Ti_3C_2T_x$ was biodegradable. Titanium concentrations in key organs (heart, liver, lung, kidney, and spleen) were negligible seven days after *in vivo* injection of MXene sheets into BALB/c mice. Researchers have also explored the impact of MXene sheet morphology on cell viability. In their work comparing ML and DL forms, Ozulumba et al. [10] demonstrated that $Ti_3C_2T_x$ had no significant effect on mouse 3T3 fibroblast cell viability or cell membrane integrity and did not induce apoptosis in Jurkat T lymphocytes or ROS production in THP-1 monocytes. Using human peripheral blood mononuclear cells, the cytocompatibility to immune cells was also demonstrated for $Ti_3C_2T_x$, showing no significant viability loss after a 24-hour exposure [15]. Another comparative study by Scheibe et al. [16] on ML, few-layer, and single-layered $Ti_3C_2T_x$ using the WST-1 cell viability assay revealed that both human HeLa cervical cancer cells and MSU1.1 fibroblasts remained >80% viable after 48-hour treatment irrespective of sheet morphology and concentration (10–400 $\mu g\,ml^{-1}$). Studies have demonstrated the biocompatibility *in vitro* and the hemocompatibility on human whole blood of $Ti_3C_2T_x$ [12, 15]. These support the use of $Ti_3C_2T_x$ in applications ranging from extracorporeal blood purification and drug delivery to bioimaging and PTT.

Other MXene compositions assessed for biocompatibility include tantalum carbide ($Ta_4C_3T_x$), vanadium carbide (V_2CT_x), molybdenum carbide (Mo_2CT_x), and niobium carbide (Nb_2CT_x). Like $Ti_3C_2T_x$, these have all been shown to pose minimal risk to cell viability. Liu et al. [17] showed that mouse 4T1 breast cancer cell viability was unaffected after incubation with $Ta_4C_3T_x$ sheets for 24 hours. Similarly, Rafieerad et al. [18] reported that $Ta_4C_3T_x$ was nontoxic toward human bone marrow-derived mesenchymal stem cells and human induced pluripotent stem cells (hiPSC)-derived fibroblasts, cardiomyocytes, and neural progenitor cells. In their study, Feng et al. [19] demonstrated that V_2CT_x, having enzyme-mimicking properties, positively impacted the viability of pheochromocytoma (PC12) cells and mouse L929 fibroblasts by protecting the cells from oxidative stress and ROS-mediated apoptosis *in vitro*. Additionally, V_2CT_x did not cause toxicity to Kunming mice *in vivo*. Mo_2CT_x nanoflakes were not cytotoxic to mouse L929 fibroblasts and 4T1 cells after 48 hours of incubation [20]. Nb_2CT_x flakes were biocompatible with mouse 4T1 breast cancer cells [21] and human U87 glioma cells [21, 22]. Following *in* vivo administration of the MXene flakes to tumor-bearing mice for PTT, Han et al. [22] detected excretion of Nb and Si elements over a 72-hour period via elemental analysis of mice urine and feces. This finding

indicated that the Nb_2CT_x MXenes were biodegradable and posed minimal bioaccumulation risk. These reports of broad-spectrum MXene biocompatibility beyond $Ti_3C_2T_x$ provide support for the increased adoption of MXenes within nanomedicine strategies.

MXene quantum dots (QDs) are zero-dimensional nanoparticles (NPs) of MXenes with a lateral size of less than 20 nm [23]. MXene QDs take advantage of phenomena like edge effects and quantum confinement, which emerge at atomically thin dimensions, resulting in features such as fluorescence, tunable optoelectronic behavior, and photothermal conversion [23, 24]. These features render them especially useful for biomedical applications such as cellular imaging and optical biosensing. Most biocompatibility assessments of MXene QDs have reported nontoxicity against a wide range of cell types. $Ti_3C_2T_x$ QDs did not impact the viability of mouse RAW264.7 macrophages [24], rat mesenchymal stem cells [25], human peripheral blood mononuclear cells [25], human iPSC-derived fibroblasts [25], and BALB/c mice [26]. Likewise, Yu et al. [27] demonstrated that $Ti_3C_2T_x$ QDs were nontoxic to human embryonic kidney (HEK) 293 cells, HeLa cervical cancer cells, MCF-7 breast cancer cells, and U251 glioma cells. Rafieerad et al. [28] showed that $Ta_4C_3T_x$ QDs were biocompatible with human umbilical vein endothelial cells and did not induce intracellular ROS production, apoptosis, or membrane damage. Nb_2CT_x QDs did not significantly impact 3T3 fibroblast viability [29] and, in a similar manner, Mo_2CT_x QDs were not cytotoxic to mouse melanoma B16-F10 cells and human lung cancer A549 cells [30]. Using MTT assay results, Shao et al. [31] showed that titanium nitride (Ti_2NT_x) QDs had no significant impact on cell viability after 24-hour incubation with mouse 4T1 breast cancer cells, human embryonic kidney cells, and U87 glioma cells. The above results provide further evidence of biocompatibility of the MXene family of 2D nanomaterials.

In addition to their direct application, researchers have also explored the biocompatibility of MXenes combined with polymer matrices for biomedical use. This approach combines MXenes' unique physical and chemical properties with the functional properties offered by the polymers. Biocompatibility studies have shown that MXene addition to polymer scaffolds largely has no significant effect on cell viability. Awasthi et al. [32] found that mouse MC3T3-E1 pre-osteoblasts and 3T3 fibroblasts cultured on $Ti_3C_2T_x$ MXene-polycaprolactone (PCL) meshes for five days retained viability equivalent to that of the PCL only controls. Similar outcomes of *in vitro* biocompatibility have been reported for $Ti_3C_2T_x$ MXene composites with chitosan nanofibers [33], bacterial cellulose hydrogels [34], poly(lactic acid) membranes [35], polyvinyl alcohol films [36], poly-L-lactic acid nanofibers [37], intraocular lens acrylate polymers [11] and alginate bioprinting inks [38]. Overall, evidence suggests widespread MXene biocompatibility, whether in nanosheet, QD, or composite form.

Although the majority of current studies have classed MXenes as biocompatible, instances of MXene cytotoxicity have been cited in the literature [39–43] with

distinct differences found in the sensitivity of malignant and non-malignant cancerous cell lines to MXene incubation. As has been widely noted for graphene and graphene derivatives, differences in precursor quality, synthesis methods, product purity, material physicochemical properties as well as test protocols can impact the outcome of cytotoxicity assays [44, 45] and may explain some observed discrepancies. For example, Ozulumba et al. [10] showed that direct contact of DL $Ti_3C_2T_x$ MXene with DCFH (the active agent in the DCFH-DA assay probe commonly used to measure cellular ROS levels) produced DCF fluorescence signals leading to false positive results of ROS production. The authors mitigated this risk by labeling cells with the DCFH-DA probe for intracellular uptake before introducing MXene flakes thus limiting direct nanomaterial contact with the probe. This finding highlights the need to standardize methods, report on material-only controls, and alternative assay protocols in early *in vitro* cell-based assays to minimize the risk of assay interference and false positives.

26.3 MXenes, Inflammation, Infection, and the Wound Healing Response

MXenes have been investigated for potential use as antimicrobials and anti-inflammatory agents to limit infection, bind metabolic toxins, moderate hyper-inflammatory stimulus, and enable wound healing. Their structure allows intercalation of small molecules, surface group modifications, redox reactions, and a large surface area for adsorption of bioactive molecules such as slow-eluting drugs or biological metabolites for detoxification. This has been exemplified in early studies demonstrating adsorption of urea for dialysate regeneration in a portable kidney [9] and adsorption of inflammatory cytokines for suppression of hyperinflammation and life-threating infection [10] (Figure 26.3). Their potential as free radical scavengers [47] has also been considered in addition to interaction with SARS-CoV-2 viral protein activity for repressed viral transmission [15, 48].

MXenes provide a potential approach to target multi-drug-resistant bacterial strains that cannot be treated with currently available antibiotics. Studies have demonstrated dose-dependent inhibition of gram-negative *Escherichia coli* (*E. coli*) and gram-positive *Bacillus subtilis* (*B. subtilis*) by $Ti_3C_2T_x$ for water purification and reduced bio-fouling [46, 49]. In one study, DL $Ti_3C_2T_x$ induced significantly higher bacterial inhibition (>97%) in comparison to ML $Ti_3C_2T_x$ (<33.6%), Ti_3AlC_2 MAX phase (<18.3%), and graphene oxide (GO, 90%) [49]. Differences in cell membrane structure were proposed to account for the variable response of *B. subtilis* and *E. coli* to MXene. Impact on bacterial viability was hypothesized to be via physical damage to membrane integrity caused by the sharp edges of $Ti_3C_2T_x$. Contrasting results have been observed in other studies in which $Ti_3C_2T_x$

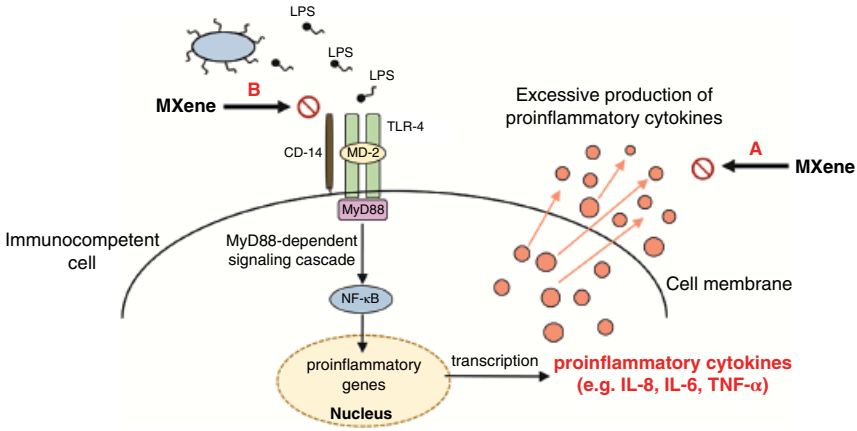


Figure 26.3 Potential mechanisms by which MXenes may impact inflammatory cytokine production in LPS-stimulated THP-1 monocytes. (a) MXenes may directly absorb pro-inflammatory cytokines secreted by the stimulated cells. (b) MXenes may inhibiting LPS binding to LBP and/or preventing binding of the LPS-LBP complex to the CD14 surface receptor, which subsequently prevents stimulation of membrane-bound Toll-like receptors. *Source:* Adapted from Solov'eva et al. [46].

was found to have no effect on *E. coli* growth characteristics in comparison to GO-silver (Ag) and Ag NPs, where significant reduction in bacterial viability was observed [10]. Different delamination and intercalation agents have been shown to alter the antimicrobial activity of MXenes [50]. This was demonstrated in a study where the time taken for 50% bacterial cell death (IC_{50}) to occur was decreased for $Ti_3C_2T_x$ by intercalation with potassium hydroxide (97 minutes), sodium hydroxide (80 minutes), hydrazine monohydrate (53 minutes), isopropylamine (76 minutes), and dimethyl sulfoxide (120 minutes) when compared to $Ti_3C_2T_x$ intercalated with water molecules (137 minutes). MXene flakes have also been used as supportive platforms for the aligned growth of other nanomaterials with antimicrobial activity. For example, the vertical growth of MnO_2 on $Ti_3C_2T_x$ flakes produced a 20% reduction in cell viability of both *B. subtilis* and *E. coli* compared to that of randomly oriented MnO_2 at the same concentration (100 $\mu g\,ml^{-1}$) [51]. Research to better understand the mechanisms by which different MXenes can be adapted to optimize any antimicrobial effects will expand their useful incorporation into technologies to more effectively target infection.

MXenes may also play a role in the development of advanced wound healing strategies for the treatment of non-healing wounds and patient pain management. Current strategies aim to produce a suitable wound dressing that maintains stability during healing, achieves good biocompatibility and antibacterial activity, creates a firm adhesion to the skin, and ideally heals the wound without antibiotics.

A multifunctional, self-healing, antibacterial, hemostatic scaffold was developed using $Ti_3C_2T_x$ as a dressing to treat infected wounds. The scaffolds consisted of branched poly(glycerol-ethylenimine) (PGE), $Ti_3C_2T_x$ MXene/polydopamine (PDA) nanosheets, and oxidized hyaluronic acid (HCHO) referred to as HPEM scaffolds [14]. On exposure to *E. coli*, *Staphylococcus aureus* (*S. aureus)*, and methicillin-resistant *S. aureus*, HPEM scaffolds showed a >98% inhibition of bacterial growth. The conductivity, flexibility, biocompatibility, and mechanical strength of $Ti_3C_2T_x$ within a wound dressing have also been exploited to investigate whether exogenous electrical stimulation (ES) could be used to improve wound healing [34]. Hydrogels consisting of regenerated bacterial cellulose (rBC) and $Ti_3C_2T_x$ were used to demonstrate improved wound healing following application of an ES potential of up to 100 mV. In a rat full-thickness skin defect model, rBC/$Ti_3C_2T_x$ hydrogel dressings demonstrated faster wound closure, neovascularization, and wound remodeling when compared to commercial controls following the application of 100 mV ES potential. Such studies indicate the useful incorporation of MXenes within wound dressings for rapid wound healing and inhibition of infection.

The properties of MXenes make them highly suited to tissue engineering applications where biomaterial scaffolds, in combination with bioactive molecules, are used to direct cell behavior in order to repair or replace damaged tissue. MXenes have been investigated for use in bone, skin, cardiovascular, and neural tissue applications. They have shown, for example, the potential to promote osteogenesis and osseointegration for improved bone graft success, the ability to support cardiomyocytes in an electrically conductive composite cardiac patch to treat damaged tissue following myocardial infarction and as a conductive, photothermal agent (PTA) to improve wound healing and reduce infection [14, 52, 53]. Further challenges exist in optimization of cell-material dynamics for tissue-specific, functional longevity.

26.4 MXenes Sensors and Biosensors in Diagnostics

Early-stage diagnosis of disease is essential for appropriate and timely treatment. By monitoring physiological changes, disease can be detected and interventions put in place at an earlier stage leading to improved outcomes [54]. Sensors and biosensors are key diagnostic tools used in medicine for the fundamental understanding and detection of diseases as well as the development of therapeutics. Achieving high selectivity and sensitivity is vital in the detection of diminutive physiological changes that may occur in diagnostic markers such as changes in pressure, analyte concentration, or bioelectrical signaling pathways. Furthermore, repeatable and cost effective, large-scale fabrication of sensors and biosensors is essential for commercialization of such devices. Nanomaterials are being

investigated to overcome many challenges in the fabrication of diagnostic tools that meet these high-performance requirements [55]. MXenes show potential in the development of sensor and biosensor technologies, combining excellent electronic, electrochemical, and optical properties [56, 57]. A number of advantages exist for MXenes over graphene and other 2D materials including their hydrophilic nature and rich surface chemistry, which enable easier biological receptor binding without complex post-processing steps [58]. A key challenge in current biosensing technology is the combination of flexible and highly sensitive transducers that can be readily incorporated for use. The flexibility and biocompatibility of MXenes enable their incorporation as durable sensors within wearable devices for point-of-care medicine. The large and growing family of MXenes provides different transition metal carbides and nitrides with tunable properties for the development of sensing and biosensing technologies for healthcare technology applications based on multiple mechanisms of transduction. These include mechanical, electrical, electrochemical, and optical sensing and biosensing (Figure 26.4).

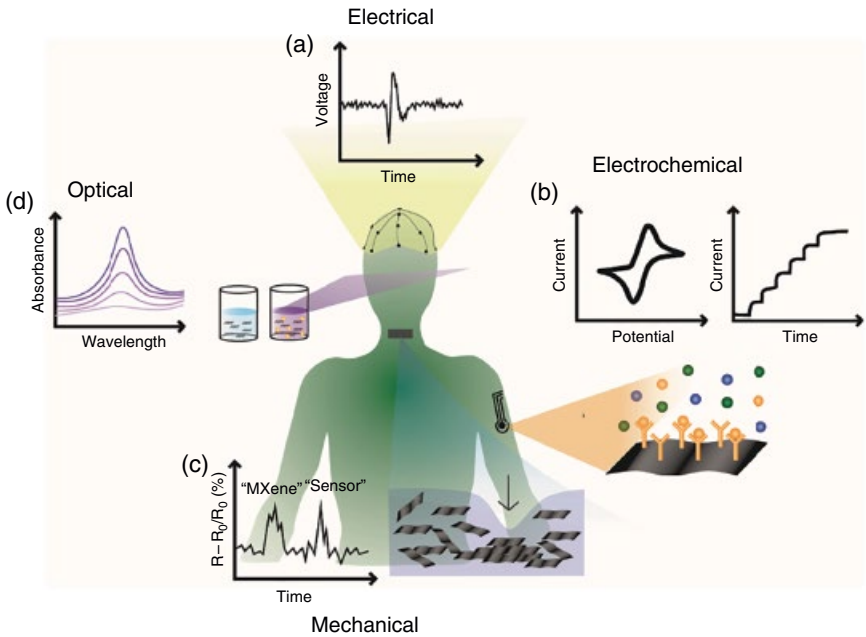


Figure 26.4 Types of MXene-sensors and biosensors (a) MXene electrical sensors for electroencephalograph recordings. *Source:* Adapted from Driscoll et al. [59]. (b) MXene skin-patch biosensors for the electrochemical detection of glucose in sweat. *Source:* Adapted from Lei et al. [60]. (c) MXene-based mechanical sensors for speech recognition. *Source:* Adapted from Li et al. [61]. (d) MXene optical biosensor for the visual detection of cholesterol. *Source:* Adapted from Li et al. [62].

26.4.1 MXene-based Mechanical Sensors

The ability to monitor human motion through mechanical sensing may be used to aid health and recovery through methods such as movement rehabilitation, speech recognition, sports performance, and pulse monitoring. This can be achieved with capacitive, piezoresistive, or piezoelectric mechanisms that rely on external mechanical stimuli to cause a change in electrical capacitance, resistivity, or charge formation, respectively [63]. The combined flexibility and electrical conductivity of MXenes make them suitable for these devices, allowing cyclic strain without loss of conductive properties over time [63]. A common fabrication approach for these sensors is the incorporation of MXenes as fillers in a composite in which the interlayer distance and orientation of MXene flakes transduce the stimuli into an electrical signal (Figure 26.4c). By changing MXene concentration and the mechanical properties of the second phase, it is possible to tailor the sensitivity, stretchability, and recyclability of the sensor for specific applications. An example is the poly(vinylidene fluoride) trifluoroetheylene/ML $Ti_3C_2T_x$ sensor, which achieved a gauge factor of 817.4 kPa^{-1} in the range of 0.072–0.74 kPa and 2213.68 kPa^{-1} in the range of 0.74–3.08 kPa^{-1} [61]. The broad pressure sensing range enabled recognition of speech, detection of knee movements, and pulse monitoring. By selecting a hydrophobic matrix, MXene oxidation from moisture was avoided resulting in long-term stability of up to 20 weeks. Furthermore, due to the easy processability of MXenes, a 10×10 array was developed to demonstrate spatial mapping, which is essential for human-machine interactions [64].

26.4.2 MXene-based Electrical Sensors

Bioelectric circuits that govern communication and activation within the human body may be mapped to enable an improved understanding of human physiology in addition to genetic, cardiac, muscular, and neurological diseases and injuries. The limitations of conventional materials currently used in multiarray electrodes to monitor these bioelectric patterns include stiffness, high impedance, and complex fabrication protocols [65]. $Ti_3C_2T_x$ electrode arrays with high spatiotemporal resolution have been developed for recording electroencephalography (Figure 26.4a), electromyography, electrocardiography, and electrooculography [66]. The highly conductive MXene electrodes (MXtrodes) show low impedance, which in turn increases the signal-to-noise ratio compared to conventional electrodes such as gold (Au) electrodes [59]. Their inherent pseudocapative behavior combined with high conductivity and excellent skin-matching mechanical properties, make MXenes safe from unwanted chemical reactions and remove the need to use a pre-electrolytic gel which causes skin irritation [67]. Due to the comparable performance of $Ti_3C_2T_x$ electrodes to those available commercially and their potential for high-scale fabrication,

MXtrodes are expected to be the next generation of epidermal electrodes for electrophysiology in healthcare and medical research [66].

Field-effect transistor (FET) sensors are another type of electrical sensors that can be used to detect biomarker concentrations within biological fluids. Since MXene electroactive surfaces are sensitive to environmental changes, FET-sensors have been developed using MXene as the semiconducting channel. For example, with an increase in dopamine concentration, dopamine molecules adsorbed onto MXene surfaces result in a change in conductance of the MXene-based FET channel [68]. The stable conductance of MXene channels was demonstrated by the linear relationship between voltage and current following Ohm's law, establishing the potential use of MXenes for other FET-sensing applications. In this manner, chemical perturbations beyond changes in biomolecule concentration, such as an increase or decrease in pH or ion fluctuations could be detected by MXene-based channels as has been demonstrated in similar applications [69, 70]. Furthermore, the tunable bandgap of different MXene types [4] makes a range of MXene based FET sensors possible.

26.4.3 MXene-based Electrochemical Sensors and Biosensors

One of the most common avenues to diagnose disease is using electroanalytical techniques to oxidize and reduce specific biomarkers found in bodily fluids including blood, tear fluid, and urine. Electrochemical techniques provide good sensitivity and low detection limits, which are essential for the small concentrations of a number of useful biomarkers found in the body. The highly conductive carbide core of MXenes as well as their outer transition metal oxide-like layers provide a unique surface for electron transfer reactions [71]. Therefore, MXene coatings and composites have been used as the working electrodes for a range of electrochemical techniques. For example, MXene-coated glassy carbon was used to reduce H_2O_2 through cyclic voltammetry and quantify it amperometrically at −500 mV vs. Ag|AgCl [72]. The limit of detection (LOD) achieved (0.7 nM) was comparable to one of the lowest LODs reported (0.3 nM) using a gold/platinum alloy NP-based electrochemical sensor [73]. Additionally, another member of the MXene family, V_2CT_x, has demonstrated enzyme-like behavior as a chemical catalyst for ROS [19]. This suggests the potential of other MXenes beyond $Ti_3C_2T_x$ to be used as catalysts for electrochemical sensing. Furthermore, fundamental studies of MXenes, as pseudocapacitive electrode materials, should be carried out to understand the range of analytes that can undergo different electron transfer mechanisms on MXene surfaces. Finally, selecting and electrochemically optimizing MXenes that can reach a more positive potential window may open avenues for the detection of multiple biomolecules that are redox active in this region.

The incorporation of biorecognition elements at the electrode surface is commonly done to provide analyte specificity. These sensors, known as biosensors, can also be developed when the analytes of interest are not easily oxidized or reduced at the bare electrode surface. The termination groups at MXene surfaces such as –O and –OH, which are rendered during the wet etch synthesis, facilitate the functionalization and modification of MXenes with recognition elements (Figure 26.4b) [57, 74, 75]. Physical adsorption is one approach for easy immobilization first demonstrated in 2015 with the encapsulation of hemoglobin (Hb) between the layers of the accordion-like structure of ML $Ti_3C_2T_x$ [75]. MXene biocompatibility and it is –OH-rich surface created a favorable microenvironment for enzyme stability which is key for the development of enzyme-based biosensors. Other recognition molecules as well as nanomaterials have been immobilized physically for the development of biosensors with improved performance. A common entrapment approach for the fabrication of these biosensors is with the aid of Nafion and chitosan in a one drop-casting step [60, 76]. Chemical bonding is an alternative method for immobilization. For example, the antibody anti-carcinoembryonic antigen (anti-CEA) was attached to MXene using (3-aminopropyl)triethoxysilane to introduce amino groups to the MXene surface that could covalently bond to the carboxyl group of anti-CEA [74]. Beyond developing approaches to attach recognition elements to the surface of MXenes for use in aptamer- [77], antibody- [78], DNA- [79], and enzyme-based [76] biosensors, it is essential to determine methods to control MXene surface terminations in order to tailor the interaction of MXenes with their biological surroundings.

26.4.4 MXene-based Optical Sensors and Biosensors

The transduction of biological events can also be investigated by the interaction of light with matter. Colorimetric sensors are one example, and these can be developed by taking advantage of the catalytic activity of MXenes. The catalysis of chemical reactions in the presence of the analyte of interest results in a change in color that can be measured through a spectrophotometer for biomarker quantification or for visual identification (Figure 26.4d). For example, a $Ti_3C_2T_x$/copper sulfide-nanocomposite was used as a nanoenzyme to catalyze the reaction of 3,3,5,5-tetramethylbenzinidine and H_2O_2 for cholesterol quantification in the presence of cholesterol oxidase [62]. The change in color from colorless to blue was measured and correlated to cholesterol concentration achieving an LOD of 1.9 μM. In a similar manner, $Ti_3C_2T_x$ sheets as nanoenzyme agents have been used in conjugation with CRISPR-Cas12a sensing technology for the sub-picomolar detection of Hepatitis B virus (HBV) [80].

The high light absorptivity of 2D MXene sheets throughout the ultraviolet-visible (UV-Vis) to near-infrared (NIR) region [3] allows their use as the quencher element within a Forster resonance energy transfer (FRET)-based biosensor, which relies on the transfer of excited energy. The mechanism can be exemplified by a MXene-based biosensor in which $Ti_3C_2T_x$ sheets were functionalized with a dual-signal-tagged chimeric DNA (dcDNA) probe. The probe contained a TAMRA-labeled MUC1 aptamer and FAM-labeled hairpin DNA for the quantification of cancer biomarkers MUC1 and miR-21 and the *in-situ* imaging of breast cancer cells [81]. Upon interaction of the probe and MUC1 or miR-21, Ti_3C_2 sheets, acting as fluorescent quenchers, were pushed away resulting in a recovery of probe fluorescence and lighting either the MUC1-containing membrane or the miR-21-containing cytoplasm [81]. MXene QDs (MQDs), in contrast to their 2D counterparts, exhibit fluorescence and therefore several MQDs, including Ti_3C_2 and Nb_2C, have been used as fluorescent probes in FRET-biosensors for the quantification of biomarkers such as glutathione [82].

Plasmonic biosensors are devices that use optical transduction for the detection of biomarkers. Since plasmons are highly sensitive to changes in their environment, surface plasmon resonance (SPR) biosensors are known to achieve low detection limits [83]. The change in reflective index can be correlated with molecular interactions happening at the surface of the film. MXene sheets and QDs, which are plasmonic materials with high charge concentrations, have been used to enhance the sensitivity of SPR biosensors for cancer biomarkers and the N-gene of SARS-CoV-2 [84]. The enhancement can be attributed to MXenes' hydrophilicity and large surface area allowing a more intimate molecular interaction with analytes present in the aqueous media as well as more interaction with the incident light. Surface-enhanced Raman Scattering (SERS) biosensors are another example of plasmonic biosensors that are known for their low, picomolar LOD and non-destructive nature. Due to their high metallic conductivity and surface plasmon resonance in the UV-Vis to NIR region, $Ti_3C_2T_x$ has been used as a SERS substrate in which the charge transfer and electromagnetic mechanism during analyte interactions resulted in SERS enhancement and enabled analyte quantification [85]. On this basis, a glucose oxidase/$Ti_3C_2T_x$/Au composite was used as a substrate for SERS determination of glucose concentration in the tears of diabetic patients [86]. Due to the quenching ability of 2D MXenes, the fluorescence background for SERS signals was reduced. The range of MXene substrates for SERS biosensing is still expanding. It is anticipated that MXenes' negatively charged surface will enable the enhancement of signals for the detection of positively charged molecules resulting in their sensitive quantification [85].

The ability of MXenes to transduce biological events into detectable signals through multiple mechanisms including electrical, electrochemical, and optical has been demonstrated for the development of sensors and biosensors.

Moreover, other transduction mechanisms combining several of the discussed properties have also been explored including photoelectrochemical [87], electrochemiluminescence [88], and photothermal mechanisms [89]. Due to their hydrophilicity, ease of handling, and facile processing, MXenes have been incorporated within composites including polymers and other nanomaterials for a synergy of properties for sensing. Often, the higher sensitivity and lower limits of detection achieved are attributed to the high conductivity and rich surface area of MXenes as well as their large surface area for immobilization of biorecognition elements. However, to further advance the field of MXenes in diagnostics, it is essential that studies report the performance of each component alone to fully understand the role of MXene in the sensing mechanism. As a result, research efforts could focus on enhancing these properties through, for example, optimization of synthesis methods, as was done to increase the conductivity of $Ti_3C_2T_x$ by one order of magnitude from initial reporting [90]. In this manner, improved understanding of the MXene properties enabling transduction tailored to each sensing and biosensing application would speed the development of these technologies, matching the high sensitivity and low LOD required for real-world devices.

26.5 MXenes in Photothermal Therapy

PTT is a non-invasive, electromagnetic radiation-based, anti-cancer treatment causing heat-induced tumor death by exposure to NIR light [91]. Within the NIR region, tissues absorb a negligible amount of light allowing deep penetration of tissue and providing a useful route for targeted therapeutic interventions. In PTT, PTAs are applied to localize the laser and transform light into heat to ablate the tumor through hyperthermia without damaging surrounding tissues [91]. MXenes are plasmonic materials and have shown potential as PTAs due to their tunable light absorption throughout the NIR region [3] and their relative cytocompatibility for healthy tissues [16].

Several key properties of MXenes have been determined as optimal for PTT in comparison with other nanomaterials. The extinction coefficient (ε), which, according to the Beer–Lambert [92] law is linearly correlated to the absorbance of a material over the light path length ($\varepsilon = C^*A/l$), is a relevant parameter for comparison of the capability of materials to effectively absorb light at certain wavelengths. Another parameter to demonstrate the competence of a material as a PTA is the material light-to-heat conversion efficiency (η), which can be determined by a study of the maximum heating temperature and the time constant for heat transfer. To date, the extinction coefficients and light-to-heat conversion efficiencies of several MXenes in the NIR window have been calculated. For example,

$Ti_3C_2T_x$ was determined to have an extinction coefficient of $\varepsilon = 25.21 g^{-1} cm^{-1}$ and $\eta = 30.6\%$ at 808 nm, which is higher than that of graphene oxide ($3.61 g^{-1} cm^{-1}$) and Au nanorods ($13.91 g^{-1} cm^{-1}$, 21%) [93]. The high light absorptivity of $Ti_3C_2T_x$ can be attributed to the wide plasmon peak in the NIR region, located at around 780 nm. Moreover, Liu et al. [12] proposed surface modification of $Ti_3C_2T_x$ with $Al(OH)_4^-$ to enhanced the localized surface plasmon resonance (LSPR). Their method consisted of supplying additive Al^{3+} during synthesis followed by tetramethylammonium hydroxide delamination to obtain highly stable Al oxo-anion terminations and overcome the loss of $Al(OH)_4^-$ reported for other conventional methods. The resulting $Al(OH)_4^-$ functionalized Ti_3C_2 showed a higher absorption at 800 nm compared to that of $Ti_3C_2T_x$, suggesting the enhancement of the LSPR effect and contributing to a higher extinction coefficient ($28.61 g^{-1} cm^{-1}$) than that reported previously for $Ti_3C_2T_x$. Furthermore, light absorption in the NIR-II window (1000–1350 nm), which allows deeper tissue-penetration compared to that of the NIR-I window (750–1000 nm) [21], was reported for Nb_2CT_x ($\varepsilon = 35.41 g^{-1} cm^{-1}$) with a higher conversion efficiency (46.65%) at 1064 nm compared to that (36.5%) at 808 nm. Moreover, MXenes showed good photothermal stability demonstrated by the lack of photobleaching after multiple cycles [94]. The reported studies demonstrate the successful use of MXenes as PTAs and support further research into the mechanisms that enable the enhancement of LSPR or efficiency coefficients through alternative synthesis methods or post-processing steps such as surface modification.

The application and efficiency of MXenes as PTAs has been demonstrated in different *in vitro* and *in vivo* models with and without NIR radiation. For example, Nb_2C for cancer phototherapeutics was exploited by Lin et al. [21] to efficiently ablate mouse tumor xenografts using PTT. The study treated Nb_2CT_x nanosheets with polyvinylpyrrolidone (PVP) for stability and improved biocompatibility. 4T1-tumor-bearing mice treated with Nb_2C-PVP, and NIR-I or NIR-II laser irradiation showed complete tumor eradication and survival of up to 50 days relative to 16–20 days in untreated mice. Nb_2C-PVP (12–200 $\mu g\,ml^{-1}$) showed no significant impact on cell survival with 4T1 breast and U87 glioma cancer cells for up to 48 hours and upon laser irradiation, a greater cancer cell death was found with an increase in laser energy. This was confirmed using an *in vivo* mouse model, which showed no significant changes in white and red blood cell count, hemoglobin, platelets, and mean corpuscular volume against controls supporting the conclusion that Nb_2C-PVP treatment did not disrupt normal physiology. Biochemical analysis showed no aberrant changes relative to the control mice with greater Nb content excreted from the treated mice. The performance of MXene QDs as PTAs has also been demonstrated. For example, Mo_2CT_x QDs ($\varepsilon = 4.424 l g^{-1} cm^{-1}$, $\eta = 42.9\%$) showed no toxicity without NIR irradiation toward mouse melanoma B16-10F cells and 90% cell death after 10 minutes of

808 nm laser radiation [30]. The PTA efficacy of Mo_2CT_x QDs *in vivo* was demonstrated through the inhibition of tumor growth in B16-10F tumor-bearing nude mice after 15 days compared to controls. Similar observations of significant tumor reduction were reported for studies using MXenes, such as $Ti_3C_2T_x$ [93] and $Ta_4C_3T_x$ [95], as PTAs upon NIR radiation.

Previously reported issues with effective PTT treatment include the lack of targeted delivery of the PTA, which subsequently reduces the efficiency of cancer ablation. To improve therapeutic effectiveness through better PTA distribution within cancer tissue, Zhou et al. [94] developed a composite bio-injection of Nb_2CT_x and the biocompatible plant protein, zein. The insolubility of zein in water due to its non-polar amino acid residues made the zein composite become solid upon solvent exchange between ethanol and water found in tumors. In this manner, Nb_2C remained trapped within the tumor allowing localized function and avoiding PTA leaching. *In vivo* investigation using 4T1 tumor model in Balb/c nude mice cells demonstrated the successful eradication of tumors through a tumor-confined, rapid increase in temperature of up to 70 °C upon composite irradiation, with significant tumor regression compared to controls. Another approach to ensure localized PTT treatment is through the specific internalization of PTA by cancerous cells. Studies using static cell culture have limited applicability to the tumor environment as they lack the stresses and fluid flow that impact NP uptake. Therefore, $Ti_3C_2T_x$ was investigated by Shurbaji [96] using a parallel plate flow chamber with a shear rate of 0.1 Dyn cm^{-2} to mimic a shear stress environment and optimize cancer cell uptake of the PTA for tumor ablation. As MXene uptake was not significantly influenced by shear stress, the authors suggested that internalization could be improved by surface modification. Additionally, other studies have shown the selective internalization and toxicity of Ti_2CT_x toward cancerous cell lines and have explained this by differences in cell metabolism and morphology [41]. Research to date has demonstrated the effective incorporation of MXenes for improved PTT efficiency and has highlighted MXenes' interaction with the microtumor environment for amelioration of PTT treatments.

Beyond, the integration of different MXene compositions in PTT for cancer treatment, MXene PTAs have been further exploited for other applications. For example, $Ti_3C_2T_x$ was used to treat infection, combining MXenes' structure with their efficient light-to-heat conversion capacity to disrupt the cell membrane of *S. aureus,* a bacterial pathogen commonly linked to hospital-acquired infections [97]. MXenes have also been used as PTAs for remote, nongenetic, cellular modulation to enhance neural signaling [98]. $Ti_3C_2T_x$ was used to stimulate dorsal root ganglion neurons (DRGs) by changing the cell membrane capacitance upon generation of thermal energy. Through the observed modulation of labeled-Ca^{2+} flux, the controlled action potential of dorsal root ganglion neurons was confirmed to

have subcellular resolution. MXenes combine properties of tunable wavelength absorption across the UV-Vis-NIR spectrum [3] with excellent photothermal conversion enabling further development as a PTA to treat a range of disorders from repression of tumorigenesis to treatment of infection and neural disorders.

26.6 MXenes in Theranostics

The properties of MXenes have enabled their use as dual-modality nanomaterials for theranostics, in which diagnostics and therapy are combined to reduce the time from disease diagnosis to treatment. For instance, MXene 2D sheets and QDs have been used to enable multiple bioimaging techniques during therapy. For example, upon NIR laser radiation, the thermoelastic expansion generated by MXene PTAs gives rise to acoustic waves that enable the *in vivo* non-invasive photoacoustic (PA) imaging of tissues during PTT [30, 99] . Temperature variations can also be monitored using infrared thermal cameras for tumor imaging for PTT assessment [100]. $Ta_4C_3T_x$ PTAs have shown enhanced X-ray computed tomography (CT) contrast for CT imaging due to the high atomic number of tantalum ($Z = 73$) and its high X-ray attenuation coefficient [95, 99] . The easy functionalization of MXenes using simple processing steps can also be used for tumor imaging. For example, MXenes including $Ti_3C_2T_x$ or $Ta_4C_3T_x$ were functionalized with paramagnetic NPs such as manganese oxide (MnO_x) [99, 101] and iron oxide [17] for tumor microenvironment-responsive enhanced magnetic resonance imaging (MRI). In this manner, the MXene sheets conjugated with paramagnetic NPs allowed multiple types of imaging including MRI, CT, and PA with simultaneous PTT to eradicate tumors in a 4T1 breast tumor-baring mouse model[99, 101]. MXene PTAs have also been used as platforms for incorporation of fluorescent imaging dyes. Xiang et al. [100] functionalized Nb_2C PTAs with Cy5.5, a NIR fluorescent dye, to study the *in vivo* bio-distribution and tumor accumulation after PTA injections [100]. In comparison to free Cy5.5 dye, the fluorescent signals of Cy5.5-Nb_2C PTA composite remained for up to 12 hours in the tumor, demonstrating enhanced permeability and the retention effect of MXene PTAs.

In addition, MXene agents have been developed for use in synergistic therapies. For example, Au NPs were grown on $Ti_3C_2T_x$ surface to develop PTAs that could also enhance the effectiveness of radiotherapy (RT) through the oxygenation of the tumor [102]. In this manner, the Au-Ti_3C_2 agents were dual-image guided using PA- and CT-imaging for PTT and RT tumor eradication in a 4T1 tumor-bearing mice model [102]. MXene PTAs have been used as platforms for drug delivery in combination with PTT. For example, $Ti_3C_2T_x$ was used in cationic, anti-cancer drug delivery using MXene as a combined PTA and anti-cancer drug-delivery platform [12]. $Ti_3C_2T_x$ sheets were mixed with doxorubicin hydrochloride (DOX) and

hyaluronic acid (HA), as an anti-cancer drug and tumor-targeting molecule, respectively. Although in the early stages of development, multiple MXene theranostics approaches have been demonstrated, combining several bioimaging techniques and synergistic therapies. Preliminary studies have shown the potential for image-guided therapy using MXene PTAs in models of breast, liver, colon, brain, and cervical cancer [103] but could also be applied to other disease processes.

26.7 Perspective on Future Outlook

The feasible use of MXenes within healthcare technologies is in the early stages of development and many potential applications have yet to be investigated. For example, the field of ophthalmology has yet to take advantage of the significant optoelectronic properties of MXenes. $Ti_3C_2T_x$ thin films have demonstrated low sheet resistance with high optical transparency corresponding to a high figure of merit, a dimensionless measure of the optoelectronic quality of transparent conductive electrodes (TCE) [104]. MXene TCEs meet the requirements of conductivity, optical transparency, and biocompatibility for use as flexible, hydrophilic, and sensitive sensors within ocular lens applications. They are capable of responding to changes in the ophthalmic environment via conductive signaling following detection of a change in, for example, pressure or analyte concentration. The first demonstration of this was in the use of $Ti_3C_2T_x$ in an adjustable focus lens to provide changes in dioptric range for an accommodative intraocular design [11] (Figure 26.5). Light-emitting diodes are another biomedical application in which MXenes could potentially be utilized for visual communication in virtual and augmented reality for point-of-care medicine. MXene TCEs could be incorporated to achieve comparable performance to that of commercially available LEDs with the added benefit of flexibility [105]. MXenes could also be considered for use in biomimetics as a platform for high-resolution, single-molecule sensing [106], in enzyme biomimicry, for example, to treat ROS-mediated inflammatory disease [19] or in artificial muscle and robotics technologies.

The multifunctionality of MXene, initially demonstrated in diverse fields including energy storage [107] and wireless communication [108] can also be applied in the healthcare setting. For example, as biodevices progress toward the Internet of Things, there is an expectation that they will be self-powered and able to communicate wirelessly with the user. One advantage of MXenes over other materials is their potential use to fabricate several components of a "smart" device including batteries [107], antennas [108], and interconnects to reduce contact resistance and improve device performance. In addition, MXenes can be incorporated into wearables through the knitting of MXene-coated yarns [109, 110]. Their high conductivity and hydrophilicity remove the need for post-processing steps

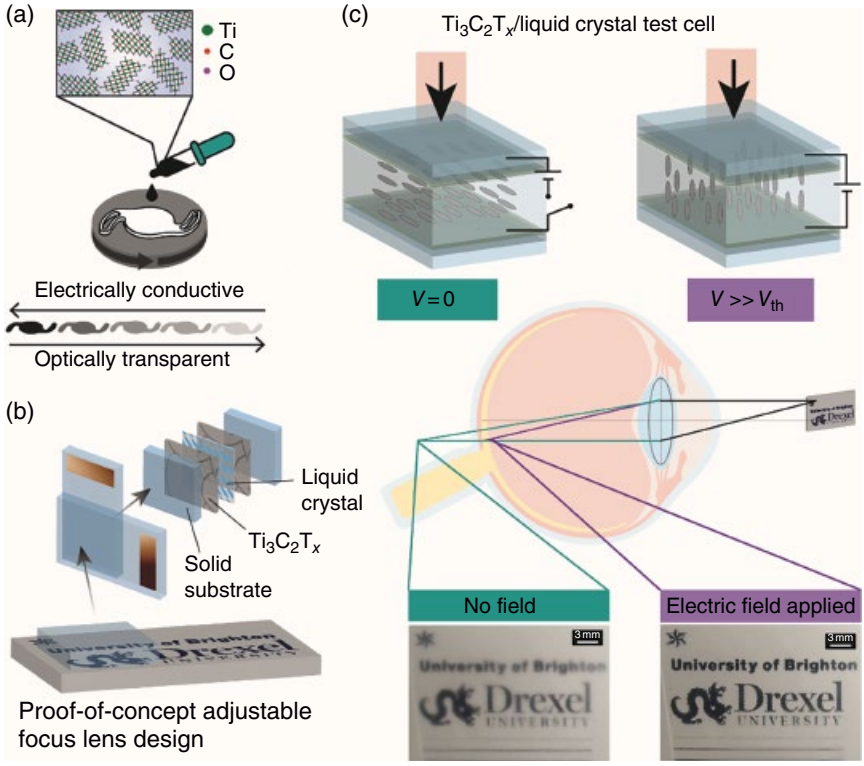


Figure 26.5 Schematic of an adjustable focus lens design. (a) A diagram of $Ti_3C_2T_x$ spin-coated on implantable intraocular lenses, with electrical conductivity and transparency retained for good optoelectronic performance and suitability in an adjustable focus lens design. (b) A diagram of a proof-of-concept design with liquid crystal confined between solid substrates spin-coated with $Ti_3C_2T_x$. (c) A diagram of the proof-of-concept $Ti_3C_2T_x$/liquid crystal test cell with and without an applied electrical field, demonstrating molecular reorientation of the liquid crystal molecules resulting in refractive index modulation and hence a change in focal length through the transparent and conductive ability of $Ti_3C_2T_x$, no field shows a digital image of the University of Brighton and Drexel University logos out of focus and then brought into focus following application of an electric field. *Source:* Ward et al. [11]/Reproduced from John Wiley & Sons, Inc./CC BY 4.0.

thus making device fabrication simple and cost-effective for large-scale device production. A number of knowledge gaps exist in the adaptation of MXene-based devices for real world use. These include a better understanding of the mechanisms by which MXene interacts with physiological pathways such as those enabling antibacterial and antiviral properties. Chemical stability in physiological media must also be improved to avoid MXene oxidation and allow improved functional longevity. This is currently addressed by surface modification or material

encapsulation within polymer composites or hydrogels to increase MXene stability for biomedical applications [111, 112]. Moreover, green routes for MXene synthesis and routes to effectively distinguish the properties of MXenes alone within composite materials via adequate controls are required. These and other considerations are best addressed within multidisciplinary teams to enable full exploitation of MXenes as tools to address emerging healthcare technology challenges.

Acknowledgments

The authors would like to thank Professor Yury Gogotsi (Drexel University) and the Drexel Nanomaterials Institute for their guidance and valuable discussions on the subjects discussed, Professor Bhavik A. Patel (University of Brighton) for useful discussions and shared perspectives on electrochemical sensing and biosensing and funding from Medical Research Council Training Grant MR/P015891/1, University Alliance Applied Biosciences for Health Training Grant, Santander International Research Scholarship, University of Brighton PhD studentship and Rayner Intraocular Lenses Ltd.

References

1 Aflori, M. (2021). Smart nanomaterials for biomedical applications—a review. *Nanomaterials* 11: 396.
2 Chimene, D., Alge, D.L., and Gaharwar, A.K. (2015). Two-dimensional nanomaterials for biomedical applications: emerging trends and future prospects. *Advanced Materials* 27: 7261–7284.
3 Maleski, K., Shuck, C.E., Fafarman, A.T., and Gogotsi, Y. (2020). The broad chromatic range of two-dimensional transition metal carbides. *Advanced Optical Materials* 9: 2001563.
4 Hantanasirisakul, K. and Gogotsi, Y. (2018). Electronic and optical properties of 2D transition metal carbides and nitrides (MXenes). *Advanced Materials* 30: 1804779.
5 Naguib, M., Mochalin, V.N., Barsoum, M.W., and Gogotsi, Y. (2014). 25th anniversary article: MXenes: a new family of two-dimensional materials. *Advanced Materials* 26: 992–1005.
6 Lukatskaya, M.R., Mashtalir, O., Ren, C.E. et al. (2013). Cation intercalation and high volumetric capacitance of two-dimensional titanium carbide. *Science* 341: 1502–1505.
7 Naguib, M., Kurtoglu, M., Presser, V. et al. (2011). Two-dimensional nanocrystals produced by exfoliation of Ti_3AlC_2. *Advanced Materials* 23: 4248–4253.

8 Oh, S.J., Kim, H., Liu, Y. et al. (2014). Incompatibility of silver nanoparticles with lactate dehydrogenase leakage assay for cellular viability test is attributed to protein binding and reactive oxygen species generation. *Toxicology Letters* 225: 422–432.

9 Meng, F., Seredych, M., Chen, C. et al. (2018). MXene sorbents for removal of urea from dialysate: a step toward the wearable artificial kidney. *ACS Nano* 12: 10518–10528.

10 Ozulumba, T., Ingavle, G., Gogotsi, Y., and Sandeman, S. (2021). Moderating cellular inflammation using 2-dimensional titanium carbide MXene and graphene variants. *Biomaterials Science* 9: 1805–1815.

11 Ward, E.J., Lacey, J., Crua, C. et al. (2020). 2D titanium carbide ($Ti_3C_2T_x$) in accommodating intraocular lens design. *Advanced Functional Materials* 30: 2000841.

12 Liu, G., Zou, J., Tang, Q. et al. (2017). Surface modified Ti_3C_2 MXene nanosheets for tumor targeting photothermal/photodynamic/chemo synergistic therapy. *ACS Applied Materials & Interfaces* 9: 40077–40086.

13 Nasrallah, G.K., Al-Asmakh, M., Rasool, K., and Mahmoud, K.A. (2018). Ecotoxicological assessment of $Ti_3C_2T_x$ (MXene) using a zebrafish embryo model. *Environmental Science. Nano* 5: 1002–1011.

14 Zhou, L., Zheng, H., Liu, Z. et al. (2021). Conductive antibacterial hemostatic multifunctional scaffolds based on $Ti_3C_2T_x$ MXene nanosheets for promoting multidrug-resistant bacteria-infected wound healing. *ACS Nano* 15: 2468–2480.

15 Unal, M.A., Bayrakdar, F., Fusco, L. et al. (2021). 2D MXenes with antiviral and immunomodulatory properties: a pilot study against SARS-CoV-2. *Nano Today* 38: 101136.

16 Scheibe, B., Wychowaniec, J.K., Scheibe, M. et al. (2019). Cytotoxicity assessment of Ti-Al-C based MAX phases and $Ti_3C_2T_x$ MXenes on human fibroblasts and cervical cancer cells. *ACS Biomaterials Science & Engineering* 5: 6557–6569.

17 Liu, Z., Lin, H., Zhao, M. et al. (2018). 2D superparamagnetic tantalum carbide composite MXenes for efficient breast-cancer theranostics. *Theranostics* 8: 1648–1664.

18 Rafieerad, A., Amiri, A., Sequiera, G.L. et al. (2021). Development of fluorine-free tantalum carbide MXene hybrid structure as a biocompatible material for supercapacitor electrodes. *Advanced Functional Materials* 31: 2100015.

19 Feng, W., Han, X., Hu, H. et al. (2021). 2D vanadium carbide MXenzyme to alleviate ROS-mediated inflammatory and neurodegenerative diseases. *Nature Communications* 12: 1–16.

20 Feng, W., Wang, R., Zhou, Y. et al. (2019). Ultrathin molybdenum carbide MXene with fast biodegradability for highly efficient theory-oriented photonic tumor hyperthermia. *Advanced Functional Materials* 29: 1901942.

21 Lin, H., Gao, S., Dai, C. et al. (2017). A two-dimensional biodegradable niobium carbide (MXene) for photothermal tumor eradication in NIR-I and NIR-II biowindows. *Journal of the American Chemical Society* 139: 16235–16247.

22 Han, X., Jing, X., Yang, D. et al. (2018). Therapeutic mesopore construction on 2D Nb_2C MXenes for targeted and enhanced chemo-photothermal cancer therapy in NIR-II biowindow. *Theranostics* 8: 4491–4508.

23 Guan, Q., Ma, J., Yang, W. et al. (2019). Highly fluorescent Ti_3C_2 MXene quantum dots for macrophage labeling and Cu^{2+} ion sensing. *Nanoscale* 11: 14123–14133.

24 Xue, Q., Zhang, H., Zhu, M. et al. (2017). Photoluminescent Ti_3C_2 MXene quantum dots for multicolor cellular imaging. *Advanced Materials* 29: 1604847.

25 Rafieerad, A., Yan, W., Sequiera, G.L. et al. (2019). Application of Ti_3C_2 MXene quantum dots for immunomodulation and regenerative medicine. *Advanced Healthcare Materials* 8: 1900569.

26 Li, X., Liu, F., Huang, D. et al. (2020). Nonoxidized MXene quantum dots prepared by microexplosion method for cancer catalytic therapy. *Advanced Functional Materials* 30: 2000308.

27 Yu, X., Cai, X., Cui, H. et al. (2017). Fluorine-free preparation of titanium carbide MXene quantum dots with high near-infrared photothermal performances for cancer therapy. *Nanoscale* 9: 17859–17864.

28 Rafieerad, A., Yan, W., Alagarsamy, K.N. et al. (2021). Fabrication of smart tantalum carbide MXene quantum dots with intrinsic immunomodulatory properties for treatment of allograft vasculopathy. *Advanced Functional Materials* 31: 2106786.

29 Yang, G., Zhao, J., Yi, S. et al. (2020). Biodegradable and photostable Nb_2C MXene quantum dots as promising nanofluorophores for metal ions sensing and fluorescence imaging. *Sensors and Actuators, B Chemical* 309: 127735.

30 Dai, W., Dong, H., and Zhang, X. (2018). A semimetal-like molybdenum carbide quantum dots photoacoustic imaging and photothermal agent with high photothermal conversion efficiency. *Materials* 11: 1776.

31 Shao, J., Zhang, J., Jiang, C. et al. (2020). Biodegradable titanium nitride MXene quantum dots for cancer phototheranostics in NIR-I/II biowindows. *Chemical Engineering Journal* 400: 126009.

32 Awasthi, G.P., Maharjan, B., Shrestha, S. et al. (2020). Synthesis, characterization, and biocompatibility evaluation of polycaprolactone–MXene electrospun fibers. *Colloids Surfaces A: Physicochemical and Engineering Aspects* 586: 124282.

33 Mayerberger, E.A., Street, R.M., McDaniel, R.M. et al. (2018). Antibacterial properties of electrospun $Ti_3C_2T_z$ (MXene)/chitosan nanofibers. *RSC Advances* 8: 35386–35394.

34 Mao, L., Hu, S., Gao, Y. et al. (2020). Biodegradable and electroactive regenerated bacterial cellulose/MXene ($Ti_3C_2T_x$) composite hydrogel as wound dressing for

accelerating skin wound healing under electrical stimulation. *Advanced Healthcare Materials* 9: 2000872.

35 Chen, K., Chen, Y., Deng, Q. et al. (2018). Strong and biocompatible poly (lactic acid) membrane enhanced by $Ti_3C_2T_z$ (MXene) nanosheets for guided bone regeneration. *Materials Letters* 229: 114–117.

36 Zhao, L., Wang, L., Zheng, Y. et al. (2021). Highly-stable polymer-crosslinked 2D MXene-based flexible biocompatible electronic skins for in vivo biomonitoring. *Nano Energy* 84: 105921.

37 Huang, R., Chen, X., Dong, Y. et al. (2020). MXene composite nanofibers for cell culture and tissue engineering. *ACS Applied Bio Materials* 3: 2125–2131.

38 Rastin, H., Zhang, B., Mazinani, A. et al. (2020). 3D bioprinting of cell-laden electroconductive MXene nanocomposite bioinks. *Nanoscale* 12: 16069–16080.

39 Jastrzębska, A.M., Szuplewska, A., Wojciechowski, T. et al. (2017). In vitro studies on cytotoxicity of delaminated Ti_3C_2 MXene. *Journal of Hazardous Materials* 339: 1–8.

40 Rozmysłowska-Wojciechowska, A., Szuplewska, A., Wojciechowski, T. et al. (2020). A simple, low-cost and green method for controlling the cytotoxicity of MXenes. *Materials Science and Engineering: C* 111: 110790.

41 Szuplewska, A., Kulpińska, D., Dybko, A. et al. (2019). 2D Ti_2C (MXene) as a novel highly efficient and selective agent for photothermal therapy. *Materials Science and Engineering: C* 98: 874–886.

42 Szuplewska, A., Wojciechowska, A.R., Poźniak, S. et al. (2019). Multilayered stable 2D nano-sheets of Ti_2NT_x MXene: synthesis, characterization, and anticancer activity. *Journal of Nanobiotechnology* 17: 114.

43 Wu, W., Ge, H., Zhang, L. et al. (2020). Evaluating the cytotoxicity of Ti_3C_2 MXene to neural stem cells. *Chemical Research in Toxicology* 33: 2953–2962.

44 Guo, X. and Mei, N. (2014). Assessment of the toxic potential of graphene family nanomaterials. *Journal of Food and Drug Analysis* 22: 105–115.

45 Ou, L., Song, B., Liang, H. et al. (2016). Toxicity of graphene-family nanoparticles: a general review of the origins and mechanisms. *Particle and Fibre Toxicology* 13: 57.

46 Solov'eva, T., Davydova, V., Krasikova, I., and Yermak, I. (2013). Marine compounds with therapeutic potential in gram-negative sepsis. *Marine Drugs* 11: 2216–2229.

47 Qi, Z., Wang, S., Li, Y. et al. (2021). Scavenging activity and reaction mechanism of $Ti_3C_2T_x$ MXene as a novel free radical scavenger. *Ceramics International* 47: 16555–16561.

48 Gordon, D., Jang, G., Bouhaddou, M. et al. (2020). A SARS-CoV-2 protein interaction map reveals targets for drug repurposing. *Nature* 583: 459–468.

49 Rasool, K., Helal, M., Ali, A. et al. (2016). Antibacterial activity of $Ti_3C_2T_x$ MXene. *ACS Nano* 10: 3674–3684.

50 Rajavel, K., Shen, S., Ke, T., and Lin, D. (2019). Achieving high bactericidal and antibiofouling activities of 2D titanium carbide ($Ti_3C_2T_x$) by delamination and intercalation. *2D Materials* 6: 35040.

51 Alimohammadi, F., Sharifian Gh., M., Attanayake, N.H. et al. (2018). Antimicrobial properties of 2D MnO_2 and MoS_2 nanomaterials vertically aligned on graphene materials and Ti_3C_2 MXene. *Langmuir* 34: 7192–7200.

52 Basara, G., Saeidi-Javash, M., Ren, X. et al. (2022). Electrically conductive 3D printed $Ti_3C_2T_x$ MXene-PEG composite constructs for cardiac tissue engineering. *Acta Biomaterialia* 139: 179–189.

53 Mi, X., Su, Z., Fu, Y. et al. (2022). 3D printing of Ti_3C_2-MXene-incorporated composite scaffolds for accelerated bone regeneration. *Biomedical Materials* 17: 035002.

54 Mehrotra, P. (2016). Biosensors and their applications – a review. *Journal of Oral Biology and Craniofacial Research* 6: 153–159.

55 Welch, E.C., Powell, J.M., Clevinger, T.B. et al. (2021). Advances in biosensors and diagnostic technologies using nanostructures and nanomaterials. *Advanced Functional Materials* 31: 2104126.

56 Bhardwaj, S.K., Singh, H., Khatri, M. et al. (2022). Advances in MXenes-based optical biosensors: a review. *Biosensors & Bioelectronics* 202: 113995.

57 Kalambate, P.K., Gadhari, N.S., Li, X. et al. (2019). Recent advances in MXene–based electrochemical sensors and biosensors. *Trends in Analytical Chemistry* 120: 115643.

58 Alhabeb, M., Maleski, K., Anasori, B. et al. (2017). Guidelines for synthesis and processing of two-dimensional titanium carbide ($Ti_3C_2T_x$ MXene). *Chemistry of Materials* 29: 7633–7644.

59 Driscoll, N., Richardson, A.G., Maleski, K. et al. (2018). Two-dimensional Ti_3C_2 MXene for high-resolution neural interfaces. *ACS Nano* 12: 10419–10429.

60 Lei, Y., Zhao, W., Zhang, Y. et al. (2019). A MXene-based wearable biosensor system for high-performance in vitro perspiration analysis. *Small* 15: 1–10.

61 Li, L., Fu, X., Chen, S. et al. (2020). Hydrophobic and stable MXene-polymer pressure sensors for wearable electronics. *ACS Applied Materials & Interfaces* 12: 15362–15369.

62 Li, Y., Kang, Z., Kong, L. et al. (2019). MXene-Ti_3C_2/CuS nanocomposites: enhanced peroxidase-like activity and sensitive colorimetric cholesterol detection. *Materials Science and Engineering: C* 104: 110000.

63 Lei, D., Liu, N., Su, T. et al. (2020). Research progress of MXenes-based wearable pressure sensors. *APL Materials* 8: 110702.

64 Yin, R., Wang, D., Zhao, S. et al. (2021). Wearable sensors-enabled human–machine interaction systems: from design to application. *Advanced Functional Materials* 31: 202008936.

65 Driscoll, N., Maleski, K., Richardson, A.G. et al. (2020). Fabrication of Ti_3C_2 MXene microelectrode arrays for in vivo neural recording. *Journal of Visualized Experiments* 12: 1–9.

66 Driscoll, N., Erickson, B., Murphy, B.B. et al. (2020). MXtrodes: MXene-infused bioelectronic interfaces for multiscale electrophysiology and stimulation. *Science Translational Medicine* 13: 433237.

67 Murphy, B.B., Mulcahey, P.J., Driscoll, N. et al. (2020). A gel-free $Ti_3C_2T_x$-based electrode array for high-density, high-resolution surface electromyography. *Advanced Materials and Technologies* 5: 1–10.

68 Xu, B., Zhu, M., Zhang, W. et al. (2016). Ultrathin MXene-micropattern-based field-effect transistor for probing neural activity. *Advanced Materials* 28: 3333–3339.

69 Liu, C., Wei, X., Hao, S. et al. (2021). Label-free, fast response, and simply operated silver ion detection with a $Ti_3C_2T_x$ MXene field-effect transistor. *Analytical Chemistry* 93: 8010–8018.

70 Liu, C., Hao, S., Chen, X. et al. (2020). High anti-interference $Ti_3C_2T_x$ MXene field-effect-transistor-based alkali indicator. *ACS Applied Materials & Interfaces* 12: 32970–32978.

71 Lukatskaya, M.R., Kota, S., Lin, Z. et al. (2017). Ultra-high-rate pseudocapactive energy storage in two-dimensional transition metal carbides. *Nature Energy* 2: 17105.

72 Lorencova, L., Bertok, T., Dosekova, E. et al. (2017). Electrochemical performance of $Ti_3C_2T_x$ MXene in aqueous media: towards ultrasensitive H_2O_2 sensing. *Electrochimica Acta* 235: 471–479.

73 Xiao, F., Zhao, F., Zhang, Y. et al. (2009). Ultrasonic electrodeposition of gold-platinum alloy nanoparticles on ionic liquid – chitosan composite film and their application in fabricating nonenzyme hydrogen peroxide sensors. *Journal of Physical Chemistry C* 113: 849–855.

74 Kumar, S., Lei, Y., Alshareef, N.H. et al. (2018). Biofunctionalized two-dimensional Ti_3C_2 MXenes for ultrasensitive detection of cancer biomarker. *Biosensors & Bioelectronics* 121: 243–249.

75 Wang, F., Yang, C., Duan, C.Y. et al. (2015). An organ-like titanium carbide material (MXene) with multilayer structure encapsulating hemoglobin for a mediator-free biosensor. *Journal of the Electrochemical Society* 162: B16–B21.

76 Rakhi, R.B., Nayuk, P., Xia, C., and Alshareef, H.N. (2016). Novel amperometric glucose biosensor based on MXene nanocomposite. *Scientific Reports* 6: 36422.

77 Vajhadin, F., Mazloum-Ardakani, M., Shahidi, M. et al. (2022). MXene-based cytosensor for the detection of HER2-positive cancer cells using $CoFe_2O_4$@Ag magnetic nanohybrids conjugated to the HB5 aptamer. *Biosensors & Bioelectronics* 195: 113626.

78 Wu, Q., Li, N., Wang, Y. et al. (2019). A 2D transition metal carbide MXene-based SPR biosensor for ultrasensitive carcinoembryonic antigen detection. *Biosensors & Bioelectronics* 144: 111697.

79 Zheng, J., Wang, B., Ding, A. et al. (2018). Synthesis of MXene/DNA/Pd/Pt nanocomposite for sensitive detection of dopamine. *Journal of Electroanalytical Chemistry* 816: 189–194.

80 Tao, Y., Yi, K., Wang, H. et al. (2022). CRISPR-Cas12a-regulated DNA adsorption and metallization on MXenes as enhanced enzyme mimics for sensitive colorimetric detection of hepatitis B virus DNA. *Journal of Colloid and Interface Science* 613: 406–414.

81 Wang, S., Wei, S., Wang, S. et al. (2019). Chimeric DNA-functionalized titanium carbide MXenes for simultaneous mapping of dual cancer biomarkers in living cells. *Analytical Chemistry* 91: 1651–1658.

82 Xu, X., Zhang, H., Diao, Q. et al. (2020). Highly sensitive fluorescent sensing for intracellular glutathione based on Ti_3C_2 quantum dots. *Journal of Materials Science: Materials in Electronics* 31: 175–181.

83 Nguyen, H.H., Lee, S.H., Lee, U.J. et al. (2019). Immobilized enzymes in biosensor applications. *Materials* 12: 1–34.

84 Chen, R., Kan, L., Duan, F. et al. (2021). Surface plasmon resonance aptasensor based on niobium carbide MXene quantum dots for nucleocapsid of SARS-CoV-2 detection. *Microchimica Acta* 188: 316.

85 Sarycheva, A., Makaryan, T., Maleski, K. et al. (2017). Two-dimensional titanium carbide (MXene) as surface-enhanced Raman scattering substrate. *Journal of Physical Chemistry C* 121: 19983–19988.

86 Cui, X., Li, J., Li, Y. et al. (2022). Detection of glucose in diabetic tears by using gold nanoparticles and MXene composite surface-enhanced Raman scattering substrates. *Spectrochimica Acta – Part A Molecular and Biomolecular Spectroscopy* 266: 120432.

87 Jiang, G., Yang, R., Liu, J. et al. (2022). Two-dimensional Ti_2C MXene-induced photocurrent polarity switching photoelectrochemical biosensing platform for ultrasensitive and selective detection of soluble CD146. *Sensors and Actuators B: Chemical* 350: 130859.

88 Zhang, K., Fan, Z., Yao, B. et al. (2021). Exploring the trans-cleavage activity of CRISPR-Cas12a for the development of a MXene based electrochemiluminescence biosensor for the detection of Siglec-5. *Biosensors & Bioelectronics* 178: 113019.

89 Cai, G., Yu, Z., Tong, P., and Tang, D. (2019). Ti_3C_2 MXene quantum dot-encapsulated liposomes for photothermal immunoassays using a portable near-infrared imaging camera on a smartphone. *Nanoscale* 11: 15659–15667.

90 Mathis, T.S., Maleski, K., Goad, A. et al. (2021). Modified MAX phase synthesis for environmentally stable and highly conductive Ti_3C_2 MXene. 15: 6420–6429.

91 Jaque, D., Maestro, L.M., del Rosal, B. et al. (2014). Nanoparticles for photothermal therapies. *Nanoscale* 6: 9494–9530.

92 Swinehart, D.F. (1962). The Beer-Lambert law. *Journal of Chemical Education* 39: 333–335.

93 Lin, H., Wang, X., Yu, L. et al. (2017). Two-dimensional ultrathin MXene ceramic nanosheets for photothermal conversion. *Nano Letters* 17: 384–391.

94 Zhou, B., Pu, Y., Lin, H. et al. (2020). In situ phase-changeable 2D MXene/Zein bio-injection for shear wave elastography-guided tumor ablation in NIR-II bio-window. *Journal of Materials Chemistry B* 8: 5257–5266.

95 Lin, H., Wang, Y., Gao, S. et al. (2018). Theranostic 2D tantalum carbide (MXene). *Advanced Materials* 30: 201703284.

96 Shurbaji, S., Manaph, N.P.A., Ltaief, S.M. et al. (2021). Characterization of MXene as a cancer photothermal agent under physiological conditions. *Frontiers in Nanotechnology* 3: 689718.

97 Wang, X., Yao, M., Ma, L. et al. (2021). NIR-responsive Ti_3C_2 MXene colloidal solution for curing purulent subcutaneous infection through the 'nanothermal blade' effect. *Advanced Healthcare Materials* 10: 2100392.

98 Wang, Y., Garg, R., Hartung, J.E. et al. (2021). $Ti_3C_2T_x$ MXene flakes for optical control of neuronal electrical activity. *ACS Nano* 15: 14662–14671.

99 Dai, C., Chen, Y., Jing, X. et al. (2017). Two-dimensional tantalum carbide (MXenes) composite nanosheets for multiple imaging-guided photothermal tumor ablation. *ACS Nano* 11: 12696–12712.

100 Xiang, H., Lin, H., Yu, L., and Chen, Y. (2019). Hypoxia-irrelevant photonic thermodynamic cancer nanomedicine. *ACS Nano* 13: 2223–2235.

101 Dai, C., Lin, H., Xu, G. et al. (2017). Biocompatible 2D titanium carbide (MXenes) composite nanosheets for pH-responsive MRI-guided tumor hyperthermia. *Chemistry of Materials* 29: 8637–8652.

102 Tang, W., Dong, Z., Zhang, R. et al. (2019). Multifunctional two-dimensional core-shell MXene@Gold nanocomposites for enhanced photo-radio combined therapy in the second biological window. *ACS Nano* 13: 284–294.

103 Fusco, L., Gazzi, A., Peng, G. et al. (2020). Graphene and other 2D materials: a multidisciplinary analysis to uncover the hidden potential as cancer theranostics. *Theranostics* 10: 5435–5488.

104 Hantanasirisakul, K., Zhao, M.-Q., Urbankowski, P. et al. (2016). Fabrication of $Ti_3C_2T_x$ MXene transparent thin films with tunable optoelectronic properties. *Advanced Electronic Materials* 2: 1600050.

105 Ahn, S., Han, T.-H., Maleski, K. et al. (2020). A 2D titanium carbide MXene flexible electrode for high-efficiency light-emitting diodes. *Advanced Materials* 32: 202000919.

106 Mojtabavi, M., Vahidmohammadi, A., Liang, W. et al. (2019). Single-molecule sensing using nanopores in two-dimensional transition metal carbide (MXene) membranes. *ACS Nano* 13: 3042–3053.

107 Anasori, B., Lukatskaya, M.R., and Gogotsi, Y. (2017). 2D metal carbides and nitrides (MXenes) for energy storage. *Nature Reviews Materials* 2: 16098.

108 Sarycheva, A., Polemi, A., Liu, Y. et al. (2018). 2D titanium carbide (MXene) for wireless communication. *Science Advances* 4: eeau0920.

109 Levitt, A., Zhang, J., Dion, G. et al. (2020). MXene-based fibers, yarns, and fabrics for wearable energy storage devices. *Advanced Functional Materials* 30: 202000739.

110 Uzun, S., Seyedin, S., Stoltzfus, A.L. et al. (2019). Knittable and washable multifunctional MXene-coated cellulose yarns. *Advanced Functional Materials* 29: 1905015.

111 George, S.M. and Kandasubramanian, B. (2020). Advancements in MXene-polymer composites for various biomedical applications. *Ceramics International* 46: 8522–8535.

112 Zhang, Y.-Z., El-Demellawi, J.K., Jiang, Q. et al. (2020). MXene hydrogels: fundamentals and applications. *Chemical Society Reviews* 49: 7229–7251.

Part V

Conclusions and Perspectives

27

Summary and Outlook

Chuanfang Zhang[1] *and Michael Naguib*[2]

[1] *College of Materials Science and Engineering, Sichuan University, Chengdu, Sichuan, China*
[2] *Department of Physics and Engineering Physics, Tulane University, New Orleans, LA, USA*

Since the discovery of two-dimensional (2D) transition metal carbides and nitrides, namely, MXenes, in 2011, tremendous efforts either focusing on the synthesis and characterizations, or finding new applications, have been dedicated to this wonder class of 2D material. Together with graphene, transition metal dichalcogenide, hydroxide, oxide, boron nitride, etc., the discovery of MXenes has broadened the knowledge of 2D materials family and greatly pushed the limits of their attractive properties, which have led to practical applications.

In the atomic structure, $n+1$ ($n = 1$–4) layers of early transition metals (M) are interleaved with n layers of carbon or nitrogen (X) with terminations (T_x) on the surface of the single-layer nanosheets [1]. Therefore, MXene can be described in a general formula of $M_{n+1}X_nT_x$. It is worth noting that these terminations are bonded to the outer M layers, with their type and amount can be precisely controlled either through different MXene etching routes, or etching time. By varying the selection of M and X as well as tuning their atomic ratios and surface chemistry, there should exist at least 100 stoichiometric MXene compositions and unlimited MXene solid solutions [2]. The rich family of MXenes thus offers unique properties covering outstanding electrical, mechanical, electrochemical, electromechanical, and optical properties, and finds applications including electrochemical energy storage, superconductivity, environmental protection, to electromagnetic interference shielding, radio frequency identification, etc. [3]. These promising applications of MXenes are introduced in Chapters 19–27.

The prerequisite for the full achievement of these outstanding properties lies in the high quality of MXenes. Here the definition of high quality refers to large

Transition Metal Carbides and Nitrides (MXenes) Handbook: Synthesis, Processing, Properties and Applications, First Edition. Edited by Chuanfang Zhang and Michael Naguib.
© 2024 John Wiley & Sons, Inc. Published 2024 by John Wiley & Sons, Inc.

crystalline size, absence of secondary phase, lack of pin holes or defects, and narrow size distribution. To achieve high-quality MXenes, one needs to re-innovate the synthesize route and avoid aggressive etching. HF etching is known for the efficiency in producing MXenes from various MAX or non-MAX phases; however, the as-synthesized MXenes possess abundant pin-holes and crystalline defects, [4] which dramatically degrade MXenes stability at ambient conditions. Replacing HF with *in-situ* HF forming route, mainly referring to the LiF-HCl (so-called MILD route) and the NH_4HF_2 etching, which *in-situ* produce HF during etching and the intercalation of Li^+ or NH_4^+/NH_3 in the interlayers, respectively [5]. Solids obtained from the *in-situ* etching routes generally possess a higher crystalline quality compared to that of HF-route. Additionally, the intercalated ions facilitate the delamination of multilayered MXenes into predominantly single-layered MXenes, allowing the direct formation of colloidal solutions when dispersed in good solvents [6]. These MXene dispersions or inks enable subsequent solution processing at ease, such as printing (inkjet printing, extrusion [or direct ink writing, DIW] printing, and aerosol-jet printing) [7] and coating (blade coating, dip coating, slot-die coating, spray coating, and so on), [8] as described in detail in Chapters 10–15.

On the other hand, when replacing the etchant with Lewis acidic molten salts, MXenes with uniform terminations can be achieved, which is impossible in the conventional MXene synthesis route. Huang's group has been dedicated to the molten salt etching of MXenes for years, demonstrating that MAX and MXenes can be structurally edited using the molten salt chemical scissors [9, 10]. Molten salt etching represents the quasi-solid to solid synthesis route, while the purity of the resultant MXenes is high. Guidelines on the MXene precursors, F-based synthesis of MXenes, low-temperature F-free synthesis, and on the molten salts etching of MXenes, as well as the subsequent MXene intercalation chemistry, can be found in Chapters 2–6.

Unlike the liquid-to-solid or quasi-solid-to-solid synthesis route, the direct chemical vapor deposition of MXene represents a brand new MXene synthesis method. The recent work from Talapin's group shows that through using $TiCl_4$ as the titanium source and CH_4 as the carbon source, by reacting this material at 950 °C, Ti_2CCl_2 can be directly achieved on the Ti foil [11]. Similarly, when replacing CH_4 with N_2, Ti_2NCl_2 can be obtained at 640 °C. Importantly, the chemical vapor deposited MXenes are vertically aligned on the metal foil, facilitating the rapid ion diffusion kinetics thus allowing a high charge–discharge rate when used for Li-ion battery anode. This work is a major milestone for the MXene field, highlighting the importance of the innovation in the material synthesis for high-performance application such as electrochemical energy storage.

These abovementioned MXenes synthesis route largely determine their properties. For instance, when processing MXene colloidal solutions into

transparent conductive films, smaller flake size results in more junctions (where electrons have to overcome before transporting to the next flake), thus leading to a much higher sheet resistance compared to films consisting of larger flake size with less junctions. Similarly, at a given flake size, flakes with less pin-holes or defects exhibit a much higher conductivity compared to that of flakes with intensive defects, which is quite common in the HF-etched MXenes. Moreover, the defects density also strongly accelerates the flakes degradation, leading to a much compromised chemical stability when dispersed in water. Methods aiming to prolong their shelf life and guidelines on MXene handling, as well as exploring new properties in multi-M MXenes, are summarized in Chapters 7–9. In addition, first-principle theoretical predictions and simulations on the work function, density of state, Femi level, etc. are also important in exploring new MXenes that are thermodynamically stable and their corresponding optical, optoelectronic, and mechanical properties, and so on. Information on this section can be found in Chapters 16–18.

With the research on MXenes going more intensive, more MXene members with exotic properties are reported, allowing new potential applications such as biomedicine, photothermal therapy of cancer, theranostics, biosensors, dialysis, and neural electrodes [12]. Nevertheless, electrochemical energy storage is still the major application for MXenes, while $Ti_3C_2T_x$ is the most extensively investigated MXene member. This gives the MXene beginners an illusion that MXene has become synonymous with $Ti_3C_2T_x$. Eventually, in many research papers, they directly mention their samples as MXene without specifying the composition, which creates confusion considering the versatile MXene members with rich atomic compositions and unlimited solid solutions. As such, it is important to explore other MXene members beyond $Ti_3C_2T_x$, and their unique properties that enable a variety of different promising applications.

Besides investigating the large, underexplored MXene family, revisiting the synthesis route should allow the preparation of high-quality MXenes. As previously discussed, the gaseous synthesis route is known for its high efficiency in the production of few-layered MXene powders with high crystallinity. Another big advantage of gaseous synthesis route is its yield, 0.5 kg of few-layered per batch, which is almost impossible for the conventional etching routes (HF or LiF-HCl, or HF-HCl) [13]. We note that the massive production of few-layered MXene powders is of significance before the practical applications, which demand quite a lot of MXene solids.

Another big concern for the MXene field is the chemical stability. As we know, the $Ti_3C_2T_x$ MXene colloidal solution only survives for five days, and turns anatase TiO_2 afterward [14]. Developing antioxidation strategies without compromising the intrinsic properties of MXenes is of essential importance for the MXene community. Despite freezing, the dispersion may slow down the oxidation

process [15]; however, this energy-consuming method is not practical. Adding polyanions or surfactants may necessarily protect the edges from being oxidized [16]; however, these species may alter the electronic and mechanical properties. In other words, a unique method to prolong the shelf life of MXene solids and dispersions in the absence of organic species or polyanions should be developed. An encouraging result is that through innovating the stoichiometry of MXene precursor (excessive Al in the MAX phase), high-quality MXene flakes can be obtained, which can survive even after a couple of months without apparent signs of degradation. This important result suggests that understanding the fundamentals in the MAX phase selection and optimization of the synthesis reaction should give stable, high-quality MXene flakes and colloidal dispersions.

Considering the rich MXene members and their unique, unconventional combination of properties through simply tuning the M and X elements, atomic ratio, and alignment, more new MXenes and applications may be enabled. There are enough reasons to believe that MXenes are at the frontier of 2D materials family, best evidenced by the MXene rush in the academic field. Nevertheless, MXenes are still in the early days and many exciting discoveries are still to come.

References

1 Gogotsi, Y. and Anasori, B. (2019). The Rise of MXenes. *ACS Nano* 13: 8491–8494.

2 Anasori, B., Lukatskaya, M.R., and Gogotsi, Y. (2017). 2D metal carbides and nitrides (MXenes) for energy storage. *Nature Reviews Materials* 2: 16098.

3 Zhang, C.J., Ma, Y., Zhang, X. et al. (2020). Two-Dimensional Transition Metal Carbides and Nitrides (MXenes): Synthesis, Properties, and Electrochemical Energy Storage Applications. *Energy & Environmental Materials* 3: 29–55.

4 (a) Sang, X., Xie, Y., Lin, M.W. et al. (2016). Atomic defects in monolayer titanium carbide (Ti3C2Tx) MXene. *ACS Nano* 10: 9193–9200. (b) Xie, Y. and Kent, P.R.C. (2013). Hybrid density functional study of structural and electronic properties of functionalized $Ti_{n+1}X_n$ (X = C, N) monolayers. *Physical Review B* 87: 235441. (c) Anasori, B., Xie, Y., Beidaghi, M. et al. (2015). Double Transition Metals Carbides (MXenes). *ACS Nano* 9: 9507–9516.

5 Alhabeb, M., Maleski, K., Anasori, B. et al. (2017). Guidelines for Synthesis and Processing of Two-Dimensional Titanium Carbide (Ti3C2Tx MXene). *Chemistry of Materials* 29: 7633–7644.

6 Maleski, K., Mochalin, V.N., and Gogotsi, Y. (2017). Dispersions of Two-Dimensional Titanium Carbide MXene in Organic Solvents. *Chemistry of Materials* 29: 1632–1640.

7 (a) Zhang, C.J., Kremer, M.P., Seral-Ascaso, A. et al. (2018). Stamping of Flexible, Coplanar Micro-Supercapacitors Using MXene Inks. *Advanced Functional Materials*

28: 1705506. (b) Zhang, C.J., McKeon, L., Kremer, M.P. et al. (2019). Additive-free MXene inks and direct printing of micro-supercapacitors. *Nature Communications* 10: 1795. (c) Zhang, Y.Z., Wang, Y., Jiang, Q. et al. (2020). MXene Printing and Patterned Coating for Device Applications. *Advanced Materials* 32: 1908486. (d) Abdolhosseinzadeh, S., Jiang, X.T., Zhang, H. et al. (2021). Perspectives on solution processing of two-dimensional MXenes. *Materials Today* 48: 214–240.

8 (a) Guo, T., Zhou, D., Deng, S. et al. (2023). Rational Design of $Ti_3C_2T_x$ MXene Inks for Conductive, Transparent Films. *ACS Nano*. (b) Guo, T., Zhou, D., Gao, M. et al. (2023). Large-Area Smooth Conductive Films Enabled by Scalable Slot-Die Coating of $Ti_3C_2T_x$ MXene Aqueous Inks. *Advanced Functional Materials* 2213183. (c) Hantanasirisakul, K. and Gogotsi, Y. (2018). Electronic and Optical Properties of 2D Transition Metal Carbides and Nitrides (MXenes). *Advanced Materials* 30.

9 (a) Li, M., Lu, J., Luo, K. et al. (2019). Element Replacement Approach by Reaction with Lewis Acidic Molten Salts to Synthesize Nanolaminated MAX Phases and MXenes. *Journal of the American Chemical Society* 141: 4730–4737. (b) Li, Y., Shao, H., Lin, Z. et al. (2020). A general Lewis acidic etching route for preparing MXenes with enhanced electrochemical performance in non-aqueous electrolyte. *Nature Materials* 19: 894–899. (c) Ding, H., Li, Y., Li, M. et al. (2023). Chemical scissor–mediated structural editing of layered transition metal carbides. *Science* 379: 1130–1135.

10 Kamysbayev, V., Filatov, A.S., Hu, H. et al. (2020). Covalent surface modifications and superconductivity of two-dimensional metal carbide MXenes. *Science* eaba8311.

11 Wang, D., Zhou, C., Filatov, A.S. et al. (2023). Direct synthesis and chemical vapor deposition of 2D carbide and nitride MXenes. *Science* 379: 1242–1247.

12 Cheng, L., Wang, X., Gong, F. et al. (2020). 2D Nanomaterials for Cancer Theranostic Applications. *Advanced Materials* 32: 1902333.

13 (a) Lipton, J., Röhr, J.A., Dang, V. et al. (2020). Highly Conductive, and Micropatternable MXene Films for Enhanced Electromagnetic Interference Shielding. *Matter* 3: 546–557. (b) Shuck, C.E., Sarycheva, A., Anayee, M. et al. (2020). Scalable Synthesis of $Ti_3C_2T_x$ MXene. *Advanced Engineering Materials* 22: 1901241.

14 Zhang, C.J., Pinilla, S., McEvoy, N. et al. (2017). Oxidation Stability of Colloidal Two-Dimensional Titanium Carbides (MXenes). *Chemistry of Materials* 29: 4848–4856.

15 Zhang, J., Kong, N., Hegh, D. et al. (2020). Freezing Titanium Carbide Aqueous Dispersions for Ultra-long-term Storage. *ACS Applied Materials & Interfaces* 12: 34032–34040.

16 Natu, V., Hart, J.L., Sokol, M. et al. (2019). Edge Capping of 2D-MXene Sheets with Polyanionic Salts To Mitigate Oxidation in Aqueous Colloidal Suspensions. *Angewandte Chemie International Edition* 58: 12655–12660.

Index

a

Ab initio 6, 388, 397, 401, 405, 412–418, 517, 520
Acid 5, 27, 28, 34, 35, 46, 50, 51, 58, 61, 64, 67, 78, 86, 89–92, 94, 96, 98, 101, 110, 116, 120, 121, 125, 147, 148, 163, 176, 177, 182–184, 192, 221, 224, 229, 246, 249–252, 256, 273, 275, 283, 305, 319, 324, 328, 347, 350, 357, 359, 364, 366, 387, 447, 455, 456, 459, 465, 500–503, 520, 521, 610, 612, 614, 637, 644, 660, 666, 669, 682, 685, 695, 710, 713, 721, 723
Adatom 403, 409, 516, 517, 520
Adsorbent 655–656, 659, 679–681, 695, 697
Aerogel 164, 317, 321, 345–369, 471, 577, 582, 583, 608, 610, 616, 617, 686
Aluminum 39, 41, 63, 65, 70, 73, 85, 97, 143, 144, 176, 180, 184, 185, 217, 223, 304, 305, 387, 454, 500, 541, 542, 571–572, 624, 640, 666
Antimicrobial treatments 691
Atomic defects 95, 174, 176, 655
Atomic structure 44, 92, 413, 420, 626, 737
Aspect ratio 318, 328, 468, 637

b

Bacterial 343, 569, 609, 691, 692, 710–713, 721
Batteries 5, 6, 34, 85, 118, 120, 123, 124, 201, 285, 294, 305, 309, 310, 331, 338, 356, 361, 367, 387, 388, 401–405, 494, 506, 514–536, 541–590, 621, 723
Basal plane 110, 174, 331, 413, 654, 660
Biocompatibility 632, 679, 706–714, 717, 720, 723
Biomaterials 343, 657, 713
Biomedicine 201, 706, 739
Biosensors 632–636, 651, 693, 713–719, 739
Boron 341, 345, 391, 394, 395, 404, 458, 737
Bottom-up 245, 294, 442

Transition Metal Carbides and Nitrides (MXenes) Handbook: Synthesis, Processing, Properties and Applications, First Edition. Edited by Chuanfang Zhang and Michael Naguib.
© 2024 John Wiley & Sons, Inc. Published 2024 by John Wiley & Sons, Inc.

Bulk processing 28, 459, 470, 491
Bulk synthesis 20
Borides 390, 391, 395, 396

c

Cancer theranostics 433, 739
Capacitors 116, 356, 361, 487, 495
Catalysis 71, 153, 202, 230, 317, 347, 397, 400, 581, 621, 693, 717
Ceramics 13, 85, 189, 190, 215, 221, 294, 678
Charge 77, 86, 112, 120, 130, 138, 167, 173, 194, 196, 204, 238, 305, 308, 310, 315, 317, 333, 338, 347, 389, 396, 397, 401, 403–406, 408, 412, 416, 417, 419, 431, 443, 487, 489–491, 493, 494, 496, 508–510, 514, 516, 518, 520, 523–525, 542, 556, 559, 560, 564, 565, 569, 571, 572, 576, 581, 582, 585, 586, 590, 612, 614, 617, 638, 655, 658, 664, 667, 679, 682, 686, 688, 690, 715, 718, 738
Charging-discharging process 419
Chemical order 14, 15, 18, 193
Chemical reaction 25, 94, 529, 587, 613, 715, 717
Chemical transformations 147, 262
Chemical vapor deposition 78, 245, 447, 616, 738
Chlorine 49, 59, 73, 98, 528, 663
Chromium 400, 460
Coatings 6, 123, 174, 183–185, 221, 224, 272–289, 301, 316–318, 321–323, 325, 328, 329, 341, 350, 354, 356, 366, 367, 369, 442, 453, 459, 460, 464, 466–468, 506, 507, 567, 580–582, 609, 622, 624, 628, 629, 654, 666, 671, 679, 683, 685, 708, 716, 738
Composite electrode 308, 339, 492
Conductive 86, 163, 184, 221, 284, 285, 307, 308, 310, 317, 323–325, 331, 335, 337, 338, 341, 343, 352, 361, 364, 366, 368, 369, 404, 443, 445, 459, 460, 465, 514, 515, 526, 528, 530, 531, 533, 557, 560, 564, 566, 576, 577, 581–583, 602, 609–612, 614, 616–618, 622, 624, 632, 637, 641, 643, 644, 652, 654, 671, 678, 679, 685, 713, 715, 716, 723, 724, 739
Copper 223, 305, 640, 641, 717
Cross-section 25, 60, 68, 80, 156, 217, 221, 222, 235, 241, 320, 326, 329, 334, 336, 339, 341, 464, 465, 467, 476, 498, 522, 534, 558, 588, 608, 612, 684
Crystals 18, 35, 79, 80, 86, 95, 155, 157, 164, 165, 170, 174, 176, 191, 215, 217, 221, 239, 246, 252, 301, 315–370, 387, 395, 396, 413, 415, 459, 462, 464, 468, 488, 489, 526, 616, 637, 656, 670, 724
Cycling performance 138, 525, 533, 558, 569–571, 574, 577, 581, 584–586

d

Dangling 359, 625
Defect structure 144, 157, 164, 175, 185, 458, 459, 617
Degradation 6, 95, 137–158, 164–183, 185, 186, 202, 221, 224, 489, 582, 629, 667, 678, 679, 686–691, 696, 739, 740

Delamination 5, 6, 50, 64, 65, 76, 77, 113, 114, 118, 122, 129, 144, 153, 196, 205, 221, 245–267, 273, 279, 283, 285, 299, 311, 444, 455, 456, 496, 503, 520, 558, 644, 659–661, 681, 707, 712, 720, 738
Density functional theory (DFT) 63, 246, 388, 489, 516, 541, 658
Detection 153, 350, 433, 434, 440, 634, 635, 657, 664, 679, 692–694, 698, 713–719, 723
Dielectric 71, 73, 267, 438, 604, 605, 618, 622, 624–626, 628, 629
Dissolved oxygen 145, 177, 182, 260, 276, 688
Diffraction 217, 442, 487
Double transition metal 3, 44, 199

e

Elastic constant 298, 299, 319, 323, 345, 357, 364, 409, 418, 456, 457, 530, 633
Electric double layer 262, 333, 356, 489
Electrical conductivity 7, 34, 71, 144, 153, 164, 176, 180, 181, 184, 185, 193, 194, 196, 199, 200, 230, 252, 294, 305, 315, 316, 318, 319, 321, 322, 324, 327–329, 331, 333, 338, 341, 349, 356, 357, 359, 361, 364, 398, 400, 404, 440, 442–444, 454, 460, 463, 464, 466, 468, 471, 472, 477, 524, 535, 554, 560, 584, 590, 604, 607, 611, 614, 616, 628, 631, 640, 641, 644, 653–656, 658, 660, 669, 707, 715, 724
Electrical properties 195, 197, 324, 453, 477, 632
Electrocatalyst 203
Electrocatalysis 201, 388
Electrochemical 6, 58–67, 70, 87, 90, 98–100, 102, 110, 120, 125, 139, 164, 197, 199, 201–204, 223, 229, 230, 240, 251, 259, 301, 304–310, 316, 317, 323, 331, 333, 338, 343, 345, 347, 361, 369, 388, 394, 397, 398, 413, 417, 418, 420, 421, 464, 487–492, 494, 496–510, 514, 517, 518, 525, 526, 529, 530, 533, 535, 536, 541, 544, 556–560, 564–569, 571, 572, 577, 581, 582, 584, 587, 634, 639, 656, 657, 664, 667, 693, 698, 714, 716–719, 725, 737–739
Electrochemistry 59, 70, 194, 197, 361, 447, 583, 635
Electrodes 61, 63, 116, 123, 175, 183–185, 288, 305, 307–309, 311, 326, 331, 333, 335, 338, 340, 342, 343, 359, 406, 408, 419, 434, 442, 445, 460, 468, 487–502, 504–506, 508, 510, 514, 516–518, 524, 525, 535, 556, 559, 560, 570–572, 584, 590, 622, 624, 625, 628–635, 643, 644, 664–667, 685, 693, 715, 716, 723, 739
Electronics 51, 281, 285, 294, 340, 364, 370, 504, 602, 605, 621–645

Electromagnetic interference shielding 7, 163, 194, 454, 477, 478, 602–618, 621, 737
Electron microscopy 455
Energy density 203, 307, 308, 310, 321, 331, 337, 350, 361, 362, 419, 491, 492, 494, 504, 508, 510, 514, 515, 565, 568, 571, 572, 575, 576, 581, 584, 587
Energy storage 6, 51, 109, 116, 120, 130, 138, 153, 163, 164, 175, 201–203, 230, 289, 294, 305, 311, 315–318, 324, 331, 333, 347, 364, 368, 369, 388, 389, 397, 400–413, 415, 418–420, 445, 487, 492, 504, 508, 514, 515, 519, 525, 528, 529, 536, 541–543, 556, 563, 572, 575, 584, 587, 590, 723, 737–739
Environment 35, 37, 51, 58, 74, 87, 102, 118, 137, 138, 141, 144–149, 153, 157, 158, 170, 172, 173, 177, 178, 182, 185, 199, 224, 232, 262, 347, 348, 352, 412, 413, 417, 471, 525, 529, 571, 616, 625, 629, 631, 632, 635, 651, 654, 656–658, 664, 666, 668, 678, 680, 682, 686, 718, 721, 723
Environmental stability 172, 177, 179, 181, 184, 185, 609, 664, 675
Etching 5, 13, 15, 18, 20, 25, 26, 35–37, 39–46, 49–52, 58–81, 85–103, 115–122, 125, 129, 130, 138, 143, 144, 163, 176, 177, 184, 185, 194, 196, 200, 202, 203, 214–216, 221–223, 229–234, 236, 240, 242, 245–253, 255–257, 259, 260, 263, 264, 267, 273, 275, 276, 311, 316, 328, 332, 387, 396, 420, 435, 447, 454–456, 459, 460, 496, 499, 500, 502, 503, 506, 519–521, 524, 565, 583, 607, 628, 629, 644, 655, 659–661, 681, 737–739
Exfoliation 35, 37–39, 41, 42, 44, 52, 65, 75, 92, 95, 176, 180, 221, 245, 254, 255, 259, 279, 387, 394, 456, 459, 496, 607, 626

f

Ferromagnetism 200, 230
Fiber 64, 164, 296, 301, 303, 304, 315–370, 440, 441, 453, 454, 463–466, 469, 472, 477, 505, 581, 697
Figure of merit 310, 442
Filaments 307
Flexographic printing 284
Fluoride 5, 35, 46, 50, 51, 58, 61, 63, 65, 67, 70, 78, 81, 87, 96, 97, 110, 175–177, 217, 229, 246, 249–253, 273, 275, 323, 434, 454, 500, 502, 519, 653, 715
Fluorine termination 429
Foam 334, 335, 352, 357, 359, 360, 469, 522, 605, 608

g

Gallium 79
Gas sensors 21, 196, 388, 651, 653, 656, 657, 660, 661, 663, 666, 667, 693
Grafted 183, 276, 316, 352, 359, 663, 680

Graphene 35, 79, 80, 85, 176, 182, 245, 289, 304, 310, 315, 316, 325, 335, 345, 349, 350, 357, 387, 398–400, 413, 418, 419, 440, 442, 444, 457–459, 461, 462, 469, 471, 477, 504, 508, 524, 526, 577, 579, 581, 587, 603, 605, 614, 616, 624, 625, 631, 641–643, 652, 653, 658, 669, 671, 680, 688, 692, 708, 711, 714, 720, 737
Graphite 20, 21, 23, 28, 34, 141, 143, 176, 179, 180, 245, 405, 514, 533
Graphitic 164
Gradient 23, 351, 357, 391, 464, 605, 616, 685
Gravure printing (GP) 279
Grinding 25, 119

h

Heavy metals 678–680
Heterostructures 79, 81, 399, 400, 410, 411, 413, 416, 418, 419, 435, 535, 560, 561, 566, 567, 581, 587, 588, 690
Heterogeneous 174, 282, 587, 617, 669, 671
Homogenous 21, 28, 304, 305, 530, 533, 612, 655
Hybrid 155, 164–166, 185, 304, 305, 307, 310, 311, 336, 337, 341–343, 350, 356–362, 391, 394, 397, 434, 469, 471, 505, 525, 530, 533, 534, 542, 560, 562, 564, 566–568, 570, 582, 583, 614, 632, 634, 641, 685, 690
Hydrogen evolution reaction (HER) 203, 230, 388, 489
Hydrogen gas 184, 519
Hydrochloric acid (HCl) 28, 35, 61, 67, 96, 110, 224, 229, 249
Hydrofluoric acid (HF) 5, 34, 50, 58, 110, 221, 246, 387, 644

i

Impedance 602, 604, 715
In-plane ordered 44, 45, 190, 199, 202–203, 390
Intercalation 5, 6, 49, 63–66, 76–78, 100–102, 109–130, 144, 153, 172, 181, 189, 193, 221, 240, 246–248, 250, 253–267, 273, 321, 350, 364, 402, 404, 405, 413, 415–420, 443–445, 468, 487, 489–496, 500, 501, 514, 515, 517, 520–521, 529, 535, 557, 566, 569, 571–573, 621, 635, 644, 657, 660, 664, 679, 681, 695, 711, 712, 738
Internal reflection 435
Iodine 73, 144, 502, 503

l

Large-scale production 85, 182, 322, 370, 508, 575, 614
Laser scribing 285, 506
Layer-by-layer (LbL) assembly 467, 468, 673, 683
Layered ceramics 190
Lithium chloride (LiCl) 65, 85, 93, 95, 98, 99, 116, 117, 256, 262, 490–492, 660
Lithium fluoride (LiF) 46, 110, 176, 249

Lithium-ion batteries (LIBs) 85, 230, 361, 404, 514–536, 541, 544
Lithium polysulfides 361, 576
Lithium–sulfur 542, 572, 575–584

m

Magnesium-ion batteries 541, 568–571
Magnetic properties 95, 121, 201, 230, 604
MAX phases 5, 13–28, 34–37, 39–44, 49, 52, 59–61, 63–68, 70, 73, 74, 86, 87, 89–92, 94–96, 98–103, 110, 118, 137, 141–144, 157, 163, 176, 179, 180, 184, 185, 190–193, 197, 199–202, 214, 215, 221–223, 229–231, 233, 234, 242, 245, 246, 248, 250, 251, 253, 258, 260, 264, 267, 273, 275, 276, 328, 387, 390, 391, 394–396, 398–400, 442, 454–456, 459, 496, 502, 503, 521, 557, 607, 612, 644, 659, 660, 711, 738, 740
Mechanical properties 6, 279, 285, 288, 308, 317–319, 333, 335, 341, 352, 367, 369, 442, 453–478, 508, 609, 612, 616, 633, 715, 739, 740
Membranes 143, 294, 329, 432–434, 456–458, 460–462, 578, 581, 666, 678, 679, 682–687, 691, 695–698, 707, 709–712, 718, 721
Metastable 185, 395
Microwave absorption 368
Modeling 205, 217, 221, 388, 405, 417, 713
Mo_2TiC_2 18, 398
$Mo_2Ti_2C_3$ 18, 319
$Mo_{4/3}CT_x$ 202–204
Molybdenum carbide 709
Molecular dynamics (MD) 155, 182, 219, 220, 388, 389, 412–420, 458, 475, 491, 493
Molten salt 5, 21, 23–25, 58, 64, 85–103, 118, 138, 140, 184, 191, 229, 230, 232–234, 236, 237, 240, 242, 253, 315, 496, 502–504, 629, 644, 662, 738
Monolayer 79, 123, 126, 128, 147, 224, 245, 250, 256, 263, 390, 392, 394–396, 398, 402, 409, 443, 444, 447, 453, 456–462, 491, 516, 517, 519–521, 523, 556, 607, 659
Multilayer MXenes 221, 223, 255, 256, 263–265, 273, 299, 557, 660, 661, 738

n

Nanolayer 96, 97, 612
Nanomaterials 294–298, 301, 304, 311, 318, 335–338, 370, 398, 420, 429, 453, 468, 469, 478, 564, 616, 618, 641, 652–657, 667, 671, 691, 695, 706, 710–713, 717, 719, 722, 725
Nanoparticles 155, 164, 166, 184, 224, 305, 308, 361, 445, 447, 526, 528, 530, 533, 535, 560, 561, 564, 588, 634, 641, 652, 691, 708, 710
Nanopore 413, 418, 419
Nanosheets 65, 74, 149, 151, 153, 164, 166, 167, 172, 173, 176, 180–182, 250, 255–257, 265, 266, 273–277, 279, 284, 285, 288, 304, 308, 310, 327, 328, 331–333, 335, 337, 338, 340, 343, 345, 347–349, 351, 352, 355–357, 361–365, 367,

Nanosheets (*cont'd*)
369, 370, 402, 409, 432, 441, 477, 497, 516, 519, 520, 522, 523, 528–530, 533, 557–560, 566, 567, 577, 580, 581, 583, 590, 610–612, 614, 632, 679, 680, 691, 695, 697, 710, 713, 720, 737
Nanostructure 85, 155, 431, 577, 582, 584, 652, 678
Nb_2C 92, 101, 103, 167, 168, 174, 403, 516, 517, 718, 720–722
Nb_4C_3 528
Neutral 50, 112, 120, 347, 352, 365, 487, 489, 491, 504, 569, 655, 660, 664, 682
Neutron 112, 125, 126, 214, 217, 219, 220, 226, 403, 415, 418, 419
Niobium carbide 709
Nitrogen 3, 13, 25, 35, 75, 87, 97, 98, 163, 221–223, 245, 251, 253, 266, 267, 294, 304, 307, 349, 351, 388, 391, 454, 461, 462, 501, 502, 524, 583, 584, 644, 657, 666, 693, 737
Non-MAX 43, 144, 738

o

Optical properties 195, 196, 200, 429–431, 438–440, 443, 447, 612, 714, 737
Orbitals 37, 236, 403
Ordered double transition metal 199
Ordered MXenes 15, 18, 44, 45, 190, 199–203, 205, 288, 515
Ordered vacancies 27, 202, 515
Orientation 24, 157, 191, 200, 214, 216, 217, 297, 328, 339, 348, 351, 367, 369, 418, 453, 454, 463, 464, 468, 477, 715, 724
Out-of-plane-ordered (o-MAX) 13, 18, 44, 190, 199–203, 214
Oxidation 13, 20, 21, 34, 39, 43, 64, 66, 67, 70, 77, 78, 86, 95, 100–102, 121, 129, 141, 144, 145, 147–151, 153, 155–157, 164–168, 170–186, 193, 196, 202, 222, 224, 225, 236–238, 240, 247, 251, 253, 259, 276, 277, 289, 297, 331, 343, 348, 359, 364, 445, 489, 491, 492, 496, 497, 502, 504, 517, 520, 524–526, 528, 535, 564, 590, 609, 656, 666, 667, 680, 688, 690, 695, 697, 698, 715, 724, 739
Oxygen 71, 96, 97, 121, 141, 143–147, 152, 164, 168, 170, 172, 174, 177, 178, 181, 182, 184, 223, 247, 251, 257, 260, 262, 276, 277, 288, 289, 308, 323, 349, 359, 361, 364, 388, 398, 408, 416, 419, 429, 454, 502, 508, 526, 608, 612, 656, 658, 662, 688, 690, 695, 707
Oxygen termination 398, 695
Organic ligands 663, 670
Organic solvents 71, 97, 118, 119, 147, 179–181, 183, 259, 276, 301, 302, 520, 557, 559, 643, 655, 695

p

Paper 4, 25, 145, 222, 223, 305, 308–310, 316, 338, 397, 506–508, 569, 610, 631, 634, 683, 739
Percolation 296, 297, 652, 668–670
Photodegradation 689, 690

Photothermal 163, 431, 433, 435, 497, 706, 710, 713, 719–722, 739
Physical vapor deposition (PVD) 21, 25
Plasmonic 429, 431–435, 446, 447, 718, 719
Polymer 110, 123, 179, 183, 184, 218, 294, 297, 301, 306–308, 317, 318, 323–325, 338, 341–343, 363–369, 388, 443, 459, 463, 465, 466, 468–470, 501, 504, 559, 581, 582, 602–618, 629, 631, 632, 640, 641, 652–654, 668–671, 675, 678, 682, 710, 719, 725
Precursor 5, 13–28, 35–46, 59, 79, 86, 87, 89, 92, 102, 103, 141, 144, 167, 176, 179, 180, 185, 190, 192, 199, 200, 246, 249, 260, 267, 324, 347, 351, 354, 365, 370, 455, 456, 459, 466, 502, 521, 524, 526, 529, 608, 616, 637, 686, 690, 711, 738, 740
Prediction 196, 236, 387, 391–397, 401, 404, 412, 417, 491, 697, 739
Processing 4–6, 11–28, 92, 121, 147, 181, 215, 239–242, 258, 260, 272–289, 294–297, 299, 301, 317, 325, 328, 345, 347, 366, 369, 370, 438, 440, 470, 506, 508, 519, 520, 616, 621, 628, 637, 640, 643, 644, 654, 664–666, 714, 719, 720, 722, 723, 738
Pseudocapacitance 310, 405, 408, 491

r

Radiation 78, 641, 642, 680, 686, 719–722
Reactive force field (ReaxFF) 417
Reduced graphene oxide (rGO) 335, 442, 504, 526, 658, 680
Reflection loss 367, 368, 604
Resonance 49, 71, 73, 110, 138, 175, 196, 200, 224, 429, 431, 433, 435, 447, 461, 462, 689, 718, 720, 722
Rheology 279, 285, 297–300
Rheological properties 6, 272, 277–279, 281, 284–286, 289, 295–301, 303–305, 307, 311, 316, 318, 319, 324, 328, 356
Ribbon 74, 348

s

Scanning transmission electron microscopy (STEM) 174, 191
Seebeck coefficients 201, 230, 400
Segregation 79
Selective etching 13, 18, 25, 35–37, 40, 42, 43, 64, 78, 86, 94, 176, 214, 221, 246, 328
Semiconductor 189, 194, 200, 429, 519, 622, 624, 625, 627–629, 643, 652, 653, 656, 688, 690, 698
Sensitivity 322, 324, 350, 364, 433, 632, 634, 635, 652, 654, 656–659, 666, 668, 669, 671, 693, 698, 711, 713, 715, 716, 718, 719
Sensors 21, 130, 185, 196, 289, 294, 317, 318, 322–324, 350, 369, 388, 443, 462, 629, 632–634, 651–675, 679, 692–694, 698, 713–719, 723
Separation 73, 109, 199, 240, 245, 294, 370, 415, 678, 679, 682–683, 685, 686, 688–691, 698

Sheets 24, 49, 62, 77, 112, 120, 121, 129, 143, 144, 155, 172, 178, 221, 222, 224, 231, 236, 237, 240, 258, 259, 282, 296, 297, 301, 304, 305, 307, 308, 316–321, 323–325, 333, 341, 345, 347, 350, 354, 356–359, 363, 370, 415, 454, 458, 459, 489, 491, 492, 494, 496, 497, 503, 523, 526, 529, 566, 577, 608, 610, 659–662, 669–671, 691, 707, 709, 717, 718, 722
Shielding 7, 144, 163, 194, 262, 288, 294, 305, 316, 317, 323, 325, 328, 335, 341, 343, 359, 364, 435, 438, 454, 468, 471, 472, 477, 478, 602–618, 621, 737
Simulation 6, 155, 157, 182, 203, 205, 219, 230, 231, 262, 387–421, 458, 475, 489, 491, 493, 496, 632, 739
Single crystalline 245
Single flake 156, 157, 171, 175, 200, 217, 259, 444, 455, 462, 654
Single-layer 3, 170, 180, 181, 225, 245, 251, 258, 260, 265, 267, 278, 279, 288, 299, 300, 403, 409, 709, 737, 738
Sodium-ion batteries 361, 494, 541–564
Solid solution 3, 13–15, 18, 44, 189, 190, 193–199, 203, 205, 398, 400, 433, 515, 737, 739
Solid-state 21, 138, 164, 301, 305, 356, 468, 506, 508, 509, 542, 635, 640, 666
Solution-processed 184, 442, 622, 624, 641
Spray 285, 287, 288, 316, 317, 321, 341, 345–347, 433, 442, 468, 506, 507, 580, 584, 622, 624, 628, 629, 679, 738
Strain 201, 202, 298, 322–324, 350, 357, 364, 396, 400, 476, 494, 565, 610, 611, 628, 632, 634, 651, 652, 668, 671, 673, 674, 711, 715
Sub-stoichiometric 28
Sulfur 59, 67, 123, 184, 338, 349, 521, 522, 524, 529, 535, 542, 559, 572–587, 693
Supercapacitor 6, 71, 123, 138, 164, 204, 285, 294, 301, 305, 311, 316, 319, 321, 323–326, 331, 333, 337, 338, 348, 350, 356, 359, 362, 363, 365, 388, 401, 405–408, 468, 487–510, 621
Supercritical 321
Superconductivity 400, 401, 421, 737
Surface chemistry 97, 137–141, 144, 153, 163, 189, 194, 203, 246, 252, 255, 266, 303, 305, 317, 335, 500–502, 504, 587, 657, 663, 668, 692, 706, 714, 737
Surface termination 3, 6, 15, 58, 79, 89, 92, 97–103, 112, 116, 138, 153, 154, 172, 184, 191, 200, 203, 220, 229–242, 246–253, 255, 279, 317, 388, 398, 420, 429, 431, 445, 447, 454, 496, 500–502, 517, 518, 520, 607, 627, 644, 693, 698, 717

t

Tactile sensor 668–675
Ta_2C_x 92, 433
Ta_4C_3 15

Tantalum carbide 709
Termination 3, 6, 15, 58, 61, 64, 78, 79, 81, 87, 89, 92, 95, 97–103, 112, 113, 116, 118, 120, 125, 138, 145, 153, 154, 172, 175, 177, 178, 184, 191, 200, 203, 220, 223, 229–242, 245–253, 257, 279, 317, 348, 387–389, 392, 395, 398, 400, 401, 404, 413, 419, 420, 429, 431, 435, 445, 447, 454, 496, 500–502, 516–520, 607, 627, 644, 693, 695, 698, 717, 718, 720, 737, 738
Textiles 303, 316–318, 323, 325, 369, 460, 466, 629, 632
Thermoelectric 201
Thin-films 6, 18, 23, 25, 43, 153, 163, 225, 239, 434, 438, 439, 442–444, 446, 496, 622, 637, 652, 666, 723
Ti_2C 15, 61, 92, 103, 157, 167, 168, 237, 262, 319, 403, 526, 527
$Ti_2C_{0.5}N_{0.5}T_x$ 41, 222, 224, 225
Ti_3CN 167, 168, 394
Ti_4N_3 96
Titanium carbide 20, 145, 179, 215, 505, 706
Titanium nitride 710
Top-down 35, 144, 245, 442, 447, 519
Topological insulator 429
Transparent 184, 224, 278, 284, 285, 317, 369, 442–445, 622, 624, 625, 631, 632, 643, 644, 723, 724, 739
Transport 288, 307, 308, 321, 326, 331, 333, 335, 336, 338, 339, 343–345, 367, 388, 389, 398, 401, 412, 418, 421, 444–446, 491, 497, 498, 500, 516, 530, 533, 535, 554, 559, 560, 566, 569, 577, 581–583, 607, 609, 614, 622, 637, 645, 653, 685, 694
Transportation 58, 501, 529, 625, 628, 635, 637, 640, 651, 683
Tungsten carbide (WC) 79
Tuning 35, 41, 153, 181, 224, 240, 277–279, 299, 351, 443, 444, 447, 500–502, 510, 667, 737, 740
Two-dimensional (2D) 3, 13, 85, 245, 294, 315, 316, 387, 453, 554, 621, 652, 706, 737

V

Vacancy 15, 95, 138, 140, 184, 202, 251, 410–412, 520
Vanadium carbides (V_2C) 612, 709
Volumetric 197, 202, 203, 307, 319, 321, 324, 325, 331, 336, 340, 419, 494, 502, 506, 508, 568

W

Washing 49, 50, 74, 87, 90, 98, 115–119, 129, 145, 192, 216, 217, 247, 276, 352
Wastewater 679, 682, 683, 686
Wearable 305, 316–318, 322, 325, 350, 364, 369, 466, 504, 618, 621, 625, 629–634, 640, 643, 653, 656, 664, 714, 723
Weight 26, 197, 296, 349, 352, 353, 408, 468, 494, 497, 516, 517, 581, 641, 652, 669
Work function 230, 398, 444, 445, 621, 622, 624–629, 631, 632, 643, 644, 739

x

X-ray 41, 46, 49, 59, 68, 88, 93, 110, 112, 138, 174, 192, 214, 217, 219, 220, 226, 232, 337, 403, 418, 464, 475, 488, 489, 661, 693, 722

y

Yield stress 298, 301, 302

z

Zinc-ion batteries 356

Zr_3C_2 18, 28, 404

WILEY END USER LICENSE AGREEMENT

Go to www.wiley.com/go/eula to access Wiley's ebook EULA.